12-2001

Three Dimensional Hydrodynamic Modeling Study, Craney Island eastward expansion, lower James River and Elizabeth River, Virginia

Harry V. Wang
Virginia Institute of Marine Science

S. C. Kim
Virginia Institute of Marine Science

John D. Boon
Virginia Institute of Marine Science

A. Y. Kuo
Virginia Institute of Marine Science

G. M. Sisson
Virginia Institute of Marine Science

See next page for additional authors

Authors
Harry V. Wang, S. C. Kim, John D. Boon, A. Y. Kuo, G. M. Sisson, J. M. Brubaker, and J. P-Y. Maa

Three Dimensional Hydrodynamic Modeling Study
Craney Island Eastward Expansion,
Lower James River and Elizabeth River, Virginia

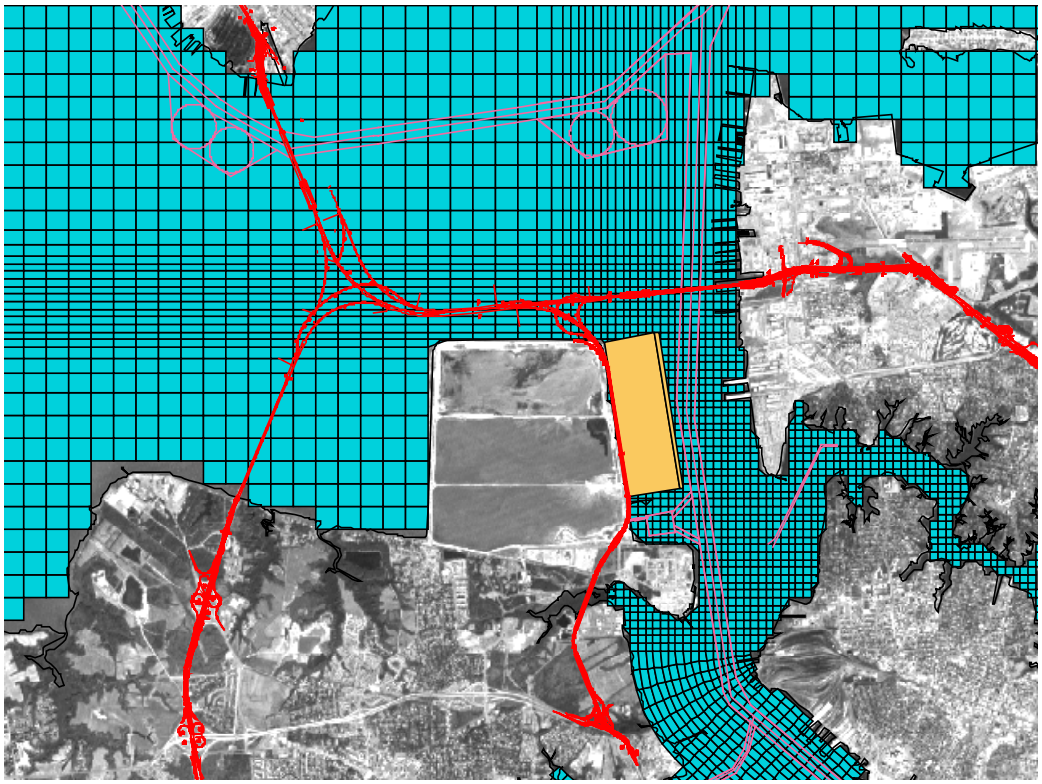

Harry V. Wang, S.C. Kim, John D. Boon, A.Y. Kuo, G.M. Sisson,
J.M. Brubaker and J.P-Y. Maa

Final Report to the
U.S. Army Corps of Engineers, Norfolk District
and the
Virginia Port Authority

Special Report No. 372
In Applied Marine Science and Ocean Engineering

Virginia Institute of Marine Science
Department of Physical Sciences
Gloucester Point, Virginia 23062

December 2001

Three Dimensional Hydrodynamic Modeling Study
Craney Island Eastward Expansion
Lower James River and Elizabeth River, Virginia

REPORT LINKS

Appendices:

WILLIAM & MARY
VIMS
VIRGINIA INSTITUTE OF MARINE SCIENCE
SCHOOL OF MARINE SCIENCE

EXECUTIVE SUMMARY

Hydrodynamic Model Study Results, Craney Island Eastward Expansion

1. The CIEE Hydrodynamic Model Study was conducted in three phases: 1) model calibration and verification for the Elizabeth River, 2) model testing of four Craney Island expansion options using *single variable runs* (using a single variable, tidal range, for model input), 3) model testing of two expansion options using *historical runs* (using multiple variables in real time for model input). The expansion option designs were evaluated for both global and local hydrodynamic change through simulation comparisons with the Base Case condition.

2. Global evaluation was conducted for Hampton Roads and the Elizabeth River by enumerating percentages of total area associated with class intervals of change in a particular property such as RMS difference in water surface elevation. Other properties evaluated by area percentile analysis included current magnitude, surface and bottom salinity, and bottom sedimentation potential.

3. Local evaluation was conducted in specific areas containing features considered important to estuarine circulation (e.g., tidal fronts, eddies, tidal prism and non-tidal flux in tributaries) and in areas of change pinpointed by global analysis.

4. Of the four expansion designs tested in the single variable runs, global analysis revealed that northward expansion (Option 6) and northeast expansion (Option 9) produced noticeably greater percentile changes in water surface elevation, current magnitude, salinity, and bottom sedimentation potential. Westward expansion (Option 5) produced a lesser degree of change. Eastward expansion (Option 7) produced only minor changes in the immediate vicinity of Craney Island.

5. Strong westerly surface and bottom currents were indicated in the berthing channel on the north side of Option 6 and are believed responsible for a significant increase in bottom salinity noted west of Craney Island and extending to the Nansemond River entrance.

6. Local analysis revealed no appreciable change in flushing ability in either the Elizabeth River basin or the Lafayette River for any of the options tested. Option 6, however, produced noticeable changes in simulated residual currents within the Elizabeth River and in areas between Newport News Point and Craney Island.

7. A tidal front near Newport News Point and a large tidal eddy over Hampton Flats appear to be affected by Options 6 and 9.

8. Historical runs tested two expansion options: Option 7 (eastward expansion) and Option 7/5a (combined eastward and westward expansion). As in the single variable runs, little change was noted in historical run comparisons for Option 7. Changes noted for Option 7/5a were slightly greater than those noted for Option 7 but were less than those noted for Option 5 (westward expansion) in the single variable runs. Streamlining of the footprint in expansion design 5a is considered to be responsible for the latter result.

Global Change – 95th Percentile (5% of area contains change greater than value listed)				
Single Variable – 50' Channel Cases				
Change in:	**Case 2 East 50' channel**	**Case 4 West 50' channel**	**Case 6 North 50' channel**	**Case 8 North/East 50' channel**
Surface Elevation	0.14 cm	0.34 cm	1.00 cm	**1.04 cm**
Surface Current	2.4 cm/s	5.3 cm/s	**12.3 cm/s**	11.7 cm/s
Bottom Current	1.6 cm/s	3.3 cm/s	**7.8 cm/s**	6.6 cm/s
Surface Salinity	0.00 ppt	0.12 ppt	**0.71 ppt**	0.23 ppt
Bottom Salinity	0.00 ppt	0.35 ppt	**1.00 ppt**	0.23 ppt
Sedimentation Potential	0.08 %	2.8 %	**8.9 %**	6.3 %
Single Variable – 55' Channel Cases				
Change in:	**Case 3 East 55' channel**	**Case 5 West 55' channel**	**Case 7 North 55' channel**	**Case 9 North/East 55' channel**
Surface Elevation	0.22 cm	0.42 cm	1.05 cm	**1.11 cm**
Surface Current	2.6 cm/s	5.5 cm/s	**12.5 cm/s**	11.8 cm/s
Bottom Current	1.7 cm/s	3.5 cm/s	**8.0 cm/s**	6.6 cm/s
Surface Salinity	0.03 ppt	0.10 ppt	**0.74 ppt**	0.23 ppt
Bottom Salinity	0.04 ppt	0.31 ppt	**1.07 ppt**	0.21 ppt
Sedimentation Potential	0.80 %	3.7 %	**10.1 %**	6.8 %

Global Change – 95th Percentile (5% of area contains change greater than value listed)				
Historical – High Discharge Event				
Change in:	**Case 2 East 50' channel**	**Case 3 East 55' channel**	**Case 10 East/West 50' channel**	**Case11 East/West 55' channel**
Surface Elevation	0.20 cm	0.22 cm	0.33 cm	**0.41 cm**
Surface Current	5.5 cm/s	5.7 cm/s	6.7 cm/s	**7.1 cm/s**
Bottom Current	2.7 cm/s	2.9 cm/s	3.7 cm/s	**3.9 cm/s**
Surface Salinity	0.00 ppt	0.03 ppt	0.02 ppt	**0.05 ppt**
Bottom Salinity	0.00 ppt	0.05 ppt	0.07 ppt	**0.09 ppt**
Sedimentation Potential	1.0 %	1.4 %	1.9 %	**2.4 %**

Historical – Low Discharge Event				
Change in:	**Case 2 East 50’ channel**	**Case 3 East 55’ channel**	**Case 10 East/West 50’ channel**	**Case11 East/West 55’ channel**
Surface Elevation	0.14 cm	0.21 cm	0.33 cm	**0.40 cm**
Surface Current	2.7 cm/s	2.8 cm/s	**4.3 cm/s**	**4.3 cm/s**
Bottom Current	1.9 cm/s	1.9 cm/s	**2.9 cm/s**	2.8 cm/s
Surface Salinity	0.00 ppt	0.00 ppt	**0.04 ppt**	0.01 ppt
Bottom Salinity	0.01 ppt	0.04 ppt	**0.09 ppt**	0.08 ppt
Sedimentation Potential	0.9 %	1.2 %	2.8 %	**3.0 %**
Historical – High Wind Event				
Change in:	**Case 2 East 50’ channel**	**Case 3 East 55’ channel**	**Case 10 East/West 50’ channel**	**Case11 East/West 55’ channel**
Surface Elevation	0.21 cm	0.25 cm	0.46 cm	**0.57 cm**
Surface Current	2.2 cm/s	2.5 cm/sec	**5.0 cm/s**	**5.0 cm/s**
Bottom Current	1.5 cm/s	2.4 cm/s	3.0 cm/s	**3.1 cm/s**
Surface Salinity	0.00 ppt	0.00 ppt	0.00 ppt	**0.01 ppt**
Bottom Salinity	0.00 ppt	**0.08 ppt**	0.02 ppt	**0.08 ppt**
Sedimentation Potential	0.8 %	0.9 %	1.7 %	**1.9 %**

TABLE OF CONTENTS

LIST OF TABLES

LIST OF FIGURES

LIST OF APPENDICES

Appendix V-B Circulation Features

I. INTRODUCTION

A. BACKGROUND

Motivation for this study derives from the joint interest of the Federal government and the Commonwealth of Virginia in a potential expansion of the Craney Island Dredged Material Management Area (CIDMMA), a Federally owned and operated facility located in Hampton Roads adjacent to the city of Portsmouth, Virginia (Figure I.1). Authorized by the U.S. River and Harbor Act of 1946, the CIDMMA has received dredged material from the deepening and maintenance of navigational channels, anchorage and berthing areas in Hampton Roads and the lower Chesapeake Bay region since the 1950's. The proposed expansion of the CIDMMA addresses a Federal interest in increasing the capacity of the CIDMMA and extending its useful life beyond the year 2050. In addition, the expansion would serve a further interest in obtaining logistical and tactical areas for the deployment of national defense forces. It simultaneously addresses the interest of the Commonwealth in future expansion of its deep-water port facilities.

The representative agencies in charge of the present development efforts are the Norfolk District, U.S. Army Corps of Engineers, and the Virginia Port Authority representing the Commonwealth Secretary of Transportation. Following a successful *Reconnaissance Study* that determined the required Federal interest, both parties signed a feasibility cost-sharing agreement and adopted a *Project Study Plan* (PSP) to determine suitable and acceptable means for designing and implementing the expansion. The PSP requires, among other items, the development and evaluation of preliminary designs for added material placement areas and new port facilities, including a marine terminal, to be incorporated in the expansion. More specifically, in order to determine the possible impact that any of these designs might have on the estuarine environment in Hampton Roads and adjacent areas, the PSP provides for a hydrodynamic modeling study to be conducted. This approach is consistent with the provisions of the National Environmental Policy Act (NEPA) that require an evaluation of preferred and alternative designs for marine construction projects in U.S. waters. Previous hydrodynamic modeling studies conducted to satisfy these requirements for similar projects in Hampton Roads include studies by Fang et al. (1972) and Boon et al. (1999).

B. PURPOSE OF THE STUDY

The purpose of the present study is to determine the nature and extent of the physical changes that may occur in the estuarine environment of Hampton Roads, including the waters of the lower James River and a major tributary, the Elizabeth River, due to the implementation of a given expansion design. The physical changes to be evaluated are:

1) tidal range and phase
2) strength and direction of tidal and tidally-averaged currents
3) salinity or salinity structure
4) circulation and flushing ability
5) sedimentation potential

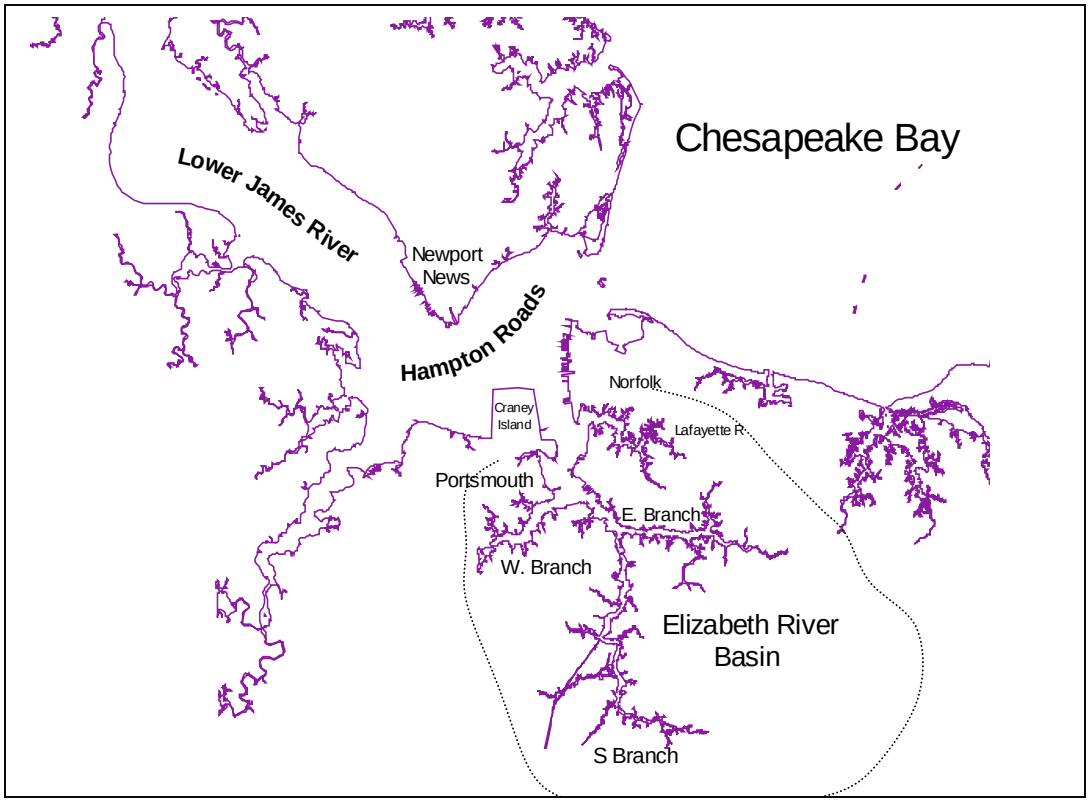

Figure I.1. Hampton Roads and the Elizabeth River Basin.

Sedimentation potential (Boon et al., 1999) is a modeled parameter computed as the percent of total time that the predicted bottom shear stress falls below a critical value permitting deposition. In concert with investigating local changes in sedimentation potential, results from a field study of possible sources of suspended sediment available for deposition are reported in Chapter III, Section D.3. In addition to the general physical characteristics listed above, specific features observed in the local estuarine environment during previous studies are examined in this report. These features include a tidal front system that regularly appears in the lower James River near Newport News Point (Kuo et al., 1988; 1990) and a non-tidal eddy system observed during the time of neap tides at the Elizabeth River entrance near Craney Island (Boon et al., 1999). The model simulation techniques described below are used to assess potential change in these features.

Another feature of key importance is the tidal prism or volume of water that enters and leaves the Elizabeth River during a tidal cycle. The magnitude of the tidal prism is an indicator of the flushing ability of the Elizabeth River Basin (Figure I.1), a system that includes not only the tidal waterways of the river stem and its four main branches but the adjacent watershed areas that deliver land-based runoff to the system as well. One of the main purposes of the present study is to determine whether any of the expansion designs would cause the tidal prism, and in turn the flushing ability of the Elizabeth River Basin, to decrease.

C. APPROACH

Potential changes in one or more of the physical characteristics or features listed above are investigated in this study through **Simulation Comparisons**. In this approach, a numerical model (described in Chapter II) is used to simulate hydrodynamic behavior at various temporal and spatial scales in the river areas under investigation. Following separate model runs, each driven by the same temporal input data including tidal height, salinity, freshwater discharges, and other boundary variables as specified, results are compared for the **Base Case** with pre-expansion conditions, and a **Test Case** including a specific **Expansion Option, with and without channel deepening,** but otherwise identical to the Base Case. Design elements of an expansion option that can be represented in the model include:

1) change in shoreline position (e.g., island creation or expansion)
2) change in water depth (e.g., channel deepening or widening)
3) change in modeling parameters[1] due to structures (e.g., bridge pilings).

The hydrodynamic model used for the simulations was previously calibrated and verified for the James River using 370 m grid spacing (Boon et al., 1999). An extension of the model into the Elizabeth River using 123 m grid spacing was completed during the present study. A description of the field data collected for calibration and verification of the Elizabeth River grid section is presented in chapter III of this report and our analysis of the results obtained is presented in Chapter IV.

1. Base Case – The Base Case for this study consists of the existing waterway conditions including bridge pilings and tunnel islands associated with the I64 and I664 highway crossings, in addition to a planned Third Crossing of Hampton Roads (Figure I.2, Alternative 9). A 50-ft inbound lane is also added to the present 50-ft outbound lane of the Norfolk Harbor Channel (NHC) leading to marine terminals in Norfolk and Portsmouth. Depths refer to the local datum of Mean Lower Low Water (MLLW).

2. Test Case – A Test Case consists of an expansion option added to the Base Case. Each test case is modeled twice, once using 50-ft depths and once using 55-ft depths in both the inbound and outbound lanes of the NHC. The 55-ft depth represents proposed channel deepening as described in the *Navigation Management Plan for the Port of Hampton Roads* (U.S. Army Corps of Engineers, 2000, p. II-45).

3. Single Variable Runs – These test four different Expansion Options described below. A basic screening approach under controlled conditions, these tests restrict the model input by allowing only a single input variable, tidal range, to vary between astronomical extremes during the course of a run. A three-constituent harmonic model is used including the M_2, S_2, and N_2 tidal constituents with phasing adjusted to produce tides of maximum (perigean-spring), mean, and minimum (apogean-neap) range during a single run of 34 days. A summary of these runs is presented in Table I.1 and Figure I.7.

[1] Modeling parameters include surface friction, local turbulence generation, and flow section porosity.

4. Historical Runs – These test two of the designs selected after evaluation of the Single Variable runs above. In these runs, actual values for several input variables are taken from the historical record over a three-month period (mid-March to mid-June, 2000). The variables include tidal and non-tidal changes in water level as well as changes in salinity at the open boundary and freshwater discharge at points along the closed boundary of the model domain. Local atmospheric winds are included through a surface stress parameter.

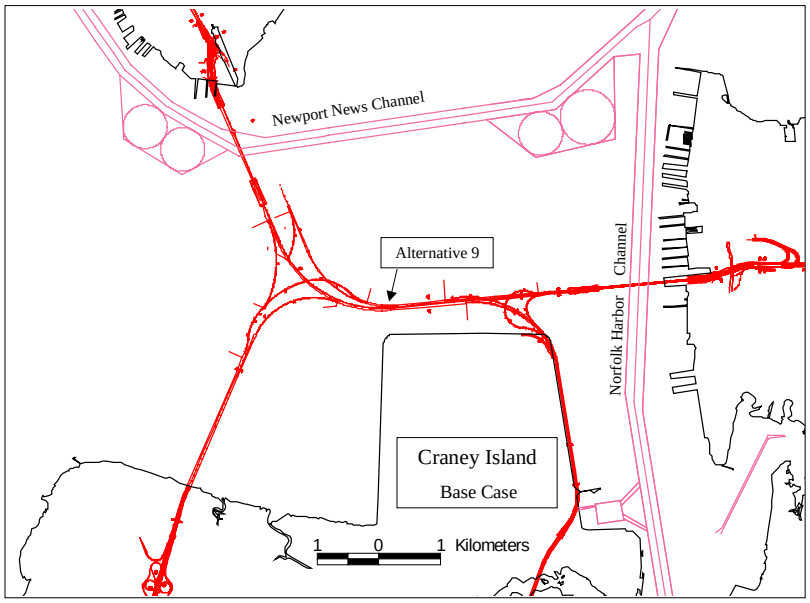

Figure I.2. Base Case with Alternative 9 Highway Crossing.

D. EXPANSION OPTIONS

Four expansion options were investigated in this study. The design of the facilities comprising these options was the joint responsibility of the federal and state partners in the feasibility cost sharing agreement, represented by the U.S. Army Corps of Engineers and the Virginia Port Authority, respectively. As previously noted, in order to satisfy NEPA requirements it was necessary to study a variety of possible alternatives, including expansion options with components expanding to the east, north, and west of Craney Island. From the perspective of estuarine hydrodynamics, a thorough testing of the resulting four designs is very desirable in order to have a broader basis for evaluation of effects, even when one design is clearly preferred for other reasons. The four options tested are described as follows:

1. Expansion Option 7 – The expansion for this option is a rectangular area to be added to the eastern side of Craney Island as shown in Figure I.3. The footprint shown has a total perimeter, all four sides included, of 7462 yd (6823 m) and a horizontal area of 539 acres (2.18 km^2). Expansion Option 7 will contain a proposed dredged material

placement area to be added first to the CIDMMA, followed by a port facility to be located above the placement area following its completion. Most of the port facility will rest on the placement fill and will serve as a container storage area. However, a docking and cargo transfer area approximately 400 ft (122 m) wide will be placed on pilings instead of fill along the entire easternmost length of the expansion. For modeling purposes, it is assumed that the water depth beneath the docking and cargo transfer area will be one-half that of the adjacent Norfolk Harbor Channel. The inbound element of the Norfolk Harbor Channel will be widened to reach the docking and cargo transfer area within the north and south boundary lines shown in Figure I.3.

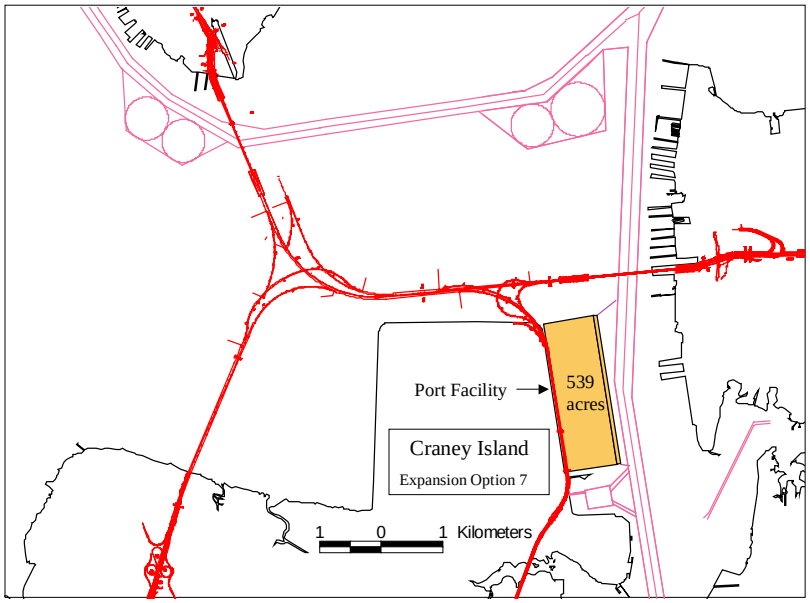

Figure I.3. Expansion Option 7 with Eastward Expansion.

2. Expansion Option 5 - This option includes a rectangular expansion added to the west side of Craney Island as shown in Figure I.4. The expansion footprint has a total perimeter of 9216 yd (8427 m) and an area of 1016 acres (4.111 km^2). The expansion in option 5 consists of a new dredged material placement area to be added to the existing CIDMMA on its west side. Conceptually, a port facility could be added building westward inside the existing CIDMMA starting from its eastern edge. However, a combination of highway access and traffic routing problems identified by the Virginia Department of Transportation (VDOT) precluded further consideration of a port facility located within the CIDMMA. Consequently, Expansion Option 5 was tested as shown in Figure I.4 with no modification of the bottom bathymetry approaching the perimeter of the expansion footprint. This design thus has no provision for an approach channel or other means of waterfront access along the eastern edge of the expansion.

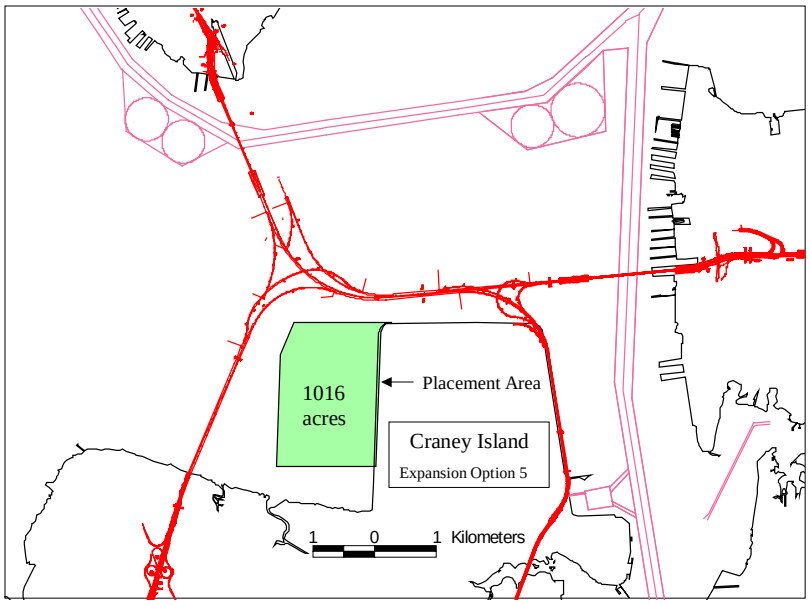

Figure I.4. Expansion Option 5 with Westward Expansion.

3. Expansion Option 6 – This option includes an expansion in the shape of a trapezoid added to the north side of Craney Island as shown in Figure I.5. The expansion footprint has a total perimeter of 9030 yd (8257 m) and an area of 811 acres (3.28 km^2). Option 6 also includes an approach channel, turning basin, and berthing areas on the north side of the expansion. The design depth in all three areas is 50 ft (15.2 m) at MLLW. The length and width of the proposed channel are approximately 12,700 ft (3871 m) and 1200 feet (366 m), respectively, with an increase in width at the western end to accommodate a turning basin approximately 1800 ft (549 m) in diameter. Most of the port facility will rest on the fill of the placement area, serving as a container storage area. However, a docking and cargo transfer area approximately 400 ft (122 m) wide will be placed on pilings instead of fill along the entire length of the northernmost edge of the expansion. For modeling purposes, it is assumed that the water depth beneath the docking and cargo transfer area will be one-half that of the adjacent approach channel. As indicated in Figure I.5, Option 6 will require a slight routing modification of Alternative 9, moving its east-west section 1200 ft (366 m) south of its proposed position for the Third Crossing of Hampton Roads.

4. Expansion Option 9 – The expansion for this option consists of a joined pair of rectangular areas to be added to the north and east sides of Craney Island as shown in Figure I.6. The footprint for Expansion Option 9 has a total perimeter of 16,045 yd (14,672 m) and covers a horizontal area of 1675 acres (6.778 km^2). The northward portion of this expansion is a dredged material placement area to be added to the existing CIDMMA. The eastward portion of this expansion will contain a port facility with approximately the same dimensions and overall configuration as those given for

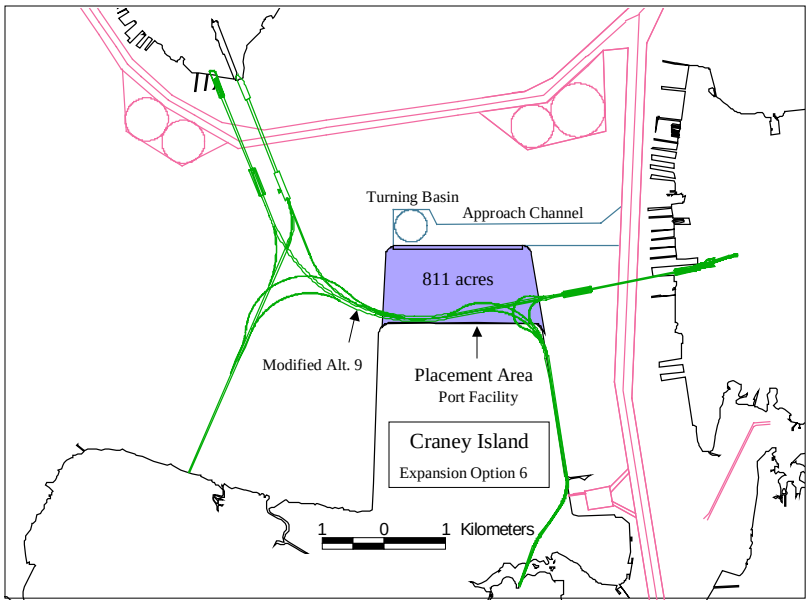

Figure I.5. Expansion Option 6 with Northward Expansion.

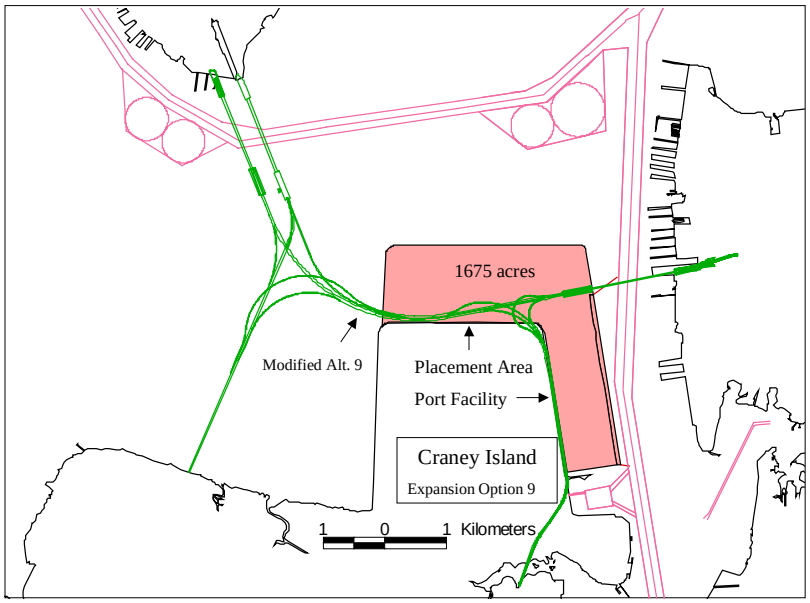

Figure I.6. Expansion Option 9 with Northward and Eastward Expansion.

expansion Option 7. This design has no provision for an approach channel or other means of waterfront access along the northern edge of the expansion. Dredging will be required along a portion of the eastern edge of the expansion, as indicated in Figure I.6, to

effectively widen the Norfolk Harbor Channel and allow vessel access to the docking and cargo transfer area of the proposed port facility. This option also requires the modified form of Alternate 9 with the southward shift of the east-west highway sector for the planned Third Crossing of Hampton Roads.

5. Method for Comparison of Results - Results from the Single Variable runs will be compared using a matrix format as illustrated in Table I.1. This format allows an objective evaluation of the four expansion options in the framework of a controlled experiment. Two options will then be selected for more extensive testing using actual conditions in a real-time experiment. Results are discussed in detail in Chapter V.

Table I.1. Single Variable Model Runs, Tidal Range Categories.

Case	Design	Channel Depth (ft)	Alternative 9	Tidal Range		
				Perigean-Spring	Mean	Apogean-Neap
1	Base Case	50	Standard	Case 1 results	…	…
2	Option 7	50	Standard	Case 2 results	…	…
3		55	Standard	Case 3 results	…	…
4	Option 5	50	Standard	Case 4 results	…	…
5		55	Standard	Case 5 results	…	…
6	Option 6	50	Modified	Case 6 results	…	…
7		55	Modified	Case 7 results	…	…
8	Option 9	50	Modified	Case 8 results	…	…
9		55	Modified	Case 9 results	…	…

In addition to analysis of data within a specific class of tidal range (Table I.1), results were also obtained as averages over a 34-day period including all classes (Figure I.7).

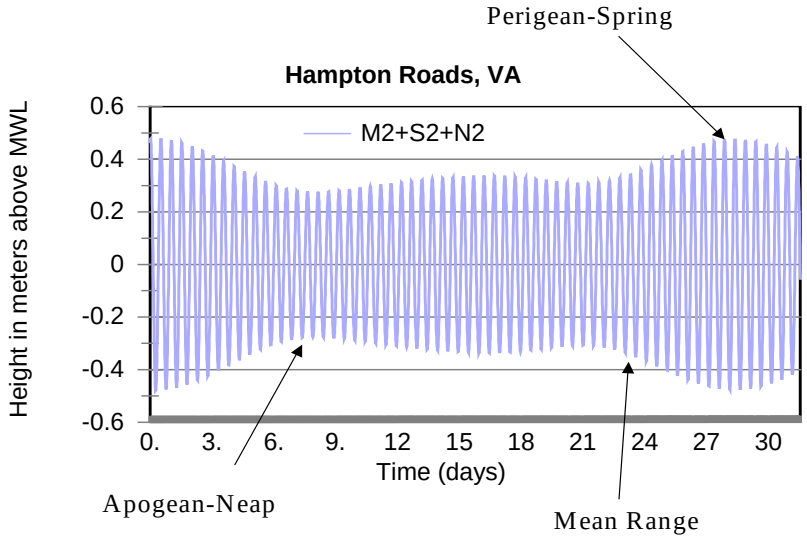

Figure I.7. Tide curve generated using M2, S2, and N2 constituent amplitudes for Hampton Roads, Virginia.

II. NUMERICAL MODEL

A. MODEL SELECTION CRITERIA

Selection of the hydrodynamic model used in this study was guided by project requirements including the basic requirement that the model must meet certain criteria in simulating the processes observed in the estuarine system under investigation. Previous studies in the lower James River (Fang et al., 1972; Kuo et al., 1988; Ruzecki and Hargis, 1988; Kuo et al., 1990; Boon et al., 1999) have shown that estuarine circulation in this region is inherently three-dimensional with important flow and material transport components simultaneously occurring in the vertical, transverse, and longitudinal directions. These observations dictate the use of a three-dimensional hydrodynamic model for adequate representation of the features being investigated in the model simulation comparisons. In addition, the comparisons technique requires the model to have adequate sensitivity for detecting both temporal and spatial changes.

In the present application, temporal change must be followed on a scale varying from hours to months. Tides and tidal currents exhibit both daily cycles on a time scale of hours and monthly cycles on a time scale of days. Although salinity structures in a river estuary such as the lower James River usually show very little change from hour to hour, they often show pronounced change when transforming from a stratified to a non-stratified state, and vice-versa, over a period of a few days. The time scale of such transitions is influenced by both monthly and semi-monthly tidal variations (e.g., the perigean-apogean, spring-neap cycles, Figure I.7) and episodic variations in freshwater inflow to tidal tributaries driven by irregular periods of storm runoff and drought. To ensure that these variations are adequately represented, a simulation period of more than one month is highly desirable.

Spatial change is dictated by the size and scale of the project being built. In the present study, the model selected must be sensitive to vertical change (incremental change in channel depth) on the order of a few feet and to horizontal change (incremental change in shoreline position) on the order of a few hundred feet. Although the size and spacing of bridge pilings is on the order of a few feet, their collective effect can be parameterized to obtain values governing flow fields at horizontal scales of a few hundred feet.

While meeting these sensitivity requirements, the model selected must remain capable of representing hydrodynamic conditions over the full extent of the model domain. The latter must include all of the James River as well as its tributary, the Elizabeth River, from their entrance at Hampton Roads to the limit of tide (at Richmond, Virginia, for the James). As noted above, it must also remain capable of representing the same conditions continuously for time periods longer than one month.

To meet these criteria, the *VIMS three-dimensional Hydrodynamic Eutrophication Model* (HEM-3D) first developed by Hamrick (1996), was selected and further modified to

permit simulations at high resolution in the Elizabeth River. This was accomplished by developing a 'step-down' model grid with dual scale resolution as shown in Figure II.1. A *fine grid* for the Elizabeth River and its entrance area was developed and embedded within the existing *coarse grid* previously developed and calibrated for the James River.

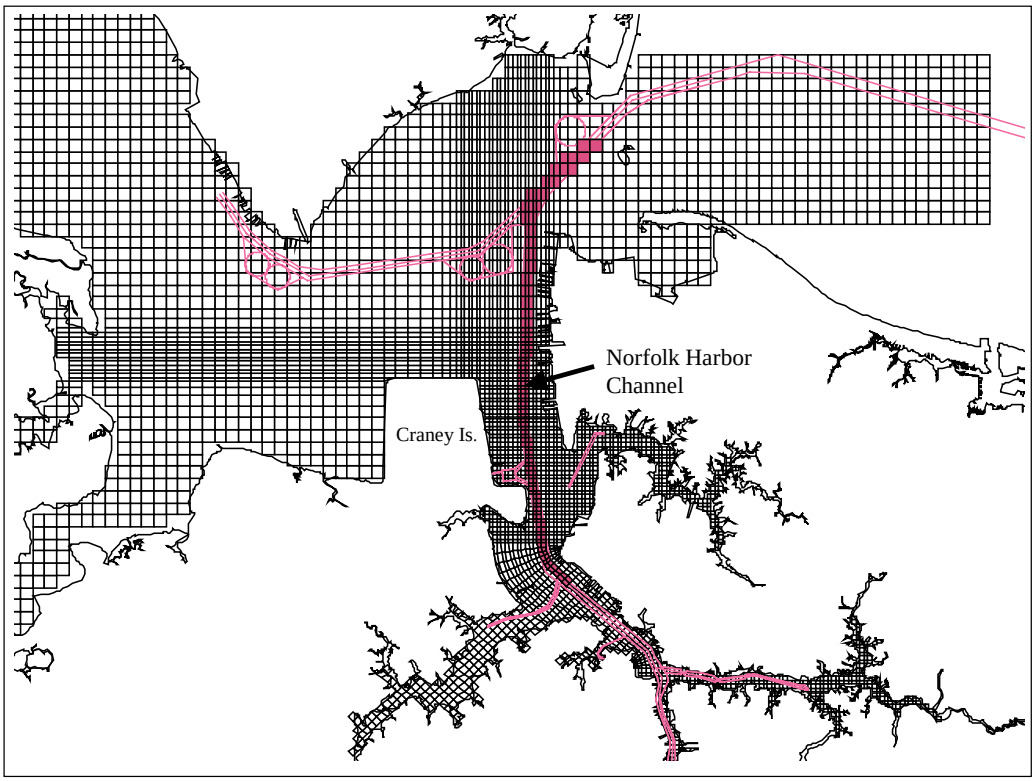

Figure II.1. Dual-scale model grid and Norfolk Harbor Channel.

B. HEM-3D MODEL DESCRIPTION

The three-dimensional Hydrodynamic-Eutrophication Model (HEM-3D) used in this study is a special purpose numerical model developed at the Virginia Institute of Marine Science (VIMS) from an innovative parent program, the Environmental Fluid Dynamics Computer Code (EFDC). The reader is referred to Hamrick (1996) for a detailed description of the EFDC. The hydrodynamic equations and the computational scheme used in this finite difference model are similar to the Blumberg-Mellor model (Blumberg and Mellor, 1987) and the U.S. Army Corps of Engineers Chesapeake Bay model (Johnson et al., 1993). In basic form, these models simulate the hydrodynamic behavior of the estuary by predicting change in surface elevation (including tides), horizontal and vertical water movement (including both tidal and non-tidal currents), and the three-dimensional distribution of conservative water properties such as the salt content (salinity). In addition, the HEM-3D model determines bed shear stress in basal layers of the model grid. Time series of bed shear stress are used to determine an index of bottom

sedimentation potential expressed as the percentage of total time that bed shear stress falls below a critical value permitting deposition to occur.

The domain of the HEM-3D model includes the entire length of the James River from its entrance in lower Chesapeake Bay to the fall line near Richmond, Virginia, using a 370 m horizontal grid. All areas of the Elizabeth River are covered using a 123 m horizontal 'step-down' grid as shown in Figure II.1. The entire model grid consists of 7529 active horizontal "cells", a portion of which covers the Hampton Roads area shown in Figure II.1. The third (vertical) dimension is implemented by stacking cells in layers one above the other from the bottom to the surface of the water column.

As implemented in Chesapeake Bay, the EFDC and its derivative programs differ from the Corps of Engineers Chesapeake Bay model in that EFDC uses stretched (sigma) coordinates in place of fixed coordinates to locate points in the vertical dimension. Each cell formed by intersecting horizontal grid lines is broken vertically into six layers of equal thickness, the thickness varying locally as a function of tidal elevation and water depth. Either rectangular or orthogonal curvilinear coordinates may be used to express the horizontal dimensions. The HEM-3D model for the James River uses State Plane Coordinates in meters and the 1983 North American Datum (NAD83) to reference all geographic positions.

The vertical reference used for all model depths in this study is the National Geodetic Vertical Datum of 1929 (NGVD). Source bathymetric data as printed on nautical charts generally refer to a tidal datum such as Mean Lower Low Water (MLLW) for their vertical reference. Hence charted depths must be converted to model depths by adding the elevation difference NGVD-MLLW. For Sewells Point in Hampton Roads, the NGVD-MLLW difference reported by the National Oceanic and Atmospheric Administration (NOAA/NGS) is 1.17 feet (0.357m). The previously mentioned project channel depths of 50 feet and 55 feet specified for model testing within the Norfolk Channel (i.e., Norfolk Harbor Reach and Craney Island Reach) are used assuming that an additional three feet of overdepth is to be permitted during dredging. The relationship between the resulting model depths and charted depths used in model testing is as shown in Figure II-2 below.

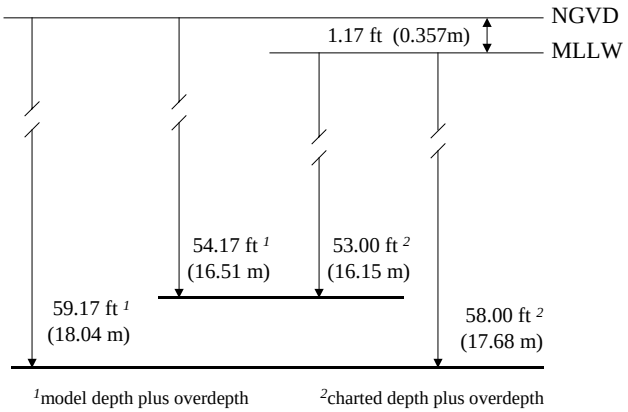

Figure II.2. Model depths and charted depths tested in the Norfolk Channel.

C. SIMULATION OF STRUCTURES AND THEIR IMPACT ON FLOW

As indicated in the previous section, the VIMS HEM-3D model set up in the James River is a dual-scale numerical model with both coarse and fine grid resolution. One of the main advantages of using a fine grid numerical model in the present project is its capability to incorporate structures from different design plans and simulate their effects on the host water body. A bridge tunnel island, for example, can be resolved by the coarse grid scale of 370 m and therefore, its effect on the water body can be simulated directly. Obviously, even with the use of fine grid spacing (123 m), it is impossible to investigate the near-field effects from the structure, such as scouring at the base of the individual pilings. But it is possible for the cumulative effect of the local processes to be parameterized at the scale of the cell size and used for studying its far-field effect. Those local processes include the constriction of flows by the spatial distribution of the bridge pilings in a cell, the impedance of flow by the collective drag forces from the individual pilings, and the corresponding turbulence mixing induced by the flow-structure interaction. Using adequate parameterization procedures, the effects of the structure on tidal fronts, eddy systems, and other far-field phenomena can then be properly investigated.

Two kinds of structures considered in this project are: 1) tunnel islands whose dimensions cover more than one grid cell (i.e., close to 740 m in length and slightly less than 370 m in width) and 2) cylindrical pilings of approximately 137 cm (54 in) in diameter standing vertically or near vertically. Based on the design drawings, the spacing between the individual pilings is more or less at regular intervals under the bridge. Both the pilings and the tunnel island extend from the water surface all the way to the bottom. Since the dimensions of the designed tunnel island are comparable to the grid resolution, it can either be treated as a 'thin wall' boundary if the shape is slender or as a land cell if it occupies most of the grid cell. Cells can be masked, depending on the position and orientation of the island, either in the west face, the south face, or both faces of a cell so that no flow is allowed to pass through the boundary. The resultant flow is thus forced to deviate and follow another path around the island boundary inserted by this procedure. The piling dimension designed, on the other hand, is smaller than the grid resolution (i.e., a sub-grid scale), and thus needs to be parameterized.

To parameterize the piling effect, first the porosity defined as the water fraction of the piling area in a cross-section is introduced into the constant x, y, z plane. These values are estimated from the actual designed plan. For example, in the application of the plan of Alternative 9, the design calls for a predominantly north-south oriented bridge piling with 70 feet (21 m) intervals and 10 feet (3 m) intervals in the cross-section direction. The porosities, once determined, are then incorporated into the mass balance control volume formulations. The continuity equation is thus given as:

$$\frac{\partial}{\partial t}(\phi_z \zeta) + \frac{\partial}{\partial x}(\phi_x Hu) + \frac{\partial}{\partial y}(\phi_y Hv) + \frac{\partial}{\partial z}(\phi_z w) = 0$$

where ζ is the water surface elevation; H is the local depth of the water column; u, v, w are the horizontal and vertical velocities; $\phi_{x,}$ $\phi_{y,}$ ϕ_{z} are porosity in x, y and z planes, respectively. The typical values of $\phi_{x,}$ ϕ_{y} are estimated as 0.93, 0.96 and ϕ_{z} in the z direction as 0.99. The mass conservation equation for a dissolved or suspended material with concentration C is:

$$\frac{\partial}{\partial t}(\phi_z C)+\frac{\partial}{\partial x}(\phi_x HuC)+\frac{\partial}{\partial y}(\phi_y HvC)+\frac{\partial}{\partial z}(\phi_z wC)=\frac{\partial}{\partial z}\left(\phi_z H^{-1}k_z\frac{\partial}{\partial z}C\right)+(\phi_z S_c)$$

where k_z is the eddy diffusivity; S_c is the source or sink term. The second step for the parameterization is to modify the momentum and the turbulence equation to include the flow-structure interaction. A resistance term was incorporated into the momentum equation as a result of the boundary shear stress introduced at and around the piling. The x- momentum equation is:

$$\frac{\partial}{\partial t}(\phi_z Hu)+\frac{\partial}{\partial x}(\phi_x Huu)+\frac{\partial}{\partial y}(\phi_y Hvu)+\frac{\partial}{\partial z}(\phi_z wu)-\mathrm{f}\,\phi_z\,\mathrm{H\,v}$$

$$=-\phi_z H\frac{\partial}{\partial x}(\mathrm{g}\zeta+\mathrm{p})+\frac{\partial}{\partial z}\left(\phi_z H^{-1}N_z\frac{\partial u}{\partial z}\right)-\mathrm{c_p}\frac{\mathrm{B_p}}{\mathrm{L_p^2}}\mathrm{H}\left(u^2+\mathrm{v}^2\right)^{0.5}u$$

where the terms on the left represent the inertial terms and the Coriolis force terms, and those on the right, the pressure gradient term, the vertical shear stress term and lastly the resistance term due to the piling. The N_z represents eddy viscosity, c_p the drag coefficient, B_p the projected piling width and L_p the separation length scale for the piling density. The resistance term is applied throughout the water column as opposed to the bottom shear stress, which is applied only at the bottom as a bottom boundary condition. The y–momentum equation (not shown) can be derived similarly.

The accompanied turbulence production and dissipation associated with the momentum resistance are also incorporated into the turbulence equations. The turbulence formulation used is the standard Mellor-Yamada turbulence closure scheme, as extended by Galperin et al. (1988) and Blumberg et al. (1992). The modifications were made to include an additional term for the turbulence energy production and dissipation induced by the bridge piling. The term which corresponding to the resistance term in the momentum equation is:

$$2\ \mathrm{c_p}\frac{\mathrm{B_p}}{\mathrm{L_p^2}}\mathrm{H}\left(u^2+\mathrm{v}^2\right)^{1.5}$$

where $c_{p,}$ $B_{p,}$ L_p are as defined in the momentum equation. The term essentially includes the effect of the turbulence flow at and around the piling as a result of the flow and the piling interaction.

D. MODEL SETUP

1. Grid Development – The existing James River grid with 370 m by 370 m cell size used in the study of the Hampton Roads Third Crossing (Boon et al., 1999) was modified to have higher resolution inside and around the mouth of the Elizabeth River (Figure II.1). First, a 123.33 m by 123.33 m cell size was imposed inside the Elizabeth River starting from the north end of the Craney Island northward extension alternative. Care was given to have a smooth transition from 370 m to 123.33 m grid—grid size was decreased in four steps with one sixth reduction of coarse grid spacing at each step. Then the reach between Lamberts Point and the entrance of the Southern Branch was represented by the combination of orthogonal curvilinear grids and rotated rectangular grids to conform to the navigational channel. Also curvilinear grids were employed for the area in the Deep Creek and the uppermost reach of the Southern Branch. Out of 252 × 303 horizontal cell grids, a total of 7529 active horizontal cells in 6 vertical layers were in the computation domain. For the existing structures, cells were masked to block flows. For bridge pilings, flow impedance and resistance was parameterized for each cell (Wang and Kim, 2000). Varying roughness heights were used ranging between 0.001 (inside the Elizabeth River) and 0.01 m (main stem of the James River) in model calibration. A time step of 30 seconds was used for all model runs.

2. Bathymetry - Existing bathymetry data for the James River model coarse grid was selected as baseline data. USACE-provided, high-resolution bathymetric survey data were used from the navigational channels to Lamberts Point reach and shoals around Craney Island. The NOAA bathymetry data were also used. The composite of data were formed by giving variable weights according to the data sources—the highest weight was given to the USACE shoal and navigational channel data, then the existing James River model grid data, and lastly the lowest weight to the NOAA data. Figure II.2 includes the final depths represented over the model grid.

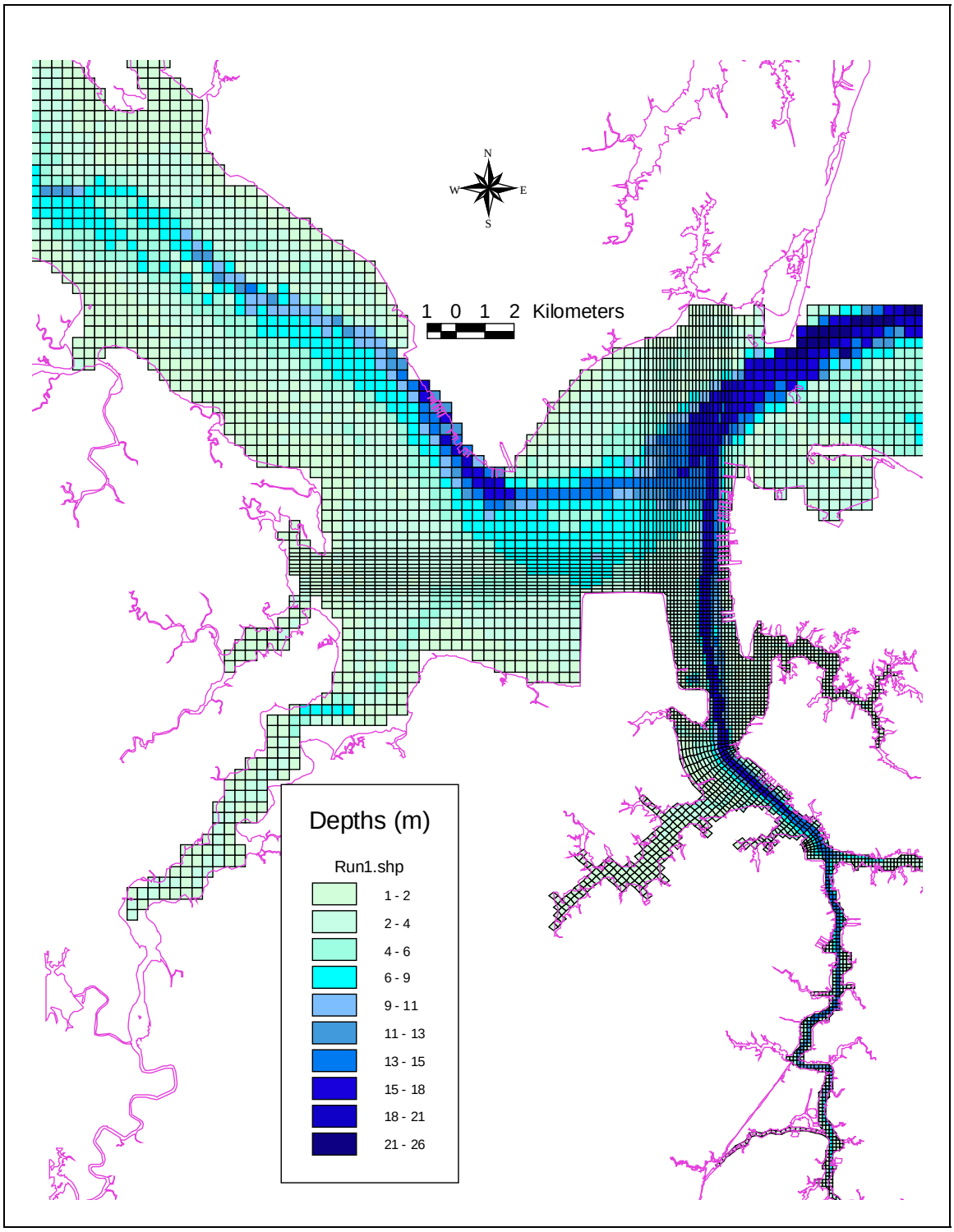

Figure II.3. Cell depths of the model grid.

III. FIELD PROGRAMS

A. PURPOSE

All hydrodynamic models require careful calibration and verification with suitable field data before they can be used to make adequate simulations of the complex hydrodynamic behavior in a given river estuary. Although the VIMS HEM-3D model for the James River estuary has been calibrated and verified as reported in an earlier study (Boon et al., 1999), that work did not include a calibration of the expanded Elizabeth River grid specifically developed for the present study. An initial search revealed that relatively few data were available for the Elizabeth River, especially observations of the current and salinity fields throughout its main stem and various branches. Accordingly, a field measurement program was designed and carried out as part of the present study. Both time series measurements at fixed stations as well as repetitive sampling data over a selected spatial region were obtained.

B. FIXED STATION TIME SERIES MEASUREMENTS

Certain types of instrumentation systems are well suited for deployment at a fixed location. These usually include self-contained electronic or electro-mechanical systems permitting selected parameters (water level, current speed and direction, salinity) to be continuously measured and recorded at fixed intervals of time. Because these systems are field-deployed and typically operate unattended for various periods of time before servicing, risk considerations are important, particularly in regions with high vessel traffic density such as Hampton Roads and the Elizabeth River. Locations for deployment of fixed current and salinity measurement systems were limited by this consideration. Shore-based water level measurements for determination of appropriate tidal parameters were less restrictive in this regard.

1. Water Level – Water level measurements in the Elizabeth River were readily available from two operational NOAA/NOS tide stations (**HRVA** and **MNPT** in Figure III.1). Sewells Point in Hampton Roads, Virginia (HRVA) is a primary tide station at the entrance to the Elizabeth River. At primary stations, tidal datums such as Mean High Water (MHW) and Mean Low Water (MLW) have been directly determined from measurements during a specific 19-year interval or Tidal Epoch. The current NOAA/NOS Tidal Epoch includes the years 1960-1978. Money Point (MNPT) in the Southern Branch of the Elizabeth River is a secondary tide station where equivalent 1960-1978 tidal datums have been determined through simultaneous comparisons with HRVA during a shorter interval. A third NOAA/NOS tide station was previously operated at the Portsmouth Naval Shipyard (PNSY) where equivalent 1960-1978 tidal datums are also available through the NOAA/NOS Coastal Operations web site - *http://co-ops.nos.noaa.gov*.

To augment the NOAA/NOS stations, VIMS personnel installed four additional tide gauges at the locations indicated in Figure III.1. These included gauges installed along the Port Norfolk Reach at Fort Norfolk, U.S. Army Corps of Engineers (**FORT**), Great

Bridge (**GRBR**) near the upstream end of the Southern Branch, one gauge within the Eastern Branch (**EAST**) and one gauge within the Western Branch (**WEST**) of the Elizabeth River. The required tidal parameters were derived as described below.

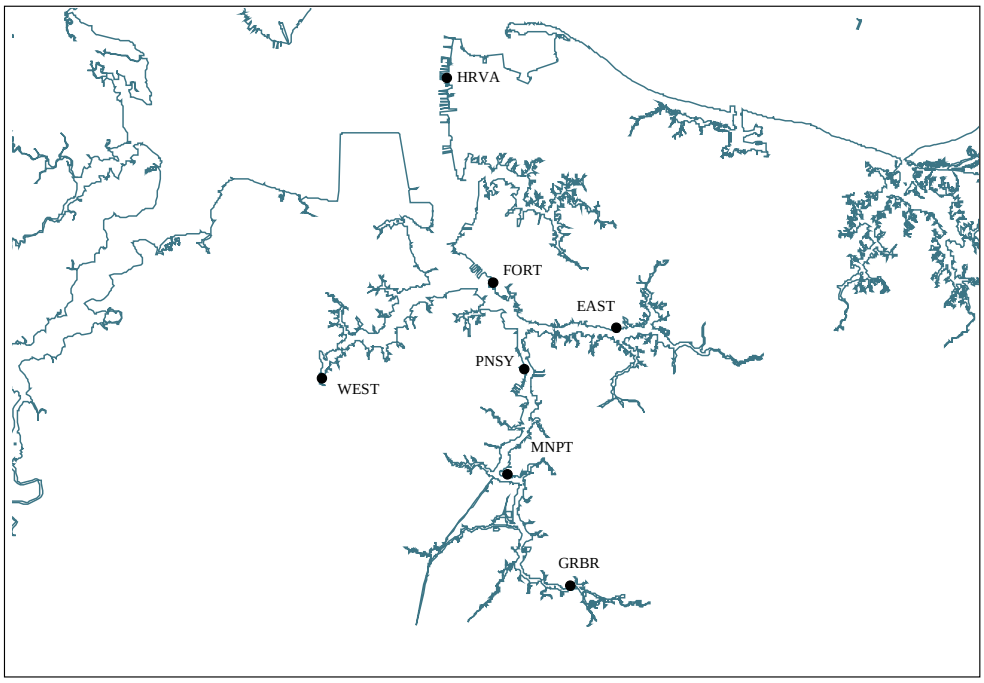

Figure III.1. Location of Elizabeth River Tide Stations.

Tide data required for model calibration in the Elizabeth River included two basic parameters: *mean tidal range* (Mn) and *mean phase lag*. The latter is expressed as either the average high water interval (HWI) or the average low water interval (LWI) between passage of the respective tidal phases at a reference station and their subsequent passage at a secondary station. The NOAA/NOS primary tide gauge at Sewells Point (HRVA) was used as the reference station. Times and heights of high and low water observed at each of the four VIMS tide stations were compared with simultaneously recorded values at HRVA to derive short-term mean values for these parameters. In each case the simultaneously recorded data covered a period of approximately two months. Since the four VIMS stations did not operate simultaneously, the months in question differed from station to station.

Mean Tidal Range - Mean tidal range is defined as the vertical distance between mean high water and mean low water, or

Mn = MHW - MLW

Short-term values of the mean tidal range were computed for the two-month period of observations obtained at each VIMS tide station. These values were in turn used to compute the average range ratio with HRVA during the corresponding two-month period. The equivalent mean range at each station for the 1960-1978 Tidal Epoch (Figure III.2) was then determined as

$Mn_B = Mn_A$ x Range Ratio

where

Mn_A = Accepted mean range (1960-1978) at primary station (HRVA)
Mn_B = Equivalent mean range (1960-1978) at secondary station

Mean Phase Lag – Mean phase lag was investigated through HWI and LWI values computed as the mean of the respective high and low water time differences recorded during the same two-month interval used to determine the range ratio between primary and secondary tide stations. Time differences (high and low water intervals) could not be determined at the Portsmouth Naval Shipyard (PNSY), where tabulated data were not available. Time differences for stations WEST and EAST averaged between 10 and 15 minutes at their respective locations off the main stem of the Elizabeth River. The results for other stations are shown in Figure III.3.

Summary Interpretation of Tidal Observations – The two tidal parameters just described are indicative of somewhat unique tidal behavior in the Elizabeth River. In contrast to the James River and other major sub-estuaries in the Chesapeake Bay region, they point to *standing wave* as opposed to *progressive wave* tidal characteristics.

As can be seen in Figure III.2, tidal range increases almost linearly with distance upstream, from 0.75 m (2.5 ft) at Sewells Point (HRVA) near the Elizabeth River entrance to 0.93 m (3.1 ft) at Great Bridge (GRBR). Figure III.3 shows that, although both high and low water intervals appear to increase in the upstream direction, the exact trend is not clear. Confidence intervals computed at the 95% level about the means of the high and low water intervals overlap at every station but one. Nevertheless it is readily apparent that the magnitude of the intervals remains small, varying from 10 minutes or less in the main stem to about 20 minutes in the Southern Branch over a distance of approximately 30 km (16 nm). In contrast, a progressive wave will take more than 50 minutes to travel a 30 km distance in a channel of 10 m depth.

These findings concerning the tide are consistent with a standing wave in a basin having an anti-node at its closed end (i.e., Great Bridge) and a nodal point lying well outside the basin. To the extent this characterization is accurate, the strength of the tidal current will be greatest in the approach region and will gradually decrease in the upstream direction to zero at Great Bridge.

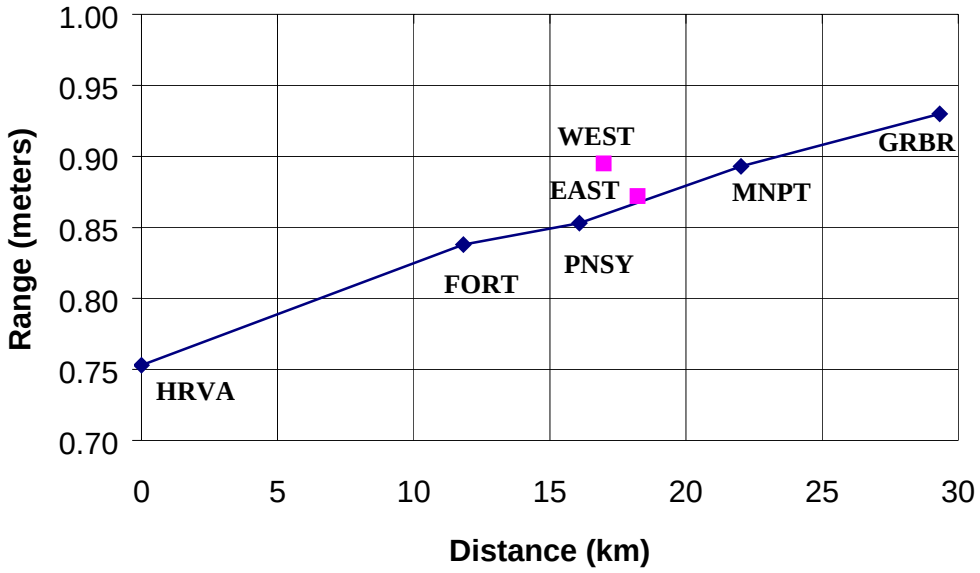

Figure III.2. Mean Tidal Range (1960-1978 Tidal Epoch), Elizabeth River.

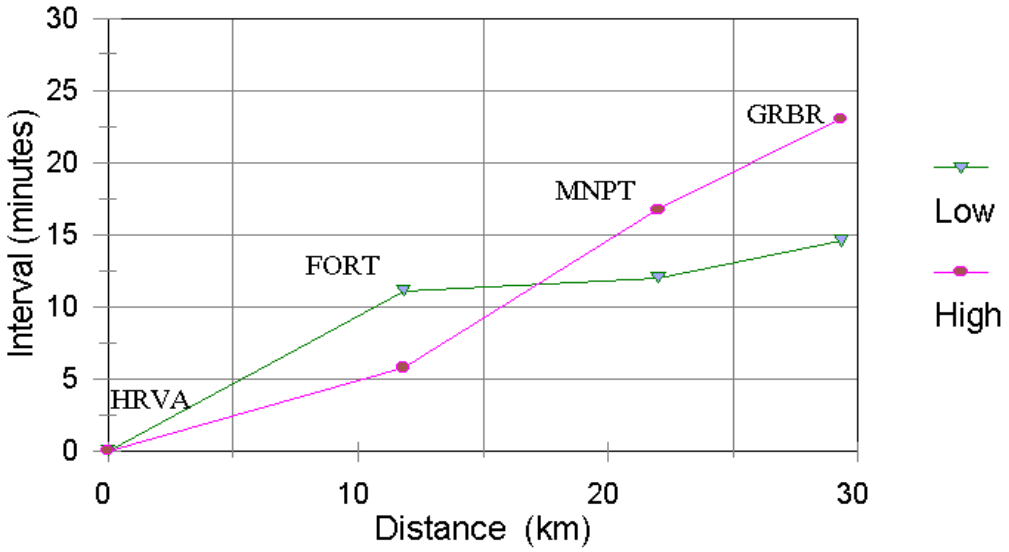

Figure III.3. Mean High and Low Water Intervals, Elizabeth River.

2. Non-tidal Water Level Change – In addition to water level variations caused by astronomical forcing at tidal frequencies, significant variations due to transient meteorological and hydrological events are routinely observed in the lower Chesapeake Bay and its tributaries. Seasonal events due to extratropical storms or "northeasters" occur on a time scale of days rather than hours and are generally uniform over a large area. These characteristics are well illustrated by the two NOAA/NOS water level records shown in Figure III.4.

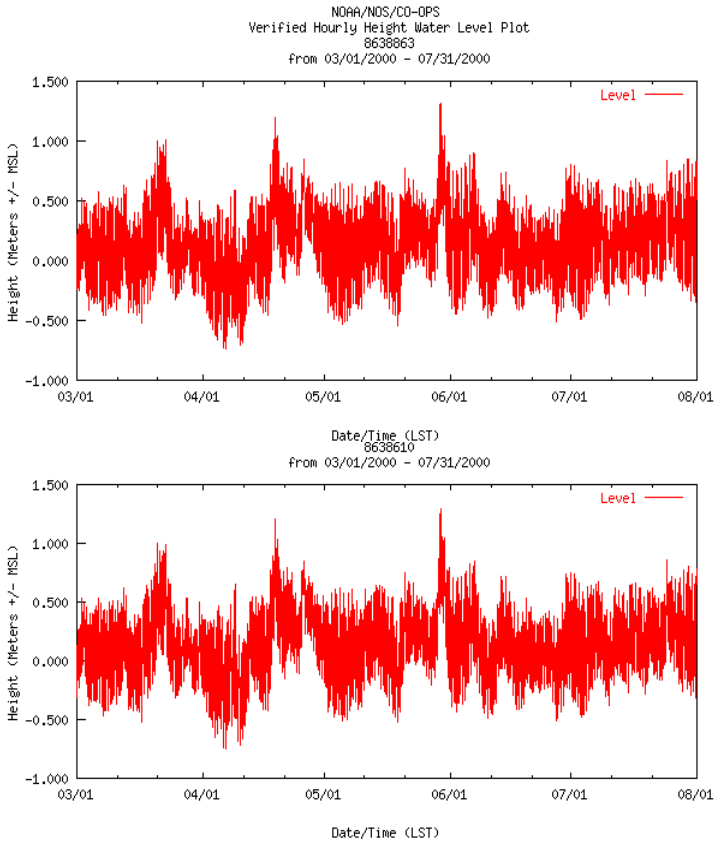

Figure III.4. Water levels at Chesapeake Bay Bridge Tunnel (upper panel) and Sewells Point, VA (lower panel) from March 1 to August 1, 2000.

In the Figure III.4 comparison, day-to-day variations in water level recorded at the Chesapeake Bay Bridge Tunnel are virtually identical to those recorded approximately 24 km (13 nm) farther inland at Sewells Point.

3. Current – Time series measurements of current were made at two locations in the Elizabeth River. A bottom-mounted Sontek 1500 KHz Acoustic Doppler Profiler (ADP)

was installed on the east side of the Norfolk Harbor channel within the Craney Island Reach at a depth of 8 m (26 ft) below MLLW. Three InterOcean S4 current meters were mounted at surface, middle, and bottom depths on a taught-wire submerged buoy platform near Hospital Point between Port Norfolk Reach and Town Point Reach. The locations of both current stations within the Elizabeth River are shown in Figure III.5.

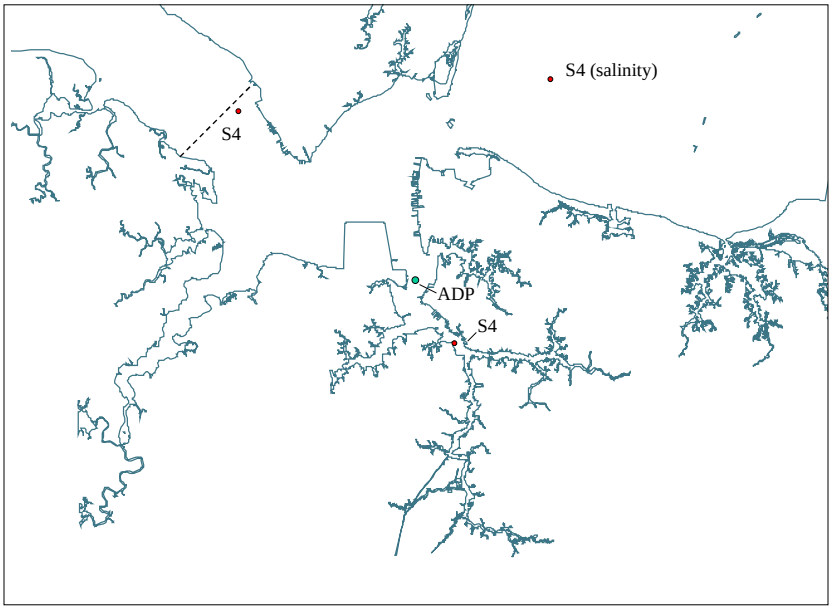

Figure III.5. Location of current stations.

Prior to analysis, current vectors were made scalar through projection on to a *principal axis* (maximum variance axis). In river estuaries, the principal axis normally lies parallel to the local channel axis. At the point of measurement, landward flow is designated *flood* current and seaward flow is designated *ebb* current by convention. Plotted as a time series, principal axis currents appear as sine waves with flood positive, ebb negative ordinate values. Chapter IV, Section B.2 of this report presents examples of time series plots from three locations (James River Bridge, Craney Island Reach, Hospital Point) that were used for model verification.

4. Salinity – Two InterOcean S4 current meters with CTD sensors were installed on a taught-wire mooring installed near Thimble Shoal Light outside the entrance to Hampton Roads at the position shown in Figure III.5. The CTD (conductivity, temperature, and depth) sensors provided salinity data from April 15 to June 8, 2000, at approximately 1 m and 11 m below the surface in 12 m water depths north of the Thimble Shoal north auxiliary shipping channel. Using an Applied Microsystems profiling CTD lowered to approximately the 15 m depth within the adjacent Thimble Shoal channel, comparative bottom salinity readings were made by field crews during monthly servicing of the S4 units. The sole purpose of this station was to obtain surface and bottom salinity data for

input to the model at its open boundary. Current data were not required at this boundary which lies outside the model domain yielding predictions.

C. 25-HOUR INTENSIVE CURRENT SURVEY

The purpose of this component of the study was to map the spatial structure of the flow field, in a portion of the Elizabeth River, at much finer horizontal scales than provided by the moored current meters at fixed stations. As a practical tradeoff, such labor-intensive sampling cannot collect data for as long or as frequently as moored meters, but still must be capable of characterizing the variability over tidal time scales. A further serious practical consideration is the presence of vessel traffic in the Elizabeth River, precluding deployment of fixed instrumentation except in limited, relatively protected locations.

The approach adopted was to measure currents with a vessel-mounted acoustic Doppler current profiler (ADCP) while underway, following a sampling trackline covering the area of interest in the desired spatial detail. By repeating the circuit at roughly hourly intervals, resolution of intra-tidal variability was achieved, and brief interruptions to give way to tugs and barges could be accommodated.

Sampling program – The intensive survey of currents was conducted in the vicinity of Lamberts Point, as indicated in Figure III.6. Aside from its proximity to Craney Island, this relatively wide reach of the Elizabeth River is of particular interest because it includes a significant bend as well as the junction with the Western Branch. An adequate characterization of the potentially complex flow in this region required relatively fine spatial resolution for which the underway sampling technique is well suited.

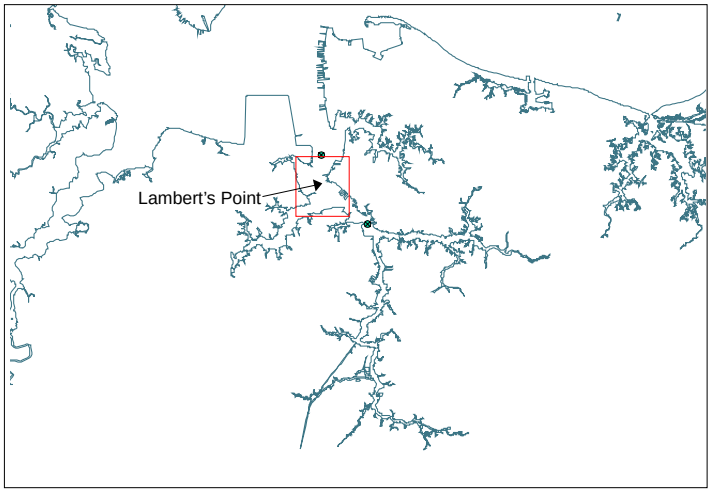

Figure III.6. Location of 25-hour intensive survey in the Elizabeth River.

The sampling trackline for the ADCP surveys is shown in Figure III.7. The total length of the line was designed so that it could be traversed easily in less than an hour at a boat speed of about 5-6 knots (2.5-3 m/s).

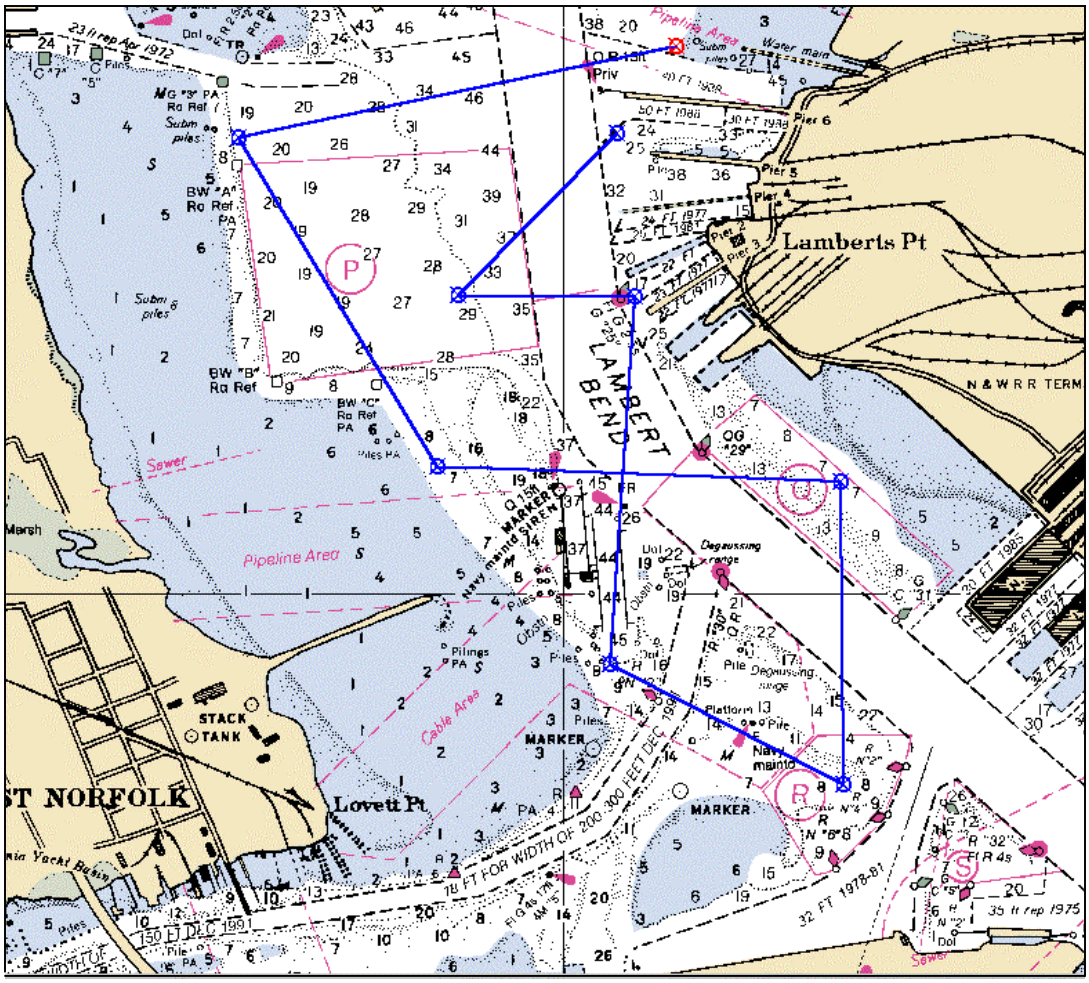

Figure III.7. Sampling trackline for the 25-hour intensive current study.

On May 16-17, 2000 currents were measured during 24 surveys along the sampling trackline. The observations spanned two semi-diurnal tidal cycles. There was a full moon on May 18; thus, the survey was conducted close to the time of a spring tide. However, predicted currents associated with this spring tide were of modest strength compared, for example, to those at the new-moon spring tide on May 4.

Instrumentation – Operations were conducted aboard the 28' *R/V Coot*. Currents were measured with a 1200 kHz ADCP (RDI Workhorse Sentinel) mounted on a rigid frame at the bow. A JRC differential GPS unit provided position data. Reflections from each acoustic "ping" of the ADCP were processed to provide flow velocity data at 25 cm

vertical intervals beneath the vessel. Because the ADCP transducers were immersed 30 cm below the surface, and a "blanking interval" of 50 cm exists just below the transducers, the measured portion of the water column begins 80 cm below the surface and extends to within about 1 m of the bottom. In the field, average velocities computed from 4-ping ensembles were recorded at 1.7 s intervals, corresponding to a data point for every 5 m of travel along the sampling trackline, assuming a nominal boat speed of about 3 m/s. The data were further averaged in post processing.

During underway sampling, the water velocity measured by the ADCP is a combination of the actual current in the water and the velocity of the boat. For example, in water not moving at all, with the boat traveling north at 3 m/s, the ADCP will measure water flowing past the sensors to the south at 3 m/s. Measurement of boat velocity is thus essential to underway current sampling. In principle, this could be accomplished with GPS data; however, direct acoustic measurement by the ADCP of its own velocity relative to the bottom, so-called "bottom tracking," is preferable whenever possible. Throughout the study, bottom tracking was used to remove boat velocity from raw data.

Representative data – The ADCP surveys measure the vertical variations in the current directly below the trackline, which spans a two-dimensional region at the water surface. Thus, each survey provides some information on the three-dimensional variability of the flow field in the region. A sample plan view of the flow field at a depth of 1 m is shown in Figure III.8 for data measured on survey 11. Here the current is represented by vectors, or sticks, indicating the direction and relative speed of the flow at all points along the trackline. Survey 11 was conducted during predicted flood current and the pattern shown in Figure III.8 shows the flow following the bend of the main channel. A different view of the flow during the same survey is shown in Figure III.9, representing the north-south (along-channel) flow through a cross section directly below leg 1, the northernmost straight segment of the trackline. This perspective reveals that the flood current (to the south) was strongest at mid-depth (5-10 m) and laterally positioned against the relatively steep bottom slope of the channel.

Data processing – The figures just discussed illustrate the general nature of the field data acquired during the intensive study. Prior to further analysis and comparisons with model output, the ADCP data were subjected to several processing steps. A simple acceleration criterion was applied to detect changes in boat speed or direction associated with the turns at the end of each leg of the sampling trackline or avoidance of vessel traffic. Data collected during those conditions were rejected. The location of each velocity data point was geo-referenced to latitude and longitude with the GPS data and then converted to state plane coordinates. ADCP velocity determinations based on only a few pings are inherently noisy and further averaging is required. For this study, 15 of the field-recorded ensembles (each of those representing a 4-ping average) were combined to produce velocity estimates based on 60 pings spanning approximately 25 seconds. At a nominal boat speed of 3 m/s, these velocity values correspond to averages over a 75 m segment of trackline. Finally, the velocity data for each of the individual surveys were interpolated onto the same uniformly spaced grid with the Matlab function GRIDDATA.

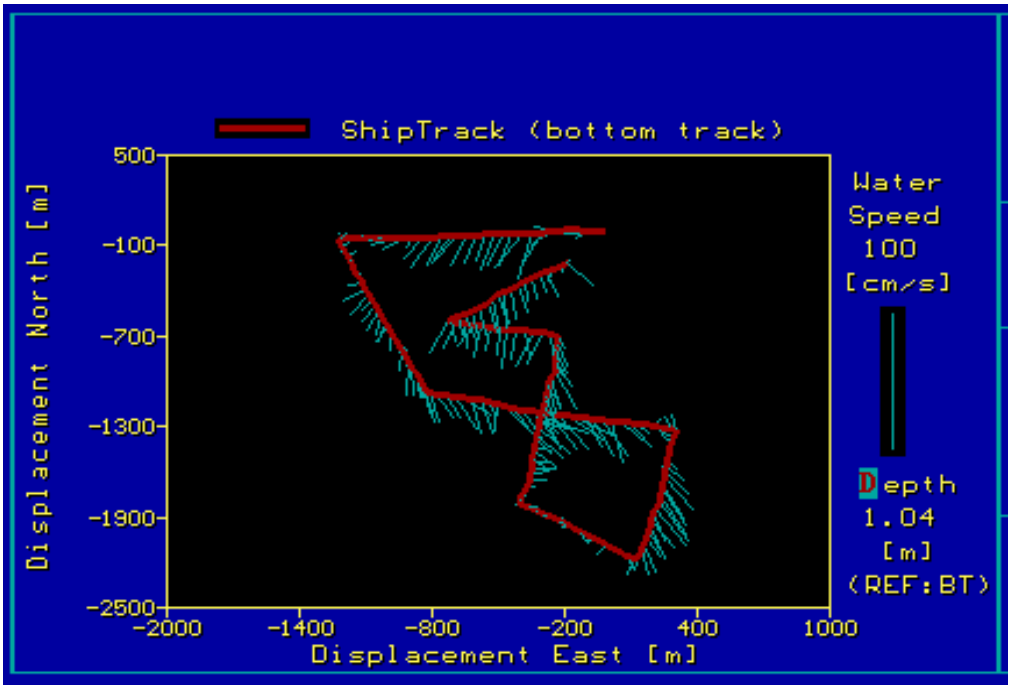

Figure III.8. ADCP survey 11 during maximum flood.
Plan view of currents 1 m below surface.

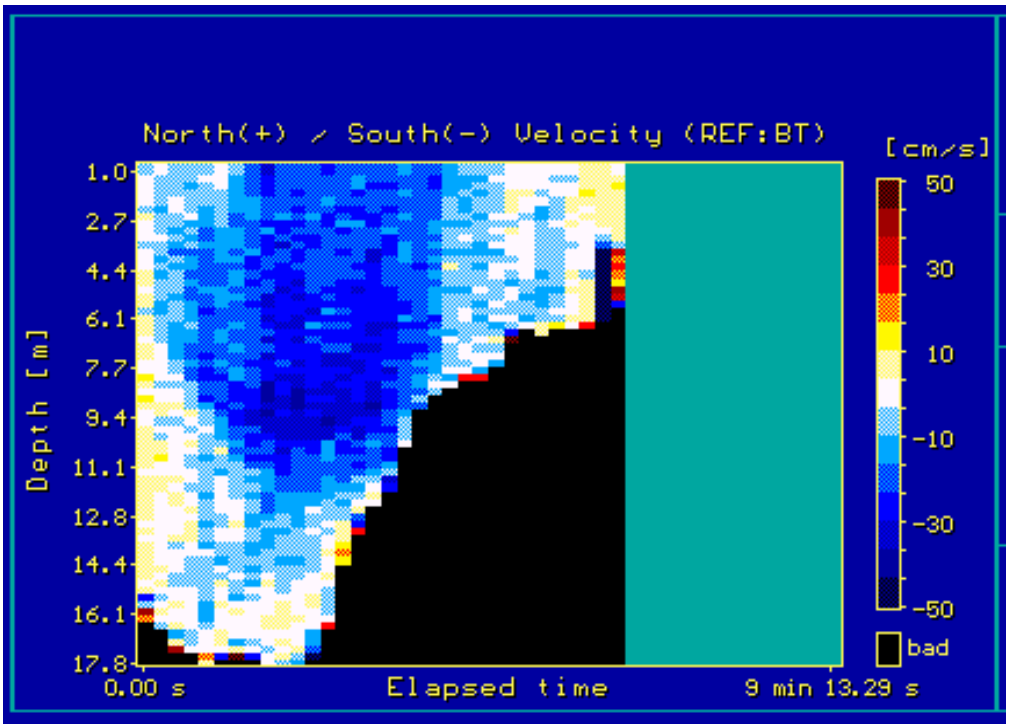

Figure III.9. ADCP survey 11 during maximum flood.
Cross-section view of currents below leg 1, looking south.

D. SLACK WATER SURVEYS

In 2000, a total of 12 slackwater surveys were conducted from April 24 to October 18. During each survey, temperature and salinity were measured at 20 stations along the mainstem of the Elizabeth and at several stations in its branches (i.e., 2 in the Eastern Branch, 3 in the Western Branch, 3 in the Lafayette River, and 3 in Deep Creek). These sampling locations are shown below in Figure III.10, where red dots signify the locations of mainstem stations and blue dots signify those of the branch stations.

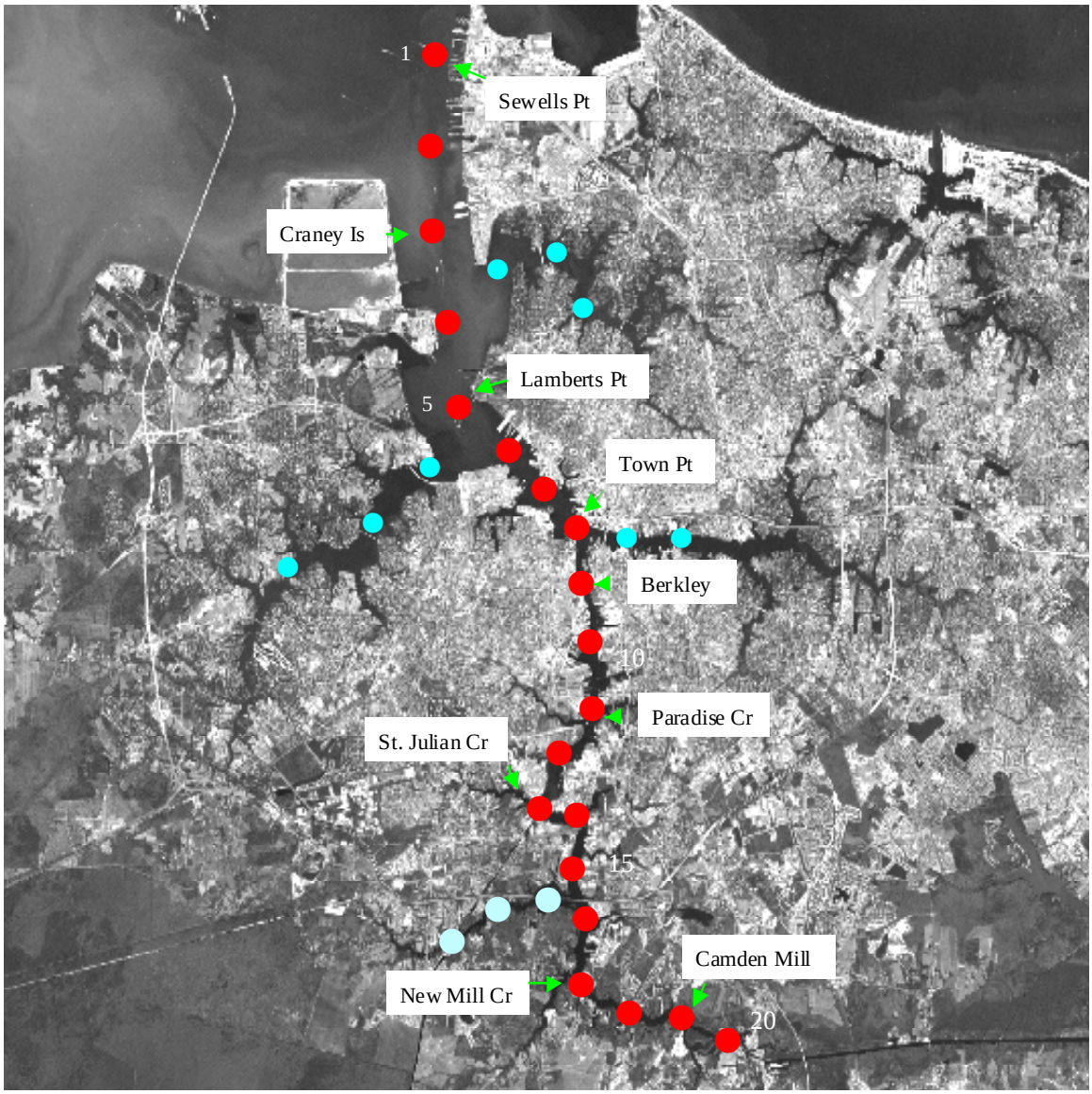

Figure III.10. Slackwater survey stations in the Elizabeth River.

Due to the standing wave condition in the Elizabeth River, slack water occurs within an average interval of 24 minutes or less throughout the system at either slack before flood

or slack before ebb. To obtain data as close as possible to slack conditions, two vessels were used to sample all stations at the predicted times of the slack phase. Temperature and conductivity were measured with an Applied Micro Systems Conductivity-Temperature-Depth probe (CTD). Conductivity and temperature readings were automatically converted to salinity values through an onboard microprocessor. Vertical profiles of salinity and temperature with resolutions of about 30 cm were obtained for each station. The sampling dates and stage of the tide (i.e., slack before flood or slack before ebb) are shown below in Table III.1.

Table III.1. Slackwater Surveys for CIEE Project.

Survey #	Date	Julian	Stage of Tide	# of Stations
1	04/24/00	115	Slack before Flood	28[1]
2	05/01/00	122	Slack before Flood	28[1]
3	05/08/00	129	Slack before Ebb	28[1]
4	05/15/00	136	Slack before Flood	31
5	05/22/00	143	Slack before Ebb	31
6	06/07/00	159	Slack before Ebb	31
7	07/28/00	210	Slack before Ebb	23[2]
8	08/29/00	242	Slack before Ebb	31
9	09/05/00	249	Slack before Ebb	31
10	09/12/00	256	Slack before Flood	31
11	10/12/00	286	Slack before Ebb	31
12	10/18/00	292	Slack before Ebb	30[3]

[1]Stations DIS1 - DIS3 not monitored for first 3 surveys.

[2]Stations EB1 - EB2, LAF1 - LAF3, and WB1 - WB3 not monitored due to equipment problems.

[3]Station ER09 eliminated from plot due to an air bubble in the instrument.

1. Salinity - The salinity distributions gathered on the 12 slackwater surveys provided high quality data essential to the HEM-3D calibration effort for the Elizabeth River section of the model domain. The distributions for the 12 surveys are shown in the Appendix to Chapter III, Section D.1. These plots display the longitudinal and depth gradients of salinity.

2. Temperature - Although temperatures were recorded along with salinities, these data were not used in the calibration effort. Plots of the temperature distributions for the 12 survey dates are shown in the Appendix to Chapter III, Section D.2.

3. Suspended Sediment - As stated in Chapter I in the introduction to this report, sedimentation potential is a modeled parameter defined as the percent of total time that the predicted bottom shear stress falls below a critical value (approximately 0.1 Pascals) that will allow fine sediment deposition to occur. Use of this parameter assumes a relationship between fluid shear stress caused by waves or currents acting on the seabed and the ability of fine-grained sediments to deposit there. Note that this is a separate assumption from one postulating a critical shear stress that must be exceeded in order for erosion of bottom sediment to occur. The latter relationship is considered more difficult to define and to apply in a hydrodynamic model because detailed information concerning the internal properties of the bed must be known (e.g., grain-size distribution, graded bedding, degree of consolidation, etc.).

The sedimentation potential is an important parameter because it allows one to assess whether a given expansion design will have the potential to cause either an increase or a decrease in bottom sedimentation at specific points in the model domain. However, merely knowing the potential for sedimentation does not guarantee that sedimentation will, in fact, occur. A supply of sediment in suspension within the water column is required at the location in question. Therefore, to 'arm' the sedimentation analysis tool offered by the HEM-3D model, it was considered necessary to know something about the distribution of suspended sediment. Information on suspended sediment in the James River exists (Nichols, 1977) but field surveys were needed to obtain it in the Elizabeth River. This was accomplished using a Seapoint optical sediment sensor in combination with the CTD profiling sensor deployed in the slack water surveys described in the previous section. Water samples collected at various depths along the profile were analyzed for total suspended solids (TSS) in the laboratory and used for *in-situ* calibration of the optical sensor. Values of TSS are expressed as mass concentrations in mg/l and are referred to as concentrations of suspended sediment.

In focusing on the distribution of suspended sediment in the Elizabeth River, the source of the sediment supply was of paramount importance. In general, sediment within an estuary may come from local bed erosion, net influx from upstream or downstream, bank erosion and lateral influx through runoff. At the outset, the first two (local bed erosion and net influx from upstream or downstream) were considered the most likely sources contributing to the total suspended load. Longitudinal and vertical gradients in suspended sediment concentration were then analyzed to infer sources.

Figures III.11a through III.11c show distributions of suspended sediment concentration in mg/l during May 2000, a month characterized by relatively high freshwater inflow. Suspended sediment concentration is relatively low (10-15 mg/l) in the upper portion of

the water column but higher concentrations (20-40 mg/l) are consistently observed in a zone near the bottom extending from the Elizabeth River entrance to approximately

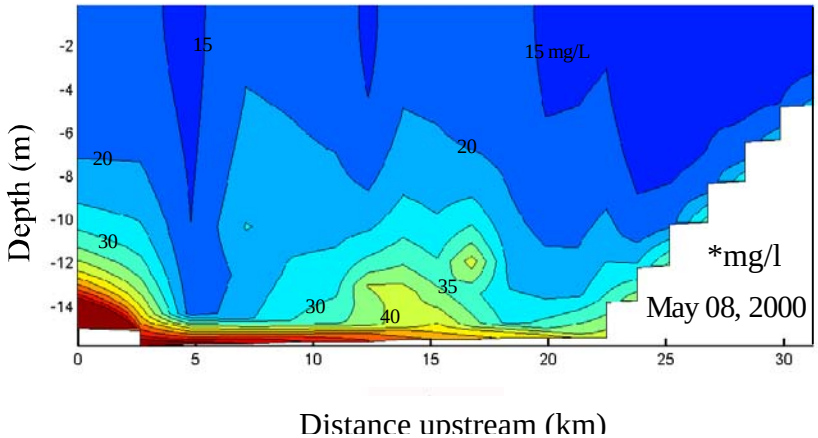

Figure III.11a. Elizabeth River suspended sediment concentration*, 5/8/2000.

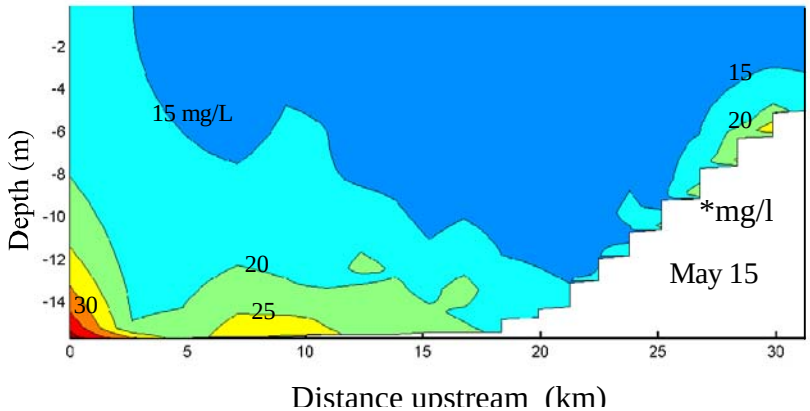

Figure III.11b. Elizabeth River suspended sediment concentration*, 5/15/2000.

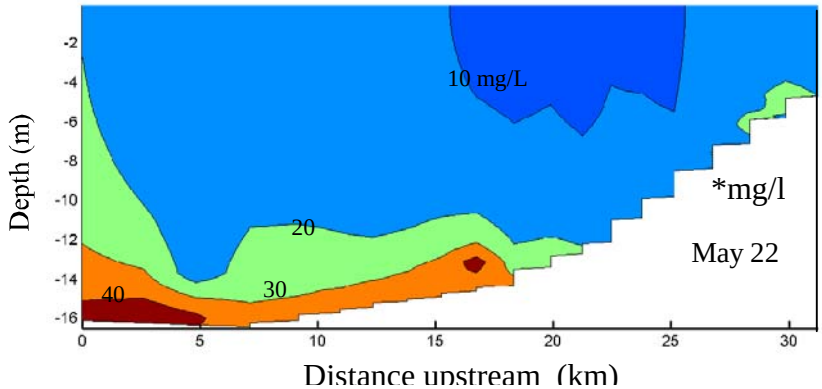

Figure III.11c. Elizabeth River suspended sediment concentration*, 5/22/2000.

18 km upstream. Highest concentrations (>40 mg/l) were found within the first 5 km upstream from the entrance. These observations clearly suggest that the James River was the primary source of suspended sediment in the Elizabeth River during the time of the May observations. Tidal phasing and advective pumping into the Elizabeth River appear to be the primary mechanism responsible for the bottom influx observed. During late ebb in the lower James River a part of the exiting flow is diverted to the right and into the Elizabeth River entrance which experiences flood at this time.

Figure III.11d and III.11e show examples of the suspended sediment concentration field in the Elizabeth River on October 12 and October 18 after an extended period of low river inflow. Concentrations of 5-10 mg/l were noted everywhere within the water column except for isolated patches of higher concentration that appear to be bottom derived. One patch of unusually high concentration coincided with the passing of a large ship near the survey vessel and is marked in Figure III.11e as propeller wash.

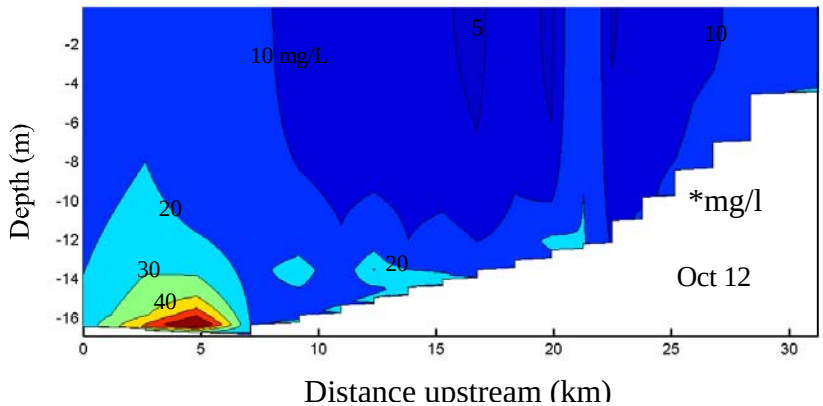

Figure III.11d. Elizabeth River suspended sediment concentration*, 10/12/2000.

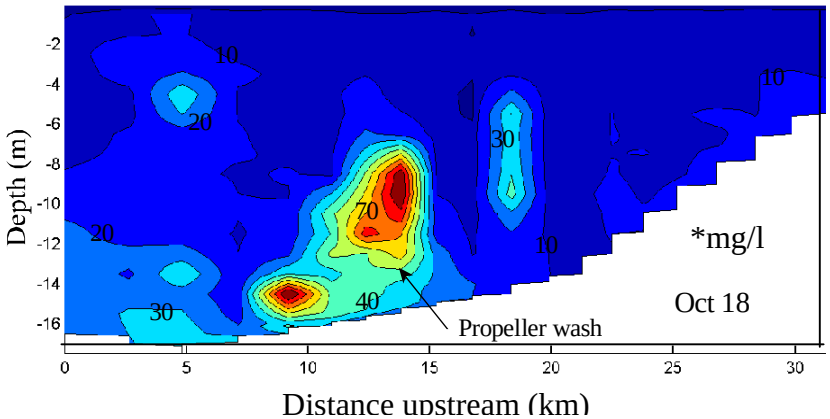

Figure III.11e. Elizabeth River suspended sediment concentration*, 10/18/2000.

The above findings suggest that bottom concentrations of suspended sediment may be expected to exceed 30 mg/l well into the Elizabeth River as far as Paradise Creek in the Southern Branch (km 18) during periods of high freshwater inflow into the James. At other times, concentrations of 30-40 mg/l are restricted to the entrance region and certain areas adjacent to the more active shipping channels.

E. DATA FROM OTHER SOURCES

In addition to the field measurements made by VIMS personnel in the course of the present study, certain data sources were also available as listed below and were incorporated into the work.

1. Water Levels – As previously stated in Section B.1 of this chapter, extensive use was made of the historical water level database available through the NOAA/NOS Coastal Operations web site - *http://co-ops.nos.noaa.gov*.

2. Salinity - In addition to the VIMS slack water survey in the Elizabeth River, we have also acquired the James River monitoring data from Cindy Johnson (Virginia Department of Environmental Quality) for the month of March and April, 2000. The primary use of the data is to provide the model with the initial conditions for salinity and temperature fields.

The James River monitoring survey, extended from the mouth of James River all the way to Richmond, consists of 16 stations including tributaries in the Chickahominy, Appomattox, and Elizabeth Rivers. Figure III.12 shows the station location map and a table listing the station names, latitude, longitude and river miles. Salinity and temperature vertical profiles were collected using standard CTD method during the periods March 23-30 and April 20-24. The salinity and temperature data at discrete locations were then linearly interpolated and contoured using the software package PGPLOT. Figures III.13-III.14 show the surface salinity and temperature field for the March, 2000 surveys and Figures III.15-III.16 show these for the April, 2000 surveys.

River	Sta. No.	(River Mile)	Location Description	Latitude	Longitude
James	TF5.1	2-JMS157.29	CartersvilleFall Line	374013.0	0780513.0
James	TF5.2	2-JMS110.30	Mayo's BridgeHead of Tide	373149.8	0772602.4
James	TF5.2A	2-JMS104.42	Buoy 166	372659.1	0772512.0
James	TF5.3	2-JMS099.30	Buoy 157	372410.6	0772331.0
App.	TF5.4A	2-APP016.38	Rt. 600 BridgeFall Line	371331.0	0772835.0
App.	TF5.4	2-APP001.53	Buoy 8	371841.0	0771749.0
James	TF5.5	2-JMS075.04	Buoy 107Plankton, Benthos	371846.0	0771359.0
James	TF5.5A	2-JMS069.08	Buoy 91	371800.0	0770?0.0
James	TF5.6	2-JMS055.94	Buoy 74	371629.0	0765918.5
Chick.	RET5.1A	2-CHK006.14	Buoy 10	371843.0	0765222.0
James	RET5.2	2-JMS042.98	Swann's Point Plankton, Benthos	371236.4	0764736.2
James	LE5.1	2-JMS032.59	Buoy 36	371224.0	0763906.0
James	LE5.2	2-JMS021.04	Buoy 12-13 Benthos	370328.1	0763500.0
James	LE5.3	2-JMS013.10	Buoy 15	365924.0	0762736.0
James	LE5.4	2-JMS005.72	Buoy 9 Benthos	365718.0	0762330.4
Eliz.	LE5.6	2-ELI002.00	Buoy 18	365412.0	0762000.0

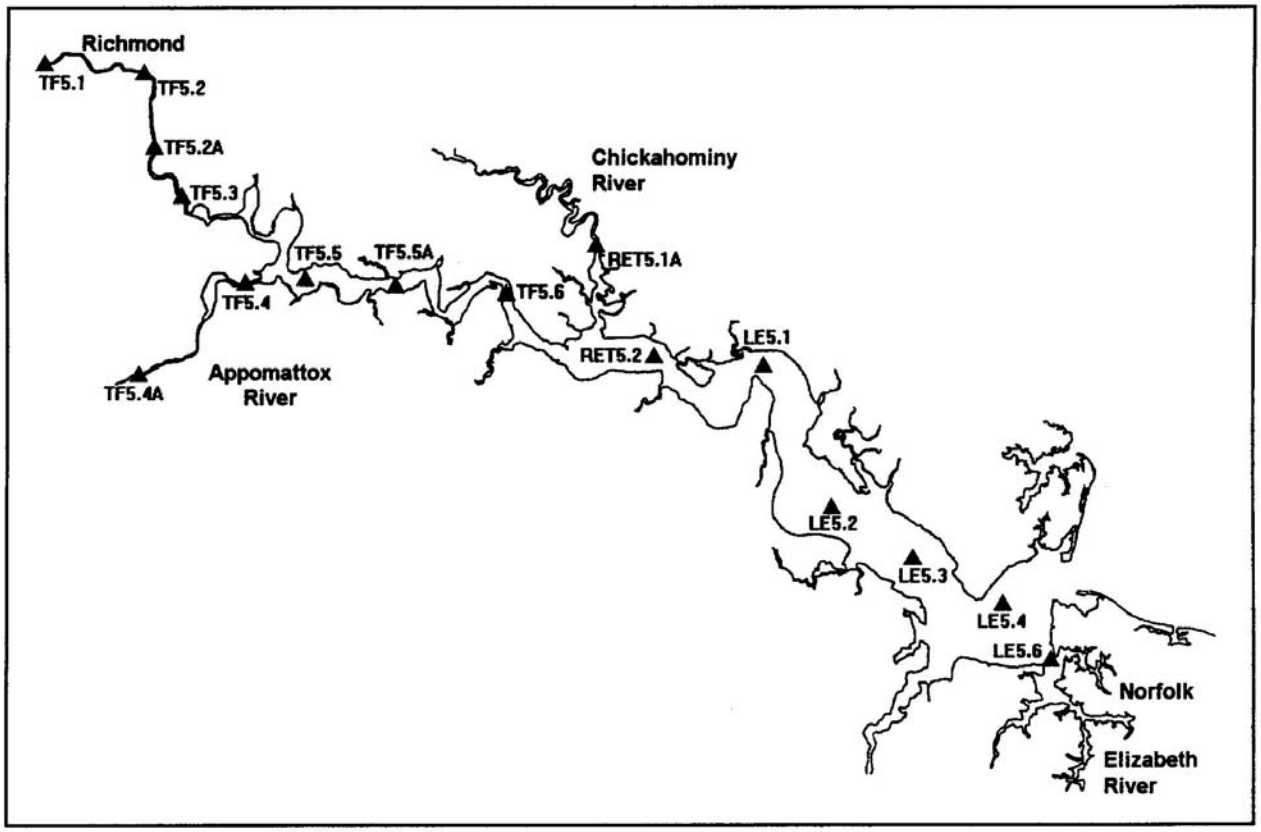

Figure III.12. Station location map.

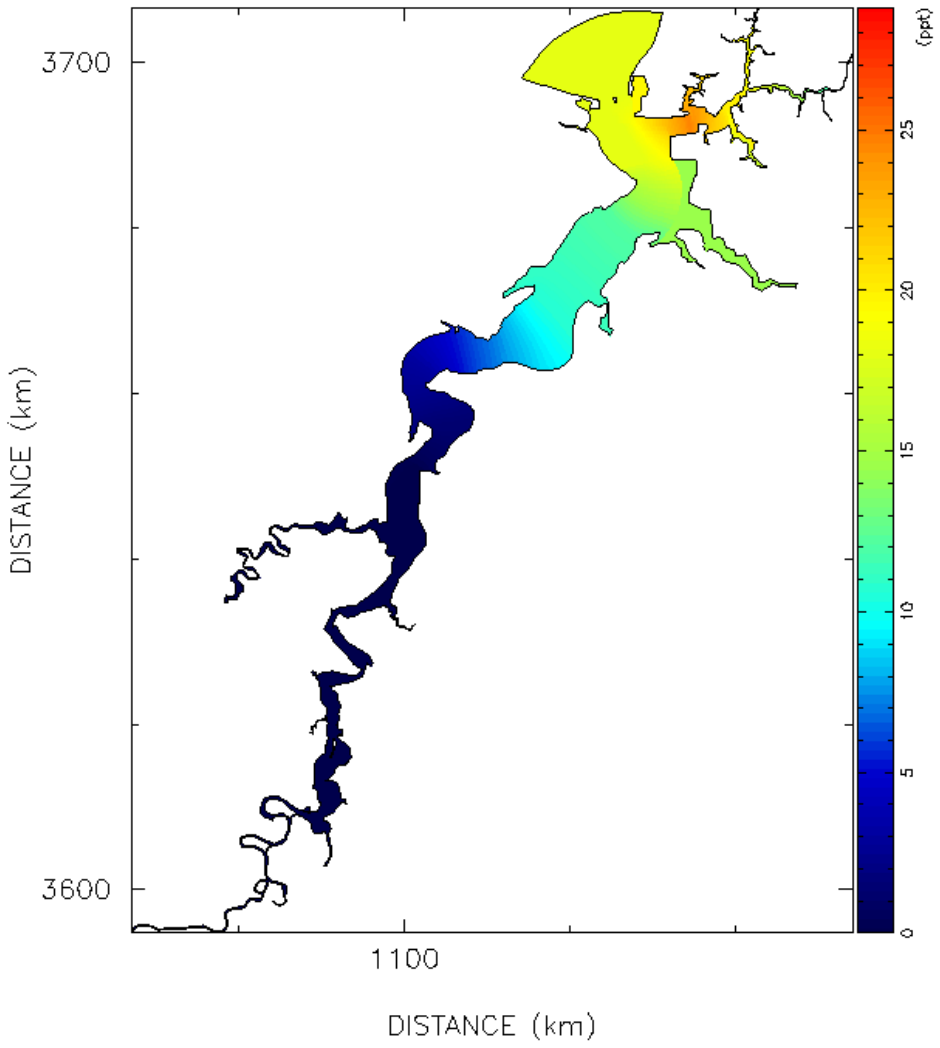

Figure III.13. Surface salinity for March, 2000 survey.

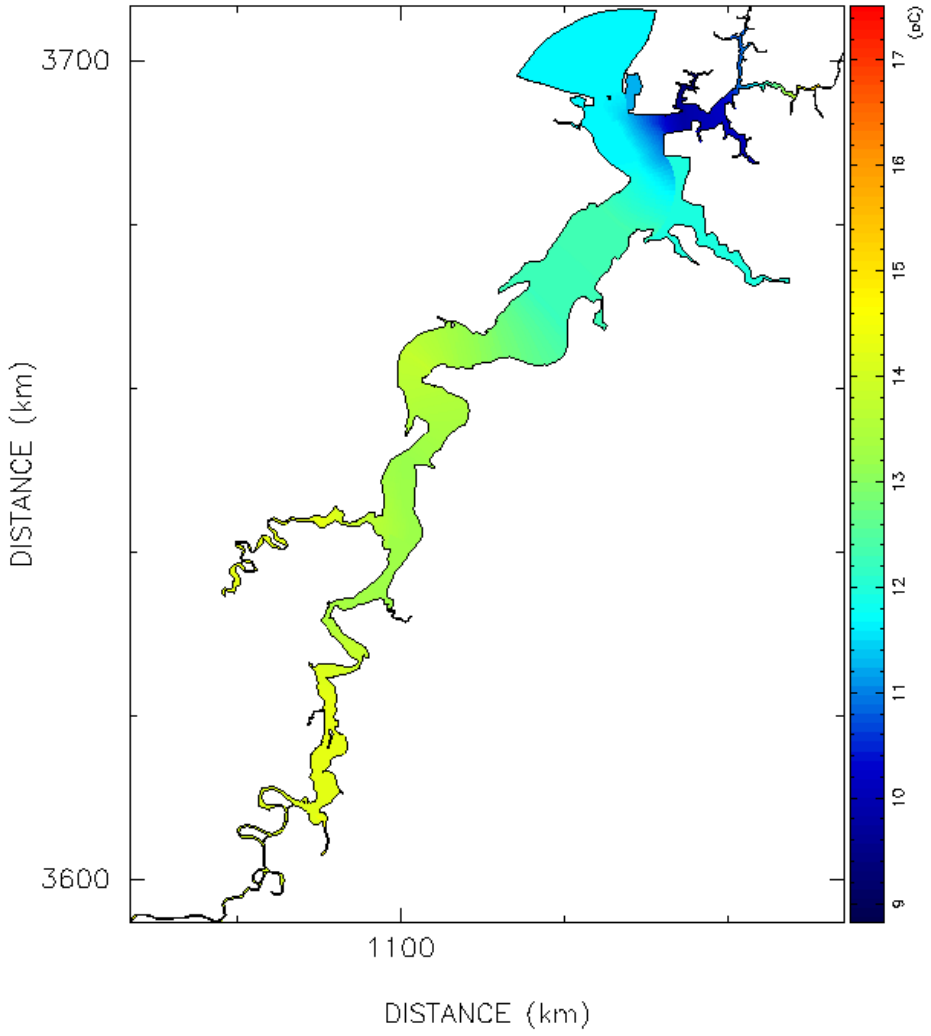

Figure III.14. Surface temperature for March, 2000 survey.

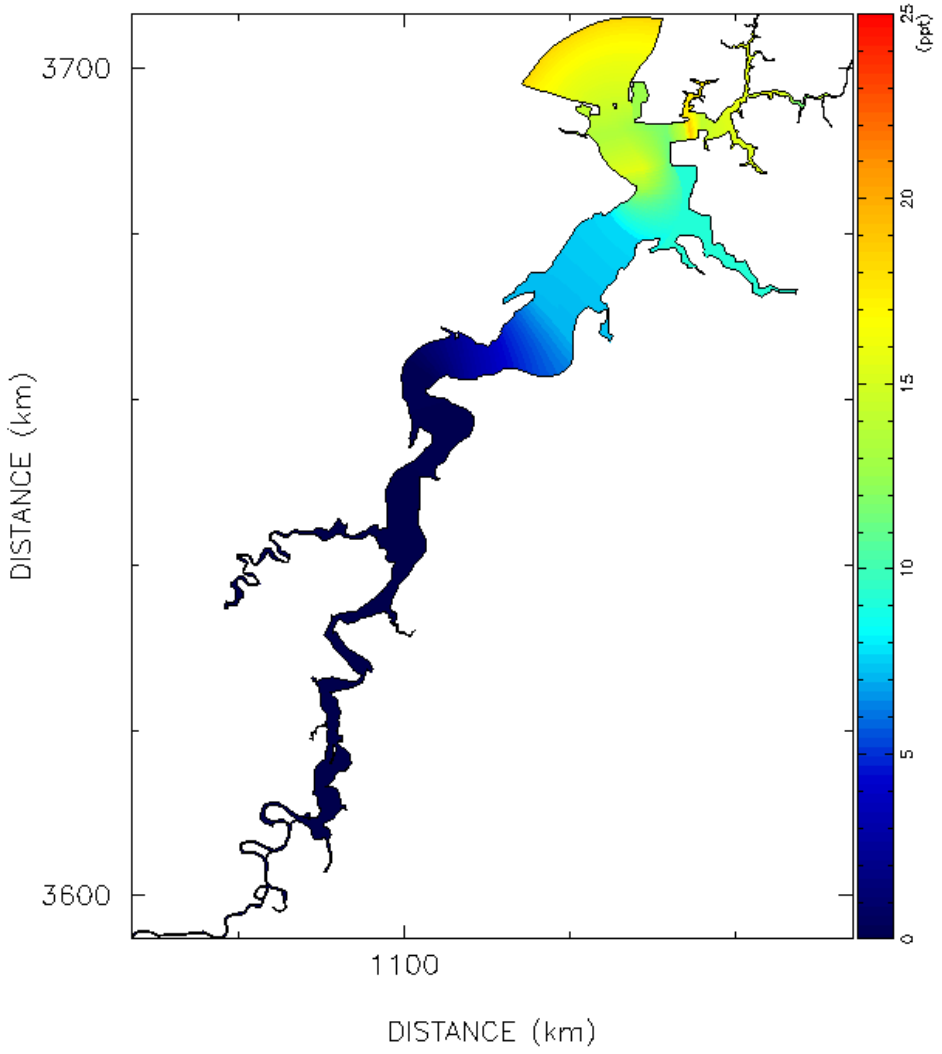

Figure III.15. Surface salinity for April, 2000 survey.

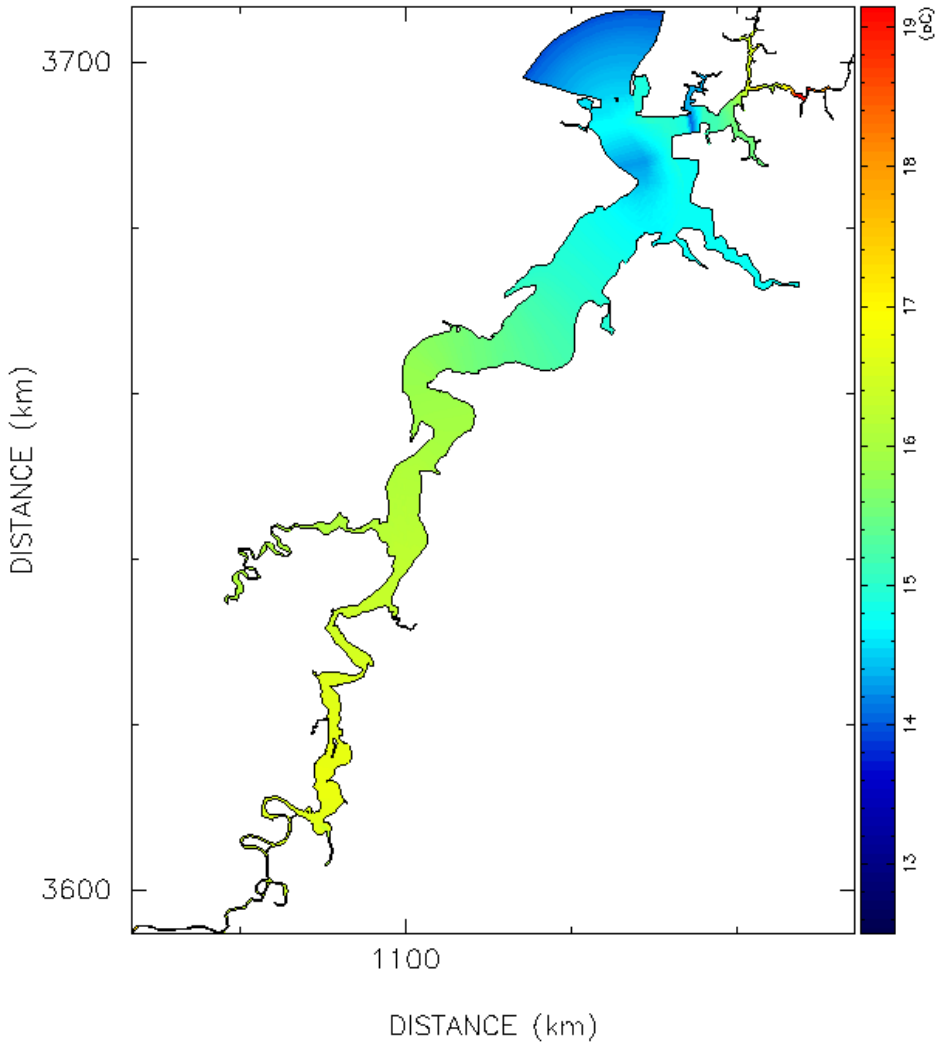

Figure III.16. Surface temperature for April, 2000 survey.

3. Freshwater Inputs - The flow rates of freshwater inputs used in the model simulations are estimated from discharge records at 4 gauging stations. The United States Geological Survey maintains one stream gauge each at a short distance upstream of tidal limit in the James, Appomattox, and Chickahominy Rivers, respectively. The discharge records at these gauges are multiplied by the ratio of the entire drainage area of each river (including the tidal portion) to that upstream of the gauging station. The resulting flow rates are input into the most upstream model cells of the respective rivers. The US Army Corps of Engineer measures the flows through the locks and spillway at the upstream end of Deep Creek, which drains the Dismal Swamp. This discharge is used, without adjustment, as input to the most upstream model cell in Deep Creek. There is no other gauging station in the Elizabeth River basin. The freshwater input from the Elizabeth River drainage area is estimated by multiplying that of the mainstem James River with the drainage area ratio. The total flow is then distributed to the heads of the Lafayette River, Eastern Branch, Western Branch, and Southern Branch according to their respective drainage areas. The drainage area for the mainstem Elizabeth River is added to that of the Southern Branch. The freshwater input through the locks at Great Bridge is negligible since both sides of the waterway are tidal (Neilson, 1975).

The magnitudes of freshwater inputs have little effect on the tidal fluctuations except during the period of very high river flows. Therefore the mean freshwater discharge is input only to the head of tide in the mainstem James River in the model simulation run for mean tide calibration. For the real time model calibration run simulating the period from April 24 to June 8, the measurements of daily discharges in the 4 gauging stations are adjusted and used for the inputs at the eight upstream model cells as described in last paragraph.

For the model scenario runs, the long-term mean freshwater discharges are used in the single variable runs. The inputs are: 234.0 cms (cubic meters per second) in the mainstem James, 46.9 cms in the Appomattox, 13.5 cms in the Chickahominy, 2.6 cms in the Deep Creek, 0.53 cms in the Lafayette River, and 0.88, 0.94, and 1.66 cms in the Eastern, Western, and Southern Branch of the Elizabeth River, respectively. The historical scenario runs use the actual measurements of daily discharges at the 4 stations to generate 8 time series input files for input to the same 8 upstream model cells in the single variable runs.

4. Meteorological Data - Water temperature is not simulated in this model study. The only meteorological data required is surface wind, which induces wind-driven circulation and enhances vertical mixing. The hourly wind speed and direction measured at Sewells Point are obtained from the NOAA web site and processed into a time series file of 4-hour averages. The corresponding data sets are then used in real time model calibration run and historical scenario runs.

IV. MODEL CALIBRATION AND VERIFICATION

The model has been calibrated with the hydrodynamic conditions in the mainstem James River in previous studies (Boon et al. 1999). For the purpose of this study, the calibration and verification of the refined grid model were focused on the Elizabeth River and the Hampton Roads area surrounding its entrance. After verifying that the refined-grid model produced the same tidal elevations at locations along the mainstem James River as the original coarse grid model, the model calibration/verification for the Elizabeth River was accomplished with a two-step process. First the model was calibrated with respect to the tidal wave propagation along the Elizabeth River under the mean tide condition. Then the model was run to simulate the prototype conditions for the period April 24 to June 8, 2000 during which field data (see Chapter III) are available for comparison. The model was verified with respect to surface elevation induced by both astronomical and meteorological tides, current velocities (tidal and residual), and salinity distributions.

A. CALIBRATION FOR MEAN TIDE

The astronomical tide accounts for about 80 % of the energy of water surface fluctuations in Hampton Roads and the Elizabeth River. Therefore an accurate reproduction of the tidal wave propagation in the Elizabeth River is of the utmost importance. Furthermore, once the model is calibrated with respect to astronomical tide, a minimum of additional adjustment is required for calculation of surface elevation and current velocity. Tidal propagation in an estuary is controlled by river geometry and frictional dissipation of energy. With river geometry and tidal range at the open boundary given, we used the distribution of tidal range as a function of distance along the Elizabeth River to calibrate against the roughness height, the model parameter for bottom friction. During the process of roughness height adjustment, minor refinements of the geometric representation by the model were performed from time to time.

Since the river inflows have no significant effect on tidal fluctuation in the lower part of estuary except during periods of extreme high flows, river inflow at Richmond was the only input used for this model calibration run. A long-term mean of 234 cms was specified at the upriver boundary of the model domain. A single tidal constituent, M2, was specified as the boundary condition at the open boundary out of the James River mouth. Since there is no tidal record at the open boundary, an inverse approach was adopted. The tidal amplitude at the open boundary was adjusted until the model produced a tidal amplitude at Sewells Point exactly half the average tidal range measured by NOAA over a 19-year tidal epoch, 75.5 cm (see Figure III.2). Figure IV.1 compares the calibrated model result of the tidal ranges with those derived from field data. The field data at some stations cover only a duration of the order of one month. The tidal ranges derived from these short-term records have been adjusted to long-term mean by simultaneous comparison with data at Sewells Point (see Chapter III, SectionB.1). The figure shows a generally increasing trend as the tide propagates upriver. The root mean

square difference between model simulation and field observation is 2.03 cm, or less than 3 % of the observed tidal range.

Figure IV.2 compares the lag times of high and low tide phases as the tide propagates upriver. It is to be noted that the time lags are very small throughout the system because of the small size of the system, compared to the tidal wave length, and the standing wave characteristics of the tide. The small discrepancies between model results and field observations may be attributed to two factors. The model calibration run used a M2 tide while the field observations include all tidal constituents. Furthermore, the observation records have a time period on the order of only one month.

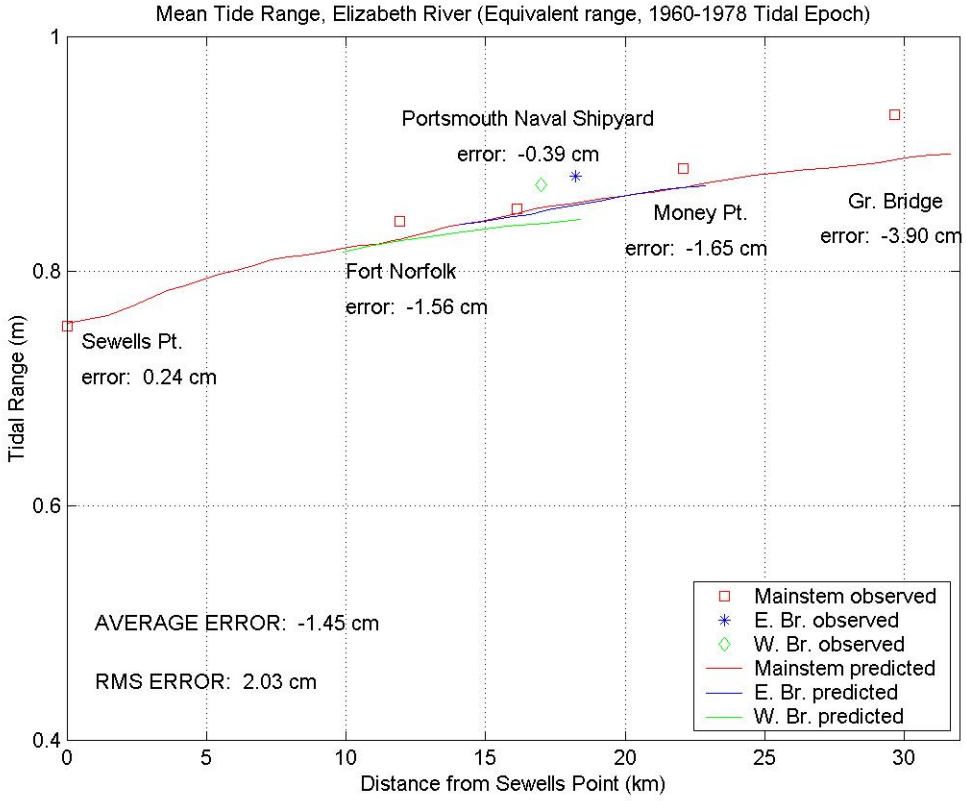

Figure IV.1. Mean Tide Range Calibration for the Elizabeth River.

B. MODEL VERIFICATION THROUGH REAL TIME SIMULATION

Verification of the model's predictive capability is regarded as an independent check on model calibration. In the present study, field data sets were collected of different variables in a time period from April to June 2000. These data sets include time series of surface elevation, current, and salinity at selected locations in the Hampton Roads and Elizabeth River regions of the model domain (see Chapter III, Section B). In addition, repetitive, quasi-synoptic measurements of the current and salinity fields were made covering selected regions within the Elizabeth River (see Chapter III, Sections C and D).

The model's real time simulation of the prototype conditions encompassed a time period from April 24 to June 8, 2000. The model was first spun up for 24 days before any salinity calculation was initiated. During the spin-up period, the salinity field observed on April 24 was imposed as a time invariant condition. The model simulation then continued until June 8, with freshwater inputs specified at 3 locations in the James River and 5 locations in the Elizabeth River (see Chapter III, Section E.3). The water surface elevation for the open boundary condition was derived from data measured at CBBT (Chesapeake Bay Bridge Tunnel). The measured time series data were delayed for half an hour to account for the time lag between CBBT and the model boundary. No adjustment on surface elevation was made. The boundary condition for salinity was constructed by interpolation of S4 current meter data measured near the model boundary (Chapter III, Section B.3). The model simulated (predicted) data were compared with measured data for the corresponding locations and time periods. The results of these comparisons are given below.

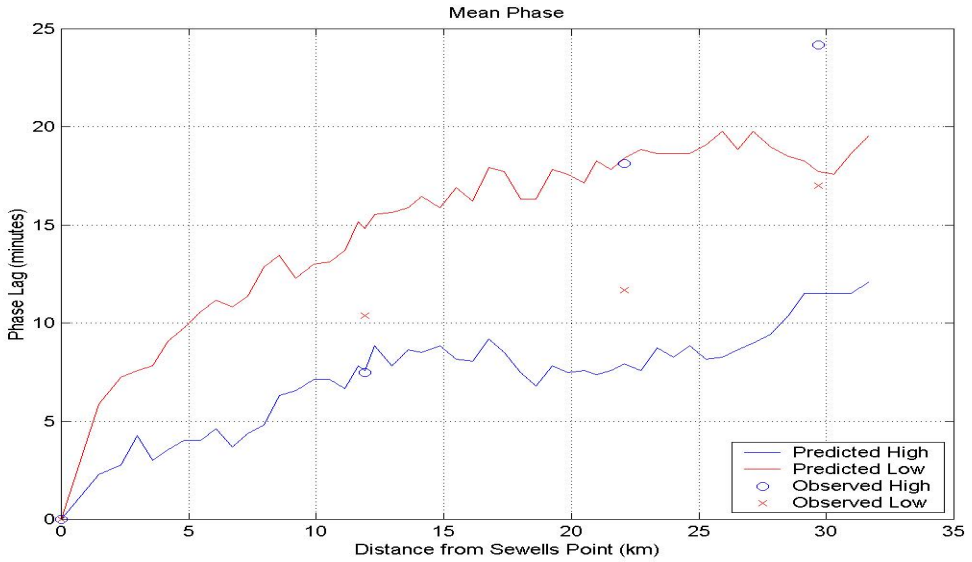

Figure IV.2. Comparison of observed and predicted high and low tide phases.

1. Surface Elevation Time Series - The model predicted time series water surface elevation was compared with observed data at Sewells Point, Fort Norfolk, Money Point, Great Bridge, Eastern Branch and Western Branch over the periods when data were available. All comparisons are characteristically the same; Figures IV.3 and IV.4 show two examples of the comparisons. The top panel of each figure compares the real time predicted and observed data. They consist of both the astronomical tide and those induced by meteorological and hydrological forcing. To isolate the non-tidal signal, both the predicted and observed time series data were passed through a low-pass filter with a 36-hour cutoff period. The low frequency time series signals were compared in the middle panel of each figure. It is noted that the model reproduced the meteorological event accurately (note the set-up around Julian day 151). The lower panels of the figures plot the difference between the predicted and observed real time data. To illustrate the level of

agreement in more detail, plots of observed versus predicted tides for Julian Day 112-127 at Sewells Point, Fort Norfolk, Eastern Branch, Money Point and Great Bridge are presented in the Appendix to Chapter IV, Section B.1 (Figures 1-5).

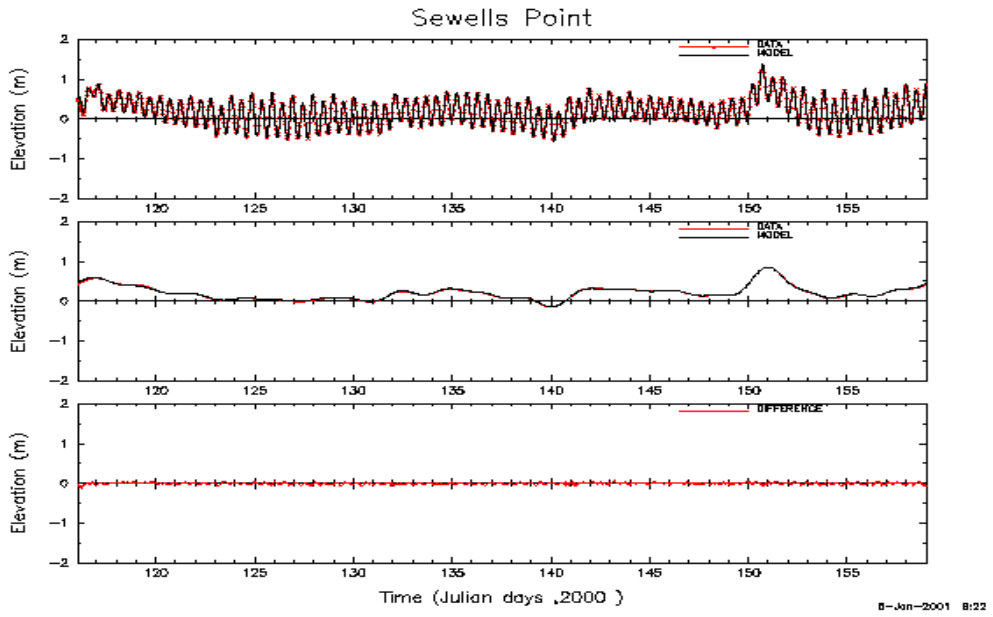

Figure IV.3. Simulated water level variation at Sewells Point.

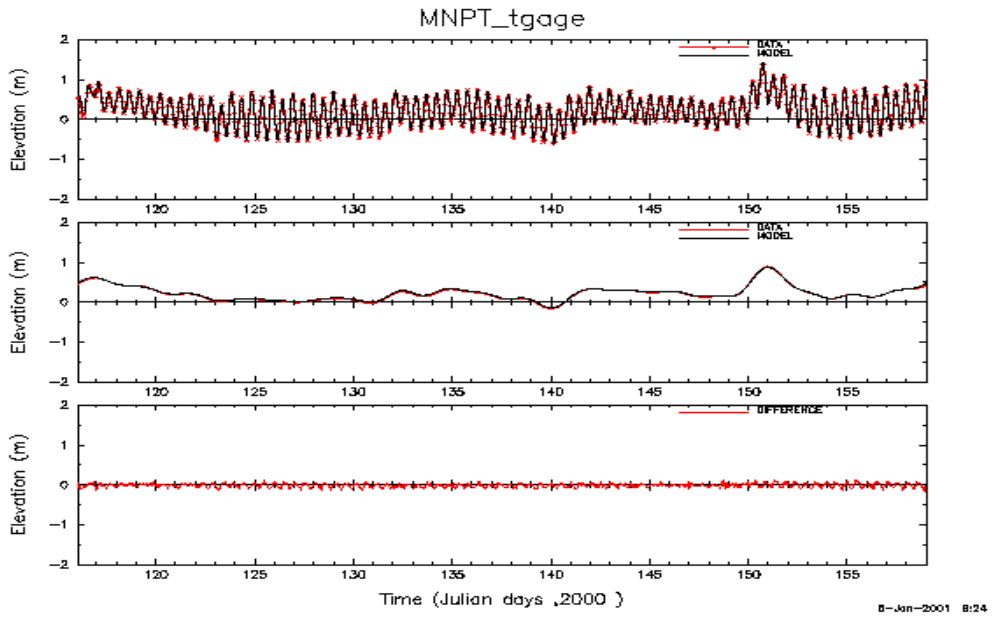

Figure IV.4. Simulated water level variation at Money Point.

2. Current Time Series - *Predicted* versus *Measured* principal axis current curves can be compared within the same time period to check amplitude, phase and mean value agreement. However, rather than visually comparing one curve with another plotted on a common set of axes (speed versus time), a quantitative comparison is made possible by plotting predicted speed against measured speed on a point-by-point basis herein termed a *P-M plot*. To provide insight into the error involved in tidal current predictions, we first consider the comparison of two simple sine waves, each with a period of 12.42 hours. These sine waves represent two hypothetical time series of predicted and measured current speed oscillating around a mean of zero. If the curves are identical (i.e., have the same amplitude, phase, and mean value), the points from the curves will plot along a straight line with 1:1 slope. If the phase of one of the current sine waves changes by 20 minutes, other parameters remaining equal, the P-M plot will appear as illustrated in Figure IV.5. Further change in phase will cause the ellipse of points in this figure to deviate further from the 1:1 line of perfect prediction, eventually degenerating into a circle when the two sine waves are a quarter cycle (90 degrees) out of phase.

In addition to phase lag, P-M plots also have the ability to display deviations between predicted and measured current amplitude. Assuming that the phase lag between sine curves remains at 20 minutes while the predicted current amplitude is reduced by 10 percent (the P-M means remaining at zero), the resulting P-M plot will appear as illustrated in Figure IV.6. The ellipse shown in this figure is identical to that shown in Figure IV.5 except that the major axis of the ellipse has rotated slightly about the centroid located by the P-M means. One or both of the P-M mean values could be changed as well, which would simply shift the centroid of the ellipse up or down, right or left.

Error Estimation - P-M plots formed with actual current data typically show a scatter of points that fall within the ellipse outline, suggesting linear regression as a means for deriving model error estimates. Statistical error estimates are made using linear regression models of predicted (Y) versus observed (X) current values from a given time series. Error is defined as the difference $(Y_i - Y_{ir})$ where Y_i is the ith model predicted current value and Y_{ir} is the ith value obtained from regression of Y on X. Assuming sinusoidal variation and no measurement error, $Y_{ir} = mX_i + b$ is the least squares regressor for differences due to phase error. Differences in this case appear as deviations from a line of best fit to the data. Regression estimates for differences due to total error (phase, amplitude and mean) use $Y_{ir} = X_i$ (m=1, b=0). Differences in this case appear as deviations from the 1:1 line of perfect prediction. Standard error is the root-mean-square (RMS) value of either difference for a sample of size n (i=1..n).

James River Bridge – Certain current calibration data previously reported for the James River HEM-3D model (Boon et al., 1999) are included in this report for completeness. Two examples prepared with model calibration data collected near the James River Bridge's main channel are shown in Figures IV.7 and IV.8. Using the regression methods described above, RMS error estimates of 6.66 cm/s and 4.25 cm/s were determined at surface and bottom, respectively, that are attributed solely to P-M phase differences. Utilizing deviations from the 1:1 line of perfect prediction, additional RMS error estimates of 9.86 cm/s and 5.07 cm/s at surface and bottom were made that are attributed

to amplitude and phase differences combined. P-M means were not significantly different from zero in these examples.

The plot of the James River Bridge surface current data (Figure IV.7) reveals a slight counter-clockwise rotation of the best-fit axis relative to the 1:1 axis. The resulting greater spread of points over the predicted current axis indicates that the model slightly over-predicts the surface current in this region. The best-fit axis in Figure IV.8 does not evidence any rotation suggesting that the model neither over-predicts nor under-predicts the bottom current at this location.

Craney Island Reach - The ADP current data obtained from the Craney Island Reach in the present study is shown first as a time series of the surface current in Figure IV.9. As noted in this figure, the model in general tends to under-predict the measured surface current with the greatest difference appearing in the ebb extremes. Figure IV.10 contains a P-M plot showing a clockwise rotation of the ellipse axis as well as an ebb-directed leftward shift in the data centroid (blue circle intersected by dashed best-fit line). The former indicates a slight under-prediction of surface tidal current. Concerning the latter, a centroid shift (negative measured current mean of approximately 6 cm/s combined with a near-zero predicted current mean) suggests that a small non-tidal surface current is present at this location that the model does not account for. The *total* RMS error attributable to both effects (11.20 cm/s) is more than the total RMS error found at the James River Bridge site (9.86 cm/s) but the RMS phase error (6.19 cm/s) is slightly less than that at the James River Bridge site (6.66 cm/s).

Because the ADP current sensor could only be installed at the eastern margin rather than within the main shipping channel, the lowest level obtainable for current measurement corresponds to the middle depth (model layer 4) in the Craney Island Reach. The resulting P-M plot is shown in Figure IV.11 with an RMS phase error of 6.42 cm/s and a total RMS error of 9.53 cm/s. The orientation of the ellipse axis is similar to that of the surface plot and shows that the model also under-predicts the current at the middle depth position. In contrast to the surface plot, both the predicted and measured current means are approximately zero at middle depth.

Hospital Point – The S4 current meters installed at Hospital Point were located on a very narrow shelf margin between the shore and the south side of the navigation channel in the Port Norfolk Reach. As with the Craney Island Reach, only model layers 6 and 4 corresponding to the surface and middle layer channel depths were represented. A time series plot (Figure IV.12) revealed an unusual situation with measured currents considerably larger than model predicted currents at peak value points. The measured sinusoidal currents are unusual here because of their extreme peakedness requiring higher than normal frequencies to represent; i.e., higher than the semi-diurnal and quarter-diurnal tidal frequencies that ordinarily account for most of the variance in coastal water level. NOAA Tidal Current Tables, in fact, list predicted maximum flood and ebb speeds of 0.4 knots (20 cm/s) and 0.3 knots (15 cm/s), respectively, for nearby stations Pinner Point (no. 5166) and Berkley, Southern Branch (no. 5181). These speeds are consistent

with the model-predicted speeds shown in Figure IV.12 but are considerably below the peak-measured speeds that briefly exceed 50 cm/s at certain times in this same figure.

P-M plots for Hospital Point are presented in Figures IV.13 and IV.14. As noted above, the maximum range for measured current speeds is considerably larger than for model predicted speeds, both in the surface layer (Figure IV.13) and in the middle layer (Figure IV.14). This fact accounts for the relatively large RMS total errors of 12.17 cm/s and 10.49 cm/s, respectively, for the surface and middle layer at Hospital Point. However, the RMS phase errors of 8.54 cm/s and 4.67 cm/s, respectively, for the surface and middle layers are more in line with current observations elsewhere. Mean speeds at both depths are close to zero. The RMS errors obtained at James River Bridge, Craney Island Reach, and Hospital point are summarized in Table IV.1.

Assessment of current verification in the Elizabeth River – The RMS errors presented in Table IV.1 apply to an individual sample of the modeled current randomly drawn from the total population of current values (i.e., the series of principal axis current values predicted at half-hour intervals for approximately 67 tidal cycles). These error estimates are therefore the appropriate ones to consider in model evaluations that utilize the complete series of current values (e.g., volume transport calculations within the Elizabeth River). We note that the Total RMS error increases proceeding into the Elizabeth River.

In addition to the above, there is sometimes a need to examine a certain current phase such as slack water or the peak value of the current (e.g., ship navigation). A visual inspection of the P-M current series shown in Figure IV.9 (Craney island Reach) and Figure IV.12 (Hospital Point) raises concern that the modeled current extremes frequently under-predict the measured current extremes at these locations. Pre- and post-deployment calibration data for our current meters were carefully checked and ruled out instrument error as the source of this discrepancy. Yet, as noted above, NOAA current table predictions for maximum flood and ebb current agreed closely with the modeled current extremes. Since NOAA current table predictions are based on the astronomical tide wherein all variation occurs at known tidal frequencies, we concluded that the discrepancies noted must occur primarily at non-tidal frequencies. Least squares harmonic analysis was then applied to the measured current data to examine both tidal and non-tidal current components in more detail.

Harmonic analysis of measured current – Tidal harmonic analysis involves the least squares (LS) fitting of tidal harmonic constituents to a time series of water level or components of current velocity such as the principal axis component. A predicted series based on these constituents is referred to as the *astronomical* tide or current. To fit the principal axis current at Craney Island Reach and Hospital Point, we chose 14.5-day current series recorded at 0.5-hour intervals beginning April 25, 2000 (Julian Day 116) and fitted them with nine tidal constituents (M_2, S_2, N_2, K_1, O_1, M_4, S_4, MS_4, M_6). The resulting astronomical current series are presented in Figures IV.15a, IV.15b, IV.16a, and IV.16b. Figures IV.15a and IV.16a show the complete measured and fitted series for the Craney Island Reach and Hospital Point, respectively. At Craney Island Reach the fitted series accounted for 88.2 percent of the measured series variance compared to 74.9

percent at Hospital Point. Adding other tidal constituents such as M_8 to the analysis did not significantly lower the proportion of variance unaccounted for in independent series. To observe the variations in greater detail, a 3-day window beginning on Julian Day 122 is shown for these stations in Figures IV.15b and IV.16b. The 3-day segments contain residual curves (difference between measured and fitted curves) that are considered to be estimates of the non-tidal current at Craney Island Reach and Hospital Point.

Examining tidal and non-tidal currents at Craney Island Reach and Hospital Point, it is apparent that large- and small-scale meteorological and hydrological 'events' exert their influence at both stations but without much consistency and amid considerable local variability. This is illustrated by an event appearing near the end of Julian Day 122 in Figures IV.15a and IV.16a. At this point in time the measured ebb current briefly increased by approximately 10 cm/s relative to the peak ebb of the fitted current at both stations. However, comparing the non-tidal (residual) current at both stations (green curves in Figures IV.15b and IV.16b), it is difficult to recognize a common event amid the numerous oscillations present at relatively high frequencies (periods less than 3 hours with no apparent phase coherence). Similarly, an even stronger event appearing in the measured ebb current near the middle of Julian Day 124 at Hospital Point does not appear at all at Craney Island Reach.

Finally, analysis shows that model predicted currents agree very well with astronomical currents independently predicted using nine tidal harmonic constituents obtained from LS-fitting of our observed current series. An example based on the surface current at Hospital Point is shown in Figures IV.17a and IV.17b. We note in Figure IV.17a that the model predicted current on Julian Day 121 contains a low-frequency (sub-tidal) meteorological event that cannot be represented at the tidal frequencies of the predicted astronomical current. Elsewhere, the agreement at tidal frequencies is quite good.

The conclusion drawn from the above analysis is that a minor but still significant portion of the variation in current speed observed within the Elizabeth River occurs at supra-tidal frequencies where it exhibits a behavior more random than deterministic. Accordingly, the ability of hydrodynamic or similar types of deterministic models to fully replicate this particular behavior is limited.

Table IV.1 – Summary of RMS Error for Predicted Principal Axis Currents at Fixed Locations

Location	RMS Error (Phase)	RMS Error (Total)
James River Bridge (surface)	6.66 cm/s	9.86 cm/s
James River Bridge (bottom)	4.25 cm/s	5.07 cm/s
Craney Island Reach (surface)	6.19 cm/s	11.20 cm/s
Craney Island Reach (middle)	6.42 cm/s	9.53 cm/s
Hospital Point (surface layer)	8.54 cm/s	12.17 cm/s
Hospital Point (middle layer)	4.67 cm/s	10.49 cm/s

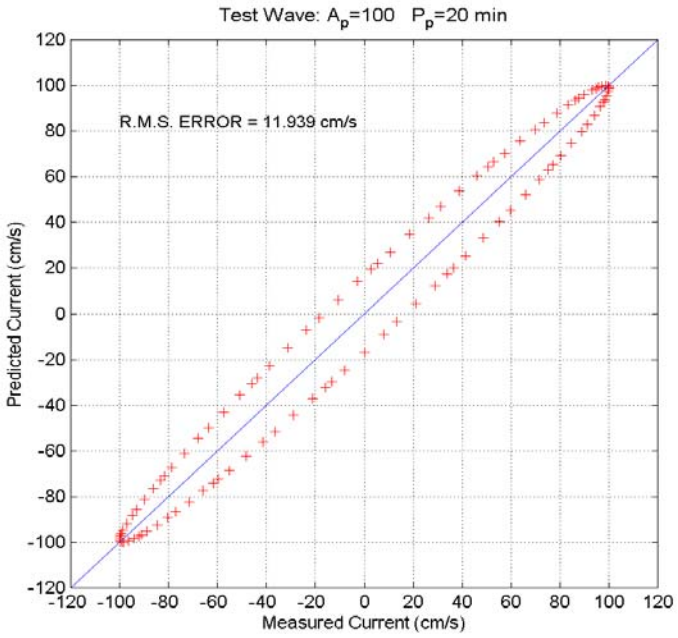

Figure IV.5. Predicted versus measured current, hypothetical example for two sine waves with a 20 minute phase difference.

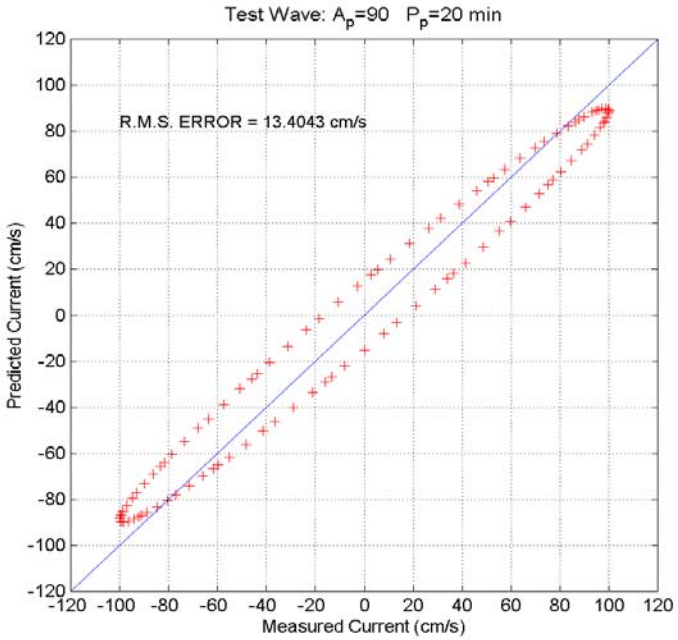

Figure IV.6. Predicted versus measured current, hypothetical example with 20 minute phase difference and 10% amplitude reduction.

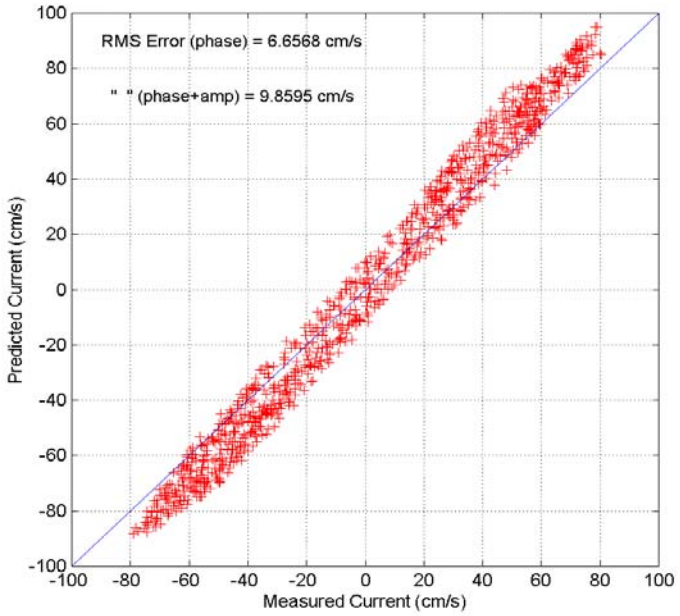

Figure IV.7. Predicted versus measured surface current, James River Bridge (Figure 14 from Boon et al., 1999).

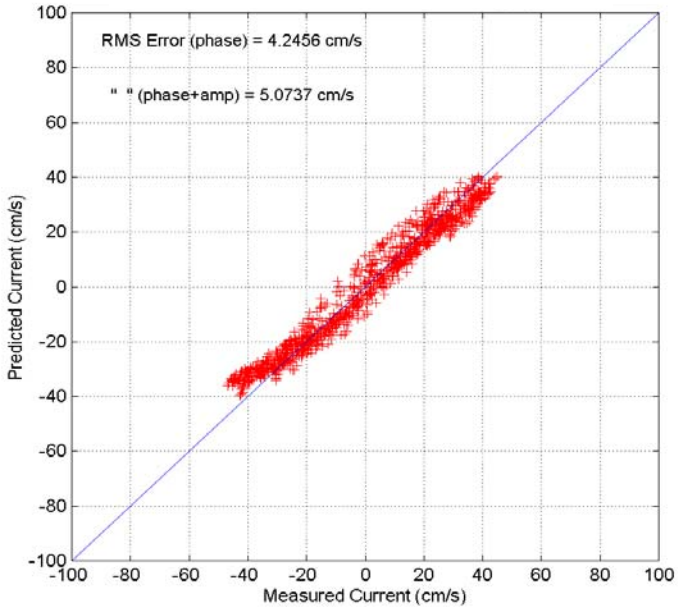

Figure IV.8. Predicted versus measured bottom current, James River Bridge (Figure 15 from Boon et al., 1999).

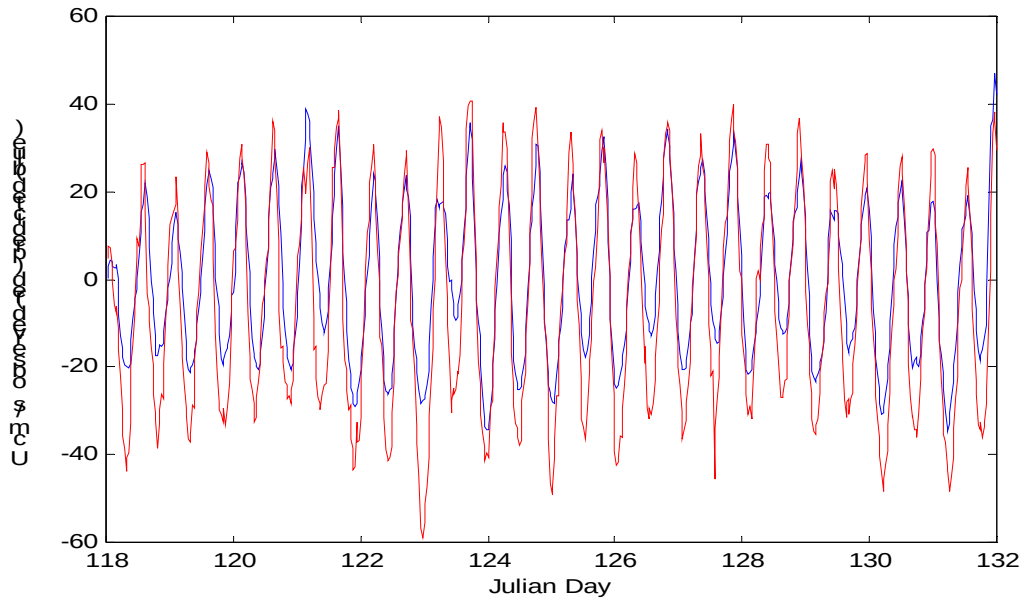

Figure IV.9. Craney Island Reach ADP station - time series of principal axis current in the surface layer (model layer 6), predicted (blue) and measured (red).

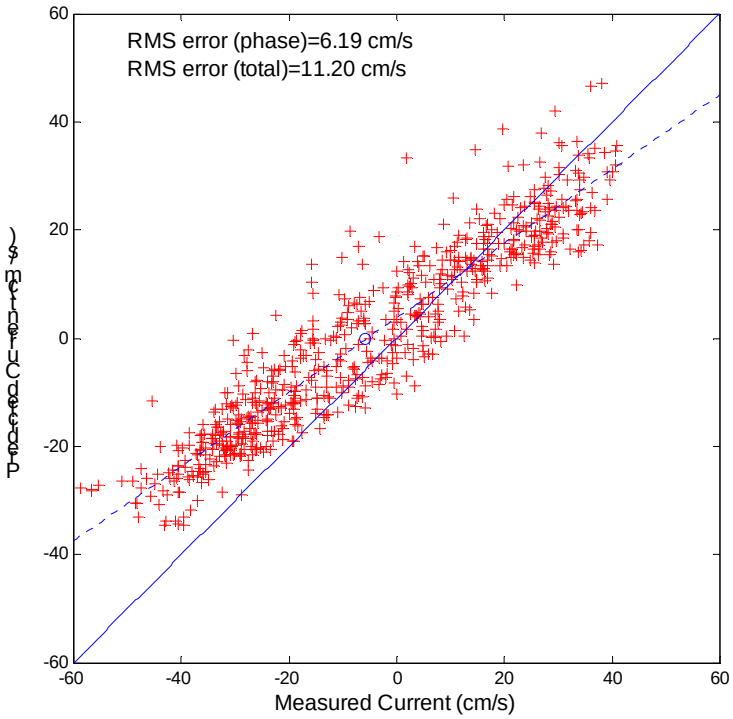

Figure IV.10. Craney Island Reach ADP station - predicted versus measured current, surface layer (model layer 6).

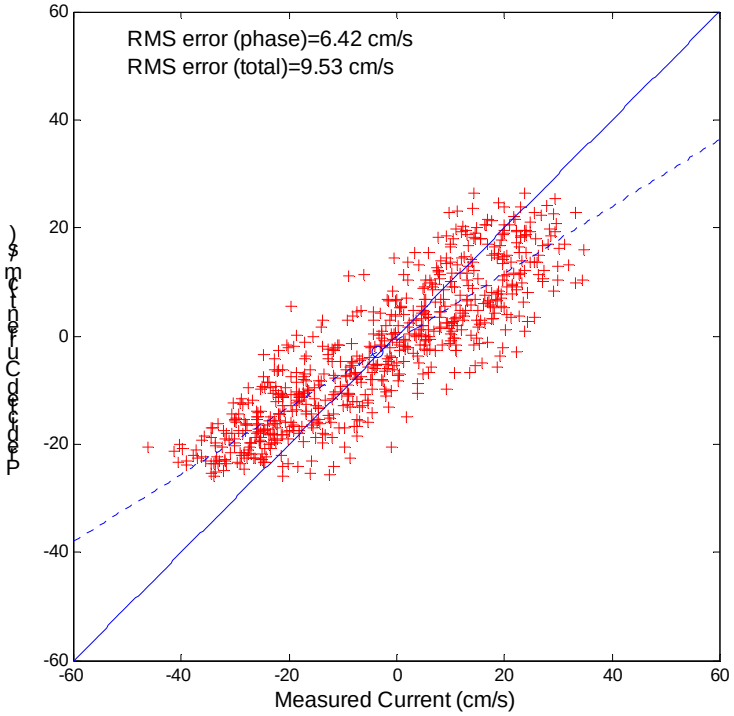

Figure IV.11. Craney Island Reach ADP station - predicted versus measured current, middle layer (model layer 4).

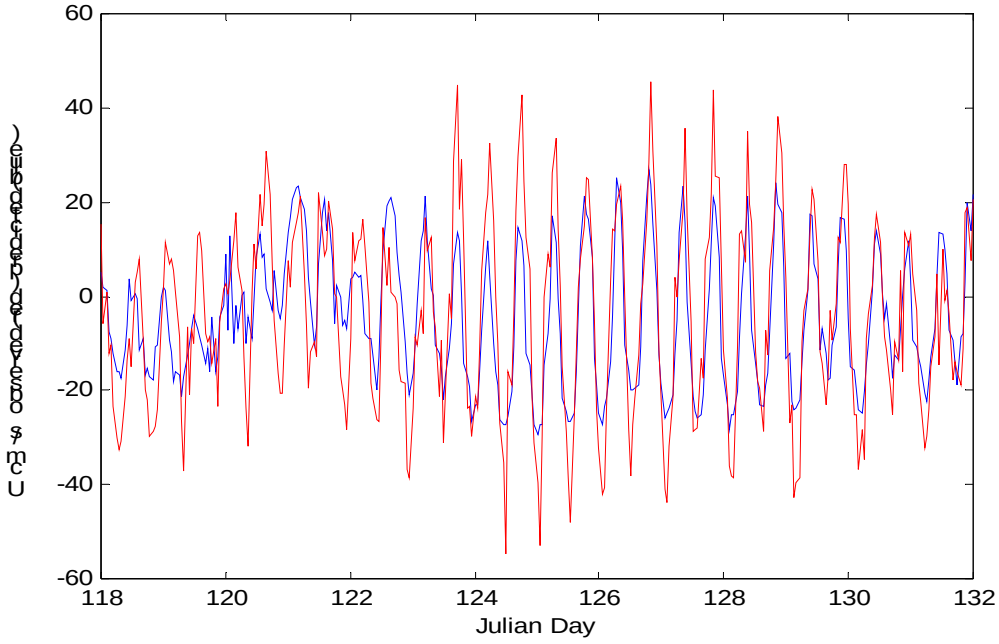

Figure IV.12. Hospital Point S4 station - time series of principal axis current in the surface layer (model layer 6), predicted (blue) and measured (red).

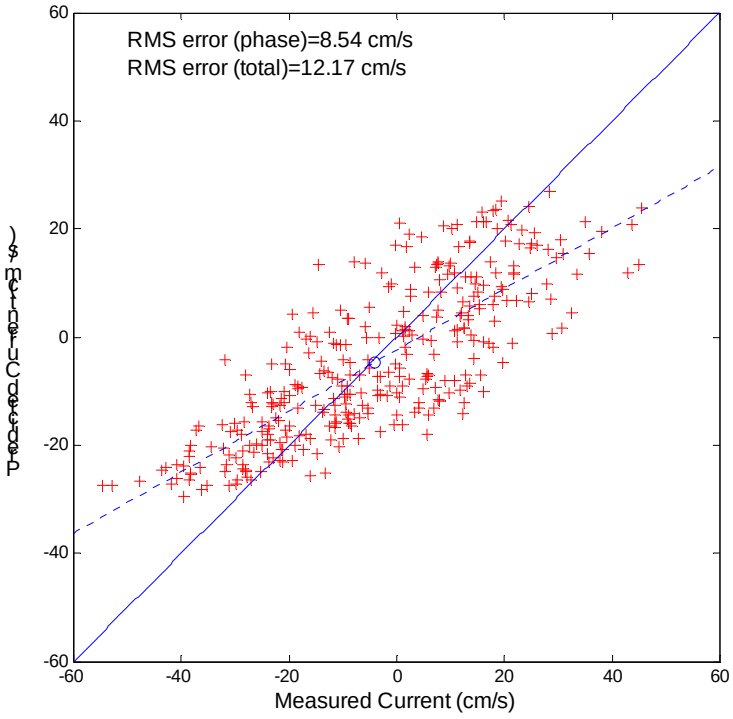

Figure IV.13. Hospital Point S4 station - predicted versus measured current, surface layer (model layer 6).

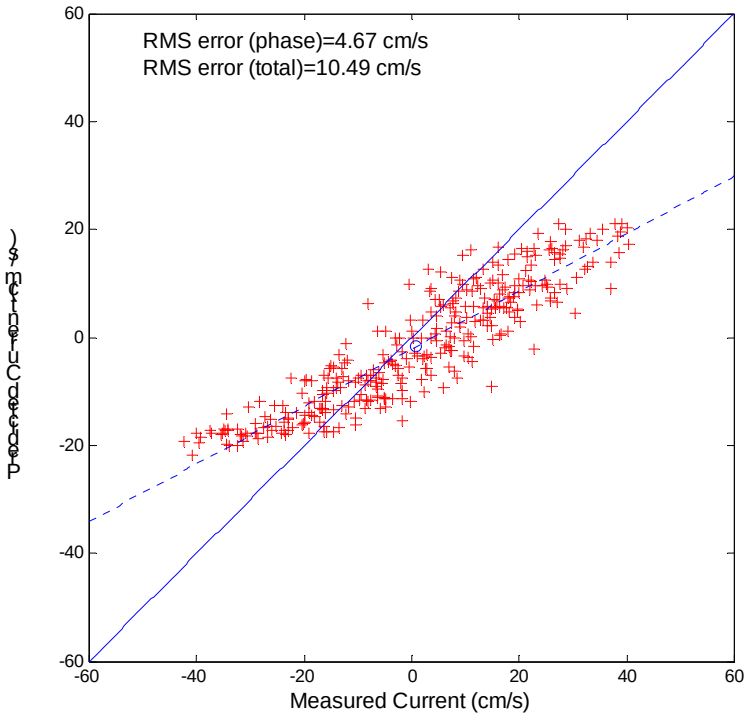

Figure IV.14. Hospital Point S4 station - predicted versus measured current, middle layer (model layer 4).

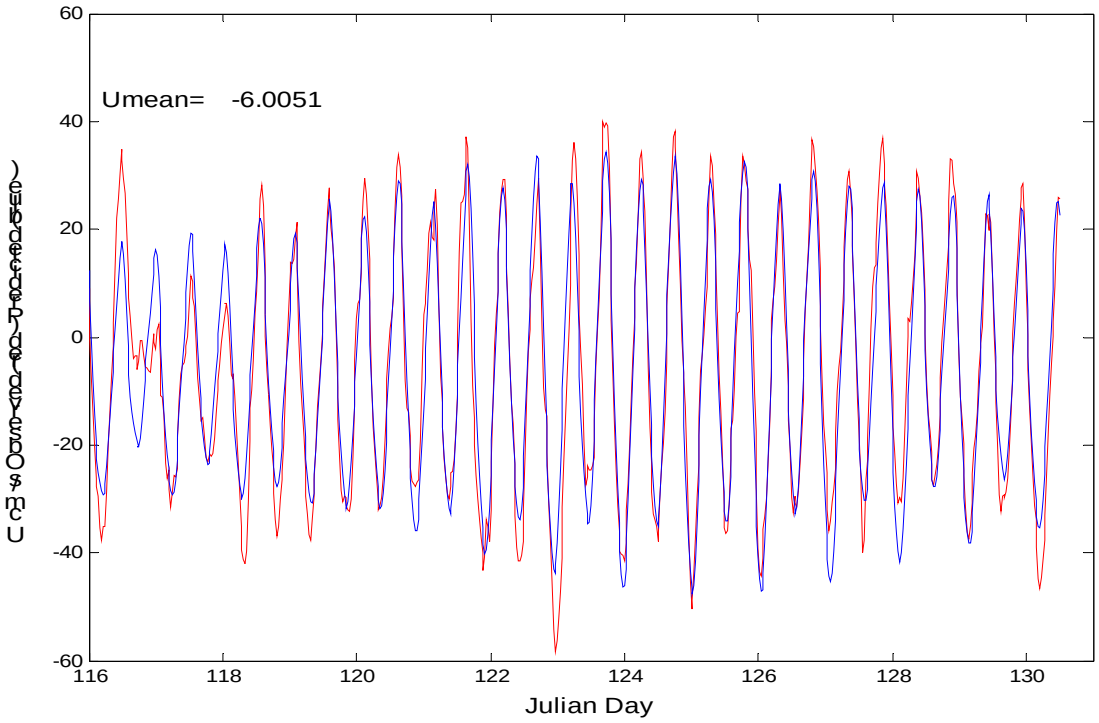

Figure IV.15a. Measured (red) and LS-fitted (blue) surface current, Craney Island Reach.

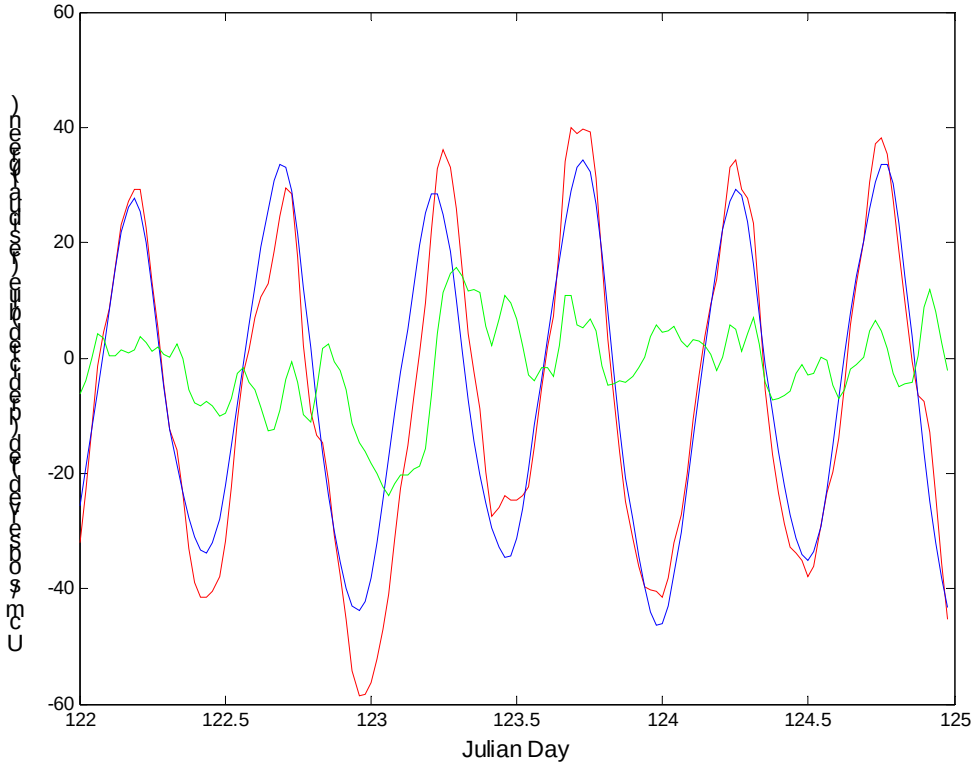

Figure IV.15b. Measured (red), LS-fitted (blue), and residual (green) surface current, Craney Island Reach.

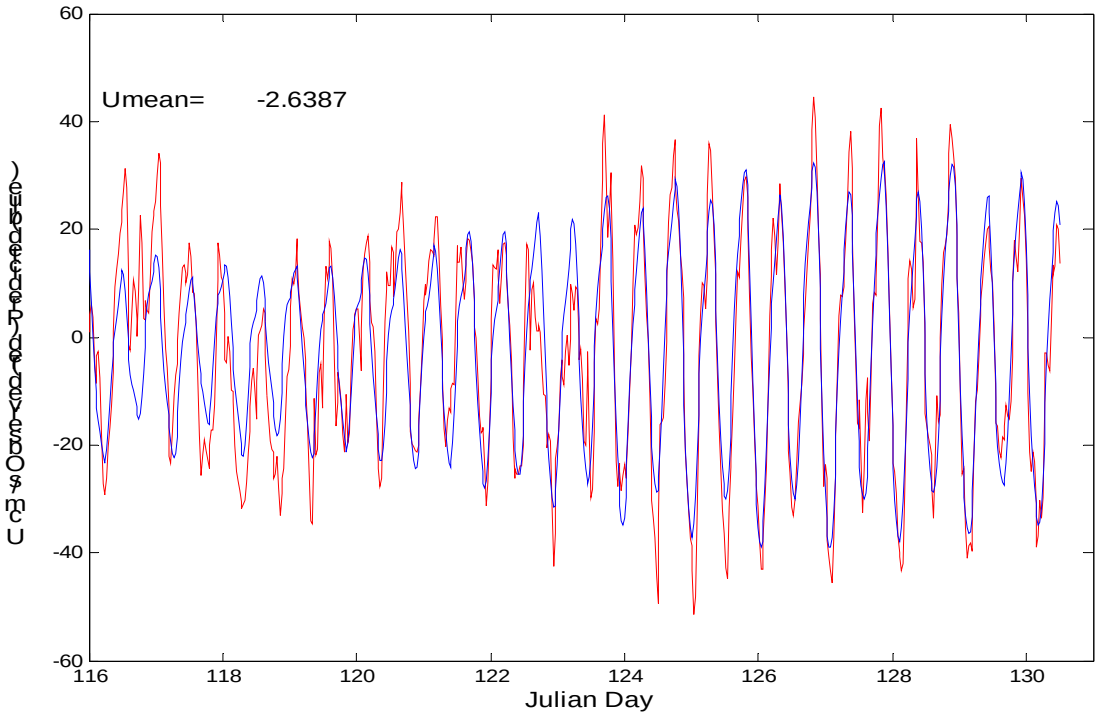

Figure IV.16a. Measured (red) and LS-fitted (blue) surface current, Hospital Point.

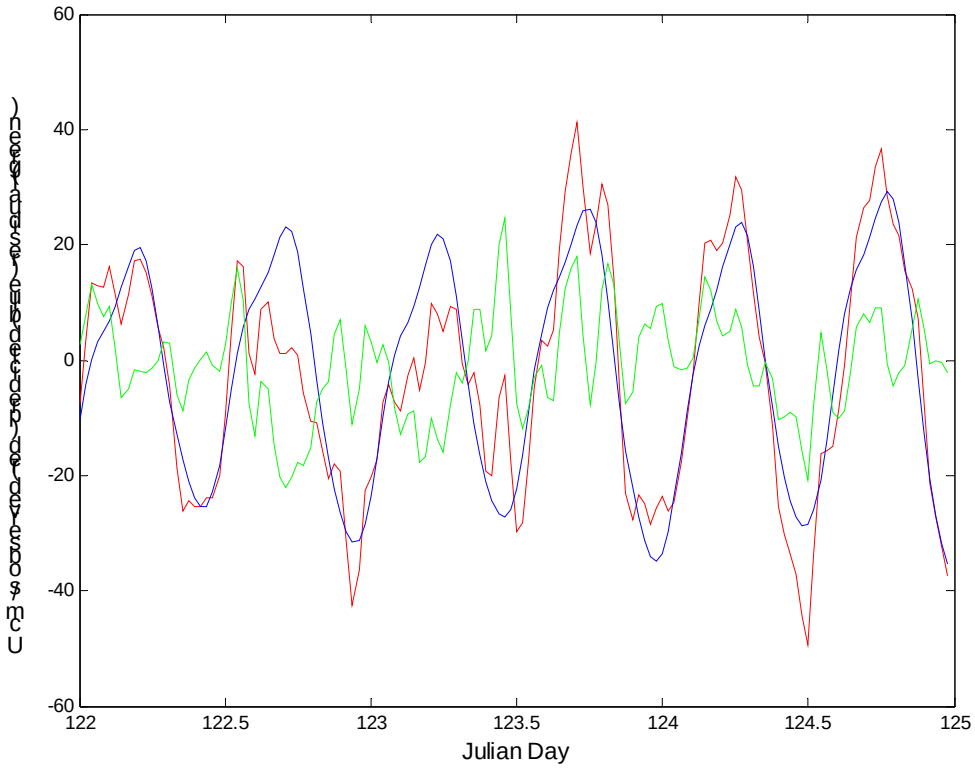

Figure IV.16b. Measured (red), LS-fitted (blue), and residual (green) surface current, Hospital Point.

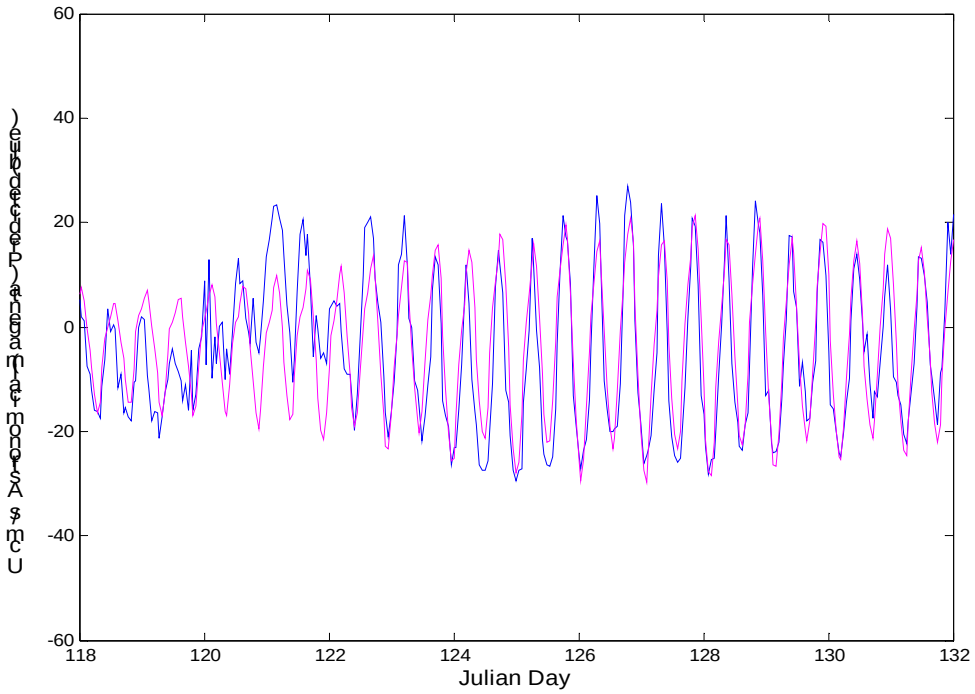

Figure IV.17a. Model predicted (blue) and astronomical (magenta) surface current, Hospital Point.

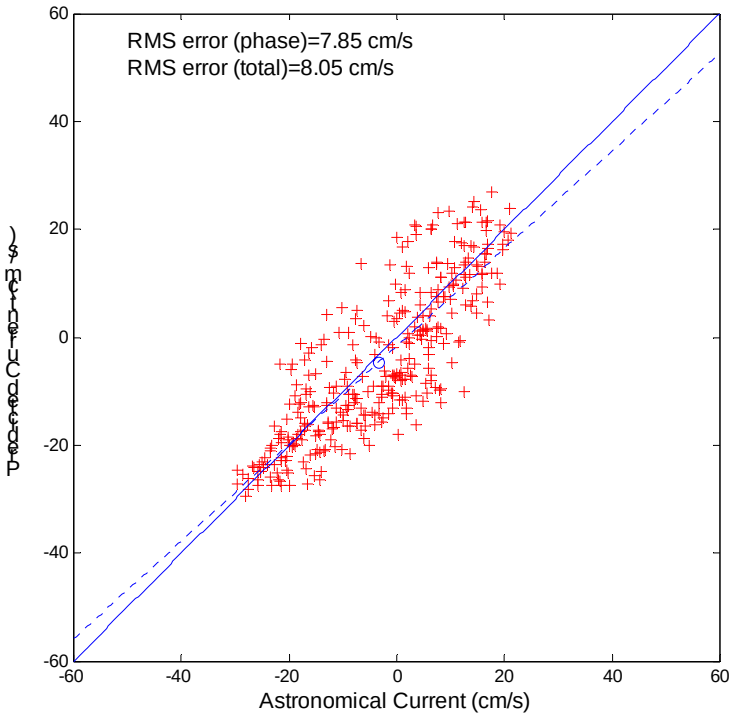

Figure IV.17b. Model predicted versus astronomical surface current, Hospital Point.

3. Residual Current – Averaging a time series of current speed at a fixed point over a semidiurnal tidal period of 12.42 hours (or a diurnal tidal period of 24.84 hours) yields the non-tidal or residual current at that point. Diurnal averaging is preferable in real time applications, especially during tropic tides when diurnal inequalities are present in both tides and currents. Residual currents, along with instantaneous currents, are used in this study to examine important circulation features depicted in spatial flow fields. When the spatial distribution of the residual current is of interest, vector averaging is performed on the u (east-west) and v (north-south) horizontal velocity components rather than simple averaging of u_m, the principal axis or maximum variance component. Assuring adequate simulation of residual current fields is an important step in model verification.

Spatial distributions of current are inherently more difficult to measure and verify than current time series. Spatial representation requires either a fixed array of simultaneously operating sensors or a moving sensor that can rapidly sample a section of the three-dimensional current field at suitable intervals of time and space. As described in Chapter II, Section C, we used the latter approach to obtain quasi-synoptic measures of the flow field at approximately hourly intervals in the Lambert Bend section of the Elizabeth River channel.

Figure IV.18a contains an example of the horizontal residual current measured at the surface in Lambert Bend during a diurnal tidal period (May 16-17, 2001). In addition to a large eddy-like feature rotating counter-clockwise southwest of Lamberts Point, this figure shows a well-organized ebb residual flow of about 8 cm/s exiting through the channel area immediately adjacent to Lamberts Point. Ebb residual flow at the surface is consistent with classical two-layer estuarine circulation. However, cross-section A-A' shown in Figure IV.18b (located by dashed line in Figure IV.18a) does not contain the corresponding classical picture of flood residual flow appearing near the bottom of the channel. Instead, a 5 cm/s flood residual flow appears at mid-depth with the area of greatest strength offset to the west of the channel. A weak ebb residual current of about 2 cm/s appears near the bottom of the channel. These measurements suggest a departure from the ideal two-layer system moving toward a three-layer system in Lambert Bend.

Comparing the measured three-dimensional flow in Lambert Bend with model predicted flow in the same section indicates broad general agreement with the patterns just described. Figure IV.19a shows both the central, counter-clockwise 'eddy' and 8 cm/s ebb residual current predicted in the surface layer at Lamberts Point, corresponding to the measured surface residual flow in Figure IV.18a. In Figure IV.19b, the middle layer (model layer 3) clearly contains horizontally extensive flood residual currents on the order of 5 cm/s offset to the west of the main channel. Figure IV.19c contains weak ebb residual flow on the order of 2-3 cm/s in the bottom layer within the channel.

Two points require emphasis in connection with model predicted residual currents. Residual current magnitudes are generally small in comparison to instantaneous current magnitudes and may therefore appear to be severely limited by the RMS error estimates presented in Table IV.1. However, because of the averaging process used to derive residual current values, the standard error associated with them is reduced accordingly

(by approximately 1/5 if n=24). Secondly, the HEM-3D model uses 'sigma' coordinates to represent the vertical dimensions of the six layers beneath each cell in the horizontal grid. This means that the bottom current velocities representing model layer 1 in Figure IV.19c appear at the same *relative* depth in the water column but clearly do not appear at the same *absolute* depth below the water surface. Thus the characterization of predicted residual flow at maximum depth in layer 1 applies only to the main navigation channel rounding Lambert Bend and its continuation along the north shore of the Port Norfolk Reach. Predicted flood residual currents shown west of the channel in Figure IV.19c correspond to the flood residual currents shown at middle depths in Figure IV.18b.

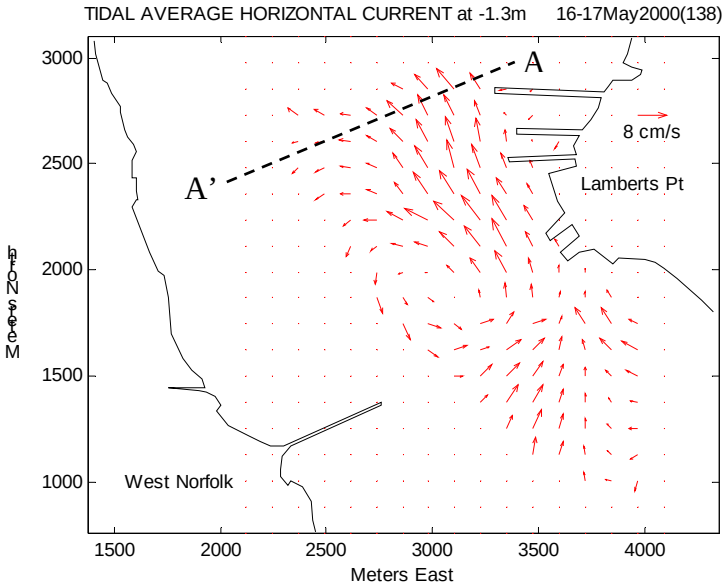

Figure IV.18a. Plan view of measured residual current, surface layer, Lamberts Point.

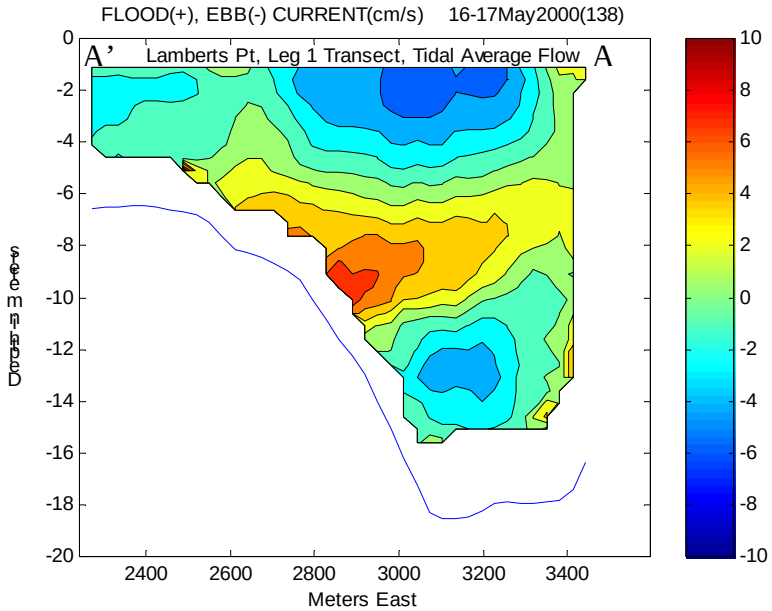

Figure IV.18b. Residual current in cross-section, transect A-A', Lamberts Point.

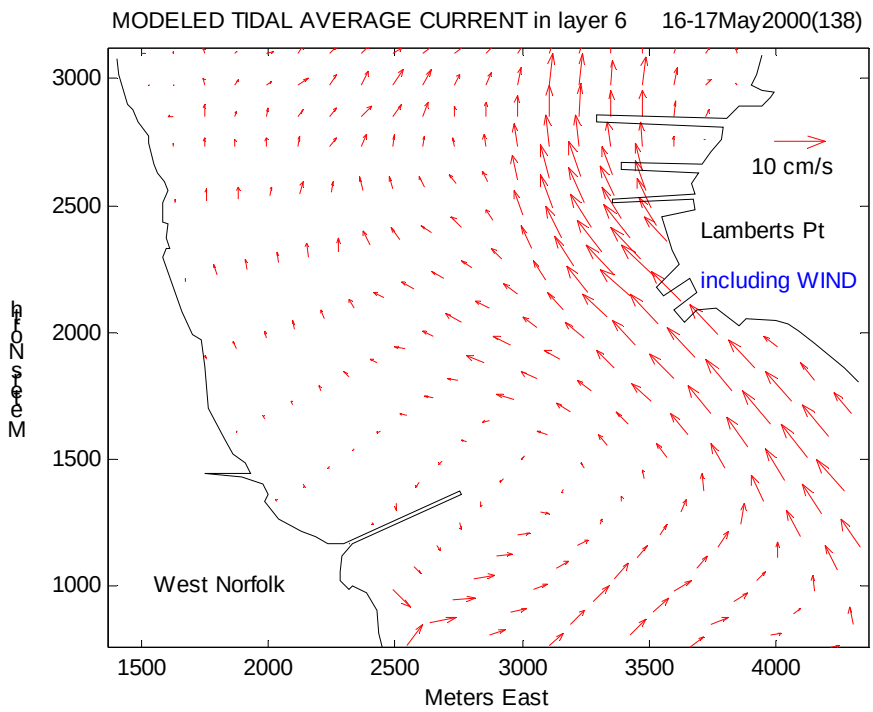

Figure IV.19a. Plan view of predicted current field, surface layer, Lamberts Point.

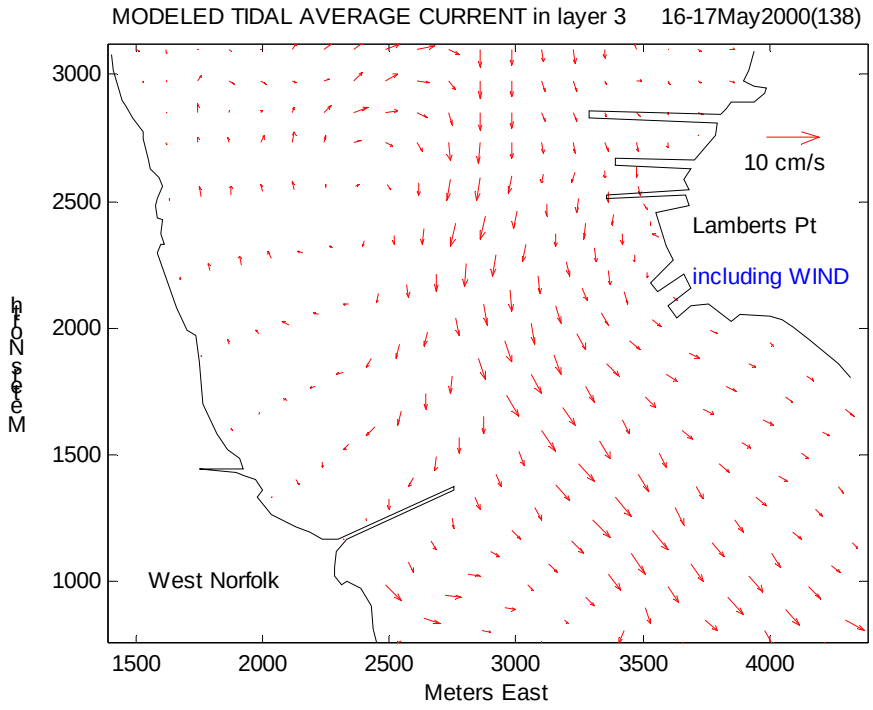

Figure IV.19b. Plan view of predicted residual current, middle layer, Lamberts Point.

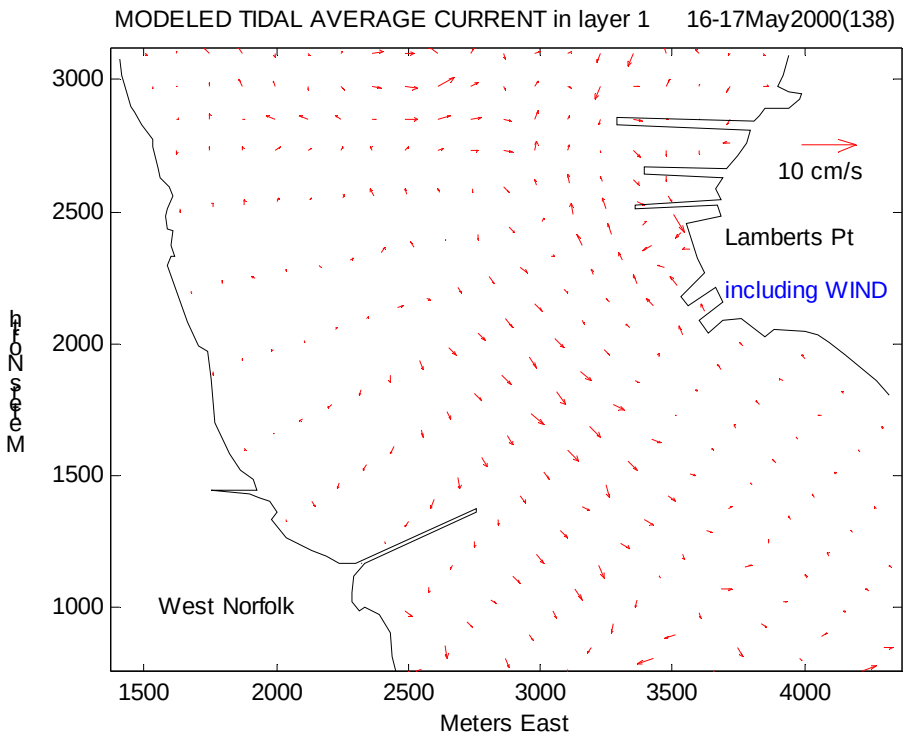

Figure IV.19c. Plan view of predicted residual current, bottom layer, Lamberts Point.

4. Salinity Distribution – In an estuary, fresh water originating from inland river sources encounters the salt water coming from the ocean to produce the longitudinal salinity distribution. The baroclinic pressure gradient generated from the fresh water at the upstream of the estuary and the salt water at the downstream then serves as the major driving force for the gravitational circulation, in which the fresh water flows seaward while the salt water flows landward. When fresh water overlays salt water, the vertical profile of salinity exhibits stratification as a result of the density difference from surface to bottom. The turbulent mixing induced by forces such as tide, wind, surface waves, internal waves and internal current shear, on the other hand, tends to homogenize property gradients in the water column both in the vertical and the horizontal direction. This turbulent activity thus counter-acts the stratification produced by the buoyancy forces.

Each estuary has its own shoreline, topography, hydrology, freshwater inputs and turbulent mixing pattern; the salinity distributions are thus different from one another. By carefully examining the salinity pattern, the characteristics of the estuary can be revealed and classified. Salinity is also an excellent natural tracer due to its conservative property. All in all, salinity is an important parameter for estuarine hydrodynamics and thus is selected to assess the performance of the estuarine hydrodynamic model. In this study, salinity time series and spatial distributions are presented from prototype measurement and compared with the model simulation results.

During the months of April – October, 2000, VIMS conducted a total of 12 slack water surveys in the Elizabeth River (see Chapter III, Section D for a detailed presentation of the monitoring program results). Among them, there are 5 consecutive weekly surveys during the months of May and early June, 2000, in which both good data coverage and data quality were obtained. We have chosen to use the salinity data measured during this intensive period to compare with the modeled results in detail. In each of these surveys, data from 31 stations were collected; 20 in the main-stem and 11 in the tributaries. The station map is shown in Figure III.10 and the observation results are shown in Figures 2-6 in Appendix to Chapter III, Section D.1, for May 1 (Julian day 122), May 8 (Julian day 129), May 15 (Julian day 136), May22 (Julian day 143), and June 7 (Julian day 159). Since the Elizabeth River is relative short in length (the propagation of tidal phase from the mouth to the head only takes about 25 minutes), the survey vessel was unable to catch the same tidal phase all the time when measuring the salinity. For this reason, caution needs to be taken when interpreting the survey data. Nevertheless, the data exhibit rich information and reveals key phenomena characterizing the Elizabeth. Several important points are summarized as follows:

(1) Both the spatial and time series plots in the Elizabeth River show an alternately stratified and de-stratified salinity pattern over the course of this 5 week period. During stratified conditions, the salinity difference from the surface to the bottom can reach as much as 10 ppt while during destratified conditions the salinity difference could be reduced to as low as1-2 ppt. It appears that the de-stratified condition generally coincides with large tidal ranges (> 2.5 feet) while the stratified condition coincides with smaller tidal ranges (< 2.5 feet). For example, May 8 and June 7, both exhibit de-stratified conditions, and both of their tidal ranges are well over 2.5 feet, nearing 3.0 feet (see Figures IV.20 and IV.21). In contrast, May 1, 15 and 22 exhibit stratified conditions, which coincide with small tidal ranges below 2.5 feet. In other cases, we also found that wind forcings, particularly those from the northwest direction, can significantly reduce the stratification in the lower James and Elizabeth.

(2) Somewhat counter-intuitively, a reverse surface salinity gradient was observed several times in the mouth region of the Elizabeth during the intensive survey period. By ‘reverse surface salinity gradient’, we mean that the observed surface salinity at the mouth of the Elizabeth is actually lower than the salinity inside the Elizabeth River. This reverse salinity gradient phenomenon, when it occurs, penetrates to about 5-10 km inside the Elizabeth and ends near Lamberts Point. In accompany with the reverse salinity, there is a relative homogeneous surface salinity zone just upstream of the salinity reverse region. The reverse salinity phenomena in the Elizabeth has not been reported in the literature, but it was documented in Baltimore Harbor where fresh water originated from the Susquehanna River to the north can intrude into the Harbor and generate the three-layered circulation. In the James/Elizabeth River system, we suspect that during the freshet period in March - May the James River may have provided excess fresh water from upstream that was carried into the Elizabeth mouth, thus producing a reversed salinity gradient. However, the reverse salinity pattern appears to be transient in nature, rather than as a steady phenomena.

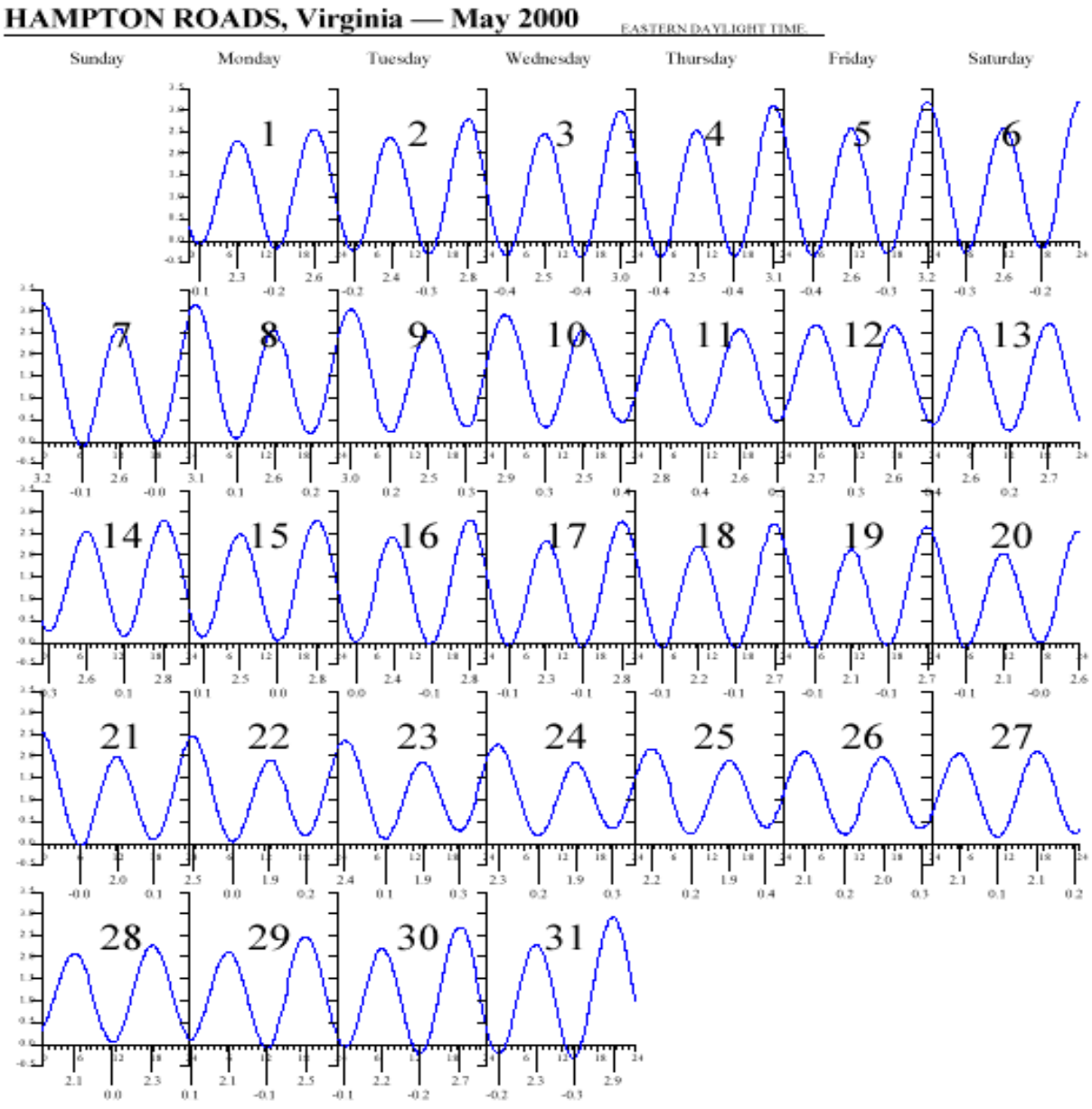

Figure IV.20. Predicted tidal height in feet above mean low water.

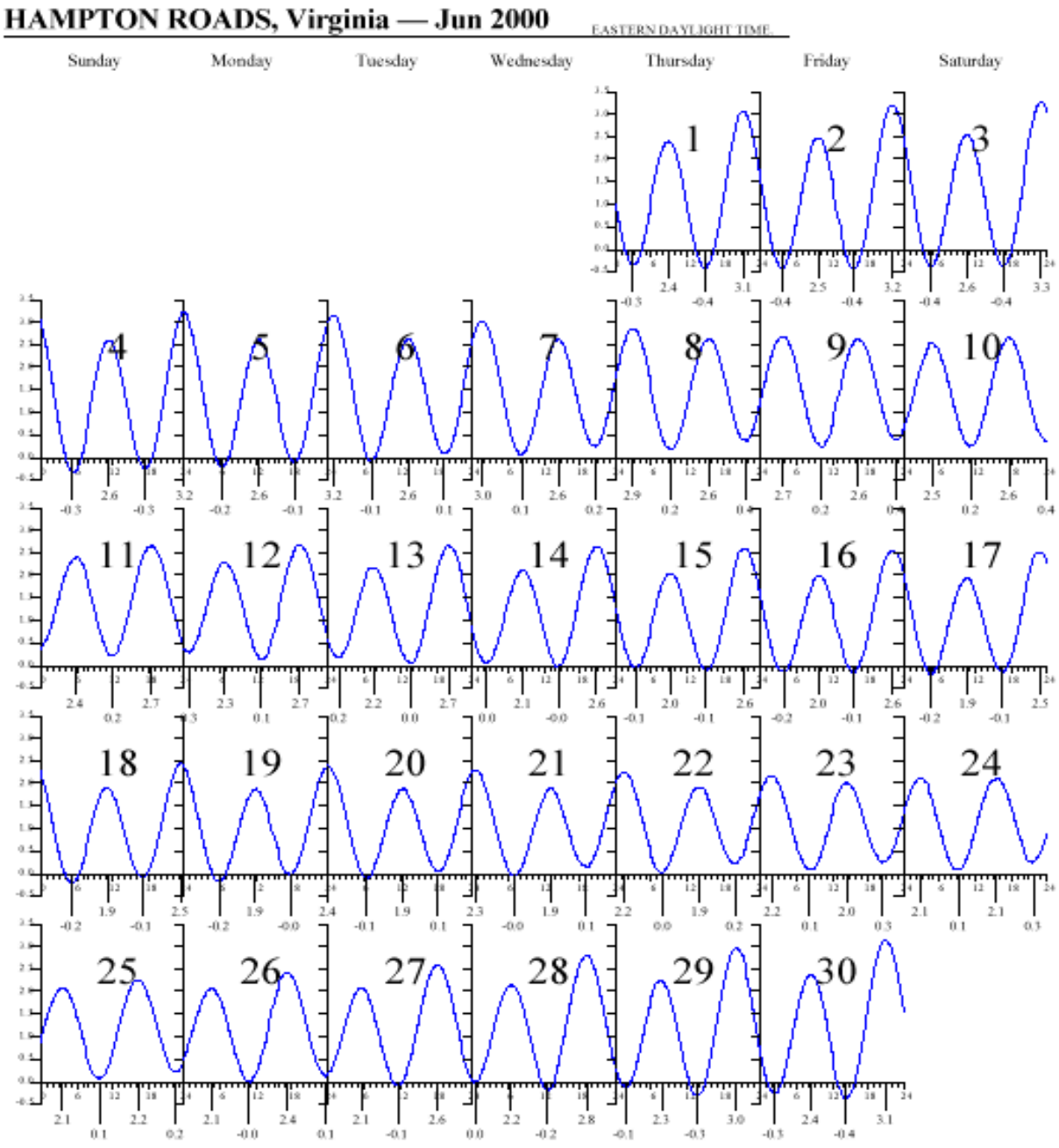

Figure IV.21. Predicted tidal height in feet above mean low water.

Whether the observed stratified-destratified condition and the reverse salinity pattern observed in the prototype data can actually be realized in the numerical model is a challenge. In order that the salinity pattern be simulated correctly, several elements are essential in the model framework that includes: correct fresh water inputs, tidal and salt boundary condition, wind forcing and the adequate turbulent closure scheme. Also one should note that the river discharges are from Richmond and the Chickahominy and Appomattox Rivers, which must be transported almost a hundred miles in order to reach the lower James. To our satisfaction, the model indeed reproduces the stratified-destratified condition at the right time, and the reversed salinity gradient at the right portion of the Elizabeth. Figures IV.22-IV.26 show the comparison of salinity contour plots for the 5 intensive surveys. For each comparison, observed salinity is shown on the upper left, modeled daily averaged on the lower left, maximum daily on the upper right, and minimum daily salinity on the lower right panels. The reason three different modeled salinity patterns were presented is because the observed salinity was not collected in the exact same tidal phase, for the reason stated before. Therefore, in order to make a reasonable comparison the modeled averaged salinity plus maximum and minimum daily values are used to compare with observed salinity. In the contour plot, salinities are marked by different color depending on the concentration with a distinct red line representing the 15 ppt isohaline. As one can see that Julian day 122 was relatively stratified with a reversed salinity gradient at the mouth. Seven days later at Julian day 129, however, the water column is very well mixed with no reversed salinity gradient. At Julian day 136, the stratification and the reversed salinity condition reappeared but then became completely well mixed at Julian day 159. In each of the surveys, the model faithfully reproduces the salinity pattern.

In conjunction with the contour plot, the modeled time series of salinity at 4 different stations inside the Elizabeth were also presented. These four stations are Sewells Point, Craney Island, Lamberts Point and Town Point and the duration was from Julian day 115 through 160, as shown in Figures IV.27-IV.30. In each of these figures, modeled salinity is shown as a solid line on the surface and at the bottom while observed salinities are shown as different symbols, squares being the surface, circles the bottom values, and the crosses indicate the intermediate values at different depths. The comparison was quite good for all 4 stations consistently throughout the period. We particularly notice that the salinity at surface and the bottom are modulated between stratified and destratified conditions for most of the period. And in the later stage after Julian day 150, one encounters a well–mixed condition toward the end of the period. The comparison of modeled and observed salinity was quite accurate throughout the Elizabeth; the overall RMS (root mean square) average error falls within around 1 ppt.

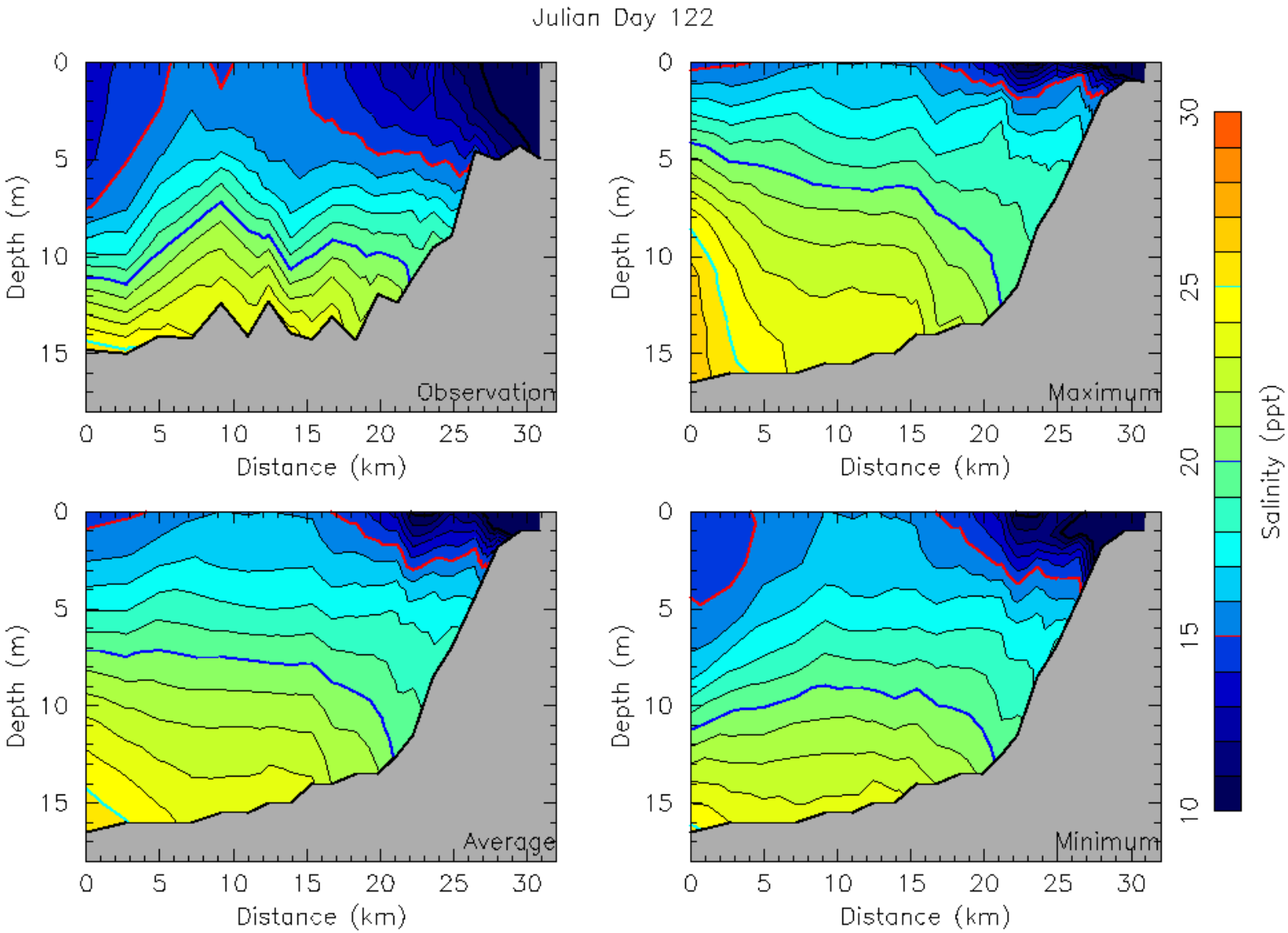

Figure IV.22. Salinity contour plots on May 1, 2000; observed (upper left), modeled (remainder).

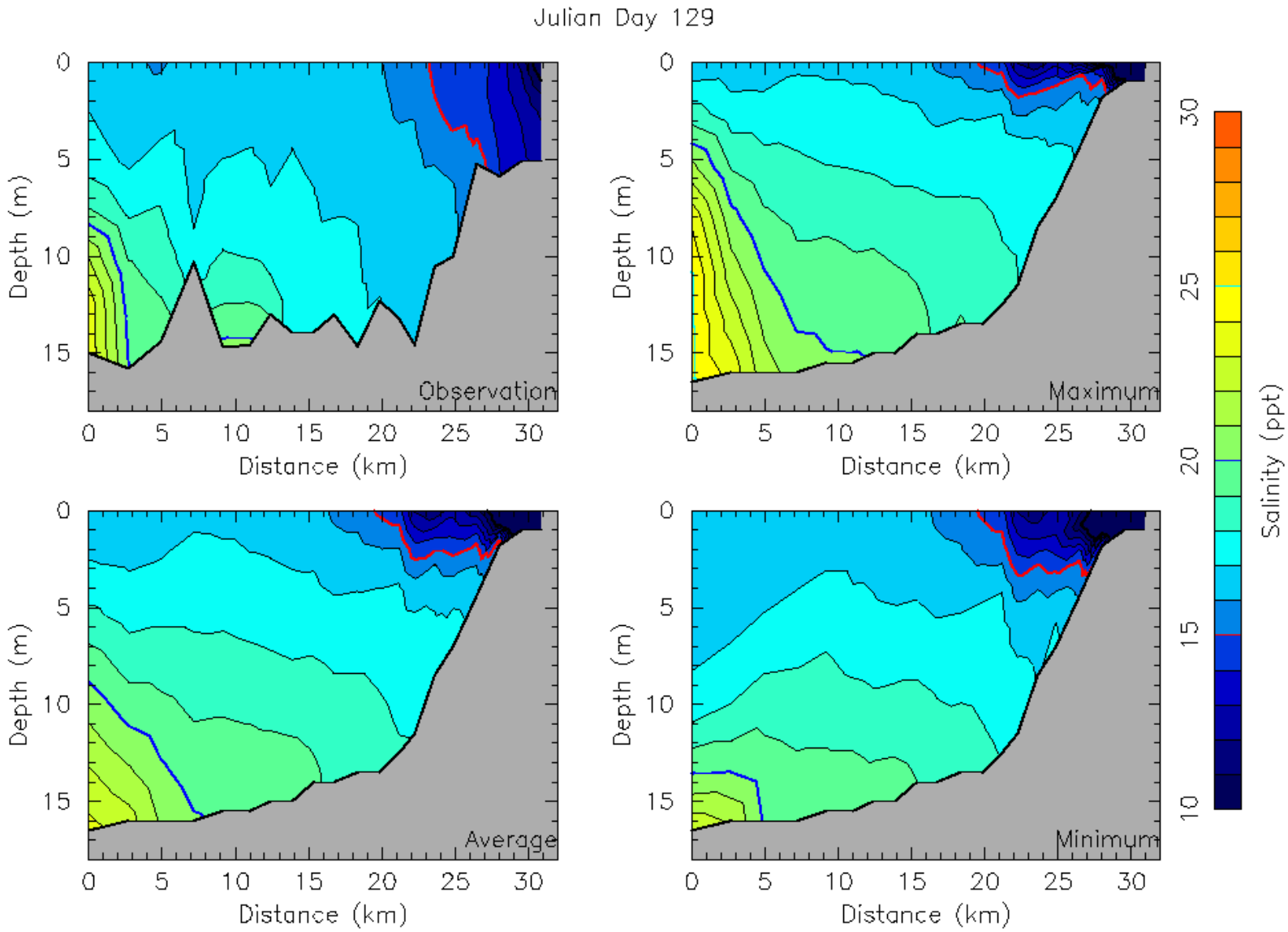

Figure IV.23. Salinity contour plots on May 8, 2000; observed (upper left), modeled (remainder).

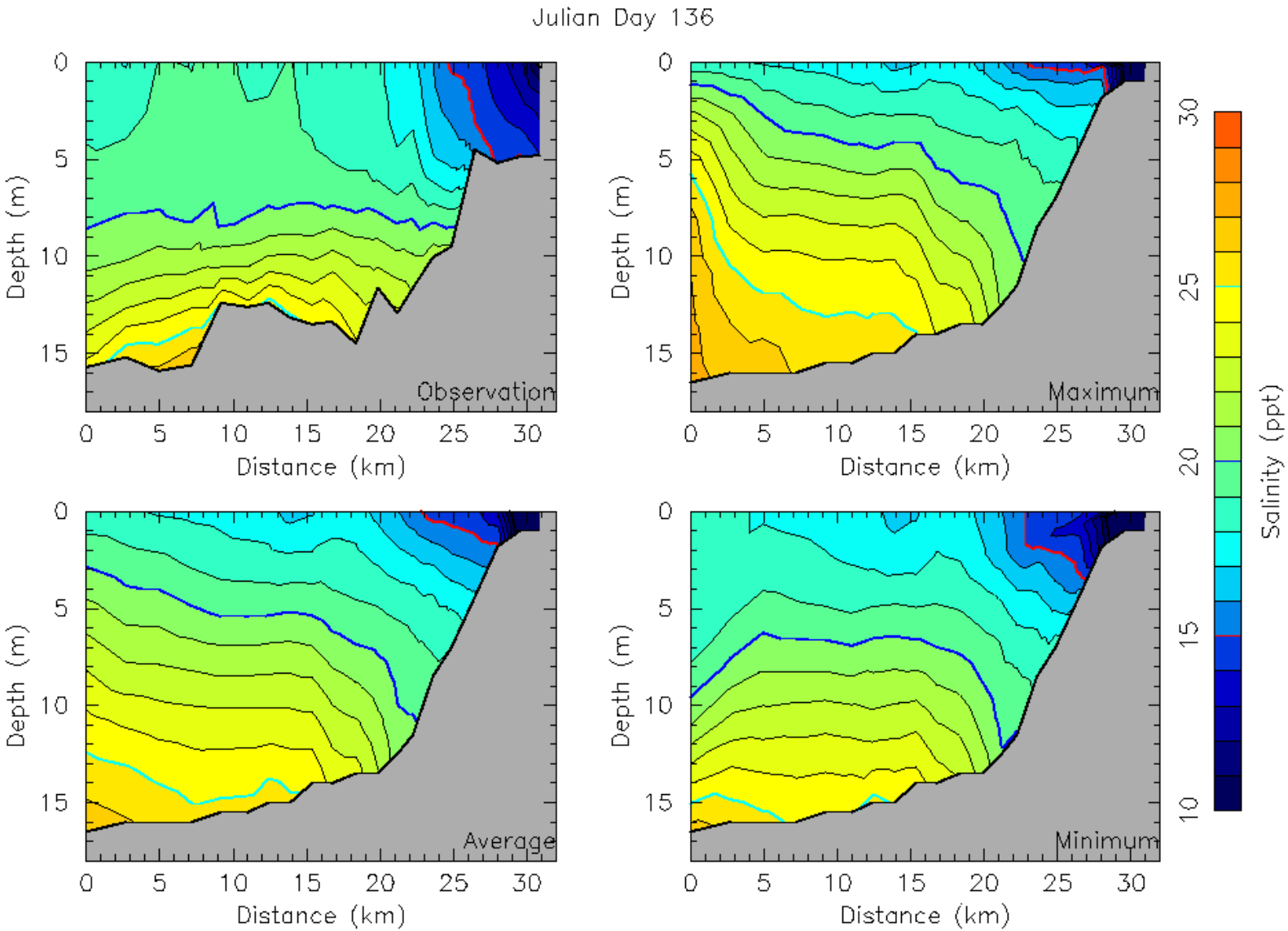

Figure IV.24. Salinity contour plots on May 15, 2000; observed (upper left), modeled (remainder).

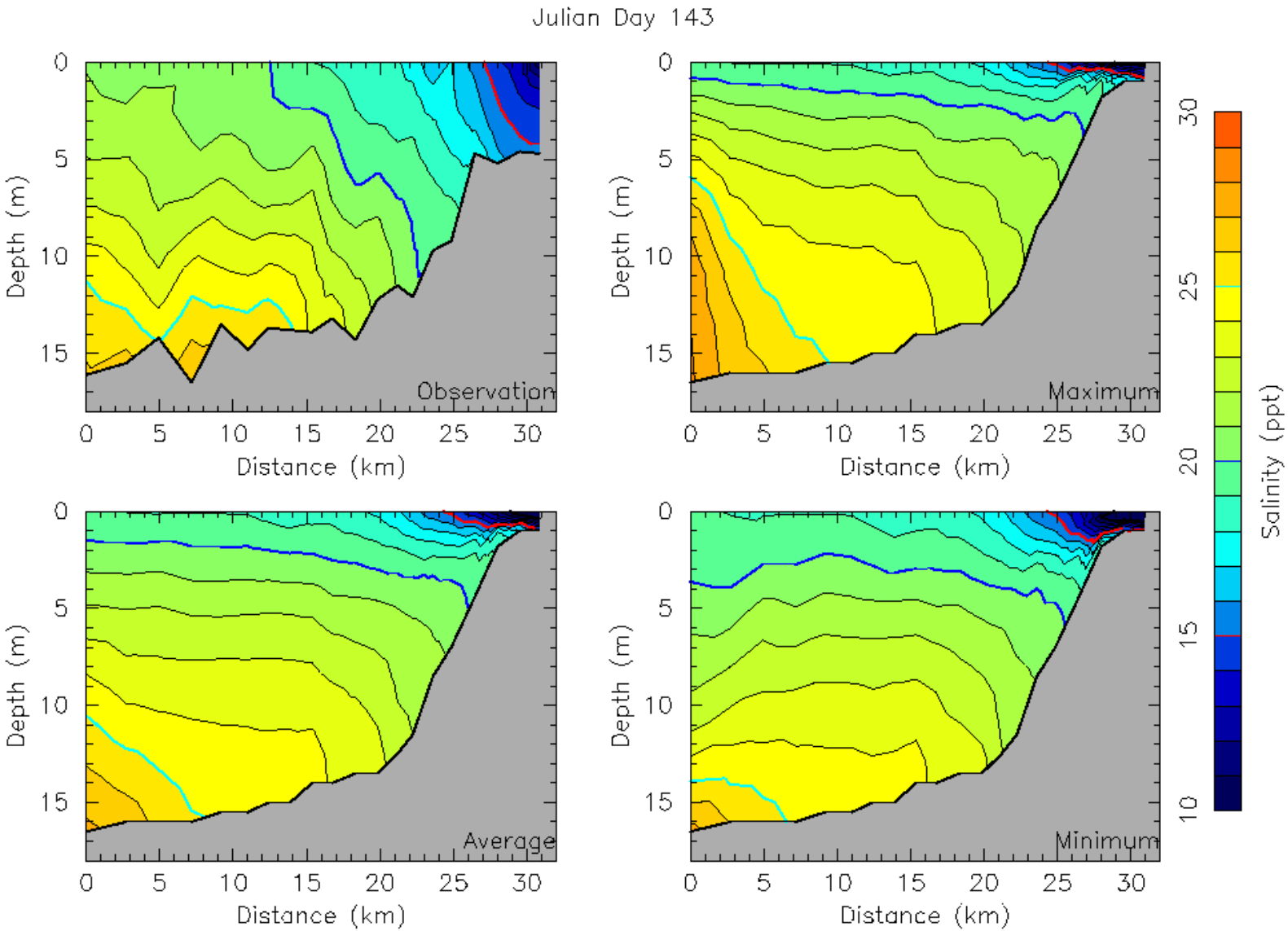

Figure IV.25. Salinity contour plots on May 22, 2000; observed (upper left), modeled (remainder).

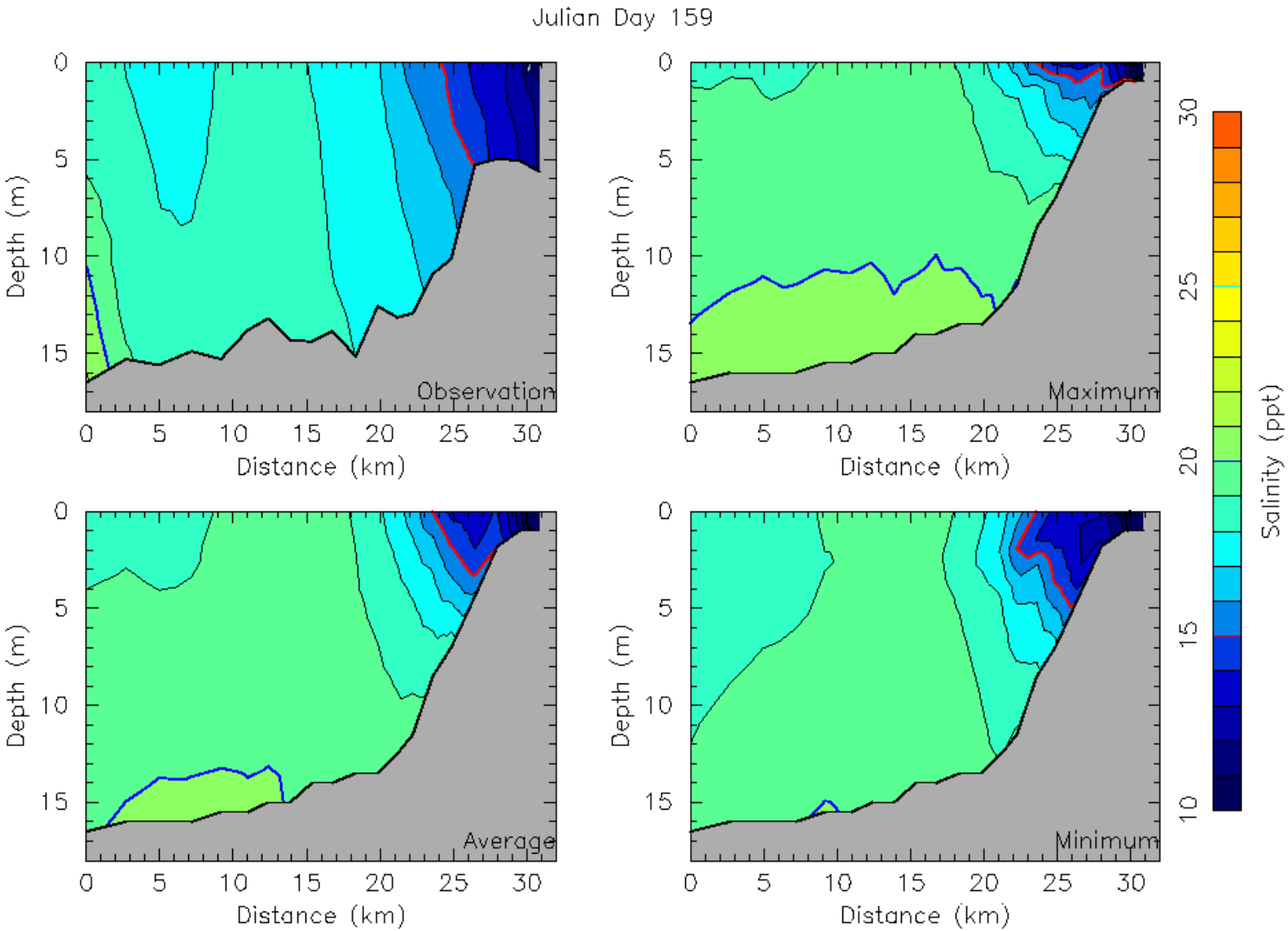

Figure IV.26. Salinity contour plots on June 7, 2000; observed (upper left), modeled (remainder).

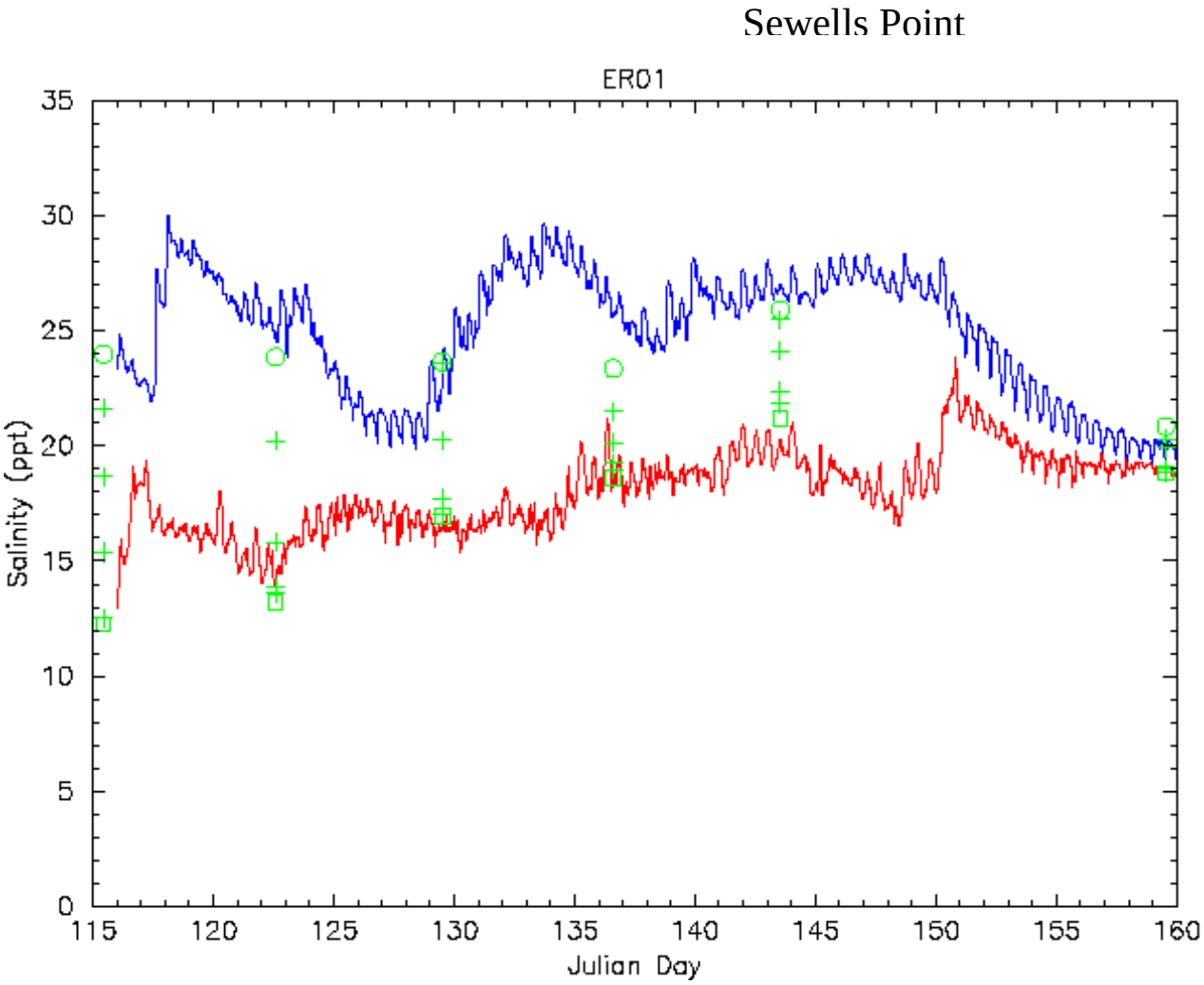

Figure IV.27. Modeled salinity time series at Sewells Point (surface-red, bottom-blue) and measured salinity (surface-squares, middle depth-crosses, bottom-circles).

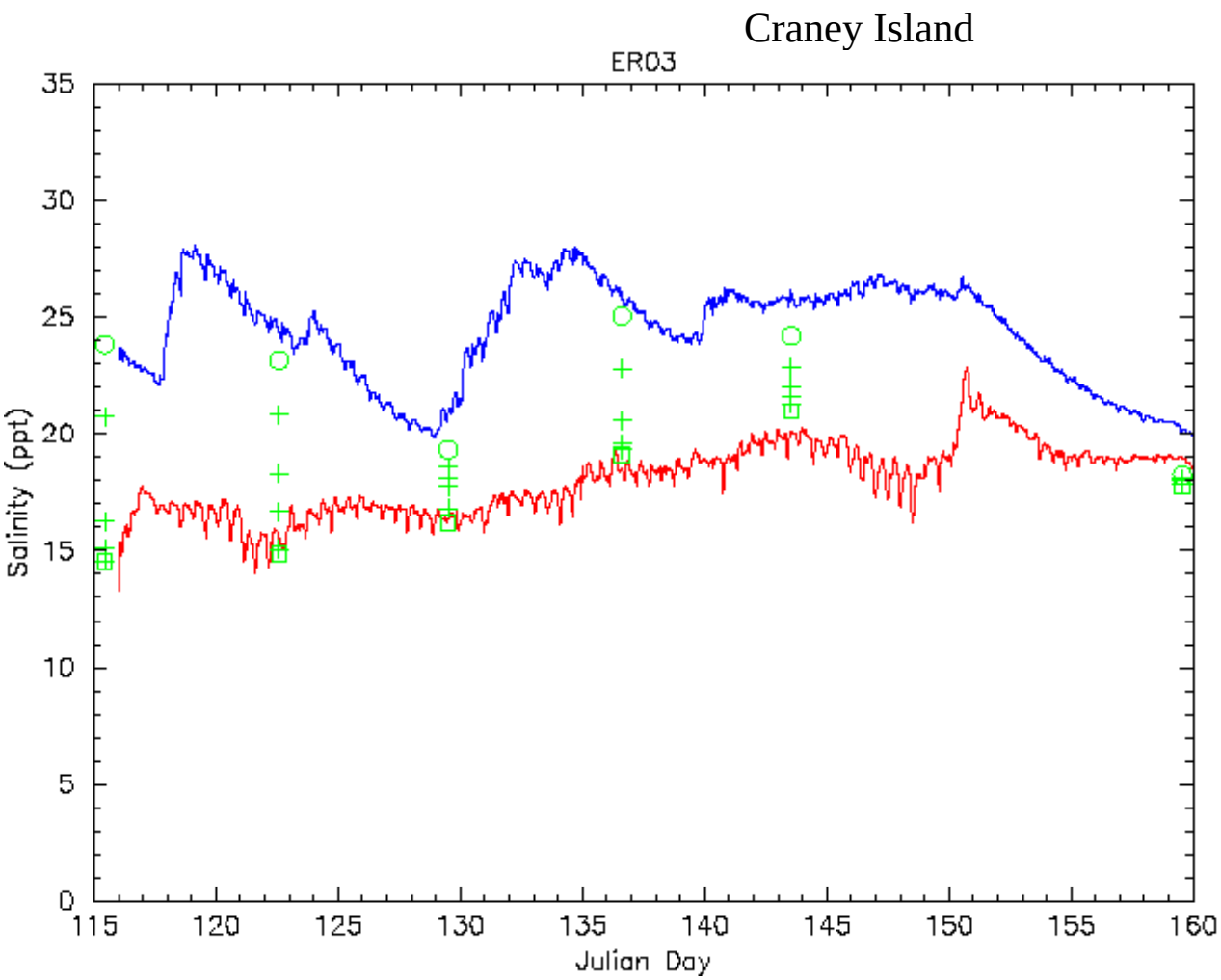

Figure IV.28. Modeled salinity time series at Craney Island (surface-red, bottom-blue) and measured salinity (surface-squares, middle depth-crosses, bottom-circles).

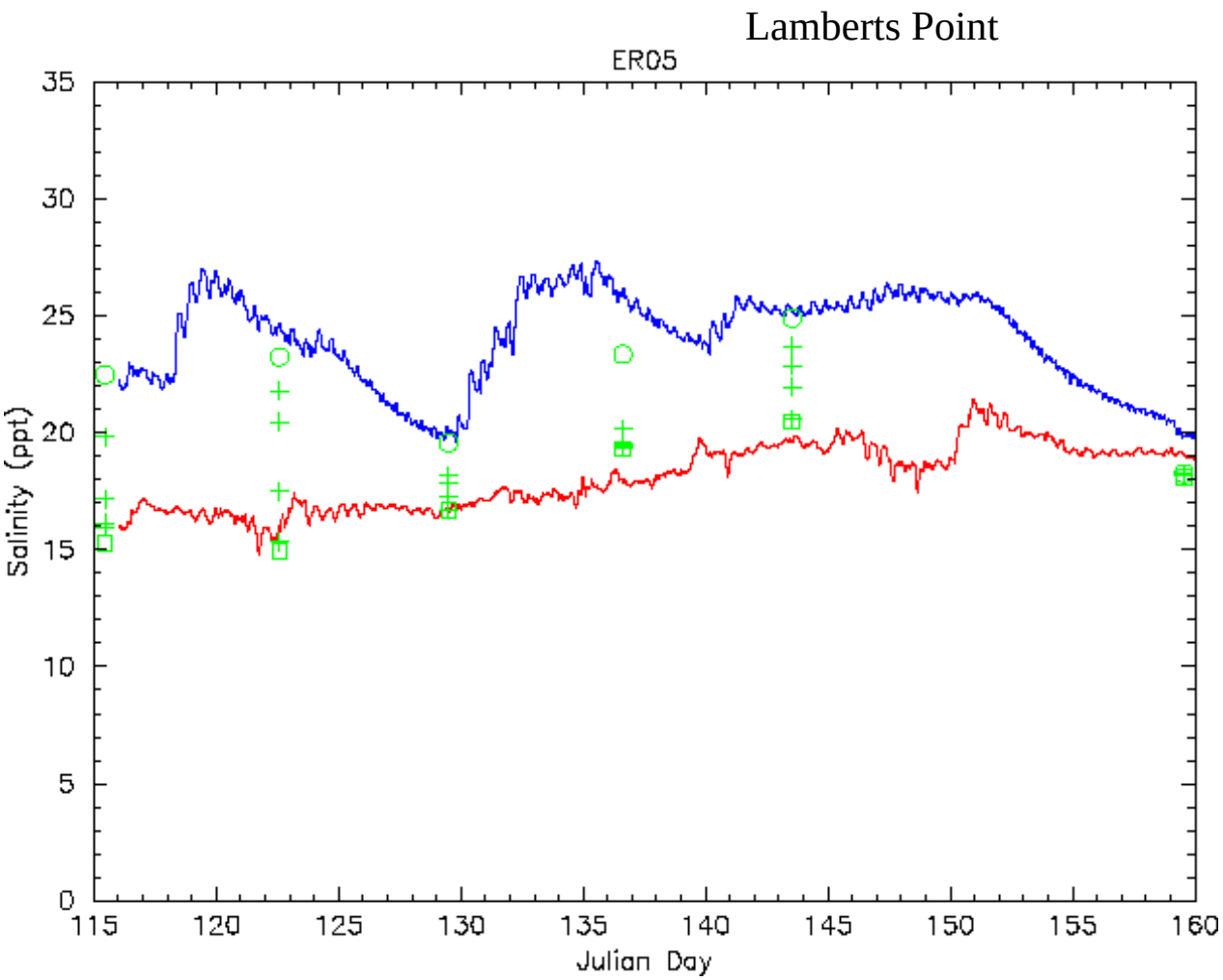

Figure IV.29. Modeled salinity time series at Lamberts Point (surface-red, bottom-blue) and measured salinity (surface-squares, middle depth-crosses, bottom-circles).

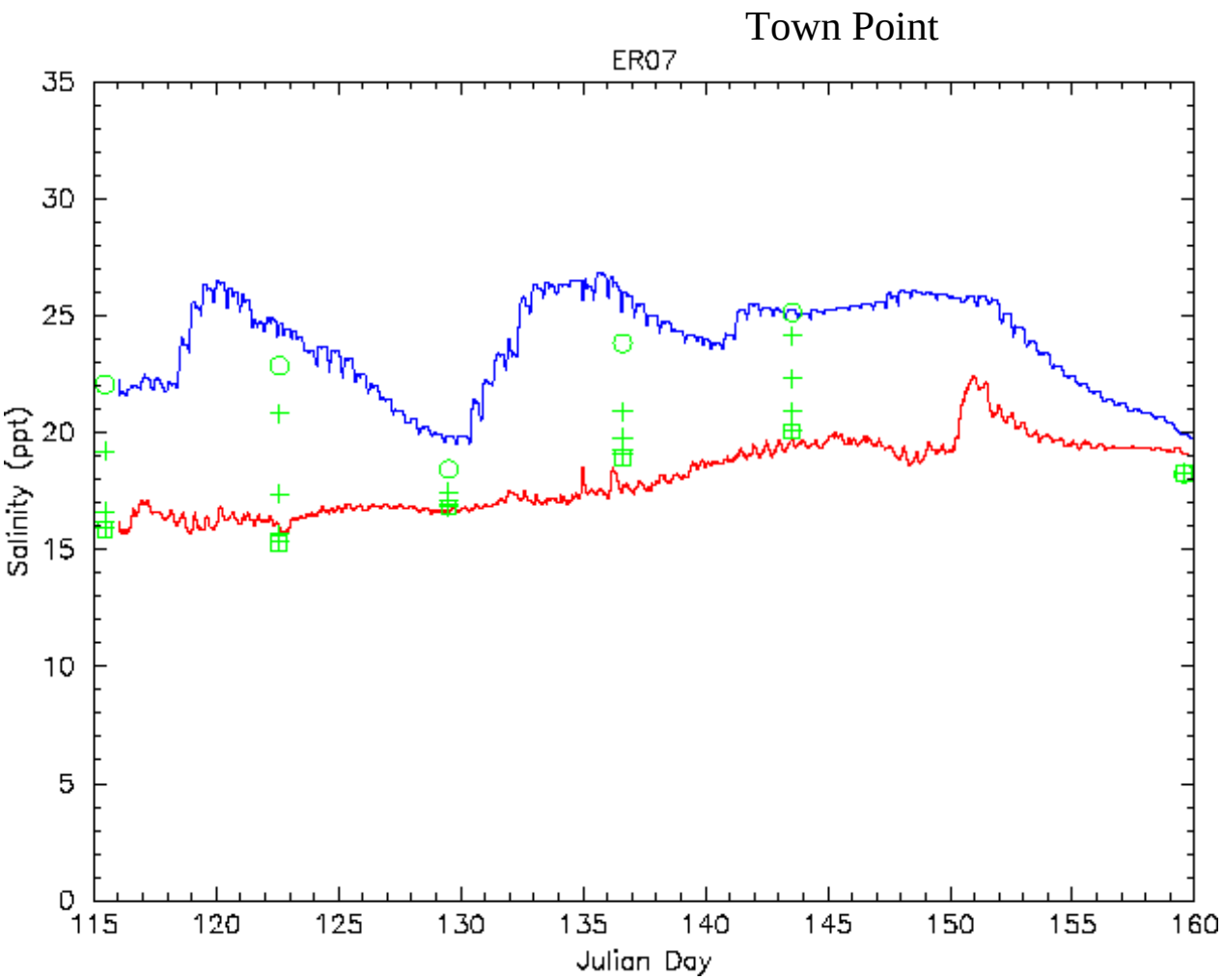

Figure IV.30. Modeled salinity time series at Town Point (surface-red, bottom-blue) and measured salinity (surface-squares, middle depth-crosses, bottom-circles).

V. SCENARIO SIMULATION COMPARISON - SINGLE VARIABLE RUNS

The proposed Craney Island expansion plan in the Lower James and Elizabeth River consists of 4 options: Eastward, Westward, Northward and the combined North and Eastward Expansions. For each option, there is also an associated ship channel deepening plan (see Chapter I, Section D for a detailed description). Two channel deepening plans for each of 4 expansion options, along with the Base Case, comprise a total of 9 model cases representing all of the scenario simulations for single variable runs. A designed time series of 74 tidal cycles was used to provide the combination of essential tidal components including spring, neap, perigean-spring and apogean-neap tides. The semimonthly progression between the extremes in tidal range for the model is shown in Chapter I, Figure I.7. The duration of each scenario run was 134 tidal cycles (including 60 tidal cycles as spin up time) and the model results were saved every half-hour throughout the entire modeling domain.

In order to assess the impacts exerted on the James/Elizabeth River system, the differences between the particular scenario run (i.e., test case) and the Base Case were obtained and analyzed. From the numerical modeling point of view, what various Craney Island expansion options introduced into the system are the perturbations from the changes in the shoreline around the Craney Island. In measuring the effect of these perturbations, we first conducted a global analysis using 4 key variables: tidal elevation, current velocity, salinity and the sediment potential. We then shifted the focus onto the local effects, including flushing characteristics from sections of the Elizabeth River, and the special circulation features known to exist in the area. By combining the global and local analysis, a balanced view of assessment from both large scale as well as local scale can be achieved in a more objective manner.

A. GLOBAL COMPARISONS

Here, the term global is used to refer to the entire spatial domain for Hampton Roads. The global technique described in this section involves the generation of a plotted spatial distribution of a long-term (i.e., 74 tidal cycles) time average comparison of parameters predicted by the model for the Base Case (Case 1) and the various test cases (Cases 2-9). The comparison is made possible by virtue of the fact that all model output for the 6 layer, 7500-cell domain of the VIMS James/Elizabeth River HEM-3D model version is saved 24 times per tidal cycle (i.e., approximately every half hour). This allows one to compare, for each location in the model domain, time series of the Base Case versus each test case and to characterize the difference as either an RMS (root mean square) difference or a simple average difference:

$$\mathrm{RMS\_DIFFERENCE} = \sqrt{\sum_{i=1}^{n} (MP_{test,i} - MP_{base,i})^2 / n}$$

for tidal elevation, velocity magnitude

$$AVERAGE\_DIFFERENCE = \sum_{i=1}^{n} (MP_{test,i} - MP_{base,i}) / n$$

for salinity, sedimentation potential,
and residual velocity

where: n is number of data points, (1776 for 74 tidal cycles)
MP_{test} is model prediction for the test case
MP_{base} is model prediction for the Base Case

In this fashion, one is able to obtain for each state variable a simple difference between the predicted value of each test case and that of the Base Case for each cell and layer of the model domain. It should be noted that each Expansion Option grid contains fewer cells than the Base Case grid so the compared locations are restricted to those common to both. Further investigation may be made in regions where larger differences appear.

1. Spatial Distribution – It is not only useful to know the relative size of the differences described above, but also their spatial distributions. Use of ArcView Avenue scripts allows for the mapping of the derived differences into the exact cell areas of this curvilinear, variable cell size grid. Differences were derived for the Hampton Roads portion of the model domain as shown in the spatial plots of Hampton Roads shown in Figures 1-72 of Appendix to Chapter V, Section A.1.

For each of the 8 test case – Base Case comparisons, the sequence of the 9 spatial plots is as follows:

1) RMS difference of tidal elevation
2) average difference of surface salinity
3) average difference of bottom salinity
4) RMS difference of surface velocity magnitude
5) RMS difference of bottom velocity magnitude
6) average difference of surface residual velocity magnitude
7) average difference of bottom residual velocity magnitude
8) sedimentation potential for test case
9) sedimentation potential difference between test case and Base Case

For purposes of comparing the analyses of the 8 case comparisons, both the area for display and the legend (class) intervals selected to report the differences were kept constant throughout the comparisons.

Whereas the differences are calculated and plotted for each of the 8 case comparisons, it was found that differences due to channel deepening were much less than those caused by the four Expansion Options themselves. It is considered appropriate to discuss Expansion Options in terms of case comparison pairs. Below is a summary of the findings in each case.

Eastward Expansion (Option 7, Cases 2 & 3) vs. Base Case (Case 1) – Plots for Case 2 (50-foot channel) are presented in Figures 1-9; those for Case 3 (55-foot channel) are presented in Figures 10-18 of the Appendix to Chapter V, Section A.1. For surface elevation (Figures 1 and 10), all RMS average differences fall below 0.25 cm except for a small area adjacent to and north of the proposed expansion area, where differences increase to 0.4 cm. This area widens and shifts slightly eastward in Case 3. Average differences in surface and bottom salinity (Figures 2-3, 11-12) fall below 0.2 ppt everywhere except in the immediate area of the expansion. Just to the north and east of the expansion, the salinity differences fall below 1.0 ppt except for a very small area of bottom salinity in the dredged region east of the expansion. Surface and bottom velocity magnitude RMS differences (Figures 4-5, 13-14) show a gradual increase to about 20 cm/sec over a very small area just north of the expansion. The small orange colorations north of the James River Bridge represent small differences relative to the currents in this area. Surface and bottom residual velocity magnitude average differences (Figures 6-7, 15-16), reveal small areas around the structure containing differences up to 5 cm/sec at the surface and up to 3 cm/sec at the bottom.

Sedimentation potential, which we define as the percent of time that the bottom shear stress computed by the model remains under 0.1 pascals, is plotted for Case 2 in Figure 8 and for Case 3 in Figure 17. One simple interpretation of these figures is that the lighter colored areas are prone to erosion whereas the darker areas (i.e., 80 to 100%) are prone to deposition assuming that fine sediment is available in the water column. Finally, a cell-by-cell average differencing of these distributions against that of the Base Case produces the sedimentation potential difference spatial distributions for Case 2 (Figure 9) and Case 3 (Figure 18). These plots show a very small area (in red) just north of the expansion with mildly increased sedimentation potential bounded by a similarly small area (in blue) just to its east with mildly decreased sedimentation potential, suggesting a tendency for a small re-allocation of deposition in this area.

Westward Expansion (Option 5, Cases 4 & 5) vs. Base Case (Case 1) – Plots for Case 4 (50-foot channel) are in Figures 19-27, and those for Case 5 (55-foot channel) are in Figures 28-36 of the Appendix to Chapter V, Section A.1. For surface elevation (Figures 19 and 28), all RMS differences east of Newport News Pt. exceed 0.25 cm, and an area extending around the westward expansion shows an RMS difference from 0.5 to 1.0 cm, increasing towards the expansion area. Average differences in surface and bottom salinity (Figures 20-21, 29-30) show both a larger impacted area (differences of 1 ppt spanning area from the expansion to the Nansemond River) and, just northwest of the expansion, higher differences (i.e., more than 1 ppt) than noted for the Eastward Expansion. Surface and bottom velocity magnitude RMS differences (Figures 22-23, 31-32) show a much larger area for the 8-12 cm/sec range with a gradual increase to about 25 cm/sec over a small area just north and west of the westward expansion. Surface and bottom residual velocity magnitude average differences (Figures 24-25, 33-34), reveal larger areas than the Eastward Expansion in the ±1 to 5 cm/sec range for the surface and ±1 to 3 cm/sec for the bottom, as well as values up to 10 cm/sec in a few cells just north and west of the Westward Expansion. Sedimentation potential difference, plotted for Case 4 vs. Base Case in Figure 27 and for Case 5 vs. Base Case in Figure 36, shows an

increased tendency for deposition to the west of the Westward Expansion, with an increased tendency for erosion to its north.

Northward Expansion (Option 6, Cases 6 & 7) vs. Base Case (Case 1) – Plots for Case 6 (50-foot channel) are in Figures 37-45, and those for Case 7 (55-foot channel) are in Figures 46-54 of the Appendix to Chapter V, Section A.1. For surface elevation (Figures 37 and 46), all RMS differences exceed 0.5 cm downstream of Newport News Pt., 0.75 cm for all areas adjacent to Craney Island, and 1.00 cm throughout most of the Elizabeth River. The highest surface elevation RMS difference (>1.50 cm) is a small area just west of the Northward Expansion. Surface salinity, shown for the Case 6 impact in Figure 38 and for that of Case 7 in Figure 47, is increased up to 1.0 ppt over much of the area north of the Northward Expansion, and up to 2.0 ppt for smaller areas both north and east of the Expansion. Bottom salinity, shown in Figure 39 for Case 6 vs. Base Case and in Figure 48 for Case 7 vs. Base Case, shows variations of 0.5 ppt covering most of Hampton Roads including the Nansemond and Elizabeth River regions, with local differences of 1.0 – 2.0 ppt just west of the Northward Expansion. Surface and bottom velocity magnitude RMS differences (Figures 31-32, and 40-41) show a much larger area for the 8-12 cm/sec legend band than did those for the Westward Expansion. The highest values (north and west of the Northward Expansion) ranged beyond 30 cm/sec. Surface and bottom residual velocity magnitude average differences (Figures 42-43, and 51-52) cover a significant area north of the Northward Expansion with differences on the order of 10 cm/sec. Sedimentation potential difference (shown in Figure 45 for Case 6 vs. Base Case and in Figure 54 for Case 7 vs. Base Case) is similar to that for the Westward Expansion, showing a depositional tendency to the west and immediately north of the Expansion and a non-depositional tendency further north, yet its area is larger and more pronounced in the Northward Expansion.

Northward and Eastward Expansion (Option 9, Cases 8 & 9) vs. Base Case (Case 1) – Plots for Case 8 (50-foot channel) are in Figures 55-63, and those for Case 9 (55-foot channel) are in Figures 64-72 of the Appendix to Chapter V, Section A.1. For surface elevation (Figures 55 and 64), some of the area north of the previously discussed Northward Expansion (Figures 37,46) which were limited to 0.75 cm, now extend to 1.00 cm, giving this Expansion Option the highest surface elevation RMS differences seen thus far. Average differences in surface and bottom salinity (Figures 56-57 and 65-66) show smaller values than for the Northward Expansion, yet cover a much larger area west of Newport News Point with a decrease on the order of 0.5 ppt. Surface and bottom velocity magnitude RMS differences (Figures 49-50 and 58-59) are quite similar to those for the Northward Expansion. Surface and bottom residual velocity magnitude average differences (Figures 60-61 and 69-70) are also similar to those of the Northward Expansion, yet somewhat less intense. Sedimentation potential differences (shown in Figure 63 for Case 8 vs. Base Case and in Figure 72 for Case 9 vs. Base Case) are very similar to those discussed in the last paragraph for the Northward Expansion.

One caution to this analysis technique should be emphasized. As we compare differences in time series (either RMS or simple differences), we know these differences result from both amplitude and phase change. To determine the issue of which contribution comes

from amplitude and which from phase, time series comparisons were made at selected points as reported in Section A.3, Chapter V.

The spatial distributions of the case comparison differences discussed in this section can be compared in the qualitative sense. They show regions of maximum change and the important gradients between these regions and those unaffected by expansion. An attempt to quantify these results involves the analysis described in the next section.

2. Percentile Analysis – In order to quantify these differences derived from the case comparisons, a technique using percentile analysis was incorporated. By dividing the aforementioned differences into class intervals and plotting the spatial accumulation as a percentage of the entire model surface area of Hampton Roads, a set of simple histograms can be constructed such as those shown in the Appendix to Chapter V, Section A.2, Figures 1-64.

Figures 1-64 are comprised of 8 figures for each case comparison in numerical order (i.e., Case 2 vs. Base Case are Figures 1-8, Case 3 vs. Base Case are Figures 9-16, …Case 9 vs. Base Case are Figures 57-64). The 8 figures present the order of state variables in the sequence of the last section, except sedimentation potential is shown only as a compared difference:

1) RMS difference of tidal elevation
2) average difference of surface salinity
3) average difference of bottom salinity
4) RMS difference of surface velocity magnitude
5) RMS difference of bottom velocity magnitude
6) average difference of surface residual velocity magnitude
7) average difference of bottom residual velocity magnitude
8) sedimentation potential difference between test case and Base Case

As with the range of legend intervals of the spatial plots discussed in the last section, the range of class intervals for each variable was selected to be large enough to contain the maximum variability encountered for all the case comparisons. An example of a histogram plot is given below to facilitate discussion. For each of the histograms shown in Figures 1-64, the class interval area is a maroon bin whose percentile value is shown on the left vertical axis. The blue curve plotted shows the cumulative percent of all bins and its value is shown on the right vertical axis.

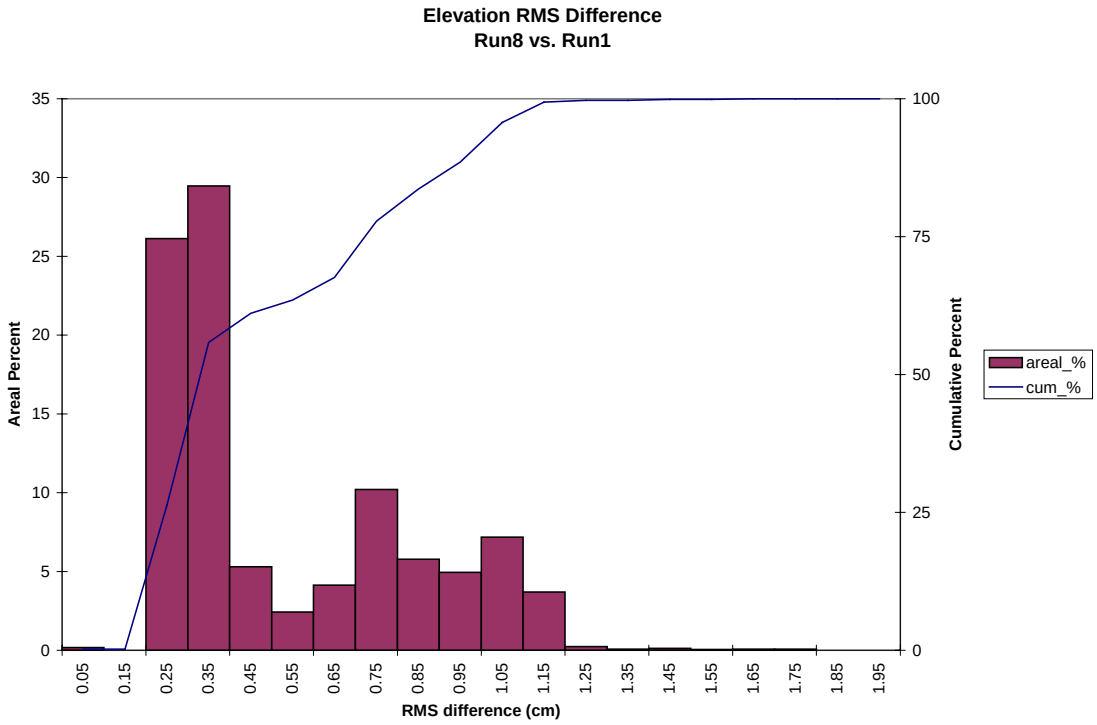

Figure V.1. Example histogram used in percentile analysis.

The final step is to extract the cumulative percentages from Figures 1-64 and group all 8 case comparisons for each state variable, as shown in Figures 65-72. Below in Figure V.2 is a copy of Figure 65, showing the cumulative curves for surface elevation. Here, the Eastward Expansion (Option 7, Cases 2-3) is shown in dark blue, the Westward Expansion (Option 5, Cases 4-5) is shown in a light (indigo) blue, the Northward Expansion (Option 6, Cases 6-7) is shown in green, and the Northward and Eastward Expansion (Option 9, Cases 8-9) is shown in red. For each option the 55-foot channel is the symboled function (i.e., Cases 3,5,7,9). Examination of these curves shows a general increase in changes as one progresses from the Eastward, to the Westward, to the Northward and Eastward, and finally to the Northward Expansion. The changes in all other state variables show the same trend among these 4 expansion options.

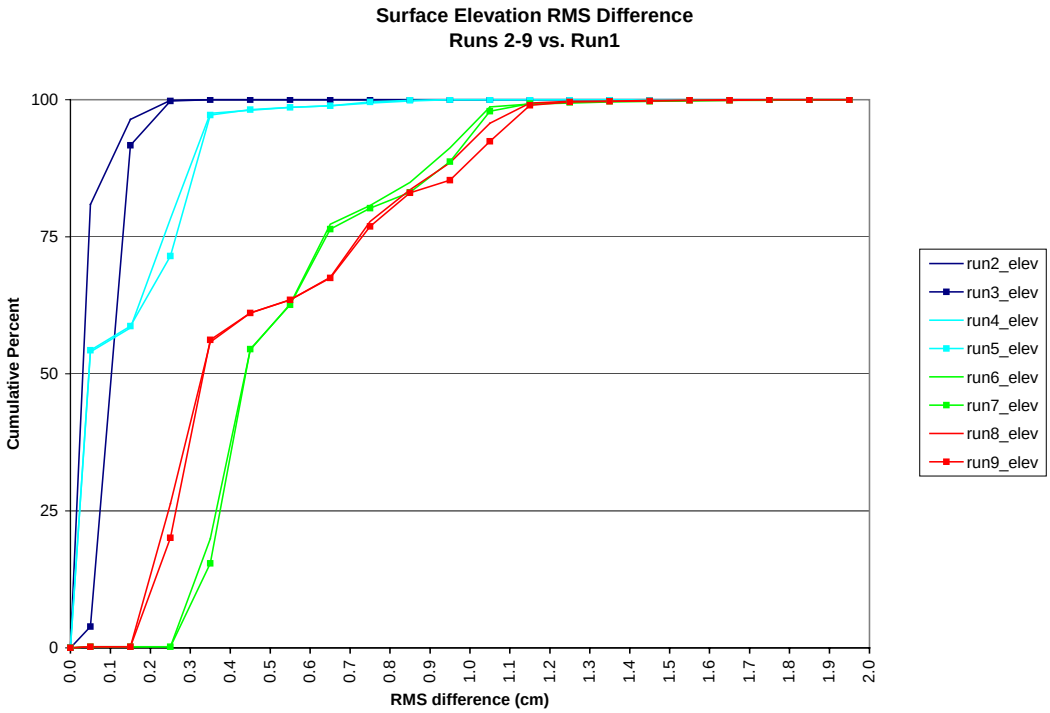

Figure V.2. Cumulative curves for surface elevation RMS differences (case comparisons 2-9).

3. Time series comparisons - So far, we have discussed the measure of difference between model results for the Base Case and various scenarios, but without considering the sources of this difference. For example, while the RMS difference provides us an integral measure of the difference, it is yet to be determined whether the difference actually occurs as a result of amplitude, phase difference, or the combination of the two. In this section, we present time series comparisons of the tidal elevation for 8 selected stations in the lower James and Elizabeth Rivers: JR01, JR02, JR03, JR04, JR05, ER03, ER05, ER13 as shown in Figure V.3. For each station, two 61-hour time series, one for the neap tide and the other for the spring tide, are analyzed. In addition to the time series, the regression analyses in a 1:1 plot (Base Case values versus test case values) are also generated. Depending on the departure of data points from the 1:1 line, the regression plots can be used to infer the source of the difference. For example, Figure IV.5 shows the regression plot with an elliptic rotation on a 1:1 line, indicating a pure phase difference of two sine curves of 20 minutes; Figure IV.6 shows a linear tilt superimposed on the elliptic circle, indicating a 10% amplitude reduction on a 20-minute phase difference sine curve.

For comparison between the Base Case (Case 1) and the northward expansion (Case 6), Figures V.4, (a) – (h), present the time series plots during neap tide at each of the 8 selected stations; Figures V.5 (a) – (h) show the associated regression plots during neap tide; Figures V.6 (a) – (h) are the time series plots during spring tide at the selected

stations and Figures V.7 (a) – (h) are the accompanying regression plots. After a process of identification, examination and comparison for both the time series and regression plots, we arrived at four major conclusions, stated as follows:

A. In a tidal estuary, where the tidal currents are oscillatory, the main source of RMS difference is neither from pure amplitude change, nor pure phase change; instead, it is the result of combined amplitude and phase change. In other words, whenever the amplitude changes, it is accompanied with the phase change and vice versa. This is consistent with the wave action conservation theory which states that, in a current and wave co-existent environment, amplitude changes are always accompanied with phase shifts; the more the amplitude changes, the more the phase will shift.

B. The tidal elevation changes inside the Elizabeth River, in most of the cases, are comparable to those in the lower James River. For example, in both the northward and northeast expansions of Craney Island, the response in the Elizabeth River is as much as that in the lower James River near Craney Island. From one point of view, the Elizabeth is dynamically coupled with the lower James; even a small change in the lower James can influence throughout the Elizabeth River with similar magnitude.

C. In most of the stations, the amplitude/phase changes are larger during the ebb tide than during the flood tide. This dependency on flow direction indicates that the effect of a given Craney Island expansion on the circulation is not uniform, but rather has more influence on the ebb tide than on the flood tide. The results are consistent with the past study that shows that flood current mainly flows through the northern portion of the lower James; in contrast, the ebb current takes a critical path near the southern side of the lower James, and thus, is more sensitive to the Craney Island expansion.

D. The station, JR02, which is located near the northwest corner of the proposed northward expansion, has the largest RMS difference with a magnitude ranging to 2.2 cm. The time series comparison indicates that during the ebb tide, its amplitude increases (or the water level drops further), while during the flood tide, its amplitude actually decreases (the water level remains lower). That means there is an overall reduction on the datum of the water level. Figure V.5 (b) clearly indicates that the test case points are mostly below the 1:1 line in the regression plot. We believe that the unusually large RMS value and the abnormal change pattern of amplitude are directly or indirectly related to the dynamics of the current around the corner, which depends on the shape of the particular structure proposed.

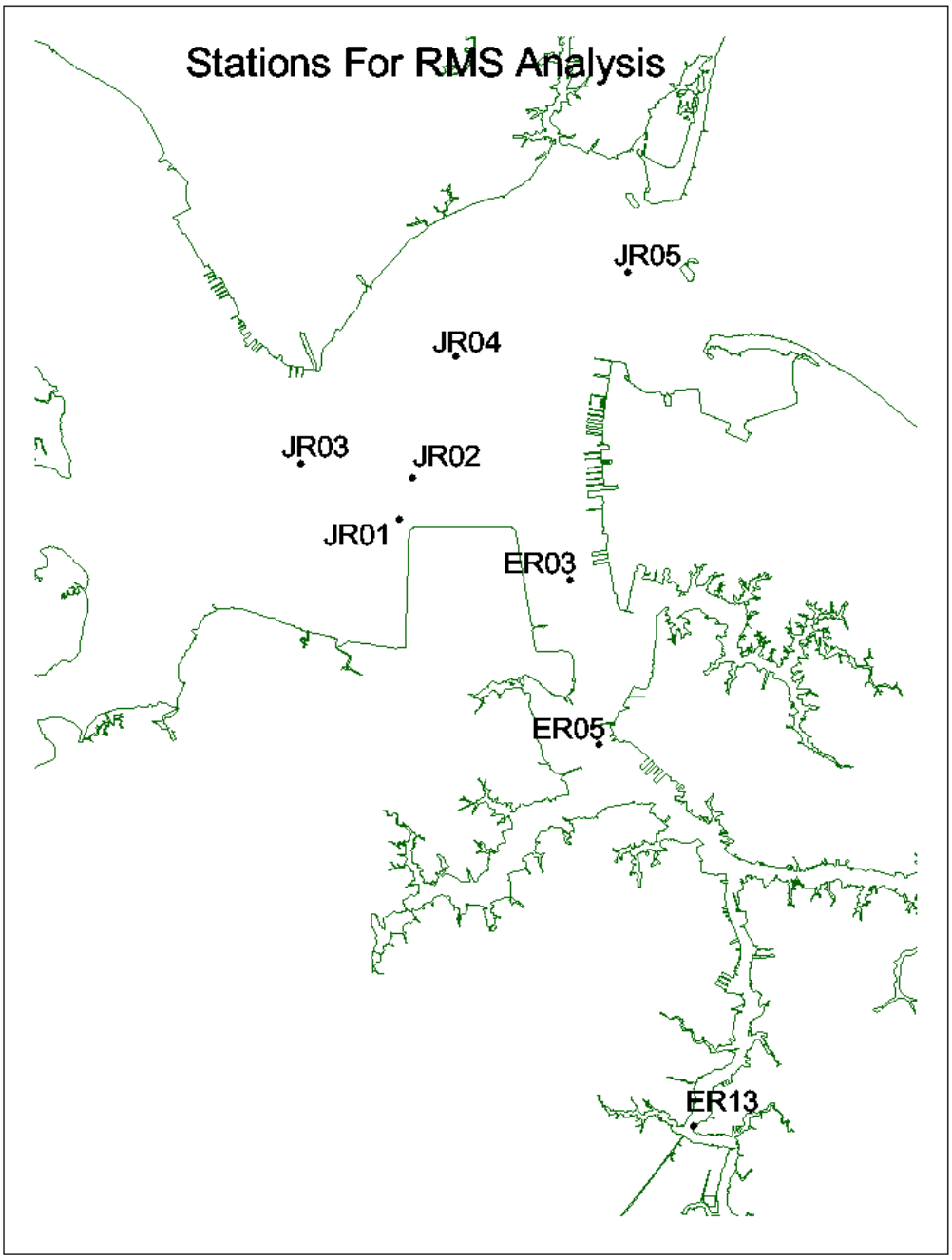

Figure V.3 Station Location Map.

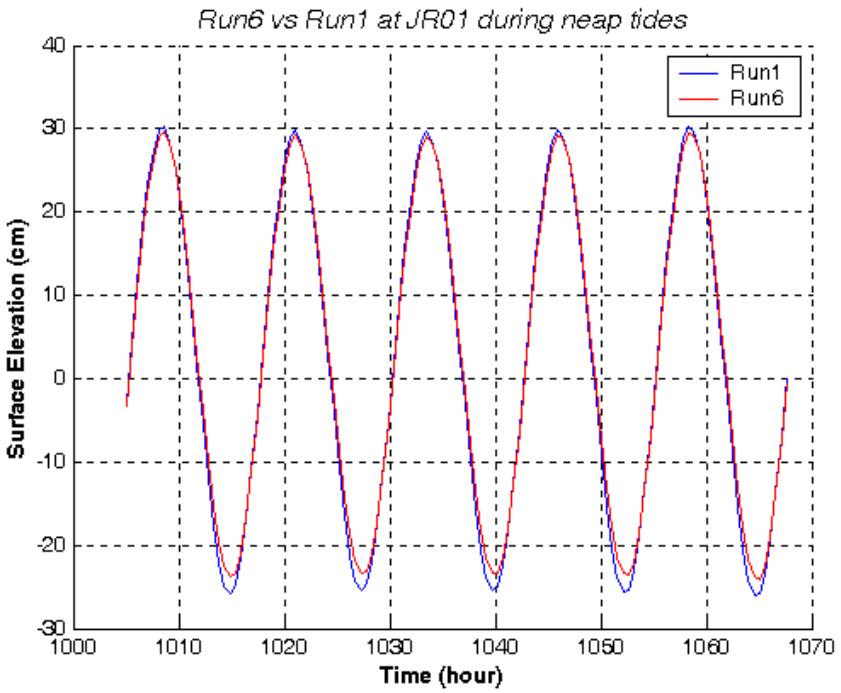

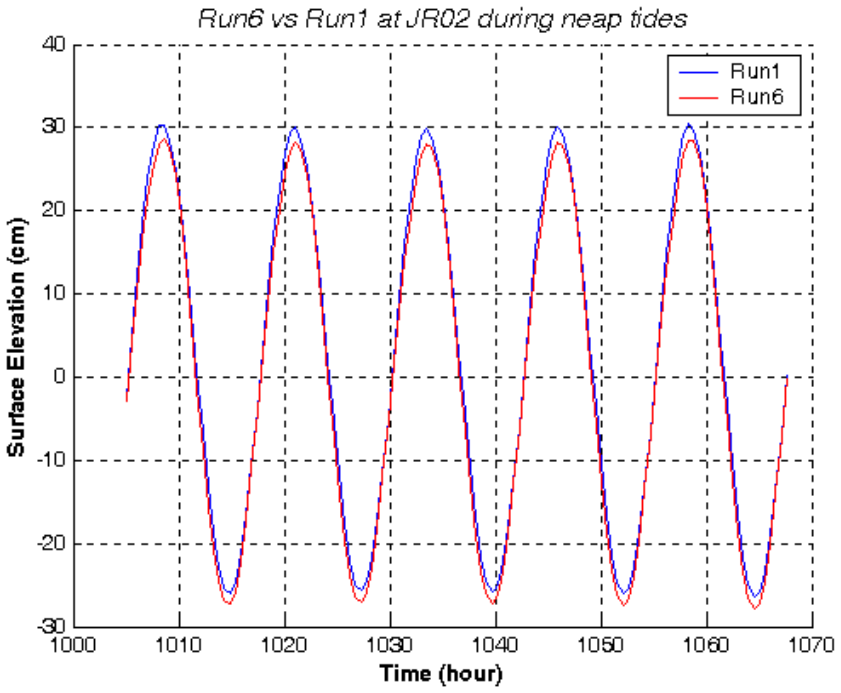

Figure V.4 Tidal Elevation time series comparison for Case 1 and Case 6 during neap tide at (a) JR01 (b) JR02 (sheet 1).

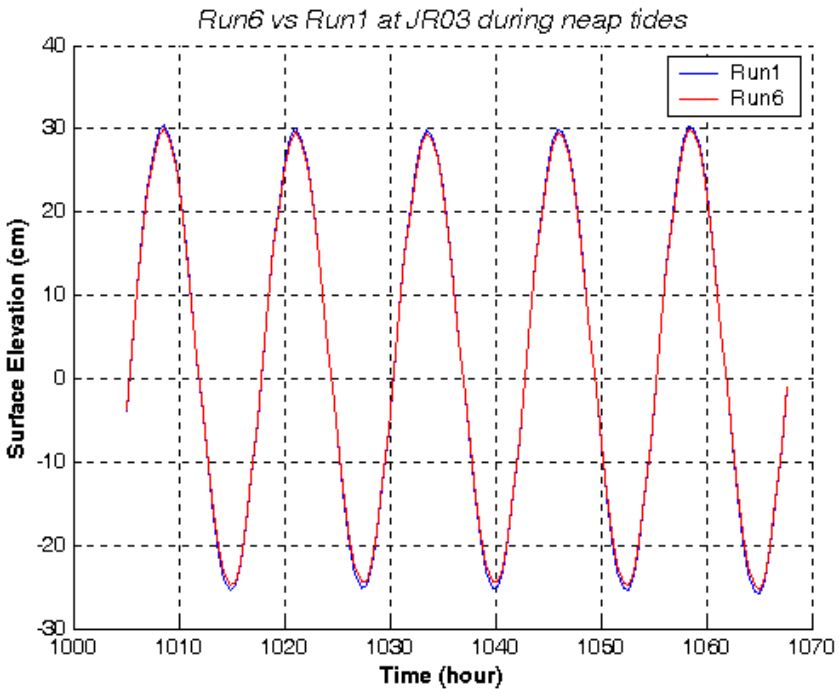

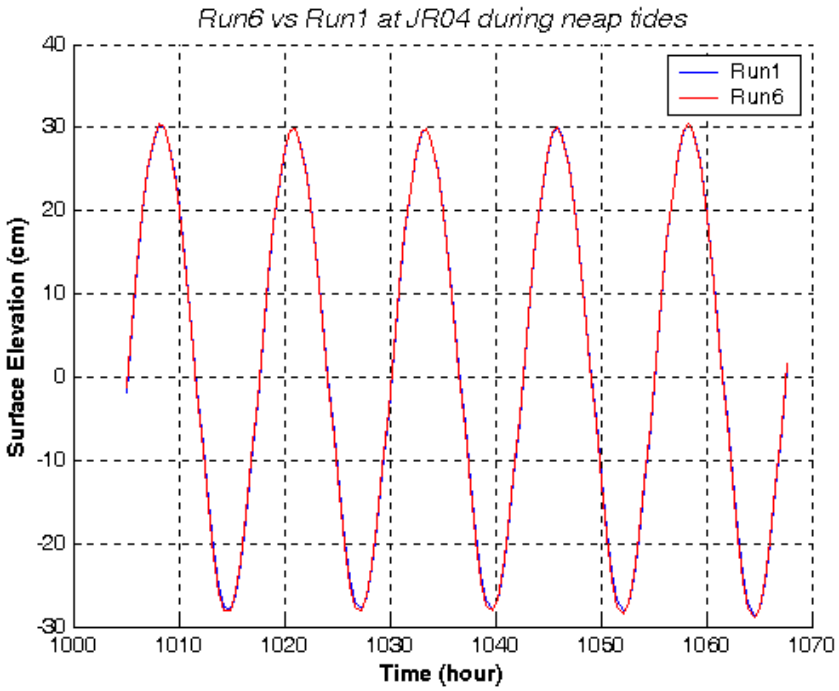

Figure V.4 (sheet 2) at (c) JR03 (d) JR04.

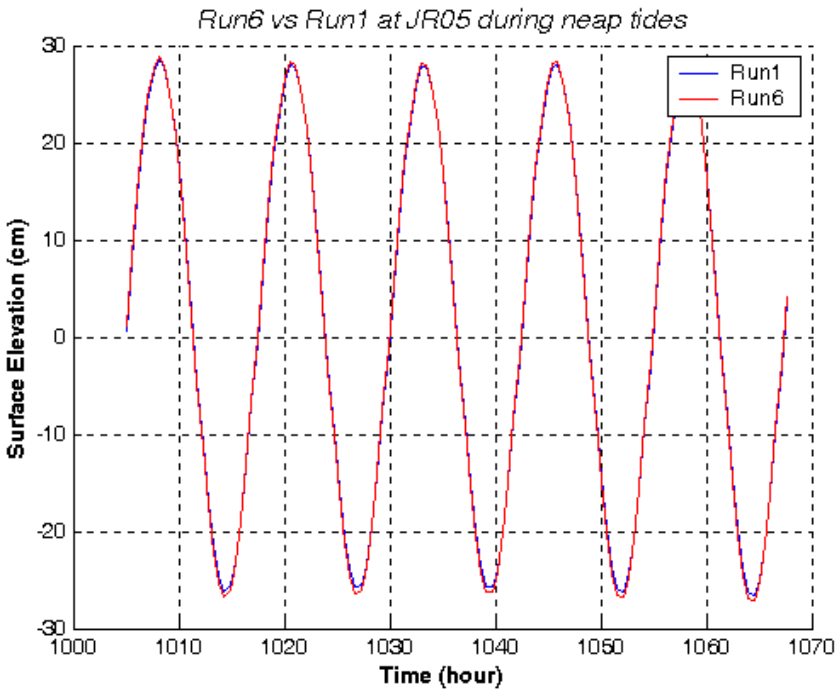

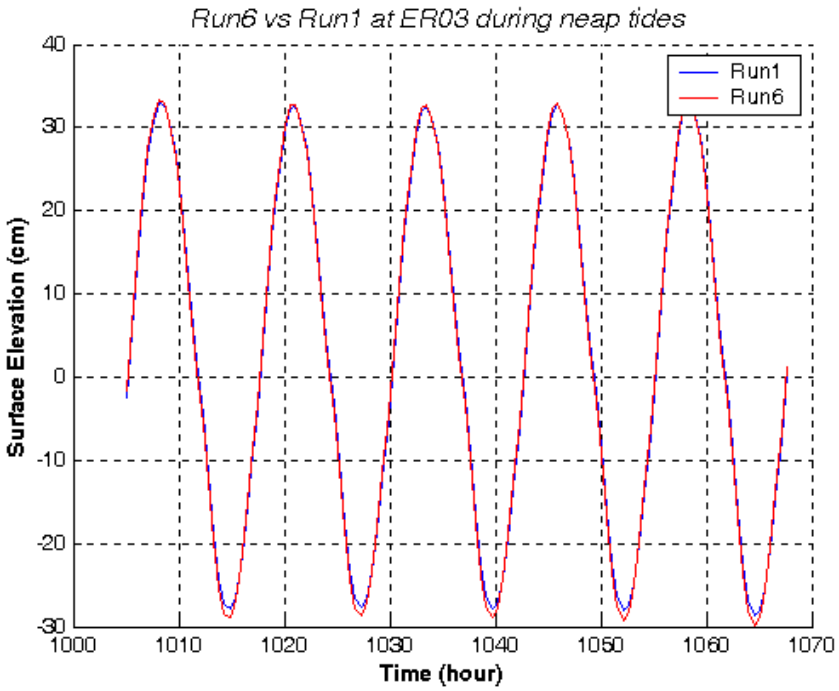

Figure V.4 (sheet 3) at (e) JR05 (f) ER03.

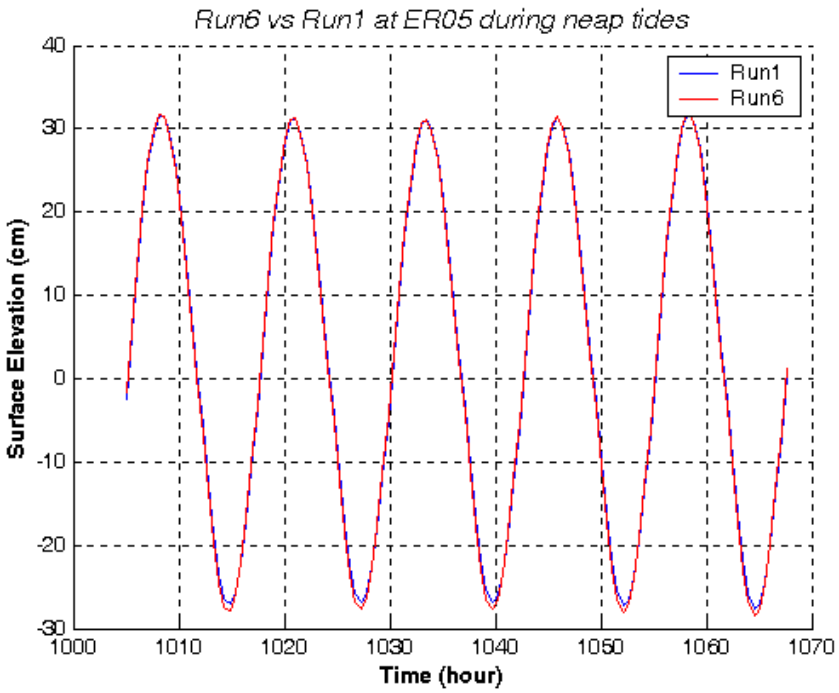

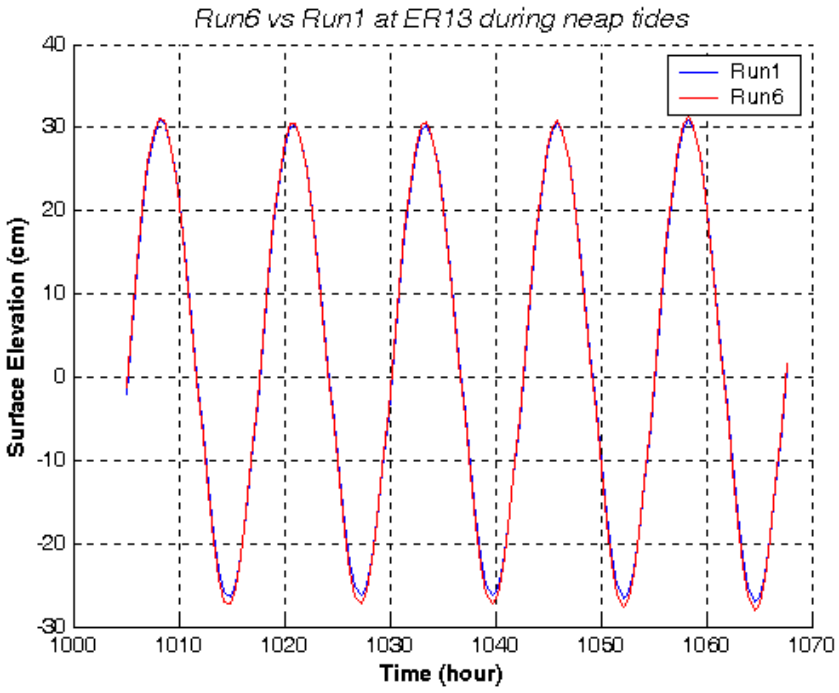

Figure V.4 (sheet 4) at (g) ER05 (h) ER13.

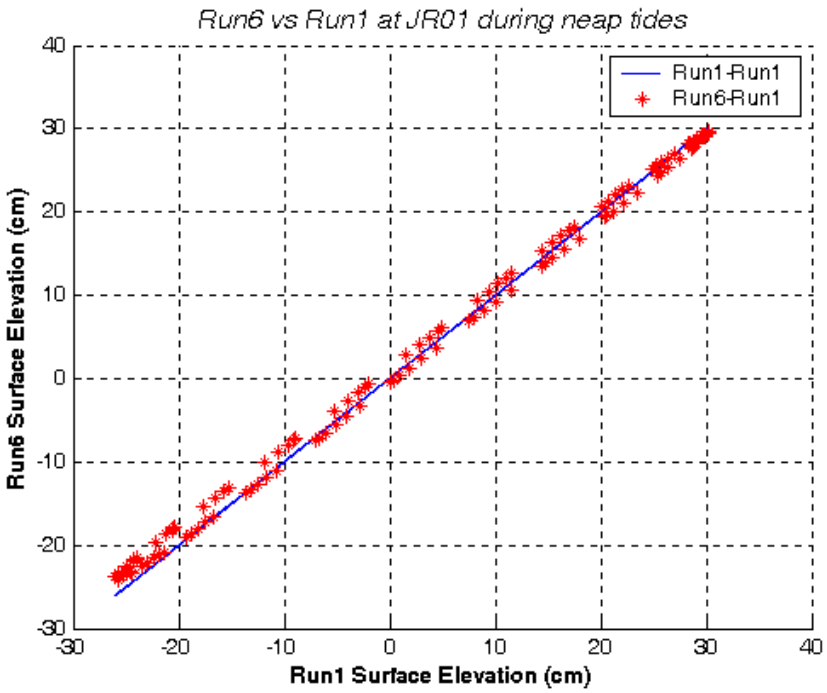

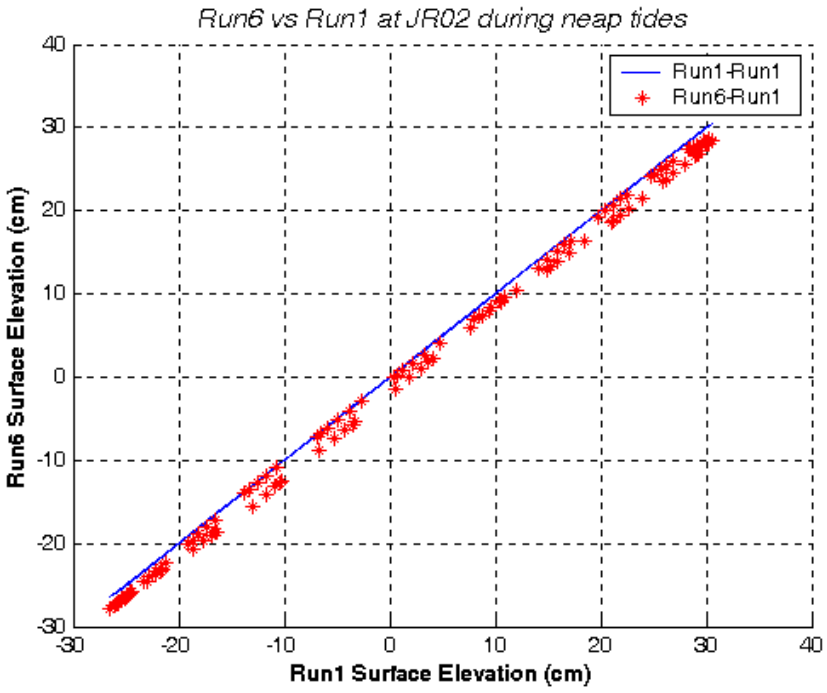

Figure V.5 Regression plot for Case 1 and Case 6 during neap tide at (a) JR01 (b) JR02 (sheet 1).

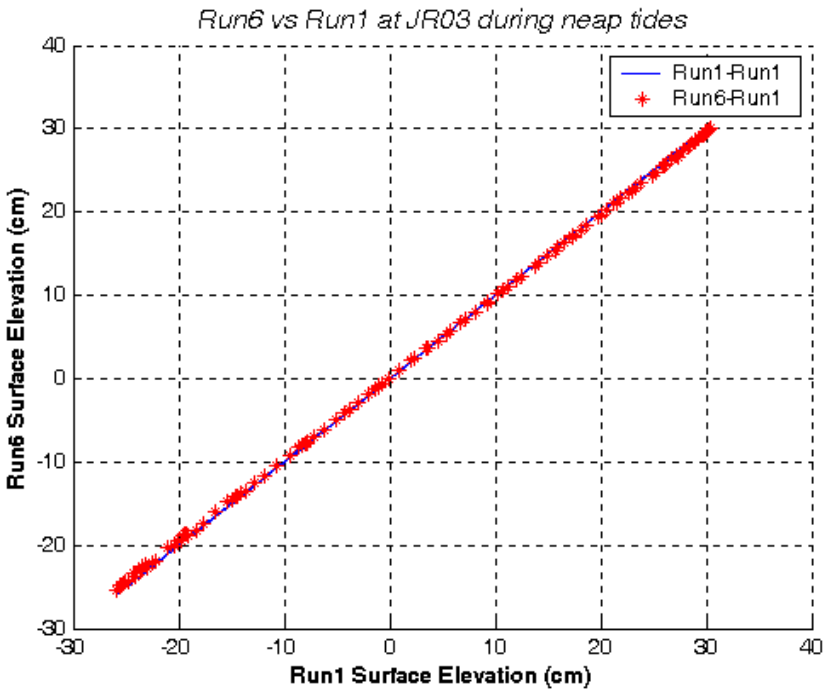

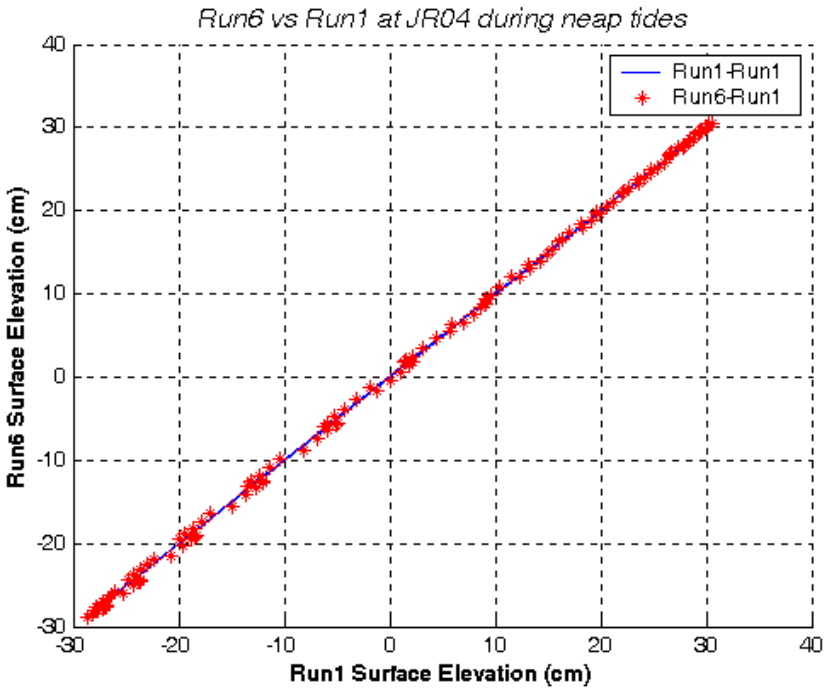

Figure V.5 (sheet 2) at (c) JR03 (d) JR04.

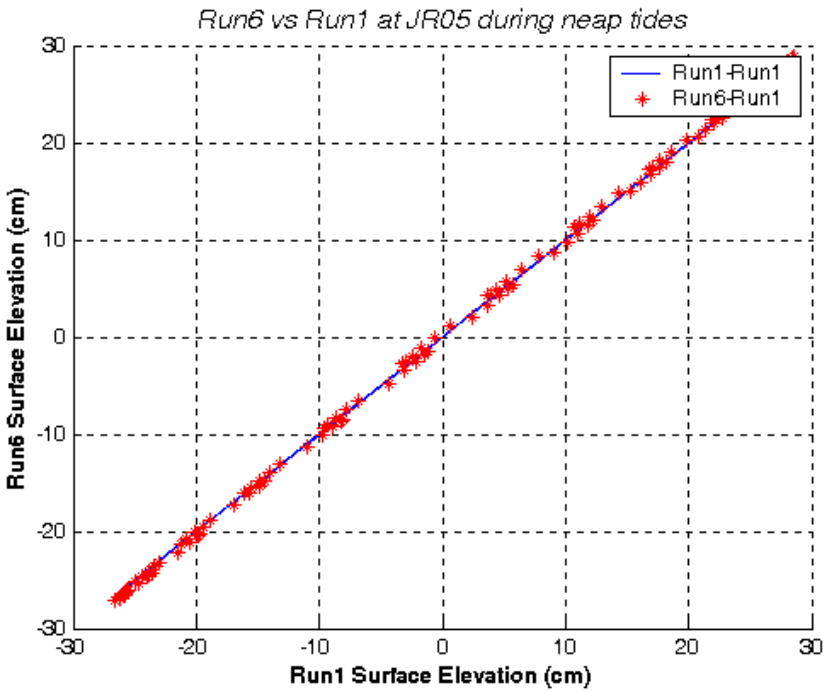

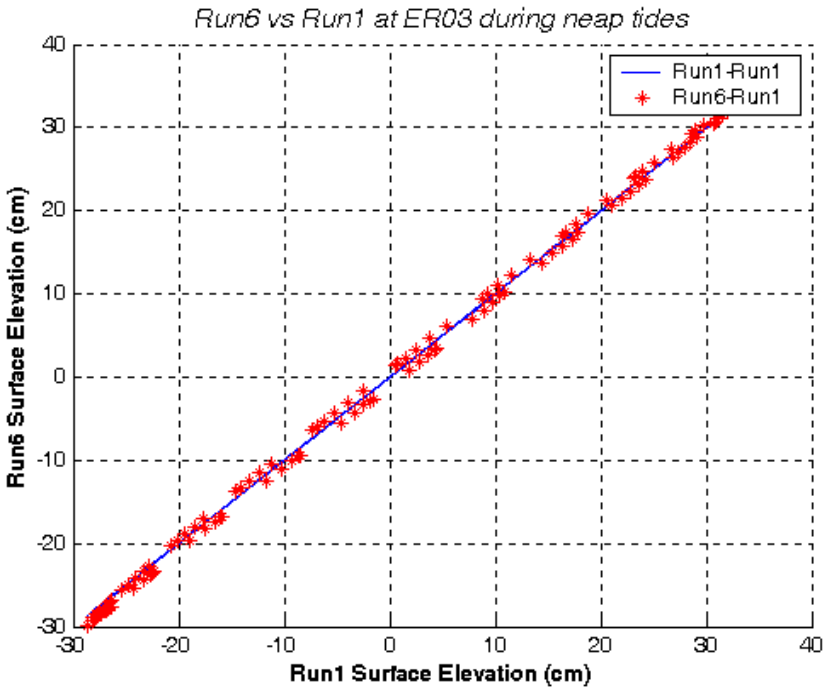

Figure V.5 (sheet 3) at (e) JR05 (f) ER03.

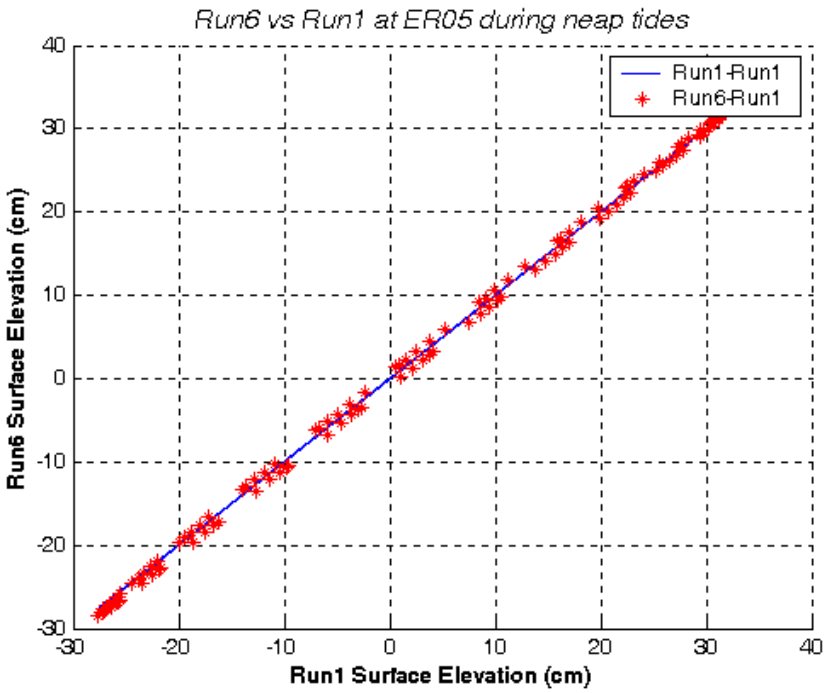

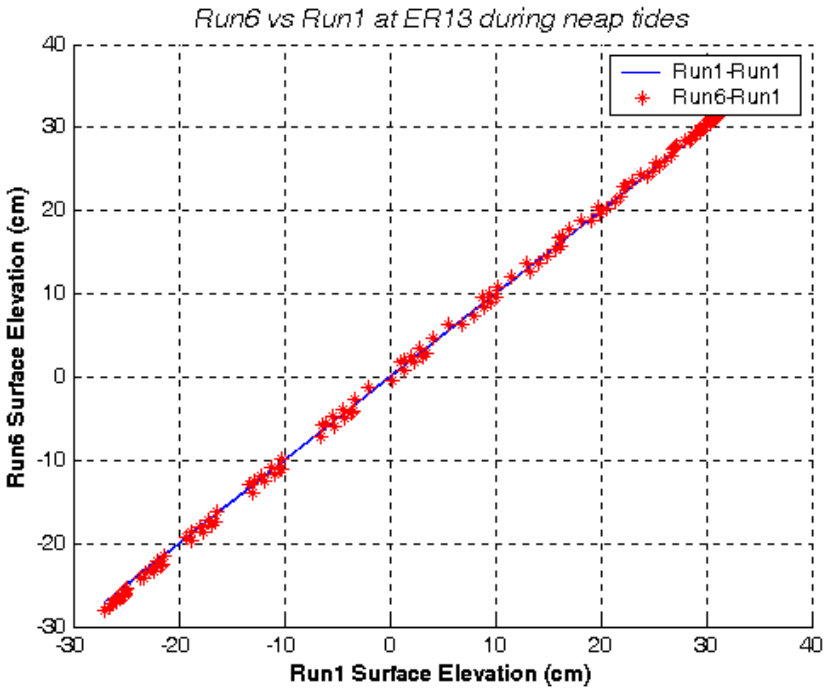

Figure V.5 (sheet 4) at (g) ER05 (h) ER13.

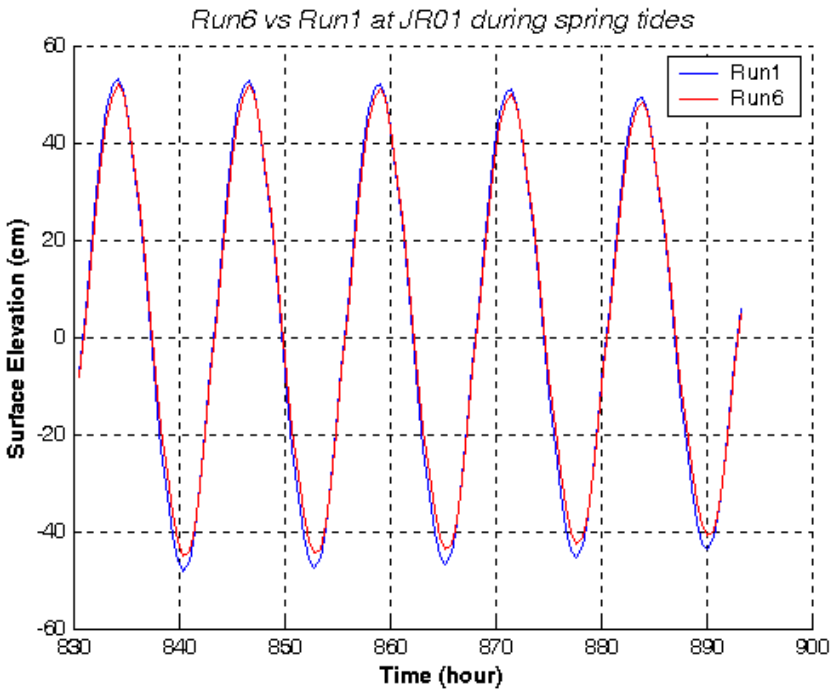

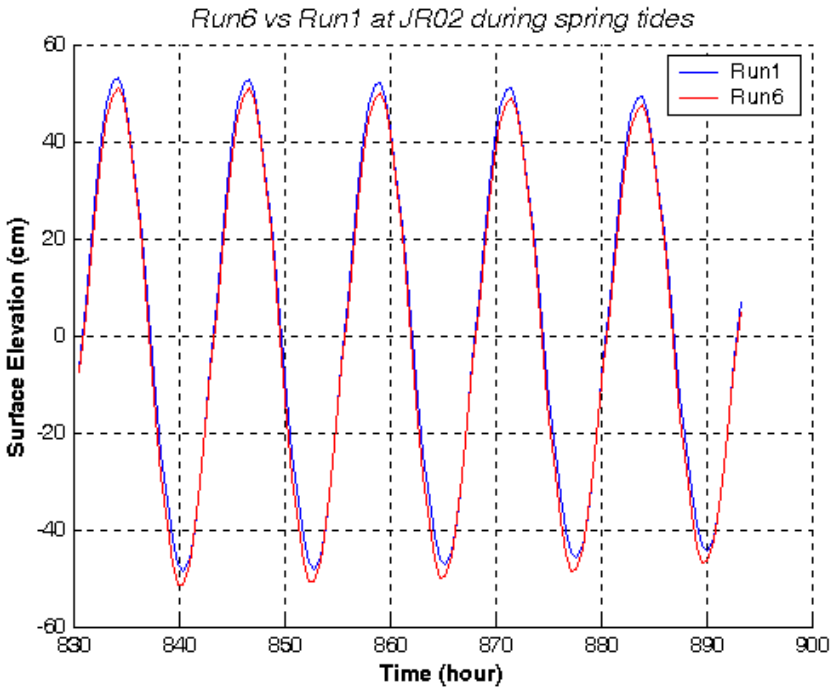

Figure V.6 Tidal elevation time series comparison for Case 1 and Case 6 during spring tide at (a) JR01 (b) JR02 (sheet 1).

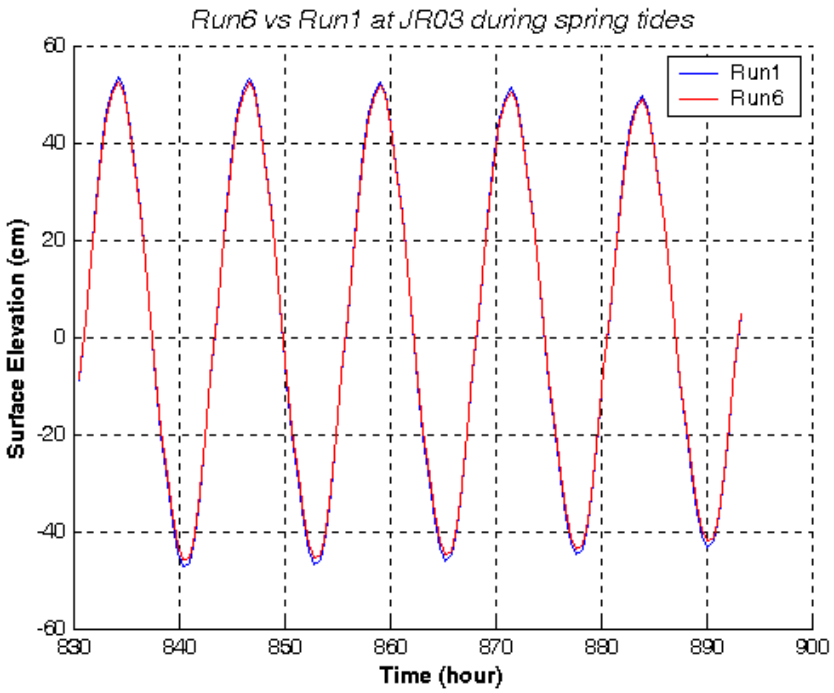

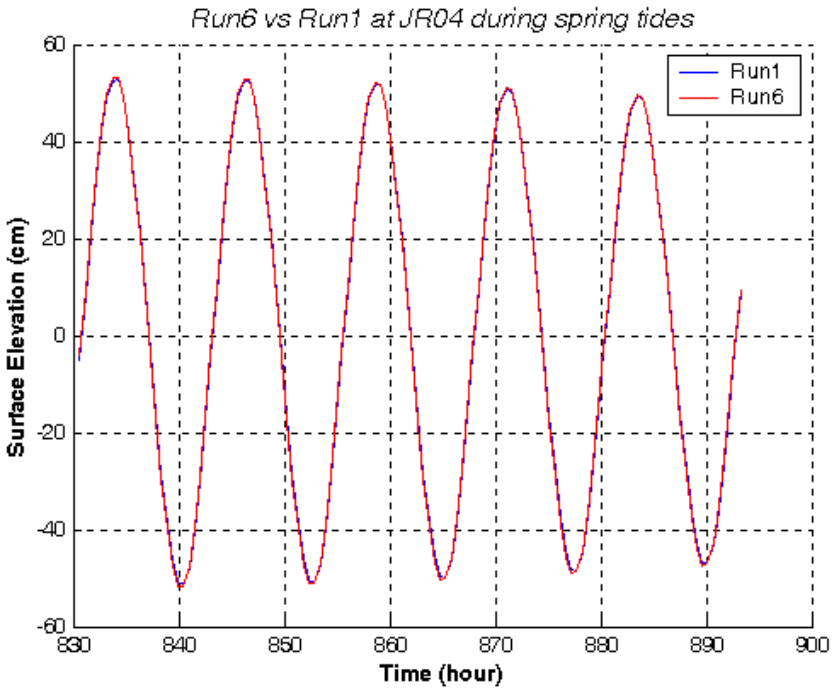

Figure V.6 (sheet 2) at (c) JR03 (d) JR04.

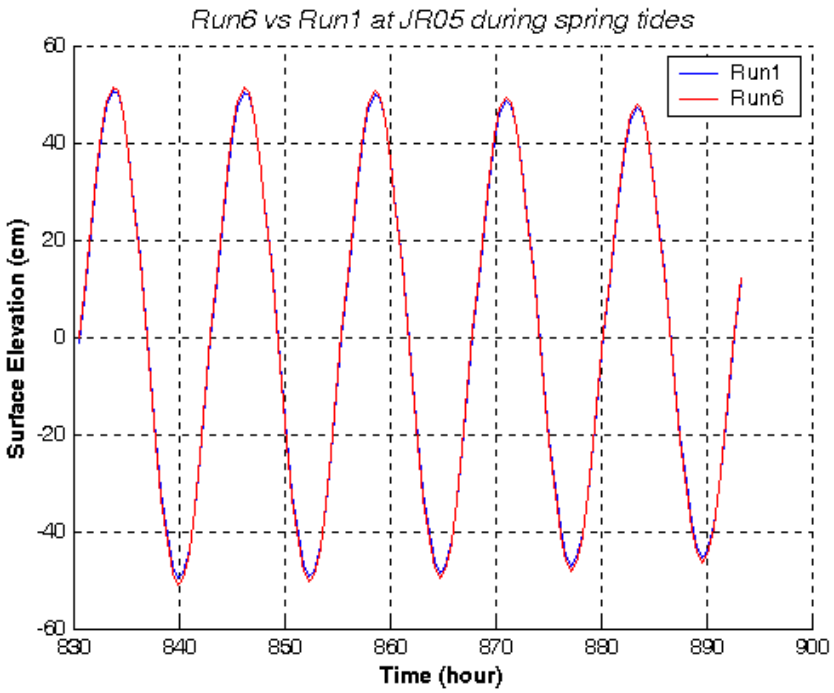

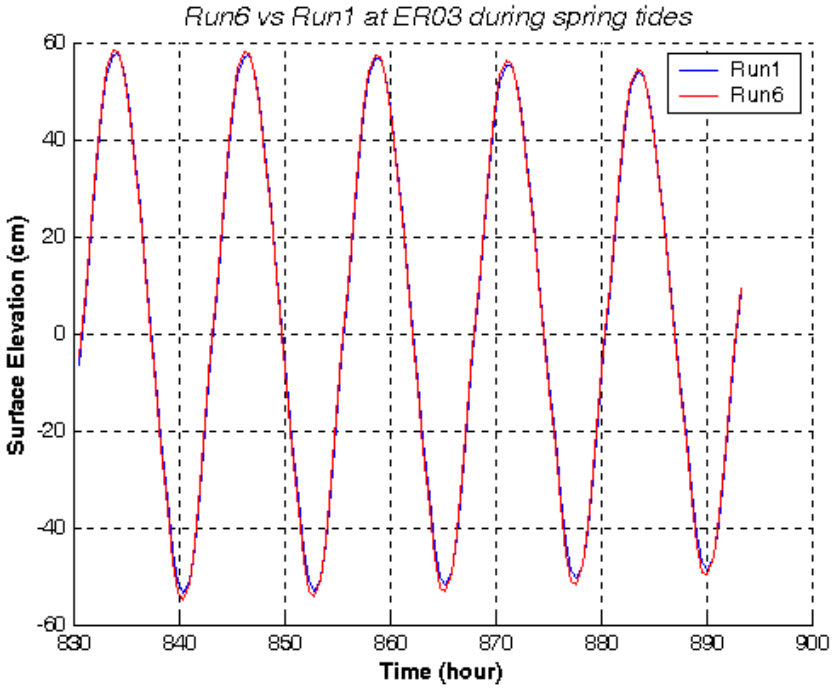

Figure V.6 (sheet 3) at (e) JR05 (f) ER03.

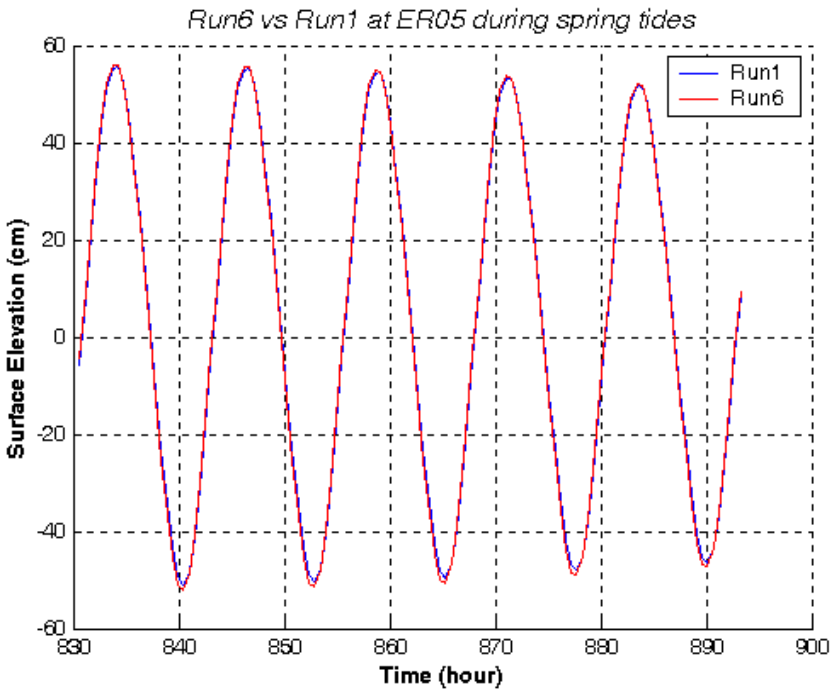

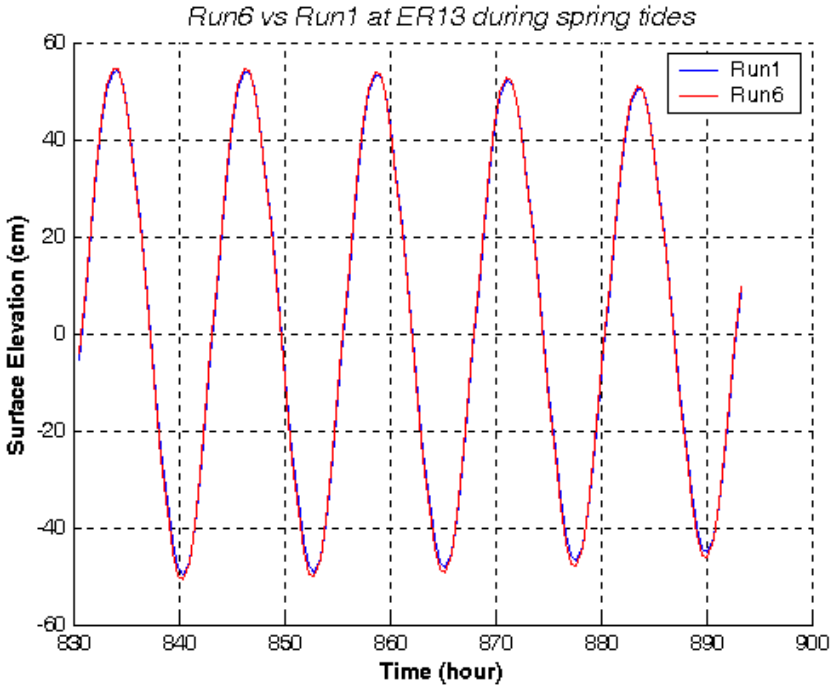

Figure V.6 (sheet 4) at (g) ER05 (h) ER13.

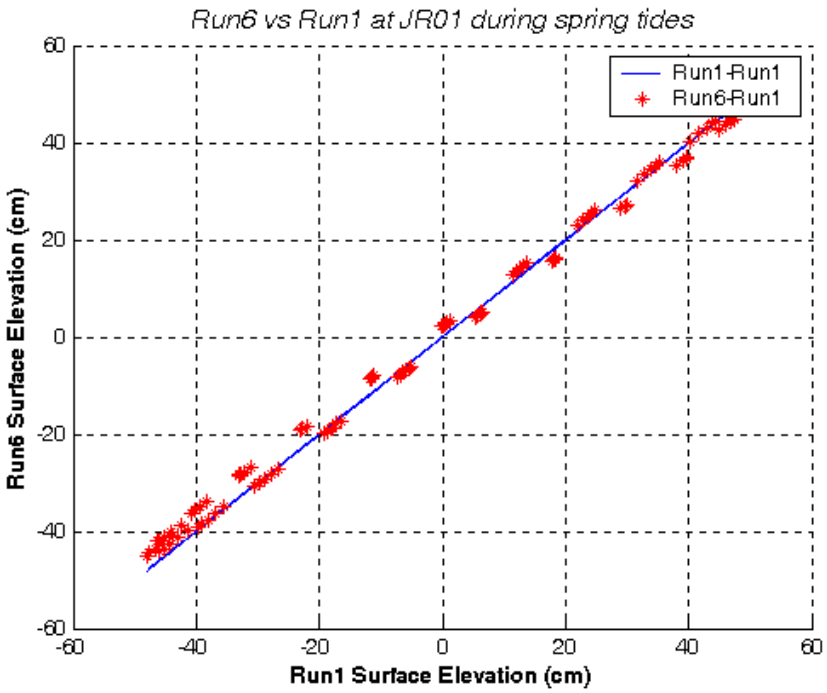

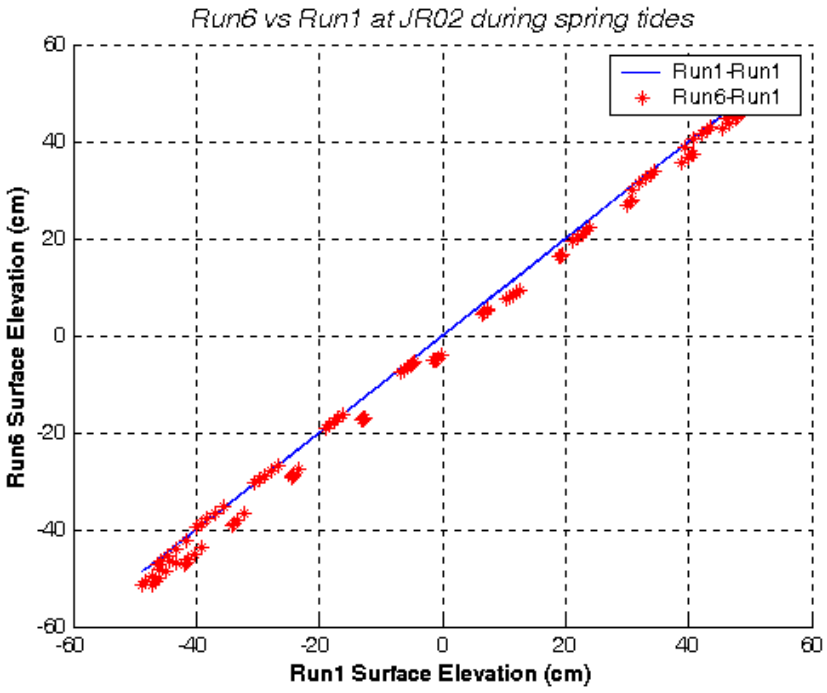

Figure V. 7 Regression plot for Case 1 and Case 6 during spring tide at (a) JR01 (b) JR02 (sheet 1).

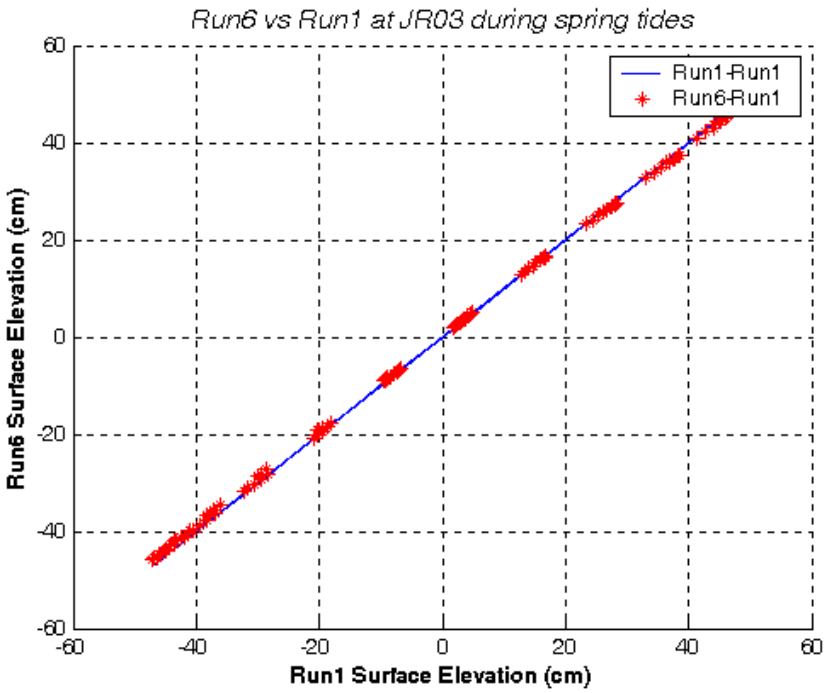

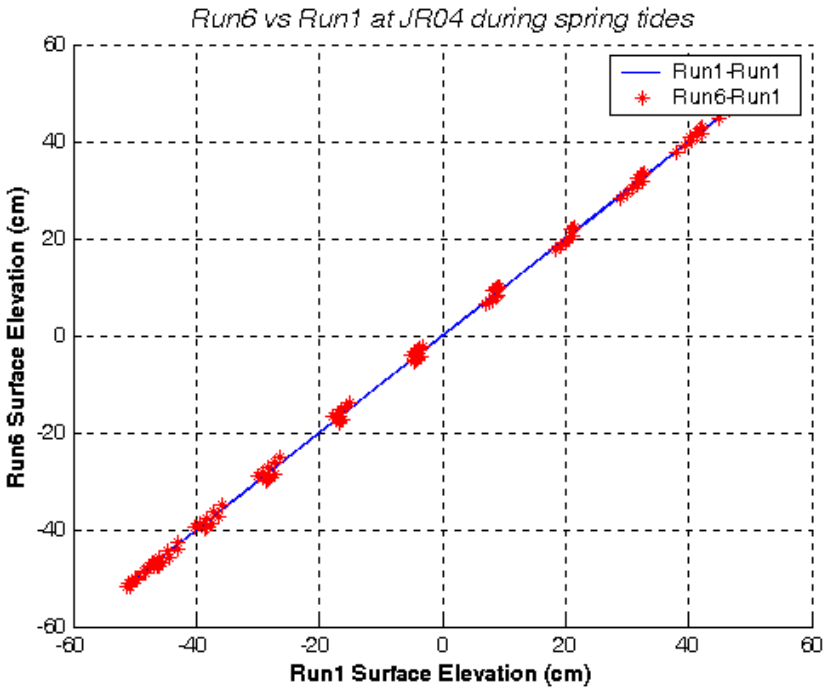

Figure V. 7 (sheet 2) (c) JR03 (d) JR04.

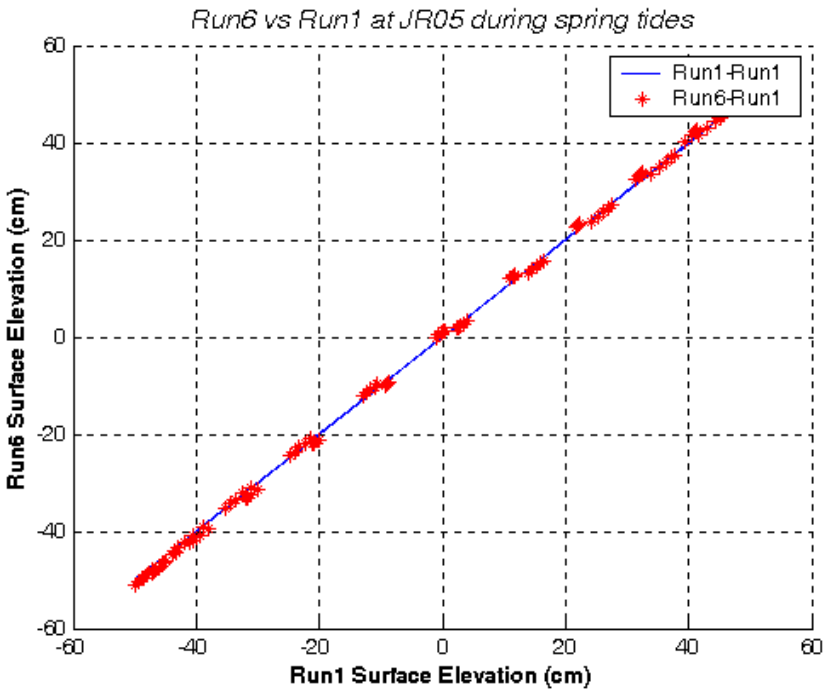

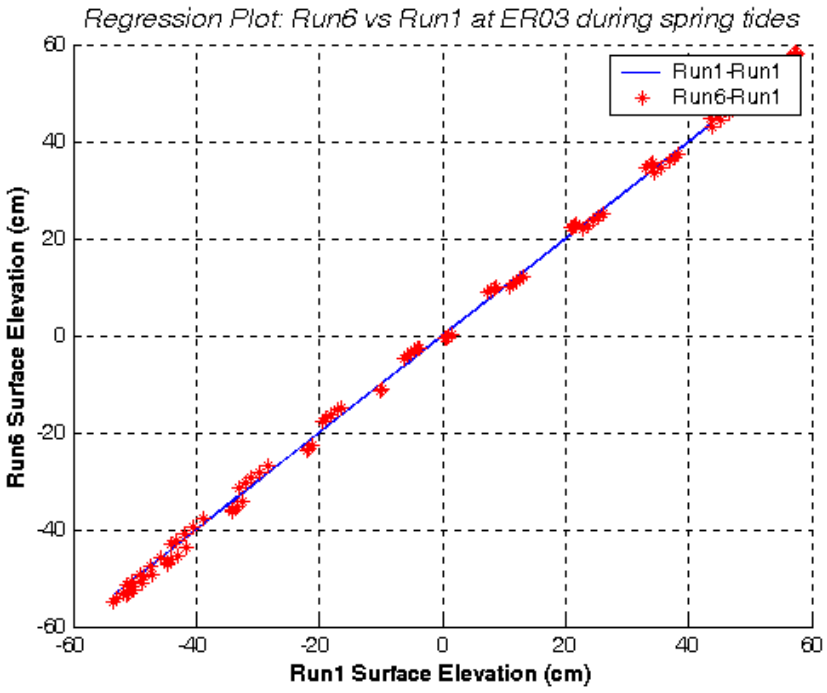

Figure V. 7 (sheet 3) (e) JR05 (f) ER03.

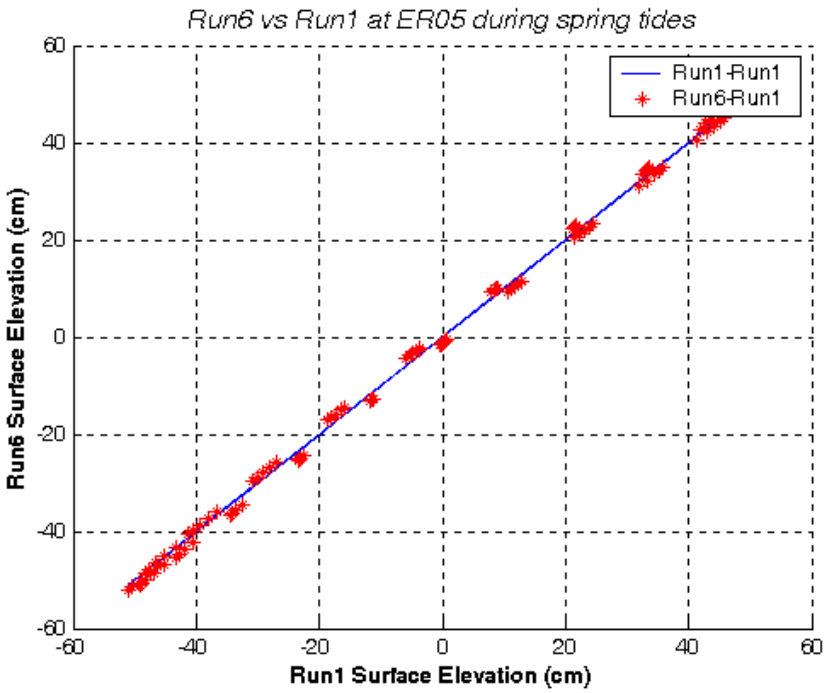

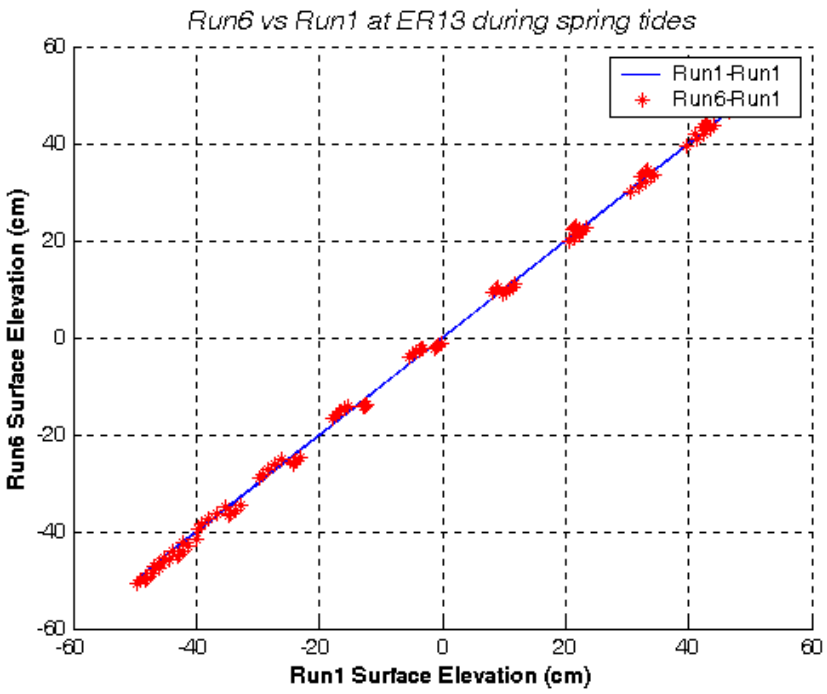

Figure V. 7 (sheet 4) (g) ER05 (h) ER13.

B. Circulation Features

Global analysis revealed that scalar changes in current magnitude are predicted to occur in a number of locations due to the effects of the expansion designs tested in this study. Only a few of these effects are likely to produce significant changes in the estuarine circulation characterized by certain flow features that depend on the way the current is organized in terms of speed and direction. Among the known circulation features within the lower James River, a tidal front and associated eddy system near Newport News Point are considered very important to the movement of aquatic organisms such as shellfish larvae (Shen, Boon, and Kuo, 1999; Shen and Kuo, 1999). We have carefully examined the modeling results for any indication that either of these features would be affected by the expansion options tested. Other circulation features within the Elizabeth River are being investigated for the first time in this study and require careful examination as well. The latter task is now possible due to the increased resolution in the 123 x 123 m Elizabeth River model grid.

Changes in circulation are addressed by examining the horizontal flow field at various depths within four 'windows' selected for this purpose. For convenience, these are named *Newport News Point, Craney Island Reach, Lambert Bend,* and *Town Point Reach.*

1. Newport News Point – The tidal front observed near Newport News Point typically appears late in the ebb phase of flow leaving the James River. Figure V.8 displays the predicted surface flow field during this time (e.g., tidal hour 9.5 in a cycle of 12 lunar hours) with the position of the front indicated by a dashed black line just below Newport News Point. The front marks the line of convergence between incoming, higher salinity water from Chesapeake Bay flowing over Hampton Flats and low salinity water still ebbing from the James River. Along the front, denser water from the bay is driven downward beneath the river water and travels upriver in the deep channel immediately west of the Newport News shoreline. Coupled with the tidal front is a large, counter-clockwise eddy positioned over Hampton Flats. The upper (inshore) segment of this eddy transports higher salinity bay water toward the front as noted above. In addition, the lower (offshore) segment transports a portion of the eastward flowing river water and diverts it to the north where it becomes entrained with incoming bay water. In this way, surface water and water-borne materials that would normally exit Hampton Roads are partially diverted back into the sub-estuary and, when encountering the tidal front, may also undergo further entrainment with bottom water moving up the James River.

Figure V.9 shows the above flow relationship along with the salinity distribution in a cross-section normal to the front (cross-section labeled A-B in Figure V.8). The current vectors shown are the horizontal velocity components lying within the transect plane. At tidal hour 9.0 in Figure V.9, the position of the tidal front is clearly delineated by opposing arrows representing horizontal flow convergence that coincides with the 16 ppt isohaline. The convergence sets up a downward flow component along the front not shown in our presentation scheme that depicts only the horizontal flow components in each of the model's six vertical layers. The vertical velocity is an order of magnitude

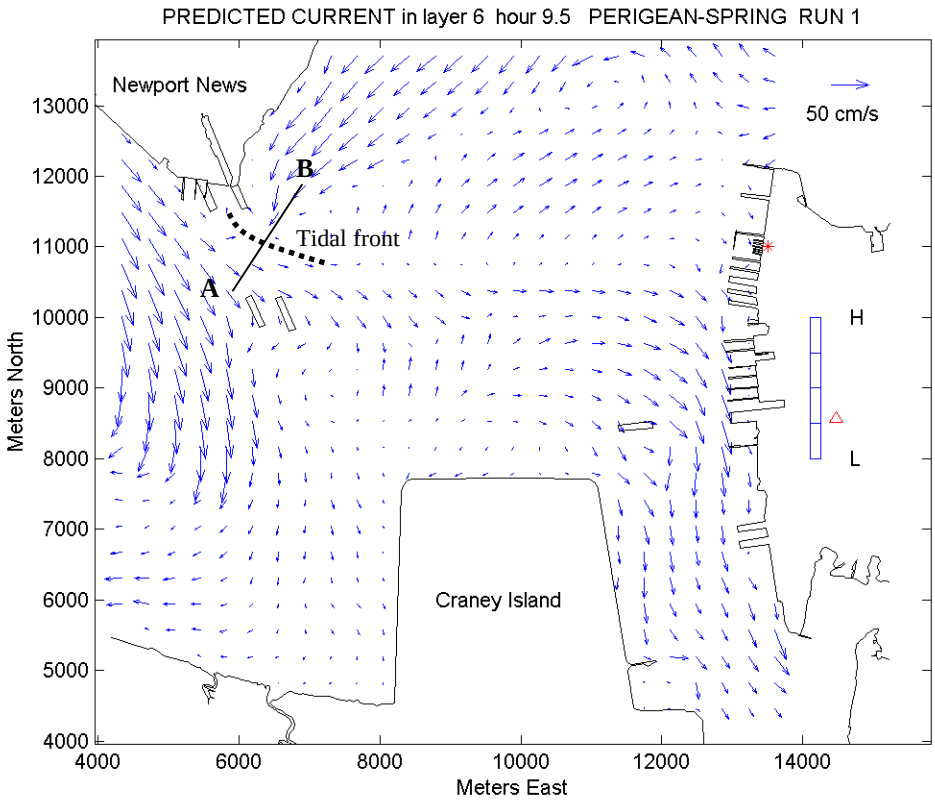

Figure V.8. Predicted surface flow for Base Case, Newport News Point, tidal hour 9.5 during a perigean-spring tide.

smaller than the horizontal velocity. Downward water transport at the front is also evidenced by the continuous layer of 18 ppt water (orange band in Figure V.9) extending from less than a meter below the surface over Hampton Flats to the bottom of the Newport News Channel at –14 m. Field observation of water mass movement aided by current measurements and dye release experiments have previously confirmed these basic features of the tidal front at this location (Kuo et al., 1988).

Another characteristic feature illustrated in Figure V.8 is the diversion of ebb flow into the Elizabeth River entrance as part of an action known as 'tidal pumping'. This phenomenon occurs in branching estuaries and explains why certain tributaries may at times show a reverse salinity gradient (saltier water occurring in the upstream direction rather than the normal downstream direction) near the mouth. This is due to the injection of river water from far upstream into the branch tributary (the Elizabeth River in this instance) during the latter part of the ebb cycle, an occurrence particularly noted during the larger spring cycles (perigean-spring tide) when tidal excursion lengths are greatest.

Residual current - The flow field shown in Figure V.8 represents the instantaneous current predicted at a specific time. To examine the net behavior of water movement in a tidal estuary, it is useful to map the residual current field obtained by vector averaging.

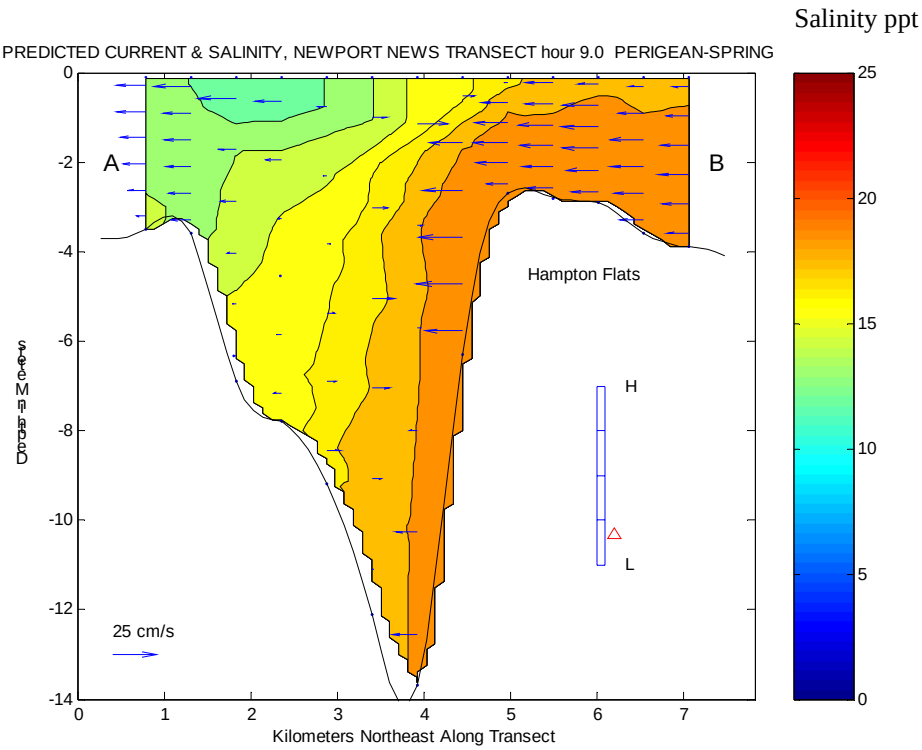

Figure V.9. Predicted current and salinity for Base Case, Newport News Point Transect A-B at tidal hour 9.0 during a perigean-spring tide.

Vector averaging involves simple averaging of the two horizontal velocity components, U (east-west) and V (north-south), predicted at a fixed time interval at each grid point over one or more complete tidal cycles. The residual current field in Figure V.10, for example, shows the extent of the counter-clockwise eddy over Hampton Flats. It is noted that this eddy is most pronounced during tides of minimal range (apogean-neap tides). Within the main current field, Figure V.10 illustrates the dominant seaward flow characteristic of the surface layer in a stratified estuary. However, looking again at Figure V.10 it is obvious that the lower James River has an unusual type of channel morphology that forces the residual flow to turn to the left just before it reaches the river mouth. In making what might otherwise be a smooth left turn, part of the eastward flow encounters a barrier, Craney Island, forcing it to accelerate and setting up a strong northward residual current near the northwest corner of the island (Figure V.10). Above this point, the residual flow resumes eastward movement across the northern edge of Craney Island until it reaches the entrance to the Elizabeth River. There it joins an eddy, or eddy-like feature, turning in a clockwise direction. We use the term ‘eddy- like’ to emphasize that this feature may result in part from vector averaging of a biased flow distribution, the bias arising during a brief period in which strong instantaneous flow is diverted into the Elizabeth River entrance during late ebb (Figure V.8). This brief pulse of water separating from the fresh water stream exiting the main stem of the James River is referred to as tidal pumping. It is noted that tidal pumping also appears to be reflected in the flow field occurring near the entrance to the Western Branch within the Elizabeth River interior.

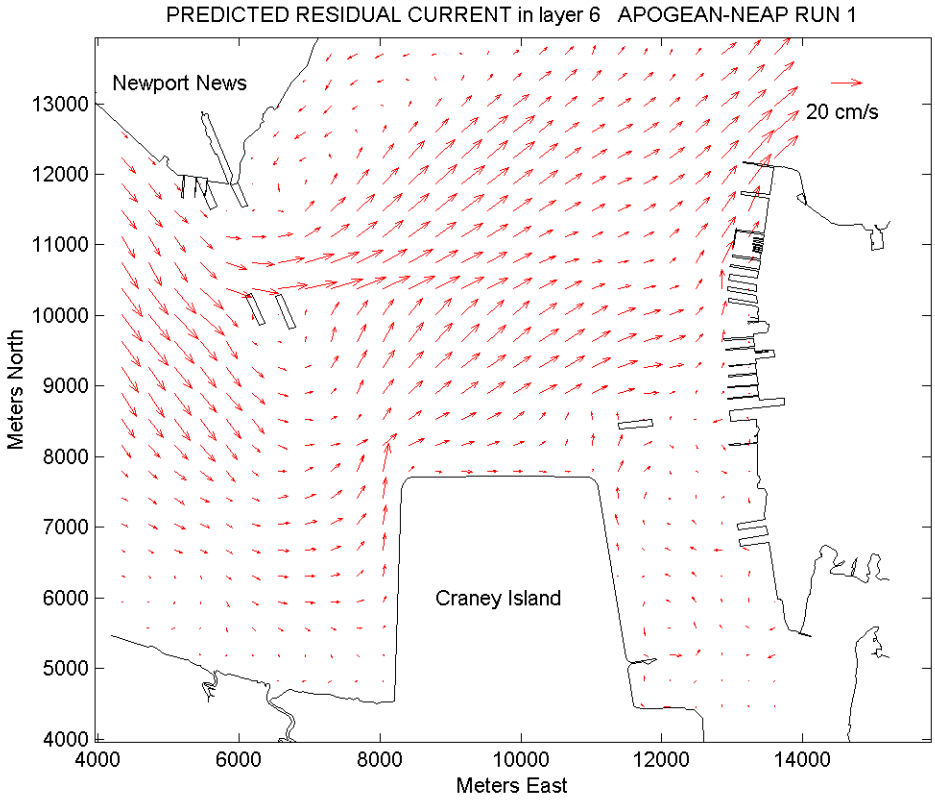

Figure V.10. Predicted surface residual flow for Base Case, Newport News Point, during an apogean-neap tide.

Changes in Circulation – To depict the changes highlighted by the model simulation comparisons between the Base Case and each of the four Test Cases, plots of the surface and bottom residual current field were constructed. These are presented in the Appendix to Chapter V, Section B. As suggested by the results of the global analysis presented in Section A of this chapter, the Northward Expansion (Option 6) and the North/East Expansion (Option 9) produced the greatest degree of change. Local analysis suggests that the changes predicted for both options are significant in terms of at least two of the features described above. In the first instance, the large eddy on Hampton Flats is considerably weakened as seen in the surface residual current predicted for both Options 6 and 9 (Appendix to Chapter V Section B, Figure 7 and Figure 9). In the second instance, the directions of the surface and bottom residual currents along the northern edge of Craney Island are reversed and the northward moving current along the western edge is strengthened, producing a large counter-clockwise eddy northwest of the northwest corner of Craney Island (Appendix to Chapter V, Section B, Figures 7,8,9,10).

With respect to changes affecting the tidal front below Newport News Point, Figures V.11 and V.12 contain the predicted current and salinity distributions for Northward Expansion (Case 6). These figures show that the tidal front is still evident in the case of Northward Expansion but the form of the front has changed and full insertion of 18 ppt water at the bottom of the channel is somewhat delayed.

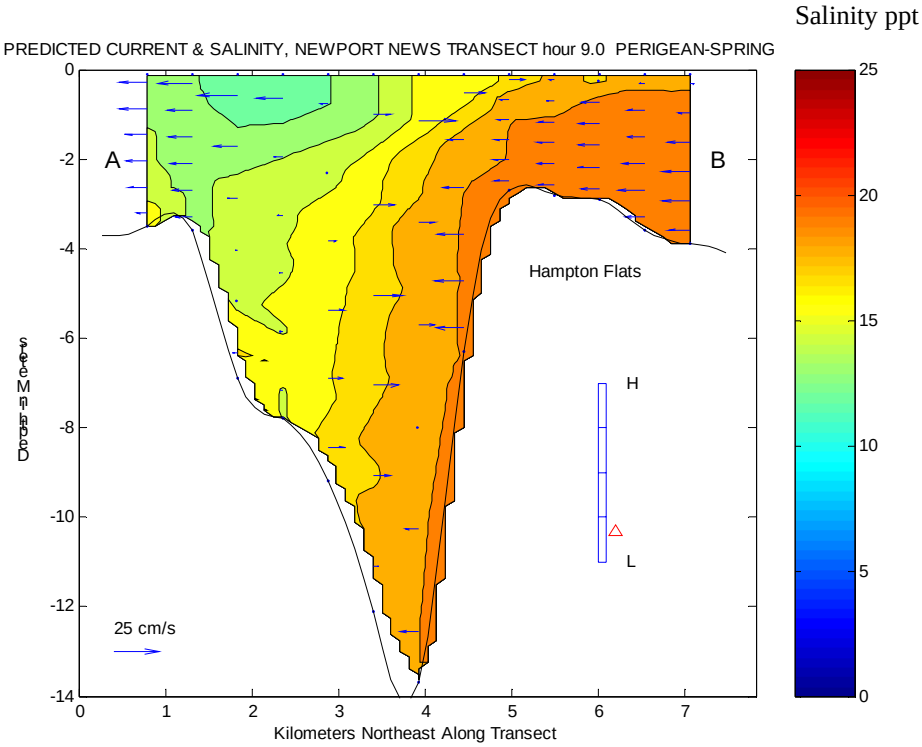

Figure V.11. Predicted current and salinity for Northward Expansion (Case 6), Newport News Point Transect A-B at tidal hour 9.0 during a perigean-spring tide.

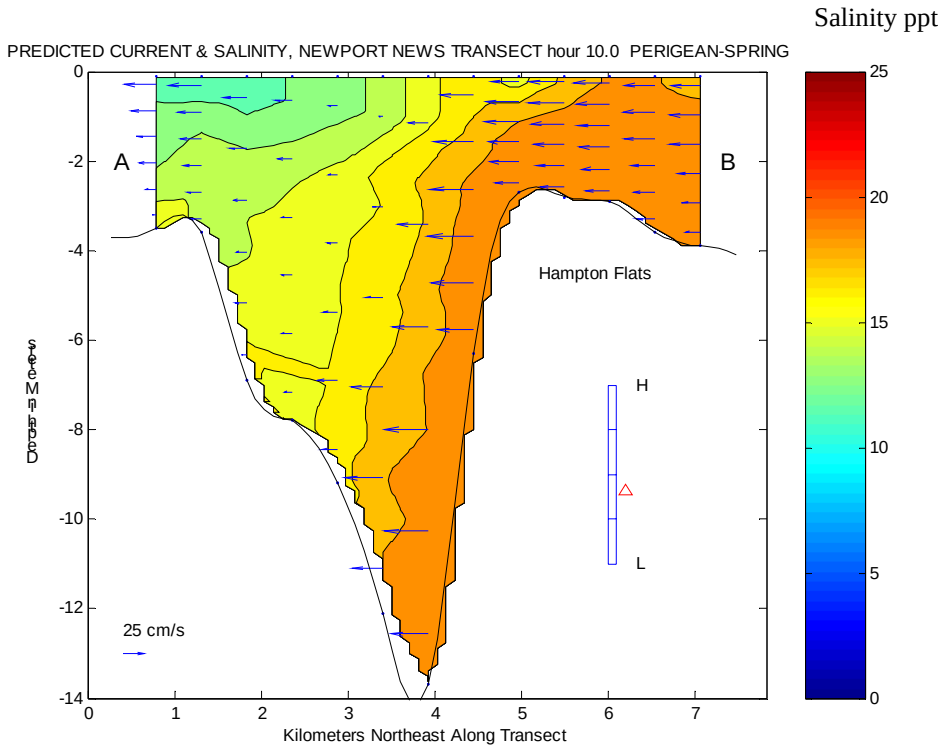

Figure V.12. Predicted current and salinity for Northward Expansion (Case 6), Newport News Point Transect A-B at tidal hour 10.0 during a perigean-spring tide.

2. Craney Island Reach – The window for Craney Island Reach covers both the entrance to the Elizabeth River and the entrance to one of its branches, the Lafayette River. In contrast to the eddy systems that are best developed in the Newport News Point window during apogean-neap tides, those within the Elizabeth River show optimum development during perigean-spring tides. This is due to the fact that eddies within the Elizabeth River are smaller and tend to develop as wakes in the lee of a breakwater or promontory where they are governed by bottom topography. The higher current velocities associated with perigean spring tides are conducive to eddy (wake) formation of this kind. Large eddies in the James River, such as the one previously described at Hampton Flats, are strongly influenced by water column stratification, a state more often observed during neap tides as opposed to spring tides.

The higher resolution of the model grid within the Craney Island Reach window permits the small clock-wise eddy in the surface residual current field at the Elizabeth River entrance to be clearly seen (Figure V.13) along with a small counter- clockwise eddy present at the entrance to the Lafayette River. During perigean-spring tides the eddy-like features seen in Figure V.13 are the dominant form of flow organization present in the surface layer with no clearly defined seaward flow being at all apparent. In contrast, Figure V.14 illustrates that the bottom residual flow in the Craney Island Reach is largely confined to the main channel where it is uniform and directed upstream.

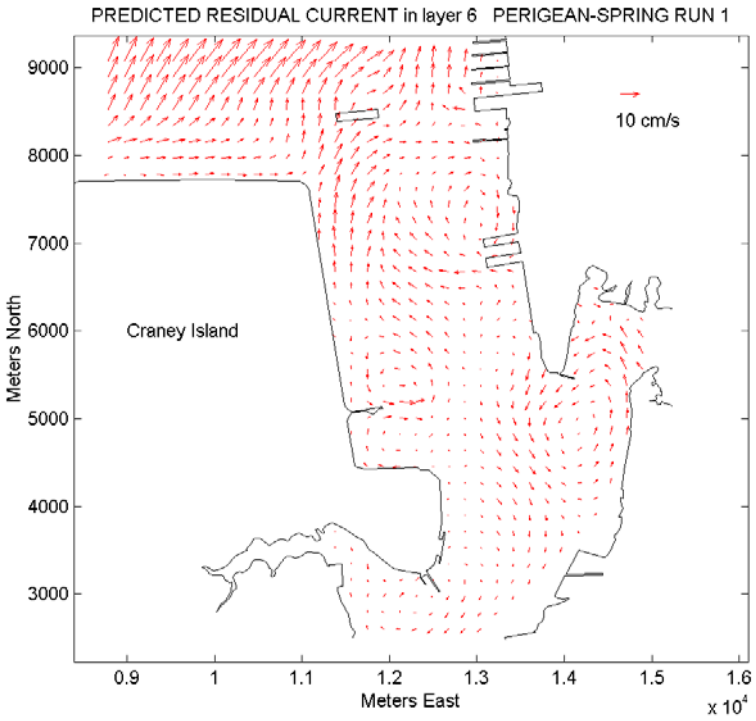

Figure V.13. Predicted surface residual flow, Craney Island Reach, during a perigean-spring tide (Base Case).

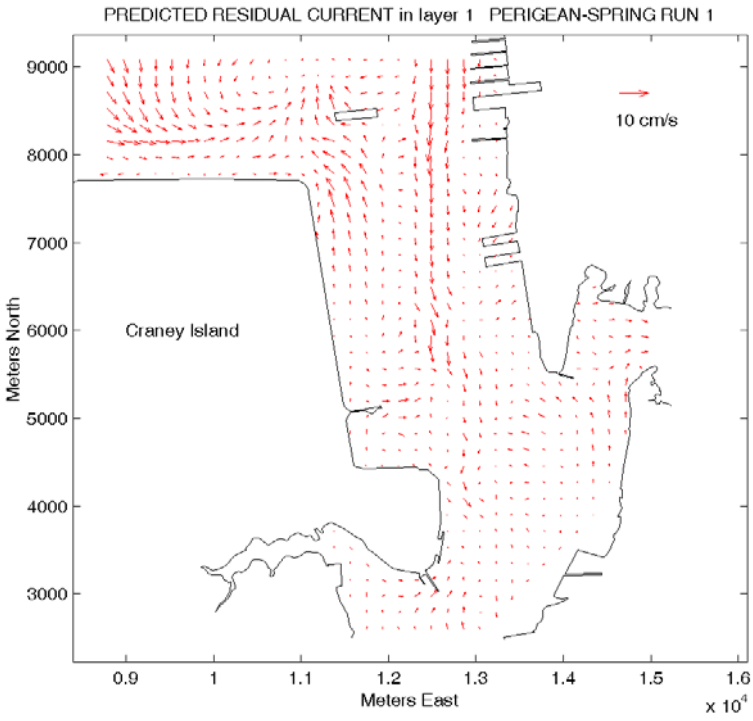

Figure V.14. Predicted bottom residual flow, Craney Island Reach, during a perigean-spring tide (Base Case).

Changes in Circulation – Surface and bottom residual flows for the Craney Island Reach window are presented in Appendix to Chapter V, Section B. There are no pronounced changes in the general circulation patterns just described in Figures V.13 and V.14 above for any of the Test Cases. The only question to emerge in the evaluation was whether a slight intensification of the current velocity and eddy structure shown in Figure V.13 might affect the transport of water-borne materials through a convergence or trapping effect. Estimates of the tidal excursion, or distance traveled by a water particle during either flood or ebb, were considered long in comparison to eddy diameter, implying that no trapping effect was likely. This view was confirmed by conducting a particle tracking experiment through model simulation involving three different release points in the surface layer at the entrance to the Lafayette River. Each of the particles released was tracked by determining its position at half-hour intervals during a perigean-spring tide as shown in Figure V.15. All three particles shown gave no indication of any tendency towards trapping within the eddy feature located at the mouth of the Lafayette River. All three required less than three complete tidal cycles to exit the Elizabeth River and begin large excursions at the entrance to the James River. We consider this test to be a valid diagnostic applicable to a considerable number of wakes and eddy-like features in the residual flow - features that appear to be the rule rather than the exception in the Elizabeth River. In other words, relative strengthening or weakening of these features due to whatever cause is not likely to affect the transport of water or water-borne materials through irregular waterways at the scale of the Elizabeth River and its branches.

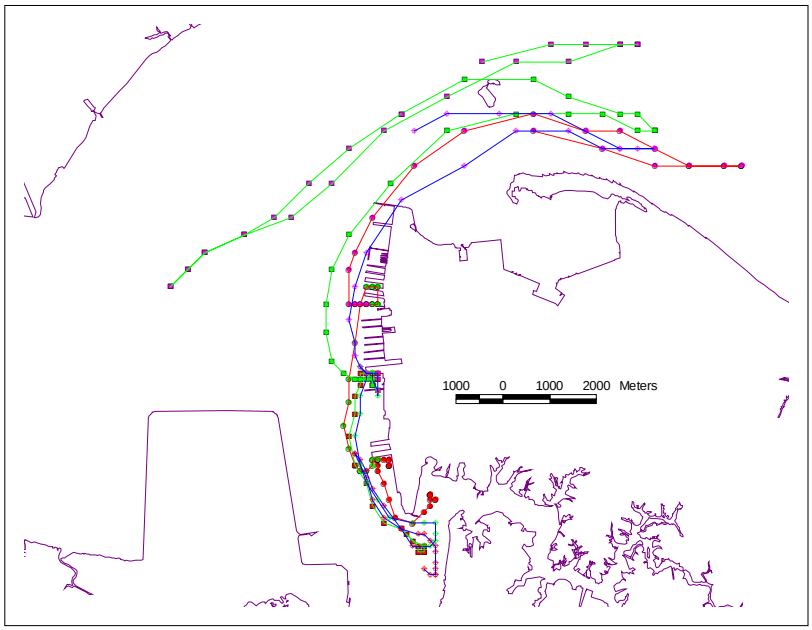

Figure V.15. Track lines of surface particles released at the Lafayette River entrance, perigean-spring tide simulation, Base Case.

3. Lambert Bend – The window for Lambert Bend covers a sharp left turn around Lamberts Point in the Elizabeth River as shown in Figure V.16. Certain details concerning the circulation in this region were provided earlier in Chapter IV on calibration/verification of the model. Among other features, the existence and general form of the central counter-clockwise eddy between Lamberts Point and the entrance to the Western Branch was confirmed by field measurements using an ADCP device (Acoustic Doppler Current Profiler). As can be seen in Figure V.16, the northeast limb of the surface eddy is coupled with a straight line of exiting channel flow in the Port Norfolk Reach just below Lamberts Point. Flow in the southwest limb of the eddy actually intensifies over the shallow bottom west of the channel (Appendix to Chapter V, Section B, Figure 22) where it conveys most of the residual flow going upstream from this point. Residual flow in the deepest layer next to the bottom is not well organized except in the channel area where it tends to be weak and seaward directed.

Changes in Circulation – There appear to be no discernable changes in the residual circulation in this segment of the Elizabeth River with one exception. As can be seen in Figure V.17 for Northward Expansion, the ebb-directed surface current appears noticeably strengthened over the Port Norfolk Reach channel when compared to the Base Case condition. Other change is difficult to assess in a complex region of the Elizabeth River where circulation is simultaneously affected by a near right-angle turn rounding Lambert Point (similar to flow turning around Newport News Point) and the proximity of the Western Branch where flow is diverted in tidal pumping.

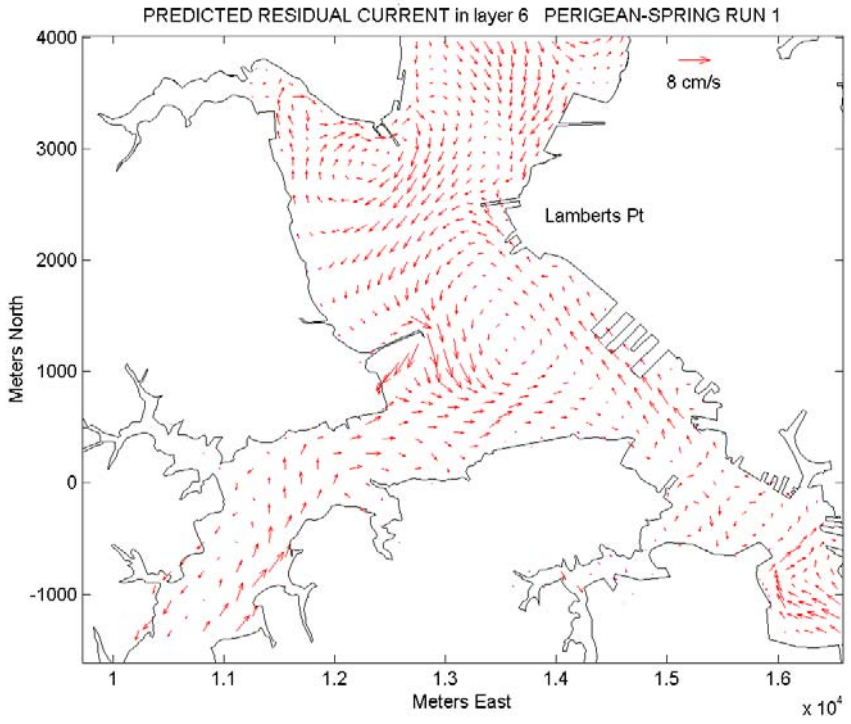

Figure V.16. Predicted surface residual flow, Lambert Bend, during a perigean-spring tide (Base Case).

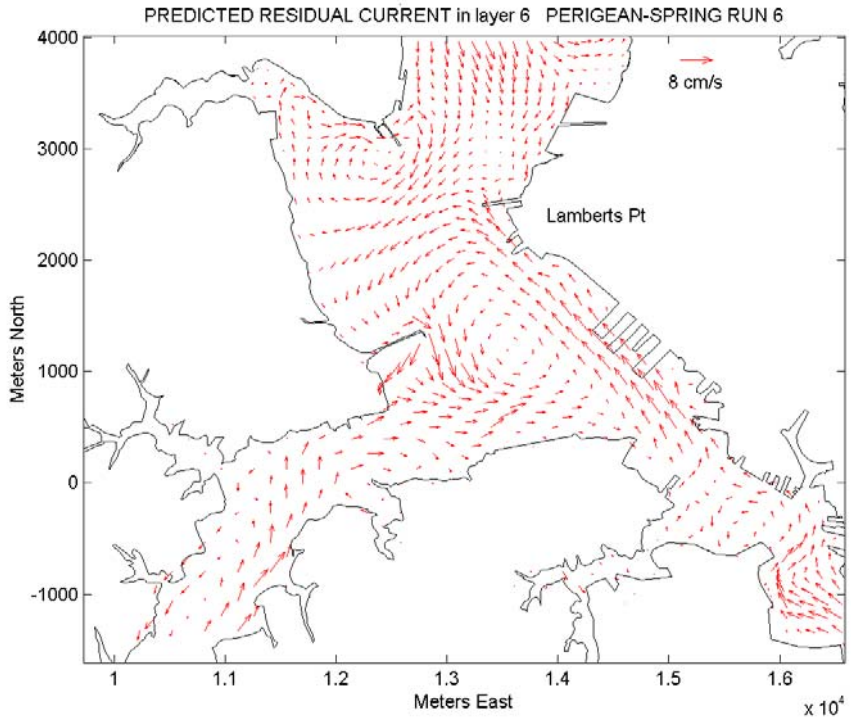

Figure V.17. Predicted surface residual flow, Lambert Bend, during a perigean-spring tide, Northward Expansion (Case 6).

4. Town Point Reach – Surface and bottom residual currents for the Town Point Reach window are presented in Figures 31 through 40 in the Appendix to Chapter V, Section B. As shown in Figure V.18 below, this section of the Elizabeth River contains the confluence between the Eastern Branch and the Southern Branch, both of which are quite narrow in this region (widths equal to three 123 m cell lengths or less). Although the surface residual flow appears chaotic in this setting, the bottom residual current is well defined and proceeds with higher velocity into the Southern Branch channel as opposed to the Eastern Branch channel.

Circulation changes - No changes in the residual circulation within the Town Point Reach window are noted for any of the Test Case simulations when compared with the Base Case.

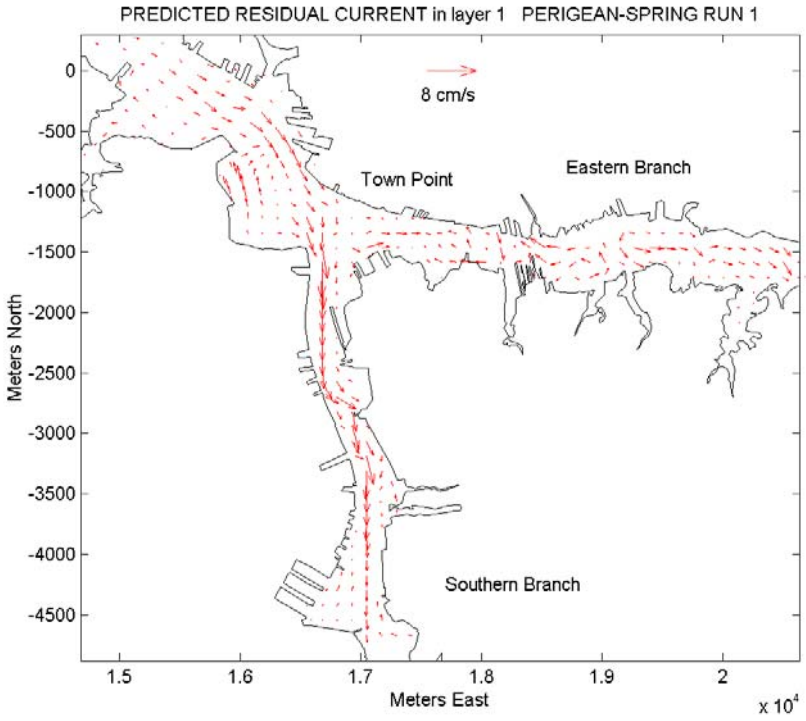

Figure V.18. Predicted bottom residual flow, Town Point Reach, during a perigean-spring tide, Base Case.

C. FLUSHING CHARACTERISTICS

The flushing capacity of an estuarine system may be estimated in two ways. One is to calculate the rate of the water exchange through a cross-section delineating the mouth of the estuary. The other is the direct simulation of flushing of material artificially introduced into the estuary. Both approaches were utilized in this study by simulation comparisons. The following two sections describe the methods of calculation and the results comparing various expansion options. In addition, some numerical experiments of particle tracking were also performed and presented. The fates of particles may serve as a qualitative indication of flushing characteristics at local region of particle release.

1. Flux Calculation - The water exchange through a cross-section may be classified into tidal and non-tidal components. Flushing is the cumulative effect of these two modes of transport in an estuarine system. The tidal prism, defined as the volume of water transported back and forth through a cross-section during a tidal cycle, quantifies the tidal flushing. The flood tide brings in the tidal prism volume of water, mixes it with the water in the system, and then removes the same volume of water during ebb tide. The non-tidal residual circulation brings in the water from one part of the cross-section, displaces the water in the system and pushes it out through another part of the cross-section. The non-tidal transport is driven by freshwater inflow at the landward end of an estuary, balanced by saltwater inflow at the seaward end of the estuary. Therefore, the calculation of volume flux through a cross-section is separated into two parts, tidal and non-tidal (or residual).

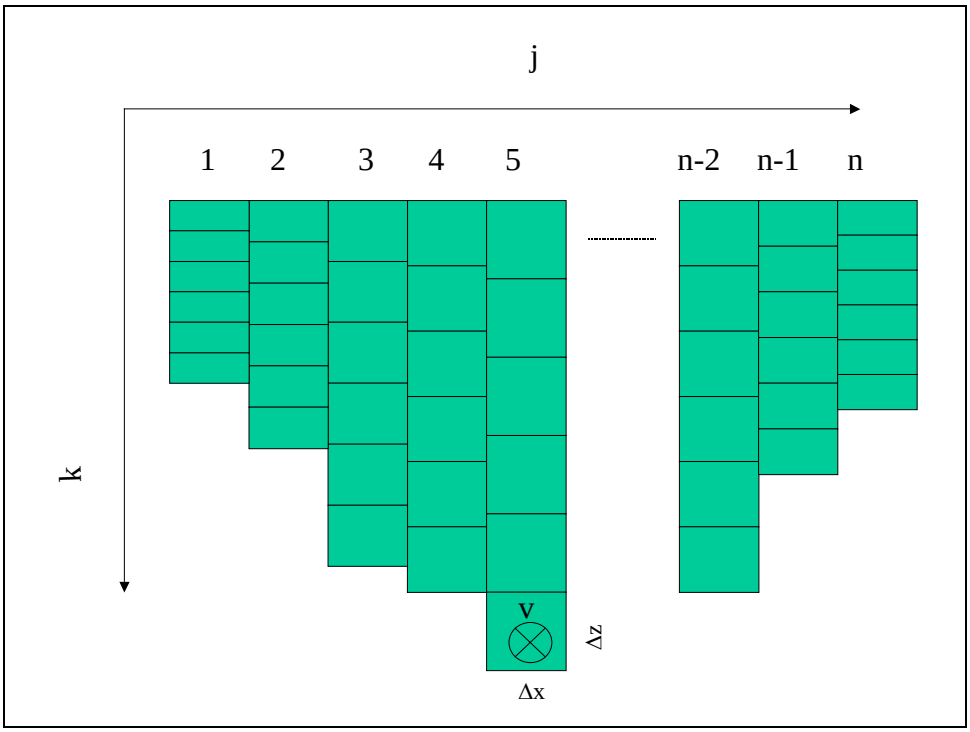

Figure V.19. Definition sketch for flux calculation.

As shown in Figure V.19, consider an estuarine cross-section in the *x*-*z* plane, which is divided into an array of computation cells by the numerical model. Let the *j*-index vary along the *x*-axis in the horizontal direction and the *k*-index vary along the *z*-axis in the vertical direction. Also, let *n* be the number of columns with constant width, Δx, in the *x*-direction, with 6 cells of variable thickness, Δz, in the *z*-direction. The volume transport, q_{ijk}, over the time interval Δt at time *i* is then calculated as $q_{ijk} = \Delta x \cdot \Delta z \cdot \Delta t \cdot \mathrm{v}_{ijk}$ where Δt is the time step and v_{ijk} is the velocity normal to the cross-section . If *nrec* is the number of time steps in a tidal cycle, then, the total residual (non-tidal) volume transport through the *j*-*k* cell during the tidal cycle is $qr_{jk} = \sum_{i=1}^{nrec} q_{ijk}$, and the mean residual transport for each time step becomes $\overline{qr_{jk}} = qr_{jk} / nrec$. The residual volume transports through the cross-section in the flood direction, QR_{flood}, and in the ebb direction, QR_{ebb}, are defined as

$$QR_{flood} = \sum_{j=1}^{n}\sum_{k=1}^{6} qr_{jk} \; if \; qr_{jk} \le 0$$

$$QR_{ebb} = \sum_{j=1}^{n}\sum_{k=1}^{6} qr_{jk} \; if \; qr_{jk} \ge 0$$

The net residual volume transport becomes the difference between the ebb and flood residuals and this should be the same as the freshwater inflow to the system, $Q_{freshwater}$

$$QR_{net} = QR_{ebb} - QR_{flood} \approx Q_{freshwater}$$

The tidal volume transport through each cell is defined as the difference between the instantaneous volume transport and the mean residual transport:

$$qt_{ijk} = q_{ijk} - \overline{qr_{jk}}$$

Then the volume transports induced by flood and ebb tides are defined for a tidal cycle as

$$QT_{flood} = \sum_{i=1}^{nrec}\sum_{j=1}^{n}\sum_{k=1}^{6} qt_{ijk} \; if \; qt_{ijk} \le 0$$

$$QT_{ebb} = \sum_{i=1}^{nrec}\sum_{j=1}^{n}\sum_{k=1}^{6} qt_{ijk} \; if \; qt_{ijk} \ge 0$$

The ebb and flood volume transport should be the same and identical to the tidal prism that is defined as the volume of water exchanged through a cross-section by the oscillating tidal flow.

Seven cross-sections were selected for investigating potential changes of volume transport, which may result from various expansion options. Two (A, C) are located in the entrance reach of the Elizabeth River. Four are at the mouths of sub-tributaries—the Lafayette River (L), the Western Branch (W), the Eastern Branch (E), and the Southern Branch (S) (Figure V.20). The remaining one is located at the entrance to the Nansemond River (N). The calculated tidal prism and residual volume transport for Base Case are shown in Figure V.21 along the entrance reach. Fluxes through 2 additional cross-sections (B, D) in the Elizabeth were also calculated for the purpose of constructing this figure. The figure shows the characteristics of the volume transport in a partially mixed

estuary. The tidal prism is an order of magnitude larger than the residual transport, and both decrease in the upriver direction.

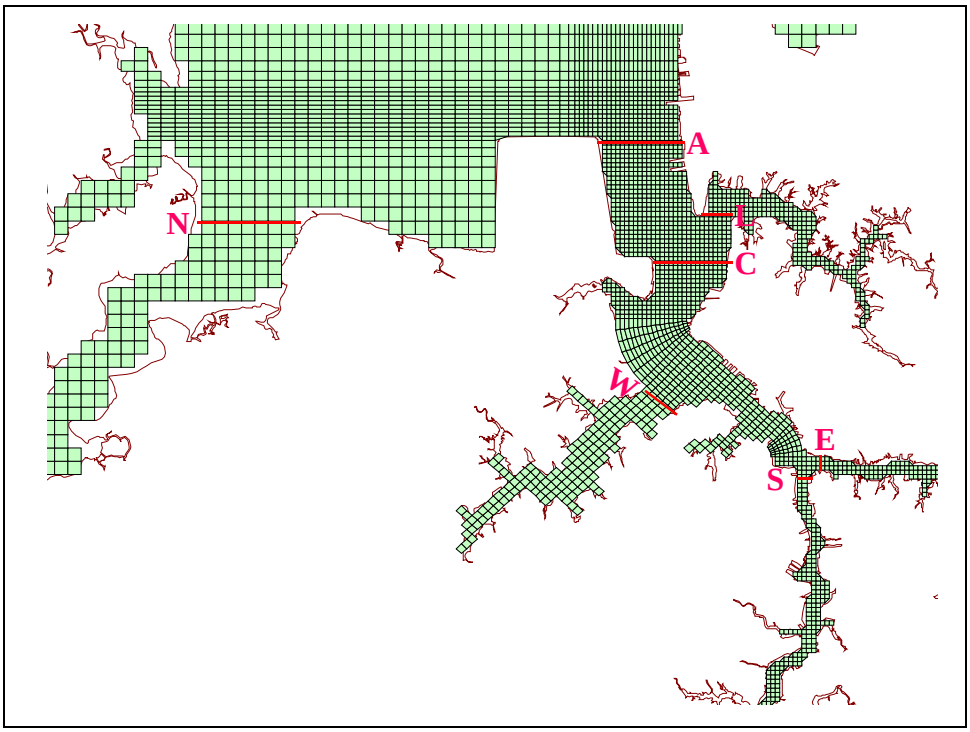

Figure V.20. Cross-sections for flux estimation.

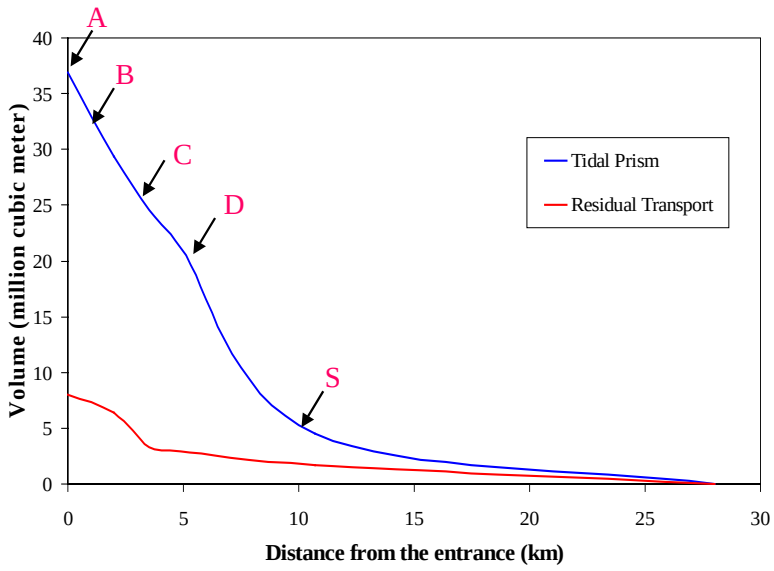

Figure V.21. Along channel variation of tidal prism and residual volume transport per tidal cycle (Case 1-Base Case, the numbers are in million cubic meters).

The calculated tidal prism and residual volume transport for all expansion options are listed in Tables V.1 through V.7 for the 7 cross-sections selected for investigation. Figure V.22 provides a graphical presentation of tidal prism and residual transport variations with location as well as expansion option. The tables and figure indicate that different channel depths with the same expansion option (for example, Cases 2 and 3, Cases 4 and 5) do not result in much difference in tidal prisms nor residual transports. The Westward Expansion (Cases 4 and 5) produces the least change in the tidal prism for the Elizabeth River system. There is a reduction of tidal prism from 5 to 6 % at cross-section A for the Eastward Expansion (Cases 2 and 3), however there is an increase of more than 20 % in residual transport. It is reasonable to assume that the opposite signs for the changes in these transports (i.e., tidal prism decreases and residual transport increases) will have opposite effects on the flushing capacity but the net effect cannot be determined on the basis of flux calculations alone. For this reason, simulated tracer release experiments were carried out (see Chapter V, Section B.2) to determine the combined effect for a particular release point. The changes due to the Eastward Expansion diminish in the upriver cross-sections. The Northward Expansion (Cases 6 and 7) and the Northward-Eastward Expansion combined (Cases 8 and 9) also reduce tidal prism and increase residual transport through cross-section A, however the increase in residual transport is much smaller when compared with the Eastward Expansion (Cases 2 and 3).

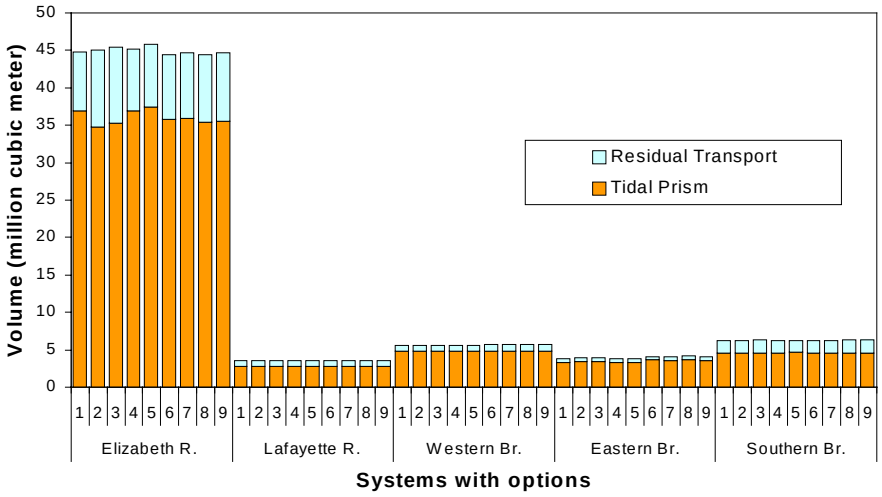

Figure V.22. Tidal prism variation with location and expansion options.

Changes in tidal prism and residual transport associated with Eastward Expansion (Cases 2 and 3) are consistent with design changes affecting cross-section A at the entrance to the Elizabeth River (Figure V.23). The fill zone producing expansion to the east clearly reduces the surface area and thus the tidal prism. However the cut zone providing the berthing area effectively widens the deeper portion of the channel and produces a slight increase in cross-sectional area. This appears to be the cause of the larger increase in residual transport for Cases 2 and 3 in the Elizabeth River shown in Figure V.22.

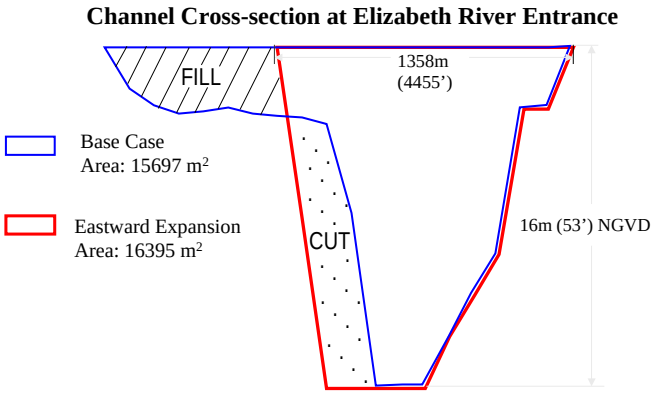

Figure V.23. Channel cross-sections for Base Case and Eastward Expansion, Elizabeth River Entrance at Craney Island.

2. Tracer Experiments – To evaluate the overall flushing rate (or residence time) of the system, numerical experiments of dye (tracer) release studies were conducted for the Base Case and the Eastward Expansion option (Cases 2 and 3). A unit mass of a neutrally buoyant tracer was released in the Southern Branch near the Jordan Bridge (Figure V.24). The tracer was released instantaneously near the end of flood tide and its concentration distribution was calculated by the mass-balance equation as the model simulation advances through successive time steps.

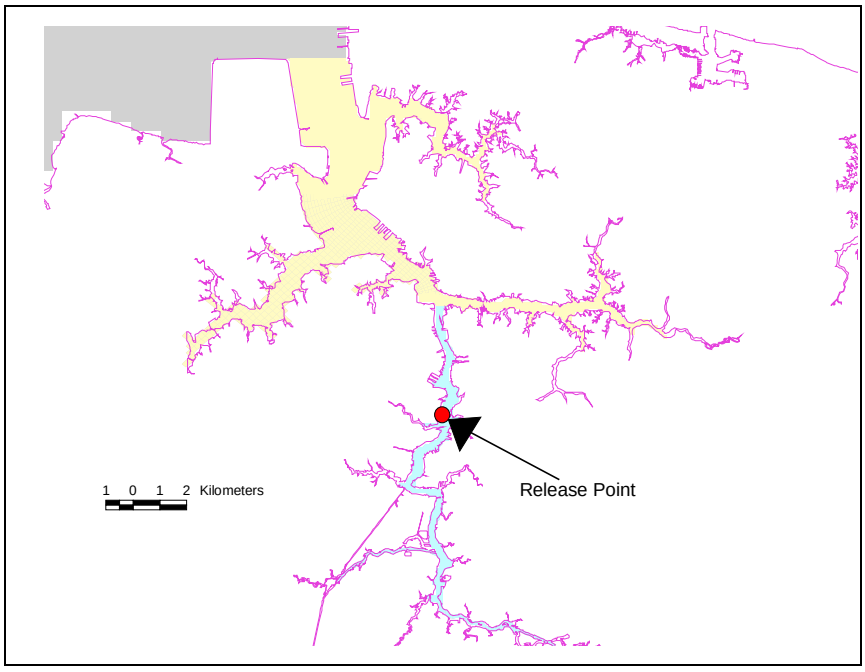

Figure V.24. Location of tracer release in the Southern Branch near the Jordan Bridge.

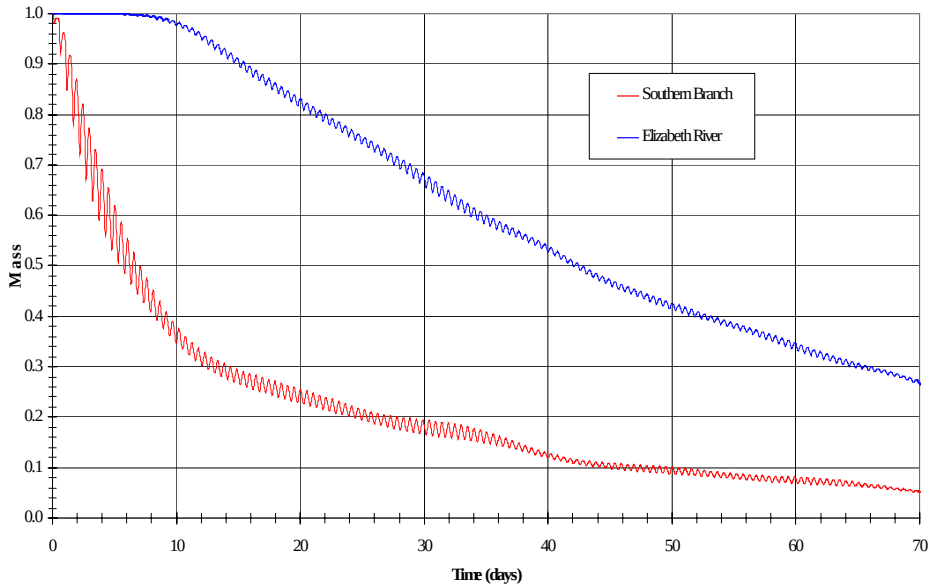

Figure V.25. Time series of tracer mass (released near the Jordan Bridge) remaining in the Southern Branch (red) and in the Elizabeth River (blue).

Total mass of the tracer remaining within the Southern Branch or within the whole Elizabeth River system was tracked over time. Figure V.25 presents the results for the Base Case (Case 1). The half-life, at which the total mass of the tracer remains in a system is reduced to half of the original mass, is a good measure of residence time. The half-life is about 6.5 days for the Southern Branch and 42.5 days for the entire Elizabeth River system. It is to be noted that the residence time of the tracer depends on the release location and on the system in which the residence is defined. The residence time will increase as the release location moves upriver, or a larger system is defined.

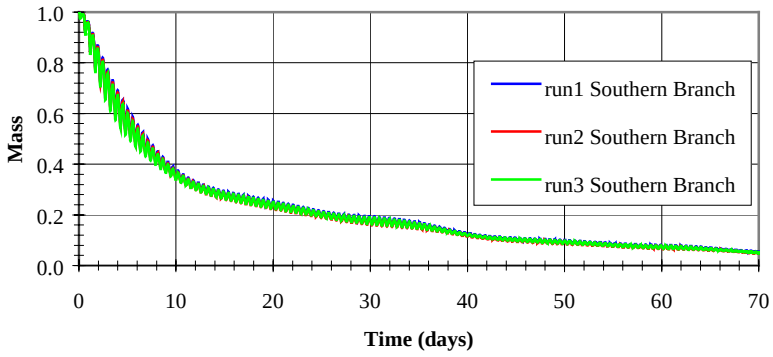

Figure V.26. Time series of mass in the Southern Branch for Case 1 (blue), Case 2 (red), and Case 3 (green).

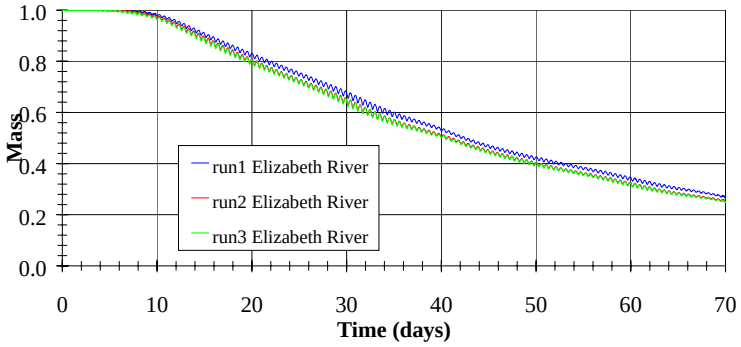

Figure V.27. Time series of mass in the Elizabeth River for Case 1 (blue), Case 2 (red), and Case 3 (green).

The results of tracer release experiments with the Eastward Expansion (Cases 2 and 3) were compared with the Base Case in Figures V.26 and V.27. There is no change in residence time caused by the Eastward Expansion for the Southern Branch (Figure V.26). This is consistent with the small changes in flux calculations listed in Table V.3. The Eastward Expansion improves flushing by decreasing the half-life by about 1.5 days for the Elizabeth River system (Figure V.27). No detectable differences were observed between Case 2 (Eastward Expansion) and Case 3 (Eastward Expansion with a deeper channel). Comparing with the results of flux calculation listed in Table V.1, it may be concluded that the more than 20 % increase in residual transport by Eastward Expansion is more than enough to compensate for the 5 to 6 % reduction in tidal prism through the mouth of the Elizabeth River. Since the flux calculation shows that all other changes in both tidal prism and residual volume transport are smaller than that of Eastward Expansion at cross-section A, it is expected that the change in flushing capacity will be smaller. No further tracer study was warranted.

3. Particle Tracking - In order to investigate the possible trapping of materials in the Lafayette River, numerical experiments of particle tracking were performed. Several particles were released near the entrance of the Lafayette River near the end of flood tide. Particles released at the surface were flushed out quickly (within 3 tidal cycles) from the system to the James River main channel (shown earlier in Figure V.15). Particles released near the bottom took a longer time (about 13 tidal cycles) to be flushed out from the system.

Table V.1. Calculated transports at cross-section A.

Case	Tidal Prism		Ebb Residual		Flood Residual	
	Flux (10^6 m^3)	Percent Change	Flux (10^6 m^3)	Percent Change	Flux (10^6 m^3)	Percent Change
1	36.87		7.96		8.04	
2	34.80	-5.61	10.24	28.58	9.94	23.73
3	35.31	-4.23	10.15	27.49	9.85	22.59
4	36.91	0.11	8.26	3.68	8.30	3.27
5	37.46	1.61	8.31	4.31	8.35	3.94
6	35.82	-2.85	8.66	8.82	8.38	4.31
7	35.95	-2.49	8.76	9.97	8.48	5.51
8	35.41	-3.94	9.02	13.30	8.72	8.52
9	35.53	-3.62	9.16	15.01	8.86	10.19

Table V.2. Calculated transports at cross-section C.

Case	Tidal Prism		Ebb Residual		Flood Residual	
	Flux (10^6 m^3)	Percent Change	Flux (10^6 m^3)	Percent Change	Flux (10^6 m^3)	Percent Change
1	24.59		3.26		2.94	
2	24.56	-0.12	3.36	3.05	3.03	3.09
3	25.12	2.15	3.24	-0.73	2.91	-1.04
4	24.59	-0.02	3.35	2.68	3.03	2.92
5	25.08	2.01	3.37	3.30	3.05	3.58
6	23.65	-3.83	3.24	-0.71	2.90	-1.28
7	24.01	-2.36	3.14	-3.79	2.80	-4.78
8	24.31	-1.15	3.52	8.02	3.19	8.56
9	24.85	1.08	3.39	3.98	3.06	4.09

Table V.3. Calculated transports at the Lafayette River Entrance.

Case	Tidal Prism		Ebb Residual		Flood Residual	
	Flux (10^6 m^3)	Percent Change	Flux (10^6 m^3)	Percent Change	Flux (10^6 m^3)	Percent Change
1	2.76		0.79		0.90	
2	2.77	0.20	0.75	-4.72	0.86	-4.04
3	2.77	0.33	0.75	-4.40	0.86	-3.84
4	2.77	0.40	0.80	1.25	0.91	1.16
5	2.78	0.52	0.80	1.34	0.91	1.18
6	2.80	1.47	0.78	-1.40	0.89	-1.33
7	2.80	1.51	0.78	-1.37	0.88	-1.57
8	2.80	1.40	0.76	-3.03	0.88	-2.36
9	2.80	1.52	0.77	-2.90	0.88	-2.39

Table V.4. Calculated transports at the Western Branch Entrance.

Case	Tidal Prism		Ebb Residual		Flood Residual	
	Flux (10^6 m^3)	Percent Change	Flux (10^6 m^3)	Percent Change	Flux (10^6 m^3)	Percent Change
1	4.77		0.77		0.65	
2	4.78	0.24	0.78	1.50	0.67	3.56
3	4.78	0.31	0.77	0.73	0.67	2.91
4	4.79	0.46	0.77	-0.32	0.65	-0.29
5	4.79	0.60	0.77	0.13	0.64	-0.54
6	4.85	1.68	0.84	9.55	0.71	10.25
7	4.85	1.69	0.83	8.62	0.71	10.29
8	4.84	1.49	0.83	8.22	0.72	11.12
9	4.84	1.48	0.81	6.08	0.71	10.03

Table V.5. Calculated transports at the Eastern Branch Entrance.

Case	Tidal Prism		Ebb Residual		Flood Residual	
	Flux (10^6 m^3)	Percent Change	Flux (10^6 m^3)	Percent Change	Flux (10^6 m^3)	Percent Change
1	3.33		0.50		0.45	
2	3.45	3.50	0.51	1.53	0.46	1.78
3	3.37	1.19	0.53	5.60	0.48	6.46
4	3.35	0.43	0.50	0.01	0.45	-0.01
5	3.31	-0.78	0.50	1.02	0.46	1.35
6	3.62	8.63	0.46	-7.59	0.42	-8.71
7	3.58	7.40	0.48	-4.43	0.43	-5.20
8	3.64	9.37	0.51	2.62	0.47	2.90
9	3.57	7.09	0.53	6.83	0.49	7.70

Table V.6. Calculated transports at the Southern Branch Entrance.

Case	Tidal Prism		Ebb Residual		Flood Residual	
	Flux (10^6 m^3)	Percent Change	Flux (10^6 m^3)	Percent Change	Flux (10^6 m^3)	Percent Change
1	4.56		1.66		1.47	
2	4.54	-0.49	1.71	2.95	1.52	3.39
3	4.61	1.11	1.71	2.84	1.52	3.23
4	4.58	0.35	1.67	0.23	1.48	0.28
5	4.64	1.69	1.63	-1.77	1.44	-1.99
6	4.56	-0.09	1.66	0.08	1.47	0.03
7	4.57	0.08	1.71	2.52	1.51	2.80
8	4.57	0.11	1.72	3.38	1.53	3.86
9	4.61	1.08	1.75	5.45	1.56	6.19

Table V.7. Calculated transports at the Nansemond River Entrance.

Case	Tidal Prism		Ebb Residual		Flood Residual	
	Flux (10^6 m^3)	Percent Change	Flux (10^6 m^3)	Percent Change	Flux (10^6 m^3)	Percent Change
1	11.95		2.32		2.58	
2	11.97	0.13	2.33	0.37	2.59	0.33
3	11.97	0.18	2.32	0.32	2.59	0.23
4	11.96	0.11	2.33	0.49	2.57	-0.73
5	11.97	0.15	2.33	0.64	2.57	-0.58
6	11.82	-1.12	2.51	8.11	2.77	7.08
7	11.82	-1.11	2.51	8.15	2.77	7.10
8	11.86	-0.76	2.37	2.38	2.63	1.90
9	11.87	-0.68	2.37	2.41	2.64	2.06

VI. SCENARIO SIMULATION COMPARISON -- HISTORICAL RUNS

The second of the two types of scenario simulation comparisons performed in this project involved real-time simulations incorporating all available input conditions (discharge at 8 locations, winds, and open boundary tidal elevation and salinity specifications). These simulations were done for the 180-day period corresponding to Julian days 60-240 of calendar year 2000 (i.e., March 1 to August 27). A total of 5 cases were simulated, as shown in table VI.1.

Case	Design	Channel Depth (ft)	Event		
			High discharge	High wind	Low discharge
1	Base Case	50	Case 1 results	Case 1 results	Case 1 results
2	Option 7	50	Case 2 results	Case 2 results	Case 2 results
3		55	Case 3 results	Case 3 results	Case 3 results
10	Option 7/5A	50	Case 10 results	Case 10 results	Case 10 results
11		55	Case 11 results	Case 11 results	Case 11 results

Table VI.1. Historical Model Cases, Event Categories.

The Base Case (Case 1) and the Eastward Expansion (Cases 2 and 3), brought forward from the single variable runs, were shown earlier in Figures I.2 and I.3. Cases 10 and 11 are shown in Figure VI.1 below:

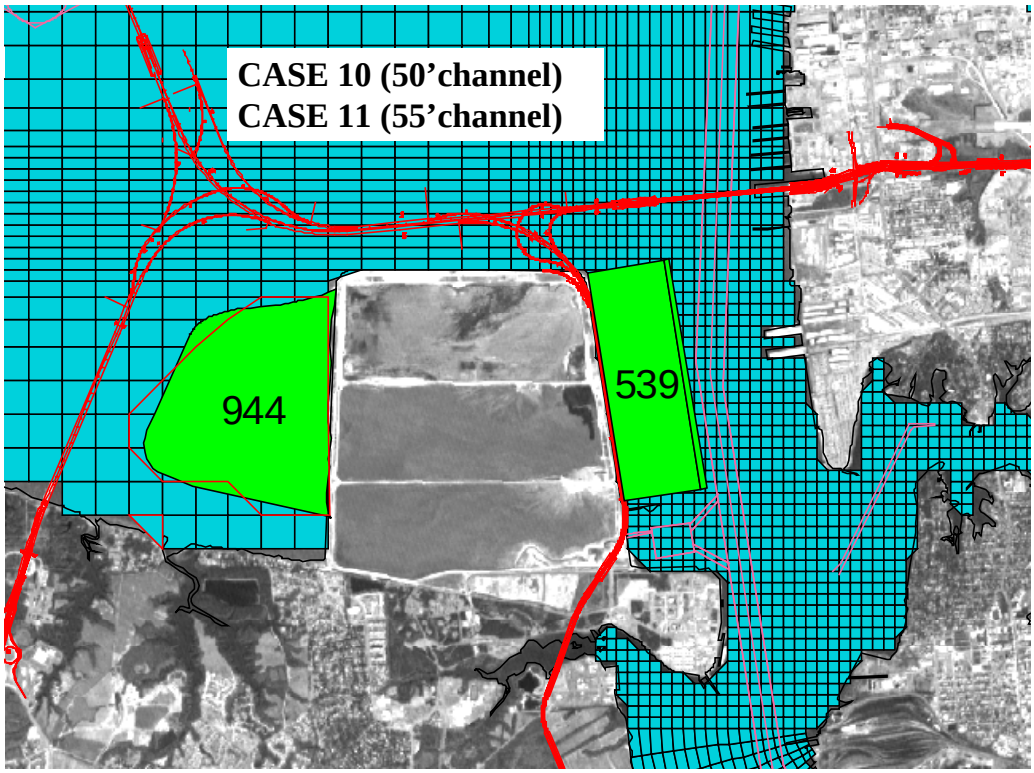

Figure VI.1. Cases 10 and 11 used in historical simulations.

From within this simulation period, three 7-day event periods were selected to represent the relatively extreme conditions of 'high discharge event' [Julian days 111-117], 'high wind event' [Julian days 149-155], and 'low discharge event' [Julian days 197-203]. A time series plot of discharge measurements upstream at Richmond is shown in Figure VI.2 and a time series of wind measured at Sewells Pt, VA is shown in Figure VI.3.

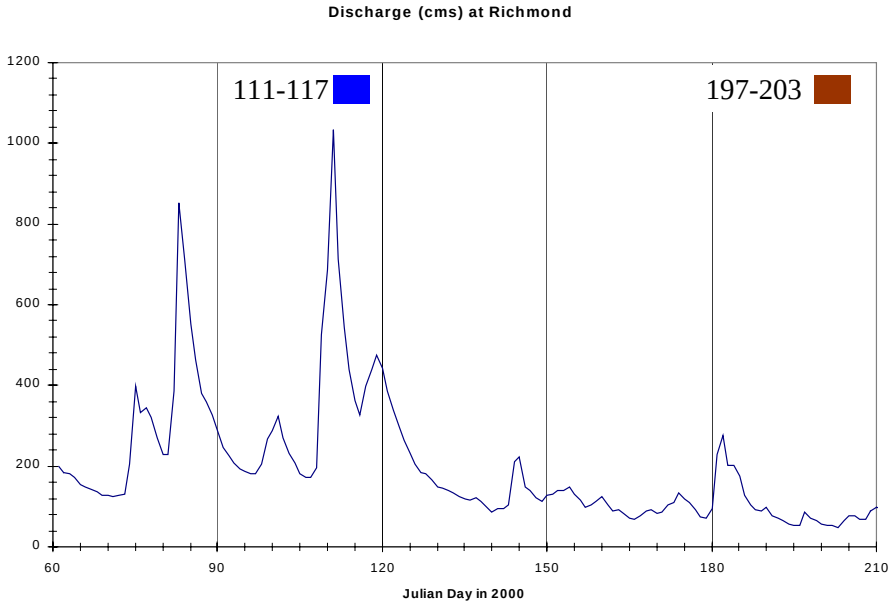

Figure VI.2. Discharge measured at Richmond, VA.

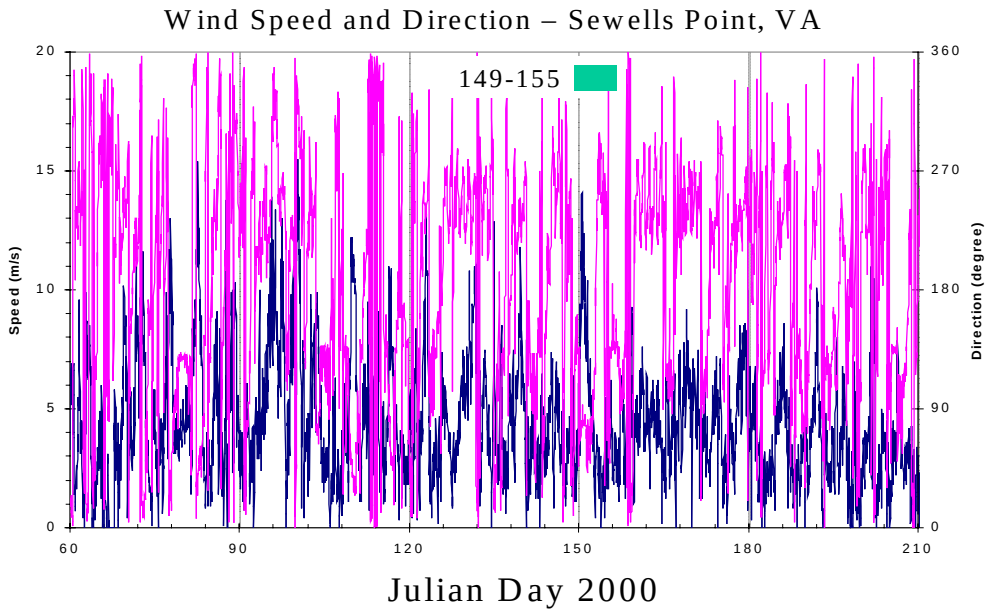

Figure VI.3. Wind measured at Sewells Pt., VA.

Whereas the duration of these events varied, the period of analysis for comparing Cases 2, 3, 10, and 11 to the Base Case was kept constant at 7 days.

A. GLOBAL COMPARISONS

Here, the reader is referred to Chapter V, Section A for a general discussion of global analysis as it was performed for the single variable runs. The difference in its use for the historical simulations is that, for each case compared to the Base Case, it was applied separately to the 3 event periods in the comparison. Therefore, the number of data points used is 336 (the number of half-hour intervals in a week), rather than 1776 as used for the single variable scenarios.

1. Spatial Distribution – Again, the reader is referred to Chapter V, Section A.1 for a general discussion of spatial plotting of differences of selected state variables between each test case and the Base Case. It should be noted here that the total number of spatial plots is 108, which results from 4 case comparisons each having 3 events with each event involving the following 9 spatial plots:

1) RMS difference of tidal elevation
2) average difference of surface salinity
3) average difference of bottom salinity
4) RMS difference of surface velocity magnitude
5) RMS difference of bottom velocity magnitude
6) average difference of surface residual velocity magnitude
7) average difference of bottom residual velocity magnitude
8) sedimentation potential for test case
9) sedimentation potential difference between test case and Base Case

These spatial plots are shown in Figures 1-108 of Appendix to Chapter VI, Section A.1. The sequence of presentation within this Appendix is as follows:

Case 2 versus Base Case	high discharge	Figures 1-9
Case 2 versus Base Case	low discharge	Figures 10-18
Case 2 versus Base Case	high wind	Figures 19-27
Case 3 versus Base Case	high discharge	Figures 28-36
Case 3 versus Base Case	low discharge	Figures 37-45
Case 3 versus Base Case	high wind	Figures 46-54
Case 10 versus Base Case	high discharge	Figures 55-63
Case 10 versus Base Case	low discharge	Figures 64-72
Case 10 versus Base Case	high wind	Figures 73-81
Case 11 versus Base Case	high discharge	Figures 82-90
Case 11 versus Base Case	low discharge	Figures 91-99
Case 11 versus Base Case	high wind	Figures 100-108

The differences were plotted for each of the case/event comparisons. Below is a summary of the findings in each:

Eastward Expansion (Option 7, Case 2 [50-foot channel] vs. Base Case, High Discharge Event) – Plots contrasting Case 2 against the Base Case for the high discharge event are shown in Figures 1-9 of the Appendix to Chapter VI, Section A.1. For surface elevation (Figure 1), all RMS average differences fall below 0.25 cm except for a small area adjacent to the proposed expansion option, where differences above 0.25 cm are shown in pink. Average differences in surface salinity (Figure 2) fall below ±0.2 ppt everywhere except directly adjacent to the expansion option. Bottom salinity average differences (Figure 3) are everywhere under ±0.2 ppt except in small areas around the option and northward in the Norfolk Harbor Channel where differences range to ±1.0 ppt. Surface velocity magnitude differences (Figure 4) and bottom velocity magnitude differences (Figure 5) reach 12 cm/sec and 8 cm/sec, respectively, near the eastward expansion but are limited to 4 cm/sec in the far field. Surface and bottom residual velocity magnitude differences (Figures 6 and 7) show, respectively, limits of ±5 cm/sec and ±3 cm/sec in areas immediately adjacent to the structure. Sedimentation potential for Case 2, high discharge event, is shown in Figure 8. Its difference from the Base Case is plotted in Figure 9, impacting a very small area north of the expansion option with a difference of about ±10%.

Eastward Expansion (Option 7, Case 2 [50-foot channel] vs. Base Case, Low Discharge Event) – Plots contrasting Case 2 against the Base Case for the low discharge event are shown in Figures 10-18 of the Appendix to Chapter VI, Section A.1. For surface elevation (Figure 10), all RMS average differences fall below 0.25 cm except for a small area adjacent to the expansion option, where differences above 0.25 cm are shown in pink. Average differences in surface salinity (Figure 11) fall below ±0.2 ppt everywhere except directly adjacent to the expansion option. Bottom salinity average differences (Figure 12) are everywhere under ±0.2 ppt except in small areas around the option where differences range to ±1.0 ppt. Surface velocity magnitude differences (Figure 13) and bottom velocity magnitude differences (Figure 14) reach 12 cm/sec and 8 cm/sec, respectively, near the eastward expansion but are limited to 4 cm/sec in the far field. Surface and bottom residual velocity magnitude differences (Figures 15 and 16) show, respectively, limits of ±5 cm/sec and ±3 cm/sec in areas immediately adjacent to the structure. Sedimentation potential for Case 2, low discharge event, is shown in Figure 17. Its difference from the Base Case is plotted in Figure 18, impacting a very small area north of the expansion option with a difference of about ±10%.

Eastward Expansion (Option 7, Case 2 [50-foot channel] vs. Base Case, High Wind Event) – Plots contrasting Case 2 against the Base Case for the high wind event are shown in Figures 19-27 of the Appendix to Chapter VI, Section A.1. For surface elevation (Figure 19), all RMS average differences fall below 0.25 cm except for a small area northeast the expansion option and the southern portion of the Southern Branch, where differences above 0.25 cm are shown in pink. Average differences in surface salinity (Figure 20) fall below ±0.2 ppt everywhere except directly adjacent to the expansion option. Bottom salinity average differences (Figure 21) are everywhere under

±0.2 ppt except in small areas around the option where differences range to ±1.0 ppt. Surface velocity magnitude differences (Figure 22) and bottom velocity magnitude differences (Figure 23) reach 12 cm/sec and 8 cm/sec, respectively, near the eastward expansion but are limited to 4 cm/sec in the far field. Surface and bottom residual velocity magnitude differences (Figures 24 and 25) show, respectively, limits of ±10 cm/sec and ± 3 cm/sec in areas immediately adjacent to the structure. Sedimentation potential for Case 2, high wind event, is shown in Figure 26. Its difference from the Base Case is plotted in Figure 27, impacting a very small area north of the expansion option with a difference of about ±10%.

Eastward Expansion (Option 7, Case 3 [55-foot channel] vs. Base Case, High Discharge Event) – Plots contrasting Case 3 against the Base Case for the high discharge event are shown in Figures 28-36 of the Appendix to Chapter VI, Section A.1. For surface elevation (Figure 28), all RMS average differences fall below 0.25 cm except for most of the surface area of the Elizabeth River, where differences above 0.25 cm are shown in pink. Average differences in surface salinity (Figure 29) fall below ±0.2 ppt everywhere except for an area adjacent to the expansion option and about its size. Bottom salinity average differences (Figure 30) are everywhere under ±0.2 ppt except in small areas around the option and northward in the Norfolk Harbor Channel where differences range to ±1.0 ppt. Surface velocity magnitude differences (Figure 31) and bottom velocity magnitude differences (Figure 32) reach 12 cm/sec and 8 cm/sec, respectively, near the eastward expansion but are limited to 4 cm/sec in the far field. Surface and bottom residual velocity magnitude differences (Figures 33 and 34) show, respectively, limits of ± 5 cm/sec and ±3 cm/sec in areas either immediately adjacent to the expansion option or following the Norfolk Harbor Channel. Sedimentation potential for Case 3, high discharge event, is shown in Figure 35. Its difference from the Base Case is plotted in Figure 36, impacting a very small area north of the expansion option and extending along the Norfolk Harbor Channel with a difference of about ±10%.

Eastward Expansion (Option 7, Case 3 [55-foot channel] vs. Base Case, Low Discharge Event) – Plots contrasting Case 3 against the Base Case for the low discharge event are shown in Figures 37-45 of the Appendix to Chapter VI, Section A.1. For surface elevation (Figure 37), all RMS average differences fall below 0.25 cm except for a small area mainly east of the expansion option, where differences above 0.25 cm are shown in pink. Average differences in surface salinity (Figure 38) fall below ±0.2 ppt everywhere except directly adjacent to the expansion option. Bottom salinity average differences (Figure 39) are everywhere under ±0.2 ppt except in small areas around the option where differences range to 1.0 ppt. Surface velocity magnitude differences (Figure 40) and bottom velocity magnitude differences (Figure 41) reach 16 cm/sec and 8 cm/sec, respectively, near the eastward expansion but are limited to 4 cm/sec in the far field. Surface and bottom residual velocity magnitude differences (Figures 42 and 43) show, respectively, limits of about ±5 cm/sec and ±3 cm/sec in areas immediately adjacent to the structure. Sedimentation potential for Case 3, low discharge event, is shown in Figure 44. Its difference from the Base Case is plotted in Figure 45, impacting a very small area north of the expansion option with a difference of about ±10%, as where as isolated cells upstream to Burwell's Bay.

Eastward Expansion (Option 7, Case 3 [55-foot channel] vs. Base Case, High Wind Event) – Plots contrasting Case 3 against the Base Case for the high wind event are shown in Figures 46-54 of the Appendix to Chapter VI, Section A.1. For surface elevation (Figure 46), all RMS average differences fall below 0.25 cm except for the entire Elizabeth River, where differences above 0.25 cm are shown in pink. Average differences in surface salinity (Figure 47) fall below ±0.2 ppt everywhere except directly adjacent to the expansion option. Bottom salinity average differences (Figure 48) are everywhere under ±0.2 ppt except in small areas around the option and along the Norfolk Harbor Channel where differences range to 1.0 ppt. Surface velocity magnitude differences (Figure 49) and bottom velocity magnitude differences (Figure 50) reach 16 cm/sec and 12 cm/sec, respectively, near the eastward expansion but are limited to 4 cm/sec in the far field. Surface and bottom residual velocity magnitude differences (Figures 51 and 52) show, respectively, limits of ±10 cm/sec and ± 3 cm/sec in areas immediately adjacent to the structure. Sedimentation potential for Case 3, high wind event, is shown in Figure 53. Its difference from the Base Case is plotted in Figure 54, impacting an area north of the expansion option with a difference of about ±10%.

East/West Expansion (Option 7/5A, Case 10 [50-foot channel] vs. Base Case, High Discharge Event) – Plots contrasting Case 10 against the Base Case for the high discharge event are shown in Figures 55-63 of the Appendix to Chapter VI, Section A.1. For surface elevation (Figure 55), all RMS average differences west of Newport News Pt. fall between 0.25 - 0.50 cm except for very small areas just north and south of the proposed westward expansion option, where differences of 0.50-1.50 cm are shown. Average differences in surface salinity (Figure 56) fall below ±0.2 ppt everywhere except directly south of the westward expansion option. Bottom salinity average differences (Figure 57) are everywhere under ±0.2 ppt except in small areas around the expansion options where differences are on the average ±0.5 ppt but range to ±2.0 ppt for a few cell locations. Surface velocity magnitude differences (Figure 58) and bottom velocity magnitude differences (Figure 59) reach 25 cm/sec and 12 cm/sec, respectively, near the eastward expansion but are limited to 4 cm/sec in the far field. Surface and bottom residual velocity magnitude differences (Figures 60 and 61) both show limits of ±5 cm/sec in areas immediately adjacent to the expansion options. Sedimentation potential for Case 10, high discharge event, is shown in Figure 62. Its difference from the Base Case is plotted in Figure 63, impacting a very small area west of the westward expansion option with a difference of about ±20 to 40%.

East/West Expansion (Option 7/5A, Case 10 [50-foot channel] vs. Base Case, Low Discharge Event) – Plots contrasting Case 10 against the Base Case for the low discharge event are shown in Figures 64-72 of the Appendix to Chapter VI, Section A.1. For surface elevation (Figure 64), all RMS average differences fall between 0.25 - 0.50 cm except for very small areas just north and south of the proposed westward expansion option, where differences of 0.50-1.50 cm are shown. Average differences in surface salinity (Figure 65) fall below ±0.2 ppt everywhere except directly adjacent to the expansion option, where they range to ±1.0 ppt. Bottom salinity average differences (Figure 66) are everywhere under ±0.2 ppt except in small areas around the option where

differences range to ±2.0 ppt. Surface velocity magnitude differences (Figure 67) and bottom velocity magnitude differences (Figure 68) reach 25 cm/sec and 12 cm/sec, respectively, near the eastward expansion but are limited to 4 cm/sec in the far field. Surface and bottom residual velocity magnitude differences (Figures 69 and 70) show, respectively, limits of ±5 cm/sec and ±3 cm/sec in areas throughout Hampton Roads. Sedimentation potential for Case 10, low discharge event, is shown in Figure 71. Its difference from the Base Case is plotted in Figure 72, impacting mainly to the west of the westward expansions with differences up to ±20-40%.

East/West Expansion (Option 7/5A, Case 10 [50-foot channel] vs. Base Case, High Wind Event) – Plots contrasting Case 10 against the Base Case for the high wind event are shown in Figures 73-81 of the Appendix to Chapter VI, Section A.1. For surface elevation (Figure 73), RMS average differences fall between 0.25 cm and 0.50 cm for most of Hampton Roads, except for small areas near the expansion options and the upriver portions of the Western, Southern, and Eastern Branches, where differences above 0.50 cm are shown in gold. Average differences in surface salinity (Figure 74) fall below ±0.2 ppt everywhere except north of the expansion option, where they range to ±1.0 ppt. Bottom salinity average differences (Figure 75) are everywhere under ±0.2 ppt except in small areas around the option where differences range to ±2.0 ppt. Surface velocity magnitude differences (Figure 76) and bottom velocity magnitude differences (Figure 77) reach 25 cm/sec and 16 cm/sec, respectively, near the eastward expansion but are limited to 4 cm/sec in the far field. Surface and bottom residual velocity magnitude differences (Figures 78 and 79) show, respectively, limits of ±10 cm/sec and ± 3 cm/sec in areas immediately adjacent to the structure. Sedimentation potential for Case 10, high wind event, is shown in Figure 80. Its difference from the Base Case is plotted in Figure 81, impacting a small area west of the westward expansion option with a difference of up to 40%.

East/West Expansion (Option 7/5A, Case 11 [55-foot channel] vs. Base Case, High Discharge Event) – Plots contrasting Case 11 against the Base Case for the high discharge event are shown in Figures 82-90 of the Appendix to Chapter VI, Section A.1. For surface elevation (Figure 82), RMS average differences fall below 0.25 cm for most of the area west of Newport News Pt. and are between 0.25 cm and 0.50 cm for most of the area east of Newport News Pt., with a very small area around the westward expansion exceeding 0.50 cm. Average differences in surface salinity (Figure 83) fall below ±0.2 ppt everywhere except for small areas adjacent to and north of the expansion options which range to ±1.0 ppt. Bottom salinity average differences (Figure 84) are everywhere under ±0.2 ppt except in small areas around the option and northward in the Norfolk Harbor Channel where differences range to ±1.0 ppt. Surface velocity magnitude differences (Figure 85) and bottom velocity magnitude differences (Figure 86) reach 25 cm/sec and 12 cm/sec, respectively, near the eastward expansion but are limited to 4 cm/sec in the far field. Surface and bottom residual velocity magnitude differences (Figures 87 and 88) show, respectively, limits of ± 5 cm/sec and ±3 cm/sec in areas either immediately adjacent to the expansion option or following the Norfolk Harbor Channel. Sedimentation potential for Case 11, high discharge event, is shown in Figure 89. Its difference from the Base Case is plotted in Figure 90, impacting a very small area north

of the expansion option and extending along the Norfolk Harbor Channel with a difference of about ±20%.

East/West Expansion (Option 7/5A, Case 11 [55-foot channel] vs. Base Case, Low Discharge Event) – Plots contrasting Case 11 against the Base Case for the low discharge event are shown in Figures 91-99 of the Appendix to Chapter VI, Section A.1. For surface elevation (Figure 91), RMS average differences fall below 0.25 cm for most of the area west of Newport News Pt. and are between 0.25 cm and 0.50 cm for most of the area east of Newport News Pt., with a very small area around the westward expansion exceeding 0.50 cm. Average differences in surface salinity (Figure 92) fall below ±0.2 ppt everywhere except directly adjacent to the expansion options, where values range to ±1.0 ppt. Bottom salinity average differences (Figure 93) are everywhere under ±0.2 ppt except in small areas around the option where differences range to ±1.0 ppt. Surface velocity magnitude differences (Figure 94) and bottom velocity magnitude differences (Figure 95) reach 25 cm/sec and 12 cm/sec, respectively, near the eastward expansion but are limited to 4 cm/sec in the far field. Surface and bottom residual velocity magnitude differences (Figures 96 and 97) show, respectively, limits of about ±5 cm/sec and ±3 cm/sec in and cover areas extending up past the James River Bridge. Sedimentation potential for Case 11, low discharge event, is shown in Figure 98. Its difference from the Base Case is plotted in Figure 99, impacting primarily an area west of the expansion option with a difference of up to 40%, whereas isolated cells showing differences exist upstream towards Burwell's Bay.

East/West Expansion (Option 7/5A, Case 11 [55-foot channel] vs. Base Case, High Wind Event) – Plots contrasting Case 11 against the Base Case for the high wind event are shown in Figures 100-108 of the Appendix to Chapter VI, Section A.1. For surface elevation (Figure 100), almost all RMS average differences fall between 0.25-0.50 cm except for the entire Elizabeth River, where differences between 0.50-0.75 cm are shown in gold. Average differences in surface salinity (Figure 101) fall below ±0.2 ppt everywhere except north of and adjacent to the expansion options, where differences range to –2.0 ppt. Bottom salinity average differences (Figure 102) are everywhere under ±0.2 ppt except in small areas around the option and along the Norfolk Harbor Channel where differences range to 1.0 ppt. Surface velocity magnitude differences (Figure 103) and bottom velocity magnitude differences (Figure 104) reach 25 cm/sec and 12 cm/sec, respectively, near the eastward expansion but are limited to 4 cm/sec in the far field. Surface and bottom residual velocity magnitude differences (Figures 105 and 106) show, respectively, limits of ±10 cm/sec and ±3 cm/sec in areas immediately adjacent to the structure. Sedimentation potential for Case 11, high wind event, is shown in Figure 107. Its difference from the Base Case is plotted in Figure 108, impacting an area west of the westward expansion option with a difference of up to 40%.

The spatial distributions of the case comparison differences are useful in delineating areas of maximum impact and yet, they are qualitative in nature. An attempt to quantify this analysis is described in the next section.

2. **Percentile Analysis** – As was done to compare the single variable test cases against the single variable base case (see Chapter V, Section A.2), the differences of historical test case results from the historical Base Case results were divided into class intervals. Then each interval's accumulated spatial distribution was plotted as a percentage of the entire model surface area of Hampton Roads. In this fashion, a set of simple histograms showing the distribution of class interval differences of each variable for each test case versus the base case can be constructed, as shown in the Appendix to Chapter VI, Section A.2, Figures 1-96.

For each of the 3 events of the 4 test cases compared to the base case, a histogram was provided for each of the following 8 selected differences in this specified sequence:

1) RMS difference of tidal elevation
2) average difference of surface salinity
3) average difference of bottom salinity
4) RMS difference of surface velocity magnitude
5) RMS difference of bottom velocity magnitude
6) average difference of surface residual velocity magnitude
7) average difference of bottom residual velocity magnitude
8) sedimentation potential difference between test case and Base Case

The differences for the high discharge, low discharge, and high wind events comparing Case 2 to the base case are shown, respectively, in Figures 1-8, 9-16, and 17-24. Retaining this sequence of these events, those comparing Case 3 to the base case are shown in Figures 25-48. Case 4 versus the Base Case is shown in Figures 49-72 and Case 5 versus the base case is shown in Figures 73-96. For each of the histograms shown in Figures 1-96, the class interval area is a maroon bin whose percentile value is shown on the left vertical axis, whereas the blue curve plotted shows a cumulative percentage of all bins the value of which is shown on the right vertical axis.

The next step is to extract the cumulative percentages from Figures 1-96 and group all 4 case comparisons, event by event, for each variable, as shown in Figures 97-120. Here, the comparison of the Eastward Expansion (Cases 2 and 3) to the base case are shown in dark blue and the comparison of the Eastward and Westward Expansions (Cases 10 and 11) to the Base Case are shown in red. The 55-foot channel cases (i.e., Cases 3 and 11) are denoted by symboled functions. In general, the difference from the test case to the base case increases as one proceeds from Case 2, to Case 3, to Case 10, and to Case 11 showing this trend among almost all the variables examined.

A final step in comparing the impacts from the different test cases is to construct a table with the 95^{th} percentile values of the aforementioned cumulative curves, as shown in Table VI.2 below:

Global Change – 95th Percentile (5% of area contains change greater than value listed)				
Historical – High Discharge Event				
Change in:	**Case 2 East 50' channel**	**Case 3 East 55' channel**	**Case 10 East/West 50' channel**	**Case11 East/West 55' channel**
Surface Elevation	0.20 cm	0.22 cm	0.33 cm	**0.41 cm**
Surface Current	5.5 cm/s	5.7 cm/s	6.7 cm/s	**7.1 cm/s**
Bottom Current	2.7 cm/s	2.9 cm/s	3.7 cm/s	**3.9 cm/s**
Surface Salinity	0.00 ppt	0.03 ppt	0.02 ppt	**0.05 ppt**
Bottom Salinity	0.00 ppt	0.05 ppt	0.07 ppt	**0.09 ppt**
Sedimentation Potential	1.0 %	1.4 %	1.9 %	**2.4 %**
Historical – Low Discharge Event				
Change in:	**Case 2 East 50' channel**	**Case 3 East 55' channel**	**Case 10 East/West 50' channel**	**Case11 East/West 55' channel**
Surface Elevation	0.14 cm	0.21 cm	0.33 cm	**0.40 cm**
Surface Current	2.7 cm/s	2.8 cm/s	**4.3 cm/s**	**4.3 cm/s**
Bottom Current	1.9 cm/s	1.9 cm/s	**2.9 cm/s**	2.8 cm/s
Surface Salinity	0.00 ppt	0.00 ppt	**0.04 ppt**	0.01 ppt
Bottom Salinity	0.01 ppt	0.04 ppt	**0.09 ppt**	0.08 ppt
Sedimentation Potential	0.9 %	1.2 %	2.8 %	**3.0 %**
Historical – High Wind Event				
Change in:	**Case 2 East 50' channel**	**Case 3 East 55' channel**	**Case 10 East/West 50' channel**	**Case11 East/West 55' channel**
Surface Elevation	0.21 cm	0.25 cm	0.46 cm	**0.57 cm**
Surface Current	2.2 cm/s	2.5 cm/sec	**5.0 cm/s**	**5.0 cm/s**
Bottom Current	1.5 cm/s	2.4 cm/s	3.0 cm/s	**3.1 cm/s**
Surface Salinity	0.00 ppt	0.00 ppt	0.00 ppt	**0.01 ppt**
Bottom Salinity	0.00 ppt	**0.08 ppt**	0.02 ppt	**0.08 ppt**
Sedimentation Potential	0.8 %	0.9 %	1.7 %	**1.9 %**

Table VI.2. Summary of 95th percentile values for cumulative curves of differences of selected state variables for each historical case versus the base case. For each state variable, the maximum value within each event is displayed as **bold**.

B. Historical Circulation Features – Local Analysis

The circulation features described in this chapter are based on model simulations produced with real time data from spring and summer 2000. For a single case, these simulations exhibit considerably more variability on a day-to-day basis than do the single variable model runs described in Chapter V. But as the previous section shows, global simulation comparisons *between* cases, e.g., Case 1 (Base Case) vs. Case 2 (Expansion Option 7), do not reflect the increased variability associated with historical data. In particular, the spatial distributions of each predicted change category in residual current magnitude for Case 1 and Case 2 are very similar in most areas regardless of whether single variable or historical data are used. Local analysis of specific circulation features that do appear to experience a degree of change are investigated here through time series comparisons at selected locations. Because of the similarities, a seven-day segment of the model output was analyzed for only one of the three event conditions (high discharge) previously described in this chapter. Results include analytical comparisons for Case 1 (Base Case) vs. Case 2 (Expansion Option 7) and Case 10 (Expansion Option 7/5a).

Methods - The real tide in Hampton Roads contains *diurnal inequalities* in the strength of flood and ebb currents similar to those appearing in the heights of high and low waters. It is therefore necessary to develop the residual (tidally averaged) current field by averaging model-predicted u (positive east) and v (positive north) velocity components over a lunar day. Since model output was generated at half-hour intervals, 50 readings approximating 24 lunar hours were used in the averaging starting midnight of each Julian (solar) day. An example of the residual surface current vector field for the high discharge condition in Hampton Roads is shown in Figure VI.4.

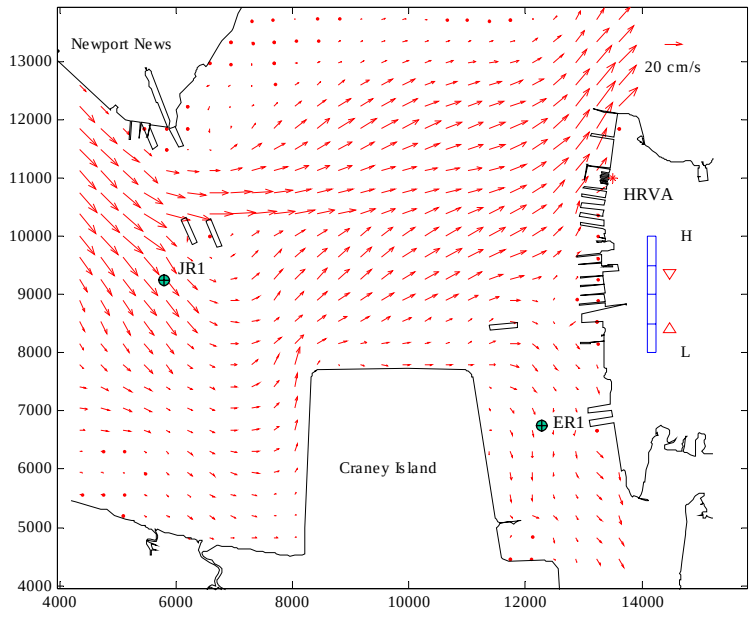

Figure VI.4. Residual surface current in Hampton Roads, April 20, 2000 (Julian Day 111). Plan view showing location of time series stations JR1 and ER1.

Three stations were selected for local time series analysis at the positions indicated in Figures VI.4 and VI.9. These include station JR1 in the main stem of the James River below Newport News Point, station ER1 at the entrance to the Elizabeth River immediately east of Craney Island, and station ER2 below Lamberts Point in the Elizabeth River. As shown in Figure VI.4, both the direction and the magnitude of the residual currents vary from point to point. The instantaneous currents (not shown) do the same but their direction and magnitude also vary with time. In order to examine the time varying current most effectively at JR1, ER1, and ER2, a uv coordinate system rotation was performed at each station to obtain the current component in the direction of maximum variance (u' or principal axis component as explained below). Each coordinate system was further adjusted by a 180º rotation as needed to orient the positive (flood) axis upstream. The resulting principal axis surface currents for the high discharge condition at stations JR1 and ER1 are shown in Figures VI.5 and VI.6, respectively.

Figure VI.5 (station JR1) shows that the time series current curves representing Case 1 and Case 2 are virtually identical. Note that both curves oscillate about a mean flow over this seven-day period of about –17.3 cm/s (ebb direction). The RMSD (root-mean-square difference) value for this pair of curves is 0.5 cm/s.

Figure VI.6 (station ER1), on the other hand, indicates a clear difference in its Case 1 and Case 2 comparison, not only in terms of the magnitude of the current but through differences in their respective means: 4.8 cm/s for Case 1 and -1.3 cm/s for Case 2. The RMSD (root-mean-square difference) value for this pair of curves is 9.1 cm/s.

The RMSD value referred to above is the same statistical index used in the global analyses for this report, the only difference being the variable in use - here it is the principal axis current, u', a sinusoidal series. The present RMSD value is computed as

$$RMSD = \sqrt{\sum \{u'_2 - u'_1\}^2 / n}$$

where u'_1 and u'_2 are the n-point time series for Case 1 and Case 2, respectively. The series difference, $\{u'_2-u'_1\}$, is usually a sinusoid resulting from differences in amplitude, phase, and the means of the two series in whatever combination they may occur.

Principal Component Analysis - While it is easy to determine the mean difference between two series, it is difficult to determine differences in *amplitude* and *phase* when the time series are short and contain periodic components representing multiple frequencies. Fortunately the dominant frequency involved here is the M_2 tidal frequency, 1/T, where T = 12.42 hours. This fact supports a method for estimating amplitude and phase differences based on Principal Component Analysis (PCA) of bivariate data. PCA analyzes a bivariate (nx2) data matrix, U, by first determining the eigenvectors of the variance-covariance matrix, VCV = $Z^T Z/(n-1)$, where Z is the bivariate data matrix in deviate form (means removed) and Z^T is Z transposed. If U = [u v], then [u' v'] = [u v][e_1 e_2] where [e_1 e_2] is a 2x2 matrix of eigenvectors. The effect of this operation is a coordinate axis rotation such that u' contains the maximum variance possible in a single component of the current velocity while v' contains the minimum variance possible. In

tidal rivers, the former is usually the current component parallel to the river channel while the latter is the component perpendicular to it.

The same procedure can be applied using U = [u'$_1$ u'$_2$] where u'$_1$ and u'$_2$ are the principal axis currents for Case 1 and Case 2. These data are plotted against each other as shown in Figures VI.7 and VI.8. The ratio of the elements in the first eigenvector determines the slope of the corresponding *principal component axis* (e.g., magenta-colored line through data points in Figure VI.8; note that this is NOT a regression line).

Determining the slope as b = $e_1(2)/e_1(1)$ and ignoring the sign,

$$A_2 = bA_1$$

where A_1 and A_2 are the *current amplitudes* for Case 1 and Case 2, respectively. A_1 and A_2 may be estimated as

$$A_1 = \sqrt{2}RMS_1$$

$$A_2 = \sqrt{2}RMS_2$$

where RMS_1 and RMS_2 are the root-mean-square values for u''$_1$ and u''$_2$, the deviate form of u'$_1$ and u'$_2$. Small differences in *current phase* between u'$_1$ and u'$_2$ can be estimated as

$$PD = \frac{T}{\pi}\arcsin(RMSD_e / 2RMS_1)$$

in which

$$RMSD_e = \sqrt{(u''_2 - bu''_1)^T (u''_2 - bu''_1)/n}$$

is the RMS deviation in u''$_2$ about the principal component axis. In contrast, RMSD is an all-inclusive value based on RMS deviation in u'$_2$ about the 1:1 axis (blue line in Figure VI.8).

Time Series near Lamberts Point in the Elizabeth River – To make an additional case comparison inside the Elizabeth River, a third time series station, ER2, was chosen near Lamberts Point at the position shown in Figure VI.9. This station is considered to be representative of Elizabeth River circulation away from the immediate influence of the eastward expansion associated with Cases 2 and 10 but within the zone where global comparisons have highlighted smaller changes that tend to spread over larger areas. The parameters just described were calculated for station ER2 during the high discharge condition to obtain a representative example of this change. Time series plots constructed for this purpose are shown in Figures VI.10 and VI.11.

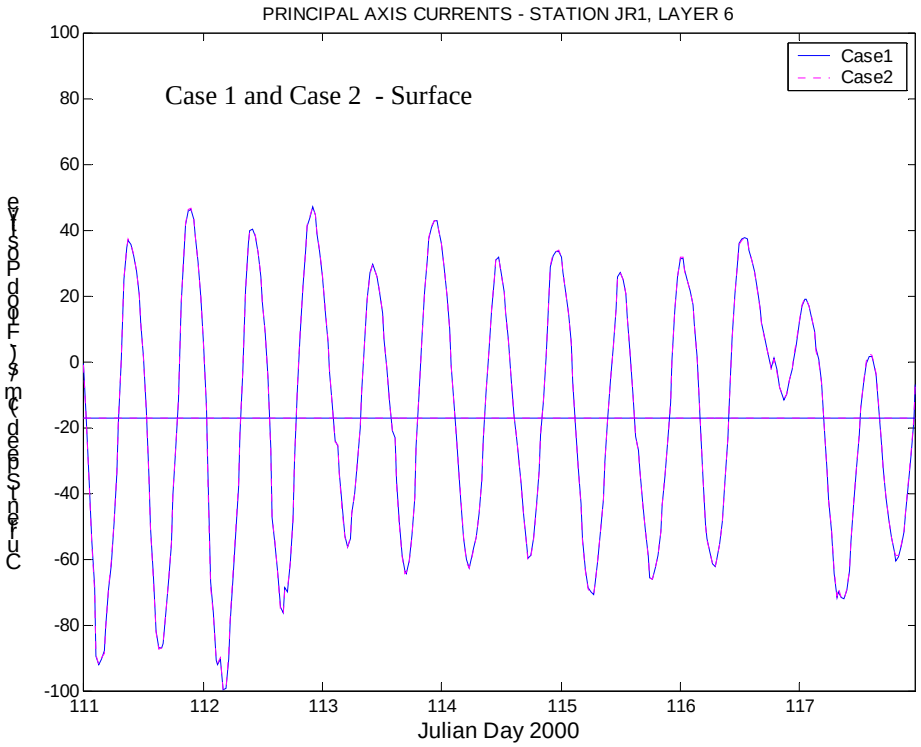

Figure VI.5. Principal axis current at Station JR1; Case 1 and Case 2 (surface layer).

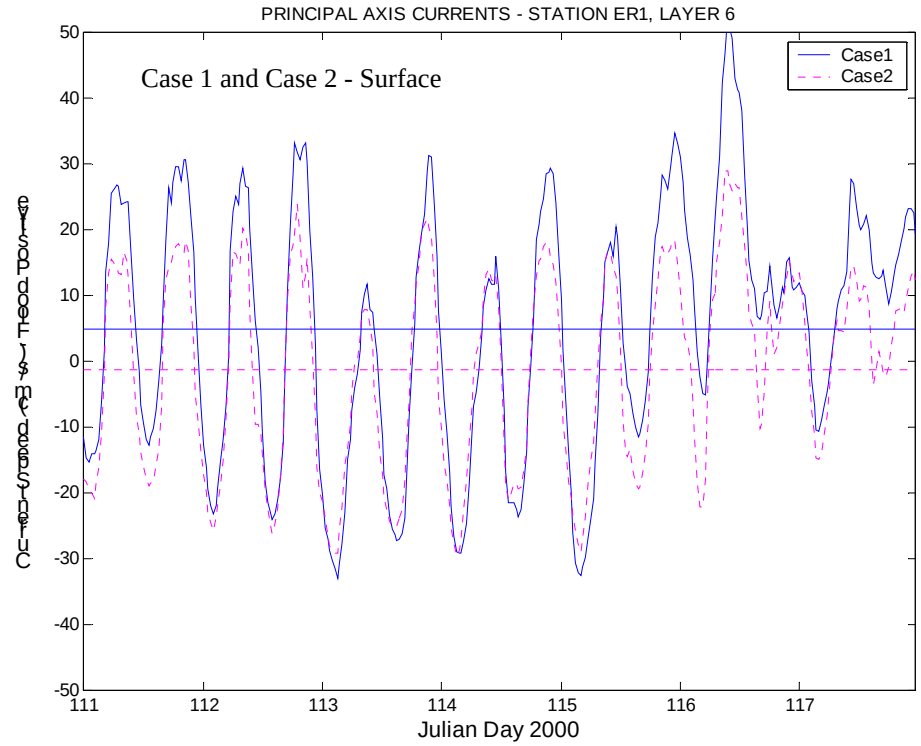

Figure VI.6. Principal axis currents at Station ER1; Case 1 and Case 2 (surface layer).

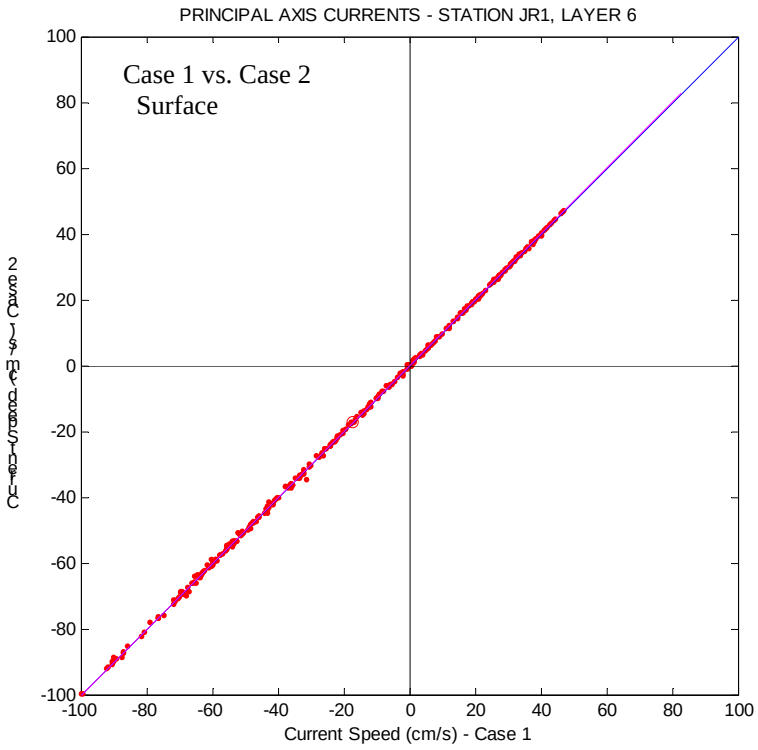

Figure VI.7. Principal axis current at Station JR1, Case 1 vs. Case 2 (surface layer).

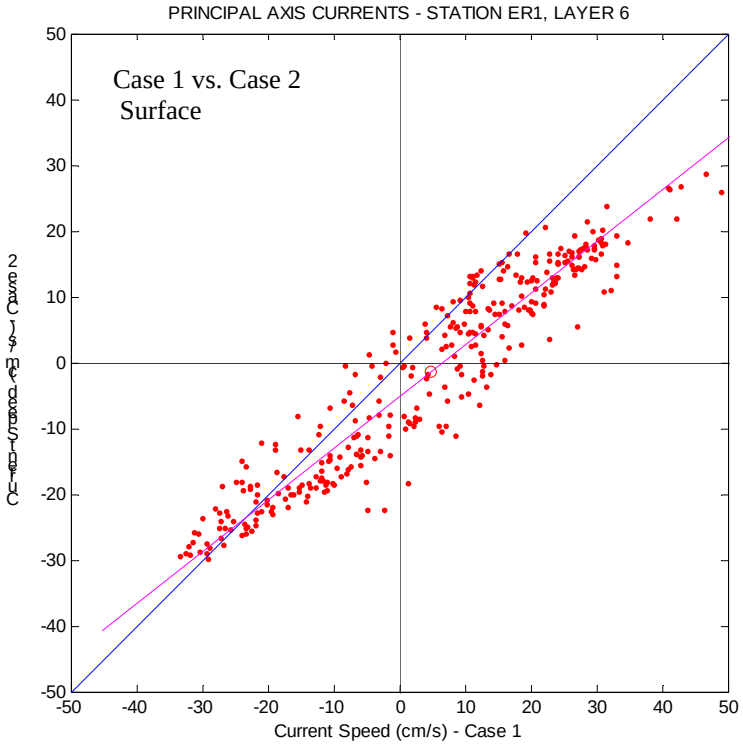

Figure VI.8. Principal axis current at Station JR1, Case 1 vs. Case 2 (surface layer).

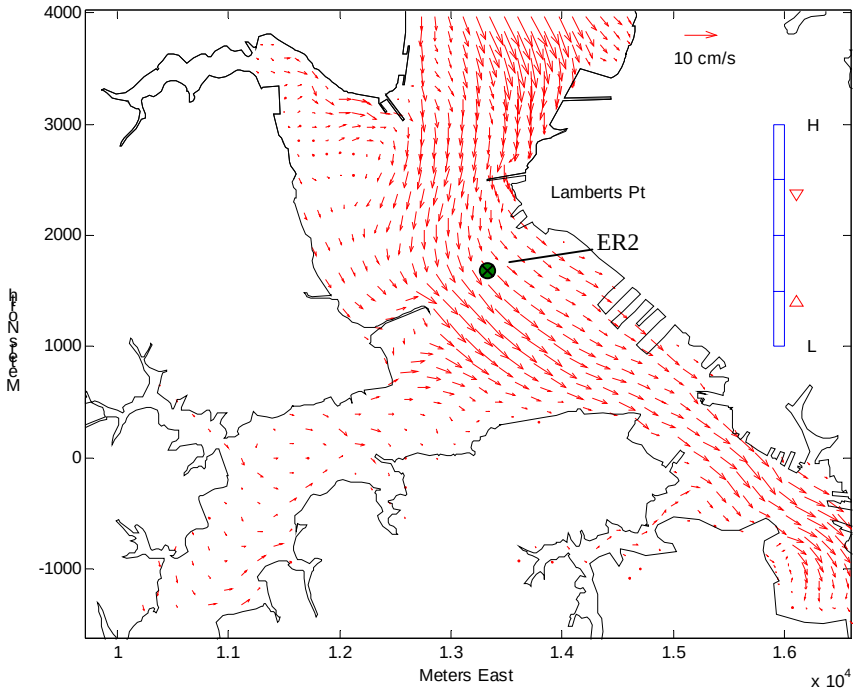

Figure VI.9. Residual surface current, Elizabeth River, April 20, 2000 (Julian day 111). Plan view showing location of time series station ER2.

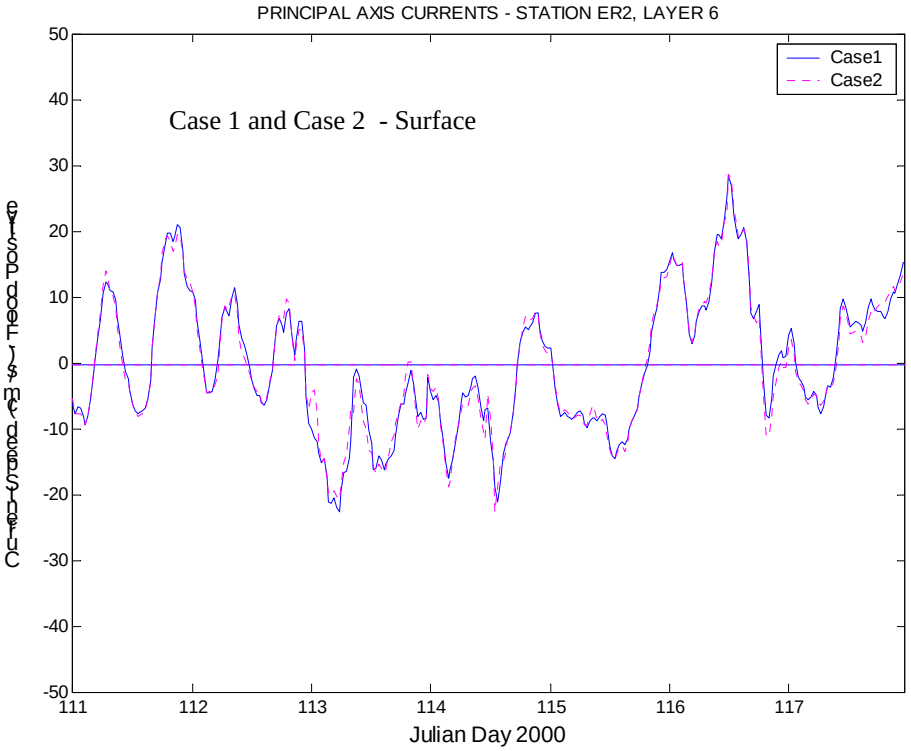

Figure VI.10. Principal axis currents at Station ER2; Case 1 and Case 2 (surface layer).

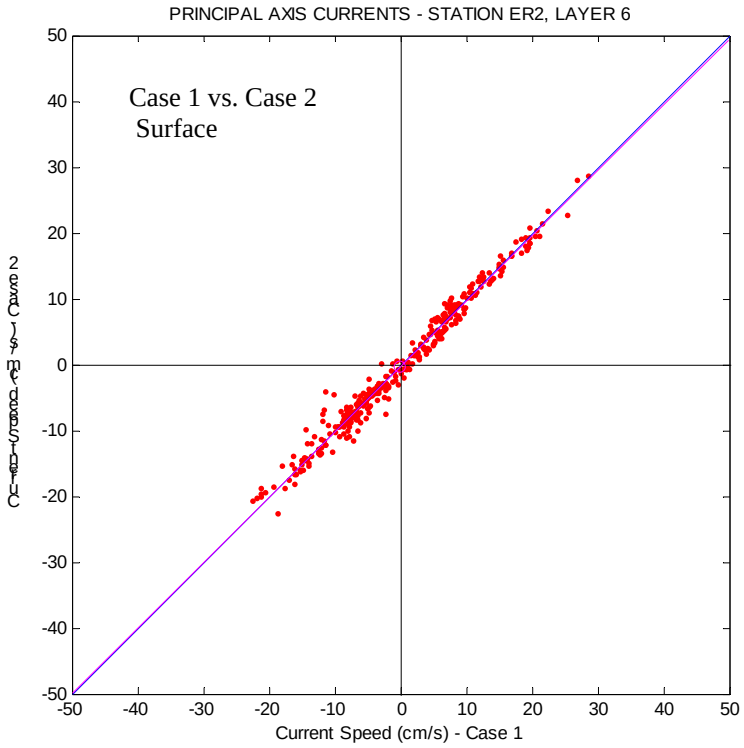

Figure VI.11. Principal axis current at Station ER2, Case 1 vs. Case 2 (surface layer).

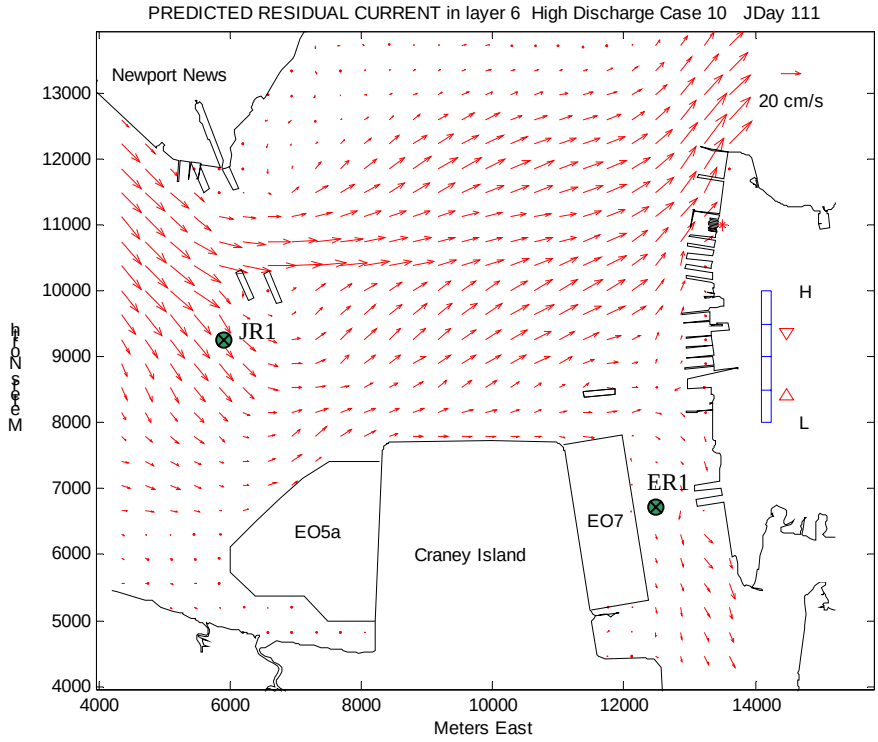

Figure VI.12. Residual surface current in Hampton Roads, April 20, 2000 (Julian Day 111). Plan view showing location of time series stations JR1 and ER1 with Expansion Option 7/5a.

Mean, amplitude and phase difference estimates - Mean, amplitude and phase difference estimates for Case 1 compared with Case 2 and Case 10 during the high discharge event (Julian day 111 –117) are presented in Tables VI.3 and VI.4. The tables contain values of the principal axis current mean, amplitude, and phase at three different depths centered within the model's surface, middle and near-bottom layers. These correspond to model layers 6, 4, and 2, respectively, where the thickness of each layer equals $1/6^{th}$ of the total depth at the station. Figures VI.5 through VI.42 show the results graphically.

For clarity, amplitude and phase differences are reported here in the same units one would use to compare a pair of simple sine waves with RMS values equivalent to those of the complex wave forms produced in real time simulations. Thus while phase difference estimates are given in minutes, it is noted that the RMS value representing phase difference is the quantity $RMSD_e$ as defined above. Its value is similar to the RMS phase error presented in Table IV.1 in Chapter IV, Model Calibration. For a 30-minute phase difference, $RMSD_e$. 5 cm/s which is roughly the same level of error as reported for phase during current calibration. In a similar fashion, model calibration data indicate that modeled current amplitudes may over-predict or under-predict observed current amplitudes by as much as 10% depending upon the location. We note in passing that the model's precision is only a fraction of this error and that field measurement error cannot be ignored as a contributor to model accuracy estimates.

Station JR1 - Examining the current time series at station JR1, the effect of the proposed expansions tested in the Case 1 vs. Case 2 comparison (Table VI.3) are minimal in terms of all three current parameters computed at all three depths. The differences resulting from these comparisons all lie well within the accuracy limits of the model. Comparing Case 1 vs. Case 10 (Table VI.4), differences in mean current, current amplitude, and current phase are slightly larger as can be expected due to the placement of new structure nearby as depicted for Case 10 (Figure VI.12). The changes, however, remain small as compared to conservative estimates of model accuracy and support the conclusion that the current field north and west of Craney Island is essentially unchanged by either Expansion Option 7 or 7/5a.

Station ER1 – In contrast to the results at station JR1, the mean, amplitude and phase of the modeled current at station ER1 exhibit significant change in both Case 2 and Case 10 comparisons with Case 1. The phase for Case 2 is predicted to lead that for Case 1 by approximately 30 minutes at the surface and approximately 52 minutes near the bottom with similar differences indicated for Case 10. Current amplitude is predicted to decrease by about 6 cm/s at the surface and 5 cm/s near bottom for these cases. Change of this magnitude is not unexpected at ER1 given its location in an area of maximum change in channel dimensions immediately east of the eastward expansion (Option 7).

Station ER2 – While a change of less than 1 cm/s is indicated in current mean and current amplitude, phase leads varying between 17 minutes at the surface and 12-13 minutes in the mid-depth and near bottom layers are predicted for Cases 2 and 10 at station ER2. The significance of a predicted change in current phase is difficult to interpret due to the standing wave properties of the tide within the Elizabeth River.

a. Surface layer

Station	Case 1	Case 2	Difference
JR1 Mean (cm/s)	-17.36	-17.33	0.03
Amp (cm/s)	53.99	54.05	0.05
Phase (min)	0	1.58	1.58
ER1 Mean (cm/s)	4.77	-1.34	-6.11
Amp (cm/s)	27.14	21.37	-5.77
Phase (min)	0	30.12	30.12
ER2 Mean (cm/s)	-0.25	-0.42	-0.17
Amp (cm/s)	14.52	14.41	-0.11
Phase (min)	0	16.51	16.51

b. Middle layer

Station	Case 1	Case 2	Difference
JR1 Mean (cm/s)	-9.55	-9.60	-0.05
Amp (cm/s)	45.62	45.81	0.19
Phase (min)	0	2.44	2.44
ER1 Mean (cm/s)	0.02	-2.91	-2.93
Amp (cm/s)	20.00	14.53	-5.47
Phase (min)	0	45.15	45.15
ER2 Mean (cm/s)	-0.31	-0.23	0.08
Amp (cm/s)	10.33	9.86	-0.47
Phase (min)	0	12.62	12.62

c. Near-bottom layer

Station	Case 1	Case 2	Difference
JR1 Mean (cm/s)	-3.31	-3.29	0.02
Amp (cm/s)	36.23	36.38	0.15
Phase (min)	0	2.75	2.75
ER1 Mean (cm/s)	-2.06	-0.39	1.67
Amp (cm/s)	13.81	9.16	-4.64
Phase (min)	0	52.37	52.37
ER2 Mean (cm/s)	-0.39	-0.32	0.07
Amp (cm/s)	13.15	13.34	0.19
Phase (min)	0	13.27	13.27

Table VI.3. Principal axis current comparisons, Cases 1 and 2, high discharge event (day 111-117): a. surface layer, b. middle layer, c. near-bottom layer of water column.

a. Surface Layer

Station	Case 1	Case 10	Difference
JR1 Mean (cm/s)	-17.36	-16.44	0.92
Amp (cm/s)	53.99	54.55	0.56
Phase (min)	0	5.20	5.20
ER1 Mean (cm/s)	4.77	-1.29	-6.06
Amp (cm/s)	27.14	21.28	-5.87
Phase (min)	0	32.31	32.31
ER2 Mean (cm/s)	-0.25	-0.29	-0.04
Amp (cm/s)	14.52	14.43	-0.09
Phase (min)	0	17.35	17.35

b. Middle layer

Station	Case 1	Case 10	Difference
JR1 Mean (cm/s)	-9.55	-9.19	0.36
Amp (cm/s)	45.62	46.77	1.14
Phase (min)	0	6.22	6.22
ER1 Mean (cm/s)	0.02	-2.98	-3.00
Amp (cm/s)	20.00	14.20	-5.80
Phase (min)	0	45.52	45.52
ER2 Mean (cm/s)	-0.31	-0.44	-0.13
Amp (cm/s)	10.33	9.79	-0.54
Phase (min)	0	13.76	13.76

c. Near-bottom layer

Station	Case 1	Case 10	Difference
JR1 Mean (cm/s)	-3.31	-3.56	-0.25
Amp (cm/s)	36.23	37.60	1.37
Phase (min)	0	7.35	7.35
ER1 Mean (cm/s)	-2.06	-0.40	1.66
Amp (cm/s)	13.81	9.07	-4.73
Phase (min)	0	51.10	51.10
ER2 Mean (cm/s)	-0.39	-0.32	0.07
Amp (cm/s)	13.15	13.39	0.24
Phase (min)	0	11.70	11.70

Table VI.4. Principal axis current comparisons, Cases 1 and 10, high discharge event (day 111-117): a. surface layer, b. middle layer, c. near-bottom layer of water column.

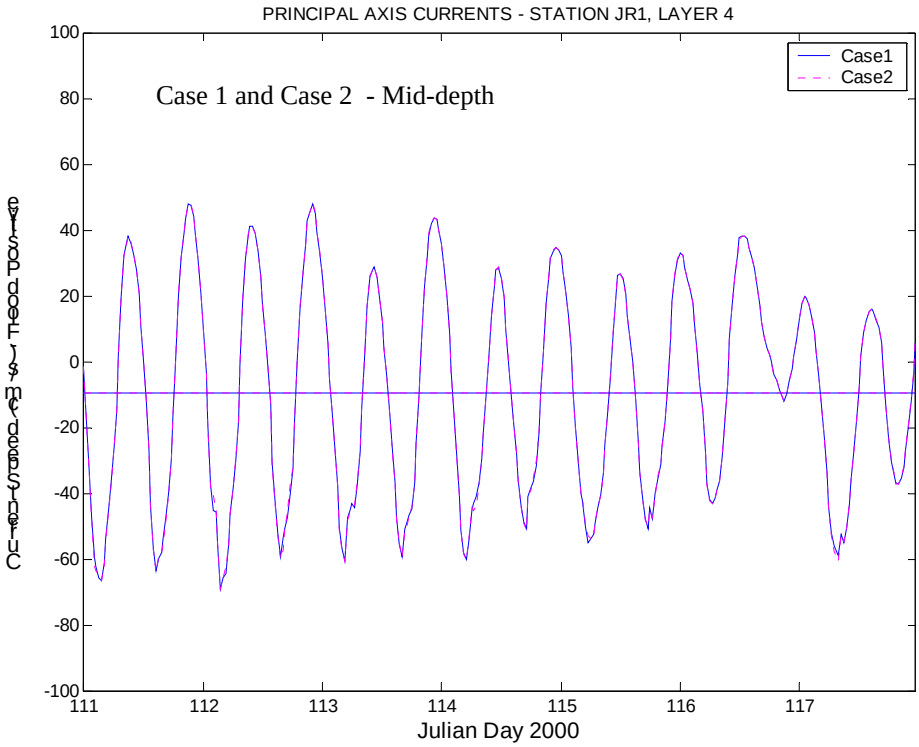

Figure VI.13. Principal axis currents at Station JR1; Case 1 and Case 2 (middle layer).

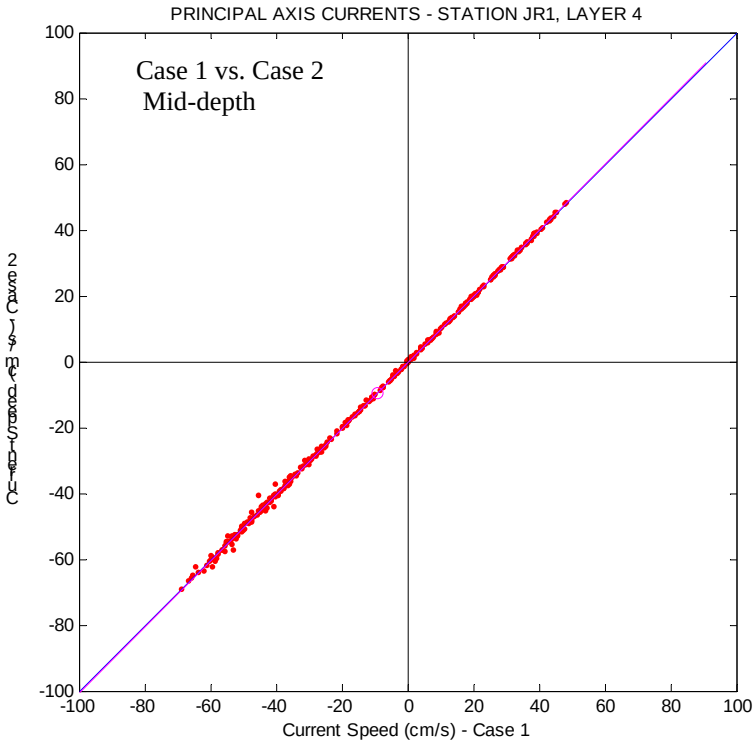

Figure VI.14. Principal axis currents at Station JR1; Case 1 vs. Case 2 (middle layer).

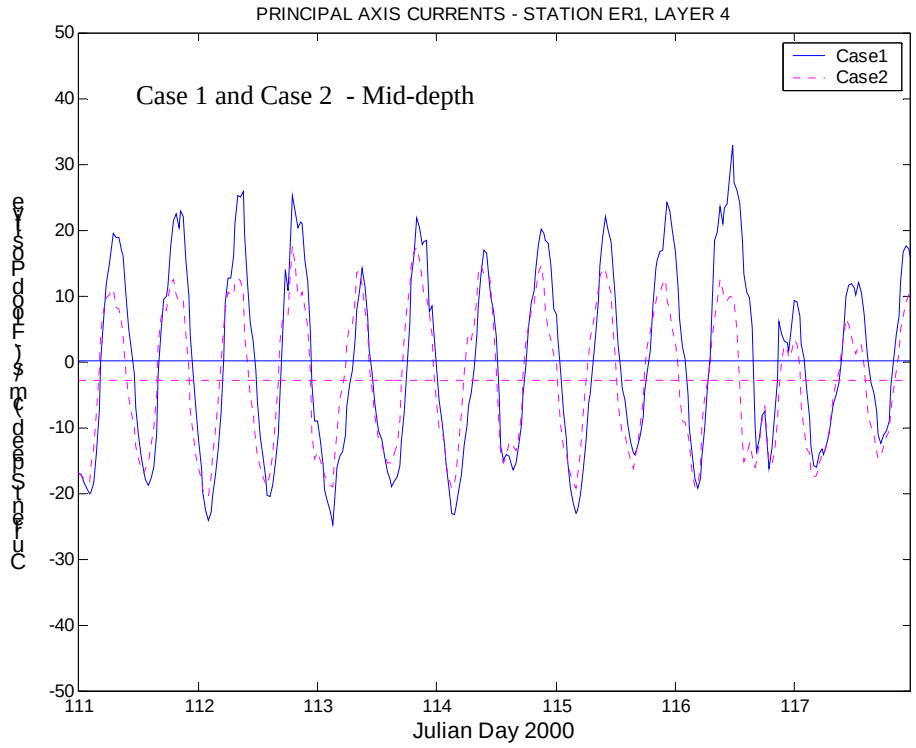

Figure VI.15. Principal axis currents at Station ER1; Case 1 and Case 2 (middle layer).

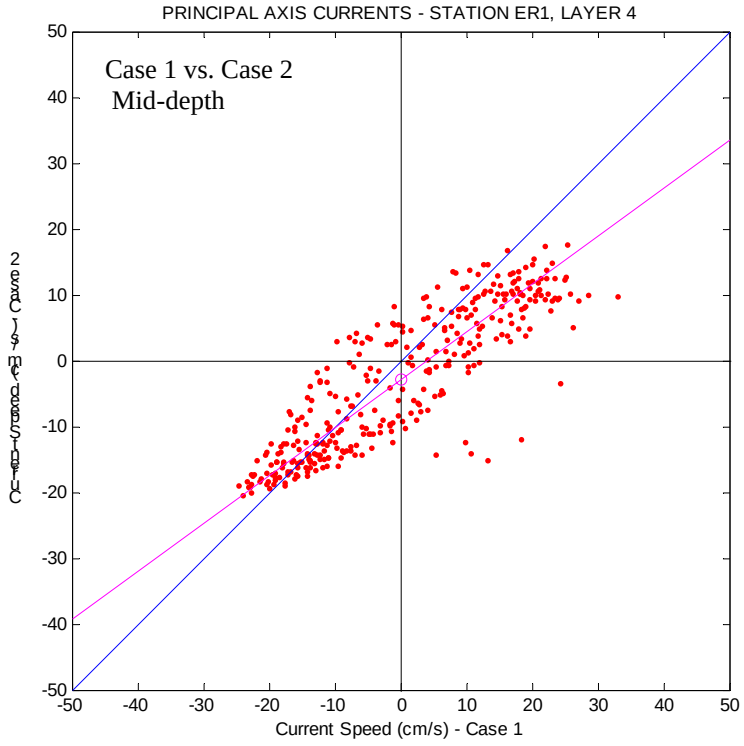

Figure VI.16. Principal axis currents at Station ER1; Case 1 vs. Case 2 (middle layer).

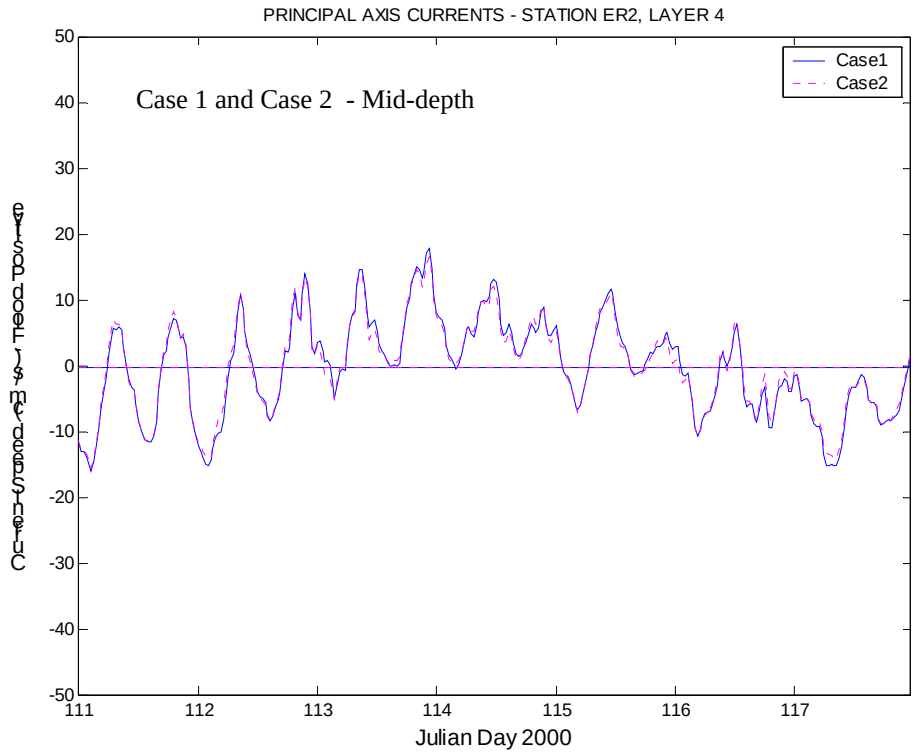

Figure VI.17. Principal axis currents at Station ER2; Case 1 and Case 2 (middle layer).

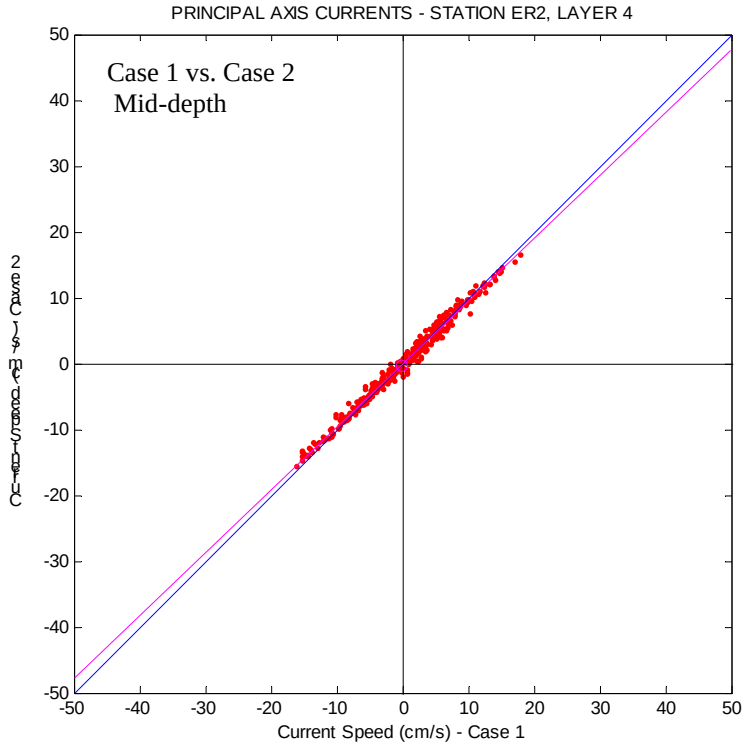

Figure VI.18. Principal axis currents at Station ER2; Case 1 vs. Case 2 (middle layer).

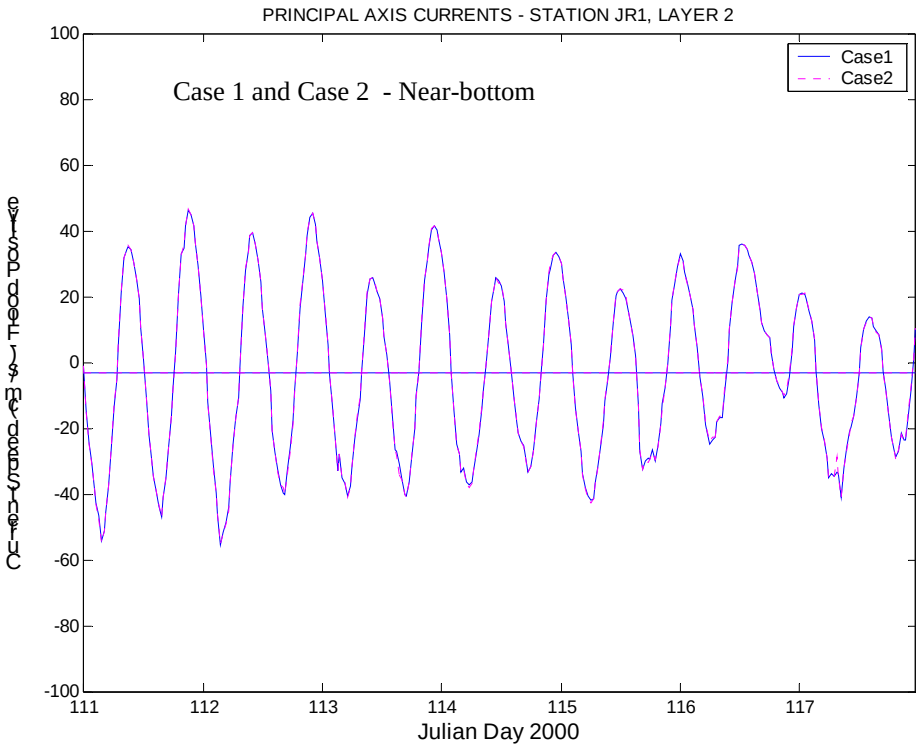

Figure VI.19. Principal axis currents at Station JR1; Case 1 and Case 2 (near bottom).

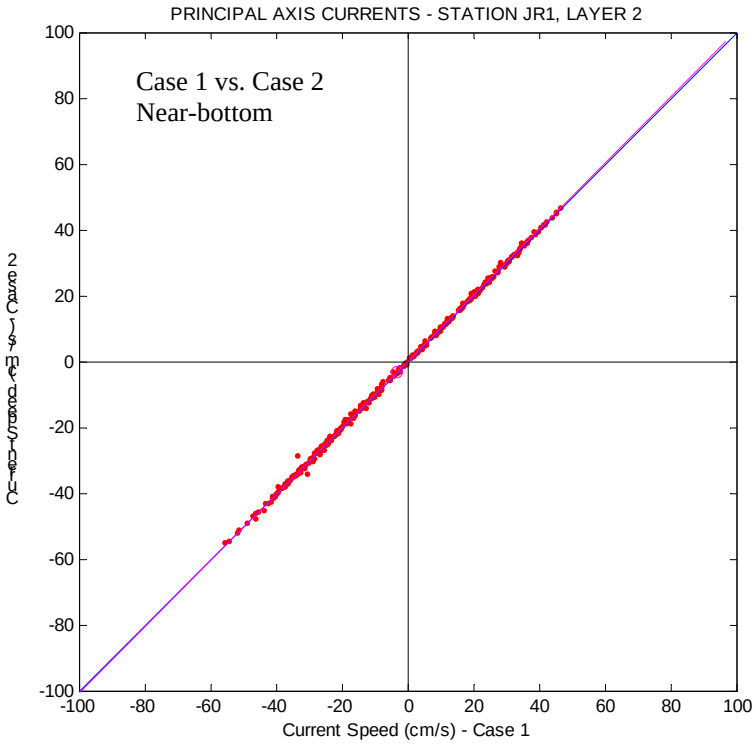

Figure VI.20. Principal axis currents at Station JR1; Case 1 vs. Case 2 (near bottom).

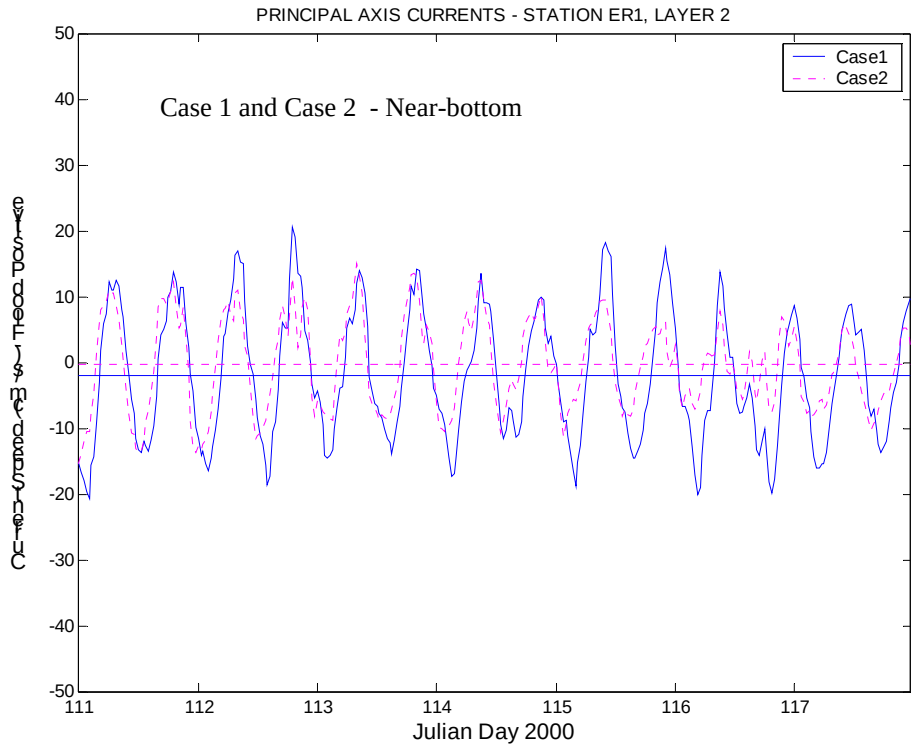

Figure VI.21. Principal axis currents at Station ER1; Case 1 and Case 2 (near bottom).

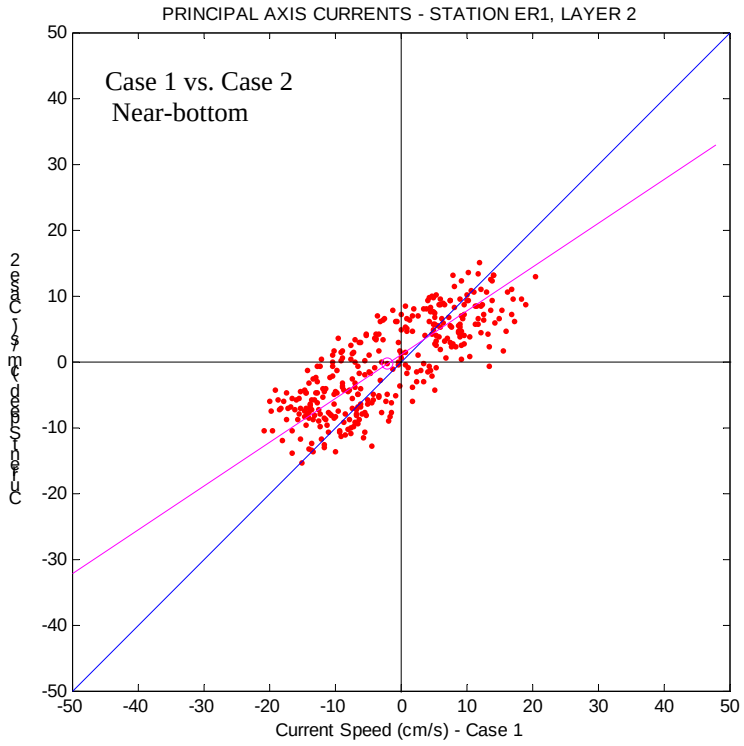

Figure VI.22. Principal axis currents at Station ER1; Case 1 vs. Case 2 (near bottom).

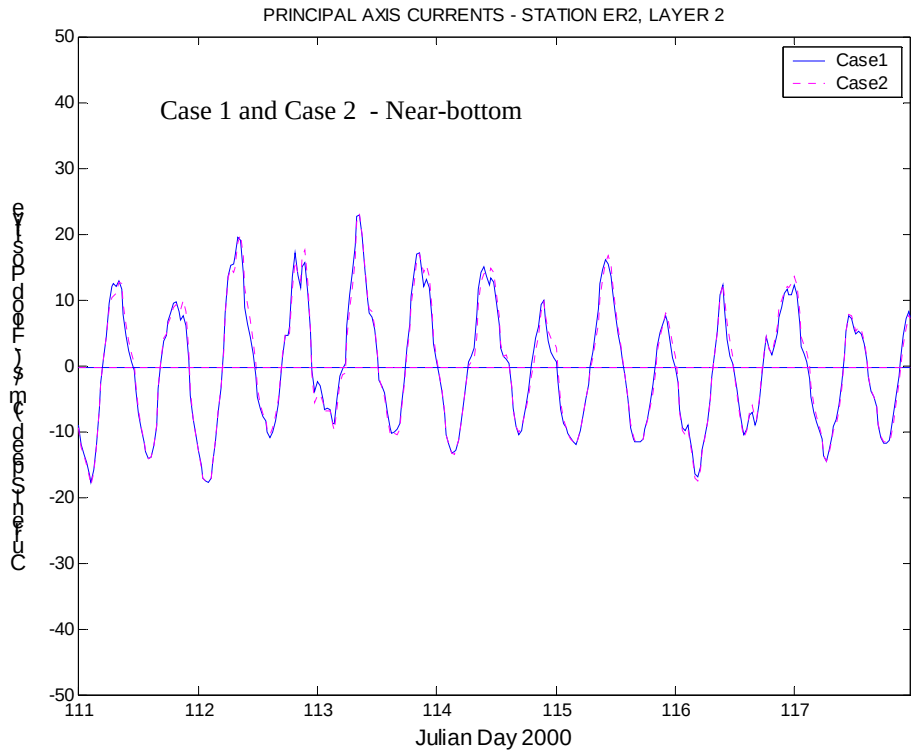

Figure VI.23. Principal axis currents at Station ER2; Case 1 and Case 2 (near bottom).

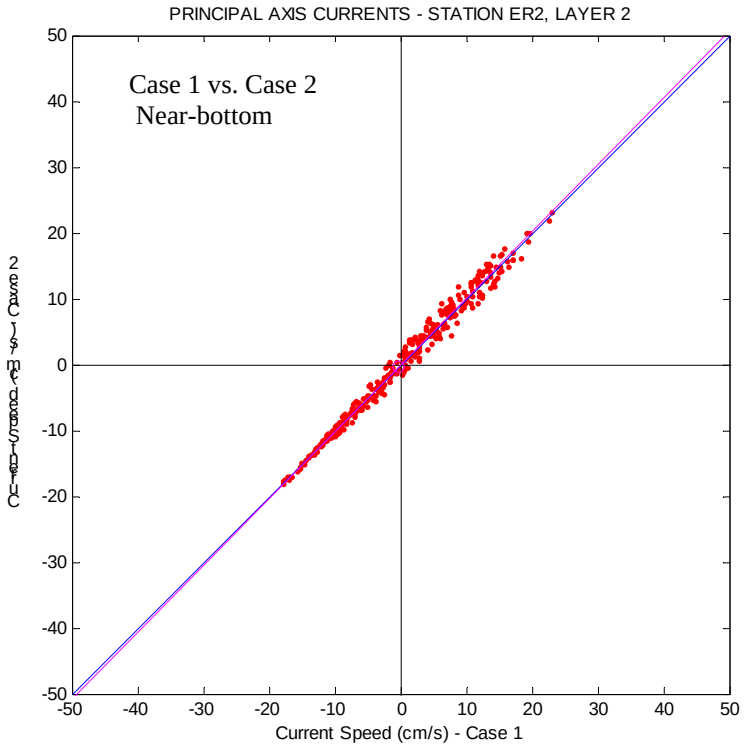

Figure VI.24. Principal axis currents at Station ER2; Case 1 vs. Case 2 (near bottom).

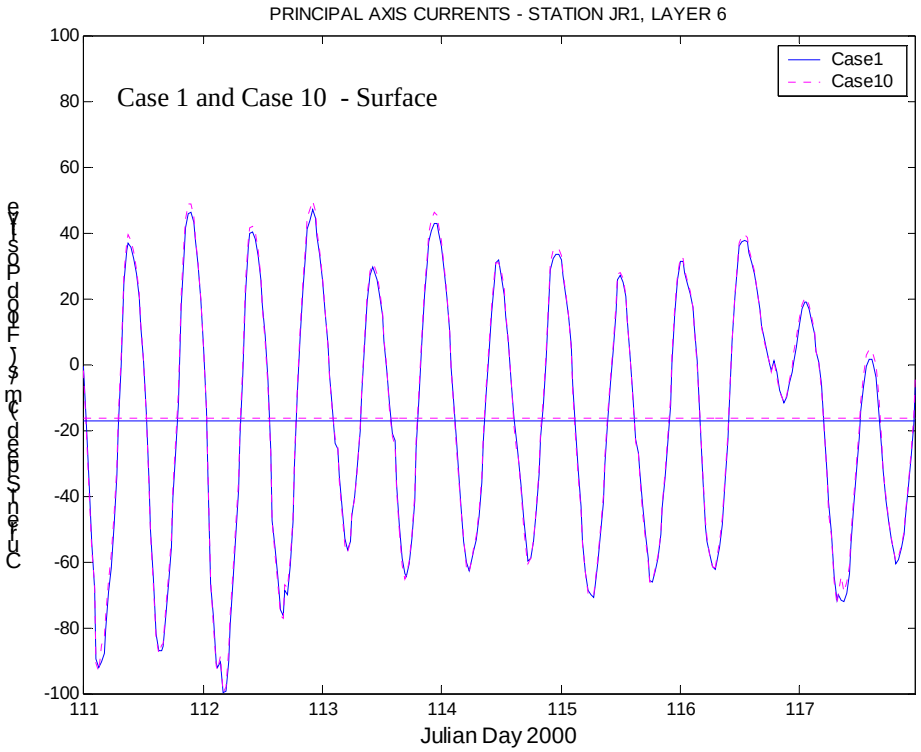

Figure VI.25. Principal axis currents at Station JR1; Case 1 and Case 10 (surface layer).

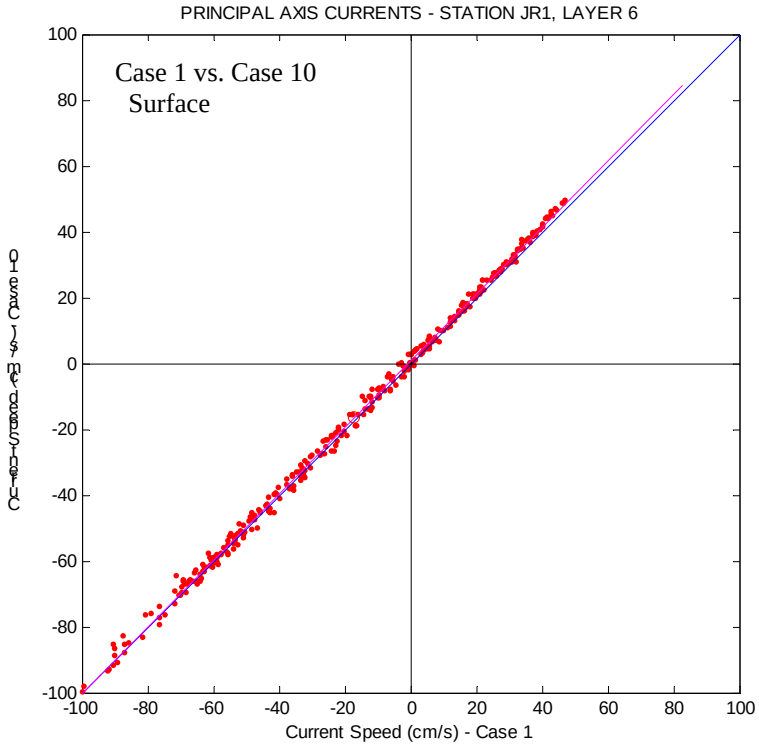

Figure VI.26. Principal axis currents at Station JR1; Case 1 vs. Case 10 (surface layer).

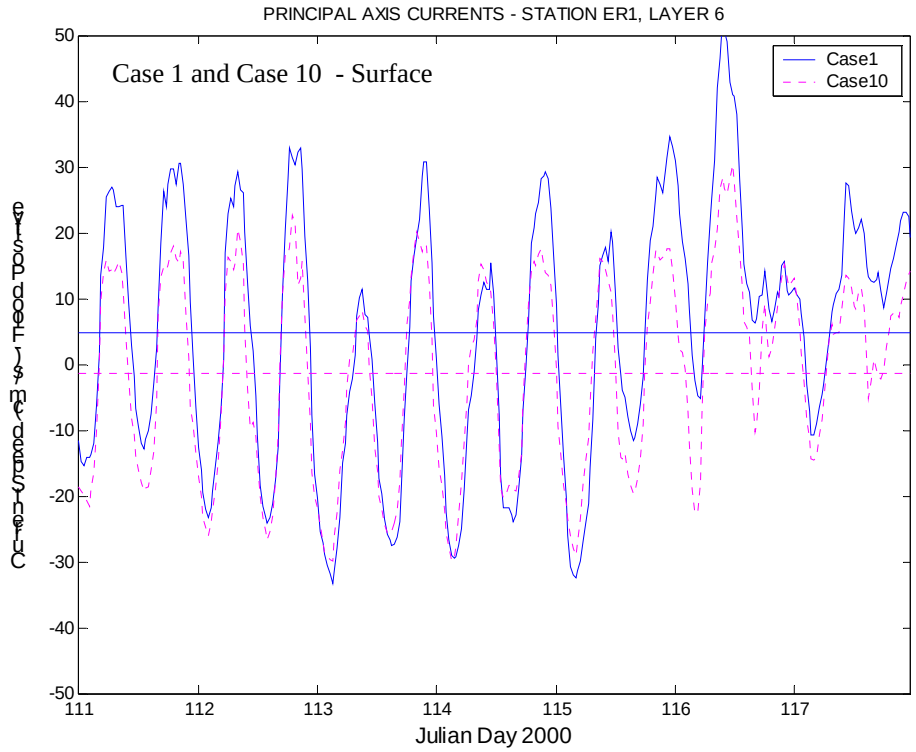

Figure VI.27. Principal axis currents at Station ER1; Case 1 and Case 10 (surface layer).

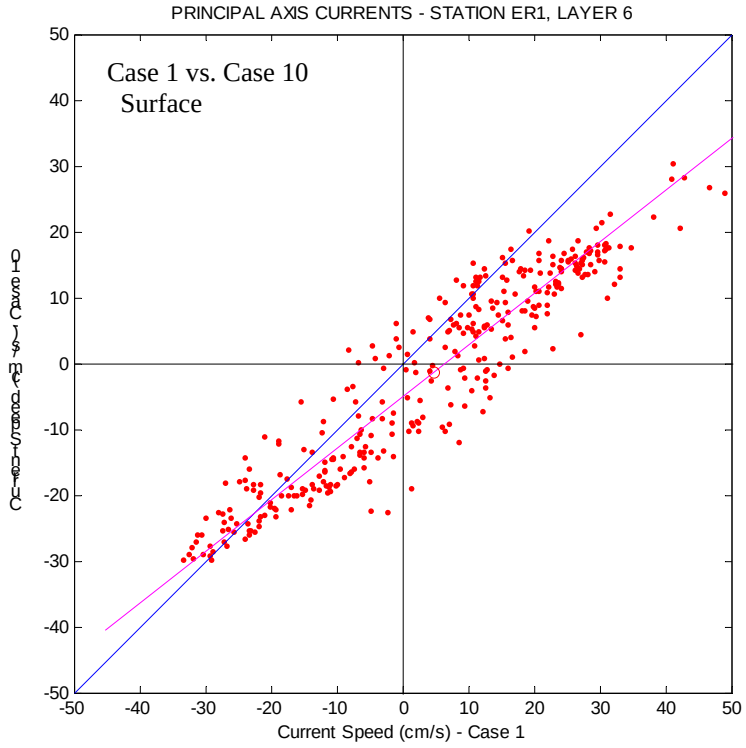

Figure VI.28. Principal axis currents at Station ER1; Case 1 vs. Case 10 (surface layer).

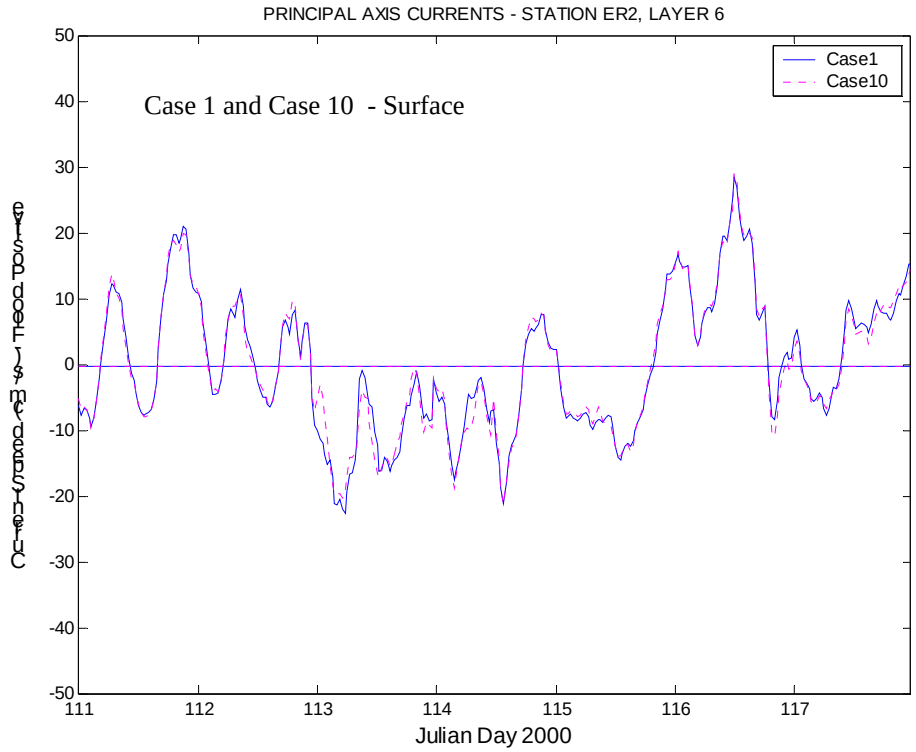

Figure VI.29. Principal axis currents at Station ER2; Case 1 and Case 10 (surface layer).

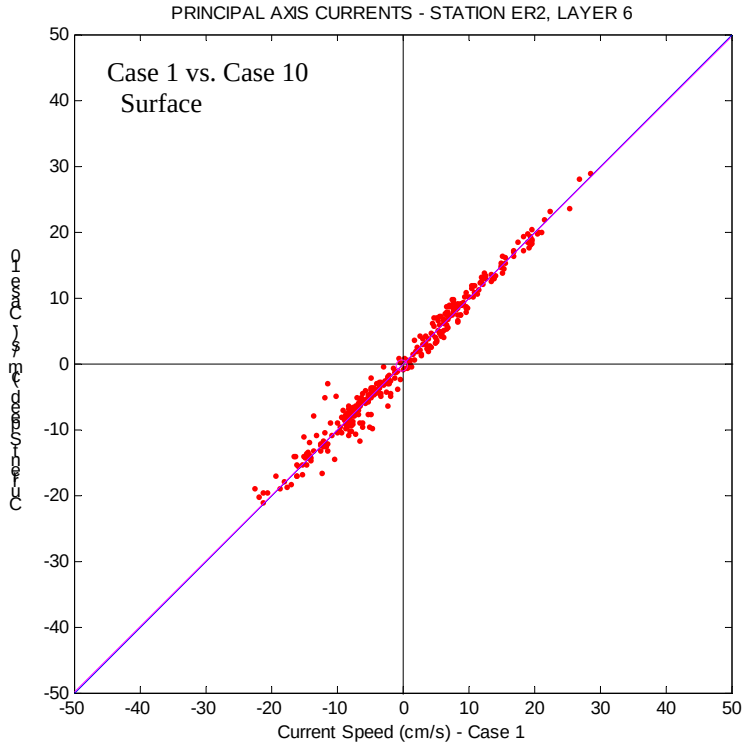

Figure VI.30. Principal axis currents at Station ER2; Case 1 vs. Case 10 (surface layer).

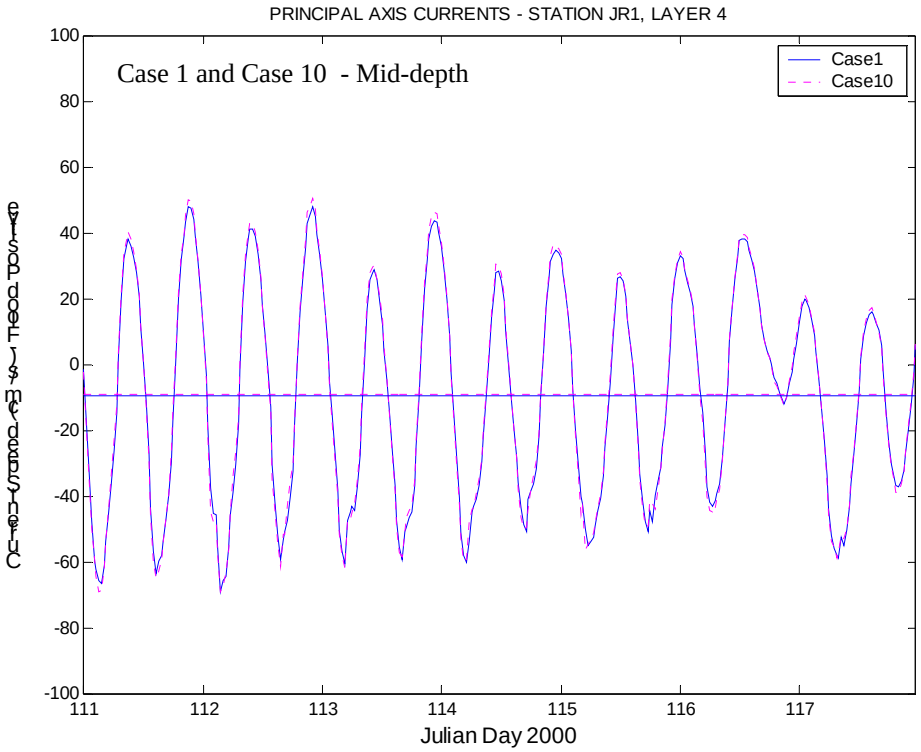

Figure VI.31. Principal axis currents at Station JR1; Case 1 and Case 10 (middle layer).

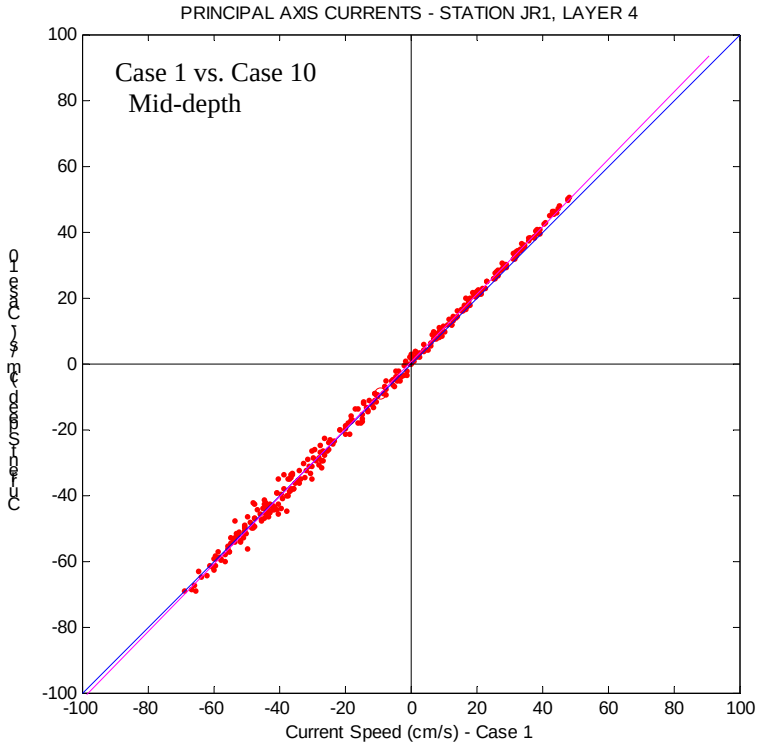

Figure VI.32. Principal axis currents at Station JR1; Case 1 vs. Case 10 (middle layer).

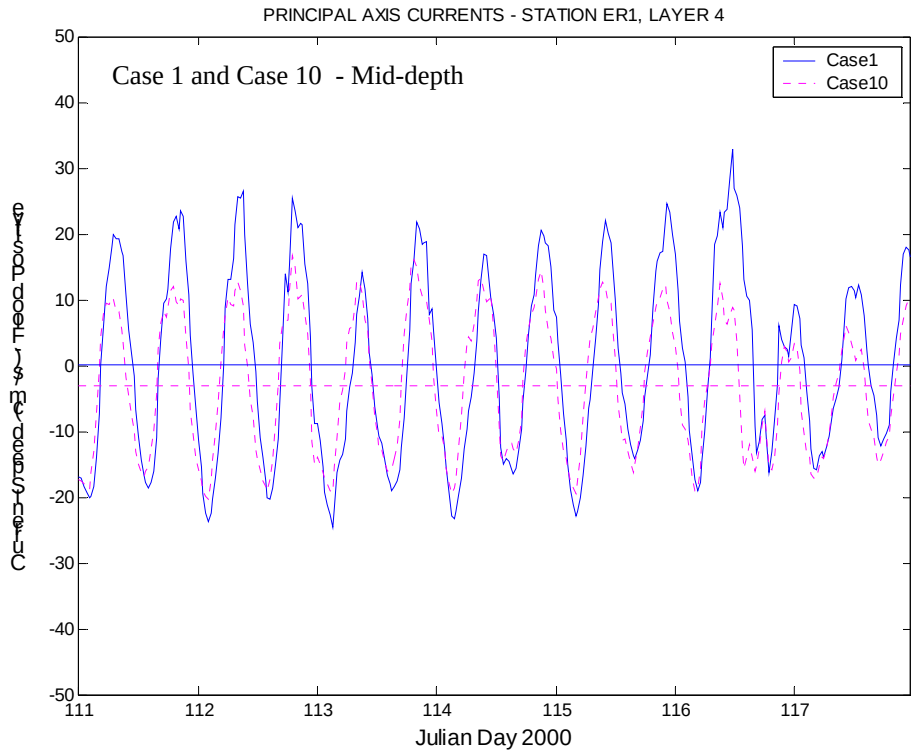

Figure VI.33. Principal axis currents at Station ER1; Case 1 and Case 10 (middle layer).

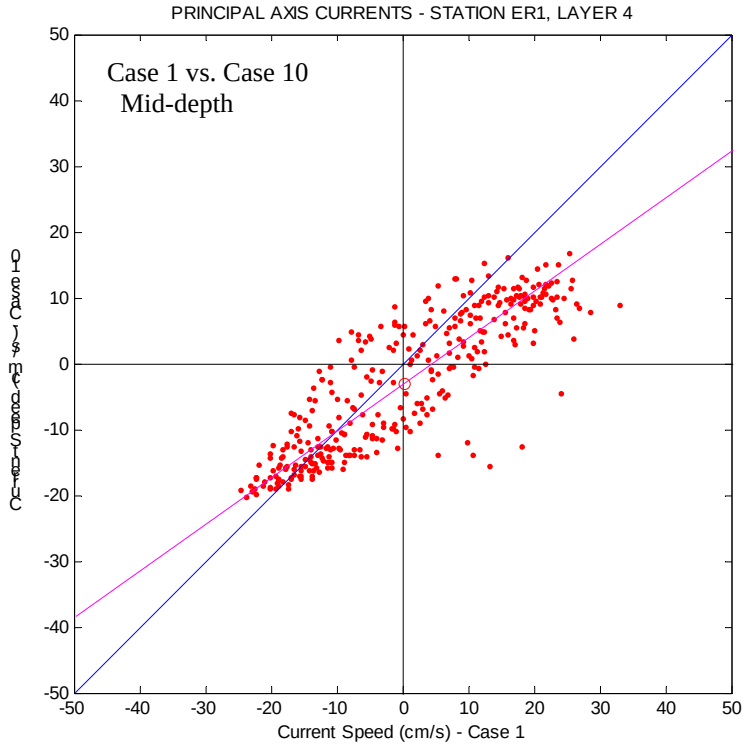

Figure VI.34. Principal axis currents at Station ER1; Case 1 vs. Case 10 (middle layer).

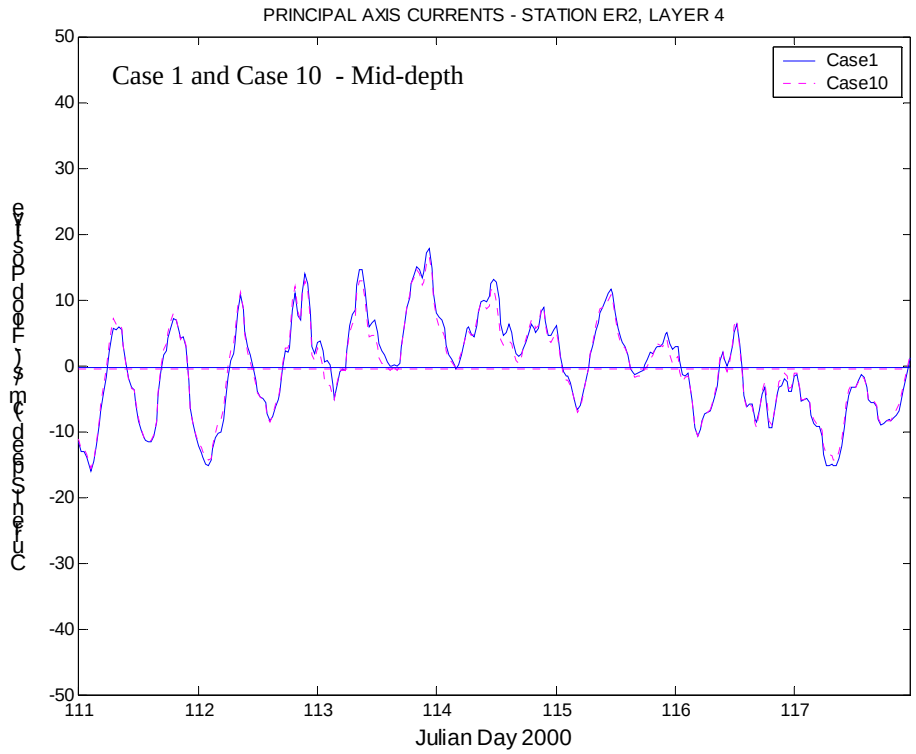

Figure VI.35. Principal axis currents at Station ER2; Case 1 and Case 10 (middle layer).

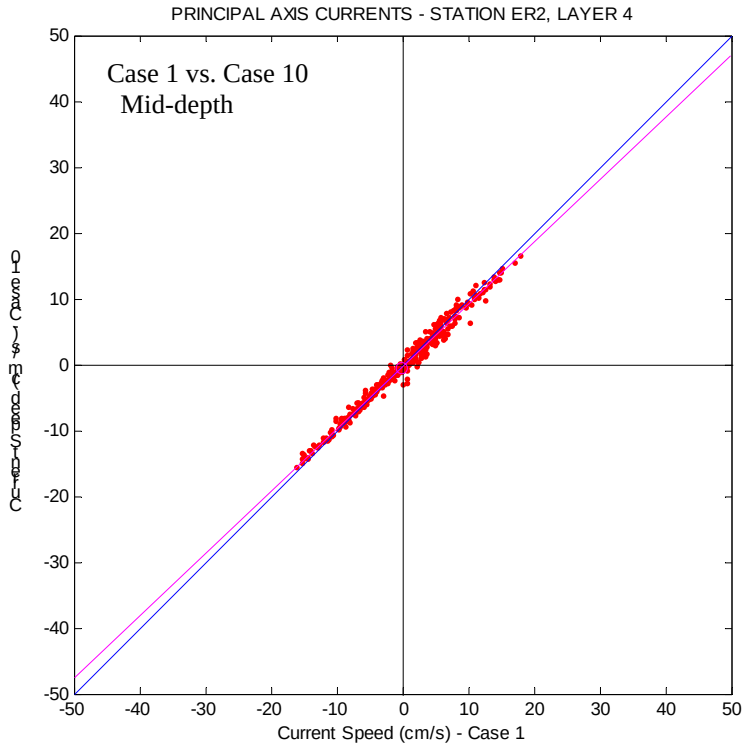

Figure VI.36. Principal axis currents at Station ER2; Case 1 vs. Case 10 (middle layer).

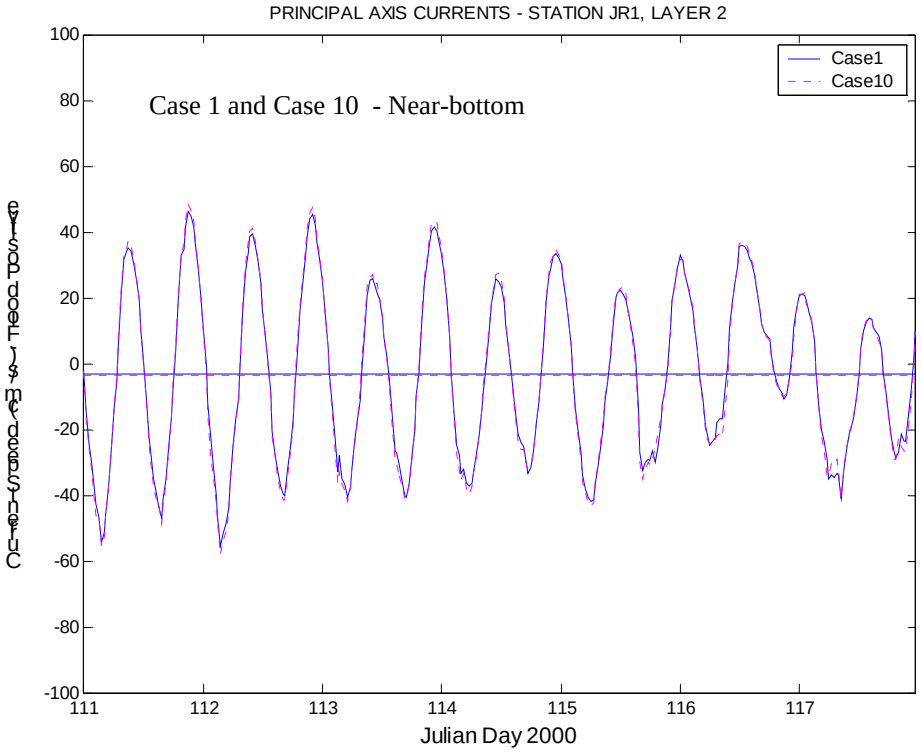

Figure VI.37. Principal axis currents at Station JR1; Case 1 and Case 10 (near bottom).

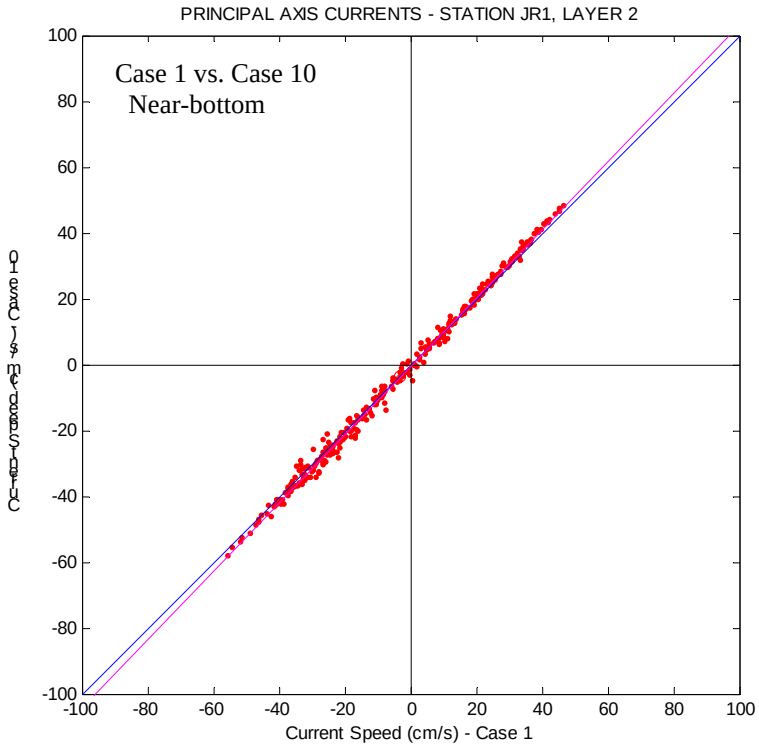

Figure VI.38. Principal axis currents at Station JR1; Case 1 vs. Case 10 (near-bottom).

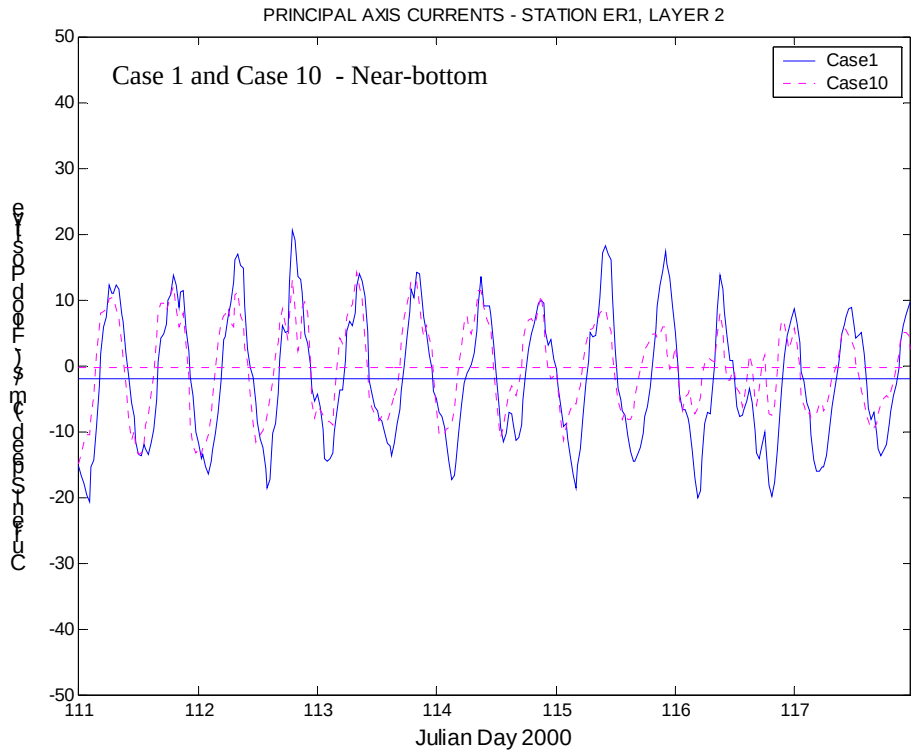

Figure VI.39. Principal axis currents at Station ER1; Case 1 and Case 10 (near bottom).

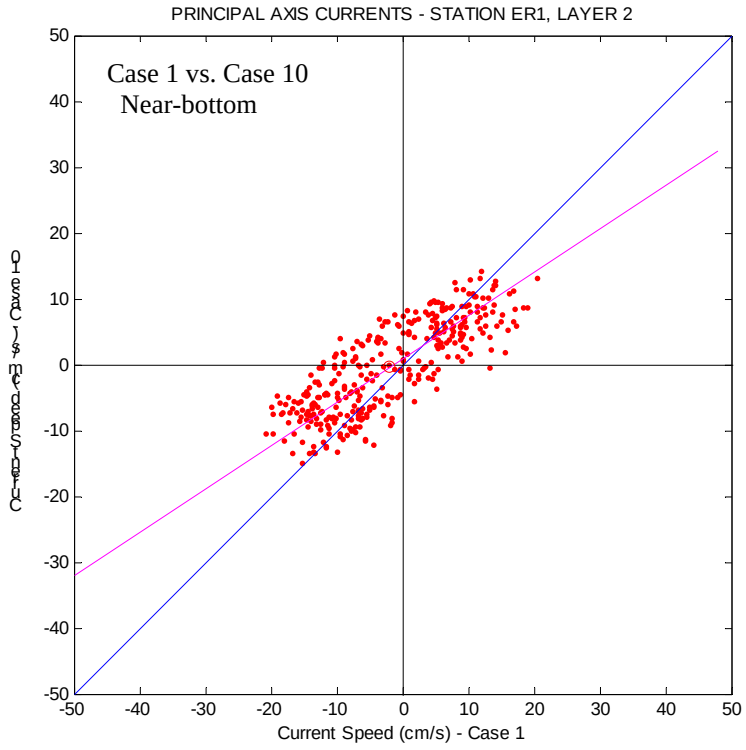

Figure VI.40. Principal axis currents at Station ER1; Case 1 vs. Case 10 (near-bottom).

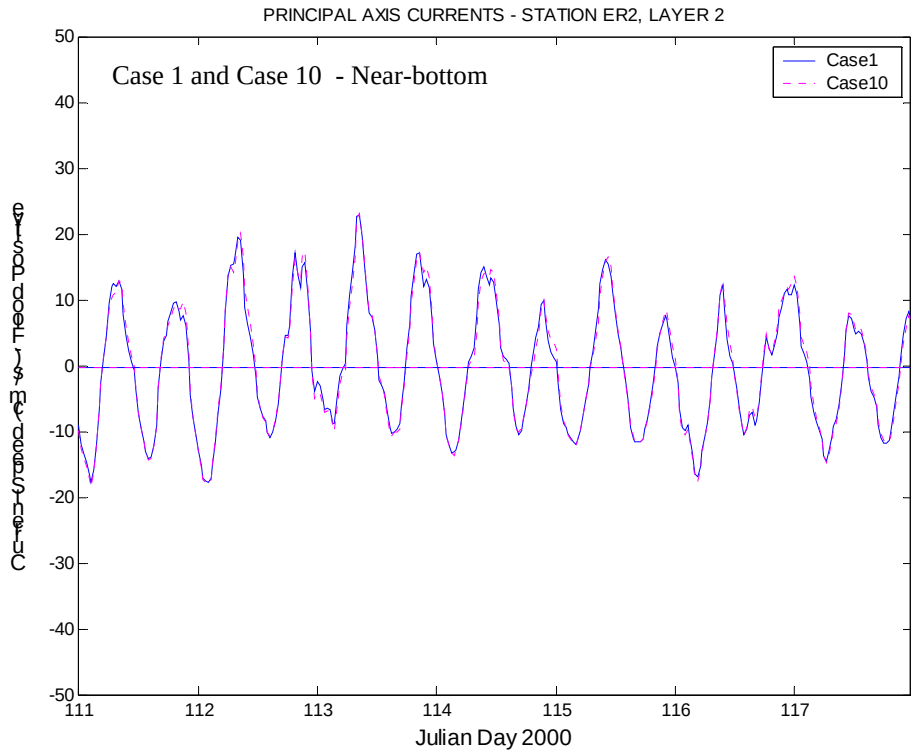

Figure VI.41. Principal axis currents at Station ER2; Case 1 and Case 10 (near bottom).

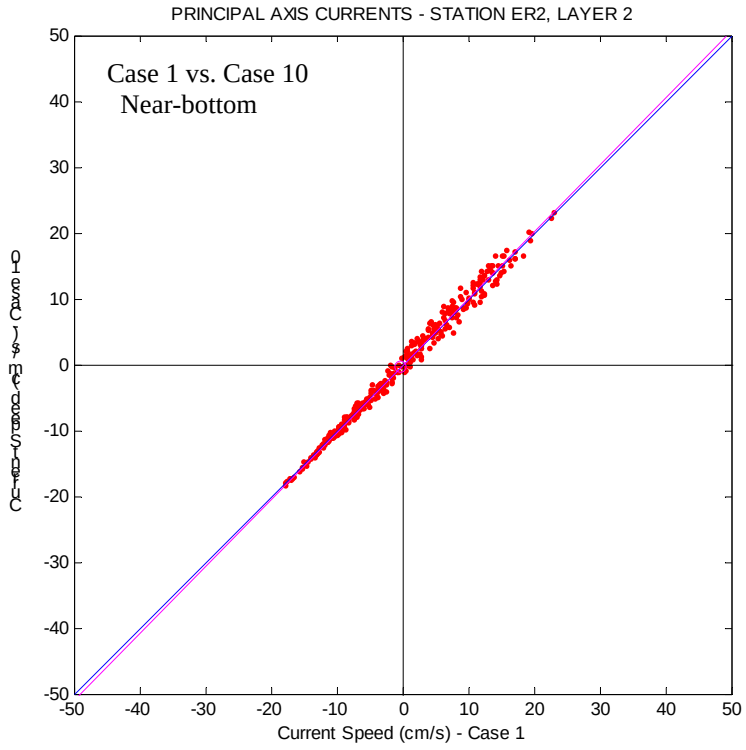

Figure VI.42. Principal axis currents at Station ER2; Case 1 vs. Case 10 (near-bottom).

C. FLUSHING CHARACTERISTICS

Two methods of estimating the flushing capacity of an estuarine system, such as the Elizabeth River or one of its branches, were described in Chapter V, Section C. Both tidal prism and residual transport calculations were shown for Cases 2-9. The reader is referred to that section for a full derivation of the flux calculation. In this section, the new expansion option (i.e., Option 7/5a, Cases 10 and 11) will be compared to the other cases for both tidal prism and residual transport. Next, simulated dye releases at the Jordan Bridge in the Southern Branch of the Elizabeth will be re-visited, this time for releases coinciding with the high discharge, the low discharge, and the high wind events of the historical runs. Finally, the influence of the western portion of Cases 10 and 11 on local flushing ability will be examined.

1. Flux Calculation – Again, the reader is referred to the earlier discussion in Chapter V, Section C.1 for a discussion of tidal and non-tidal components of volume flux through a cross section in an estuary. A separate single variable simulation of Cases 10 and 11 provided the output needed to estimate tidal prism and residual transport. These estimates are shown for all 11 cases in Figure VI.43.

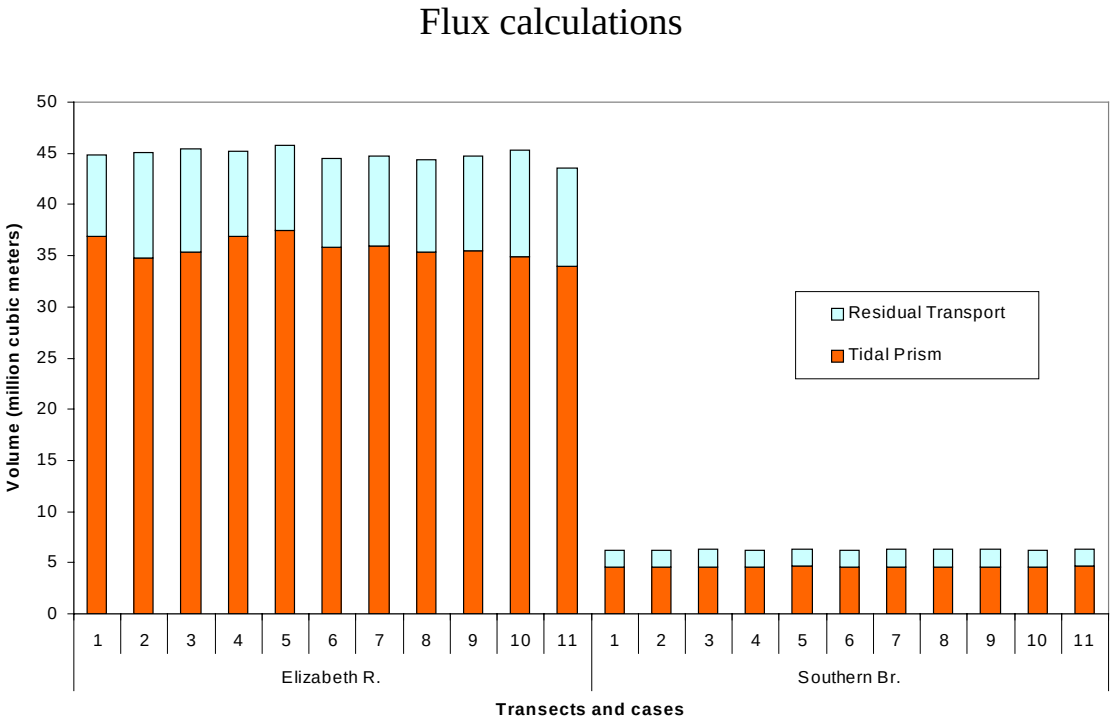

Figure VI.43. Flux calculations for the entire Elizabeth River and the Southern Branch for all 11 Cases of the single variable runs.

2. Tracer Experiments (Release in Southern Branch)– As was done for Cases 1-3 using the single variable simulations, historical Cases 1, 2, and 10 were tested for flushing capacity by releasing a unit mass of a neutrally buoyant tracer in the Southern Branch near the Jordan Bridge, shown again in Figure VI.44. These releases, however, were set to coincide with the exact beginning of each of the 3 one-week event periods (high discharge, low discharge, and high wind). As in the single variable simulations, the tracer was released instantaneously and its concentration distribution was calculated by the mass-balance equation as the model simulation advances through successive time steps.

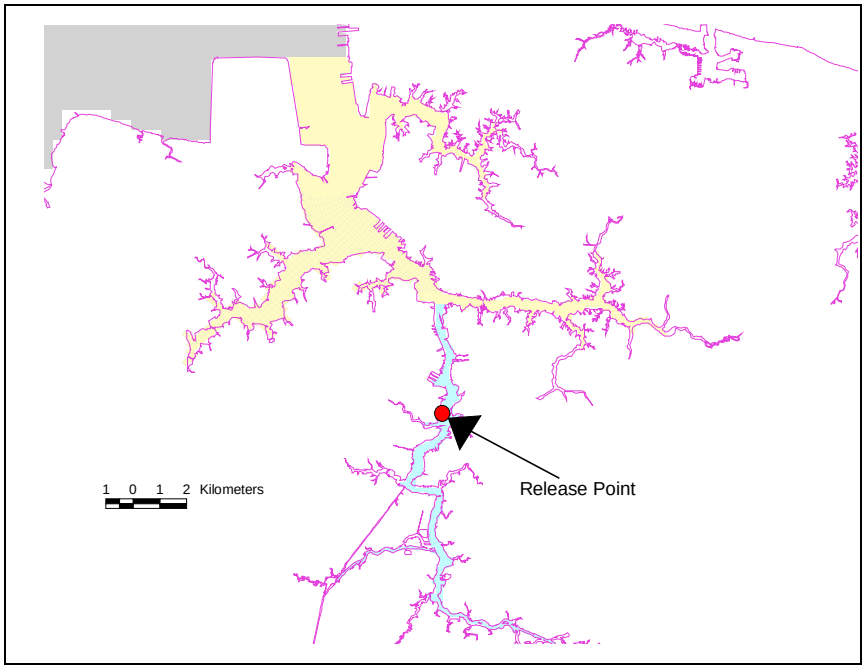

Figure VI.44. Location of tracer releases in the Southern Branch near the Jordan Bridge.

For each case and event simulation, the decay of mass remaining in the Southern Branch was plotted as a function of time, as shown in Figure VI.45. Although the decay varied significantly depending on the event occurring during release, almost no difference was noted between the cases tested. This result is summarized in Table VI.5.

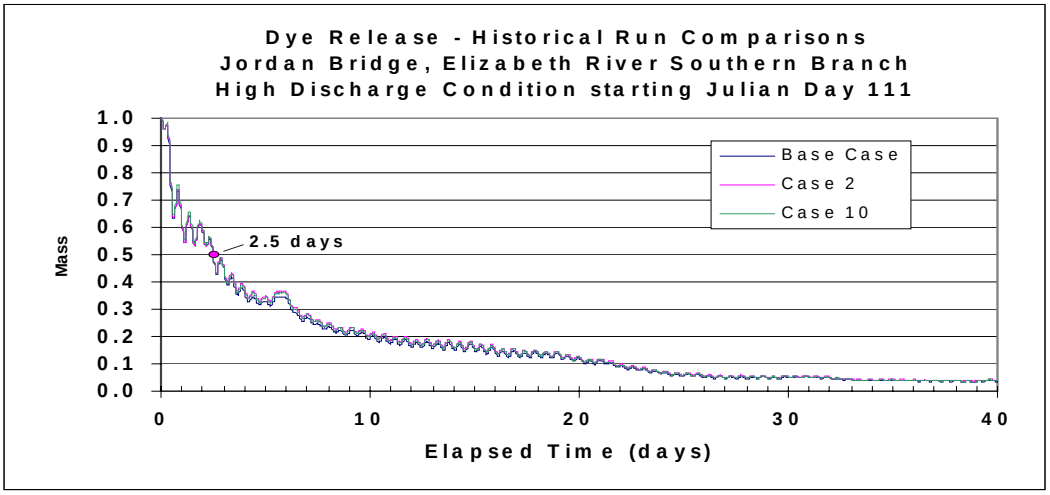

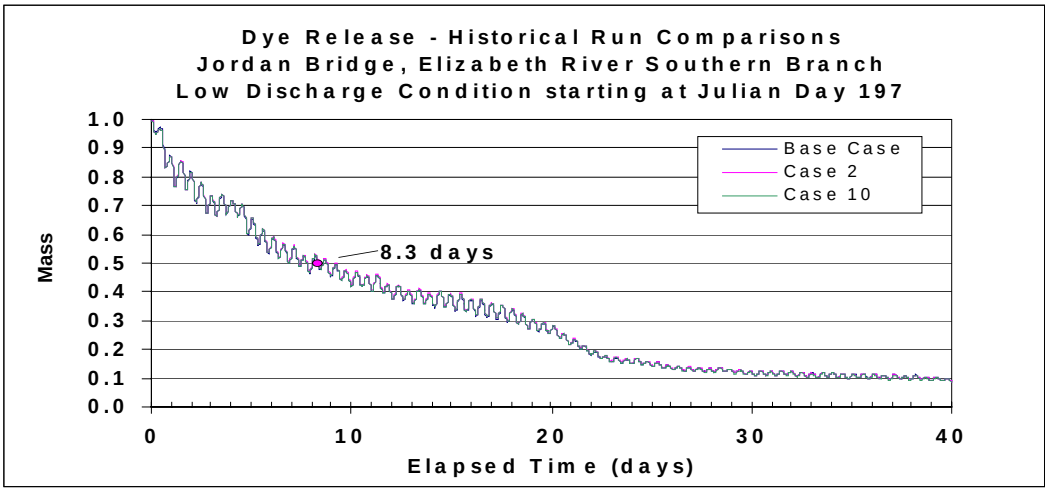

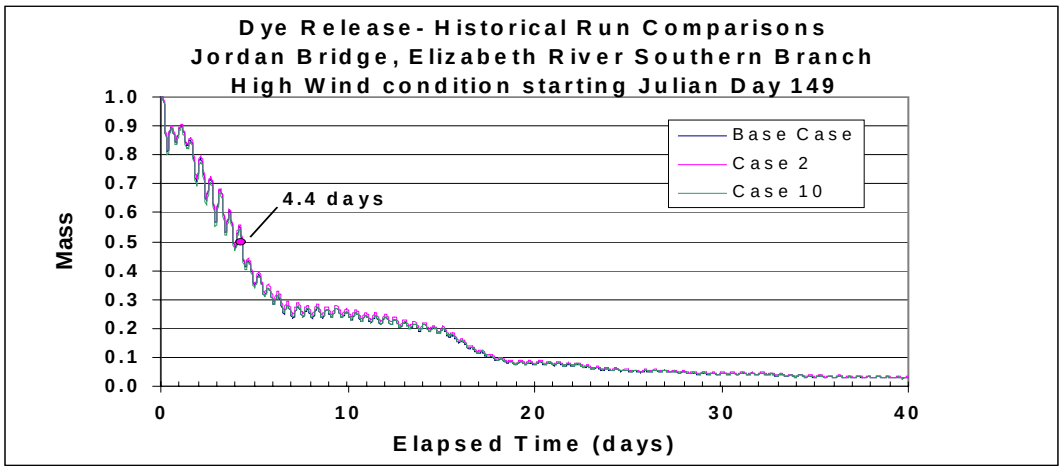

Figure VI.45. Time series of tracer mass (released near the Jordan Bridge) remaining in the Southern Branch shown for the Base Case (black), Case 2 (pink) and Case 10 (green).

Run Type	Case	Condition	Domain	Half Life
Single Var.	1	Spring-Neap	Southern Br.	6.5 days
Single Var.	2	Spring-Neap	Southern Br.	6.5 days
Historical	1	High Discharge	Southern Br.	2.5 days
Historical	2	High Discharge	Southern Br.	2.5 days
Historical	10	High Discharge	Southern Br.	2.5 days
Historical	1	Low Discharge	Southern Br.	8.3 days
Historical	2	Low Discharge	Southern Br.	8.3 days
Historical	10	Low Discharge	Southern Br.	8.3 days
Historical	1	High Wind	Southern Br.	4.4 days
Historical	2	High Wind	Southern Br.	4.4 days
Historical	10	High Wind	Southern Br.	4.4 days

Table VI.5. Summary of dye release in the Southern Branch.

2. Tracer Experiments (Release west of Craney Island)– In an attempt to address concerns about the impairment of flushing ability west of Craney Island, releases at the most confined grid cell south of the west side of Craney Island were performed for both the Base Case and for Case 10 (see Figure VI.46).

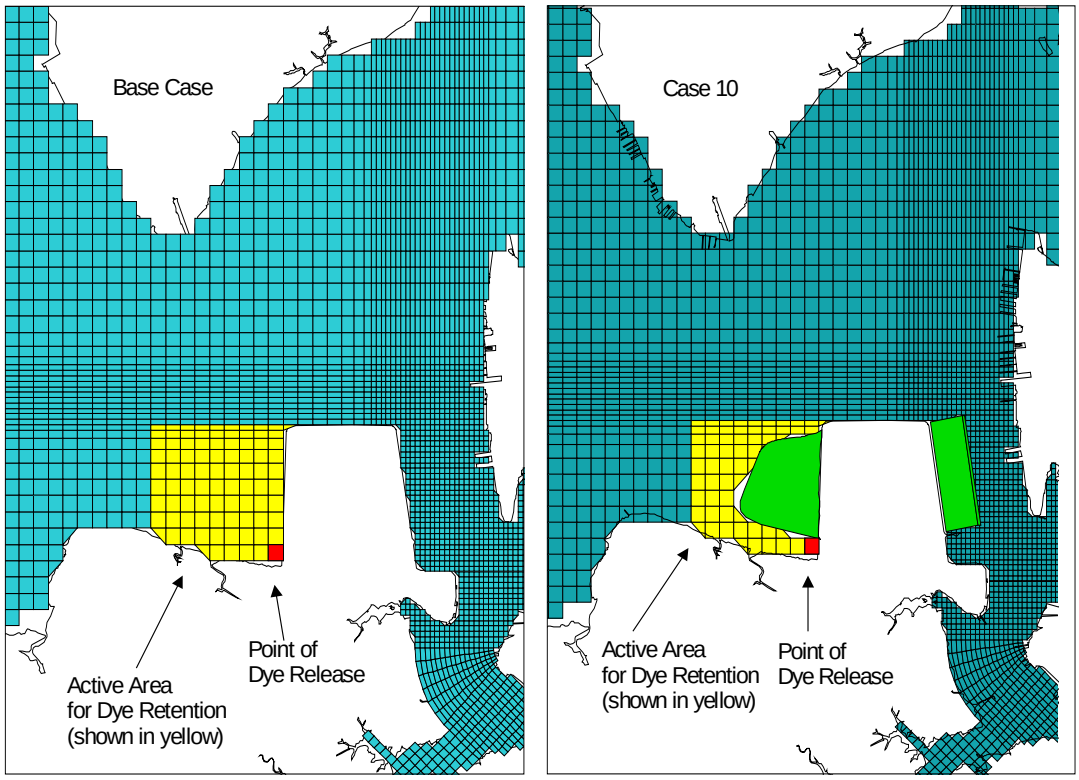

Figure VI.46. Dye test to assess flushing on the west side of Craney Island.

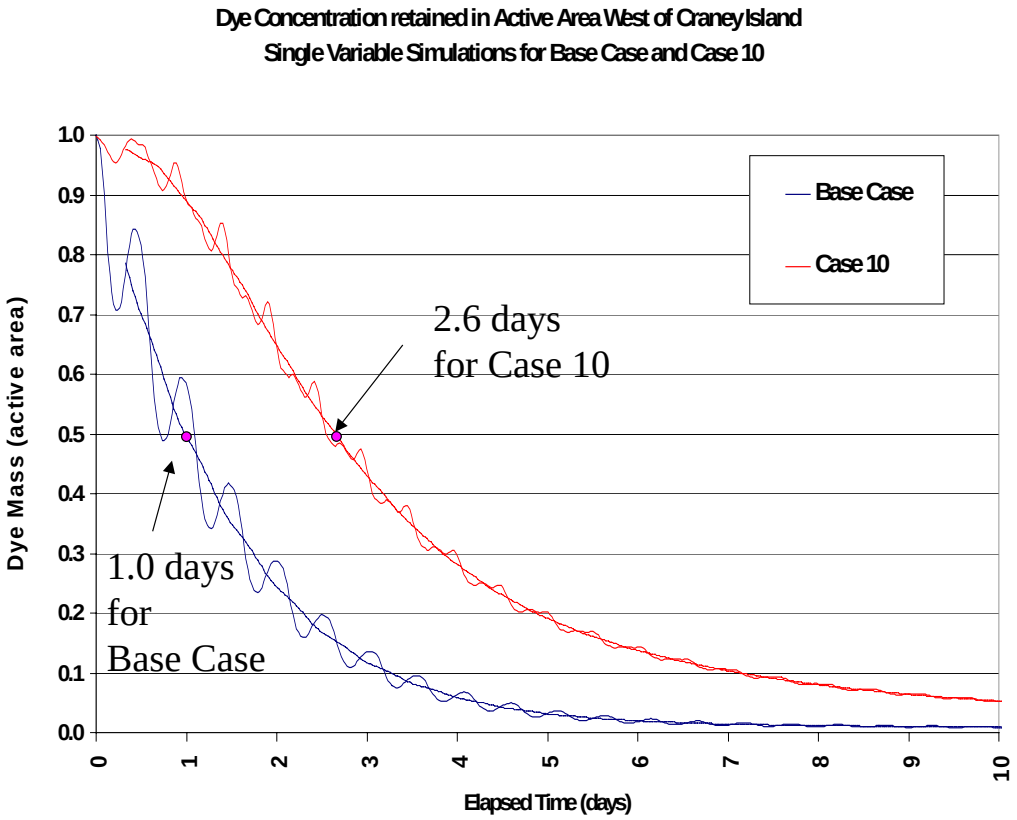

Figure VI.47. Comparison of decay rates of locally-retained dye mass for Base Case and Case 10 for a release west of Craney Island.

The total amount of dye retained in the yellow regions shown in Figure VI.46 was plotted against time for both the Base Case and Case 10 in Figure VI.47, which shows both the decay curves and a 25-hour moving average selected to smooth out tidal effects. The result showed that the half-life was increased from 1.0 days to 2.6 days due to the addition of Expansion Option 7/5a.

VII. REFERENCES

Blumberg, A. F., B. Galperin, and D. J. O'Connor (1992): Modeling vertical structure of open channel flows. Journal of Hydraulic Engineering, 118: 1119-1134.

Blumberg, A. F. and G. L. Mellor (1987): A description of a three-dimensional coastal ocean circulation model, in Three-dimensional Coastal Ocean Models, Vol. 4, edited by N. Heaps, American Geophysical Union, Washington, D. C. 208 pp.

Boon, J. D., A. Y. Kuo, H. V. Wang, and J. M. Brubaker (1999): Proposed third crossing of Hampton Roads, James River, Virginia: feature-based criteria for evaluation of model study results. In M. L. Spaulding and H. L. Butler (eds.), ASCE 6th international conference on estuarine and coastal modeling, New Orleans, LA. pp. 223-237.

Boon, J. D., H. V. Wang, S. C. Kim, A. Y. Kuo, and G. M. Sisson (1999): Three Dimensional Hydrodynamic-Sedimentation Modeling Study, Hampton Roads Crossing, Lower James River, Virginia: Report to the Virginia Department of Transportation. Special Report No. 354 in Applied Science and Ocean Engineering, Virginia Institute of Marine Science, Gloucester Point, Virginia. 36pp, 3 Appendices.

Casulli, V. and R. T. Cheng (1993): Semi-implicit finite difference methods for three-dimensional shallow water flow. Inter. J. for numerical Methods in Fluids, Vol. 15, pp 629-648.

Fang, C. S., B. J. Neilson, A. Y. Kuo, R. J. Byrne, and C. S. Welch (1972): Physical and geological studies of the proposed bridge-tunnel crossing of Hampton Roads near Craney Island. Special Report in Applied Marine Science and Ocean Engineering No. 24, Virginia Institute of Marine Science, Gloucester Point, VA, pp. 199-241.

Galperin, B., L. H. Kantha, D. Hassid, and A. Rosati (1988): A quasi-equilibrium turbulent energy model for geophysical flow. Journal of Atmospheric Science, 45: 55-62.

Hamrick, J. M. (1996): User's manual for the environmental fluid dynamics computer code. Special report in Applied Marine Science and Ocean Engineering No. 331, Virginia Institute of Marine Science, Gloucester Point, VA, 223 pp.

Johnson, B. H., K. W. Kim, R. E. Heath, B. B. Hsieh, and H. L. Butler (1993): Validation of a three-dimensional hydrodynamic model of Chesapeake Bay. Journal of Hydraulic Engineering, 119: 2-20.

Kuo, A. Y., R. J. Byrne, J. M. Brubaker, and J. H. Posenau (1988): Vertical transport across an estuary front. In J. Dronkers and W. van Leussen (eds.), Physical Processes in Estuaries, Springer-Verlag, Berlin, pp. 93-109.

Kuo, A. Y., R. J. Byrne, P. V. Hyer, E. P. Ruzecki, and J. M. Brubaker (1990): Practical Application of Theory for Tidal-Intrusion Fronts. Journal of Waterway, Port, Coastal, and Ocean Engineering, 116(3): 341-361.

Maa, J. P-Y, C. H. Lee, F. J. Chen (1995): VIMS sea carousel: bed shear stress measurements. Marine Geology, 129: 129-136.

Miller, J. L. and A. Valle-Levinson (1996): The effect of bridge piles on stratification in the lower Chesapeake Bay. Estuaries, vol. 19, no. 3, pp. 526-539.

Neilson, B. J. (1975): A water quality study of the Elizabeth River: the effect of the Army Base and Lambert Point STP effluent. Special Report No. 75 in Applied Marine Science and Ocean Engineering, Virginia Institute of Marine Science, Gloucester Point, Virginia. 133 pp.

Nichols, M.M. (1977): Response and recovery of an estuary following a river flood. Journal of Sediment Petrol., vol. 47, pp. 1171-1186.

Oey, L. –Y., G. Mellor, and R. Hires (1985): Three-dimensional simulation of the Hudson-Raritan estuary. Part III: salt flux analyses. Journal of Physical Oceanography 14: 629-645.

Ruzecki, E. P., and W. J. Hargis, Jr. (1988): Interaction between circulation of the estuary of the James River and transport of oyster larvae, In B. J. Neilson, A. Y. Kuo and J. M. Brubaker (eds.), Estuarine Circulation. The Humana Press, Clifton, N. J., pp. 255-278.

Shen, J., J. D. Boon, and A. Y. Kuo (1999): A modeling study of a tidal intrusion front and its impact on larval dispersion in the James River estuary, Virginia. Estuaries 22(3a):681-692.

Shen, J., and A. Y. Kuo (1999): Numerical investigation of an estuarine front and its associated eddy. Journal of Waterway, Port, Coastal, and Ocean Engineering 125(3):127-135.

Sisson, G. M., J. D. Boon, and K. L. Farnsworth (1999): The use of GIS in 3D Hydrodynamic model pre- and post-processing for feature-specific applications. In M. L. Spaulding and H. L. Butler (eds.), ASCE 6th international conference on estuarine and coastal modeling, New Orleans, LA, pp. 538-548.

Stigebrandt, A. (1992): Bridge-induced flow reduction in sea straits with reference to effects of a planned bridge across Öresund, Ambio 21:130-134.

Wang, H. V. and S.-C. Kim (2000): Simulation of Tunnel Island and Bridge Piling Effects in a Tidal Estuary. Estuarine and coastal modeling, proceedings of the 6th International Conference, edited by M. L. Spaulding and H. L. Butler. pp. 250-269.

APPENDIX to CHAPTER III, SECTION-D.1

Slack Water Surveys

Salinity distributions over depth and distance upstream

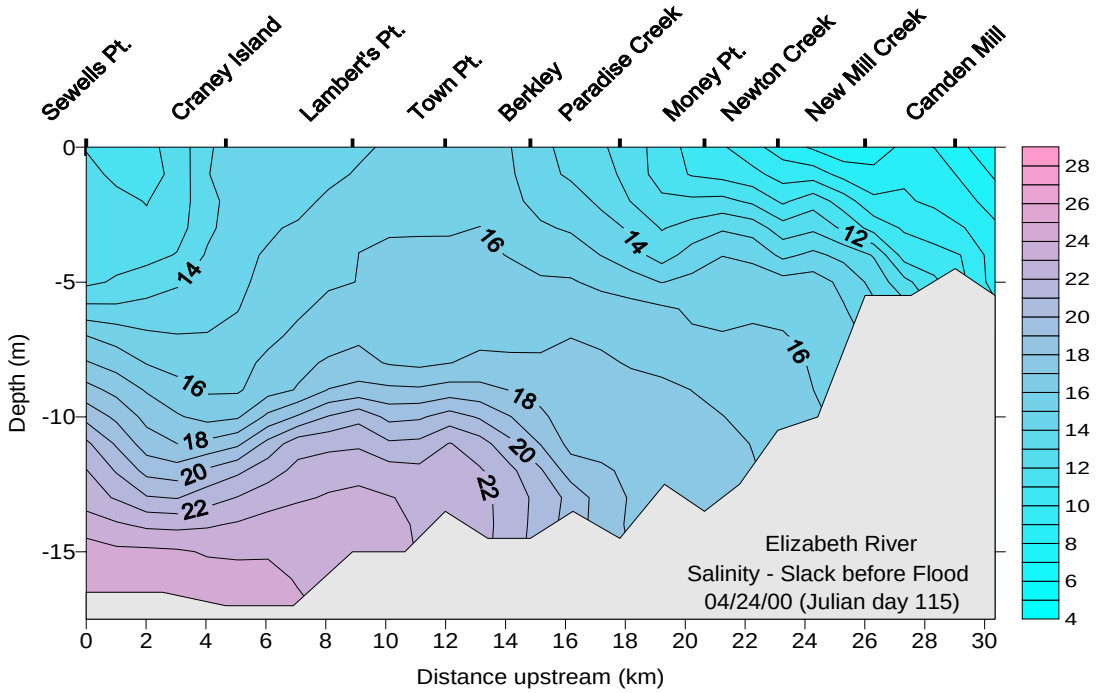

Figure 1. Salinity distribution (ppt) in the Elizabeth River on April 24, 2000.

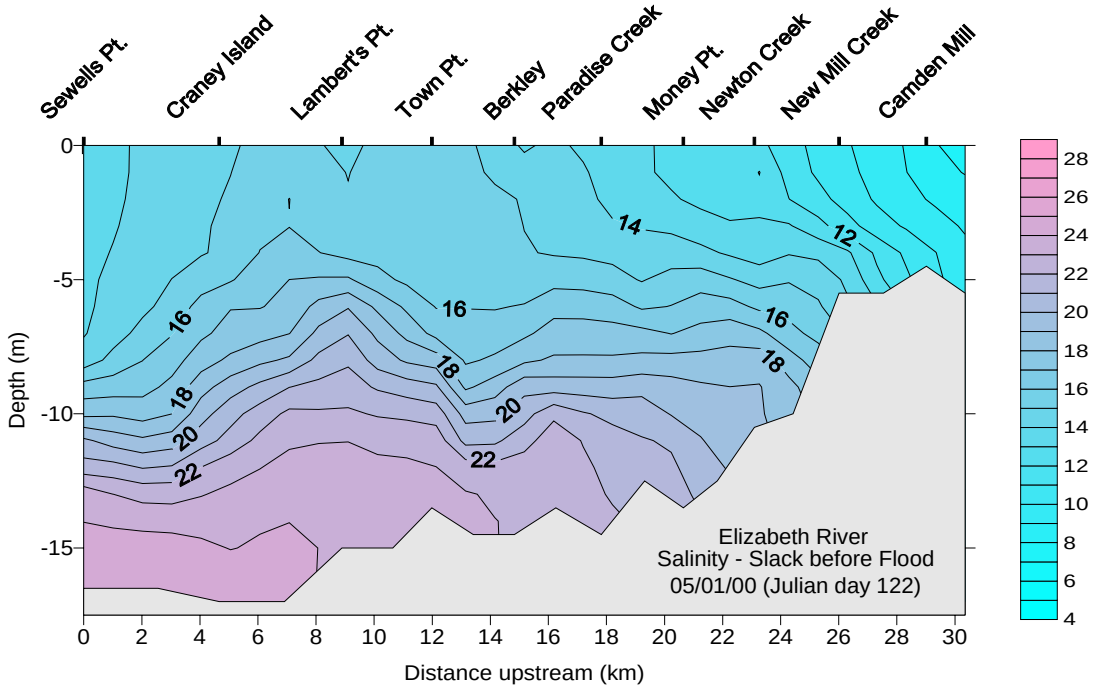

Figure 2. Salinity distribution (ppt) in the Elizabeth River on May 1, 2000.

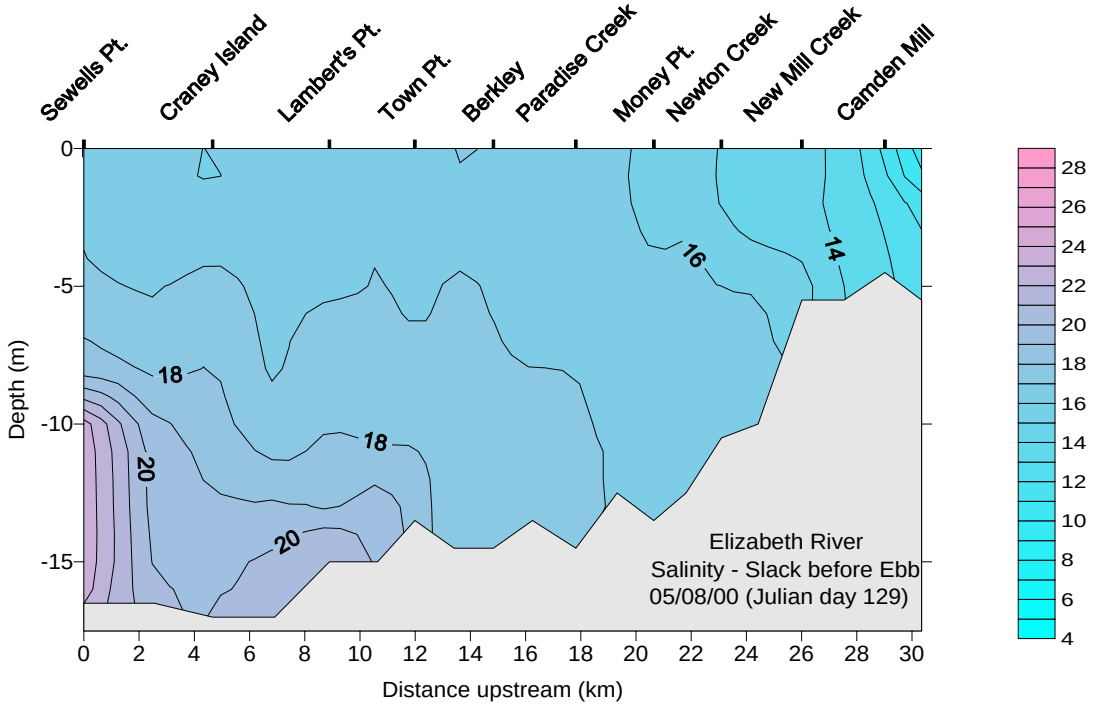

Figure 3. Salinity distribution (ppt) in the Elizabeth River on May 8, 2000.

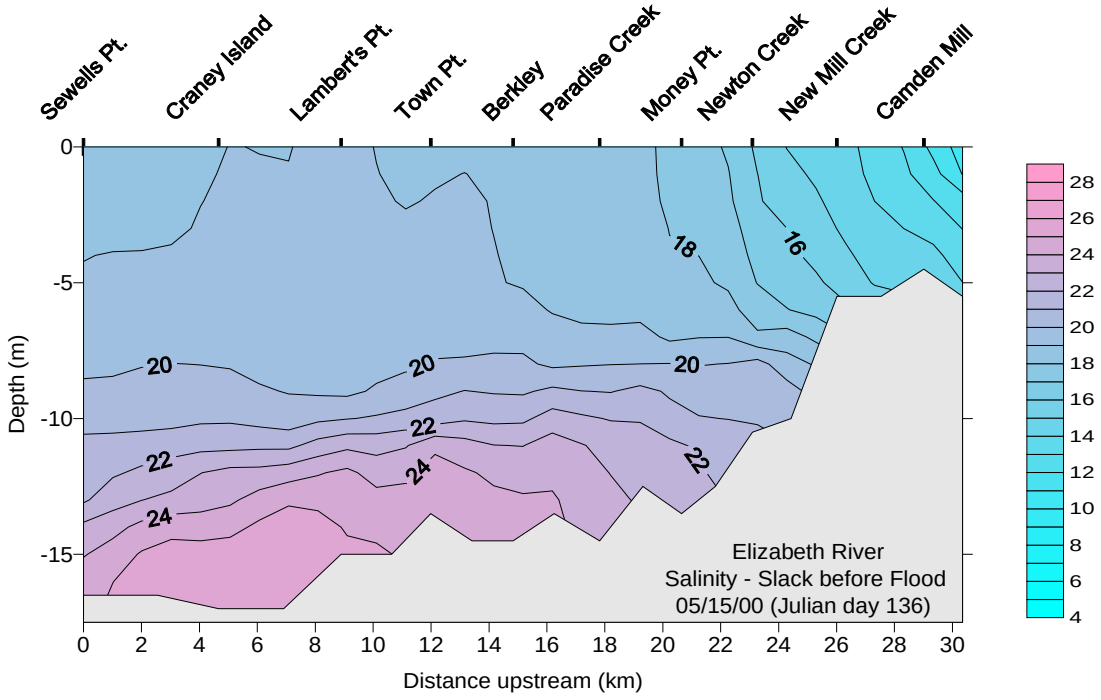

Figure 4. Salinity distribution (ppt) in the Elizabeth River on May 15, 2000.

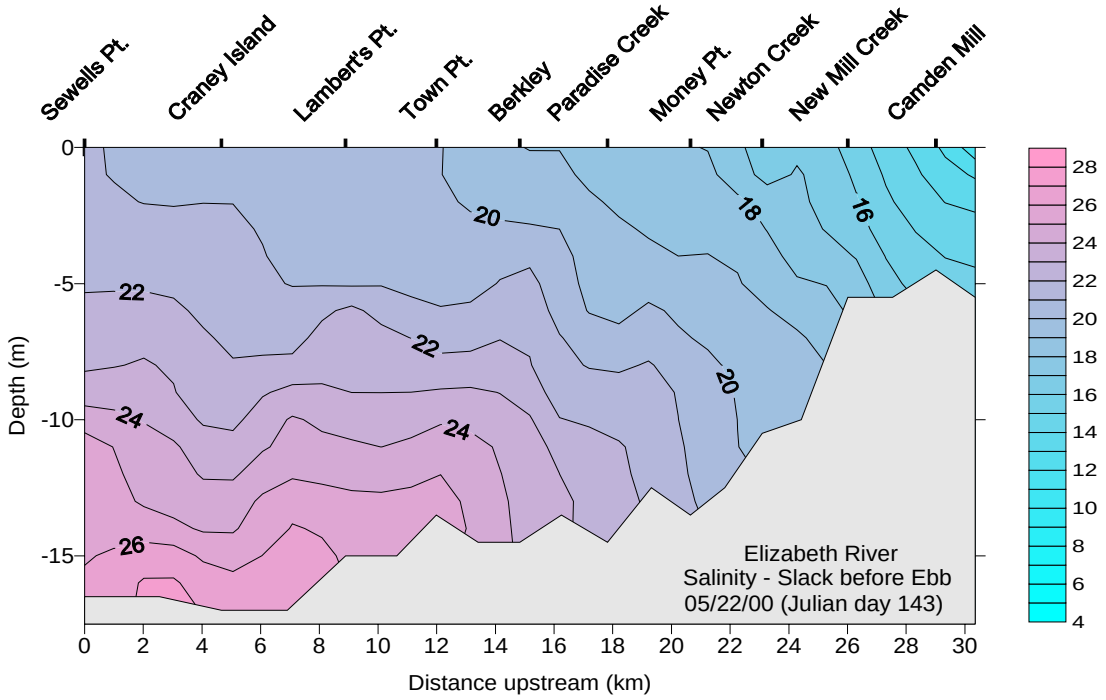

Figure 5. Salinity distribution (ppt) in the Elizabeth River on May 22, 2000.

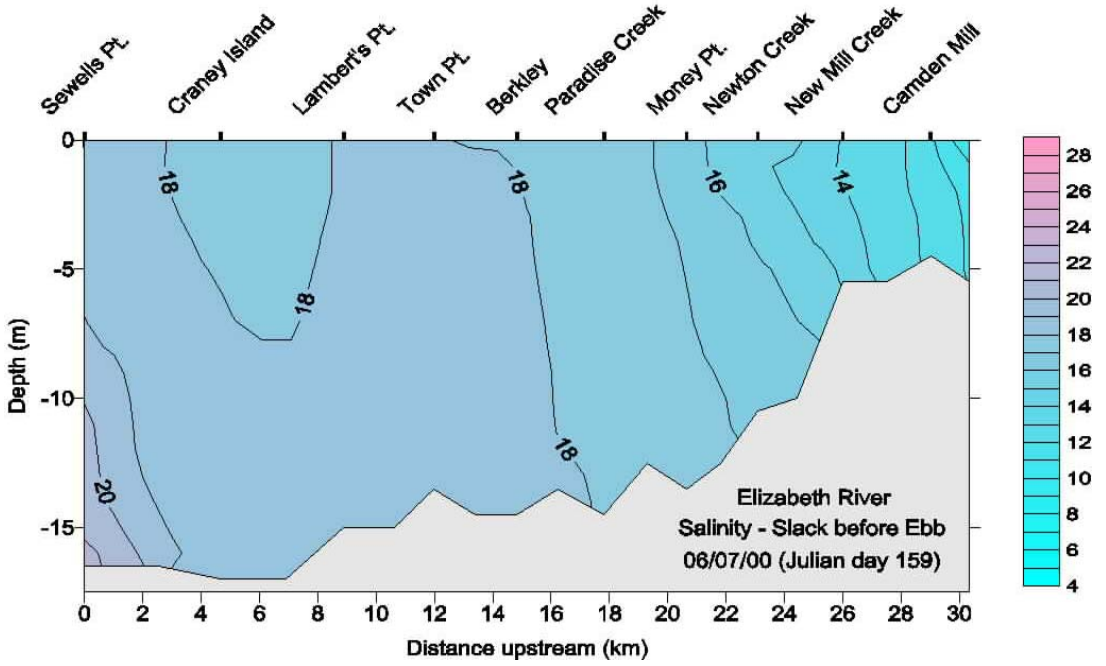

Figure 6. Salinity distribution (ppt) in the Elizabeth River on June 7, 2000.

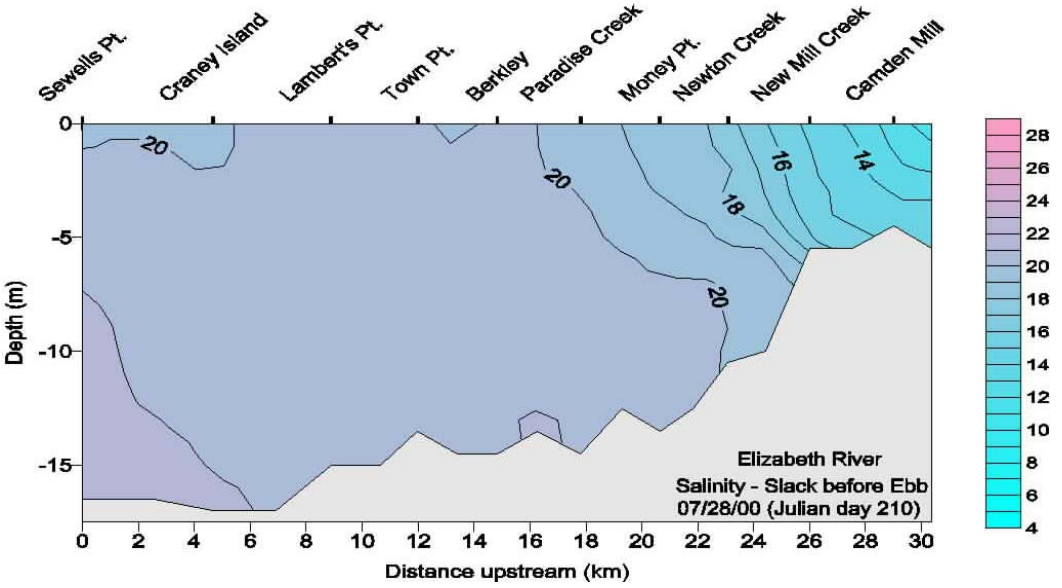

Figure 7. Salinity distribution (ppt) in the Elizabeth River on July 28, 2000.

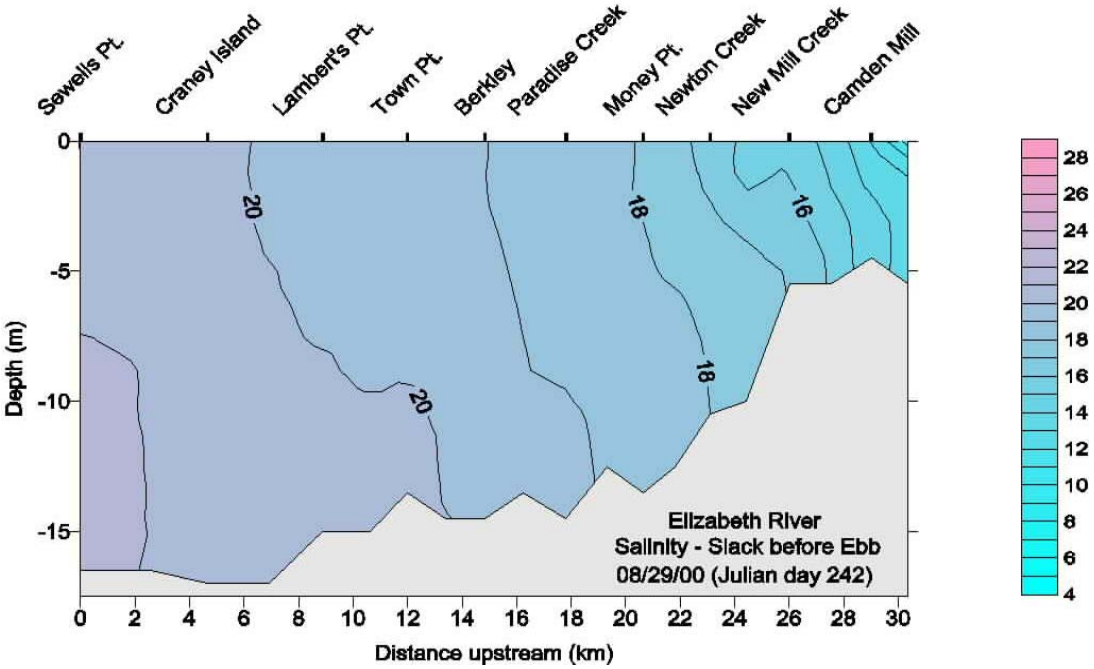

Figure 8. Salinity distribution (ppt) in the Elizabeth River on August 29, 2000.

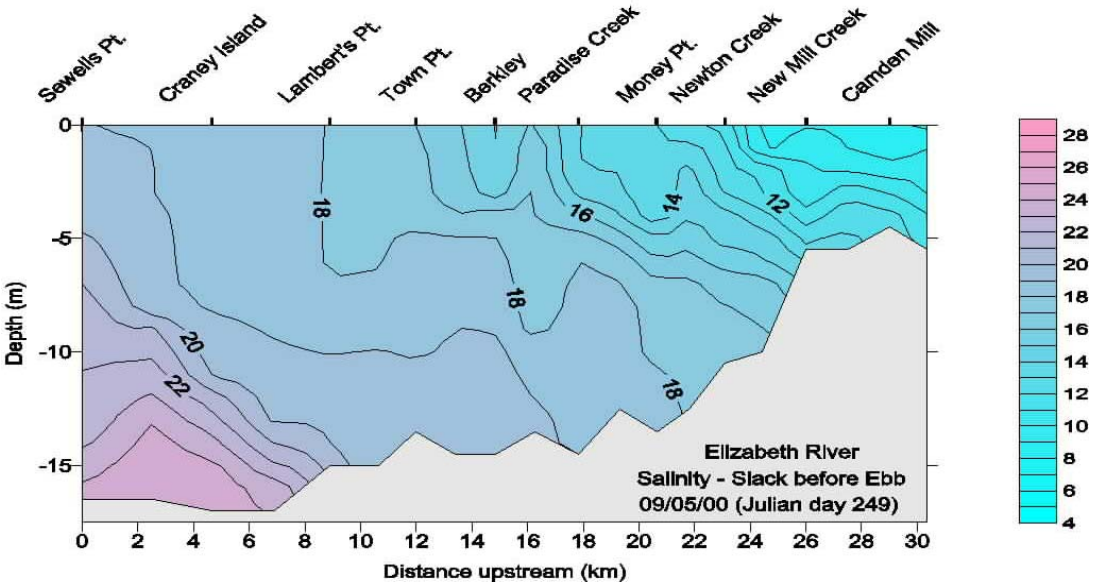

Figure 9. Salinity distribution (ppt) in the Elizabeth River on September 5, 2000.

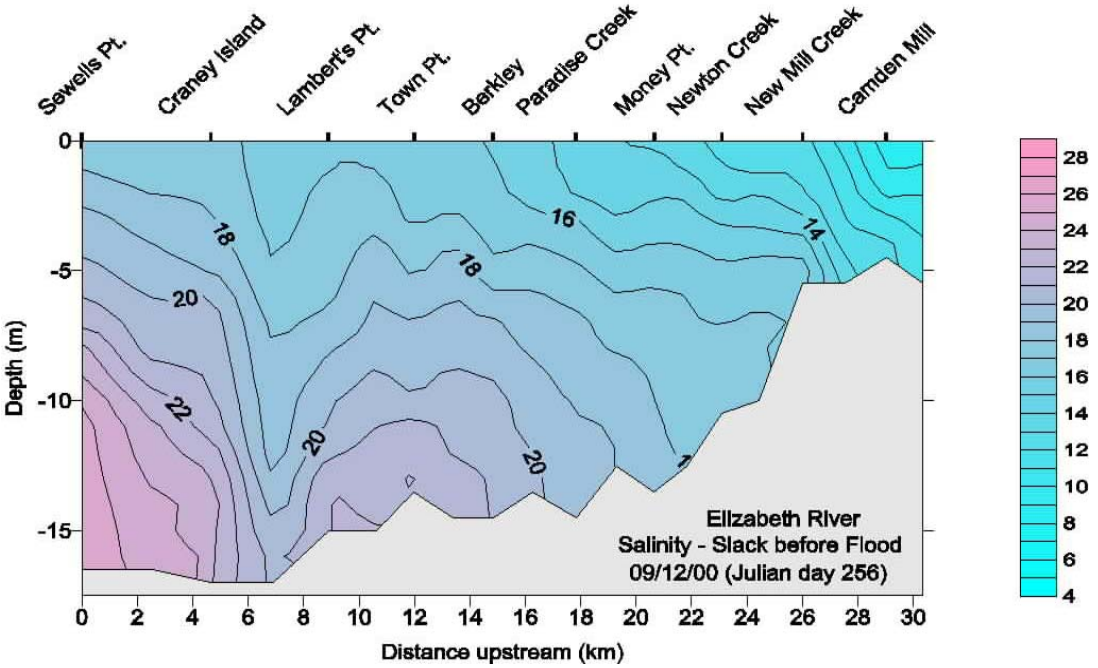

Figure 10. Salinity distribution (ppt) in the Elizabeth River on September 12, 2000.

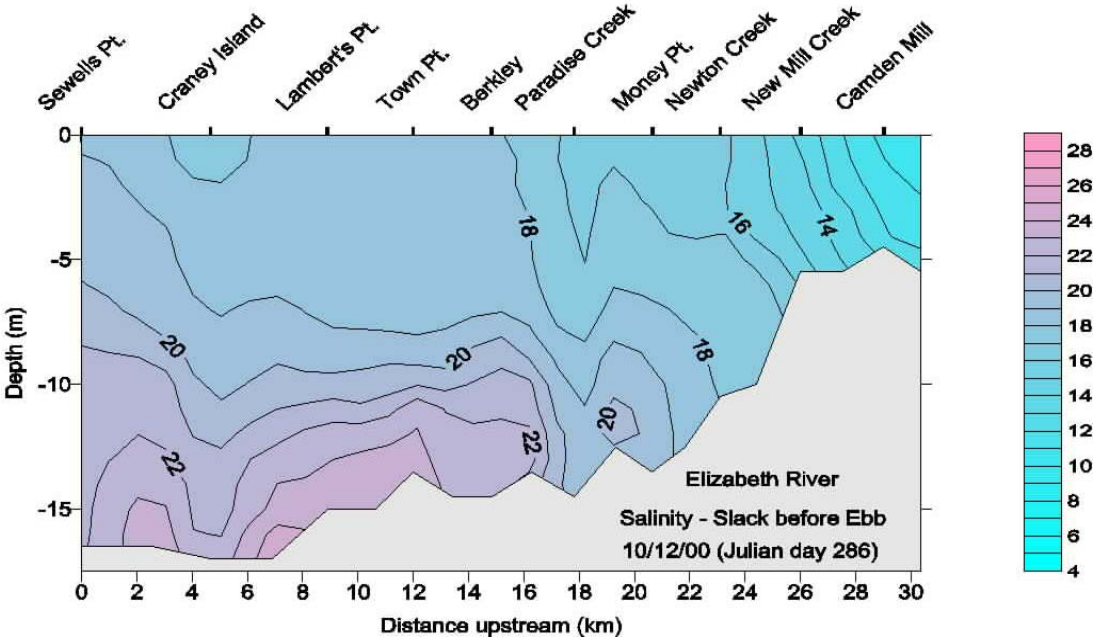

Figure 11. Salinity distribution (ppt) in the Elizabeth River on October 12, 2000.

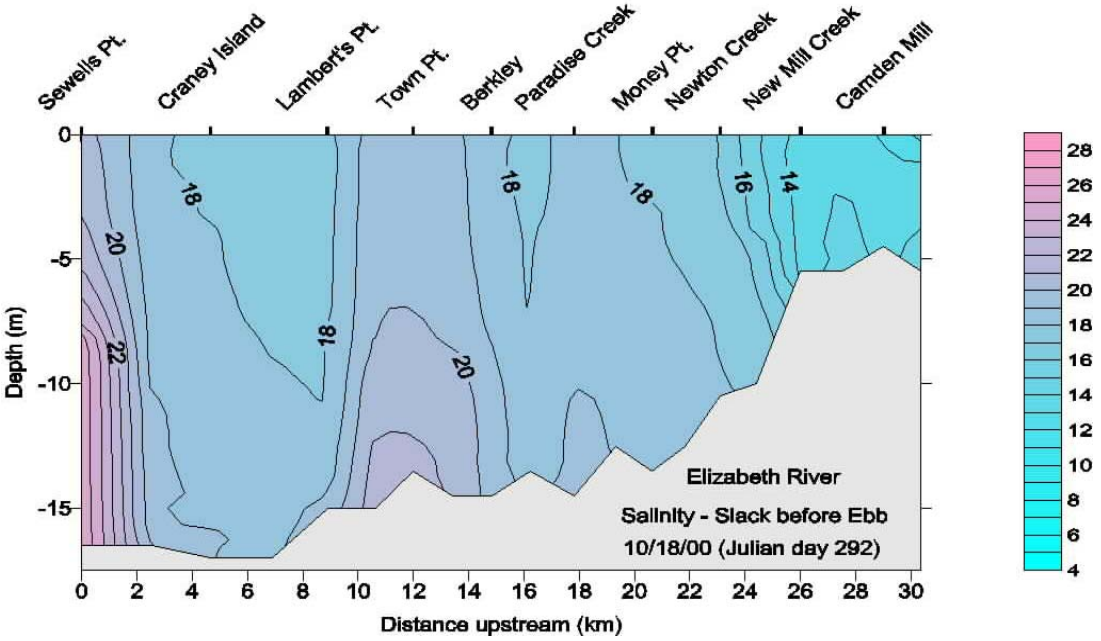

Figure 12. Salinity distribution (ppt) in the Elizabeth River on October 18, 2000.

APPENDIX to CHAPTER III, SECTION D.2

Slack Water Surveys

Temperature distributions over depth and distance upstream

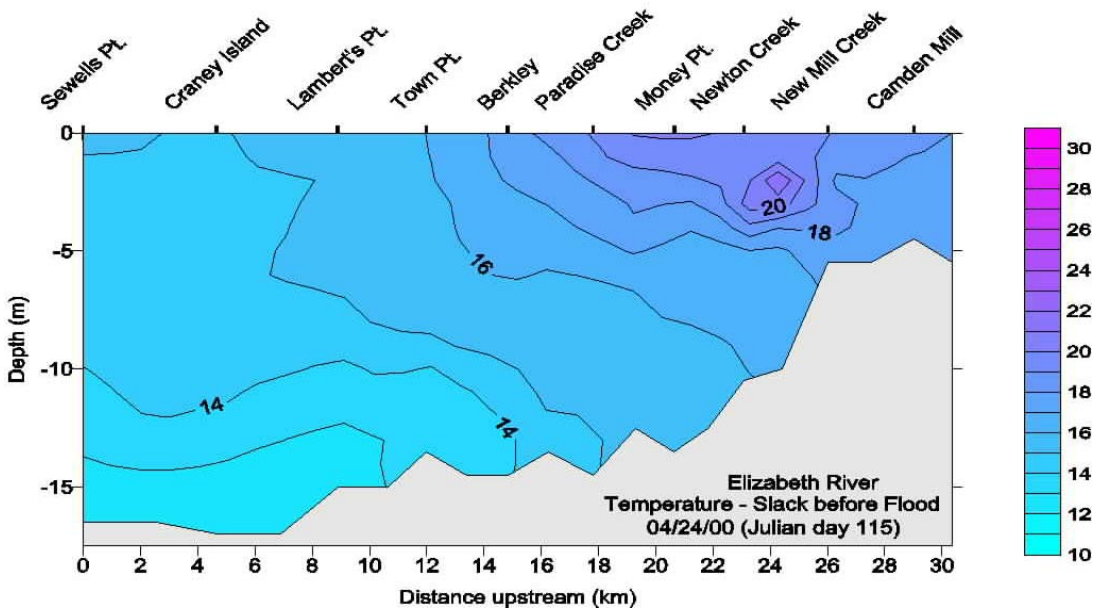

Figure 1. Temperature distribution (degrees C) in the Elizabeth River on April 24, 2000.

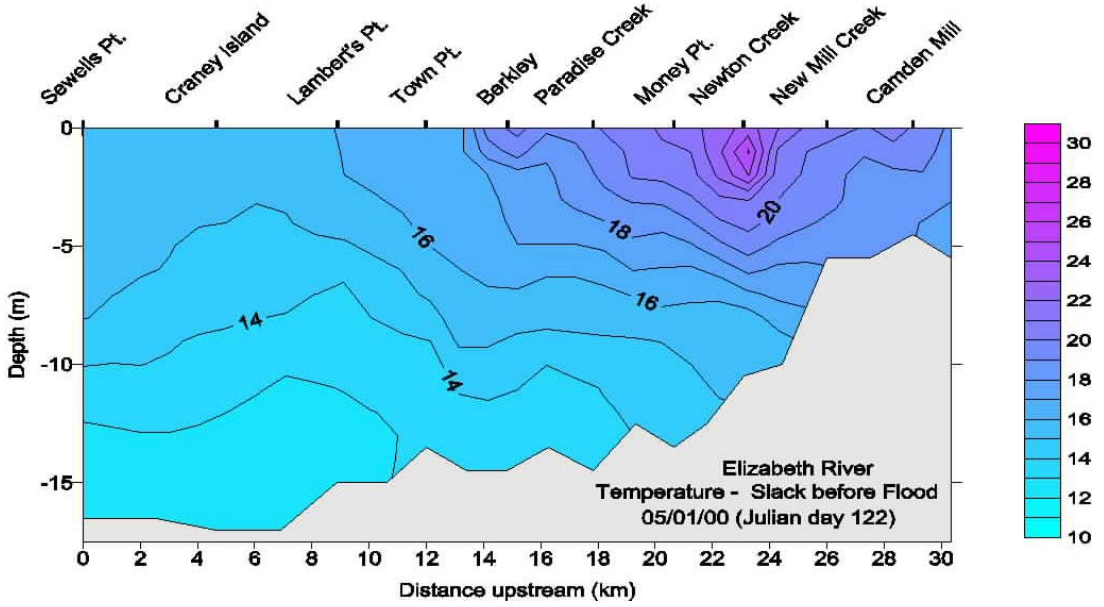

Figure 2. Temperature distribution (degrees C) in the Elizabeth River on May 1, 2000.

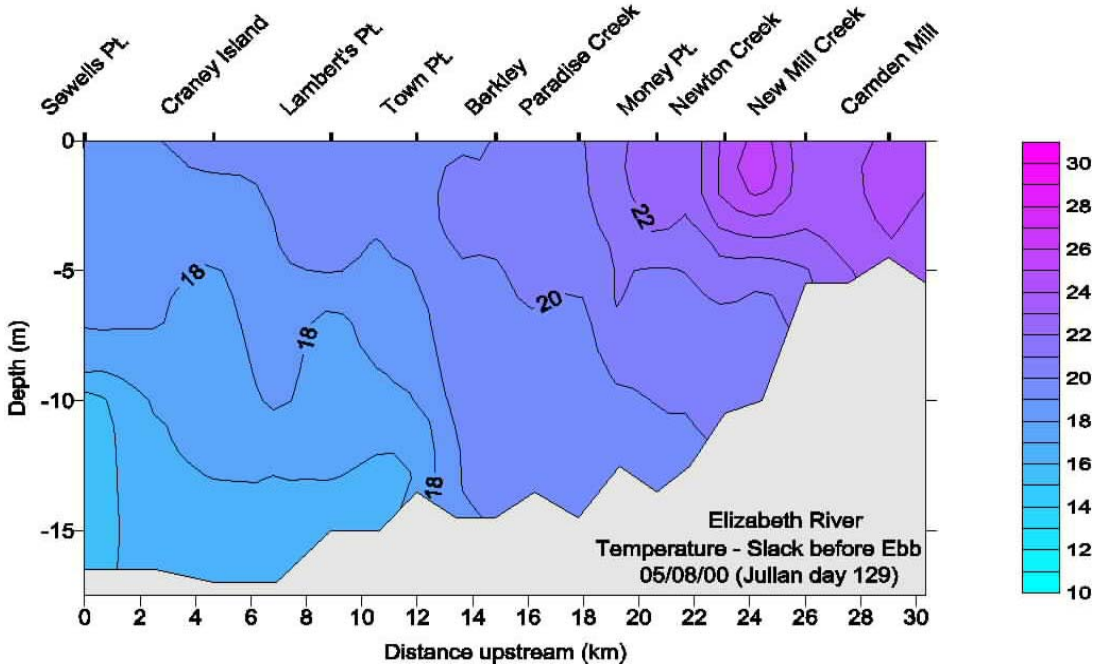

Figure 3. Temperature distribution (degrees C) in the Elizabeth River on May 8, 2000.

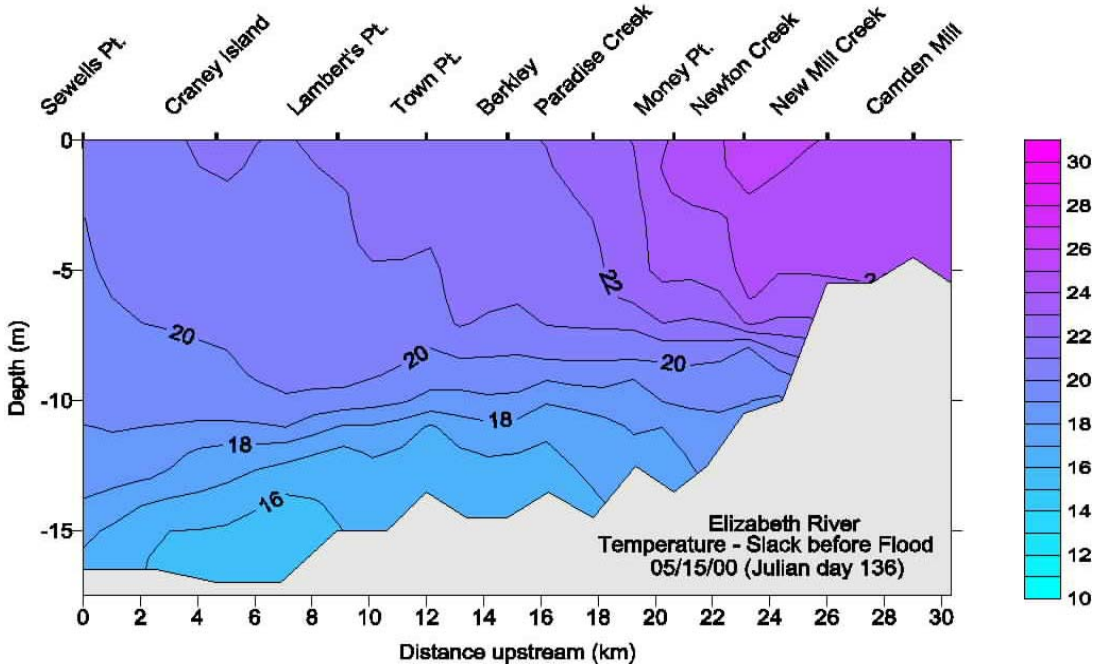

Figure 4. Temperature distribution (degrees C) in the Elizabeth River on May 15, 2000.

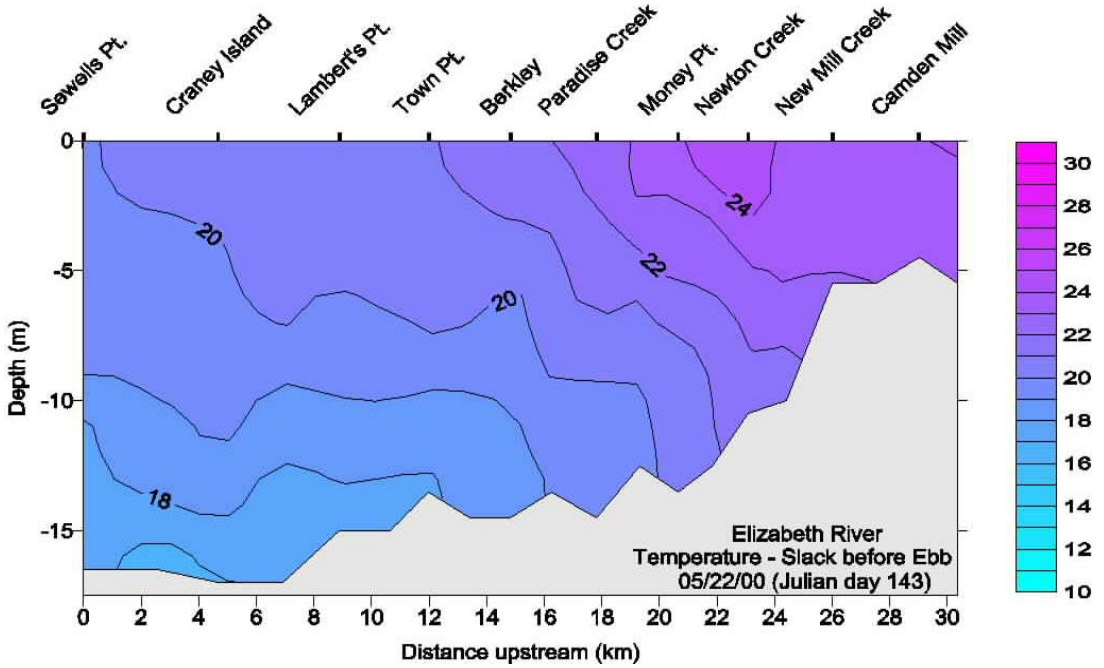

Figure 5. Temperature distribution (degrees C) in the Elizabeth River on May 22, 2000.

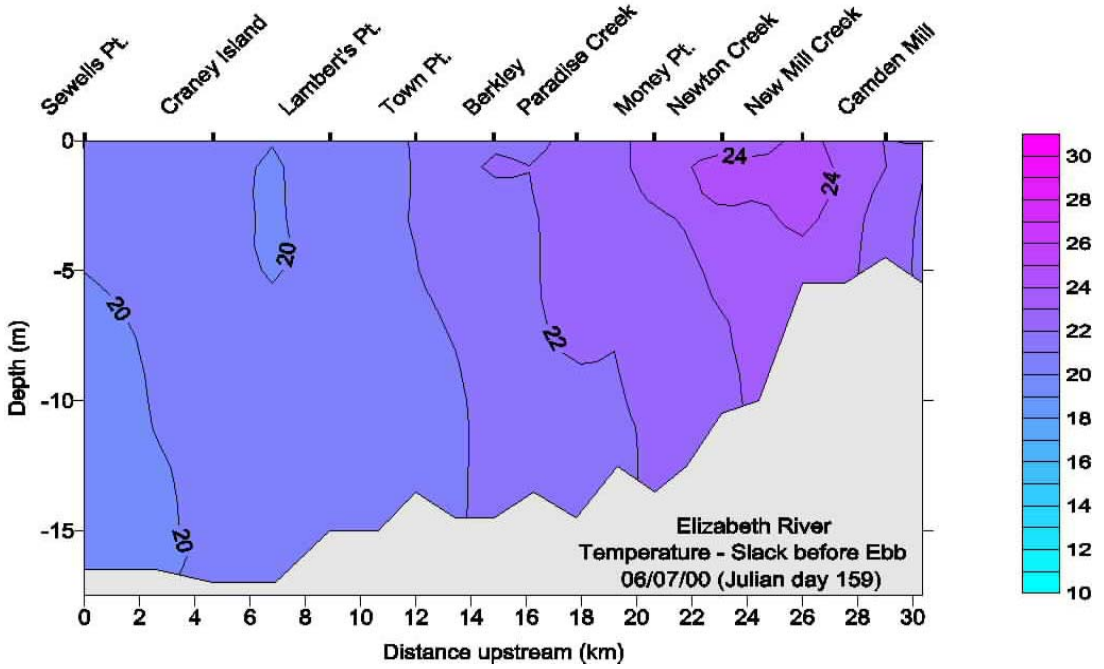

Figure 6. Temperature distribution (degrees C) in the Elizabeth River on June 7, 2000.

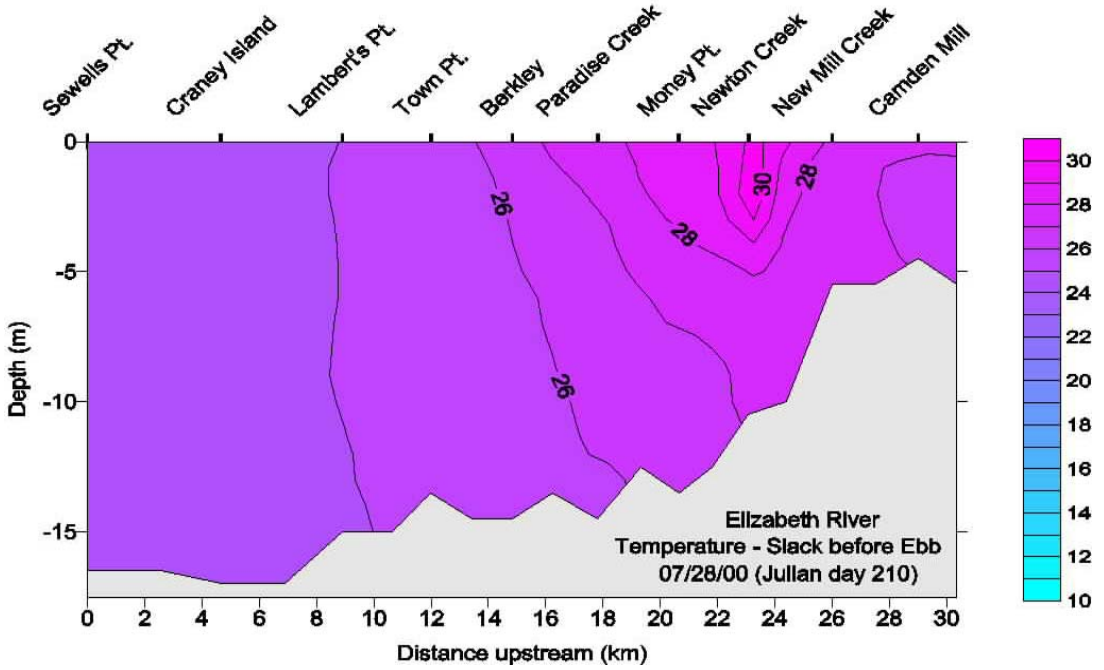

Figure 7. Temperature distribution (degrees C) in the Elizabeth River on July 28, 2000.

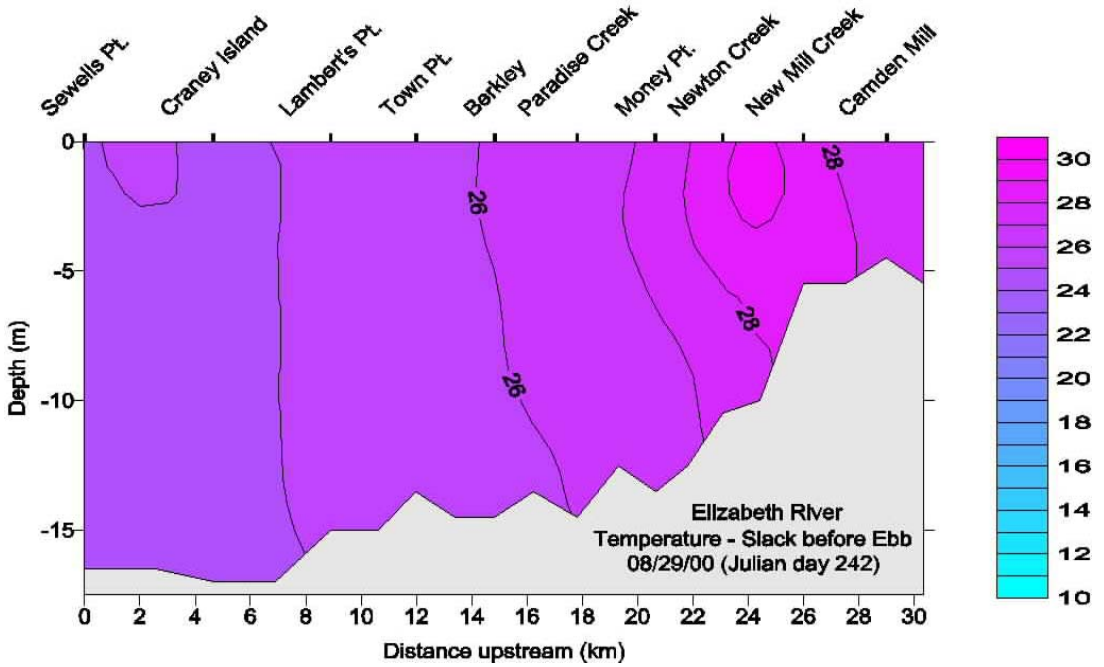

Figure 8. Temperature distribution (degrees C) in the Elizabeth on August 29, 2000.

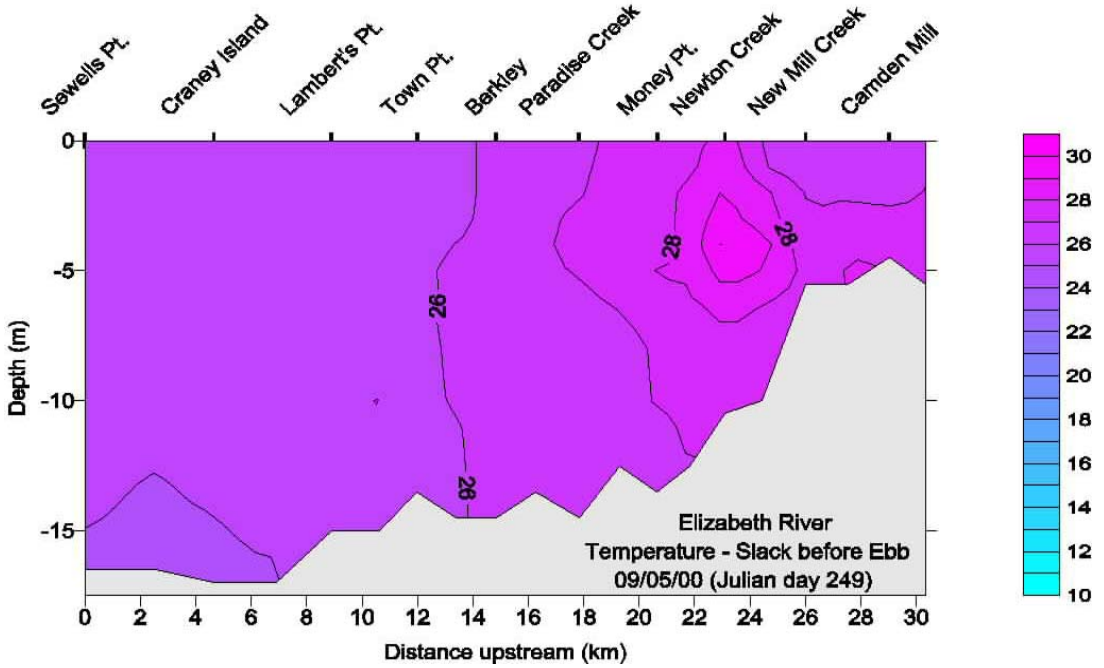

Figure 9. Temperature distribution (degrees C) in the Elizabeth on September 5, 2000.

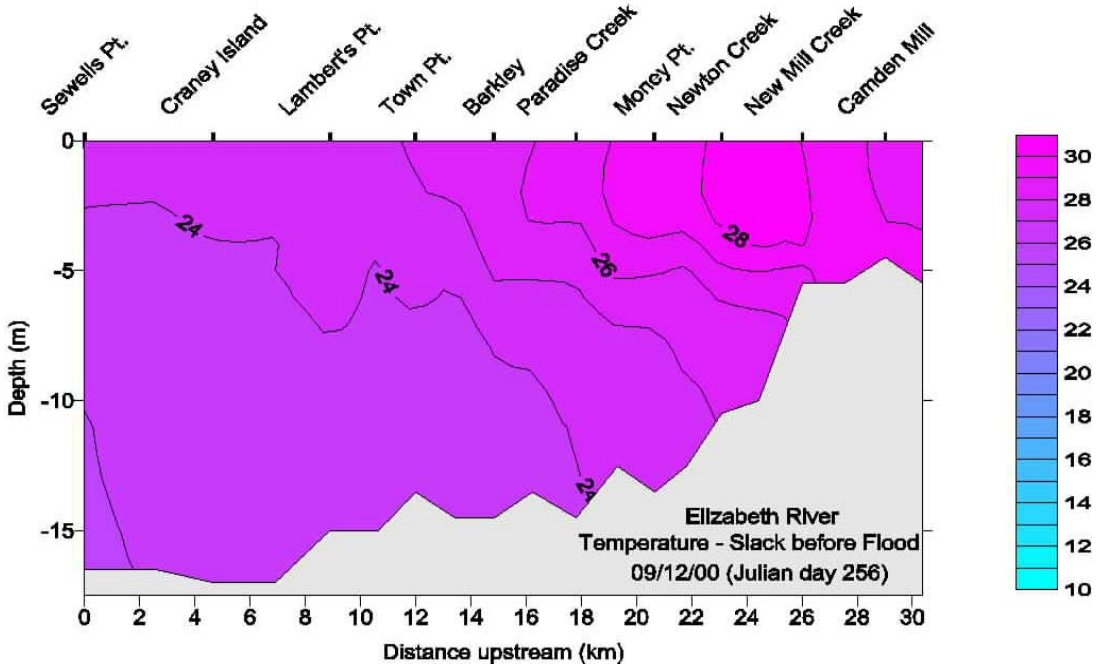

Figure 10. Temperature distribution (degrees C) in the Elizabeth on September 12, 2000.

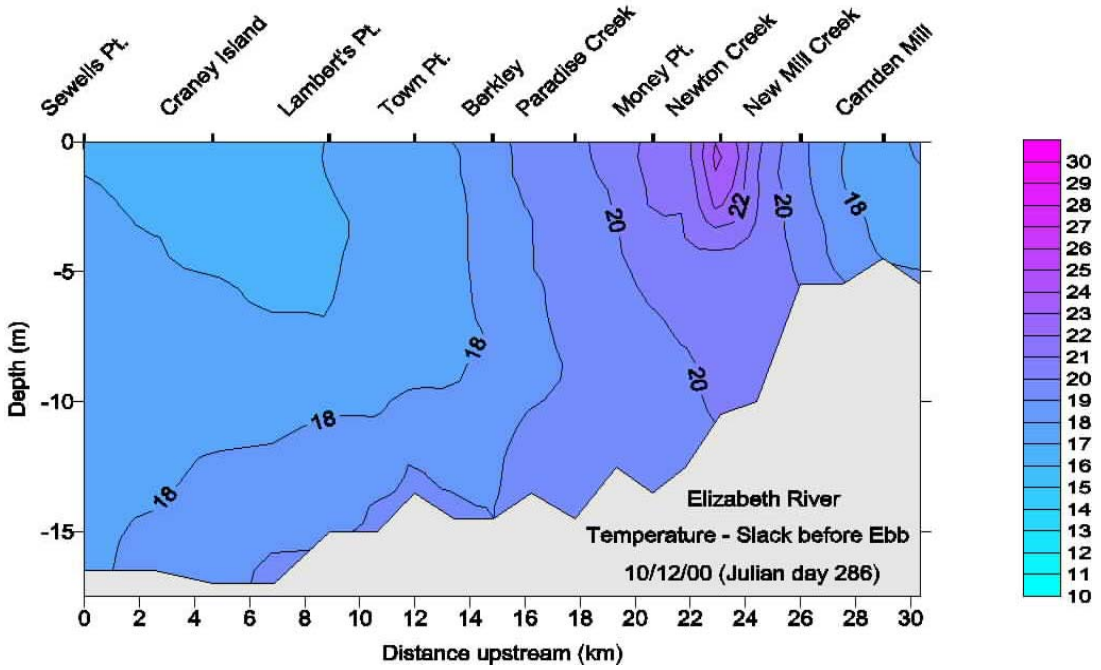

Figure 11. Temperature distribution (degrees C) in the Elizabeth on October 12, 2000.

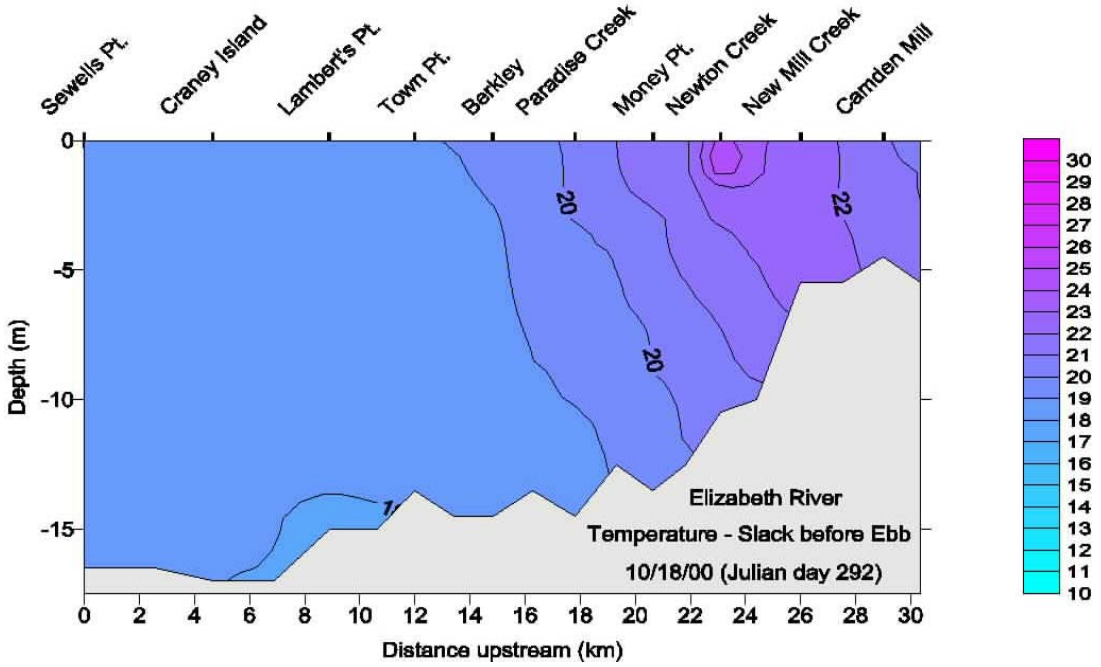

Figure 12. Temperature distribution (degrees C) in the Elizabeth on October 18, 2000.

APPENDIX to CHAPTER IV, SECTION B.1

Observed versus Predicted Time Series of Tides

Sewells Pt., Fort Norfolk, Eastern Branch, Money Pt and Great Bridge

Julian Day 112-127, 2000

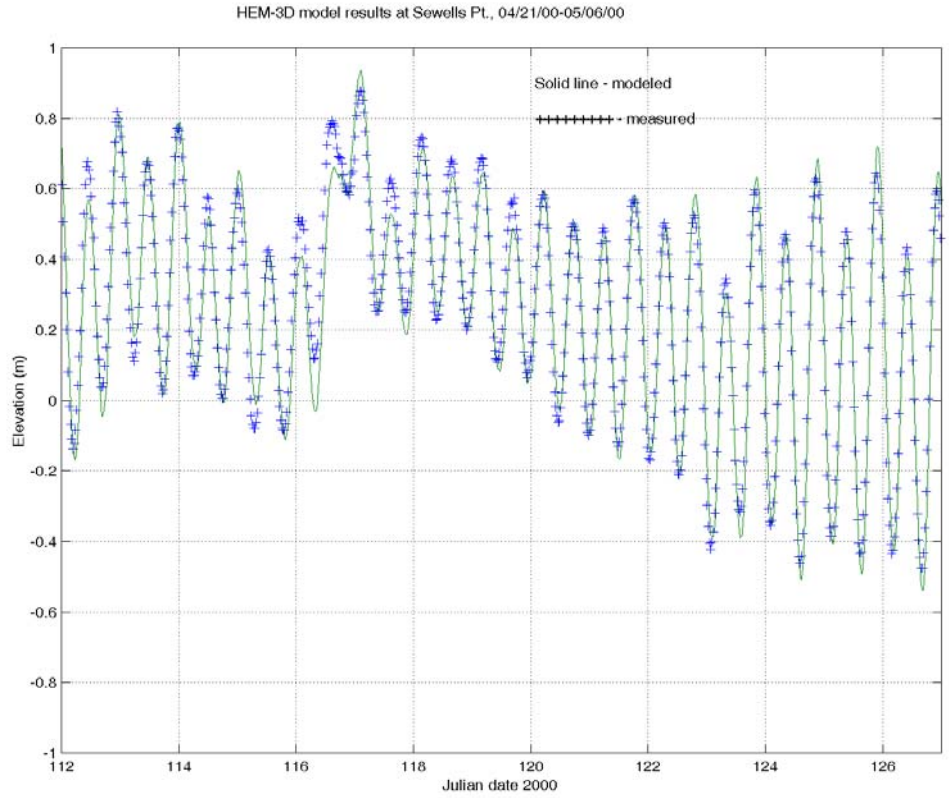

Figure 1. Observed versus predicted tide at Sewells Point.

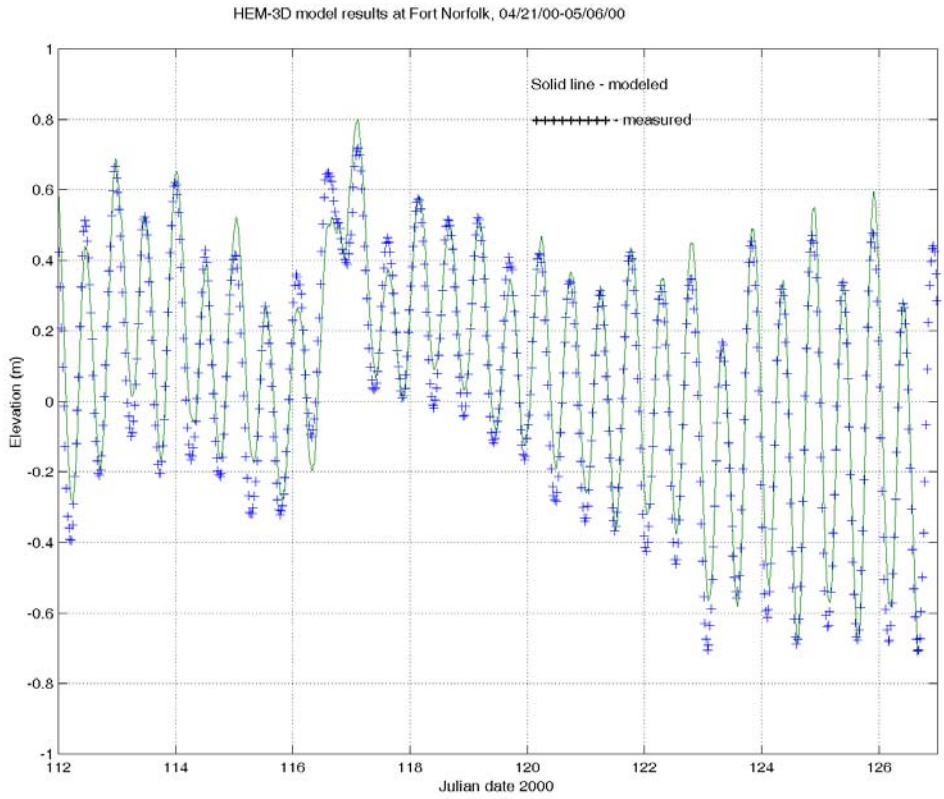

Figure 2. Observed versus predicted tide at Fort Norfolk.

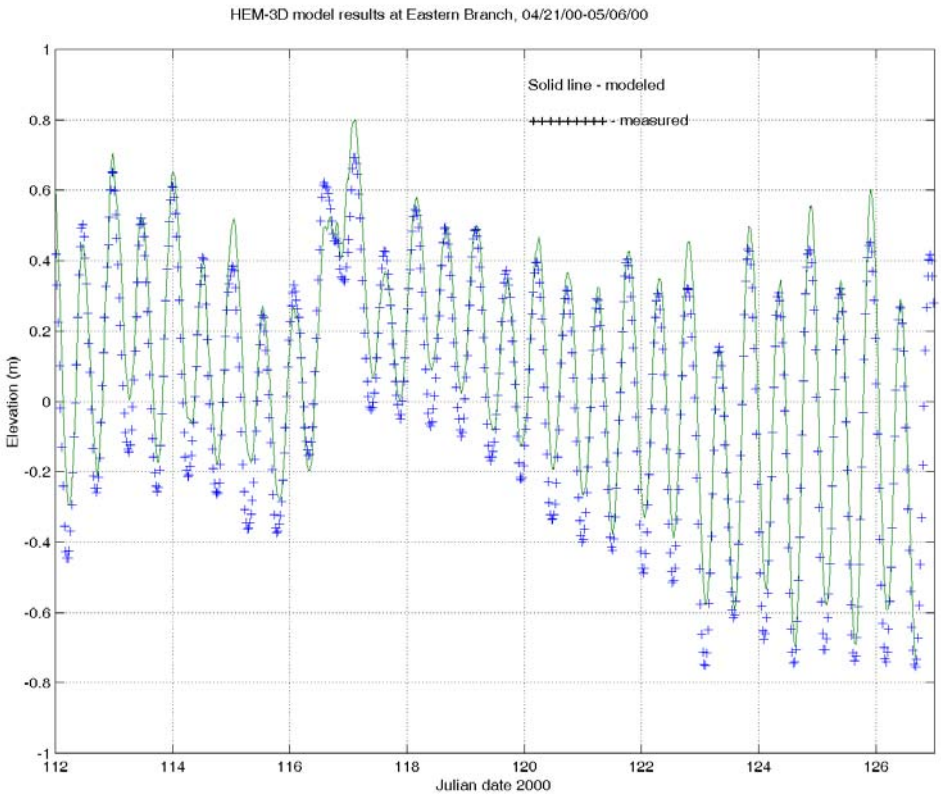

Figure 3. Observed versus predicted tide at Eastern Branch.

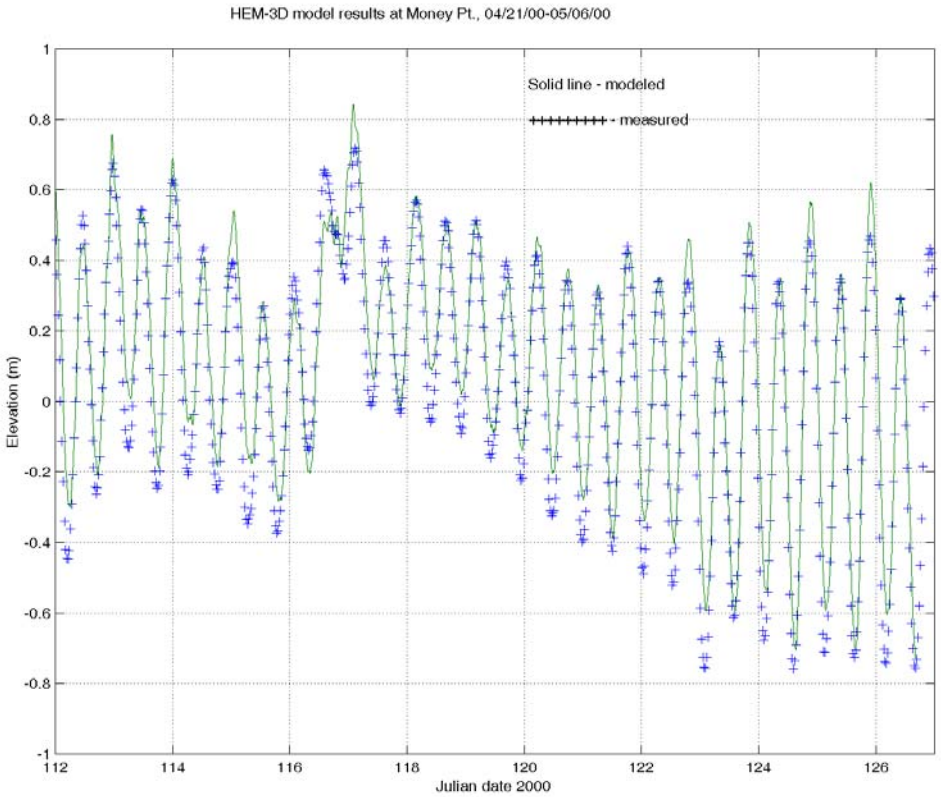

Figure 4. Observed versus predicted tide at Money Point.

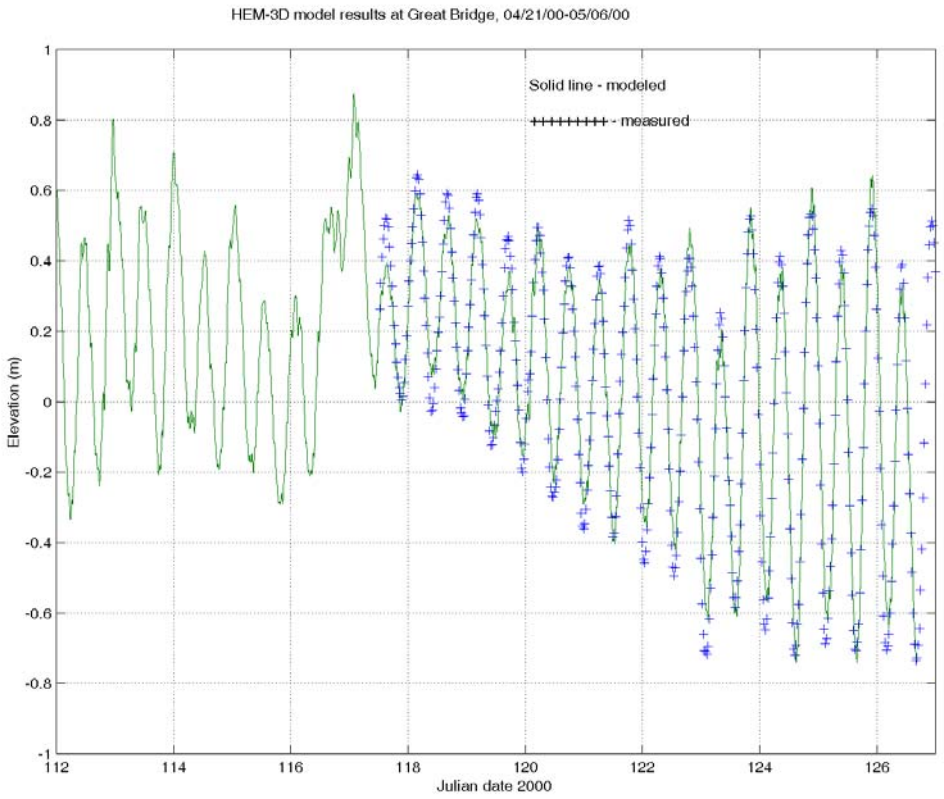

Figure 5. Observed versus predicted tide at Great Bridge.

APPENDIX to CHAPTER V, SECTION A.1

Global Comparisons of Single Variable Runs

Spatial Distributions

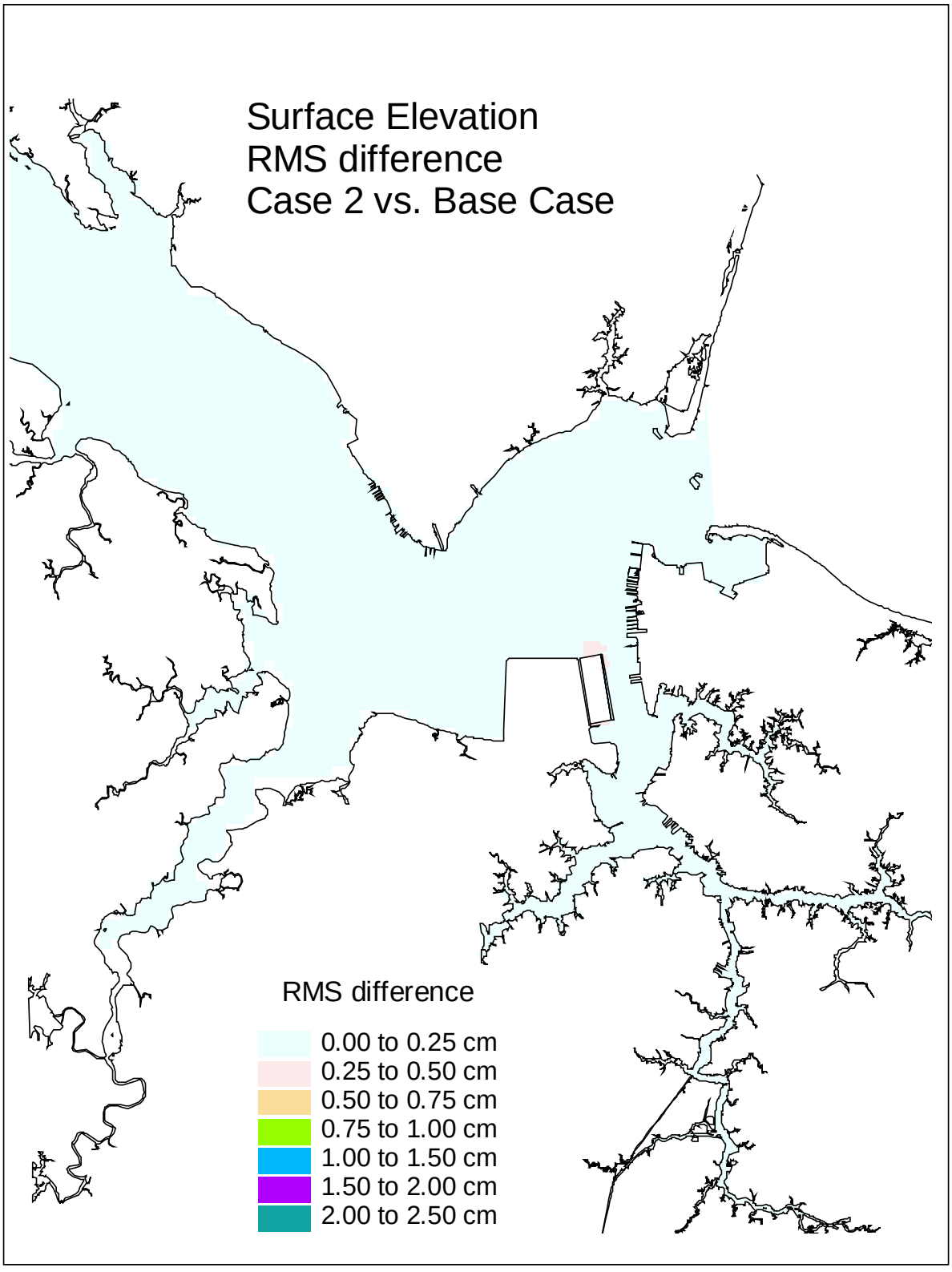

Figure 1. Single variable simulation comparison of surface elevation RMS difference for the Eastward Expansion (Option 7, 50-foot channel) versus the Base Case.

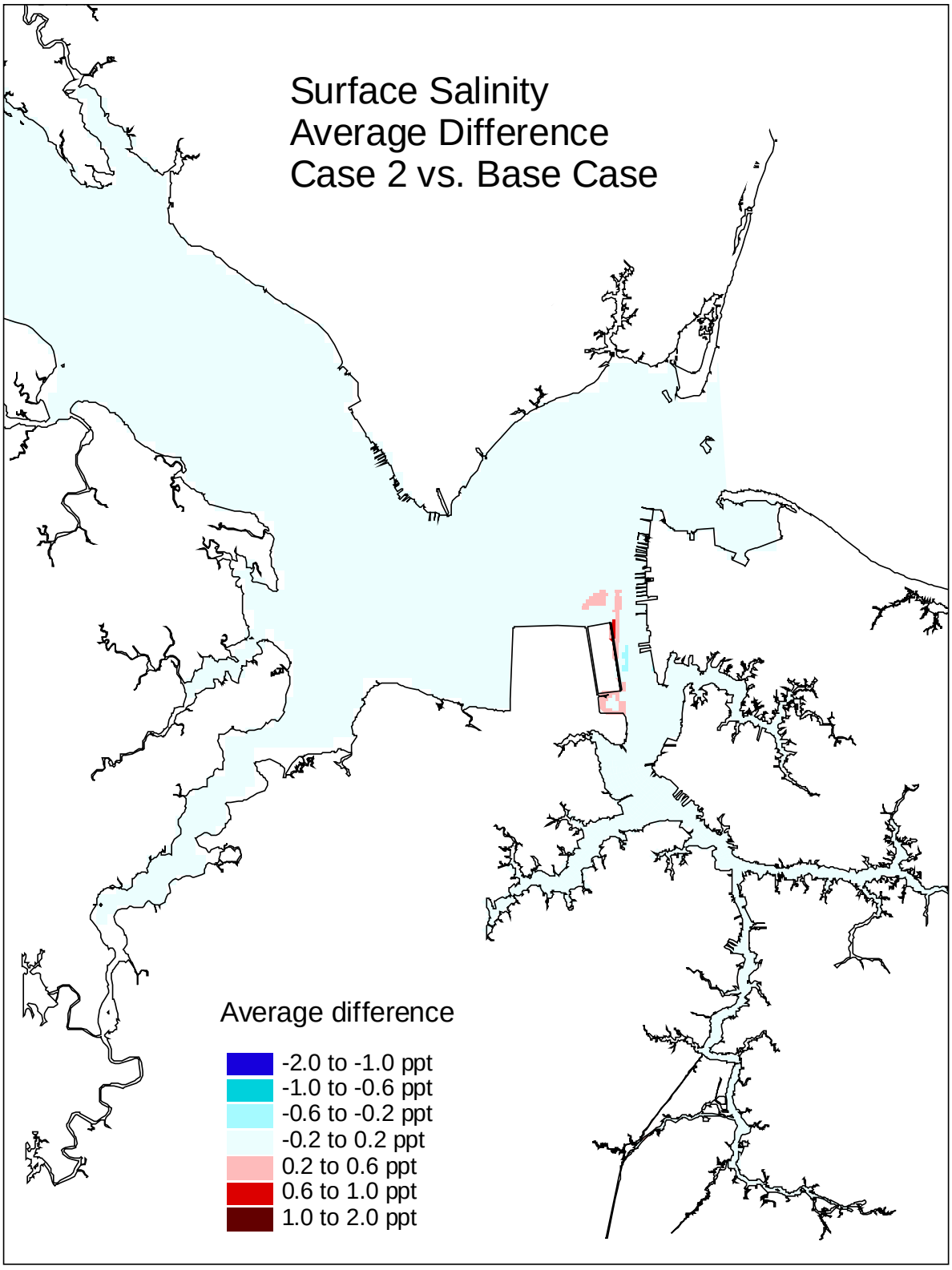

Figure 2. Single variable simulation comparison of the surface salinity average difference for the Eastward Expansion (Option 7, 50-foot channel) versus the Base Case.

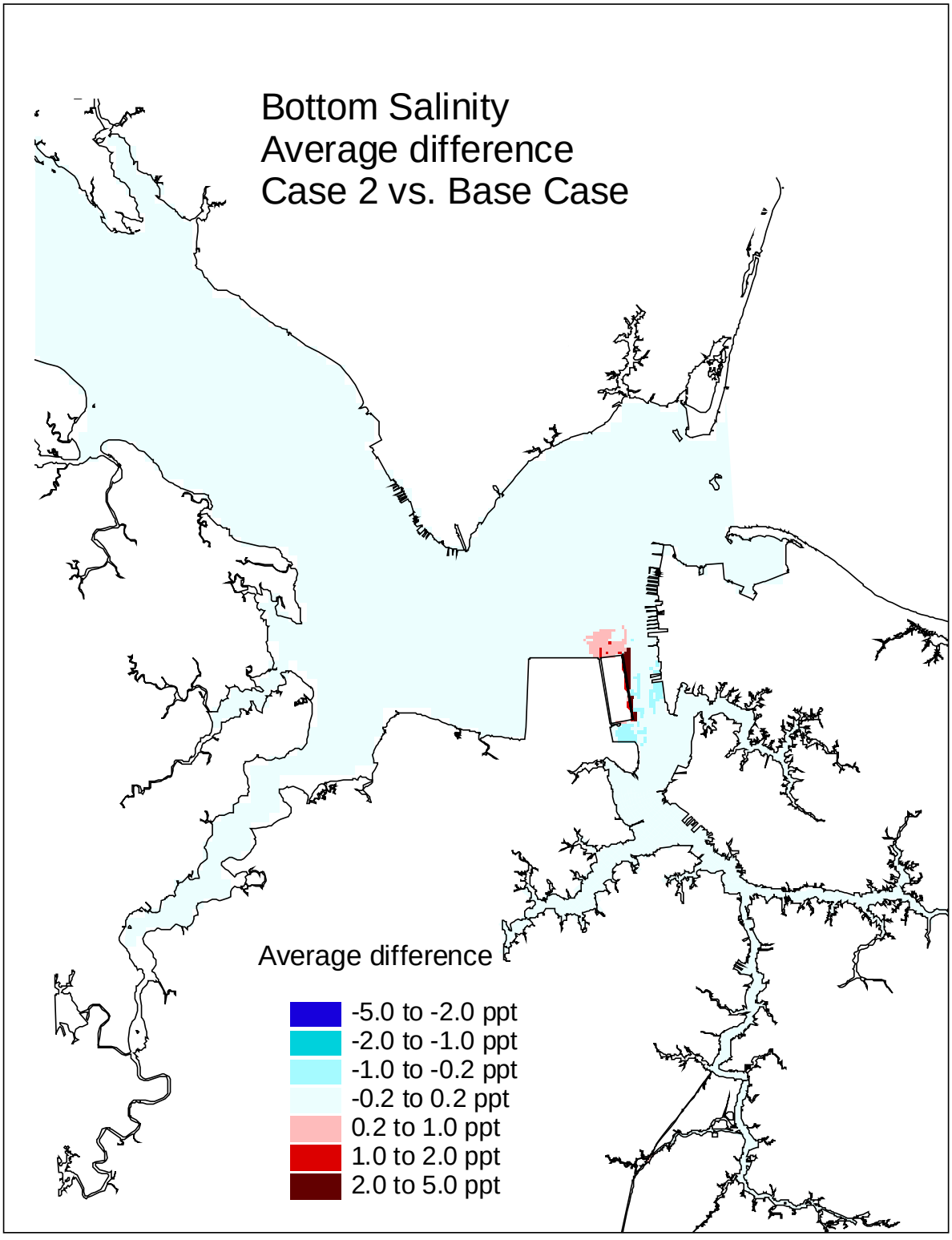

Figure 3. Single variable simulation comparison of the bottom salinity average difference for the Eastward Expansion, (Option 7, 50-foot channel) versus the Base Case.

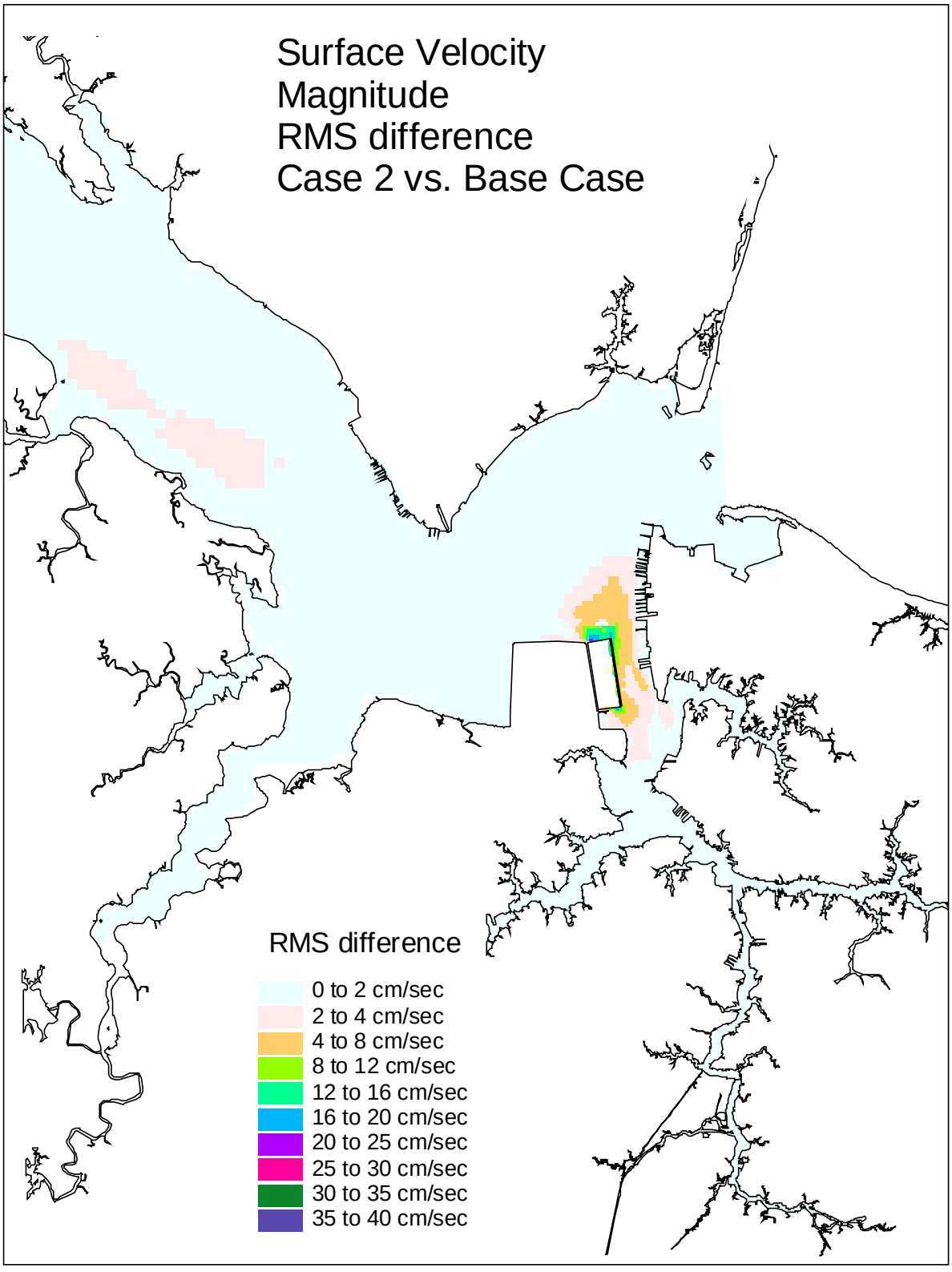

Figure 4. Single variable simulation comparison of the surface velocity RMS difference for the Eastward Expansion (Option 7, 50-foot channel) versus the Base Case.

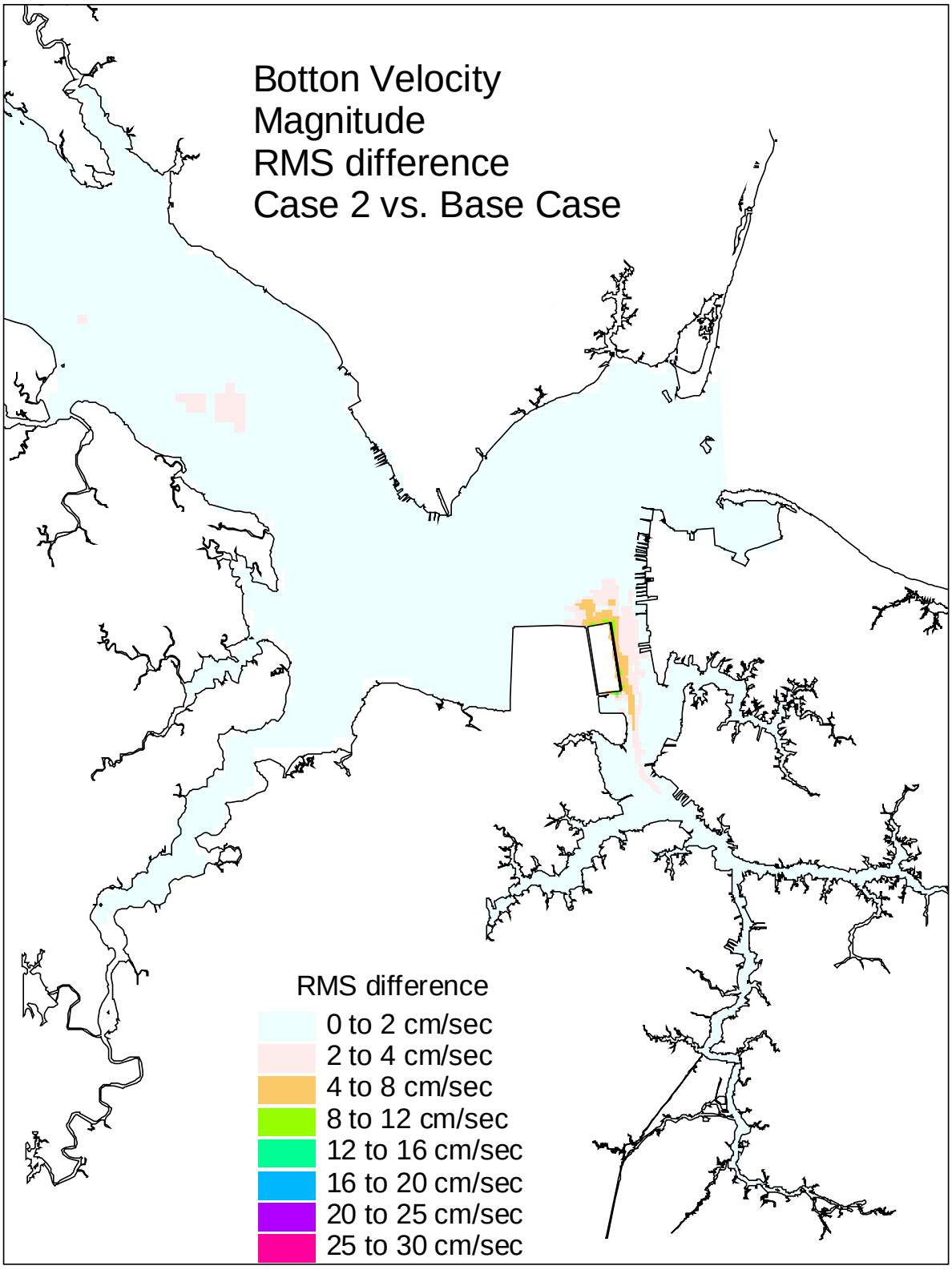

Figure 5. Single variable simulation comparison of the bottom velocity RMS difference for the Eastward Expansion, (Option 7, 50-foot channel) versus the Base Case.

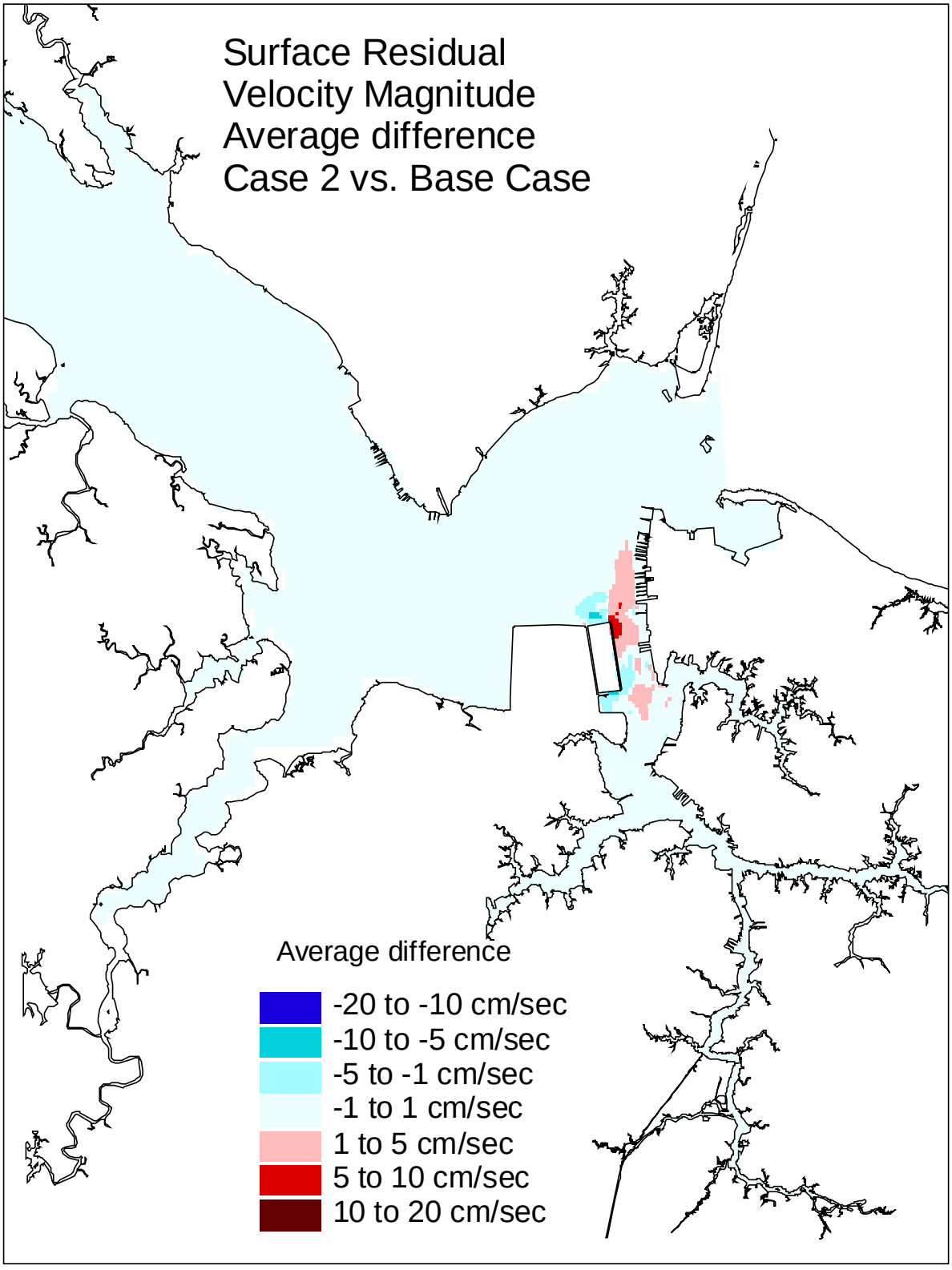

Figure 6. Single variable simulation comparison of the surface residual velocity average difference for the Eastward Expansion, (Option 7, 50-foot channel) versus the Base Case.

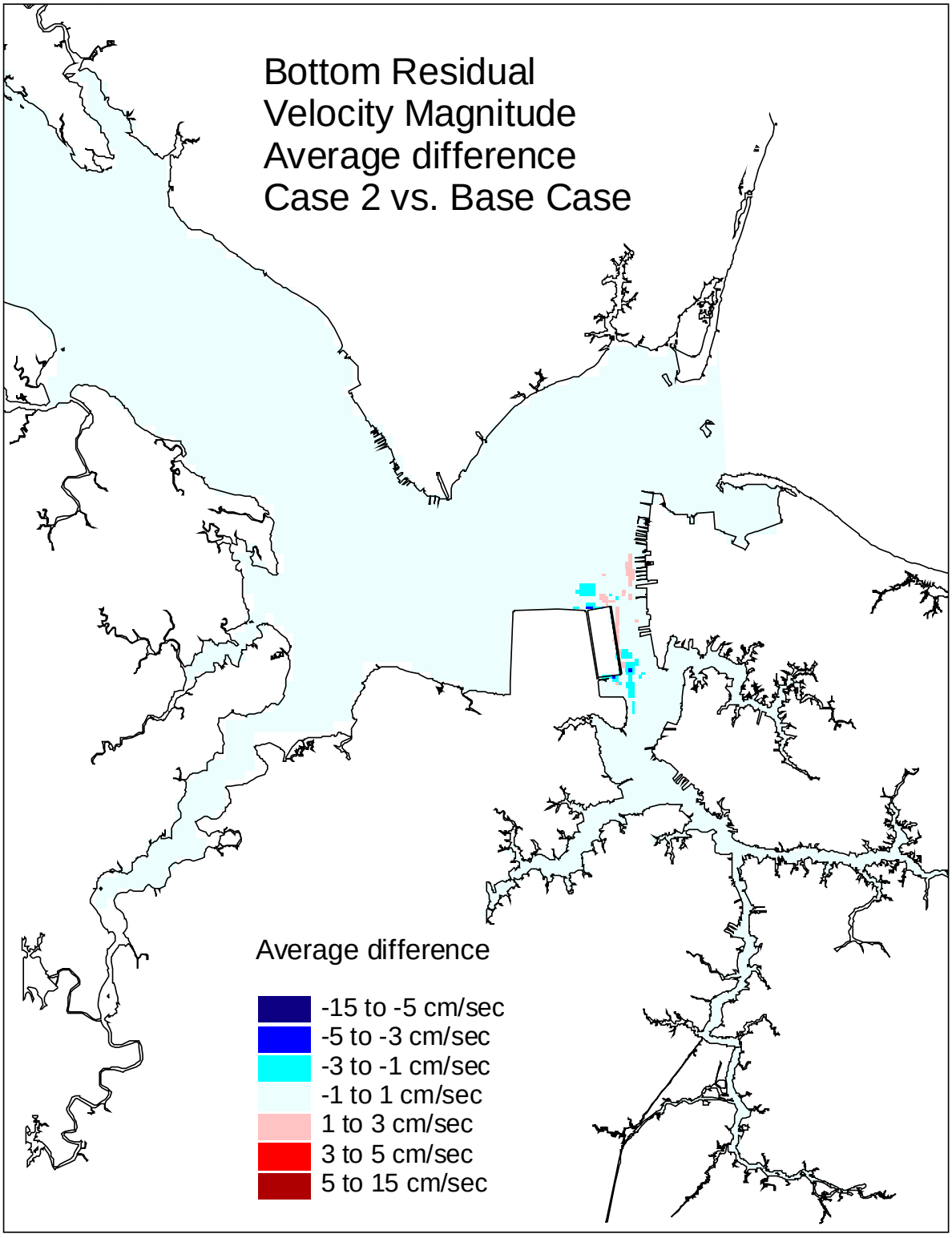

Figure 7. Single variable simulation comparison of the bottom residual velocity average difference for the Eastward Expansion, (Option 7, 50-foot channel) versus the Base Case.

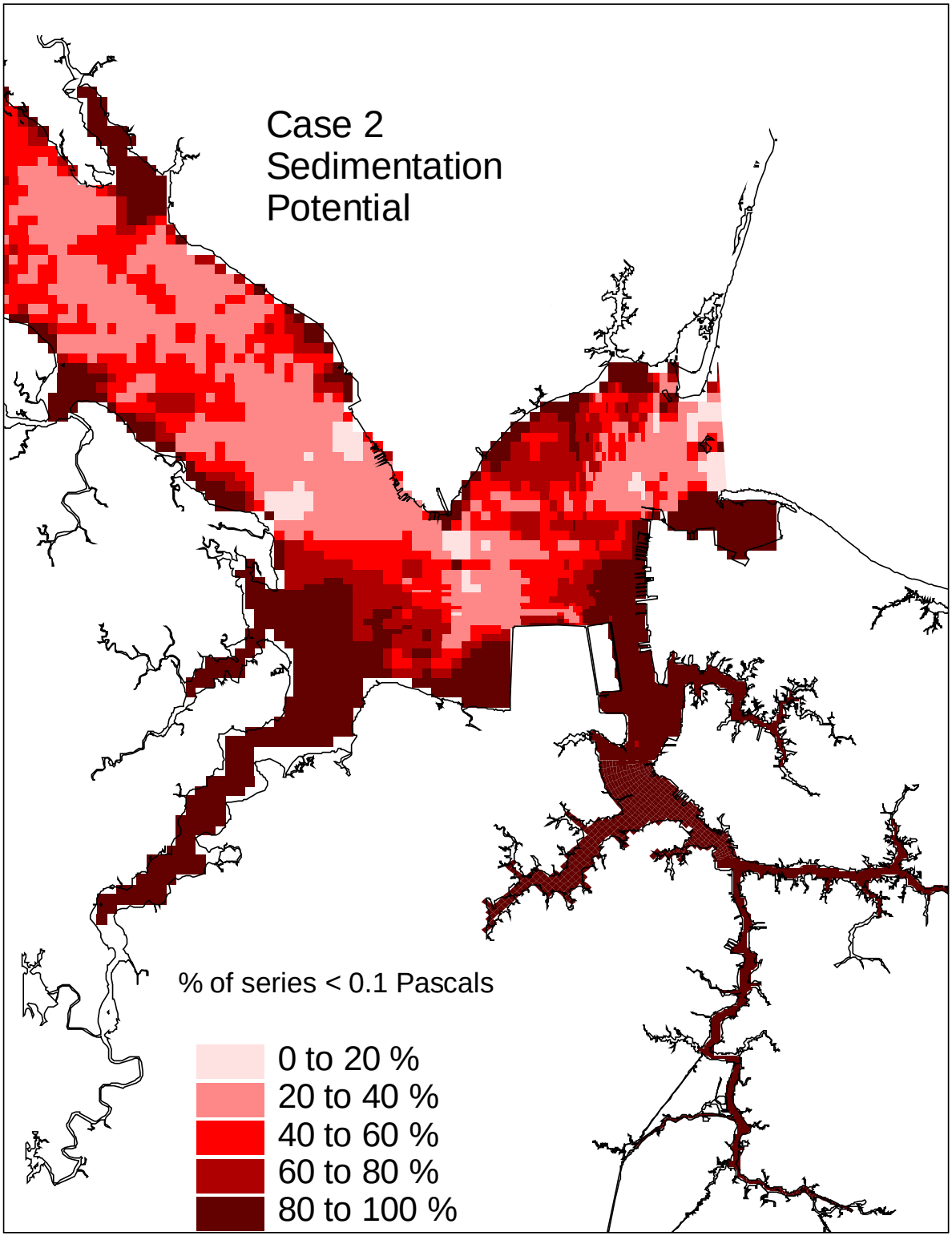

Figure 8. Single variable simulation comparison of the sedimentation potential for the Eastward Expansion, (Option 7, 50-foot channel).

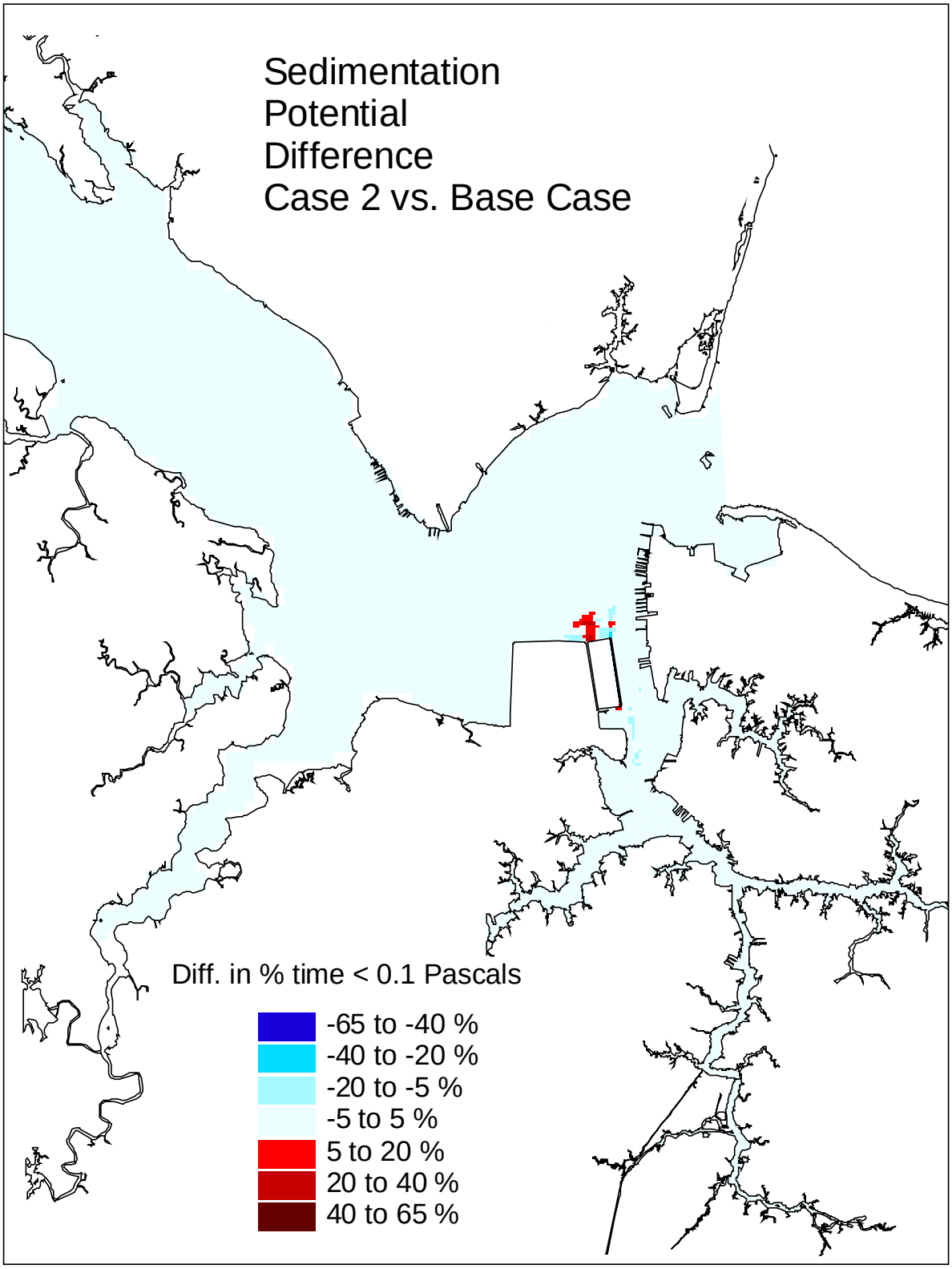

Figure 9. Single variable simulation comparison of the sedimentation potential difference for the Eastward Expansion, (Option 7, 50-foot channel) versus the Base Case.

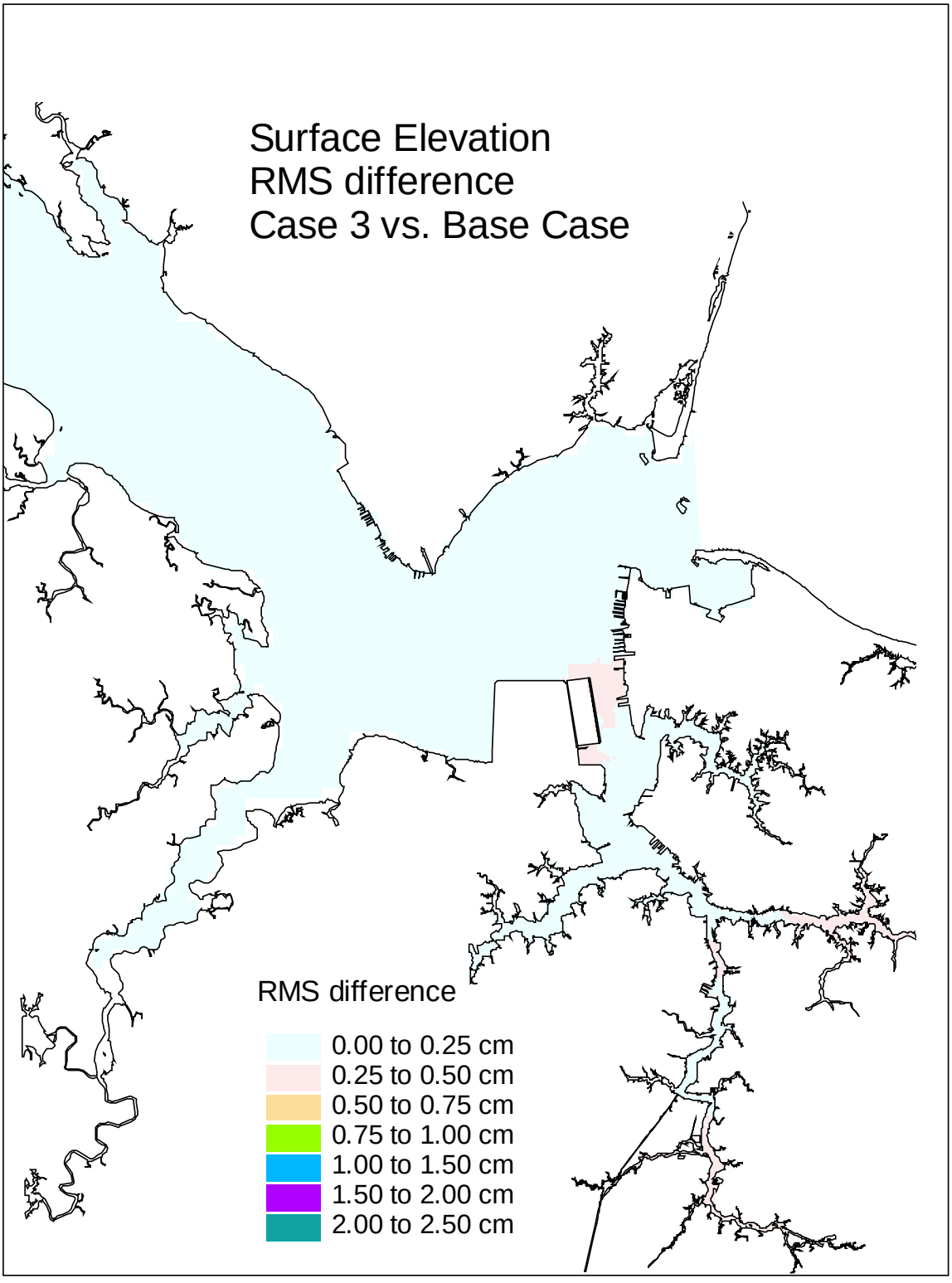

Figure 10. Single variable simulation comparison of the surface elevation RMS difference for the Eastward Expansion (Option 7, 55-foot channel) versus the Base Case.

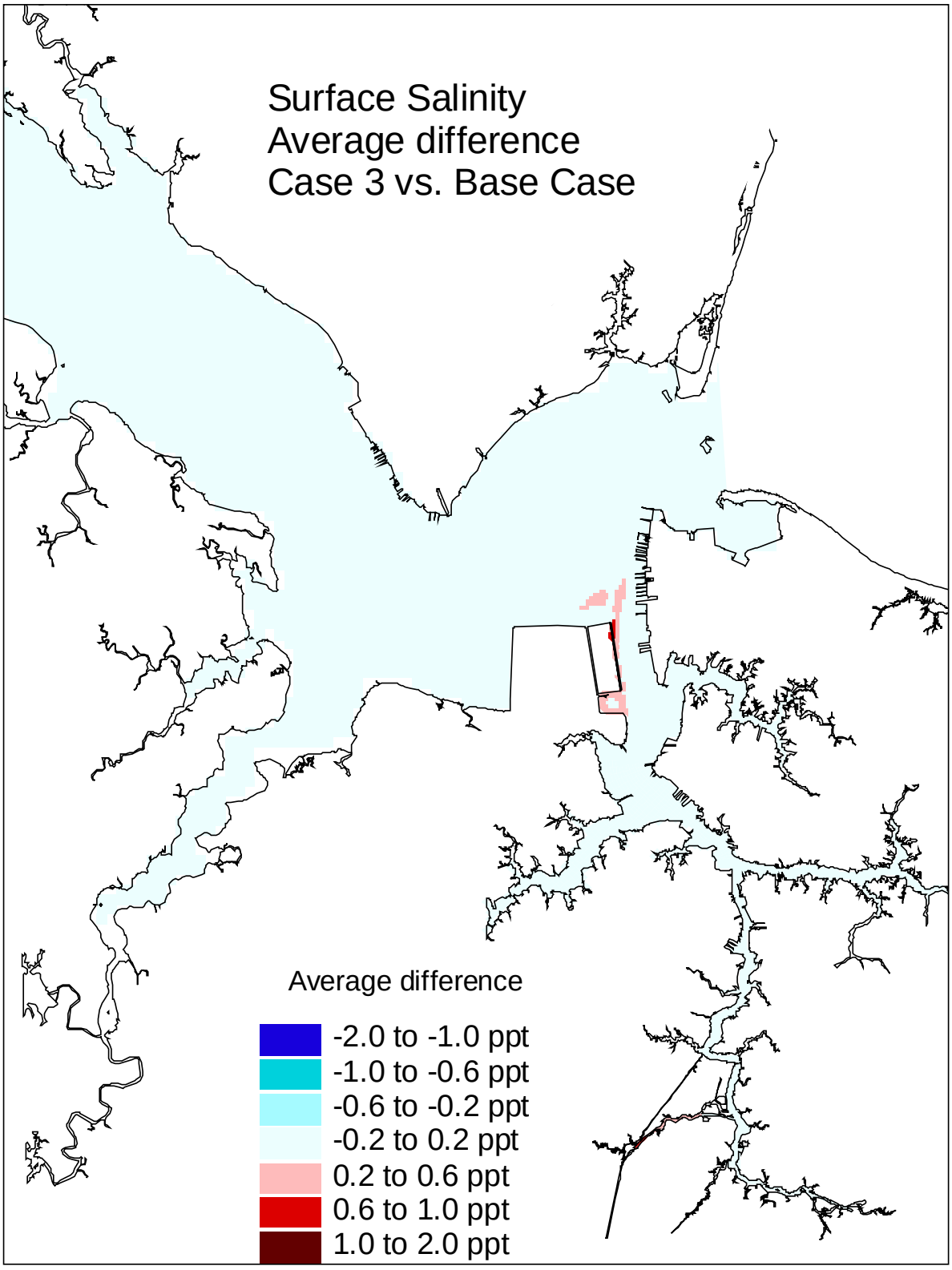

Figure 11. Single variable simulation comparison of the surface salinity average difference for the Eastward Expansion (Option 7, 55-foot channel) versus the Base Case.

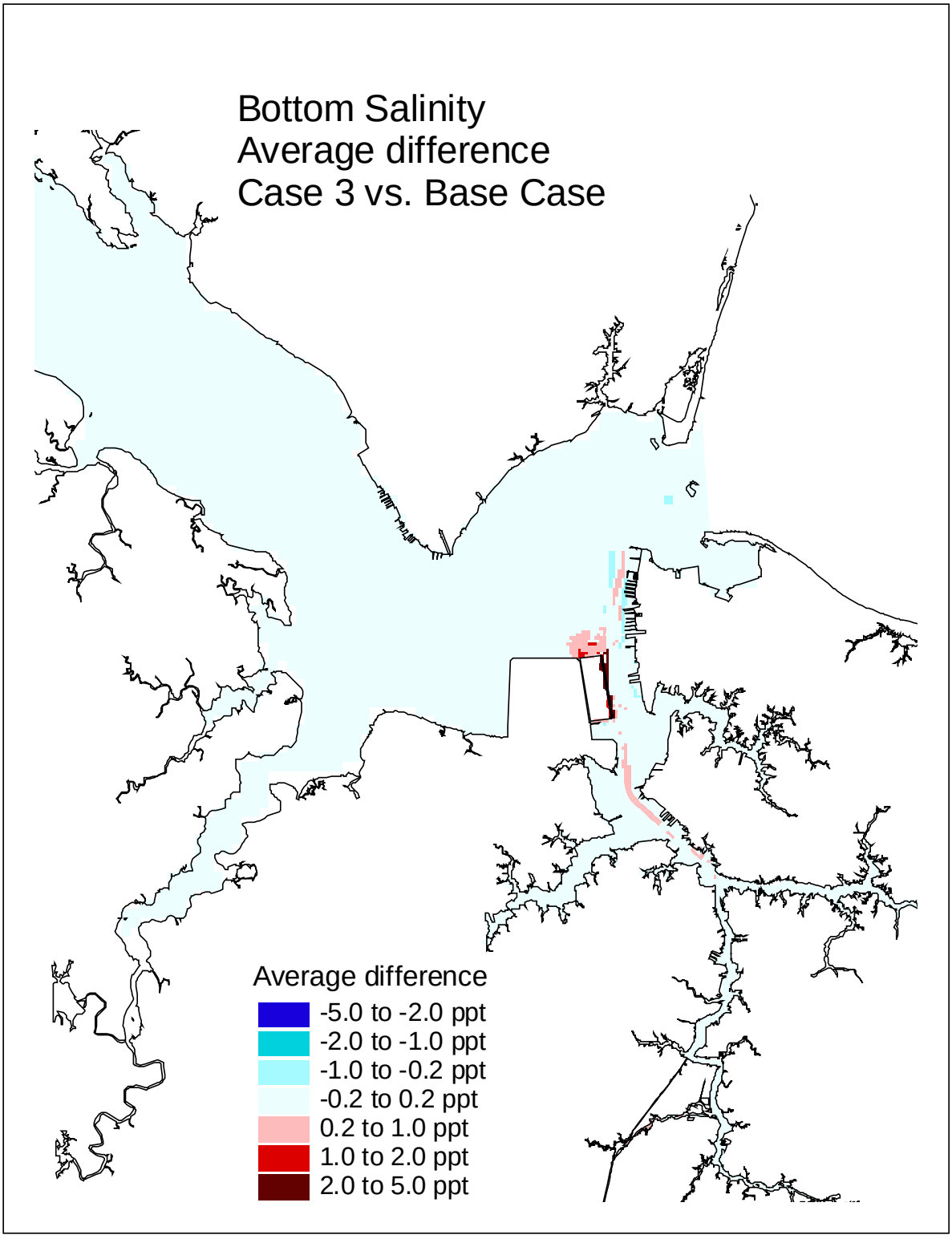

Figure 12. Single variable simulation comparison of the bottom salinity average difference for the Eastward Expansion (Option 7, 55-foot channel) versus the Base Case.

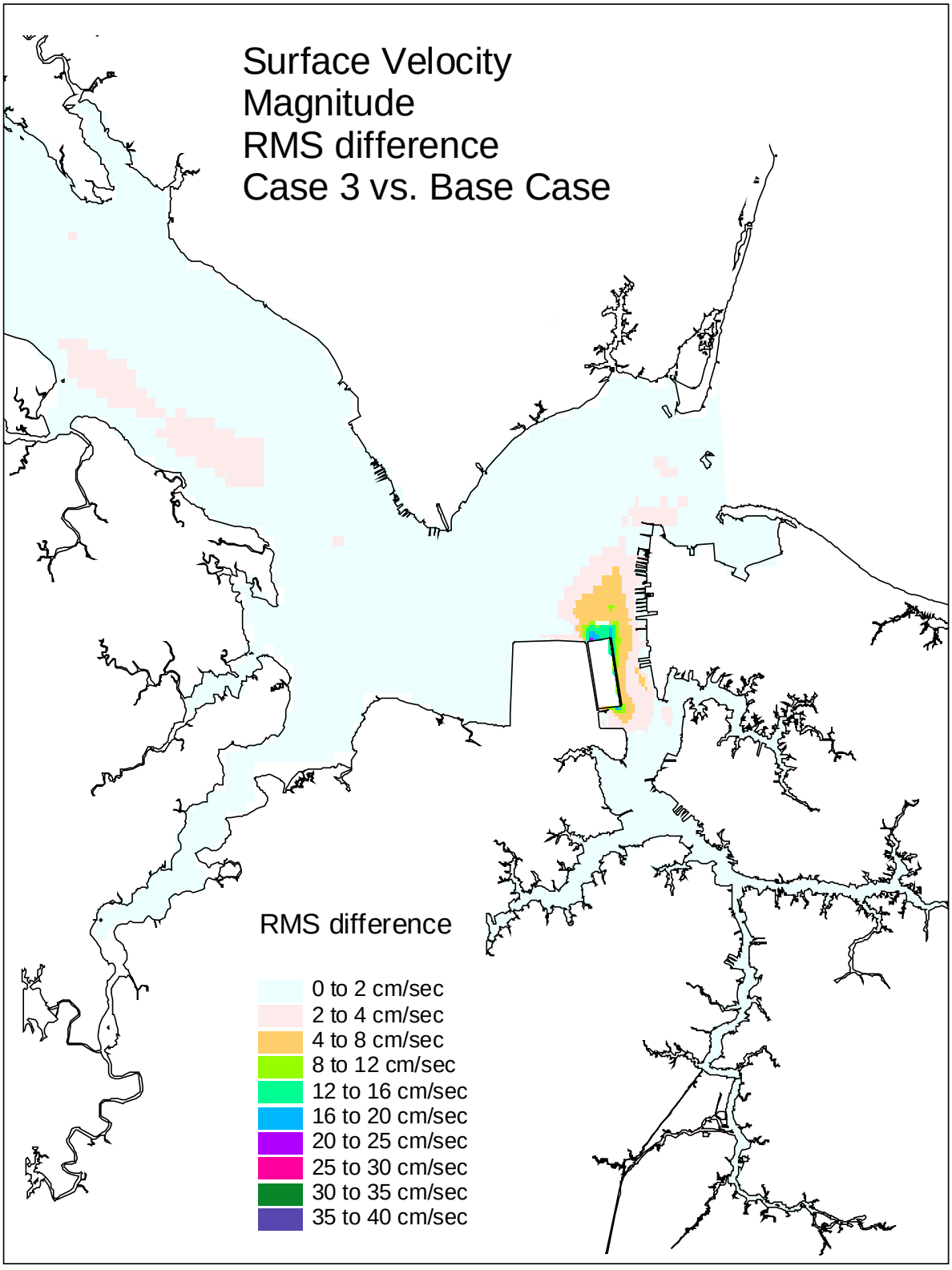

Figure 13. Single variable simulation comparison of the surface velocity RMS difference for the Eastward Expansion (Option 7, 55-foot channel) versus the Base Case.

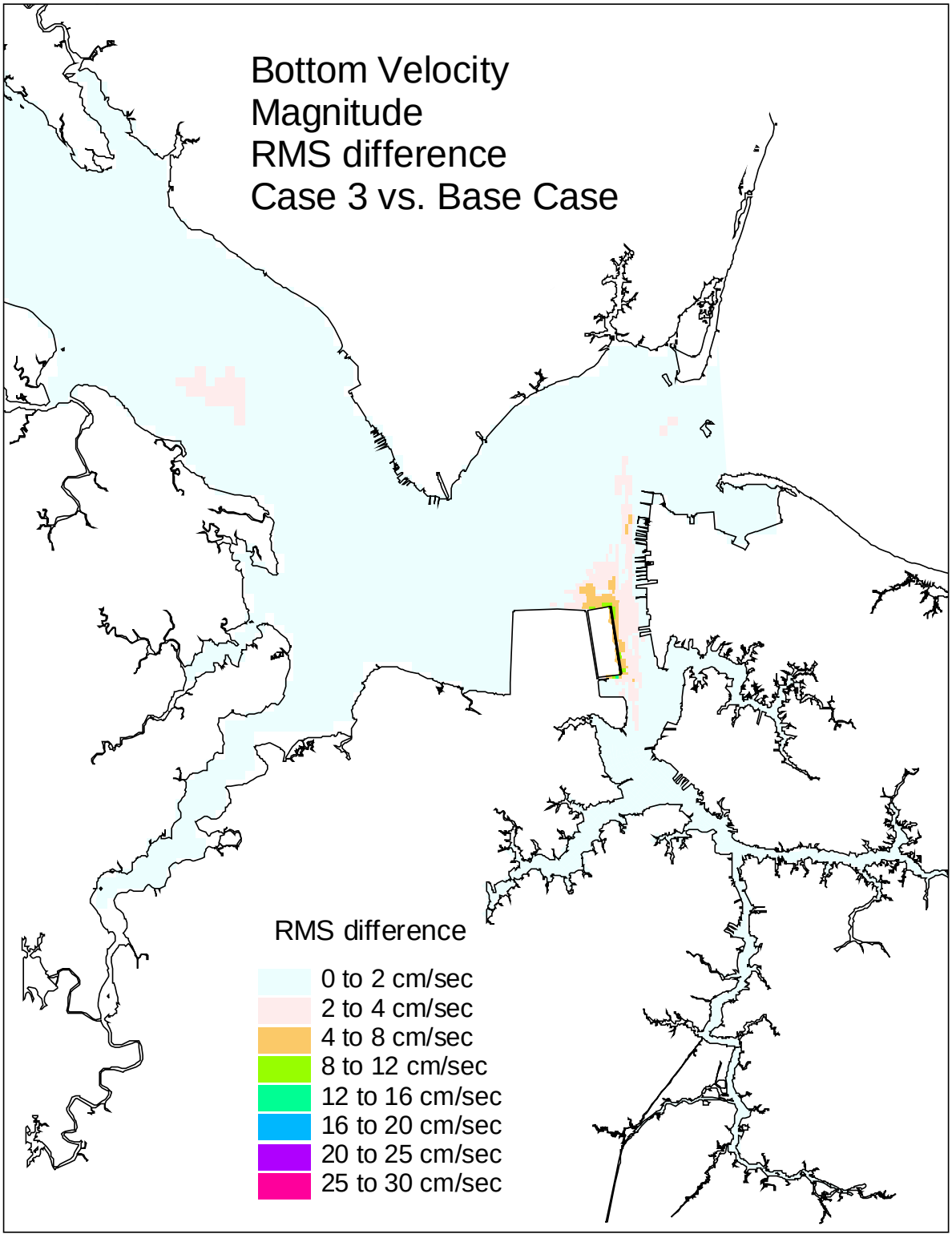

Figure 14. Single variable simulation comparison of the bottom velocity RMS difference for the Eastward Expansion, (Option 7, 55-foot channel) versus the Base Case.

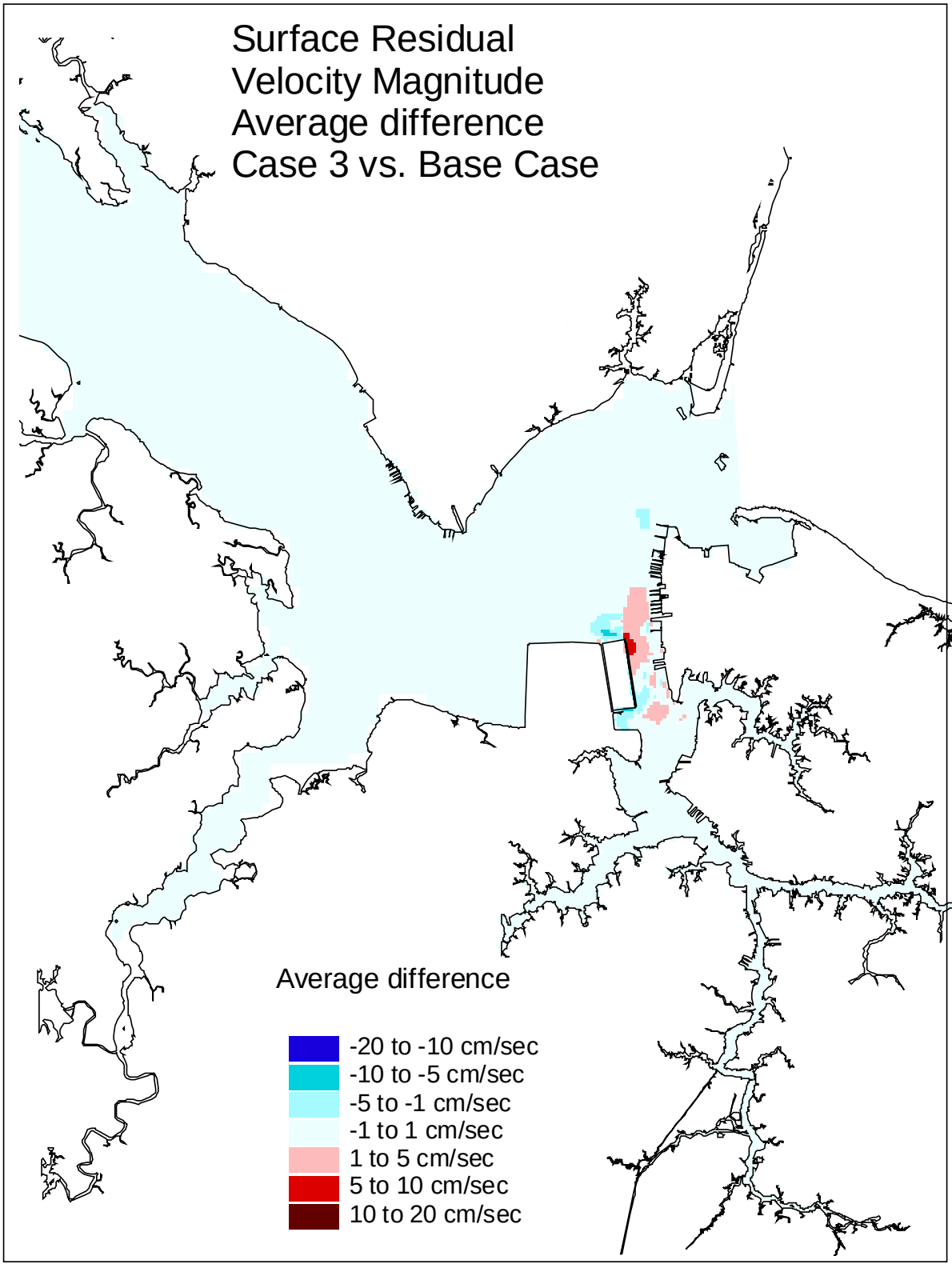

Figure 15. Single variable simulation comparison of the surface residual velocity average difference for the Eastward Expansion, (Option 7, 55-foot channel) versus the Base Case.

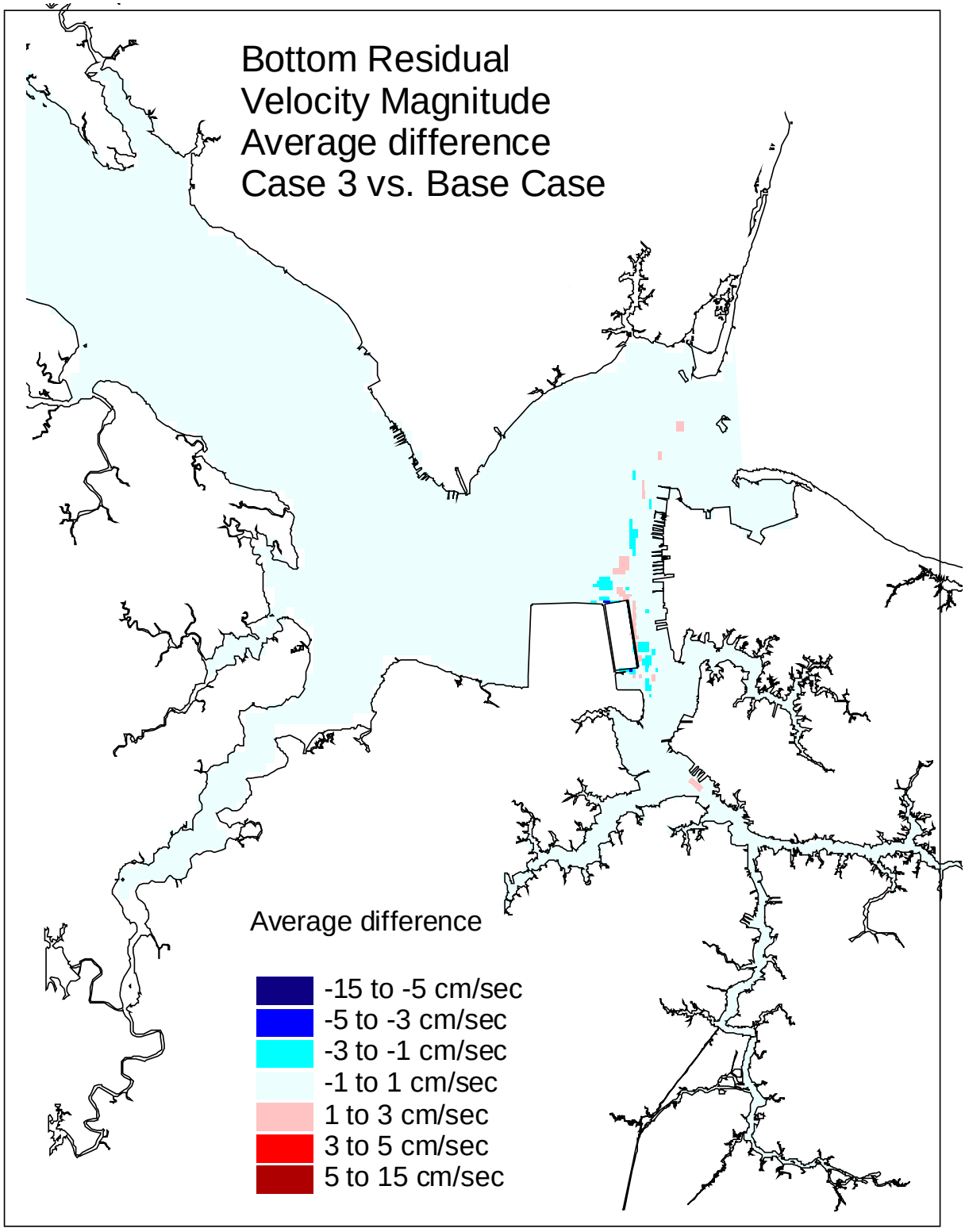

Figure 16. Single variable simulation comparison of the bottom residual velocity average difference for The Eastward Expansion, (Option 7, 55-foot channel) versus the Base Case.

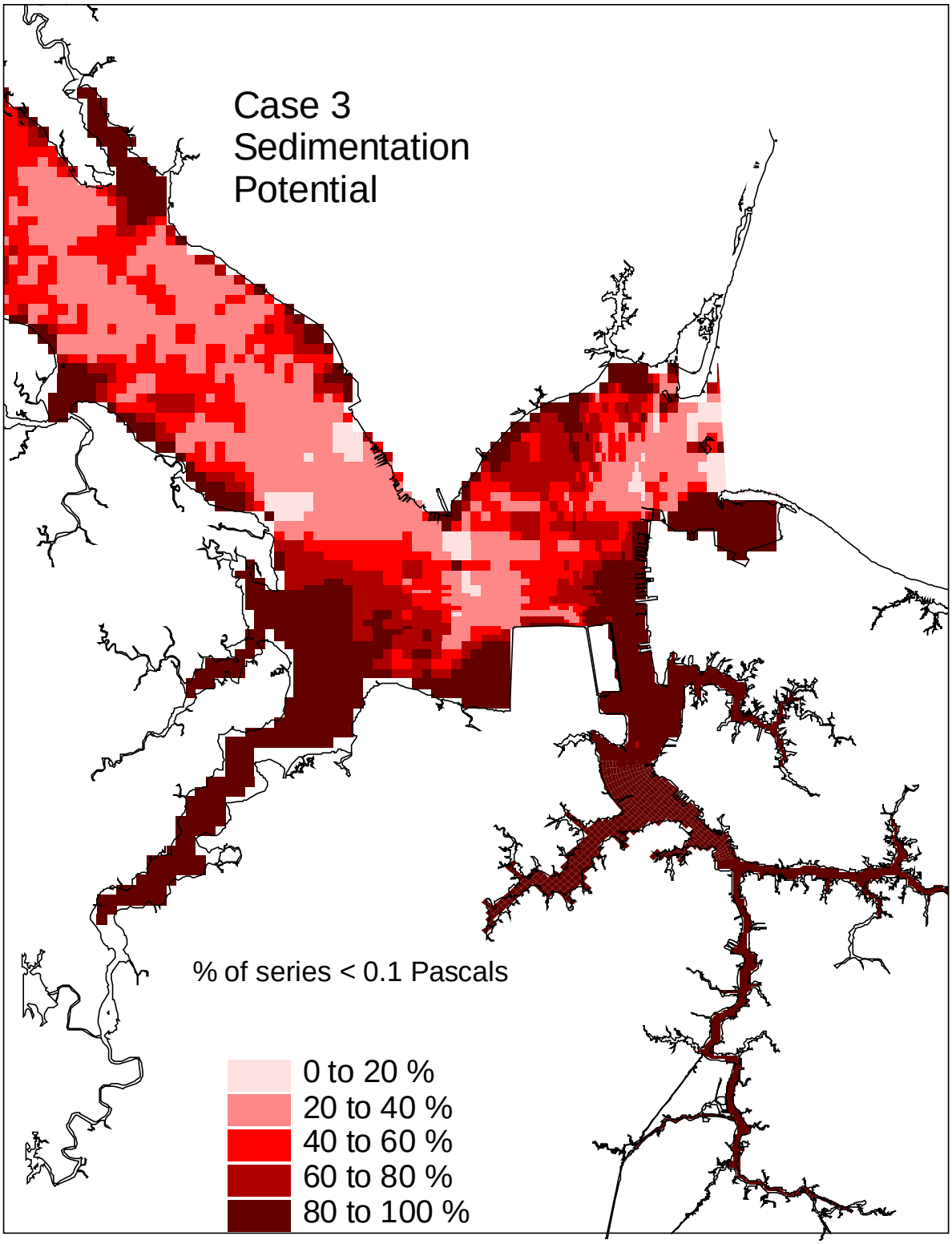

Figure 17. Single variable simulation comparison of the sedimentation potential for the Eastward Expansion, (Option 7, 55-foot channel).

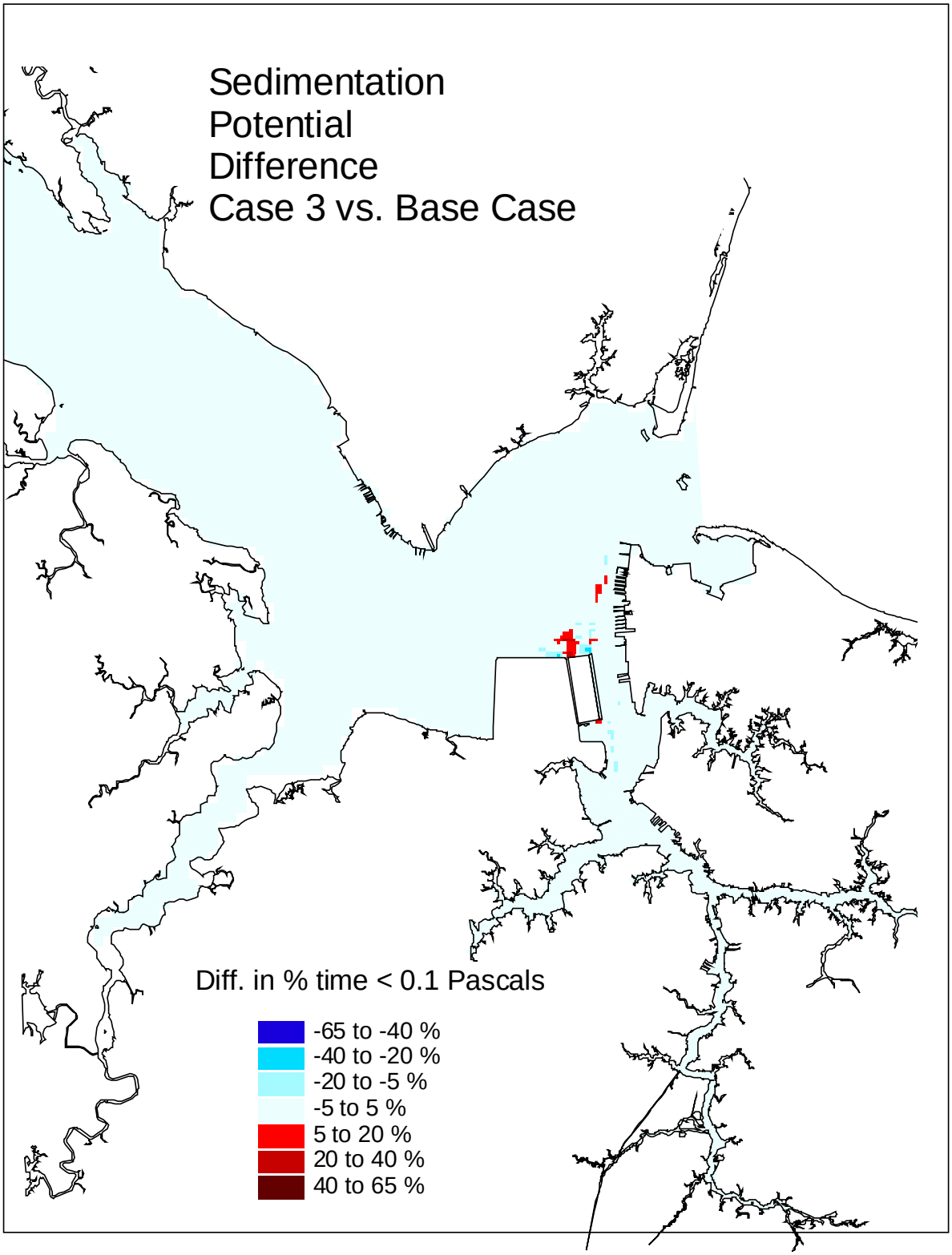

Figure 18. Single variable simulation comparison of the sedimentation potential difference for the Eastward Expansion, (Option 7, 55-foot channel) versus the Base Case.

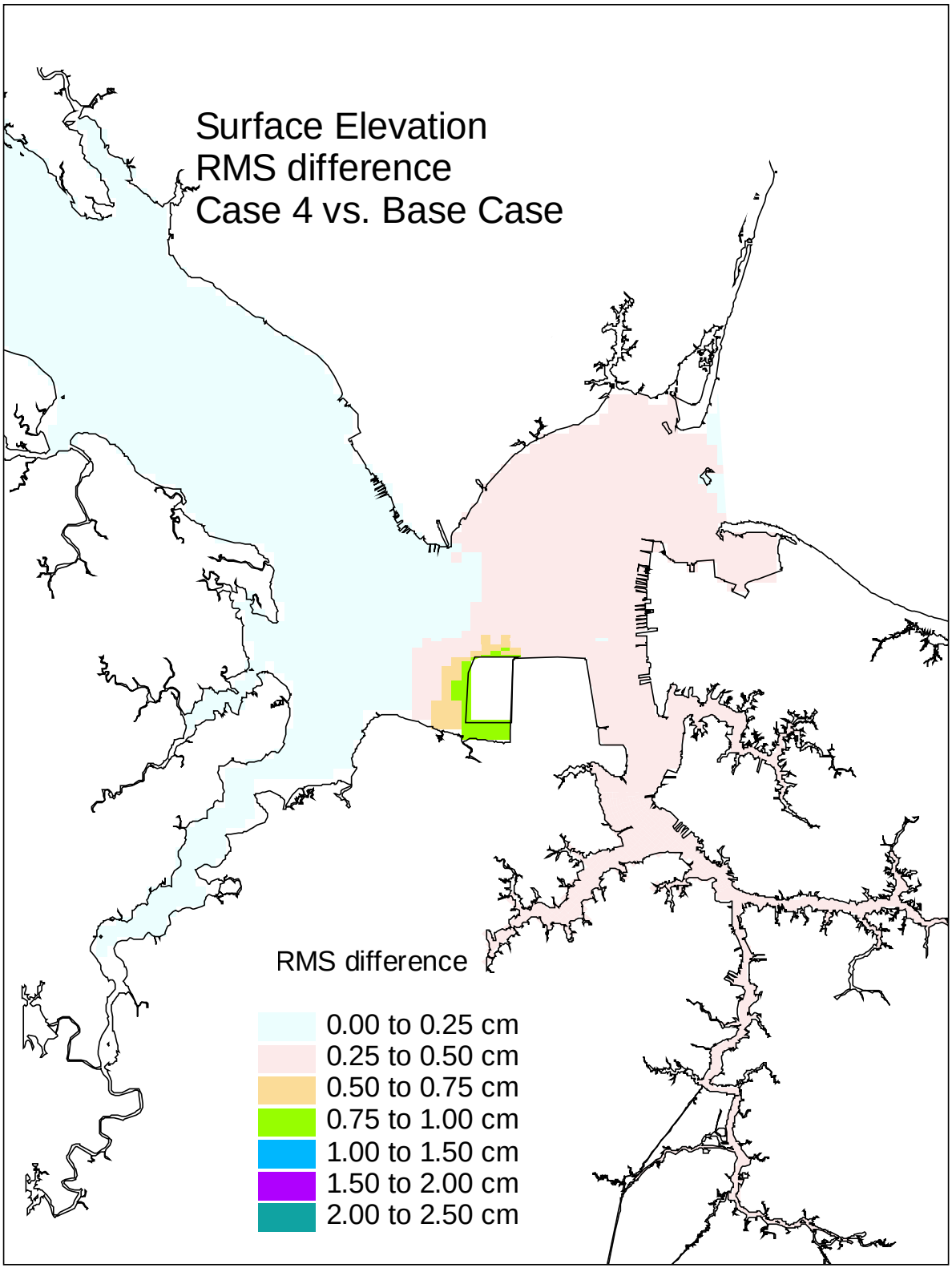

Figure 19. Single variable simulation comparison of the surface elevation RMS difference for the Westward Expansion (Option 5, 50-foot channel) versus the Base Case.

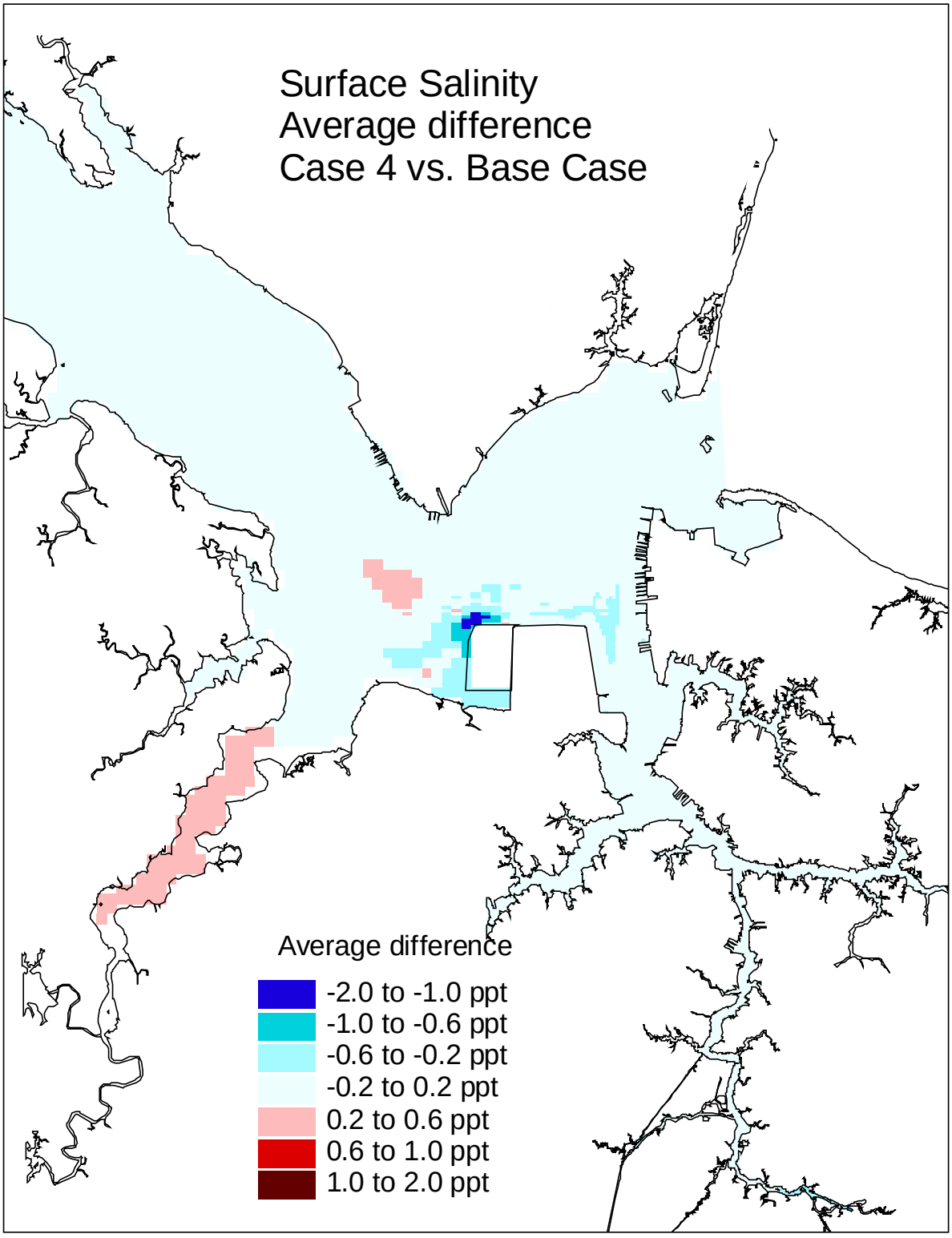

Figure 20. Single variable simulation comparison of the surface salinity average difference for the Westward Expansion (Option 5, 50-foot channel) versus the Base Case.

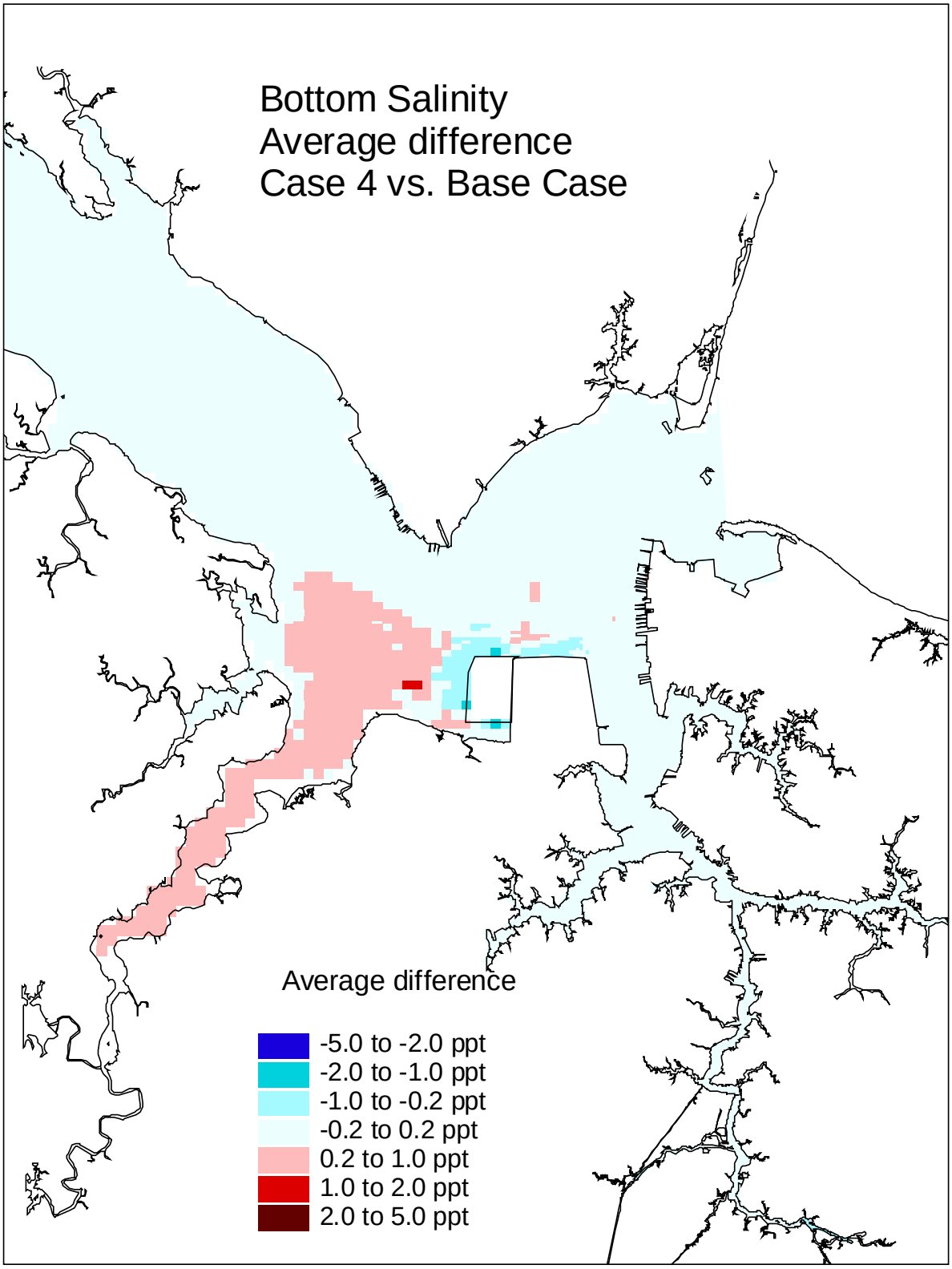

Figure 21. Single variable simulation comparison of the bottom salinity average difference for the Westward Expansion (Option 5, 50-foot channel) versus the Base Case.

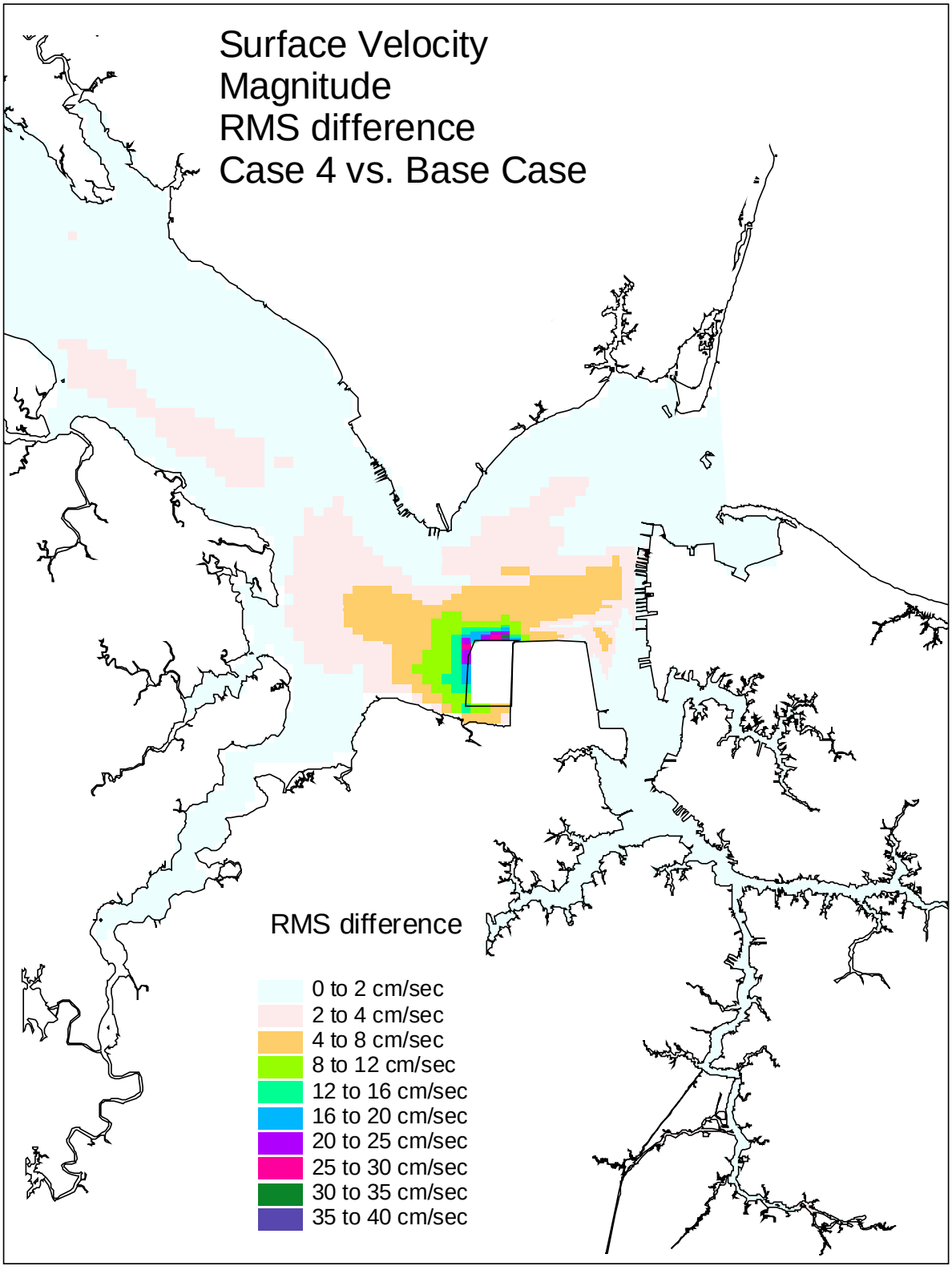

Figure 22. Single variable simulation comparison of the surface velocity RMS difference for the Westward Expansion (Option 5, 50-foot channel) versus the Base Case.

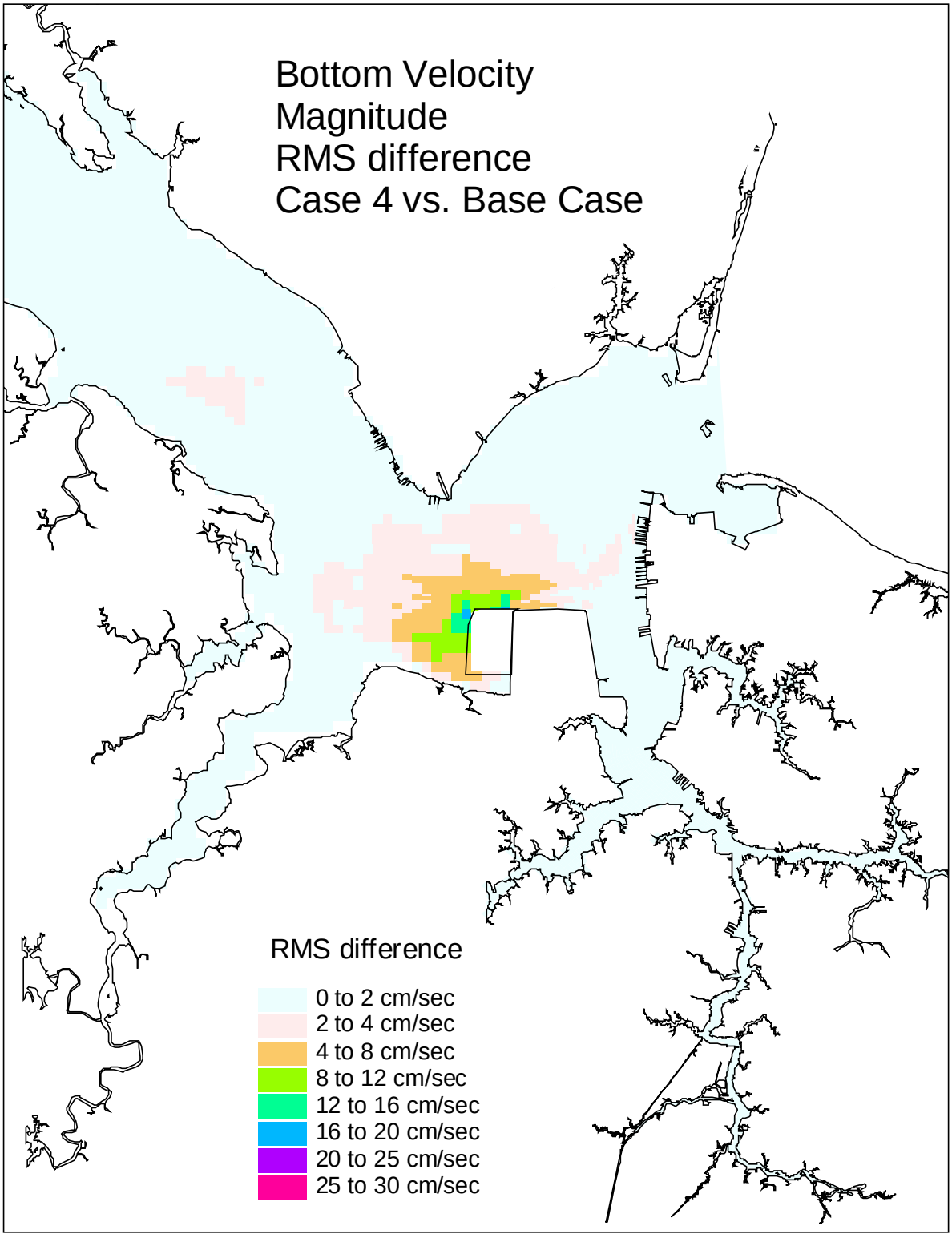

Figure 23. Single variable simulation comparison of the bottom velocity RMS difference for the Westward Expansion (Option 5, 50-foot channel) versus the Base Case.

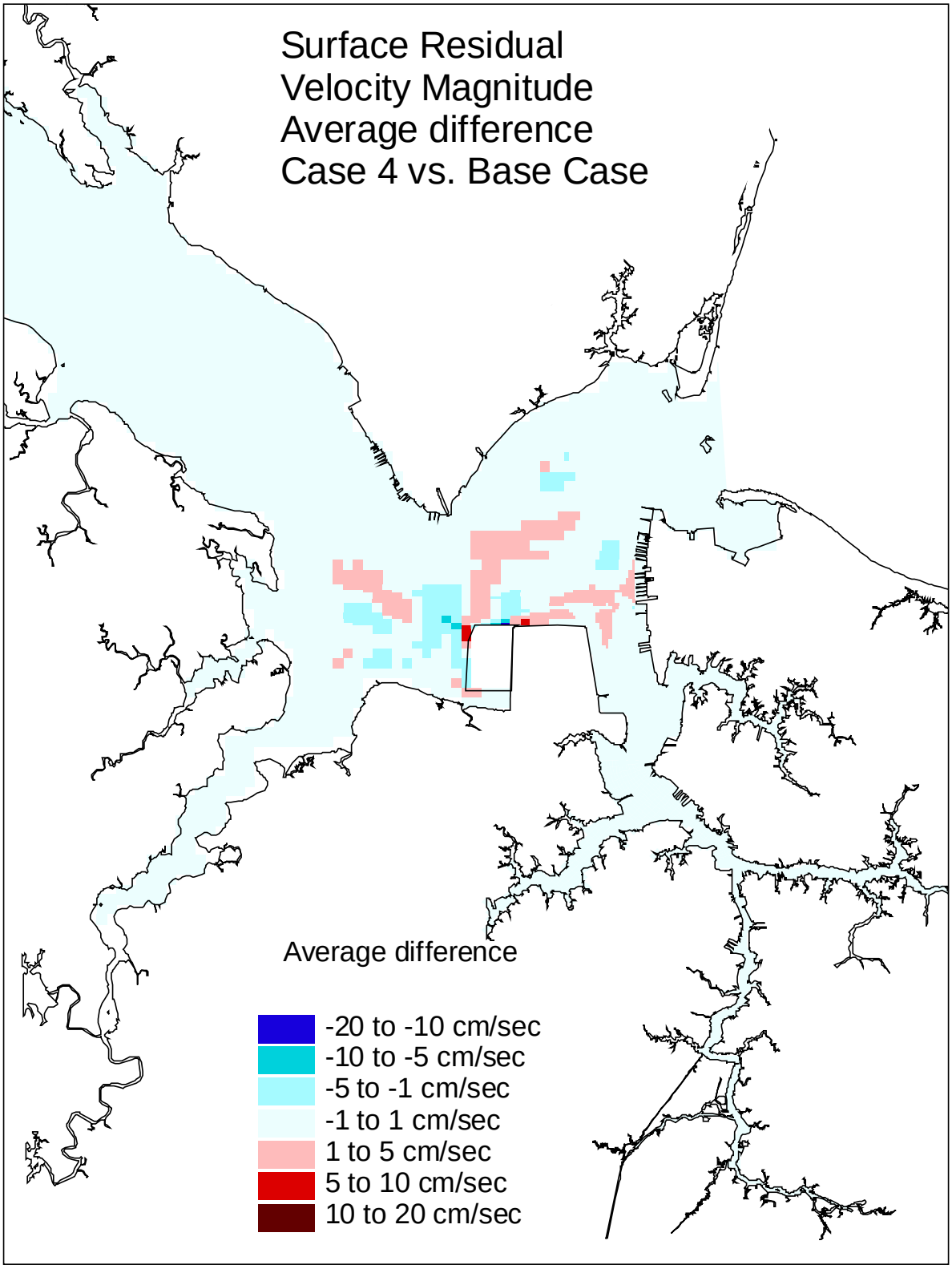

Figure 24. Single variable simulation comparison of the surface residual velocity average difference for the Westward Expansion (Option 5, 50-foot channel) versus the Base Case.

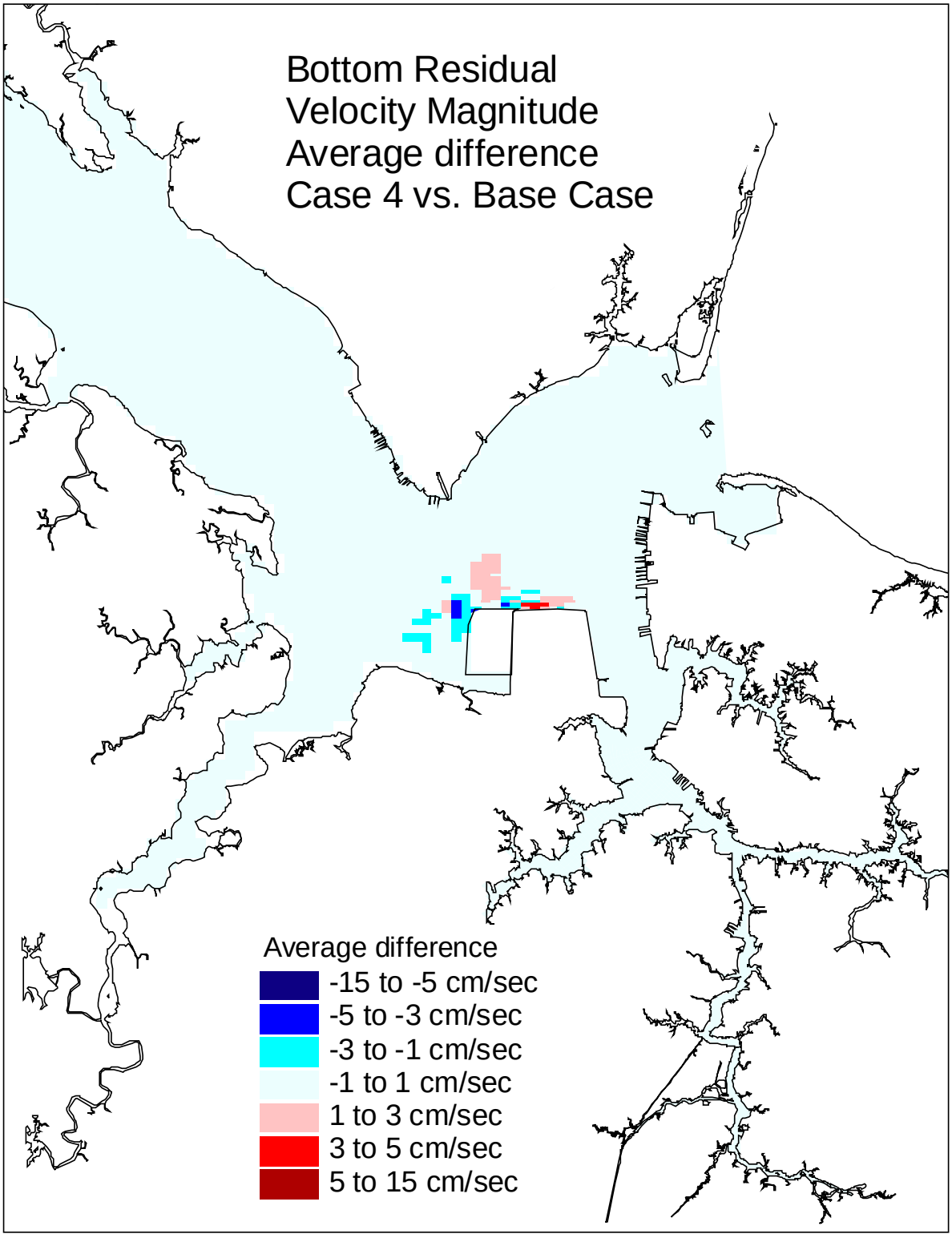

Figure 25. Single variable simulation comparison of the bottom residual velocity average difference for the Westward Expansion (Option 5, 50-foot channel) versus the Base Case.

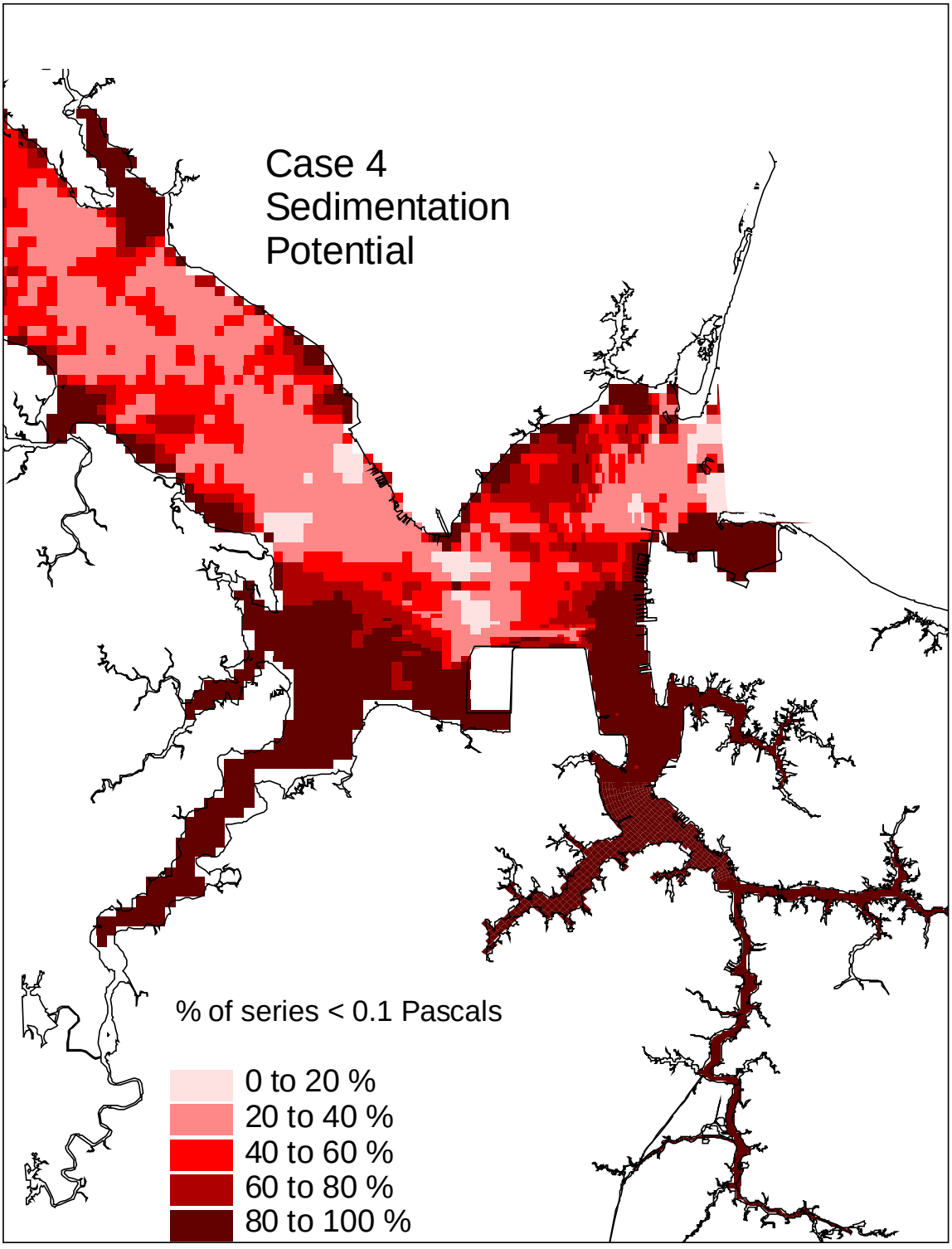

Figure 26. Single variable simulation comparison of the sedimentation potential for the Westward Expansion (Option 5, 50-foot channel).

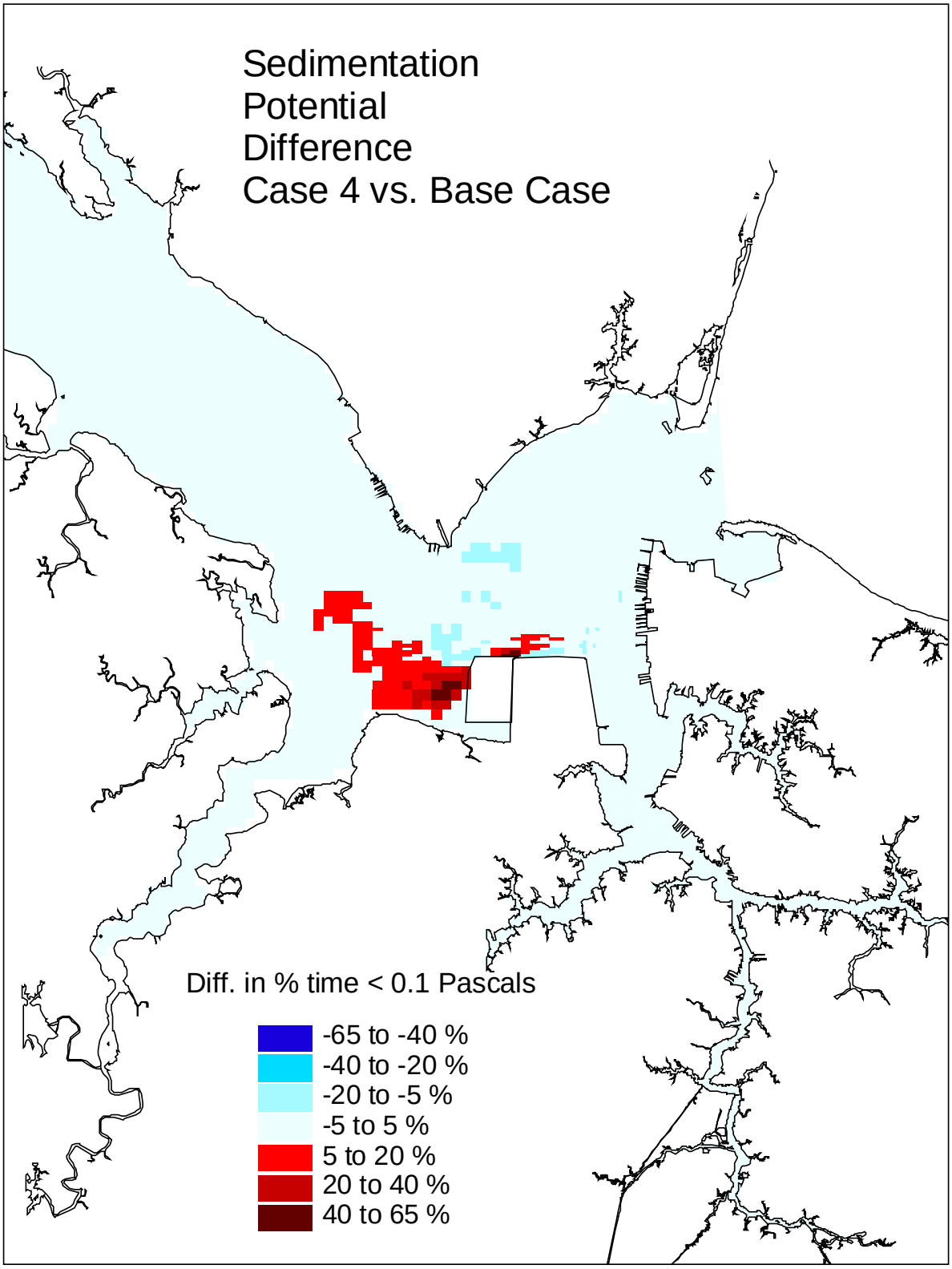

Figure 27. Single variable simulation comparison of the sedimentation potential difference for the Westward Expansion (Option 5, 50-foot channel) versus the Base Case.

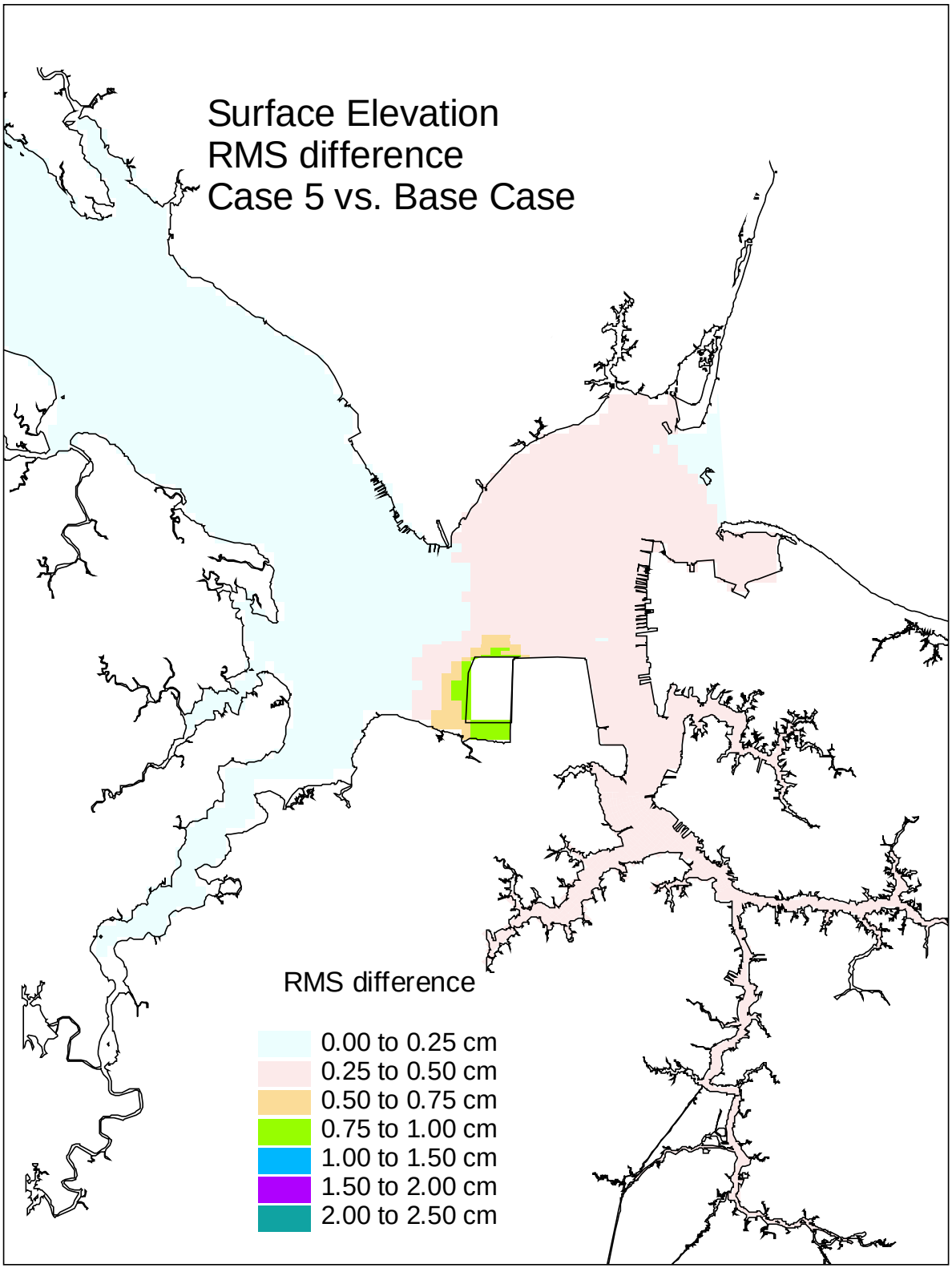

Figure 28. Single variable simulation comparison of the surface elevation RMS difference for the Westward Expansion (Option 5, 55-foot channel) versus the Base Case

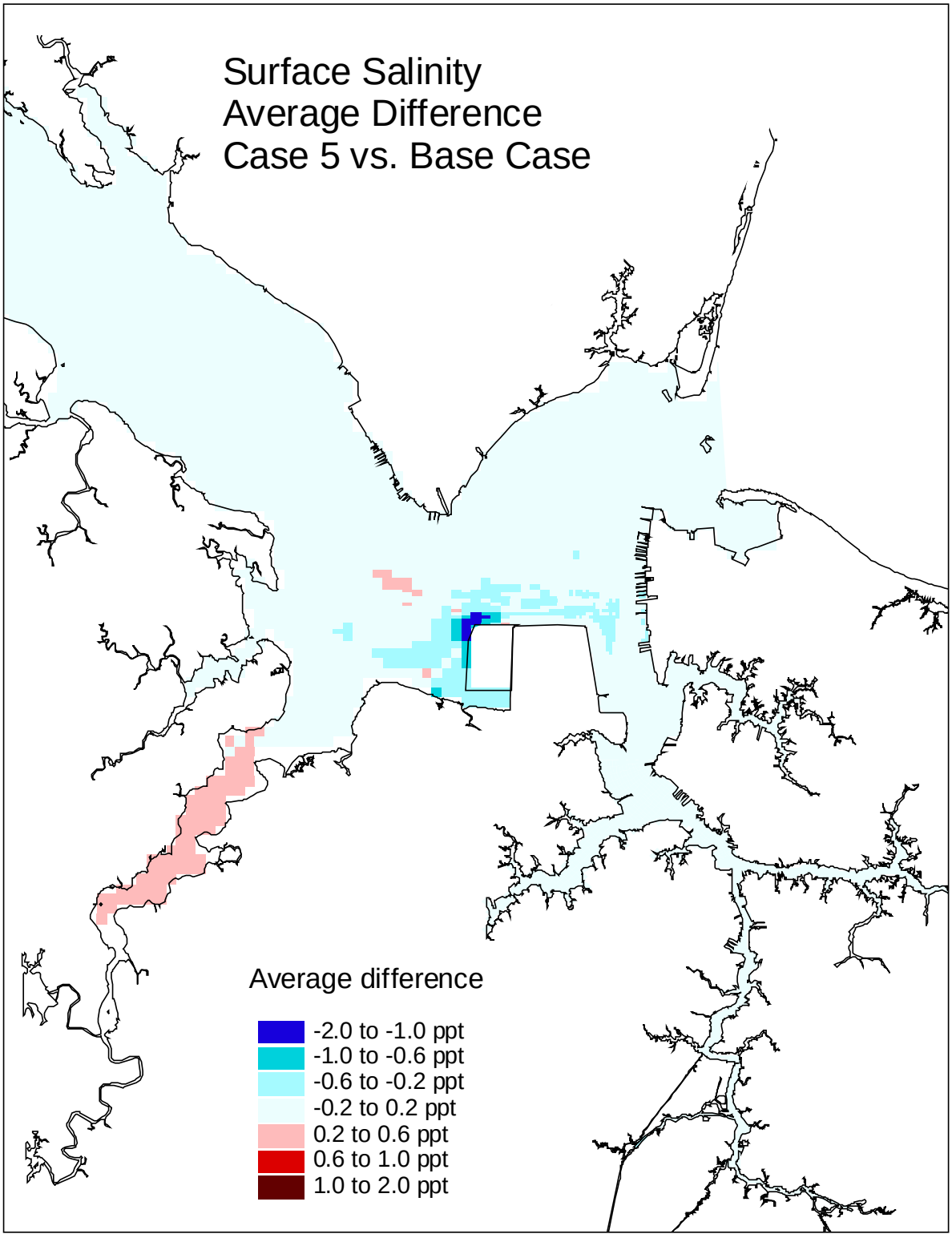

Figure 29. Single variable simulation comparison of the surface salinity average difference for the Westward Expansion (Option 5, 55-foot channel) versus the Base Case

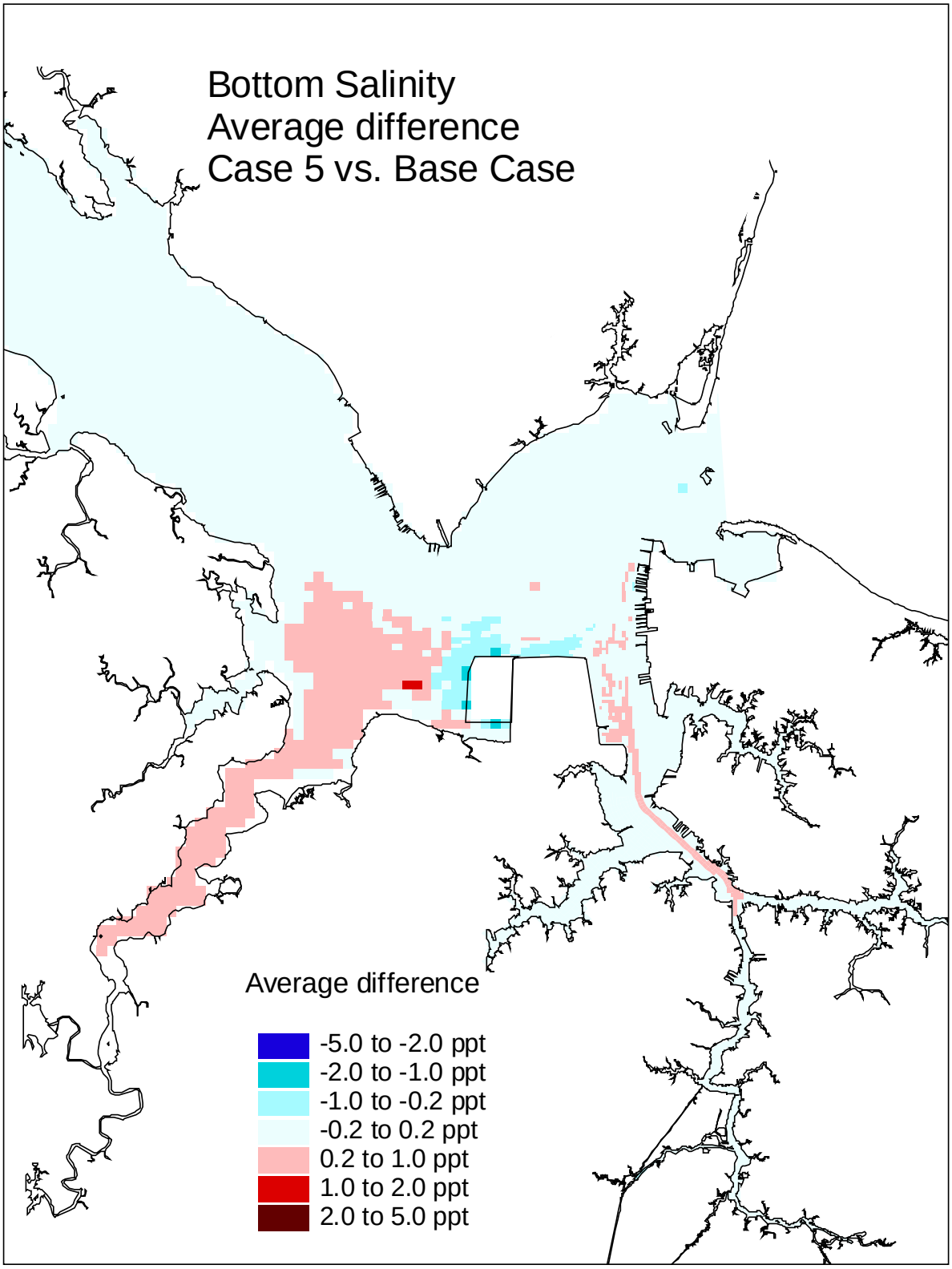

Figure 30. Single variable simulation comparison of the bottom salinity average difference for the Westward Expansion (Option 5, 55-foot channel) versus the Base Case.

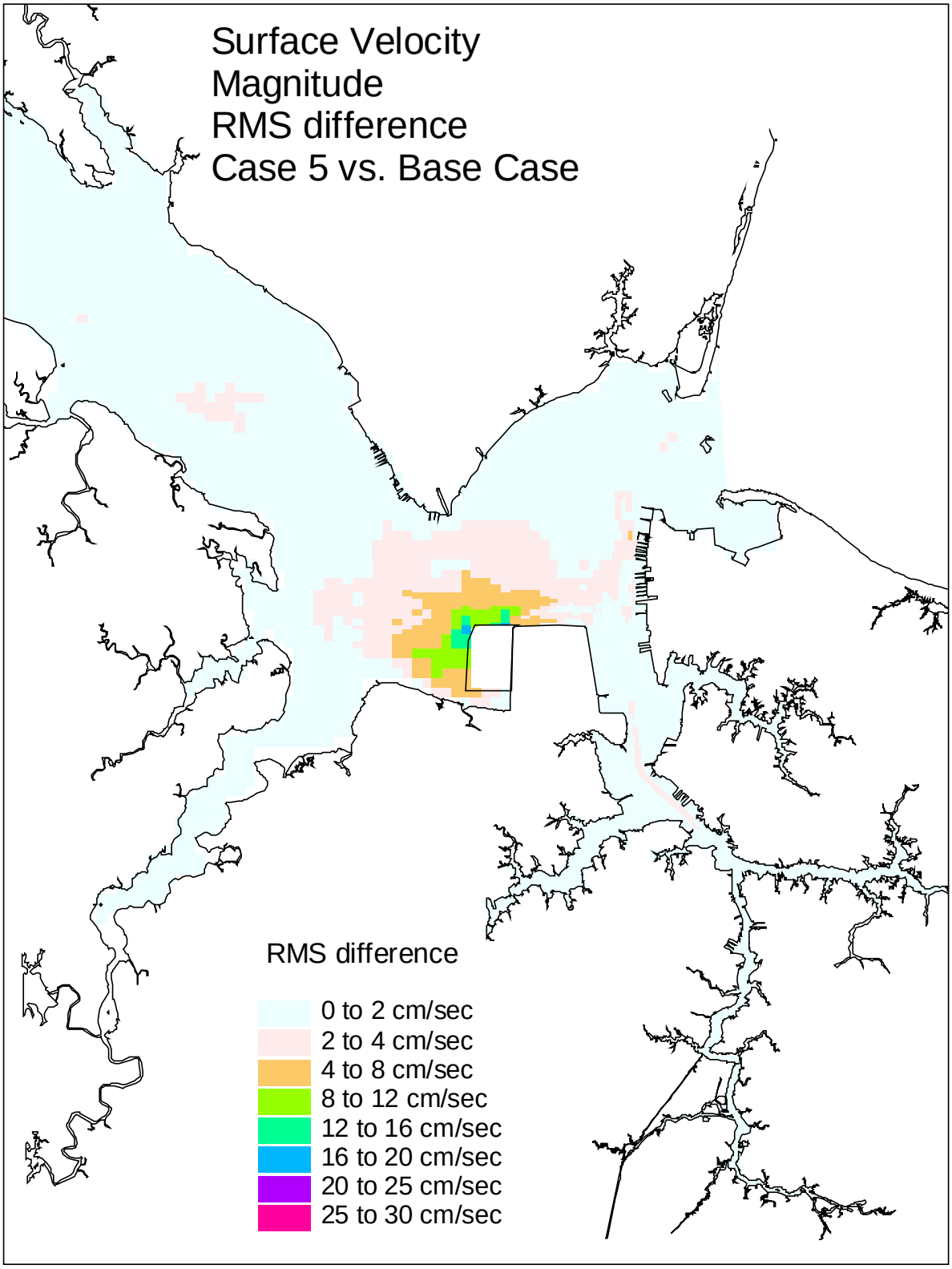

Figue 31. Single variable simulation comparison of the surface velocity RMS difference for the Westward Expansion (Option 5, 55-foot channel) versus the Base Case.

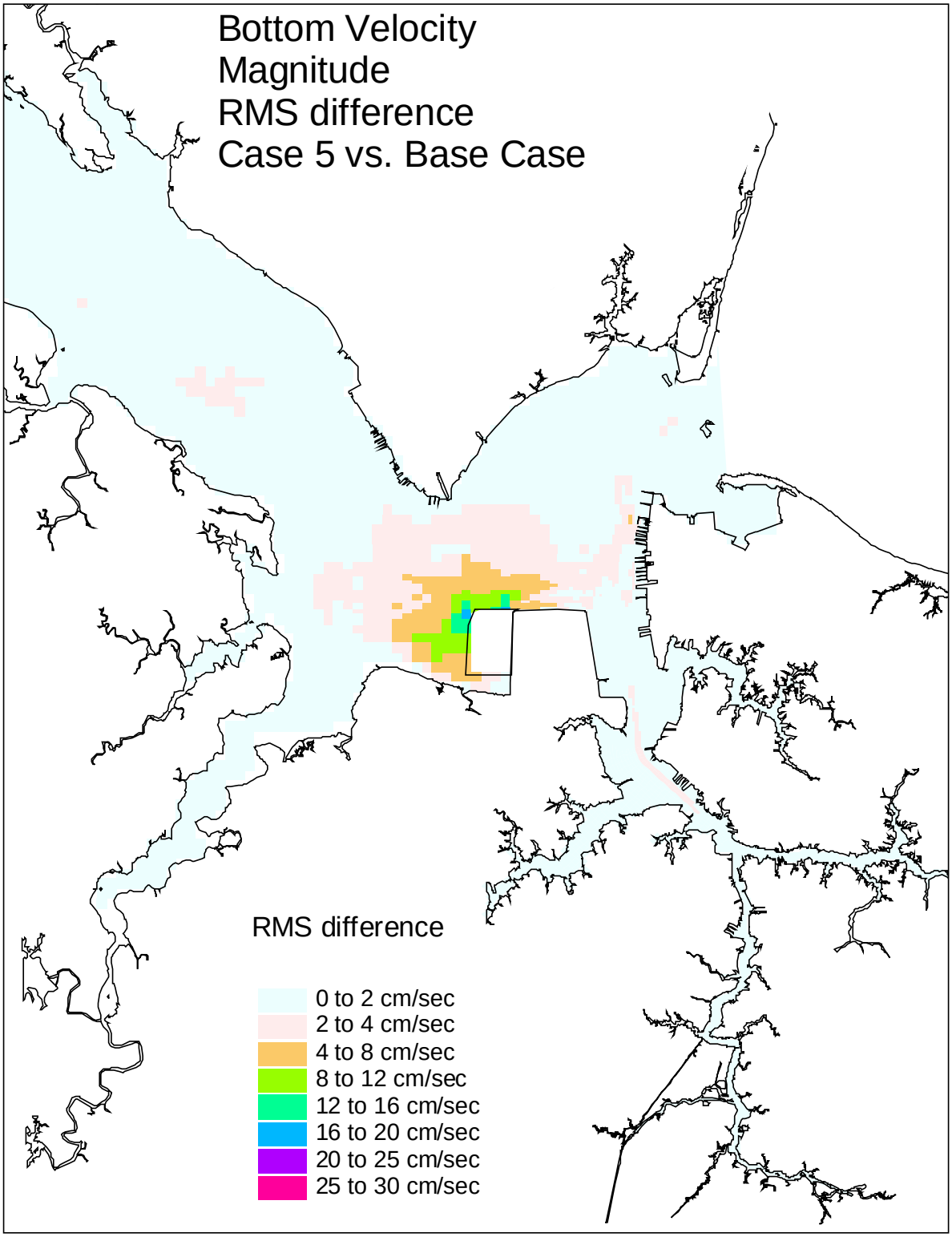

Figure 32. Single variable simulation comparison of the bottom velocity RMS difference for the Westward Expansion (Option 5, 55-foot channel) versus the Base Case.

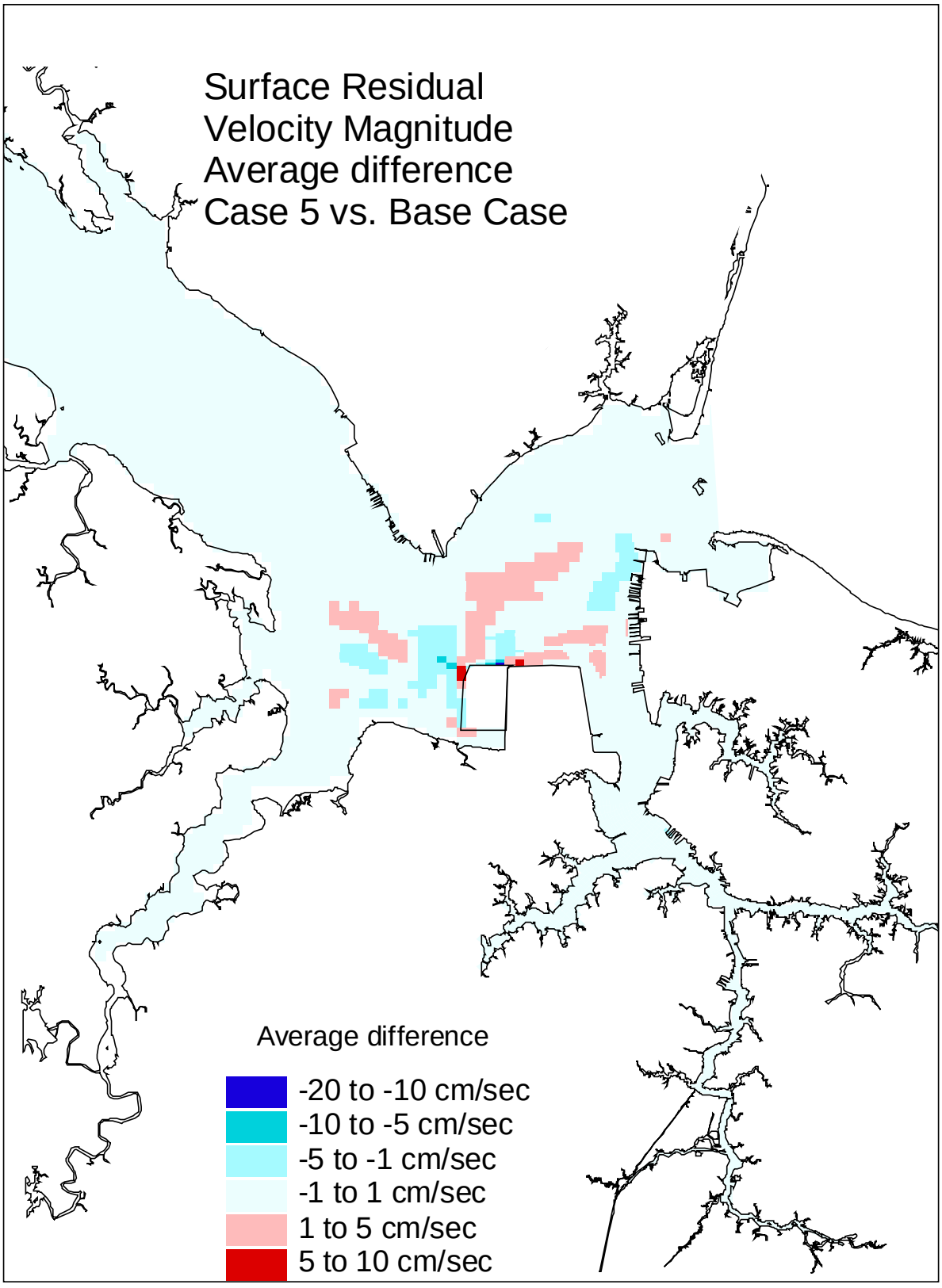

Figure 33. Single variable simulation comparison of the surface residual velocity average difference for the Westward Expansion (Option 5, 55-foot channel) versus the Base Case.

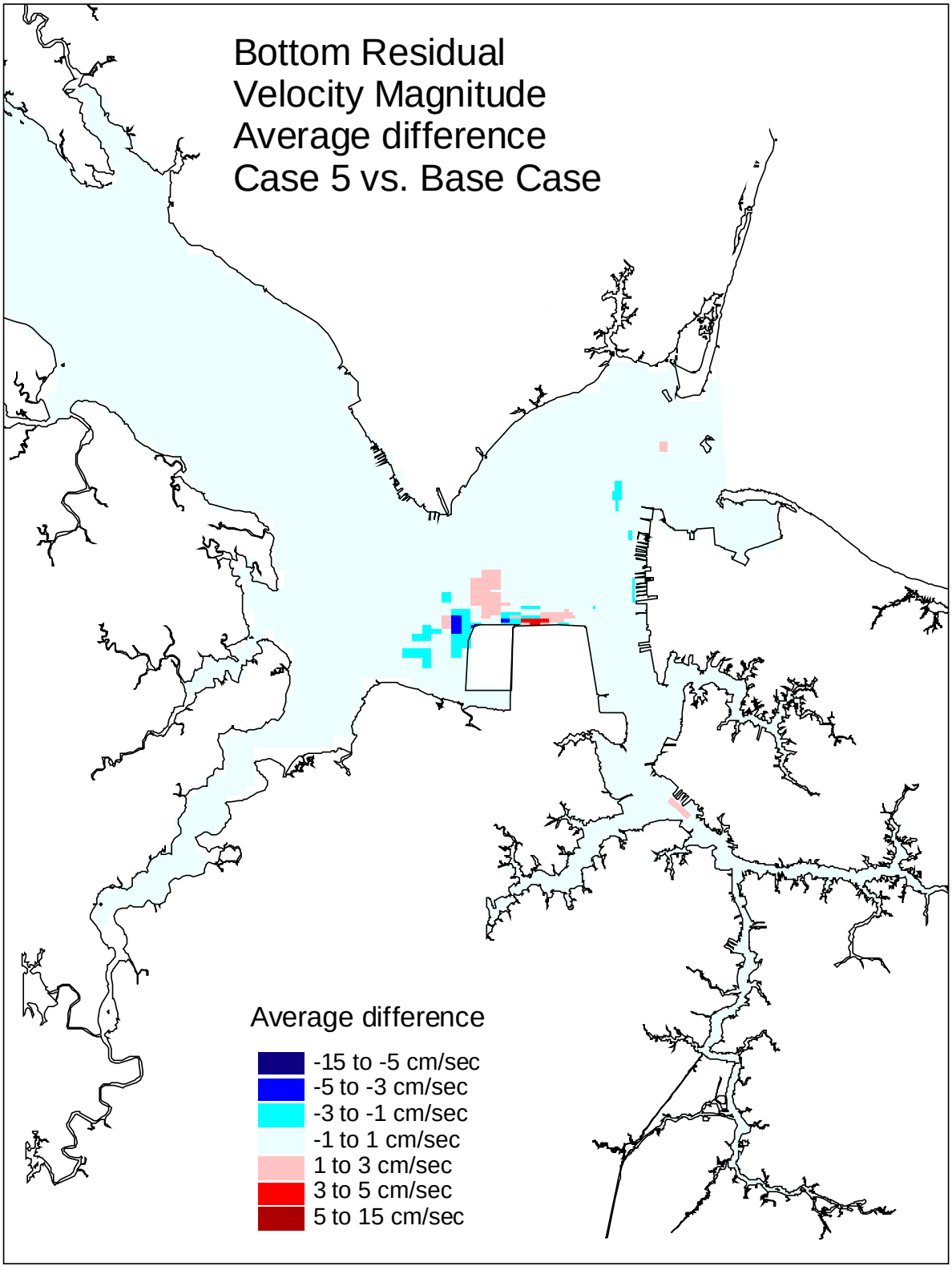

Figure 34. Single variable simulation comparison of the bottom residual velocity average difference for the Westward Expansion (Option 5, 55-foot channel) versus the Base Case.

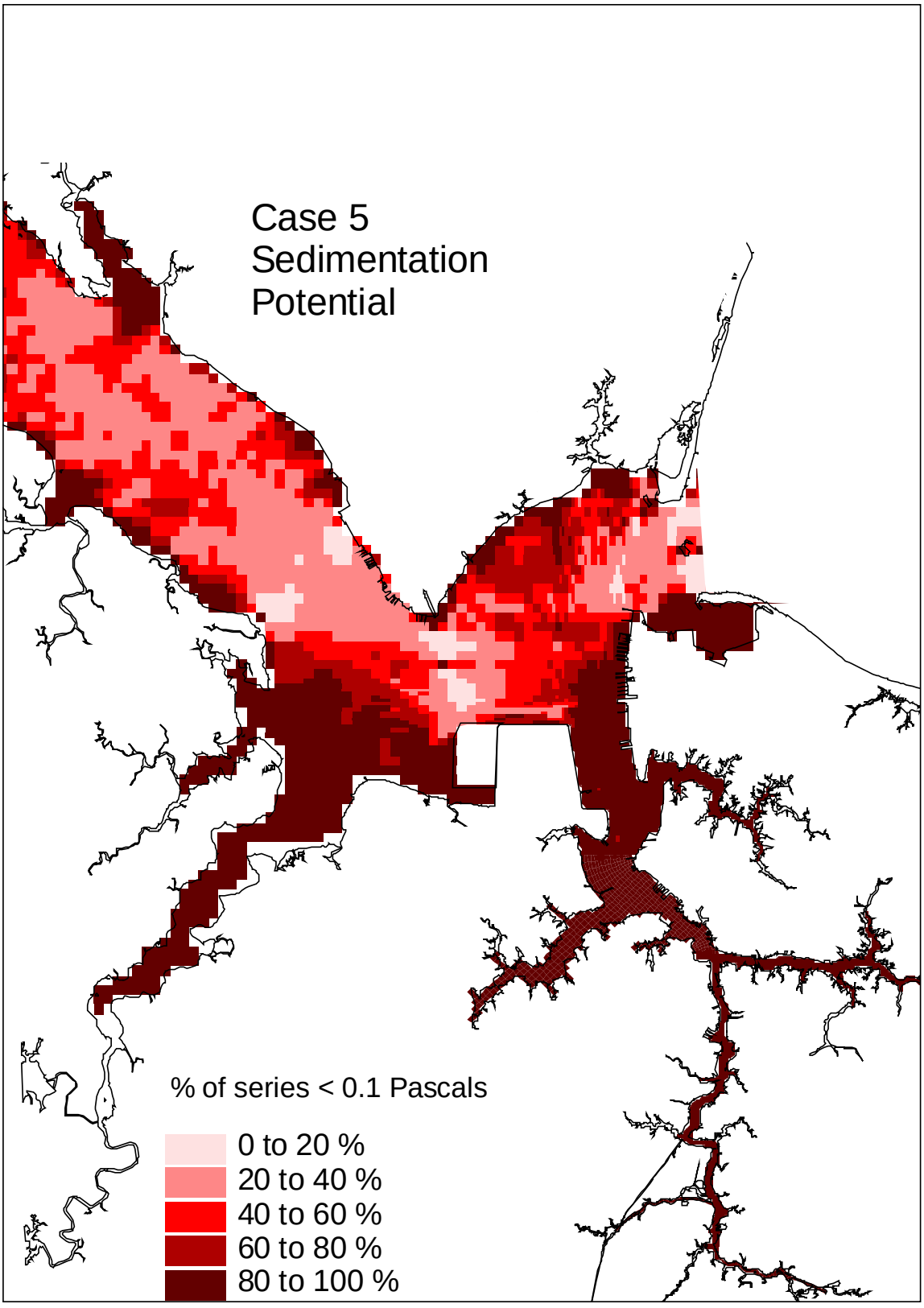

Figure 35. Single variable simulation comparison of the sedimentation potential for the Westward Expansion (Option 5, 55-foot channel).

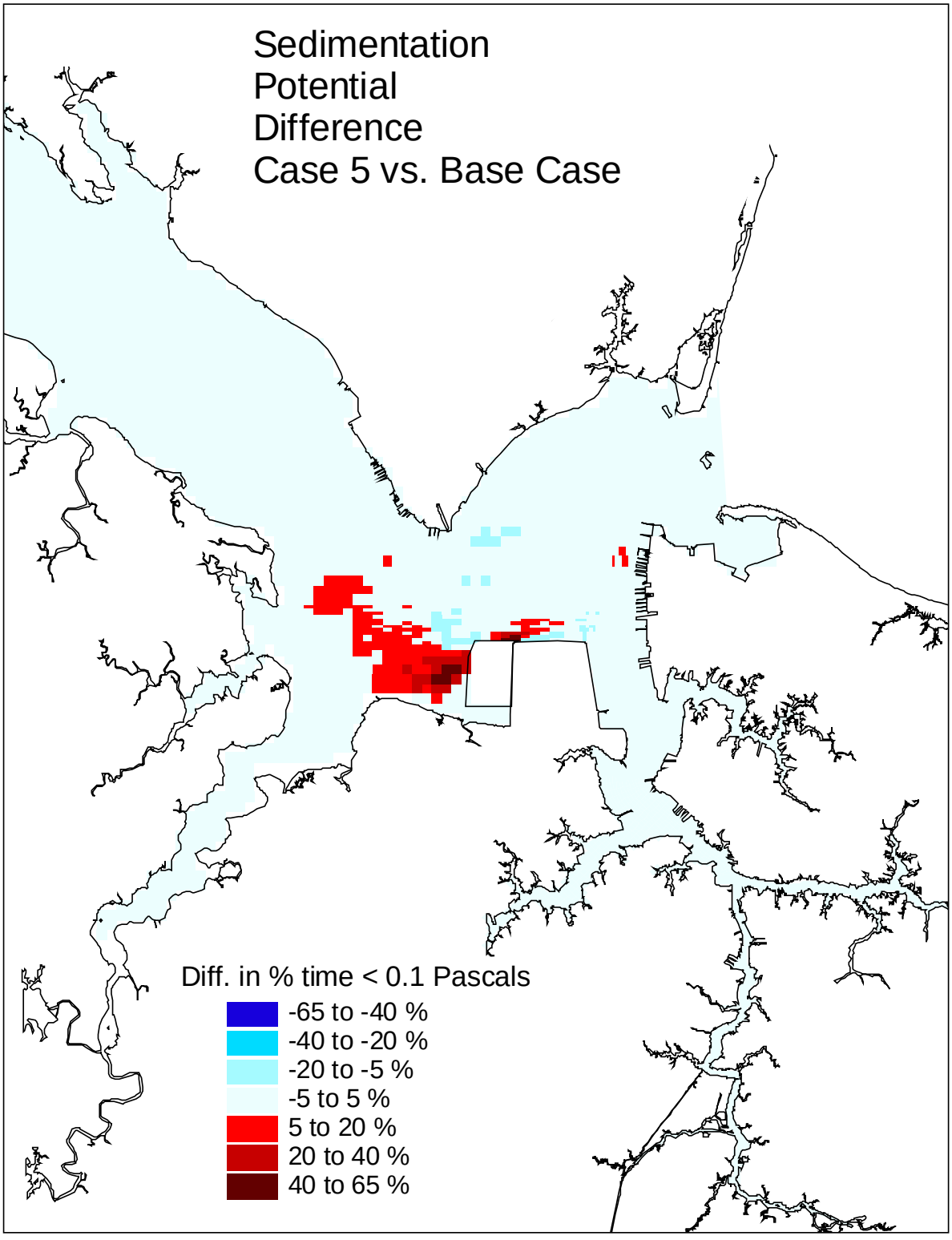

Figure 36. Single variable simulation comparison of the sedimentation potential difference for the Westward Expansion (Option 5, 55-foot channel) versus the Base Case.

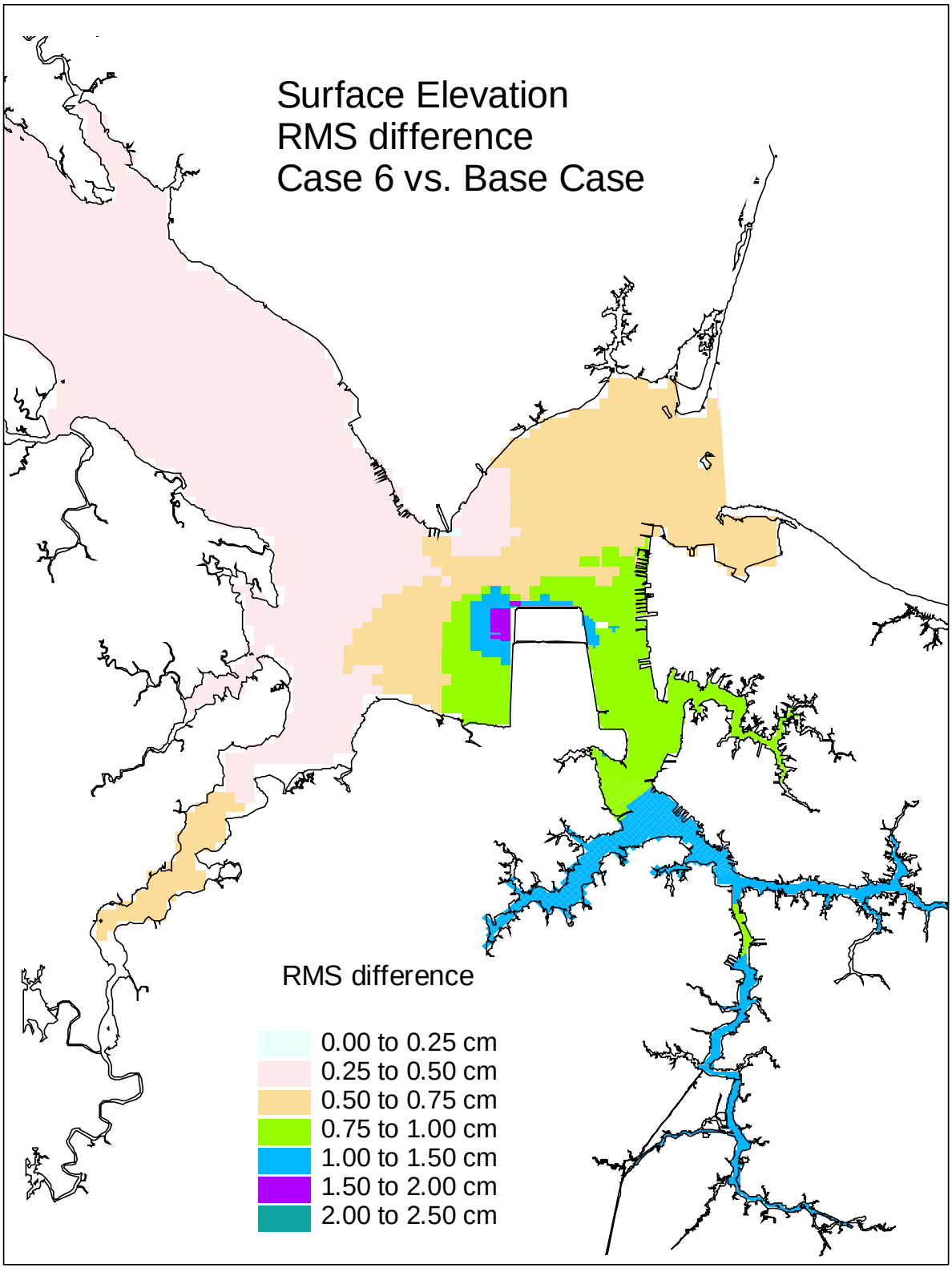

Figure 37. Single variable simulation comparison of the surface elevation RMS difference for the Northward Expansion (Option 6, 50-foot channel) versus the Base Case.

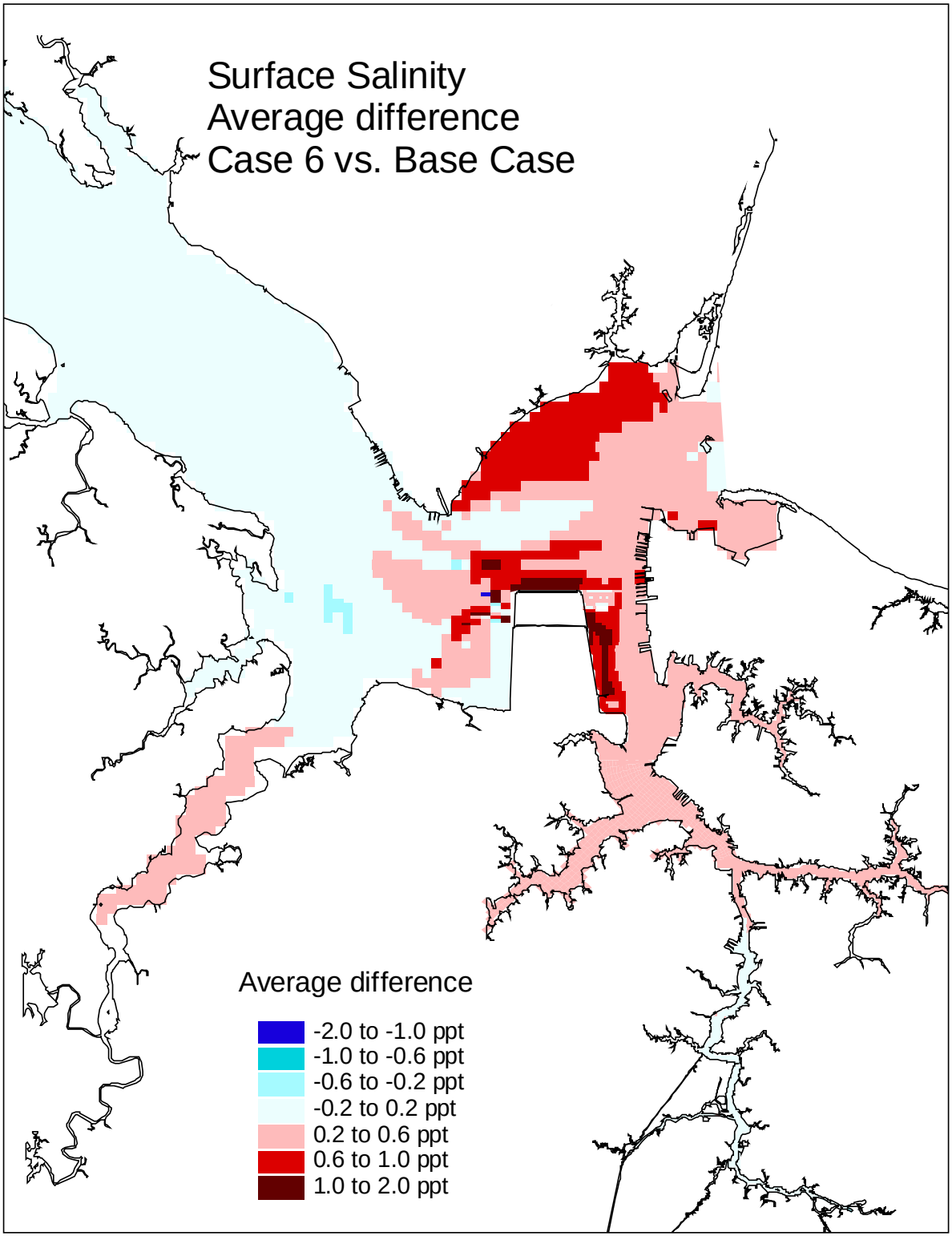

Figure 38. Single variable simulation comparison of the surface salinity average difference for the Northward Expansion (Option 6, 50-foot channel) versus the Base Case.

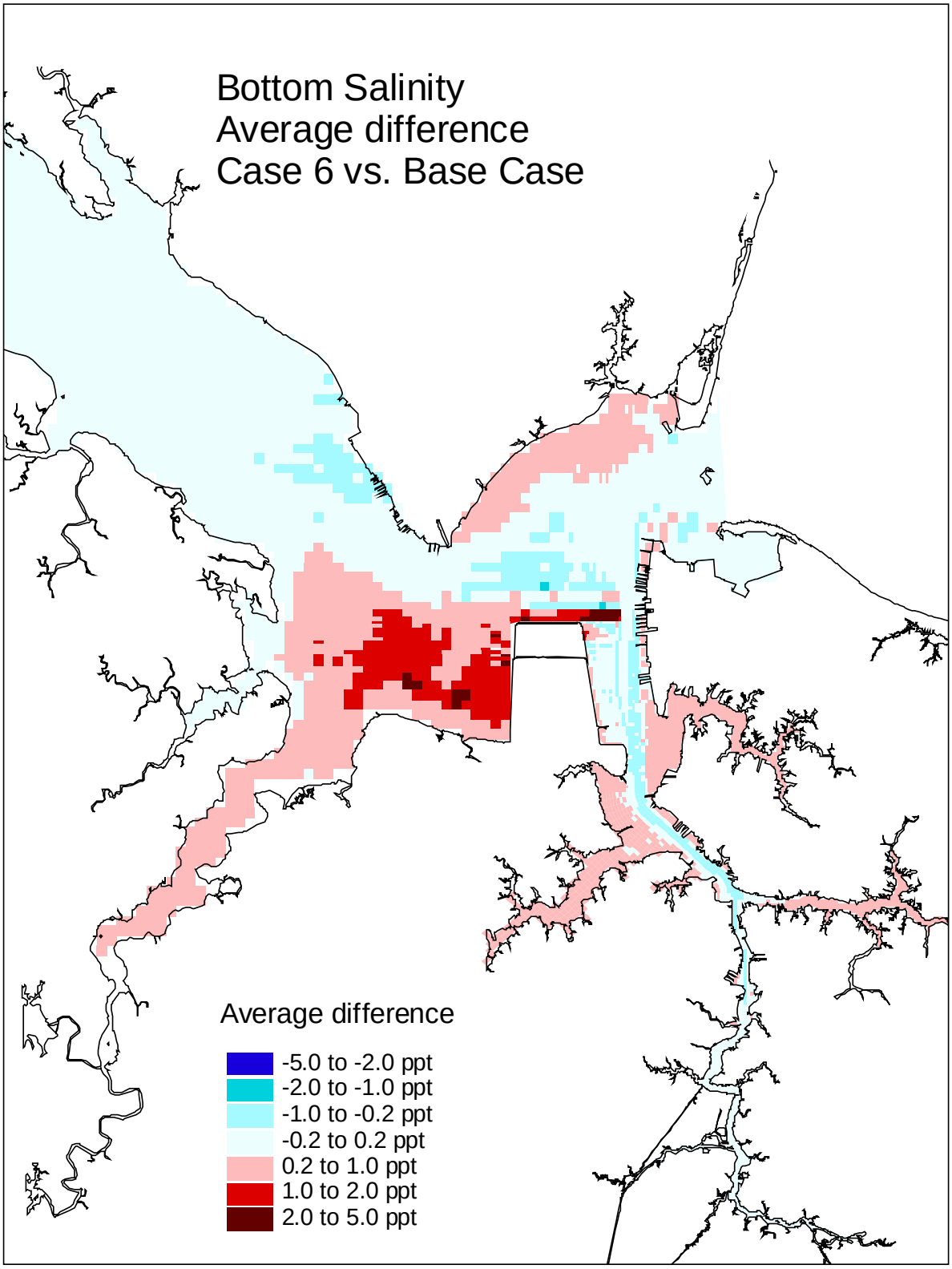

Figure 39. Single variable simulation comparison of the bottom salinity average difference for the Northward Expansion (Option 6, 50-foot channel) versus the Base Case.

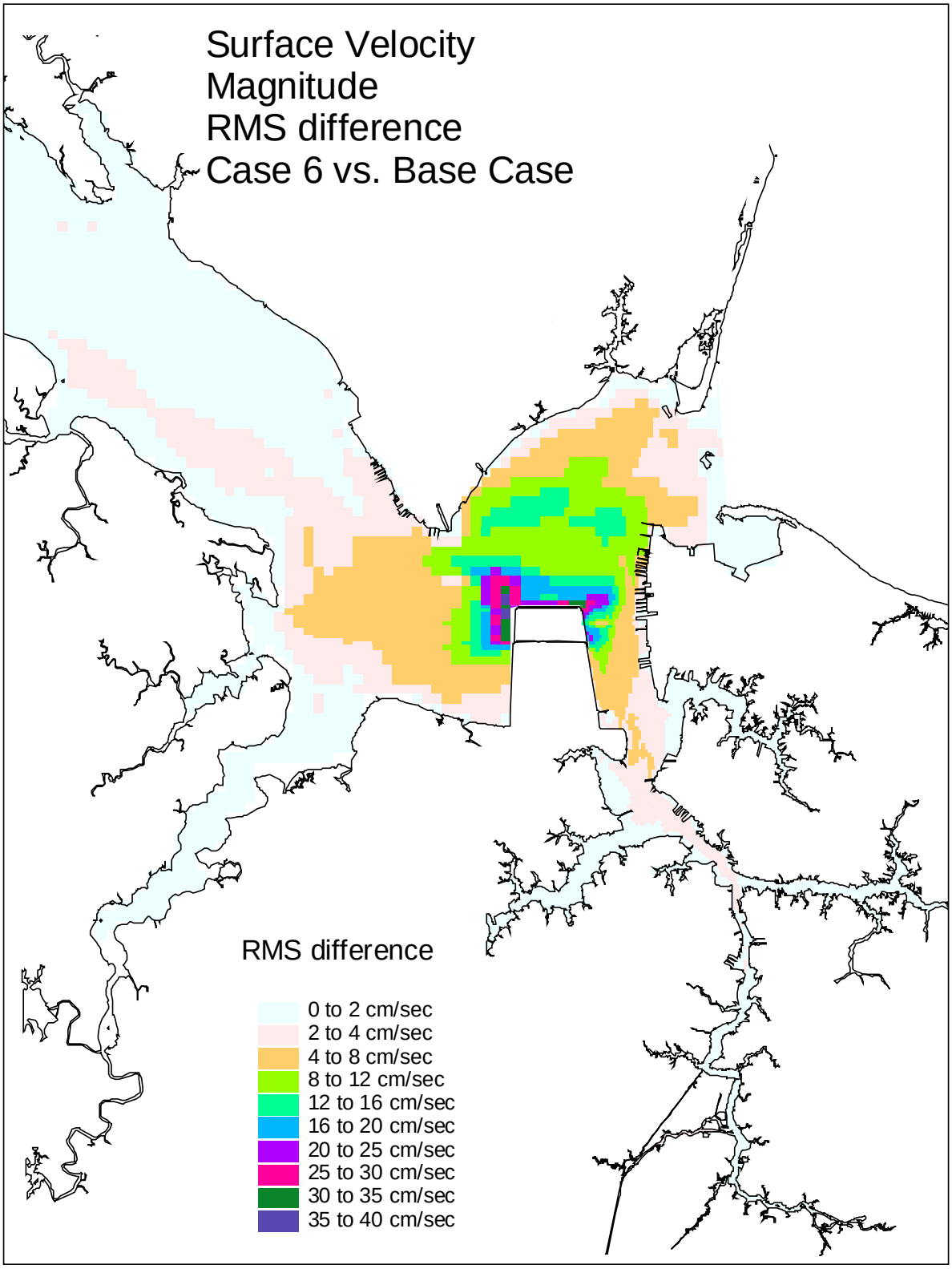

Figure 40. Single variable simulation comparison of the surface velocity RMS difference for the Northward Expansion (Option 6, 50-foot channel) versus the Base Case.

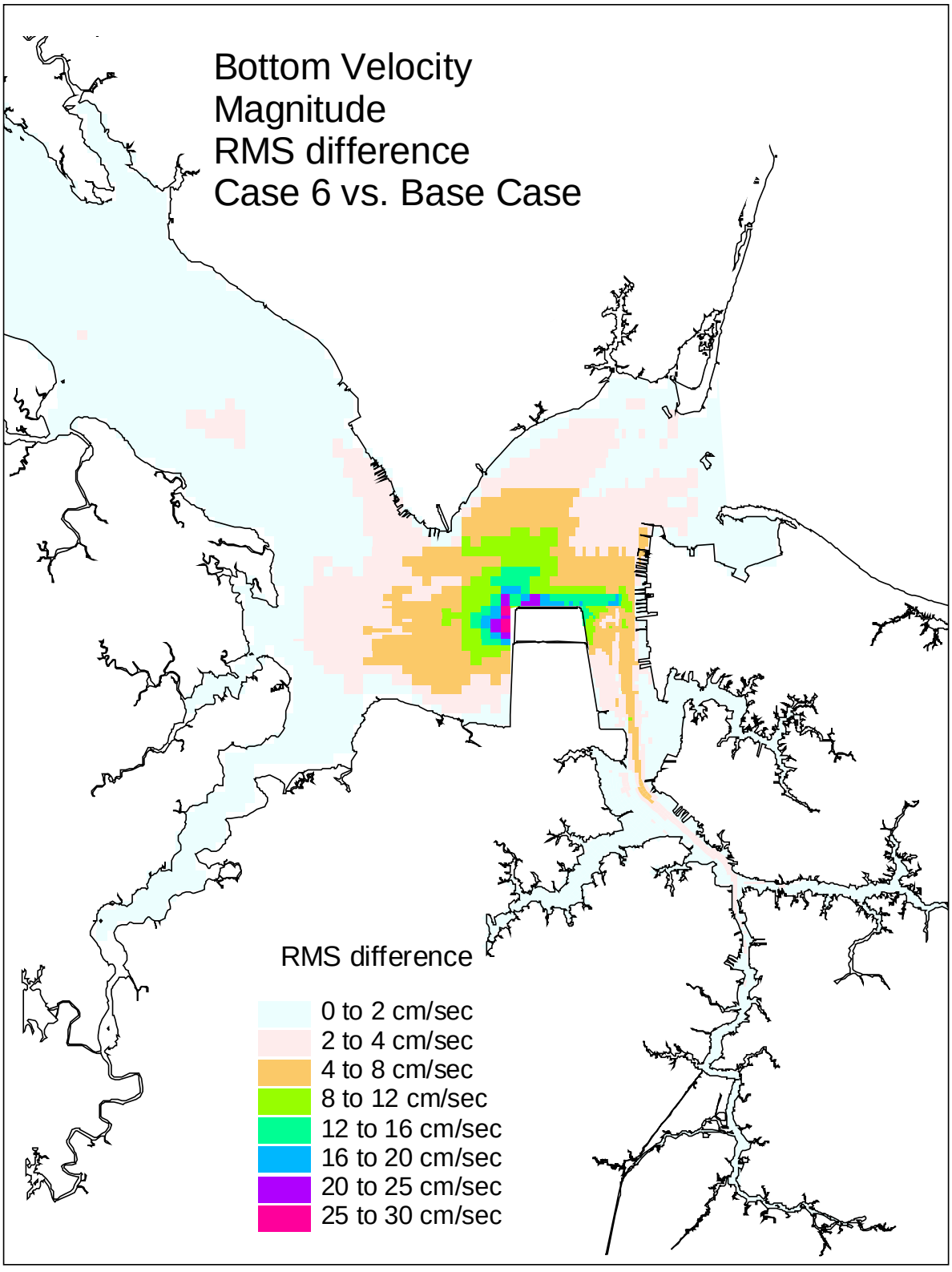

Figure 41. Single variable simulation comparison of the bottom velocity RMS difference for the Northward Expansion (Option 6, 50-foot channel) versus the Base Case.

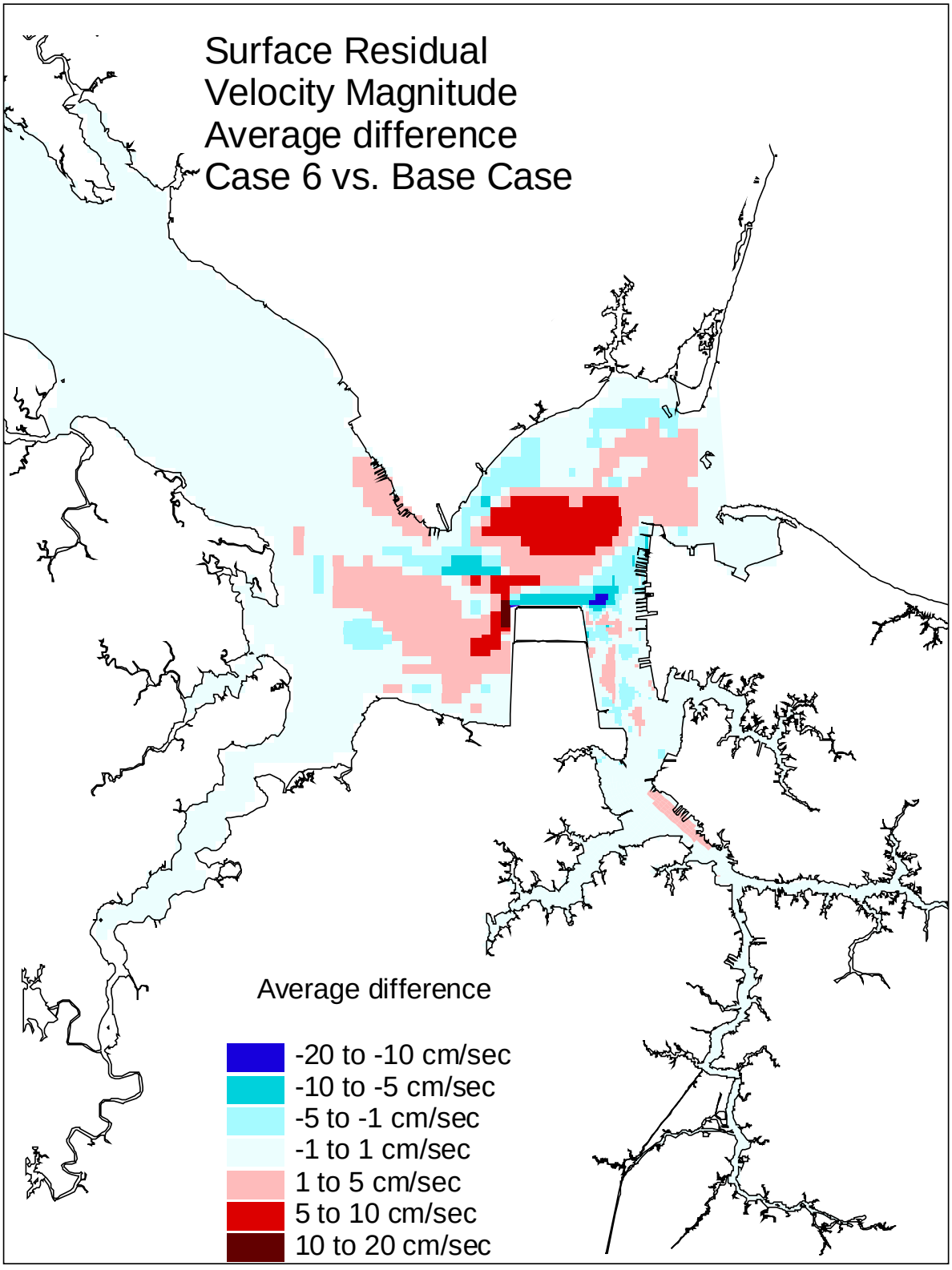

Figure 42. Single variable simulation comparison of the surface residual velocity average difference for the Northward Expansion (Option 6, 50-foot channel) versus the Base Case.

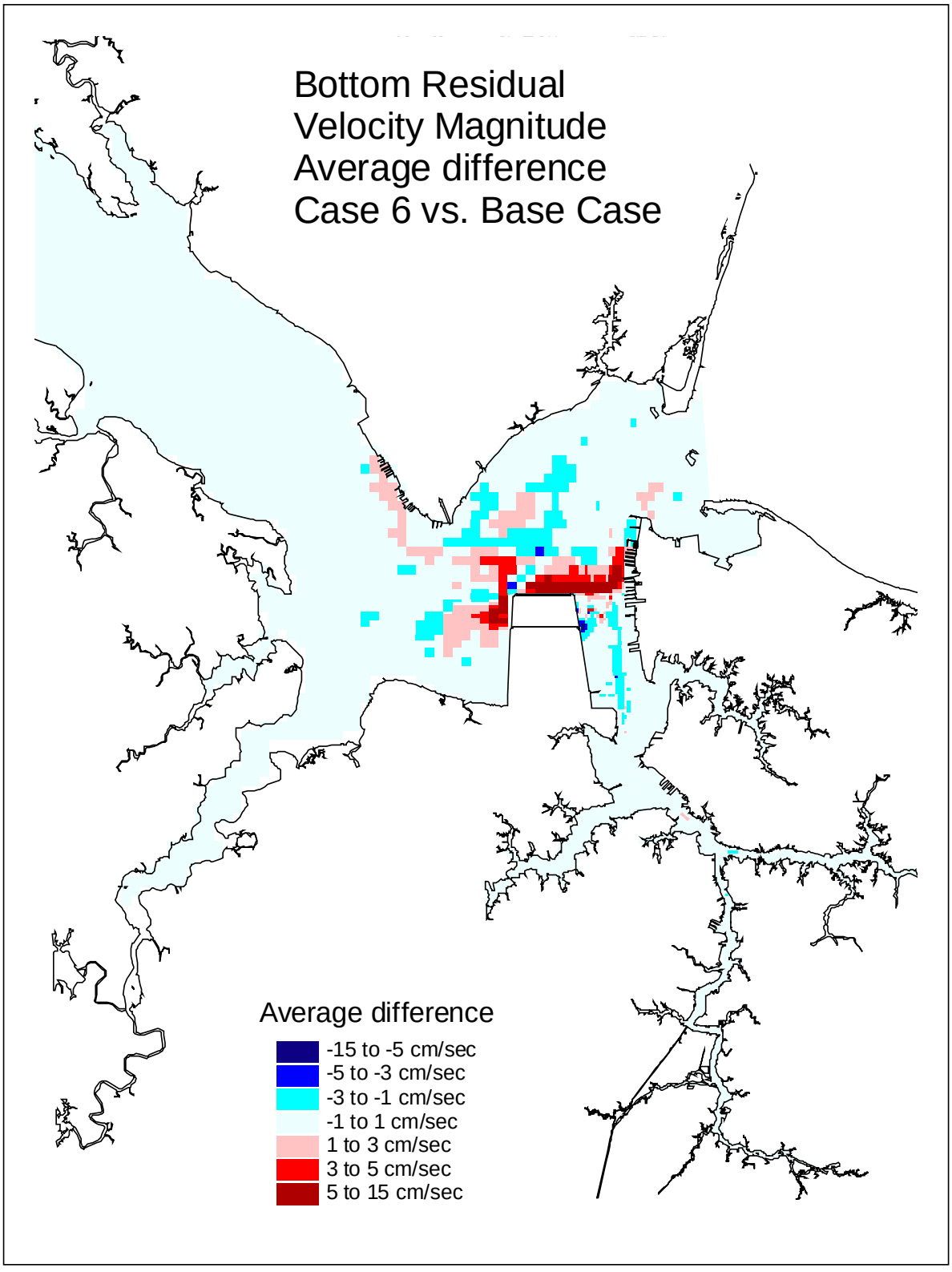

Figure 43. Single variable simulation comparison of the bottom residual velocity average difference for the Northward Expansion (Option 6, 50-foot channel) versus the Base Case.

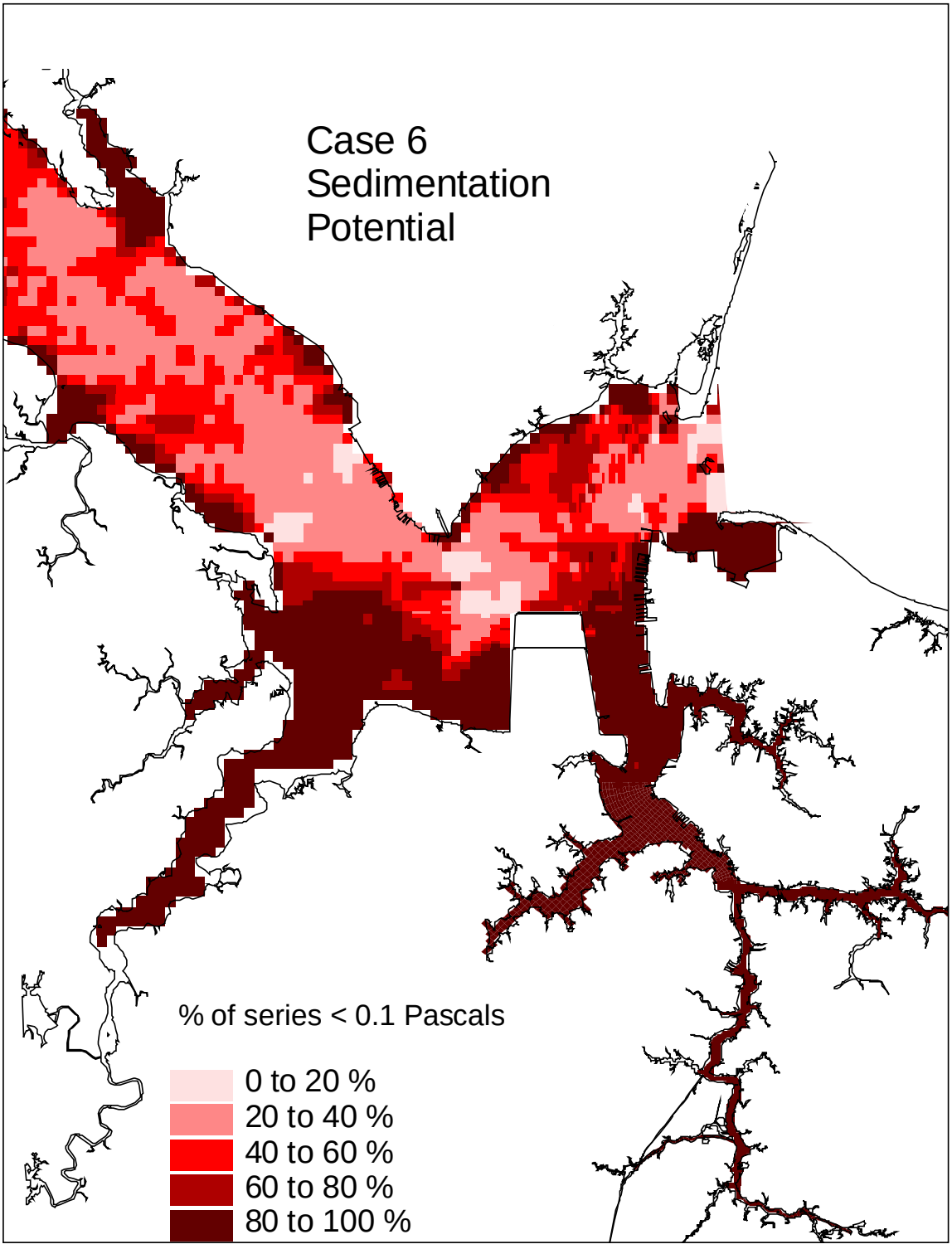

Figure 44. Single variable simulation comparison of the sedimentation potential for the Northward Expansion (Option 6, 50-foot channel).

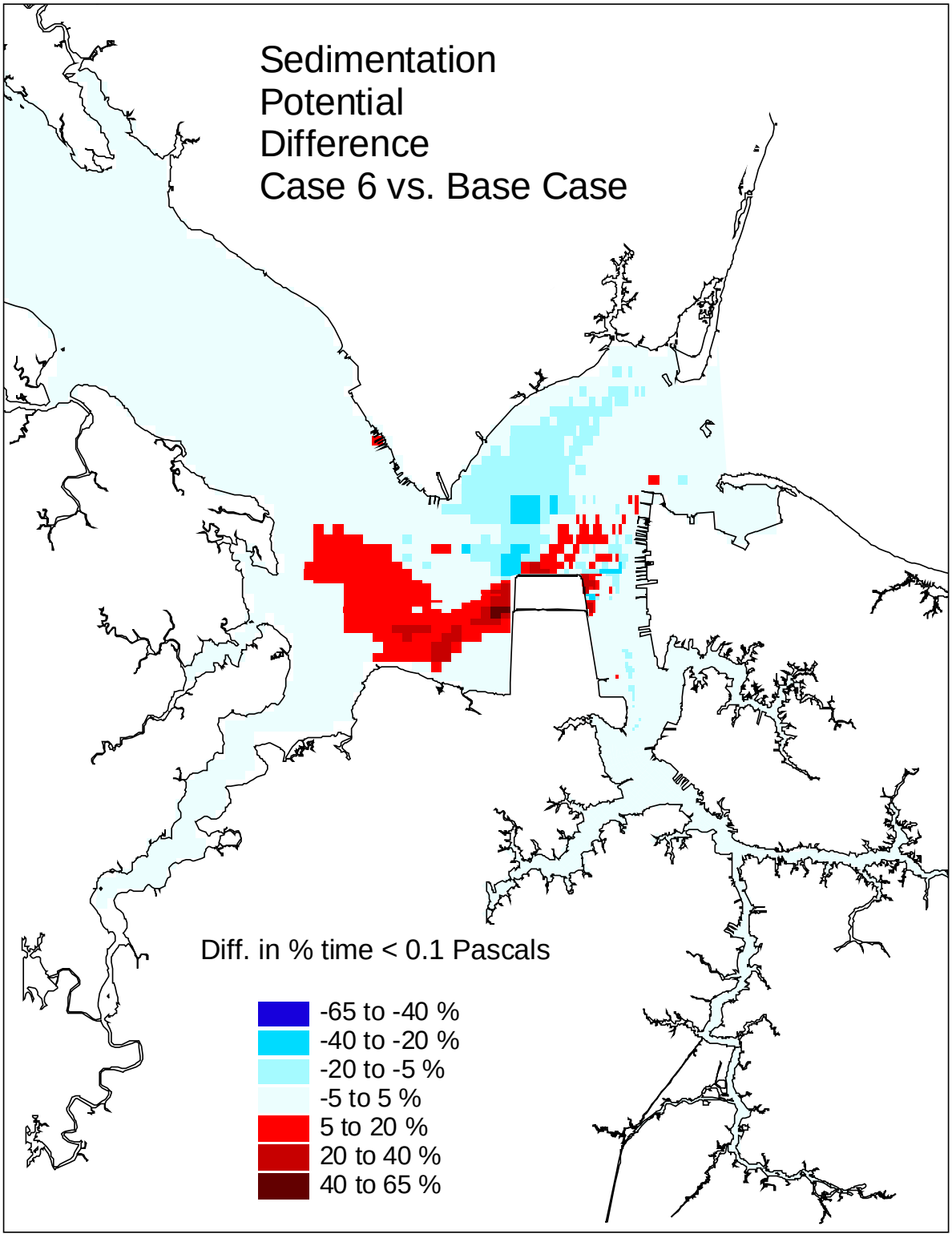

Figure 45. Single variable simulation comparison of the sedimentation potential difference for the Northward Expansion (Option 6, 50-foot channel) versus the Base Case.

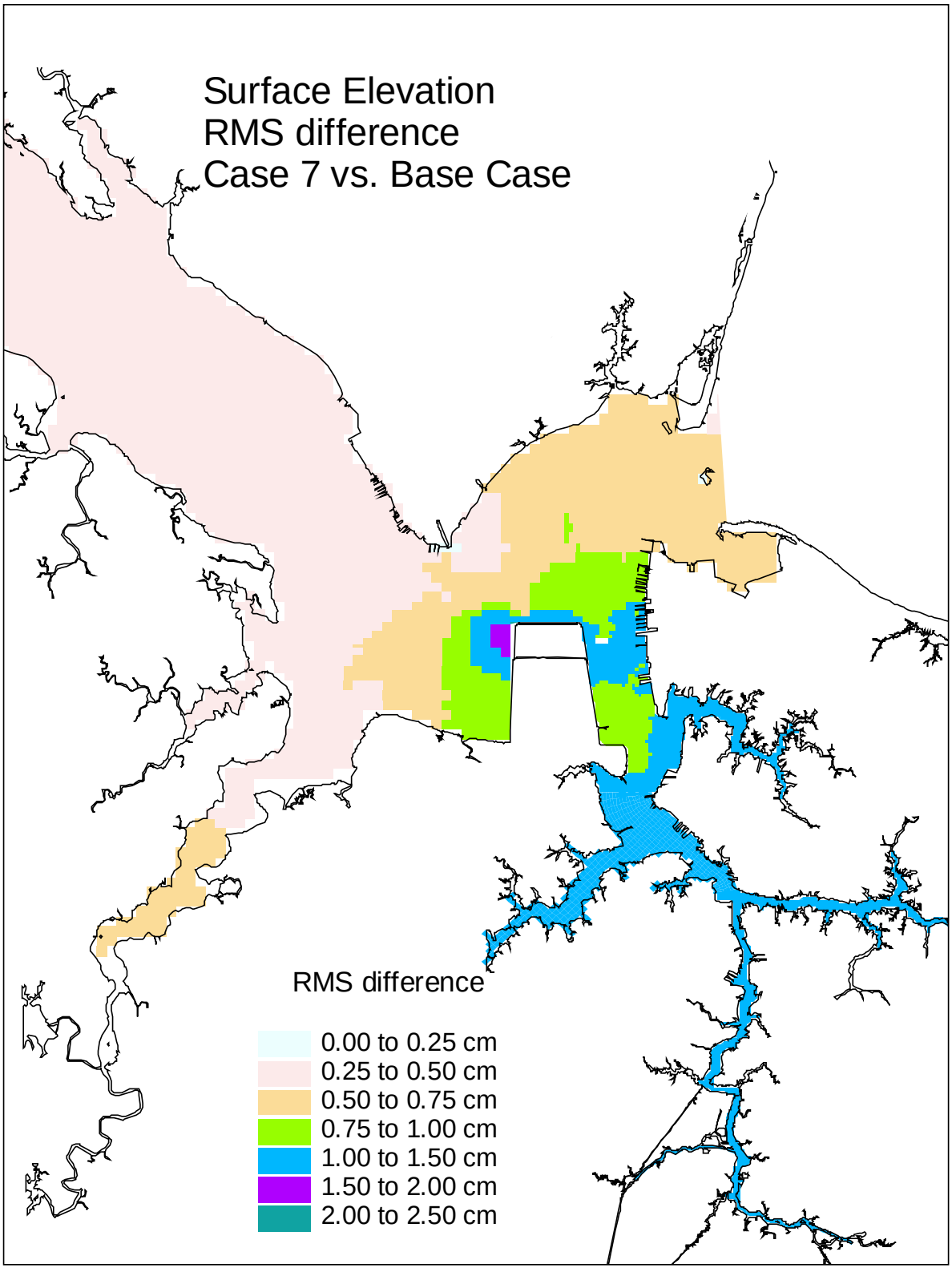

Figure 46. Single variable simulation comparison of the surface elevation RMS difference for the Northward Expansion (Option 6, 55-foot channel) versus the Base Case.

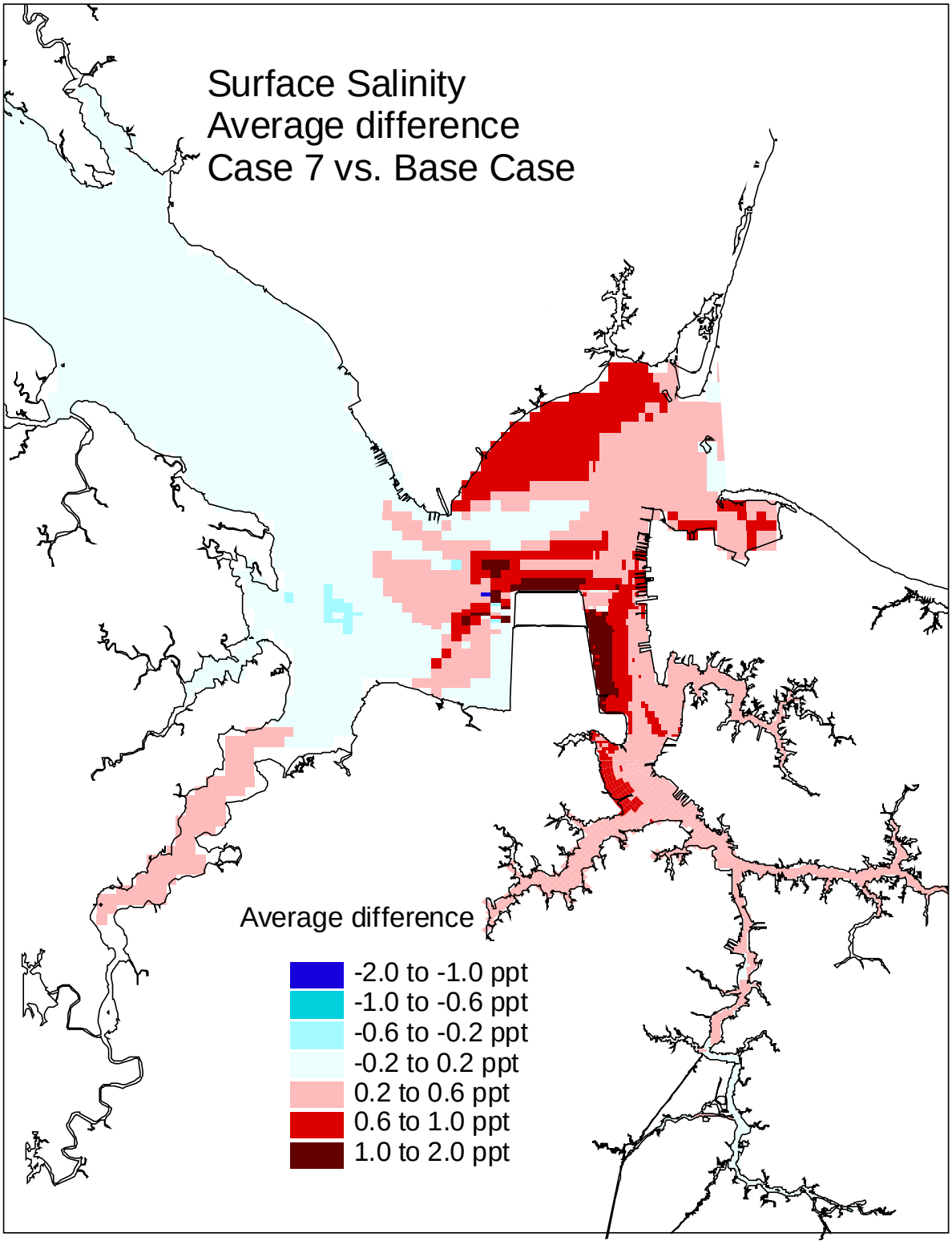

Figure 47. Single variable simulation comparison of the surface salinity average difference for the Northward Expansion (Option 6, 55-foot channel) versus the Base Case.

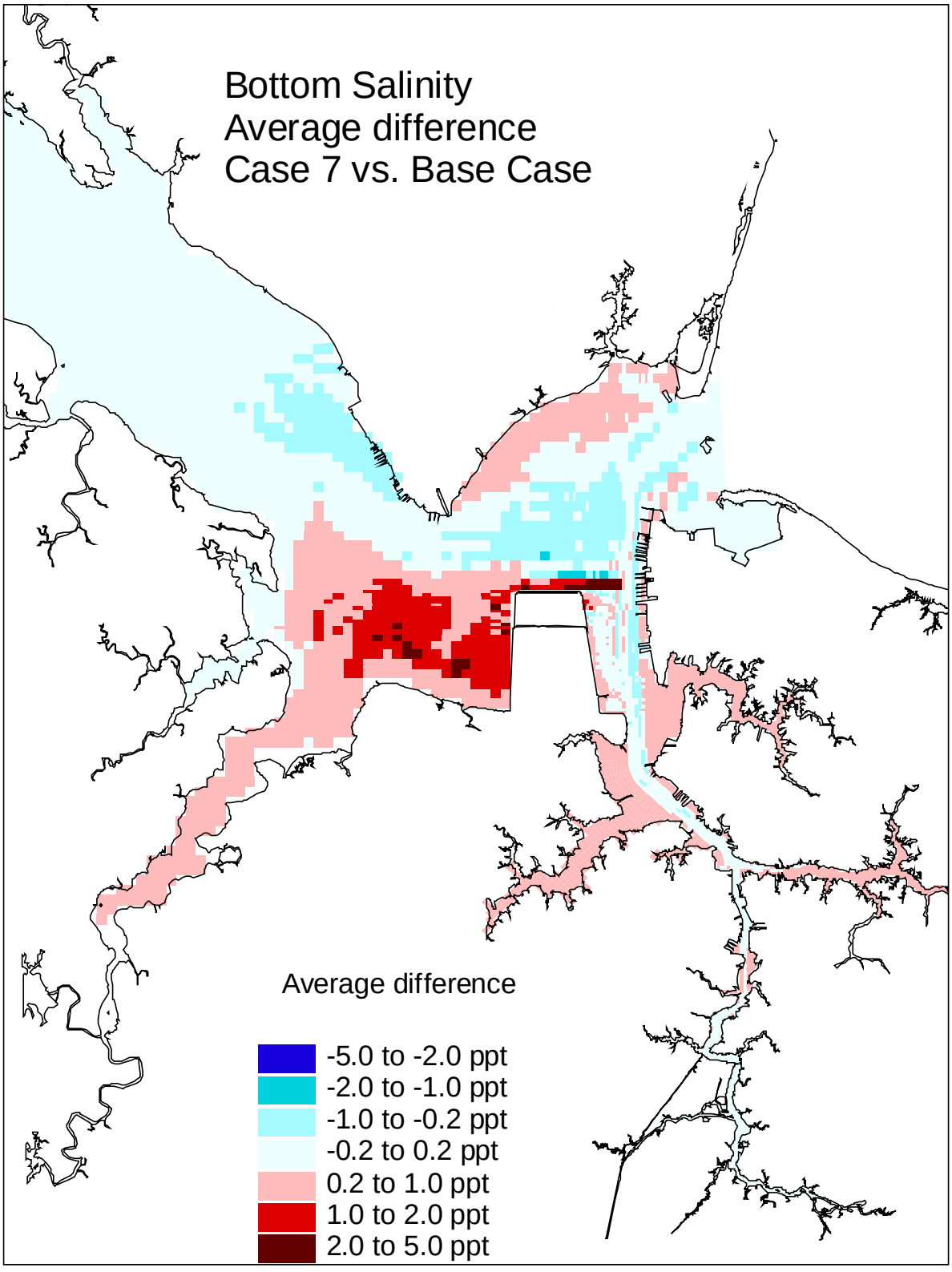

Figure 48. Single variable simulation comparison of the bottom salinity average difference for the Northward Expansion (Option 6, 55-foot channel) versus the Base Case.

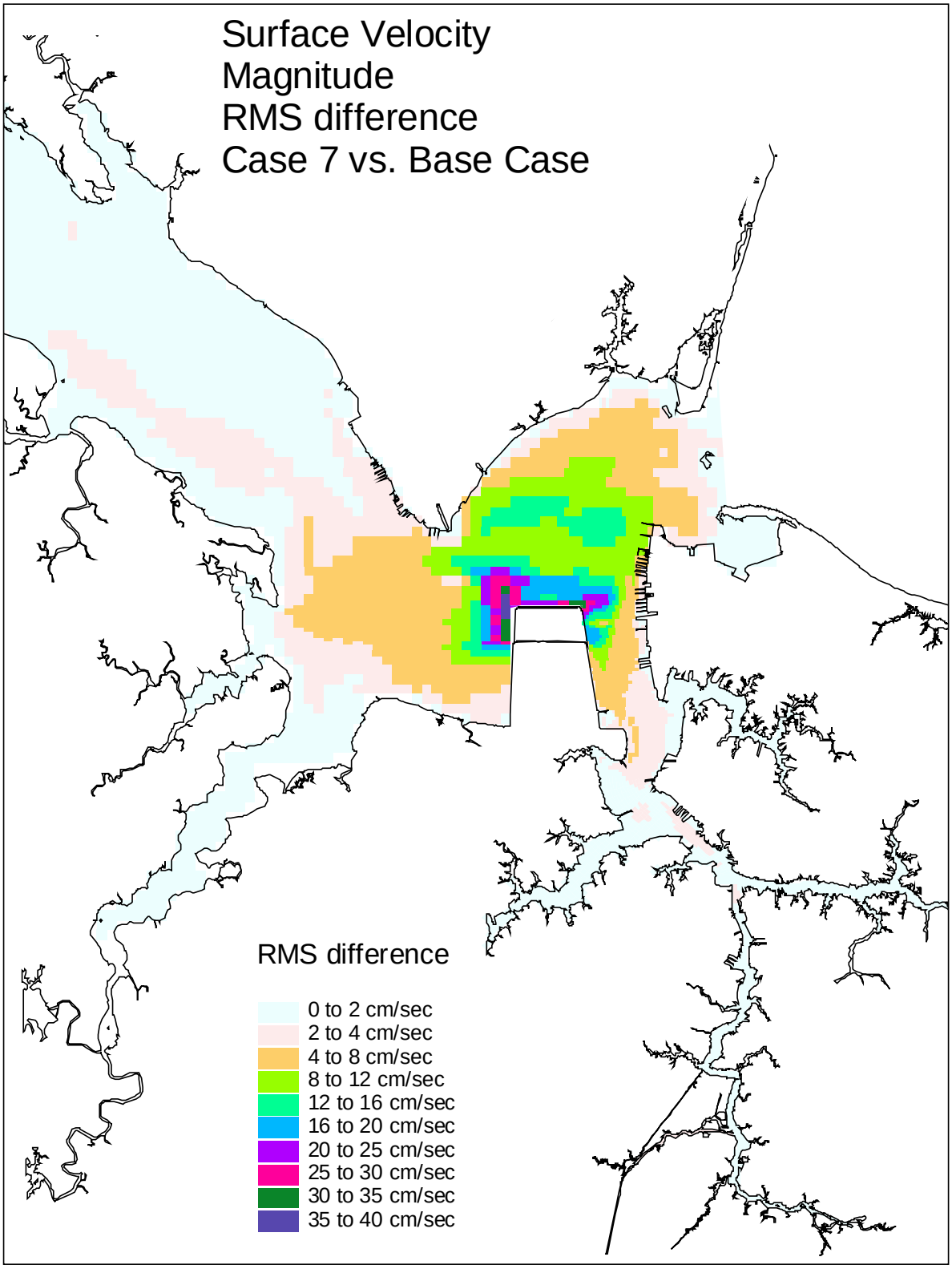

Figure 49. Single variable simulation comparison of the surface velocity RMS difference for the Northward Expansion (Option 6, 55-foot channel) versus the Base Case.

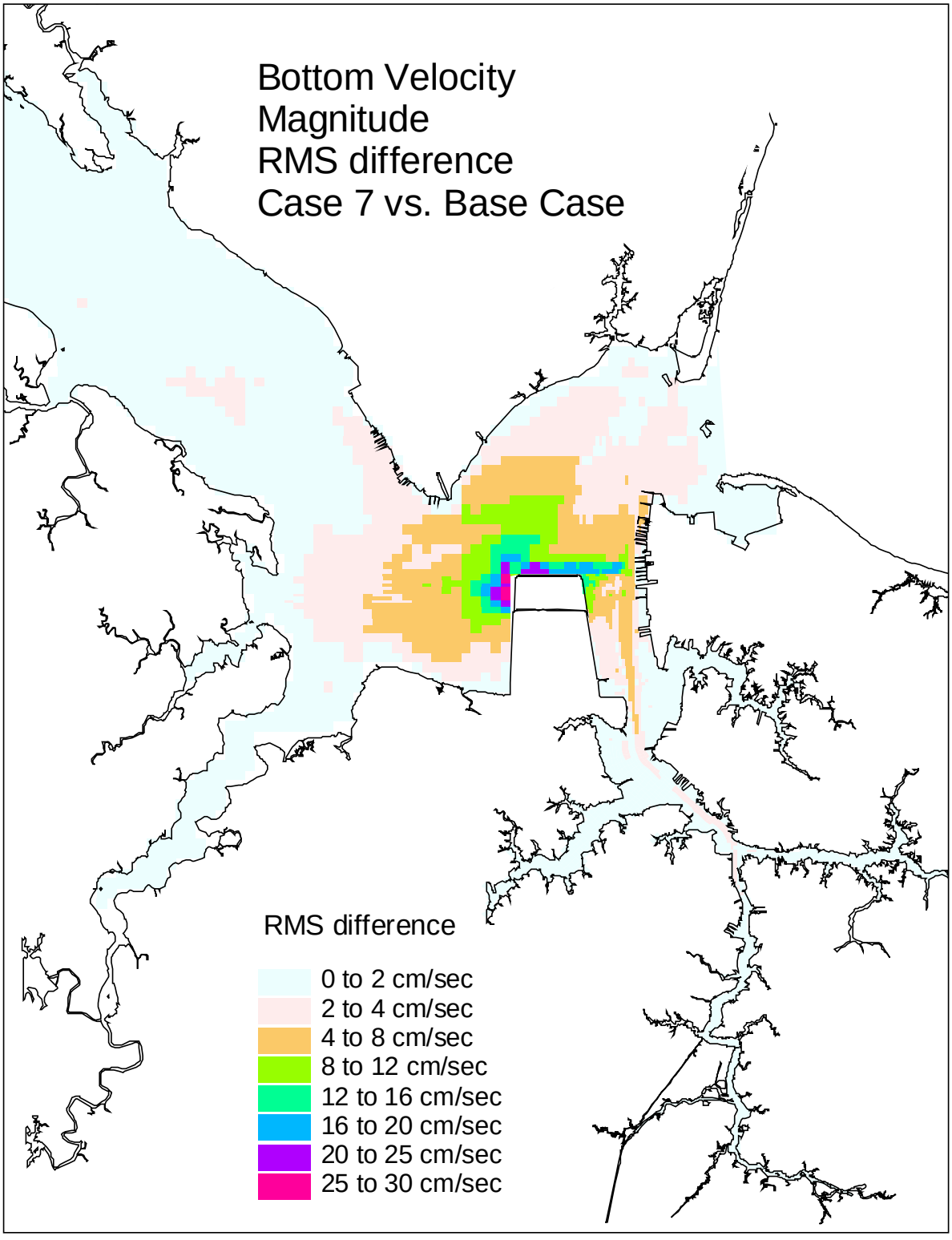

Figure 50. Single variable simulation comparison of the bottom velocity RMS difference for the Northward Expansion (Option 6, 55-foot channel) versus the Base Case.

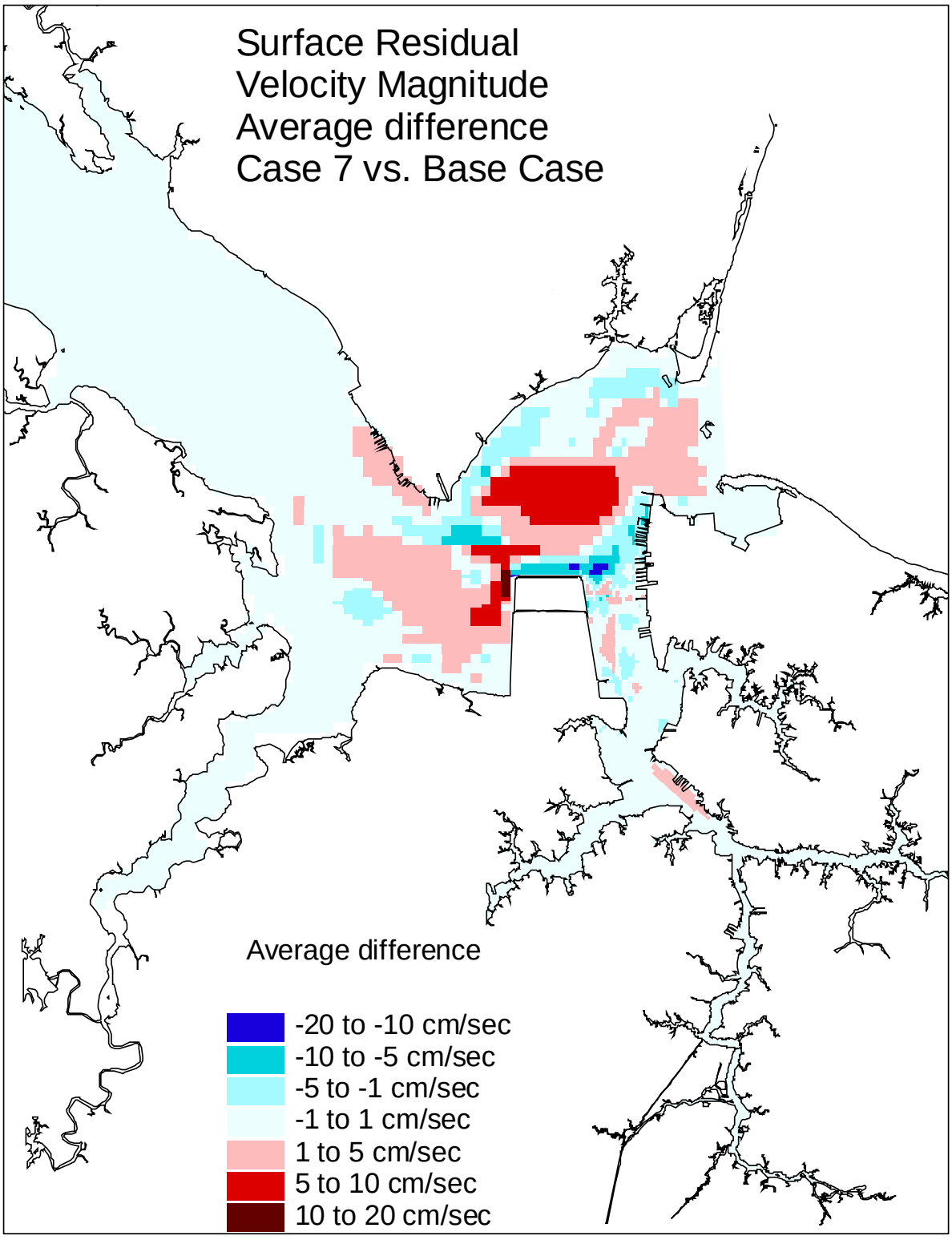

Figure 51. Single variable simulation comparison of the surface residual velocity average difference for the Northward Expansion (Option 6, 55-foot channel) versus the Base Case.

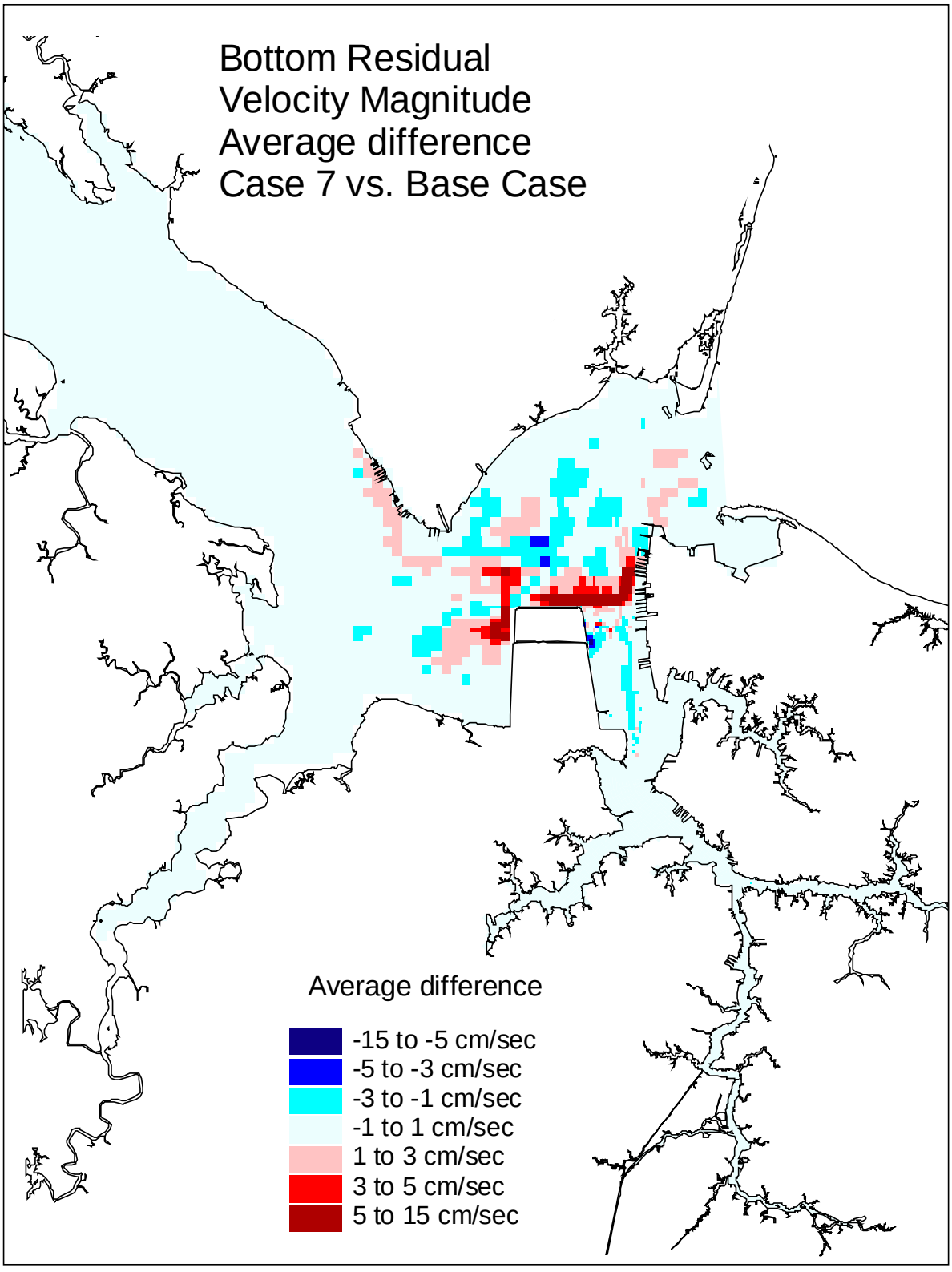

Figure 52. Single variable simulation comparison of the bottom residual velocity average difference for the Northward Expansion (Option 6, 55-foot channel) versus the Base Case.

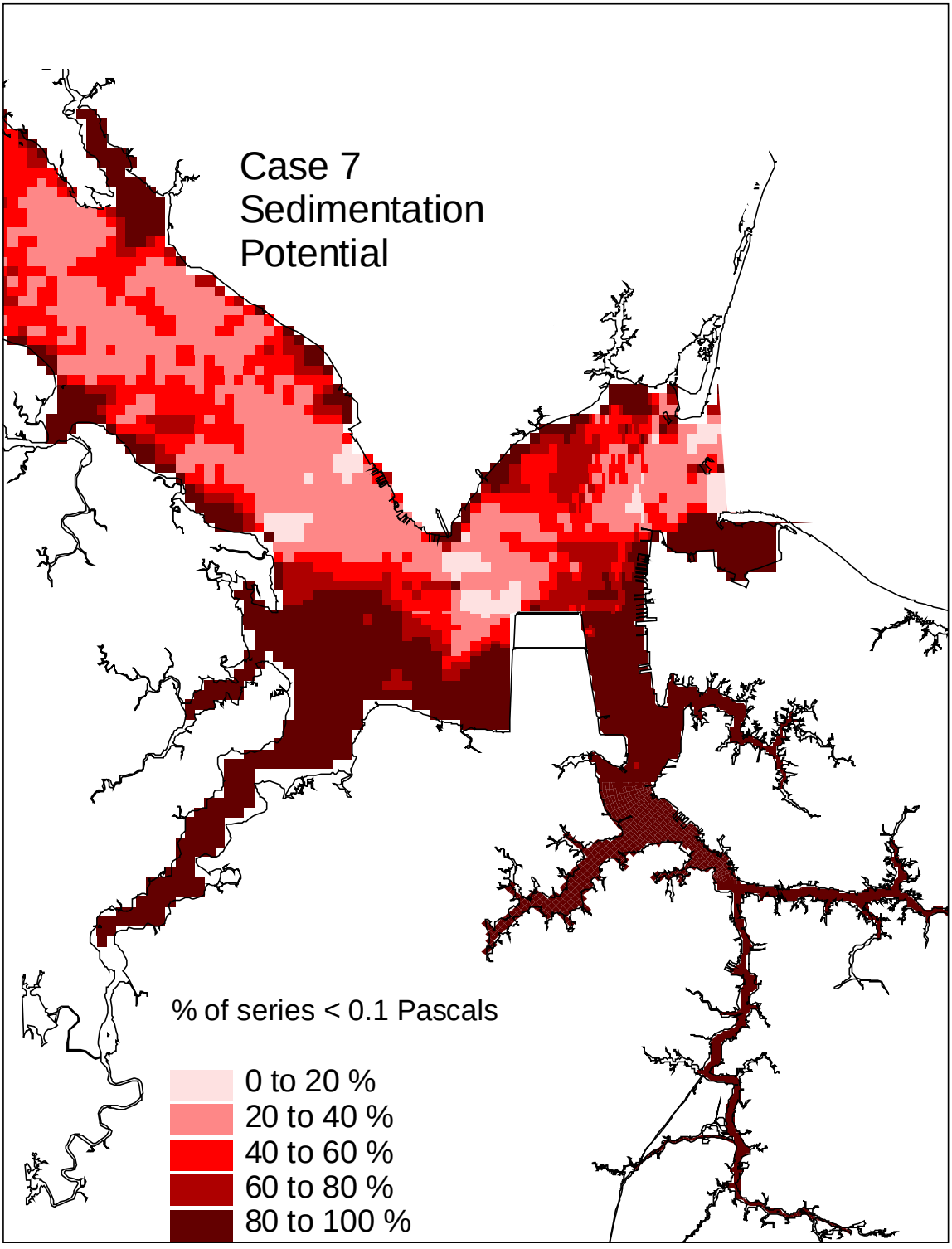

Figure 53. Single variable simulation comparison of the sedimentation potential for the Northward Expansion (Option 6, 55-foot channel)

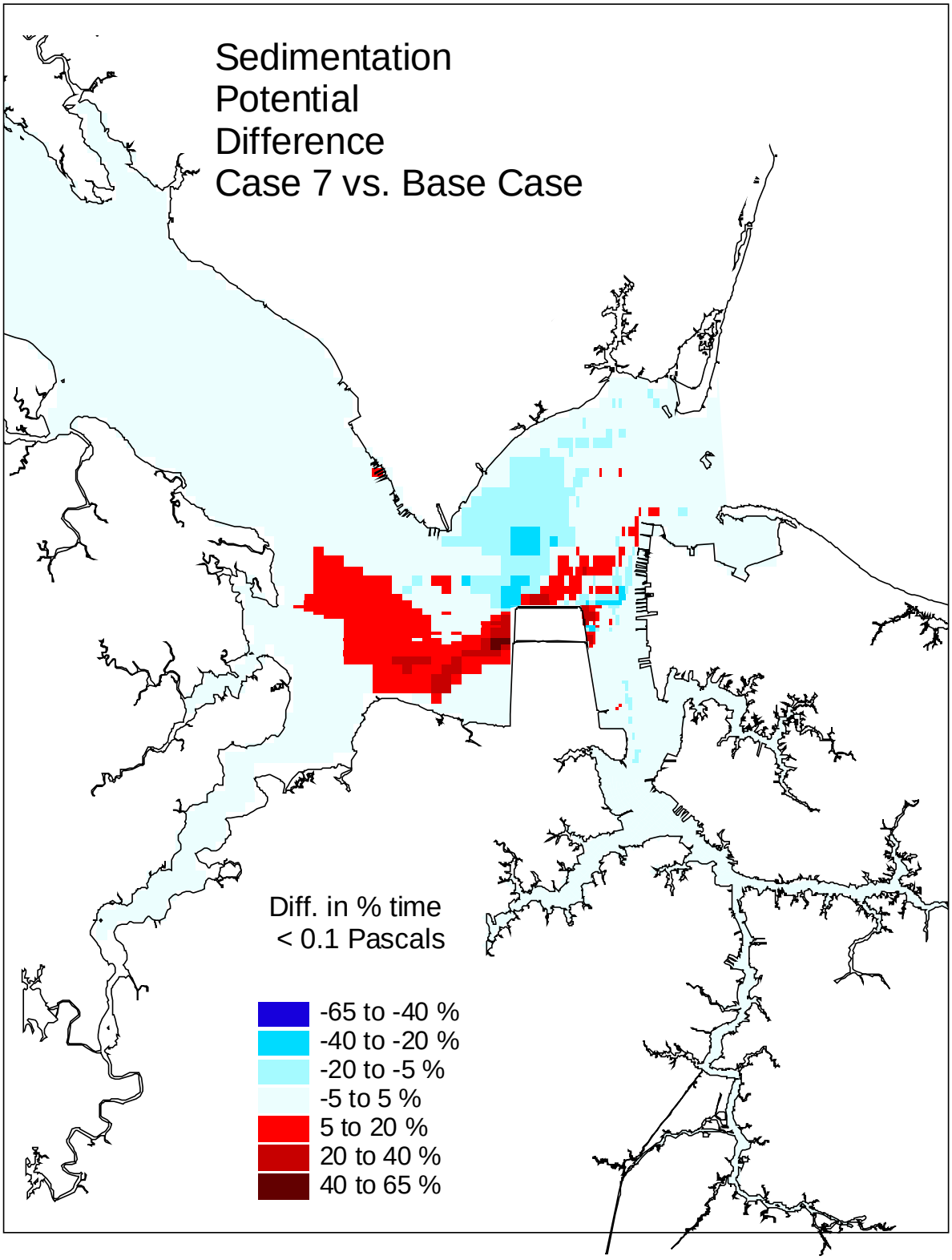

Figure 54. Single variable simulation comparison of the sedimentation potential difference for the Northward Expansion (Option 6, 55-foot channel) versus the Base Case.

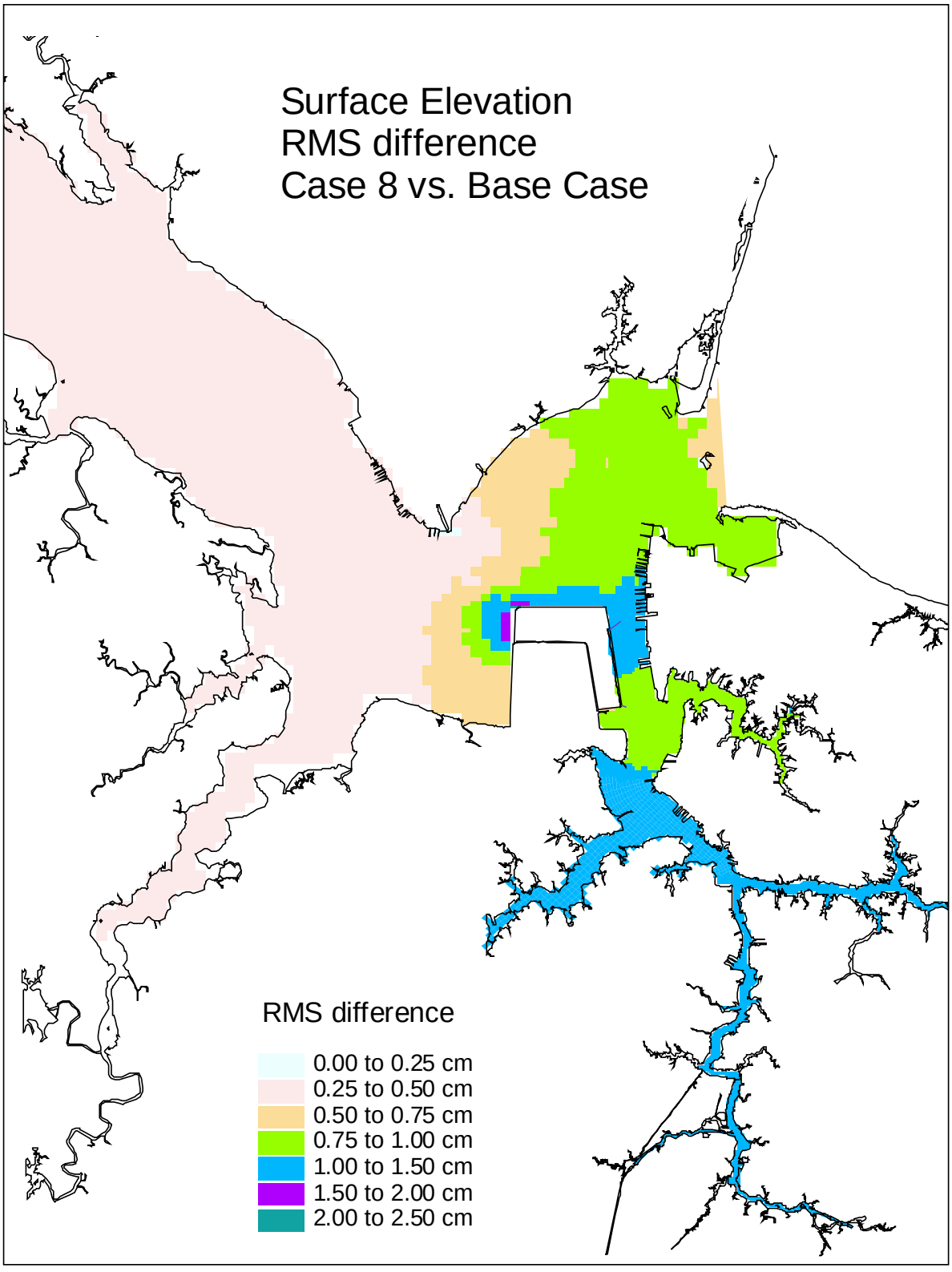

Figure 55. Single variable simulation comparison of the surface elevation RMS difference for the Northward & Eastward Expansion (Option 9, 50-foot channel) versus the Base Case.

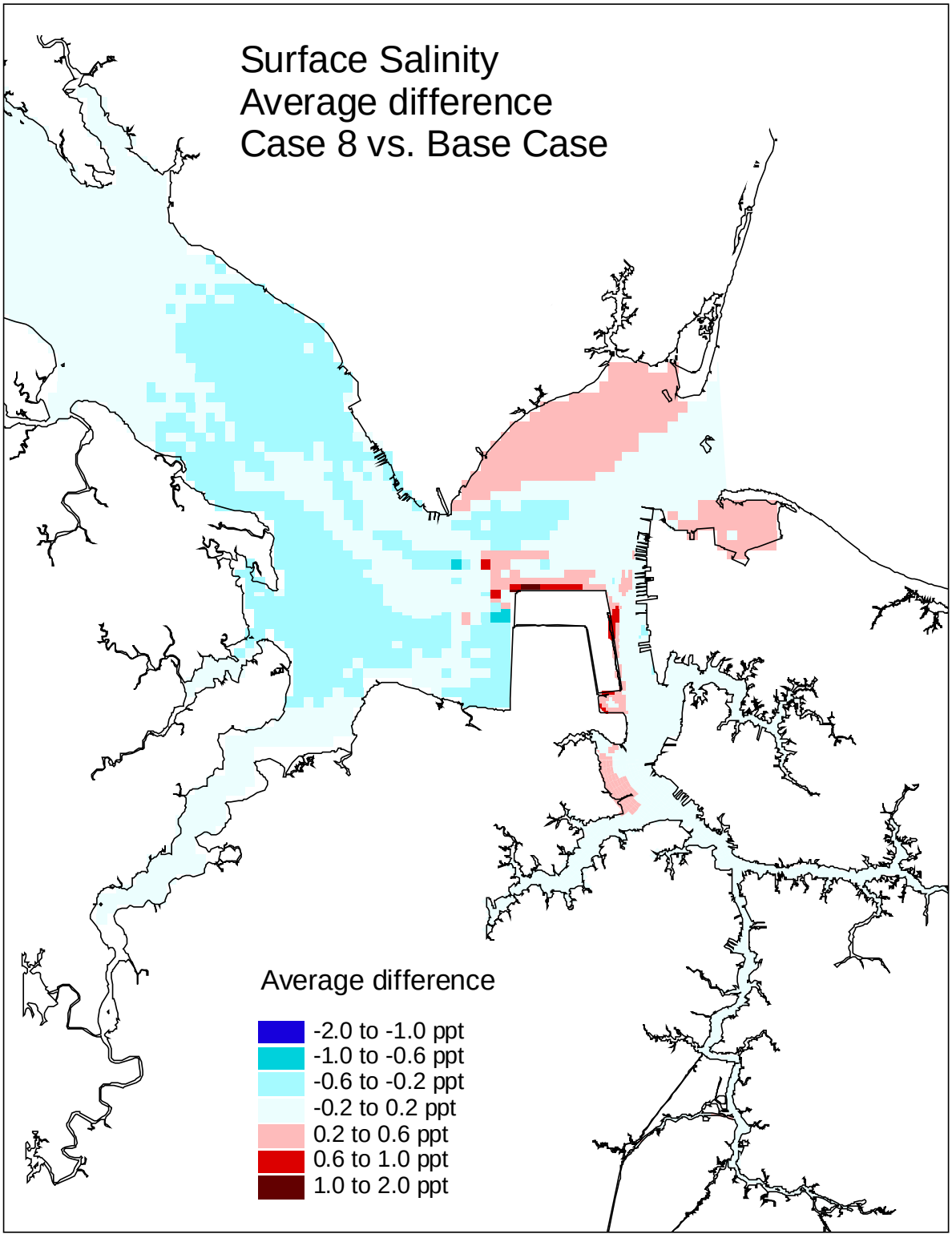

Figure 56. Single variable simulation comparison of the surface salinity average difference for the Northward & Eastward Expansion (Option 9, 50-foot channel) versus the Base Case.

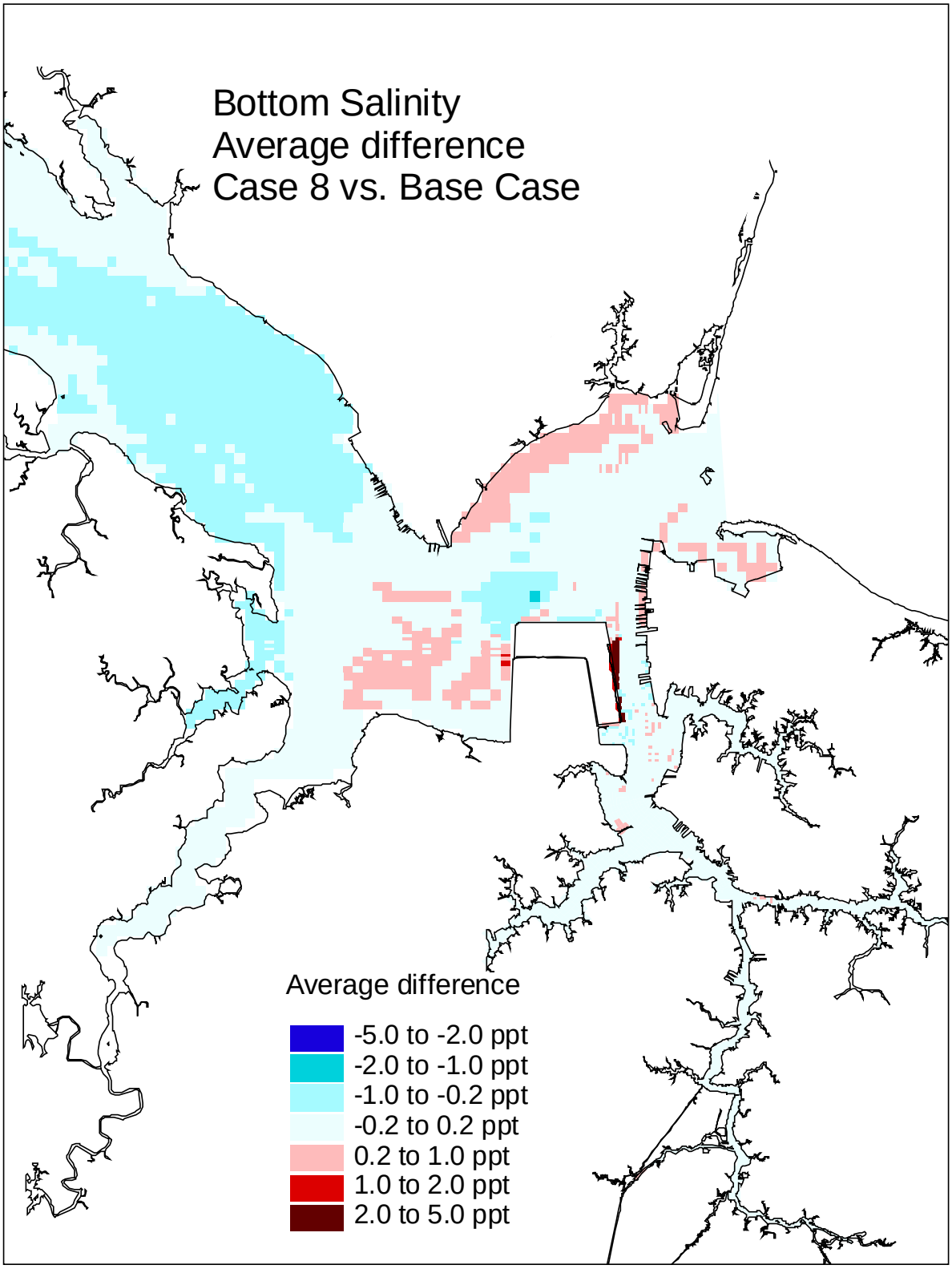

Figure 57. Single variable simulation comparison of the bottom salinity average difference for the Northward & Eastward Expansion (Option 9, 50-foot channel) versus the Base Case.

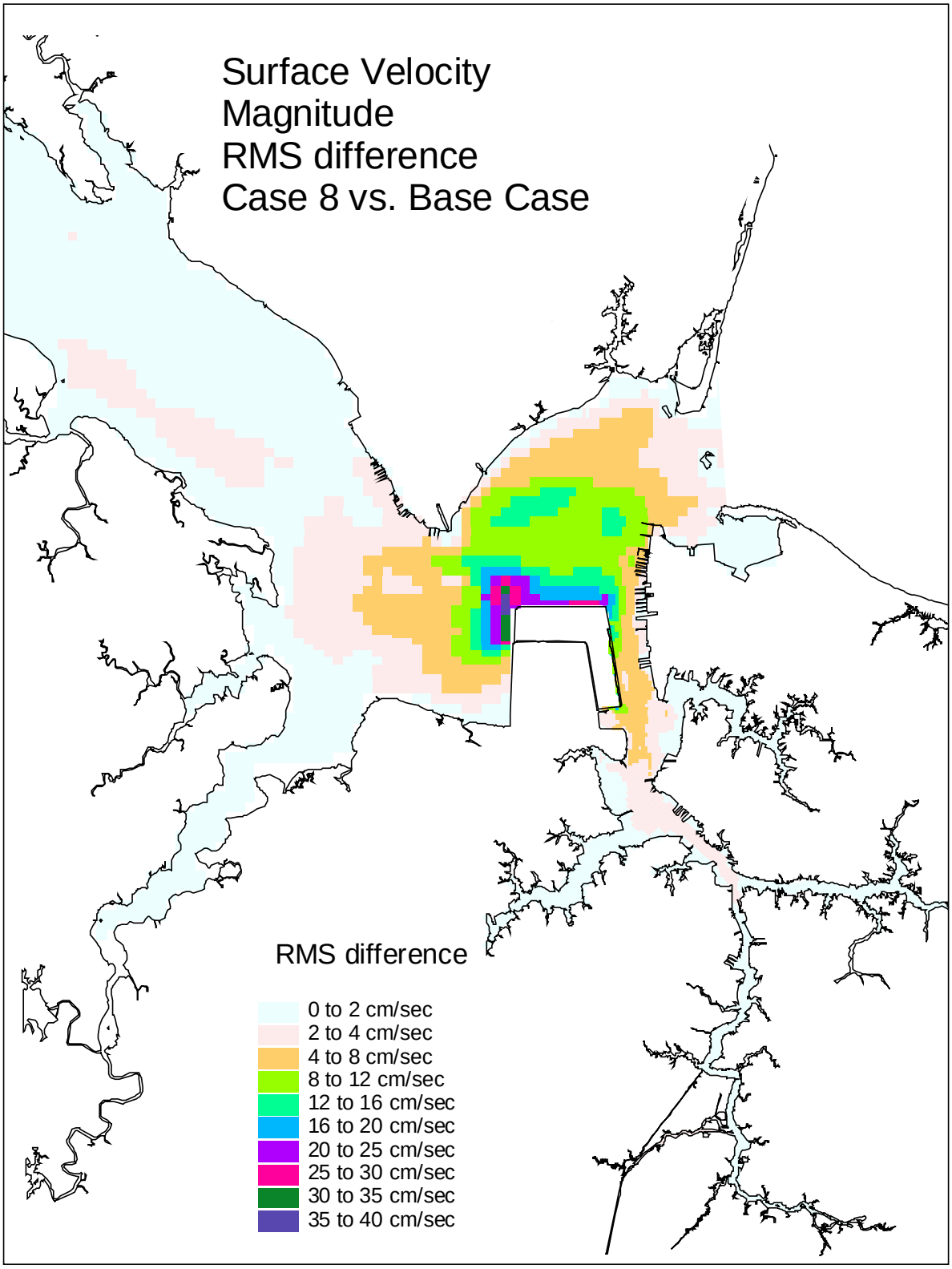

Figure 58. Single variable simulation comparison of the surface velocity RMS difference for the Northward & Eastward Expansion (Option 9, 50-foot channel) versus the Base Case.

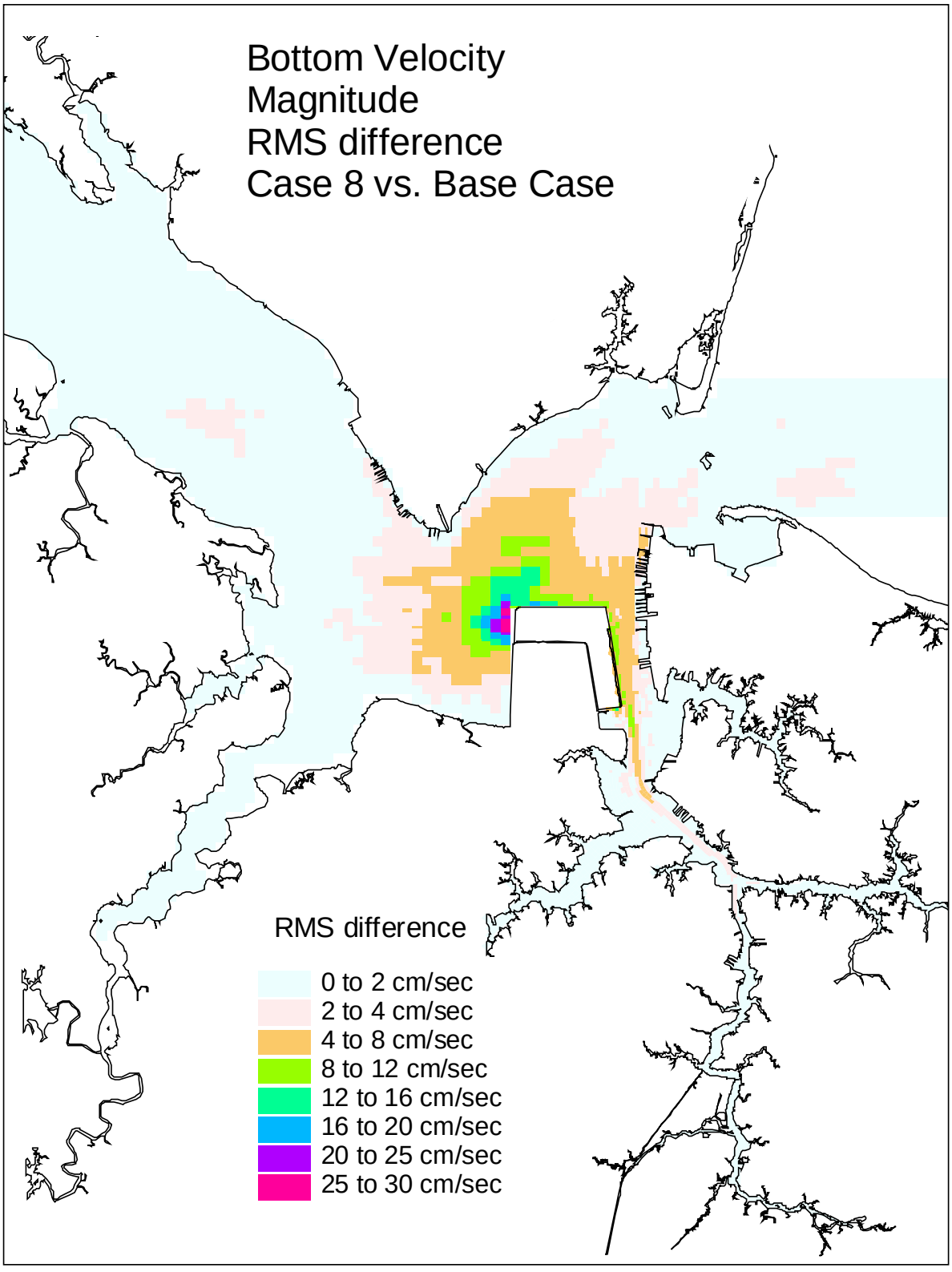

Figure 59. Single variable simulation comparison of the bottom velocity RMS difference for the Northward & Eastward Expansion (Option 9, 50-foot channel) versus the Base Case.

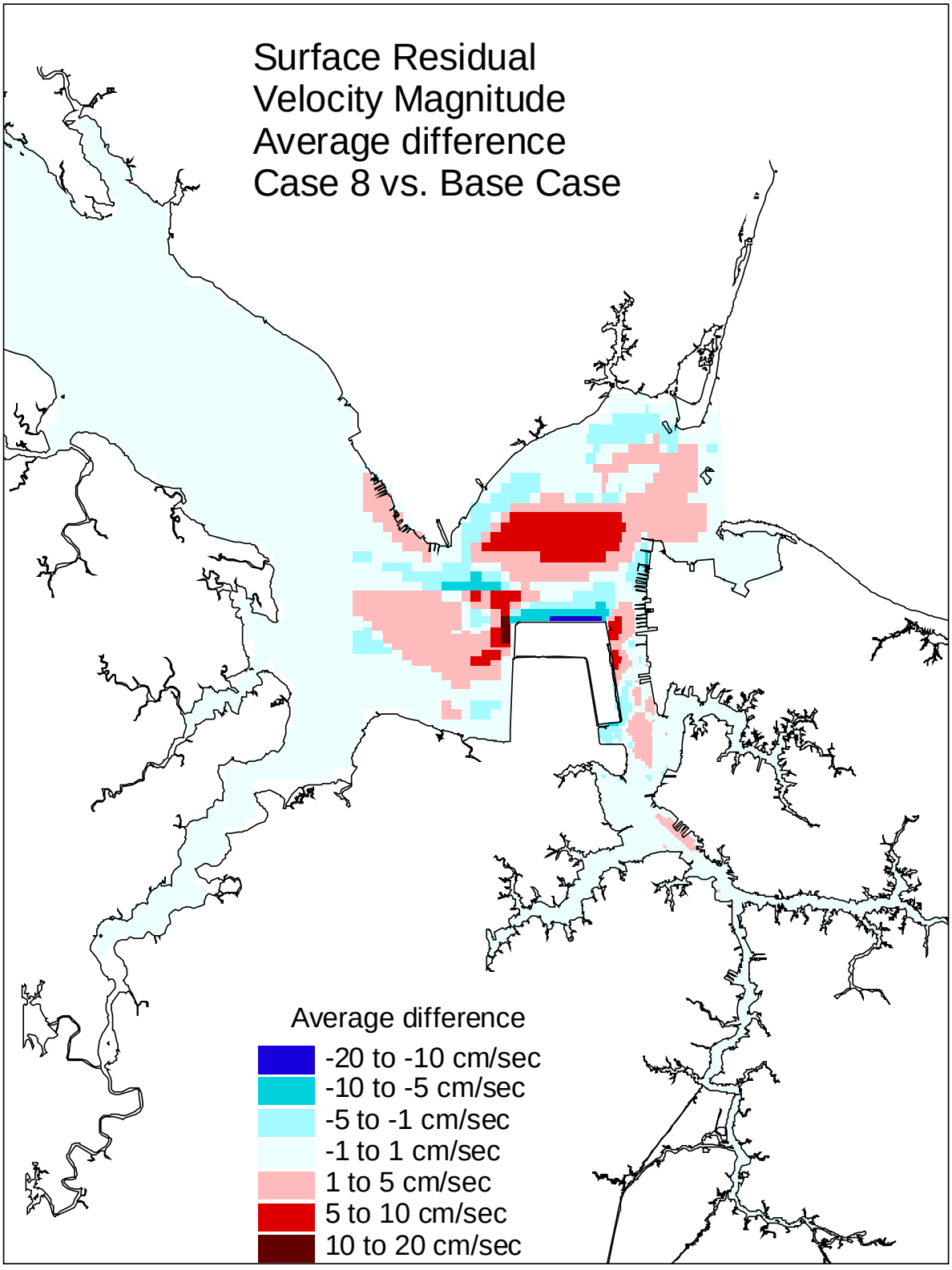

Figure 60. Single variable simulation comparison of the surface residual velocity average difference for the Northward & Eastward Expansion (Option 9, 50-ft channel) vs. the Base Case.

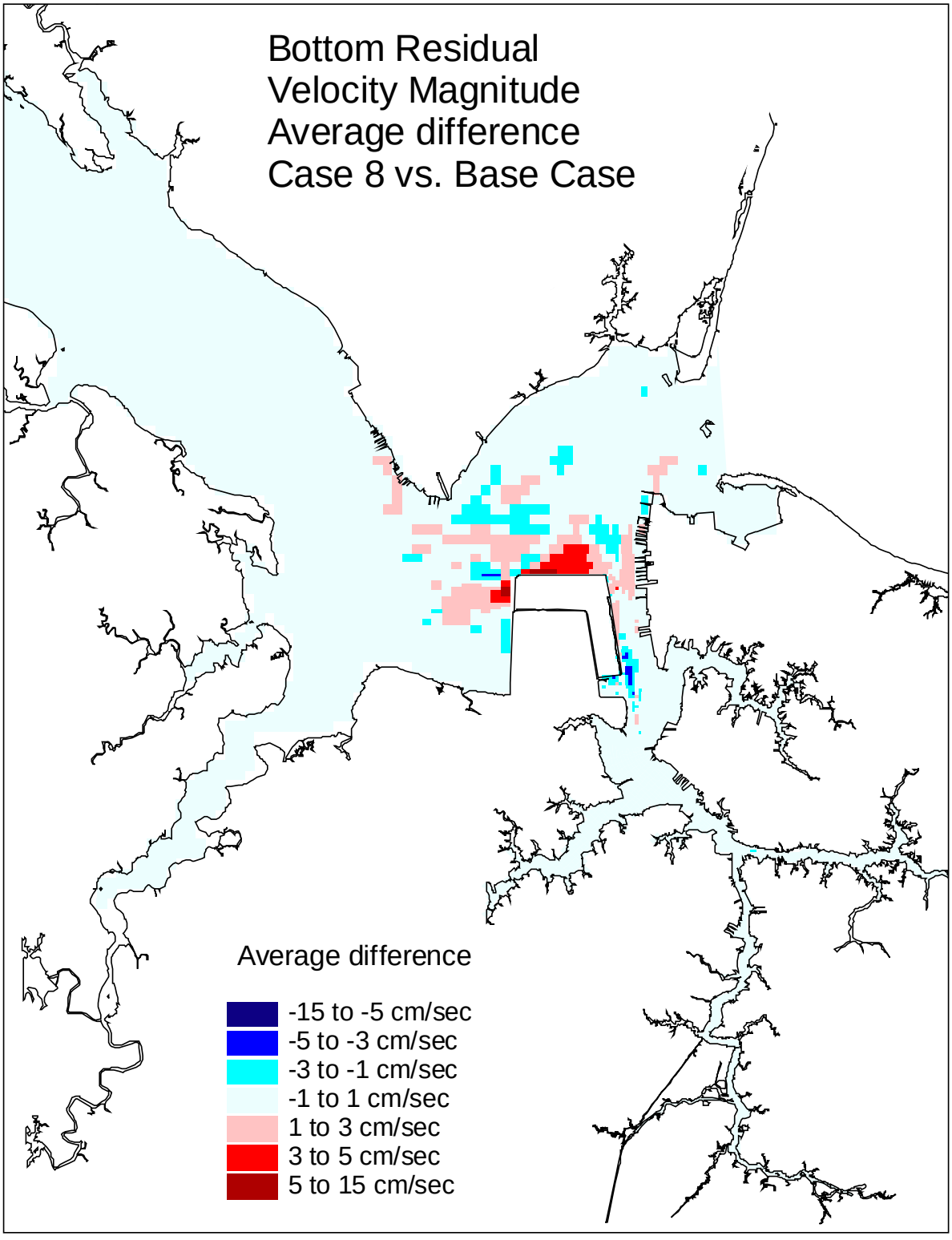

Figure 61. Single variable simulation comparison of the bottom residual velocity average difference for the Northward & Eastward Expansion (Option 9, 50-foot channel) vs. the Base Case.

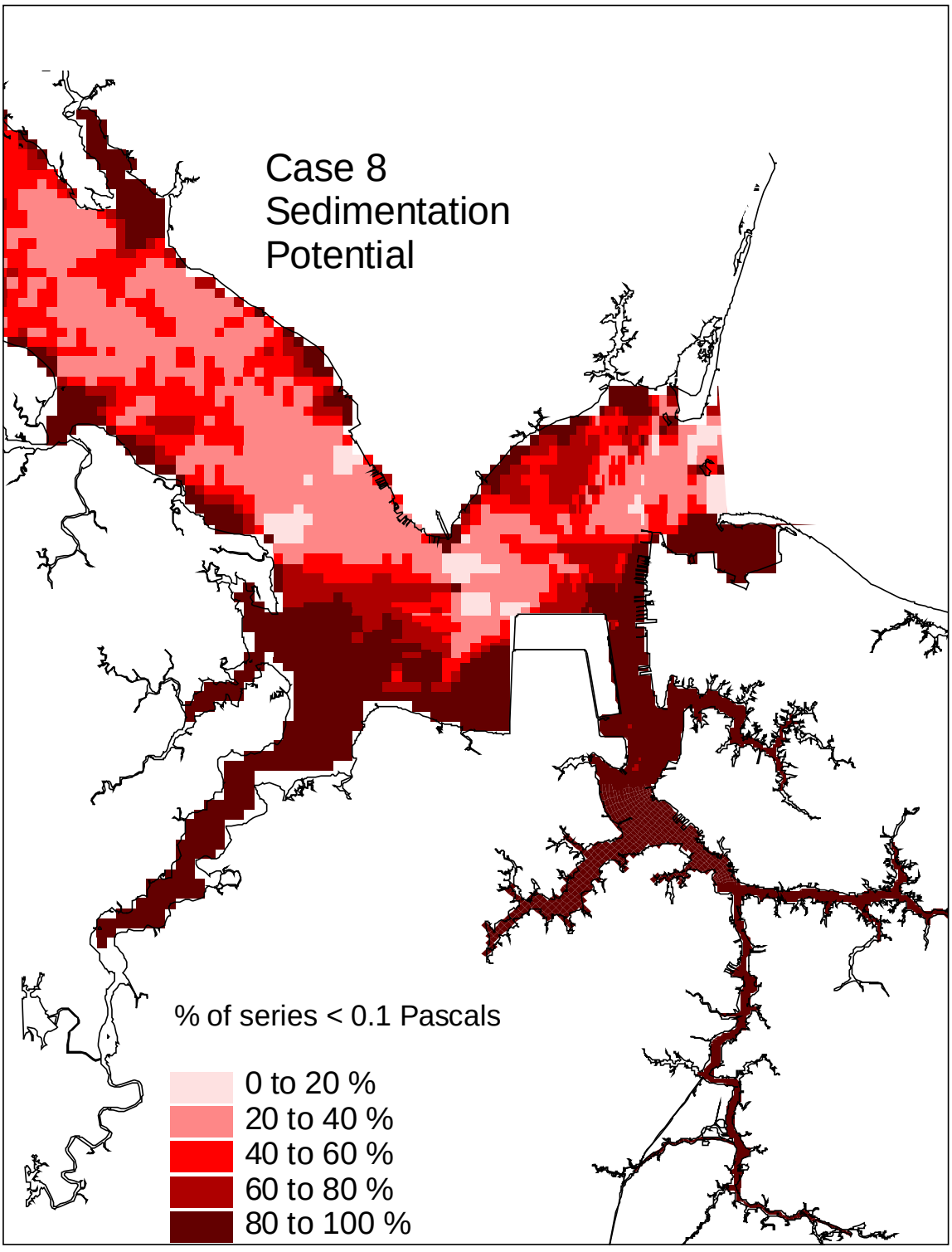

Figure 62. Single variable simulation comparison of the sedimentation potential for the Northward and Eastward Expansion (Option 9, 50-foot channel).

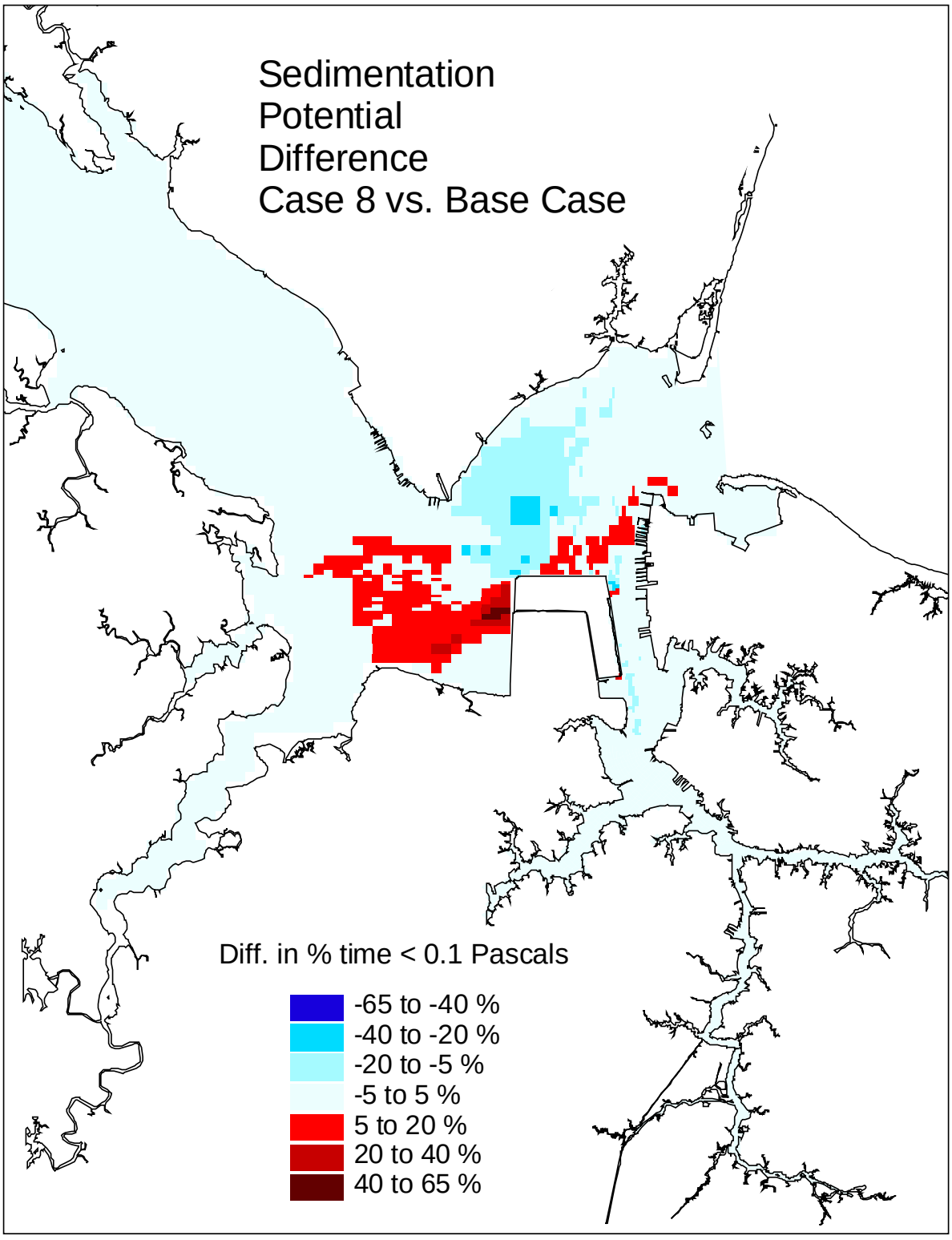

Figure 63. Single variable simulation comparison of the sedimentation potential difference for the Northward & Eastward Expansion (Option 9, 50-foot channel) versus the Base Case.

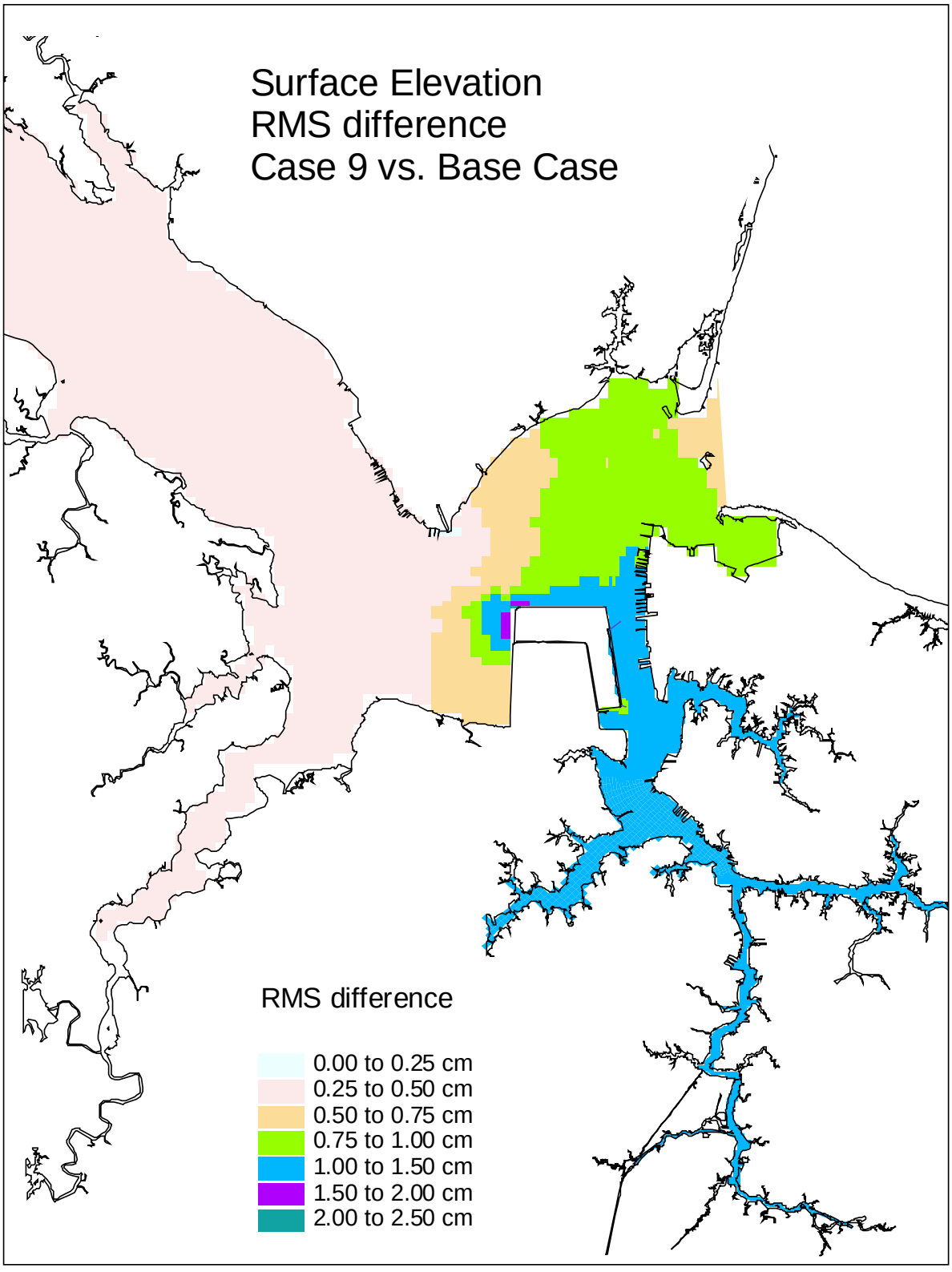

Figure 64. Single variable simulation comparison of the surface elevation RMS difference for the Northward & Eastward Expansion (Option 9, 55-foot channel) versus the Base Case.

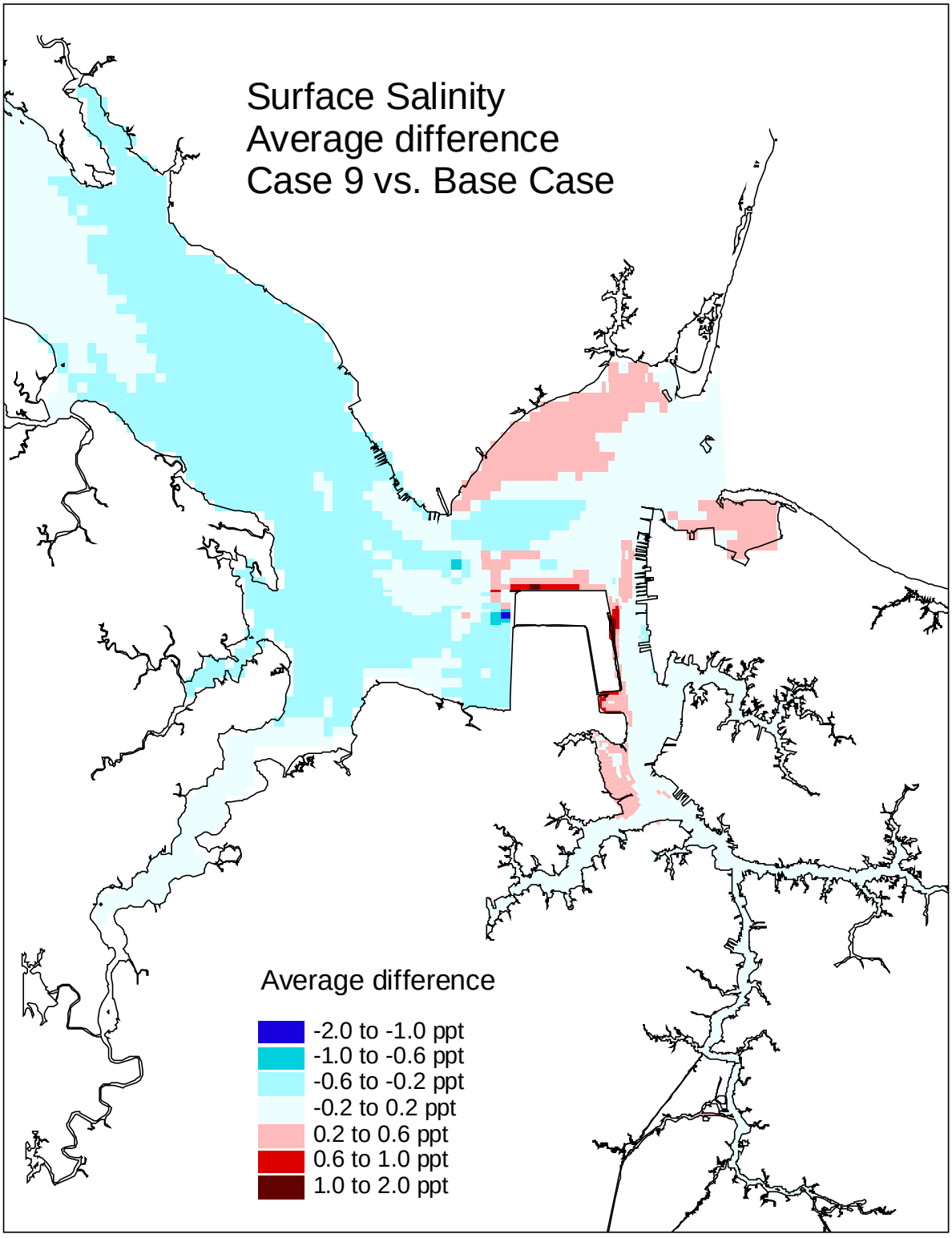

Figure 65. Single variable simulation comparison of the surface salinity average difference for the Northward and Eastward Expansion (Option 9, 55-foot channel) versus the Base Case.

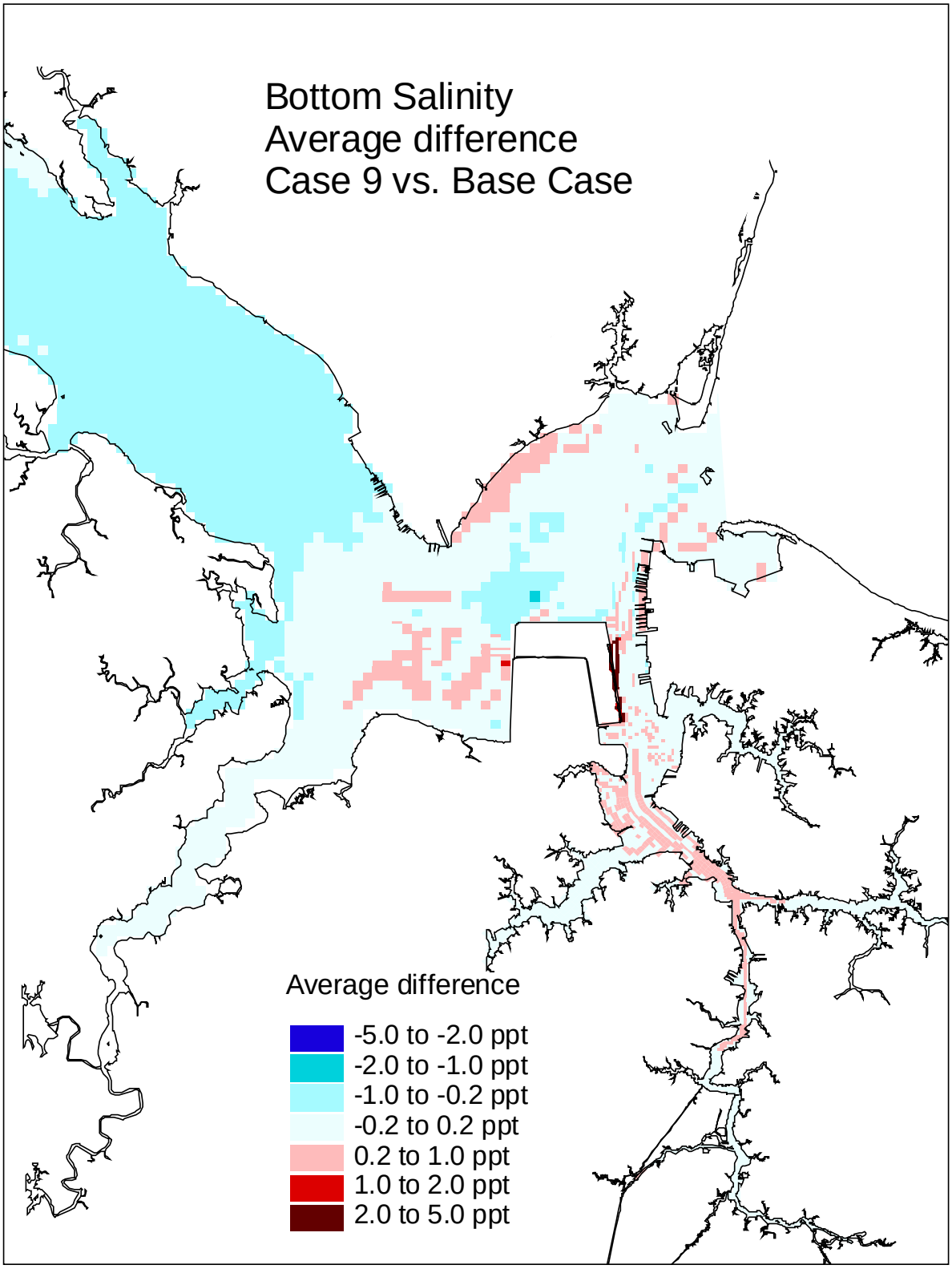

Figure 66. Single variable simulation comparison of the bottom salinity average difference for the Northward and Eastward Expansion (Option 9, 55-foot channel) versus the Base Case.

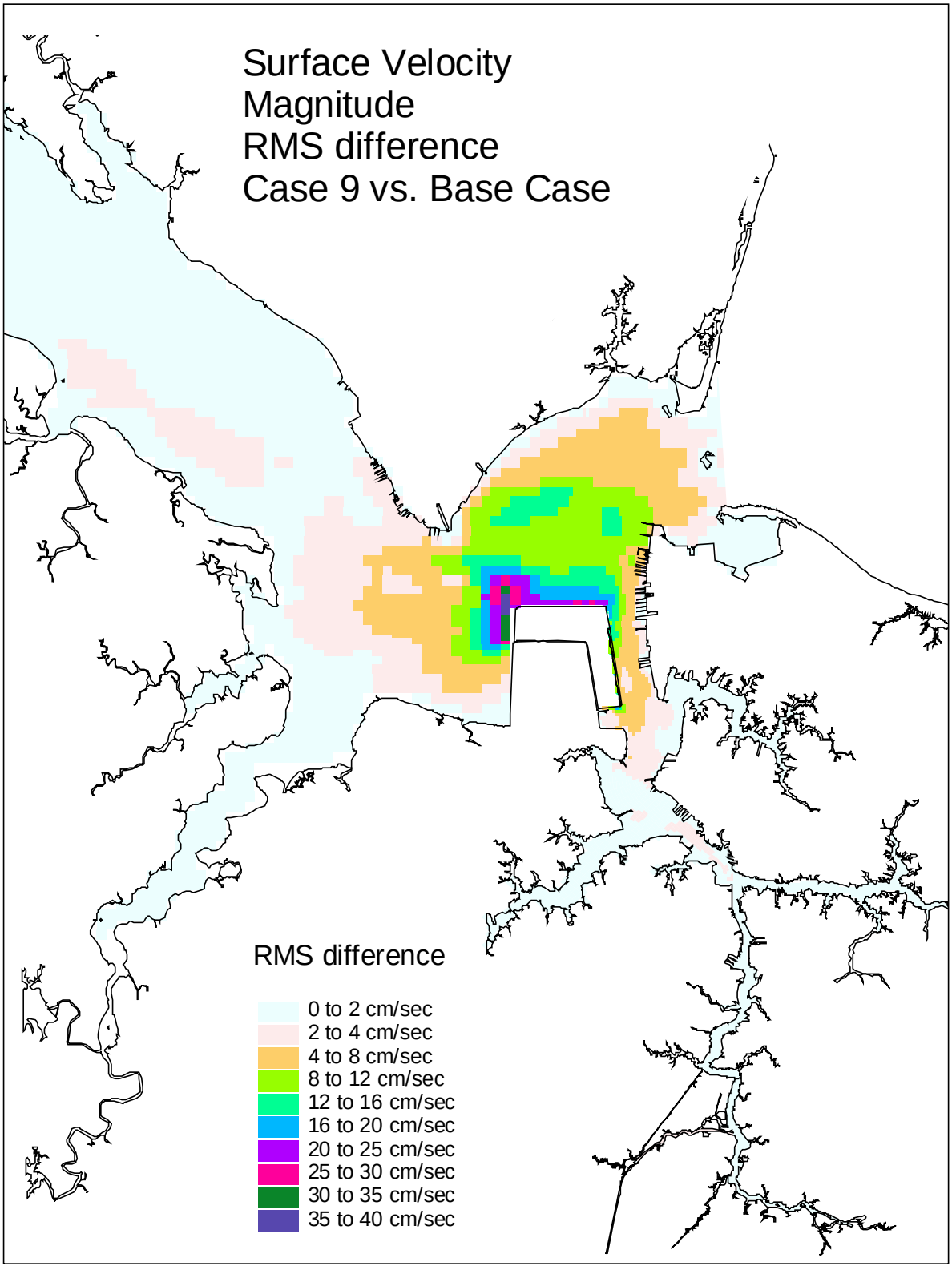

Figure 67. Single variable simulation comparison of the surface velocity RMS difference for the Northward and Eastward Expansion (Option 9, 55-foot channel) versus the Base Case.

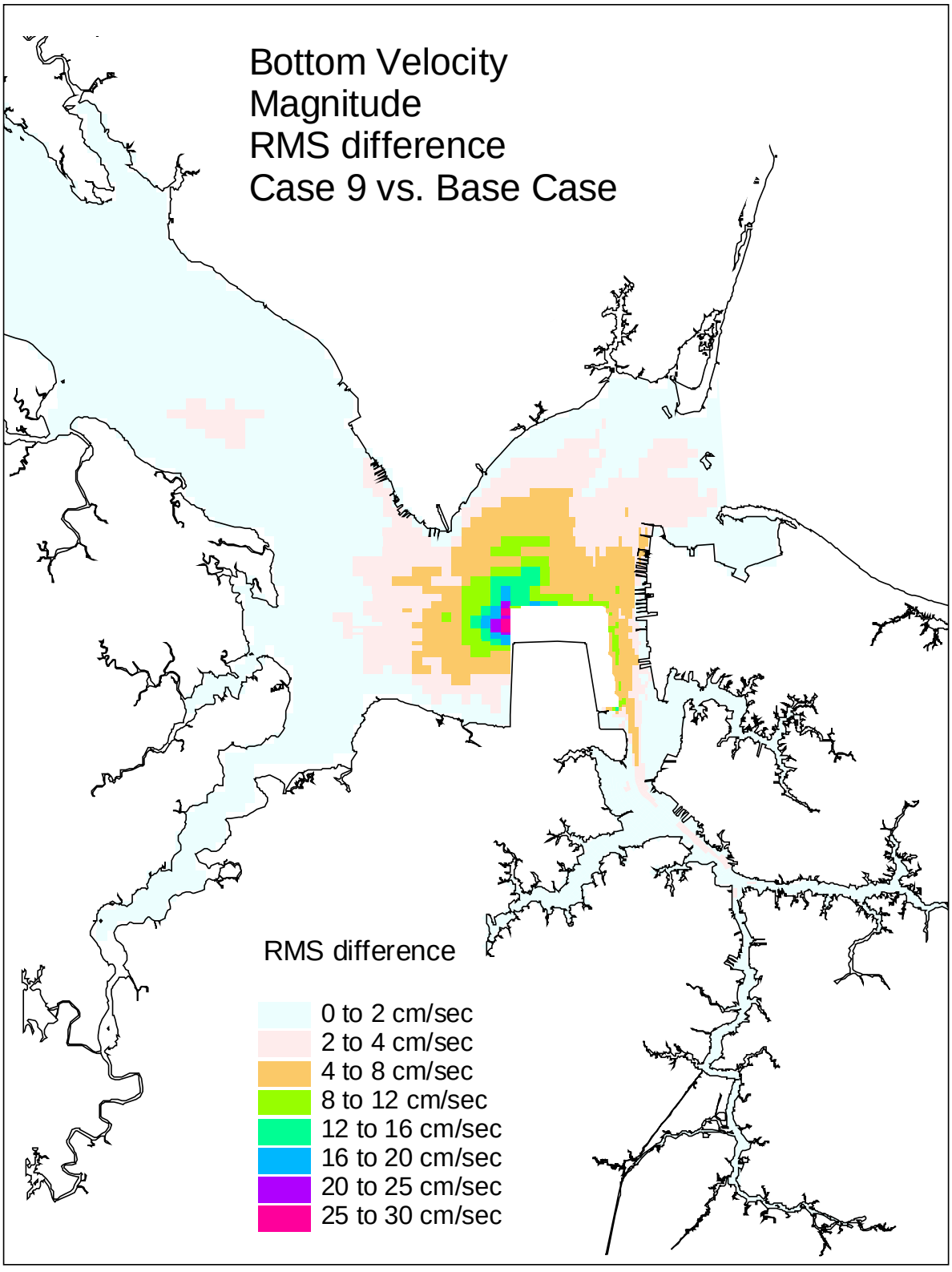

Figure 68. Single variable simulation comparison of the bottom velocity RMS difference for the Northward and Eastward Expansion (Option 9, 55-foot channel) versus the Base Case.

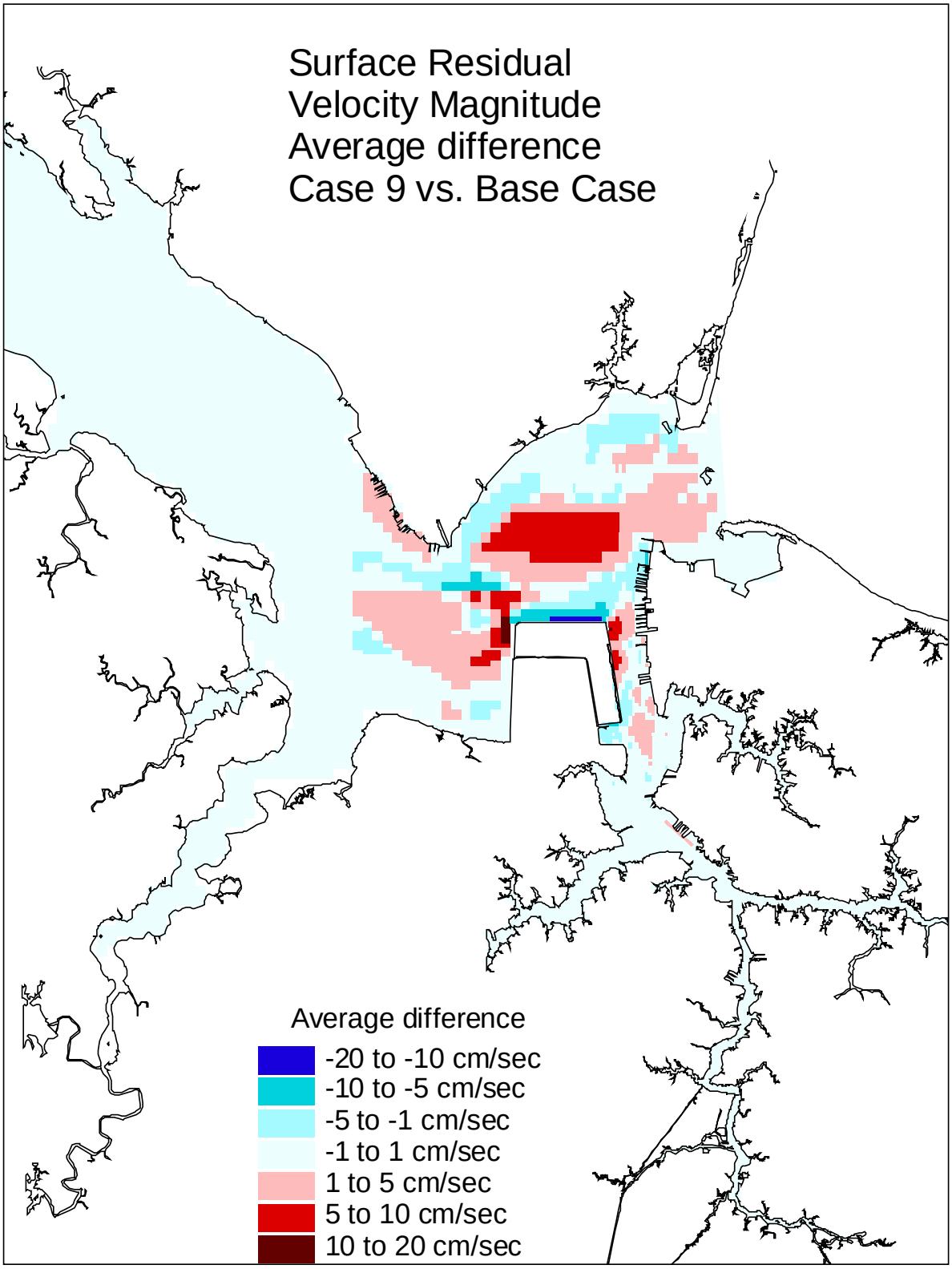

Figure 69. Single variable simulation comparison of the surface residual velocity average difference for the Northward and Eastward Expansion (Opt 9, 55-ft channel) vs. the Base Case.

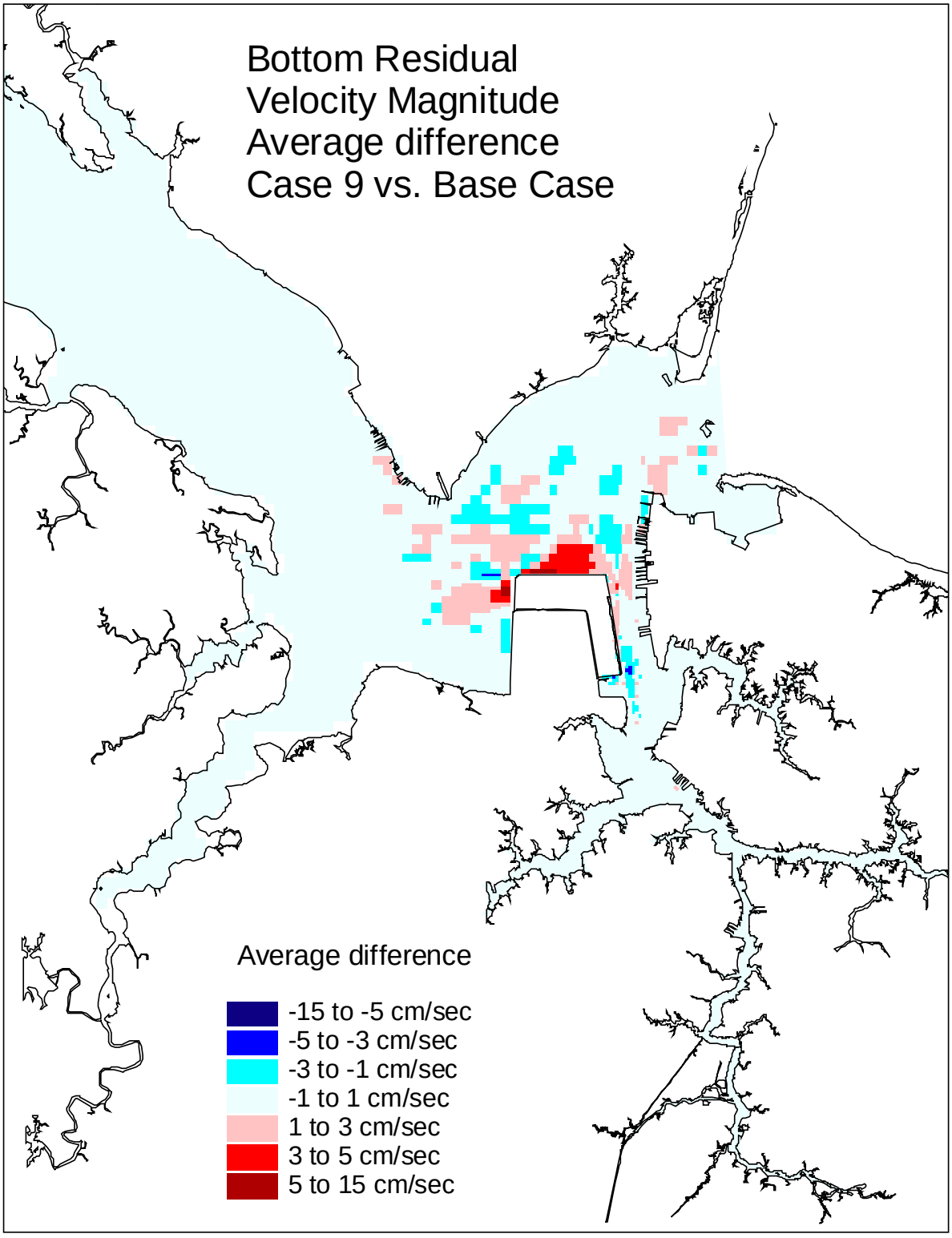

Figure 70. Single variable simulation comparison of the bottom residual velocity average difference for the Northward & Eastward Expansion (Option 9, 55-ft channel) vs. the Base Case.

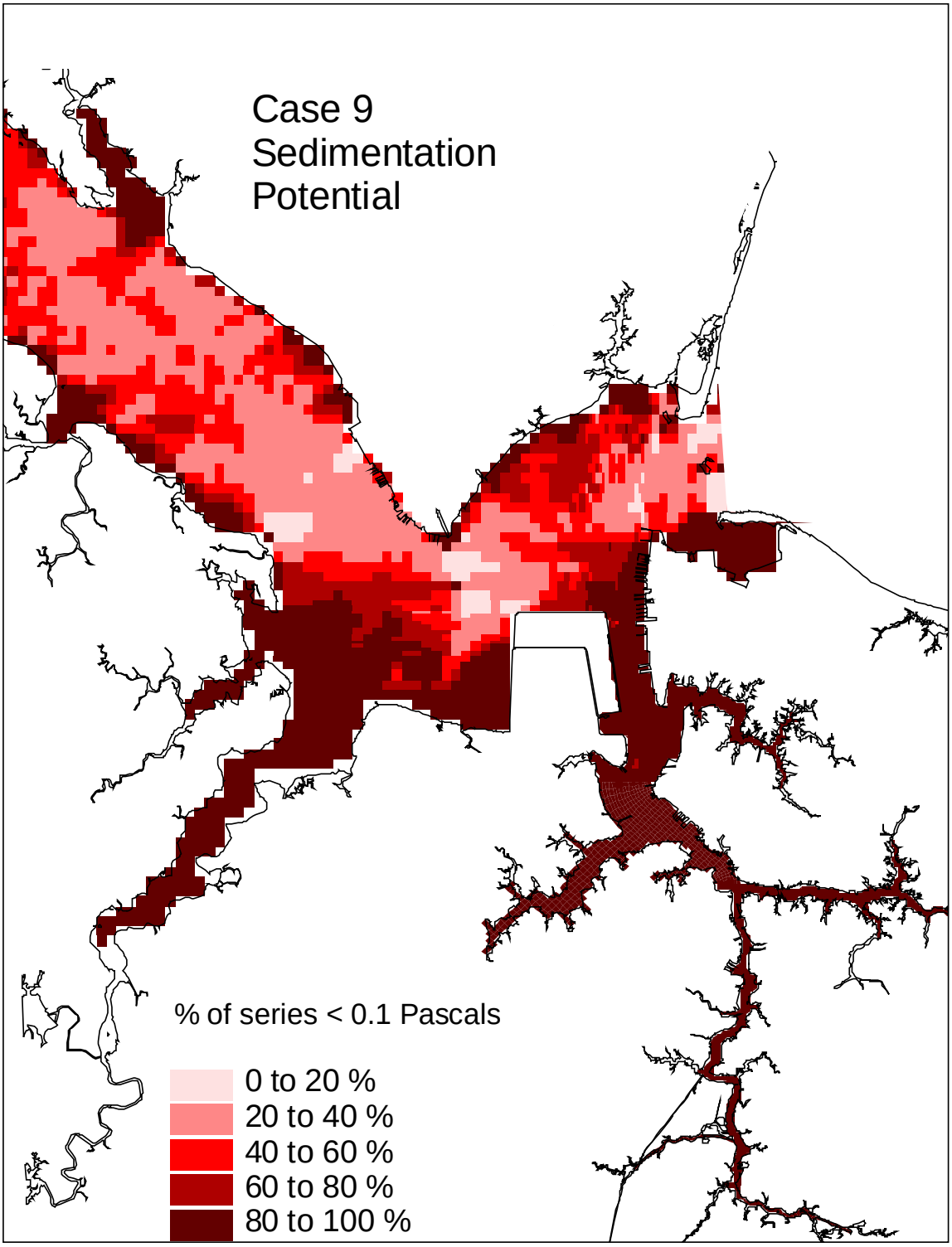

Figure 71. Single variable simulation comparison of the sedimentation potential for the Northward and Eastward Expansion (Option 9, 55-foot channel).

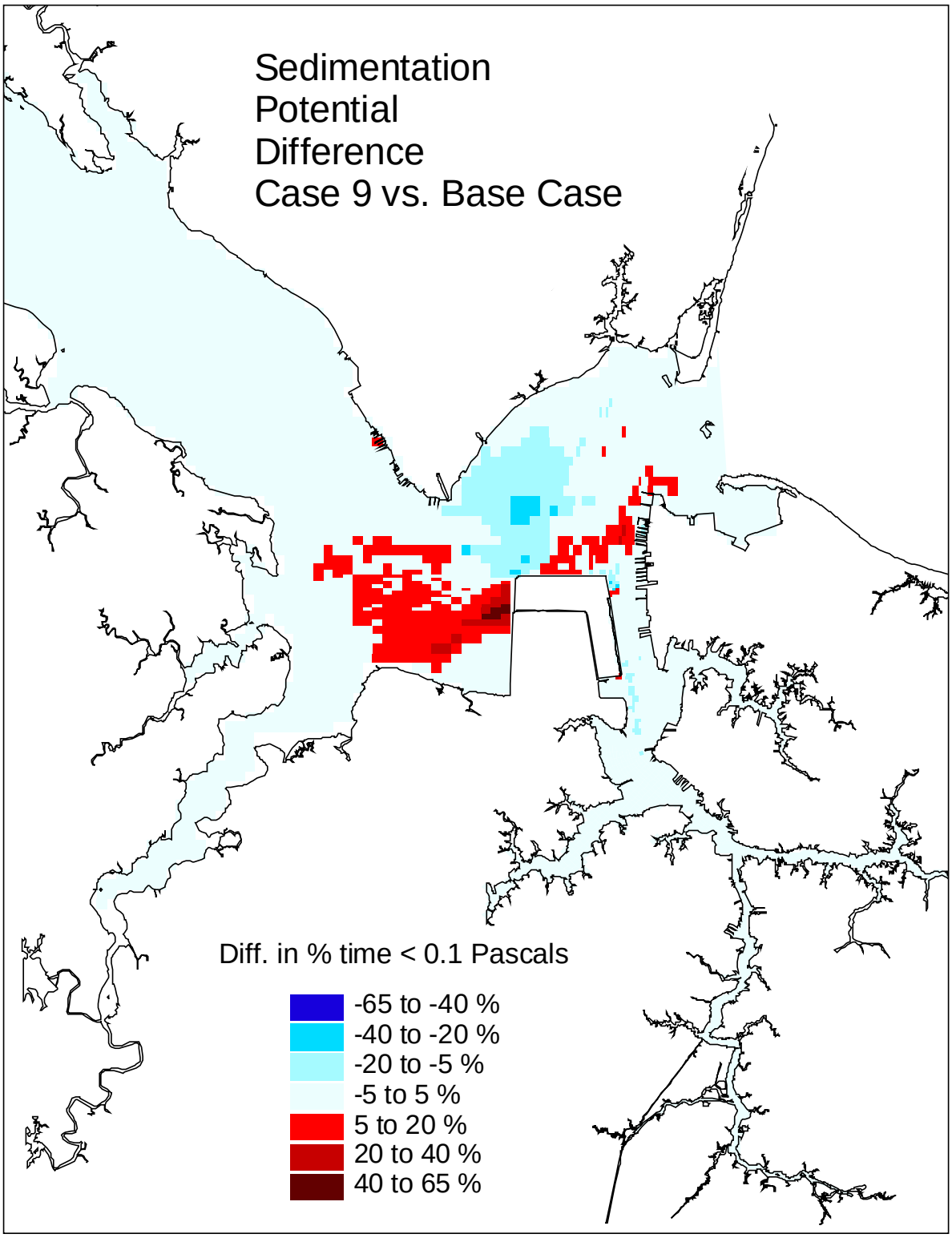

Figure 72. Single variable simulation comparison of the sedimentation potential difference for the Northward and Eastward Expansion (Option 9, 55-foot channel) versus the Base Case.

APPENDIX to CHAPTER V, SECTION A.2

Global Comparisons of Single Variable Runs

Percentile Analysis

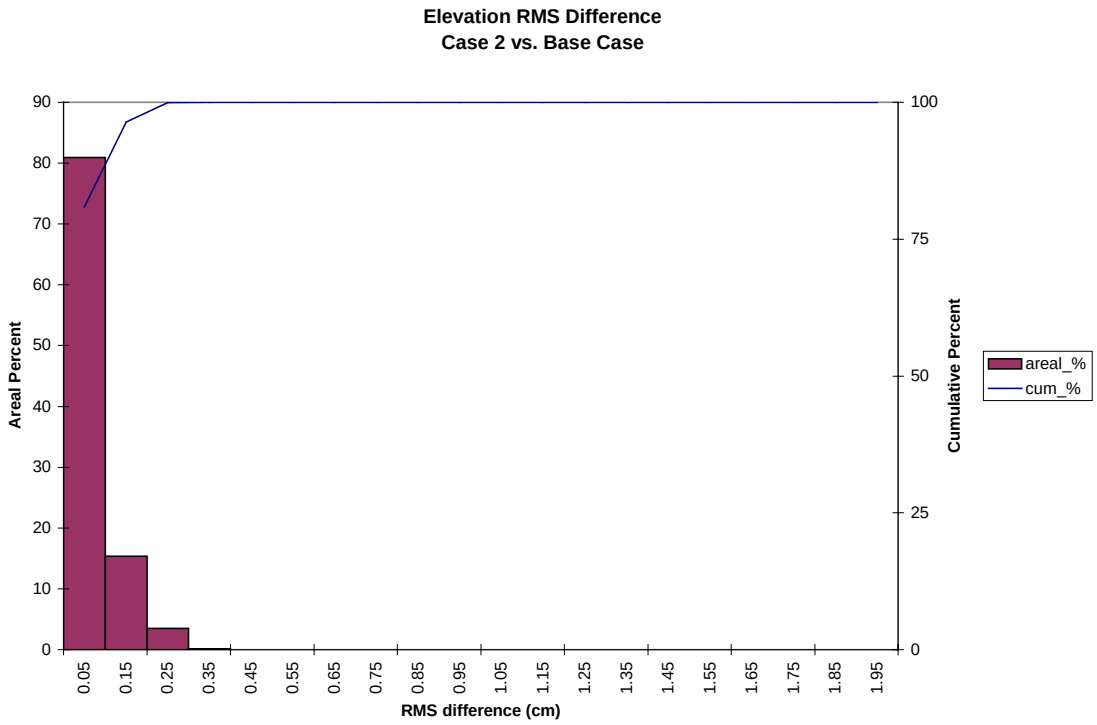

Figure 1. Frequency distribution of elevation RMS difference for the Eastward Expansion (Option 7, 50–foot channel) versus the Base Case.

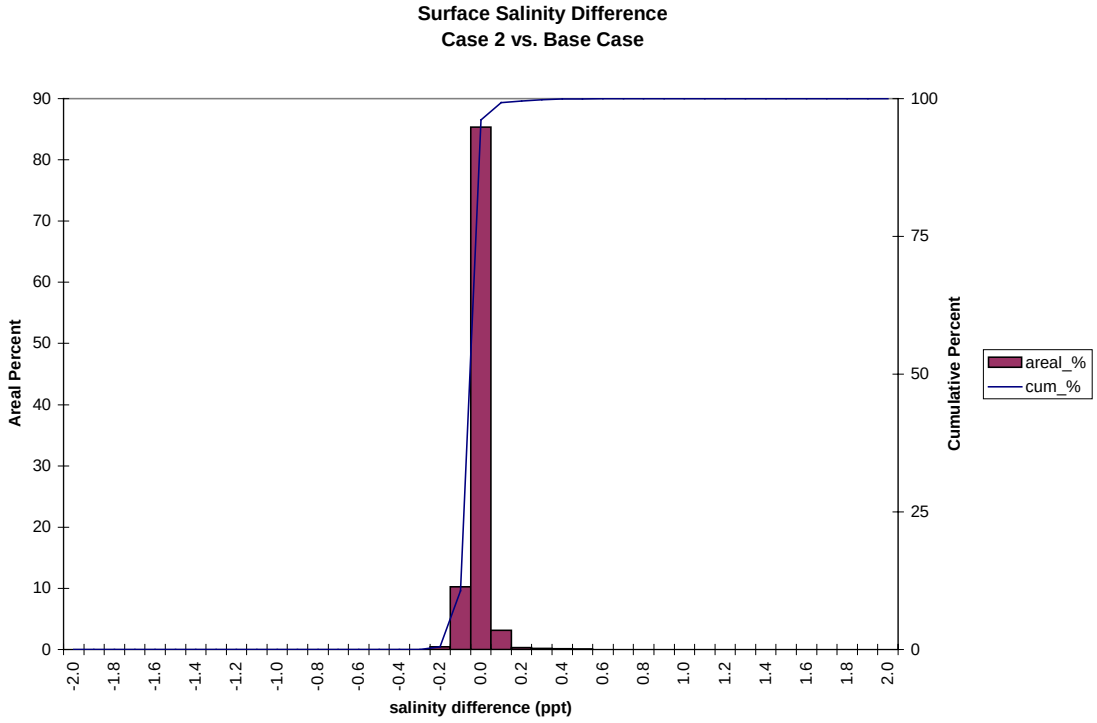

Figure 2. Frequency distribution of surface salinity average difference for the Eastward Expansion (Option 7, 50–foot channel) versus the Base Case.

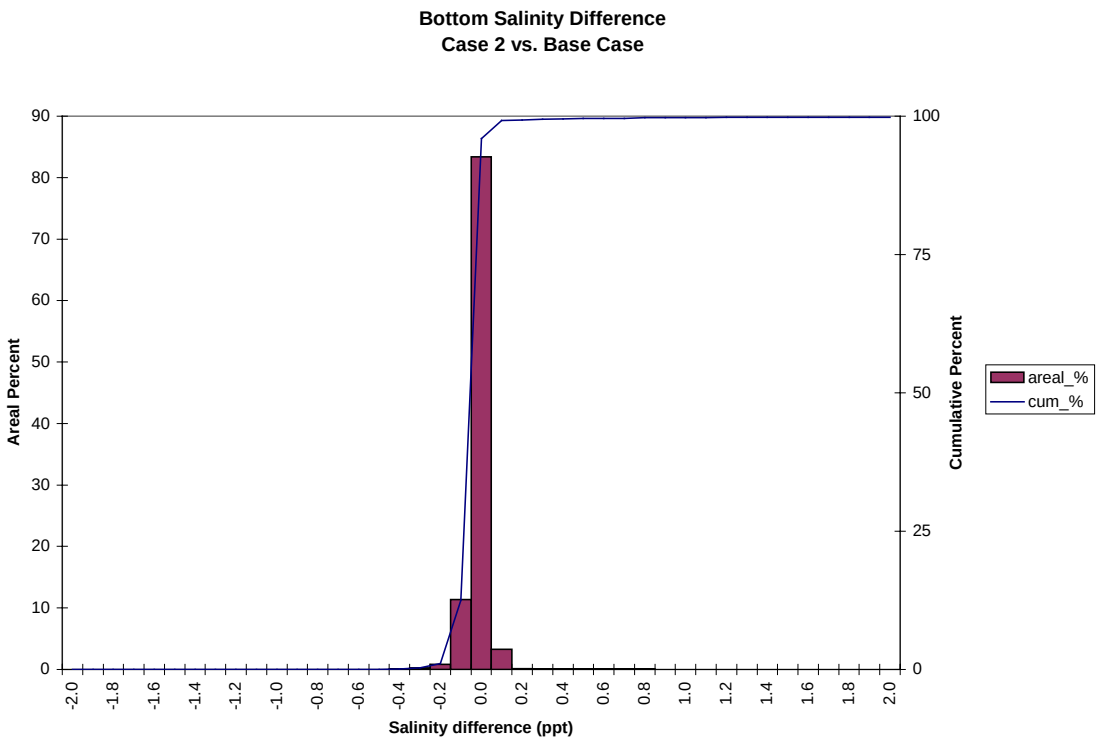

Figure 3. Frequency distribution of bottom salinity average difference for the Eastward Expansion (Option 7, 50–foot channel) versus the Base Case.

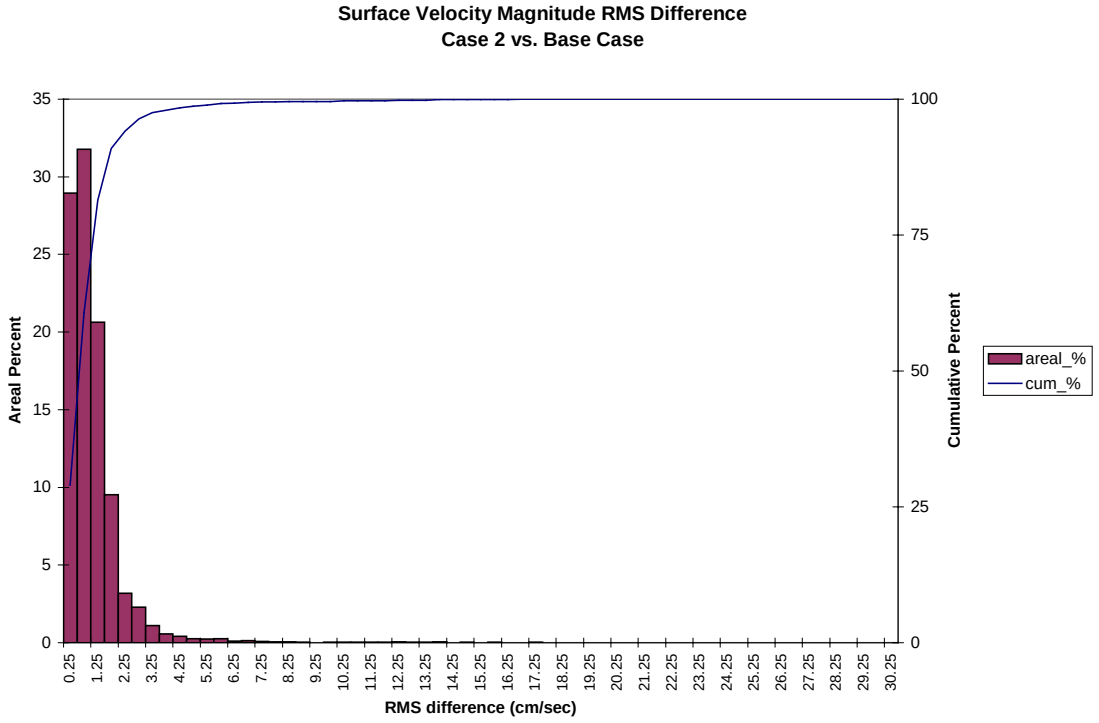

Figure 4. Frequency distribution of surface velocity RMS difference for the Eastward Expansion (Option 7, 50–foot channel) versus the Base Case.

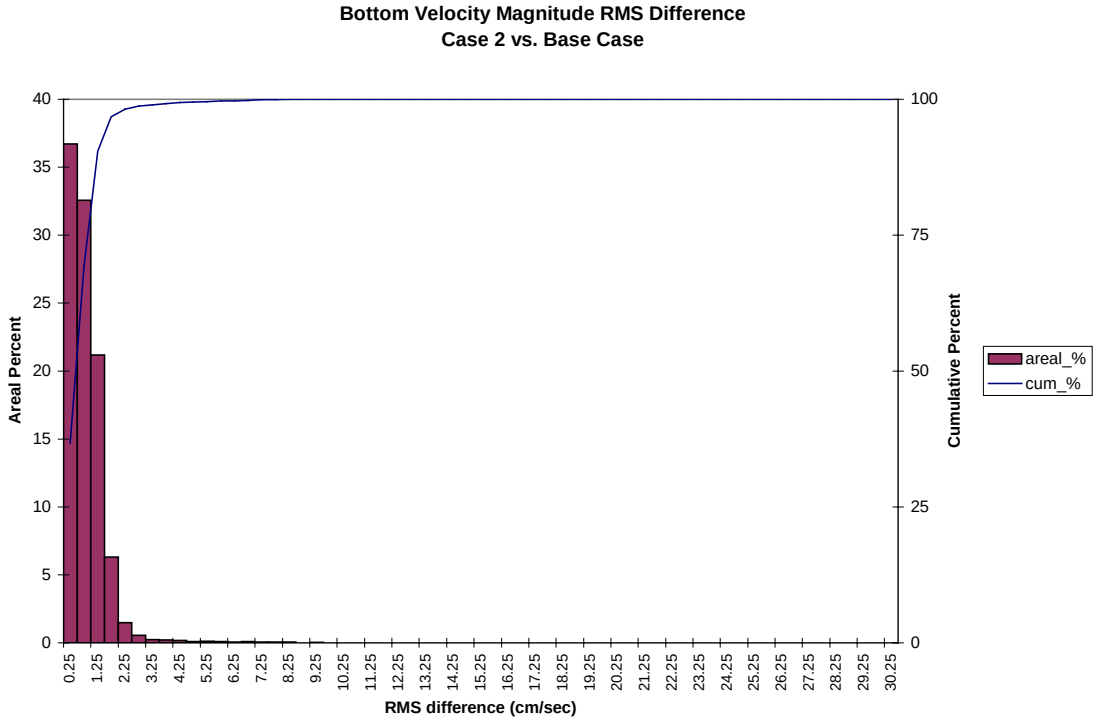

Figure 5. Frequency distribution of bottom velocity RMS difference for the Eastward Expansion (Option 7, 50–foot channel) versus the Base Case.

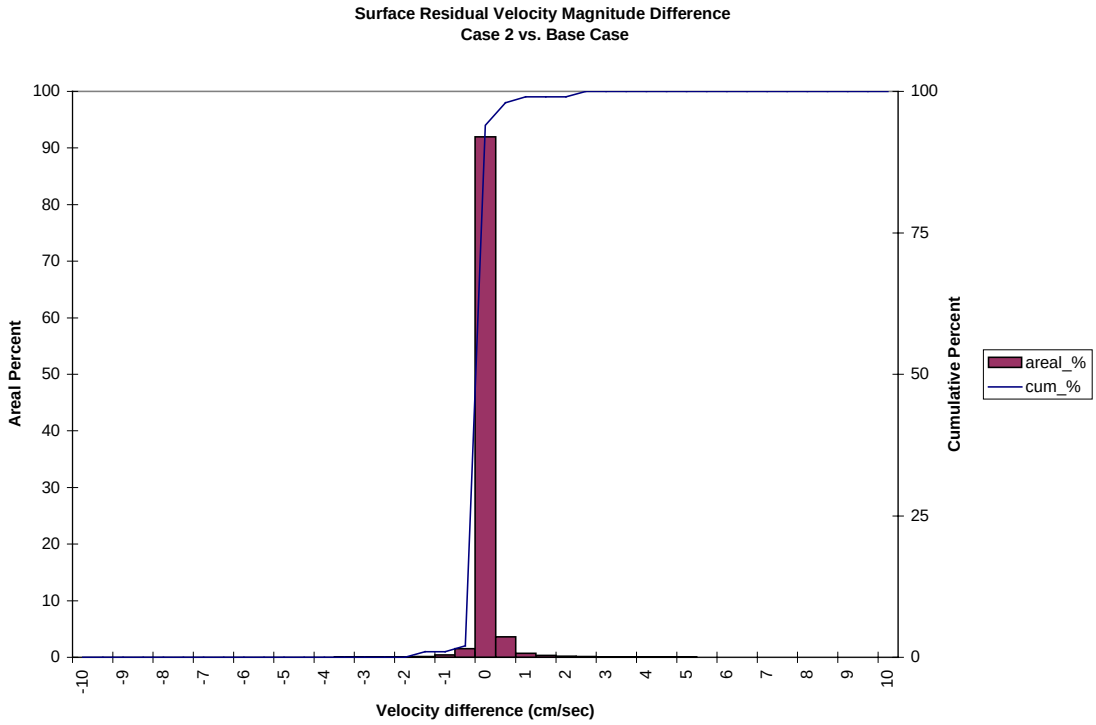

Figure 6. Frequency distribution of surface residual velocity magnitude average difference for the Eastward Expansion (Option 7, 50–foot channel) versus the Base Case.

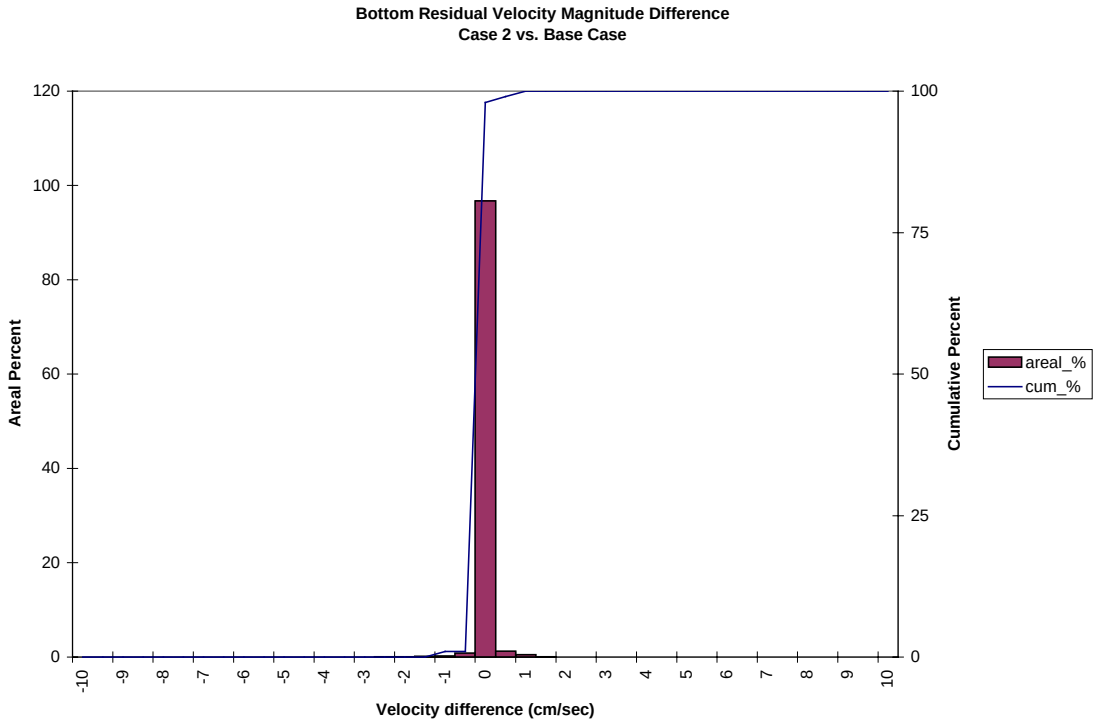

Figure 7. Frequency distribution of bottom residual velocity magnitude average difference for the Eastward Expansion (Option 7, 50–foot channel) versus the Base Case.

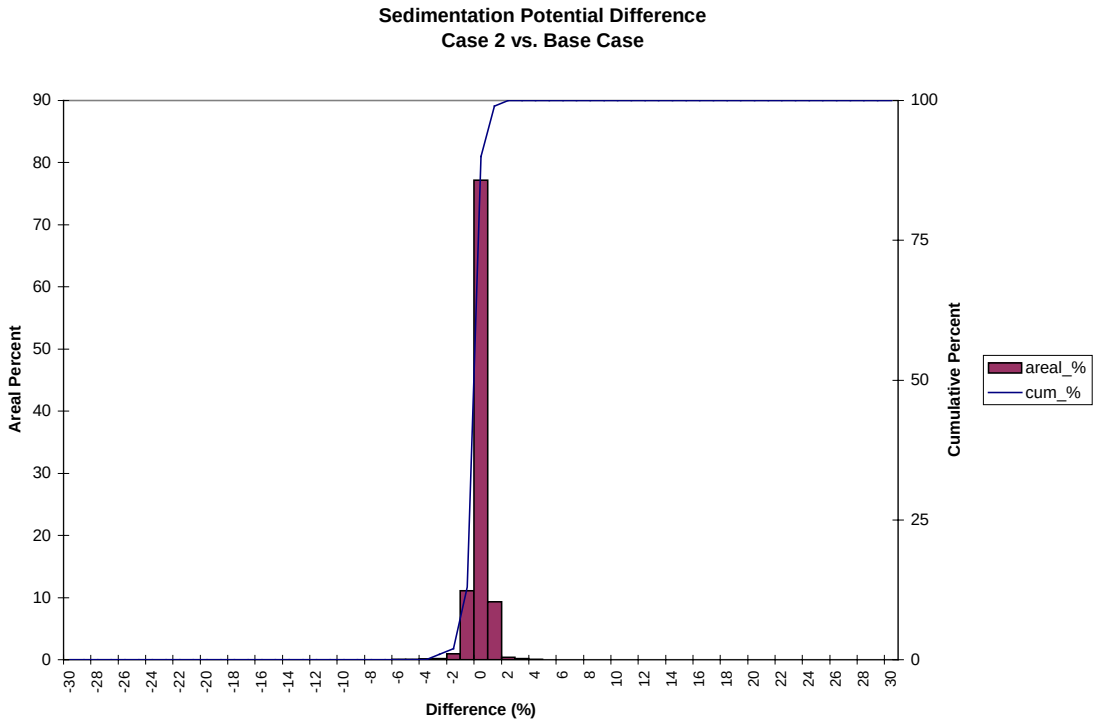

Figure 8. Frequency distribution of sedimentation potential difference for the Eastward Expansion (Option 7, 50–foot channel) versus the Base Case.

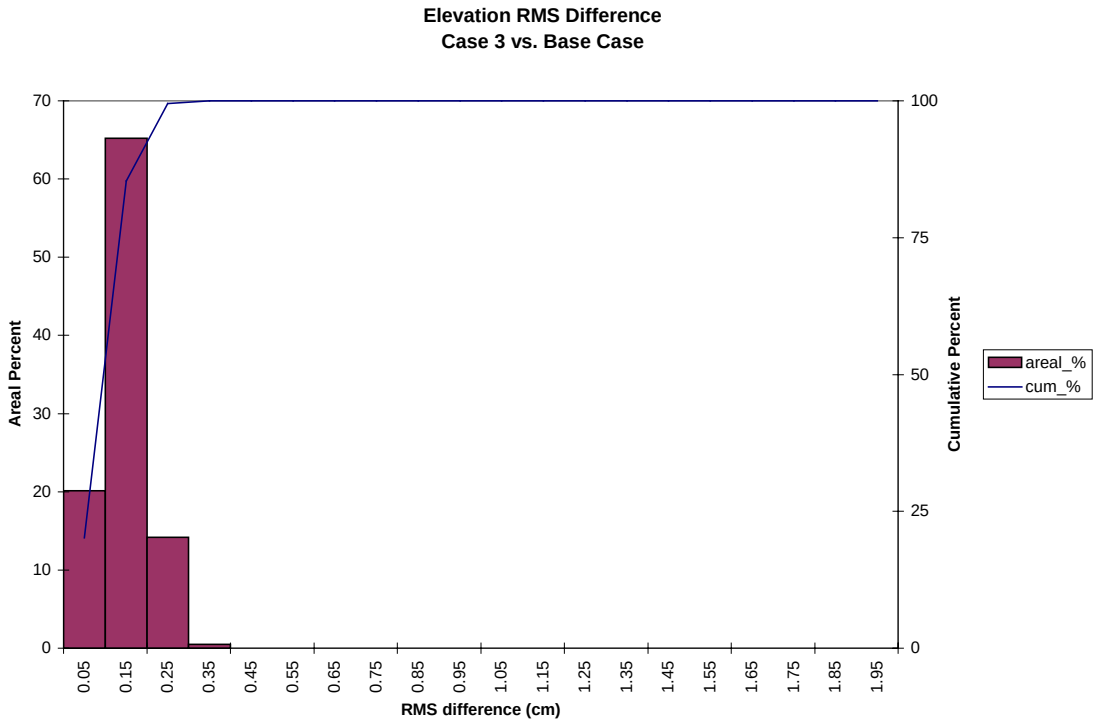

Figure 9. Frequency distribution of elevation RMS difference for the Eastward Expansion (Option 7, 55–foot channel) versus the Base Case.

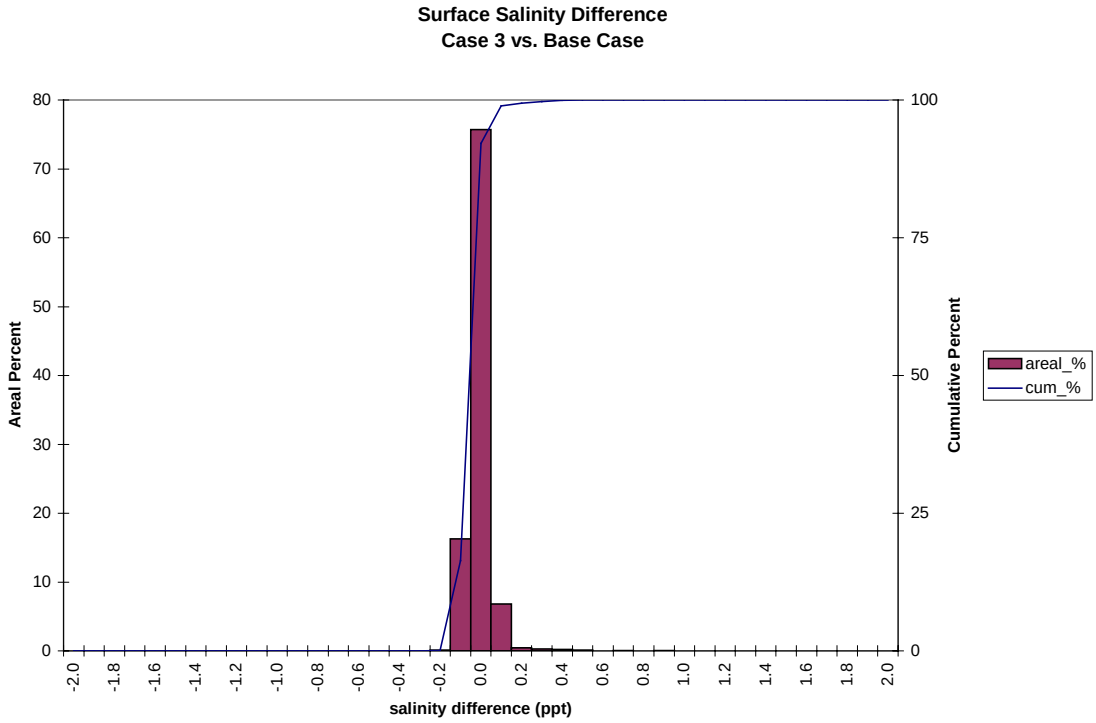

Figure 10. Frequency distribution of surface salinity average difference for the Eastward Expansion (Option 7, 55–foot channel) versus the Base Case.

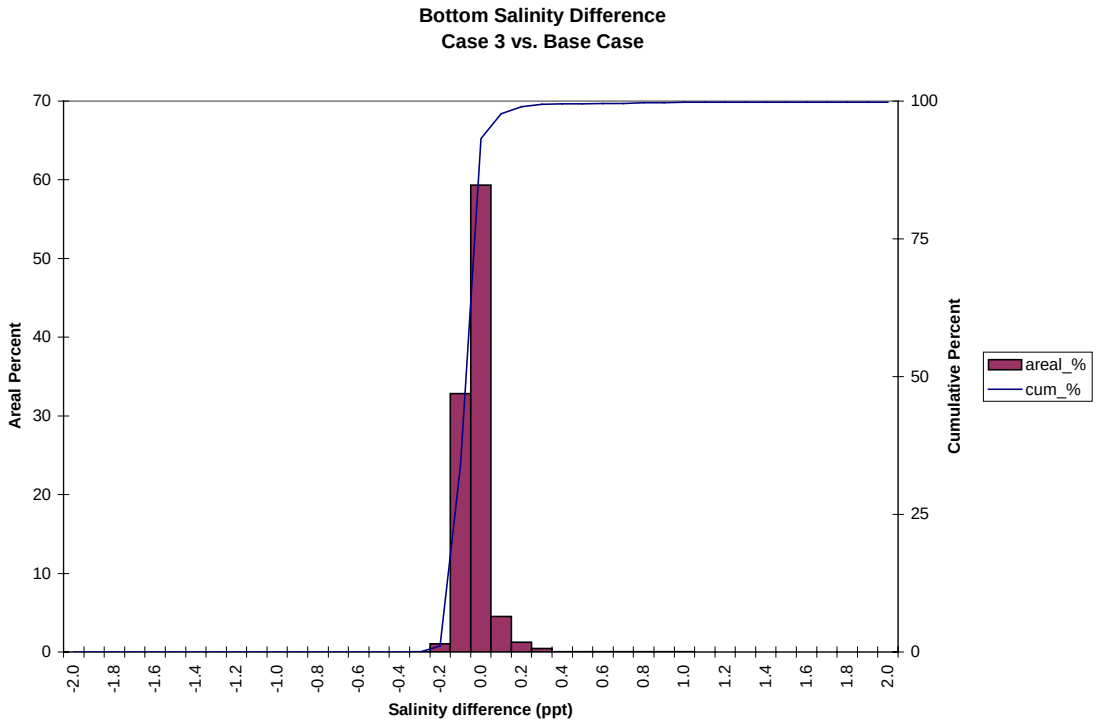

Figure 11. Frequency distribution of bottom salinity average difference for the Eastward Expansion (Option 7, 55–foot channel) versus the Base Case.

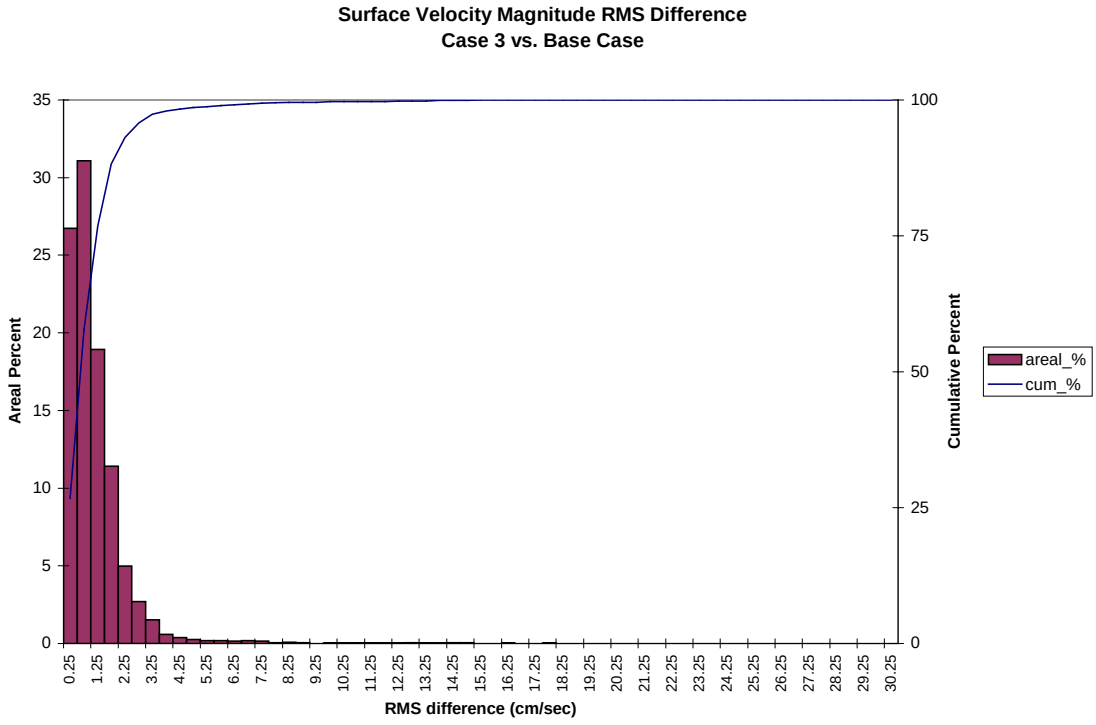

Figure 12. Frequency distribution of surface velocity RMS difference for the Eastward Expansion (Option 7, 55–foot channel) versus the Base Case.

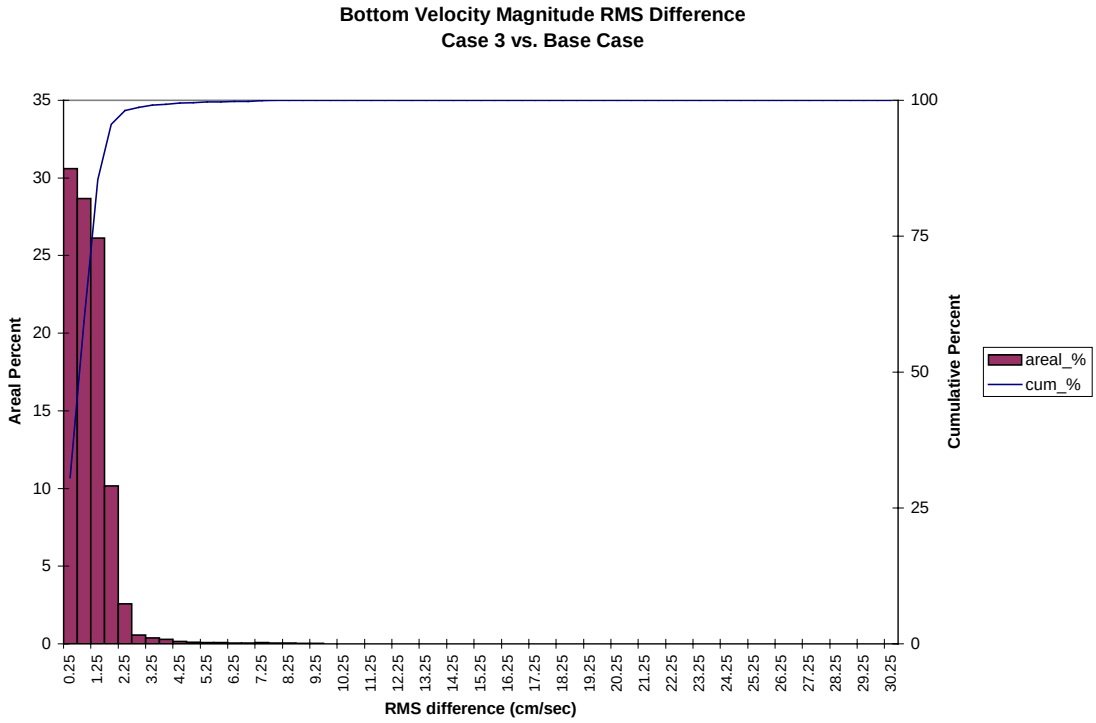

Figure 13. Frequency distribution of bottom velocity RMS difference for the Eastward Expansion (Option 7, 55–foot channel) versus the Base Case.

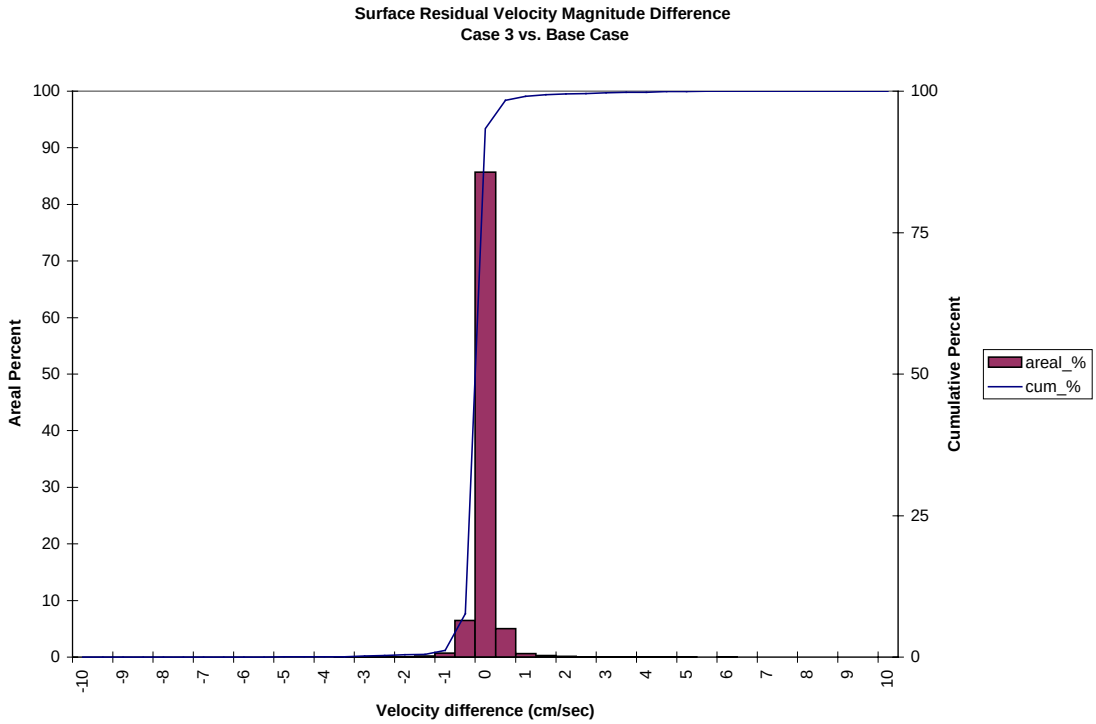

Figure 14. Frequency distribution of surface residual velocity magnitude average difference for the Eastward Expansion (Option 7, 55–foot channel) versus the Base Case.

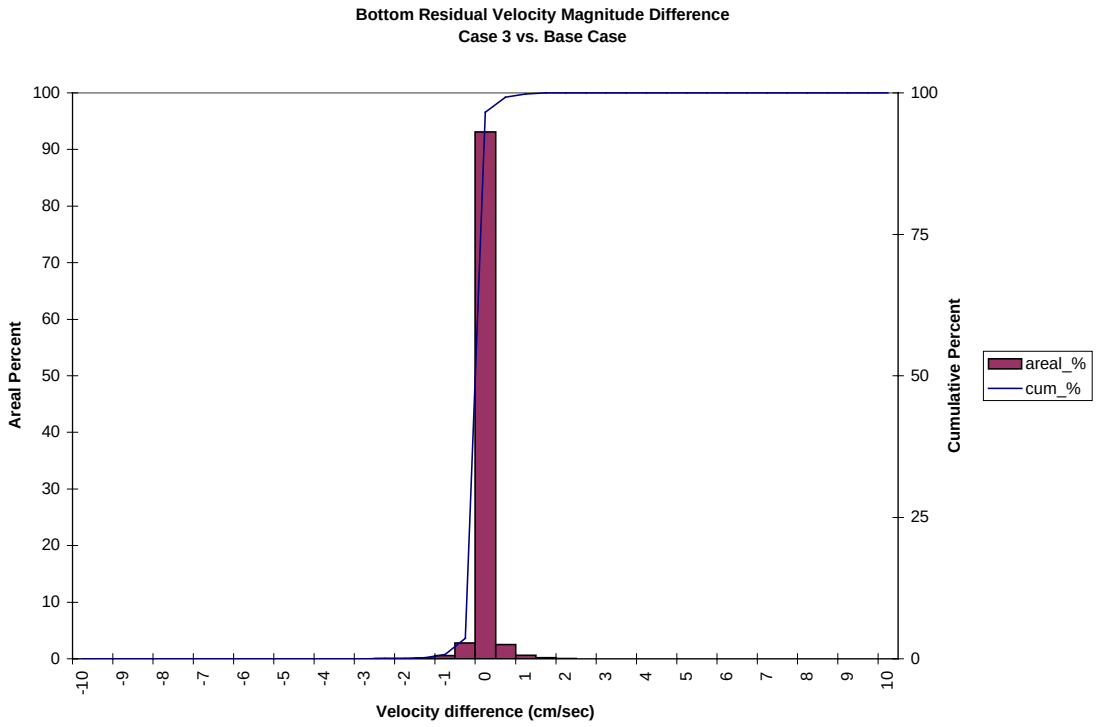

Figure 15. Frequency distribution of bottom residual velocity magnitude average difference for the Eastward Expansion (Option 7, 55–foot channel) versus the Base Case.

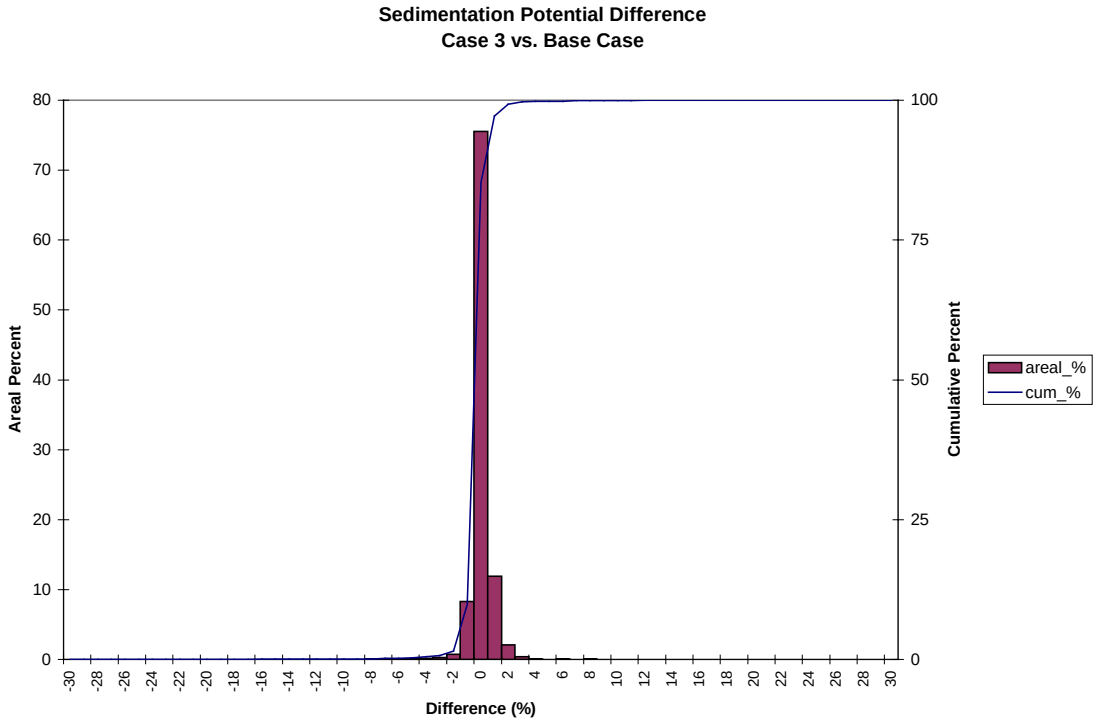

Figure 16. Frequency distribution of sedimentation potential difference for the Eastward Expansion (Option 7, 55–foot channel) versus the Base Case.

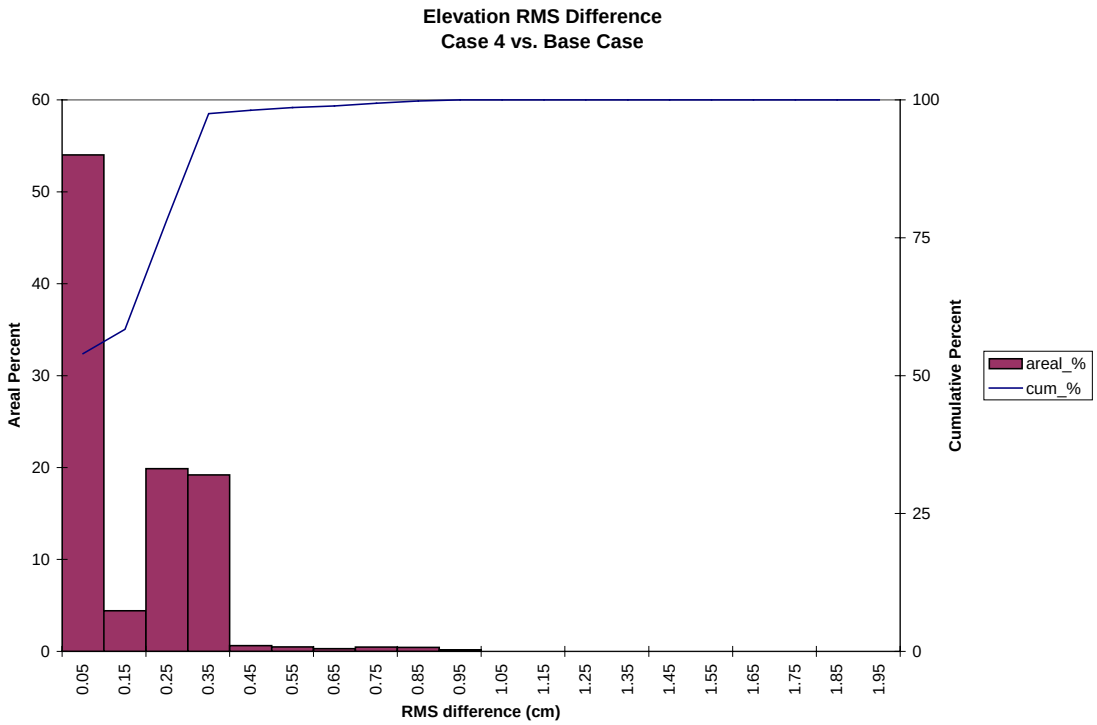

Figure 17. Frequency distribution of elevation RMS difference for the Westward Expansion (Option 5, 50–foot channel) versus the Base Case.

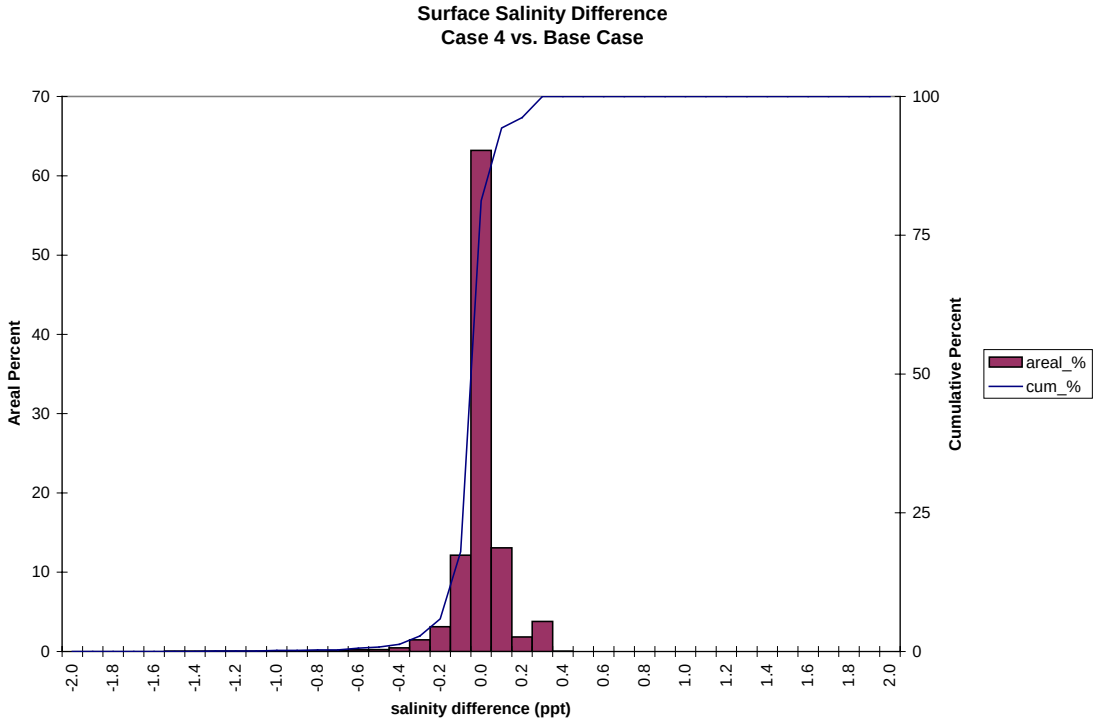

Figure 18. Frequency distribution of surface salinity difference for the Westward Expansion (Option 5, 50–foot channel) versus the Base Case.

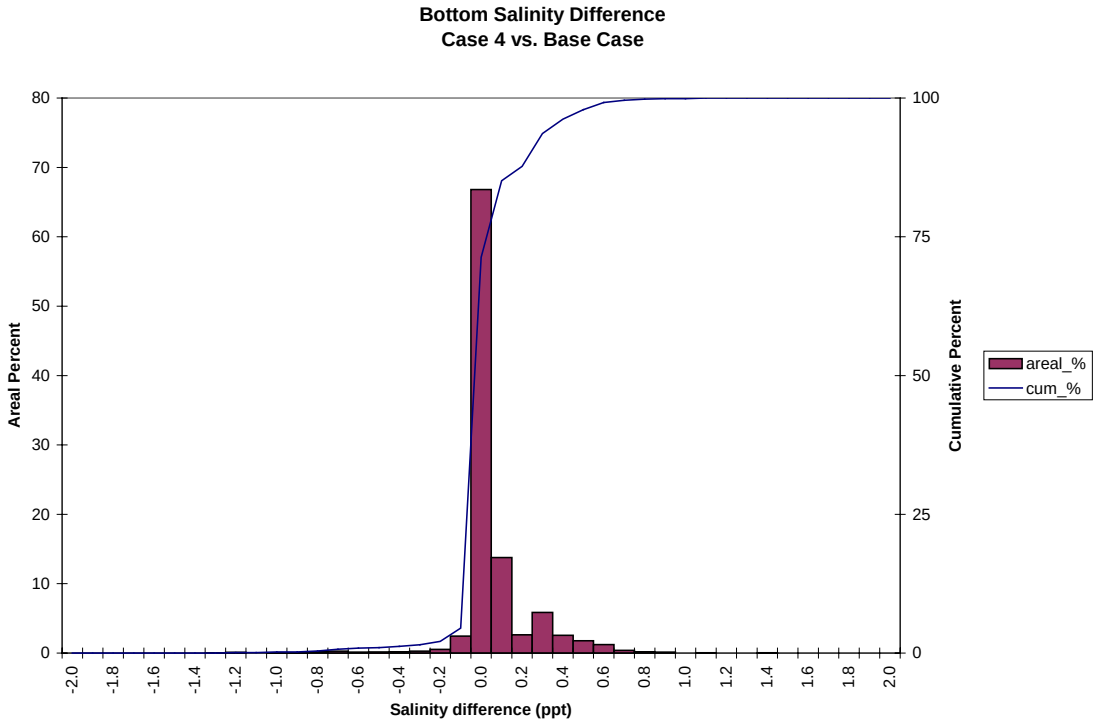

Figure 19. Frequency distribution of bottom salinity average difference for the Westward Expansion (Option 5, 50–foot channel) versus the Base Case.

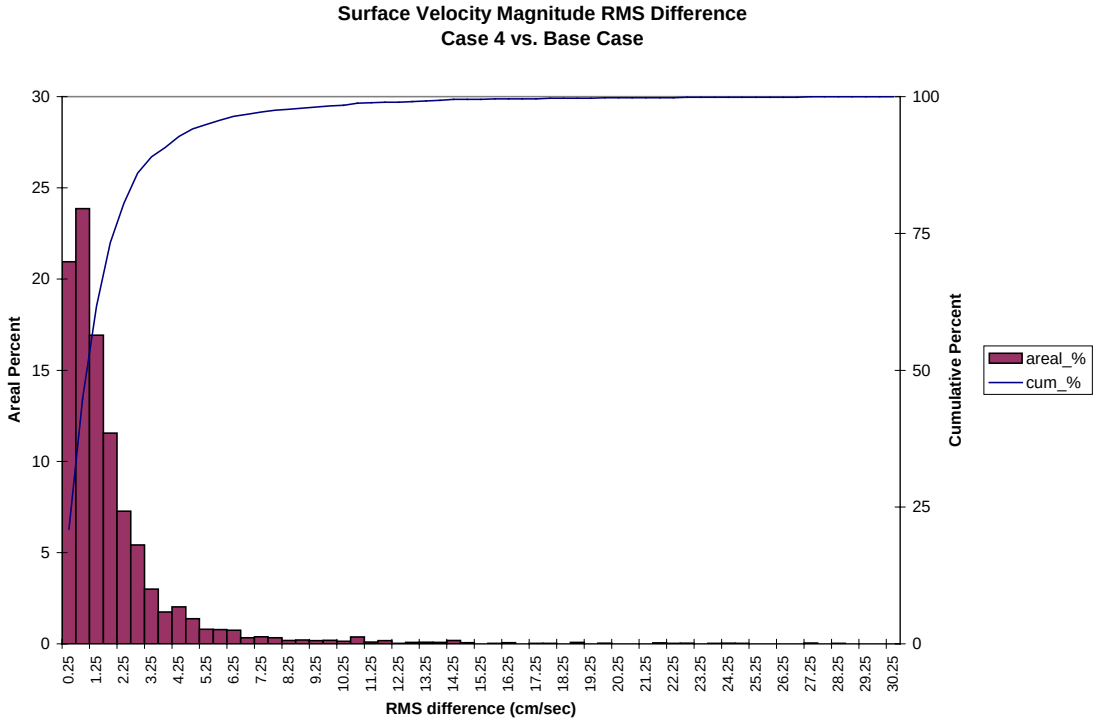

Figure 20. Frequency distribution of surface velocity RMS difference for the Westward Expansion (Option 5, 50–foot channel) versus the Base Case.

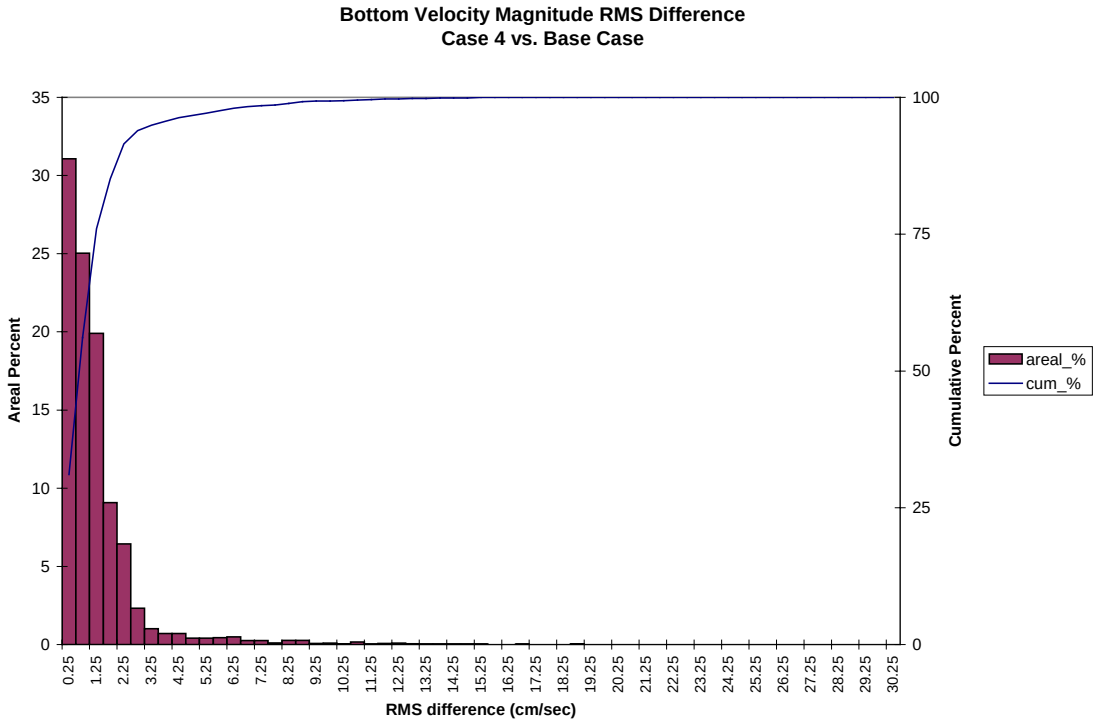

Figure 21. Frequency distribution of bottom velocity RMS difference for the Westward Expansion (Option 5, 50–foot channel) versus the Base Case.

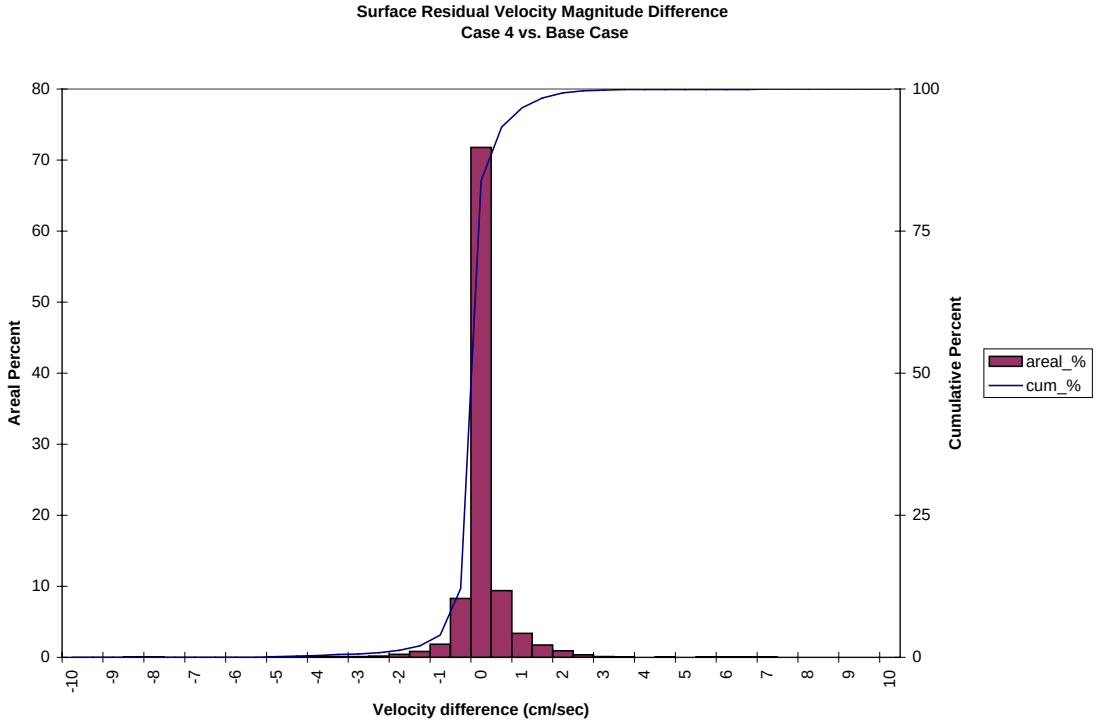

Figure 22. Frequency distribution of surface residual velocity magnitude average difference for the Westward Expansion (Option 5, 50–foot channel) versus the Base Case.

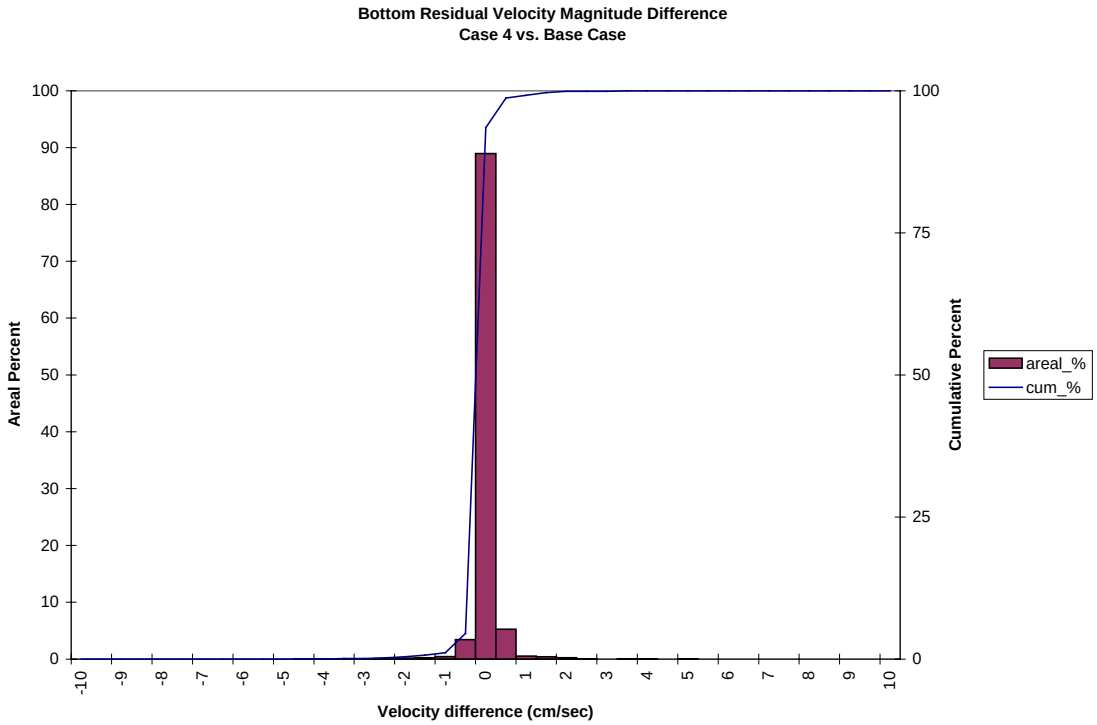

Figure 23. Frequency distribution of bottom residual velocity magnitude difference for the Westward Expansion (Option 5, 50–foot channel) versus the Base Case.

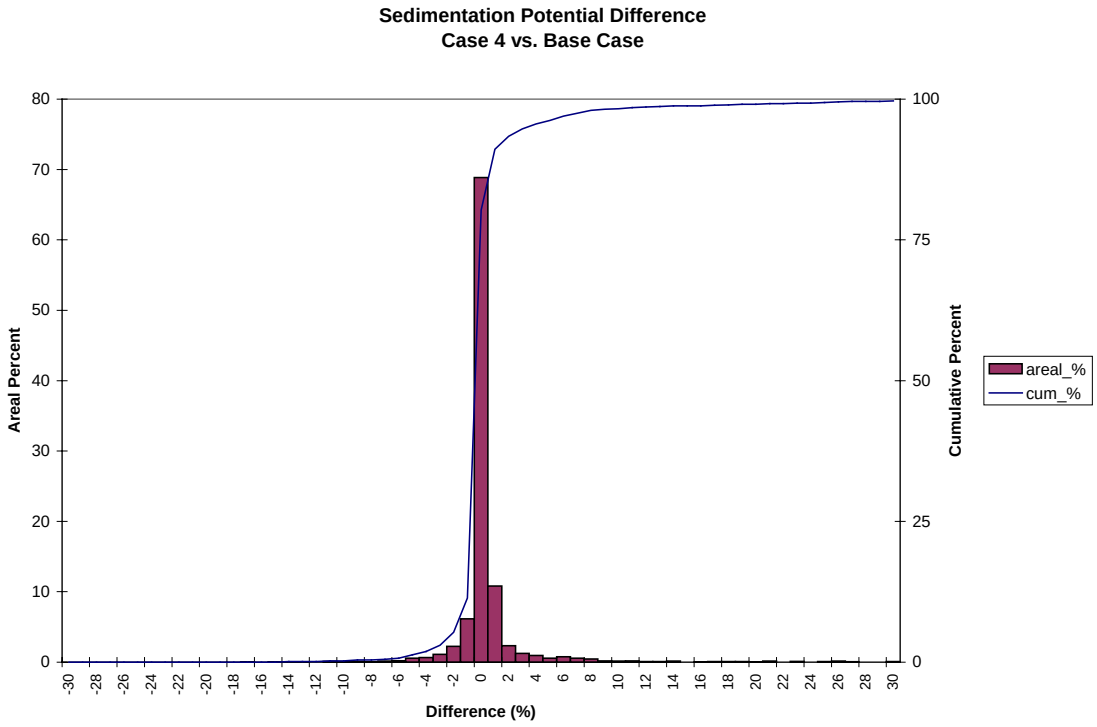

Figure 24. Frequency distribution of sedimentation potential difference for the Westward Expansion (Option 5, 50–foot channel) versus the Base Case.

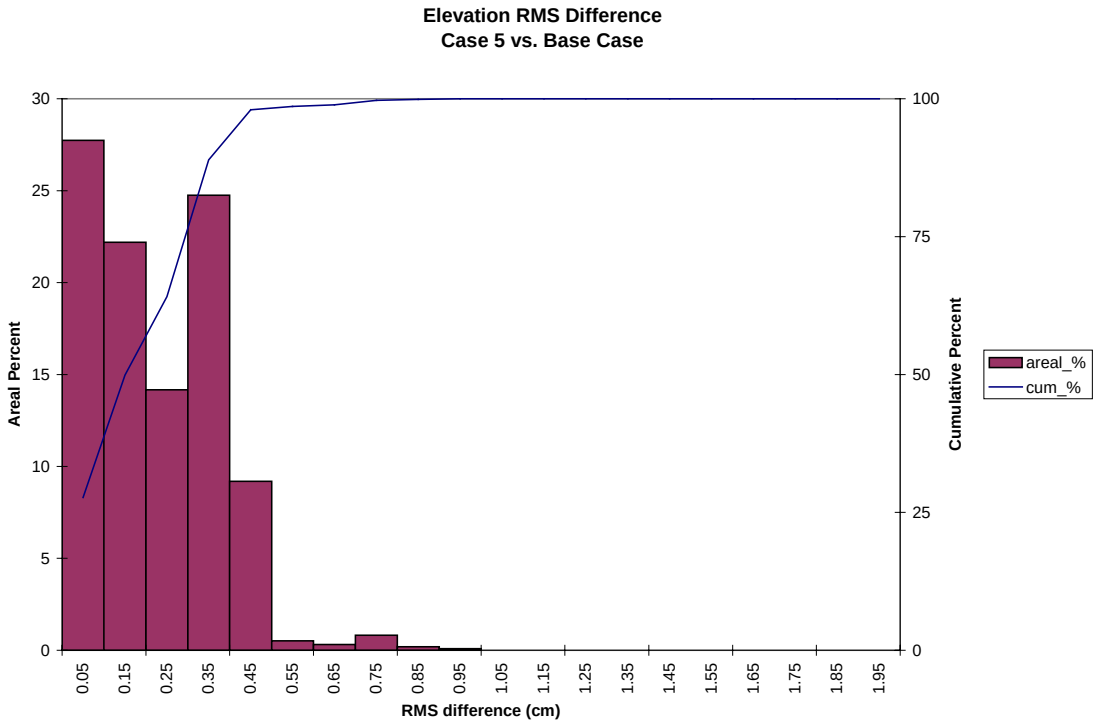

Figure 25. Frequency distribution of elevation RMS difference for the Westward Expansion (Option 5, 55–foot channel) versus the Base Case.

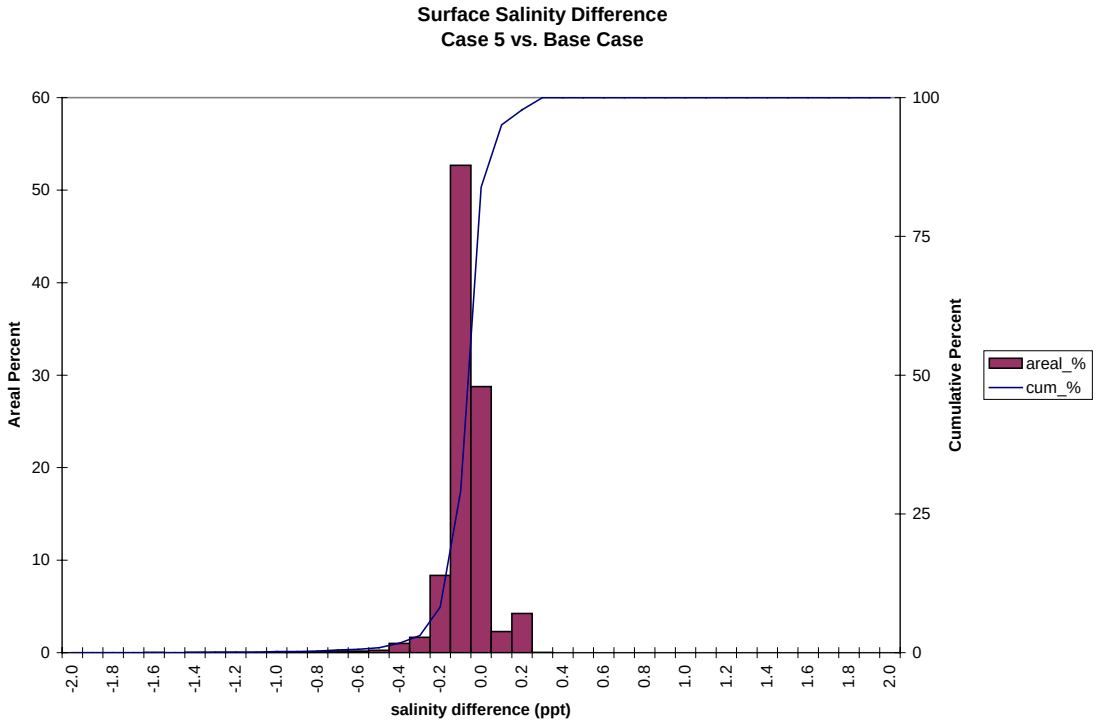

Figure 26. Frequency distribution of surface salinity difference for the Westward Expansion (Option 5, 55–foot channel) versus the Base Case.

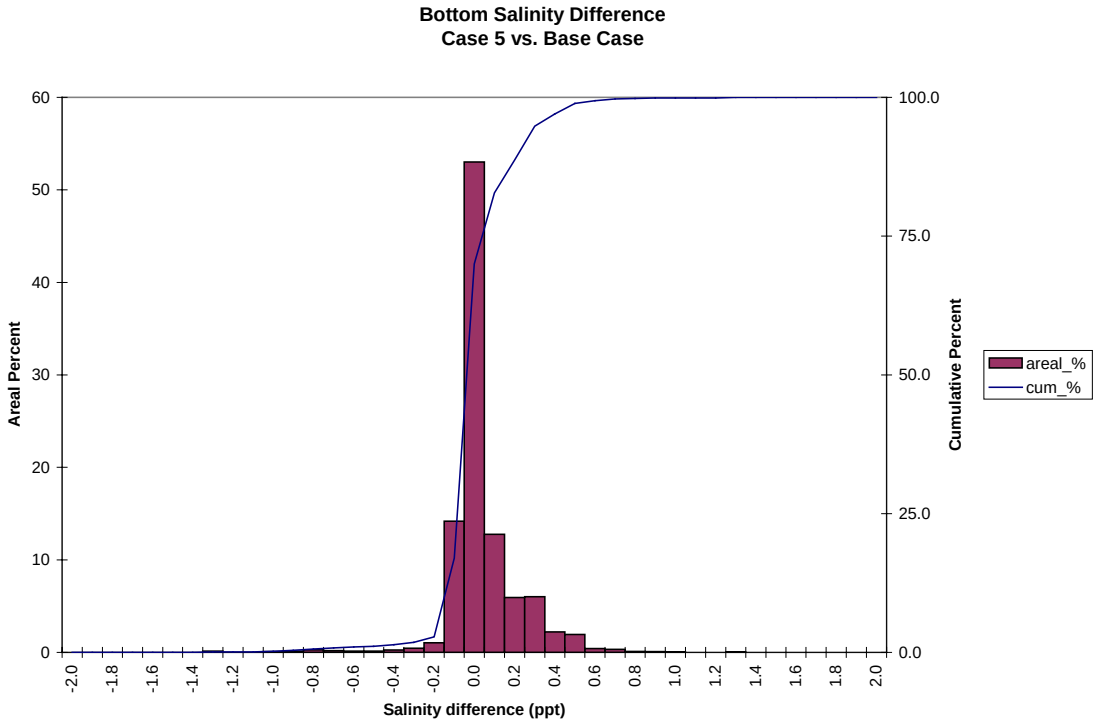

Figure 27. Frequency distribution of bottom salinity average difference for the Westward Expansion (Option 5, 55–foot channel) versus the Base Case.

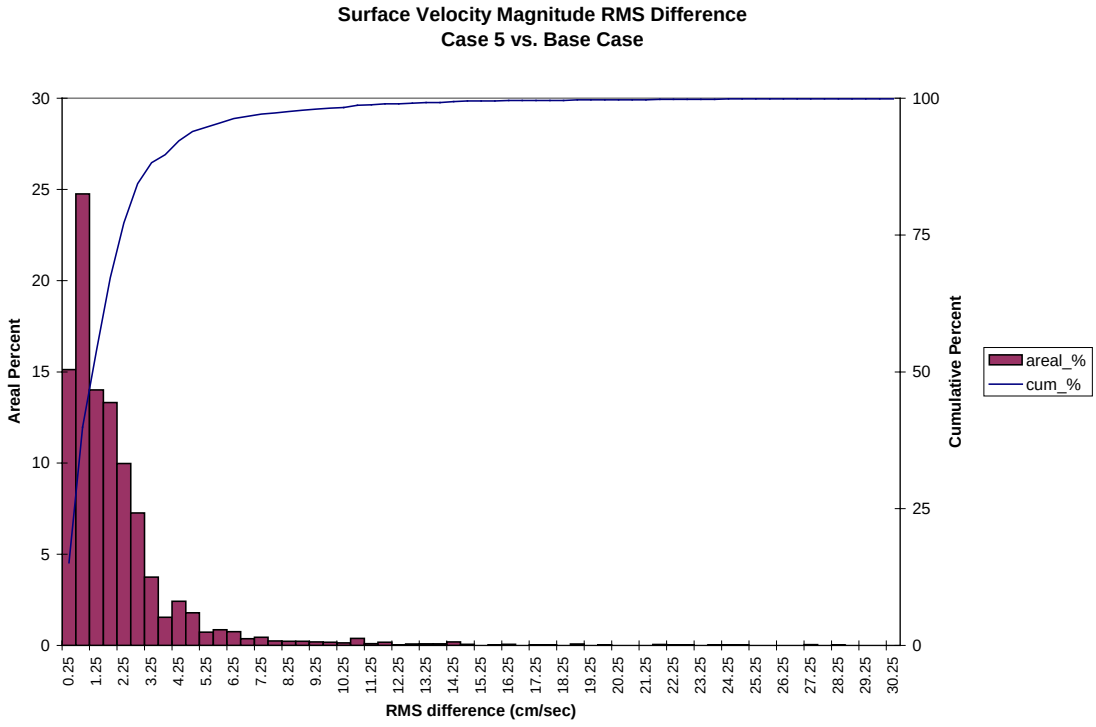

Figure 28. Frequency distribution of surface velocity RMS difference for the Westward Expansion (Option 5, 55–foot channel) versus the Base Case.

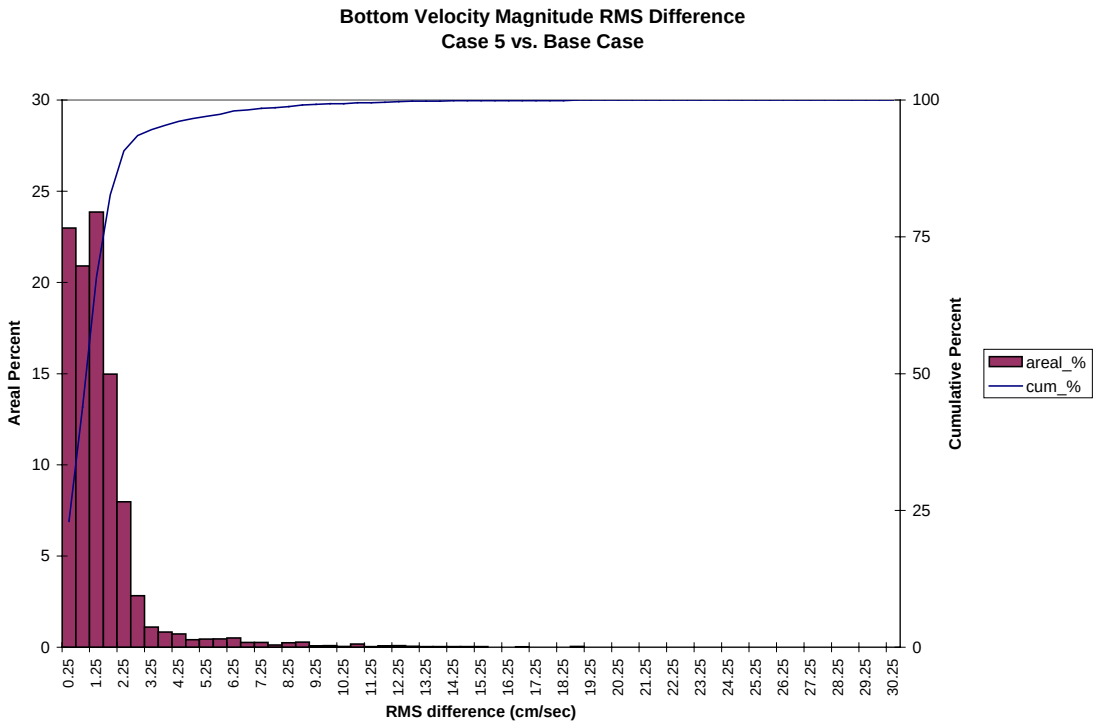

Figure 29. Frequency distribution of bottom velocity RMS difference for the Westward Expansion (Option 5, 55–foot channel) versus the Base Case.

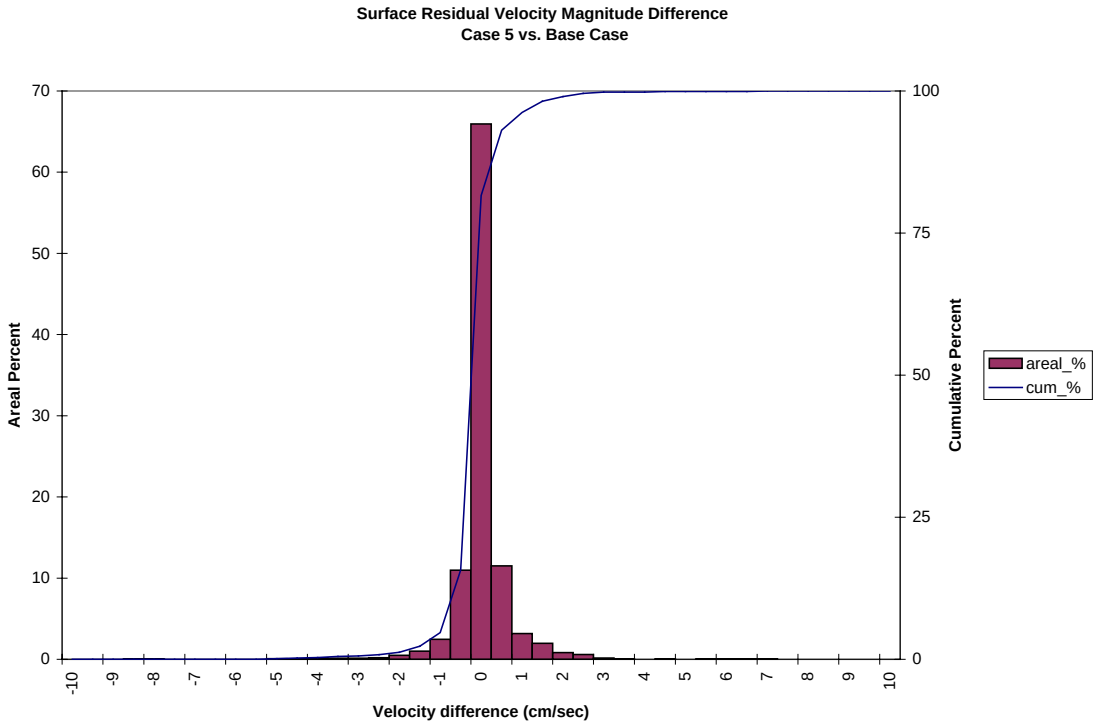

Figure 30. Frequency distribution of surface residual velocity magnitude average Difference for the Westward Expansion (Option 5, 55–foot channel) versus the Base Case.

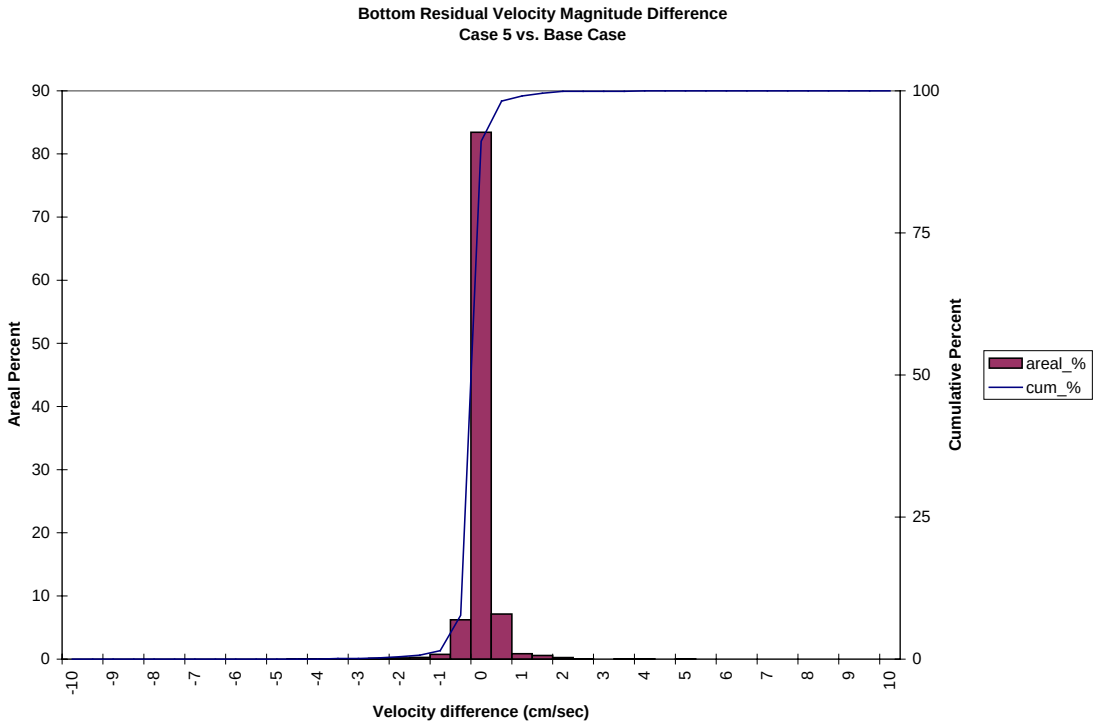

Figure 31. Frequency distribution of bottom residual velocity magnitude difference for the Westward Expansion (Option 5, 55–foot channel) versus the Base Case.

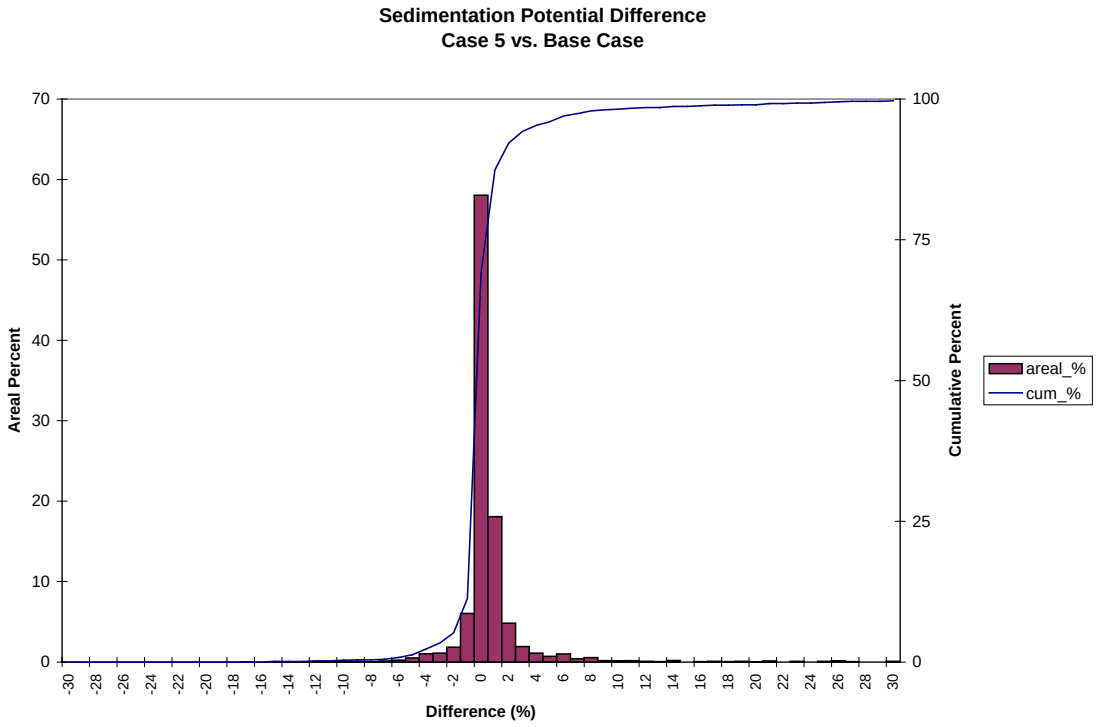

Figure 32. Frequency distribution of sedimentation potential difference for the Westward Expansion (Option 5, 55–foot channel) versus the Base Case.

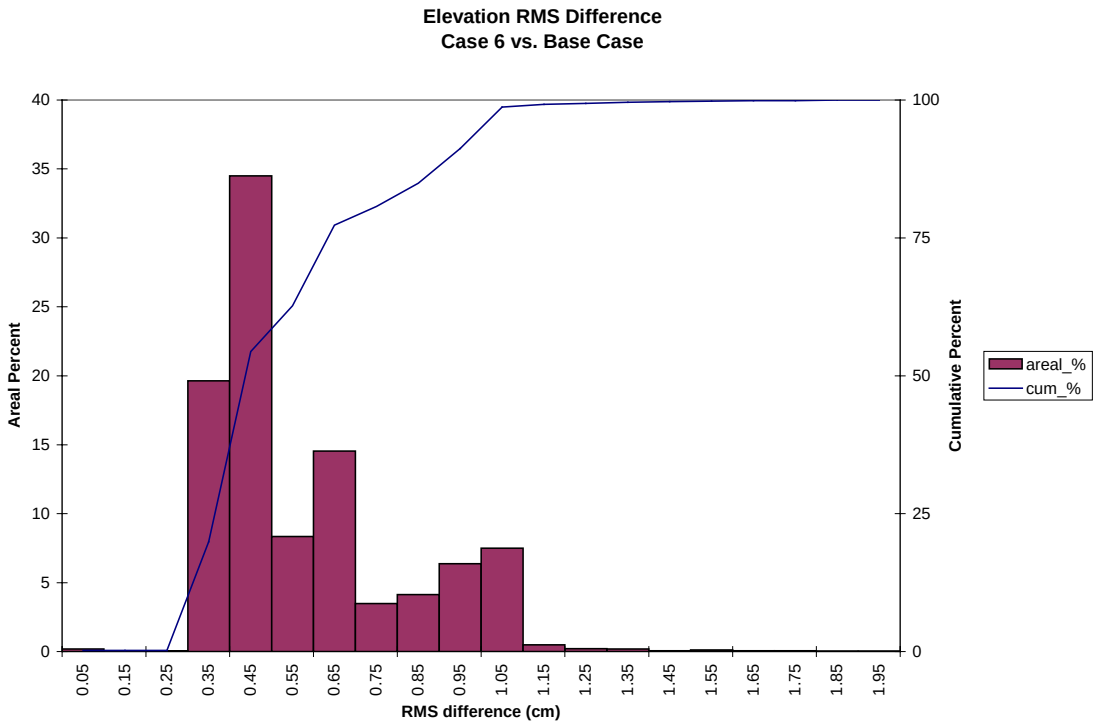

Figure 33. Frequency distribution of elevation RMS difference for the Northward Expansion (Option 6, 50–foot channel) versus the Base Case.

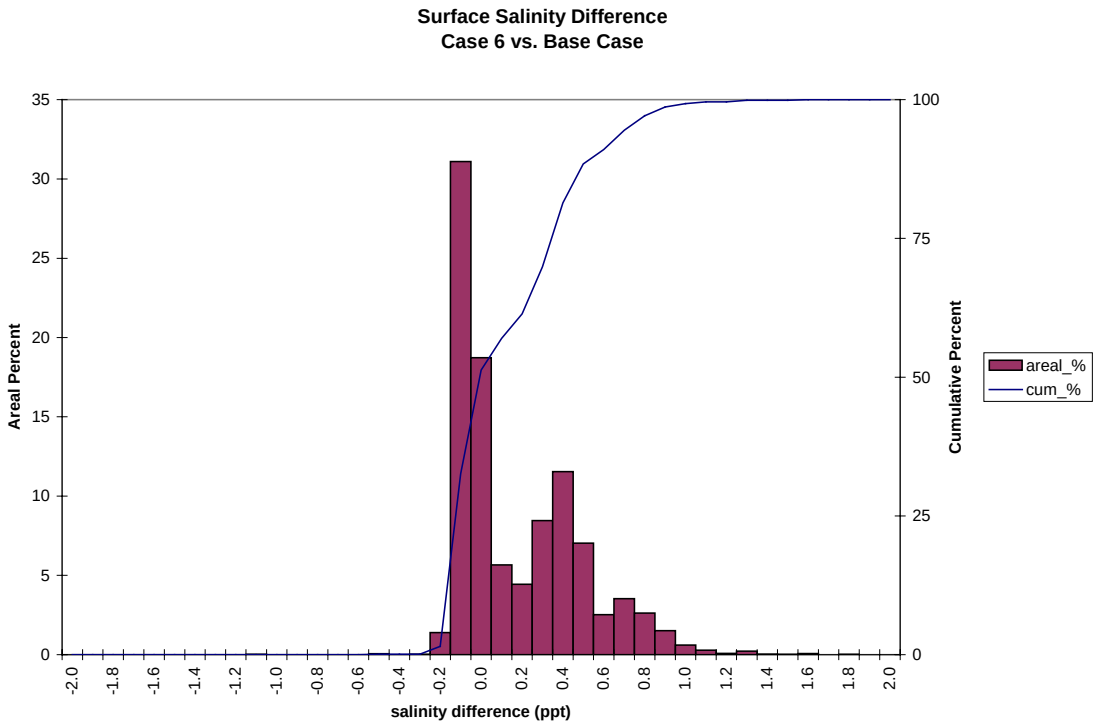

Figure 34. Frequency distribution of surface salinity difference for the Northward Expansion (Option 6, 50–foot channel) versus the Base Case.

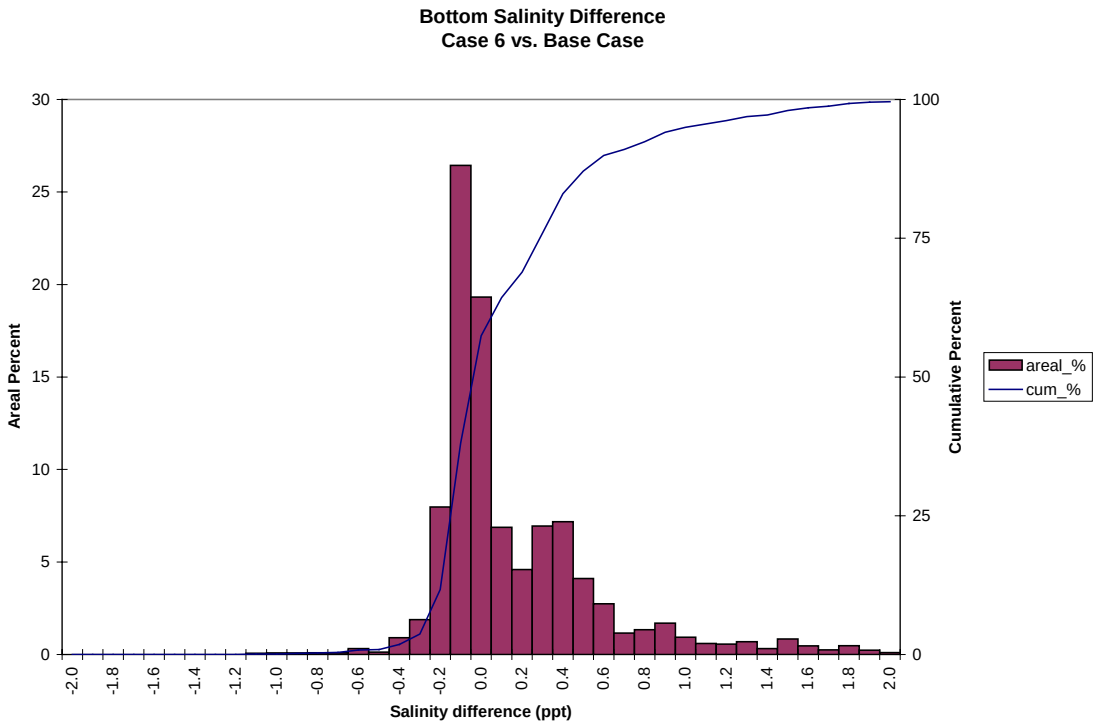

Figure 35. Frequency distribution of bottom salinity average difference for the Northward Expansion (Option 6, 50–foot channel) versus the Base Case.

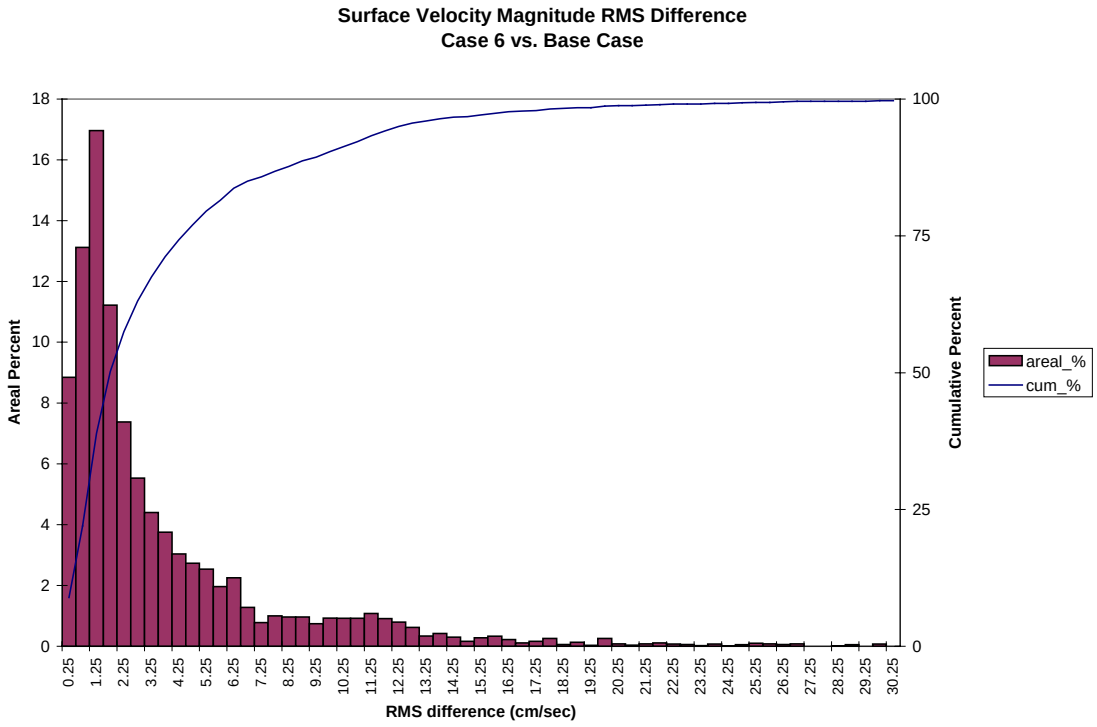

Figure 36. Frequency distribution of surface velocity RMS difference for the Northward Expansion (Option 6, 50–foot channel) versus the Base Case.

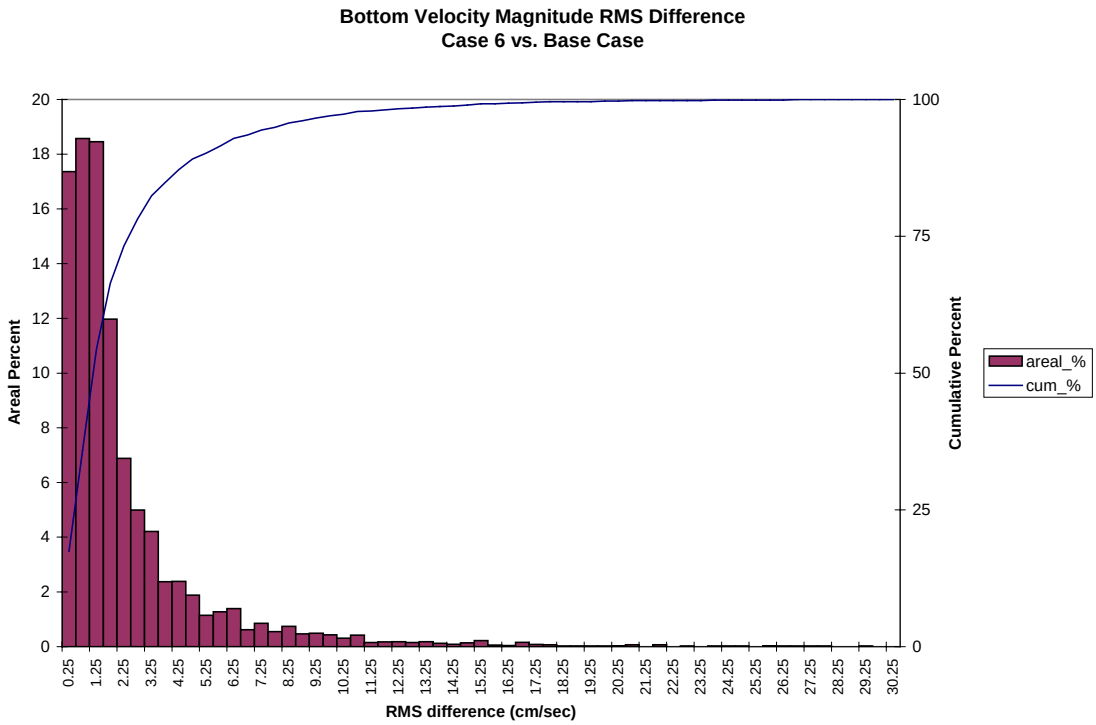

Figure 37. Frequency distribution of bottom velocity RMS difference for the Northward Expansion (Option 6, 50–foot channel) versus the Base Case.

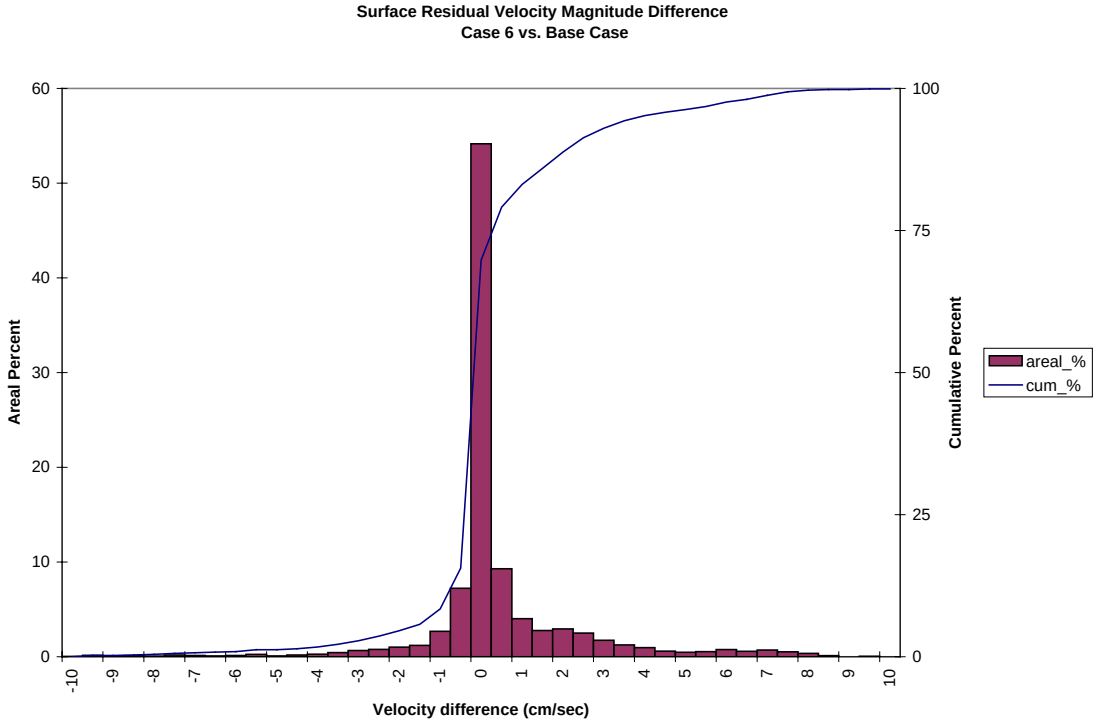

Figure 38. Frequency distribution of surface residual velocity magnitude average difference for the Northward Expansion (Option 6, 50–foot channel) versus the Base Case.

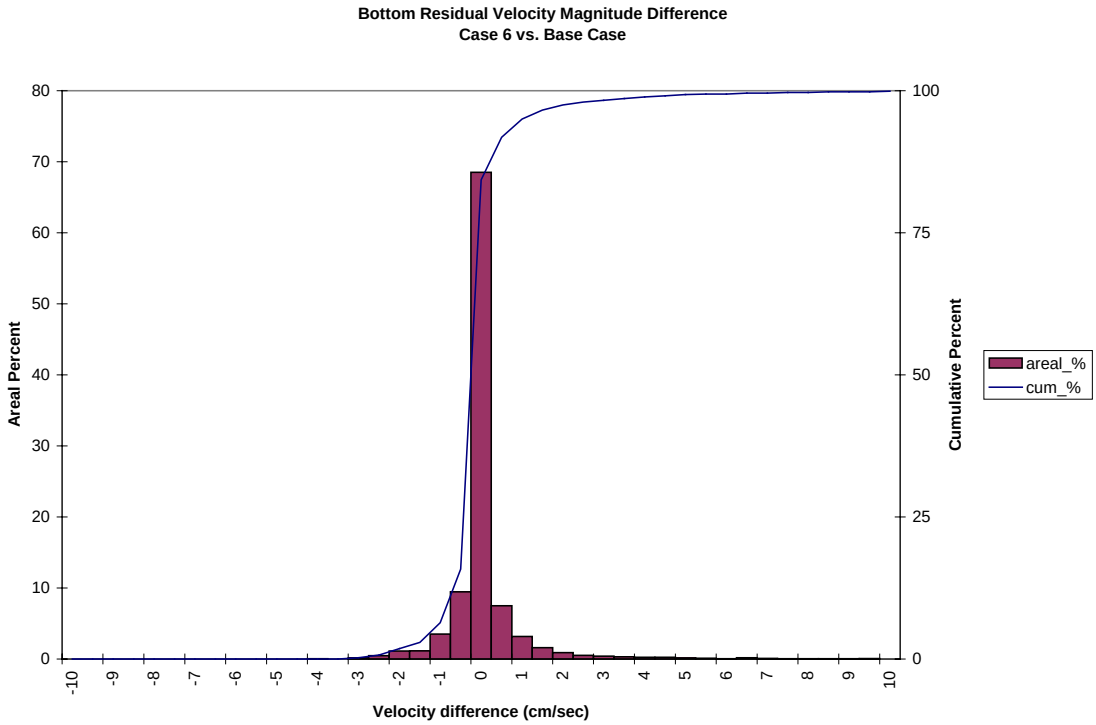

Figure 39. Frequency distribution of bottom residual velocity magnitude average difference for the Northward Expansion (Option 6, 50–foot channel) versus the Base Case.

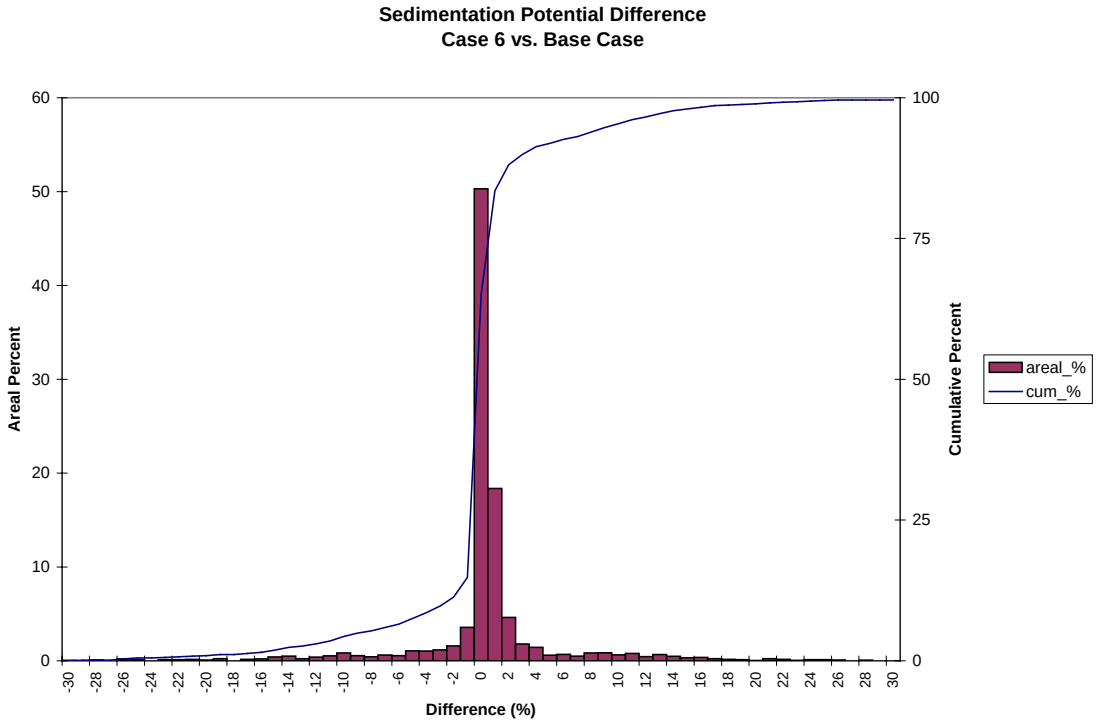

Figure 40. Frequency distribution of sedimentation potential difference for the Northward Expansion (Option 6, 50–foot channel) versus the Base Case.

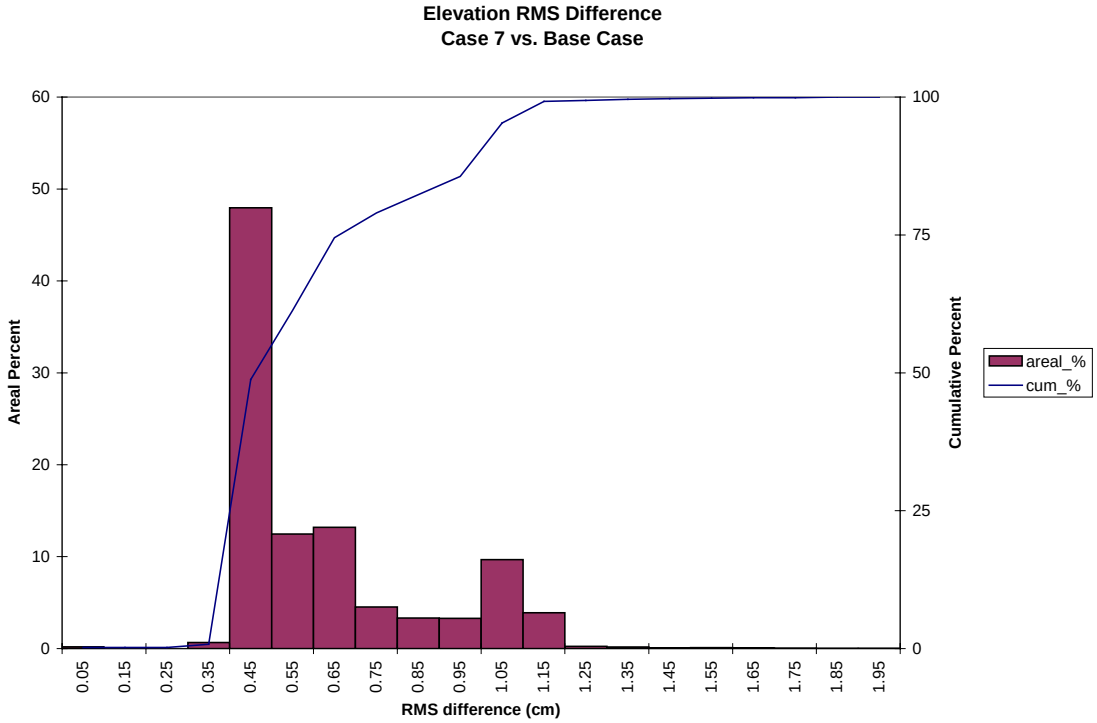

Figure 41. Frequency distribution of elevation RMS difference for the Northward Expansion (Option 6, 55–foot channel) versus the Base Case.

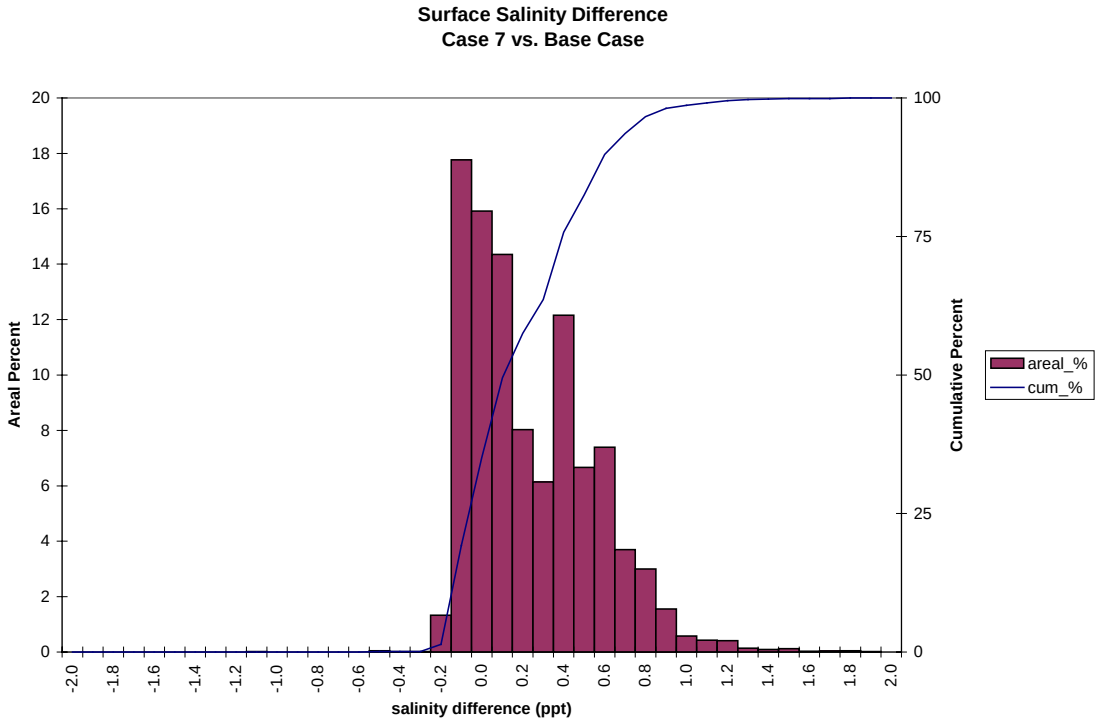

Figure 42. Frequency distribution of surface salinity average difference for the Northward Expansion (Option 6, 55–foot channel) versus the Base Case.

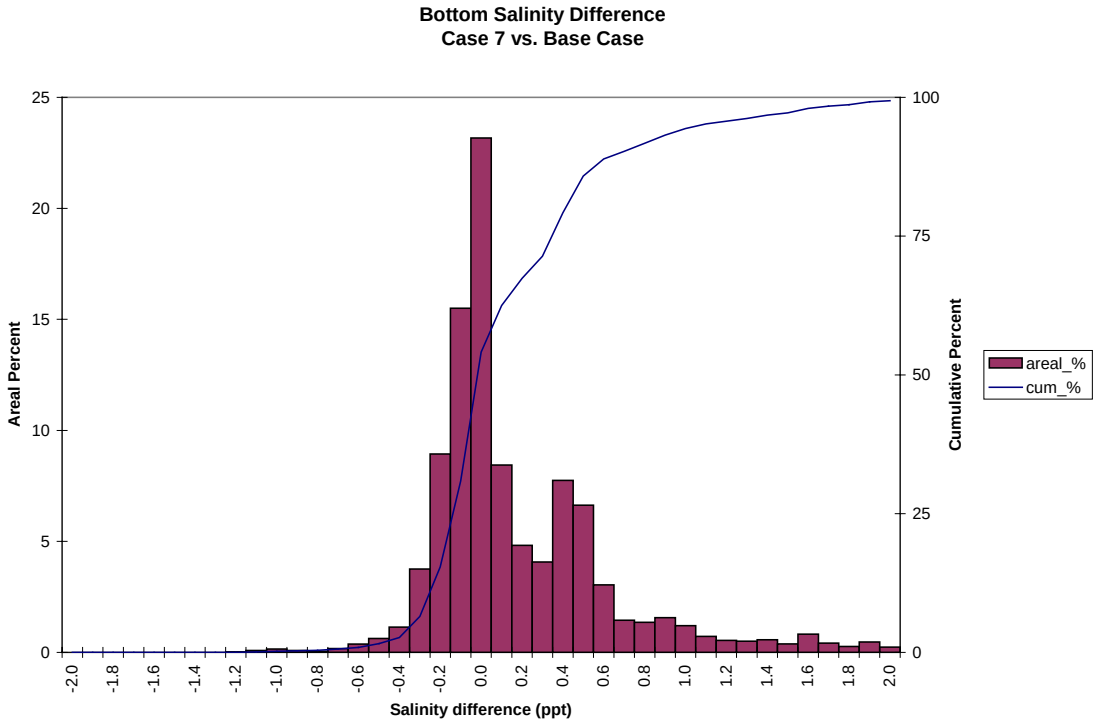

Figure 43. Frequency distribution of bottom salinity average difference for the Northward Expansion (Option 6, 55–foot channel) versus the Base Case.

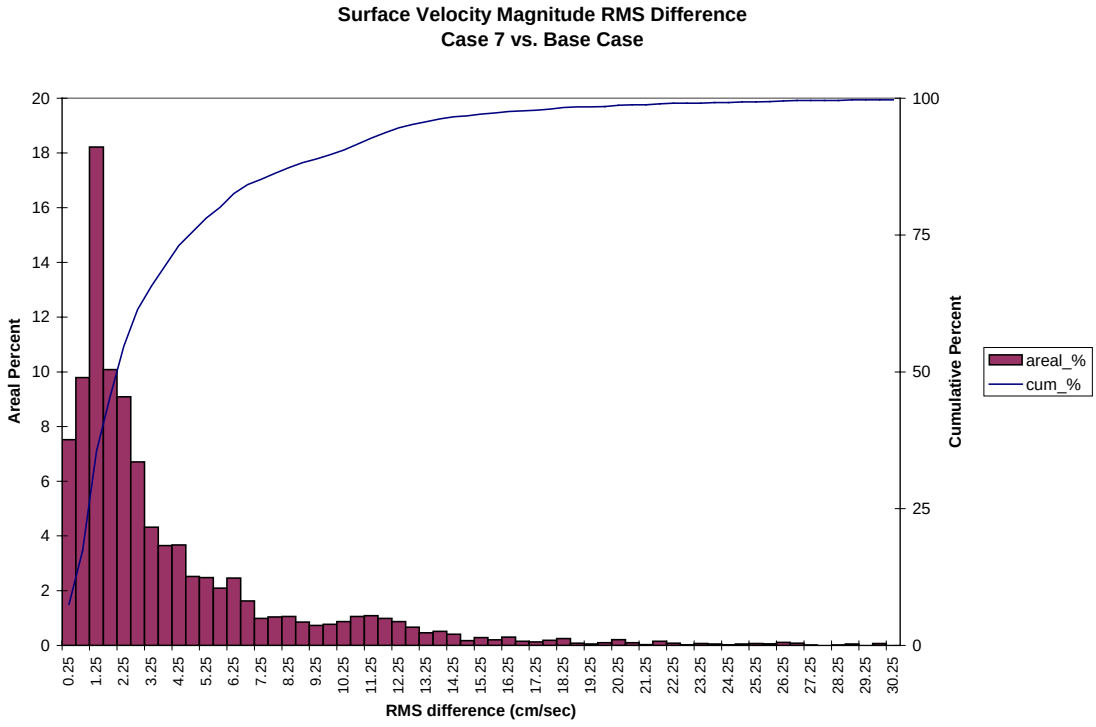

Figure 44. Frequency distribution of surface velocity RMS difference for the Northward Expansion (Option 6, 55–foot channel) versus the Base Case.

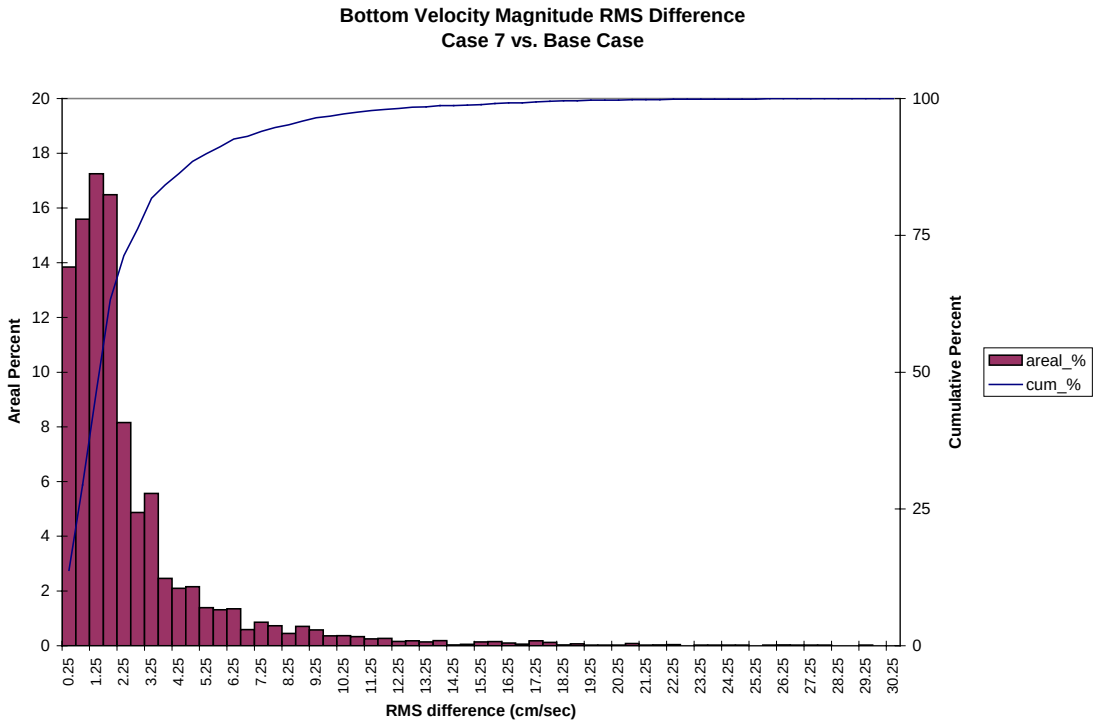

Figure 45. Frequency distribution of bottom velocity RMS difference for the Northward Expansion (Option 6, 55–foot channel) versus the Base Case.

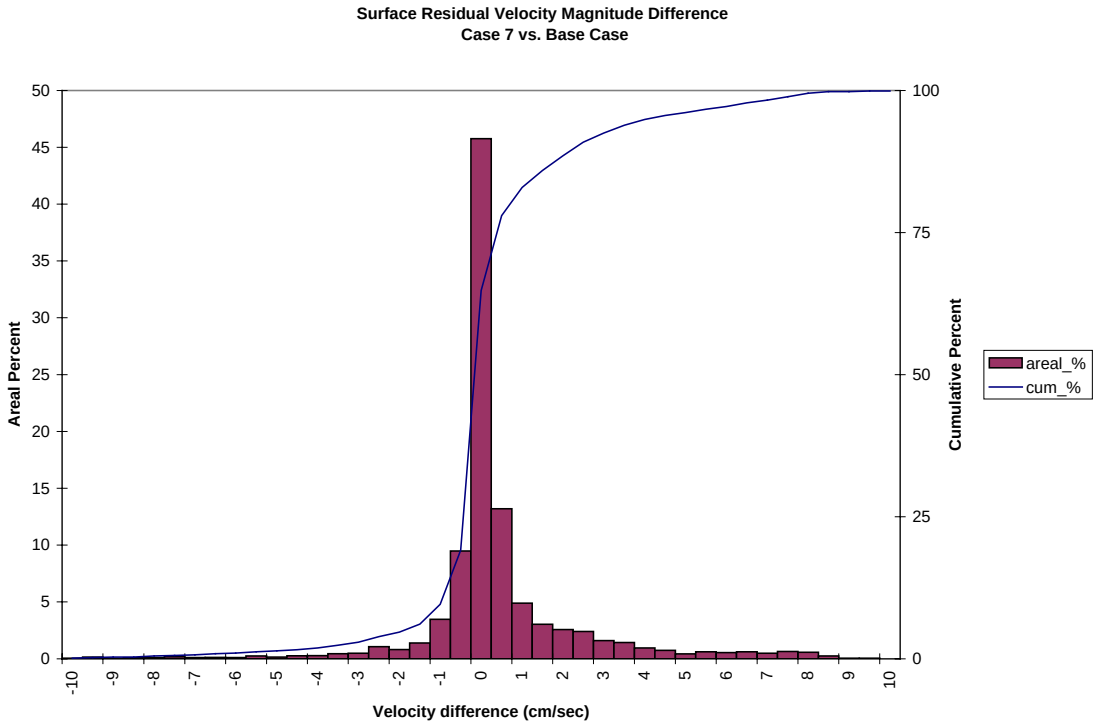

Figure 46. Frequency distribution of surface residual velocity magnitude average difference for the Northward Expansion (Option 6, 55–foot channel) versus the Base Case.

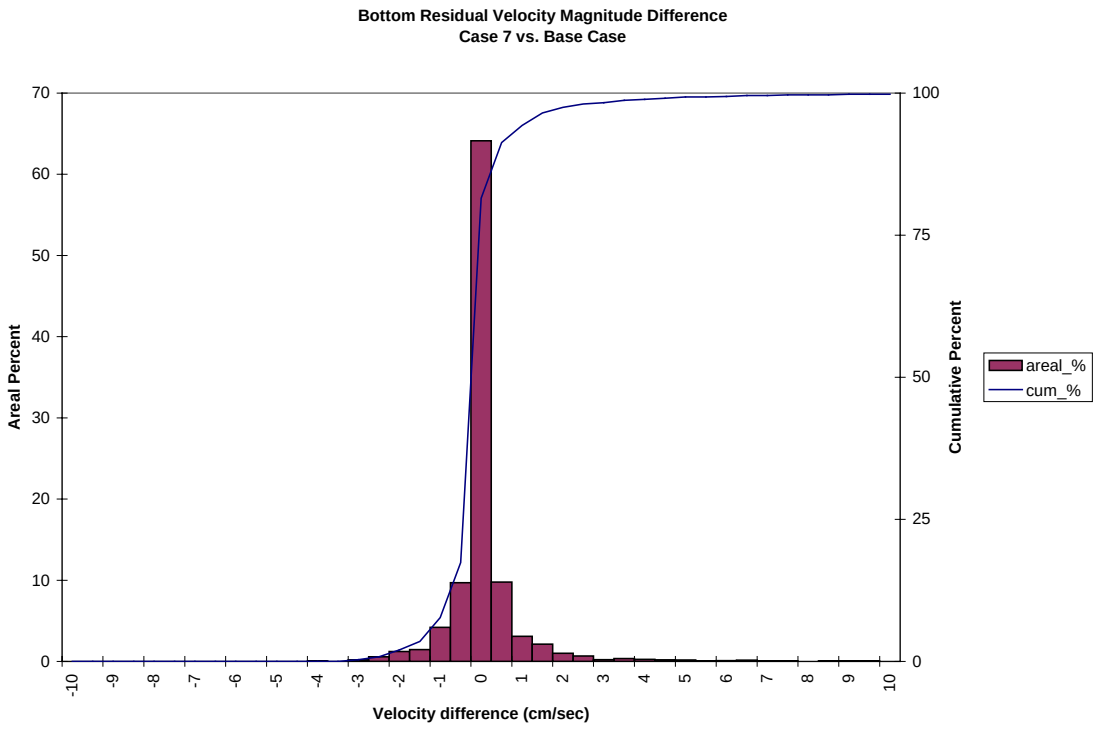

Figure 47. Frequency distribution of bottom residual velocity magnitude average difference for the Northward Expansion (Option 6, 55–foot channel) versus the Base Case.

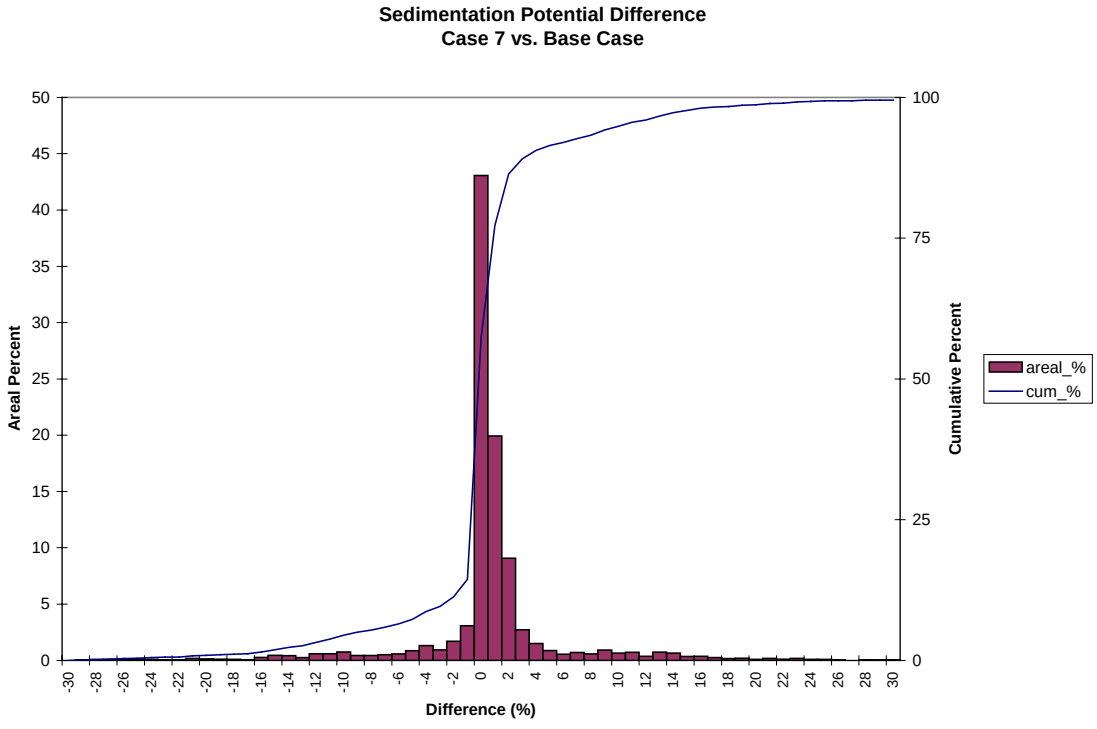

Figure 48. Frequency distribution of sedimentation potential difference for the Northward Expansion (Option 6, 55–foot channel) versus the Base Case.

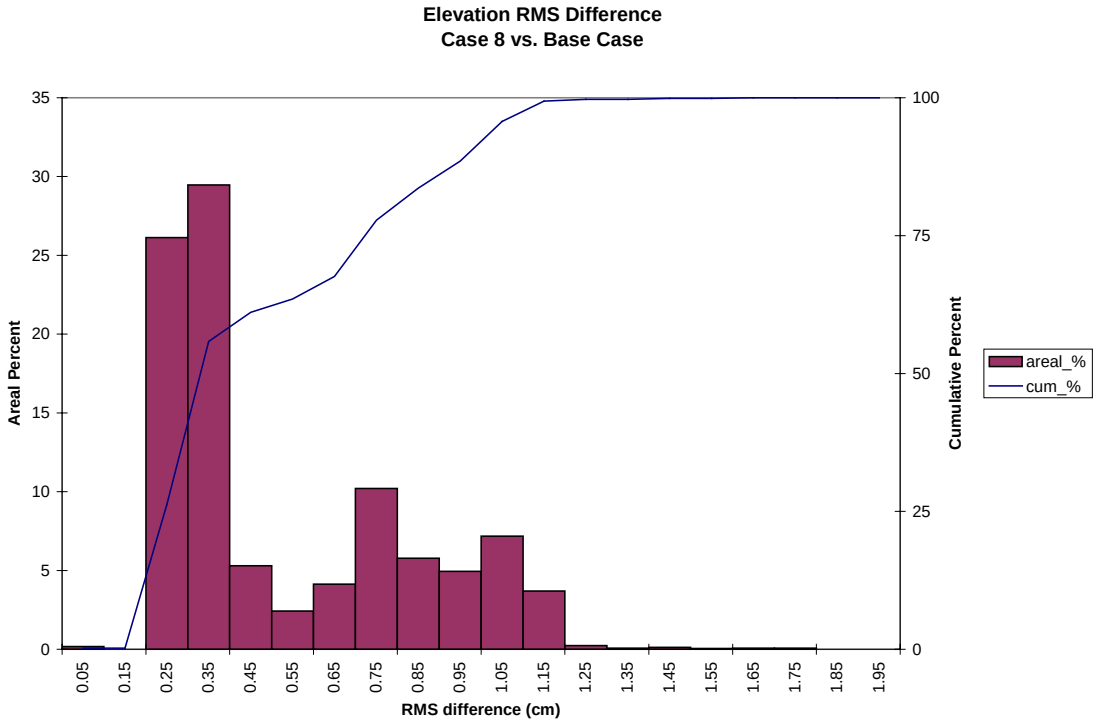

Figure 49. Frequency distribution of elevation RMS difference for the Northward and Eastward Expansion (Option 9, 50–foot channel) versus the Base Case.

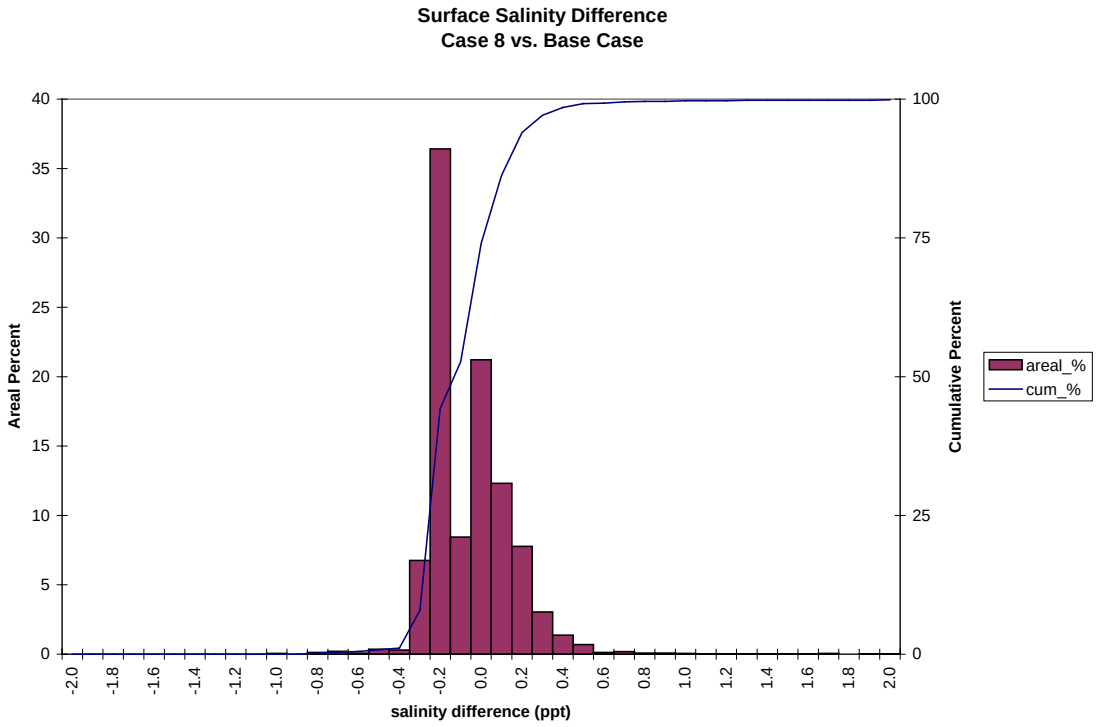

Figure 50. Frequency distribution of surface salinity average difference for the Northward and Eastward Expansion (Option 9, 50–foot channel) versus the Base Case.

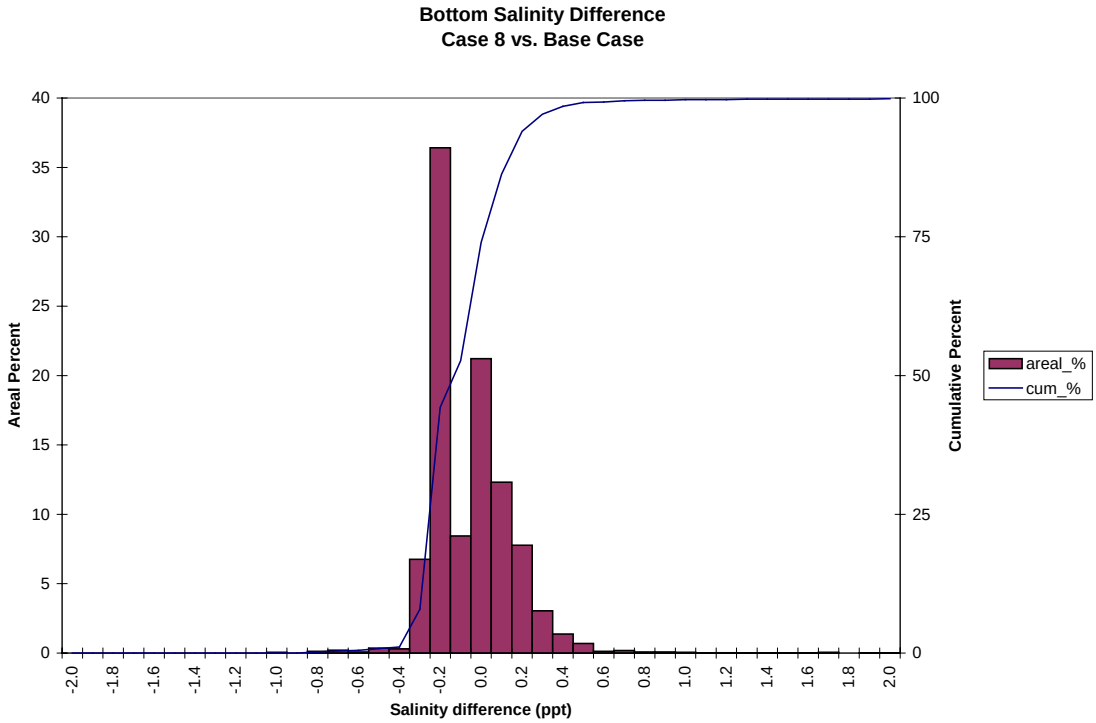

Figure 51. Frequency distribution of bottom salinity average difference for the Northward and Eastward Expansion (Option 9, 50–foot channel) versus the Base Case.

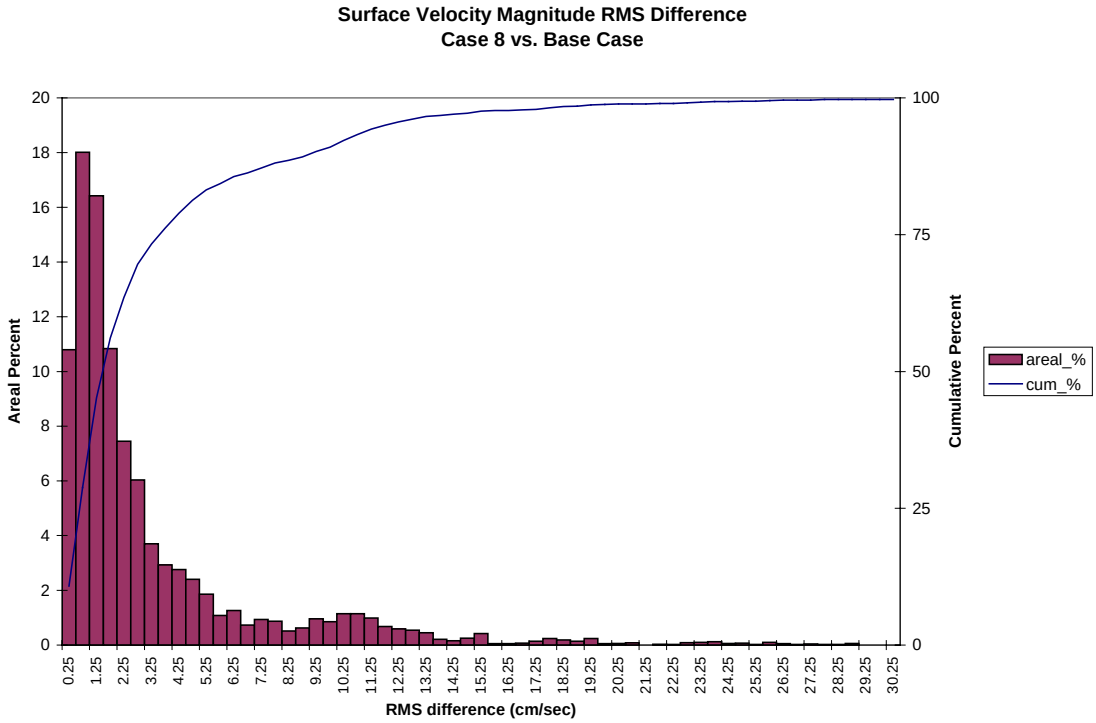

Figure 52. Frequency distribution of surface velocity RMS difference for the Northward and Eastward Expansion (Option 9, 50–foot channel) versus the Base Case.

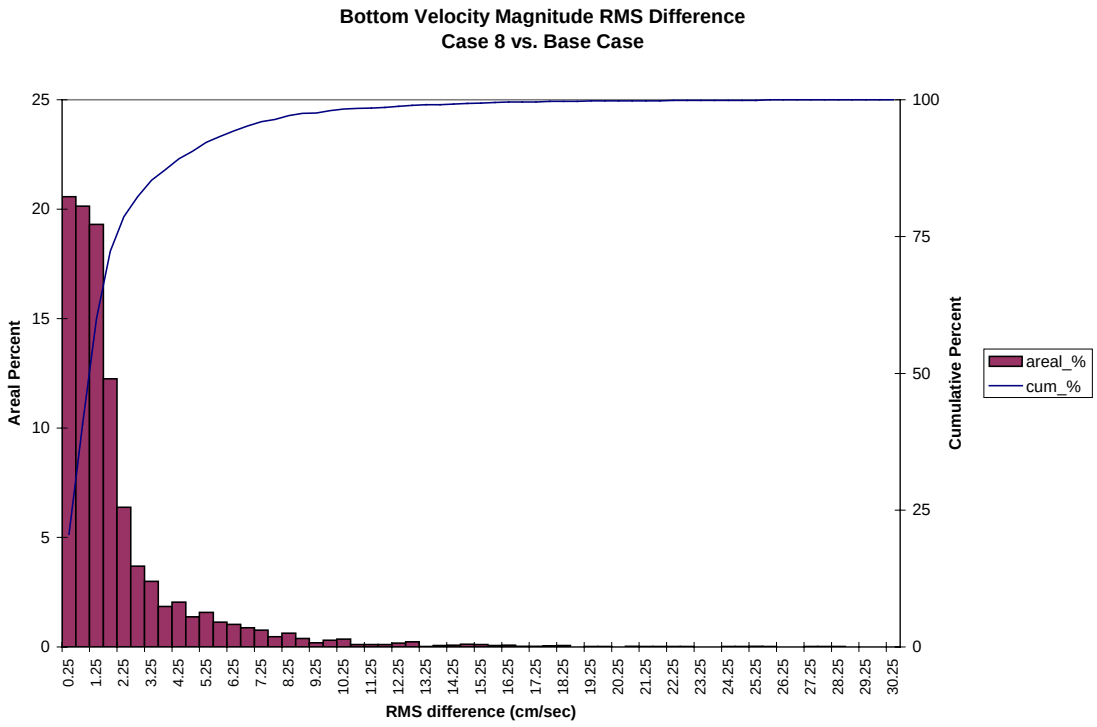

Figure 53. Frequency distribution of bottom velocity RMS difference for the Northward and Eastward Expansion (Option 9, 50–foot channel) versus the Base Case.

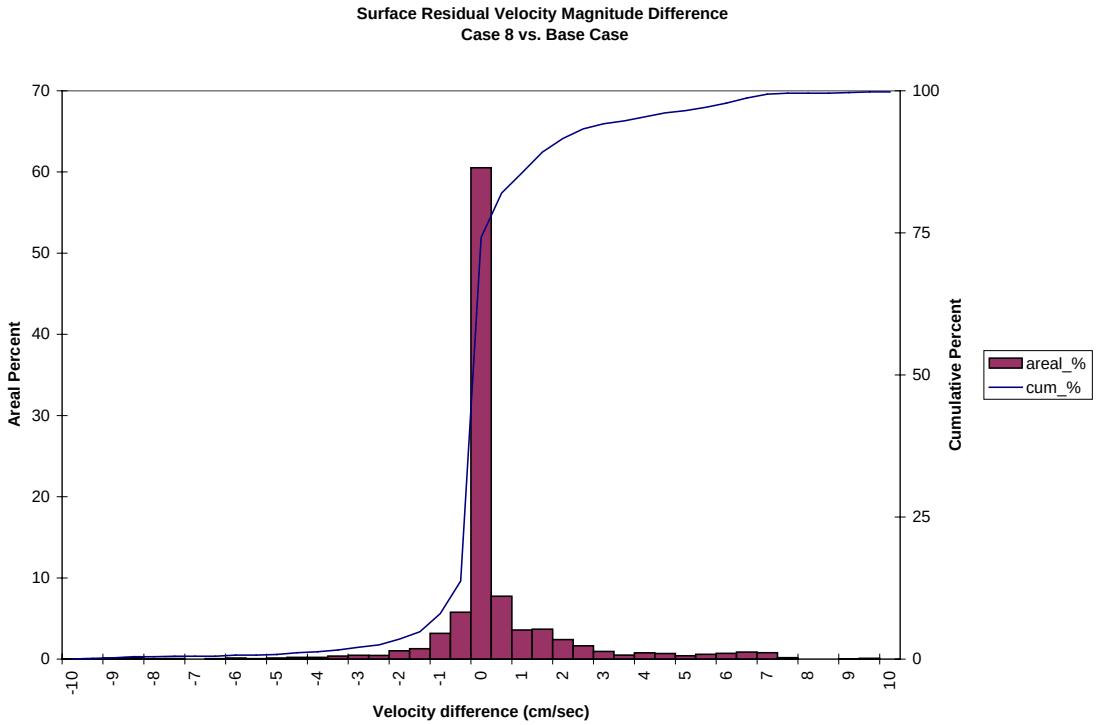

Figure 54. Frequency distribution of surface residual velocity magnitude average difference for the Northward and Eastward Expansion (Option 9, 50–foot channel) versus the Base Case.

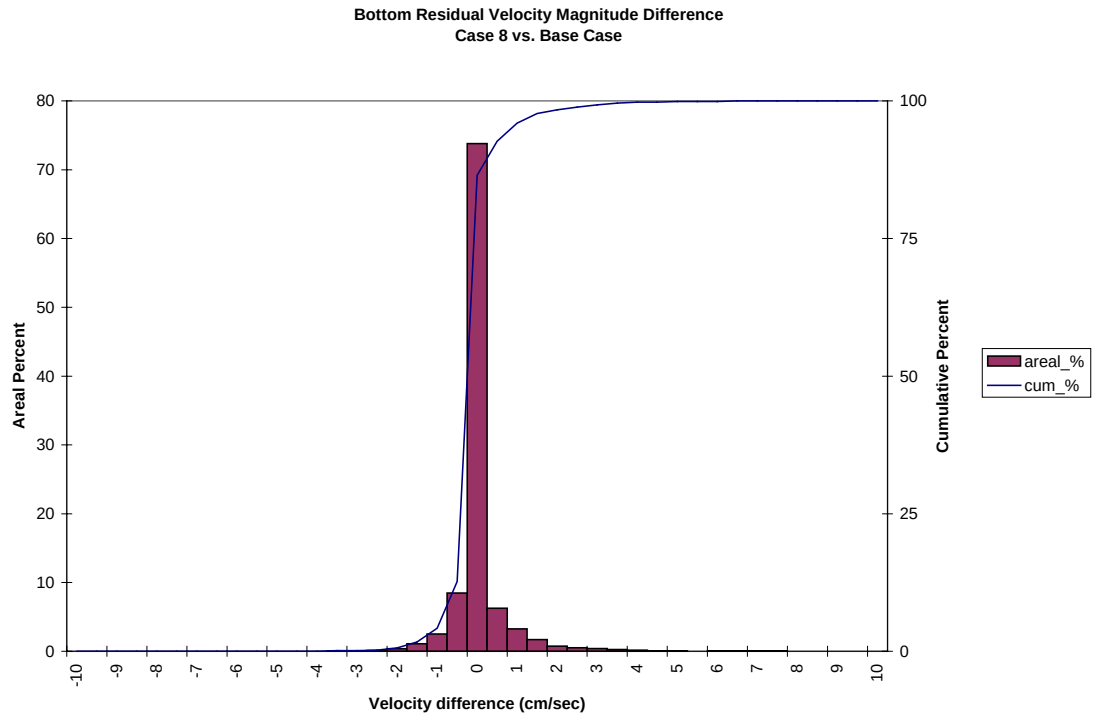

Figure 55. Frequency distribution of bottom residual velocity magnitude average difference for the Northward and Eastward Expansion (Option 9, 50–foot channel) versus the Base Case.

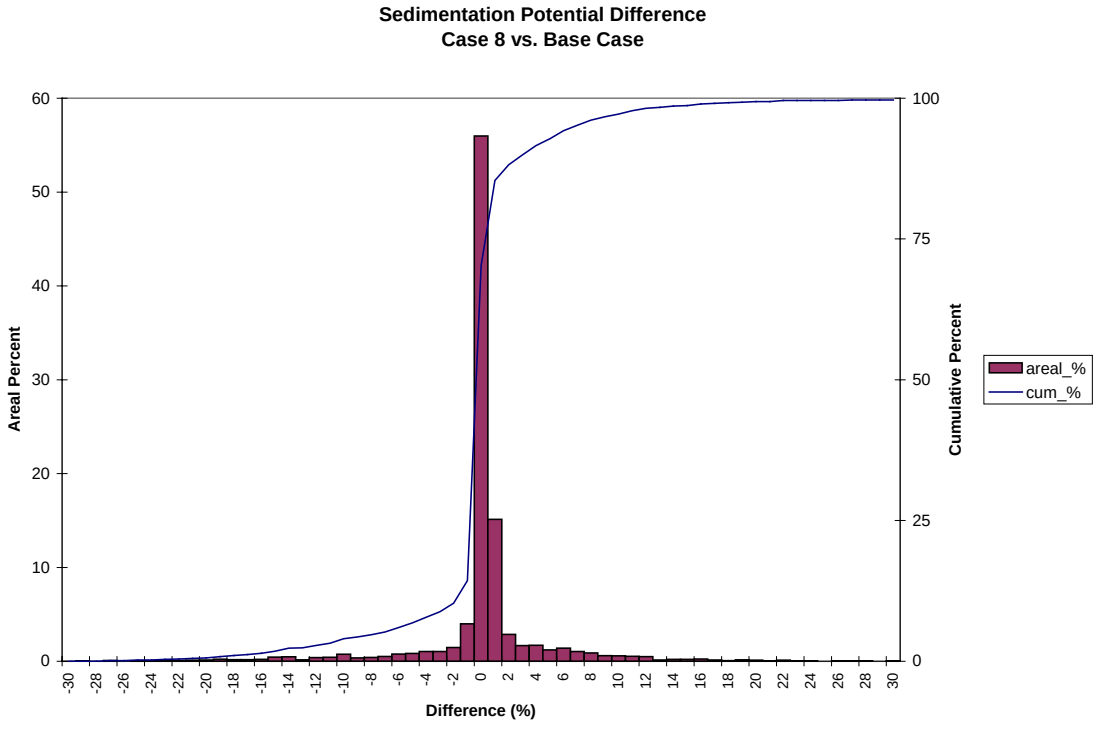

Figure 56. Frequency distribution of sedimentation potential difference for the Northward and Eastward Expansion (Option 9, 50–foot channel) versus the Base Case.

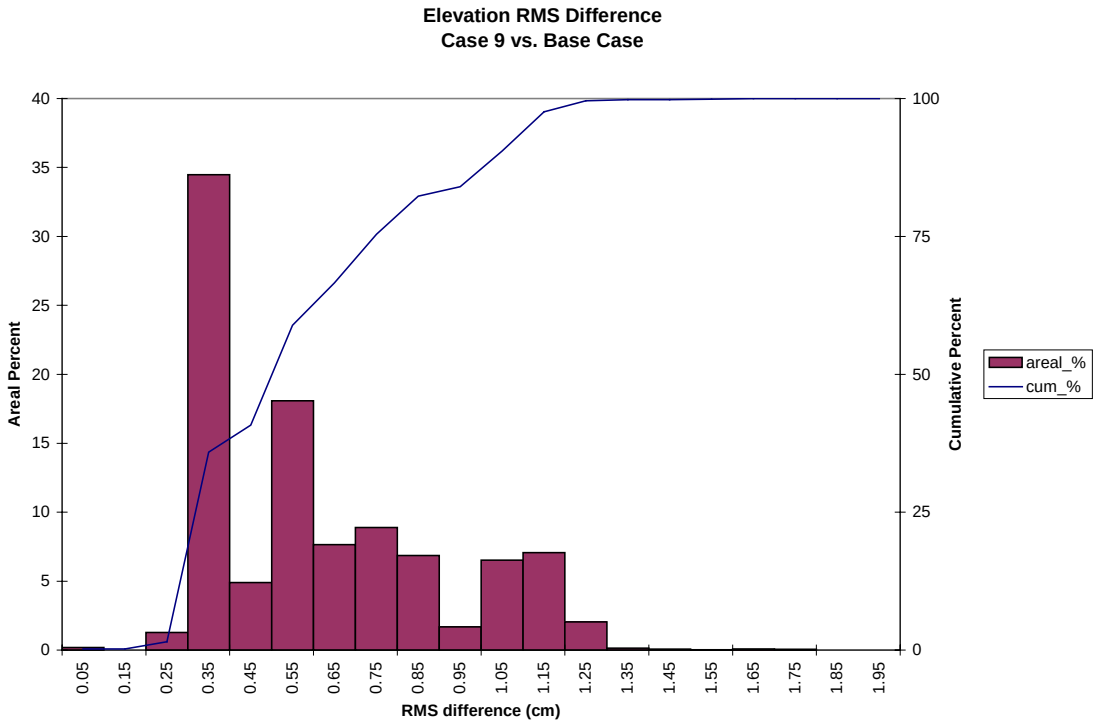

Figure 57. Frequency distribution of elevation RMS difference for the Northward and Eastward Expansion (Option 9, 55–foot channel) versus the Base Case.

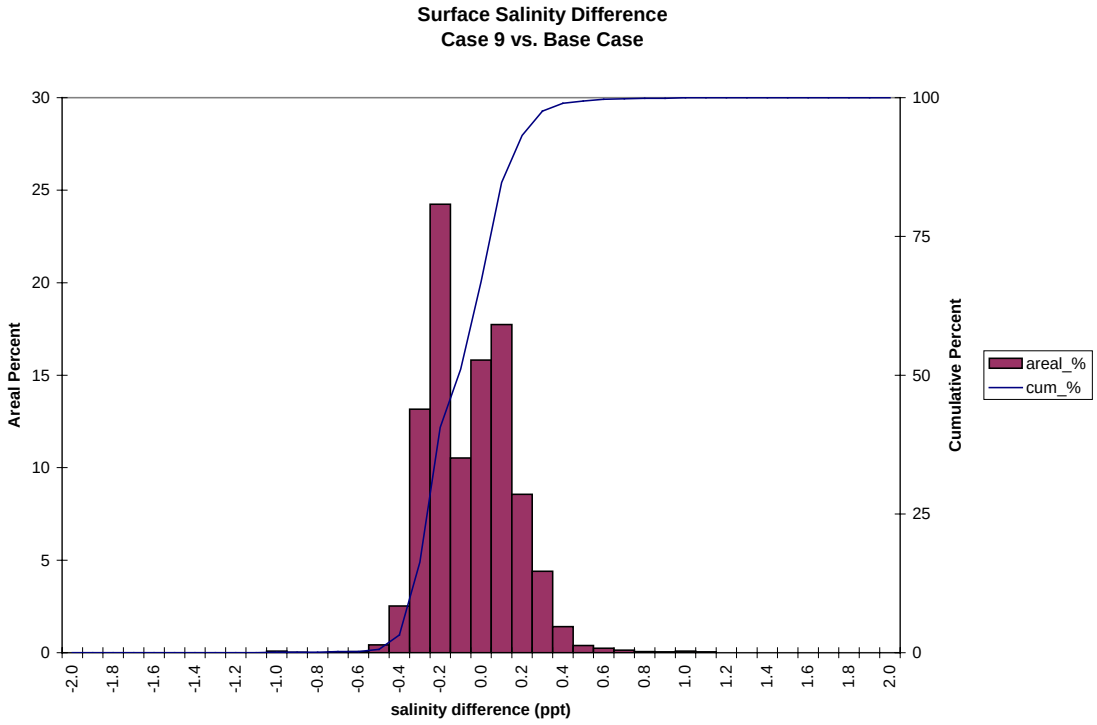

Figure 58. Frequency distribution of surface salinity average difference for the Northward and Eastward Expansion (Option 9, 55–foot channel) versus the Base Case.

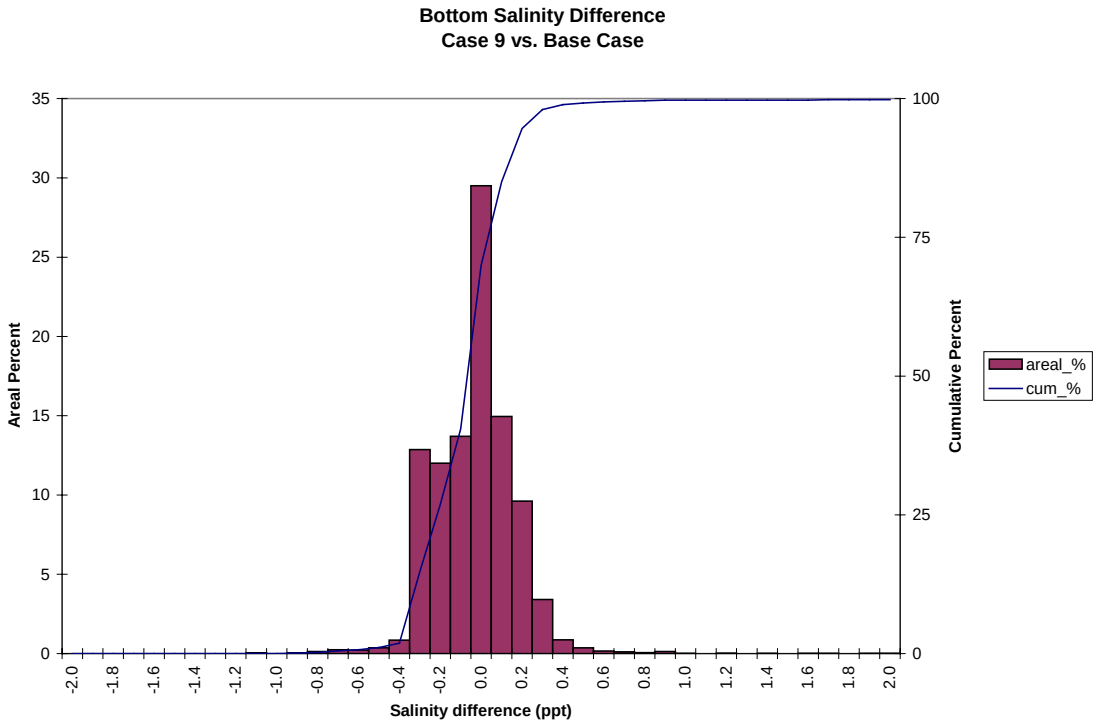

Figure 59. Frequency distribution of bottom salinity average difference for the Northward and Eastward Expansion (Option 9, 55–foot channel) versus the Base Case.

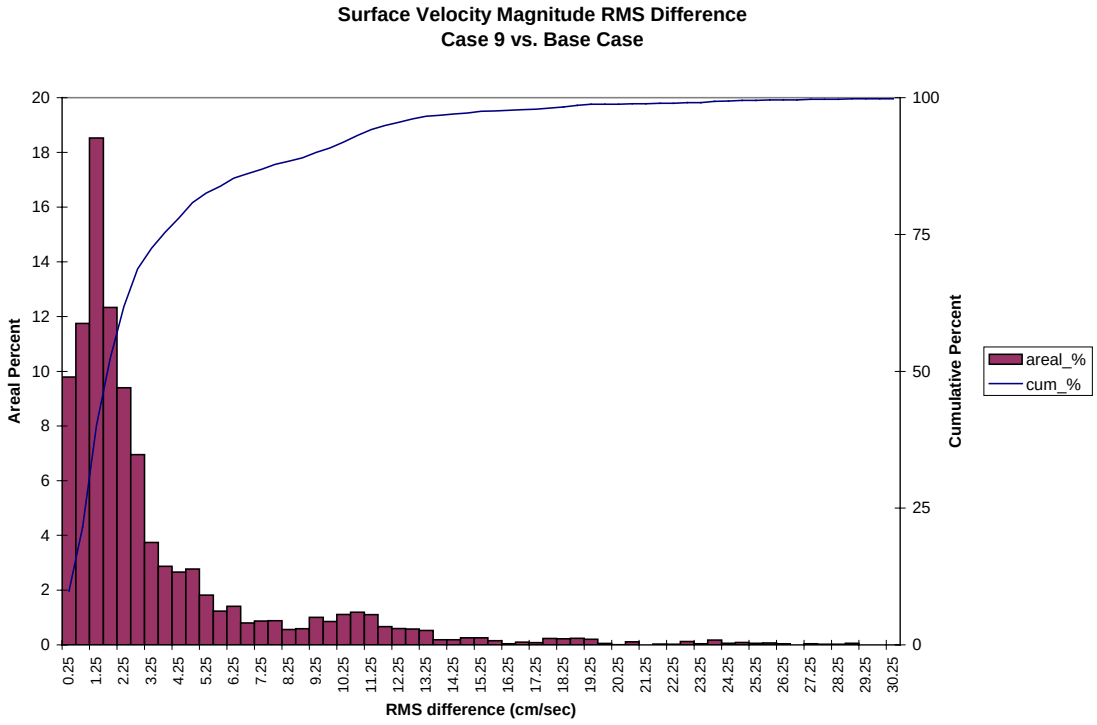

Figure 60. Frequency distribution of surface velocity RMS difference for the Northward and Eastward Expansion (Option 9, 55–foot channel) versus the Base Case.

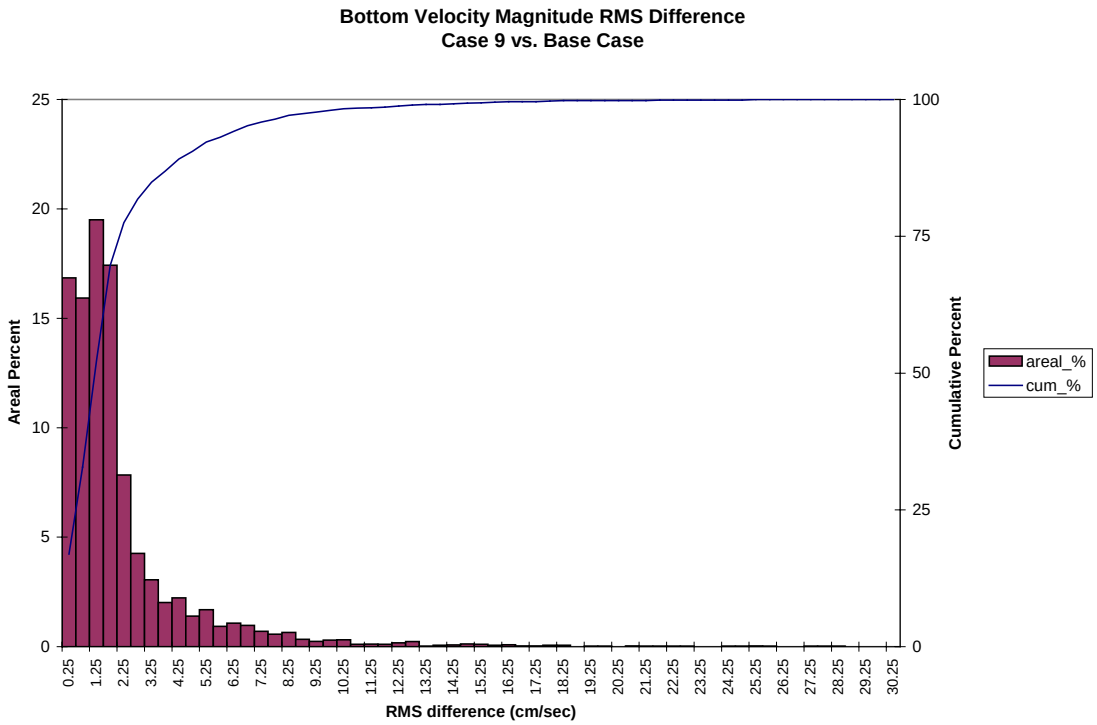

Figure 61. Frequency distribution of bottom velocity RMS difference for the Northward and Eastward Expansion (Option 9, 55–foot channel) versus the Base Case.

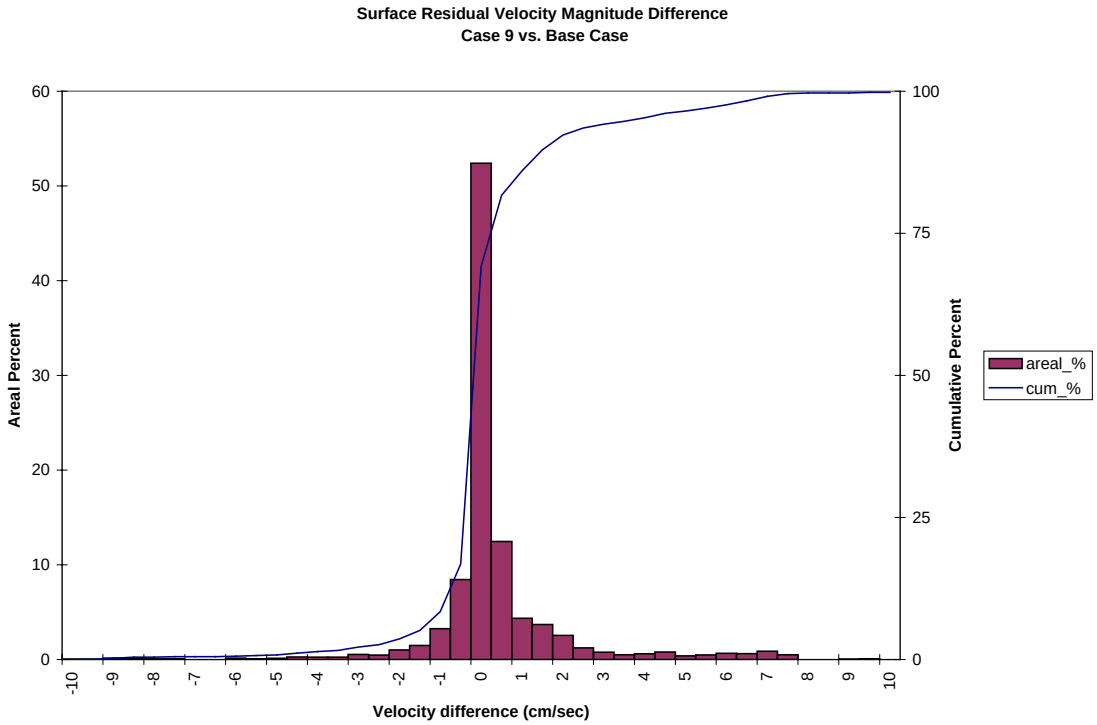

Figure 62. Frequency distribution of surface residual velocity magnitude average difference for the Northward and Eastward Expansion (Option 9, 55–foot channel) versus the Base Case.

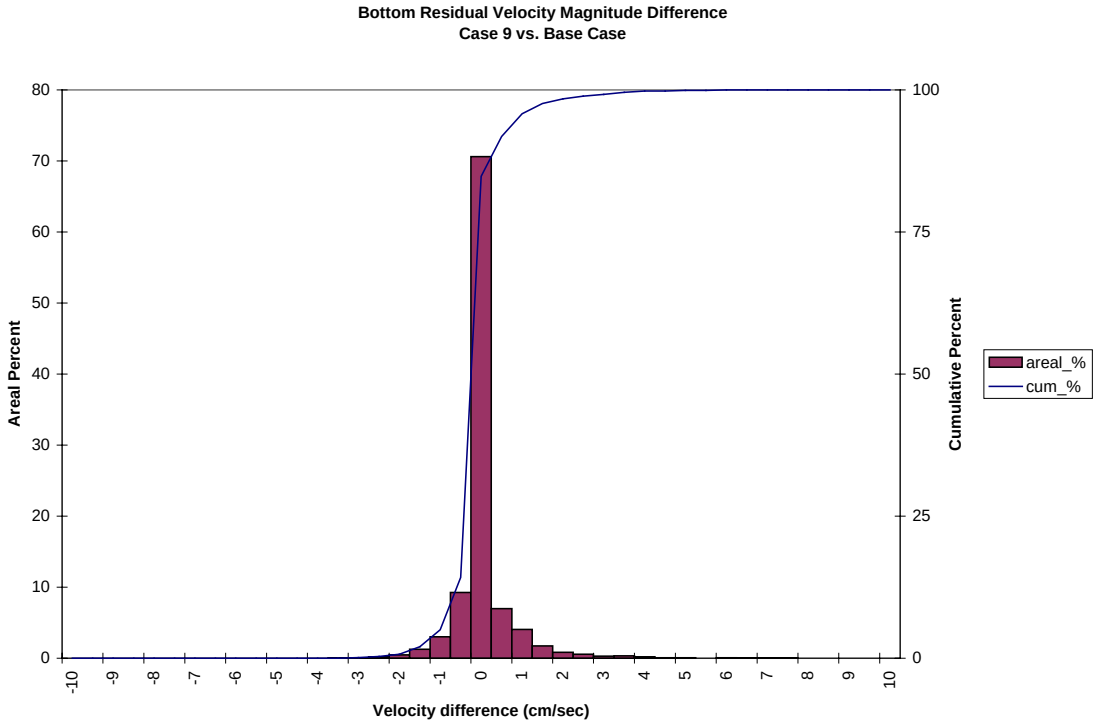

Figure 63. Frequency distribution of bottom residual velocity magnitude average difference for the Northward and Eastward Expansion (Option 9, 55–foot channel) versus the Base Case.

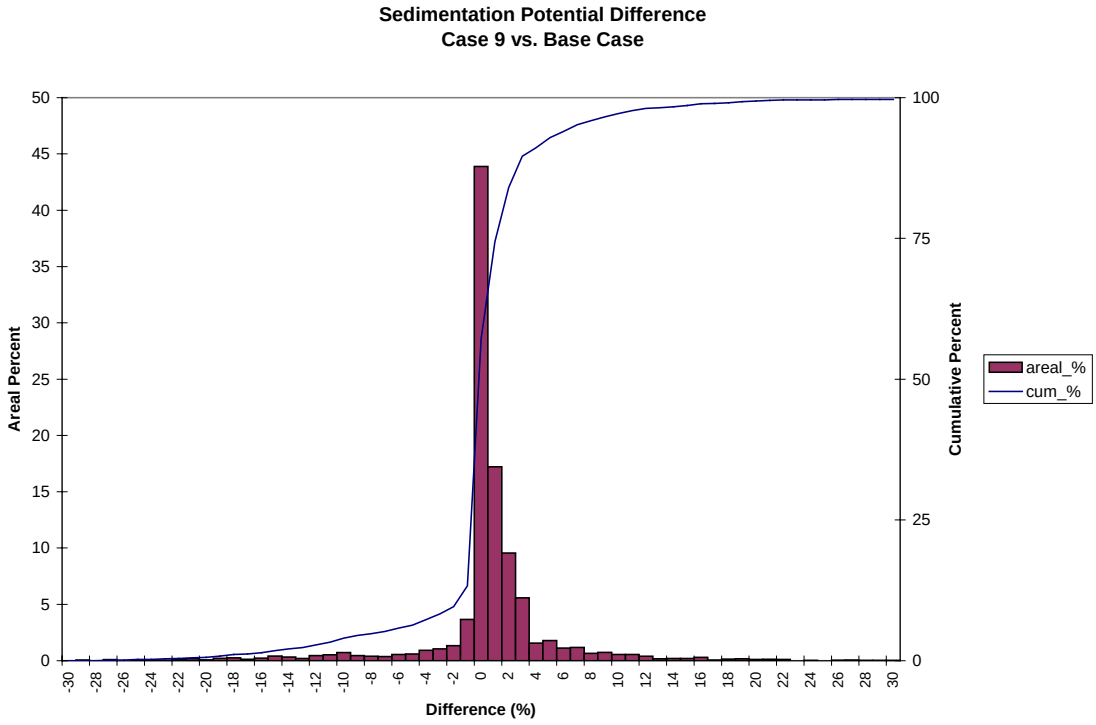

Figure 64. Frequency distribution of sedimentation potential difference for the Northward and Eastward Expansion (Option 9, 55–foot channel) versus the Base Case.

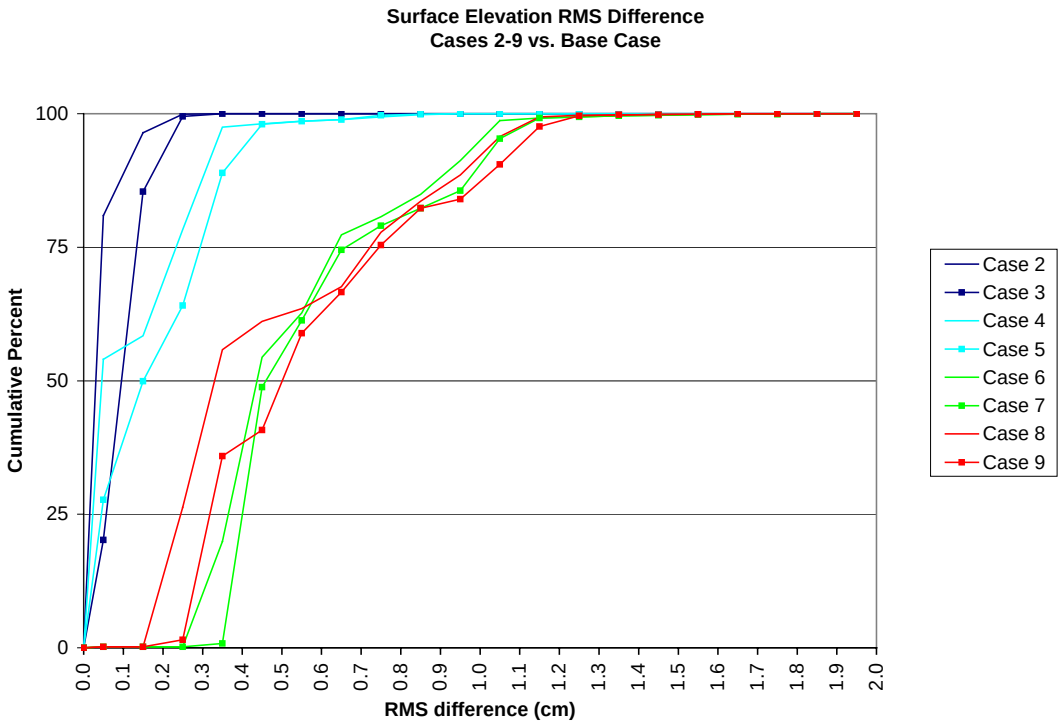

Figure 65. Cumulative percent curves of frequency distributions for surface elevation RMS differences for all Expansion Options versus the Base Case.

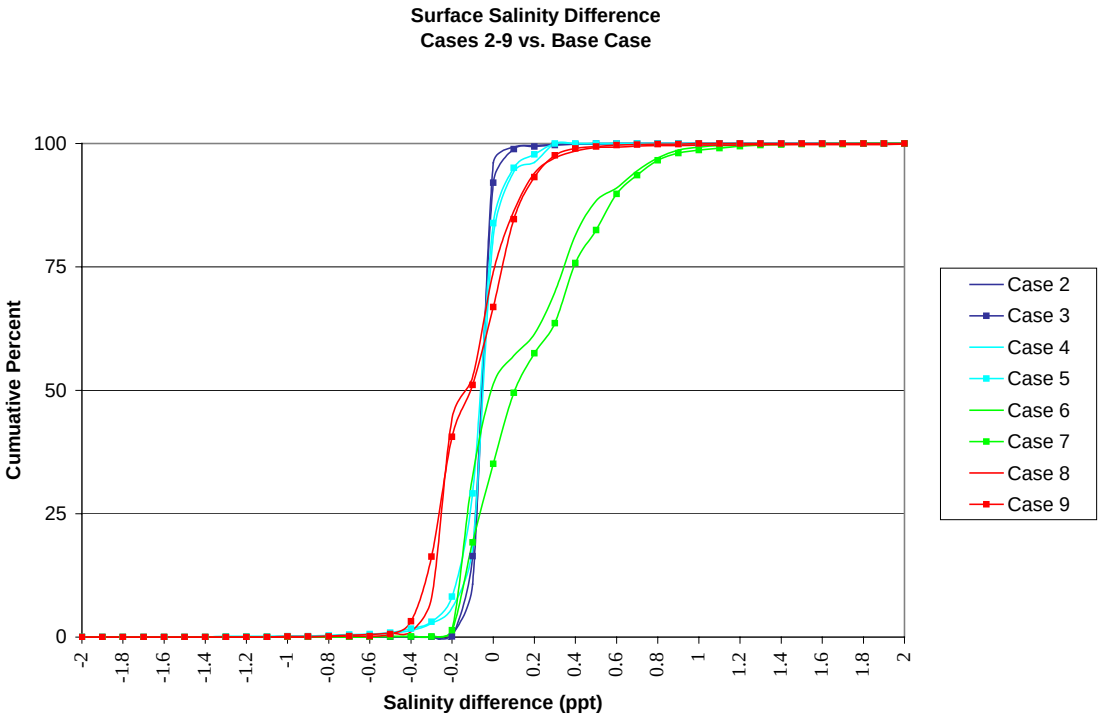

Figure 66. Cumulative percent curves of frequency distributions for surface salinity average differences for all Expansion Options versus the Base Case.

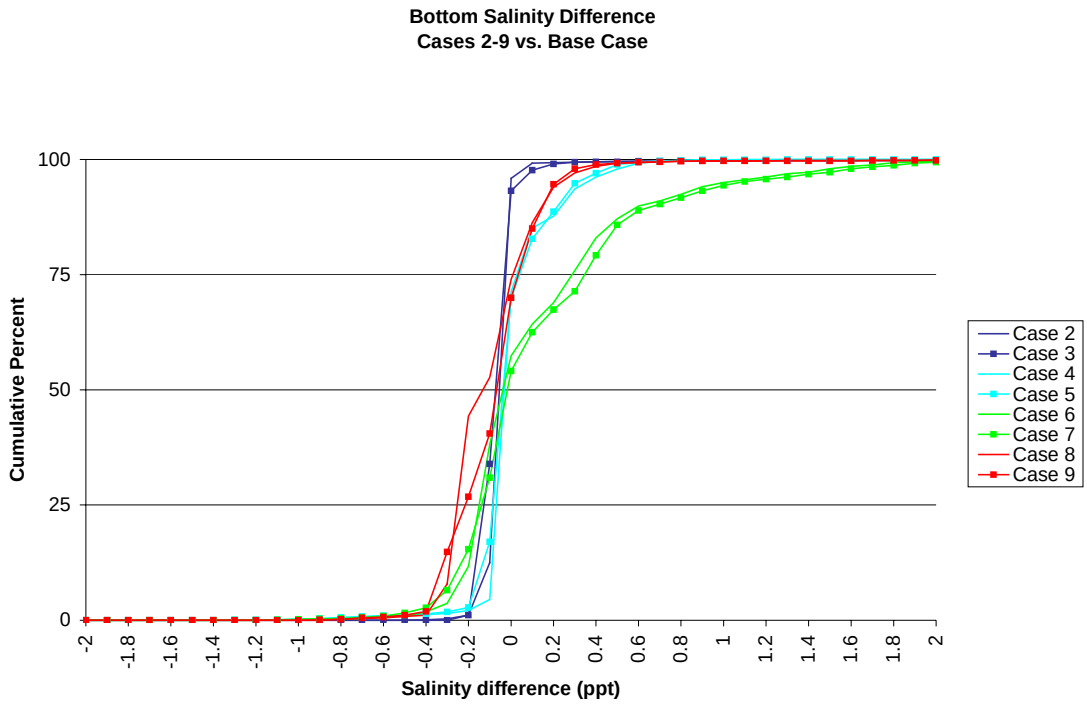

Figure 67. Cumulative percent curves of frequency distributions for bottom salinity average differences for all Expansion Options versus the Base Case.

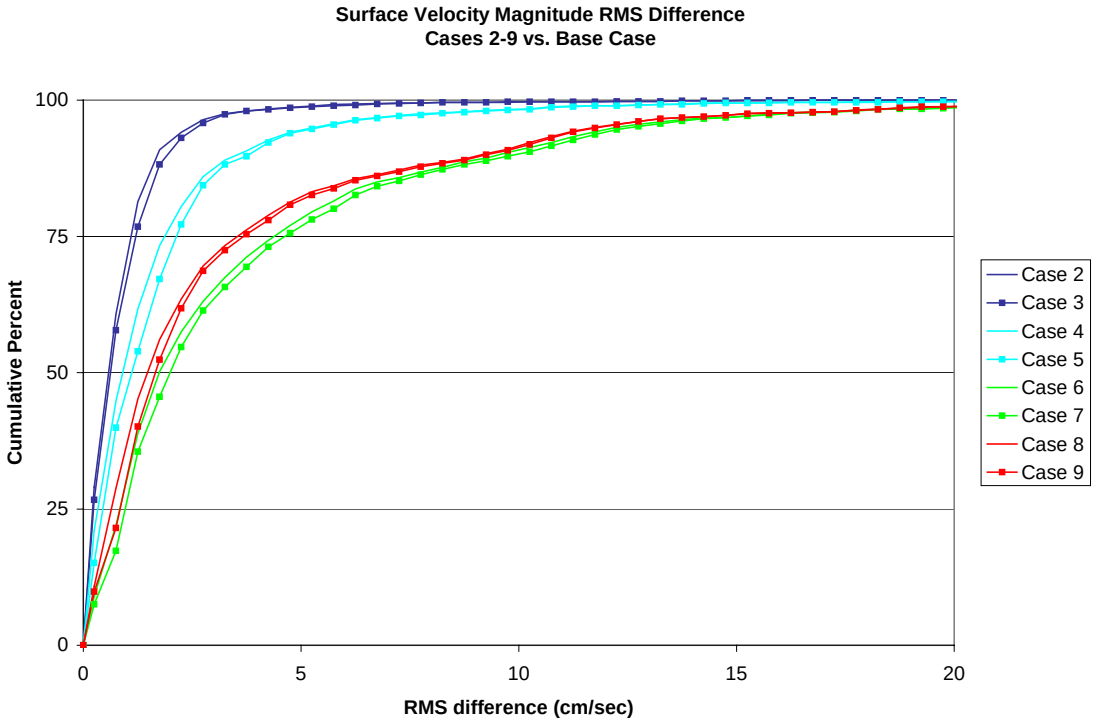

Figure 68. Cumulative percent curves of frequency distributions for surface velocity magnitude RMS differences for all Expansion Options versus the Base Case.

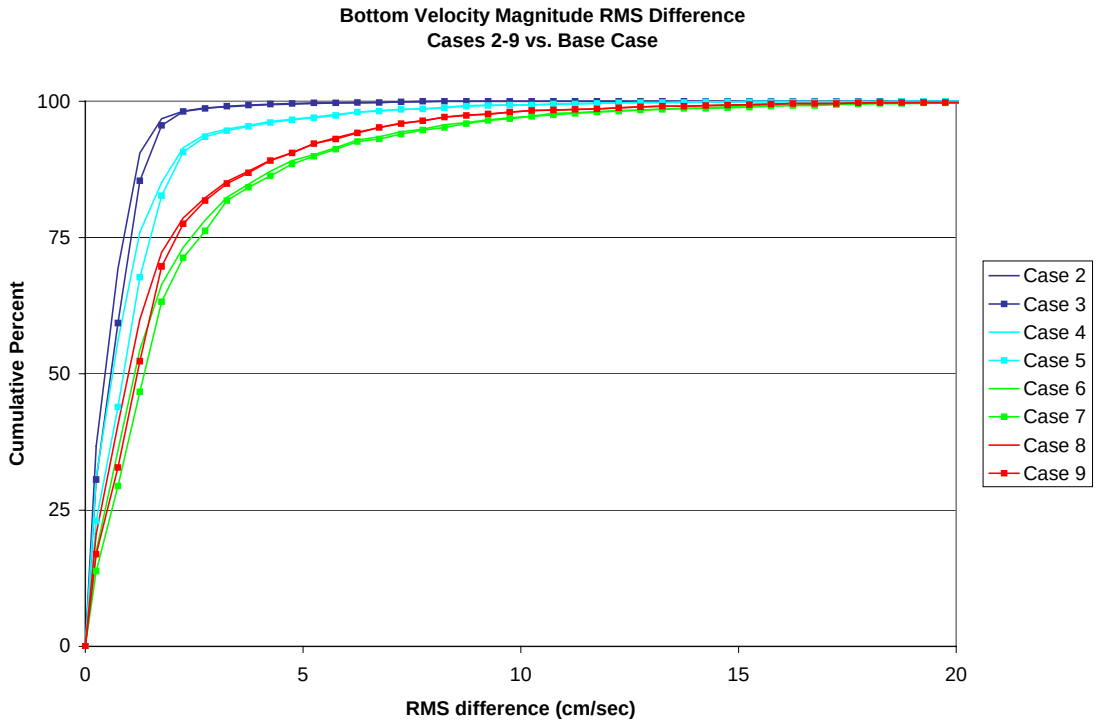

Figure 69. Cumulative percent curves of frequency distributions for bottom velocity magnitude RMS differences for all Expansion Options versus the Base Case.

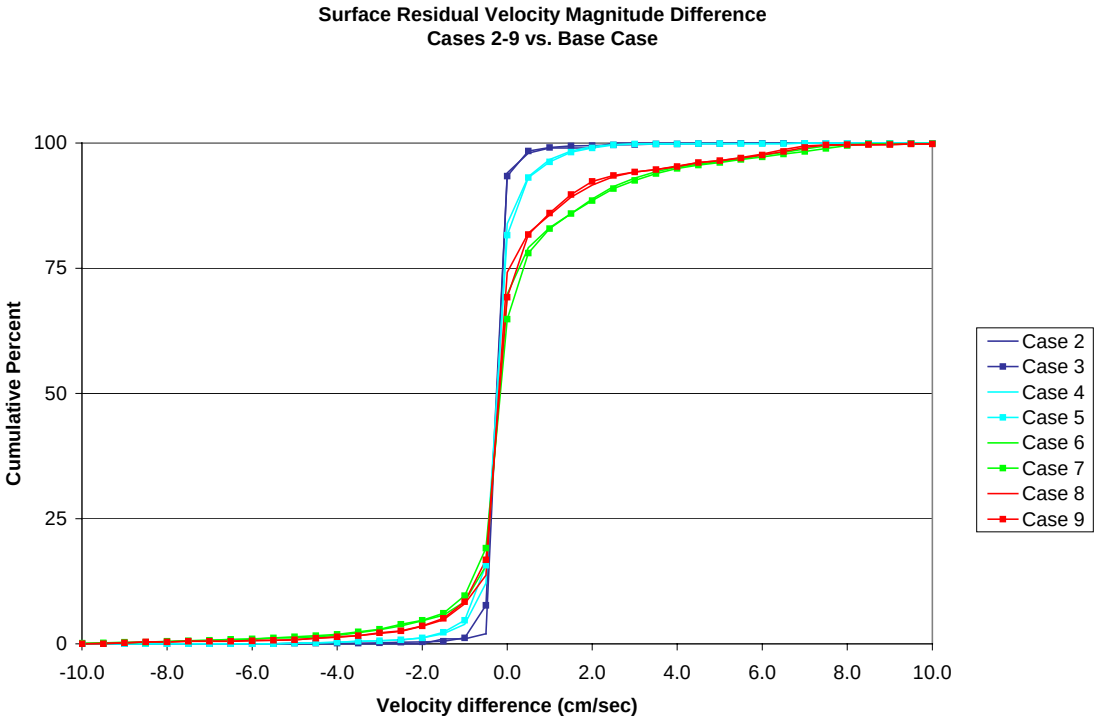

Figure 70. Cumulative percent curves of frequency distributions for surface residual velocity magnitude average differences for all Expansion Options versus the Base Case.

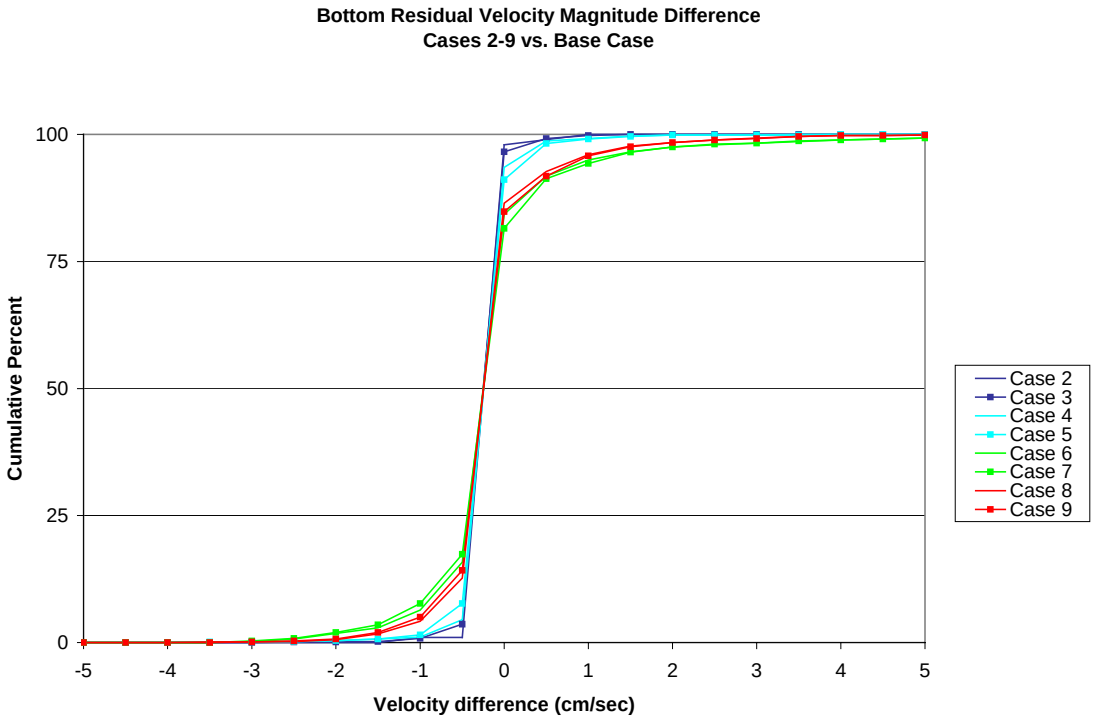

Figure 71. Cumulative percent curves of frequency distributions for bottom residual velocity magnitude average differences for all Expansion Options versus the Base Case.

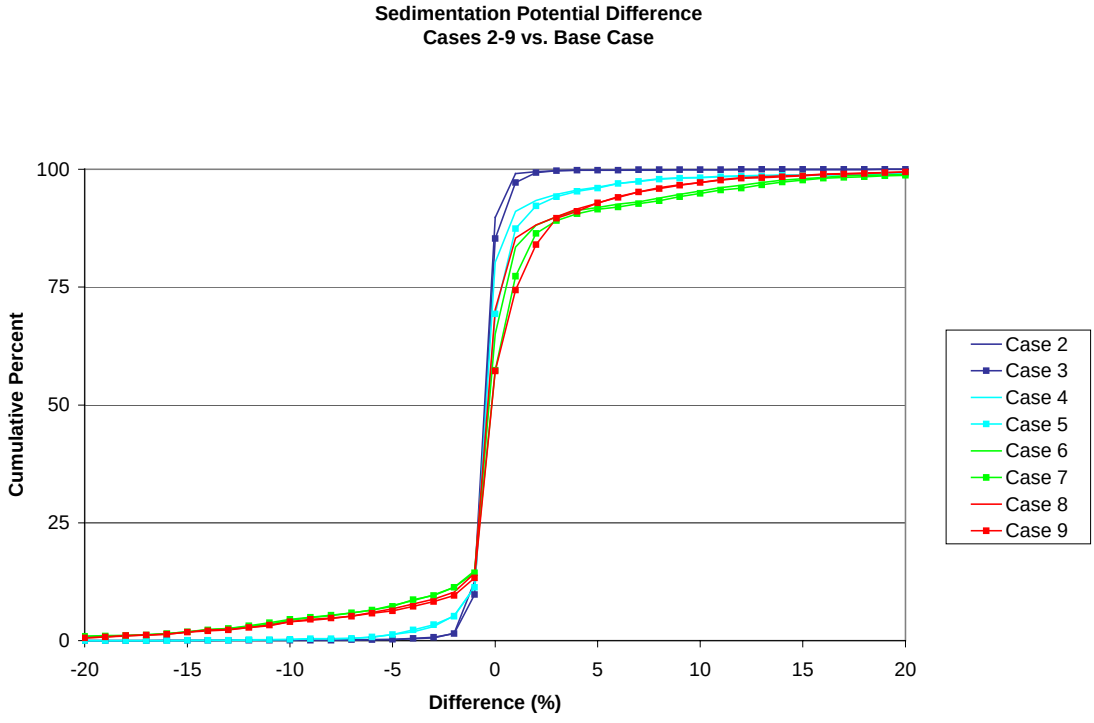

Figure 72. Cumulative percent curves of frequency distributions for sedimentation potential average differences for all Expansion Options versus the Base Case.

APPENDIX to CHAPTER V, SECTION B

Circulation Features

Window 1 of 4. Newport News Point

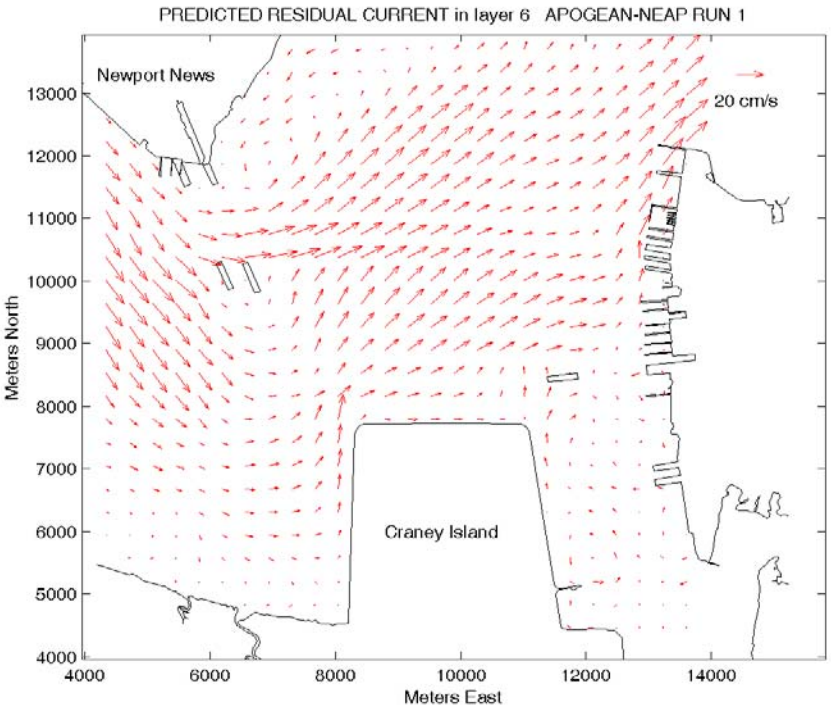

Figure 1. Predicted surface residual flow for Base Case, Newport News Point, during an apogean-neap tide.

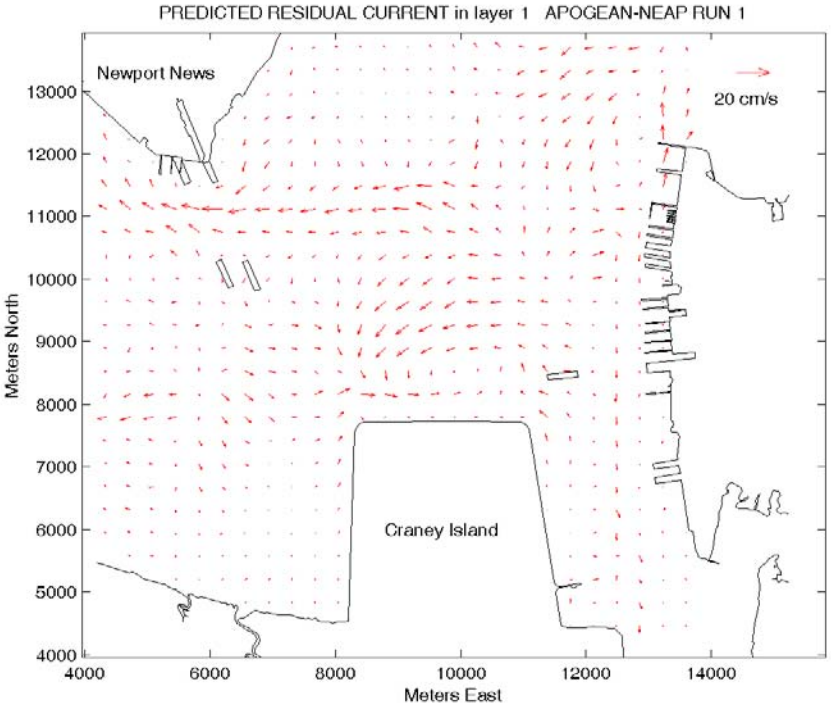

Figure 2. Predicted bottom residual flow for Base Case, Newport News Point, during an apogean-neap tide.

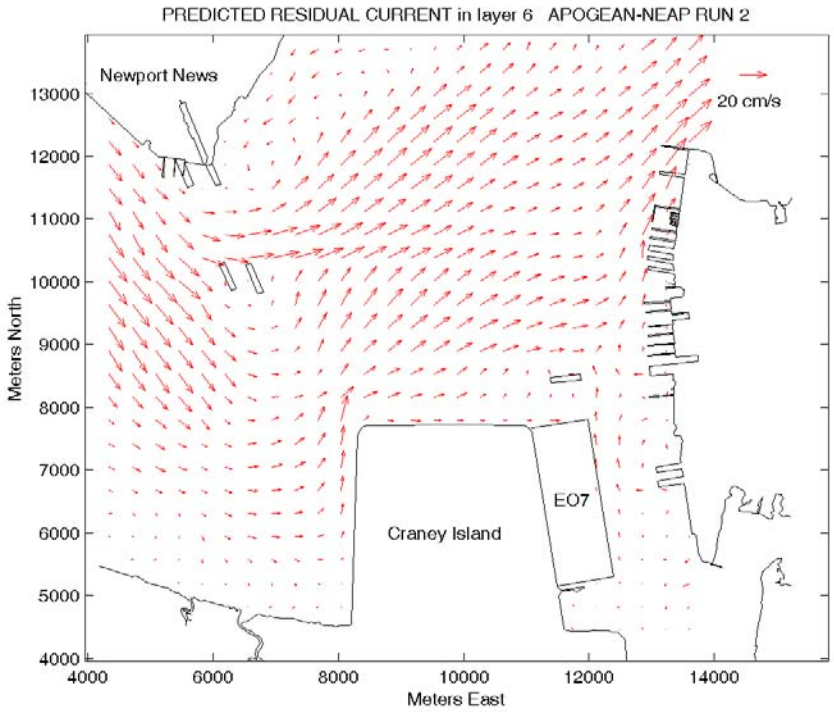

Figure 3. Predicted surface residual flow for Eastward Expansion (Case 2), Newport News Point, during an apogean-neap tide.

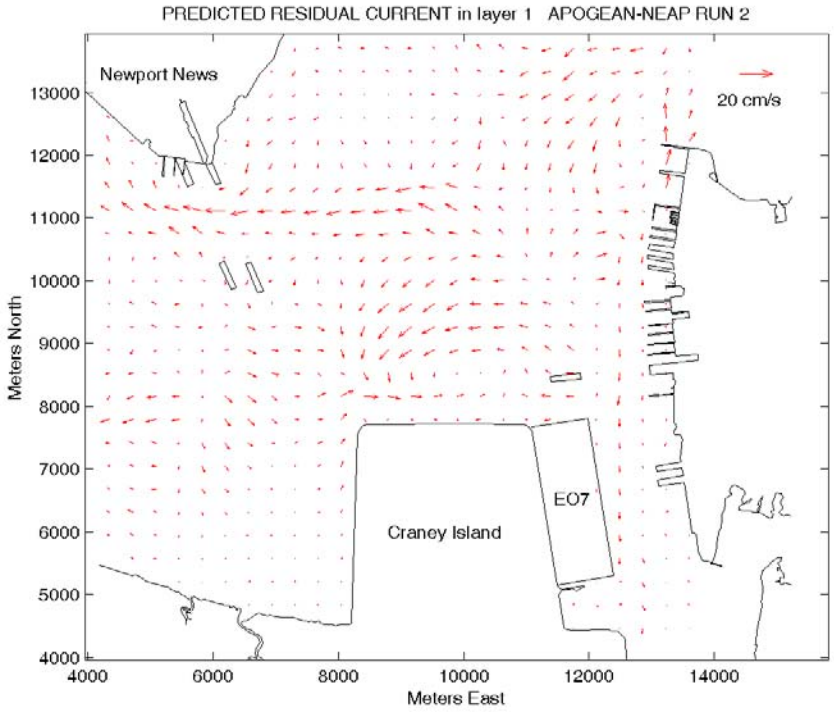

Figure 4. Predicted bottom residual flow for Eastward Expansion (Case 2), Newport News Point, during an apogean-neap tide.

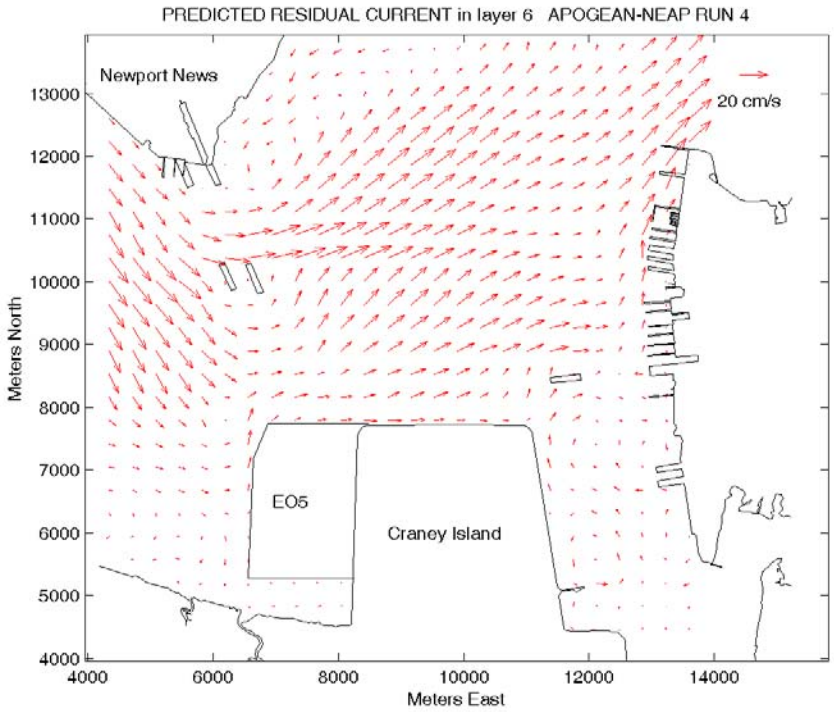

Figure 5. Predicted surface residual flow for Westward Expansion (Case 4), Newport News Point, during an apogean-neap tide.

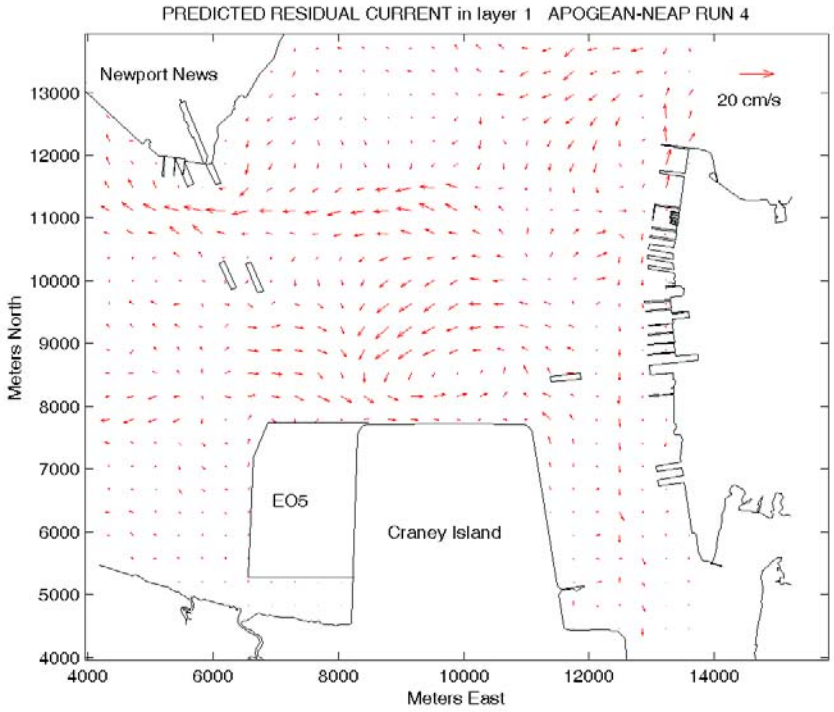

Figure 6. Predicted bottom residual flow for Westward Expansion (Case 4), Newport News Point, during an apogean-neap tide.

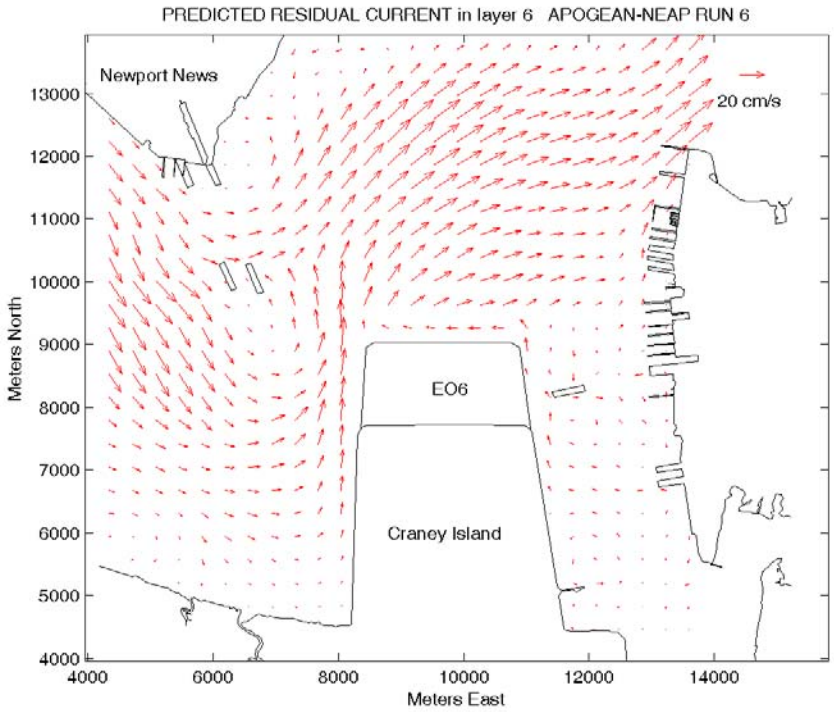

Figure 7. Predicted surface residual flow for Northward Expansion (Case 6), Newport News Point, during an apogean-neap tide.

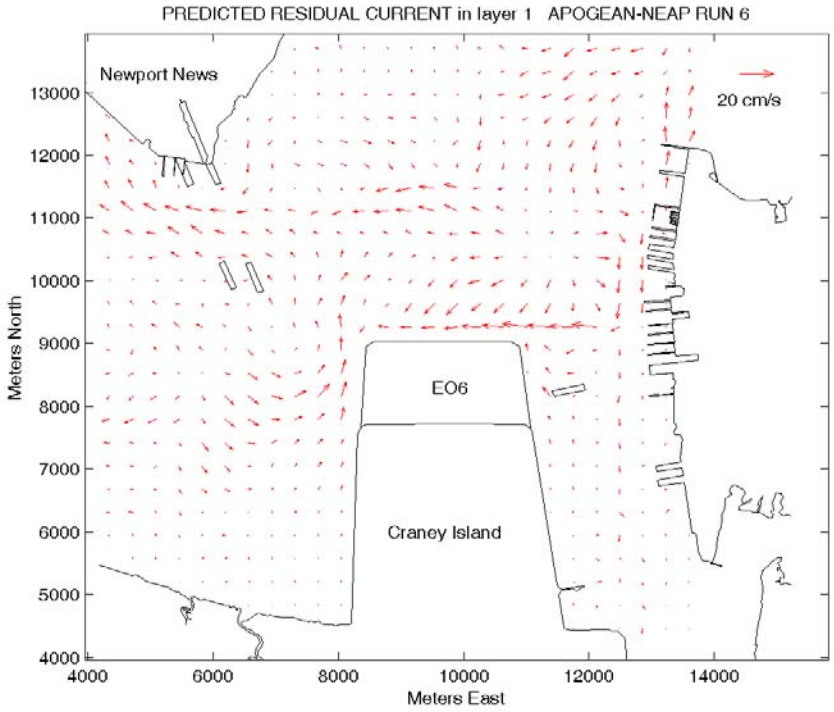

Figure 8. Predicted bottom residual flow for Northward Expansion (Case 6), Newport News Point, during an apogean-neap tide.

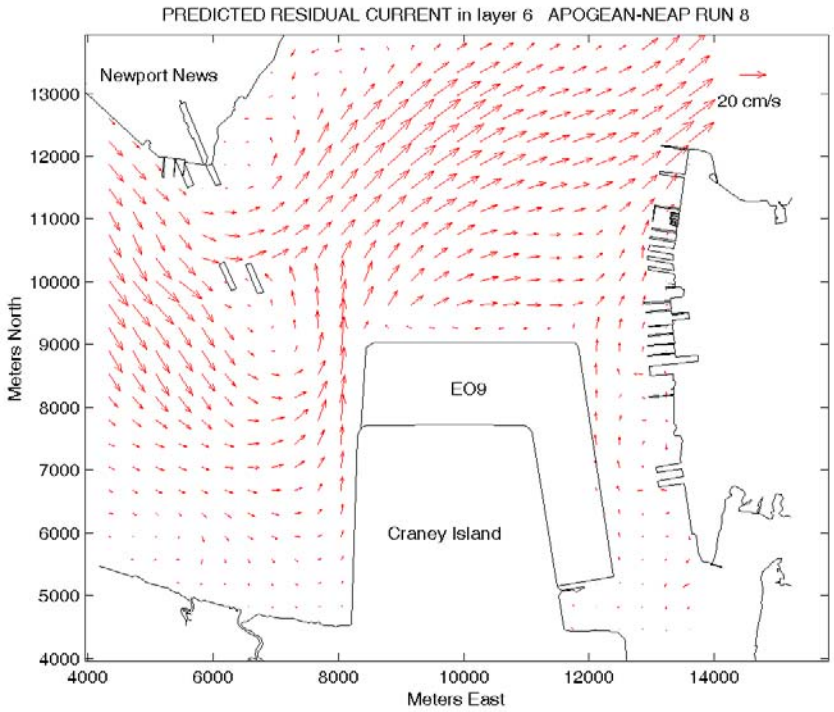

Figure 9. Predicted surface residual flow for Northward and Eastward Expansion (Case 8), Newport News Point, during an apogean-neap tide.

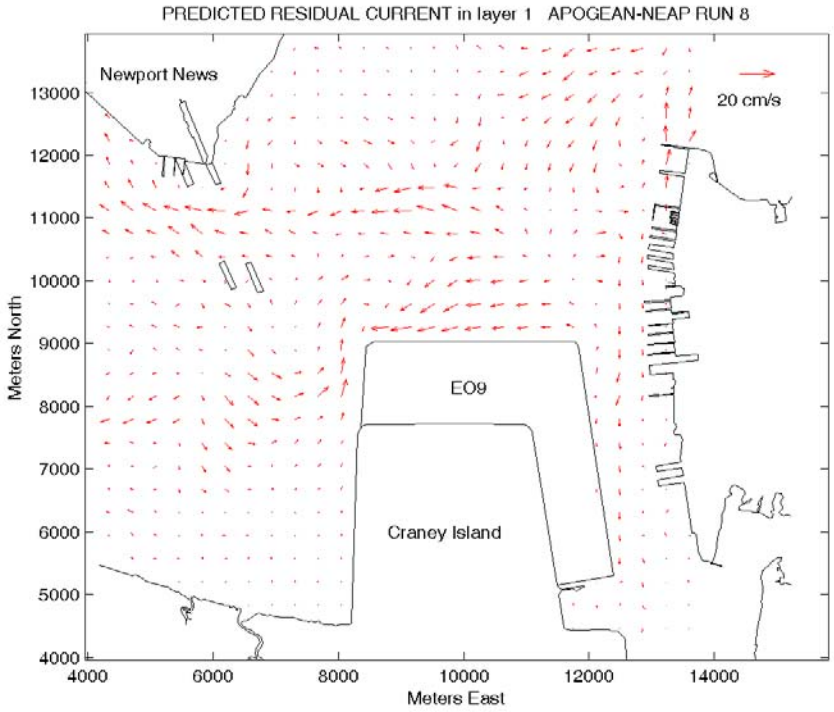

Figure 10. Predicted bottom residual flow for Northward and Eastward Expansion (Case 8), Newport News Point, during an apogean-neap tide.

Window 2 of 4. Craney Island Reach

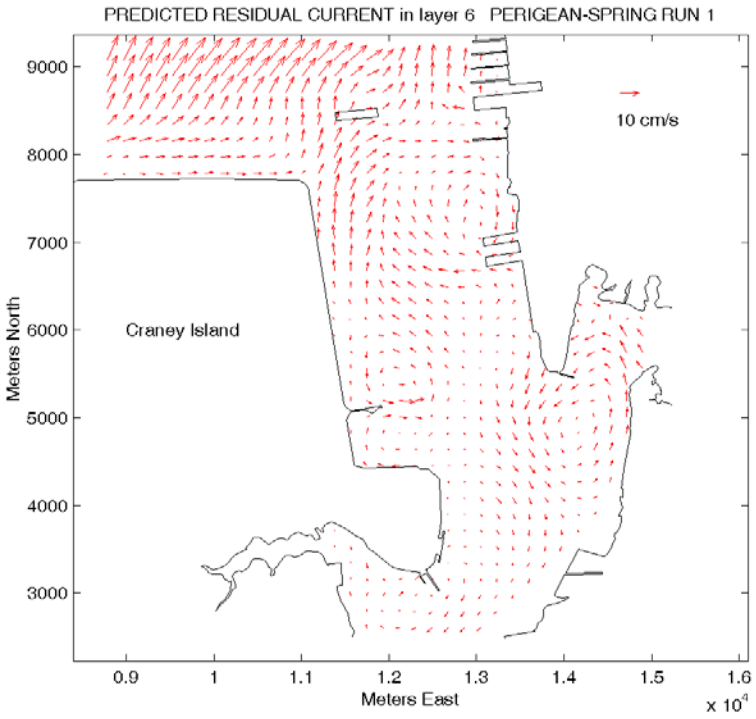

Figure 11. Predicted surface residual flow for Base Case, Craney Island Reach, during a perigean-spring tide.

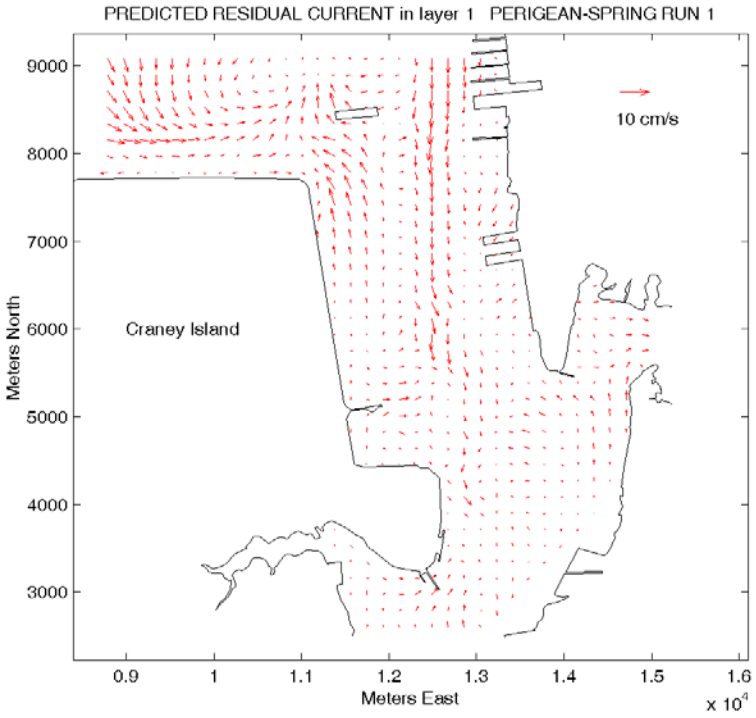

Figure 12. Predicted bottom residual flow for Base Case, Craney Island Reach, during a perigean-spring tide.

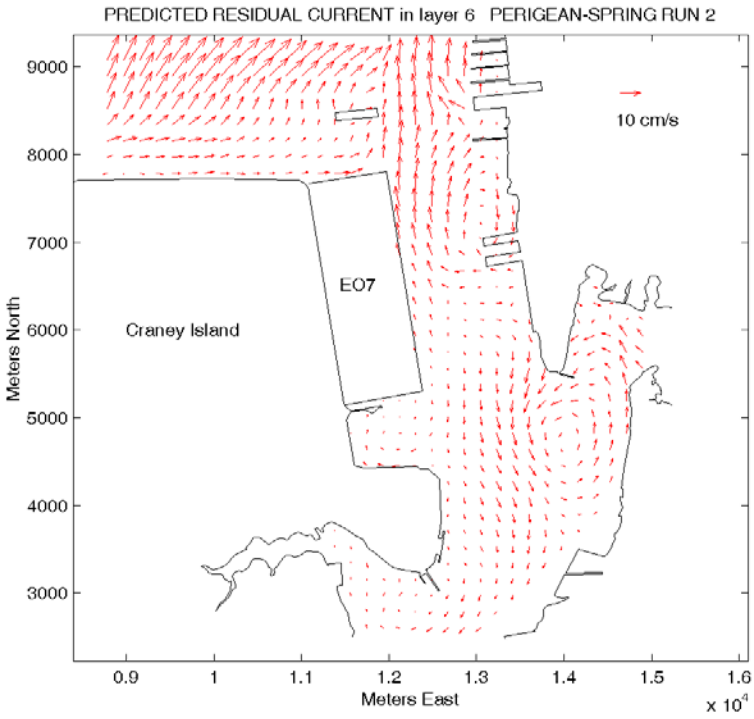

Figure 13. Predicted surface residual flow for Eastward Expansion (Case 2), Craney Island Reach, during a perigean-spring tide.

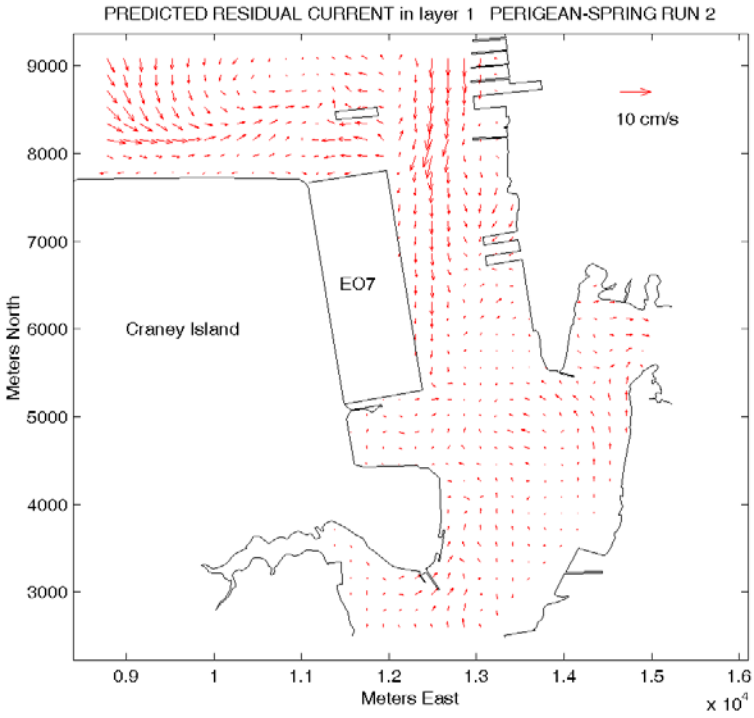

Figure 14. Predicted bottom residual flow for Eastward Expansion (Case 2), Craney Island Reach, during a perigean-spring tide.

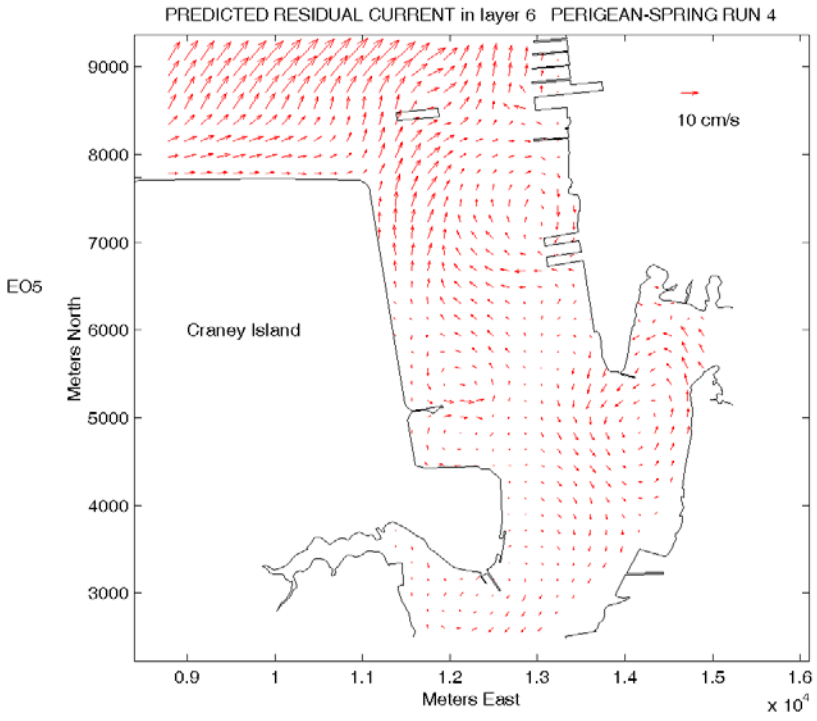

Figure 15. Predicted surface residual flow for Westward Expansion (Case 4), Craney Island Reach, during a perigean-spring tide.

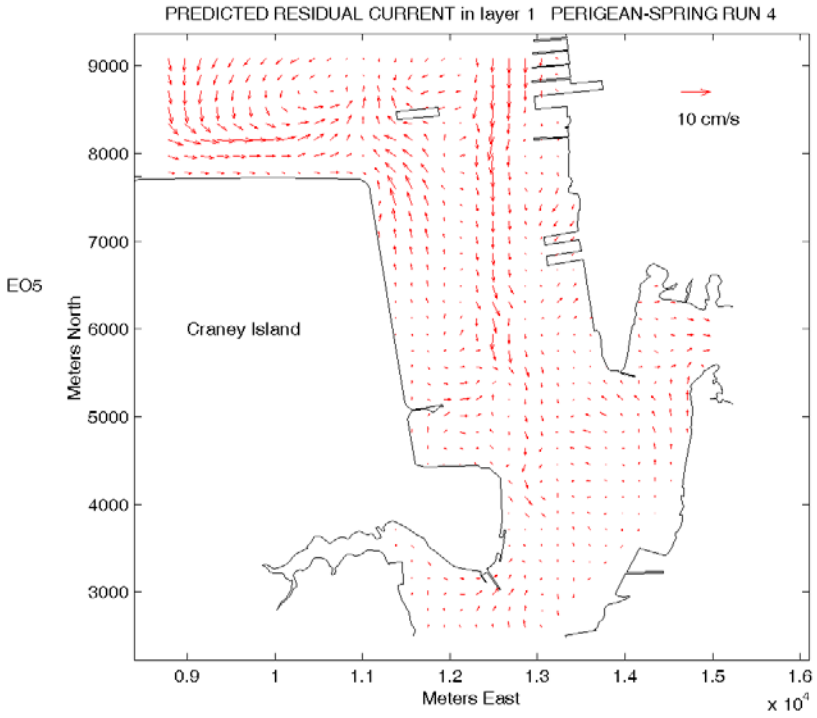

Figure 16. Predicted bottom residual flow for Westward Expansion (Case 4), Craney Island Reach, during a perigean-spring tide.

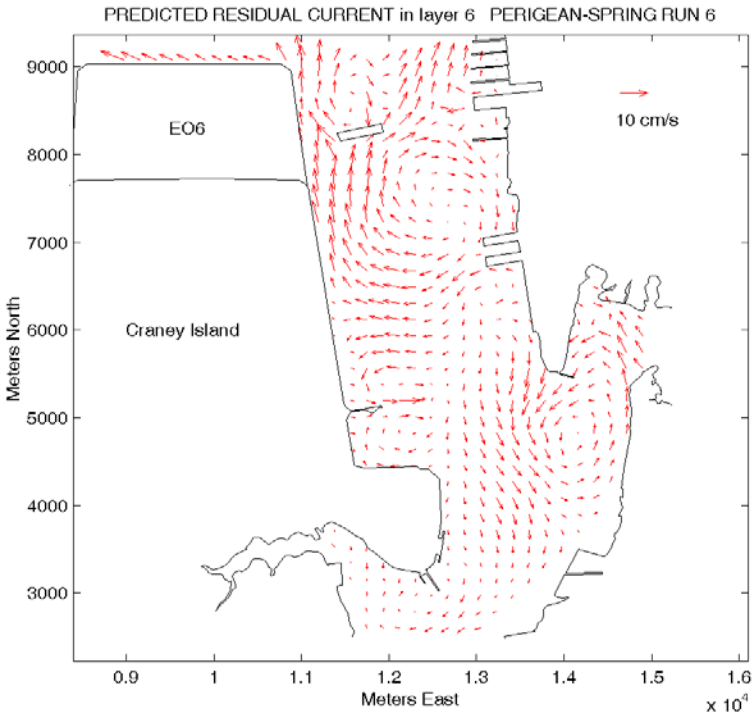

Figure 17. Predicted surface residual flow for Northward Expansion (Case 6), Craney Island Reach, during a perigean-spring tide.

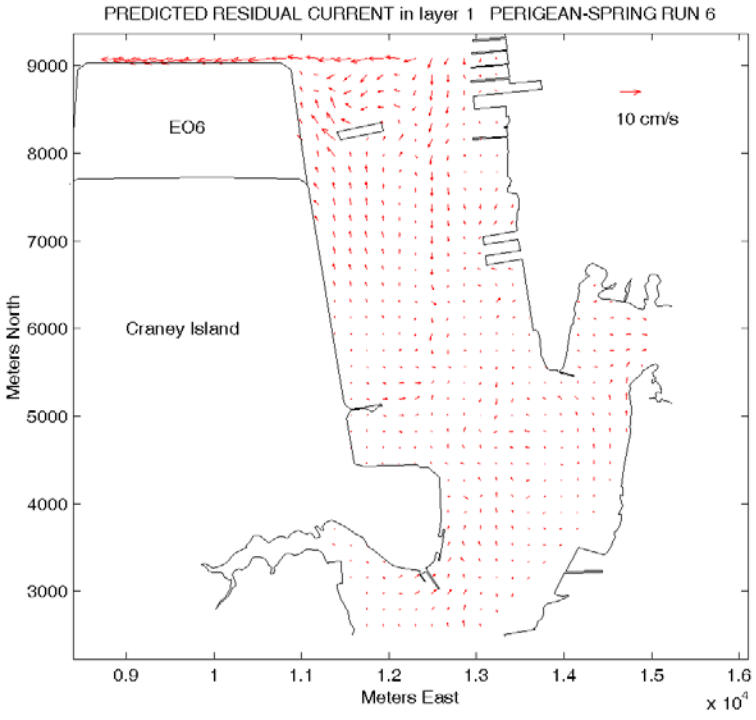

Figure 18. Predicted bottom residual flow for Northward Expansion (Case 6), Craney Island Reach, during a perigean-spring tide.

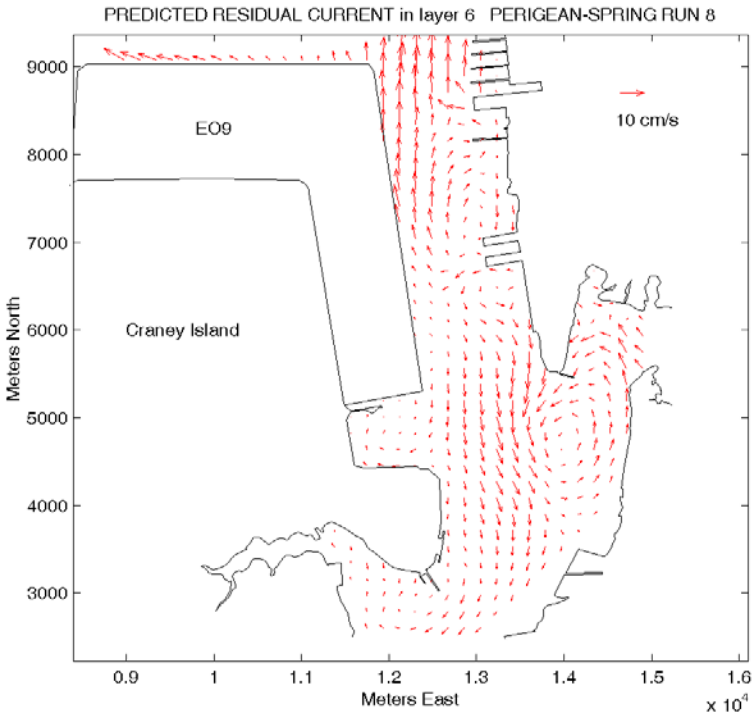

Figure 19. Predicted surface residual flow for Northward and Eastward Expansion (Case 8), Craney Island Reach, during a perigean-spring tide.

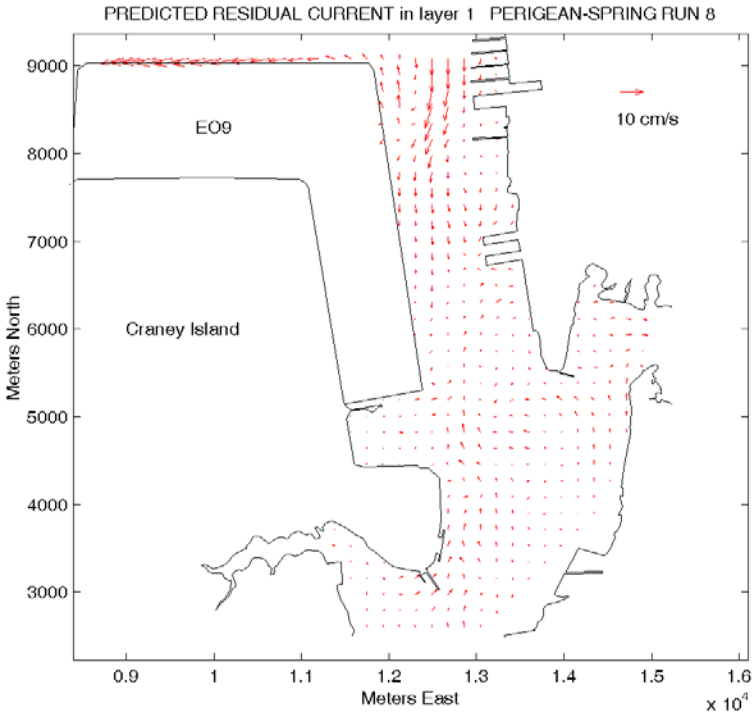

Figure 20. Predicted bottom residual flow for Northward and Eastward Expansion (Case 8), Craney Island Reach, during a perigean-spring tide.

Window 3 of 4. Lambert Bend

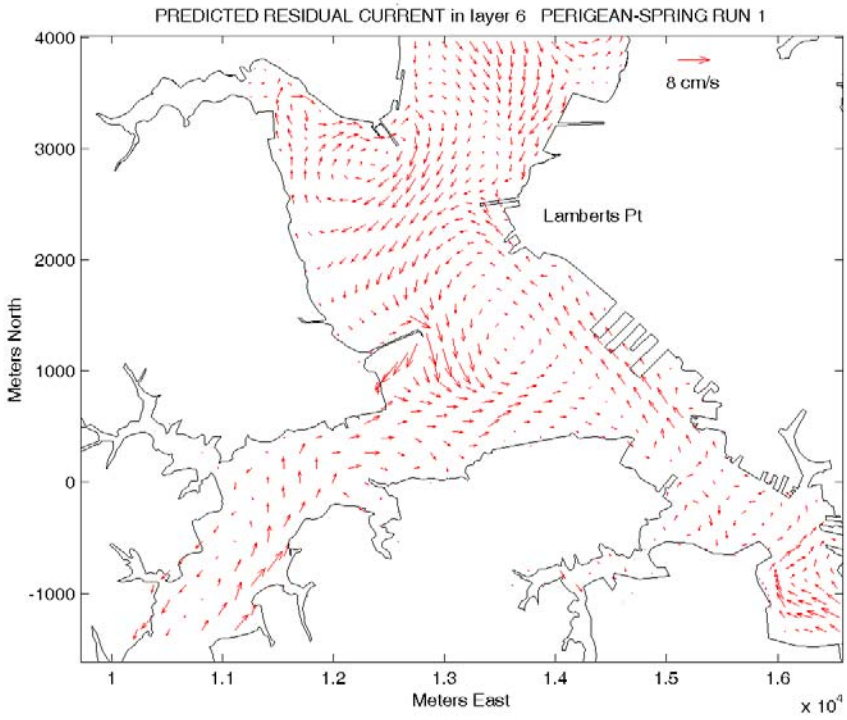

Figure 21. Predicted surface residual flow for Base Case, Lambert Bend, during a perigean-spring tide.

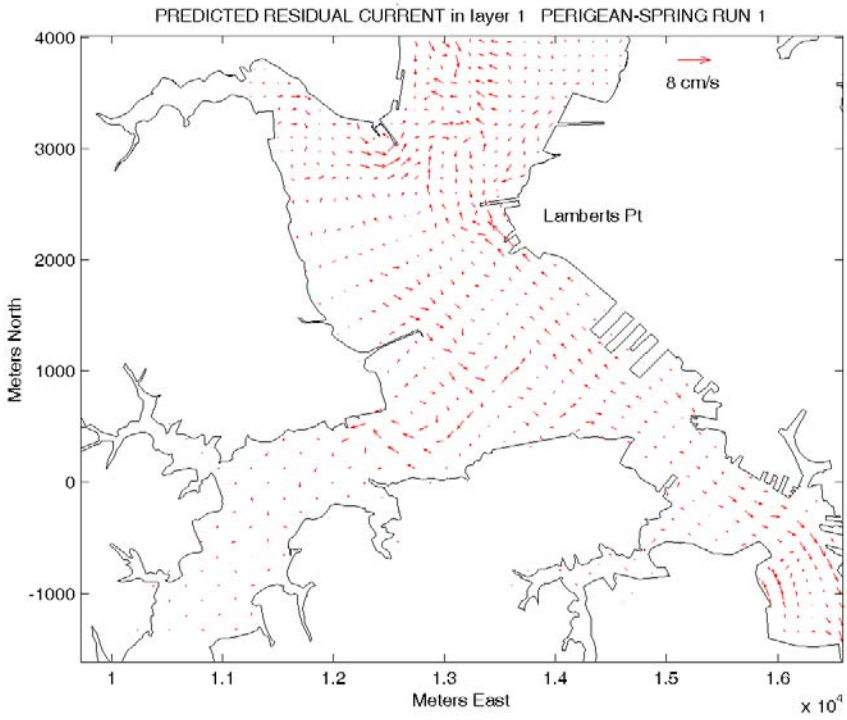

Figure 22. Predicted bottom residual flow for Base Case, Lambert Bend, during a perigean-spring tide.

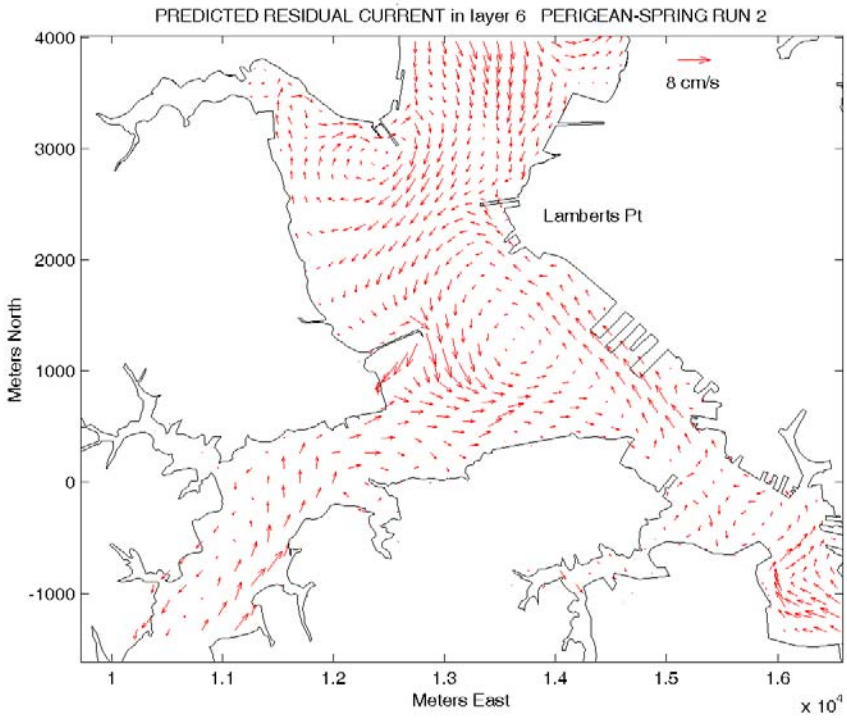

Figure 23. Predicted surface residual flow for Eastward Expansion (Case 2), Lambert Bend, during a perigean-spring tide.

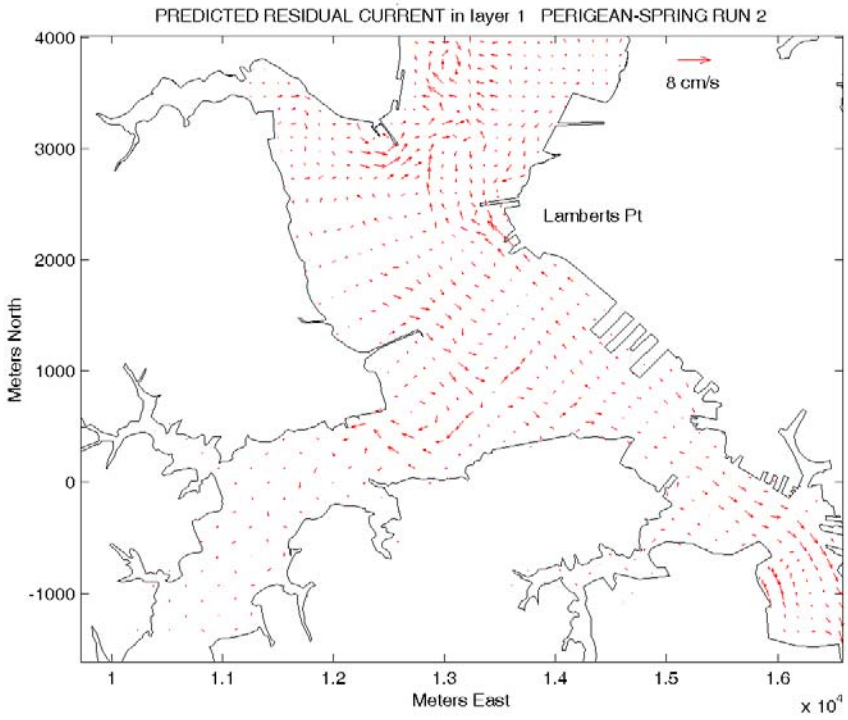

Figure 24. Predicted bottom residual flow for Eastward Expansion (Case 2), Lambert Bend, during a perigean-spring tide.

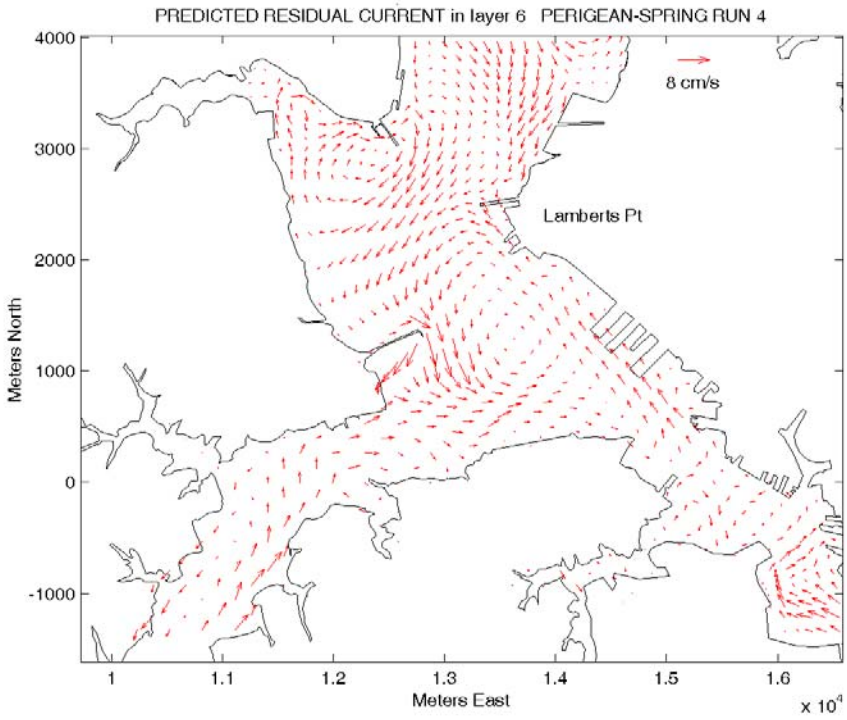

Figure 25. Predicted surface residual flow for Westward Expansion (Case 4), Lambert Bend, during a perigean-spring tide.

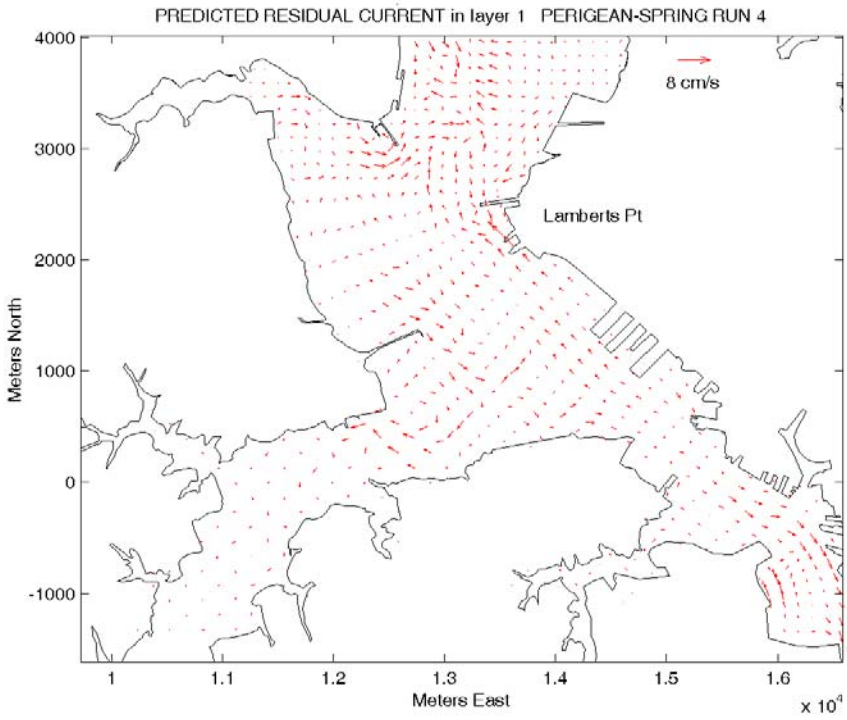

Figure 26. Predicted bottom residual flow for Westward Expansion (Case 4), Lambert Bend, during a perigean-spring tide.

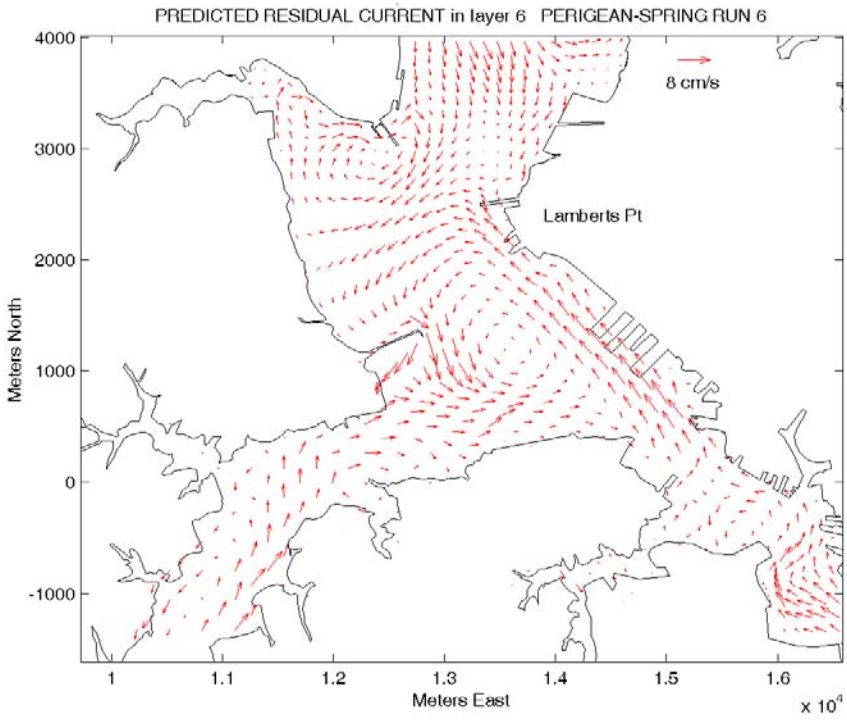

Figure 27. Predicted surface residual flow for Northward Expansion (Case 6), Lambert Bend, during a perigean-spring tide.

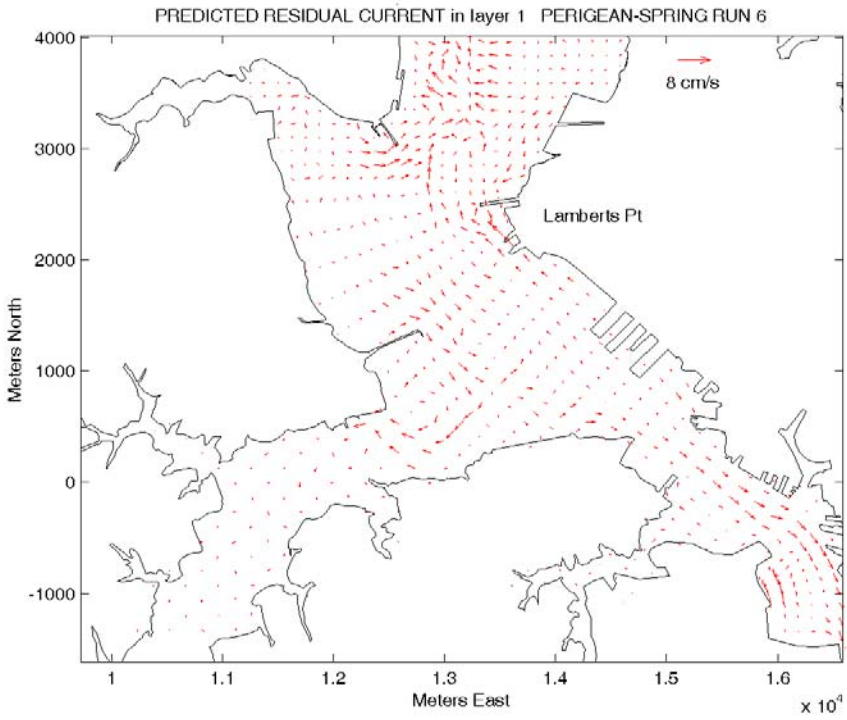

Figure 28. Predicted bottom residual flow for Northward Expansion (Case 6), Lambert Bend, during a perigean-spring tide.

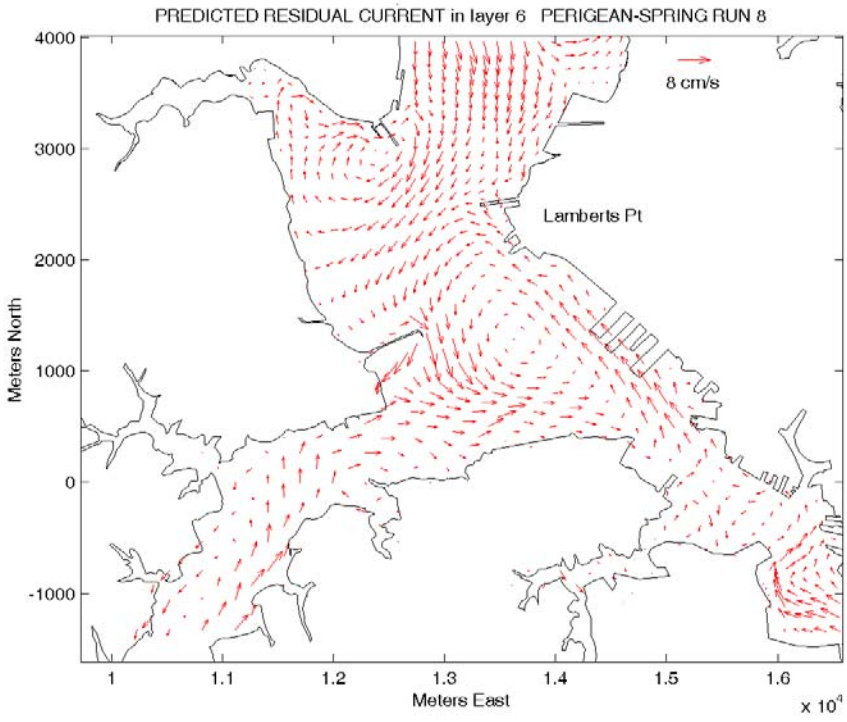

Figure 29. Predicted surface residual flow for Northward and Eastward Expansion (Case 8), Lambert Bend, during a perigean-spring tide.

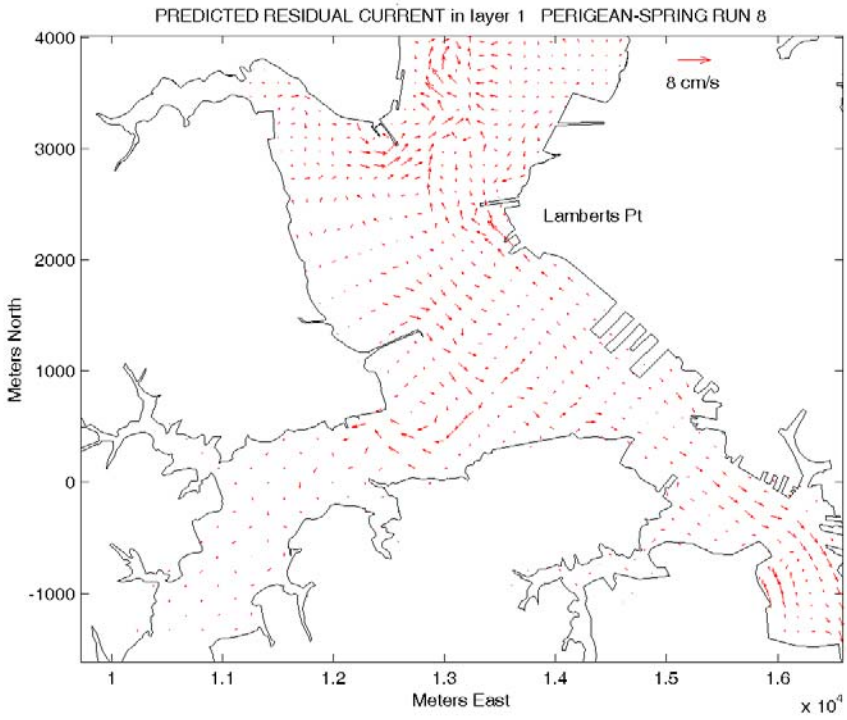

Figure 30. Predicted bottom residual flow for Northward and Eastward Expansion (Case 8), Lambert Bend, during a perigean-spring tide.

Window 4 of 4. Town Point Reach

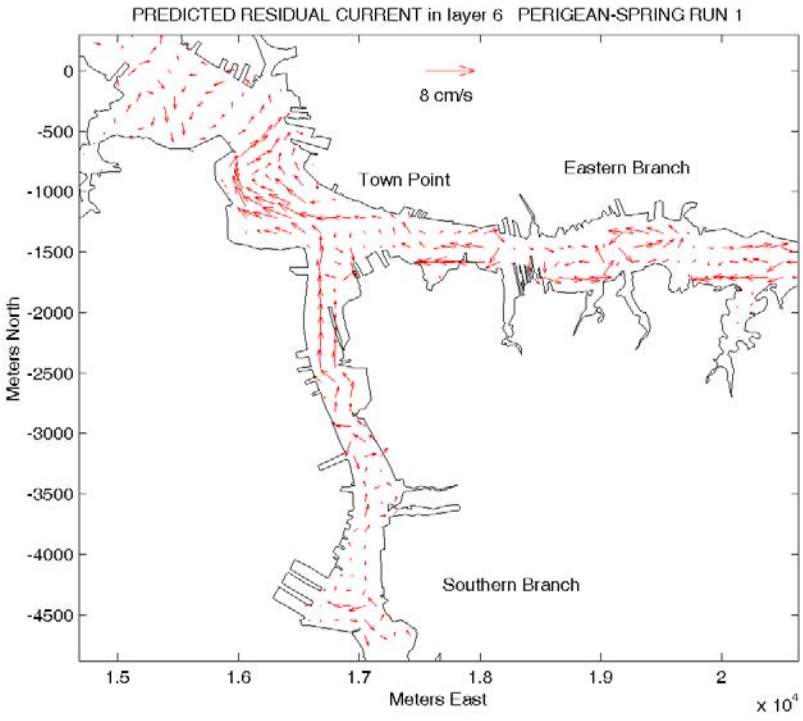

Figure 31. Predicted surface residual flow for Base Case, Town Point Reach, during a perigean-spring tide.

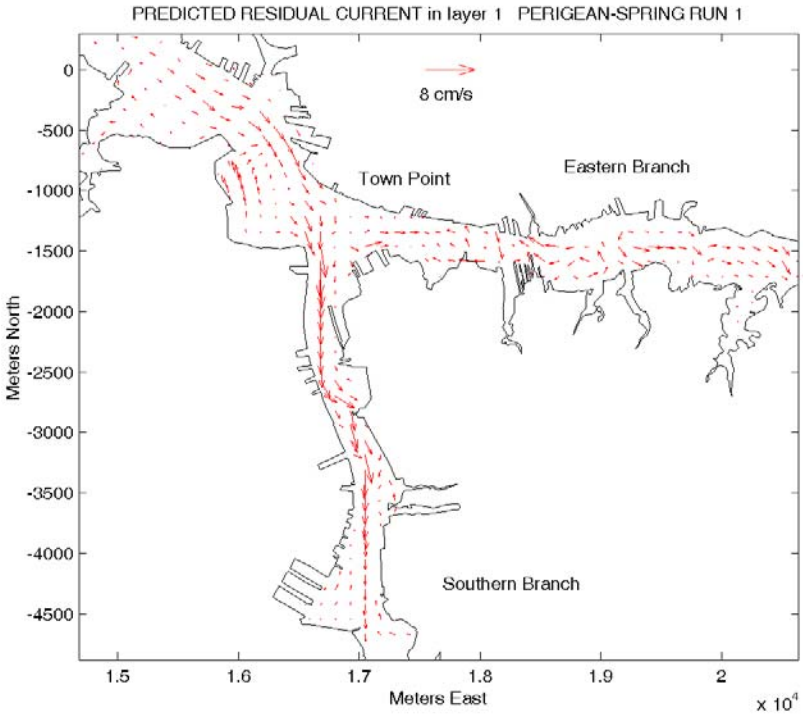

Figure 32. Predicted bottom residual flow for Base Case, Town Point Reach, during a perigean-spring tide.

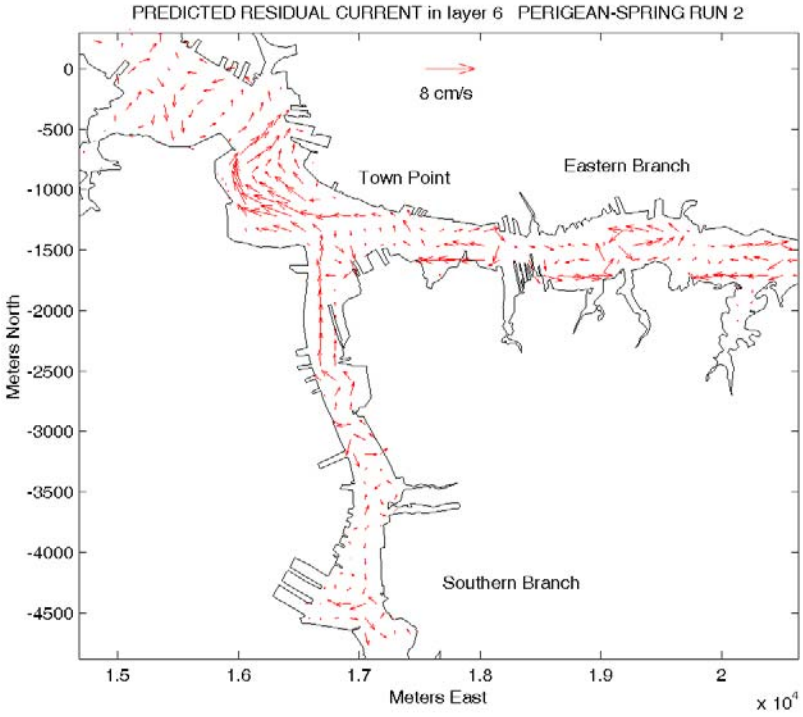

Figure 33. Predicted surface residual flow for Eastward Expansion (Case 2), Town Point Reach, during a perigean-spring tide.

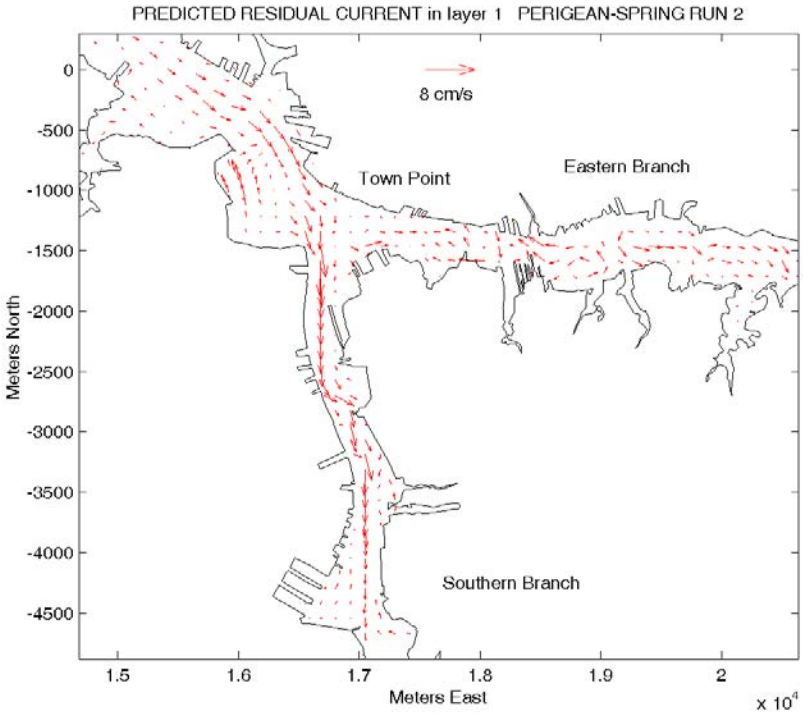

Figure 34. Predicted bottom residual flow for Eastward Expansion (Case 2), Town Point Bend, during a perigean-spring tide.

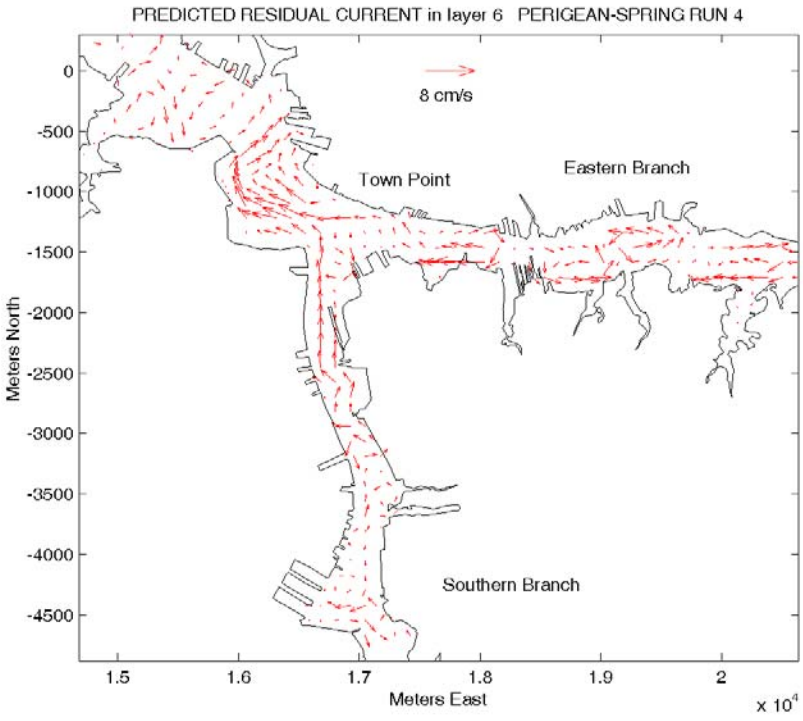

Figure 35. Predicted surface residual flow for Westward Expansion (Case 4), Town Point Bend, during a perigean-spring tide.

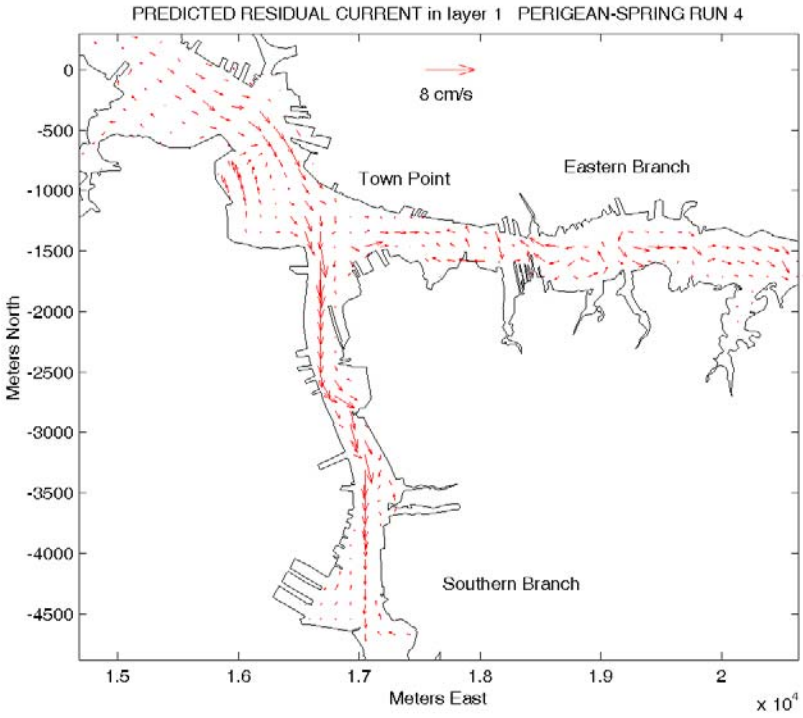

Figure 36. Predicted bottom residual flow for Westward Expansion (Case 4), Town Point Reach, during a perigean-spring tide.

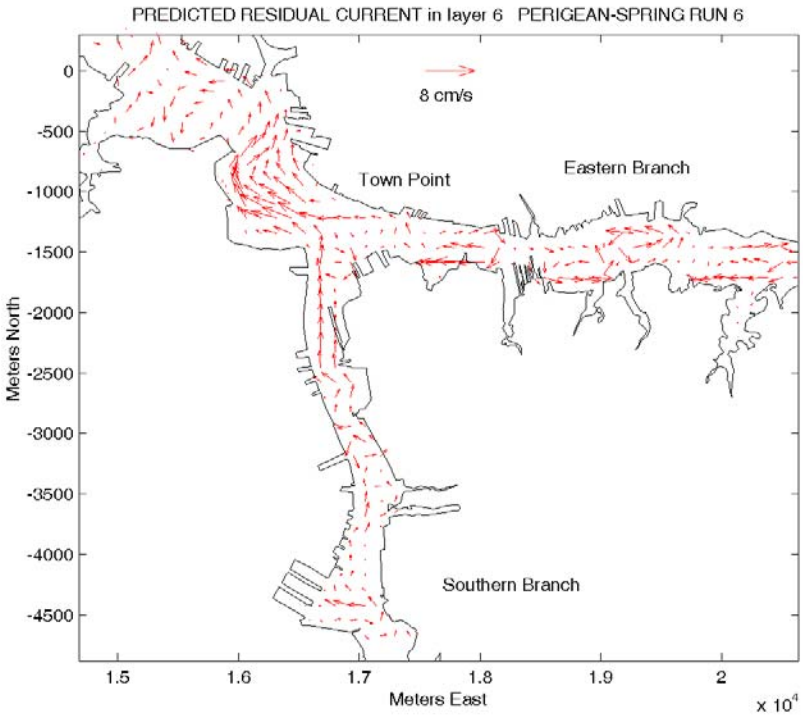

Figure 37. Predicted surface residual flow for Northward Expansion (Case 6), Town Point Reach, during a perigean-spring tide.

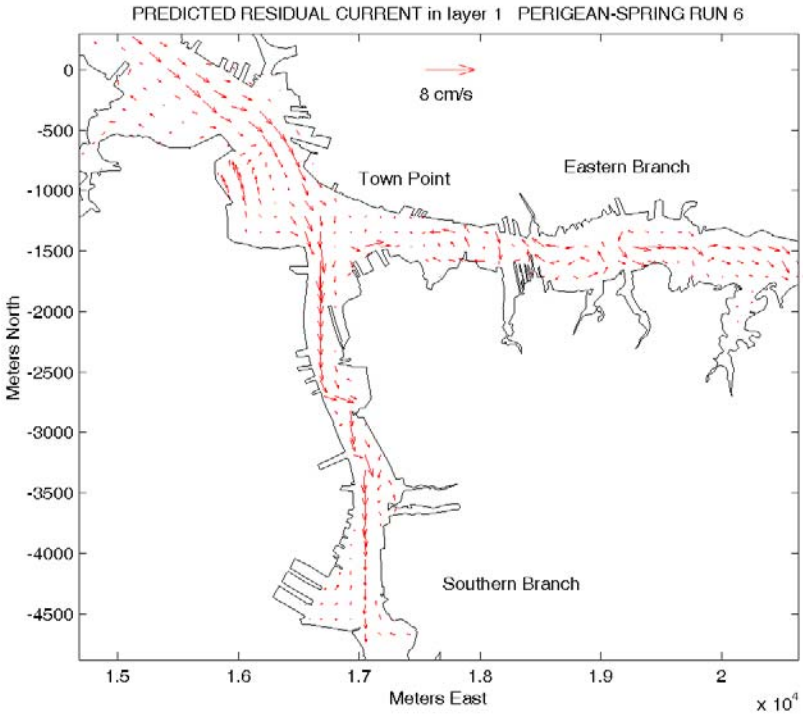

Figure 38. Predicted bottom residual flow for Northward Expansion (Case 6), Town Point Reach, during a perigean-spring tide.

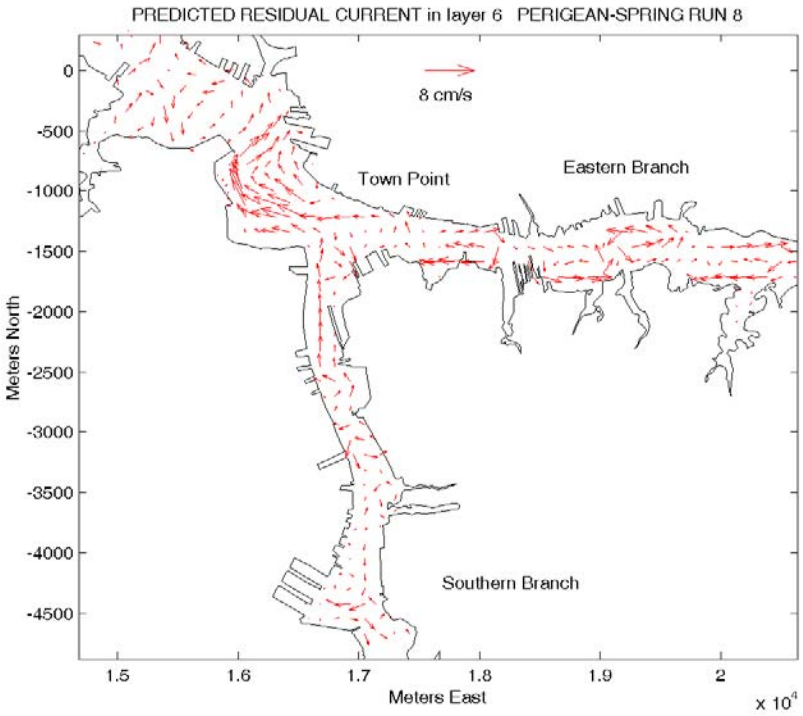

Figure 39. Predicted surface residual flow for North/East Expansion (Case 8), Town Point Reach, during a perigean-spring tide.

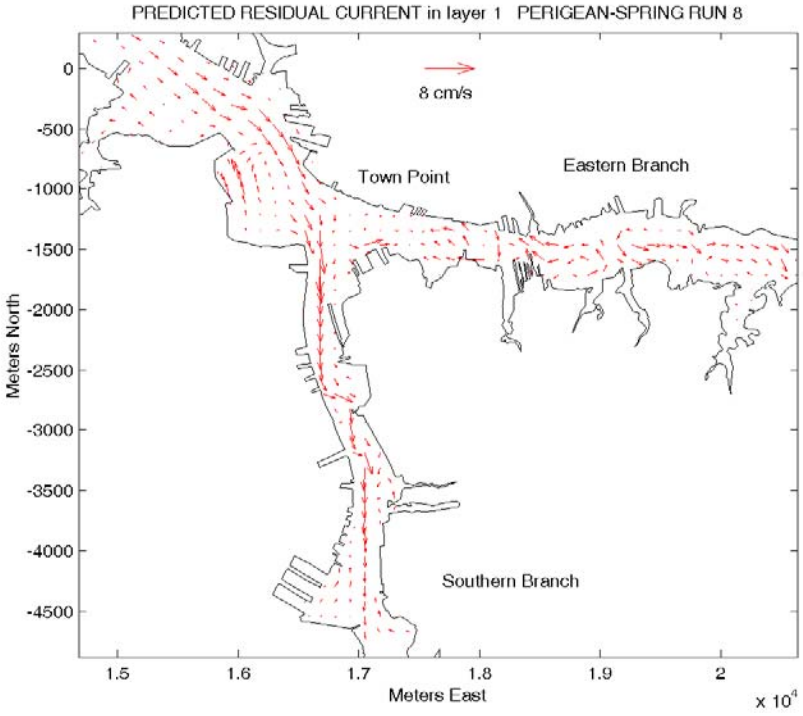

Figure 40. Predicted bottom residual flow for North/East Expansion (Case 8), Town Point Reach, during a perigean-spring tide.

APPENDIX to CHAPTER VI, SECTION A.1

Global Comparisons of Historical Runs

Spatial Distributions

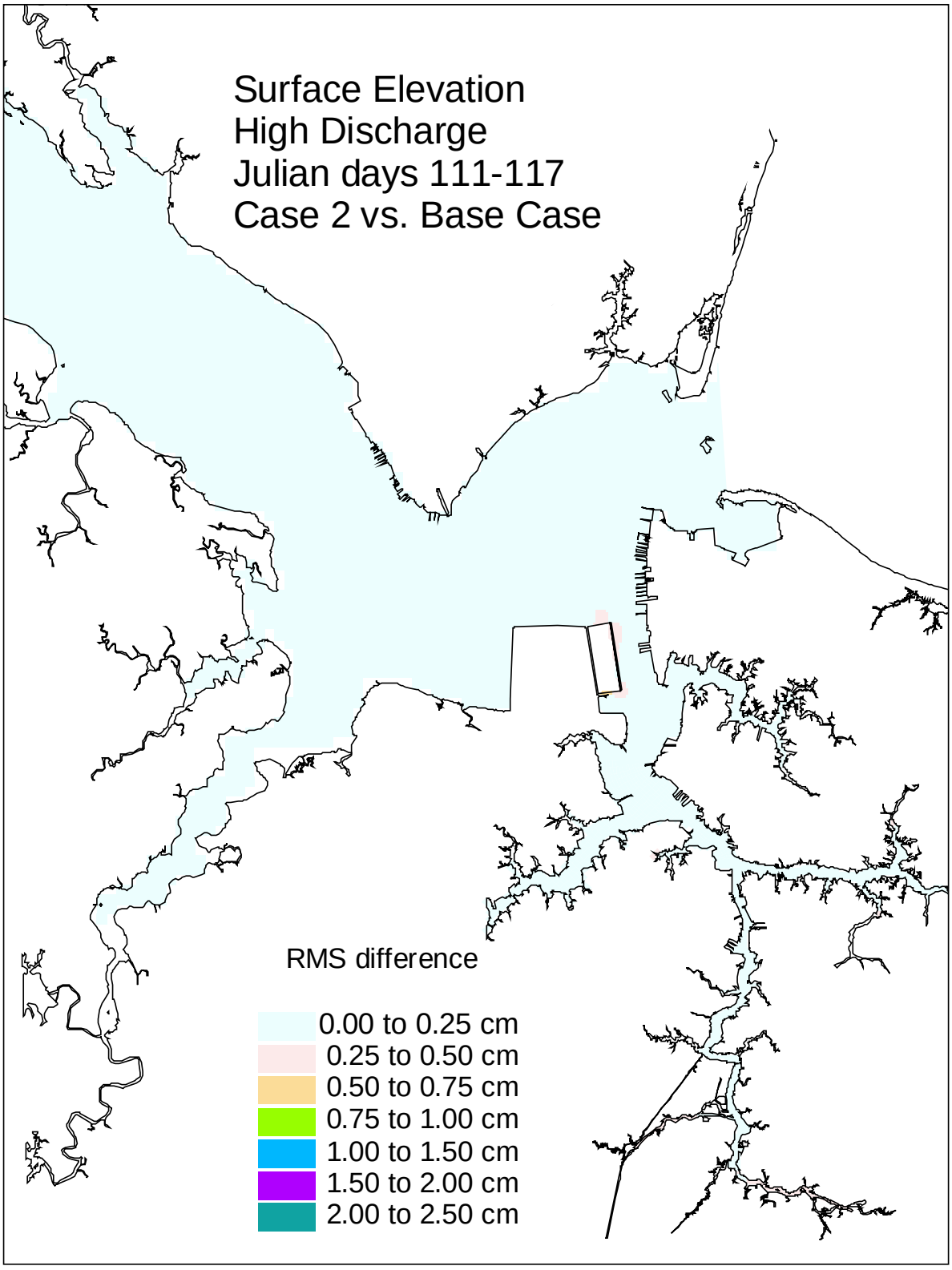

Figure 1. Historical simulation comparison (high discharge) of the surface elevation RMS difference for the Eastward Expansion (Option 7, 50-foot channel) versus the Base Case.

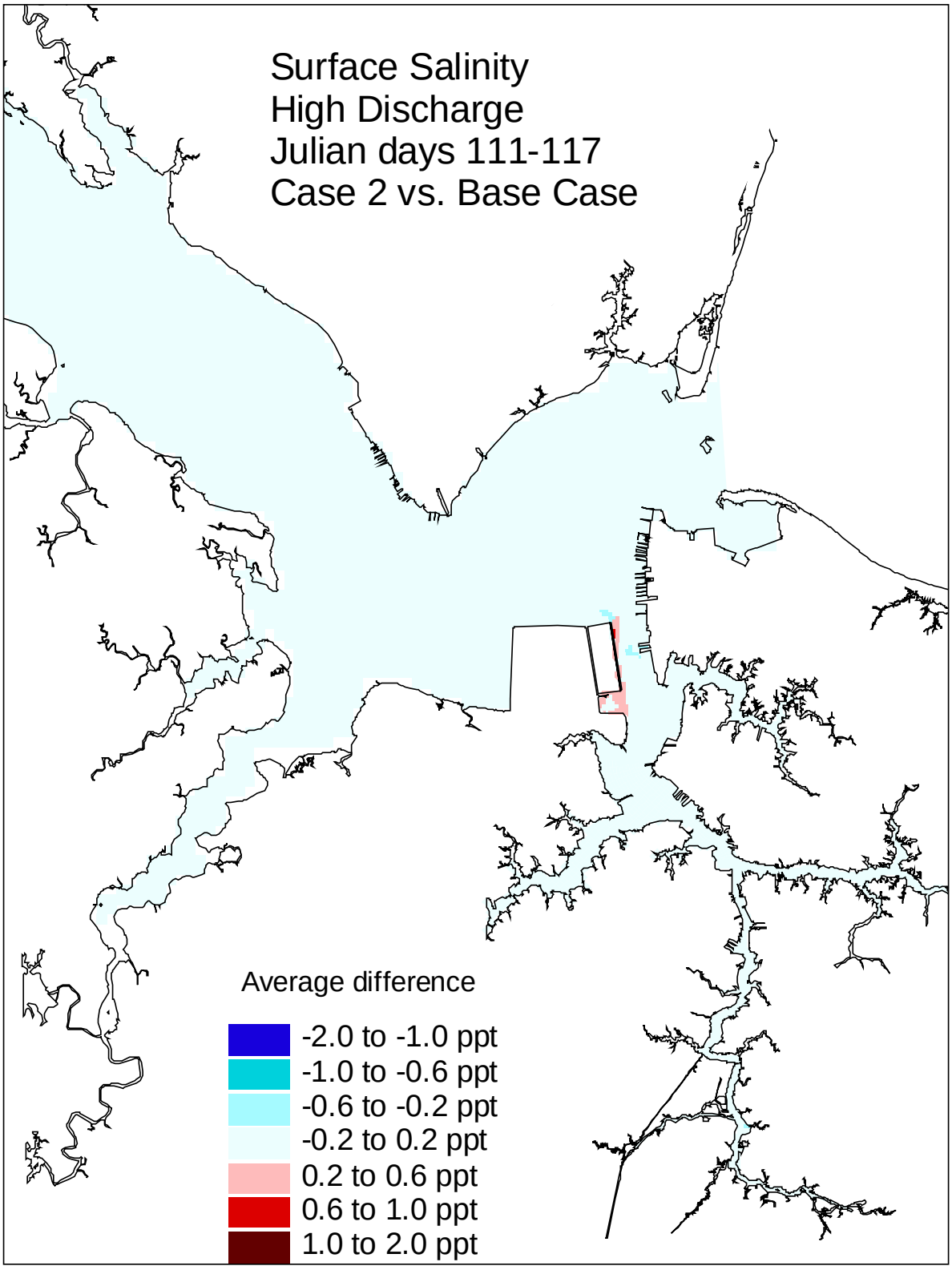

Figure 2. Historical simulation comparison (high discharge) of the surface salinity average difference for the Eastward Expansion (Option 7, 50-foot channel) versus the Base Case.

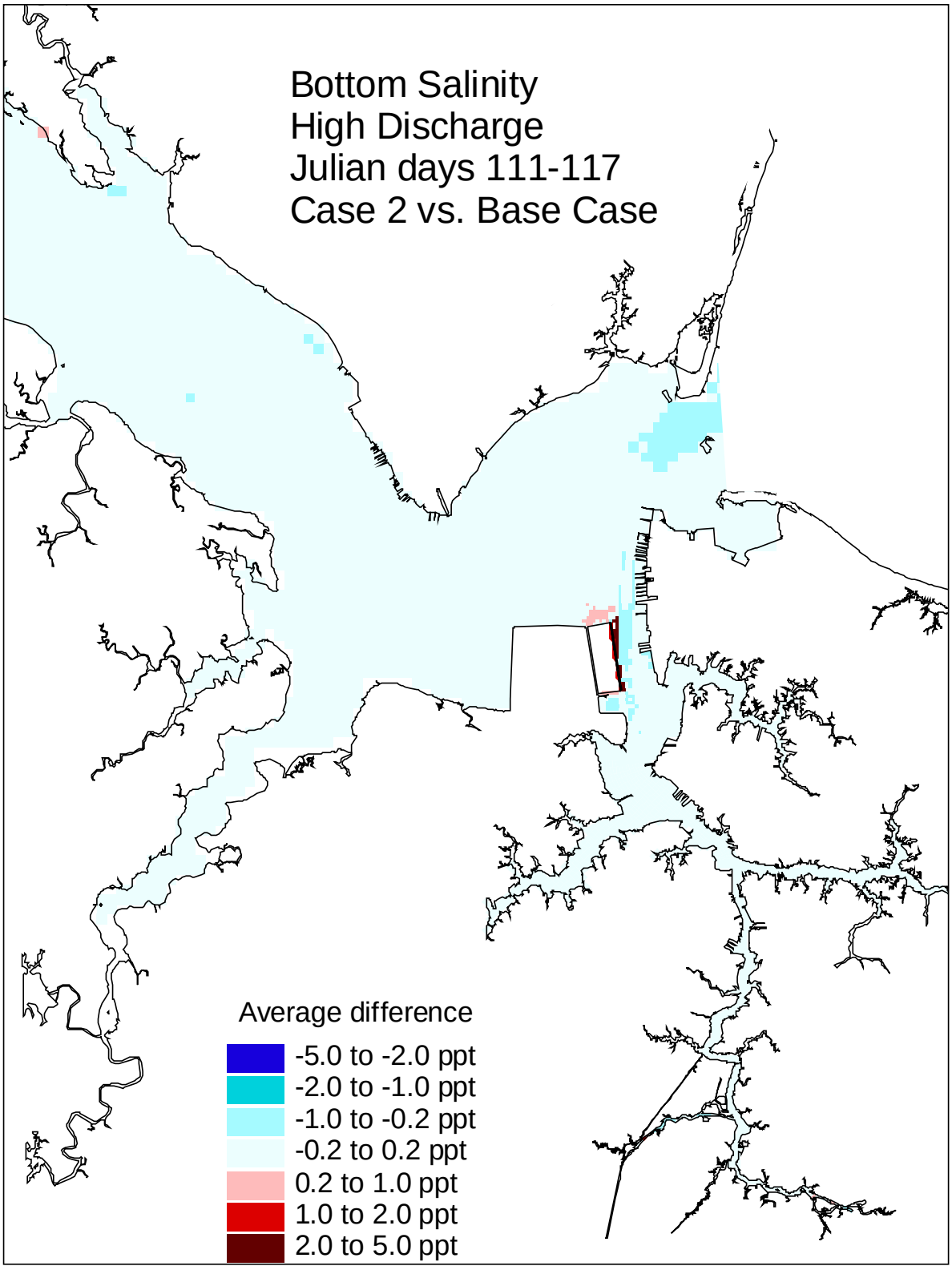

Figure 3. Historical simulation comparison (high discharge) of the bottom salinity average difference for the Eastward Expansion, (Option 7, 50-foot channel) versus the Base Case.

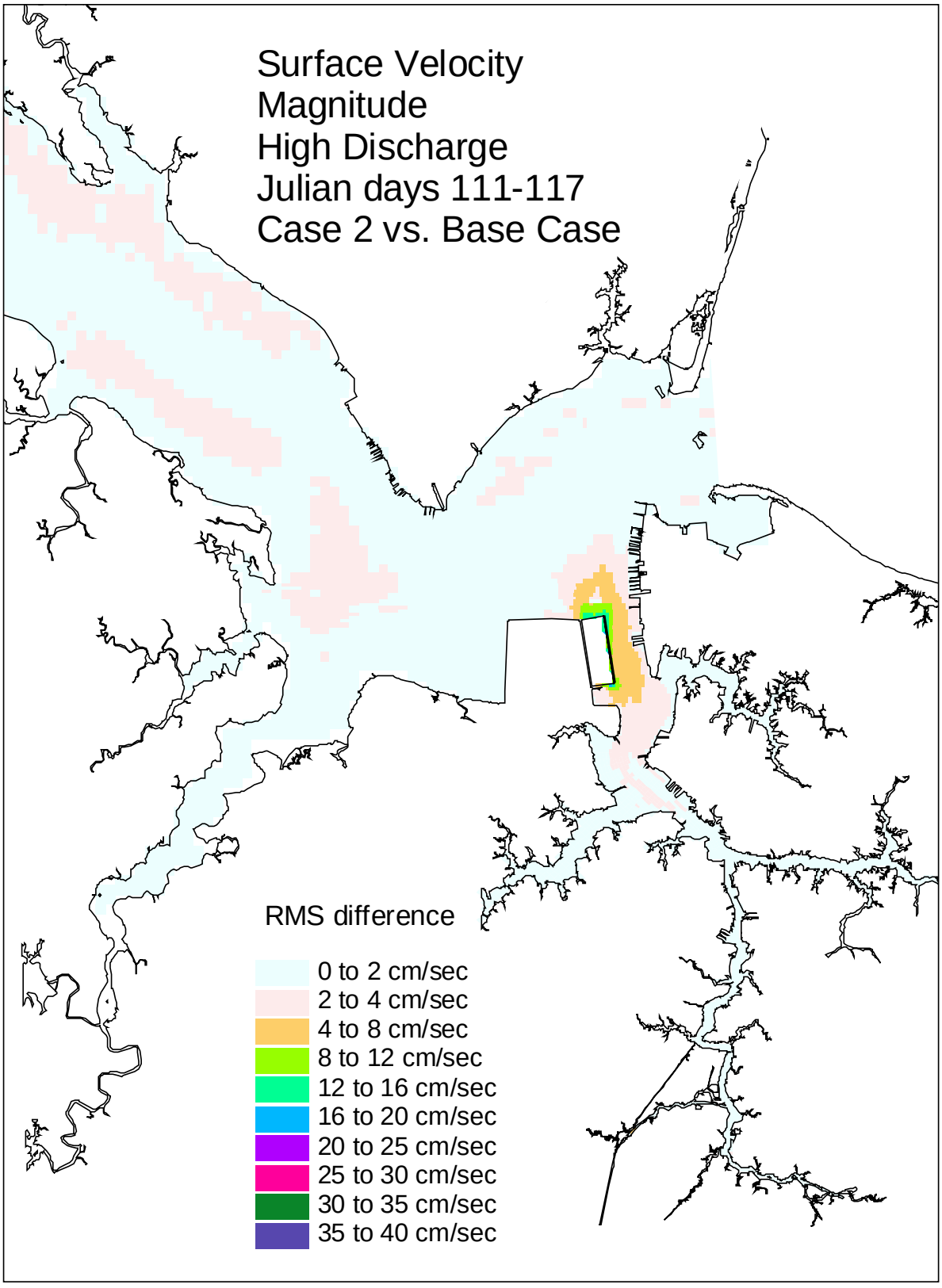

Figure 4. Historical simulation comparison (high discharge) of the surface velocity RMS difference for the Eastward Expansion (Option 7, 50-foot channel) versus the Base Case.

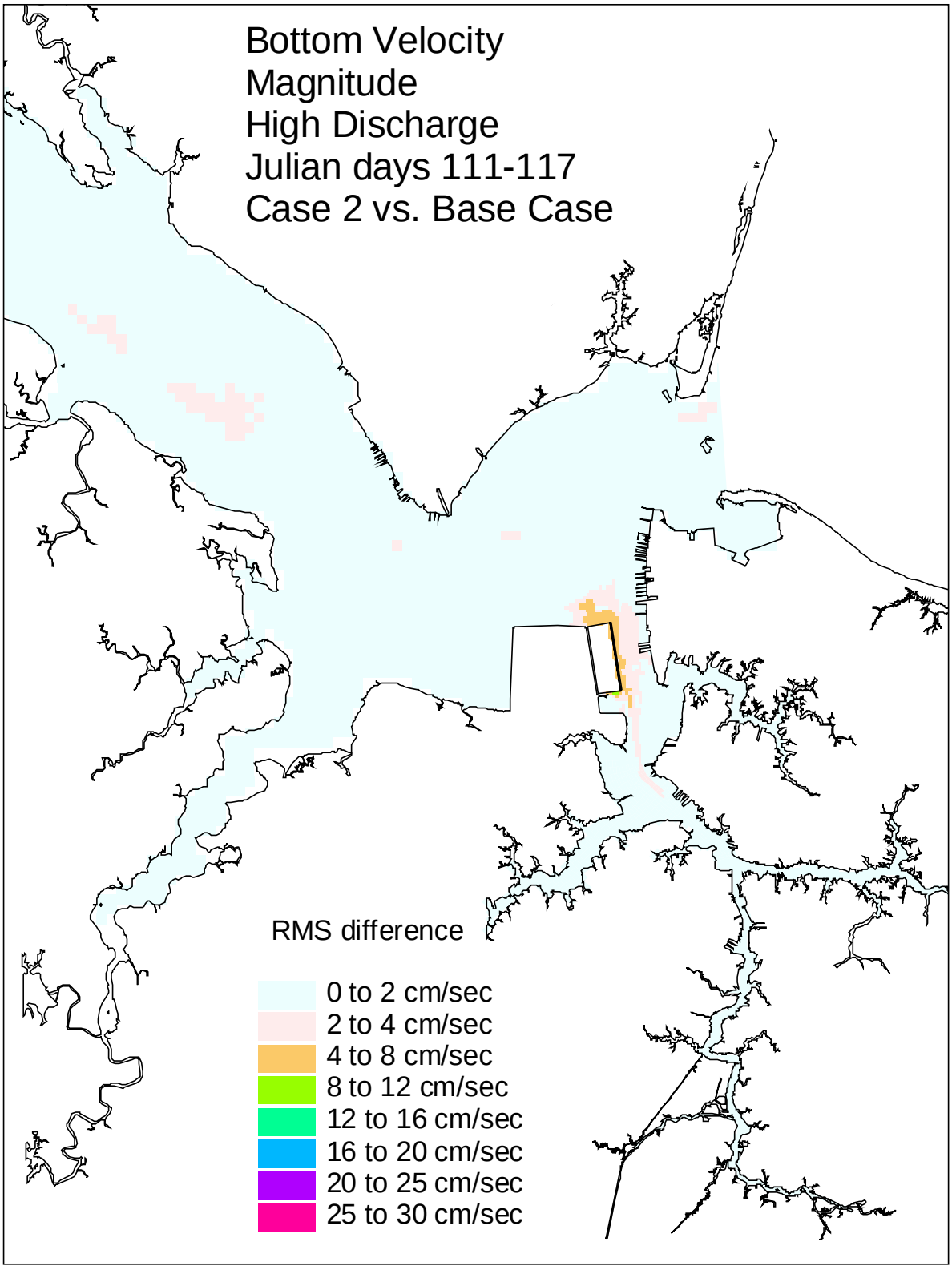

Figure 5. Historical simulation comparison (high discharge) of the bottom velocity RMS difference for the Eastward Expansion, (Option 7, 50-foot channel) versus the Base Case.

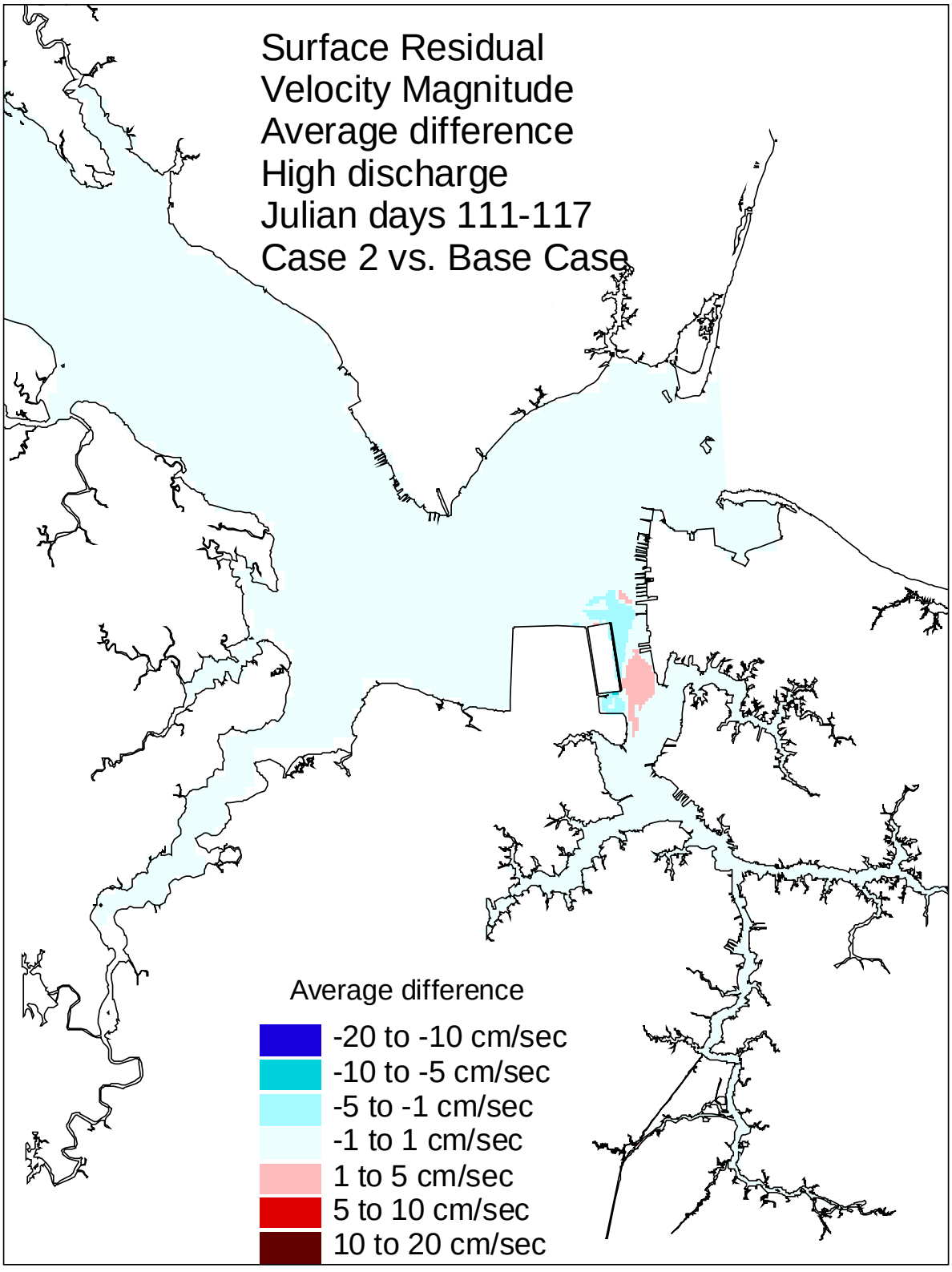

Figure 6. Historical simulation comparison (high discharge) of the surface residual velocity average difference for the Eastward Expansion, (Option 7, 50-foot channel) versus the Base Case.

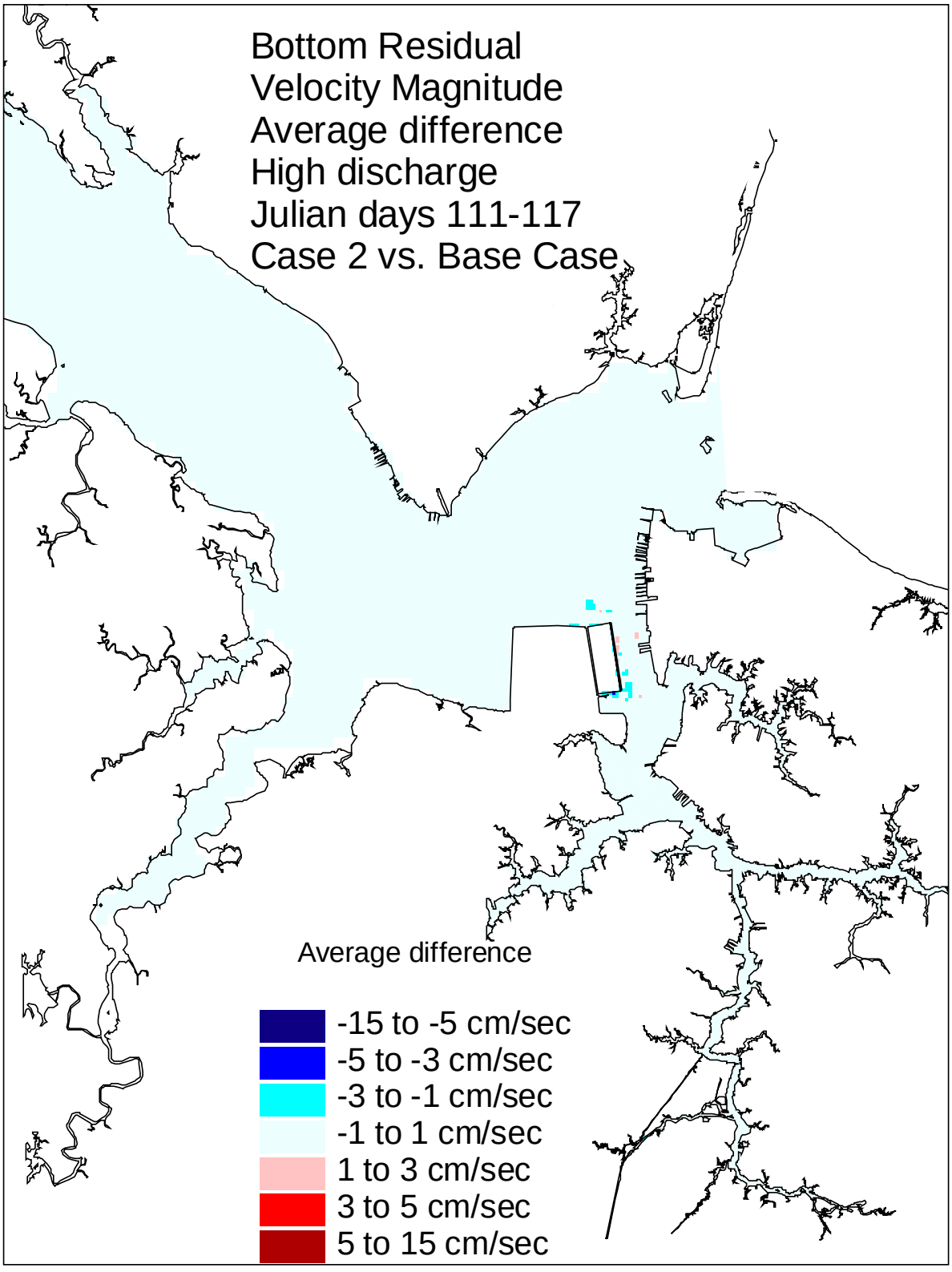

Figure 7. Historical simulation comparison (high discharge) of the bottom residual velocity average difference for the Eastward Expansion, (Option 7, 50-foot channel) versus the Base Case.

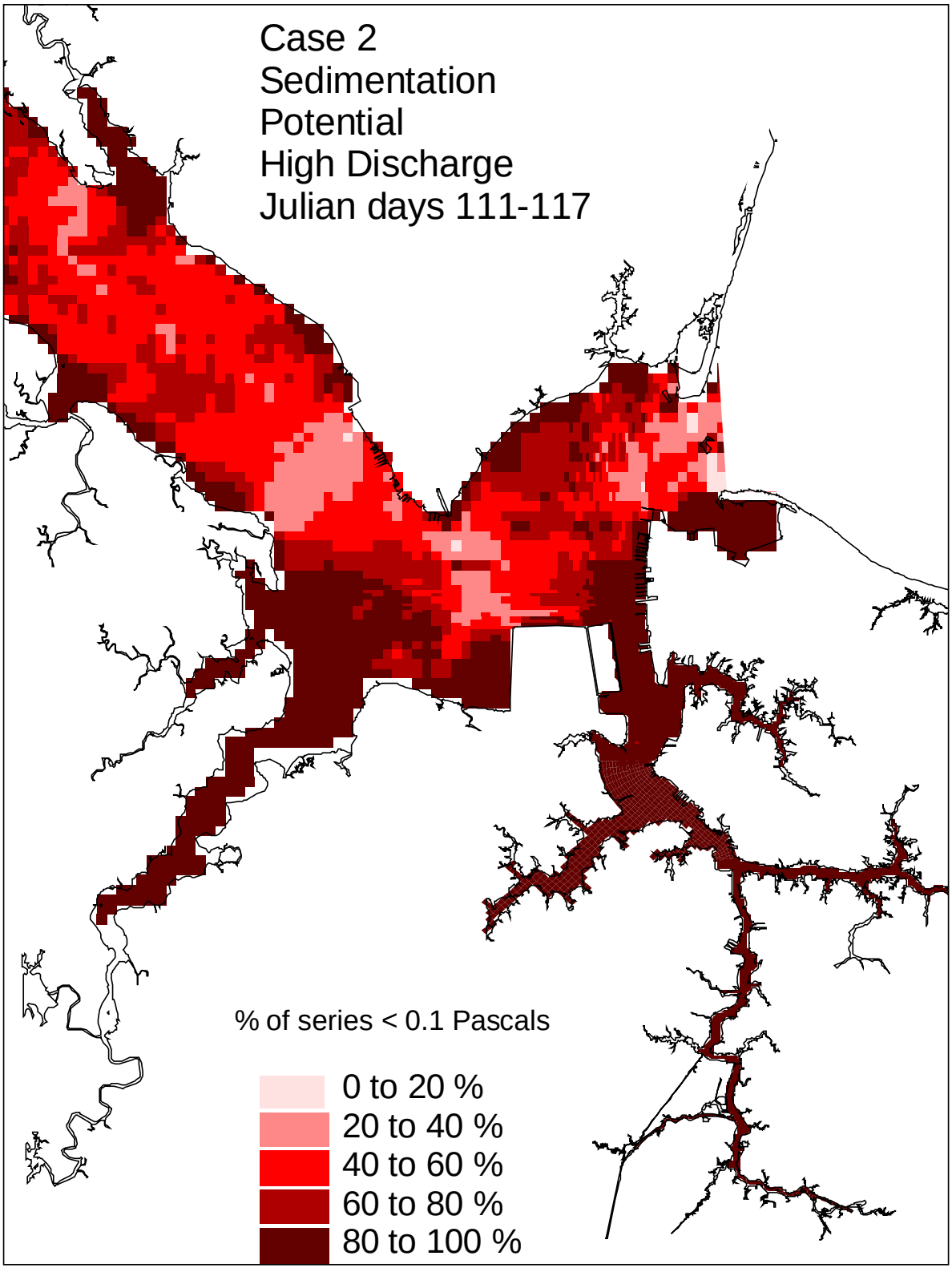

Figure 8. Historical simulation comparison (high discharge) of the sedimentation potential for the Eastward Expansion, (Option 7, 50-foot channel).

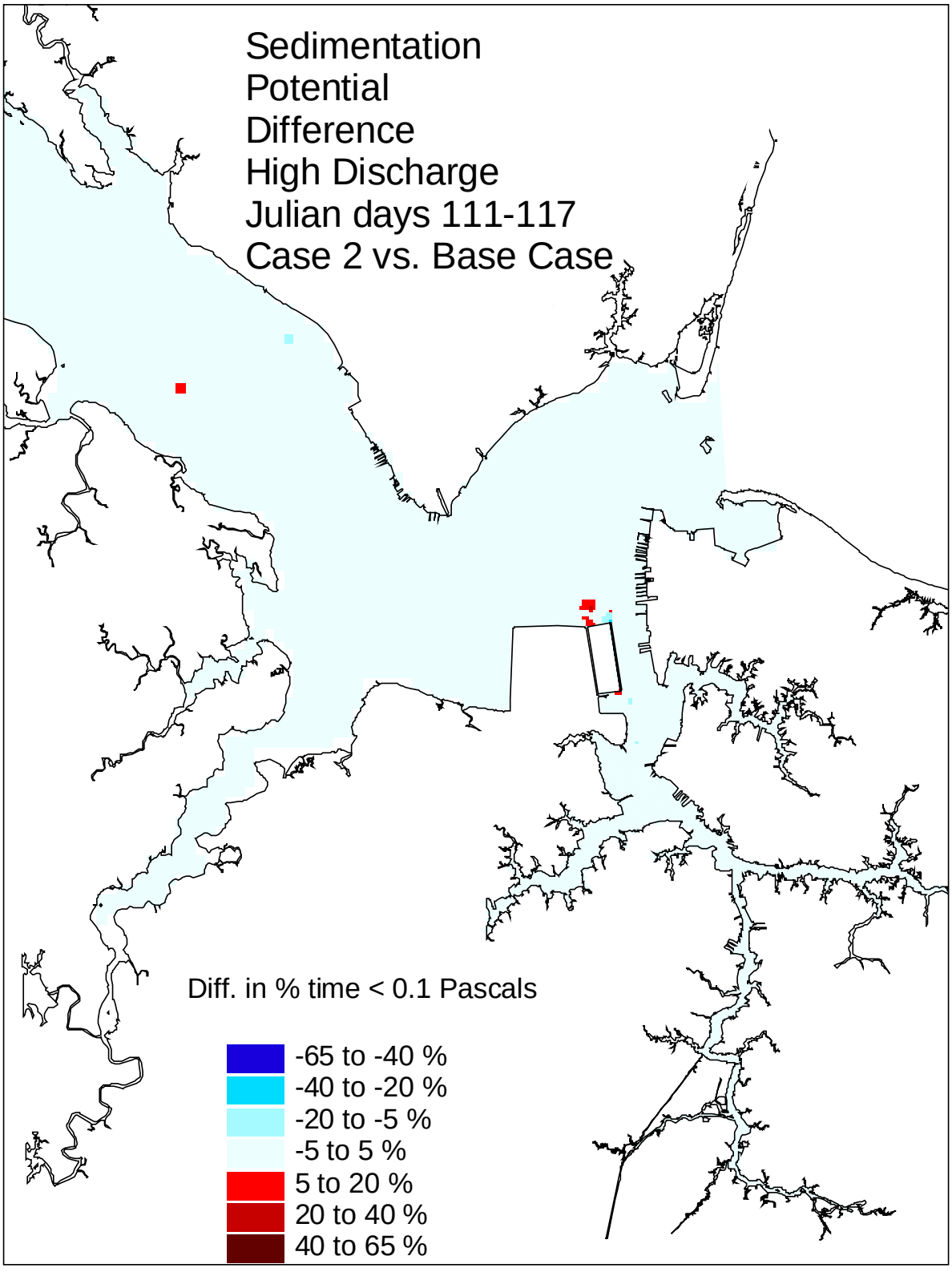

Figure 9. Historical simulation comparison (high discharge) of the sedimentation potential difference for the Eastward Expansion, (Option 7, 50-foot channel) versus the Base Case.

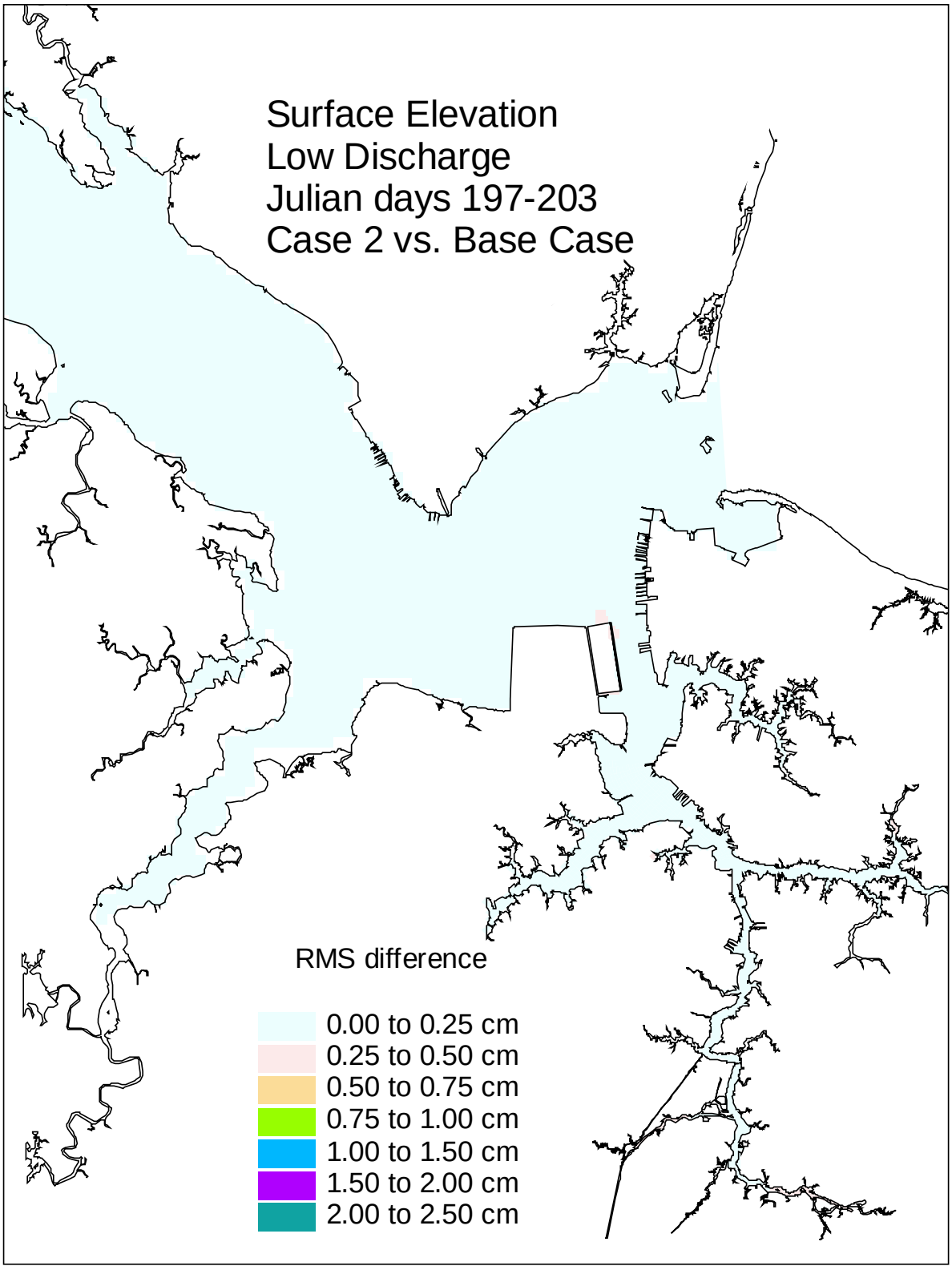

Figure 10. Historical simulation comparison (low discharge) of the surface elevation RMS difference for the Eastward Expansion (Option 7, 50-foot channel) versus the Base Case.

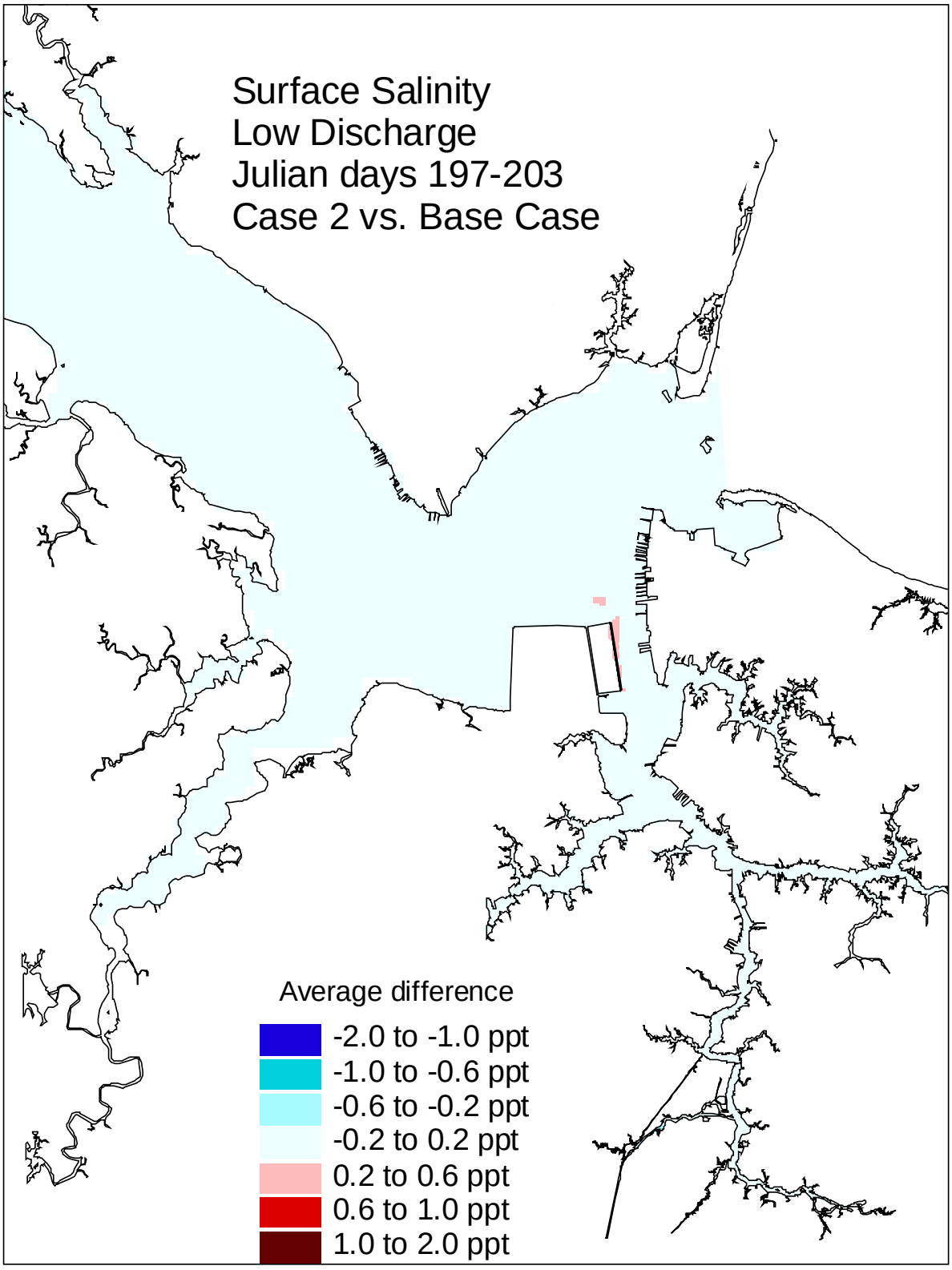

Figure 11. Historical simulation comparison (low discharge) of the surface salinity average difference for the Eastward Expansion (Option 7, 50-foot channel) versus the Base Case.

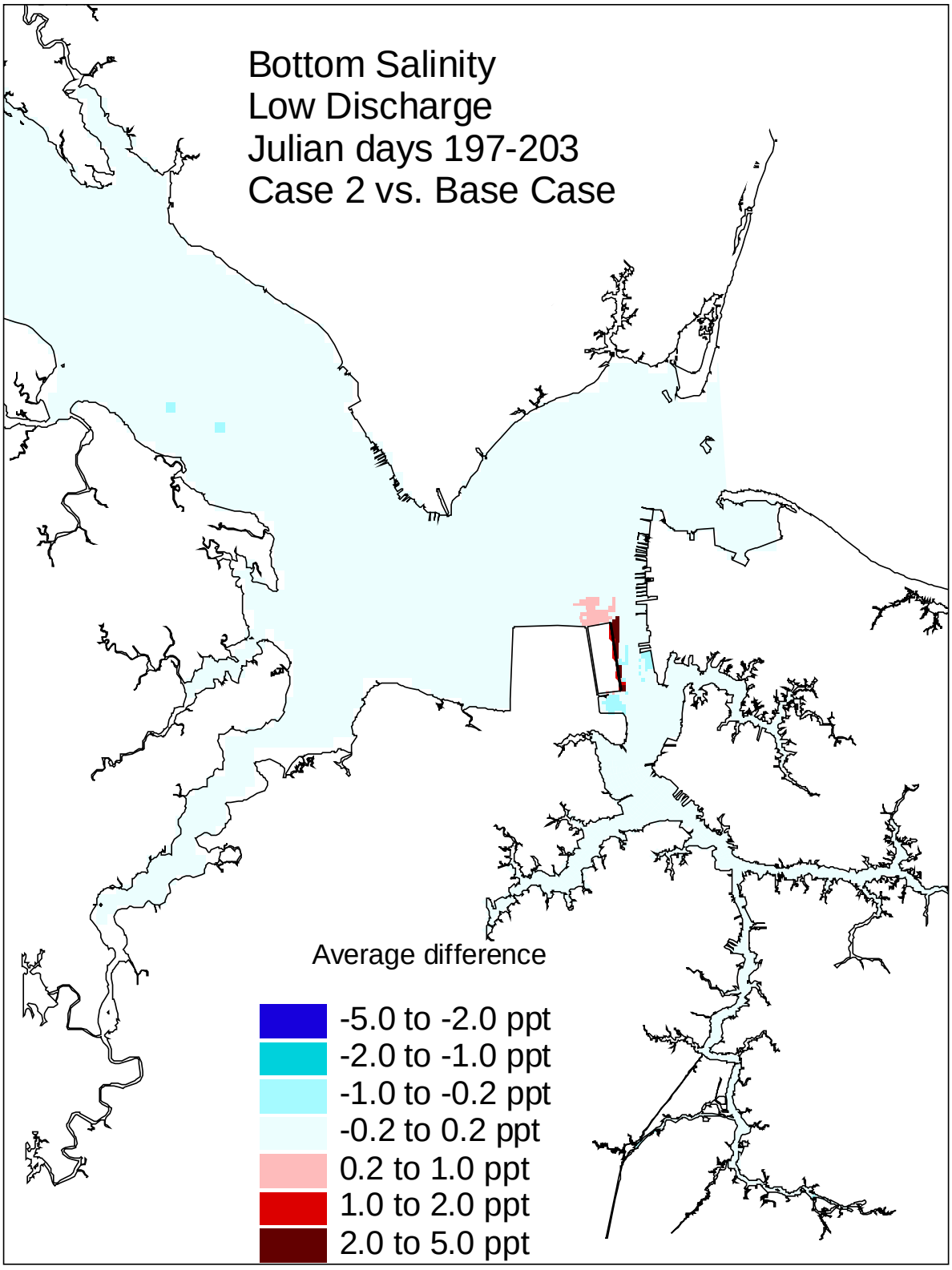

Figure 12. Historical simulation comparison (low discharge) of the bottom salinity average difference for the Eastward Expansion (Option 7, 50-foot channel) versus the Base Case.

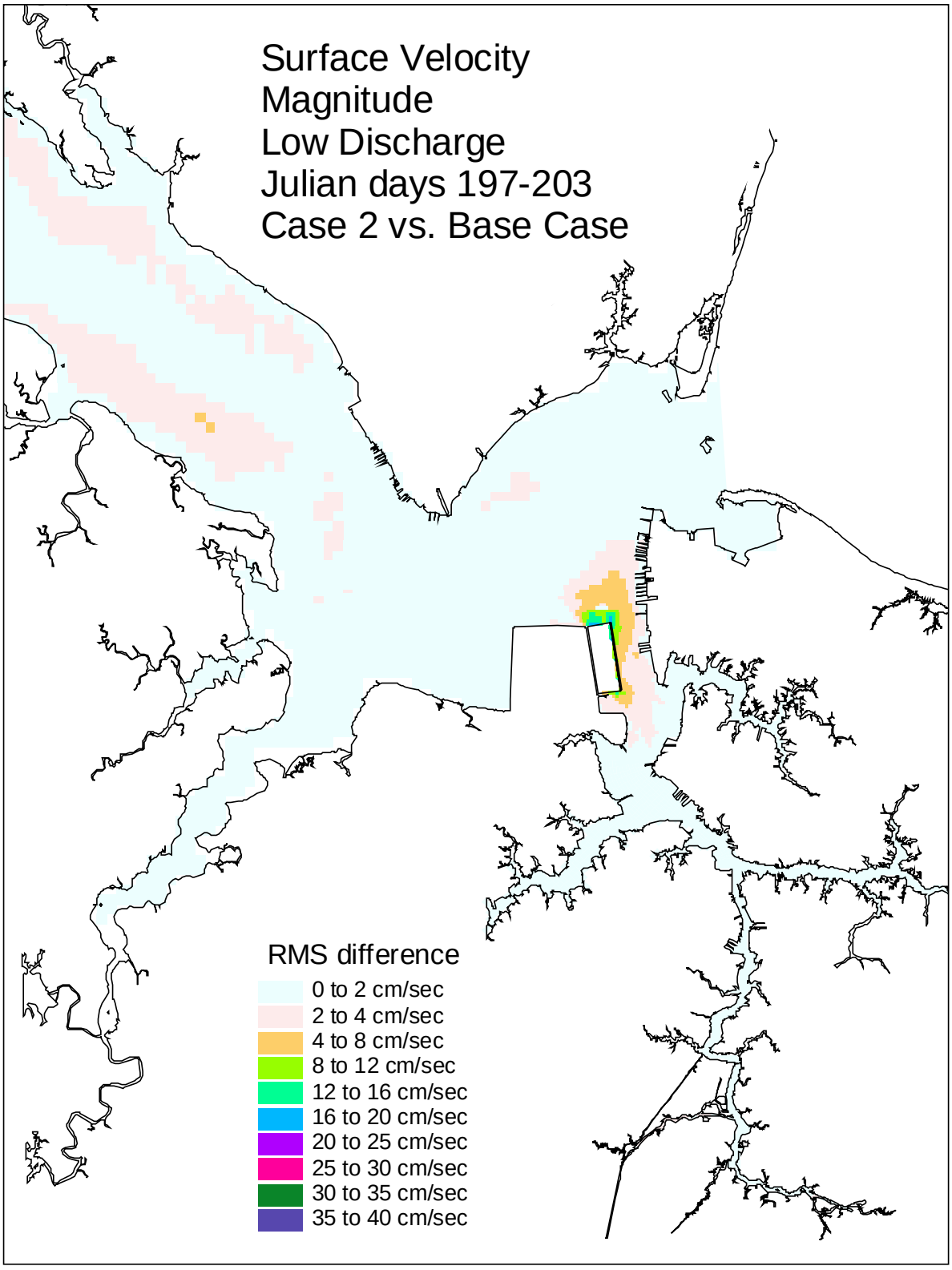

Figure 13. Historical simulation comparison (low discharge) of the surface velocity RMS difference for the Eastward Expansion (Option 7, 50-foot channel) versus the Base Case.

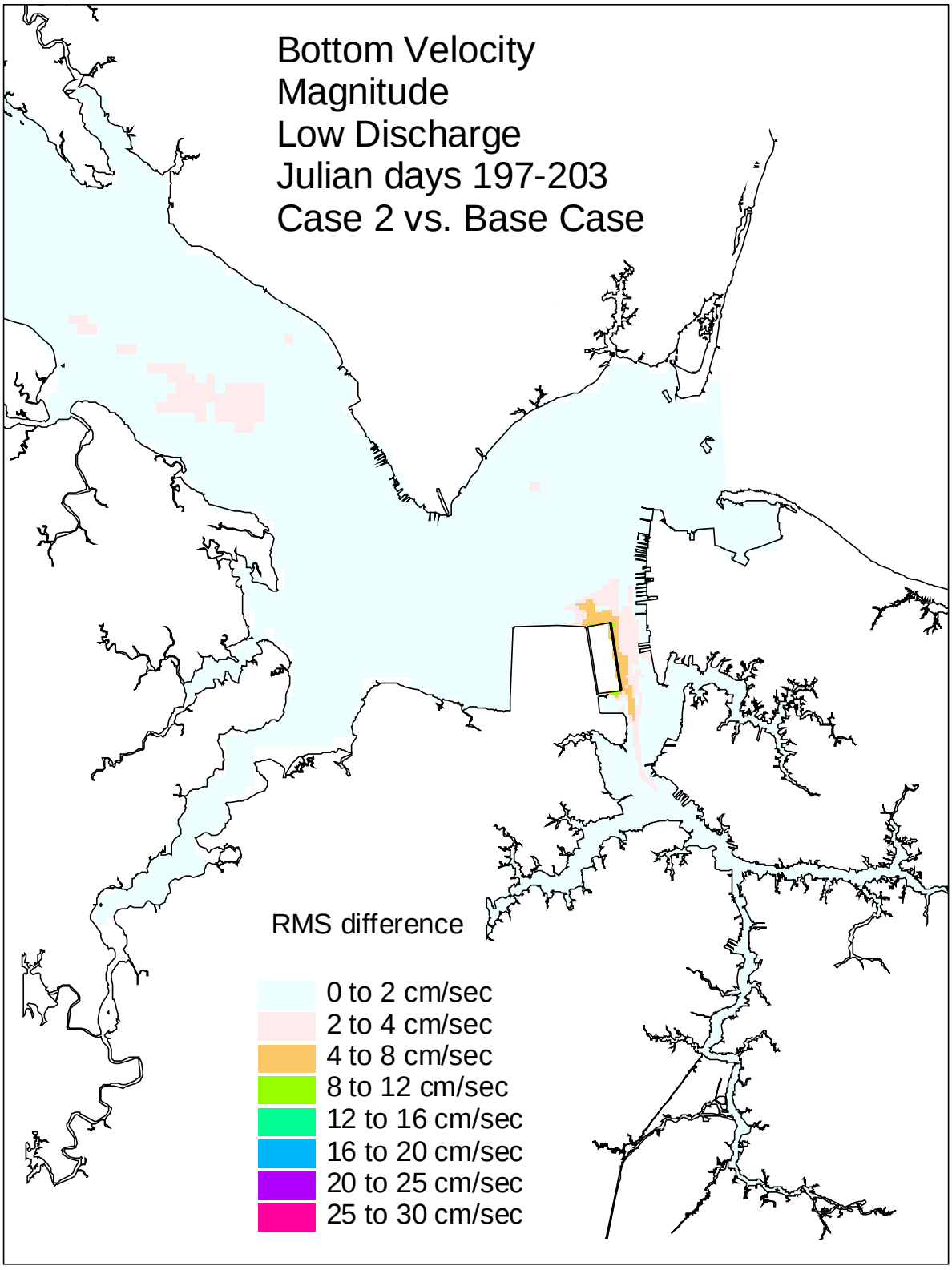

Figure 14. Historical simulation comparison (low discharge) of the bottom velocity RMS difference for the Eastward Expansion (Option 7, 50-foot channel) versus the Base Case.

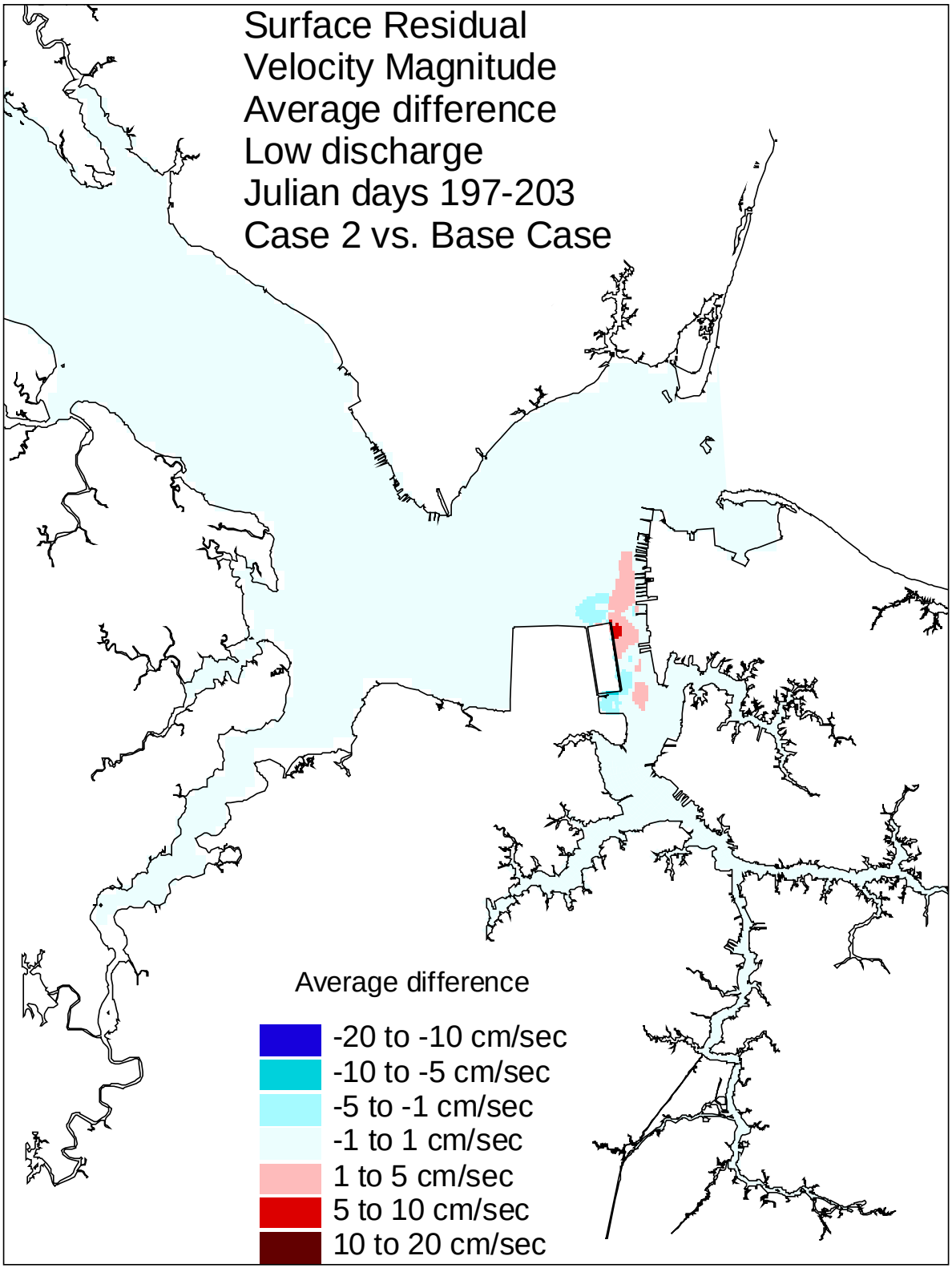

Figure 15. Historical simulation comparison (low discharge) of the surface residual velocity average difference for the Eastward Expansion (Option 7, 50-foot channel) versus the Base Case.

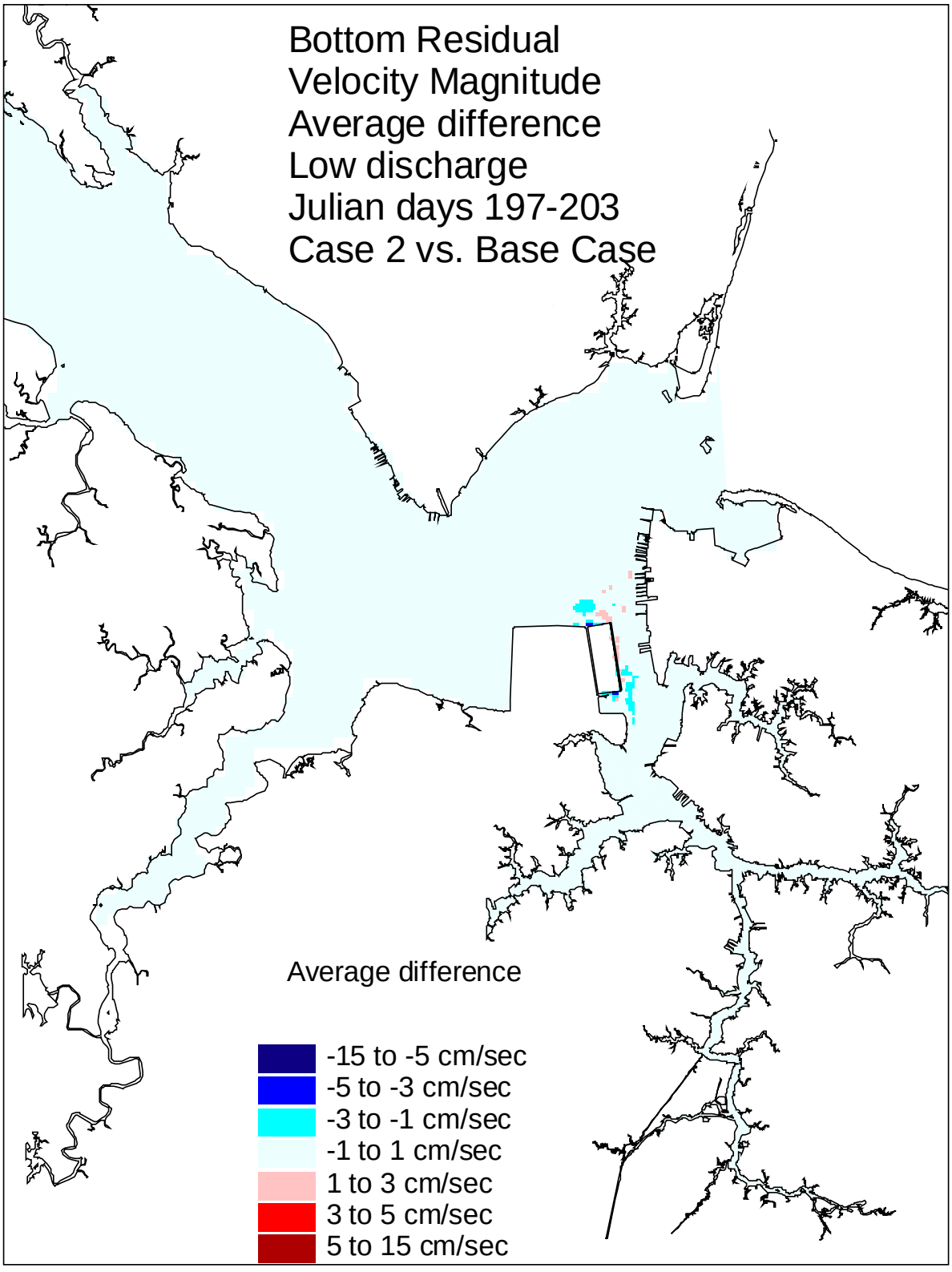

Figure 16. Historical simulation comparison (low discharge) of the bottom residual velocity average difference for the Eastward Expansion (Option 7, 50-foot channel) versus the Base Case.

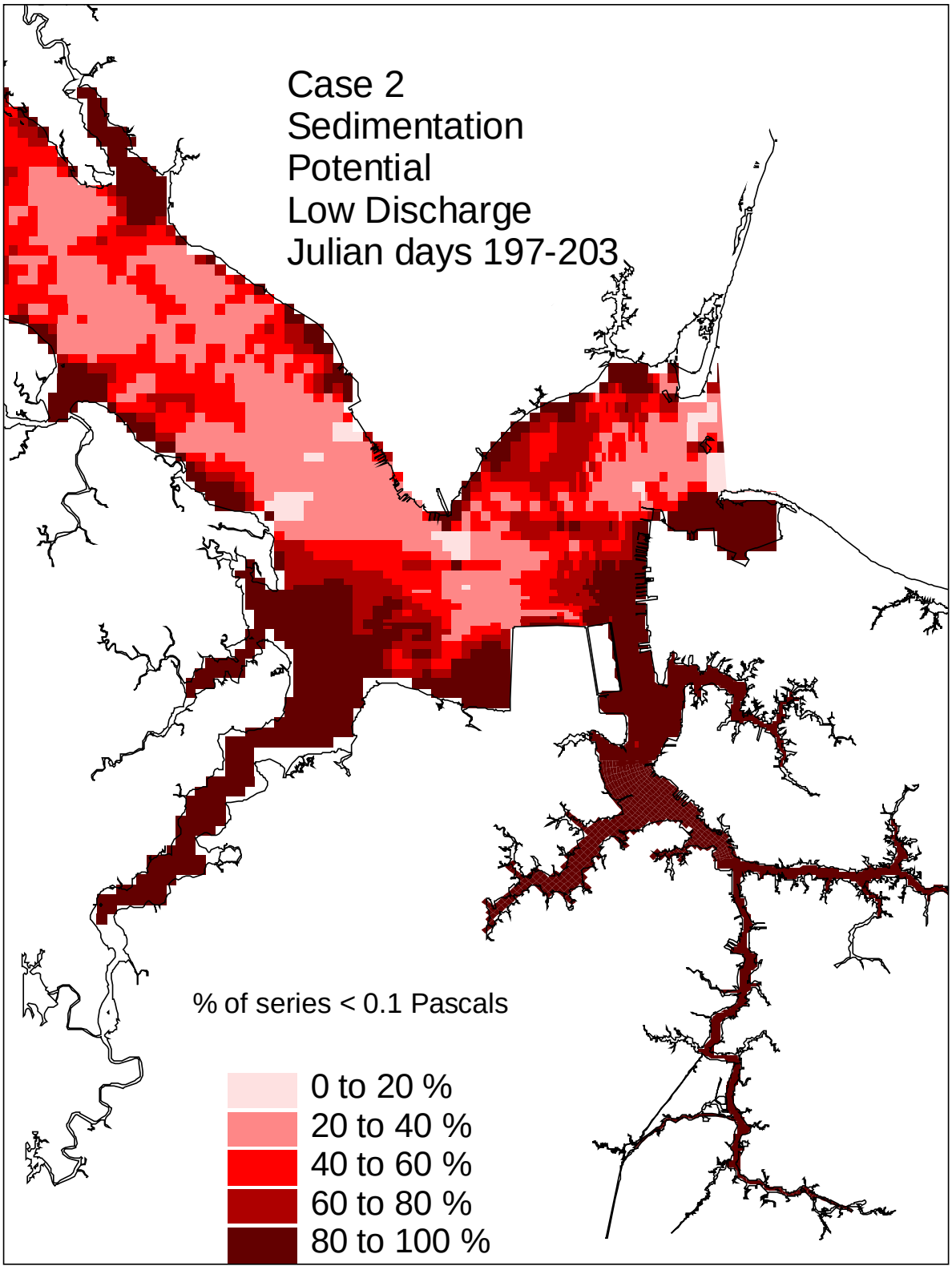

Figure 17. Historical simulation comparison (low discharge) of the sedimentation potential for the Eastward Expansion (Option 7, 50-foot channel).

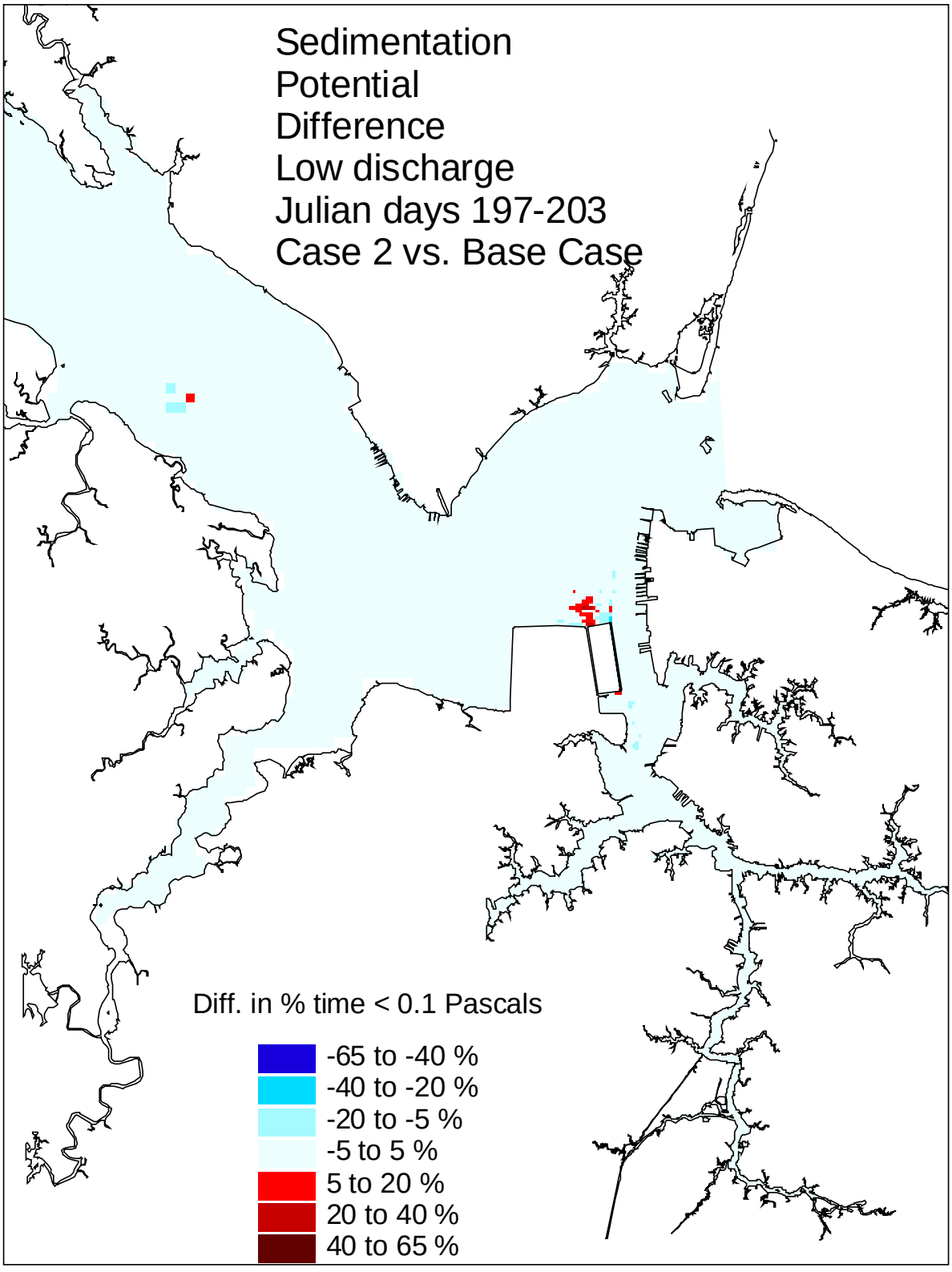

Figure 18. Historical simulation comparison (low discharge) of the sedimentation potential difference for the Eastward Expansion (Option 7, 50-foot channel) versus the Base Case.

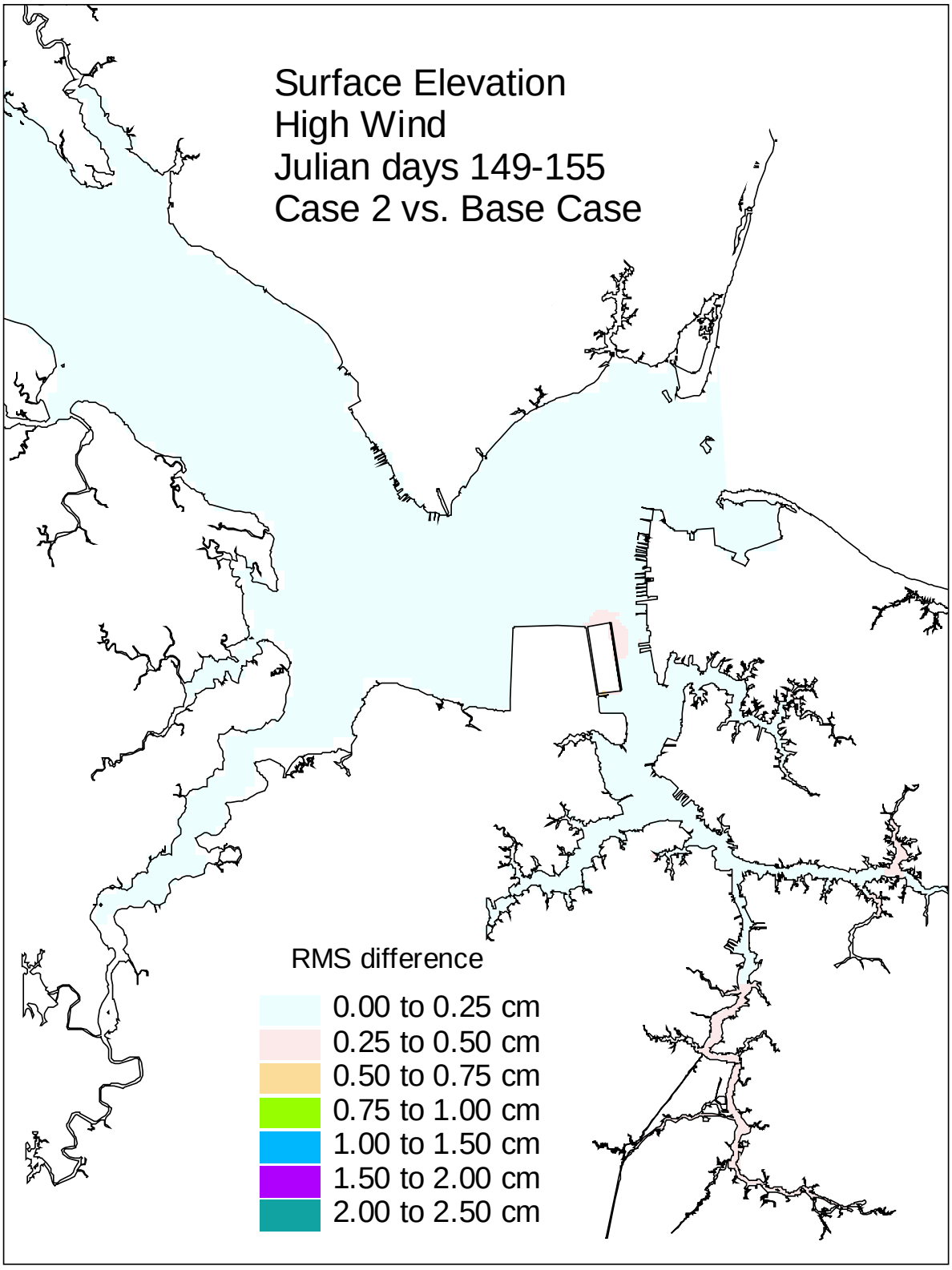

Figure 19. Historical simulation comparison (high wind) of the surface elevation RMS difference for the Eastward Expansion (Option 7, 50-foot channel) versus the Base Case.

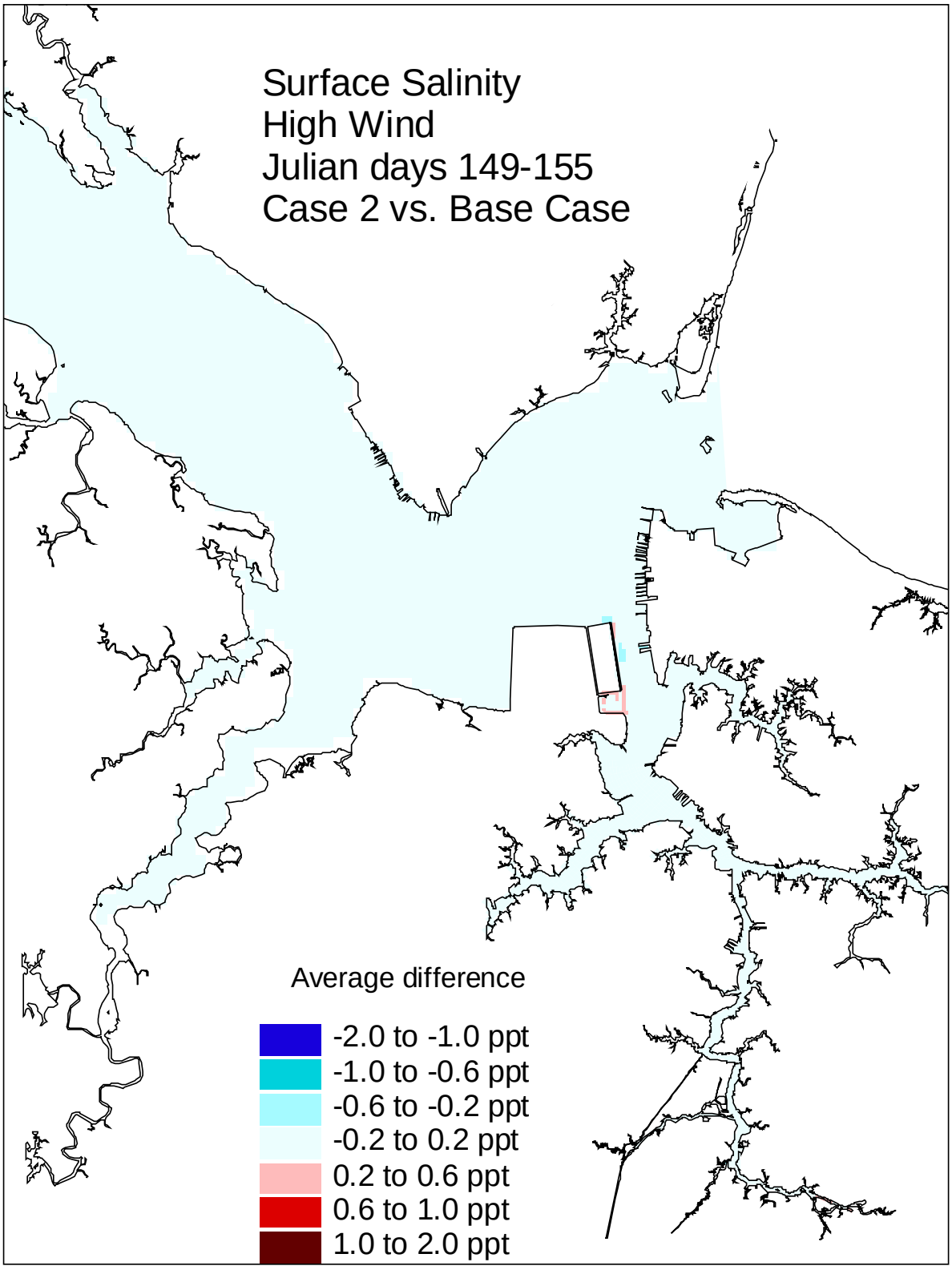

Figure 20. Historical simulation comparison (high wind) of the surface salinity average difference for the Eastward Expansion (Option 7, 50-foot channel) versus the Base Case.

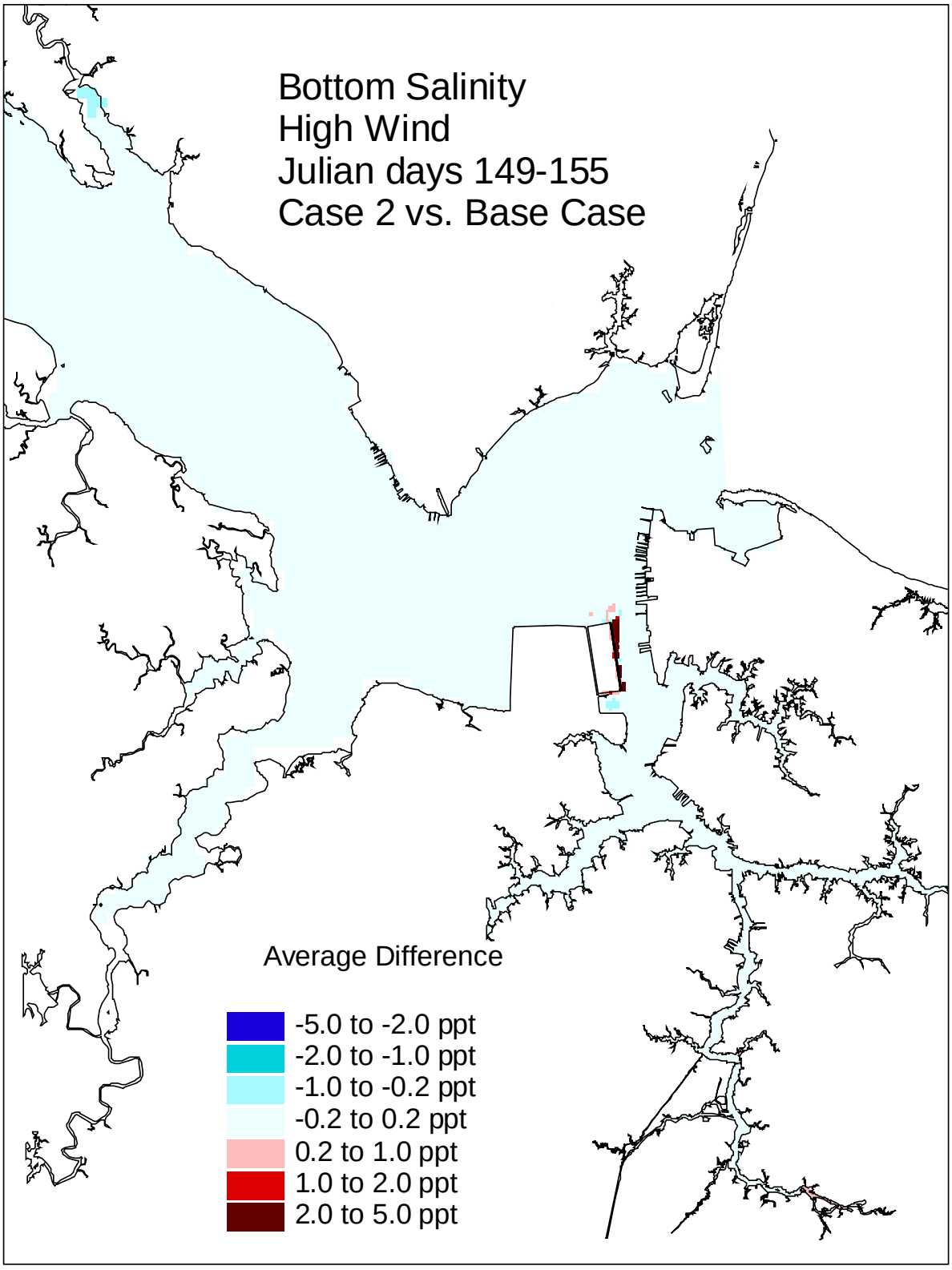

Figure 21. Historical simulation comparison (high wind) of the bottom salinity average difference for the Eastward Expansion (Option 7, 50-foot channel) versus the Base Case.

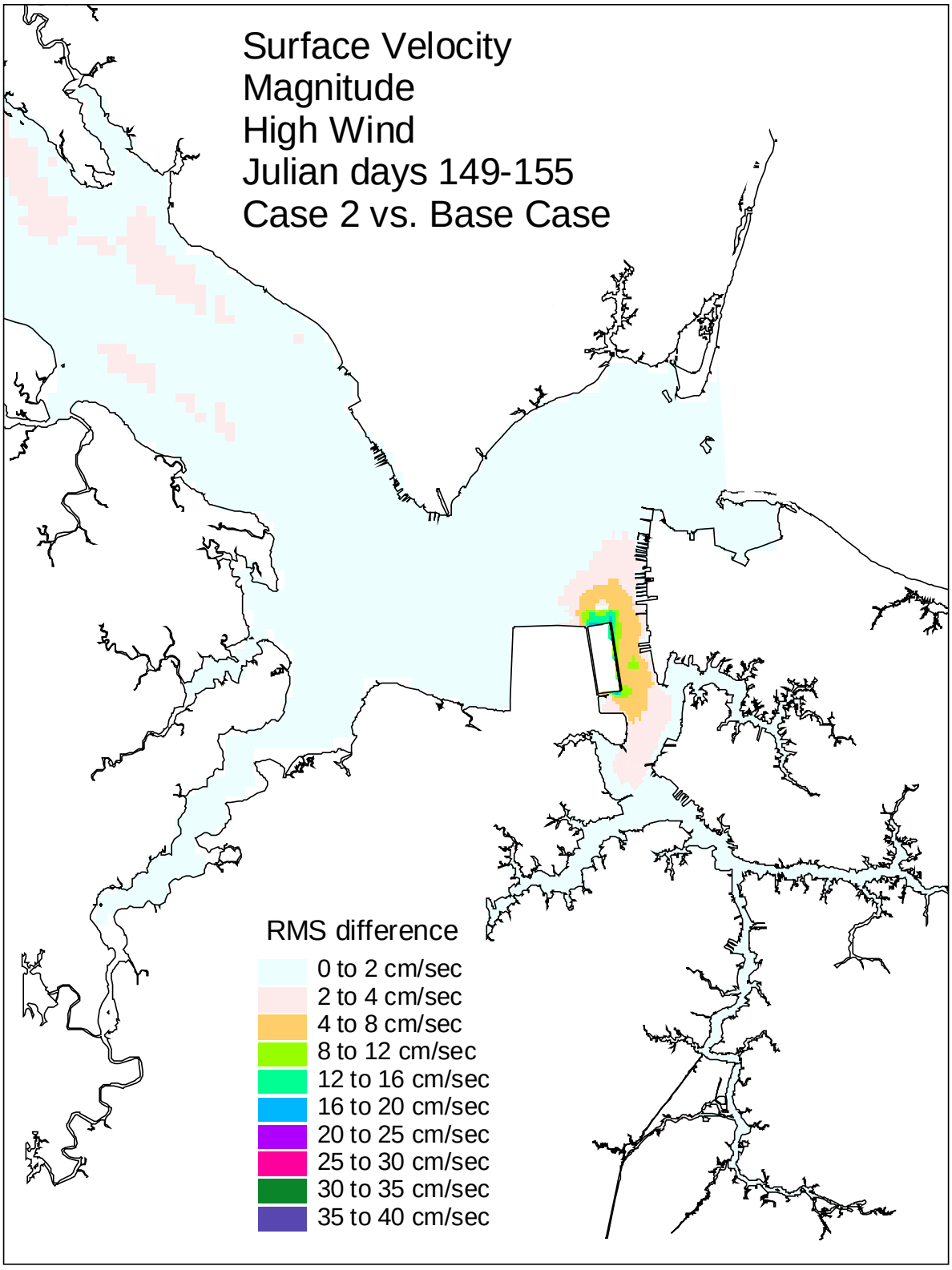

Figure 22. Historical simulation comparison (high wind) of the surface velocity RMS difference for the Eastward Expansion (Option 7, 50-foot channel) versus the Base Case.

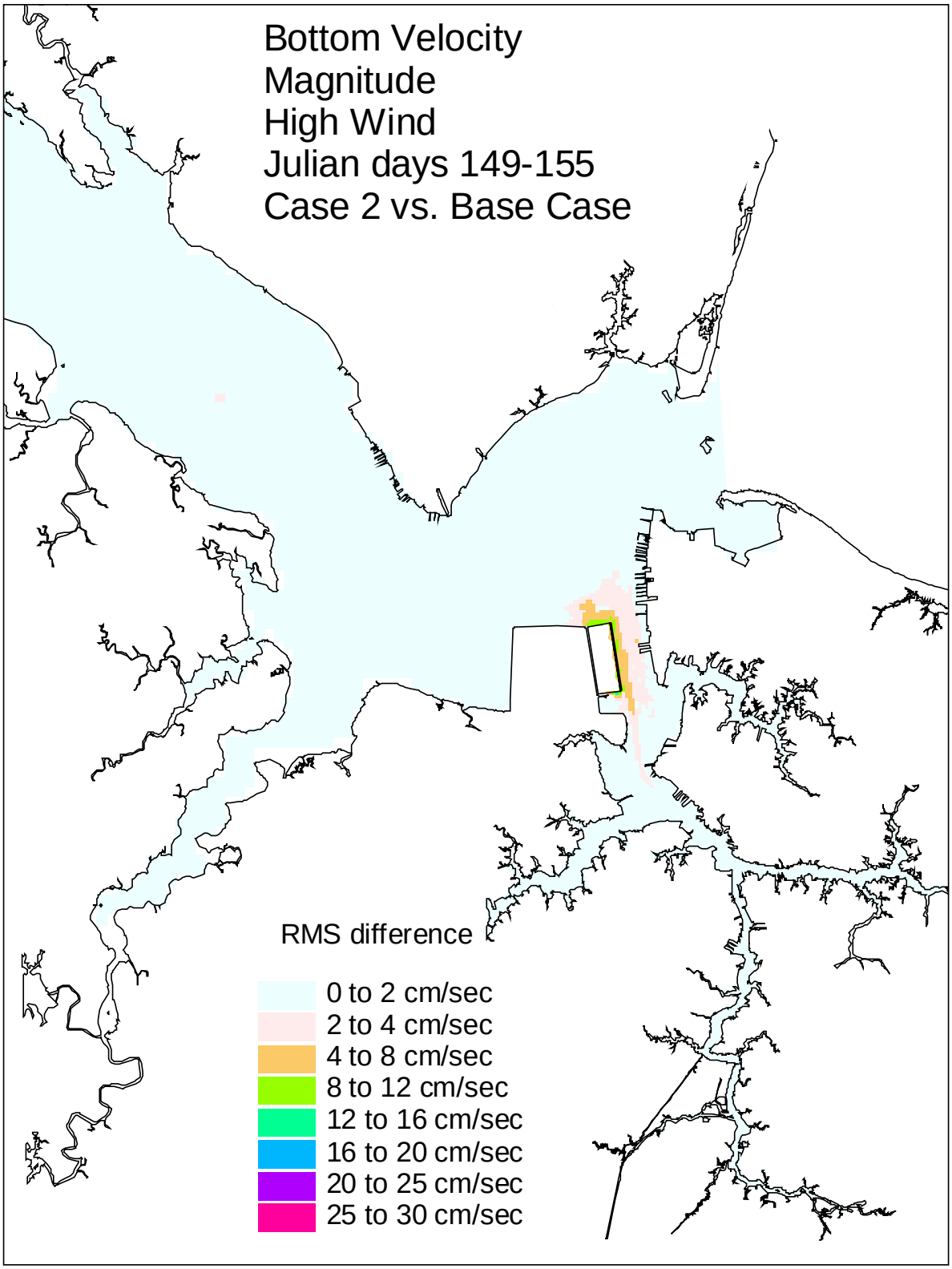

Figure 23. Historical simulation comparison (high wind) of the bottom velocity RMS difference for the Eastward Expansion (Option 7, 50-foot channel) versus the Base Case.

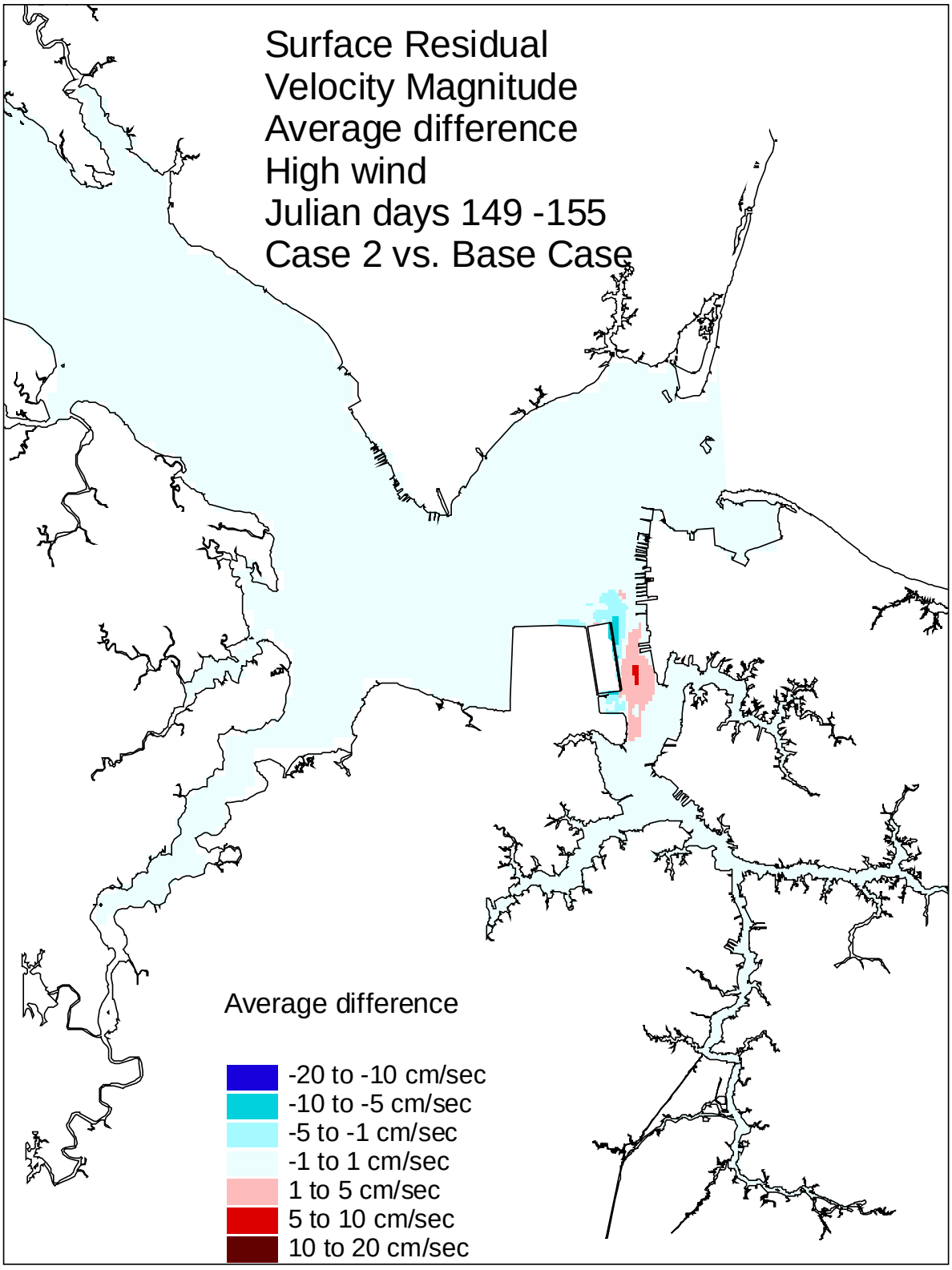

Figure 24. Historical simulation comparison (high wind) of the surface residual velocity average difference for the Eastward Expansion (Option 7, 50-foot channel) versus the Base Case.

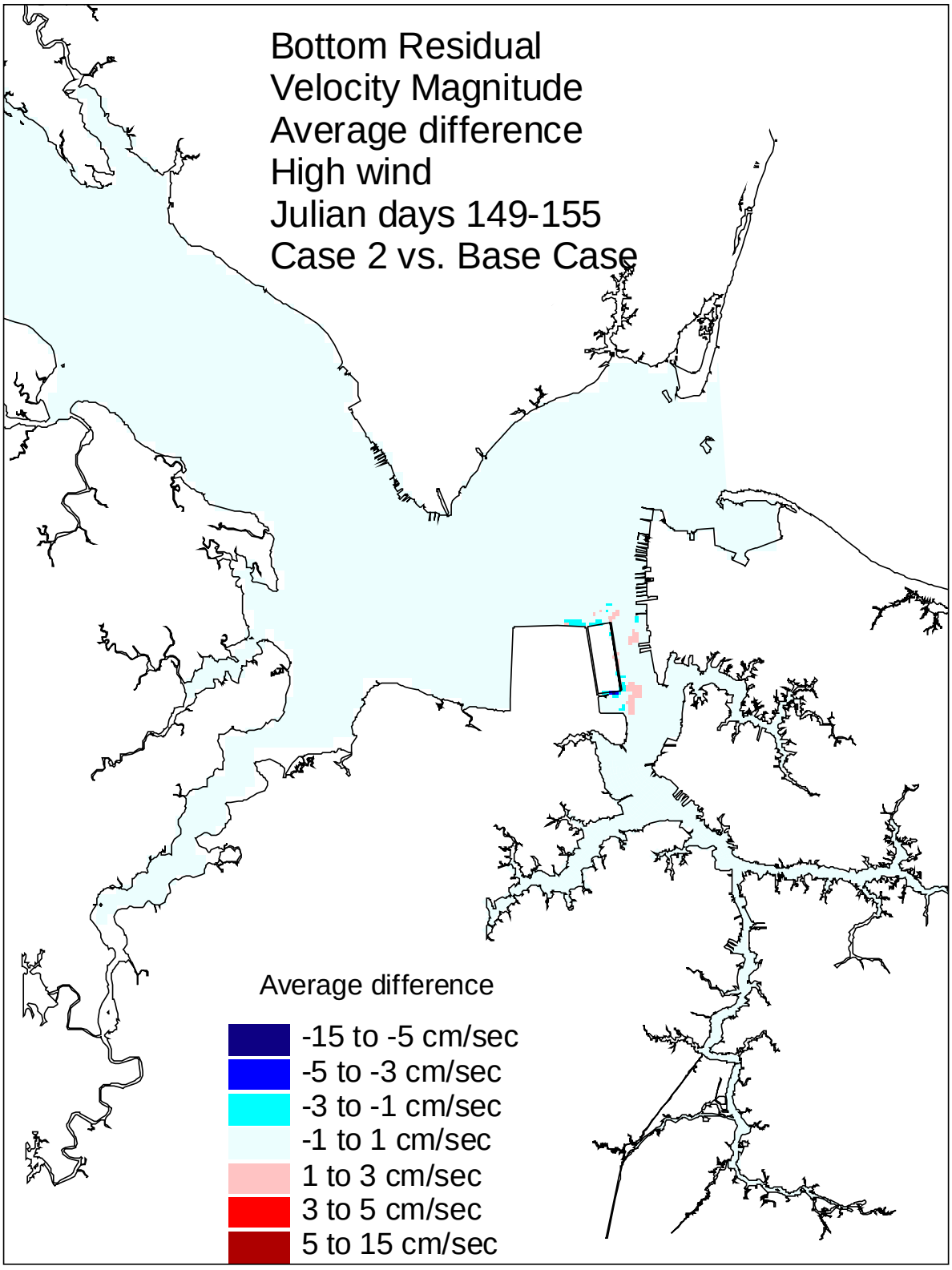

Figure 25. Historical simulation comparison (high wind) of the bottom residual velocity average difference for the Eastward Expansion (Option 7, 50-foot channel) versus the Base Case.

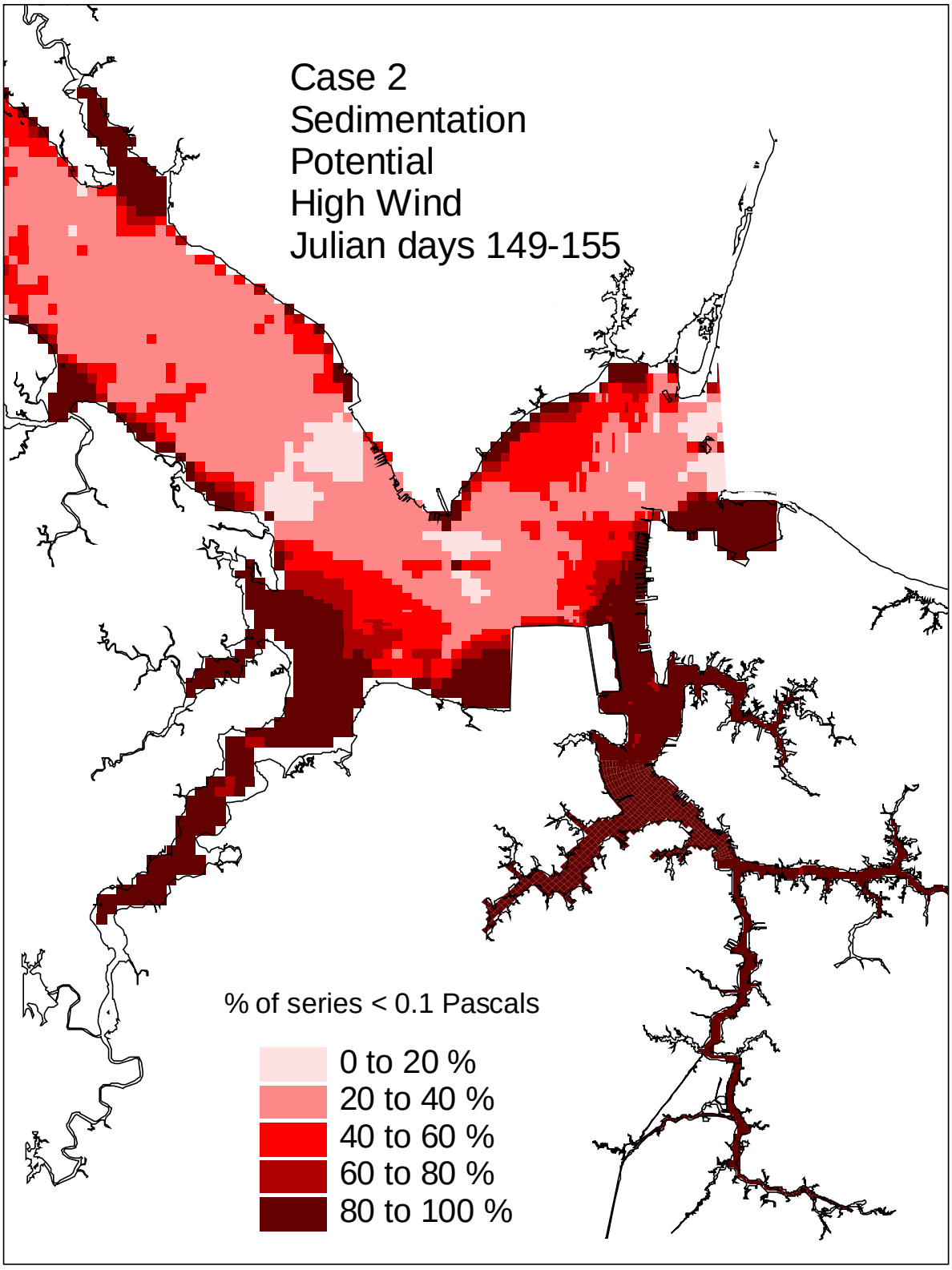

Figure 26. Historical simulation comparison (high wind) of the sedimentation potential for the Eastward Expansion (Option 7, 50-foot channel).

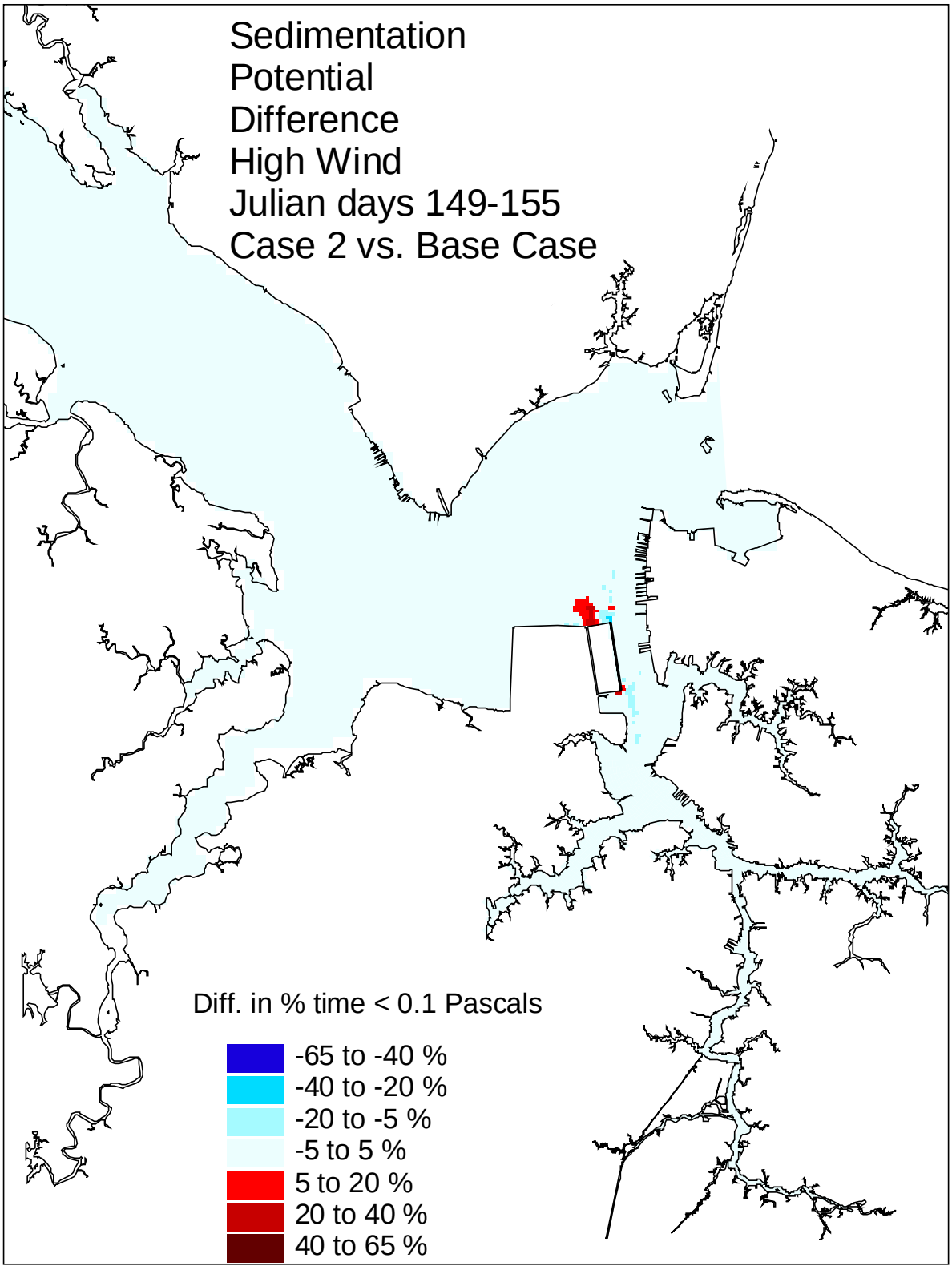

Figure 27. Historical simulation comparison (high wind) of the sedimentation potential difference for the Eastward Expansion (Option 7, 50-foot channel) versus the Base Case.

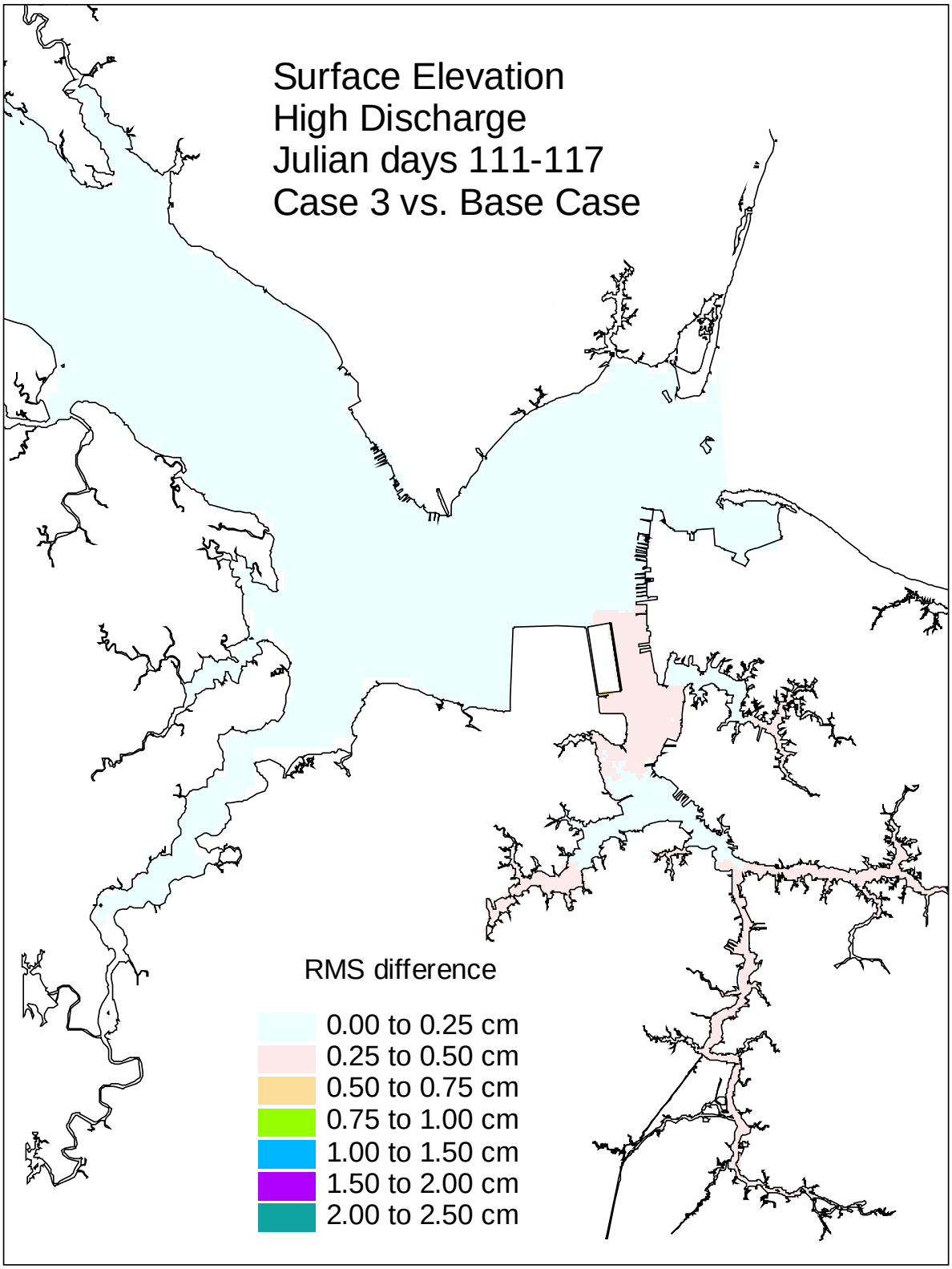

Figure 28. Historical simulation comparison (high discharge) of the surface elevation RMS difference for the Eastward Expansion (Option 7, 55-foot channel) versus the Base Case.

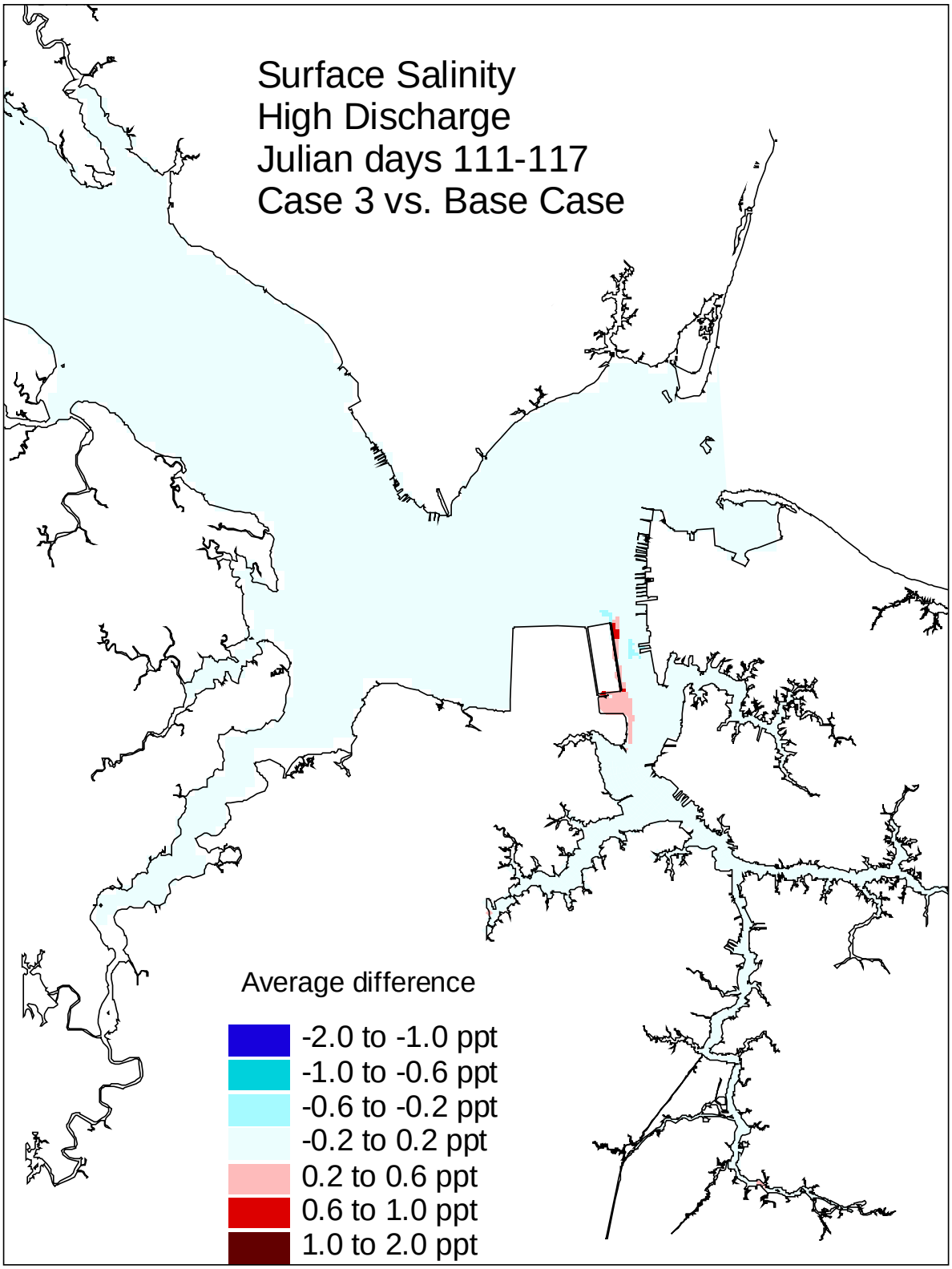

Figure 29. Historical simulation comparison (high discharge) of the surface salinity average difference for the Eastward Expansion (Option 7, 55-foot channel) versus the Base Case.

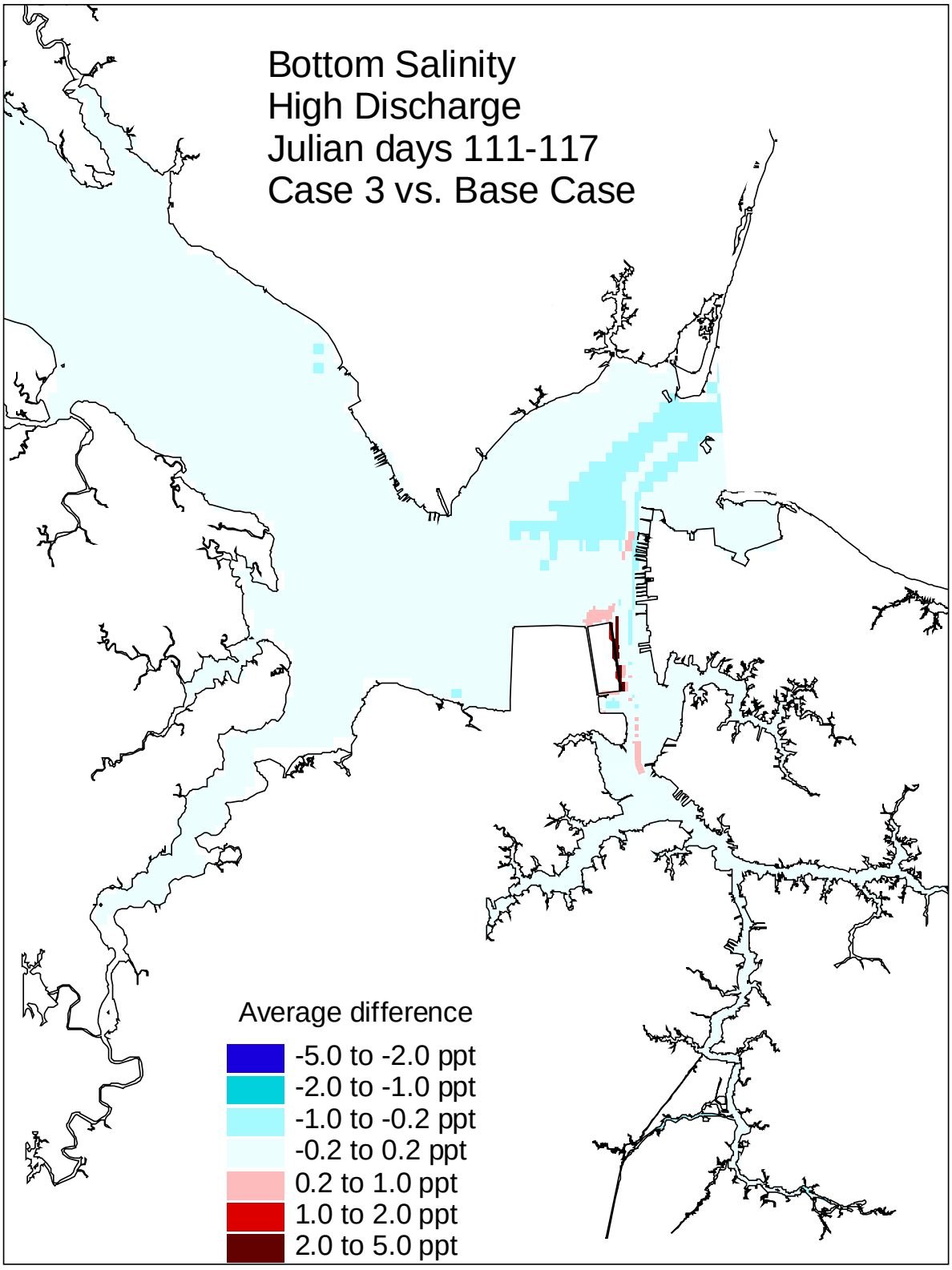

Figure 30. Historical simulation comparison (high discharge) of the bottom salinity average difference for the Eastward Expansion (Option 7, 55-foot channel) versus the Base Case.

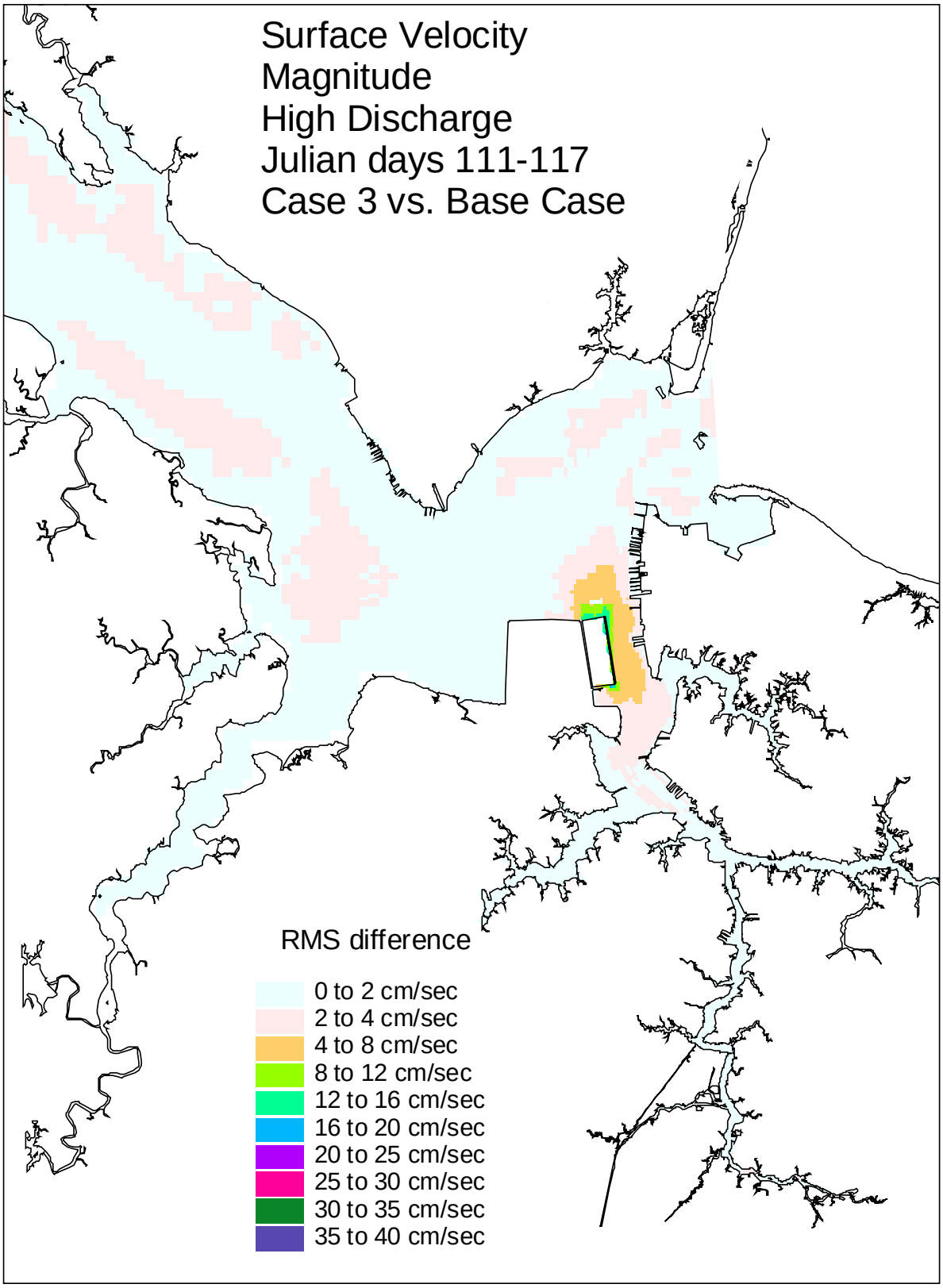

Figure 31. Historical simulation comparison (high discharge) of the surface velocity RMS difference for the Eastward Expansion (Option 7, 55-foot channel) versus the Base Case.

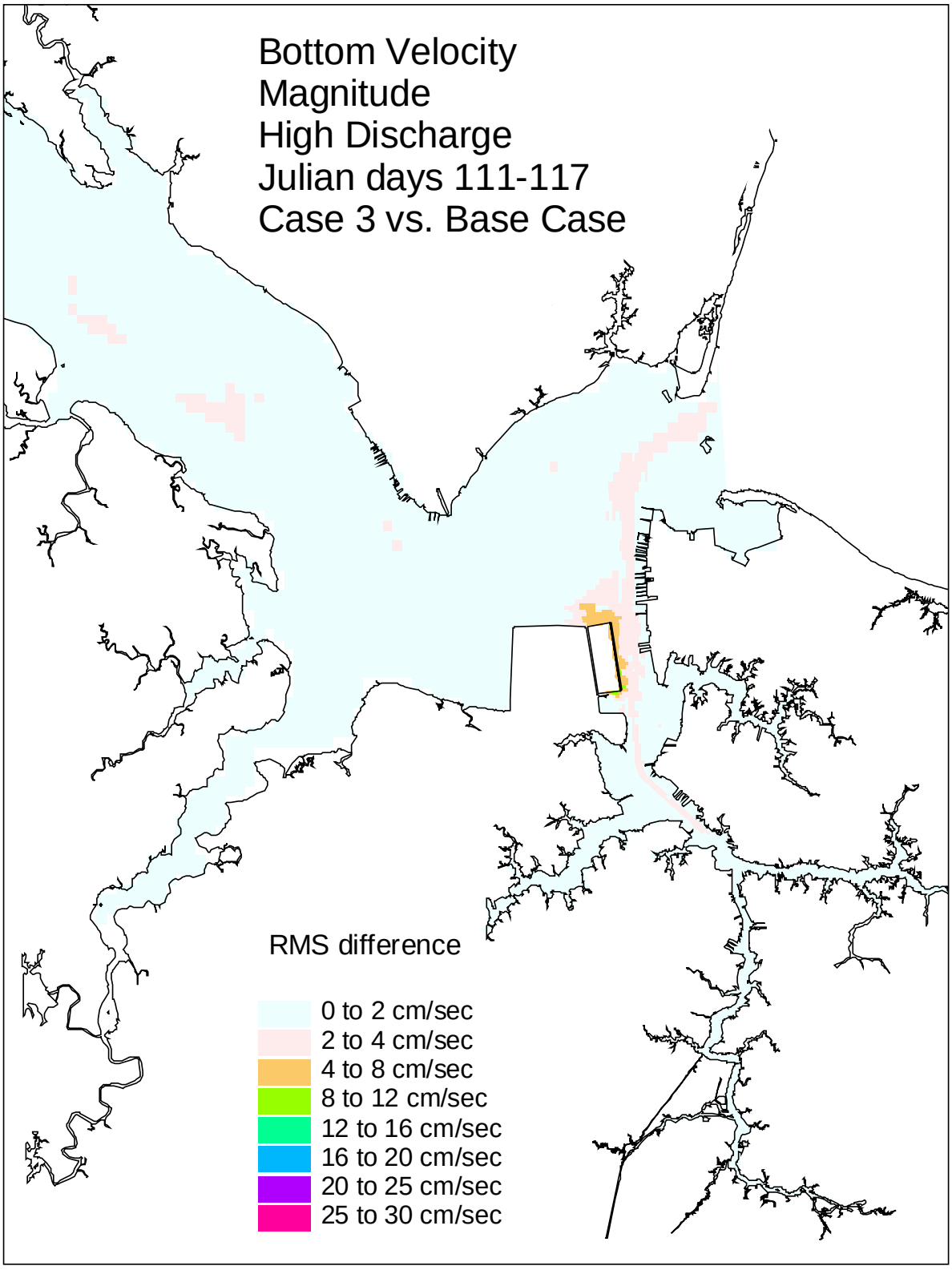

Figure 32. Historical simulation comparison (high discharge) of the bottom velocity RMS difference for the Eastward Expansion (Option 7, 55-foot channel) versus the Base Case.

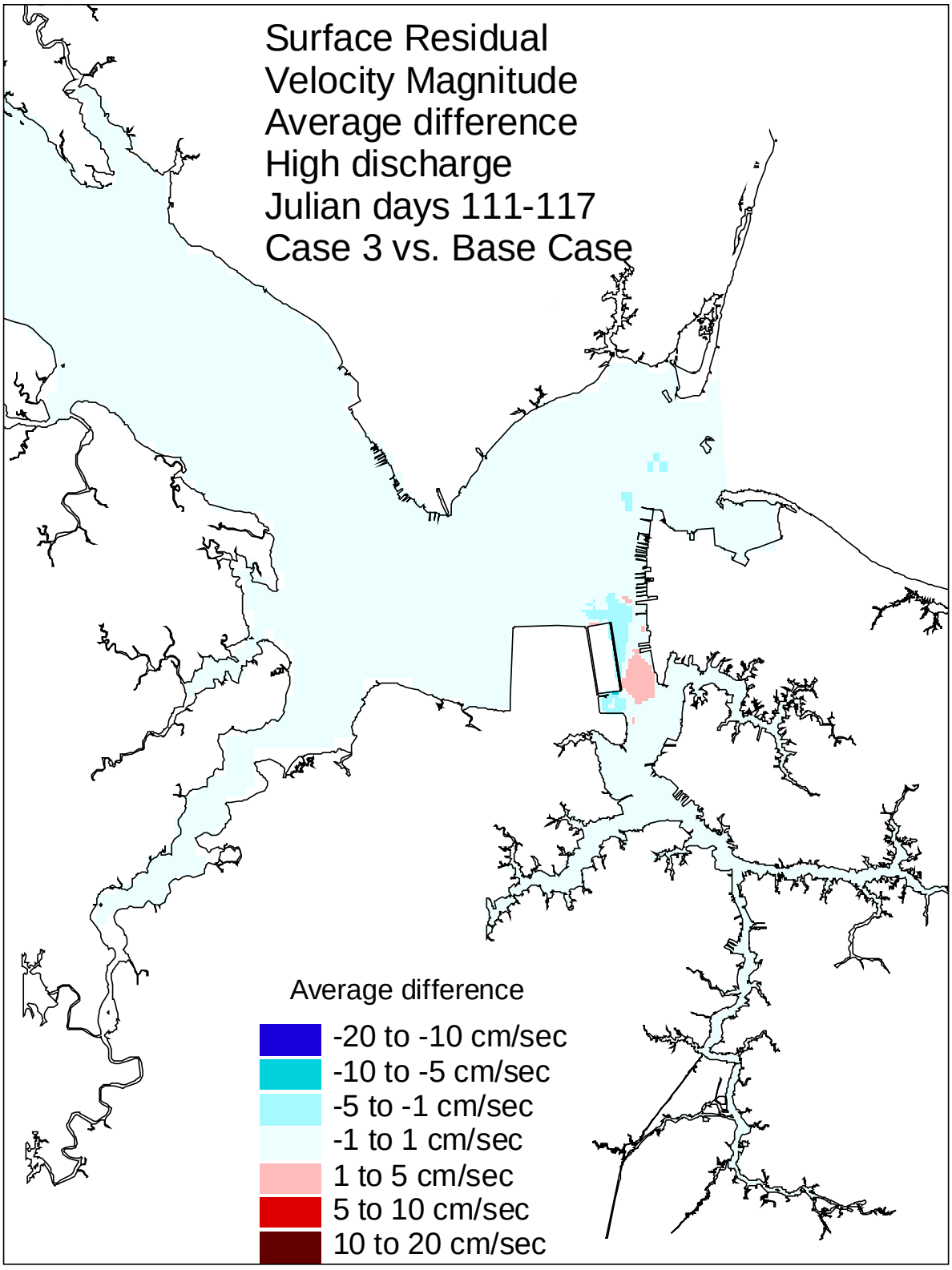

Figure 33. Historical simulation comparison (high discharge) of the surface residual velocity average difference for the Eastward Expansion (Option 7, 55-foot channel) versus the Base Case.

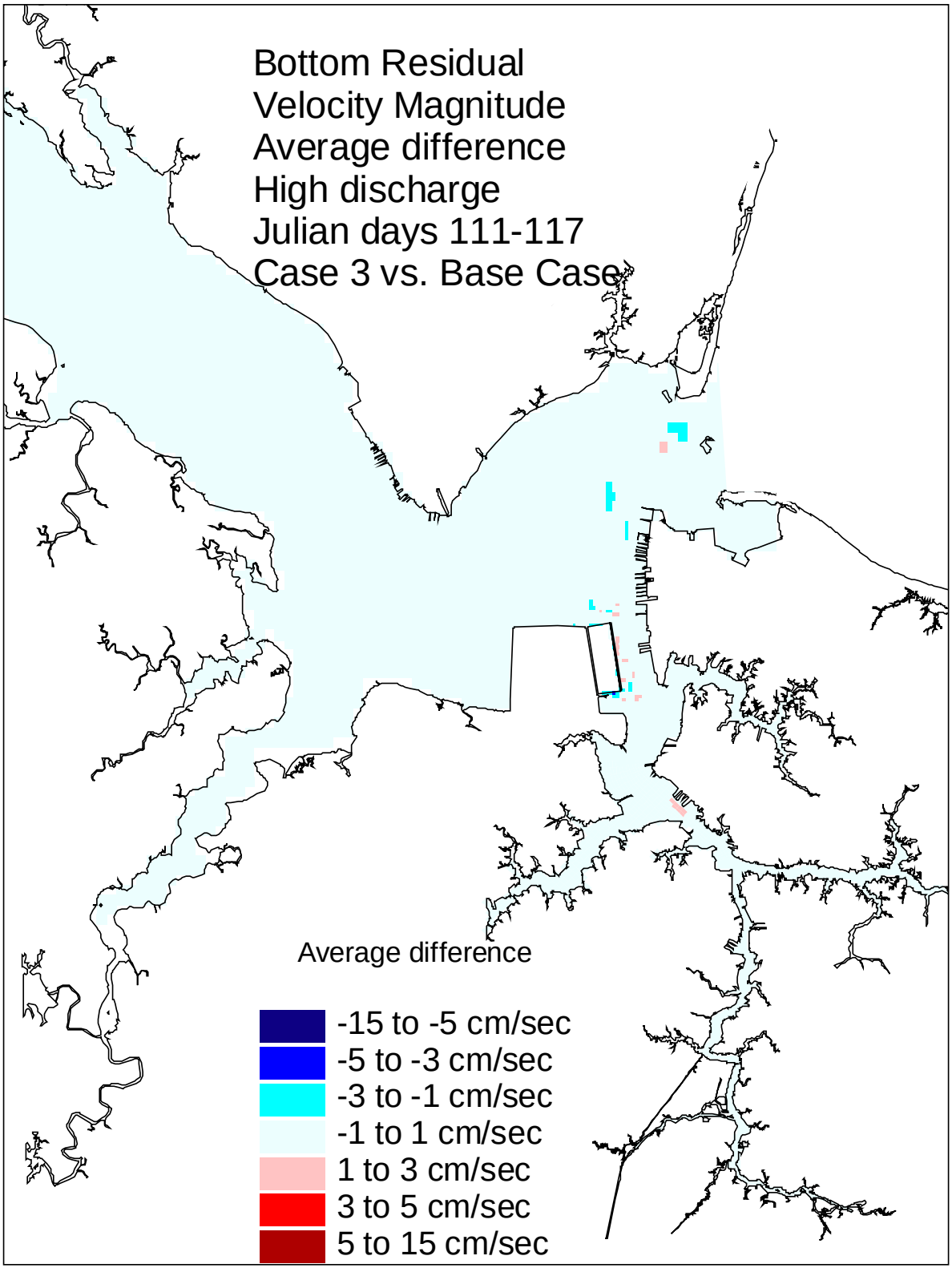

Figure 34. Historical simulation comparison (high discharge) of the bottom residual velocity average difference for the Eastward Expansion (Option 7, 55-foot channel) versus the Base Case.

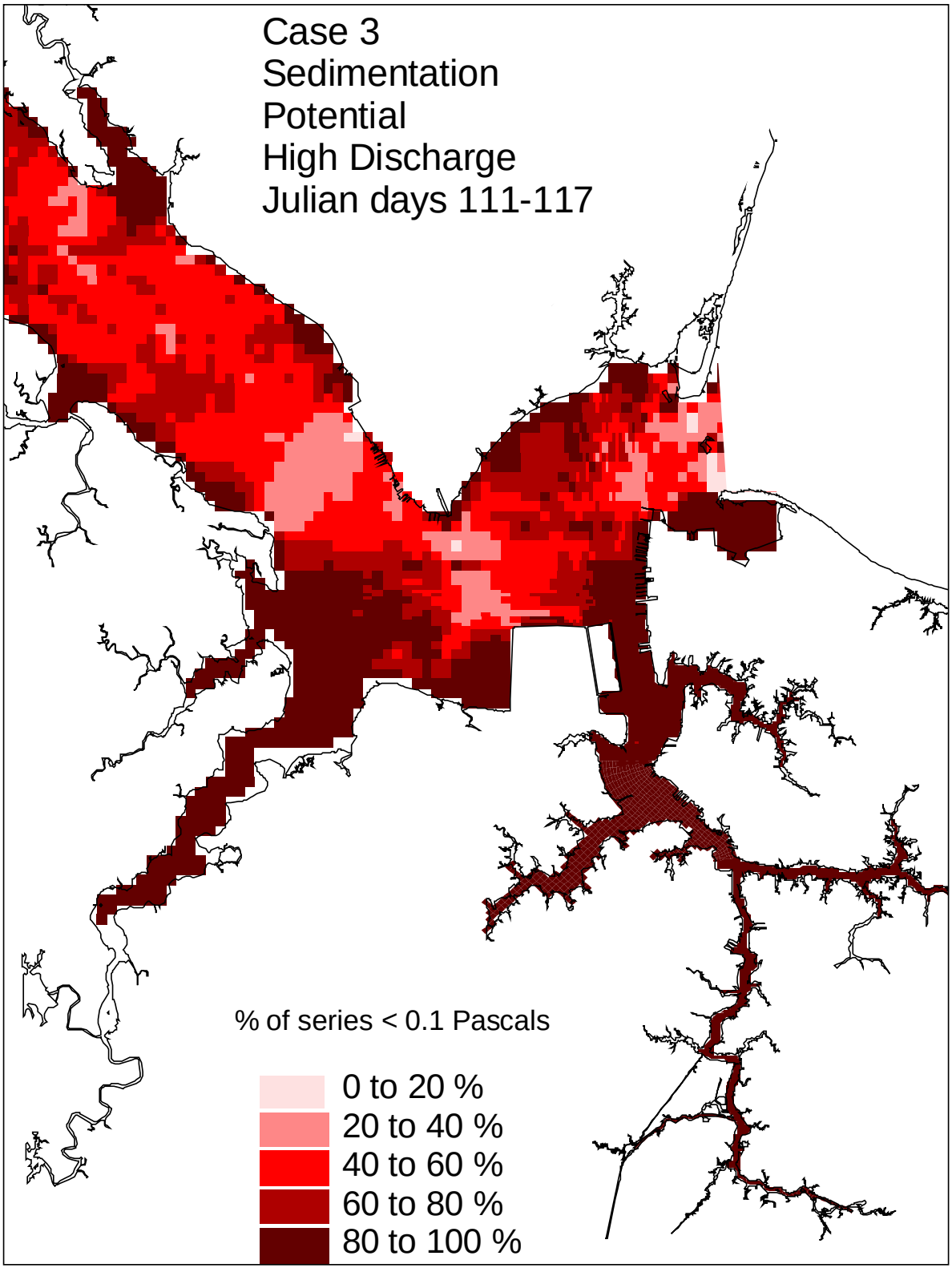

Figure 35. Historical simulation comparison (high discharge) of the sedimentation potential for the Eastward Expansion (Option 7, 55-foot channel).

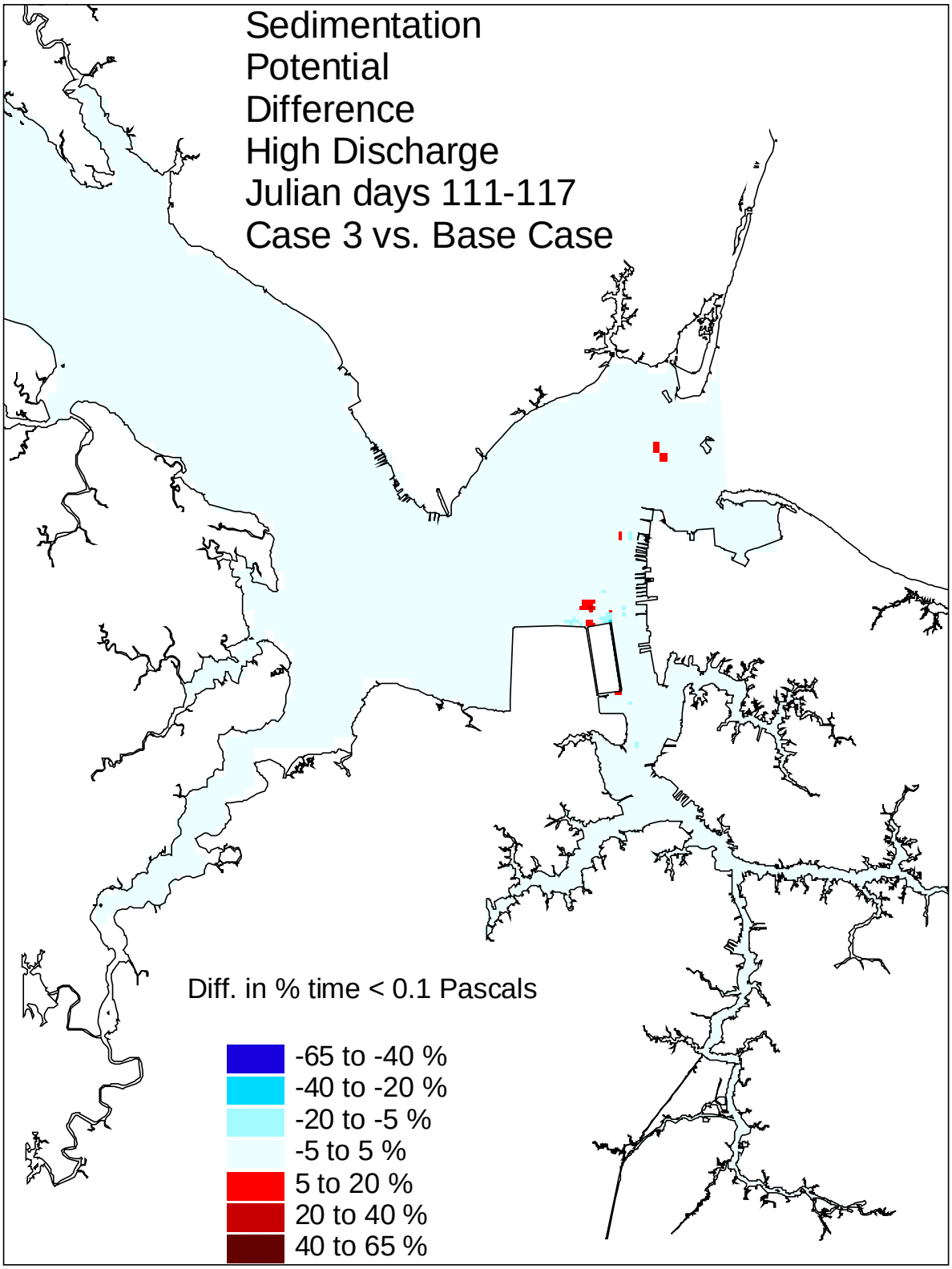

Figure 36. Historical simulation comparison (high discharge) of the sedimentation potential difference for the Eastward Expansion (Option 7, 55-foot channel) versus the Base Case.

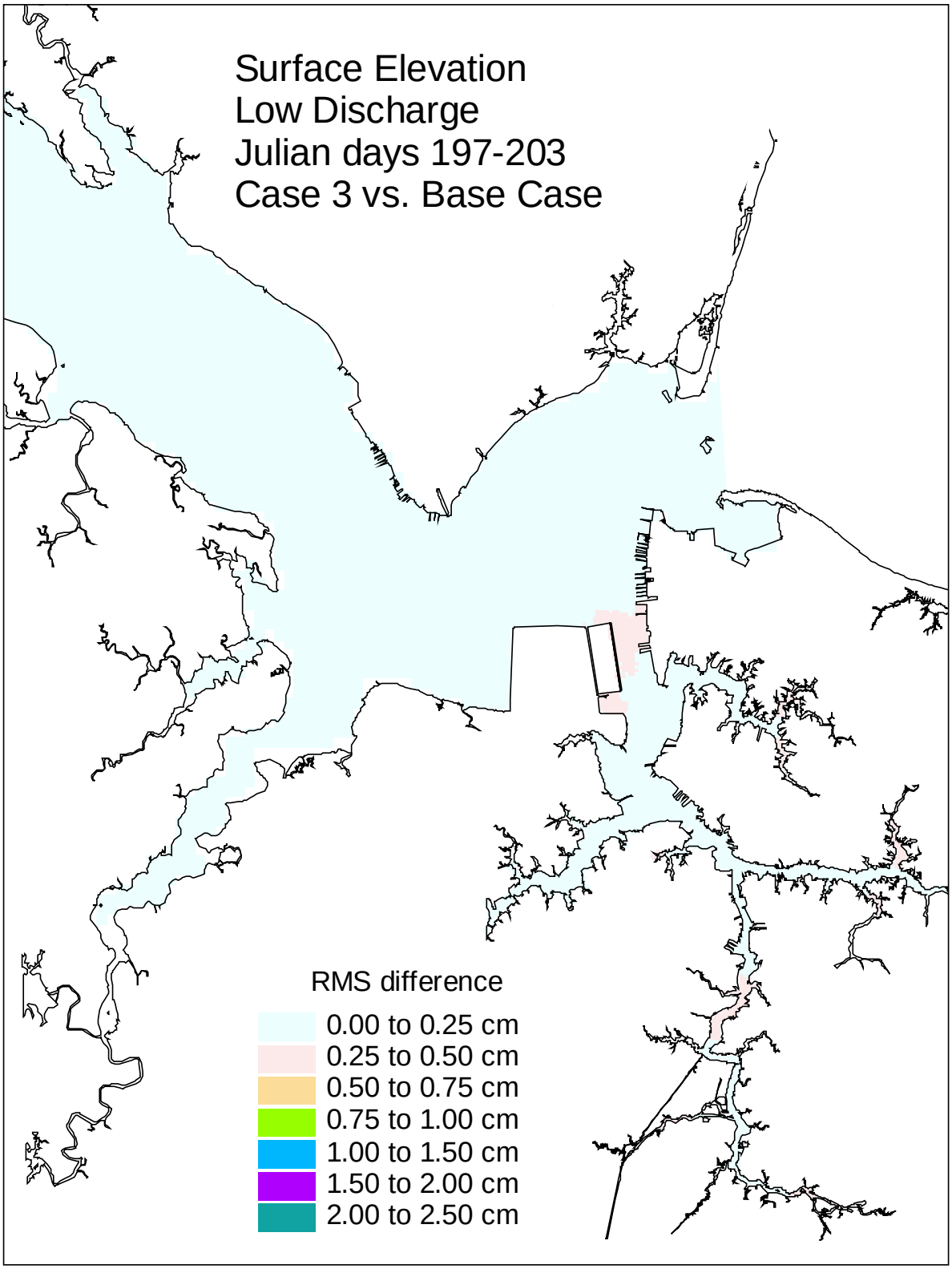

Figure 37. Historical simulation comparison (low discharge) of the surface elevation RMS difference for the Eastward Expansion (Option 7, 55-foot channel) versus the Base Case.

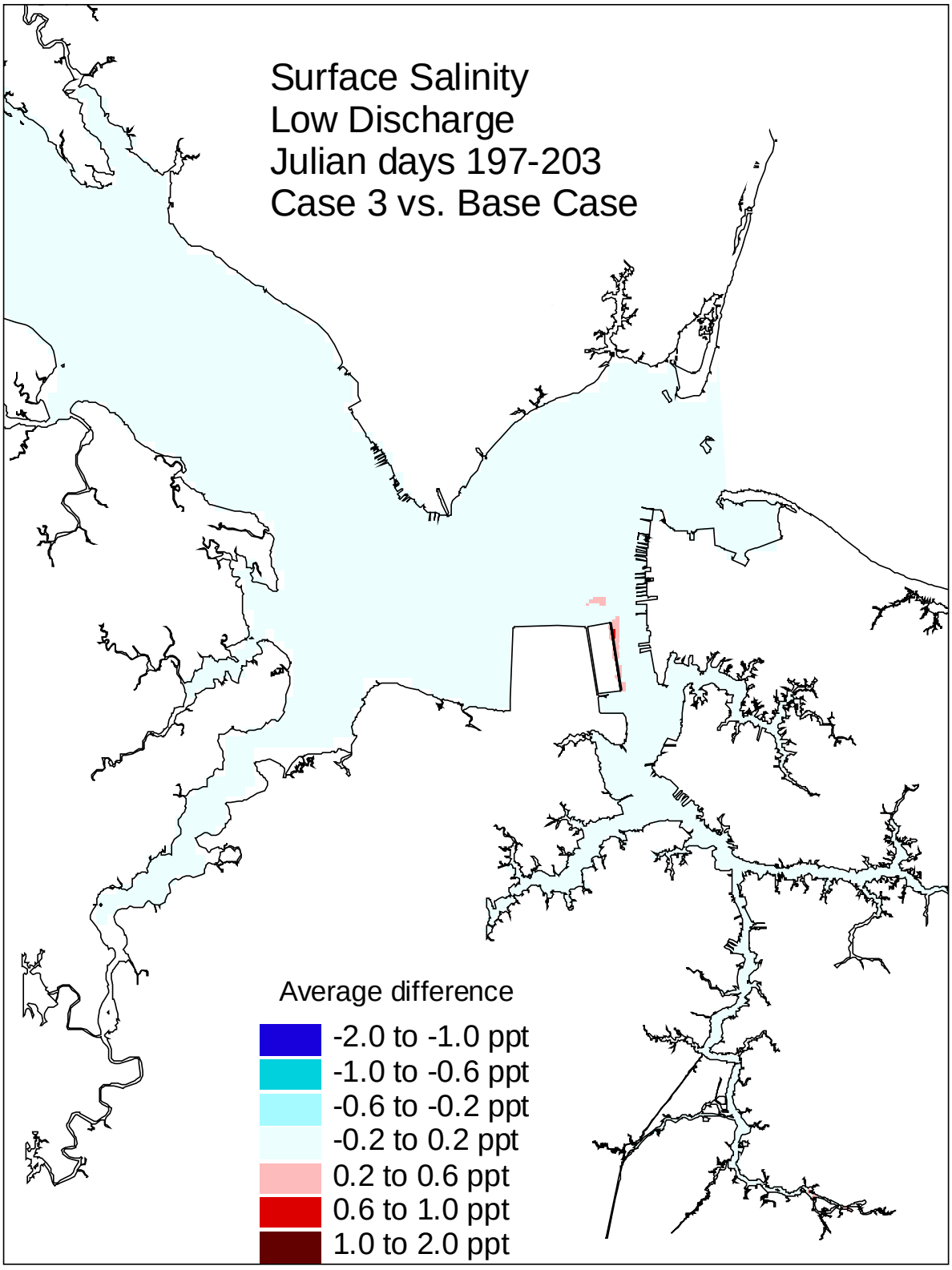

Figure 38. Historical simulation comparison (low discharge) of the surface salinity average difference for the Eastward Expansion (Option 7, 55-foot channel) versus the Base Case.

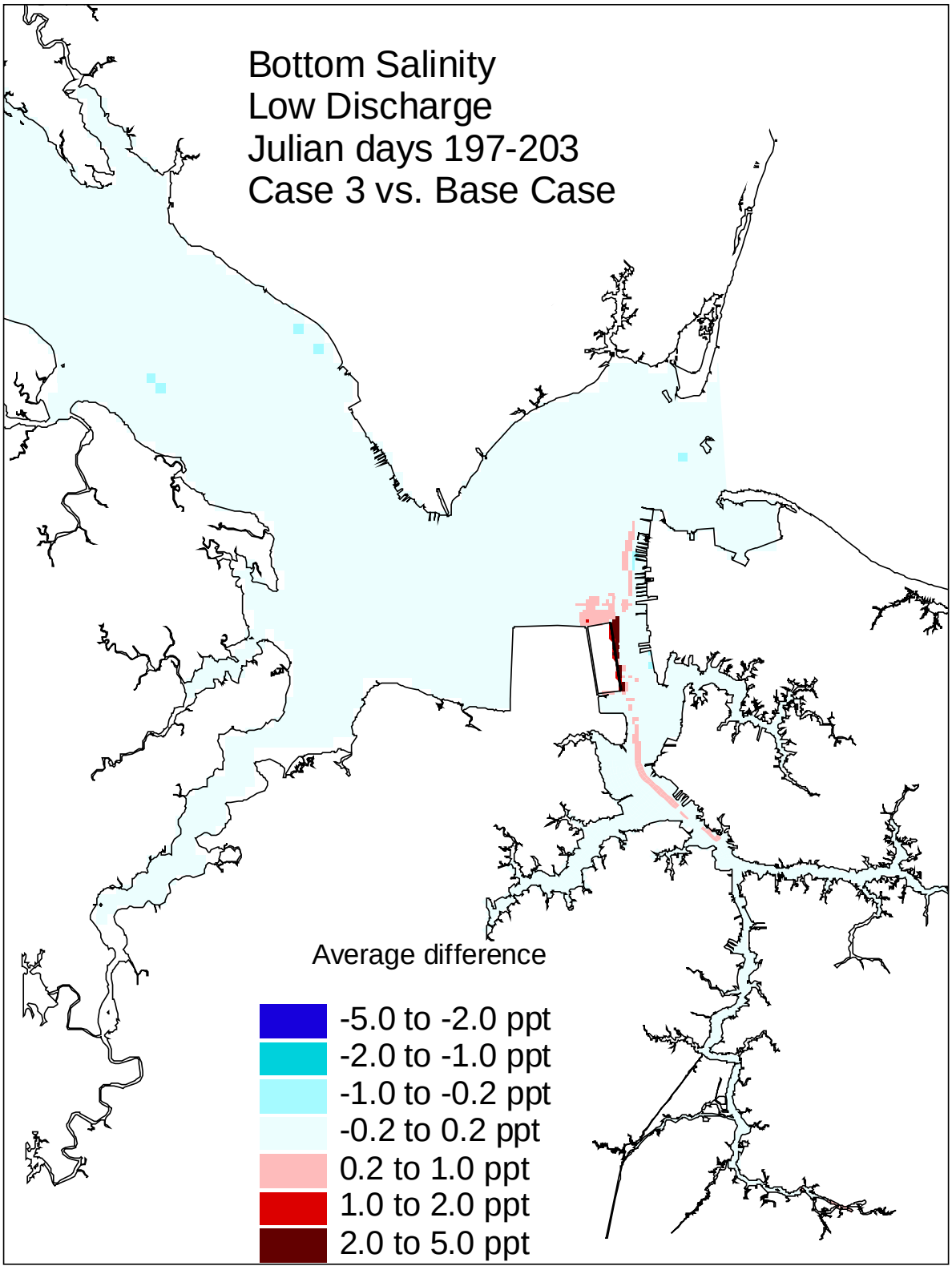

Figure 39. Historical simulation comparison (low discharge) of the bottom salinity average difference for the Eastward Expansion (Option 7, 55-foot channel) versus the Base Case.

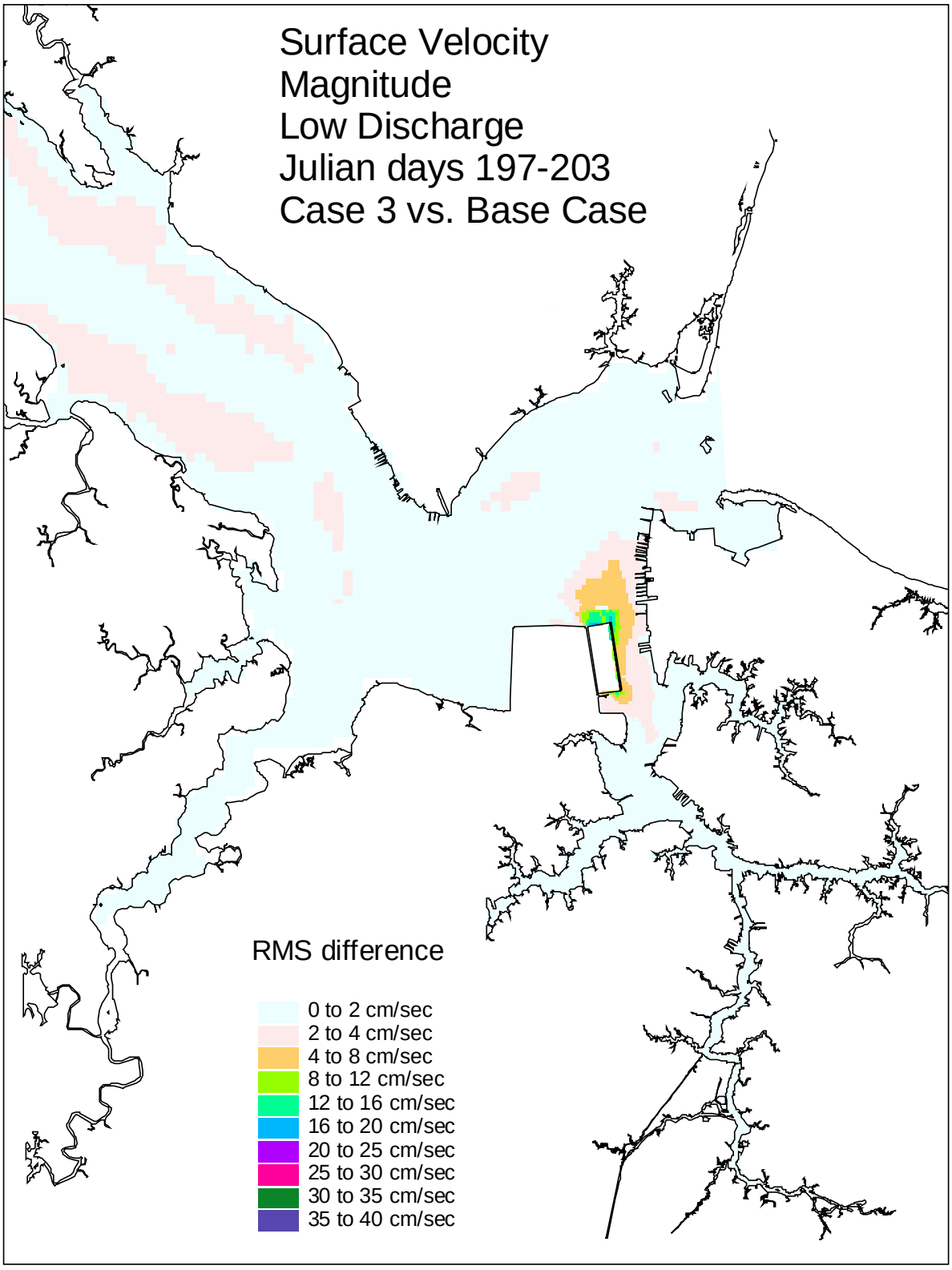

Figure 40. Historical simulation comparison (low discharge) of the surface velocity RMS difference for the Eastward Expansion (Option 7, 55-foot channel) versus the Base Case.

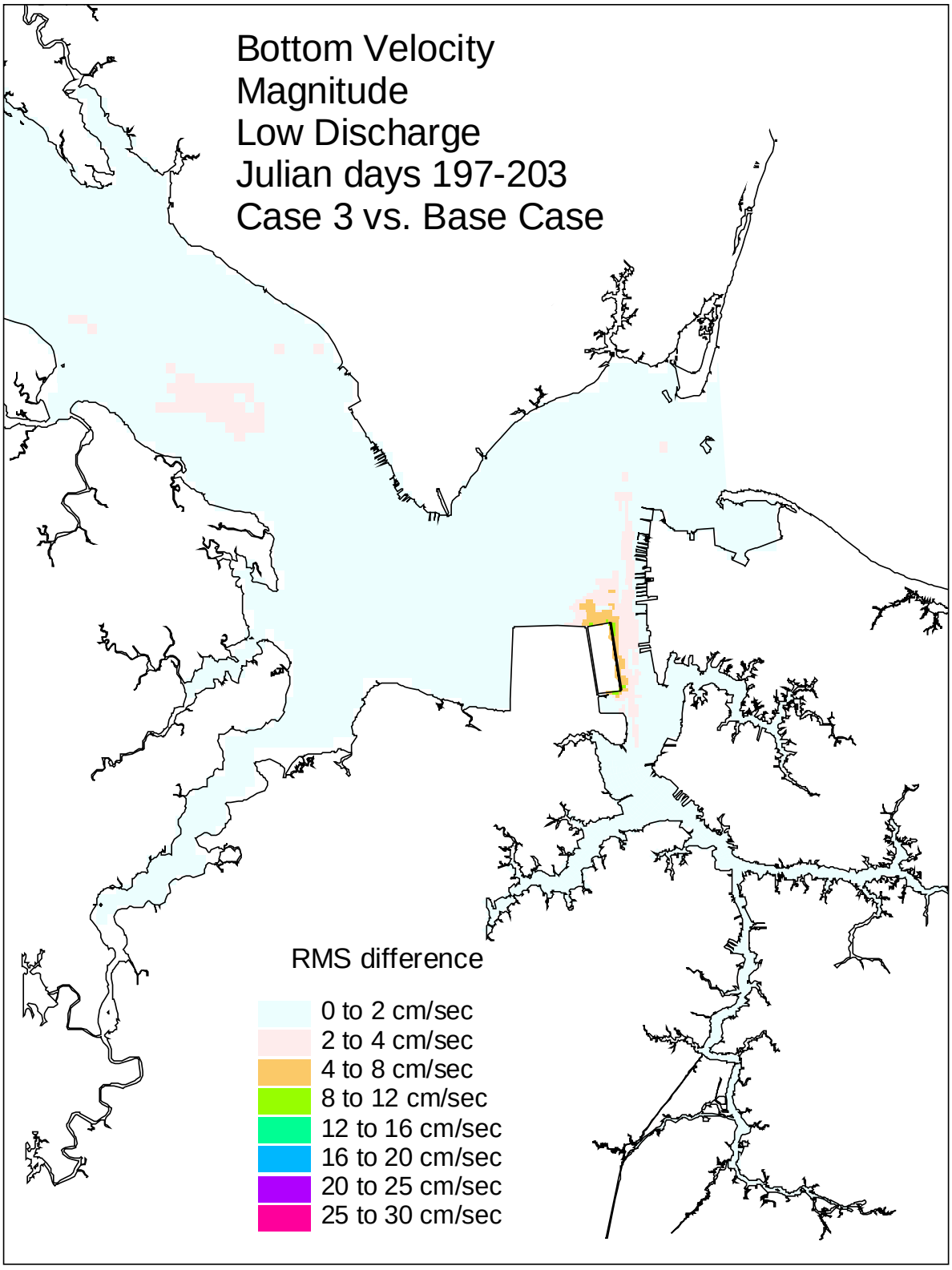

Figure 41. Historical simulation comparison (low discharge) of the bottom velocity RMS difference for the Eastward Expansion (Option 7, 55-foot channel) versus the Base Case.

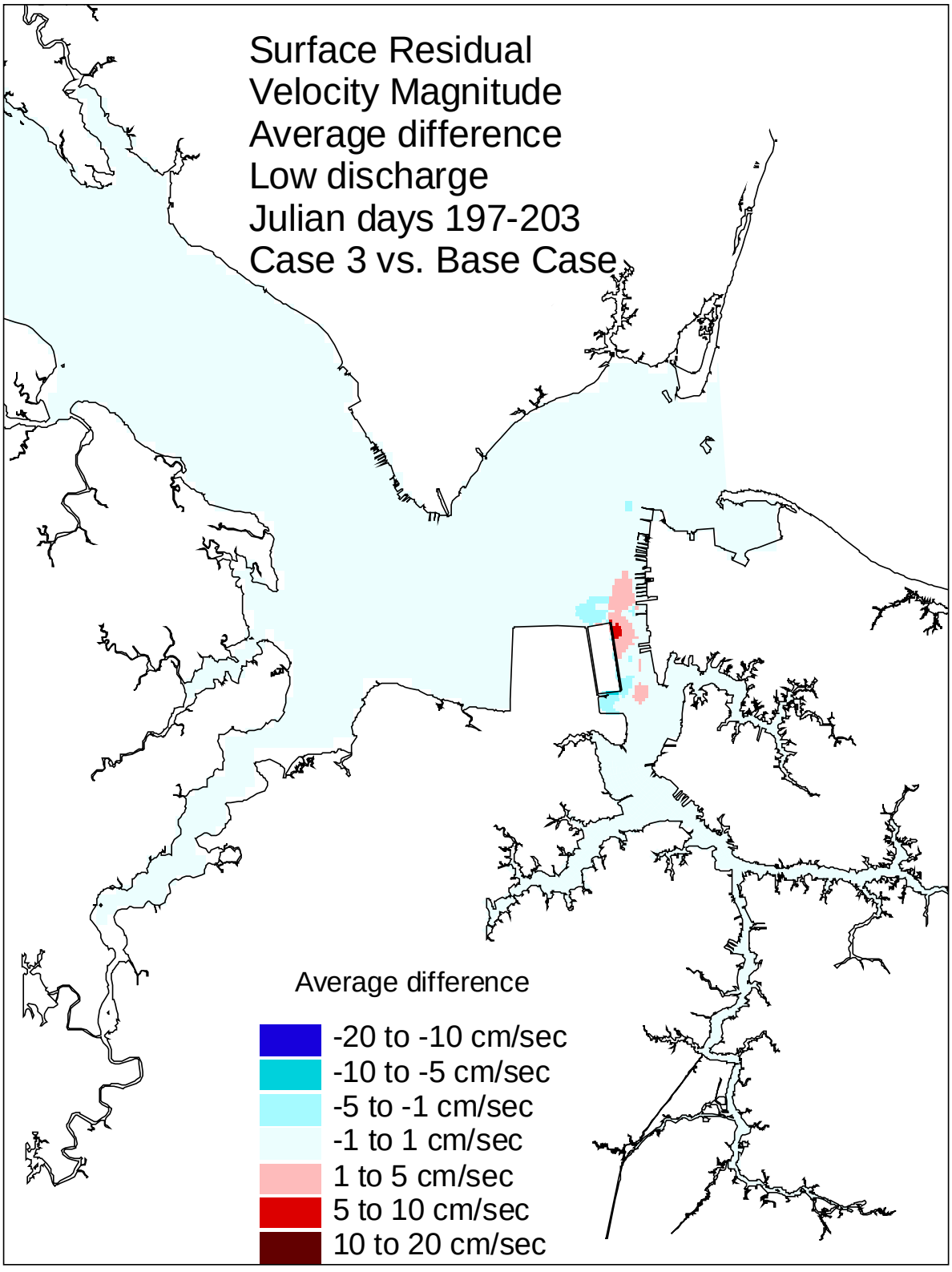

Figure 42. Historical simulation comparison (low discharge) of the surface residual velocity average difference for the Eastward Expansion (Option 7, 55-foot channel) versus the Base Case.

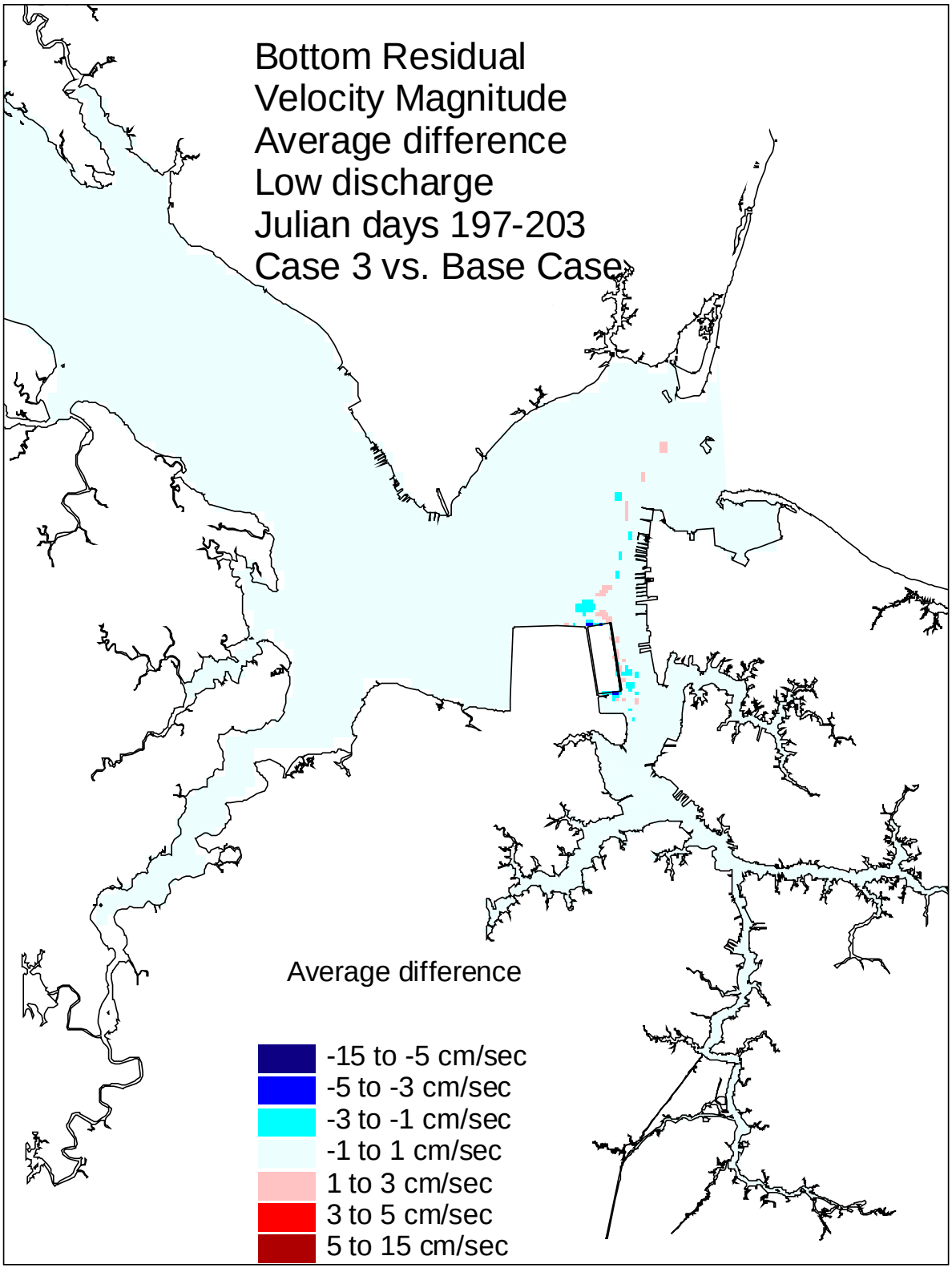

Figure 43. Historical simulation comparison (low discharge) of the bottom residual velocity average difference for the Eastward Expansion (Option 7, 55-foot channel) versus the Base Case.

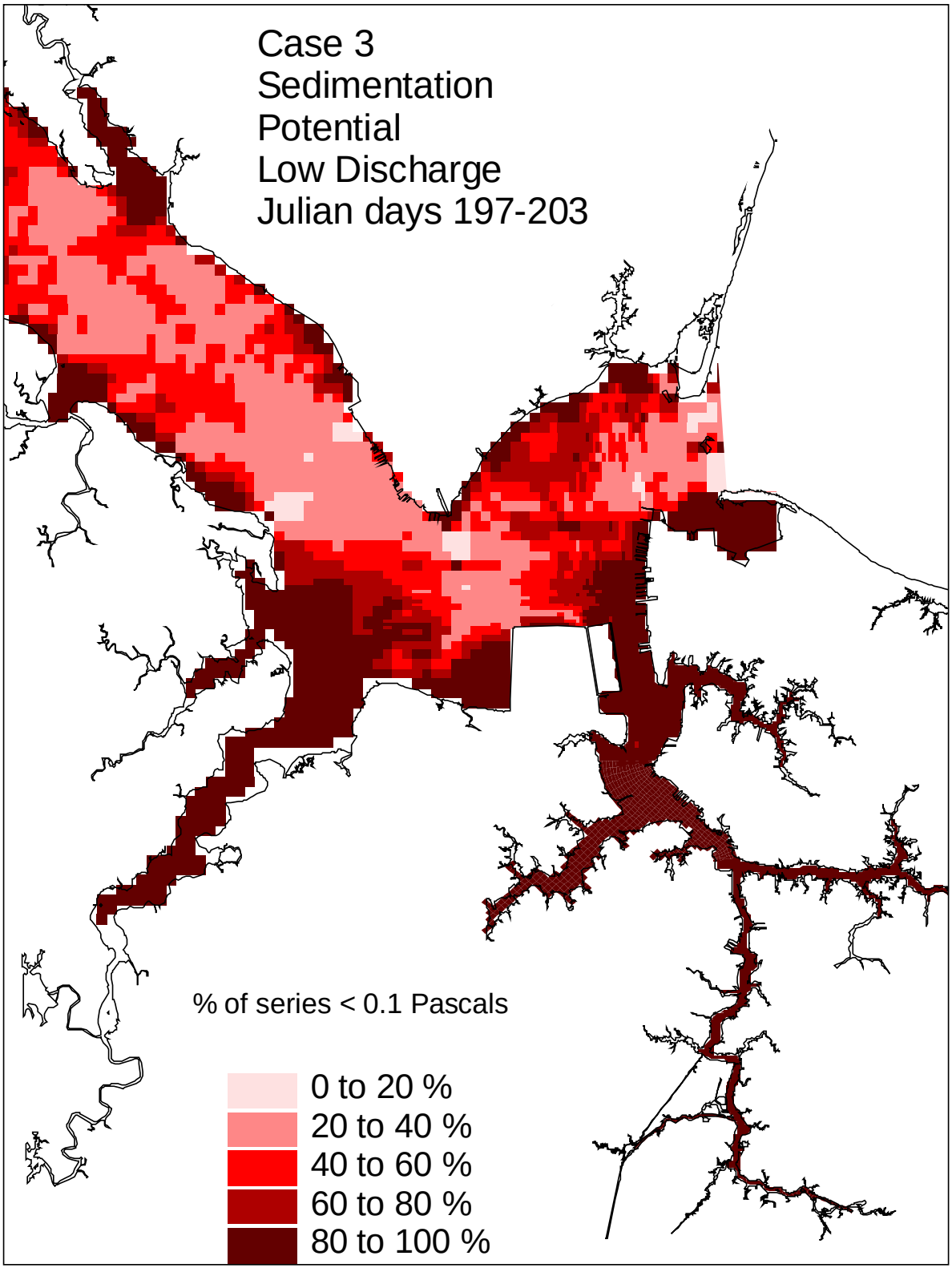

Figure 44. Historical simulation comparison (low discharge) of the sedimentation potential for the Eastward Expansion (Option 7, 55-foot channel).

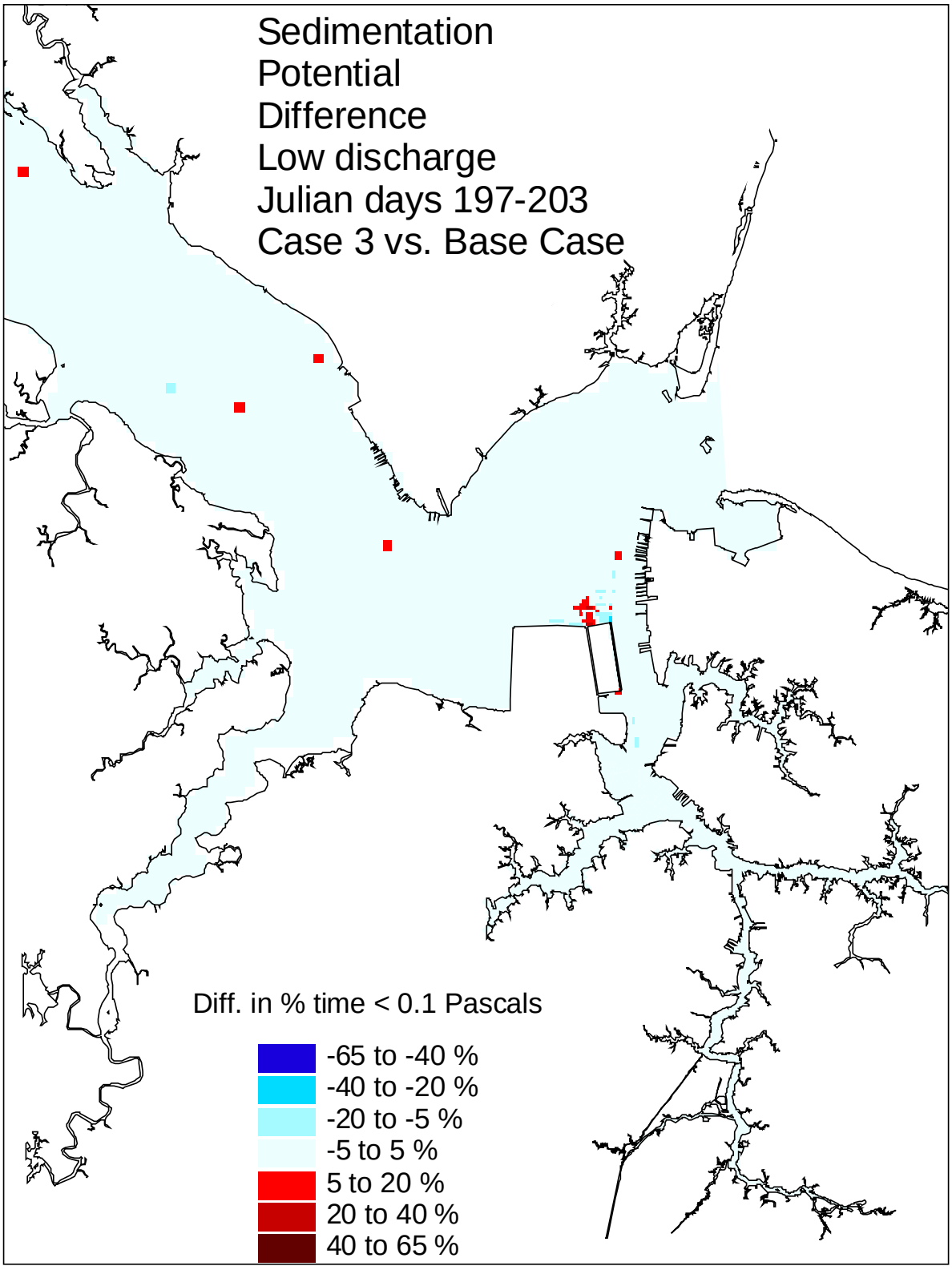

Figure 45. Historical simulation comparison (low discharge) of the sedimentation potential difference for the Eastward Expansion (Option 7, 55-foot channel) versus the Base Case.

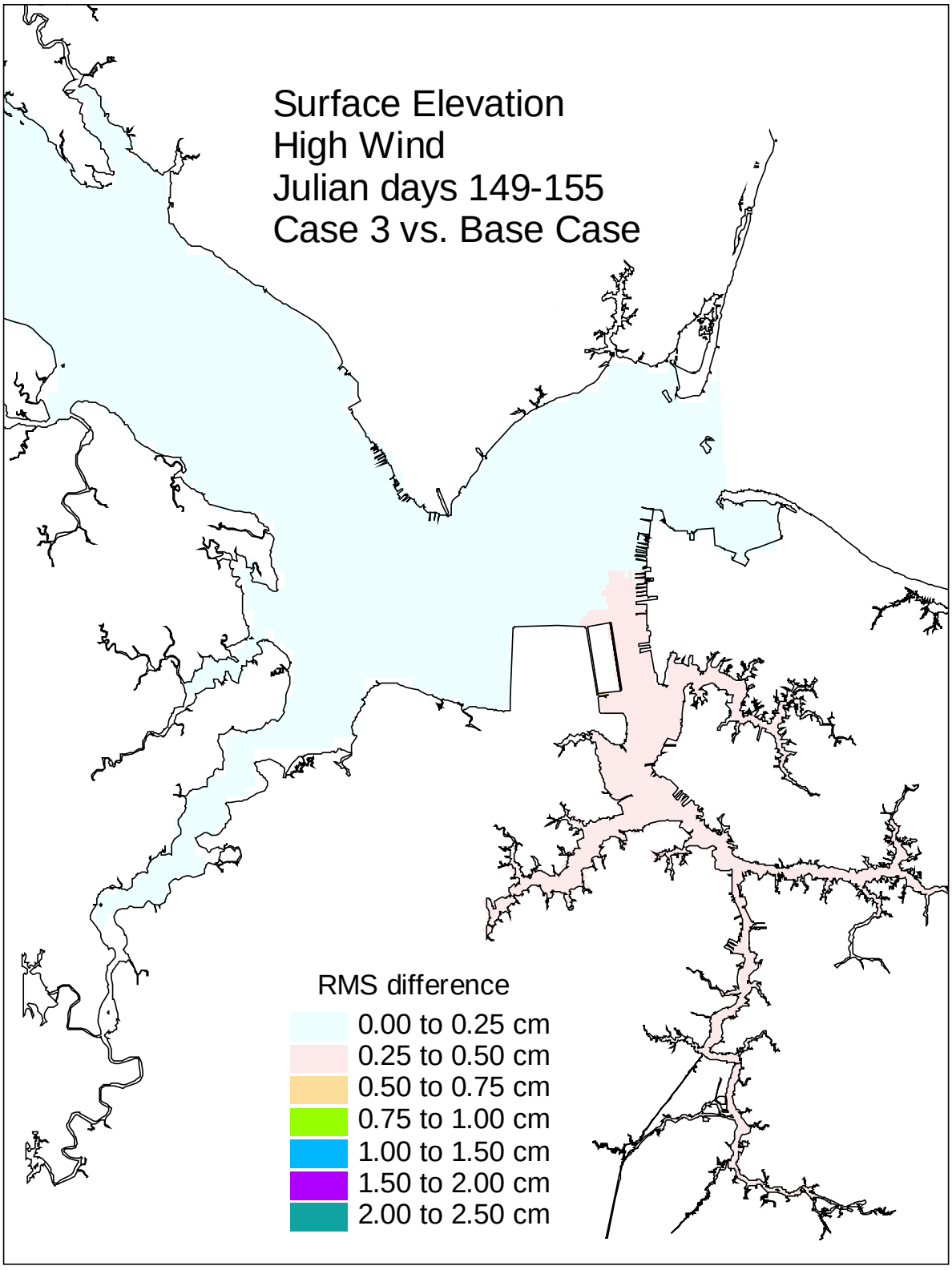

Figure 46. Historical simulation comparison (high wind) of the surface elevation RMS difference for the Eastward Expansion (Option 7, 55-foot channel) versus the Base Case.

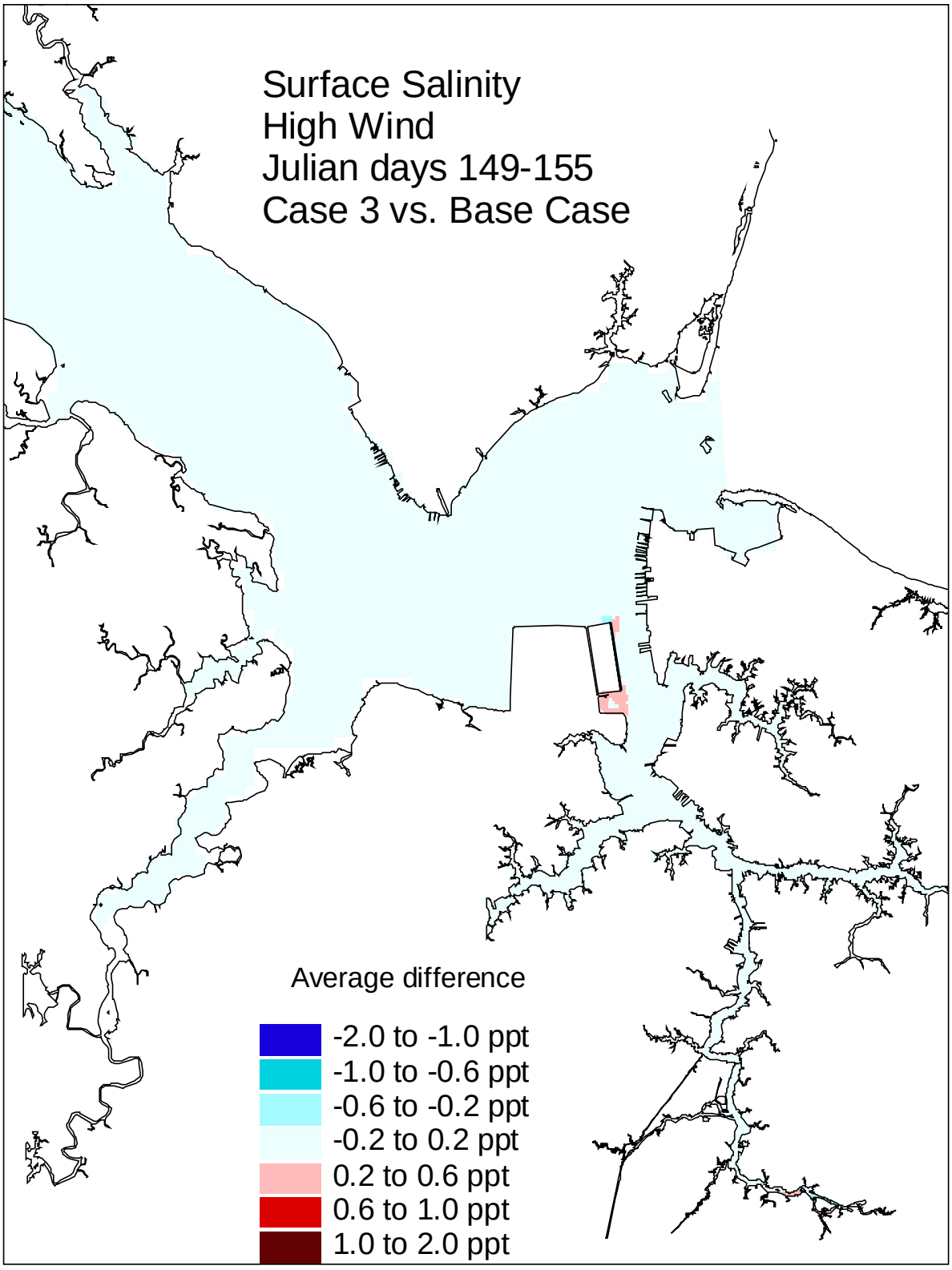

Figure 47. Historical simulation comparison (high wind) of the surface salinity average difference for the Eastward Expansion (Option 7, 55-foot channel) versus the Base Case.

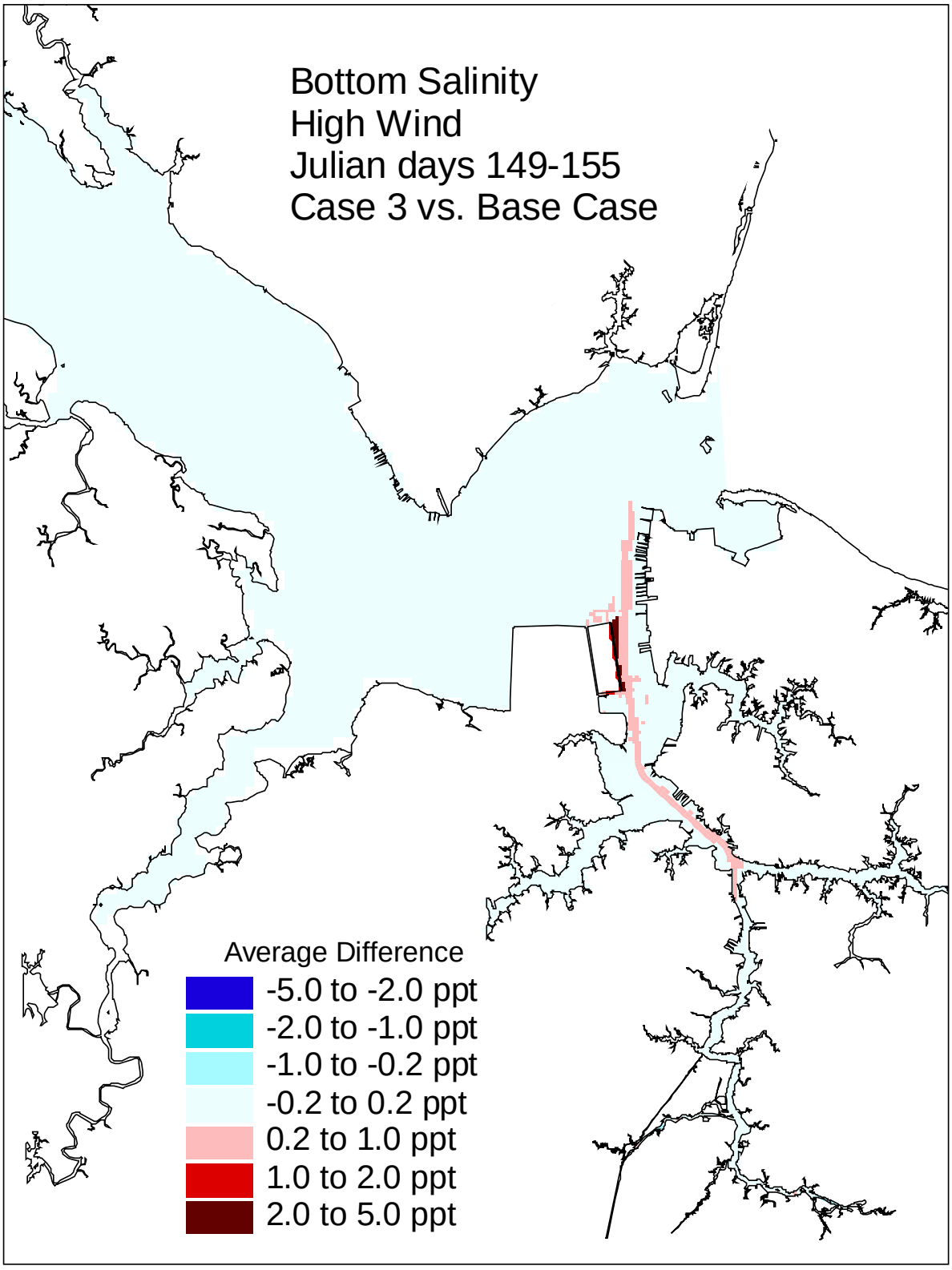

Figure 48. Historical simulation comparison (high wind) of the bottom salinity average difference for the Eastward Expansion (Option 7, 55-foot channel) versus the Base Case.

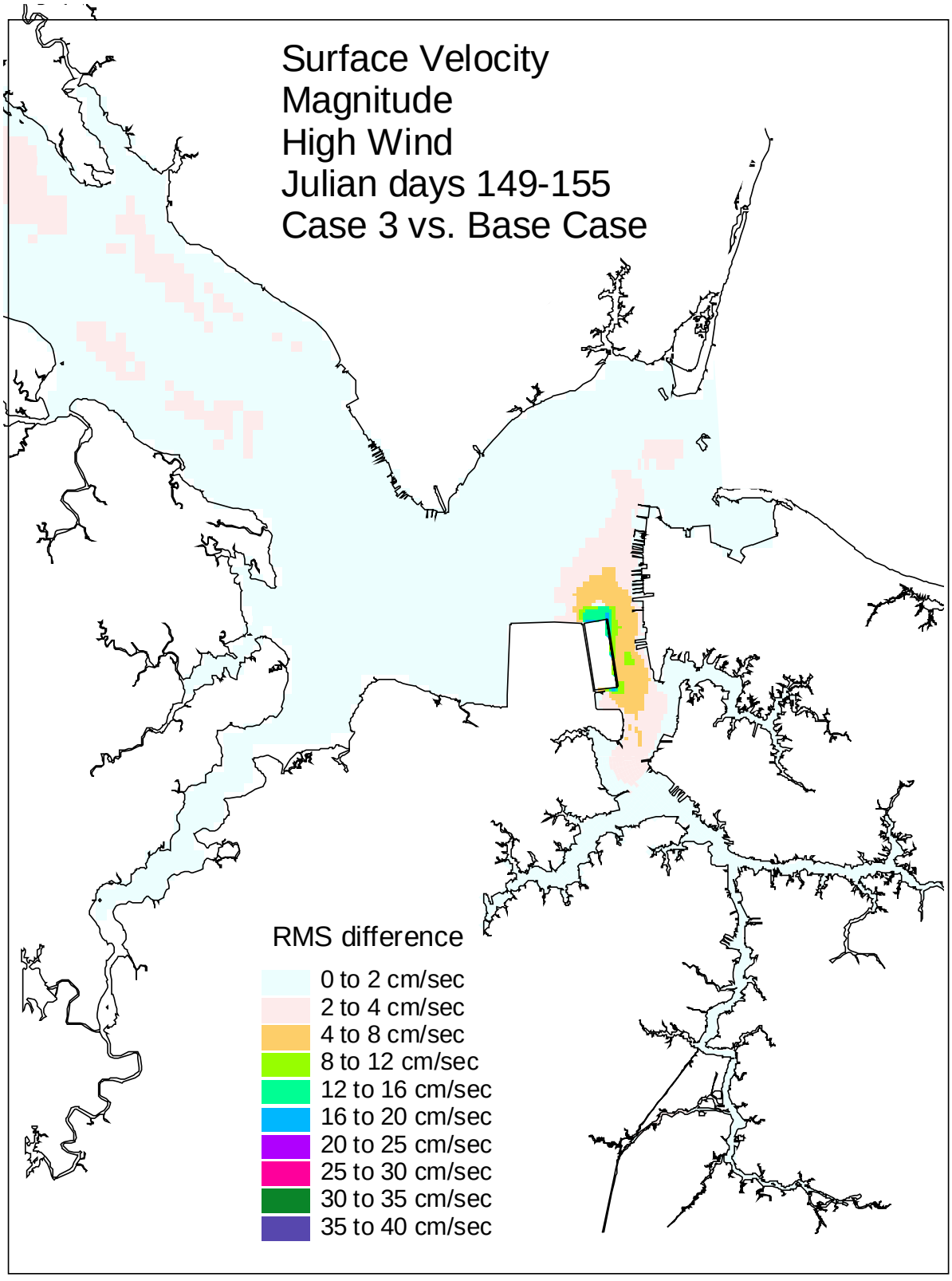

Figure 49. Historical simulation comparison (high wind) of the surface velocity RMS difference for the Eastward Expansion (Option 7, 55-foot channel) versus the Base Case.

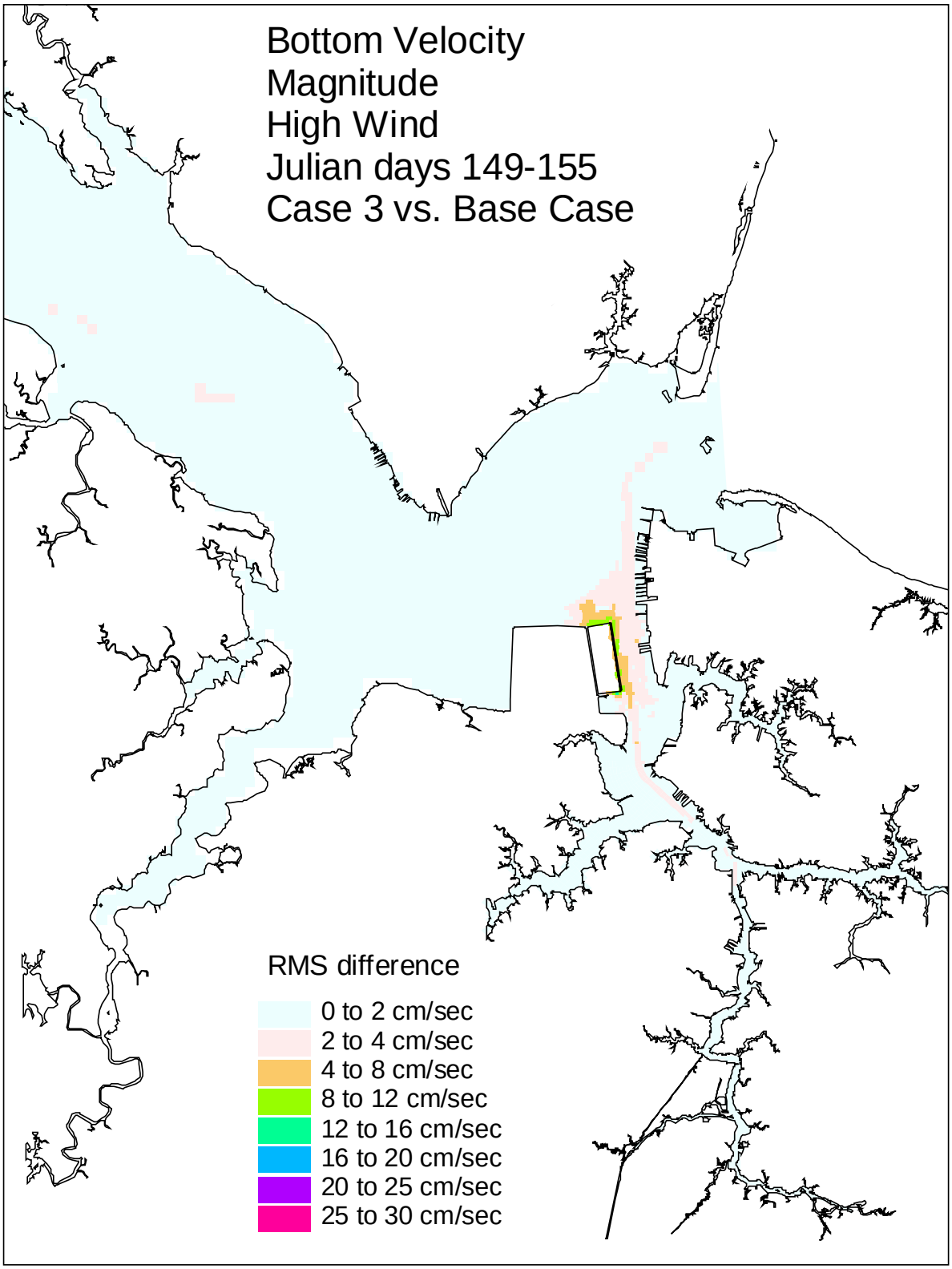

Figure 50. Historical simulation comparison (high wind) of the bottom velocity RMS difference for the Eastward Expansion (Option 7, 55-foot channel) versus the Base Case.

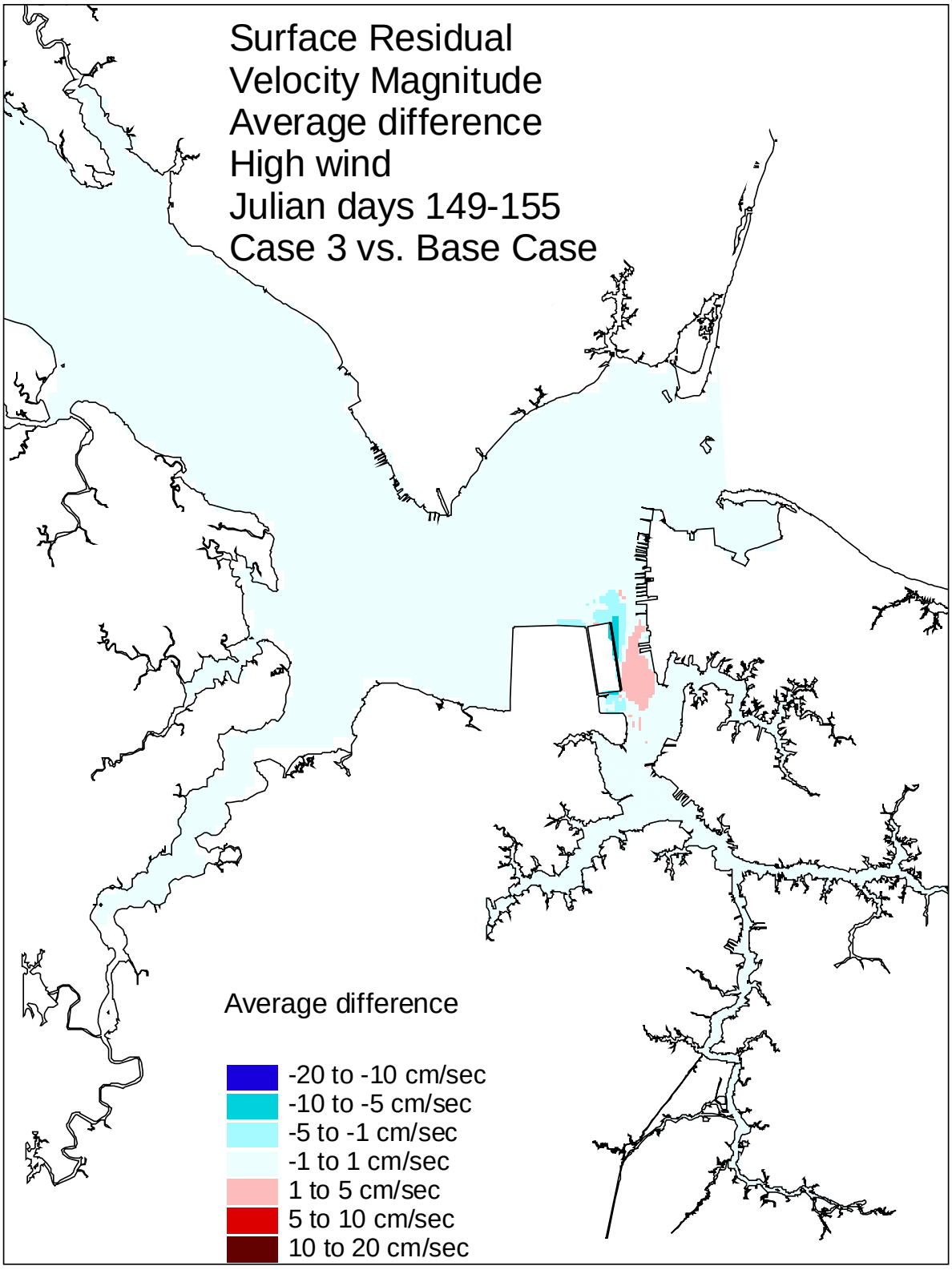

Figure 51. Historical simulation comparison (high wind) of the surface residual velocity average difference for the Eastward Expansion (Option 7, 55-foot channel) versus the Base Case.

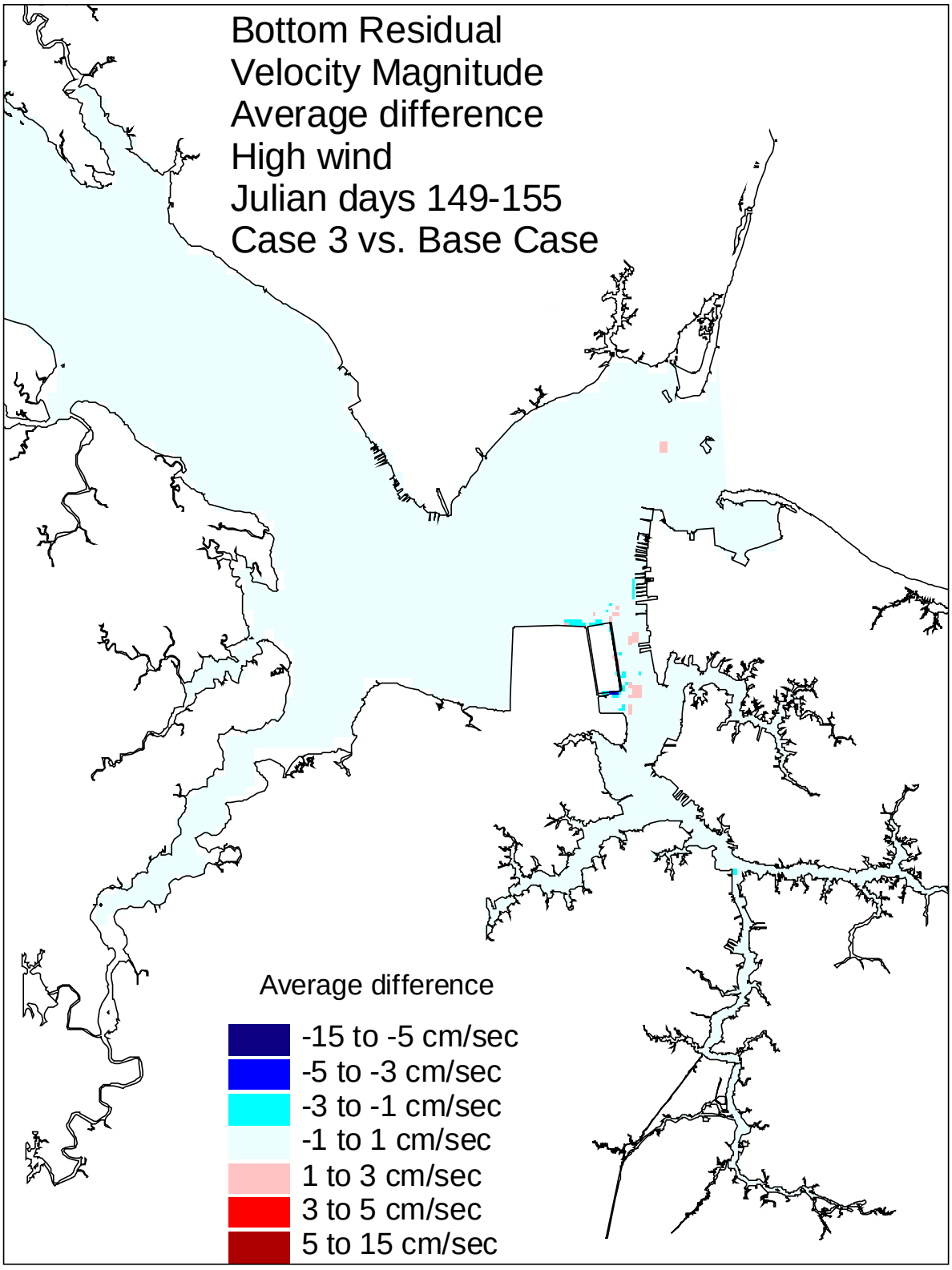

Figure 52. Historical simulation comparison (high wind) of the bottom residual velocity average difference for the Eastward Expansion (Option 7, 55-foot channel) versus the Base Case.

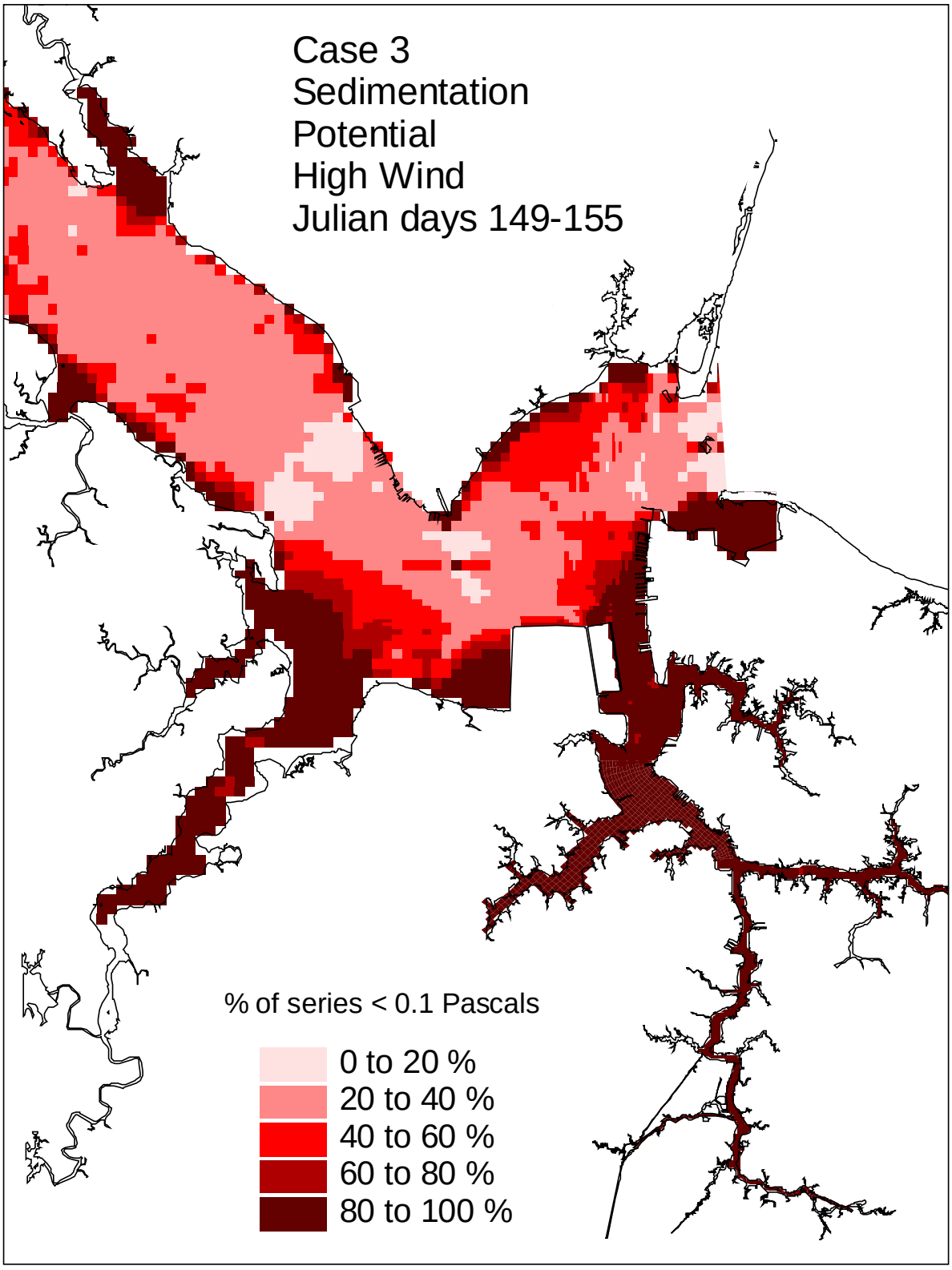

Figure 53. Historical simulation comparison (high wind) of the sedimentation potential for the Eastward Expansion (Option 7, 55-foot channel).

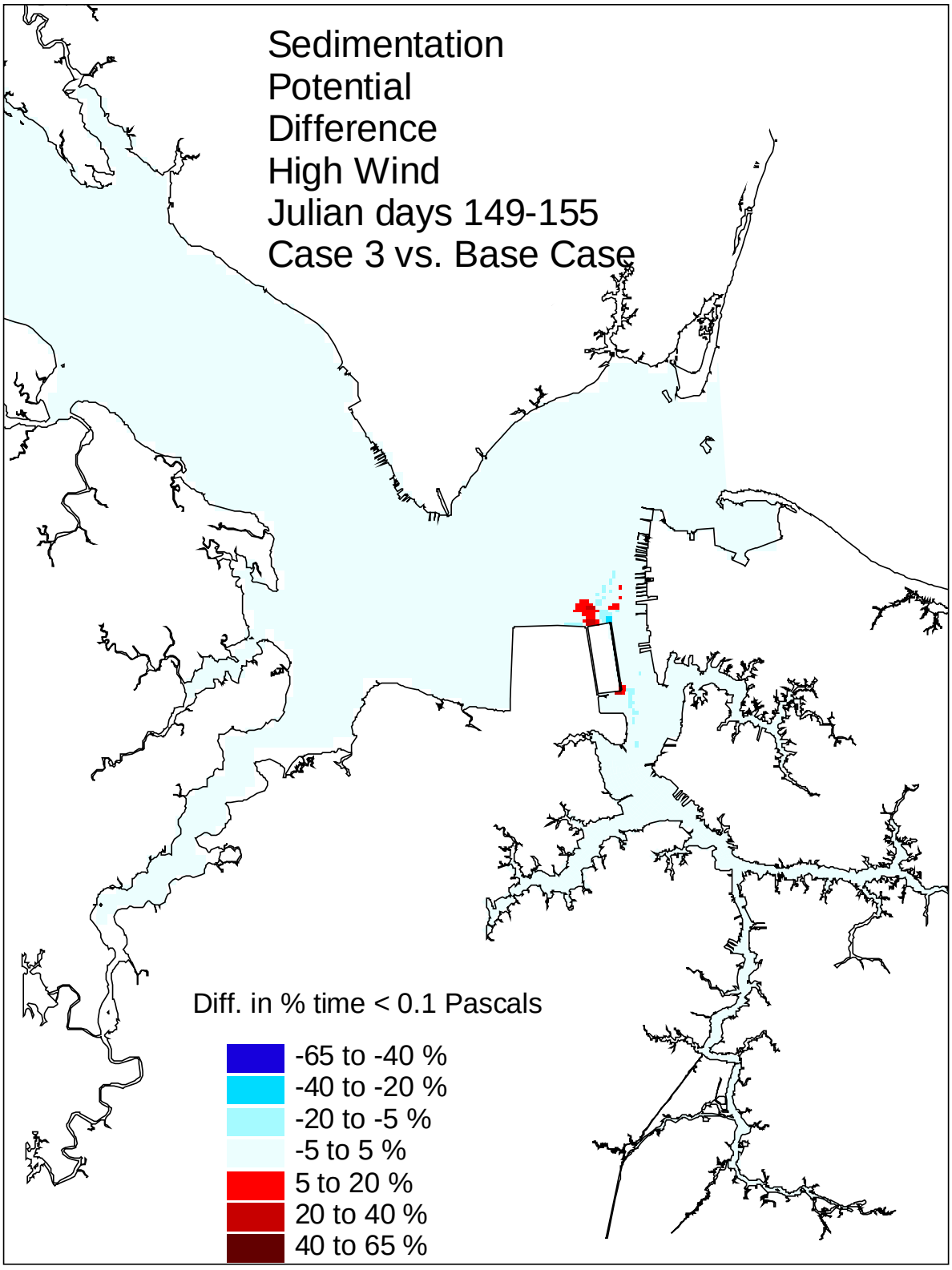

Figure 54. Historical simulation comparison (high wind) of the sedimentation potential difference for the Eastward Expansion (Option 7, 55-foot channel) versus the Base Case.

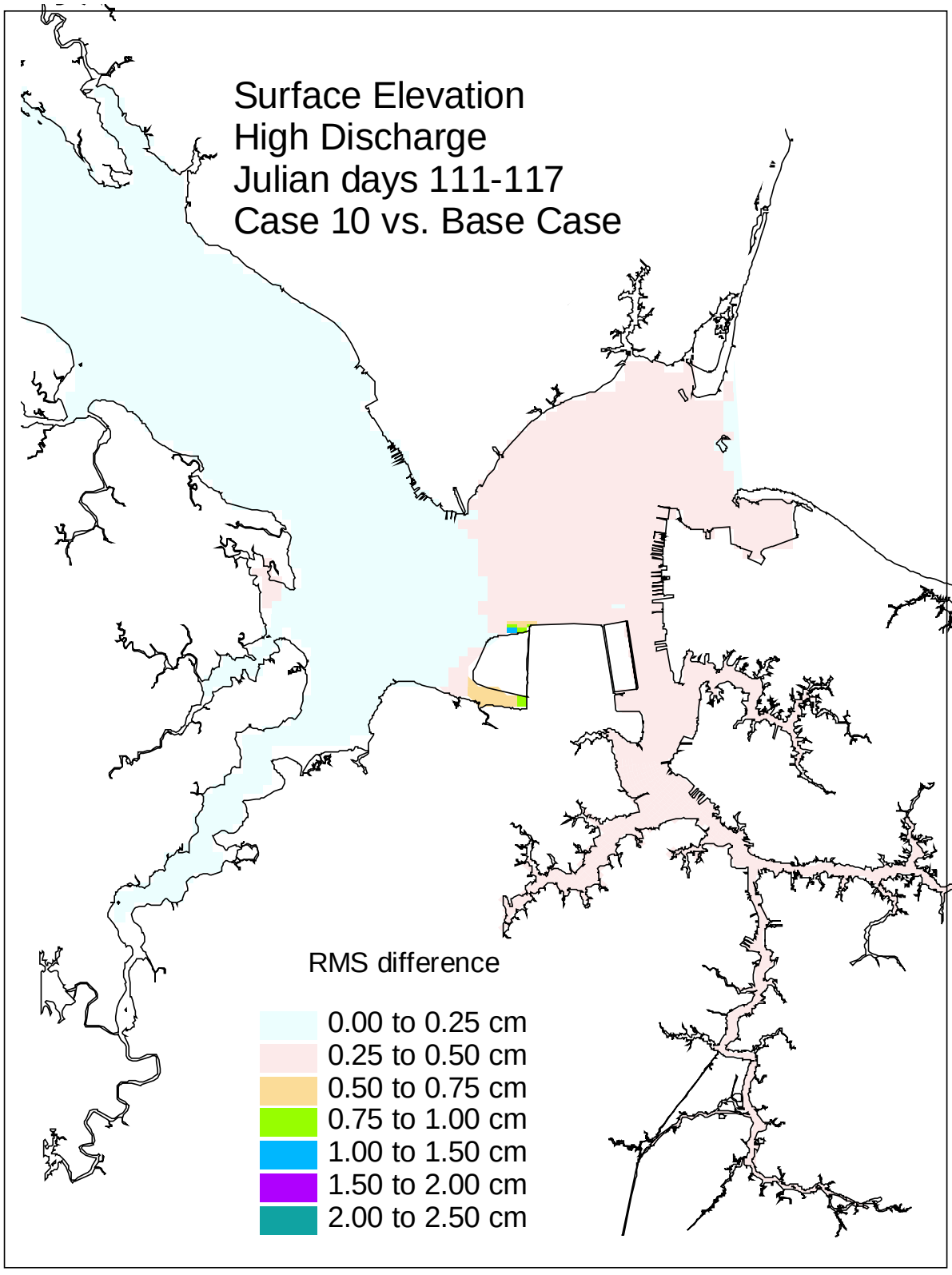

Figure 55. Historical simulation comparison (high discharge) of the surface elevation RMS difference for the Eastward and Westward Expansion (Option 7/5a, 50-foot channel) versus the Base Case.

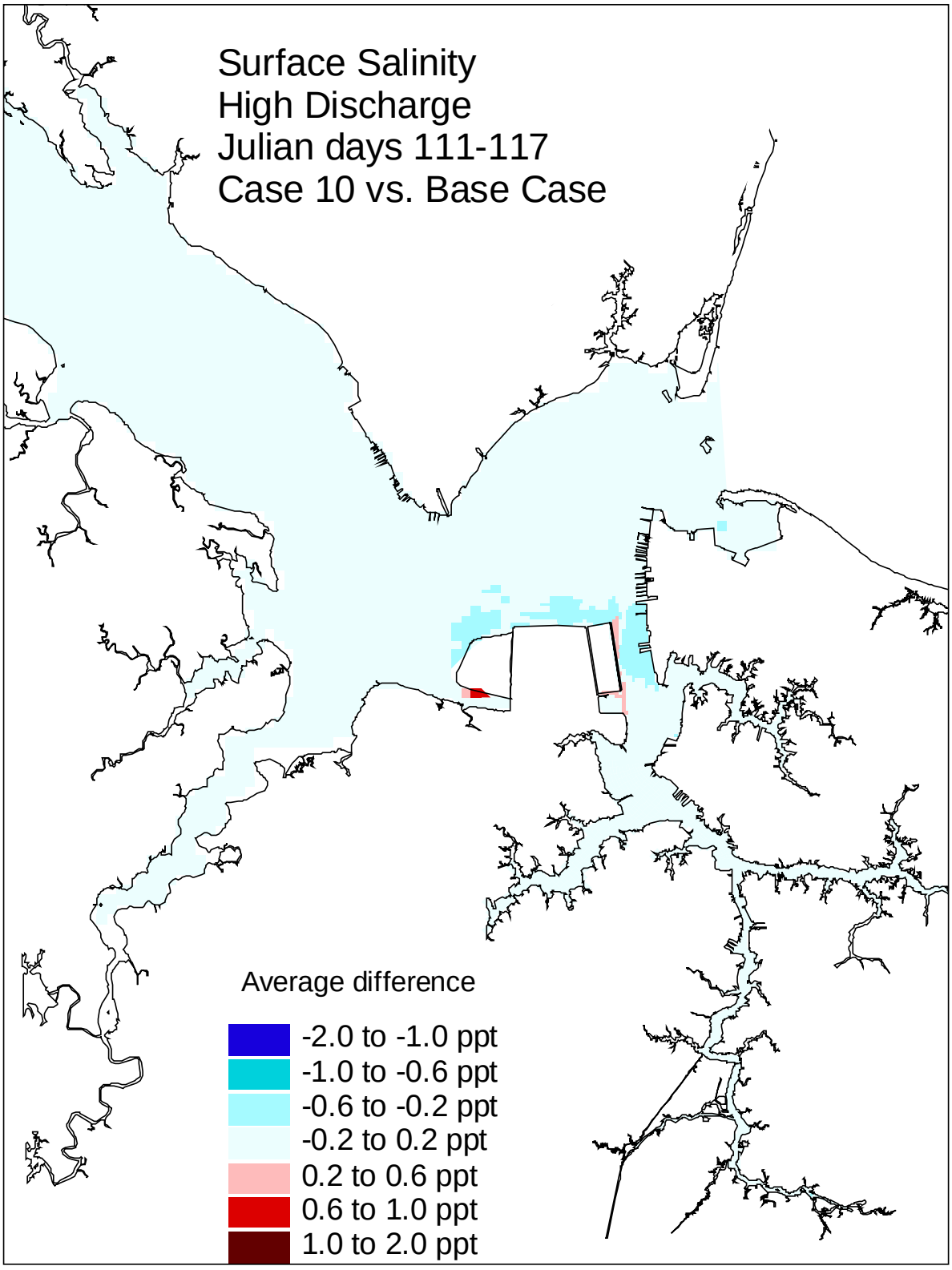

Figure 56. Historical simulation comparison (high discharge) of the surface salinity average difference for the Eastward and Westward Expansion (Option 7/5a, 50-foot channel) versus the Base Case.

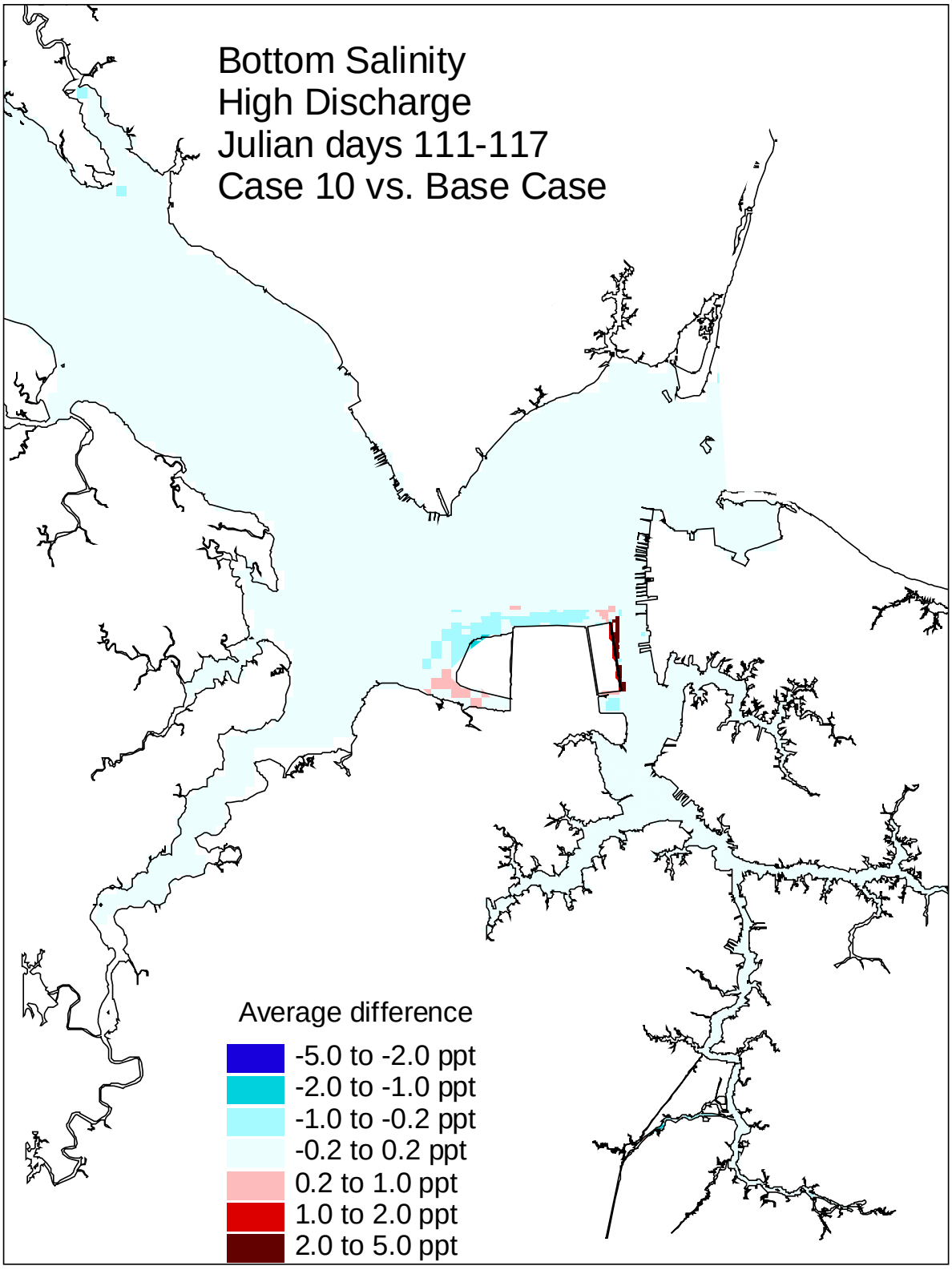

Figure 57. Historical simulation comparison (high discharge) of the bottom salinity average difference for the Eastward and Westward Expansion (Option 7/5a, 50-foot channel) versus the Base Case.

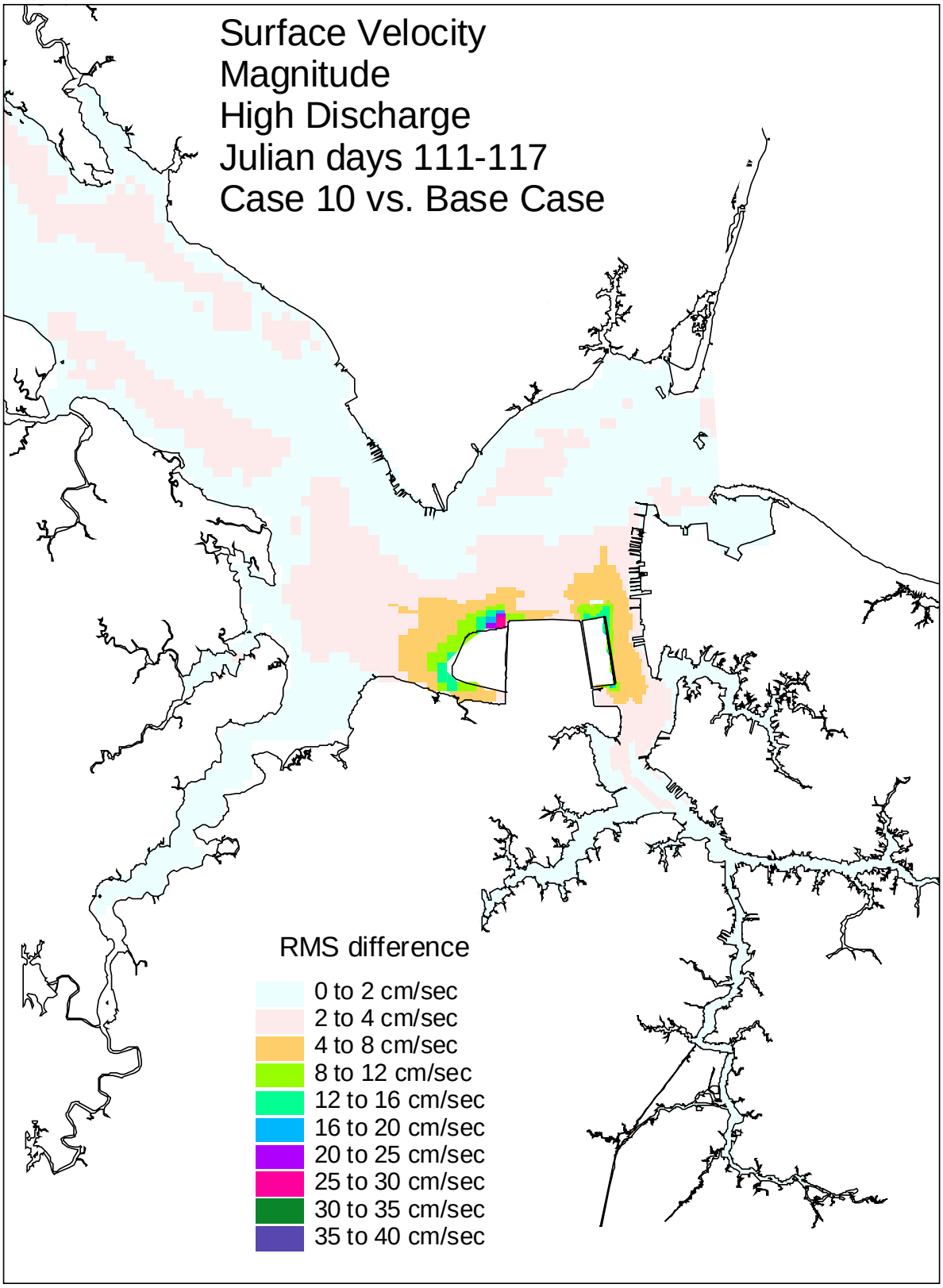

Figure 58. Historical simulation comparison (high discharge) of the surface velocity RMS difference for the Eastward and Westward Expansion (Option 7/5a, 50-foot channel) versus the Base Case.

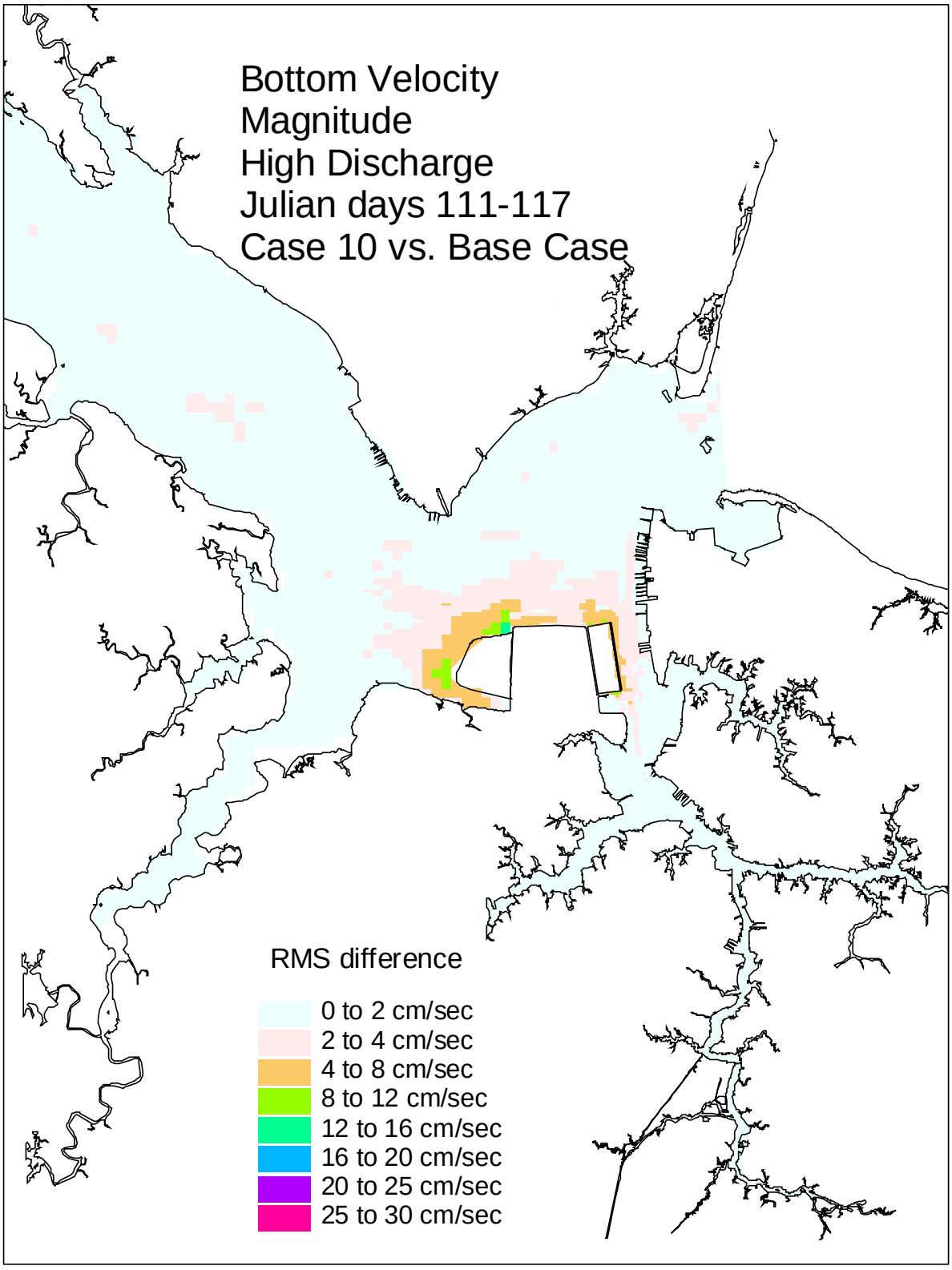

Figure 59. Historical simulation comparison (high discharge) of the bottom velocity RMS difference for the Eastward and Westward Expansion (Option 7/5a, 50-foot channel) versus the Base Case.

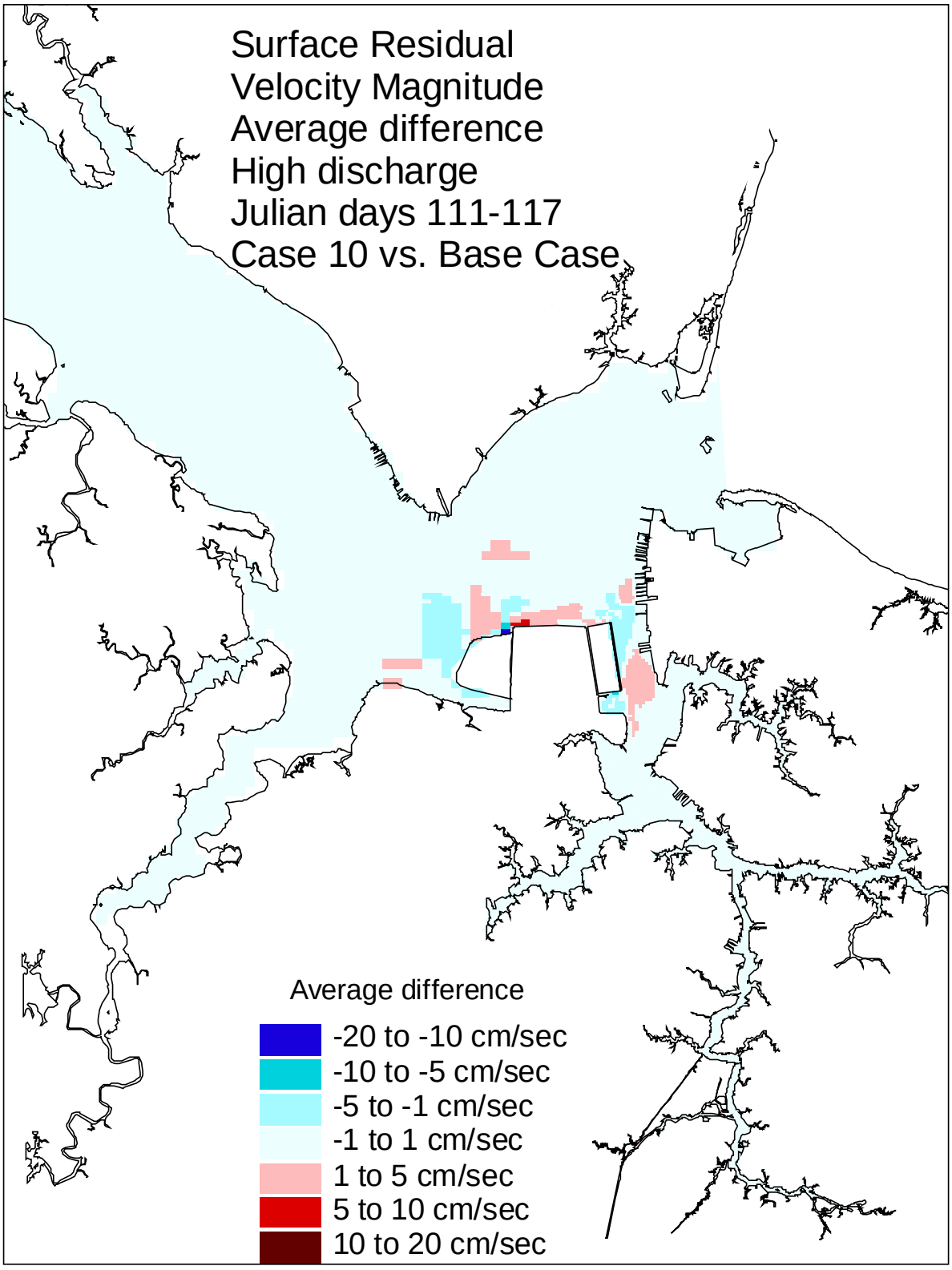

Figure 60. Historical simulation comparison (high discharge) of the surface residual velocity average difference for the Eastward and Westward Expansion (Option 7/5a, 50-foot channel) versus the Base Case.

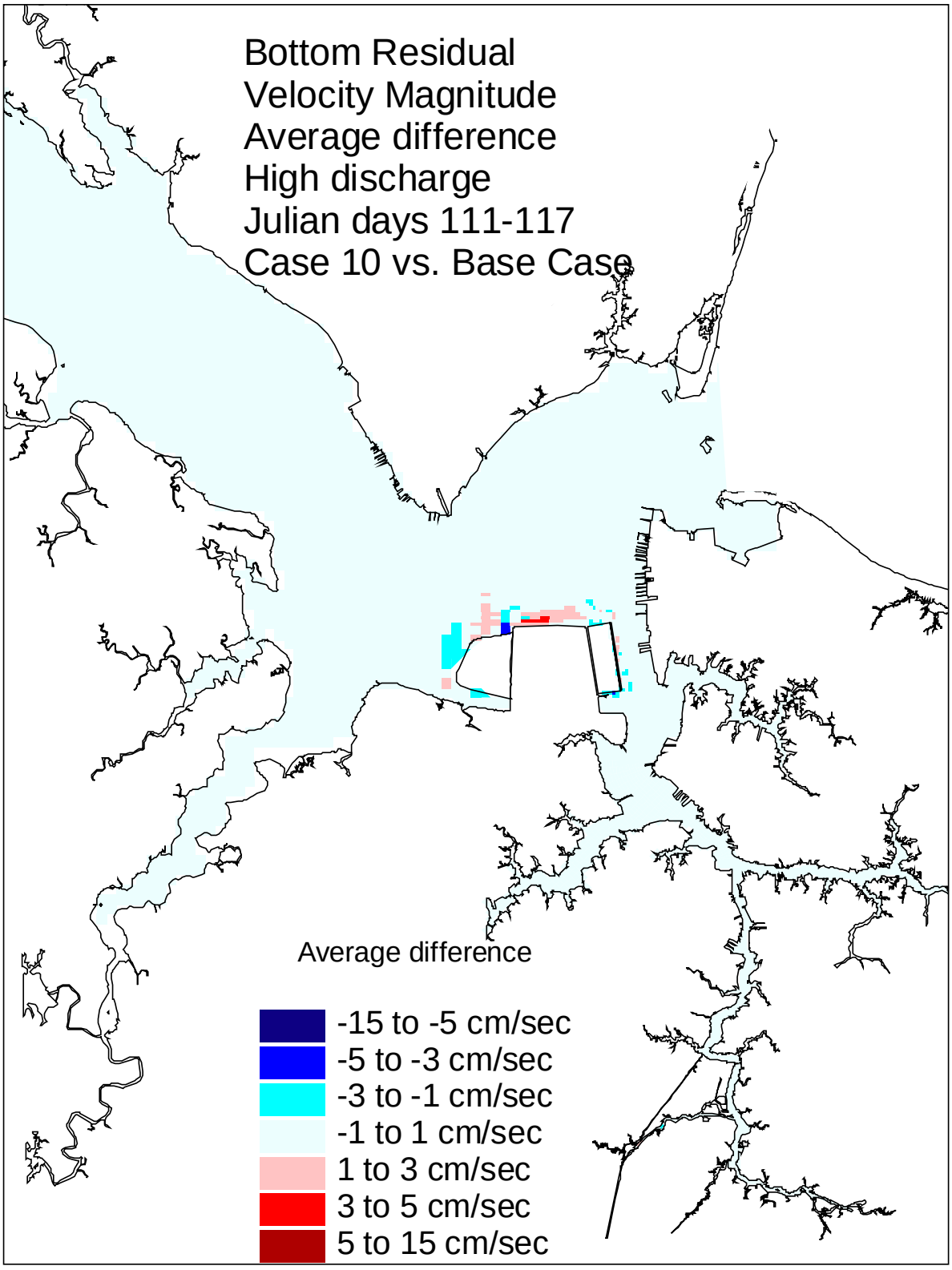

Figure 61. Historical simulation comparison (high discharge) of the bottom residual velocity average difference for the Eastward and Westward Expansion (Option 7/5a, 50-foot channel) versus the Base Case.

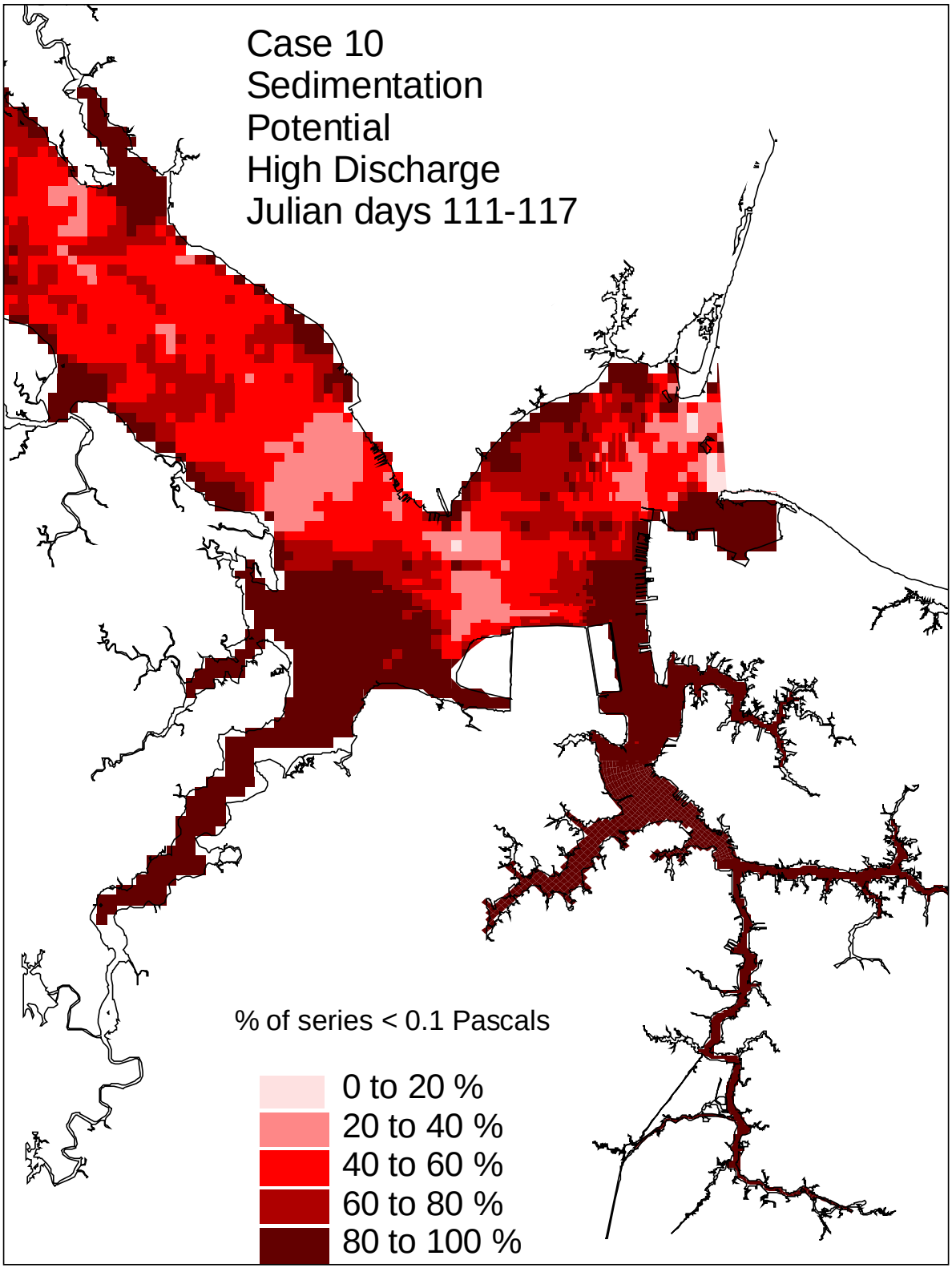

Figure 62. Historical simulation comparison (high discharge) of the sedimentation potential for the Eastward and Westward Expansion (Option 7/5a, 50-foot channel).

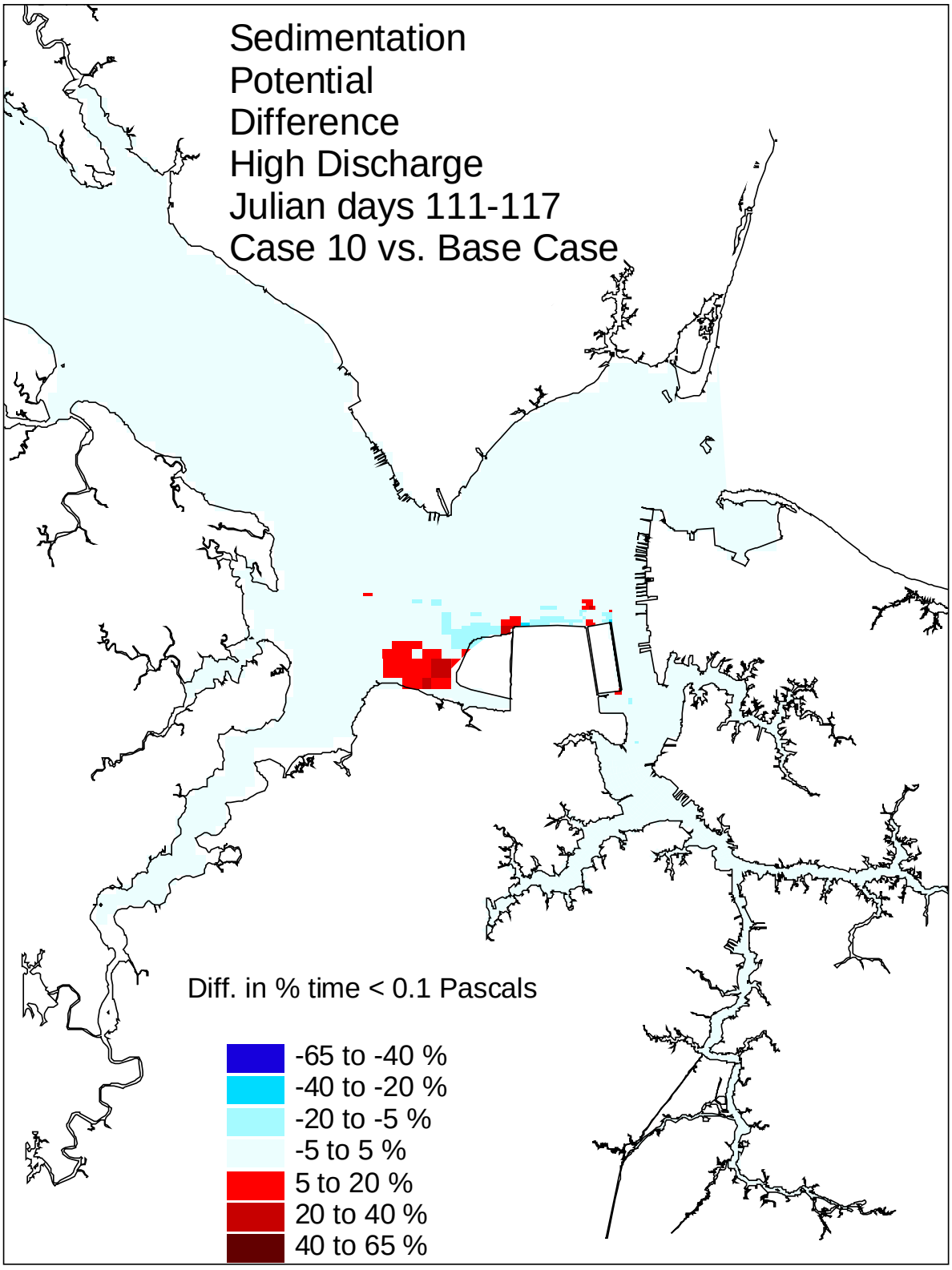

Figure 63. Historical simulation comparison (high discharge) of the sedimentation potential difference for the Eastward and Westward Expansion (Option 7/5a, 50-foot channel) versus the Base Case.

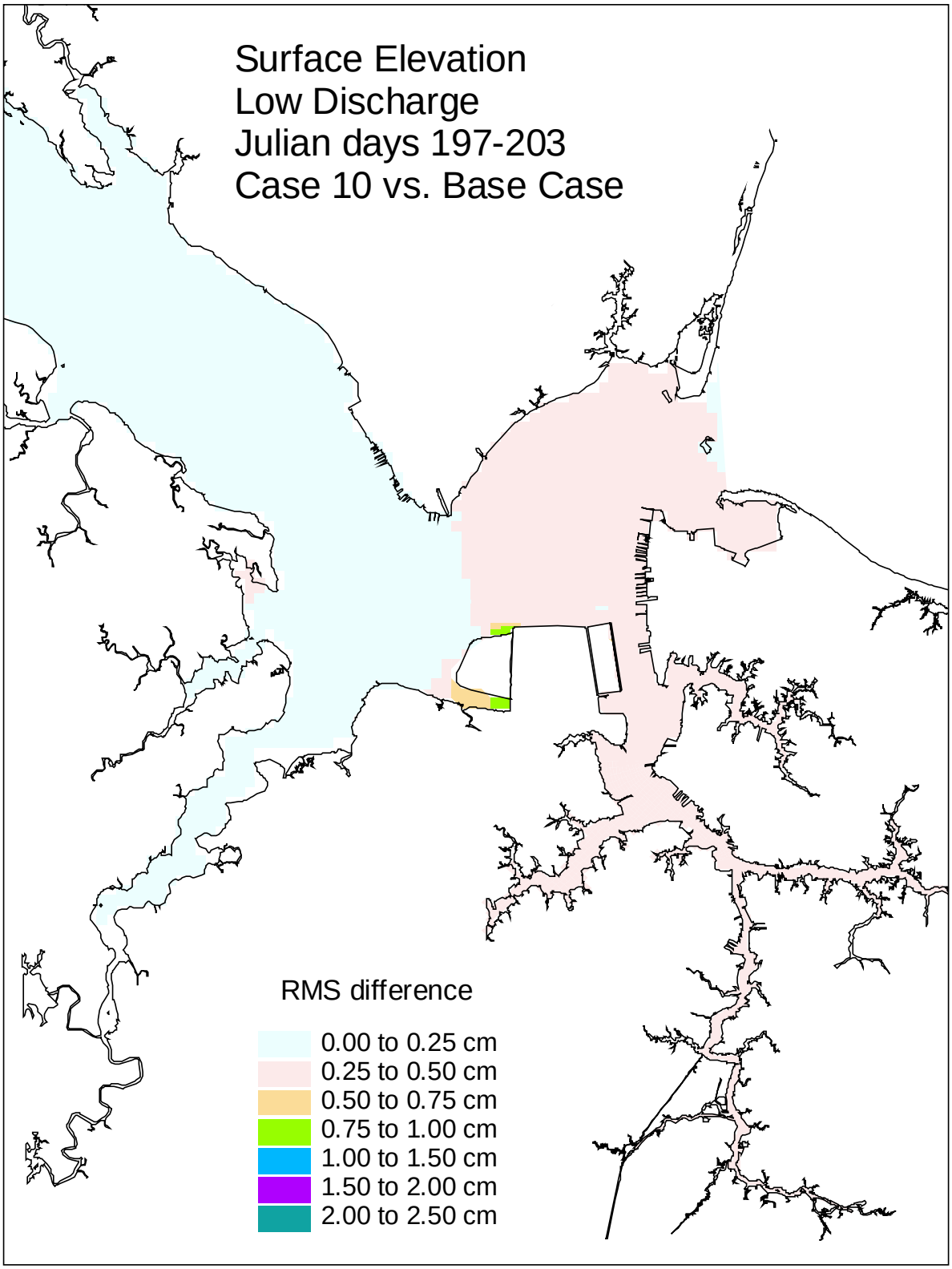

Figure 64. Historical simulation comparison (low discharge) of the surface elevation RMS difference for the Eastward and Westward Expansion (Option 7/5a, 50-foot channel) versus the Base Case.

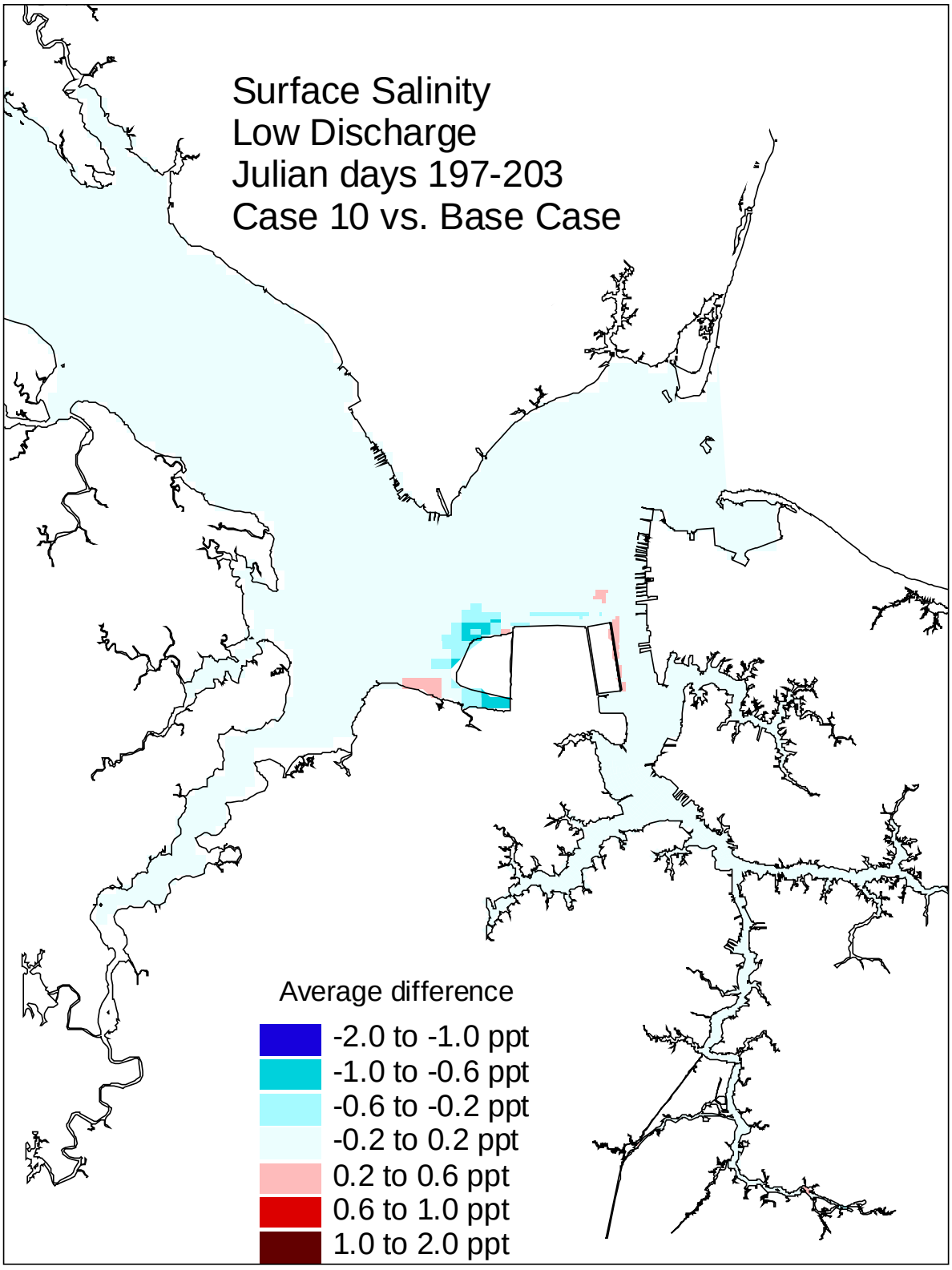

Figure 65. Historical simulation comparison (low discharge) of the surface salinity average difference for the Eastward and Westward Expansion (Option 7/5a, 50-foot channel) versus the Base Case.

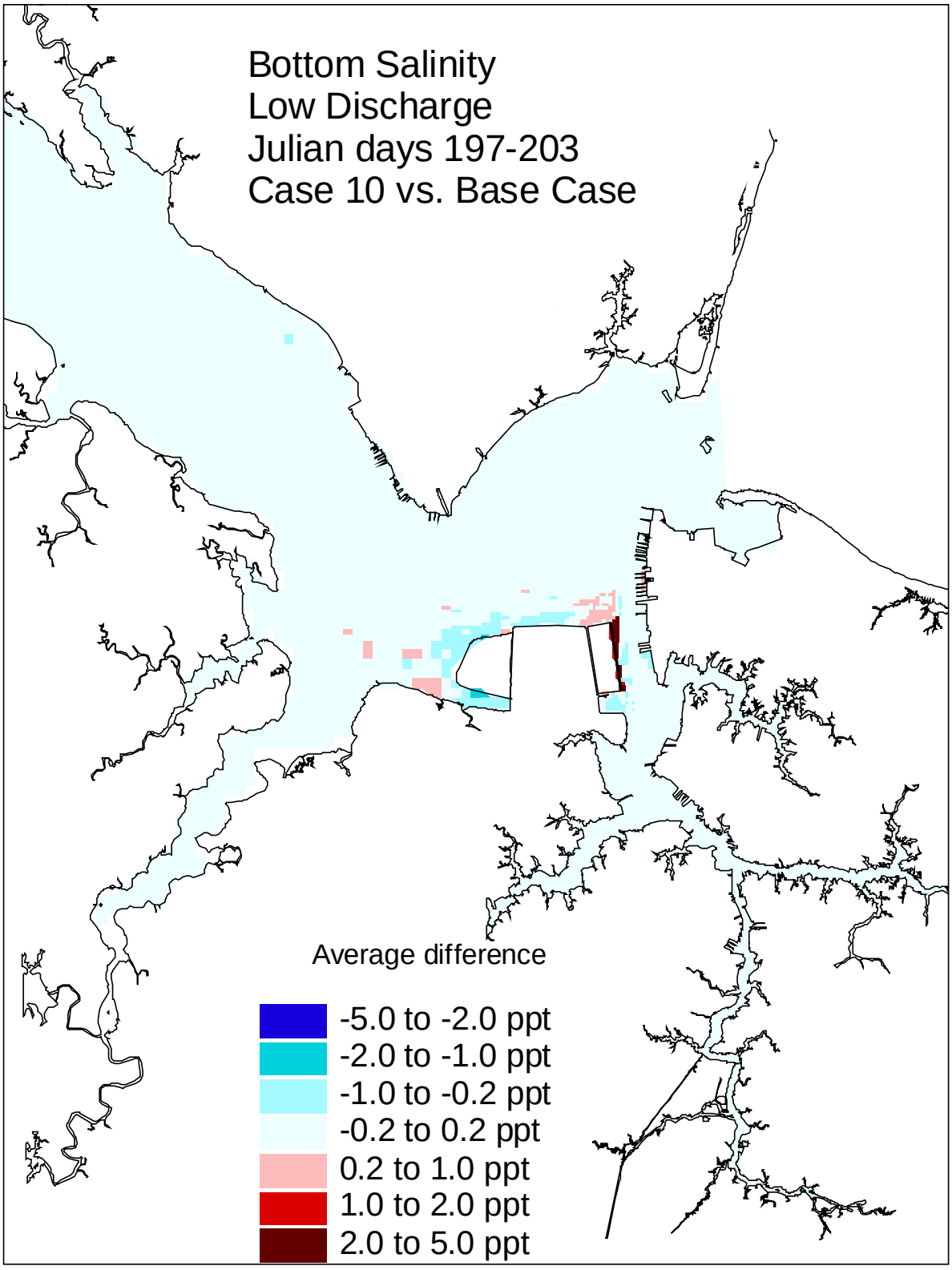

Figure 66. Historical simulation comparison (low discharge) of the bottom salinity average difference for the Eastward and Westward Expansion (Option 7/5a, 50-foot channel) versus the Base Case.

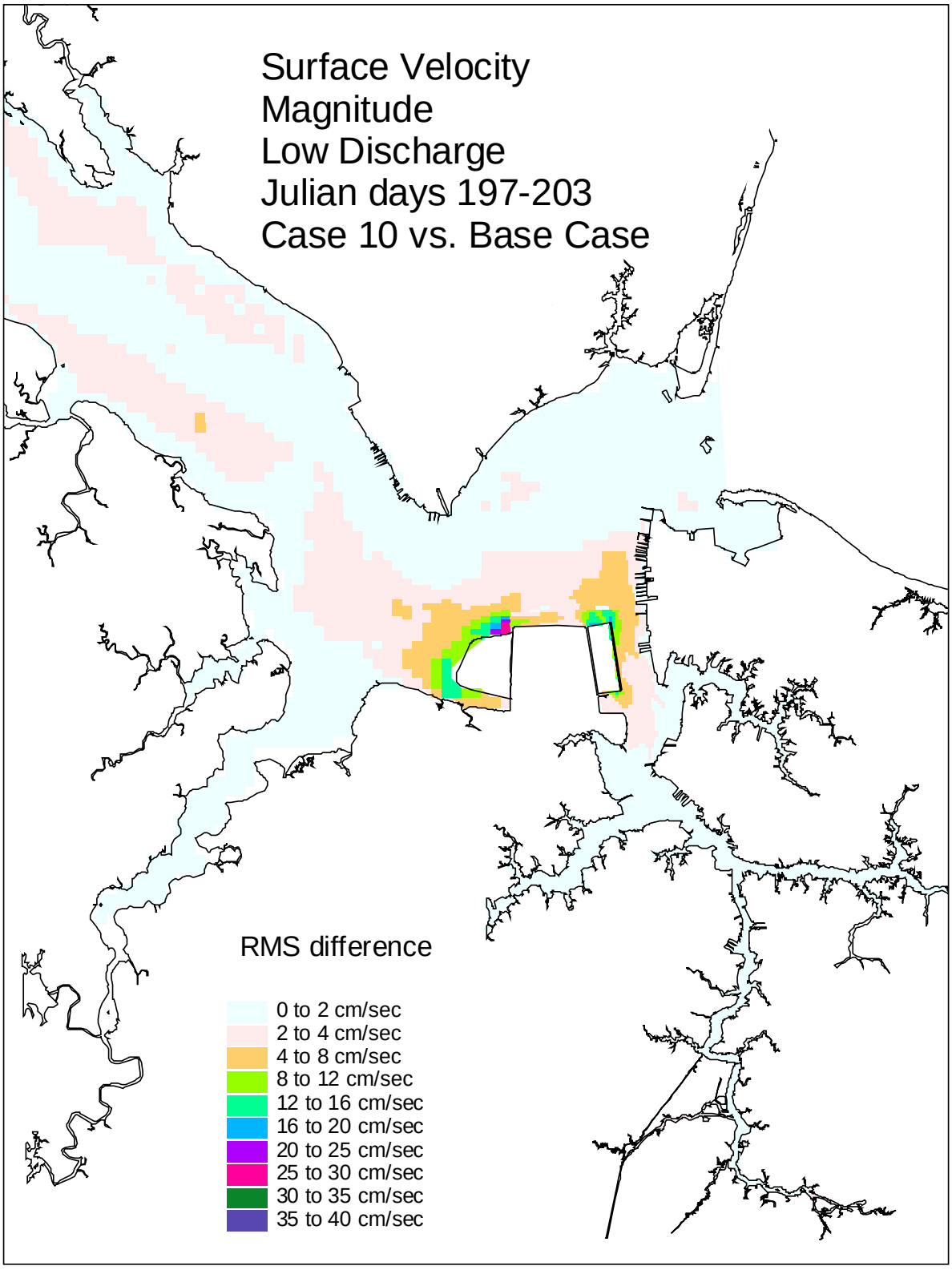

Figure 67. Historical simulation comparison (low discharge) of the surface velocity RMS difference for the Eastward and Westward Expansion (Option 7/5a, 50-foot channel) versus the Base Case.

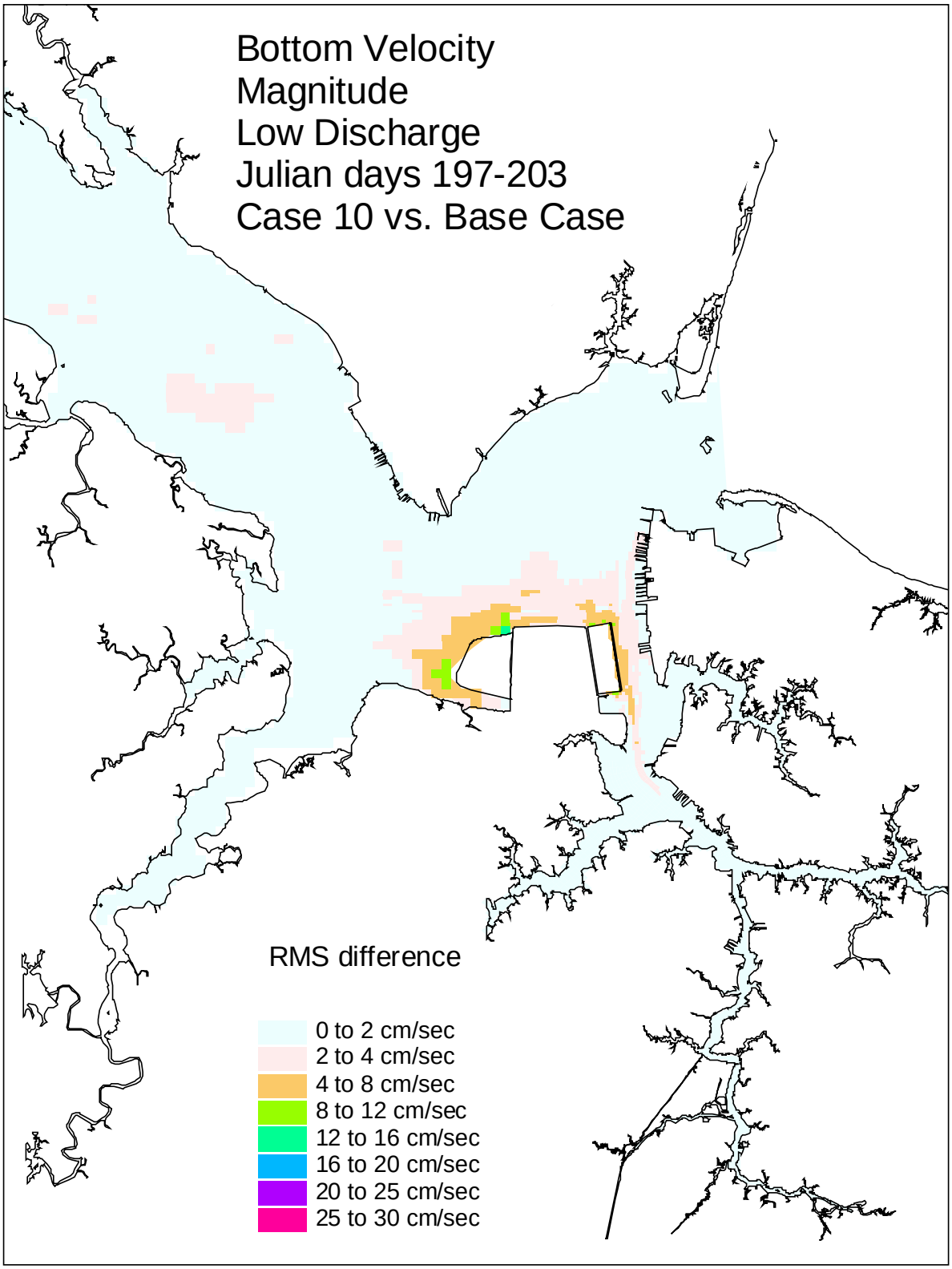

Figure 68. Historical simulation comparison (low discharge) of the bottom velocity RMS difference for the Eastward and Westward Expansion (Option 7/5a, 50-foot channel) versus the Base Case.

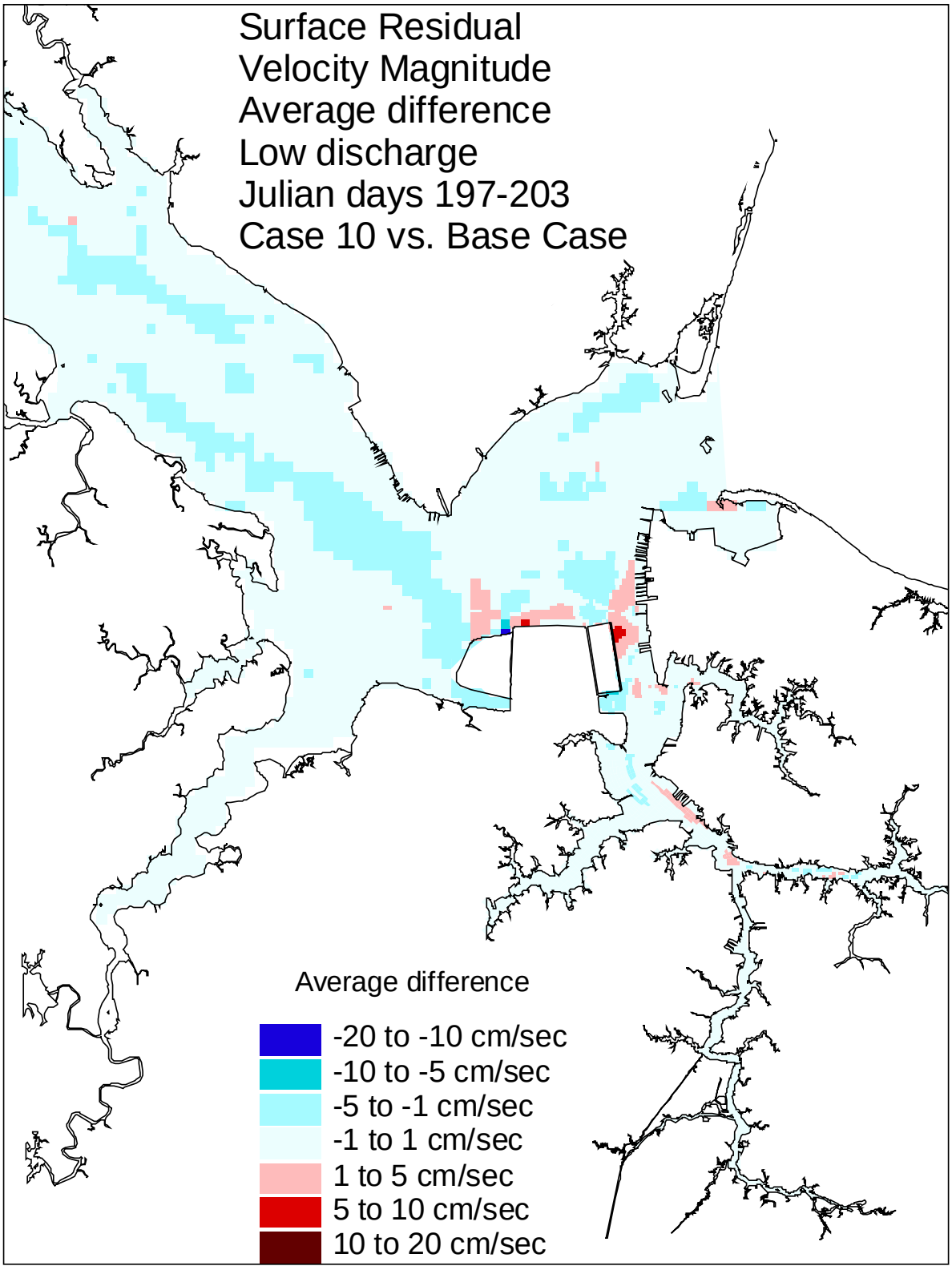

Figure 69. Historical simulation comparison (low discharge) of the surface residual velocity average difference for the Eastward and Westward Expansion (Option 7/5a, 50-foot channel) versus the Base Case.

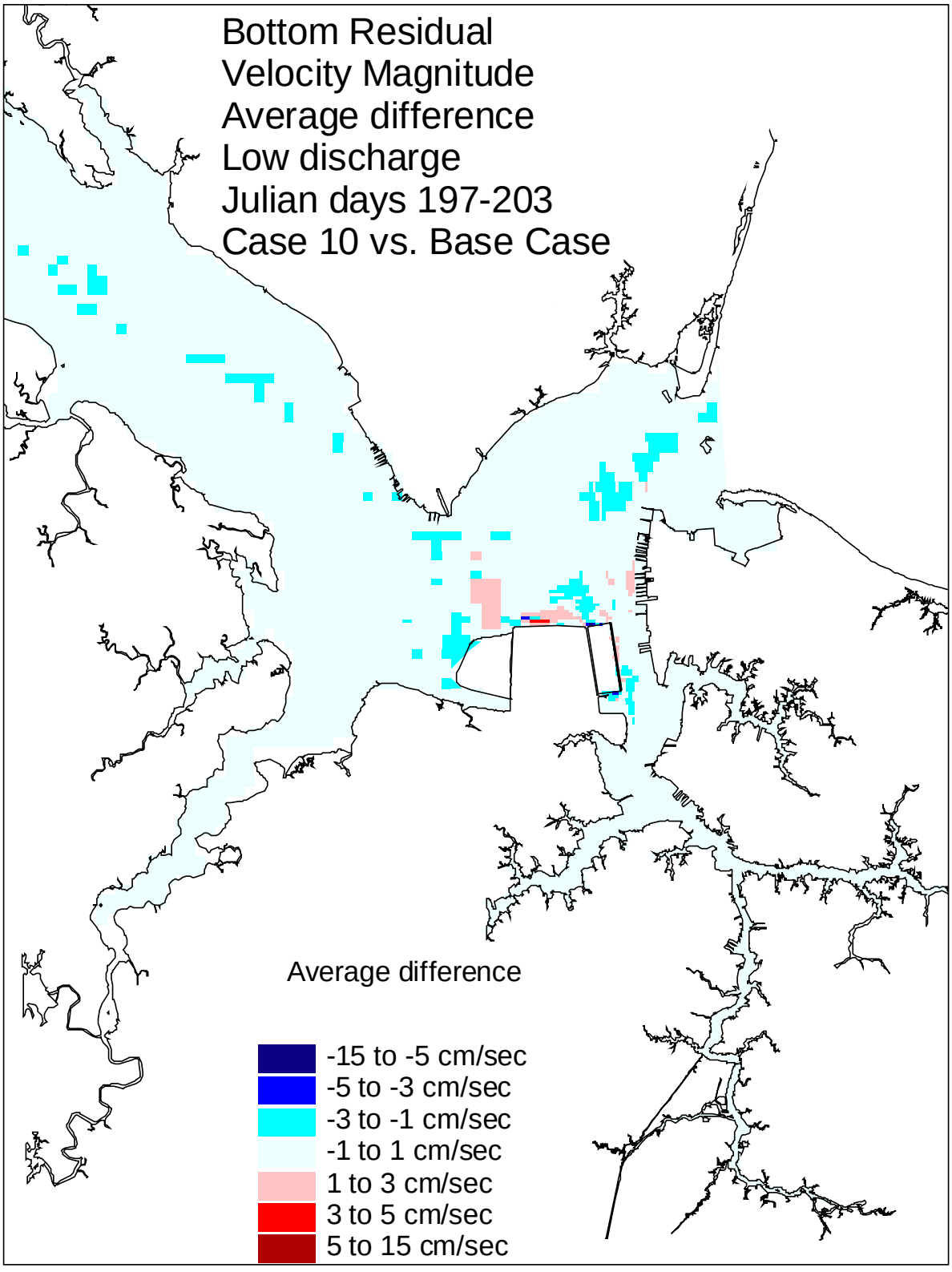

Figure 70. Historical simulation comparison (low discharge) of the bottom residual velocity average difference for the Eastward and Westward Expansion (Option 7/5a, 50-foot channel) versus the Base Case.

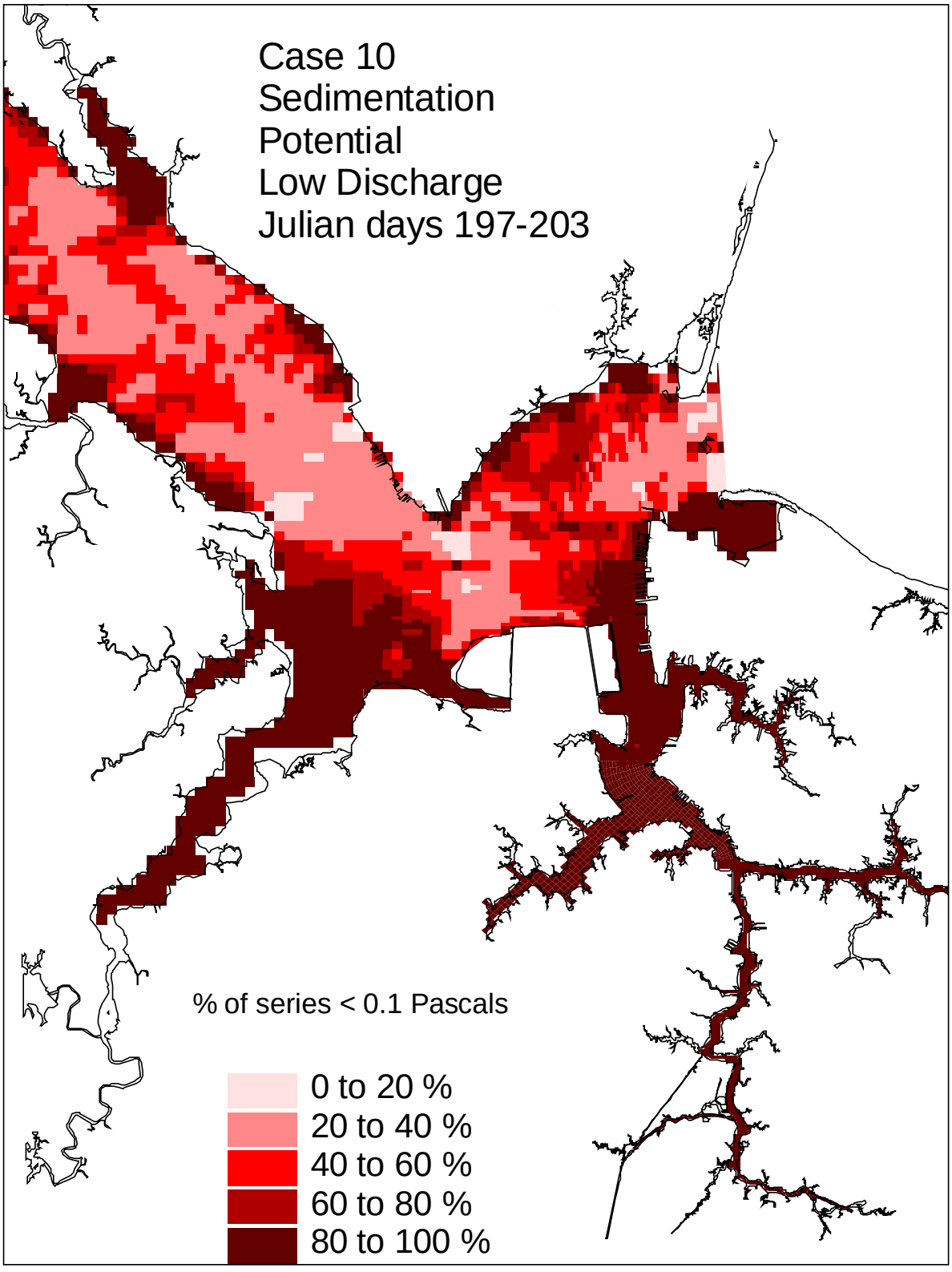

Figure 71. Historical simulation comparison (low discharge) of the sedimentation potential for the Eastward and Westward Expansion (Option 7/5a, 50-foot channel) versus the Base Case.

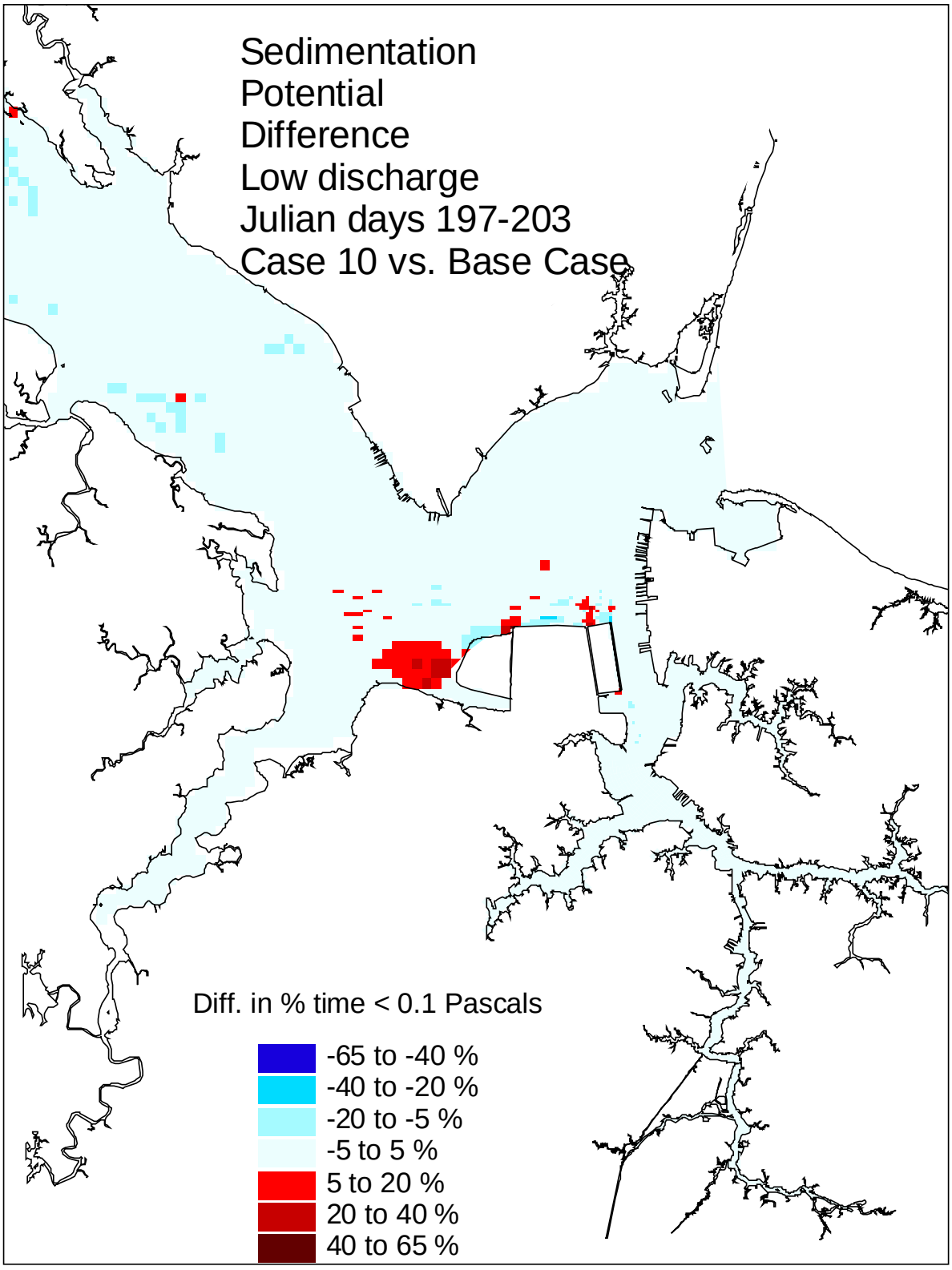

Figure 72. Historical simulation comparison (low discharge) of the sedimentation potential difference for the Eastward and Westward Expansion (Option 7/5a, 50-foot channel) versus the Base Case.

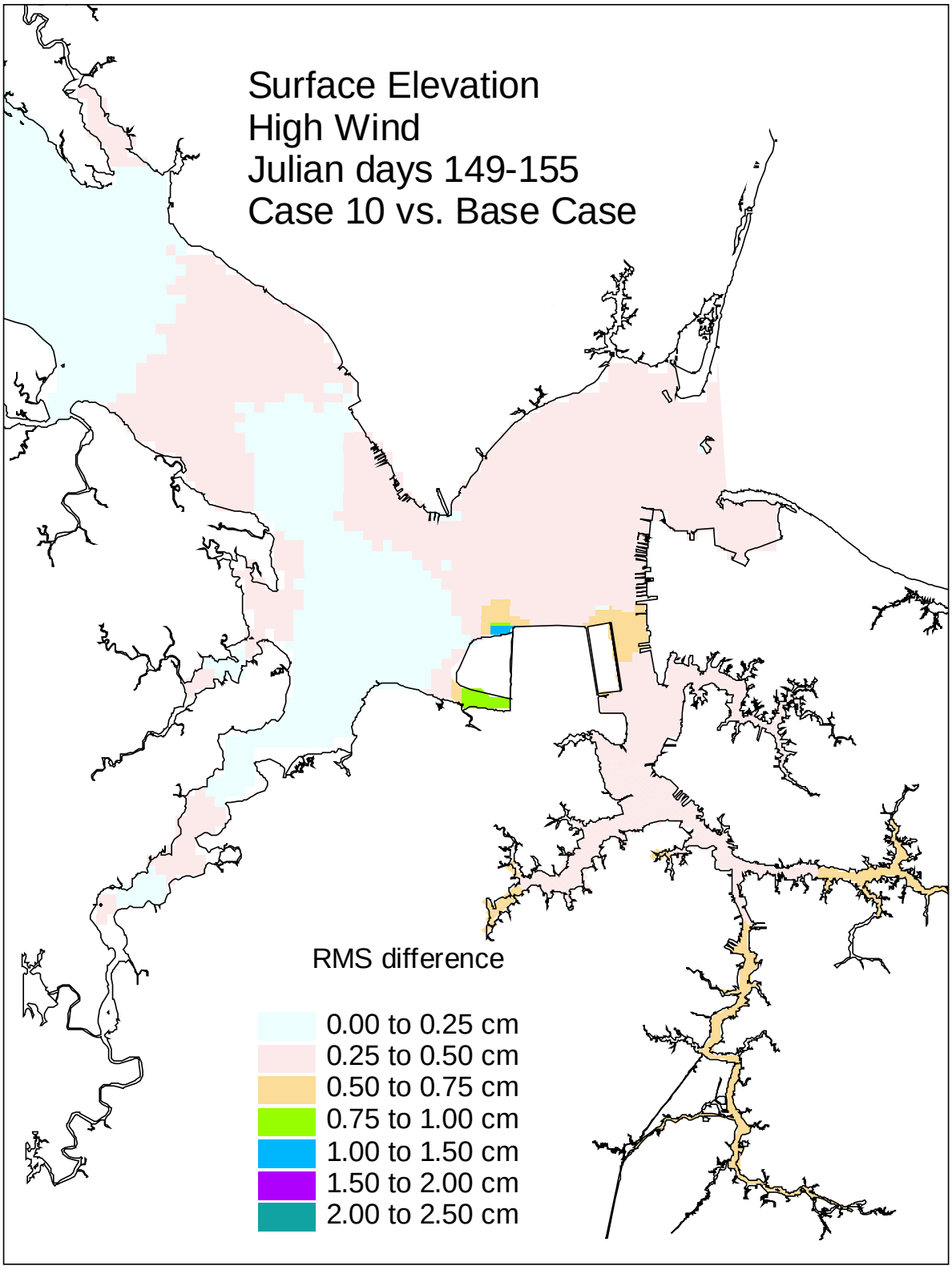

Figure 73. Historical simulation comparison (high wind) of the surface elevation RMS difference for the Eastward and Westward Expansion (Option 7/5a, 50-foot channel) versus the Base Case.

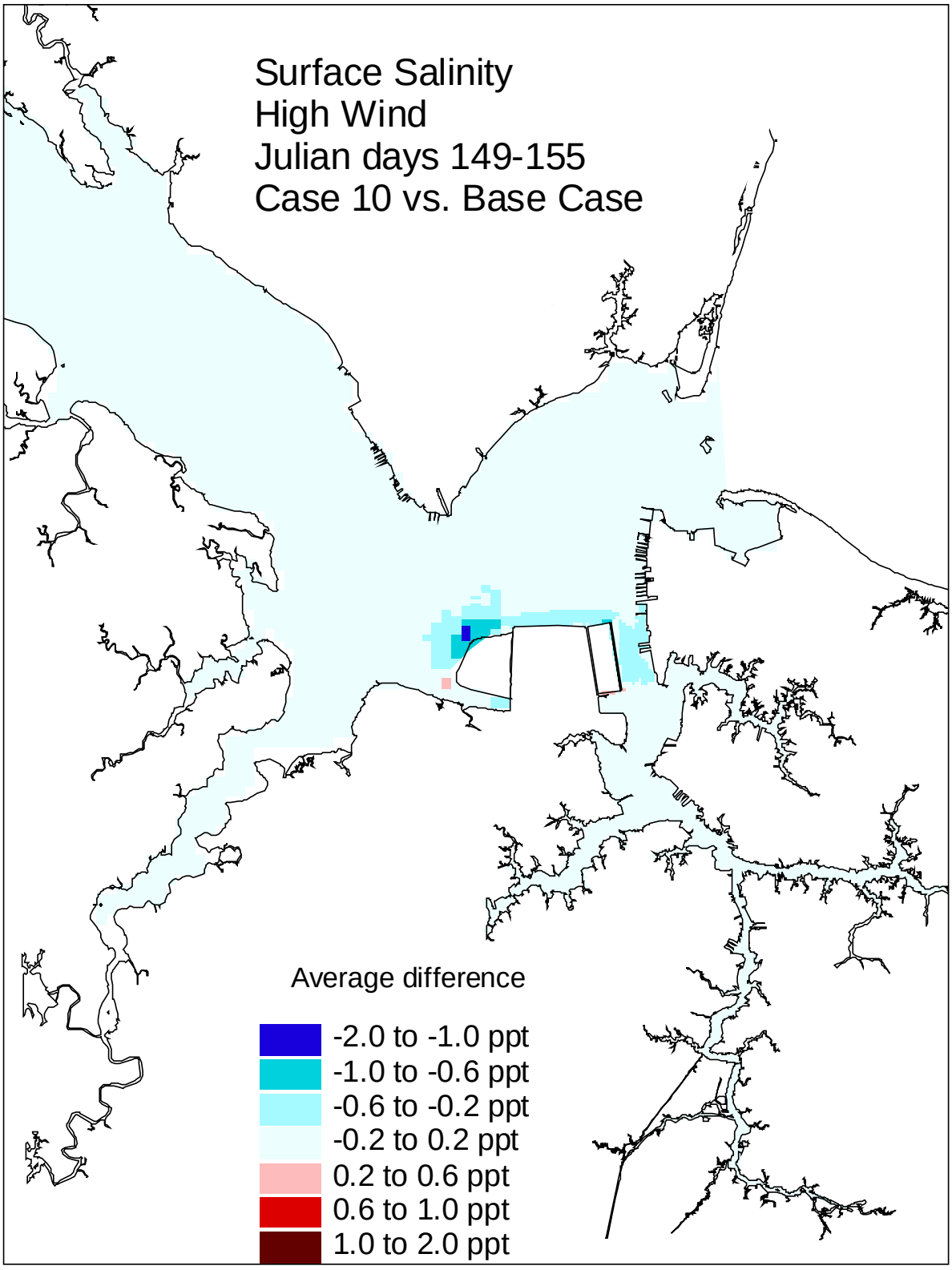

Figure 74. Historical simulation comparison (high wind) of the surface salinity average difference for the Eastward and Westward Expansion (Option 7/5a, 50-foot channel) versus the Base Case.

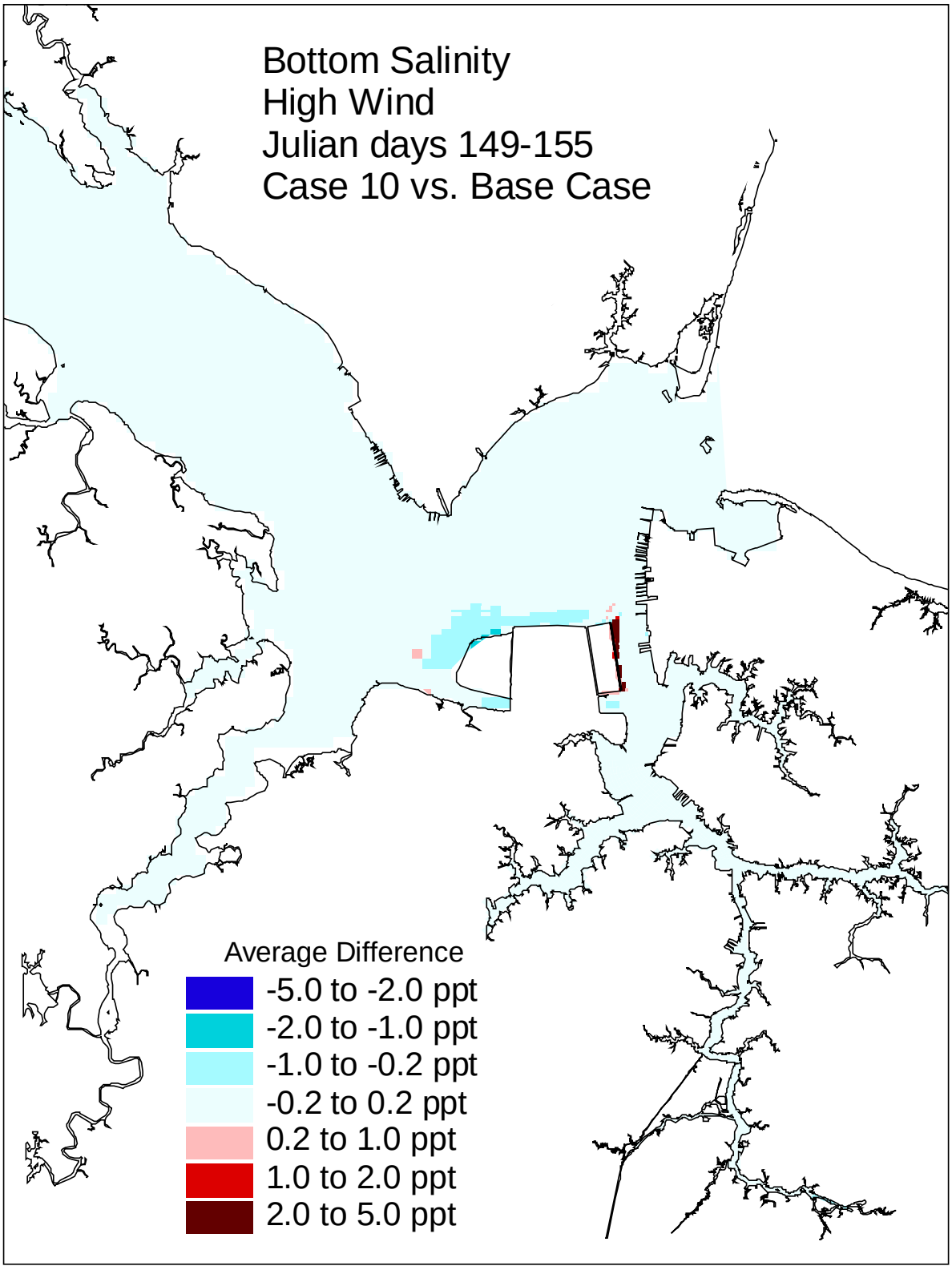

Figure 75. Historical simulation comparison (high wind) of the bottom salinity average difference for the Eastward and Westward Expansion (Option 7/5a, 50-foot channel) versus the Base Case.

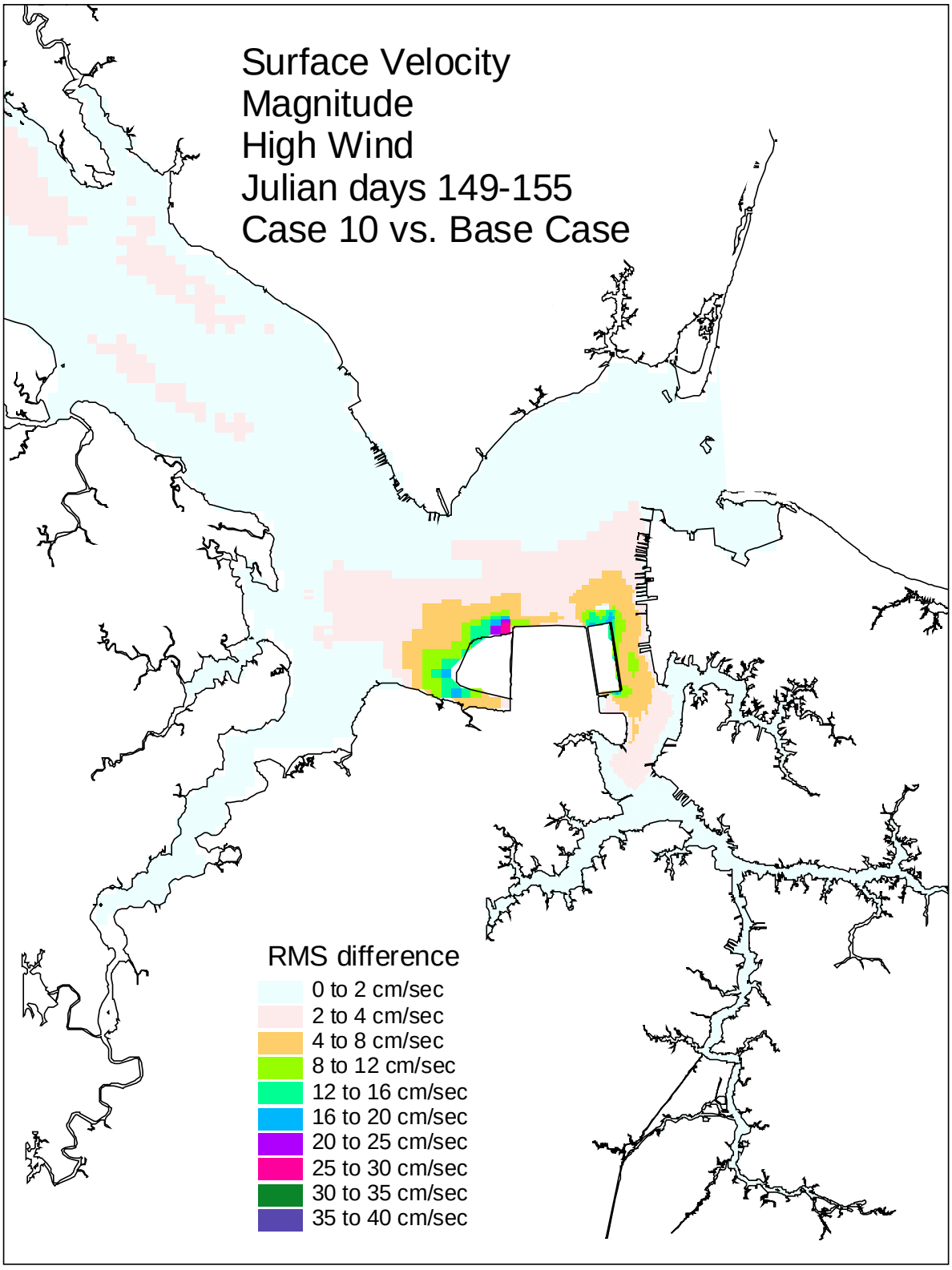

Figure 76. Historical simulation comparison (high wind) of the surface velocity RMS difference for the Eastward and Westward Expansion (Option 7/5a, 50-foot channel) versus the Base Case.

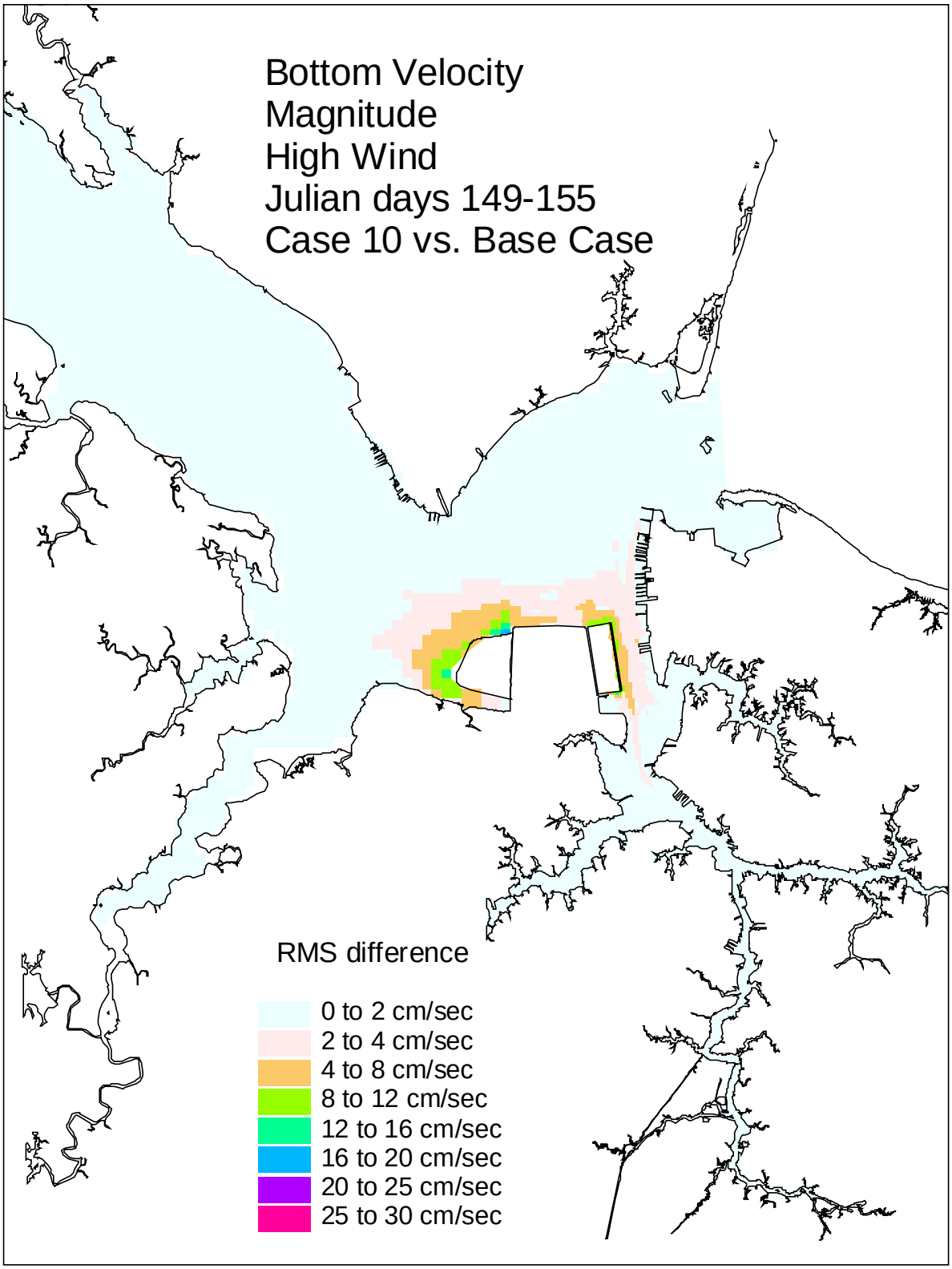

Figure 77. Historical simulation comparison (high wind) of the bottom velocity RMS difference for the Eastward and Westward Expansion (Option 7/5a, 50-foot channel) versus the Base Case.

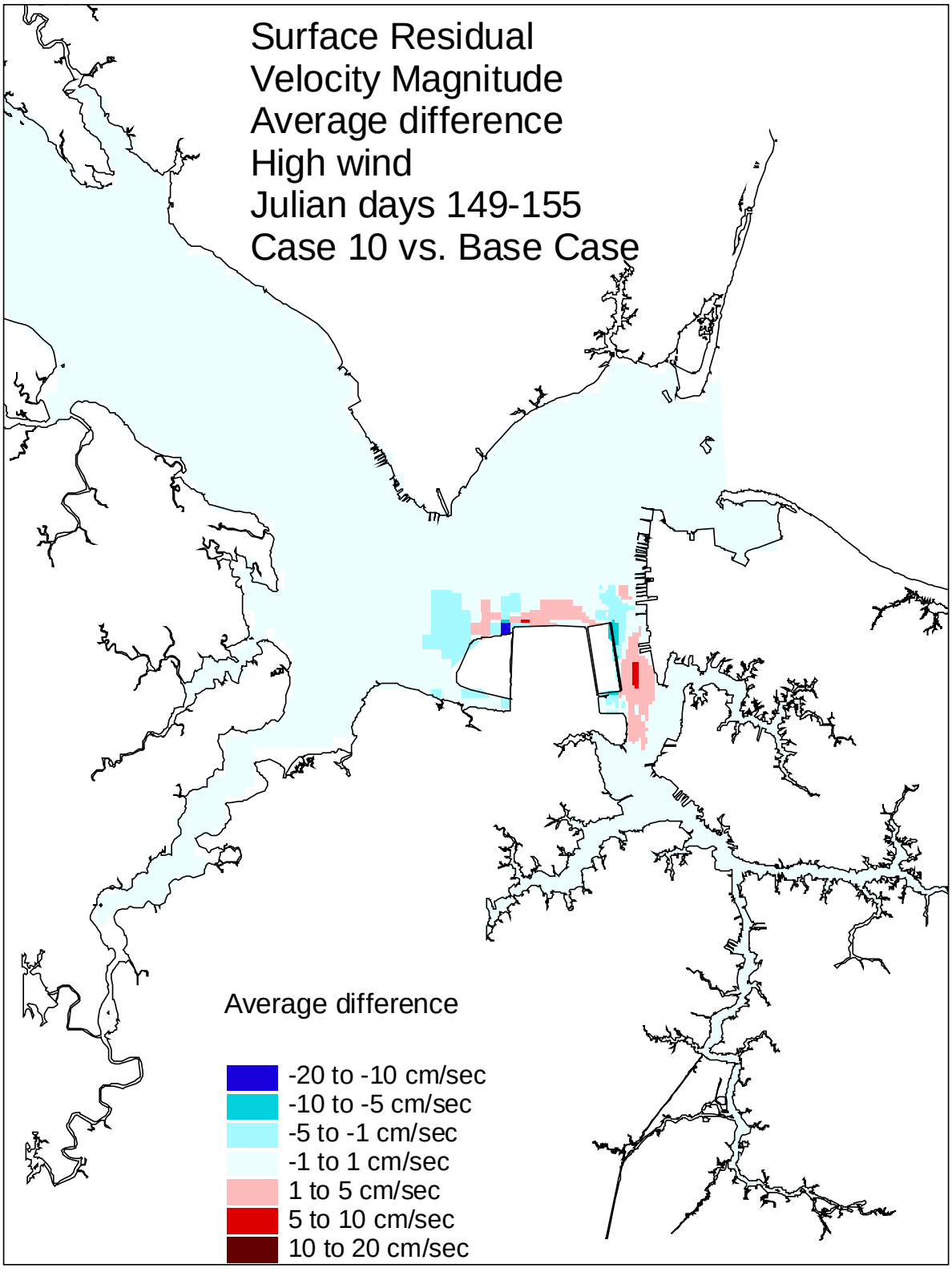

Figure 78. Historical simulation comparison (high wind) of the surface residual velocity average difference for the Eastward and Westward Expansion (Option 7/5a, 50-foot channel) versus the Base Case.

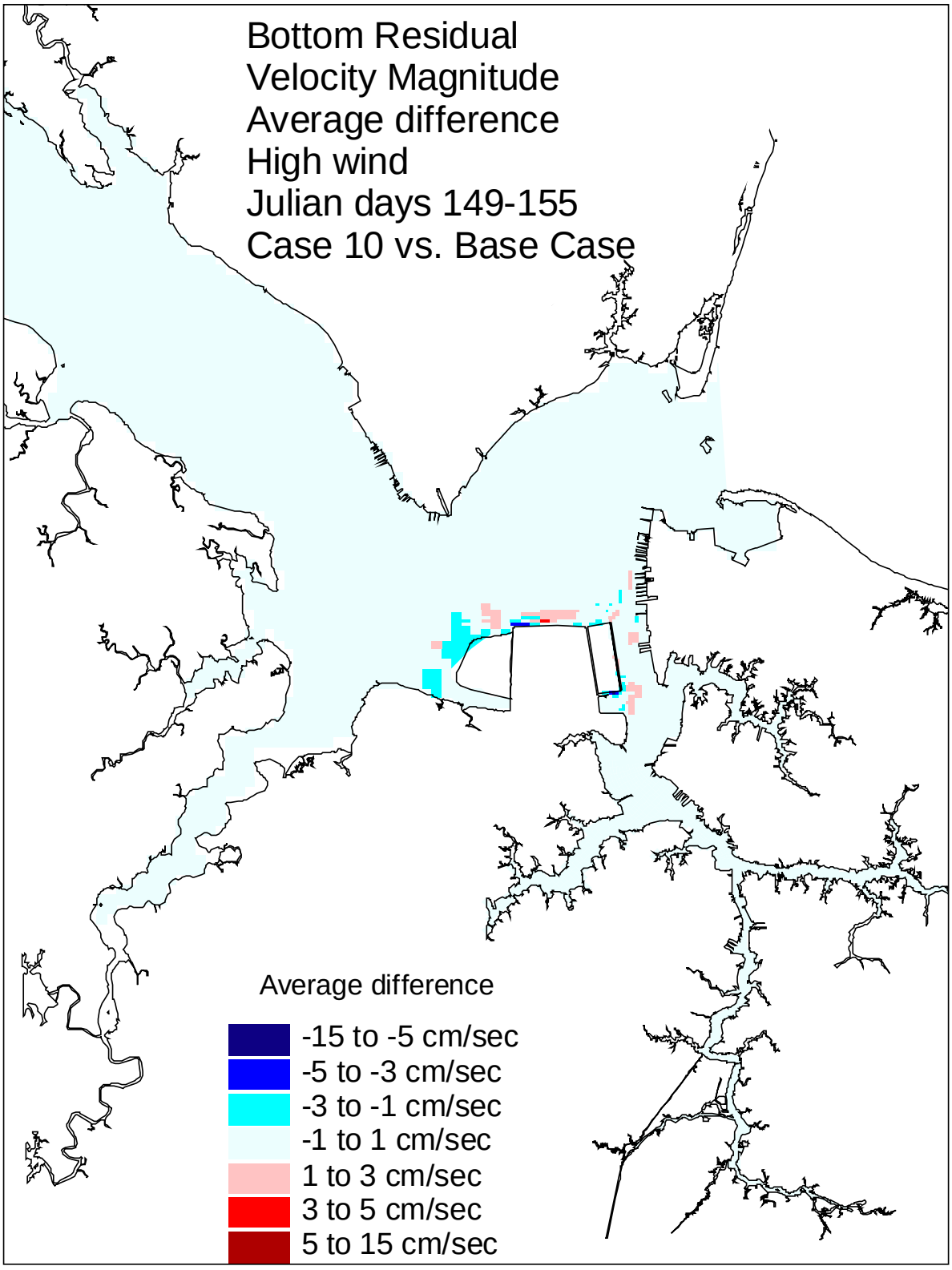

Figure 79. Historical simulation comparison (high wind) of the bottom residual velocity average difference for the Eastward and Westward Expansion (Option 7/5a, 50-foot channel) versus the Base Case.

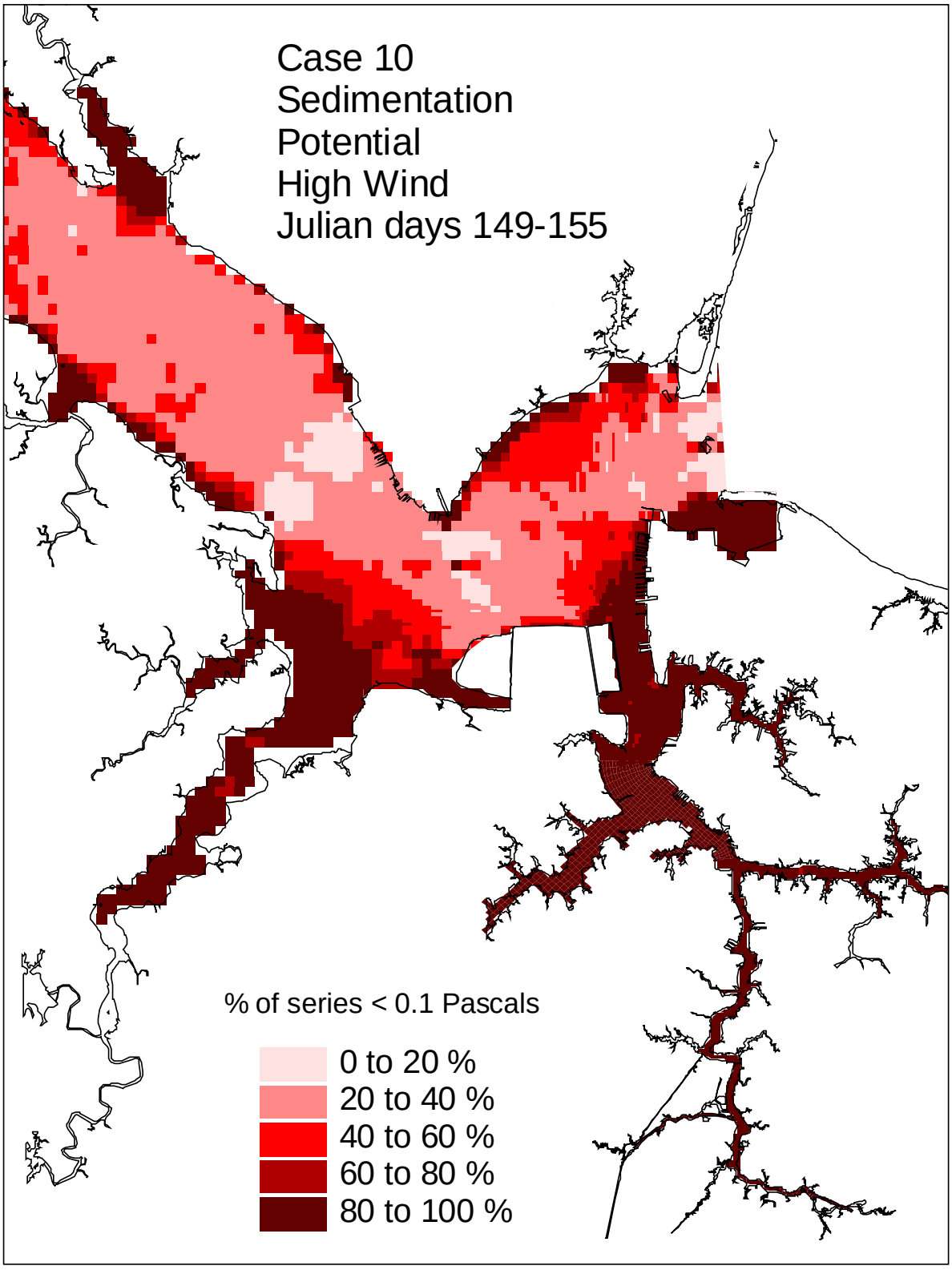

Figure 80. Historical simulation comparison (high wind) of the sedimentation potential for the Eastward and Westward Expansion (Option 7/5a, 50-foot channel).

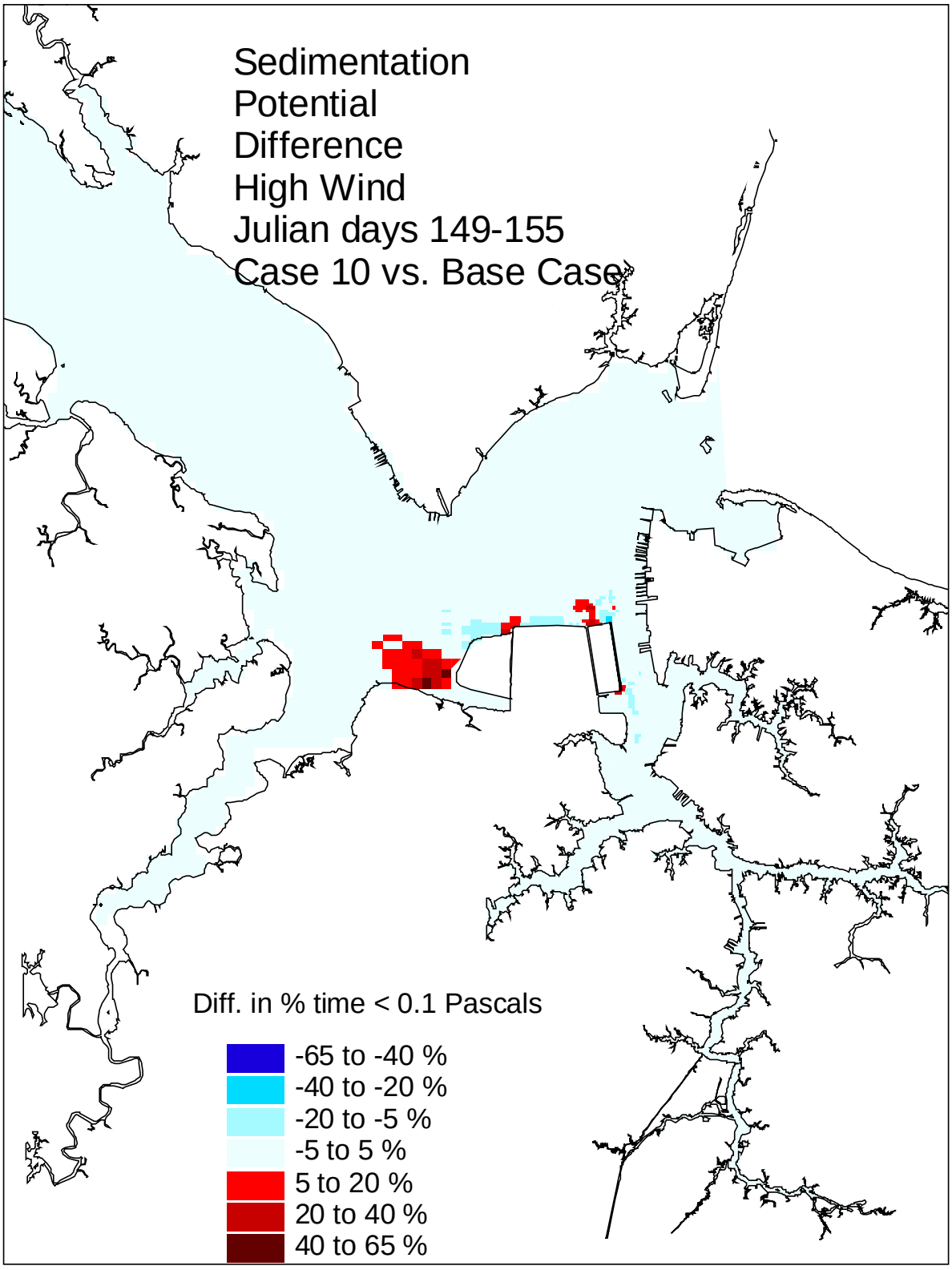

Figure 81. Historical simulation comparison (high wind) of the sedimentation potential difference for the Eastward and Westward Expansion (Option 7/5a, 50-foot channel) versus the Base Case.

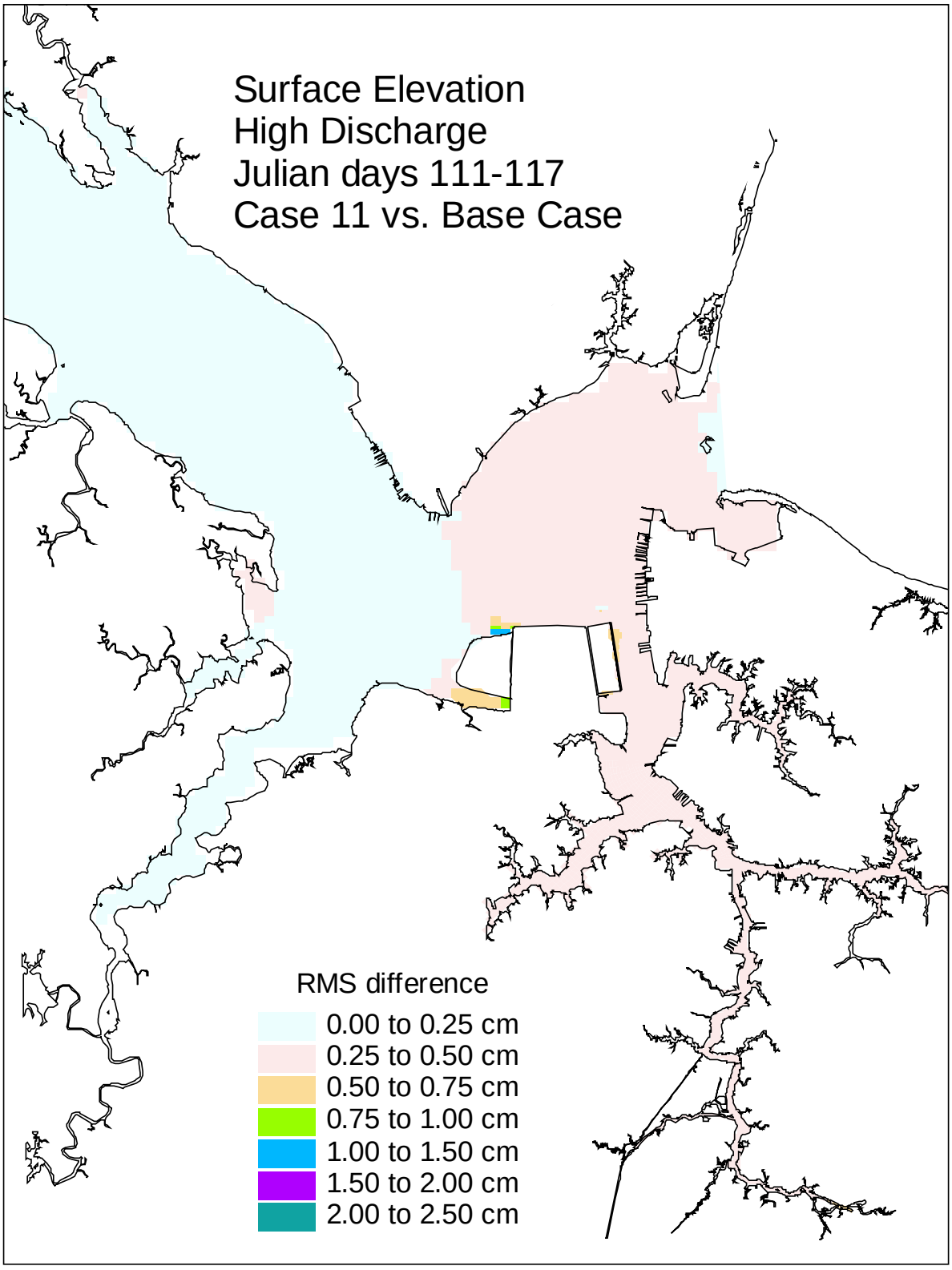

Figure 82. Historical simulation comparison (high discharge) of the surface elevation RMS difference for the Eastward and Westward Expansion (Option 7/5a, 55-foot channel) versus the Base Case.

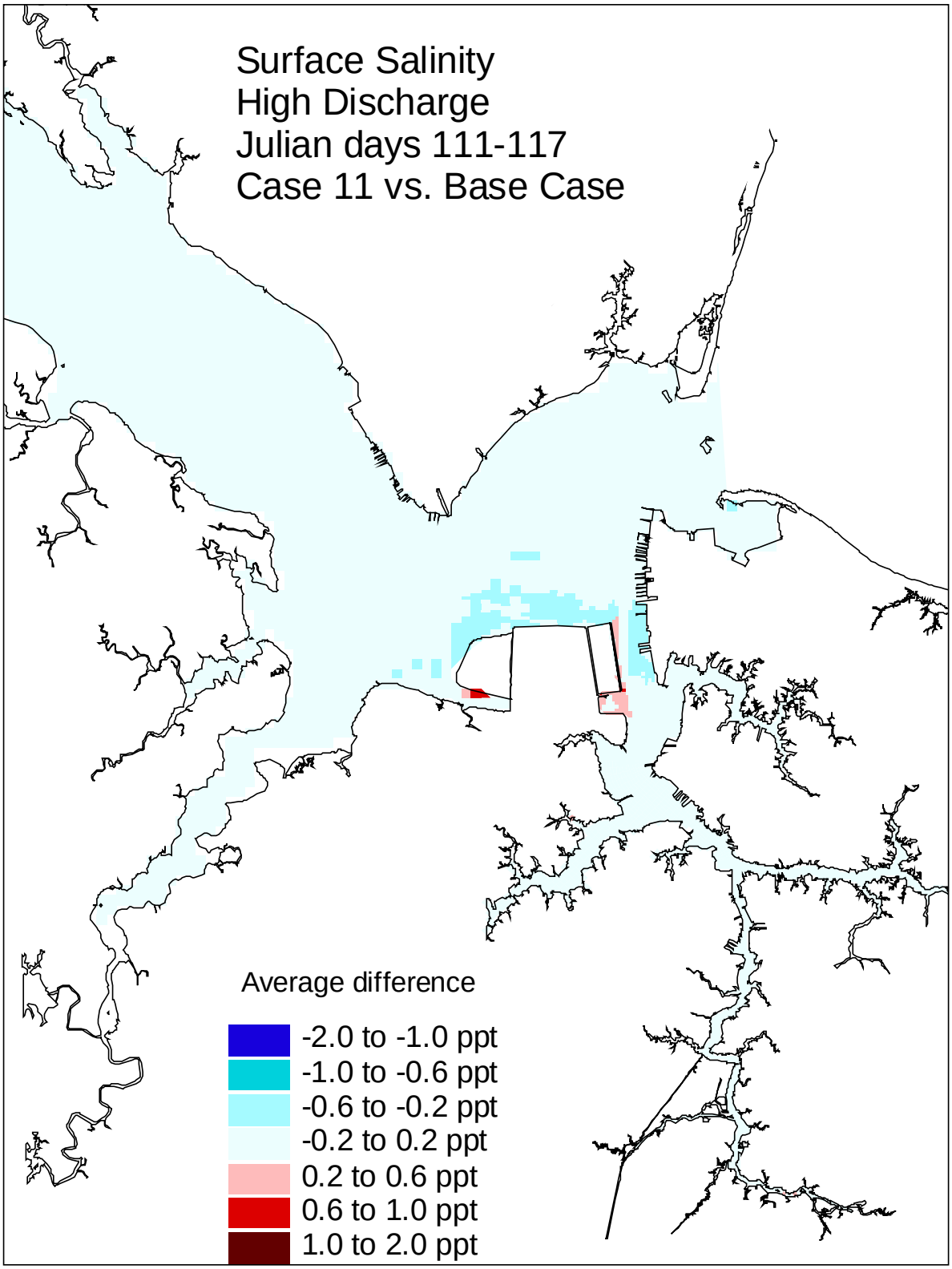

Figure 83. Historical simulation comparison (high discharge) of the surface salinity average difference for the Eastward and Westward Expansion (Option 7/5a, 55-foot channel) versus the Base Case.

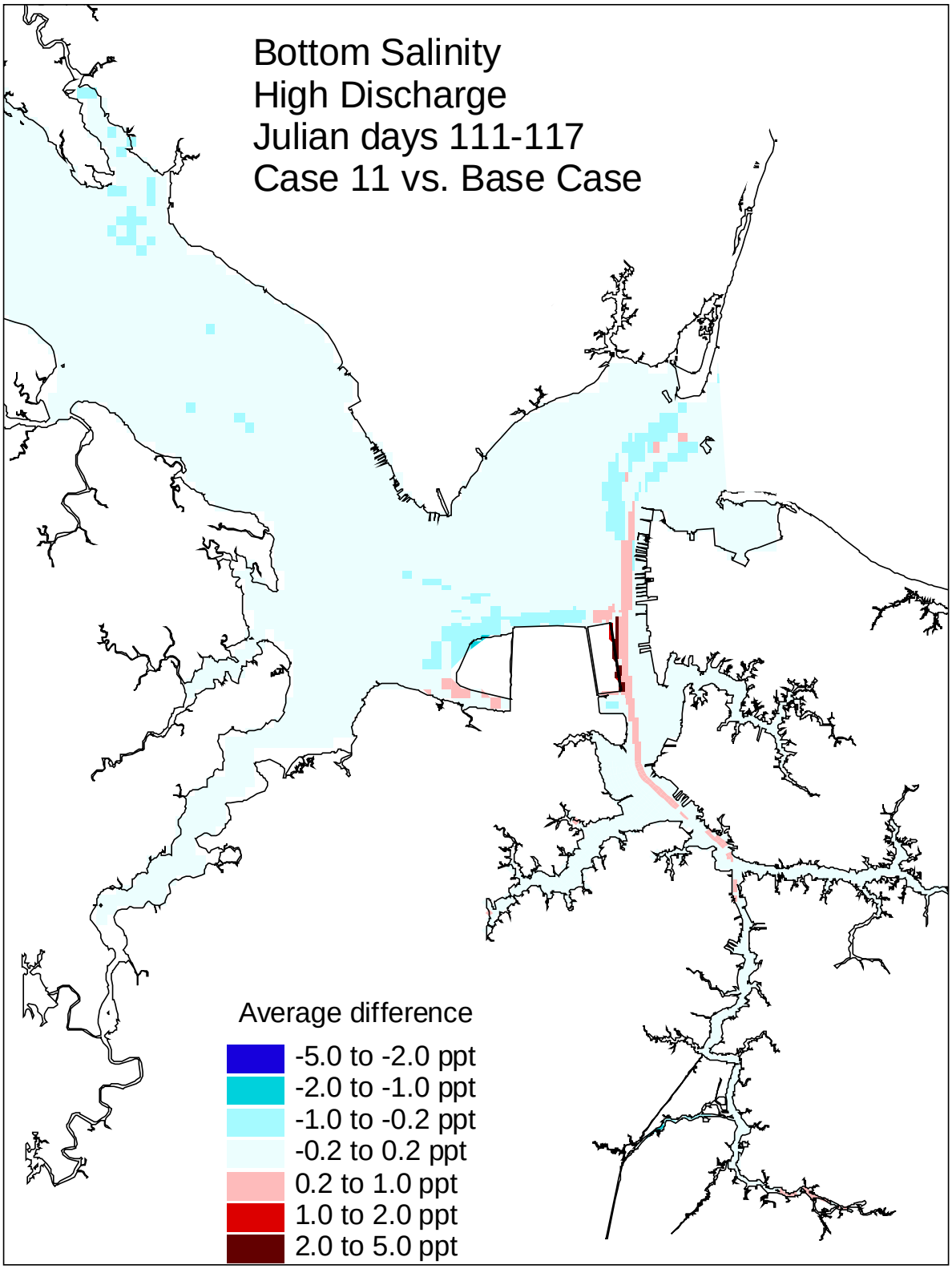

Figure 84. Historical simulation comparison (high discharge) of the bottom salinity average difference for the Eastward and Westward Expansion (Option 7/5a, 55-foot channel) versus the Base Case.

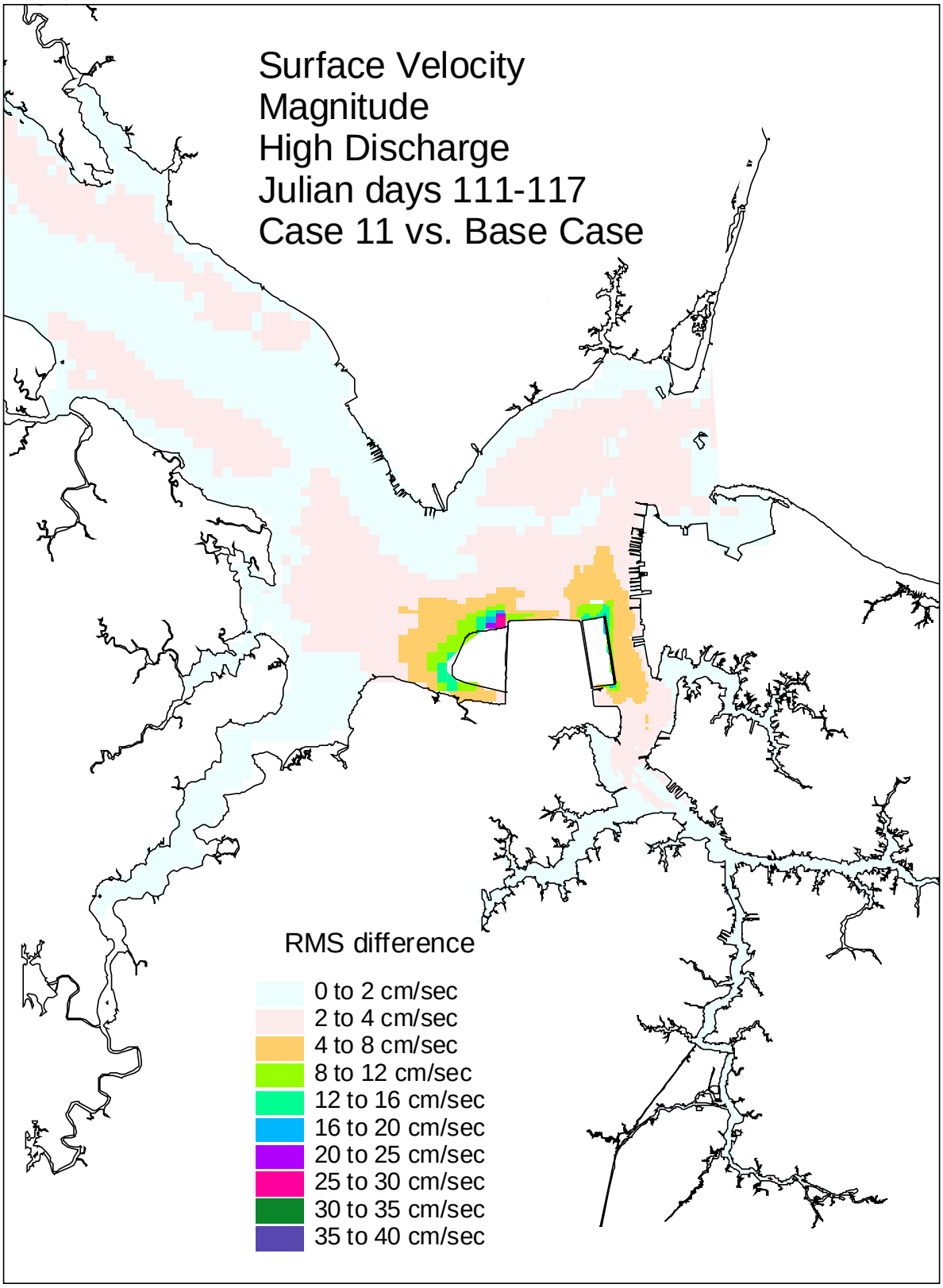

Figure 85. Historical simulation comparison (high discharge) of the surface velocity RMS difference for the Eastward and Westward Expansion (Option 7/5a, 55-foot channel) versus the Base Case.

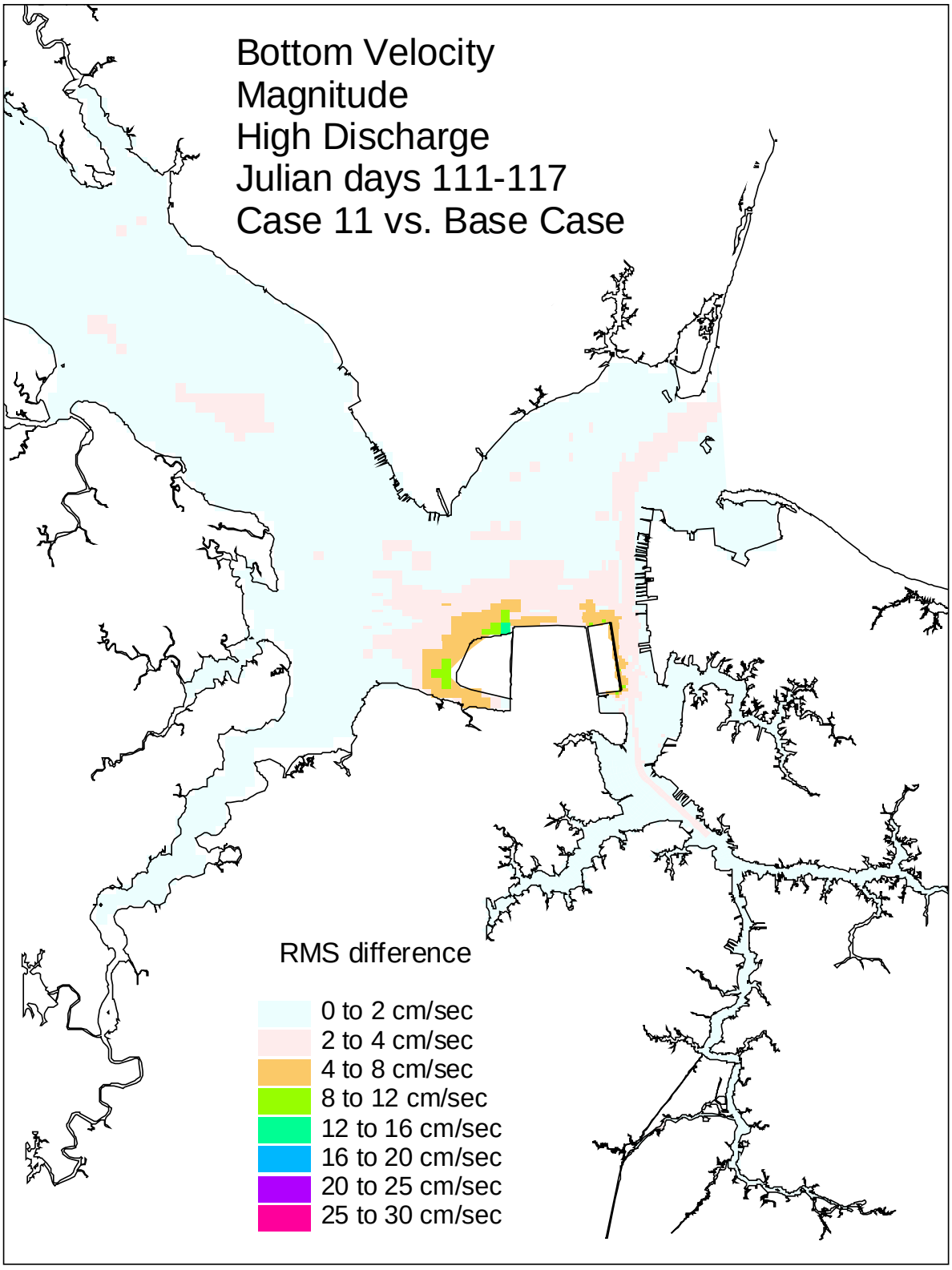

Figure 86. Historical simulation comparison (high discharge) of the bottom velocity RMS difference for the Eastward and Westward Expansion (Option 7/5a, 55-foot channel) versus the Base Case.

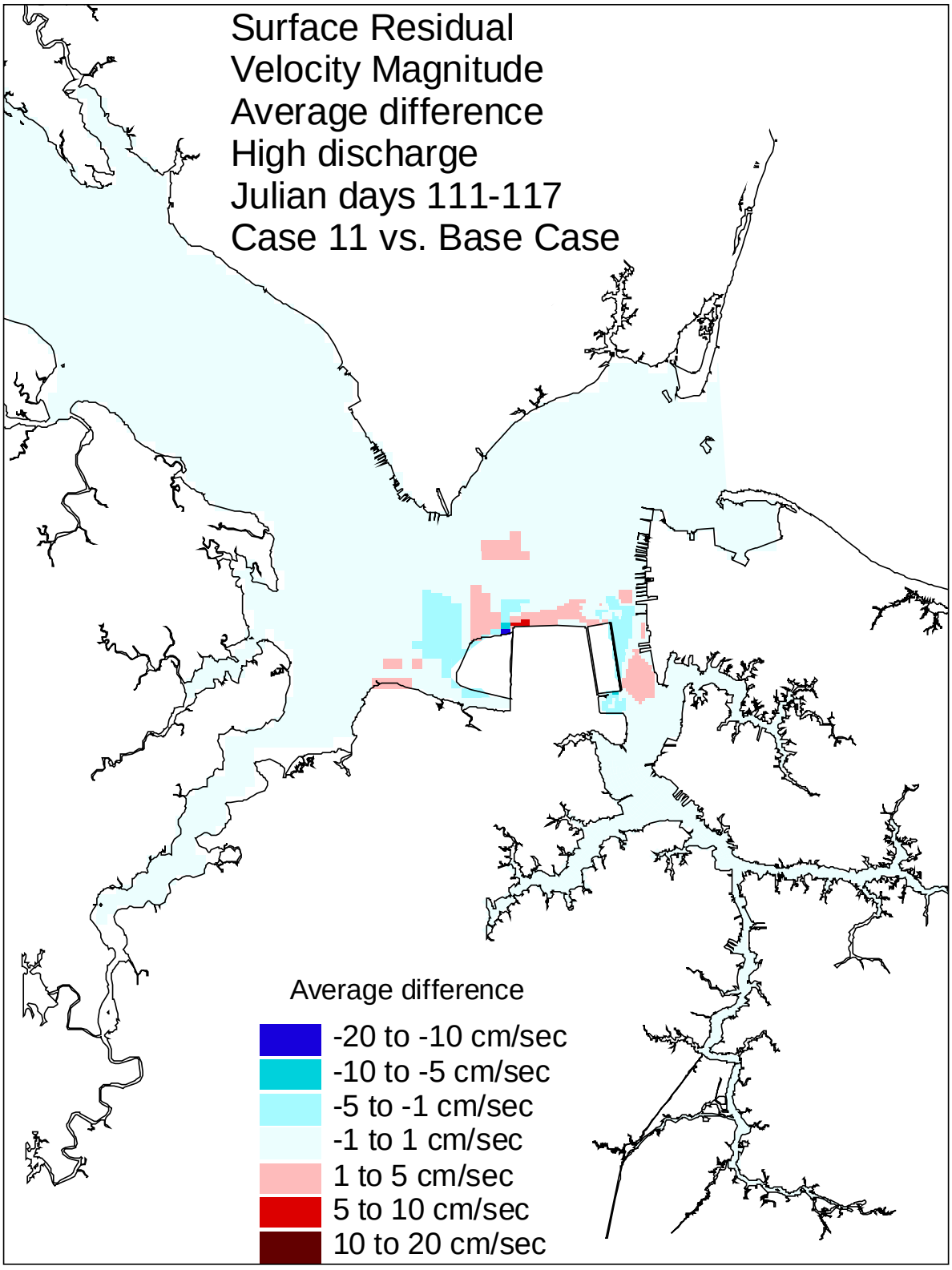

Figure 87. Historical simulation comparison (high discharge) of the surface residual velocity average difference for the Eastward and Westward Expansion (Option 7/5a, 55-foot channel) versus the Base Case.

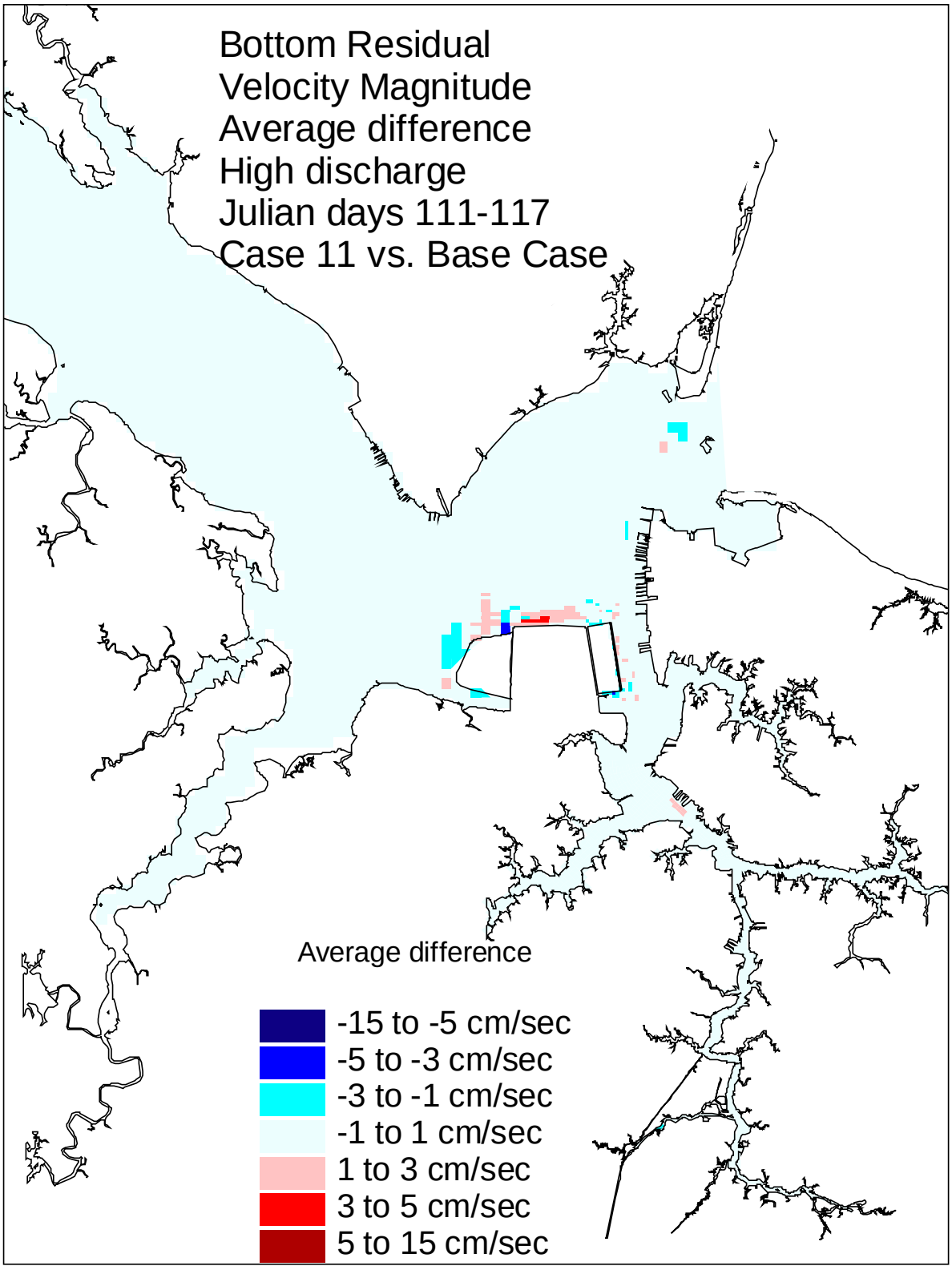

Figure 88. Historical simulation comparison (high discharge) of the bottom residual velocity average difference for the Eastward and Westward Expansion (Option 7/5a, 55-foot channel) versus the Base Case.

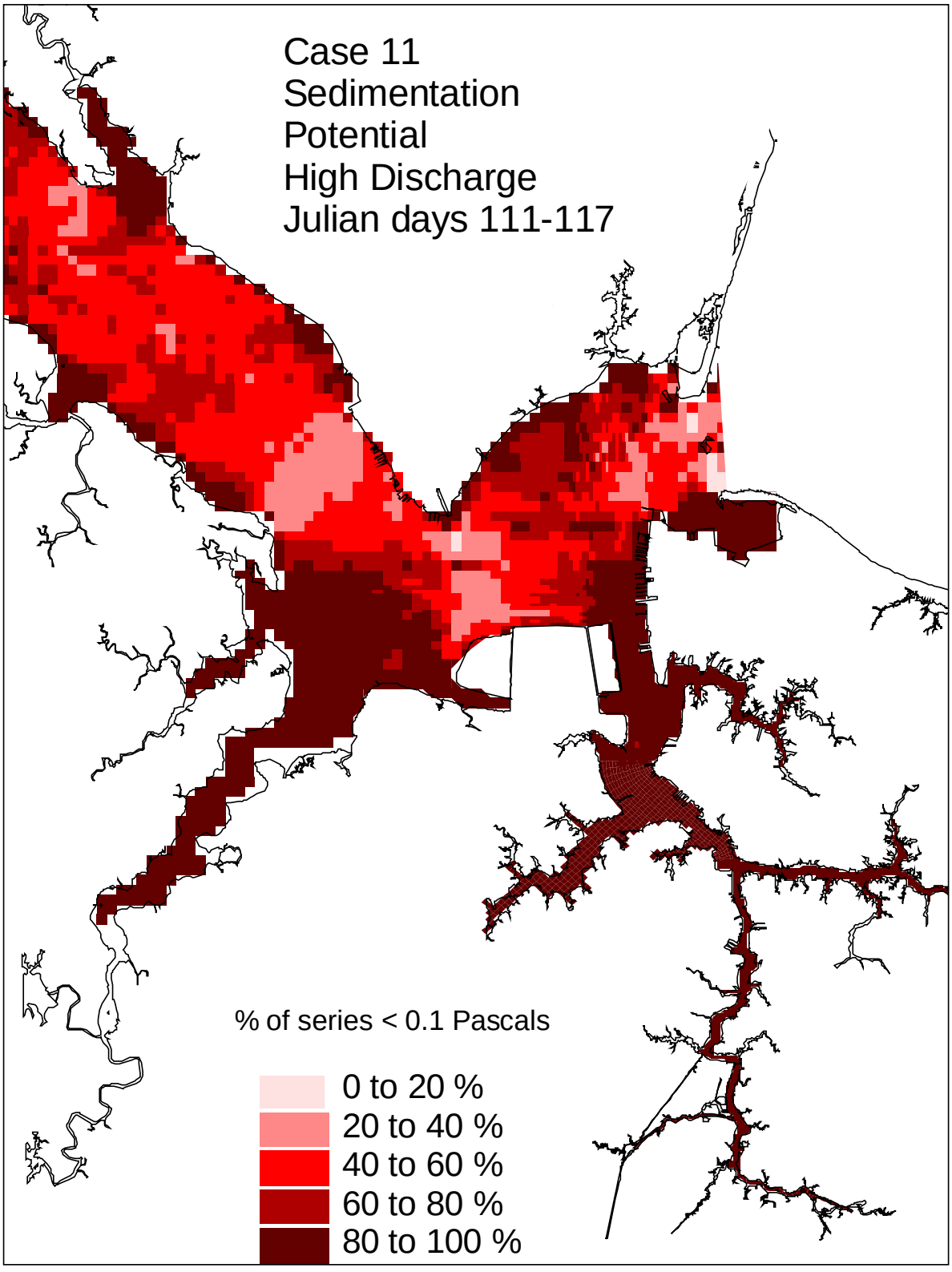

Figure 89. Historical simulation comparison (high discharge) of the sedimentation potential for the Eastward and Westward Expansion (Option 7/5a, 55-foot channel).

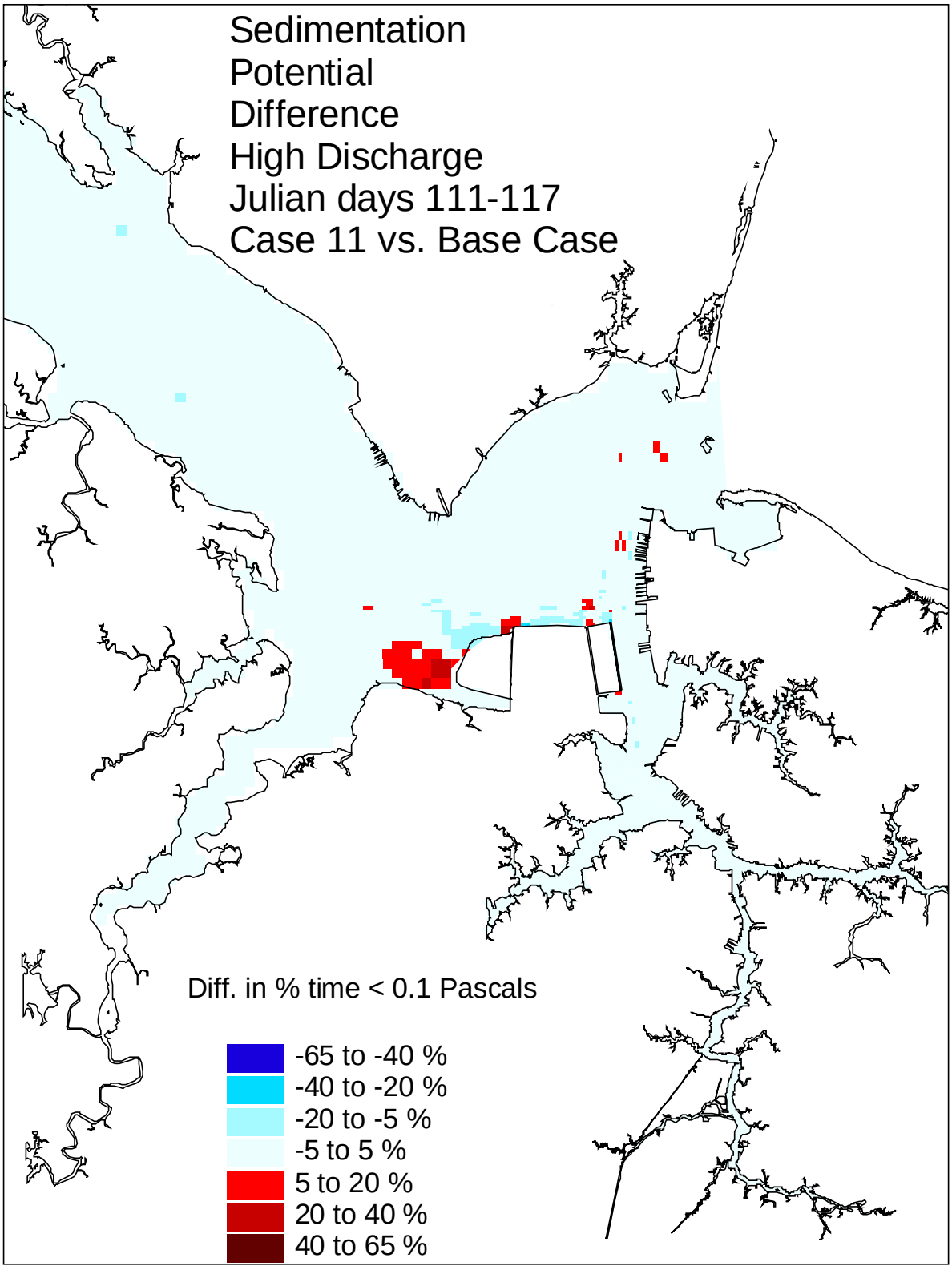

Figure 90. Historical simulation comparison (high discharge) of sedimentation potential difference for the Eastward and Westward Expansion (Option 7/5a, 55-foot channel) versus the Base Case.

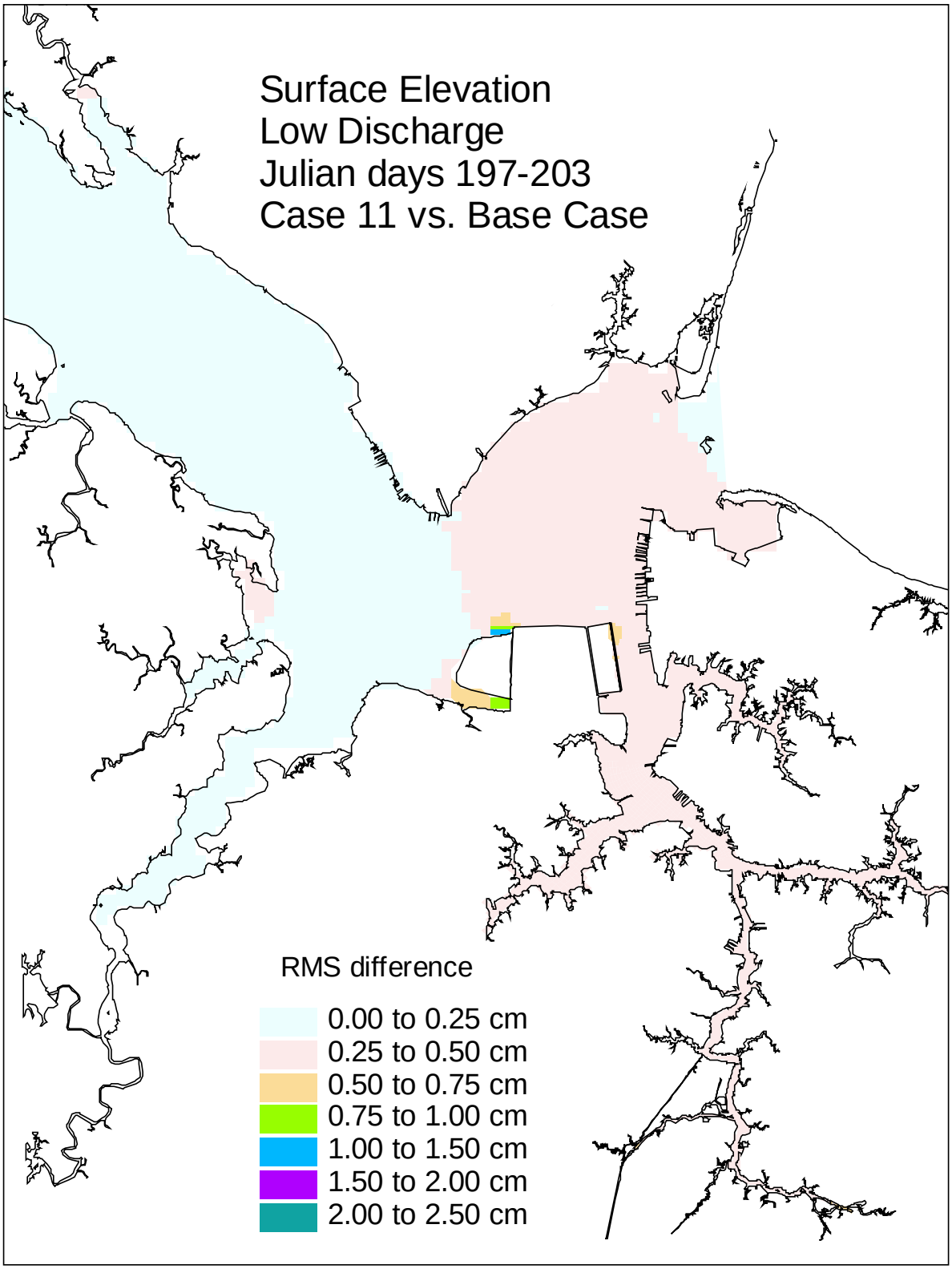

Figure 91. Historical simulation comparison (low discharge) of the surface elevation RMS difference for the Eastward and Westward Expansion (Option 7/5a, 55-foot channel) versus the Base Case.

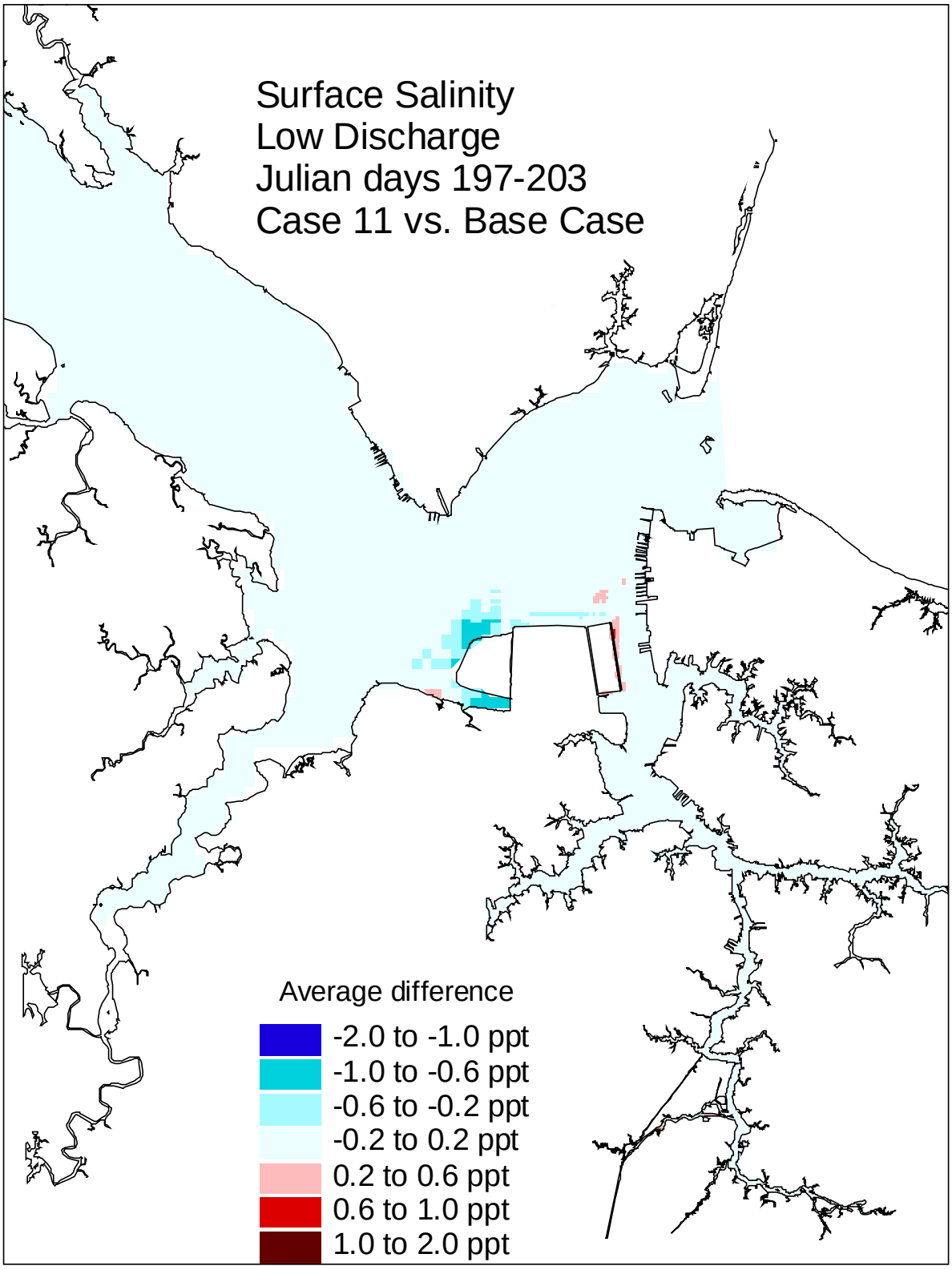

Figure 92. Historical simulation comparison (low discharge) of the surface salinity average difference for the Eastward and Westward Expansion (Option 7/5a, 55-foot channel) versus the Base Case.

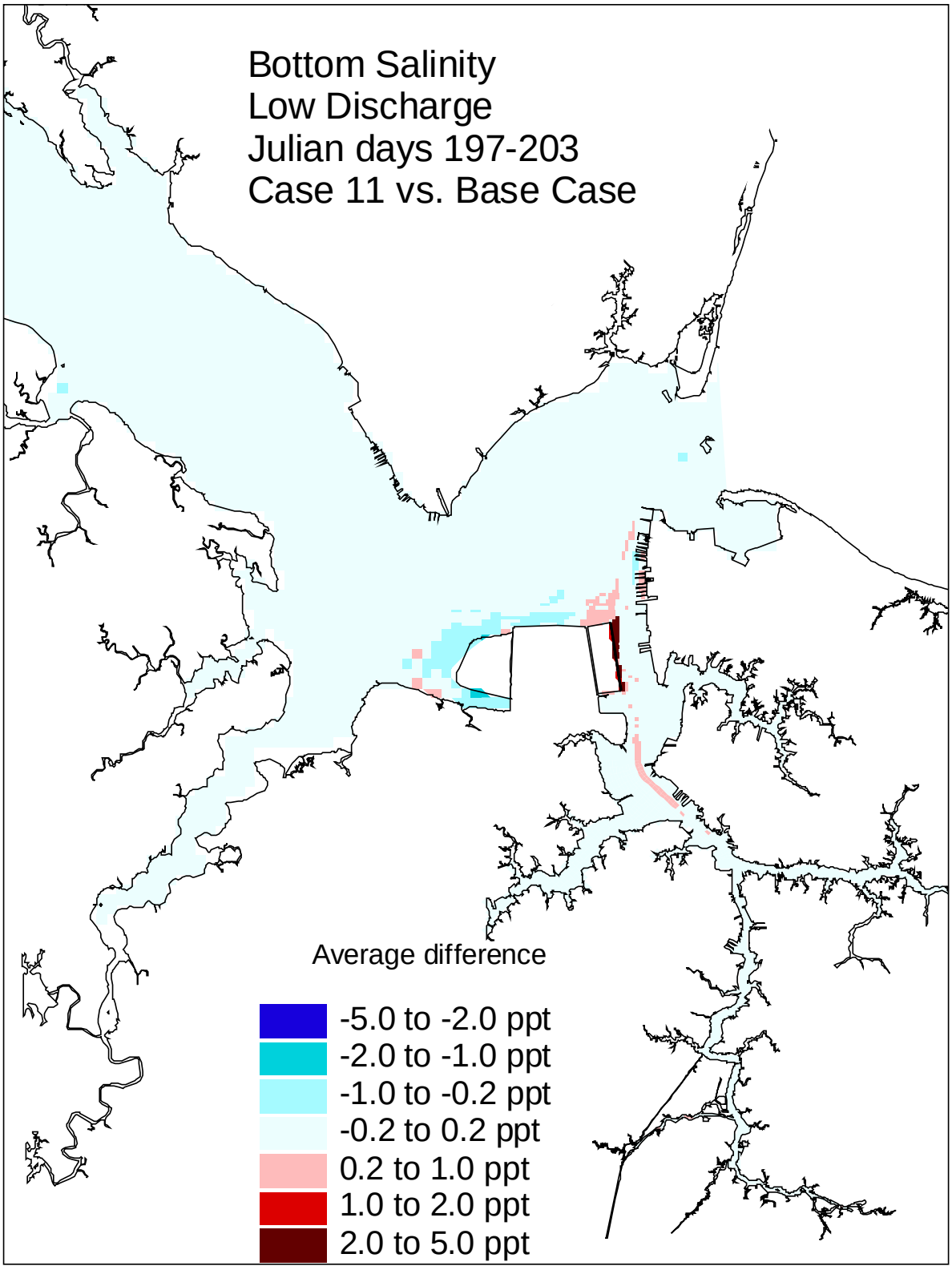

Figure 93. Historical simulation comparison (low discharge) of the bottom salinity average difference for the Eastward and Westward Expansion (Option 7/5a, 55-foot channel) versus the Base Case.

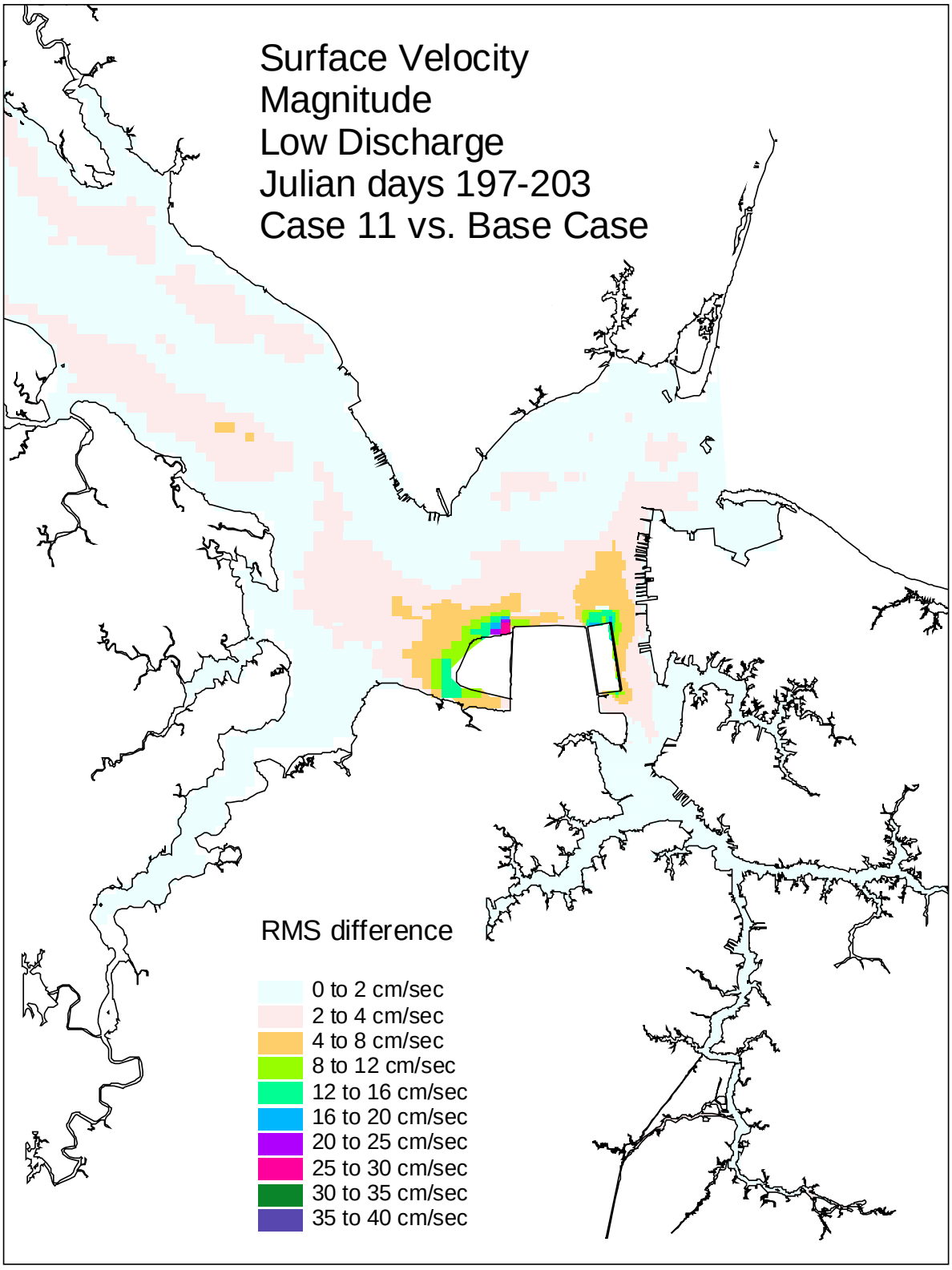

Figure 94. Historical simulation comparison (low discharge) of the surface velocity RMS difference for the Eastward and Westward Expansion (Option 7/5a, 55-foot channel) versus the Base Case.

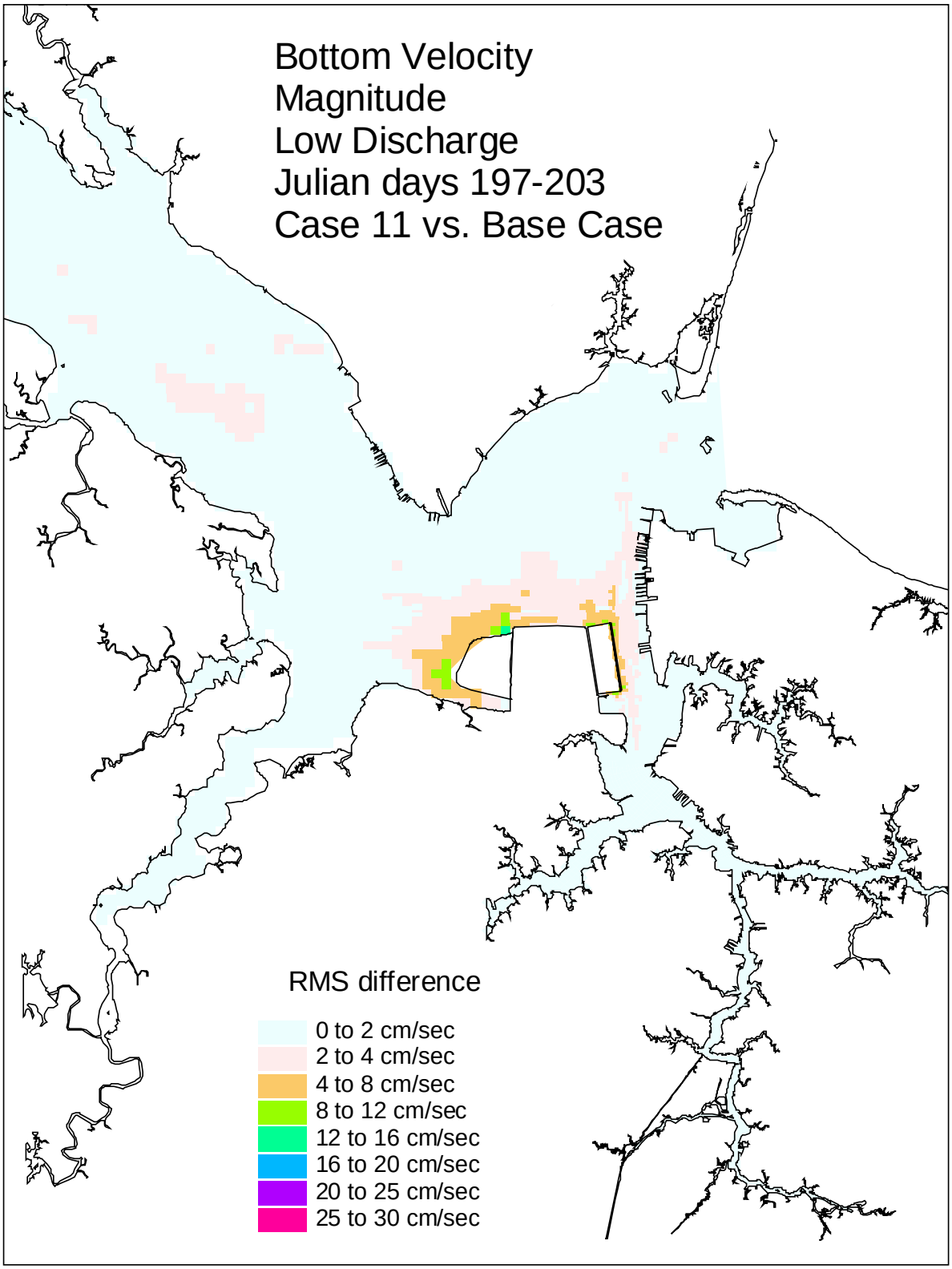

Figure 95. Historical simulation comparison (low discharge) of the bottom velocity RMS difference for the Eastward and Westward Expansion (Option 7/5a, 55-foot channel) versus the Base Case.

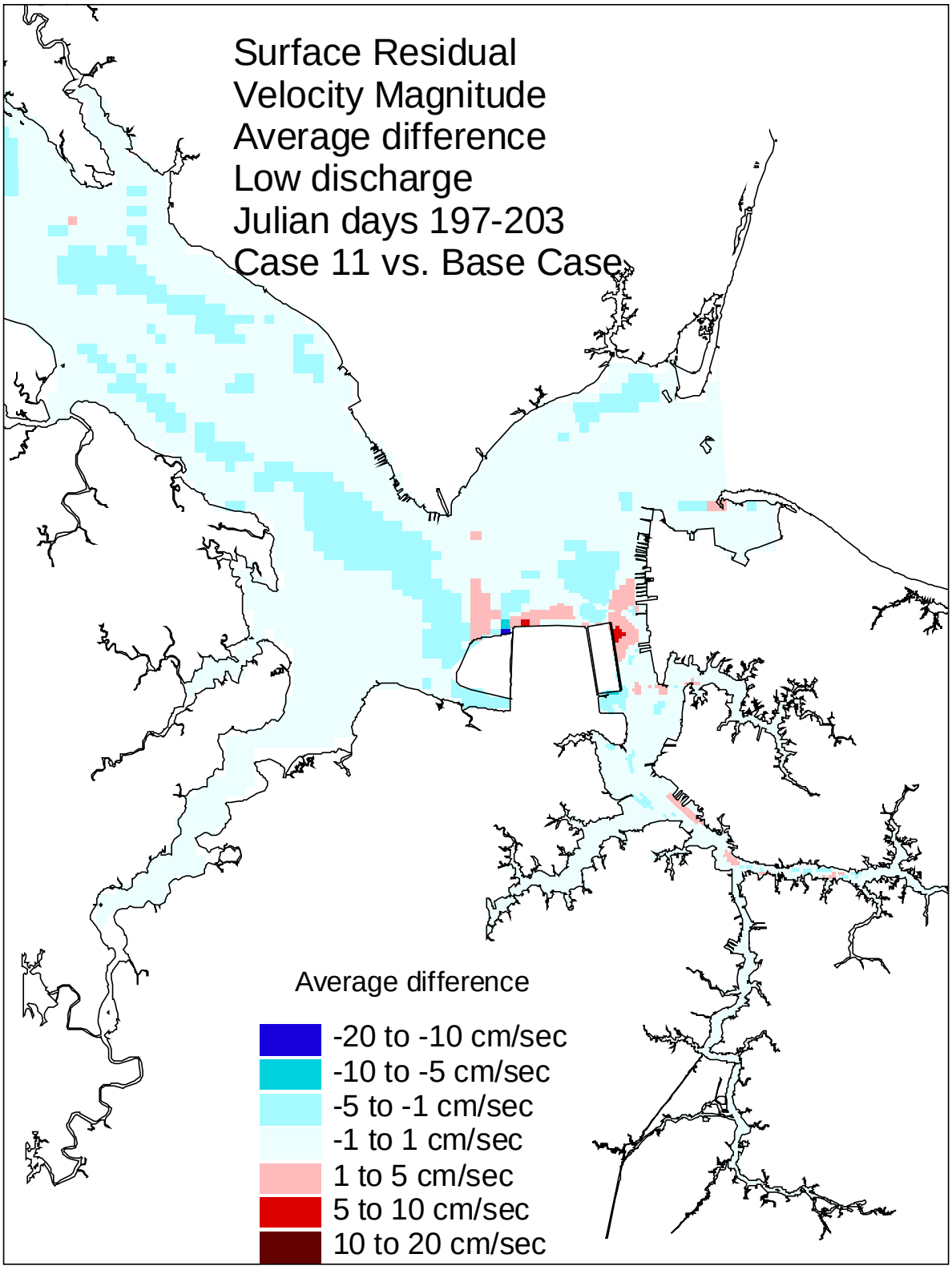

Figure 96. Historical simulation comparison (low discharge) of the surface residual velocity average difference for the Eastward and Westward Expansion (Option 7/5a, 55-foot channel) versus the Base Case.

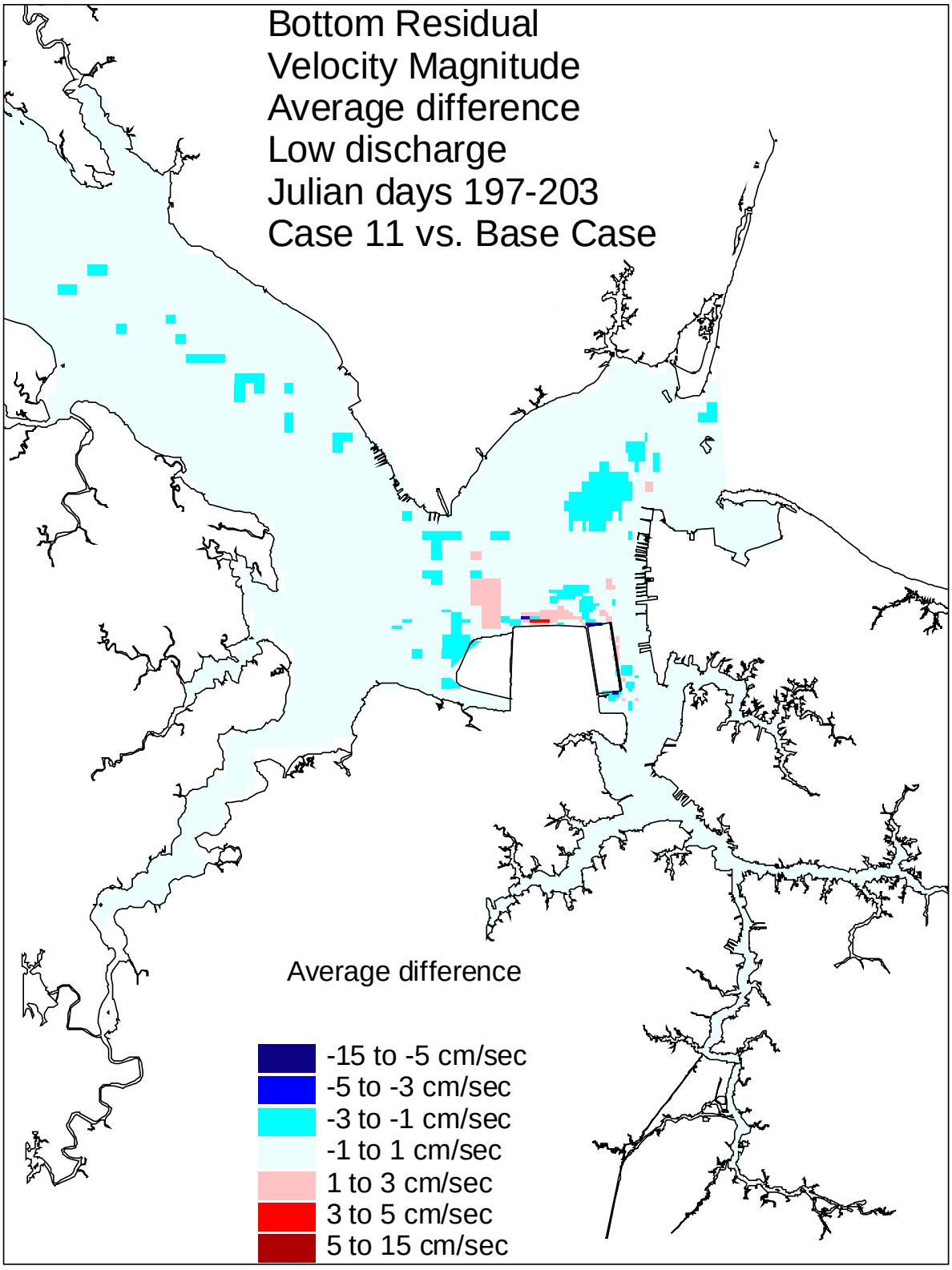

Figure 97. Historical simulation comparison (low discharge) of the bottom residual velocity average difference for the Eastward and Westward Expansion (Option 7/5a, 55-foot channel) versus the Base Case.

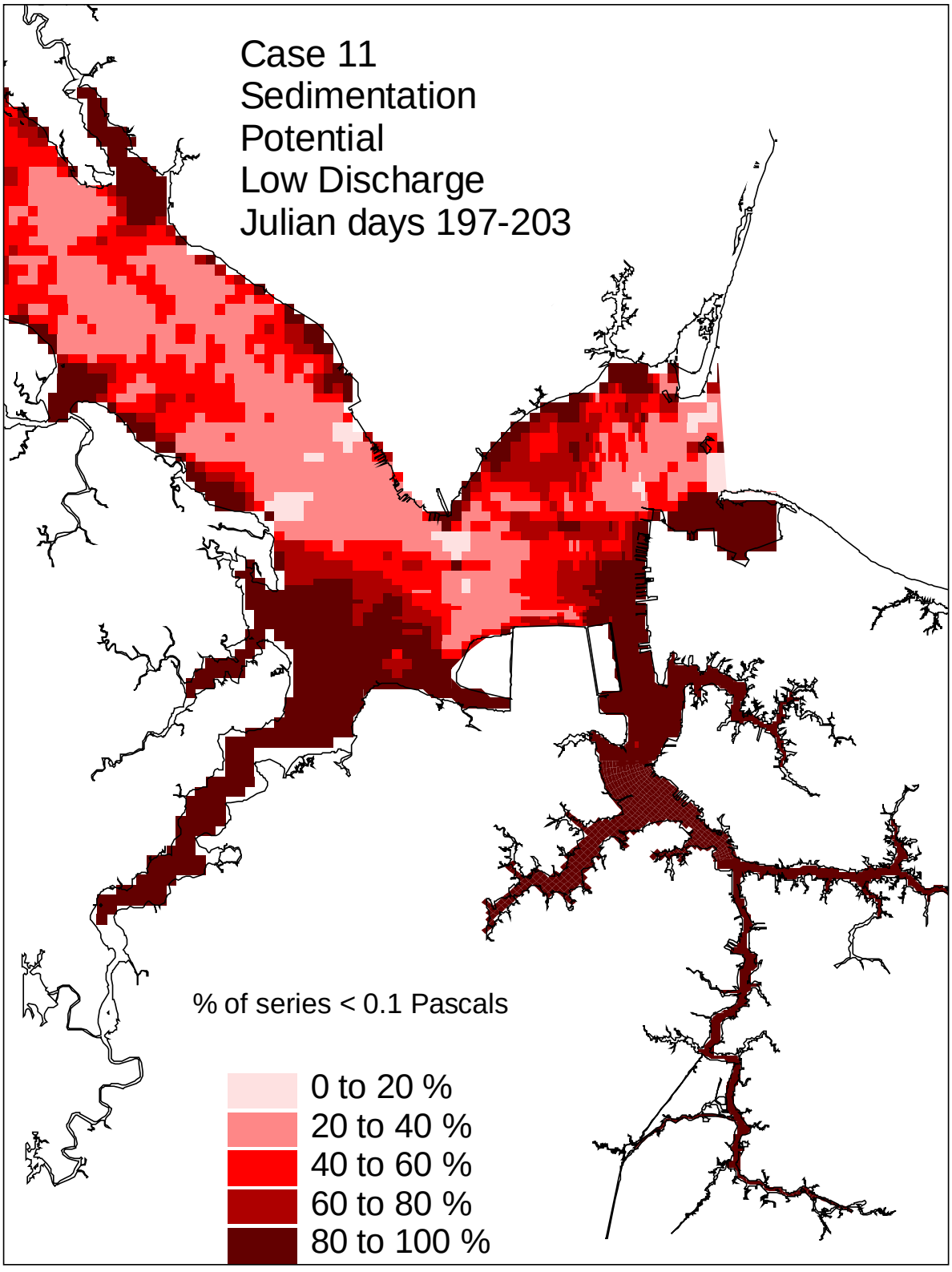

Figure 98. Historical simulation comparison (low discharge) of the sedimentation potential for the Eastward and Westward Expansion (Option 7/5a, 55-foot channel).

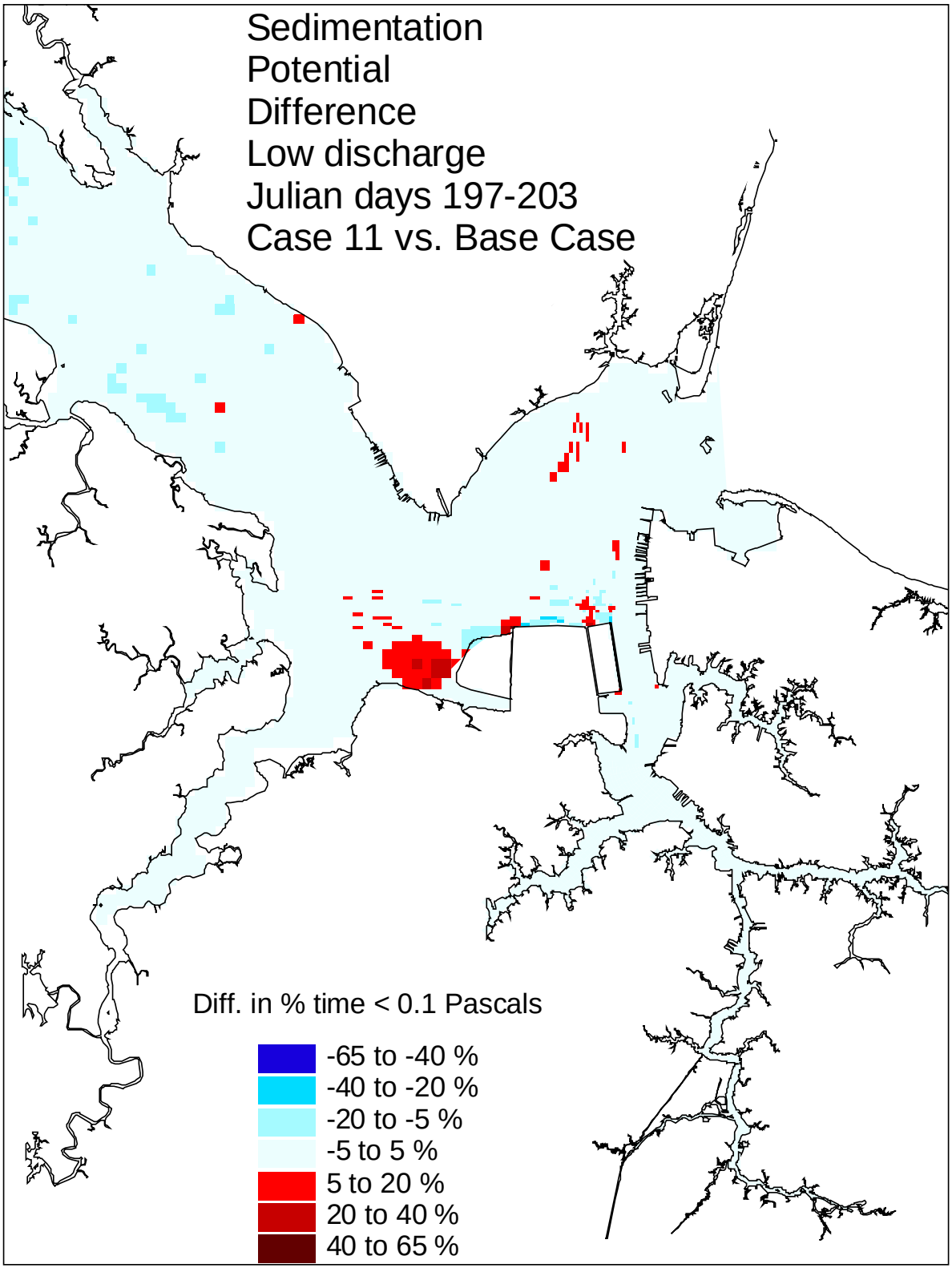

Figure 99. Historical simulation comparison (low discharge) of sedimentation potential difference for the Eastward and Westward Expansion (Option 7/5a, 55-foot channel) versus the Base Case.

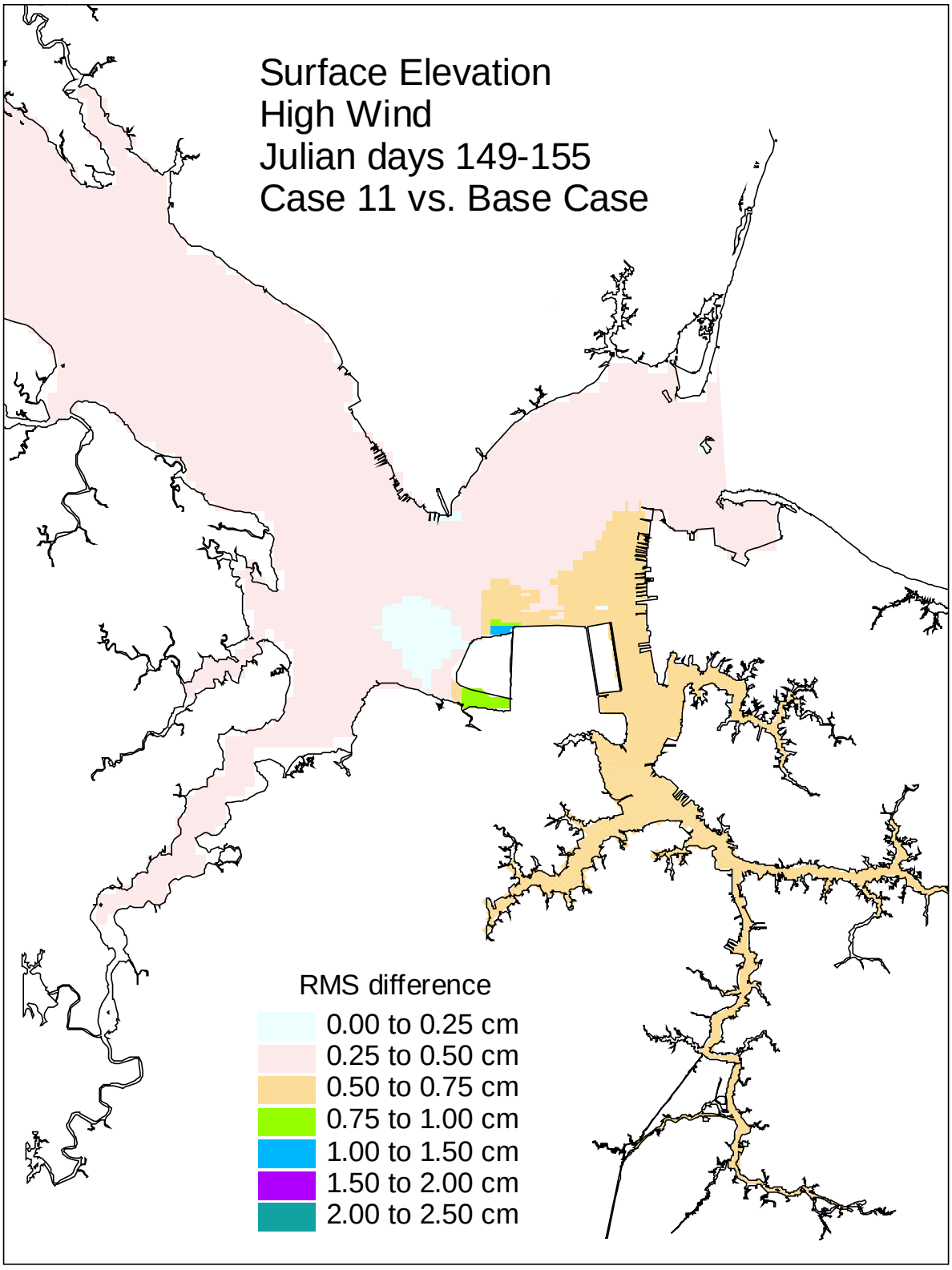

Figure 100. Historical simulation comparison (high wind) of the surface elevation RMS difference for the Eastward and Westward Expansion (Option 7/5a, 55-foot channel) versus the Base Case.

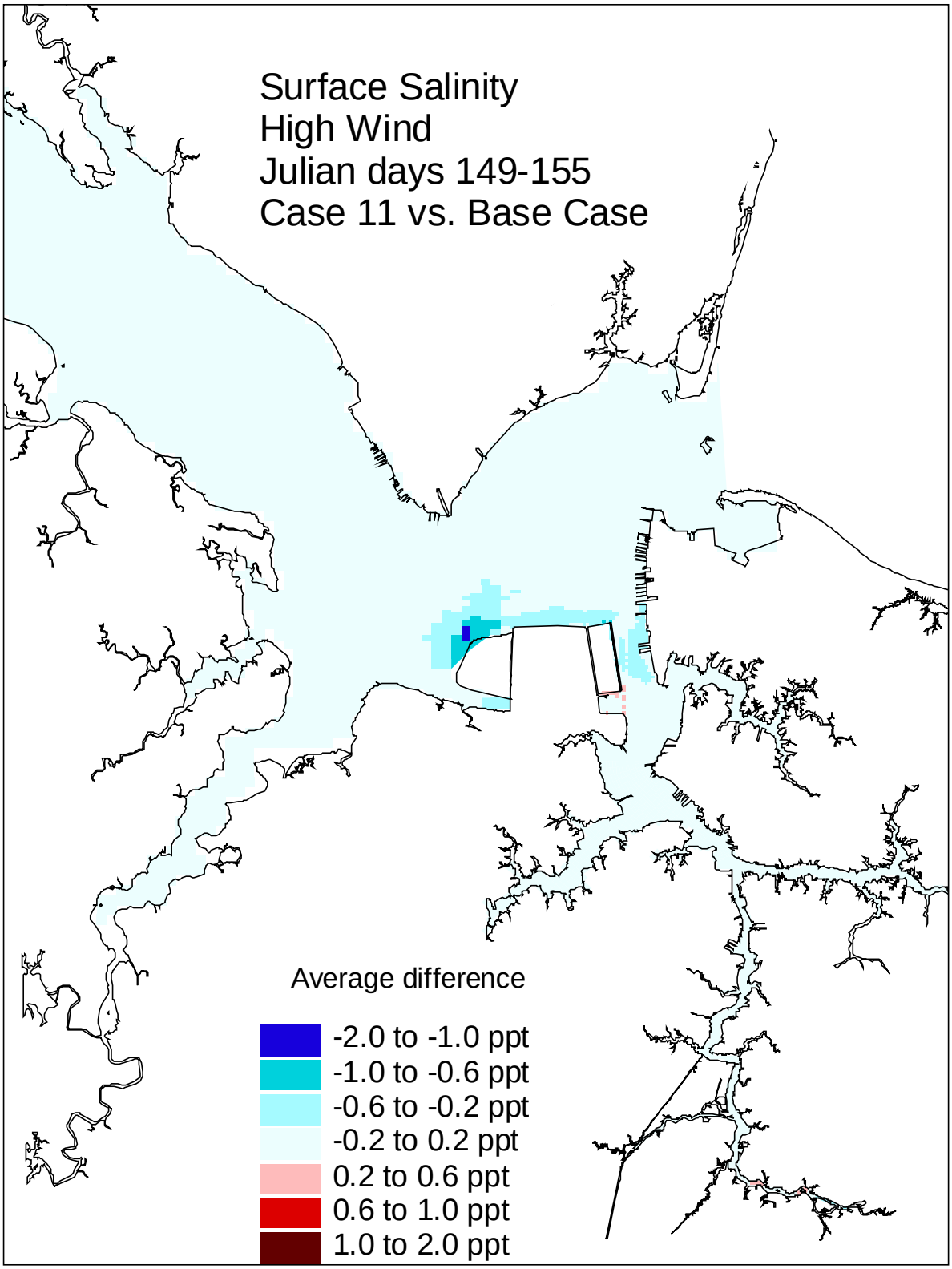

Figure 101. Historical simulation comparison (high wind) of the surface salinity average difference for the Eastward and Westward Expansion (Option 7/5a, 55-foot channel) versus the Base Case.

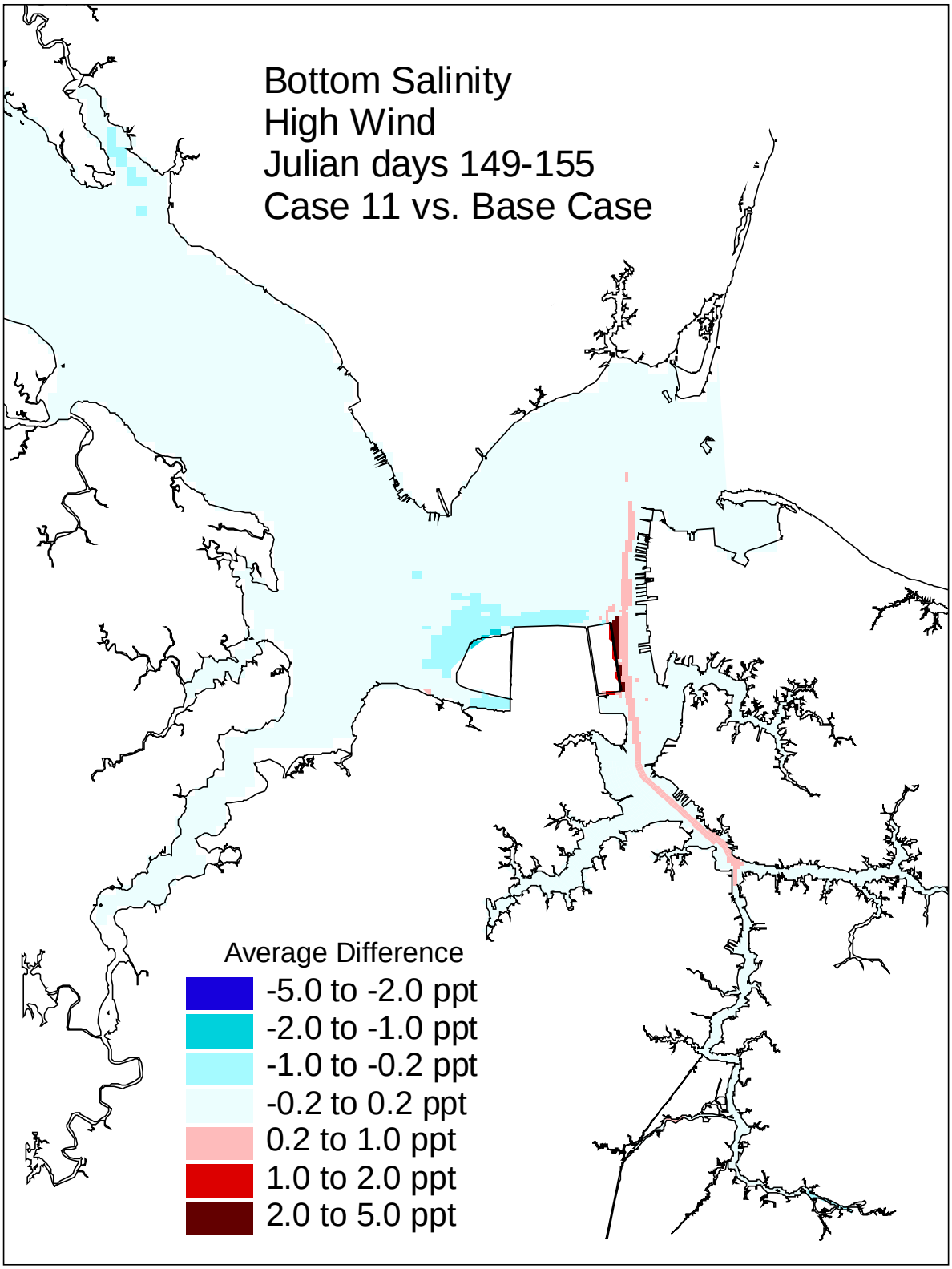

Figure 102. Historical simulation comparison (high wind) of the bottom salinity average difference for the Eastward and Westward Expansion (Option 7/5a, 55-foot channel) versus the Base Case.

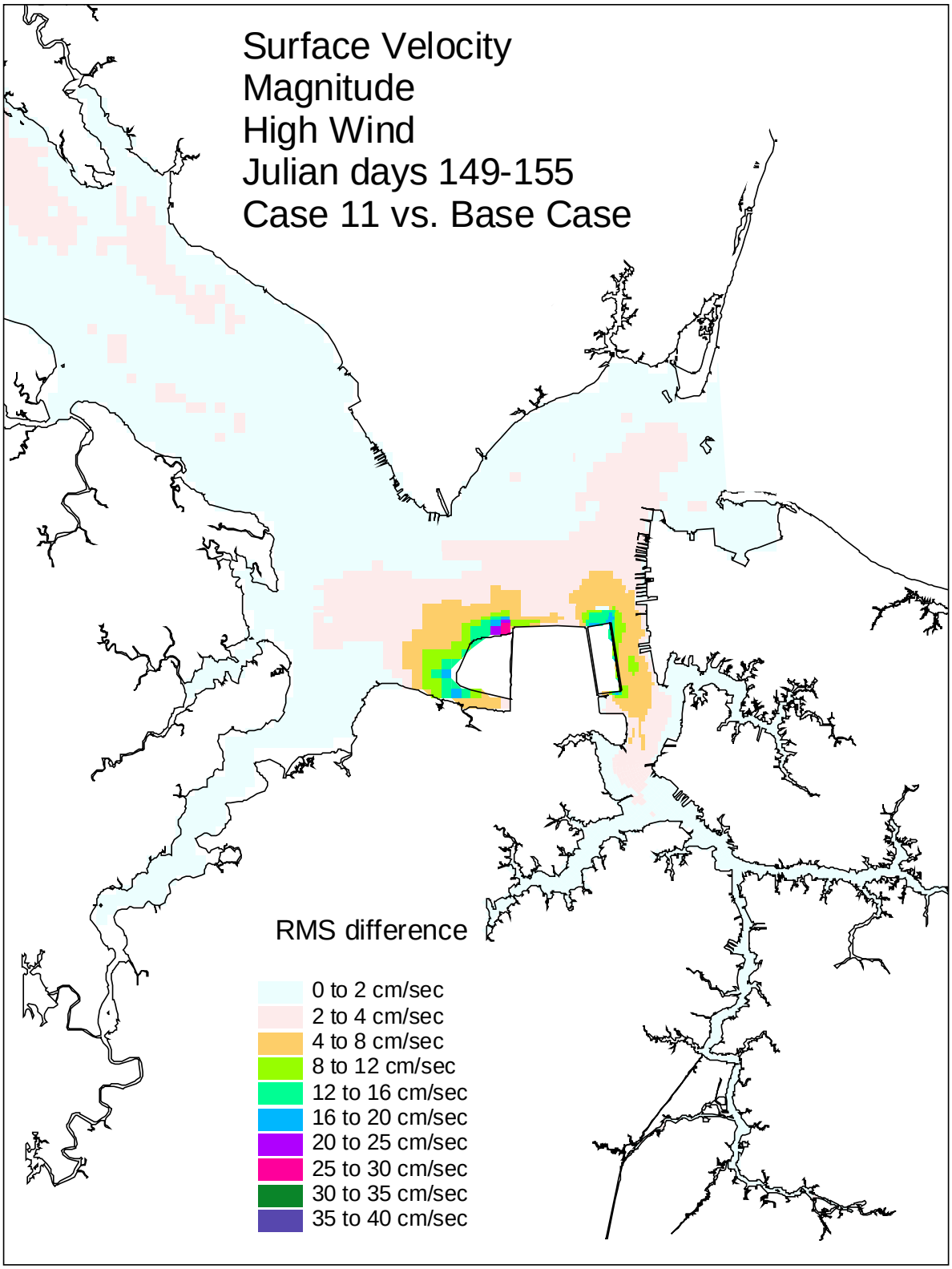

Figure 103. Historical simulation comparison (high wind) of the surface velocity RMS difference for the Eastward and Westward Expansion (Option 7/5a, 55-foot channel) versus the Base Case.

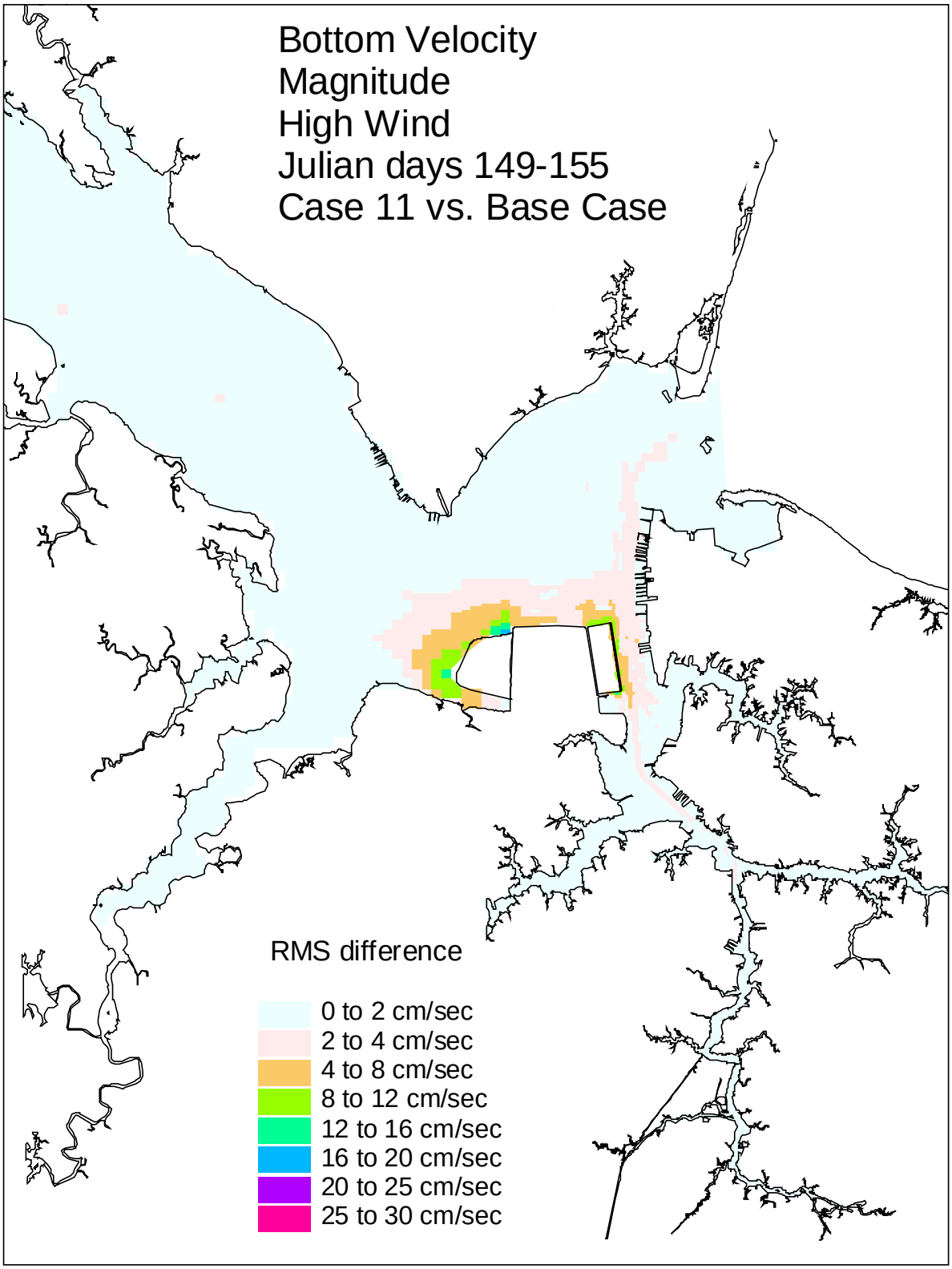

Figure 104. Historical simulation comparison (high wind) of the bottom velocity RMS difference for the Eastward and Westward Expansion (Option 7/5a, 55-foot channel) versus the Base Case.

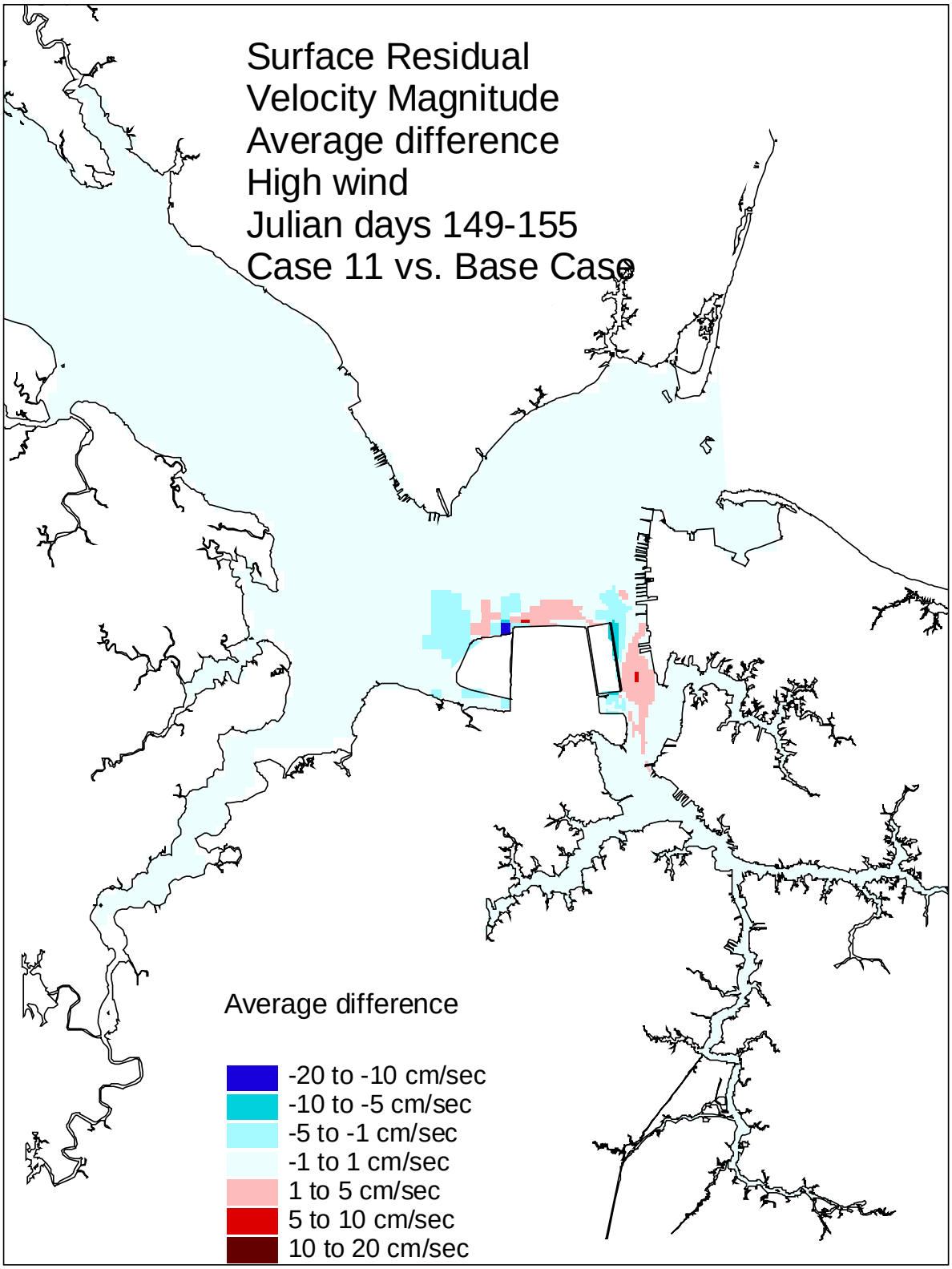

Figure 105. Historical simulation comparison (high wind) of the surface residual velocity average difference for the Eastward and Westward Expansion (Option 7/5a, 55-foot channel) versus the Base Case.

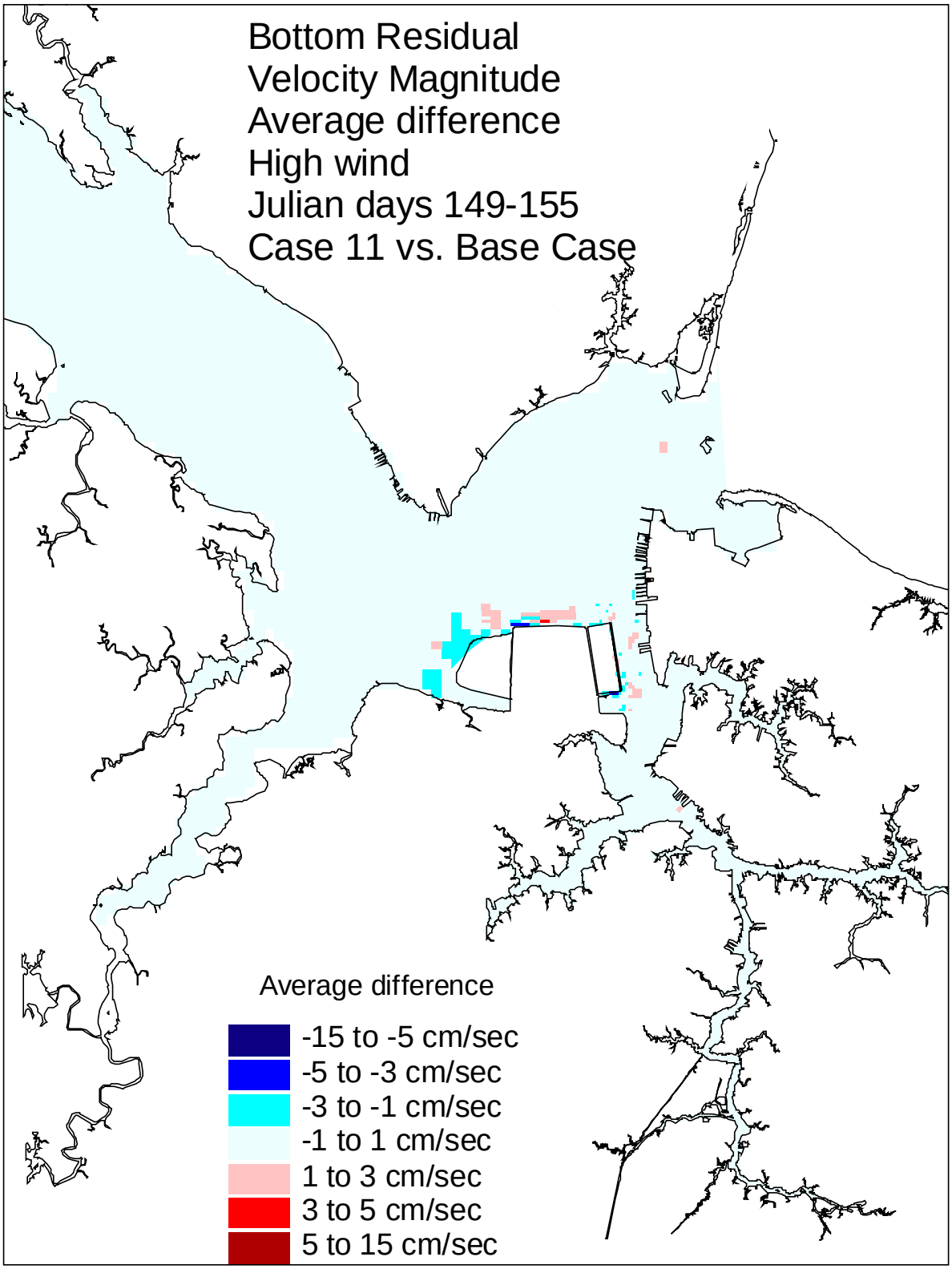

Figure 106. Historical simulation comparison (high wind) of the bottom residual velocity average difference for the Eastward and Westward Expansion (Option 7/5a, 55-foot channel) versus the Base Case.

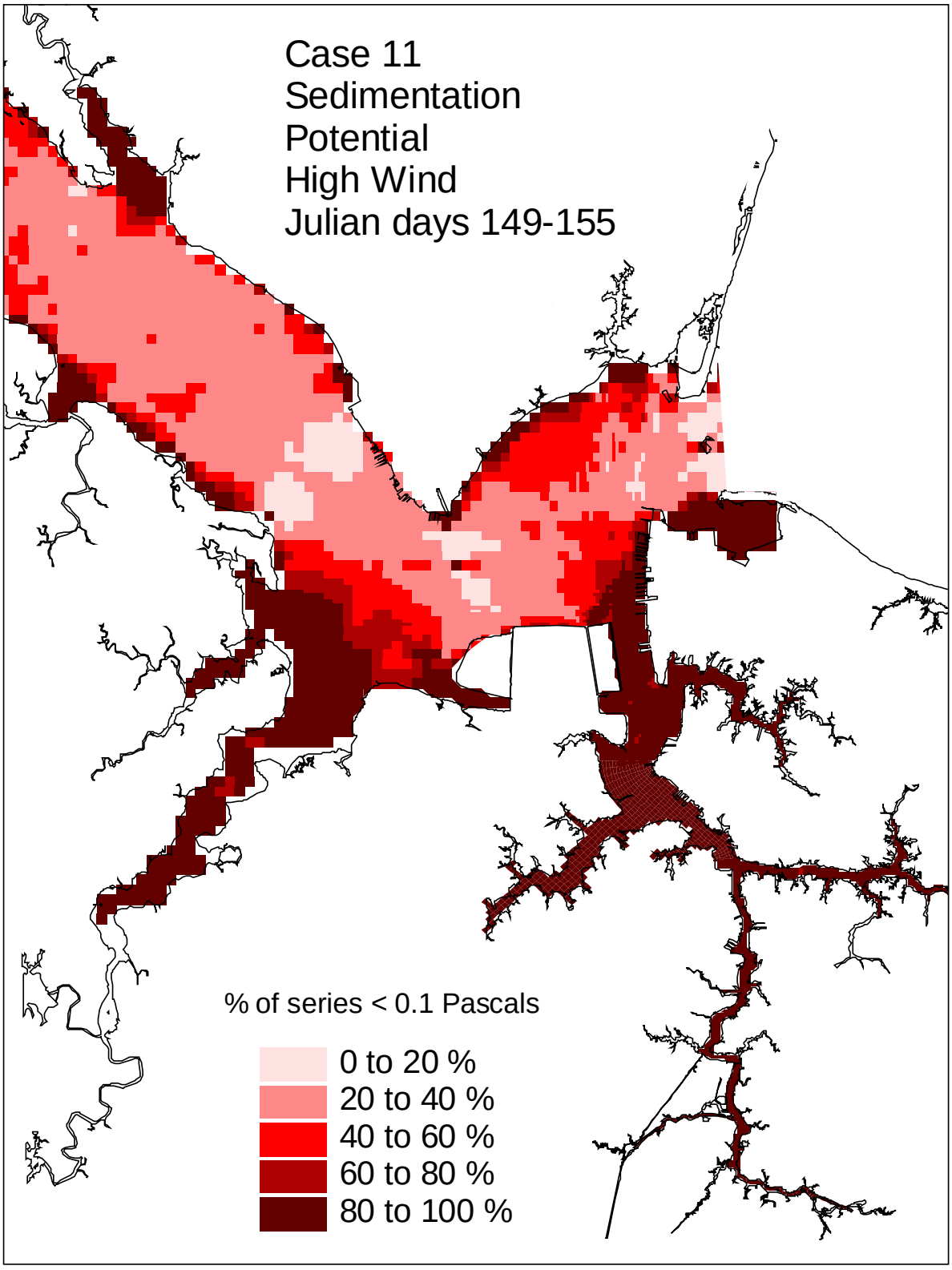

Figure 107. Historical simulation comparison (high wind) of the sedimentation potential for the Eastward and Westward Expansion (Option 7/5a, 55-foot channel).

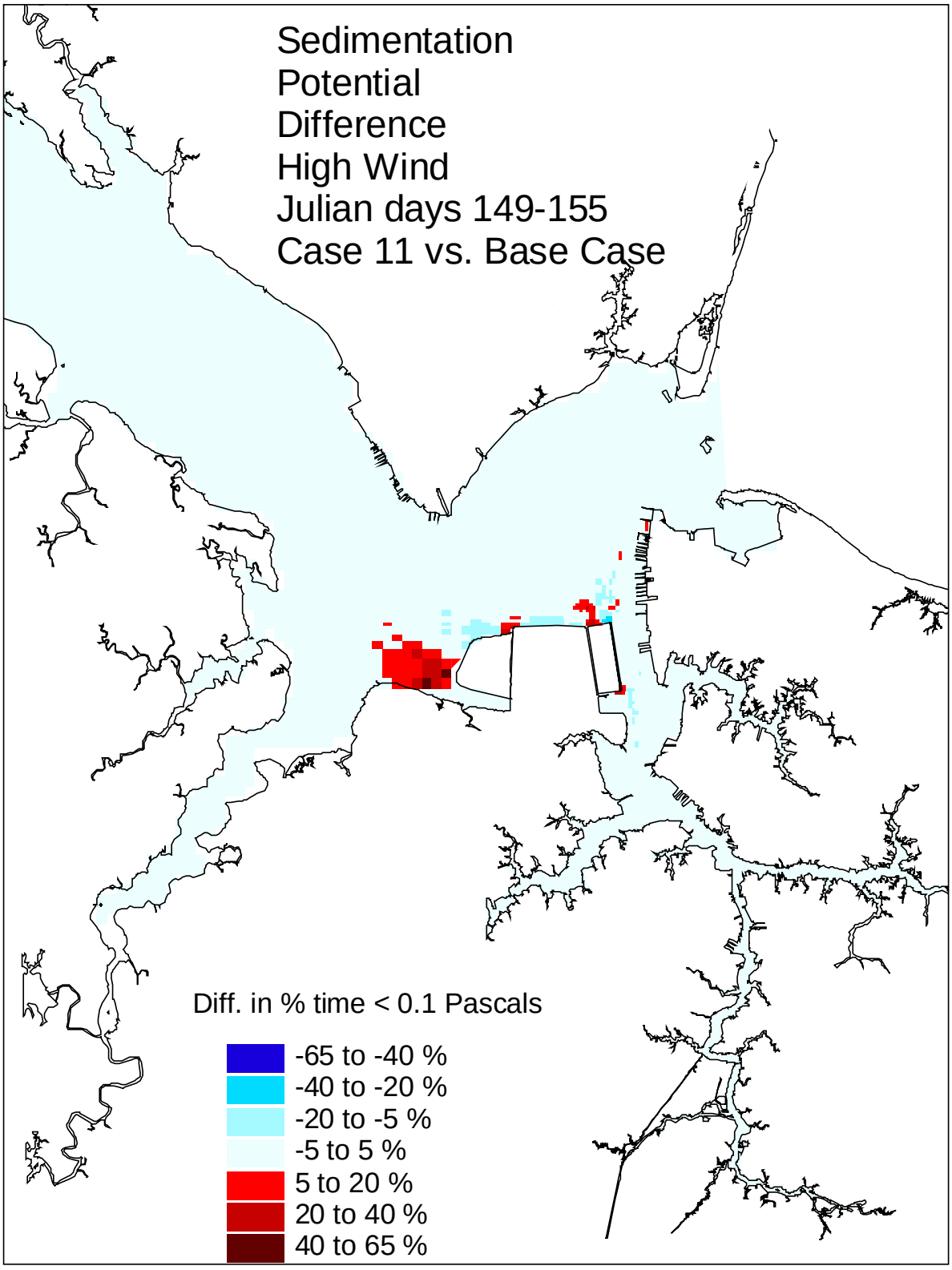

Figure 108. Historical simulation comparison (high wind) of the sedimentation potential difference for the Eastward and Westward Expansion (Option 7/5a, 55-foot channel) versus the Base Case.

APPENDIX to CHAPTER VI, SECTION A.2

Global Comparisons of Historical Runs

Percentile Analysis

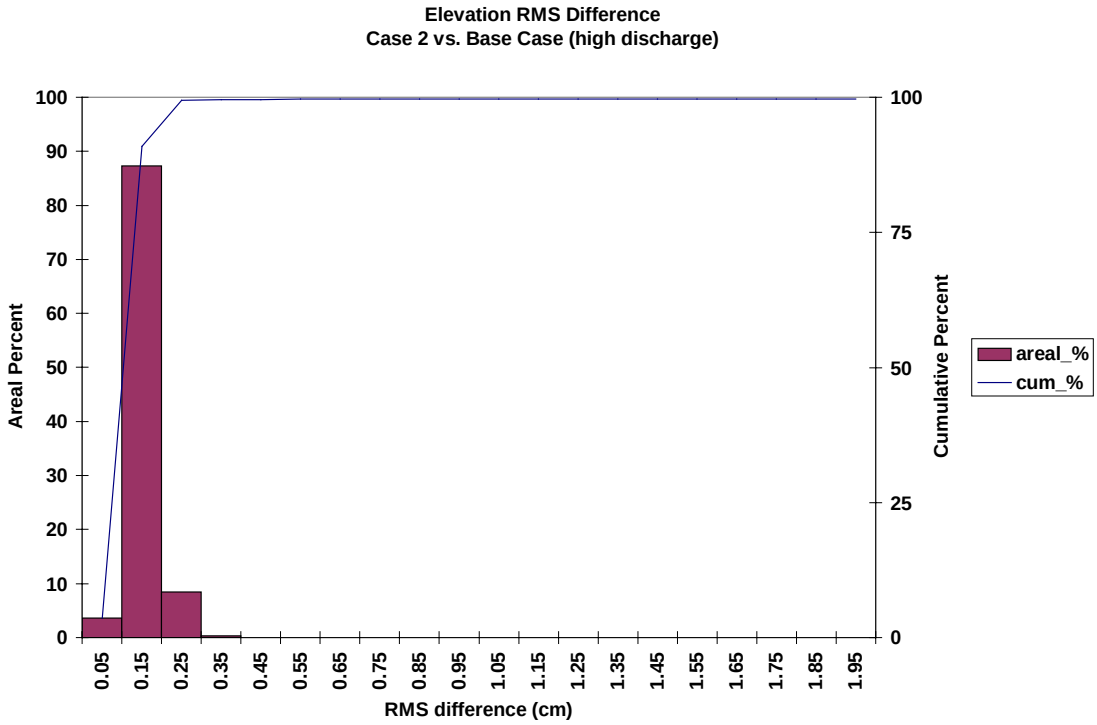

Figure 1. Frequency distribution of elevation RMS difference for the Eastward Expansion (Option 7, 50–foot channel) versus the Base Case during the highdischarge event of historical simulation.

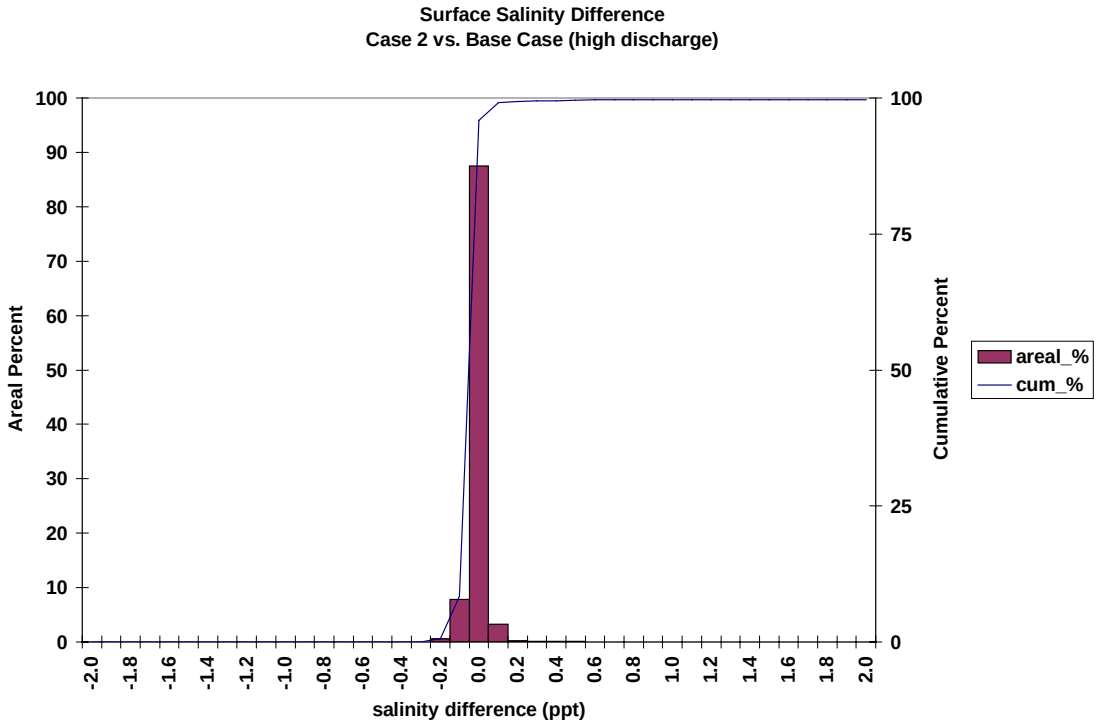

Figure 2. Frequency distribution of surface salinity average difference for the Eastward Expansion (Option 7, 50–foot channel) versus the Base Case during the high discharge event of historical simulation.

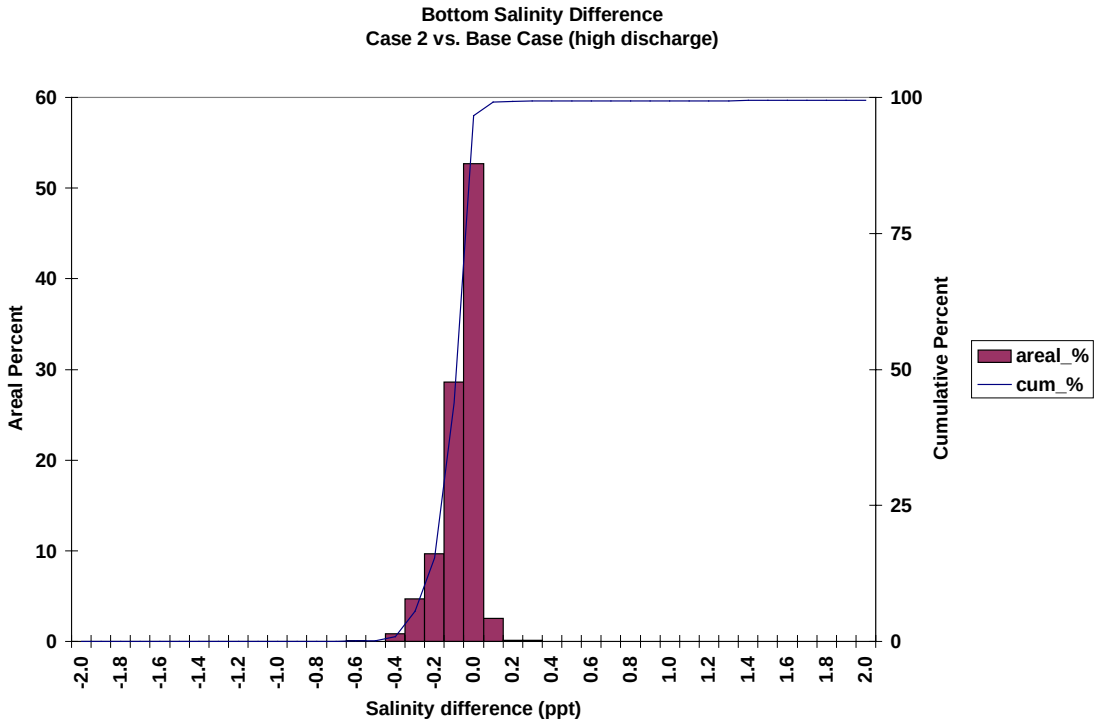

Figure 3. Frequency distribution of bottom salinity average difference for the Eastward Expansion (Option 7, 50–foot channel) versus the Base Case during the high discharge event of historical simulation.

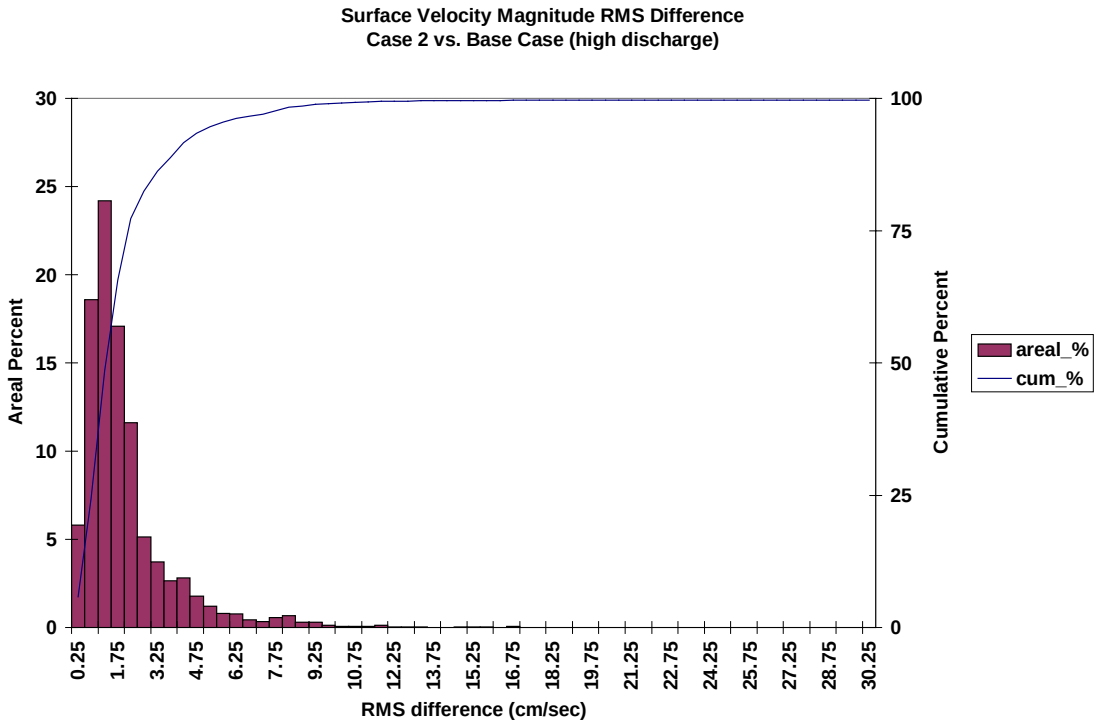

Figure 4. Frequency distribution of surface velocity RMS difference for the Eastward Expansion (Option 7, 50–foot channel) versus the Base Case during the high discharge event of historical simulation.

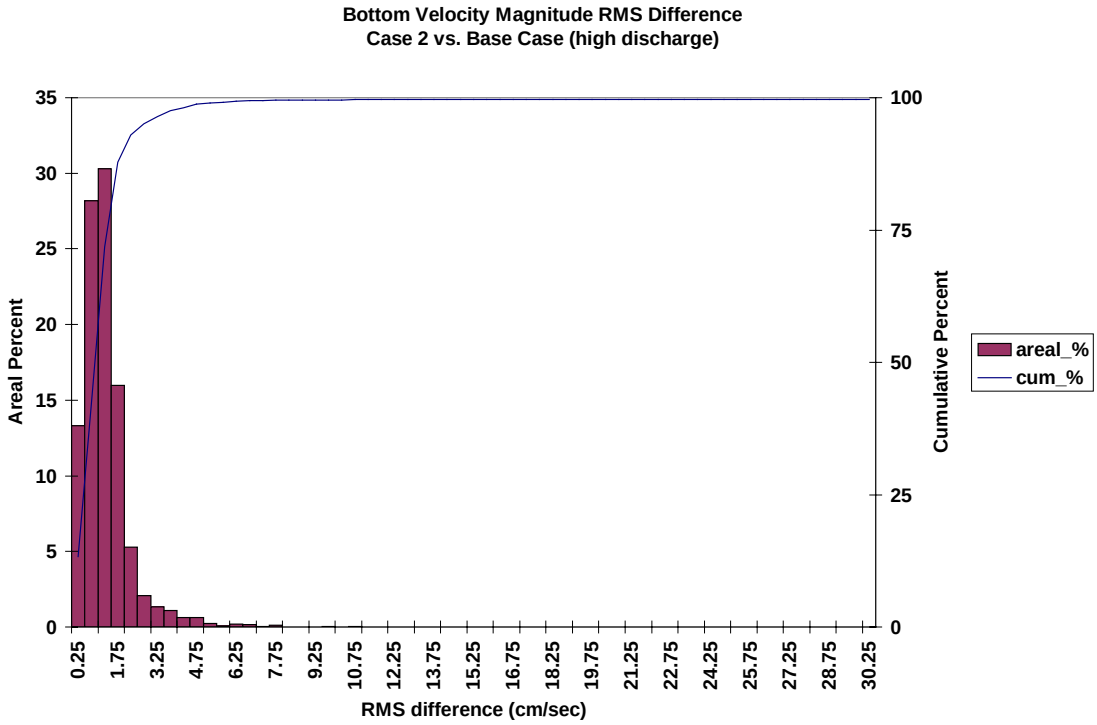

Figure 5. Frequency distribution of bottom velocity RMS difference for the Eastward Expansion (Option 7, 50–foot channel) versus the Base Case during the high discharge event of historical simulation.

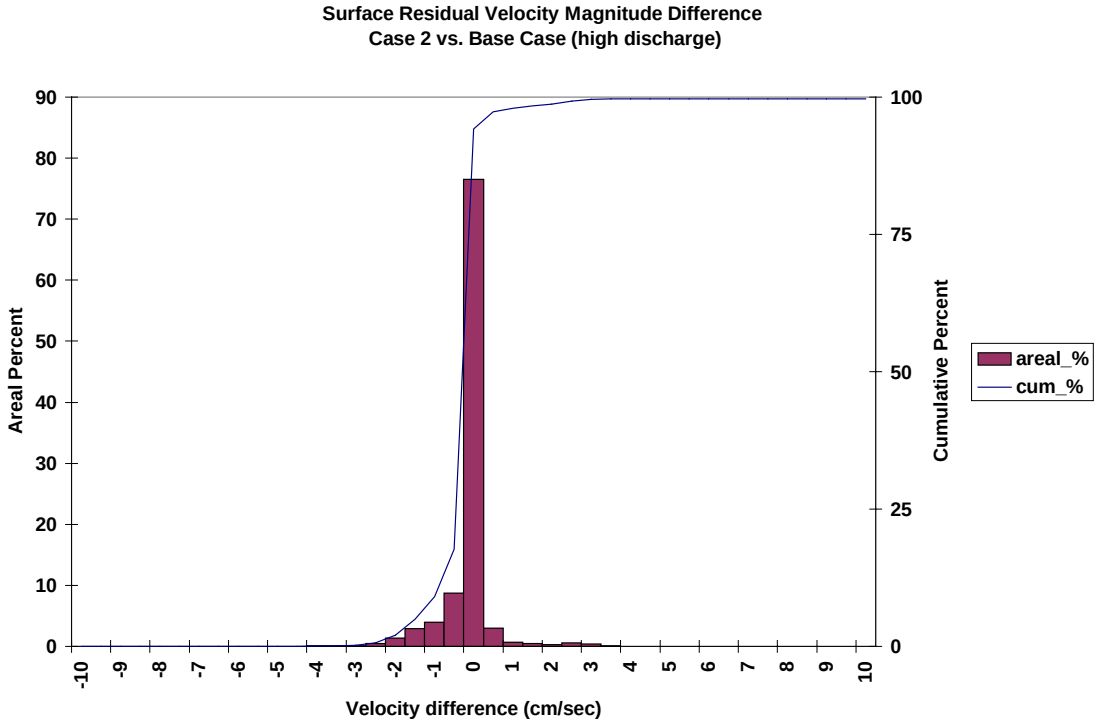

Figure 6. Frequency distribution of surface residual velocity magnitude average difference for the Eastward Expansion (Option 7, 50–foot channel) versus the Base Case during the high discharge event of historical simulation.

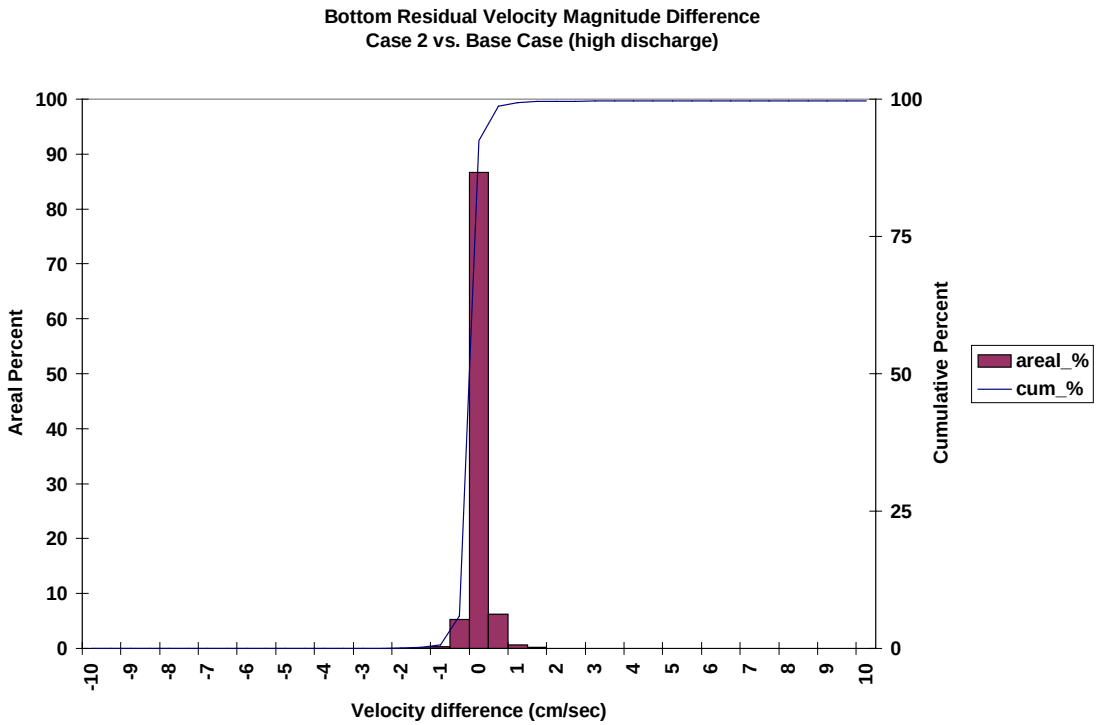

Figure 7. Frequency distribution of bottom residual velocity magnitude average difference for the Eastward Expansion (Option 7, 50–foot channel) versus the Base Case during the high discharge event of historical simulation.

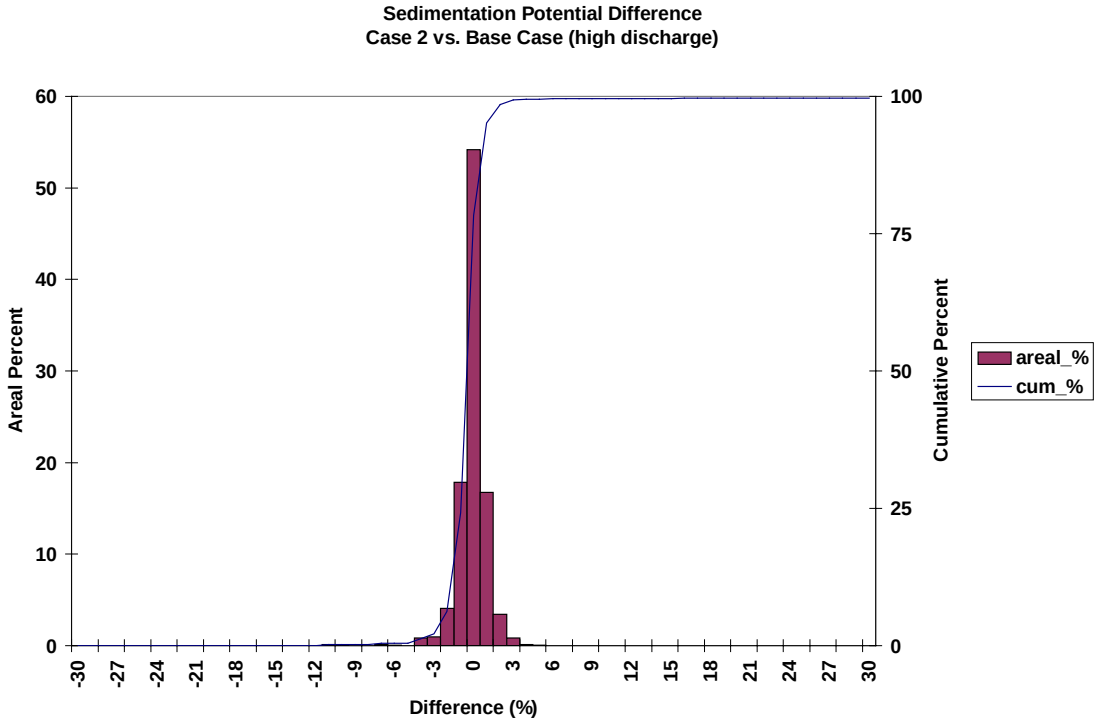

Figure 8. Frequency distribution of sedimentation potential difference for the Eastward Expansion (Option 7, 50–foot channel) versus the Base Case during the high discharge event of historical simulation.

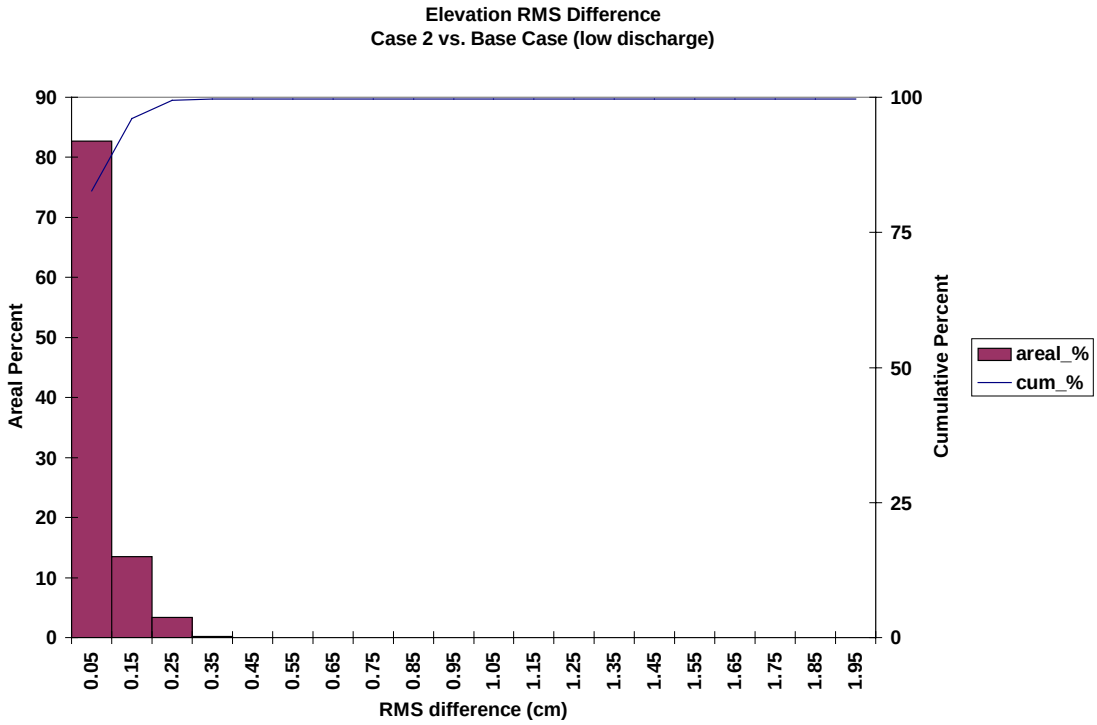

Figure 9. Frequency distribution of elevation RMS difference for the Eastward Expansion (Option 7, 50–foot channel) versus the Base Case during the low discharge event of historical simulation.

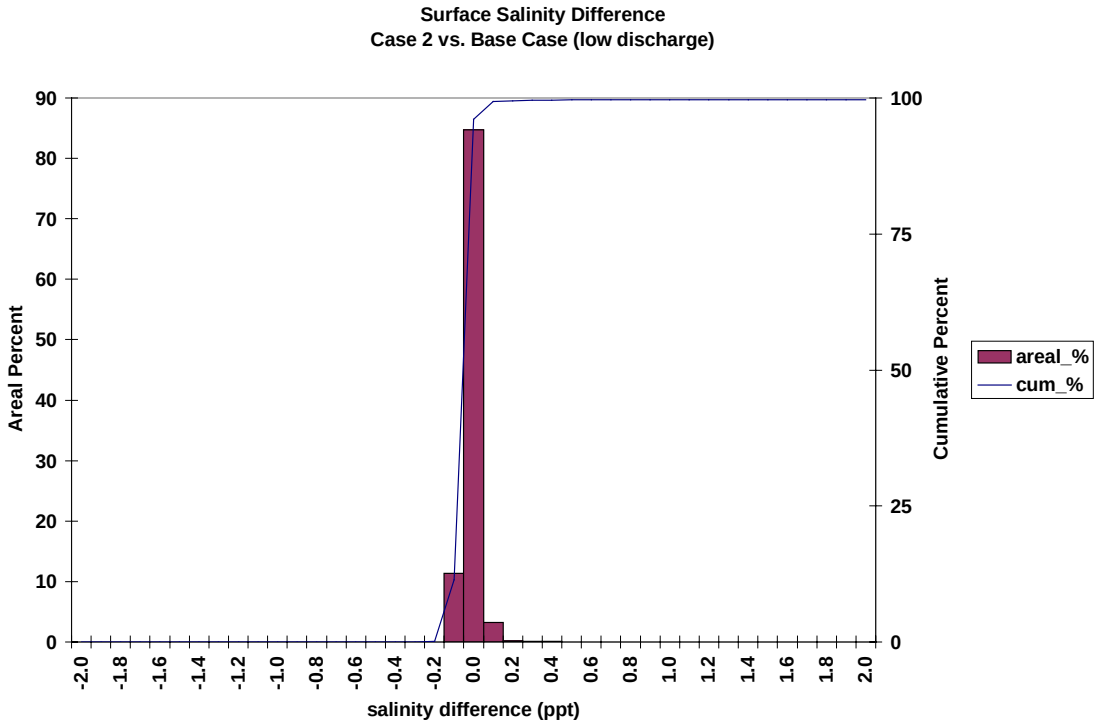

Figure 10. Frequency distribution of surface salinity average difference for the Eastward Expansion (Option 7, 50–foot channel) versus the Base Case during the low discharge event of historical simulation.

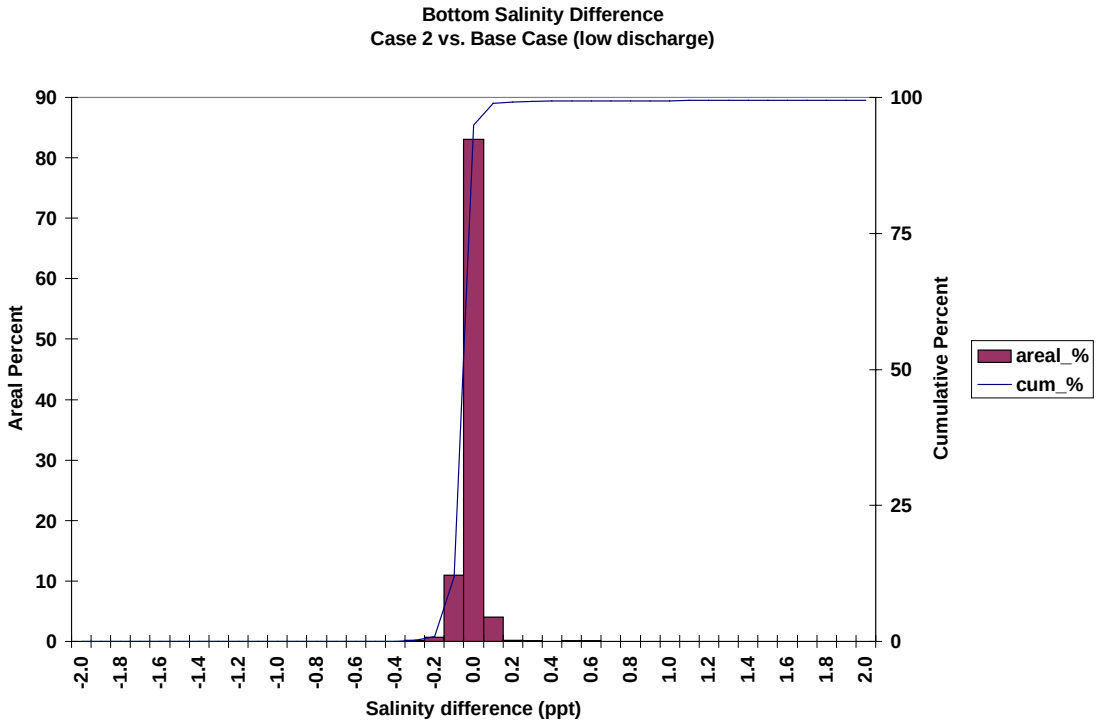

Figure 11. Frequency distribution of bottom salinity average difference for the Eastward Expansion (Option 7, 50–foot channel) versus the Base Case during the low discharge event of historical simulation.

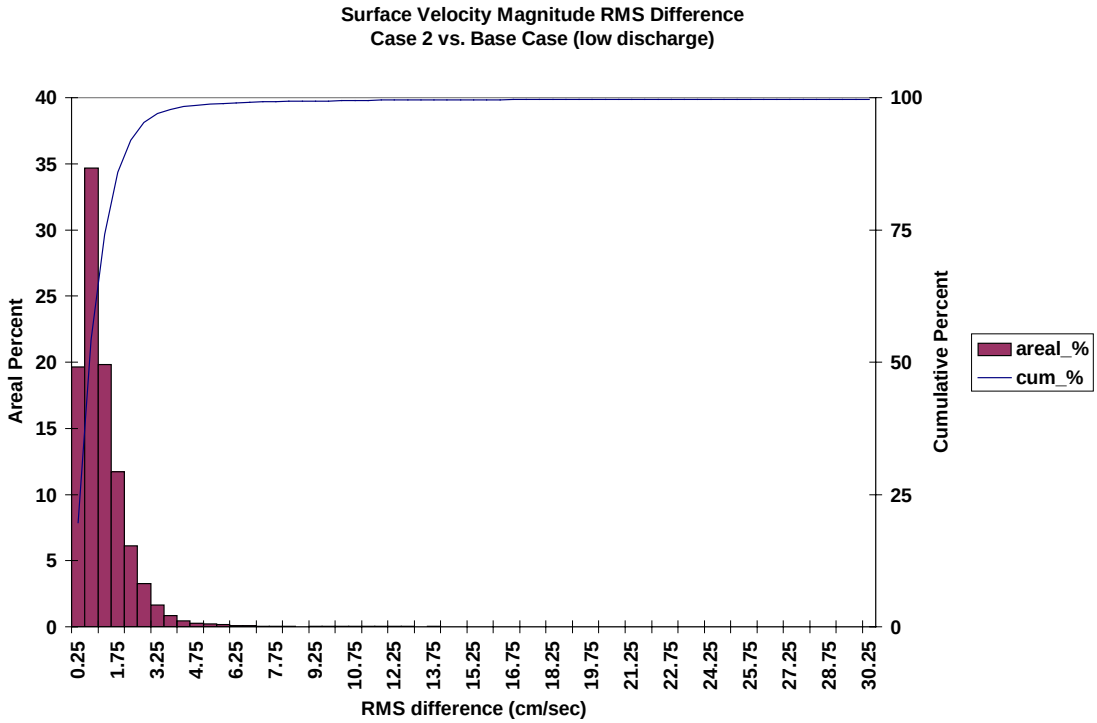

Figure 12. Frequency distribution of surface velocity RMS difference for the Eastward Expansion (Option 7, 50–foot channel) versus the Base Case during the low discharge event of historical simulation.

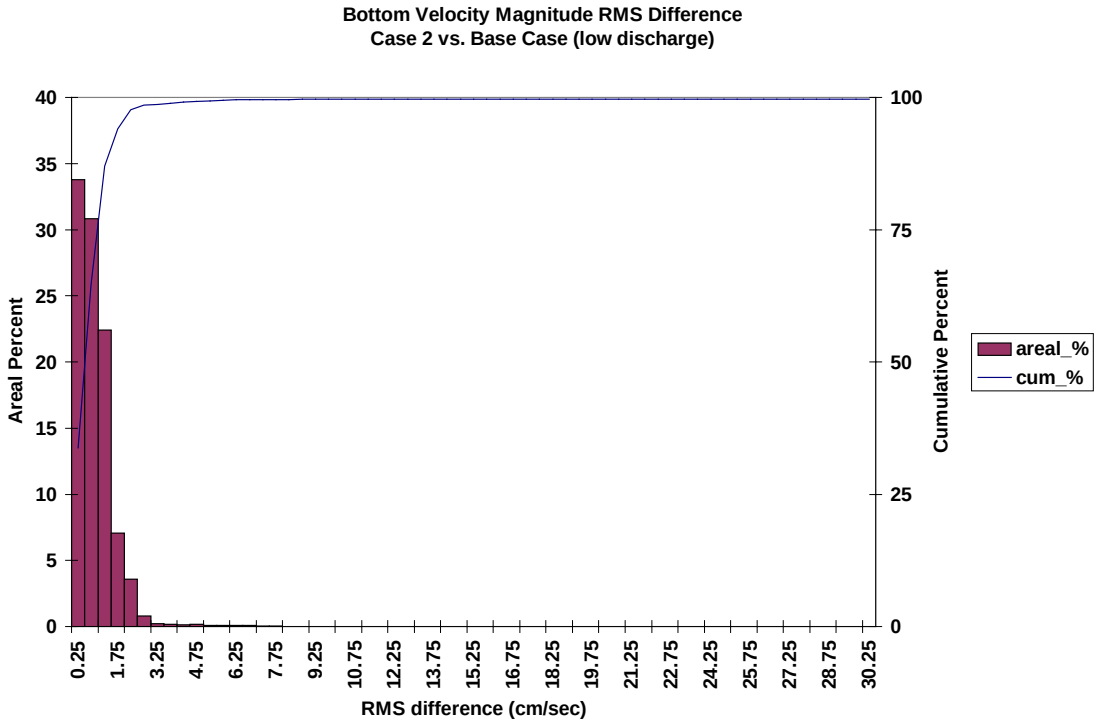

Figure 13. Frequency distribution of bottom velocity RMS difference for the Eastward Expansion (Option 7, 50–foot channel) versus the Base Case during the low discharge event of historical simulation.

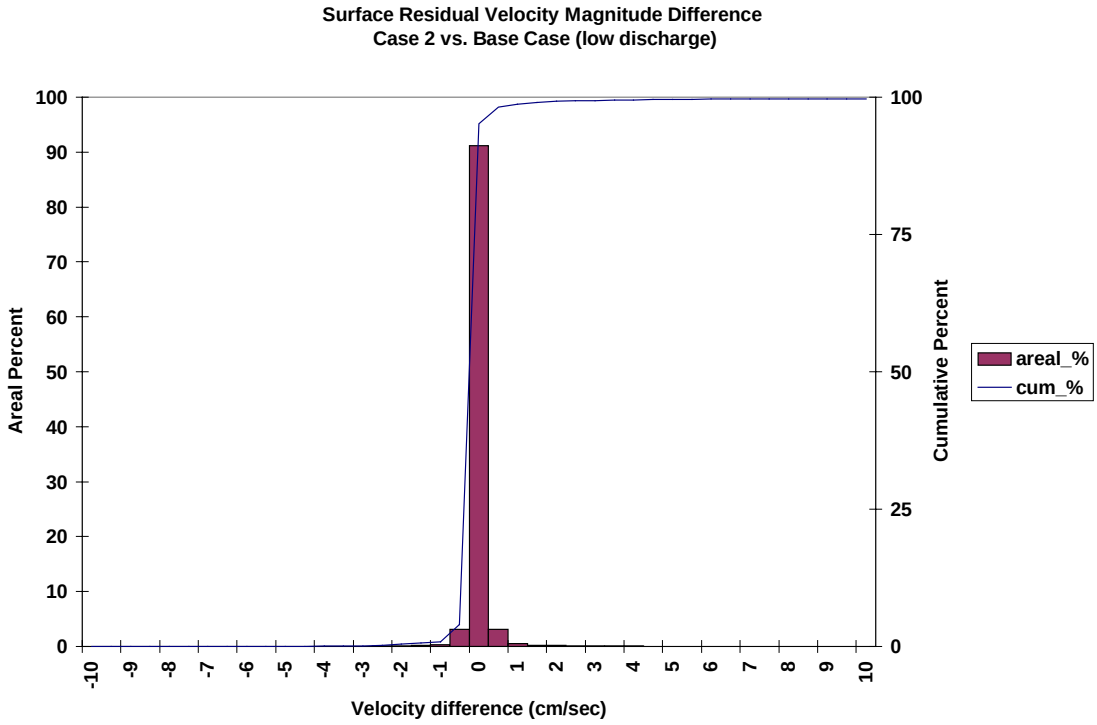

Figure 14. Frequency distribution of surface residual velocity magnitude average difference for the Eastward Expansion (Option 7, 50–foot channel) versus the Base Case during the low discharge event of historical simulation.

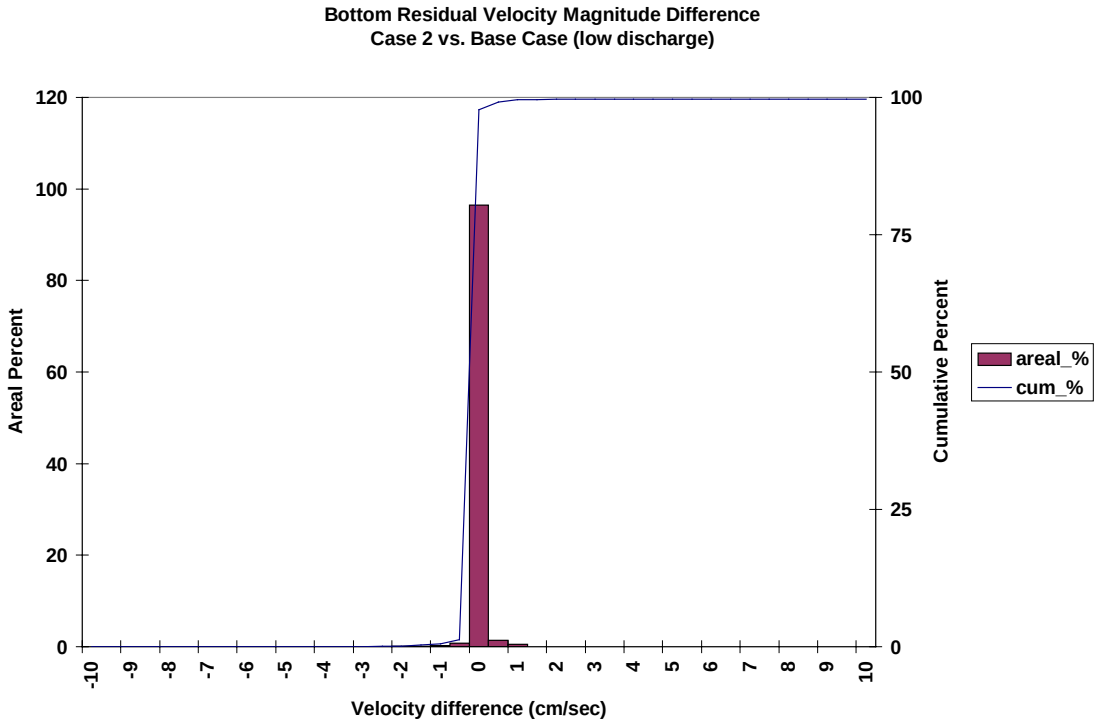

Figure 15. Frequency distribution of bottom residual velocity magnitude average difference for the Eastward Expansion (Option 7, 50–foot channel) versus the Base Case during the low discharge event of historical simulation.

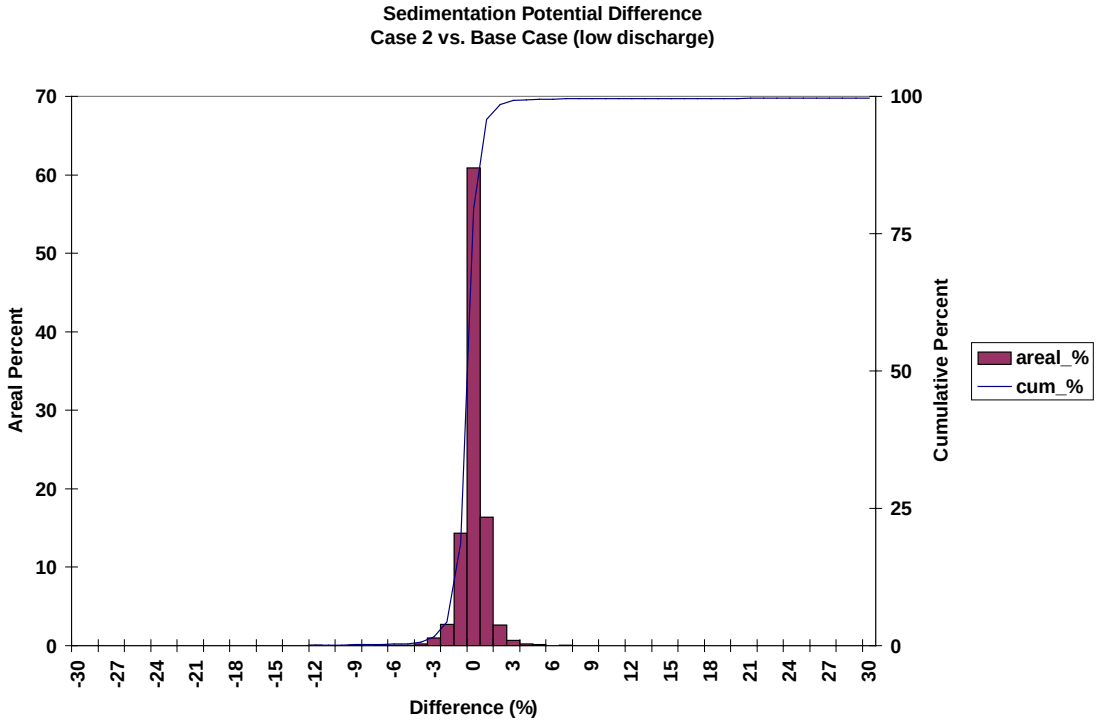

Figure 16. Frequency distribution of sedimentation potential difference for the Eastward Expansion (Option 7, 50–foot channel) versus the Base Case during the low discharge event of historical simulation.

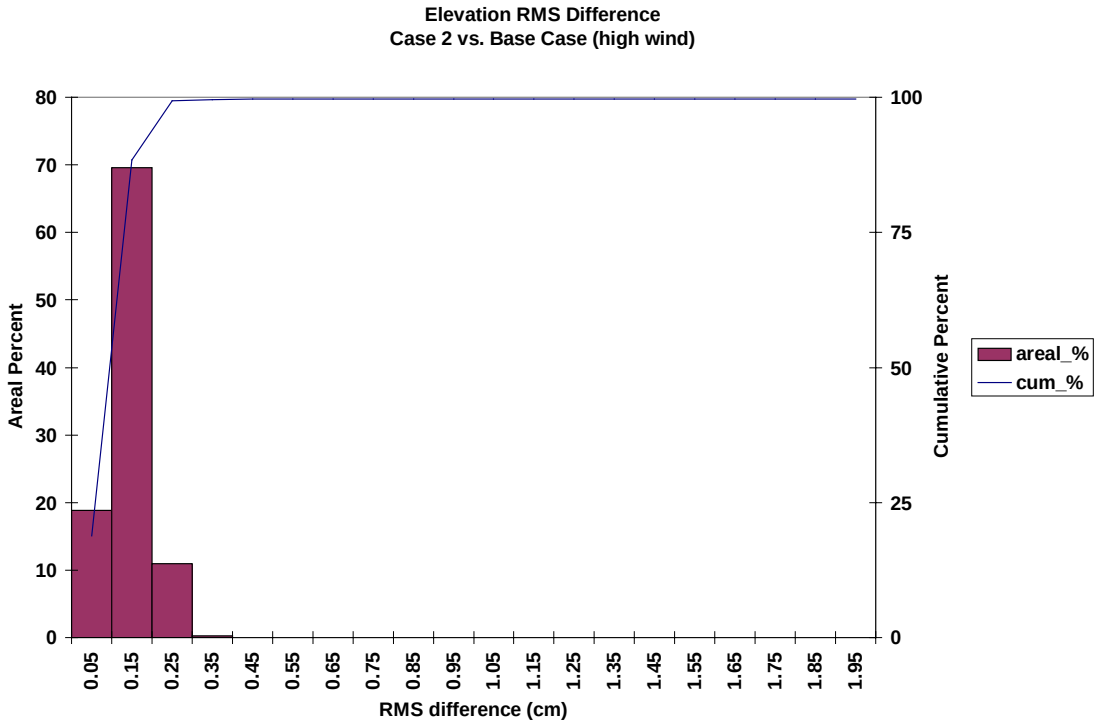

Figure 17. Frequency distribution of elevation RMS difference for the Eastward Expansion (Option 7, 50–foot channel) versus the Base Case during the high wind event of historical simulation.

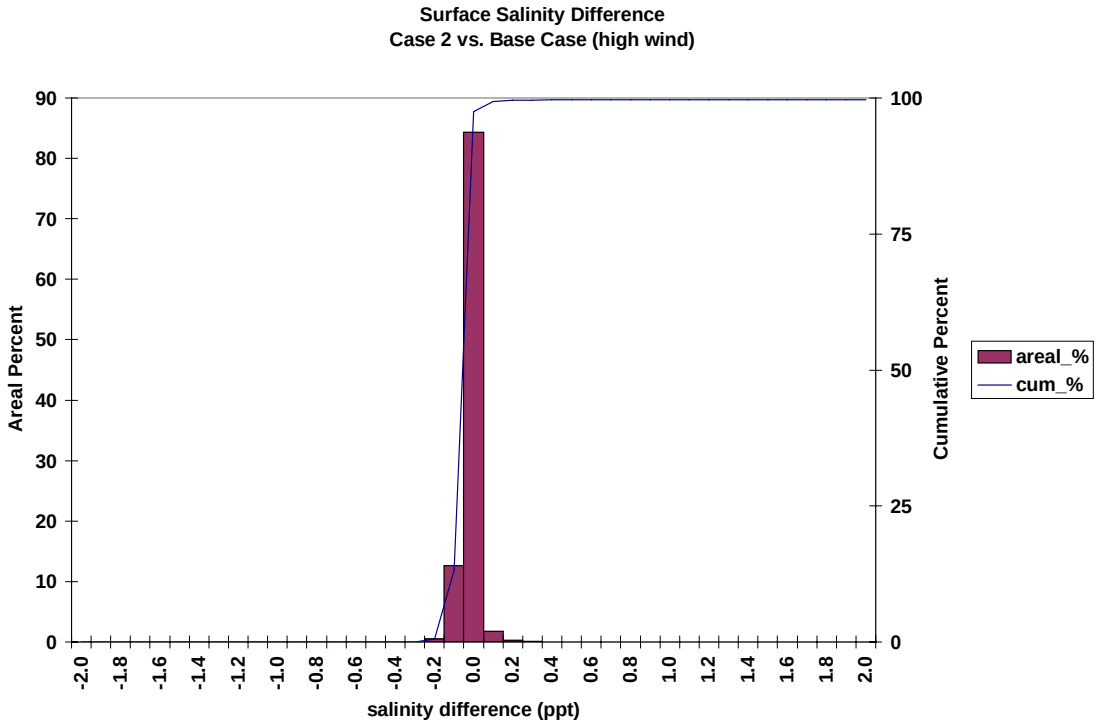

Figure 18. Frequency distribution of surface salinity average difference for the Eastward Expansion (Option 7, 50–foot channel) versus the Base Case during the high wind event of historical simulation.

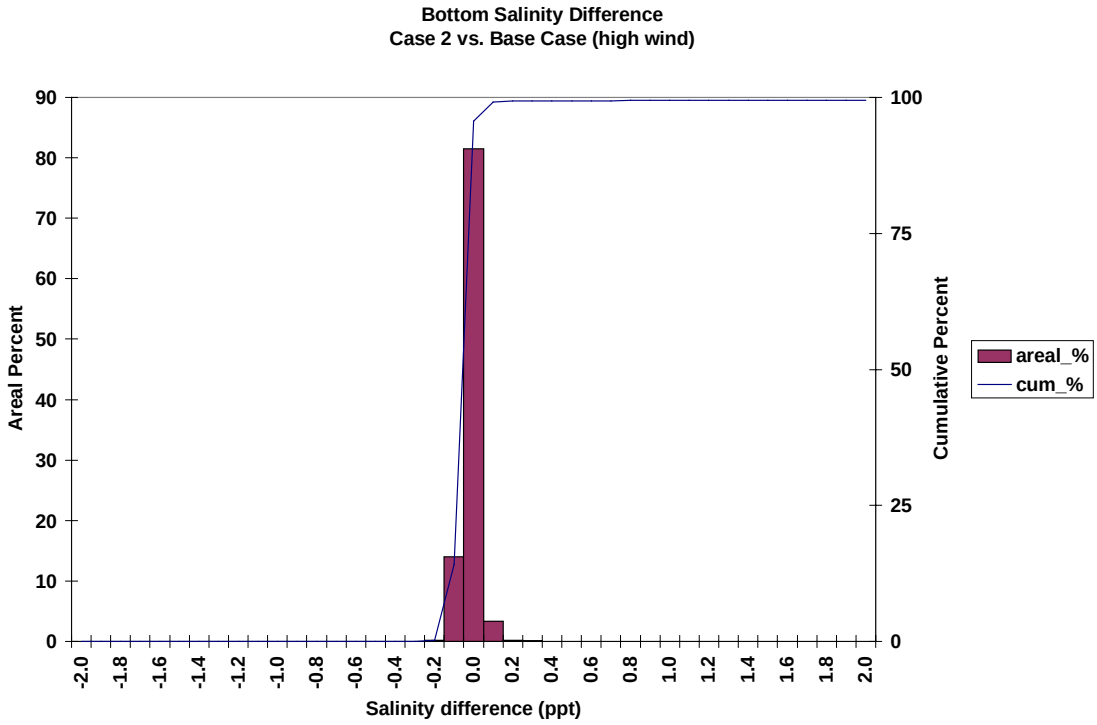

Figure 19. Frequency distribution of bottom salinity average difference for the Eastward Expansion (Option 7, 50–foot channel) versus the Base Case during the high wind event of historical simulation.

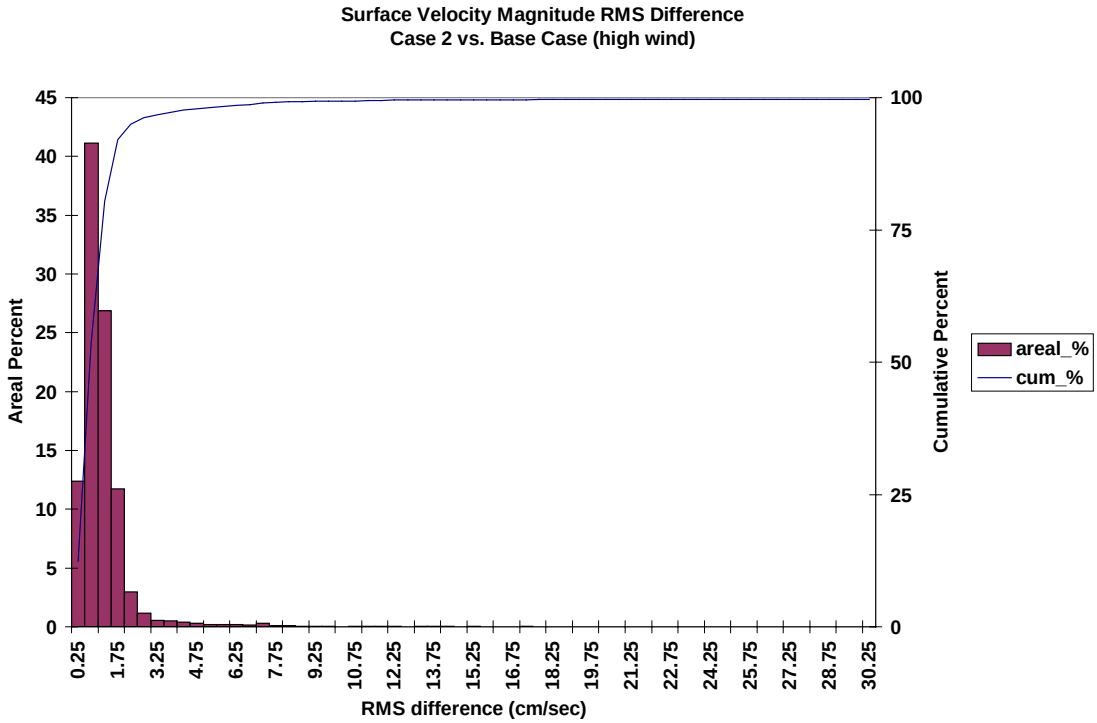

Figure 20. Frequency distribution of surface velocity RMS difference for the Eastward Expansion (Option 7, 50–foot channel) versus the Base Case during the high wind event of historical simulation.

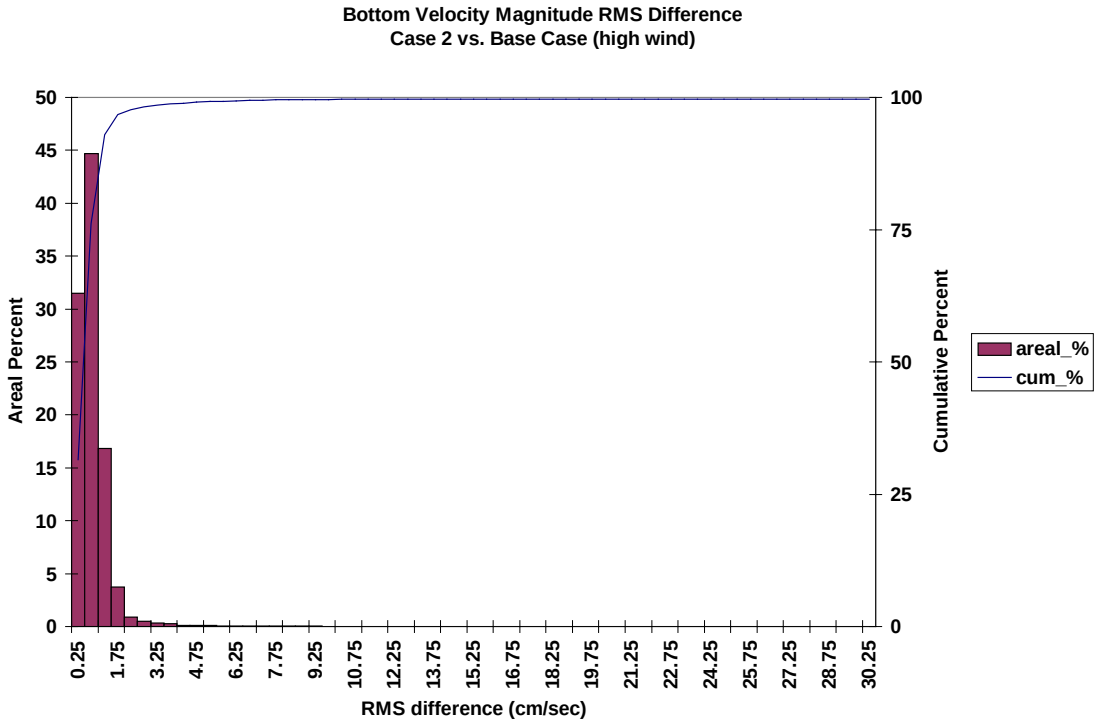

Figure 21. Frequency distribution of bottom velocity RMS difference for the Eastward Expansion (Option 7, 50–foot channel) versus the Base Case during the high wind event of historical simulation.

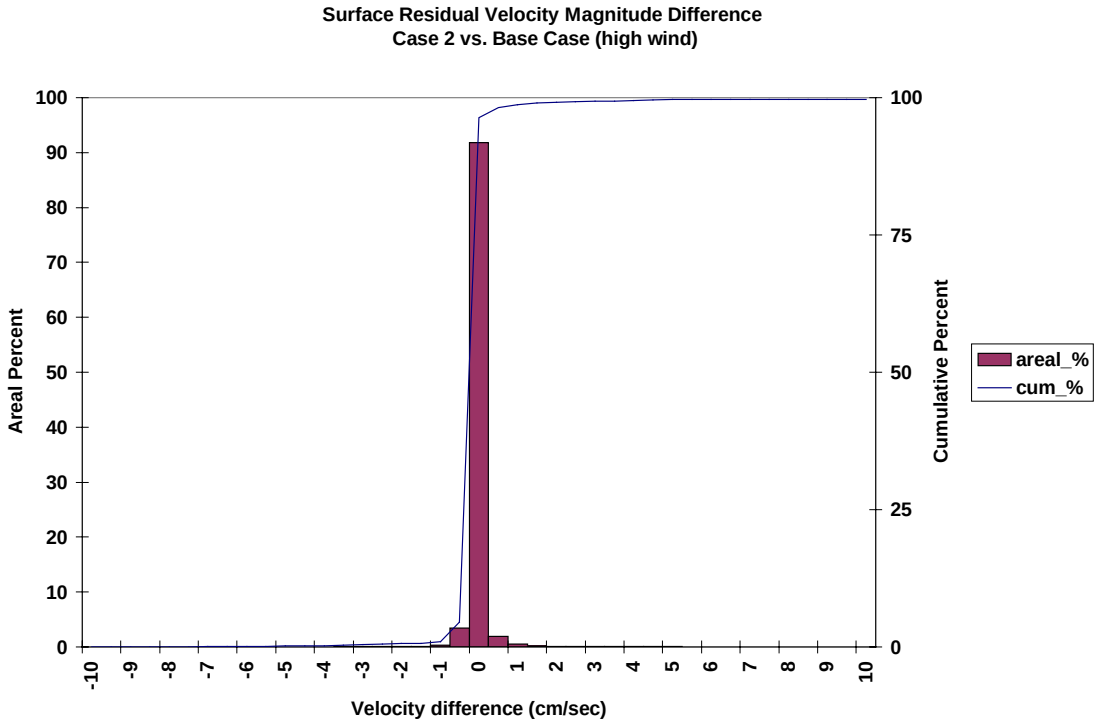

Figure 22. Frequency distribution of surface residual velocity magnitude average difference for the Eastward Expansion (Option 7, 50–foot channel) versus the Base Case during the high wind event of historical simulation.

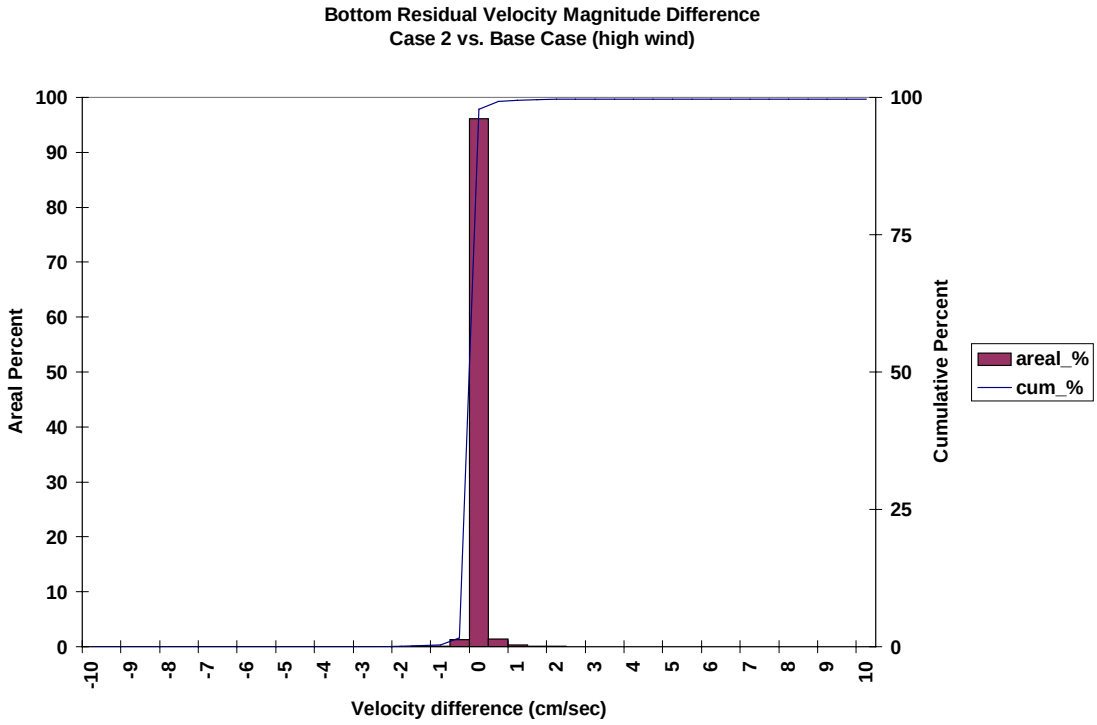

Figure 23. Frequency distribution of bottom residual velocity magnitude average difference for the Eastward Expansion (Option 7, 50–foot channel) versus the Base Case during the high wind event of historical simulation.

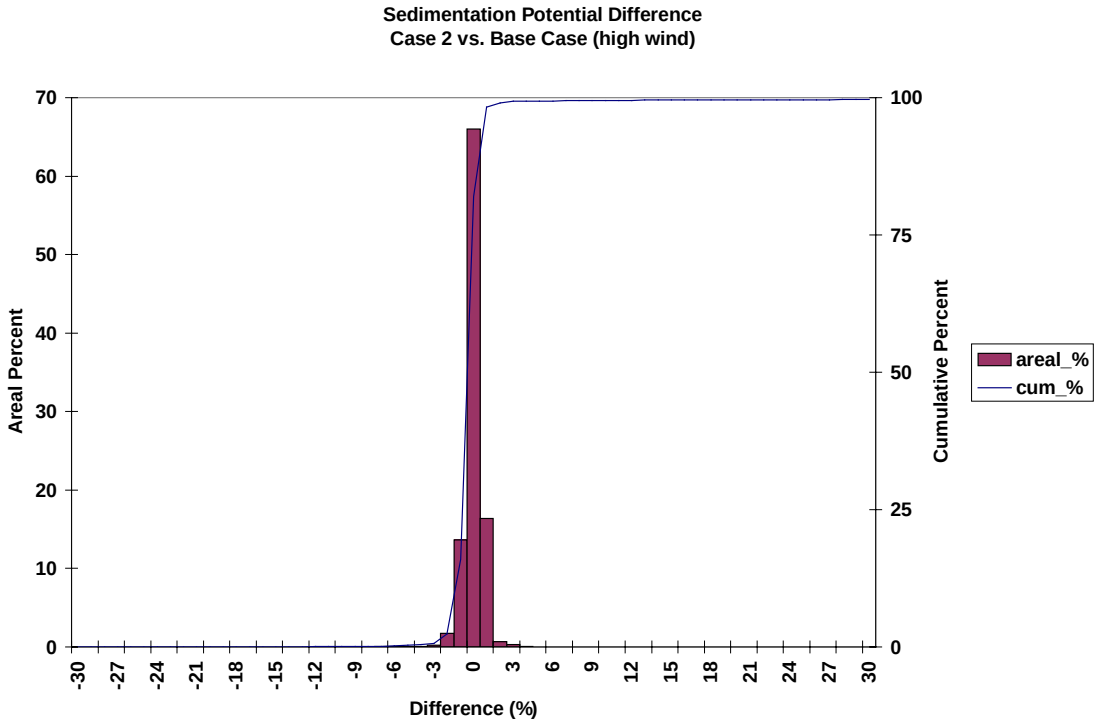

Figure 24. Frequency distribution of sedimentation potential difference for the Eastward Expansion (Option 7, 50–foot channel) versus the Base Case during the high wind event of historical simulation.

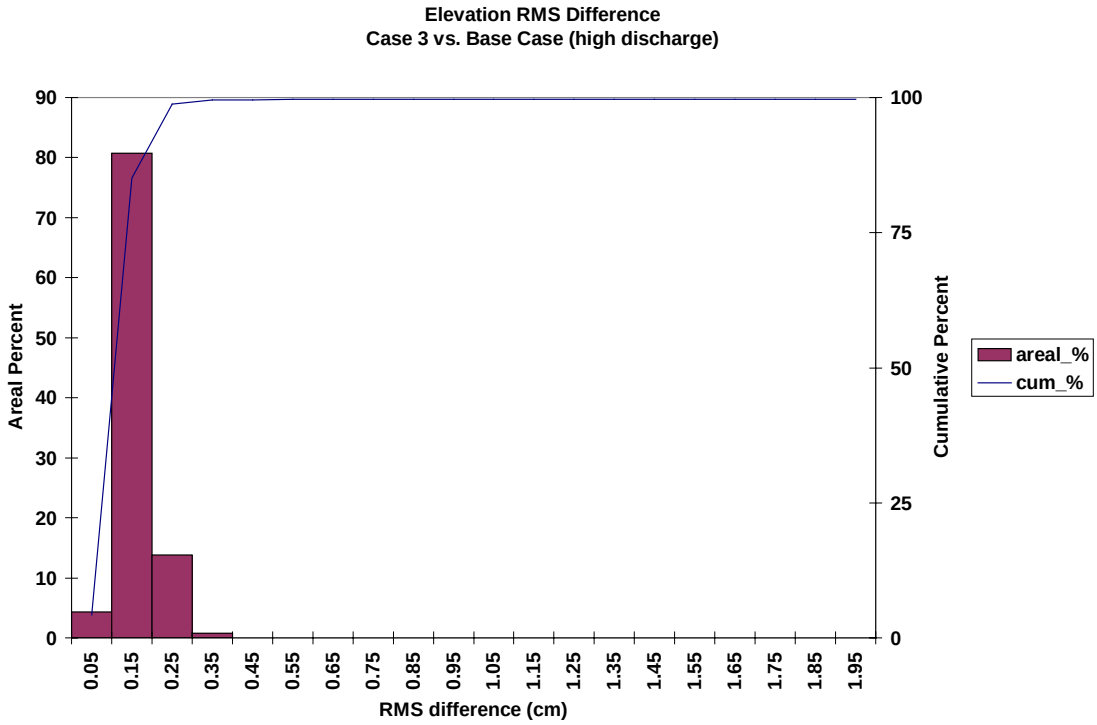

Figure 25. Frequency distribution of elevation RMS difference for the Eastward Expansion (Option 7, 55–foot channel) versus the Base Case during the high discharge event of historical simulation.

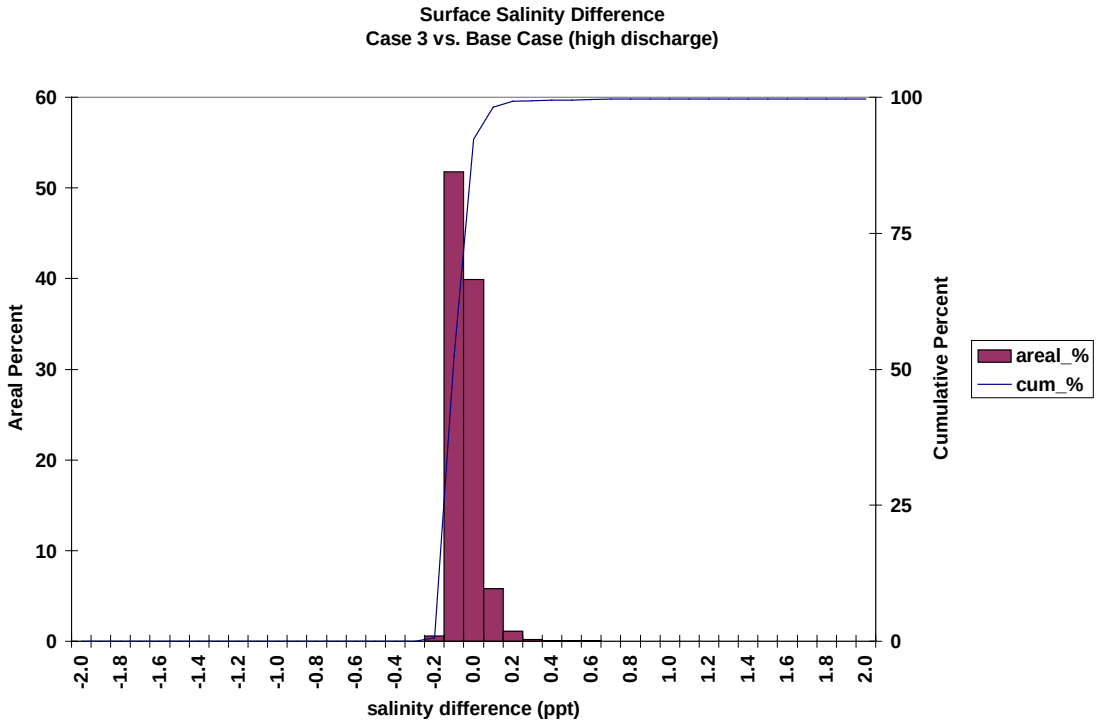

Figure 26. Frequency distribution of surface salinity average difference for the Eastward Expansion (Option 7, 55–foot channel) versus the Base Case during the high discharge event of historical simulation.

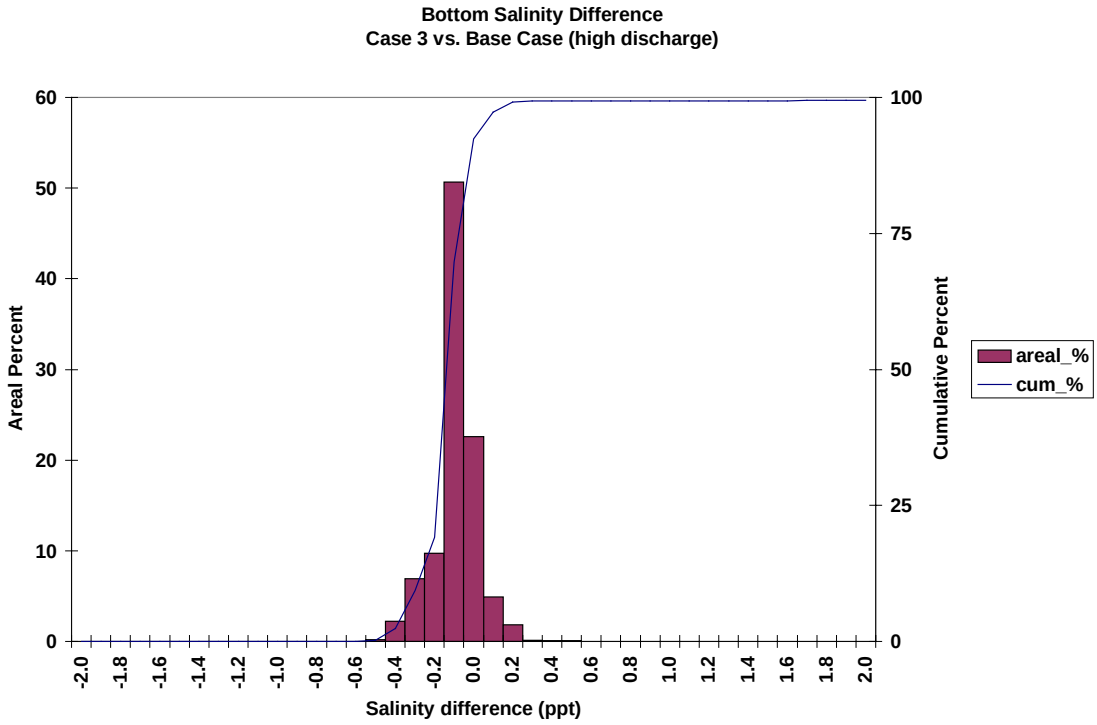

Figure 27. Frequency distribution of bottom salinity average difference for the Eastward Expansion (Option 7, 55–foot channel) versus the Base Case during the high discharge event of historical simulation.

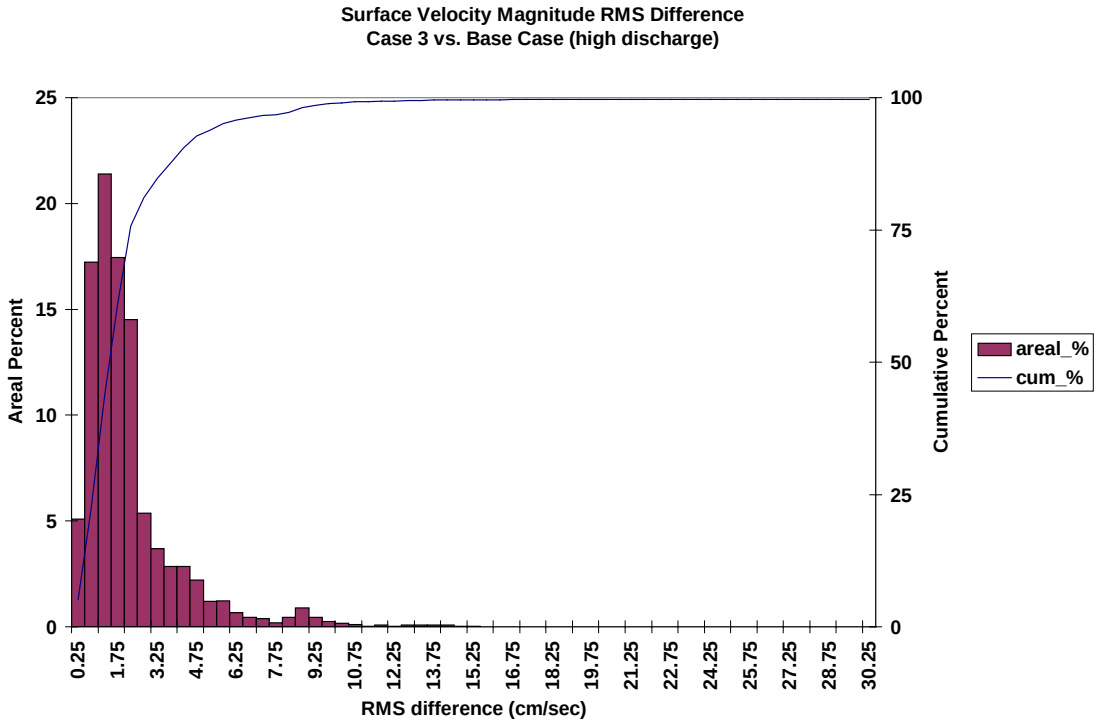

Figure 28. Frequency distribution of surface velocity RMS difference for the Eastward Expansion (Option 7, 55–foot channel) versus the Base Case during the high discharge event of historical simulation.

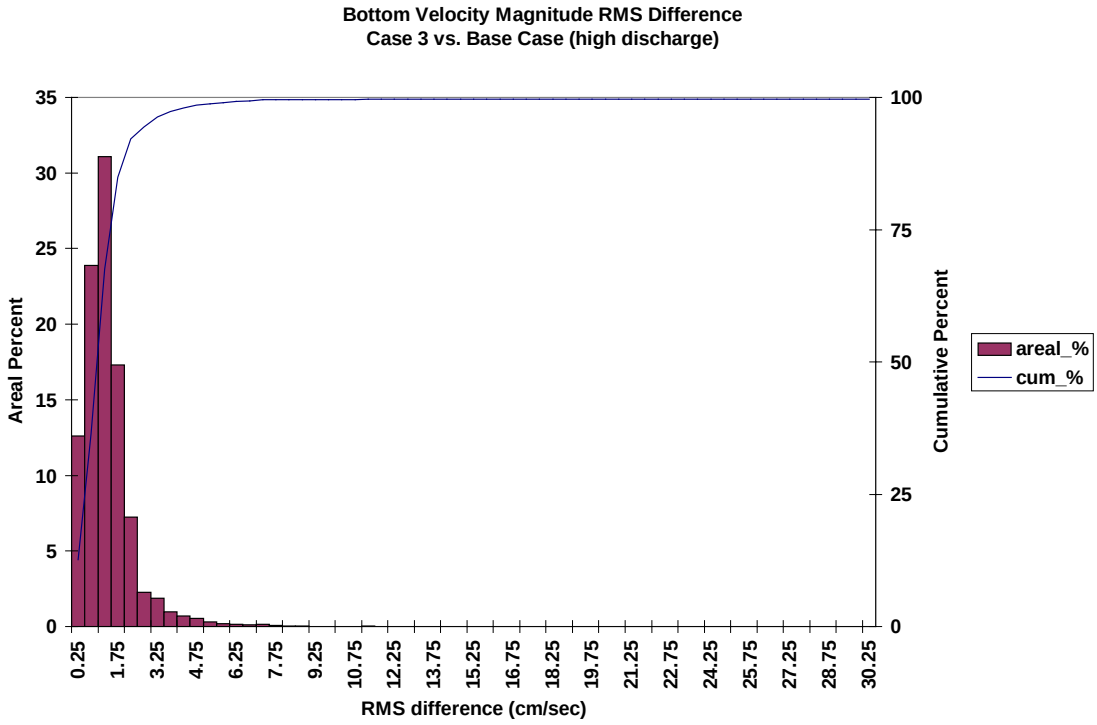

Figure 29. Frequency distribution of bottom velocity RMS difference for the Eastward Expansion (Option 7, 55–foot channel) versus the Base Case during the high discharge event of historical simulation.

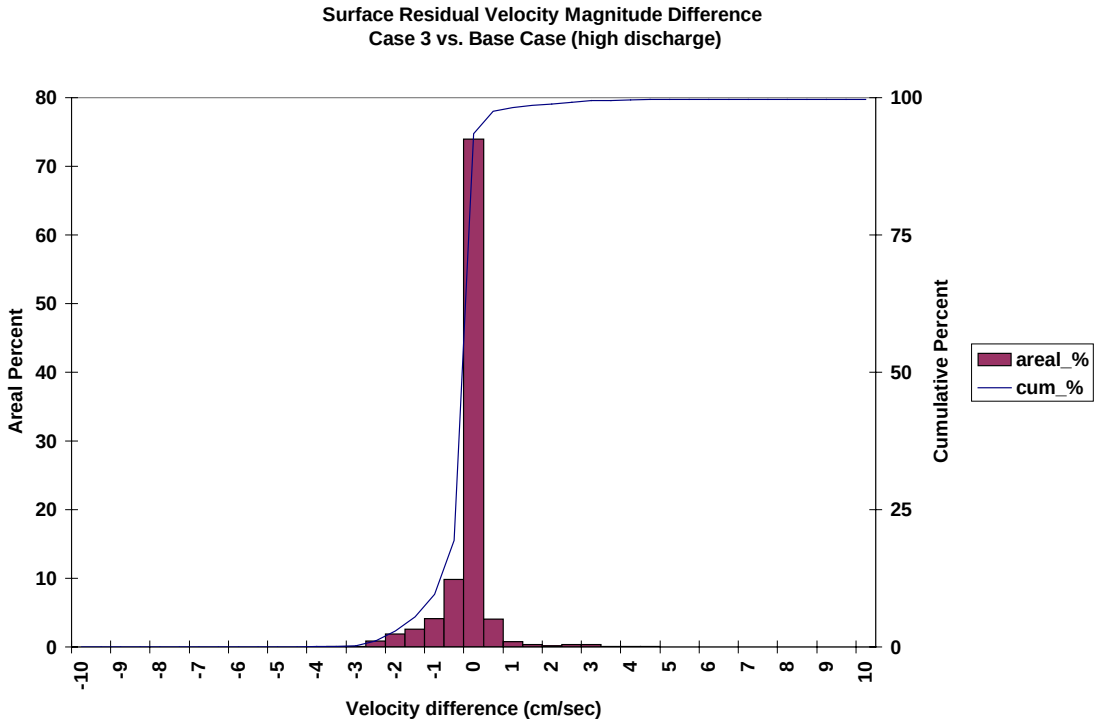

Figure 30. Frequency distribution of surface residual velocity magnitude average difference for the Eastward Expansion (Option 7, 55–foot channel) versus the Base Case during the high discharge event of historical simulation.

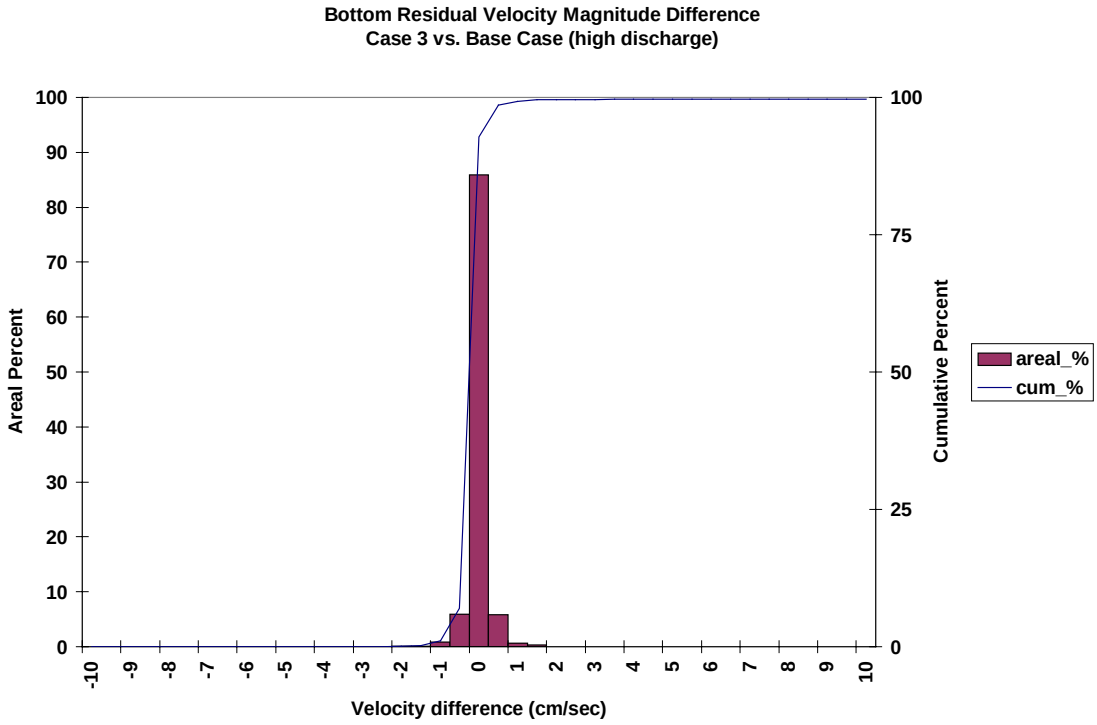

Figure 31. Frequency distribution of bottom residual velocity magnitude average difference for the Eastward Expansion (Option 7, 55–foot channel) versus the Base Case during the high discharge event of historical simulation.

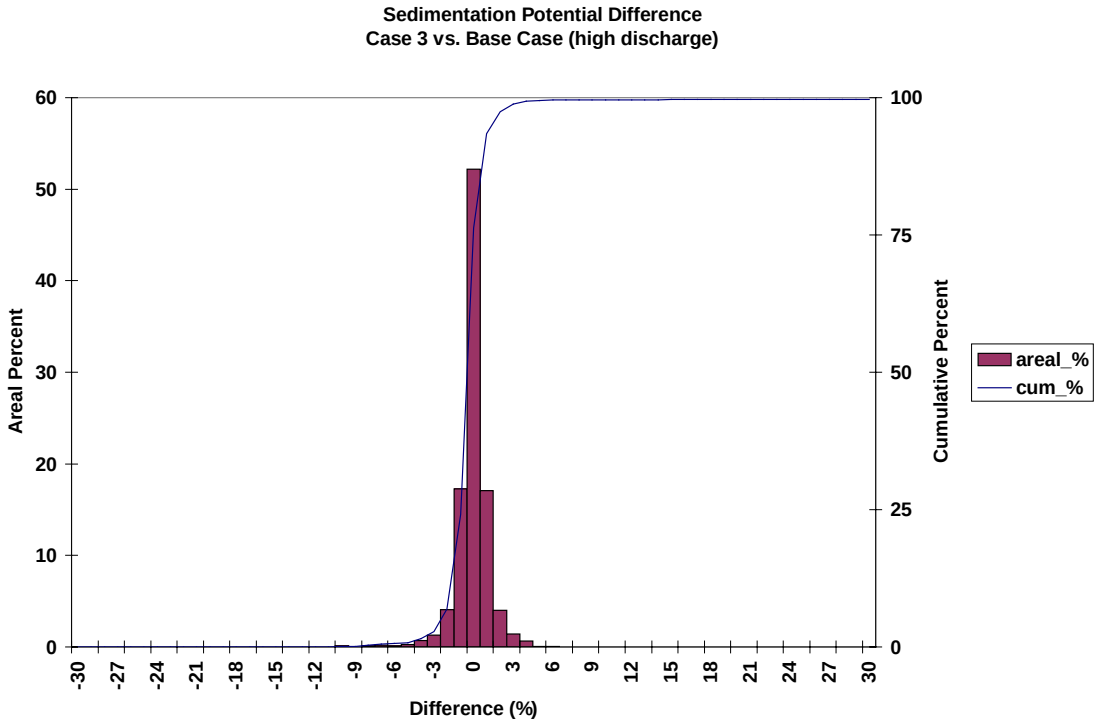

Figure 32. Frequency distribution of sedimentation potential difference for the Eastward Expansion (Option 7, 55–foot channel) versus the Base Case during the high discharge event of historical simulation.

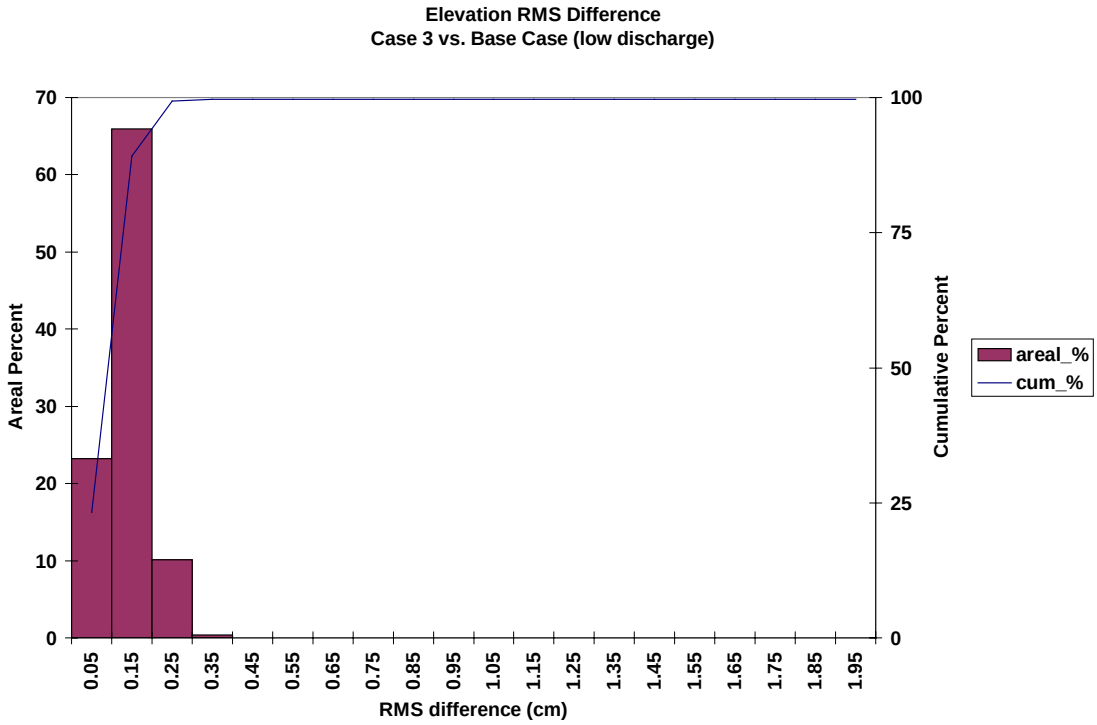

Figure 33. Frequency distribution of elevation RMS difference for the Eastward Expansion (Option 7, 55–foot channel) versus the Base Case during the low discharge event of historical simulation.

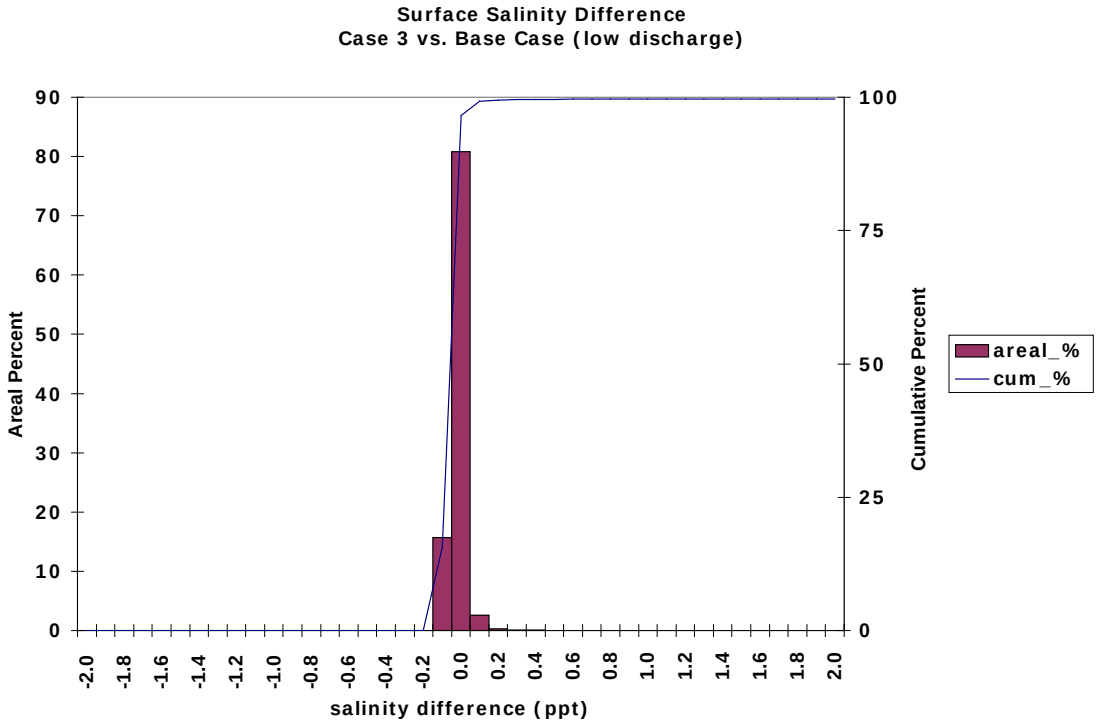

Figure 34. Frequency distribution of surface salinity average difference for the Eastward Expansion (Option 7, 55–foot channel) versus the Base Case during the low discharge event of historical simulation.

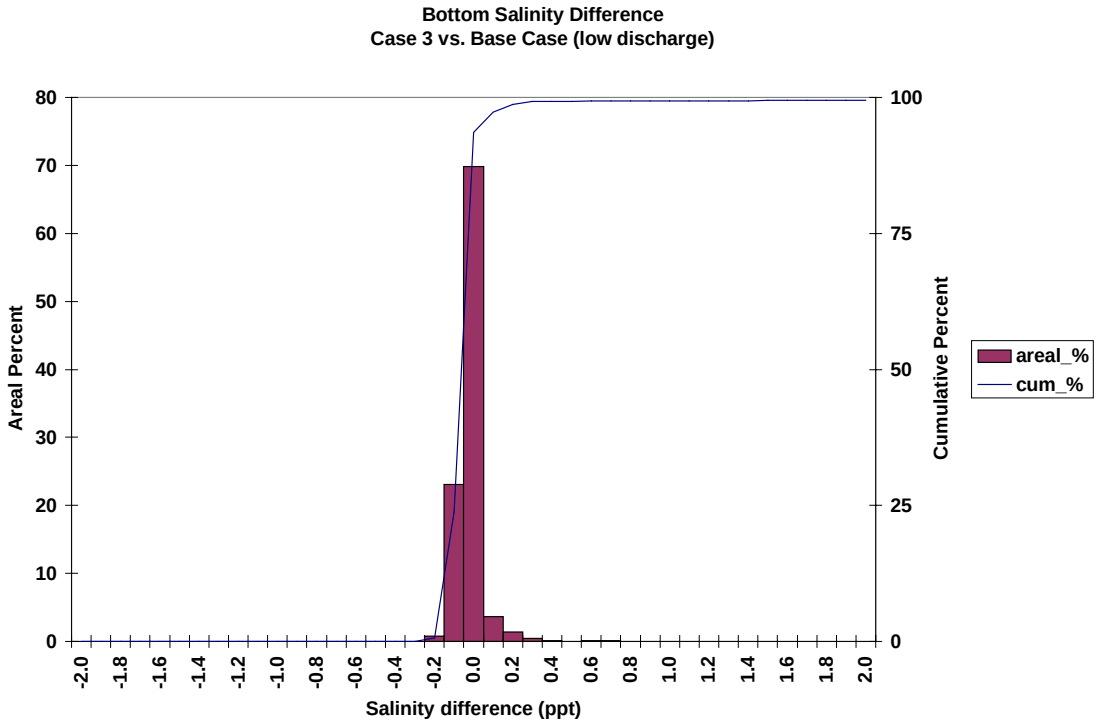

Figure 35. Frequency distribution of bottom salinity average difference for the Eastward Expansion (Option 7, 55–foot channel) versus the Base Case during the low discharge event of historical simulation.

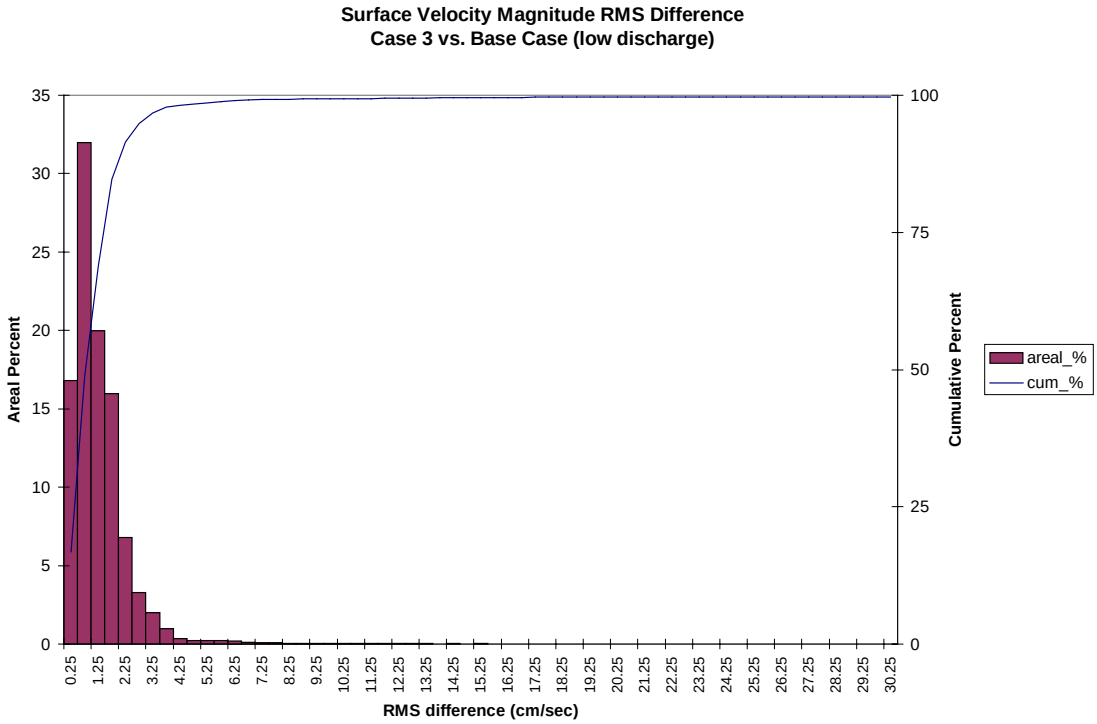

Figure 36. Frequency distribution of surface velocity RMS difference for the Eastward Expansion (Option 7, 55–foot channel) versus the Base Case during the low discharge event of historical simulation.

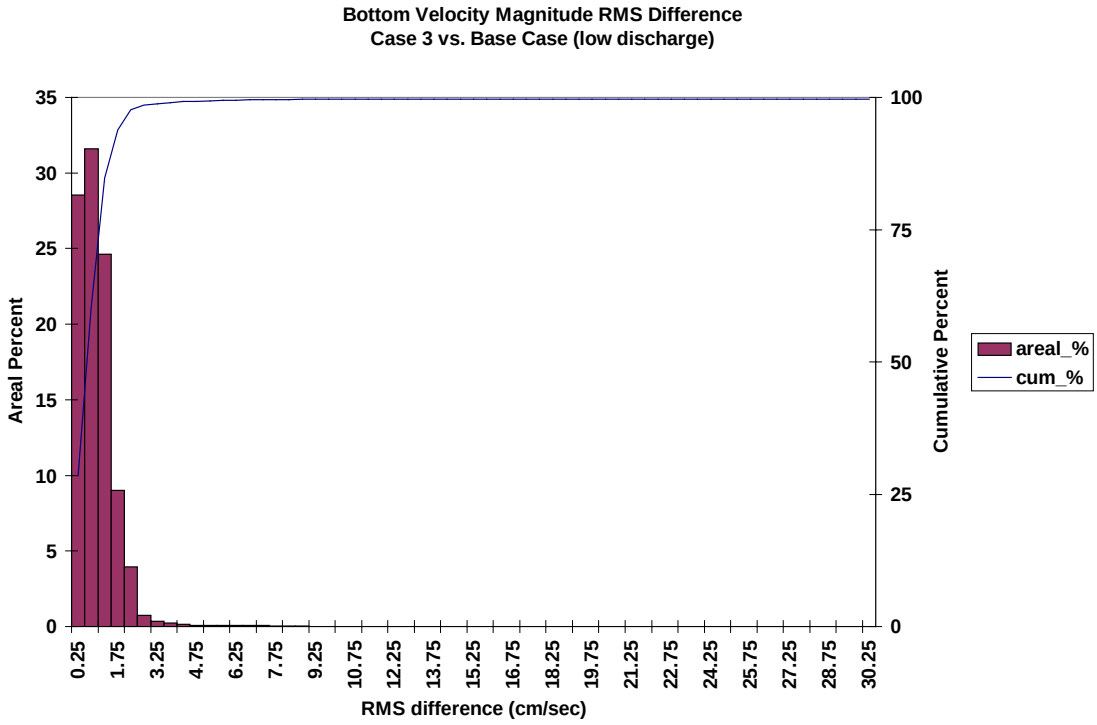

Figure 37. Frequency distribution of bottom velocity RMS difference for the Eastward Expansion (Option 7, 55–foot channel) versus the Base Case during the low discharge event of historical simulation.

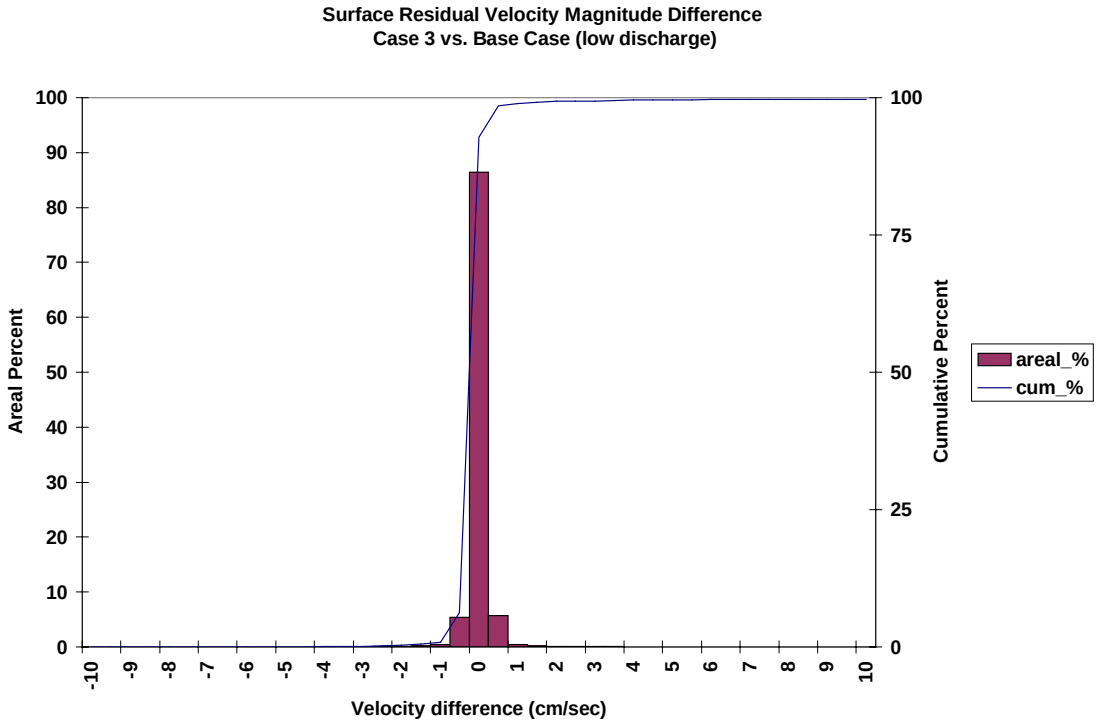

Figure 38. Frequency distribution of surface residual velocity magnitude average difference for the Eastward Expansion (Option 7, 55–foot channel) versus the Base Case during the low discharge event of historical simulation.

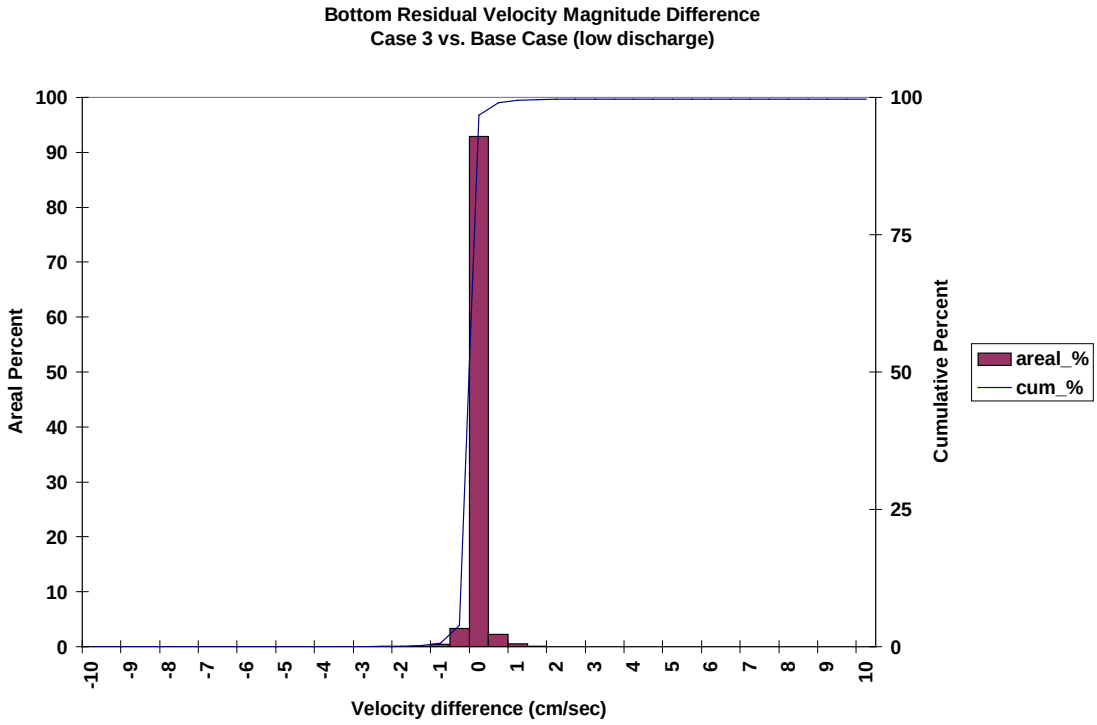

Figure 39. Frequency distribution of bottom residual velocity magnitude average difference for the Eastward Expansion (Option 7, 55–foot channel) versus the Base Case during the low discharge event of historical simulation.

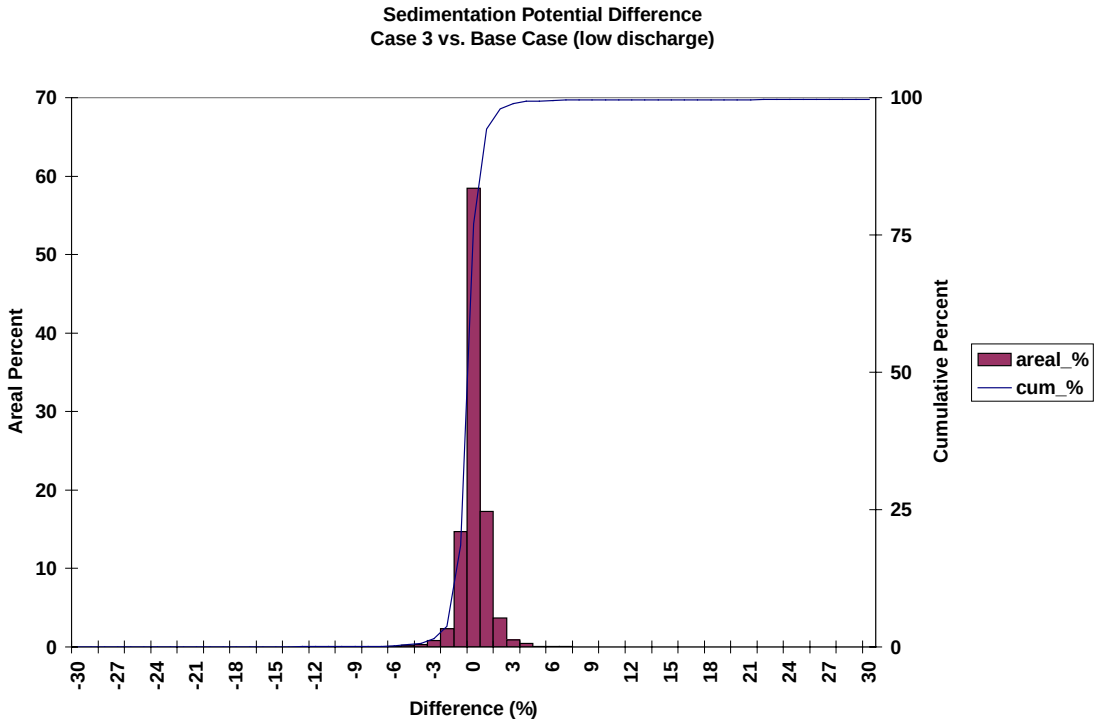

Figure 40. Frequency distribution of sedimentation potential difference for the Eastward Expansion (Option 7, 55–foot channel) versus the Base Case during the low discharge event of historical simulation.

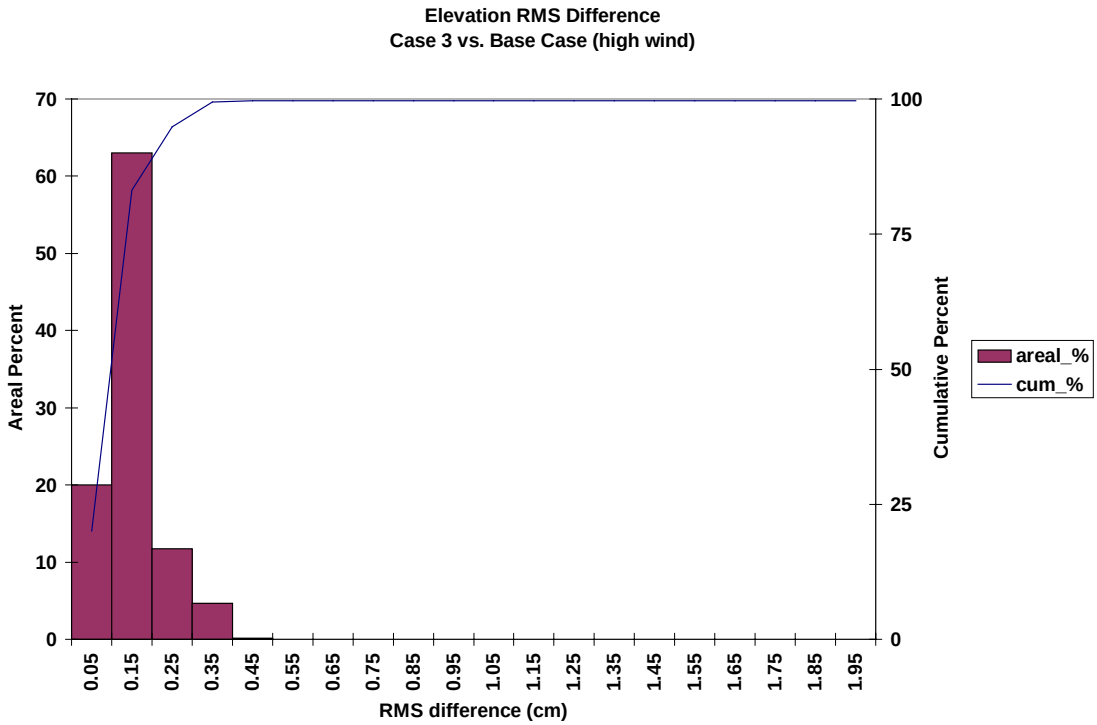

Figure 41. Frequency distribution of elevation RMS difference for the Eastward Expansion (Option 7, 55–foot channel) versus the Base Case during the high wind event of historical simulation.

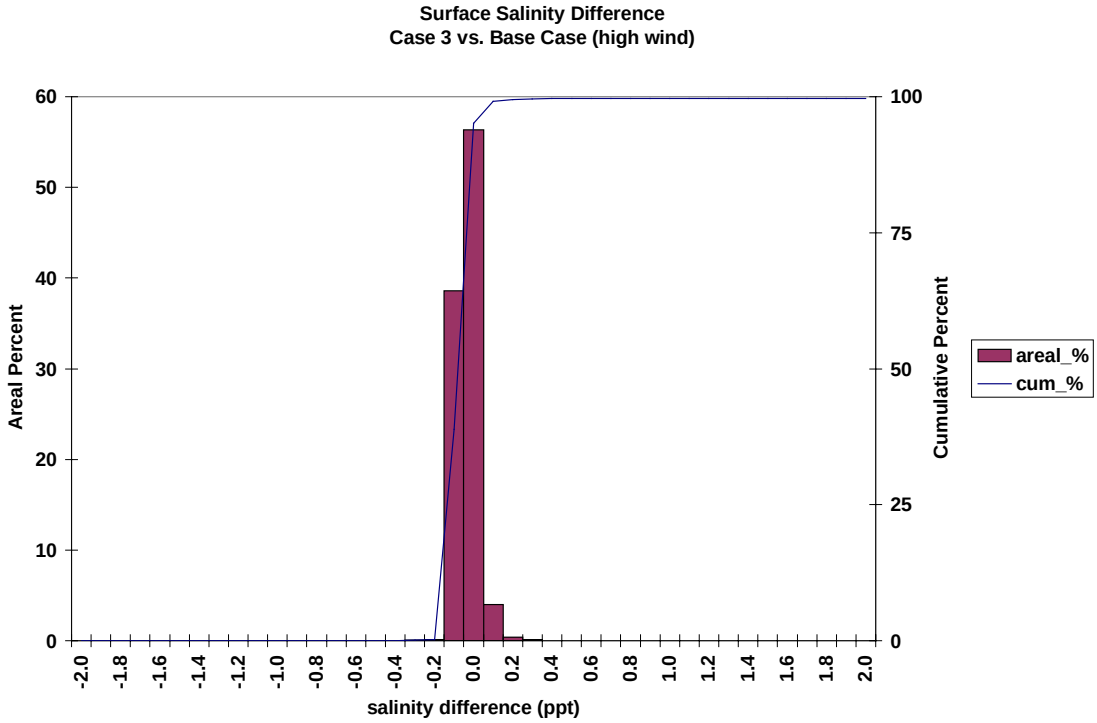

Figure 42. Frequency distribution of surface salinity average difference for the Eastward Expansion (Option 7, 55–foot channel) versus the Base Case during the high wind event of historical simulation.

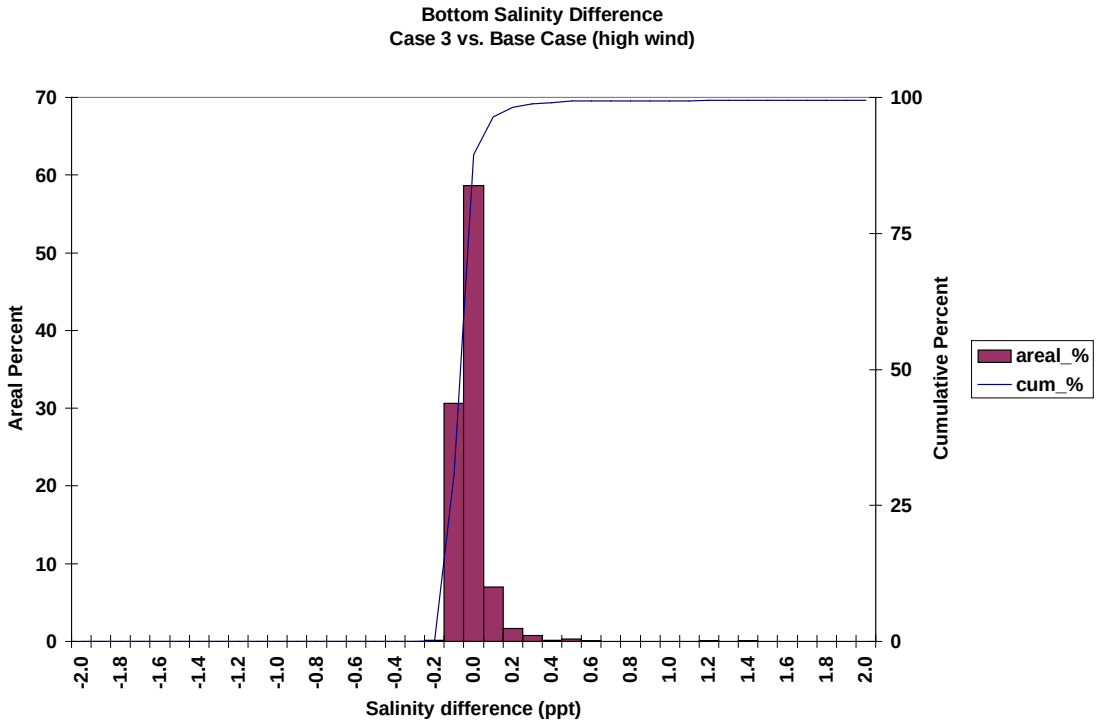

Figure 43. Frequency distribution of bottom salinity average difference for the Eastward Expansion (Option 7, 55–foot channel) versus the Base Case during the high wind event of historical simulation.

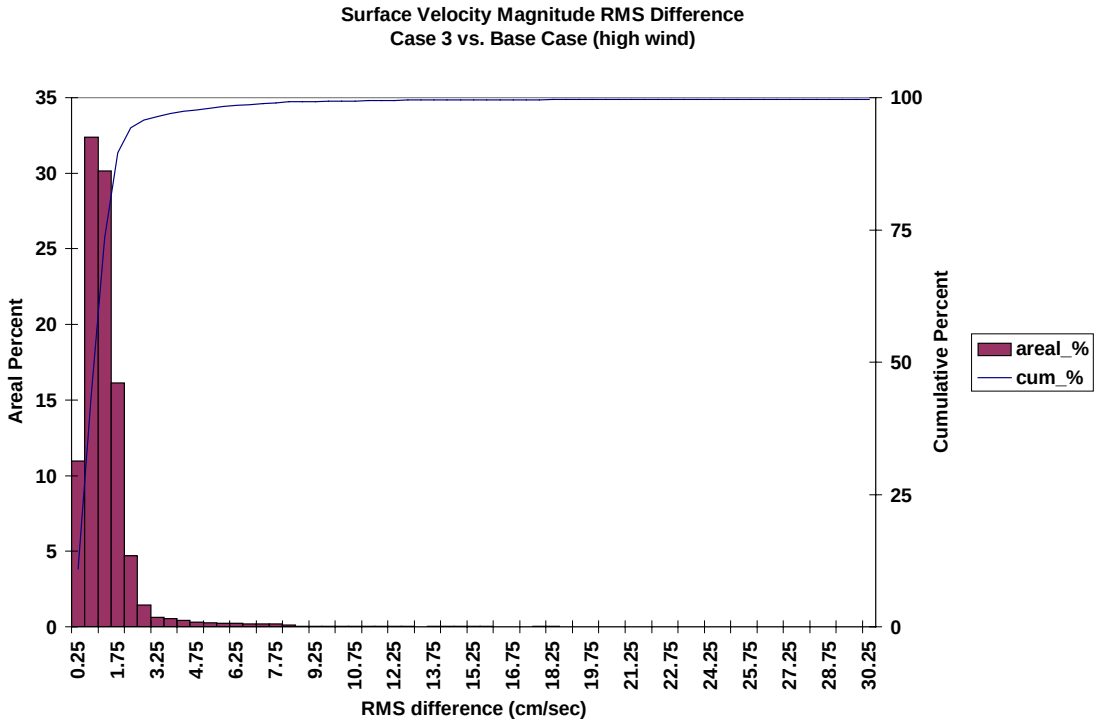

Figure 44. Frequency distribution of surface velocity RMS difference for the Eastward Expansion (Option 7, 55–foot channel) versus the Base Case during the high wind event of historical simulation.

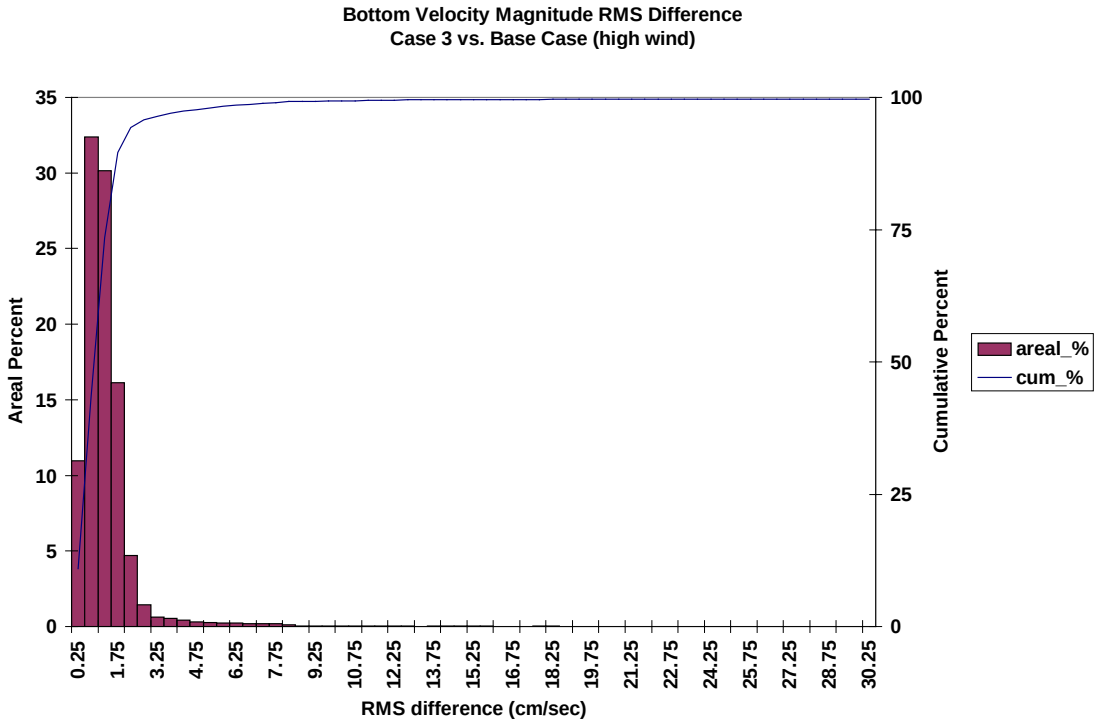

Figure 45. Frequency distribution of bottom velocity RMS difference for the Eastward Expansion (Option 7, 55–foot channel) versus the Base Case during the high wind event of historical simulation.

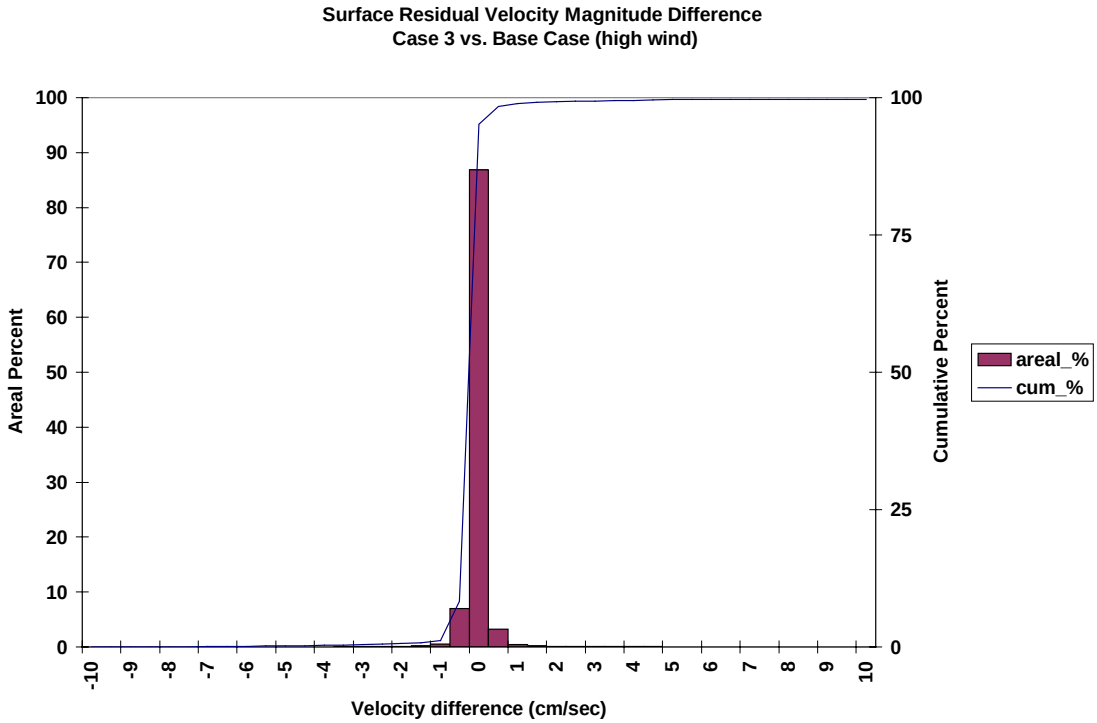

Figure 46. Frequency distribution of surface velocity residual magnitude average difference for the Eastward Expansion (Option 7, 55–foot channel) versus the Base Case during the high wind event of historical simulation.

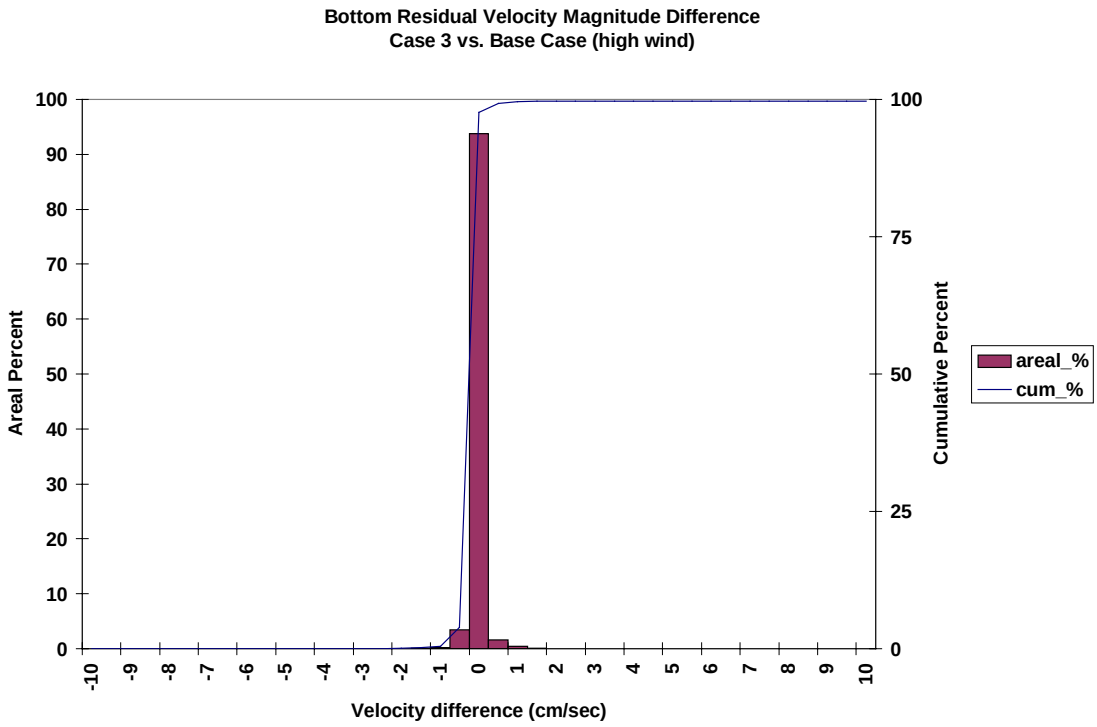

Figure 47. Frequency distribution of bottom velocity residual magnitude average difference for the Eastward Expansion (Option 7, 55–foot channel) versus the Base Case during the high wind event of historical simulation.

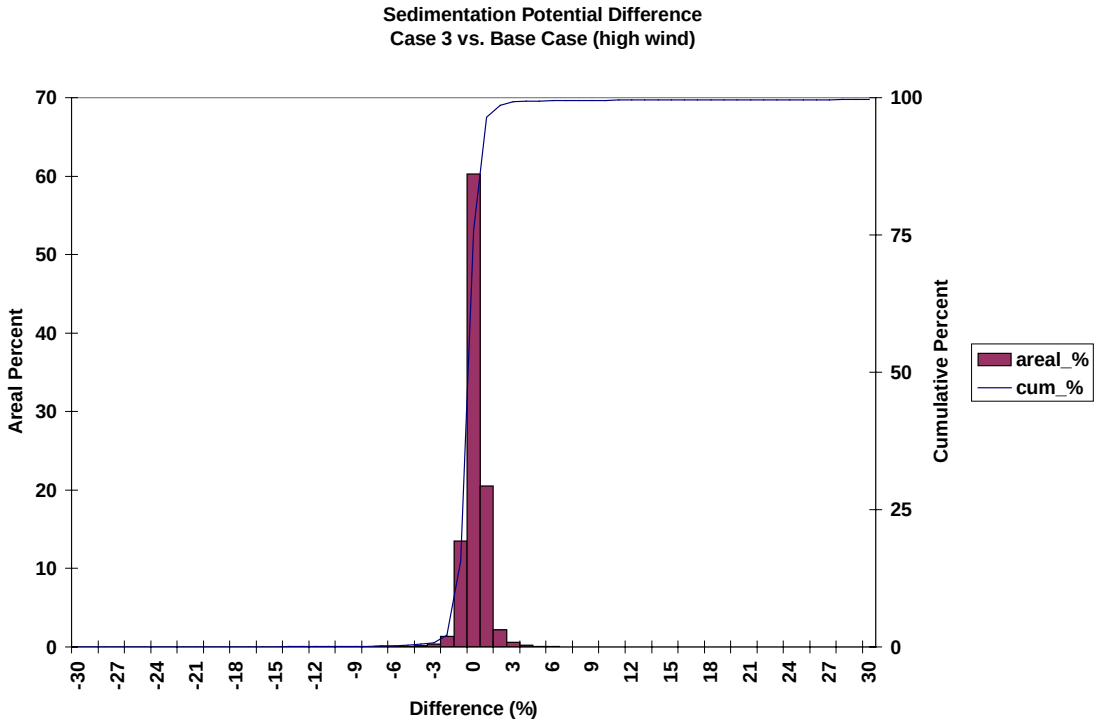

Figure 48. Frequency distribution of sedimentation potential difference for the Eastward Expansion (Option 7, 55–foot channel) versus the Base Case during the high wind event of historical simulation.

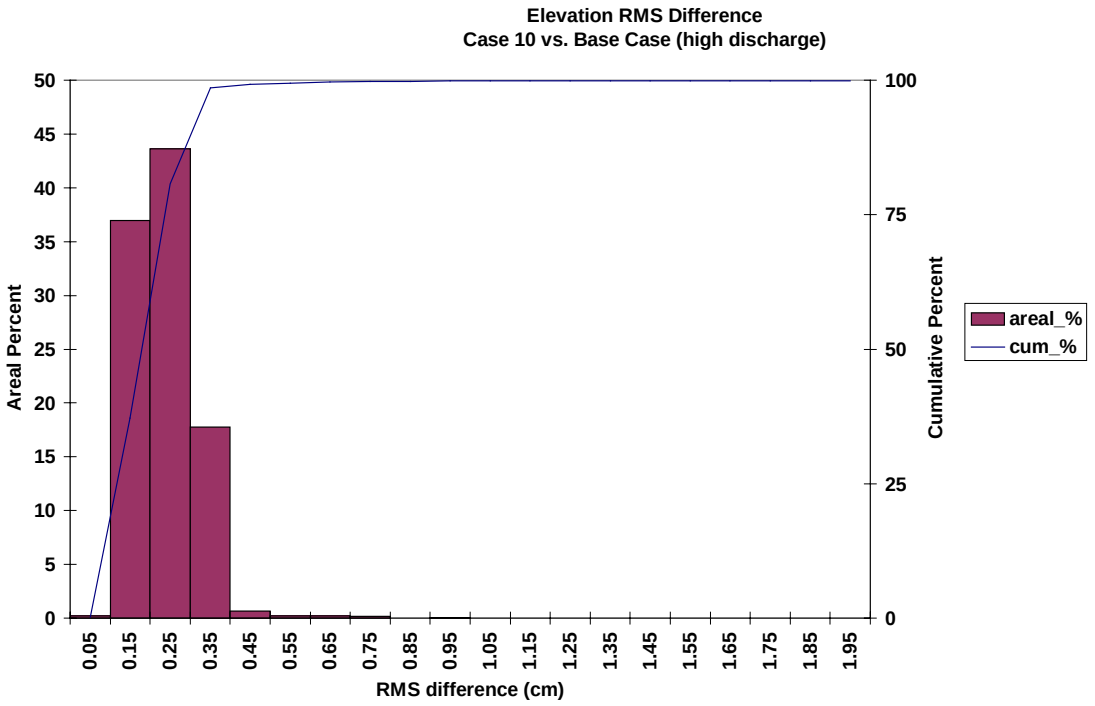

Figure 49. Frequency distribution of elevation RMS difference for the Eastward and Westward Expansion (Option 7/5a, 50–foot channel) versus the Base Case during the high discharge event of historical simulation.

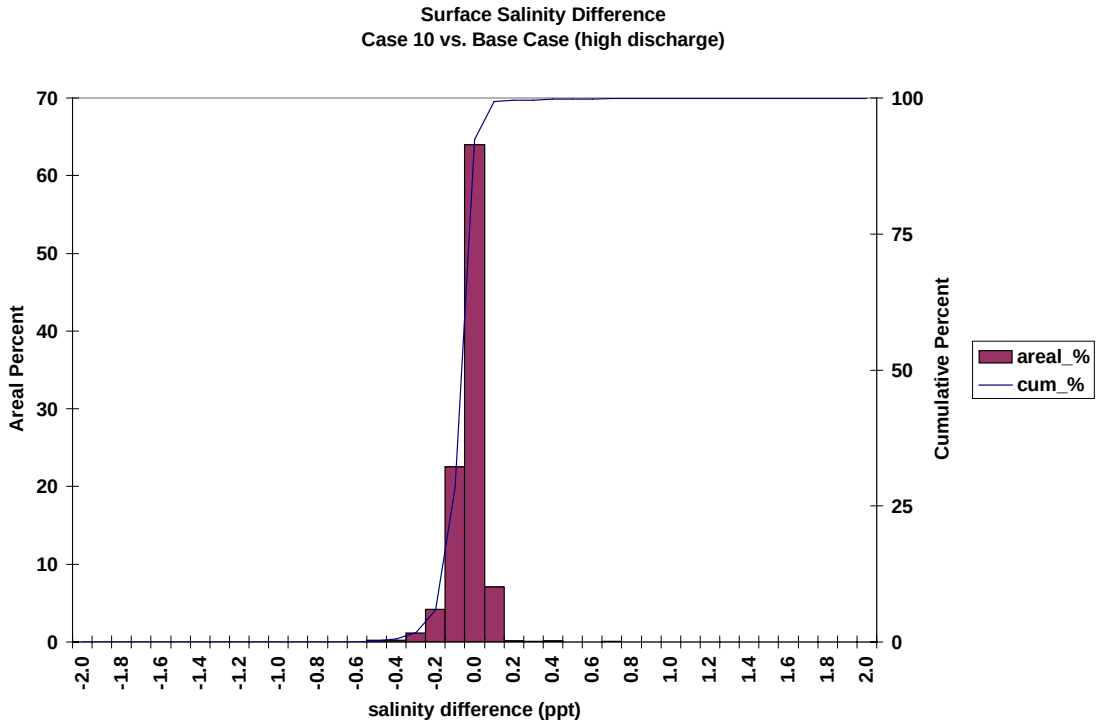

Figure 50. Frequency distribution of surface salinity average difference for the Eastward and Westward Expansion (Option 7/5a, 50–foot channel) versus the Base Case during the high discharge event of historical simulation.

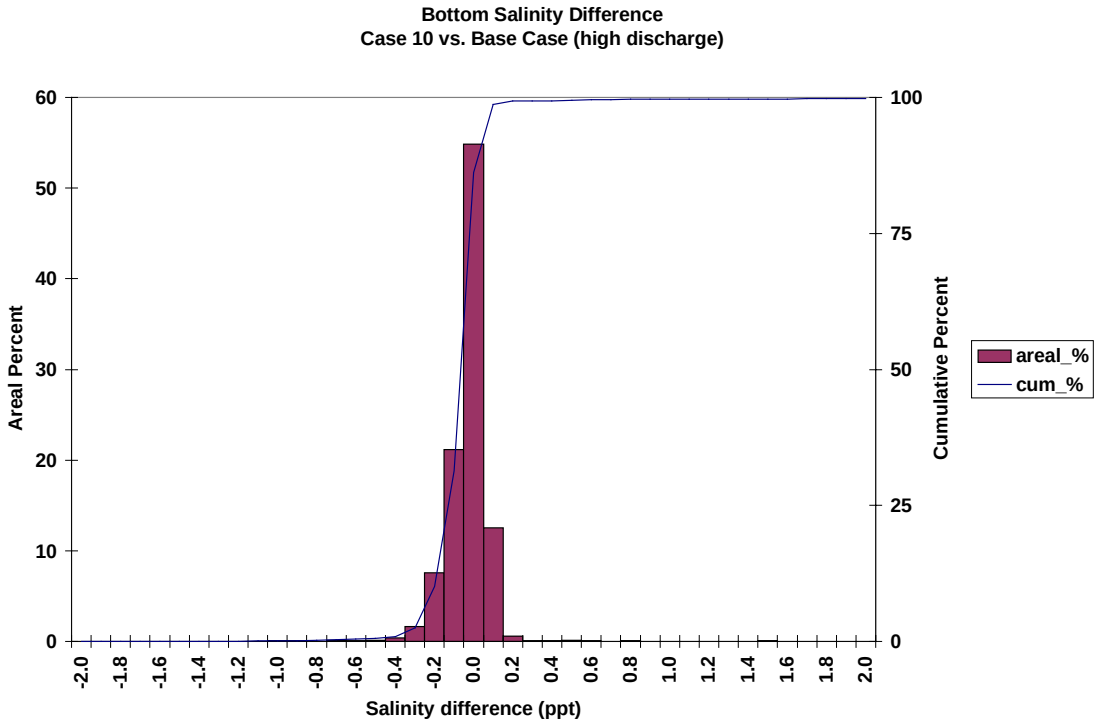

Figure 51. Frequency distribution of bottom salinity average difference for the Eastward and Westward Expansion (Option 7/5a, 50–foot channel) versus the Base Case during the high discharge event of historical simulation.

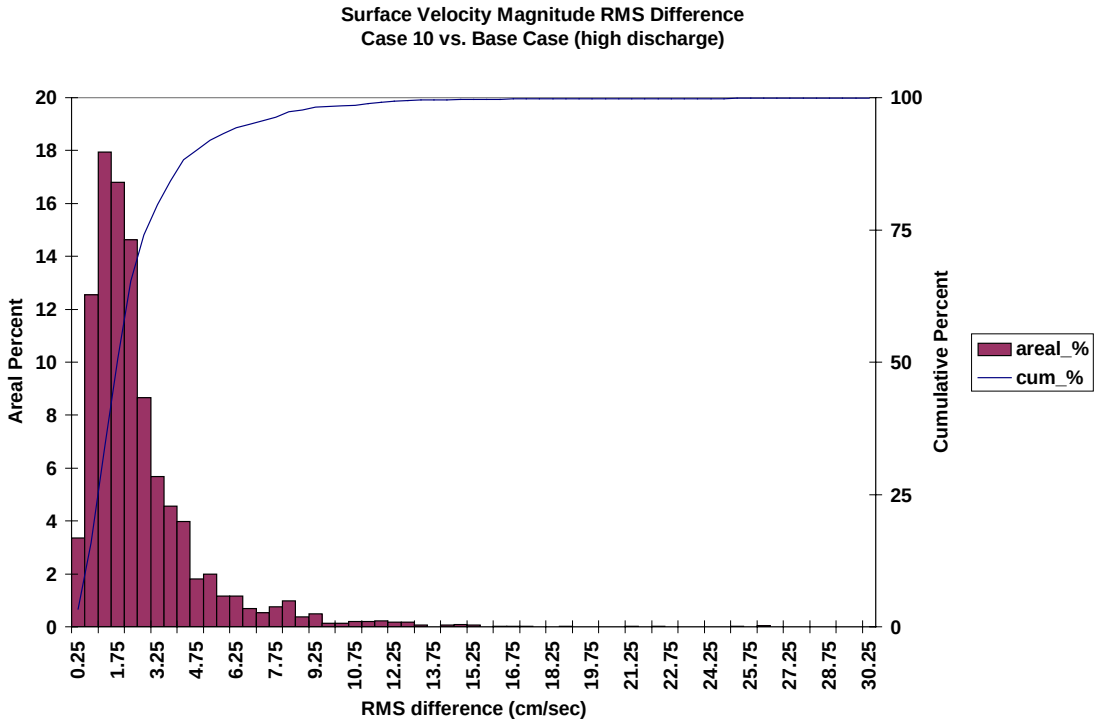

Figure 52. Frequency distribution of surface velocity RMS difference for the Eastward and Westward Expansion (Option 7/5a, 50–foot channel) versus the Base Case during the high discharge event of historical simulation.

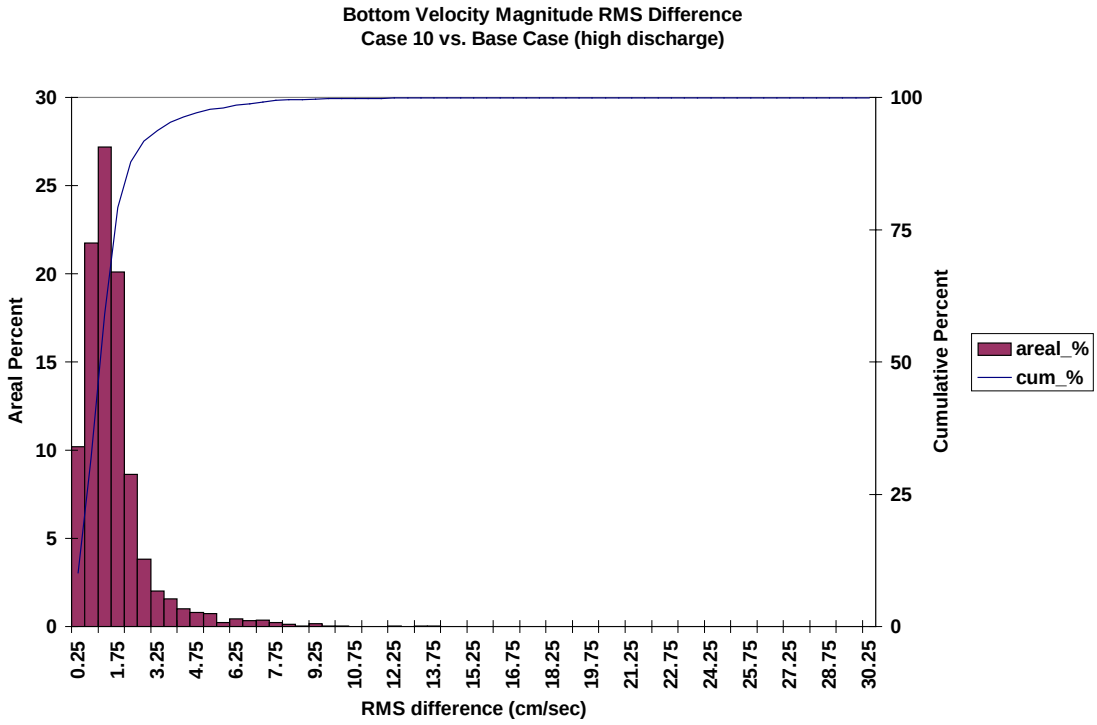

Figure 53. Frequency distribution of bottom velocity RMS difference for the Eastward and Westward Expansion (Option 7/5a, 50–foot channel) versus the Base Case during the high discharge event of historical simulation.

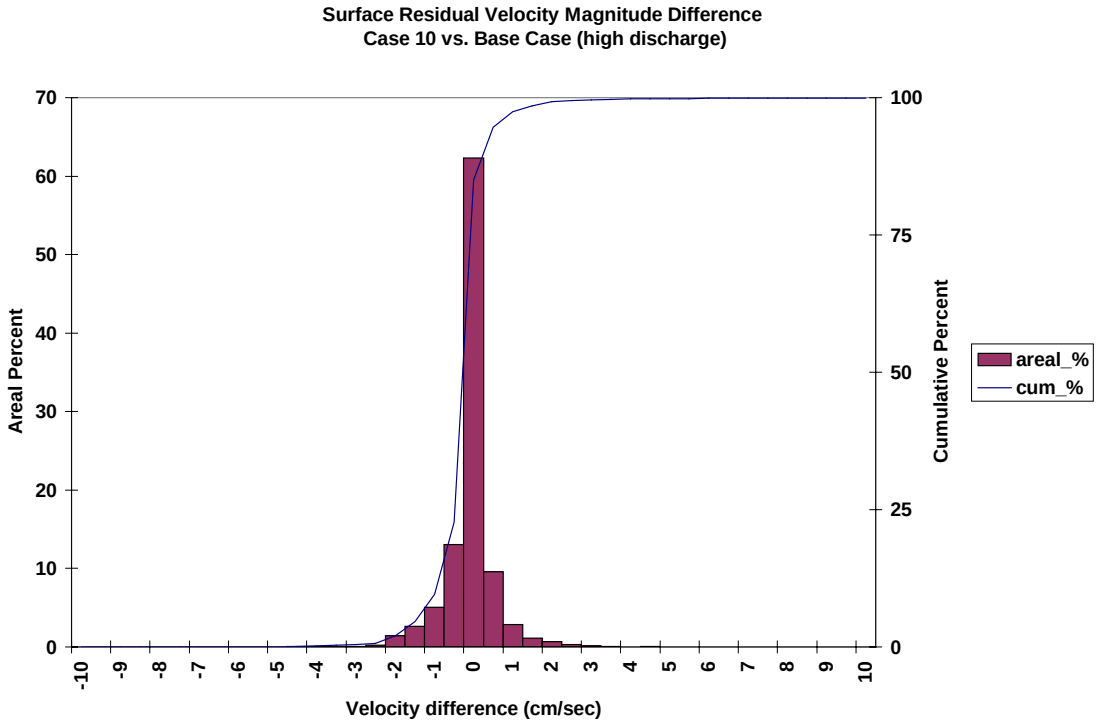

Figure 54. Frequency distribution of surface residual velocity magnitude average difference for the Eastward and Westward Expansion (Option 7/5a, 50–foot channel) versus the Base Case during the high discharge event of historical simulation.

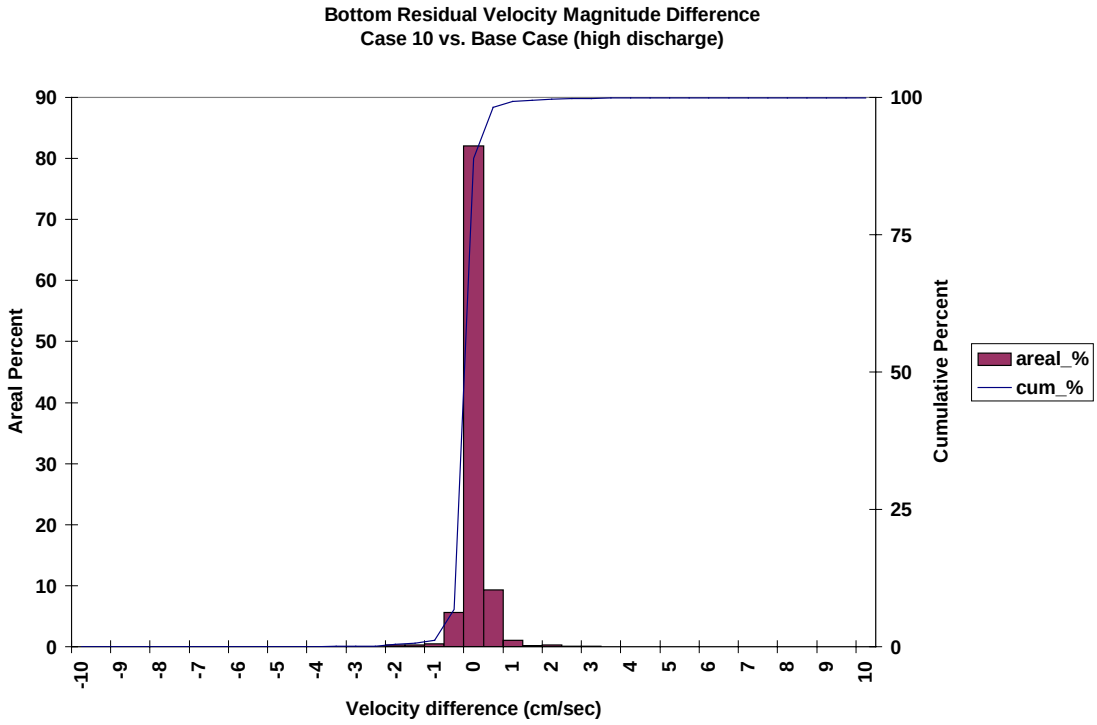

Figure 55. Frequency distribution of bottom residual velocity magnitude average difference for the Eastward and Westward Expansion (Option 7/5a, 50–foot channel) versus the Base Case during the high discharge event of historical simulation.

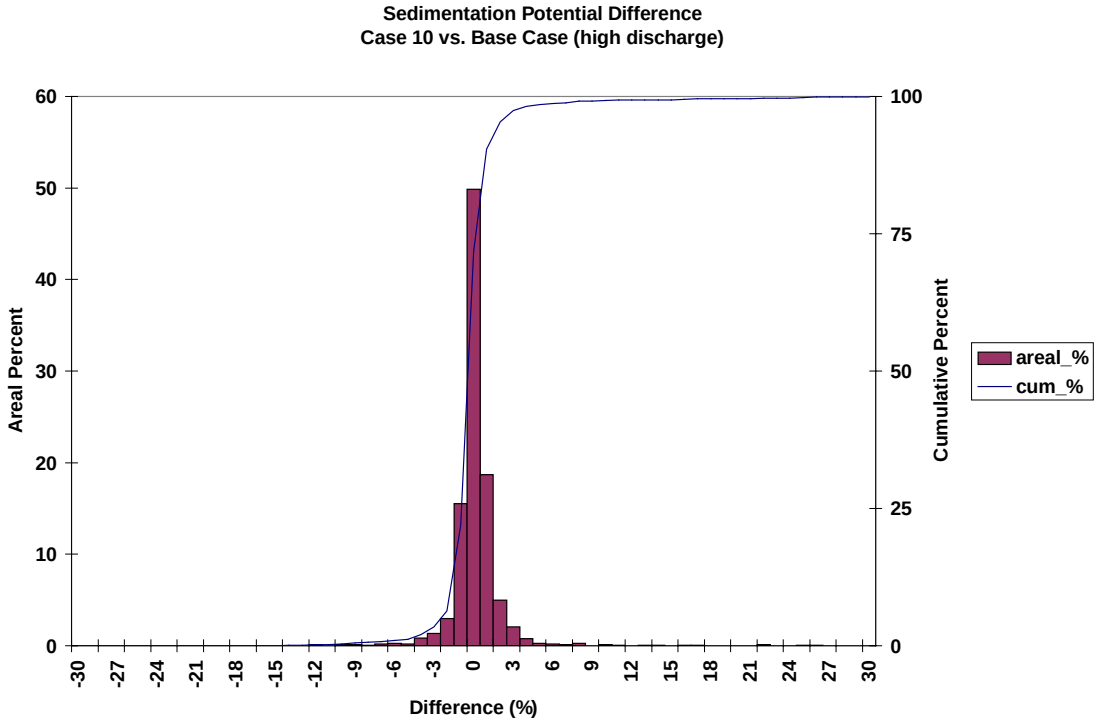

Figure 56. Frequency distribution of sedimentation potential difference for the Eastward and Westward Expansion (Option 7/5a, 50–foot channel) versus the Base Case during the high discharge event of historical simulation.

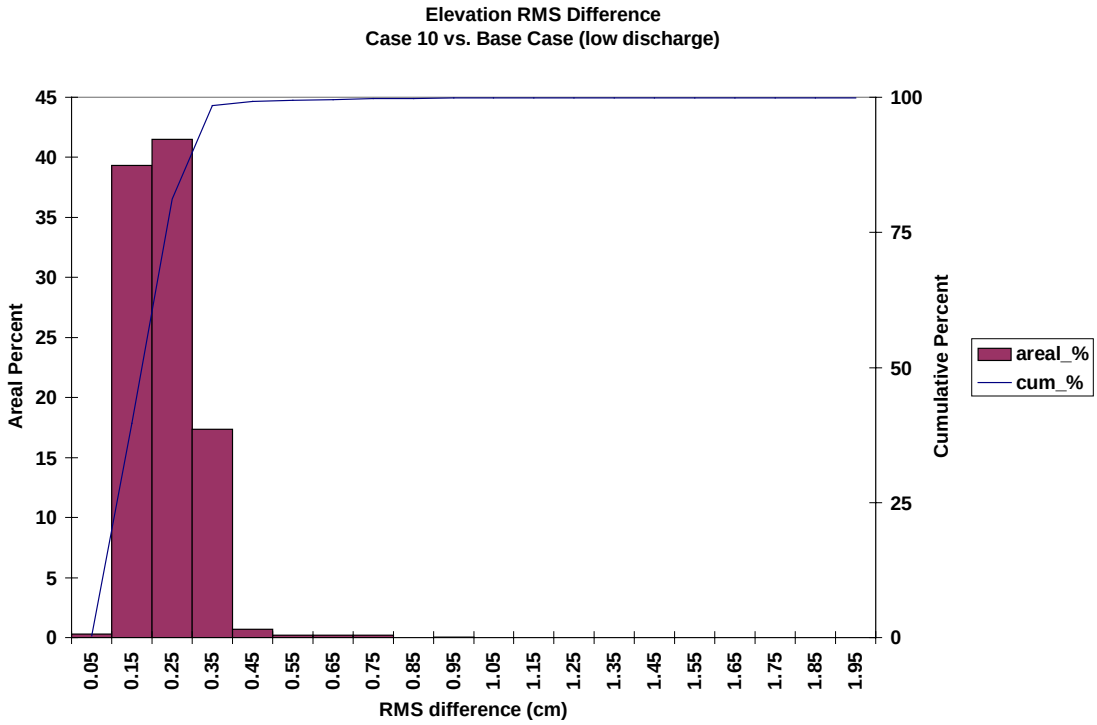

Figure 57. Frequency distribution of elevation RMS difference for the Eastward and Westward Expansion (Option 7/5a, 50–foot channel) versus the Base Case during the low discharge event of historical simulation.

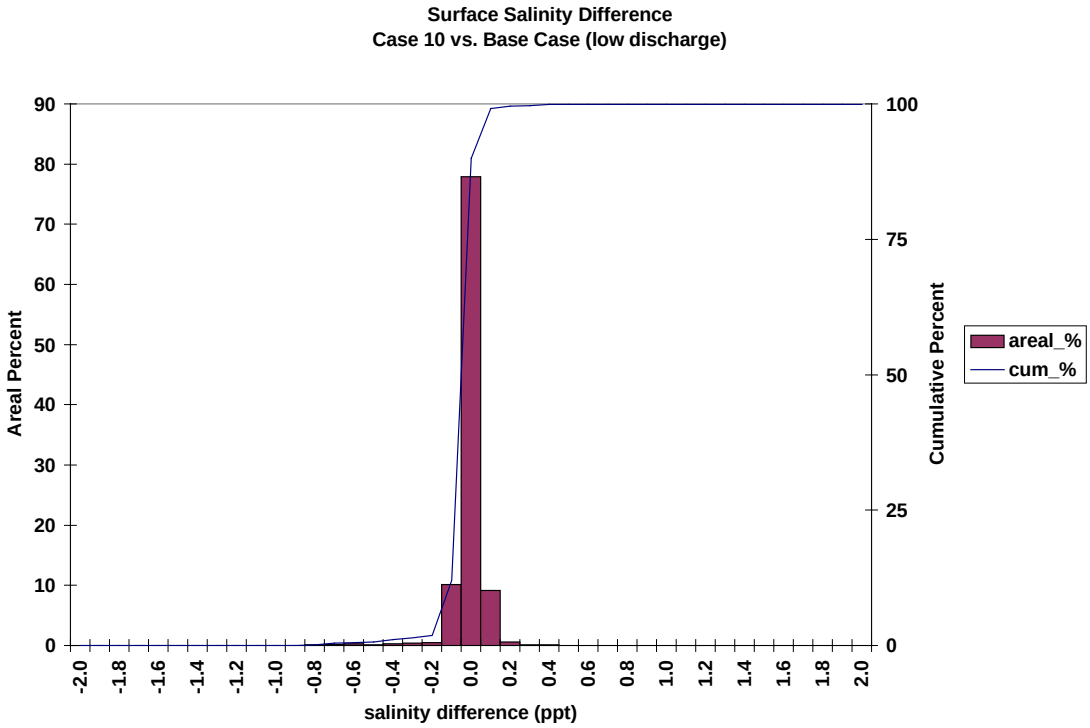

Figure 58. Frequency distribution of surface salinity average difference for the Eastward and Westward Expansion (Option 7/5a, 50–foot channel) versus the Base Case during the low discharge event of historical simulation.

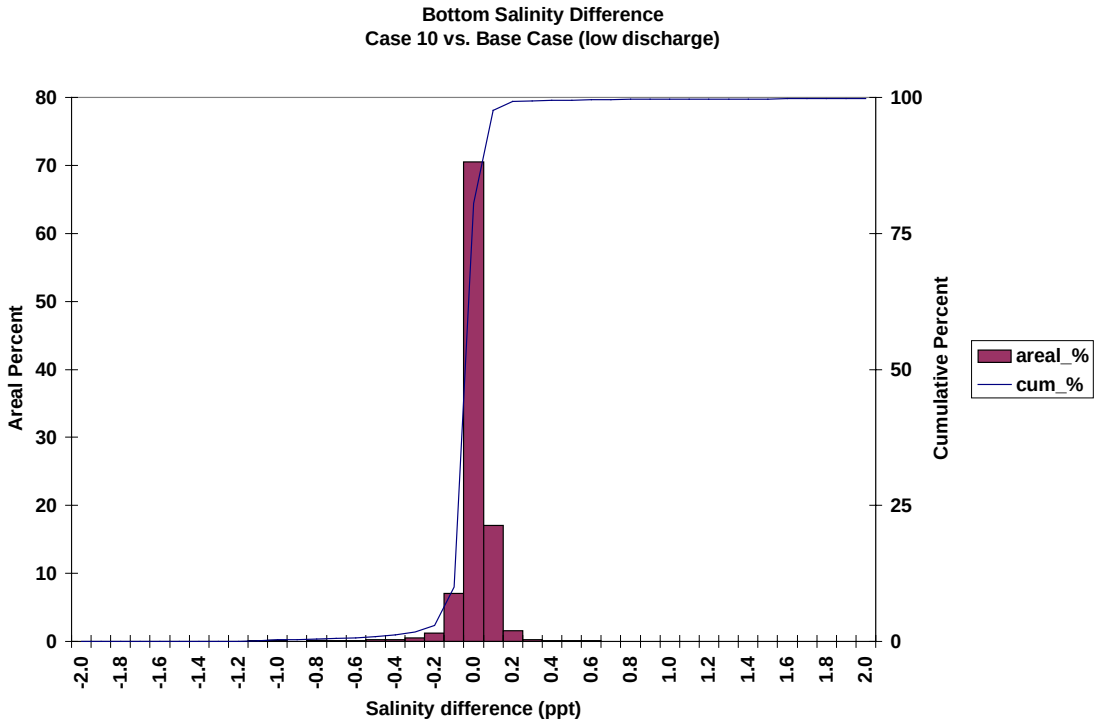

Figure 59. Frequency distribution of bottom salinity average difference for the Eastward and Westward Expansion (Option 7/5a, 50–foot channel) versus the Base Case during the low discharge event of historical simulation.

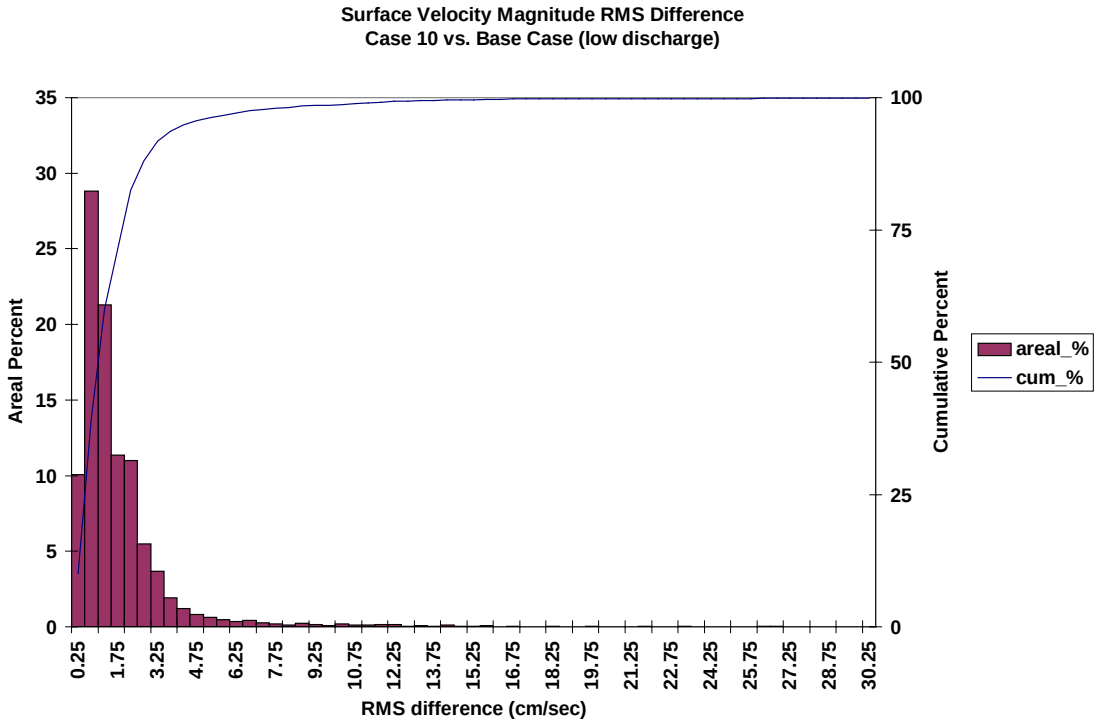

Figure 60. Frequency distribution of surface velocity RMS difference for the Eastward and Westward Expansion (Option 7/5a, 50–foot channel) versus the Base Case during the low discharge event of historical simulation.

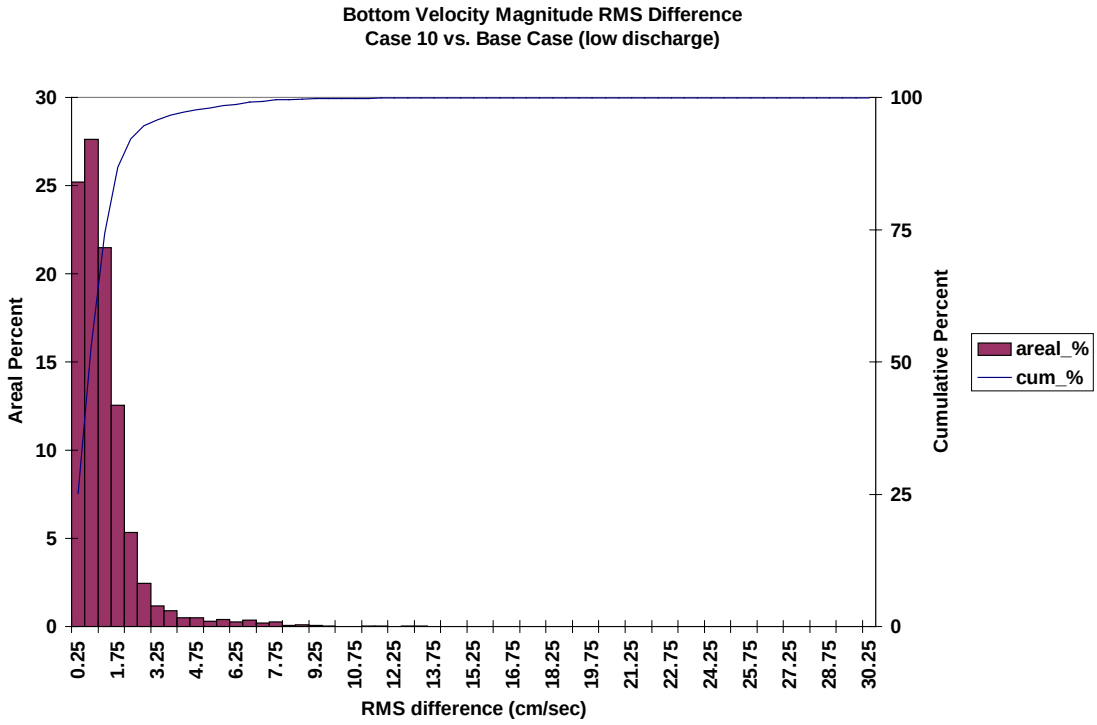

Figure 61. Frequency distribution of bottom velocity RMS difference for the Eastward and Westward Expansion (Option 7/5a, 50–foot channel) versus the Base Case during the low discharge event of historical simulation.

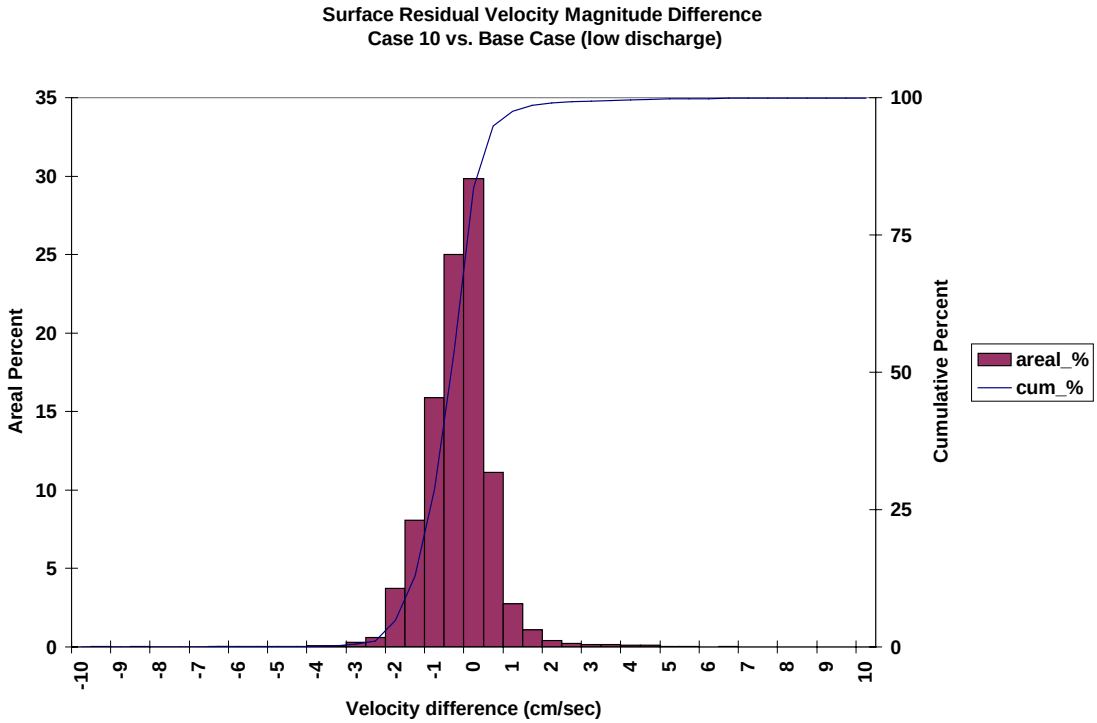

Figure 62. Frequency distribution of surface residual velocity magnitude average difference for the Eastward and Westward Expansion (Option 7/5a, 50–foot channel) versus the Base Case during the low discharge event of historical simulation.

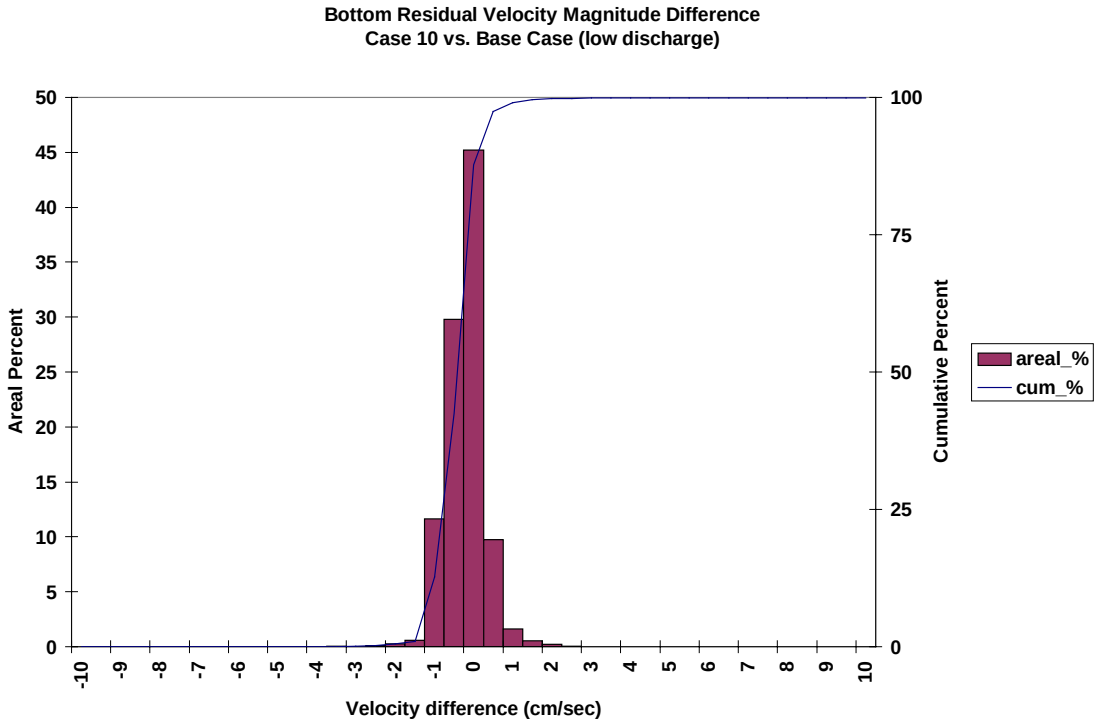

Figure 63. Frequency distribution of bottom residual velocity magnitude average difference for the Eastward and Westward Expansion (Option 7/5a, 50–foot channel) versus the Base Case during the low discharge event of historical simulation.

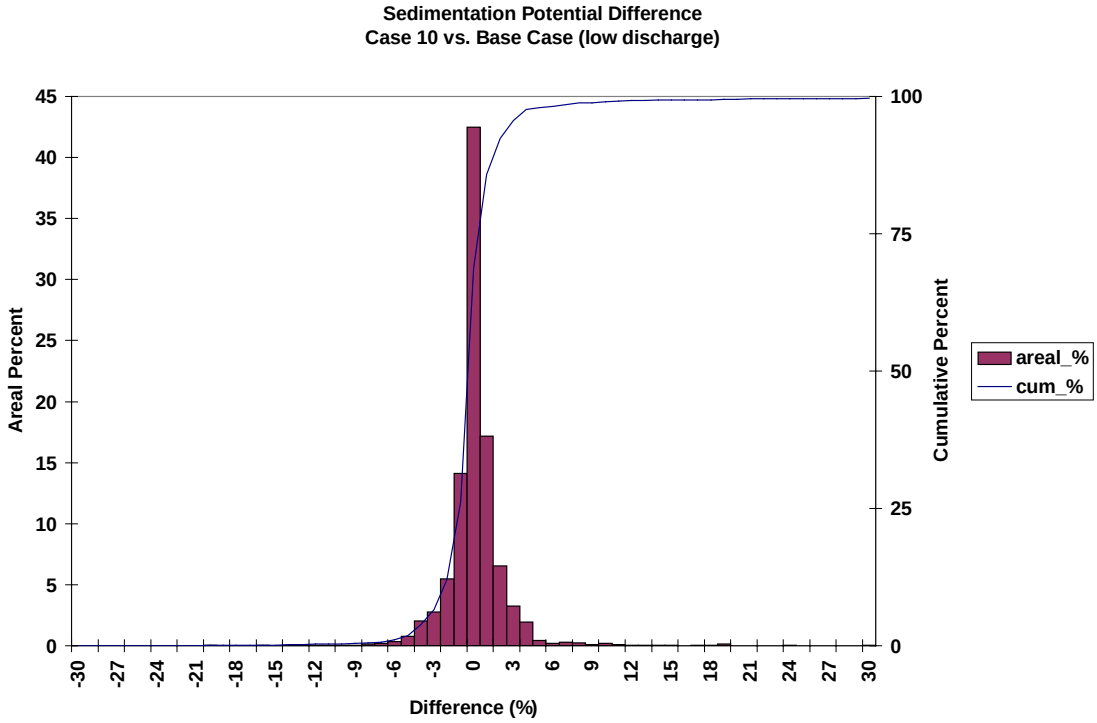

Figure 64. Frequency distribution of sedimentation potential difference for the Eastward and Westward Expansion (Option 7/5a, 50–foot channel) versus the Base Case during the low discharge event of historical simulation.

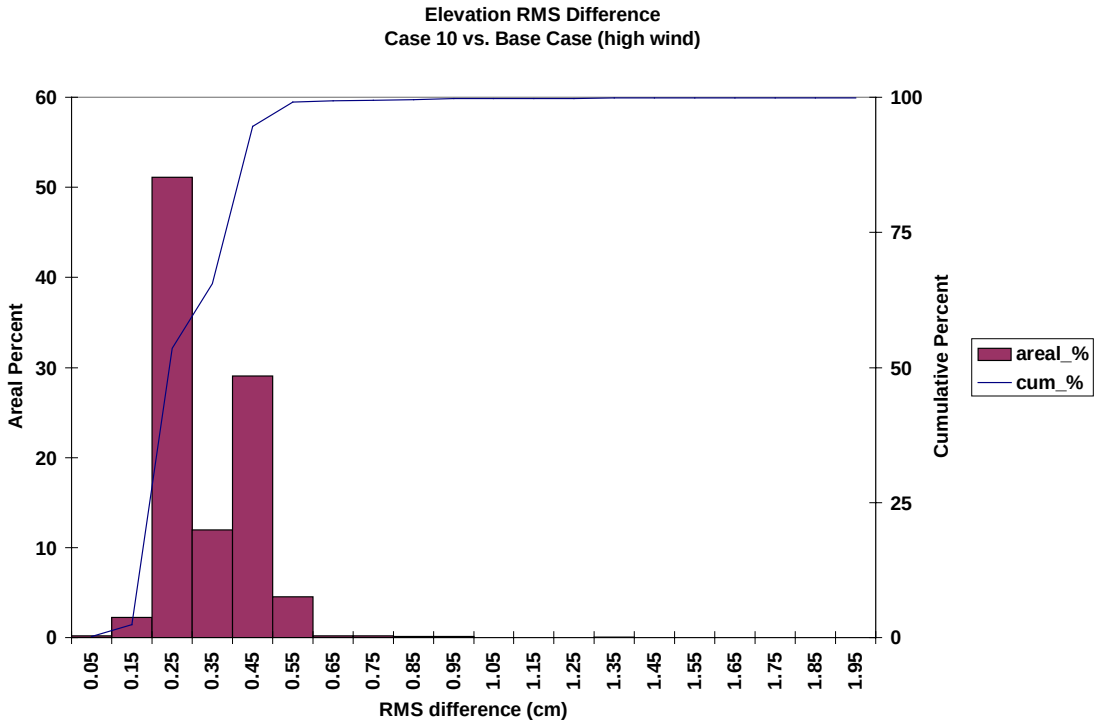

Figure 65. Frequency distribution of elevation RMS difference for the Eastward and Westward Expansion (Option 7/5a, 50–foot channel) versus the Base Case during the high wind event of historical simulation.

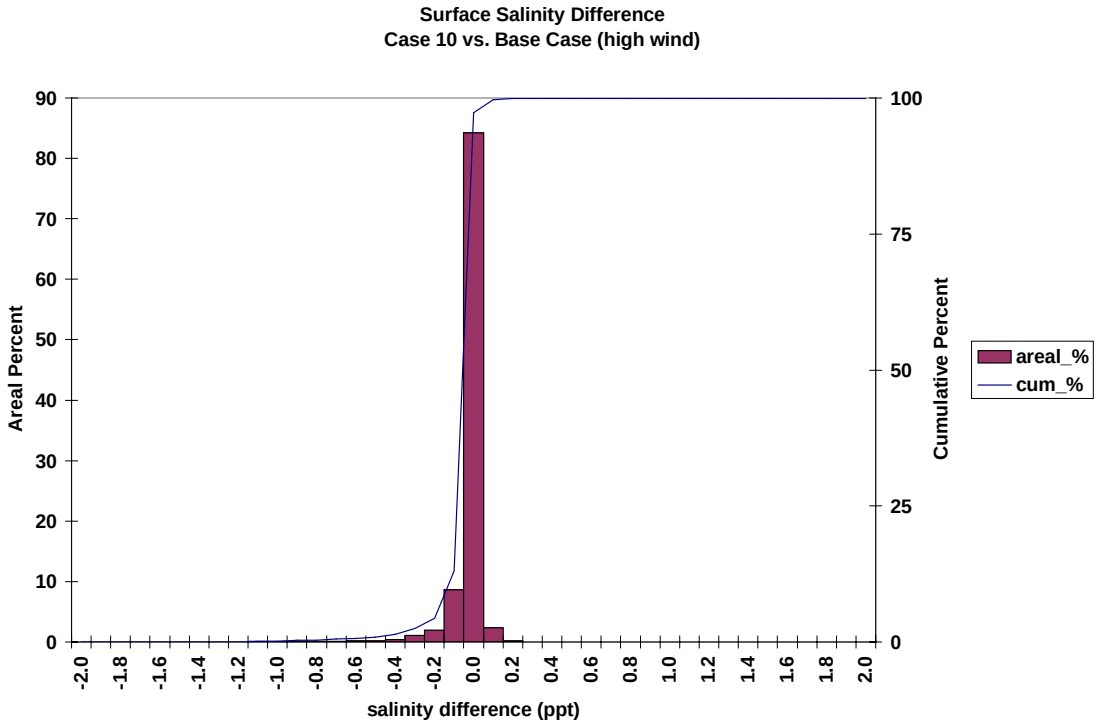

Figure 66. Frequency distribution of surface salinity average difference for the Eastward and Westward Expansion (Option 7/5a, 50–foot channel) versus the Base Case during the high wind event of historical simulation.

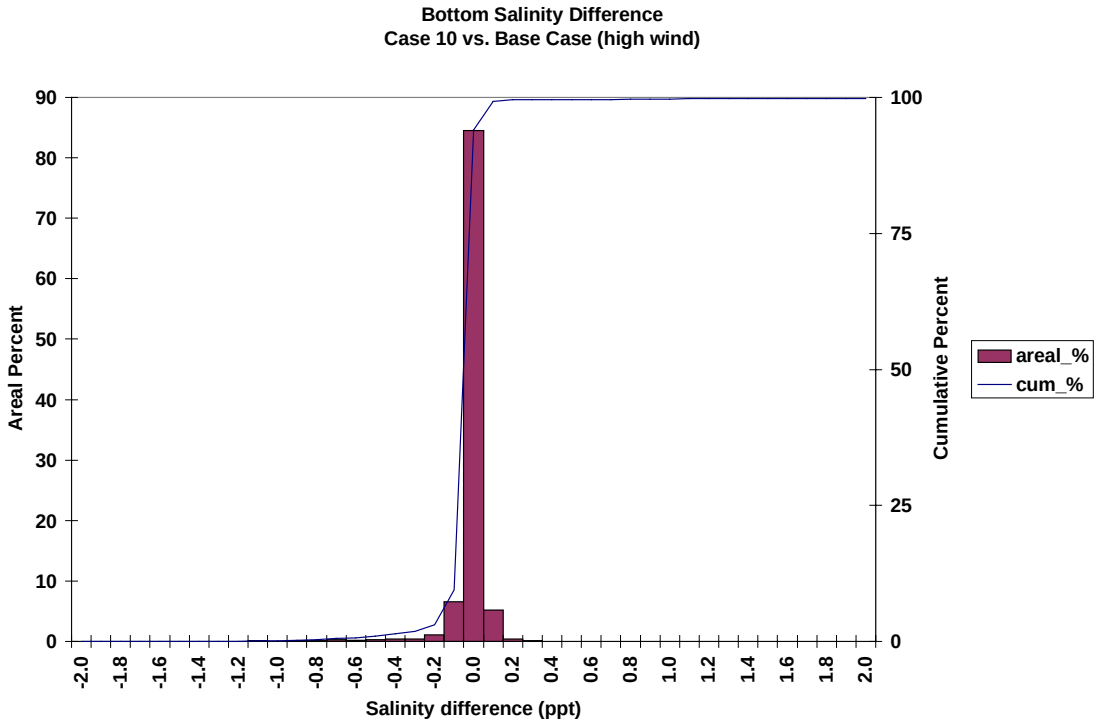

Figure 67. Frequency distribution of bottom salinity average difference for the Eastward and Westward Expansion (Option 7/5a, 50–foot channel) versus the Base Case during the high wind event of historical simulation.

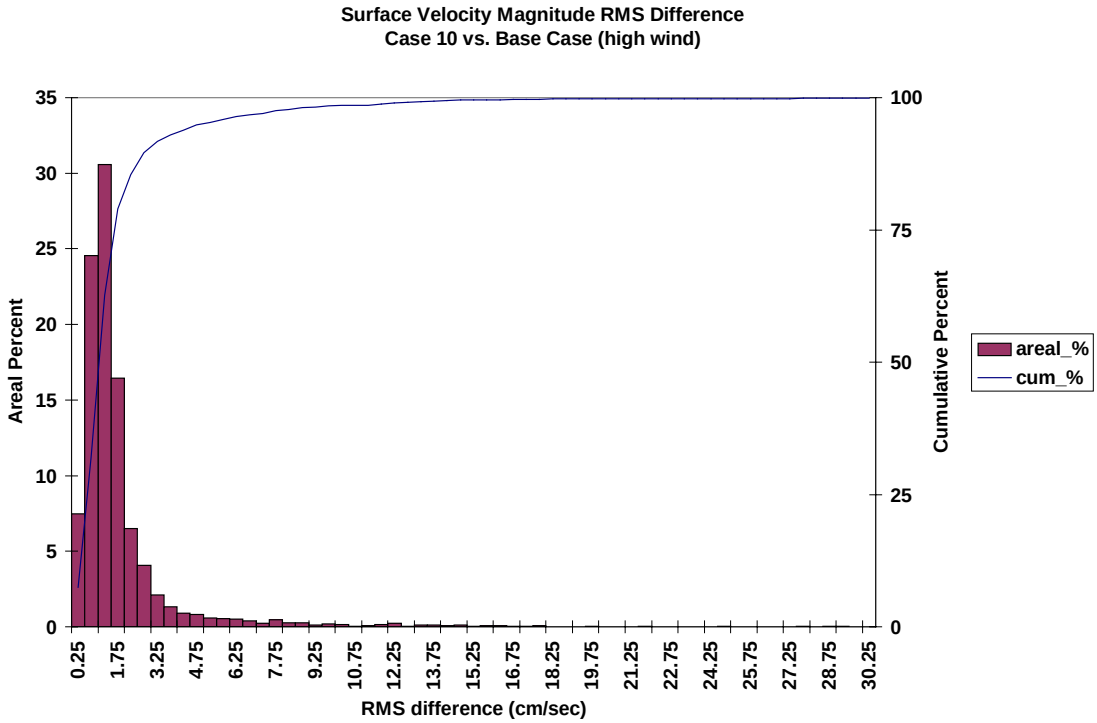

Figure 68. Frequency distribution of surface velocity RMS difference for the Eastward and Westward Expansion (Option 7/5a, 50–foot channel) versus the Base Case during the high wind event of historical simulation.

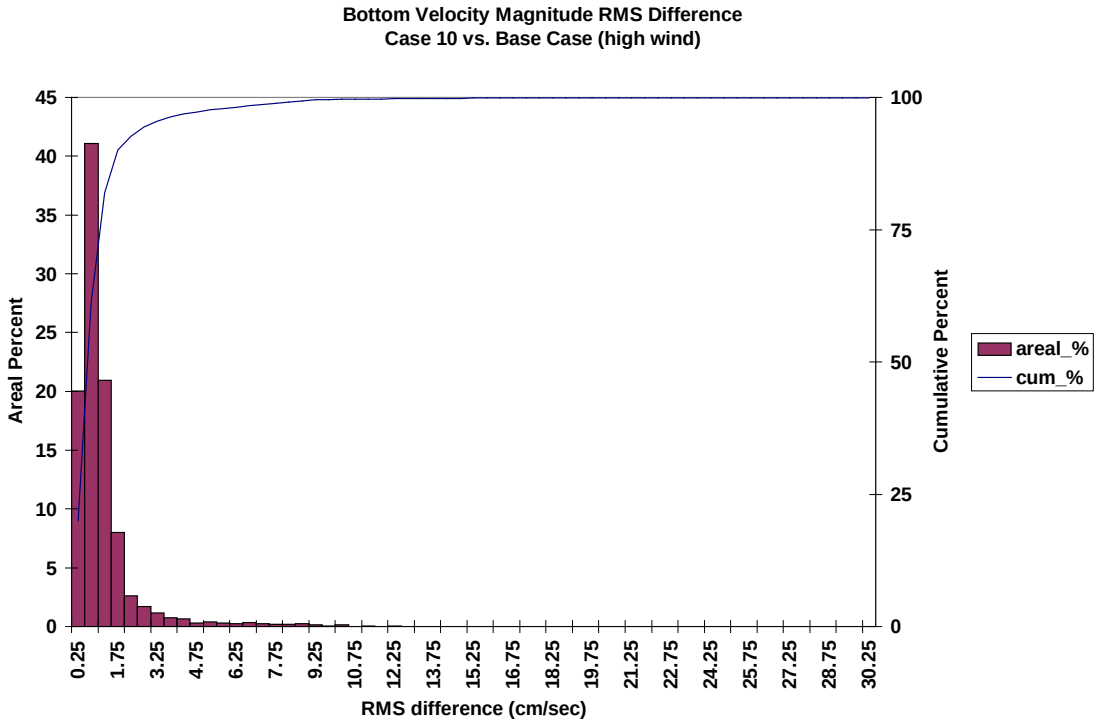

Figure 69. Frequency distribution of bottom velocity RMS difference for the Eastward and Westward Expansion (Option 7/5a, 50–foot channel) versus the Base Case during the high wind event of historical simulation.

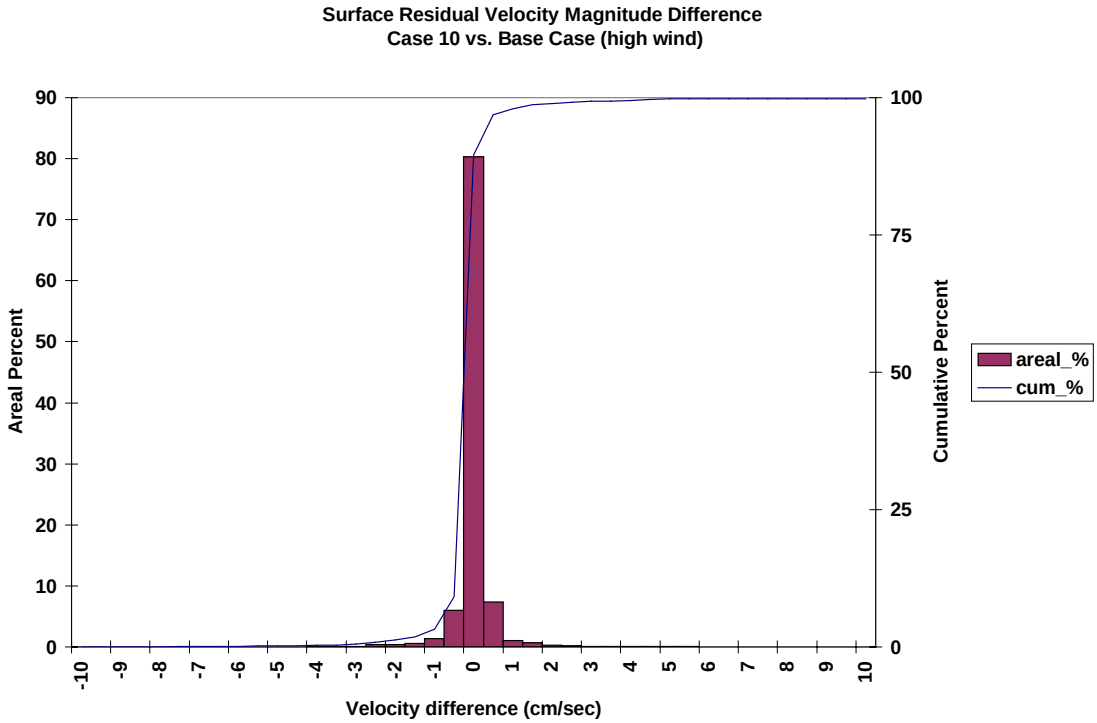

Figure 70. Frequency distribution of surface residual velocity magnitude average difference for the Eastward and Westward Expansion (Option 7/5a, 50–foot channel) versus the Base Case during the high wind event of historical simulation.

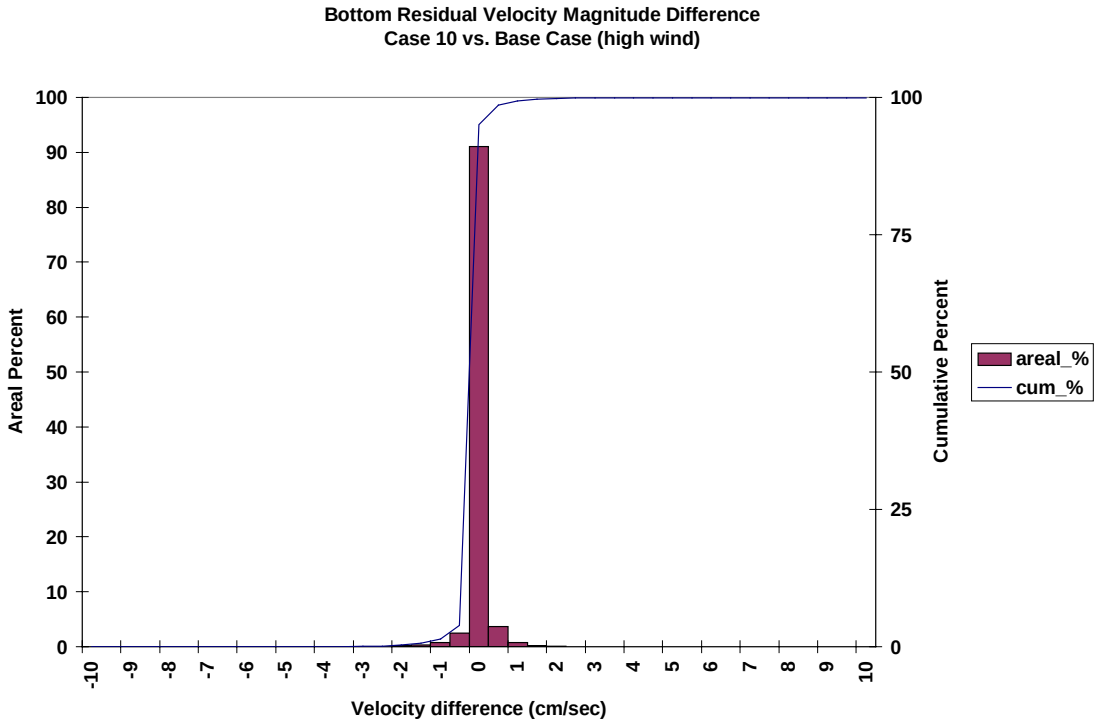

Figure 71. Frequency distribution bottom residual velocity magnitude average difference for the Eastward and Westward Expansion (Option 7/5a, 50–foot channel) versus the Base Case during the high wind event of historical simulation.

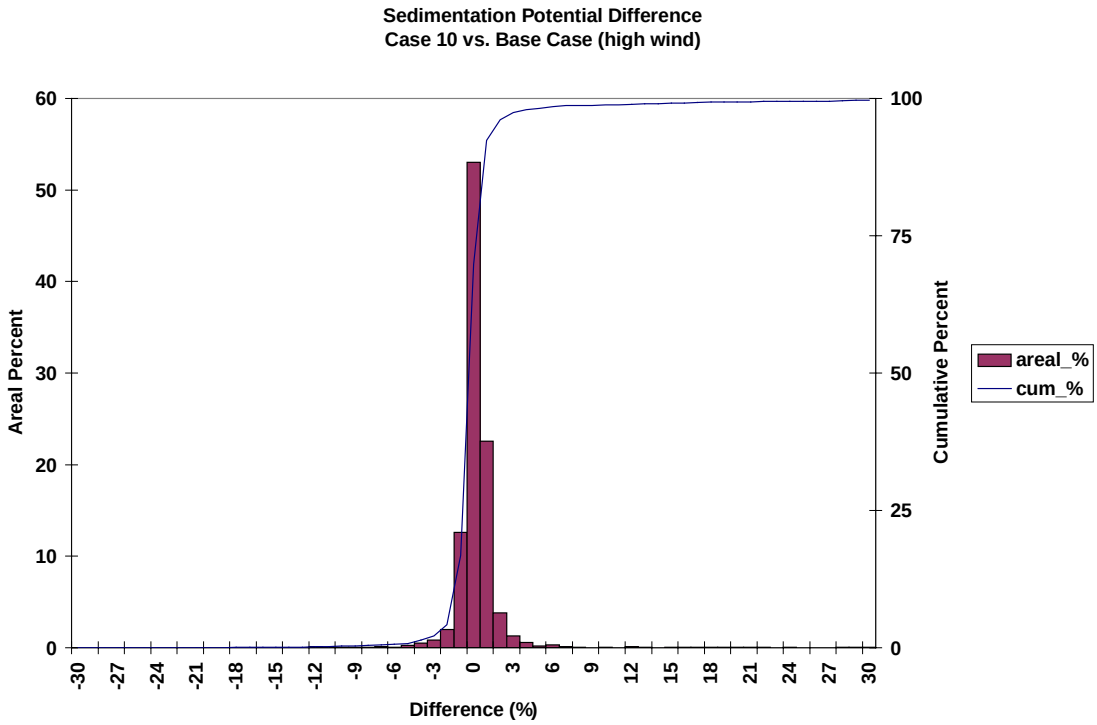

Figure 72. Frequency distribution of sedimentation potential difference for the Eastward and Westward Expansion (Option 7/5a, 50–foot channel) versus the Base Case during the high wind event of historical simulation.

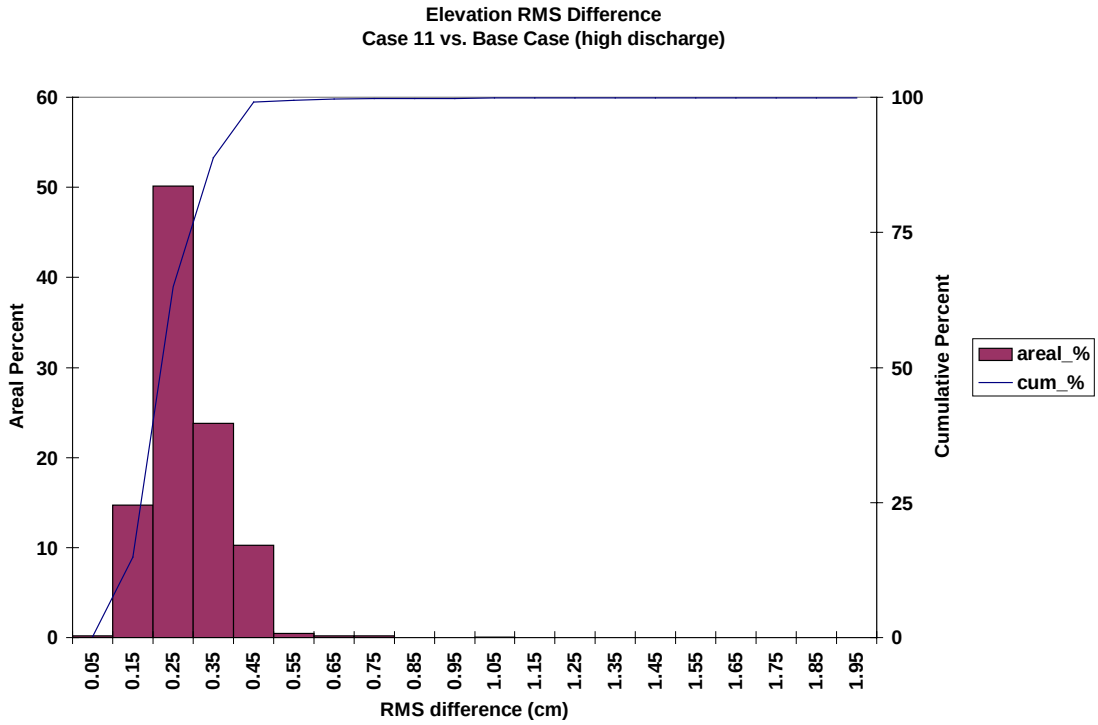

Figure 73. Frequency distribution of elevation RMS difference for the Eastward and Westward Expansion (Option 7/5a, 55–foot channel) versus the Base Case during the high discharge event of historical simulation.

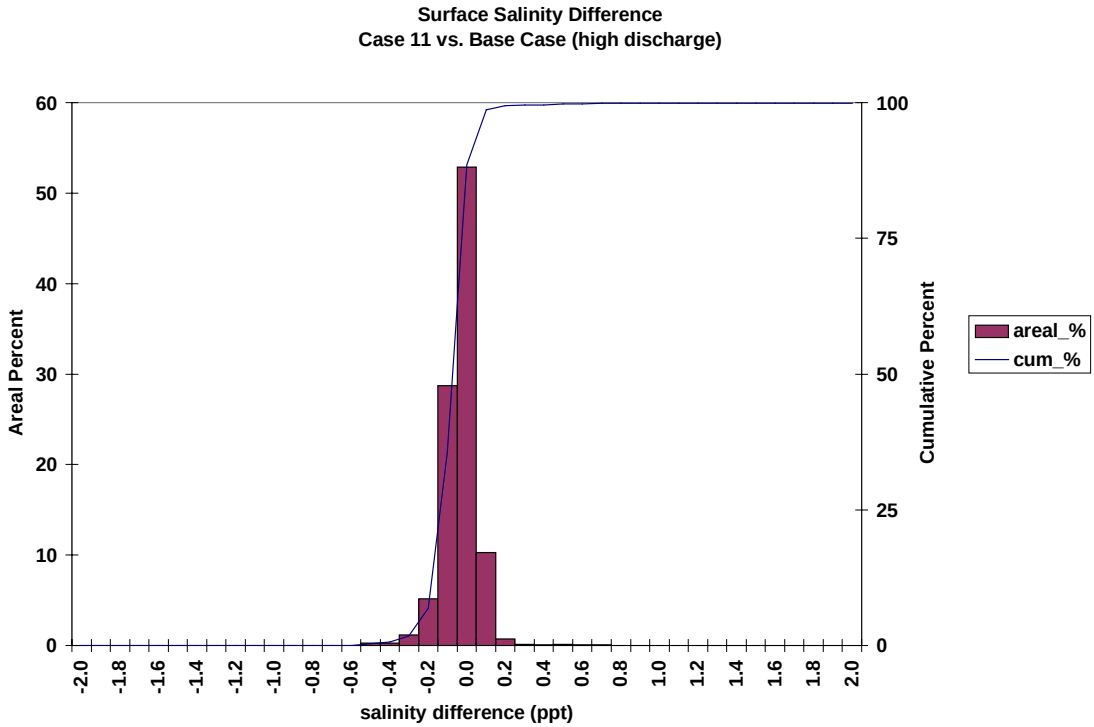

Figure 74. Frequency distribution of surface salinity average difference for the Eastward and Westward Expansion (Option 7/5a, 55–foot channel) versus the Base Case during the high discharge event of historical simulation.

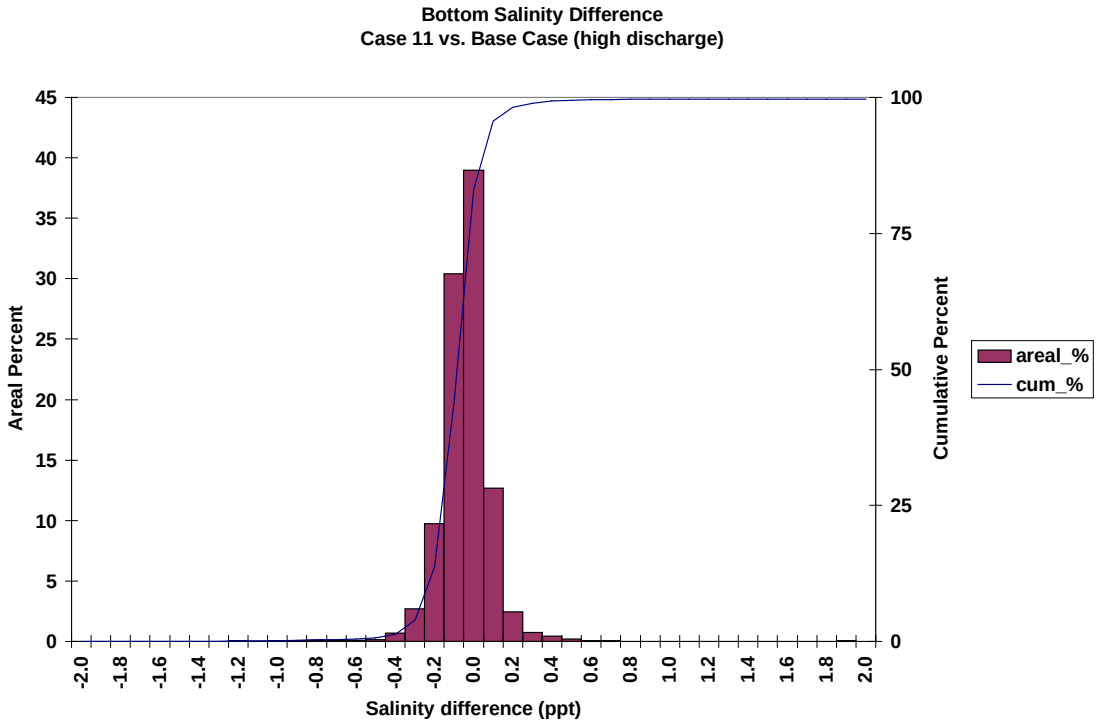

Figure 75. Frequency distribution of bottom salinity average difference for the Eastward and Westward Expansion (Option 7/5a, 55–foot channel) versus the Base Case during the high discharge event of historical simulation.

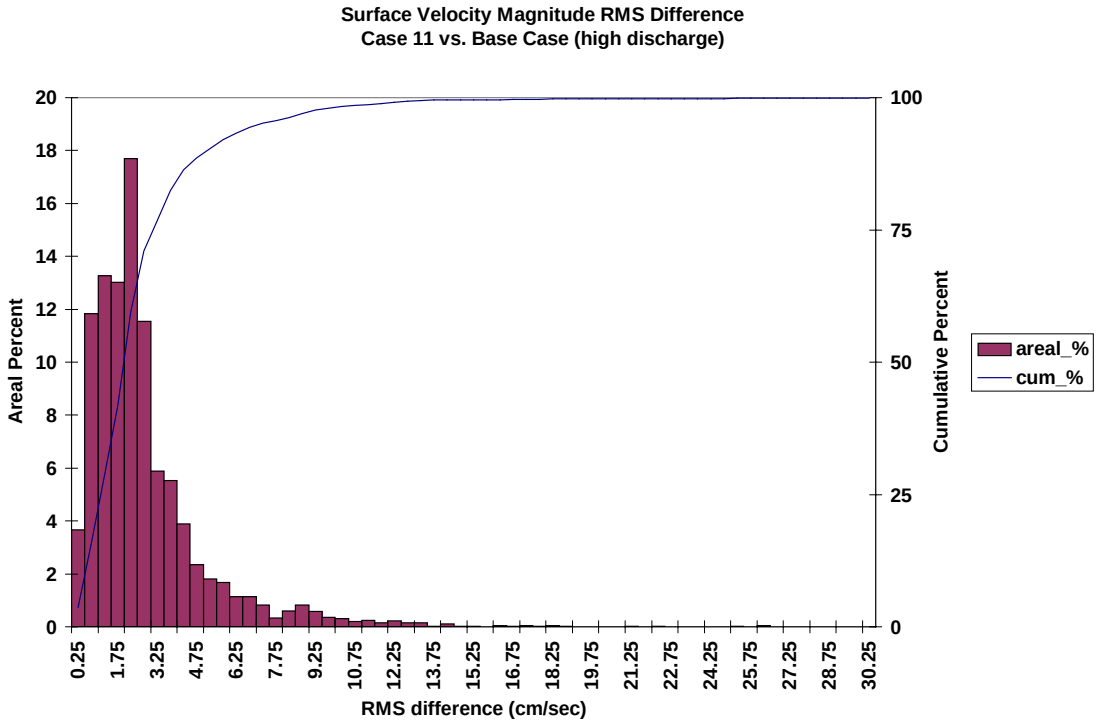

Figure 76. Frequency distribution of surface velocity RMS difference for the Eastward and Westward Expansion (Option 7/5a, 55–foot channel) versus the Base Case during the high discharge event of historical simulation.

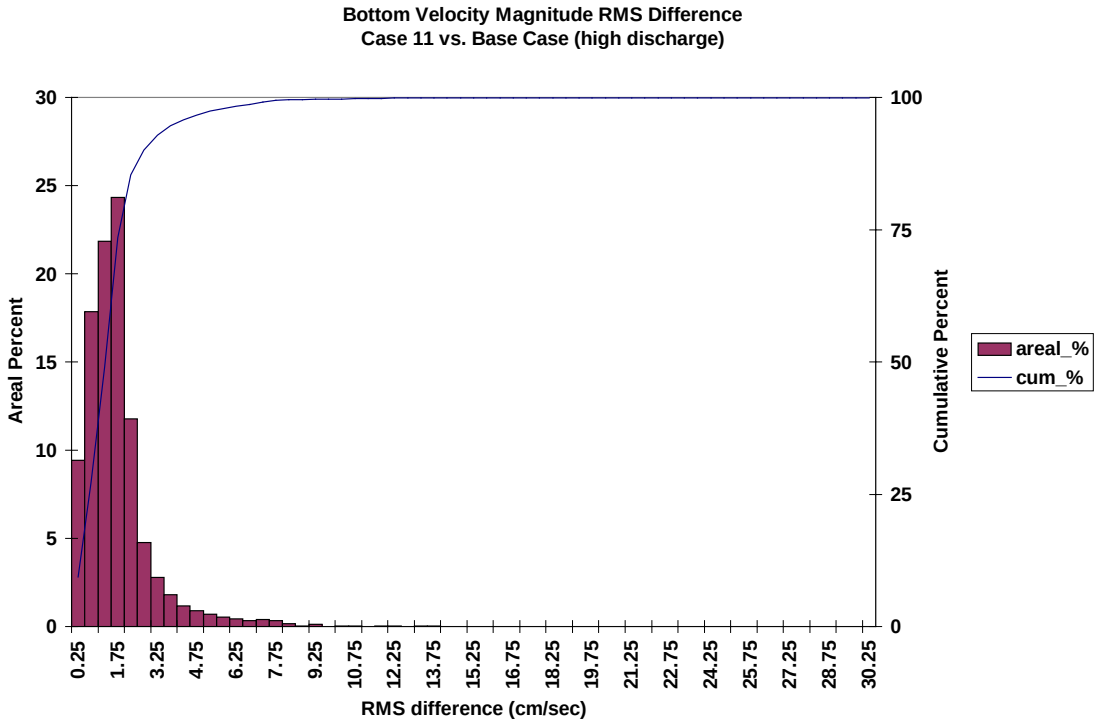

Figure 77. Frequency distribution of bottom velocity RMS difference for the Eastward and Westward Expansion (Option 7/5a, 55–foot channel) versus the Base Case during the high discharge event of historical simulation.

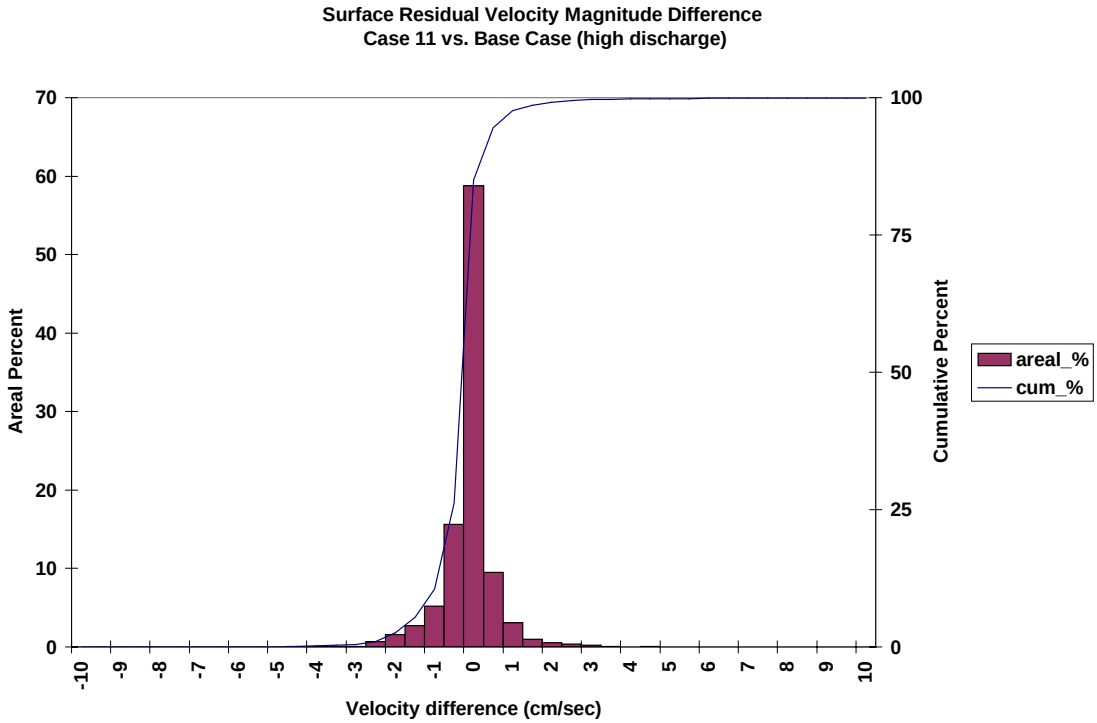

Figure 78. Frequency distribution of surface residual velocity magnitude average difference for the Eastward and Westward Expansion (Option 7/5a, 55–foot channel) versus the Base Case during the high discharge event of historical simulation.

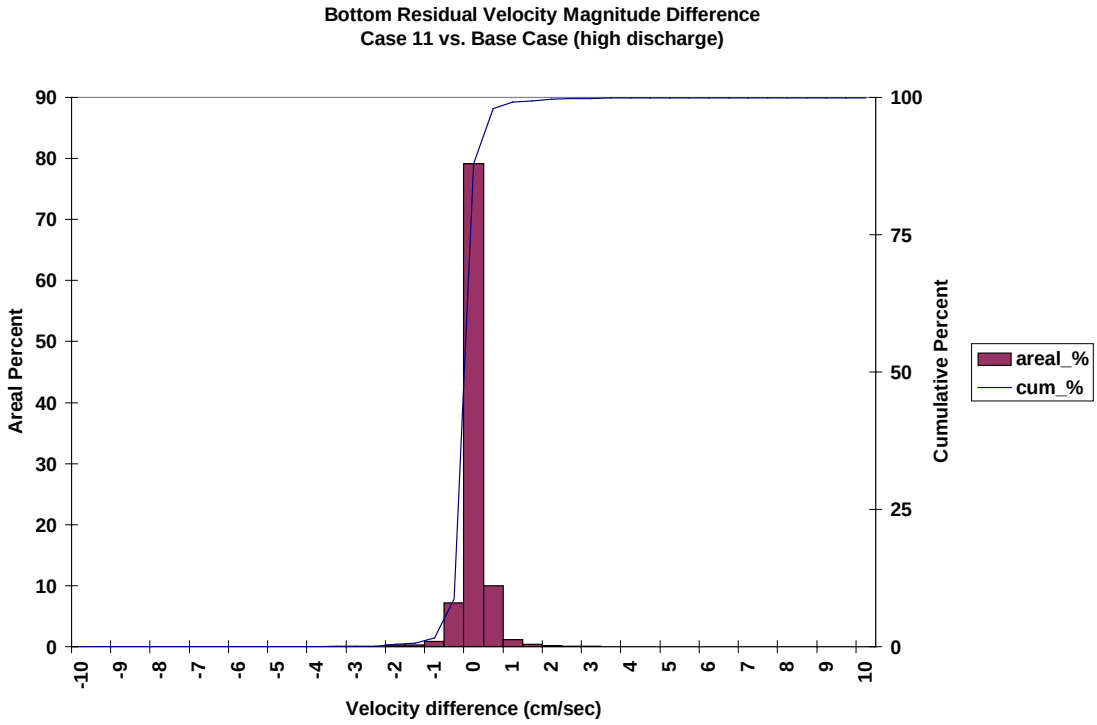

Figure 79. Frequency distribution of bottom residual velocity magnitude average difference for the Eastward and Westward Expansion (Option 7/5a, 55–foot channel) versus the Base Case during the high discharge event of historical simulation.

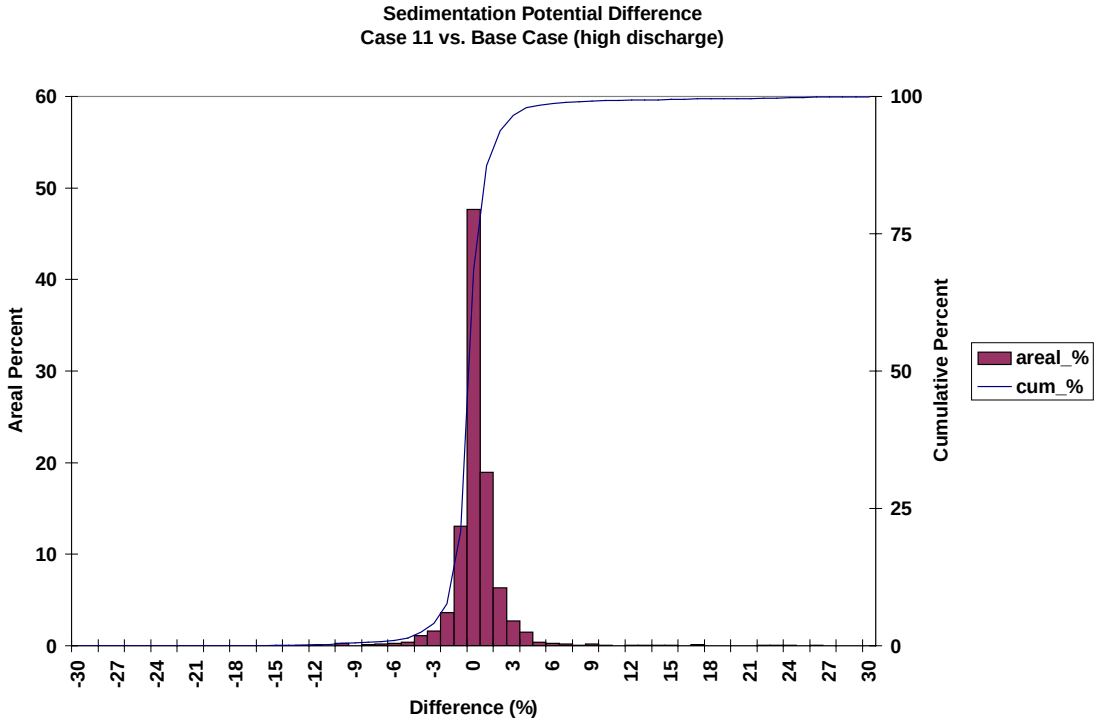

Figure 80. Frequency distribution of sedimentation potential difference for the Eastward and Westward Expansion (Option 7/5a, 55–foot channel) versus the Base Case during the high discharge event of historical simulation.

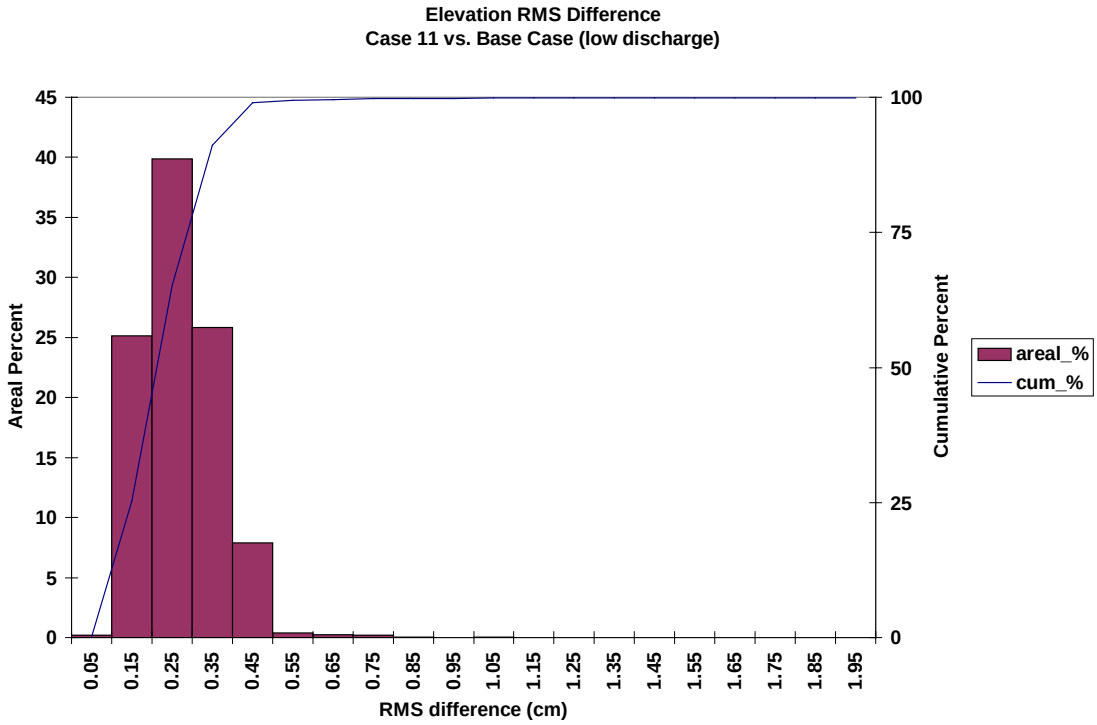

Figure 81. Frequency distribution of elevation RMS difference for the Eastward and Westward Expansion (Option 7/5a, 55–foot channel) versus the Base Case during the low discharge event of historical simulation.

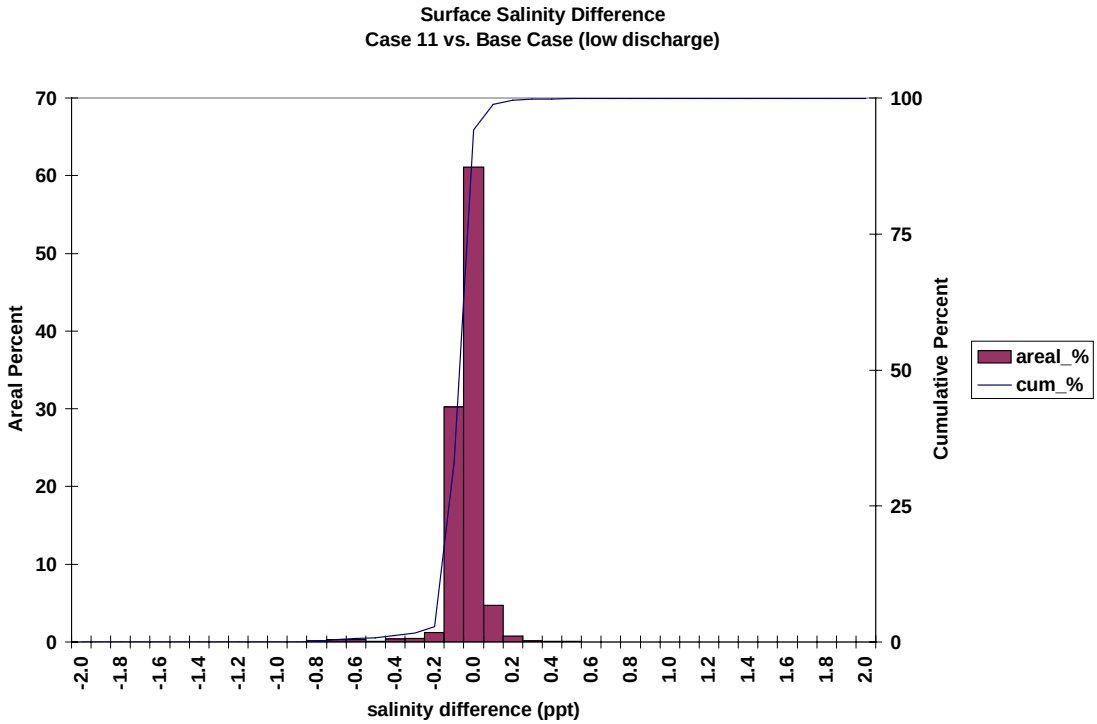

Figure 82. Frequency distribution of surface salinity average difference for the Eastward and Westward Expansion (Option 7/5a, 55–foot channel) versus the Base Case during the low discharge event of historical simulation.

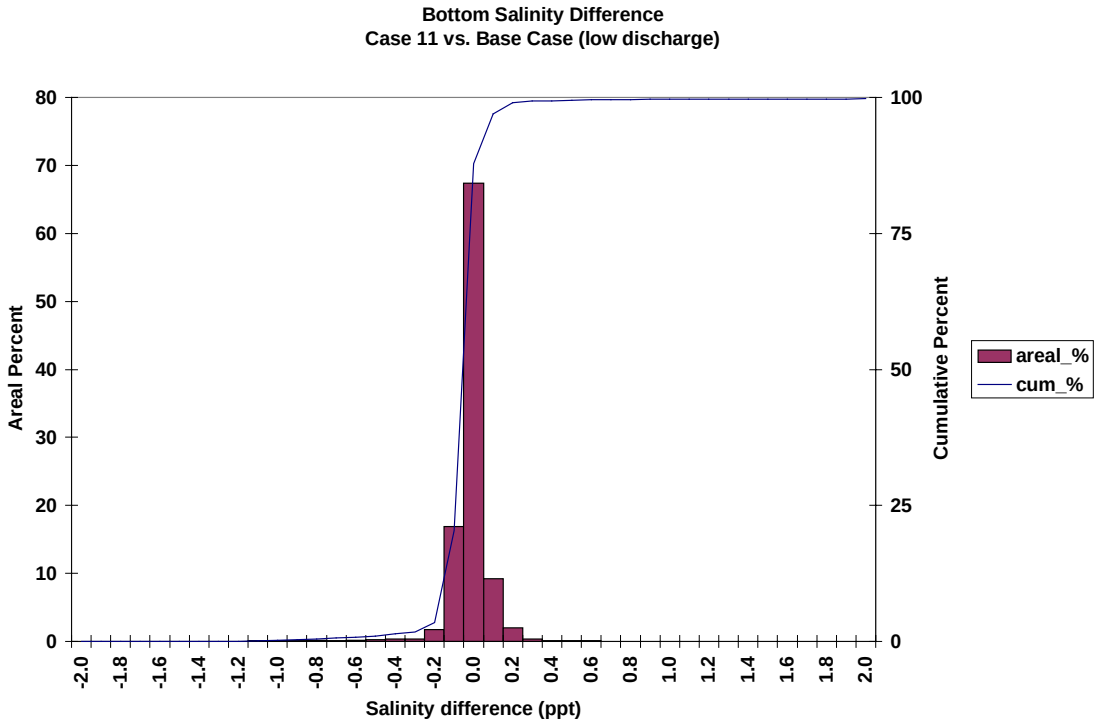

Figure 83. Frequency distribution of bottom salinity average difference for the Eastward and Westward Expansion (Option 7/5a, 55–foot channel) versus the Base Case during the low discharge event of historical simulation.

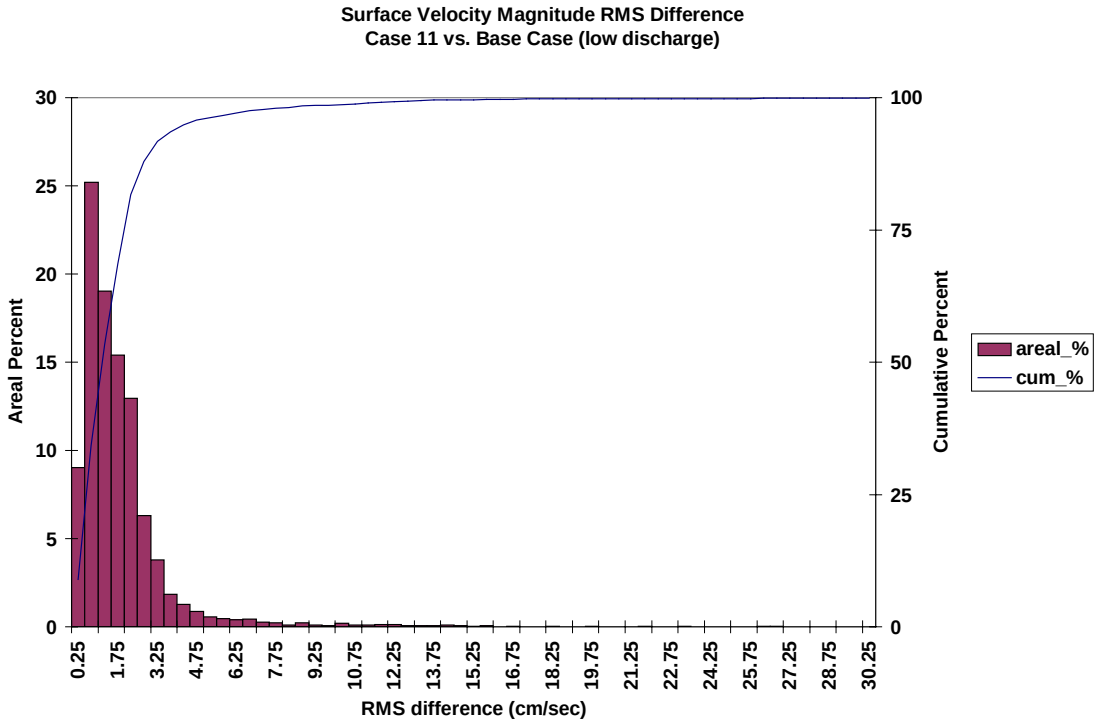

Figure 84. Frequency distribution of surface velocity RMS difference for the Eastward and Westward Expansion (Option 7/5a, 55–foot channel) versus the Base Case during the low discharge event of historical simulation.

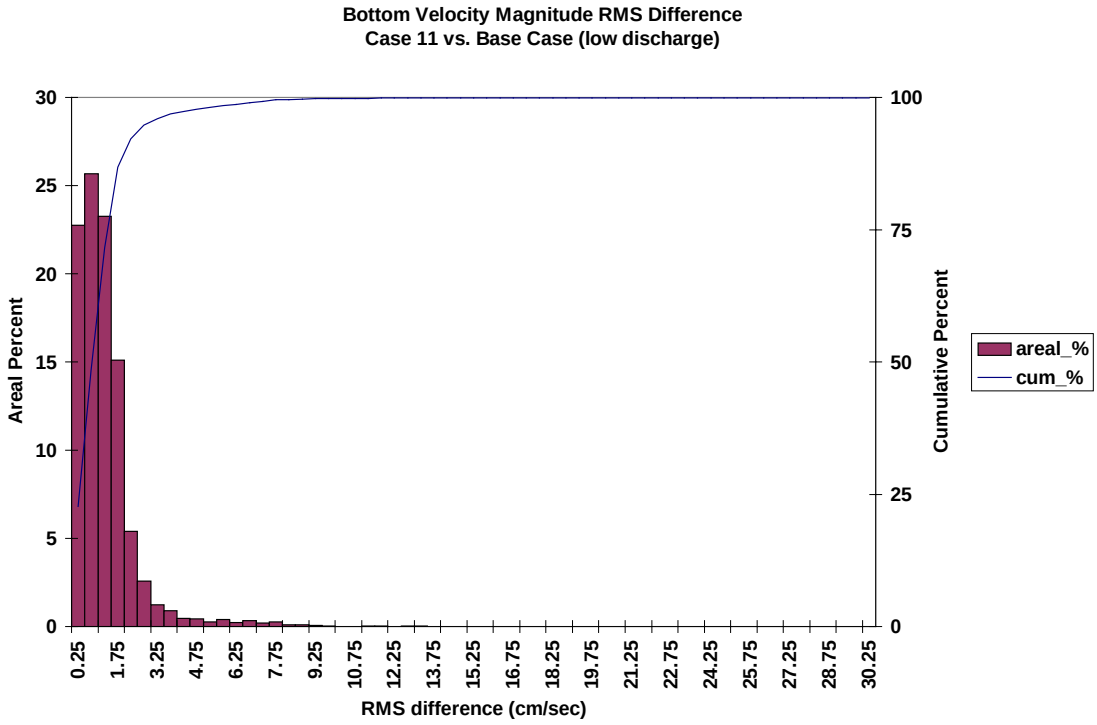

Figure 85. Frequency distribution of bottom velocity RMS difference for the Eastward and Westward Expansion (Option 7/5a, 55–foot channel) versus the Base Case during the low discharge event of historical simulation.

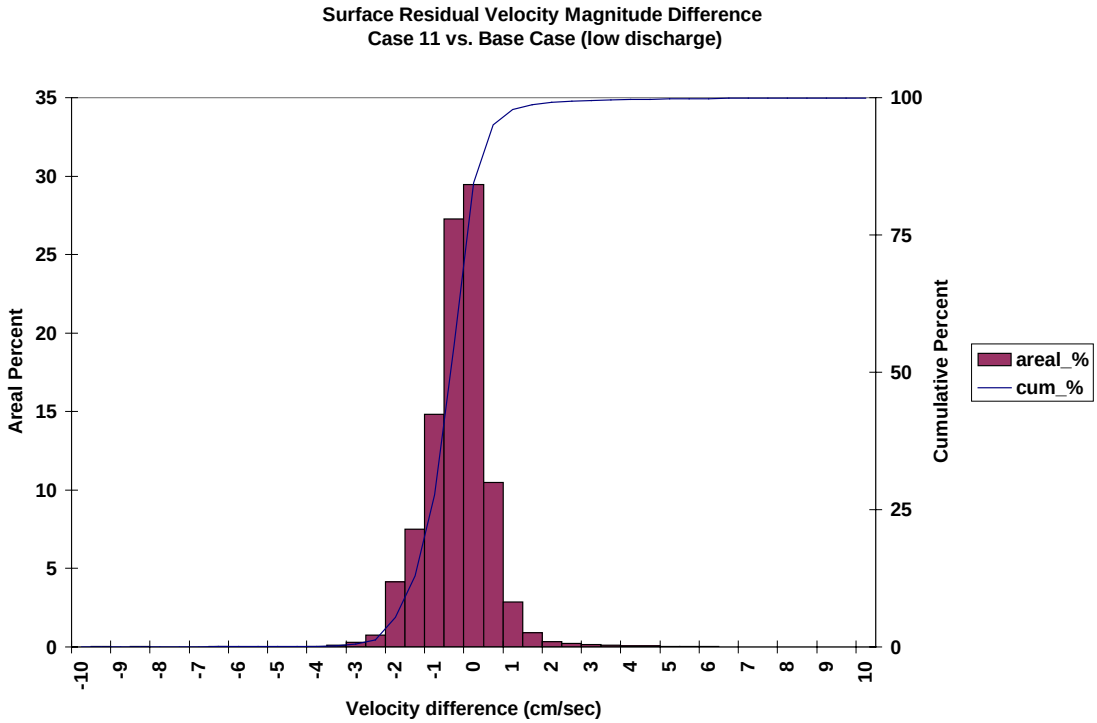

Figure 86. Frequency distribution of surface residual velocity magnitude average difference for the Eastward and Westward Expansion (Option 7/5a, 55–foot channel) versus the Base Case during the low discharge event of historical simulation.

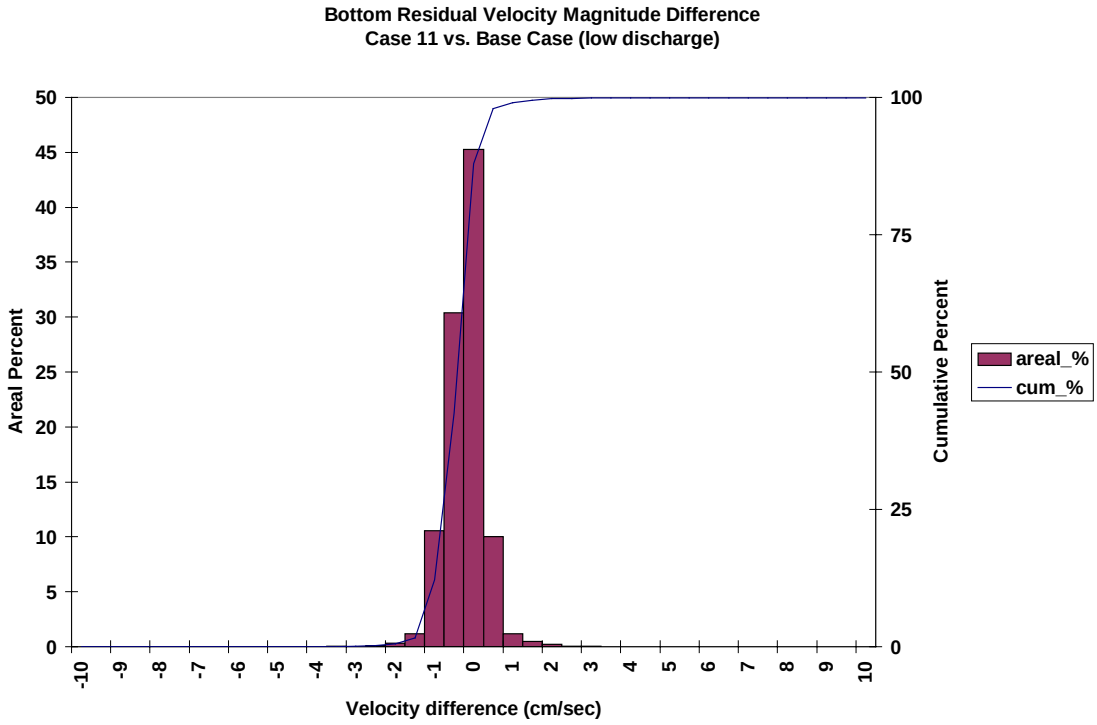

Figure 87. Frequency distribution of bottom residual velocity magnitude average difference for the Eastward and Westward Expansion (Option 7/5a, 55–foot channel) versus the Base Case during the low discharge event of historical simulation.

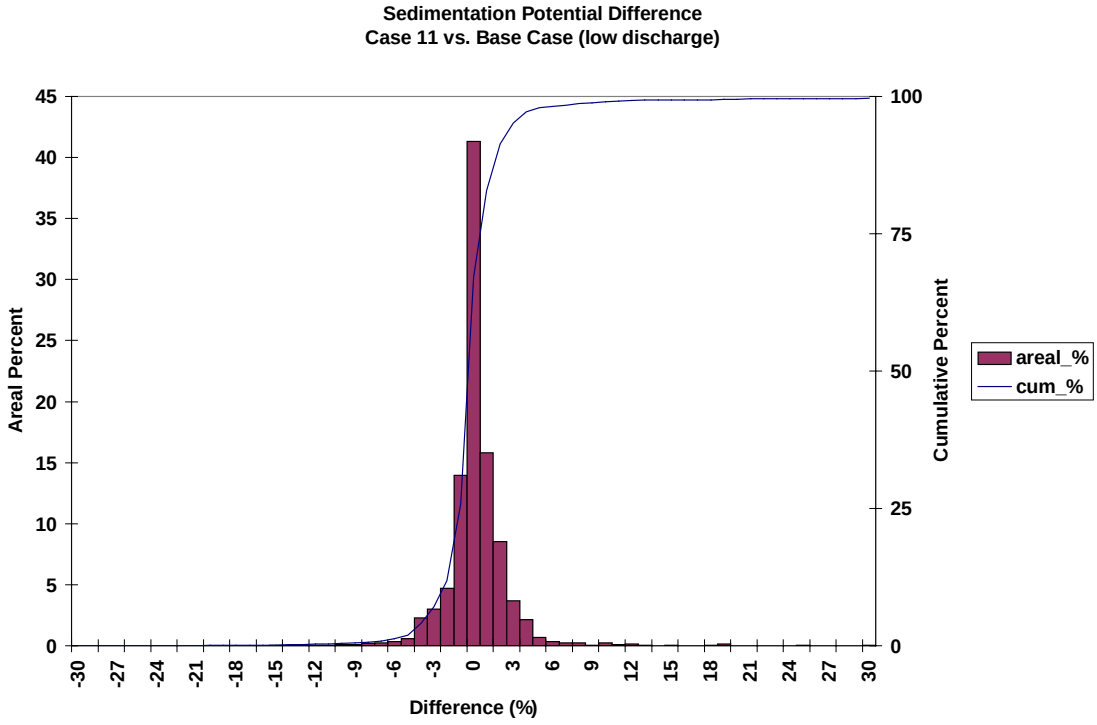

Figure 88. Frequency distribution of sedimentation potential difference for the Eastward and Westward Expansion (Option 7/5a, 55–foot channel) versus the Base Case during the low discharge event of historical simulation.

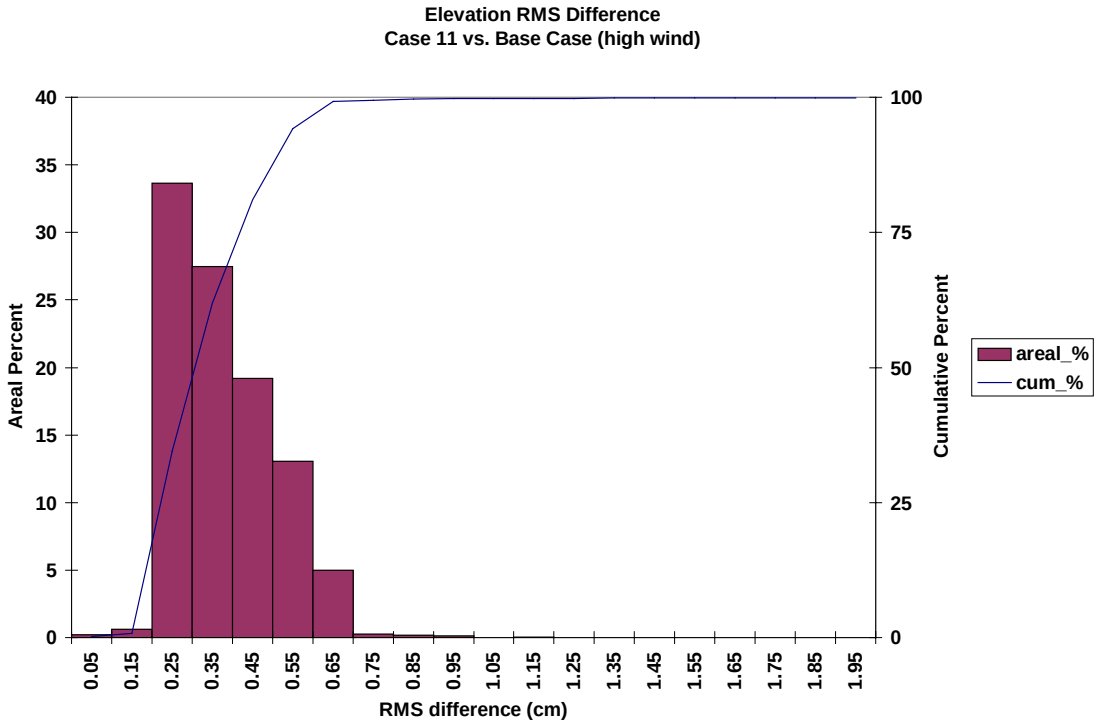

Figure 89. Frequency distribution of elevation RMS difference for the Eastward and Westward Expansion (Option 7/5a, 55–foot channel) versus the Base Case during the high wind event of historical simulation.

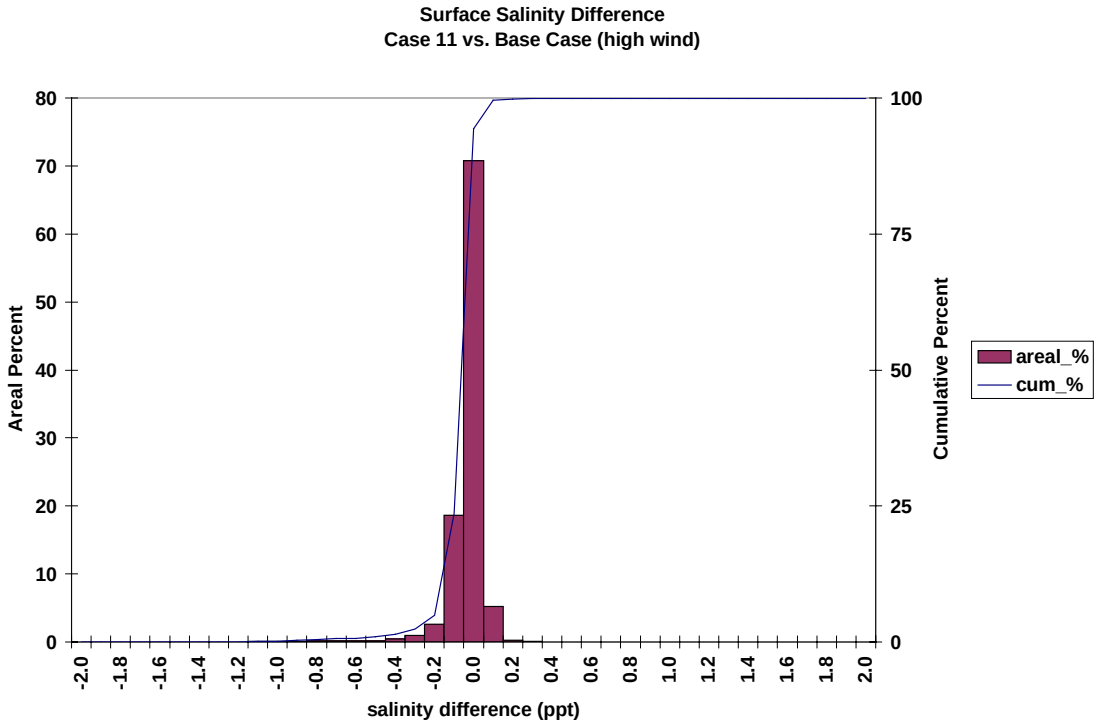

Figure 90. Frequency distribution of surface salinity average difference for the Eastward and Westward Expansion (Option 7/5a, 55–foot channel) versus the Base Case during the high wind event of historical simulation.

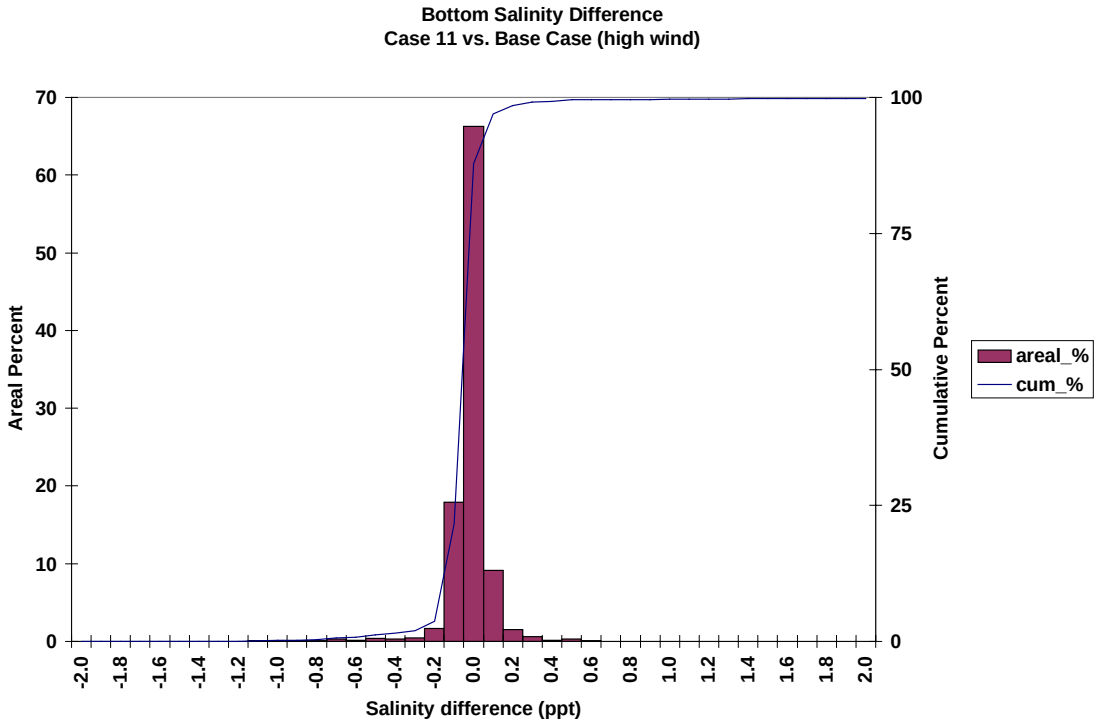

Figure 91. Frequency distribution of bottom salinity average difference for the Eastward and Westward Expansion (Option 7/5a, 55–foot channel) versus the Base Case during the high wind event of historical simulation.

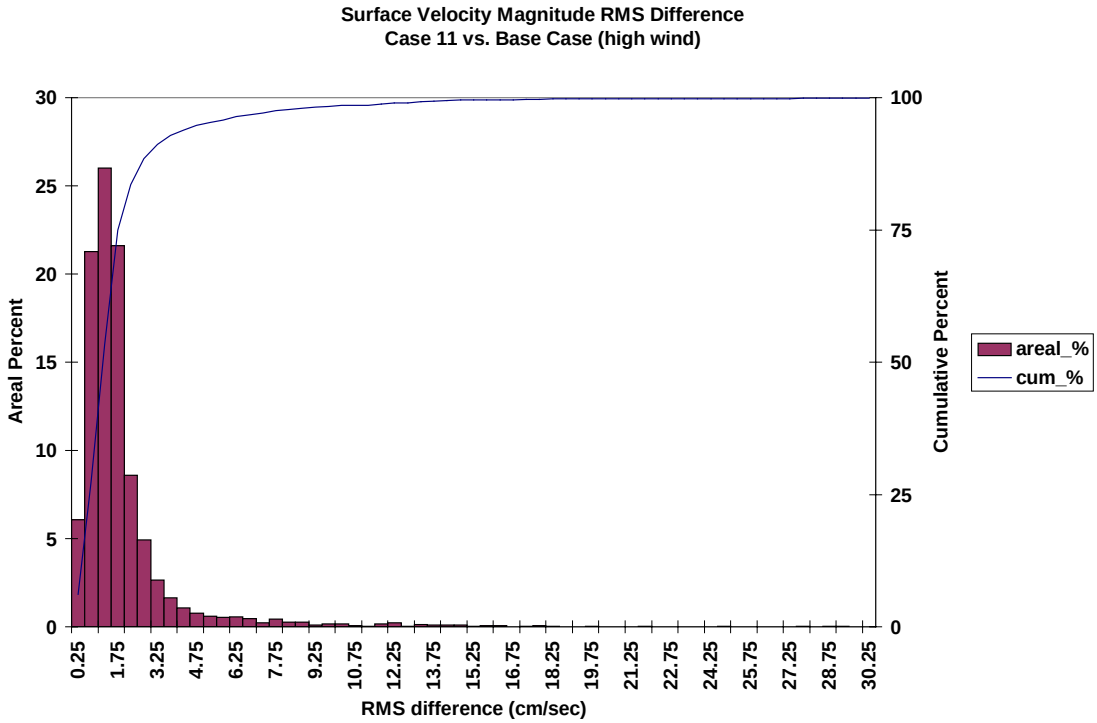

Figure 92. Frequency distribution of surface velocity RMS difference for the Eastward and Westward Expansion (Option 7/5a, 55–foot channel) versus the Base Case during the high wind event of historical simulation.

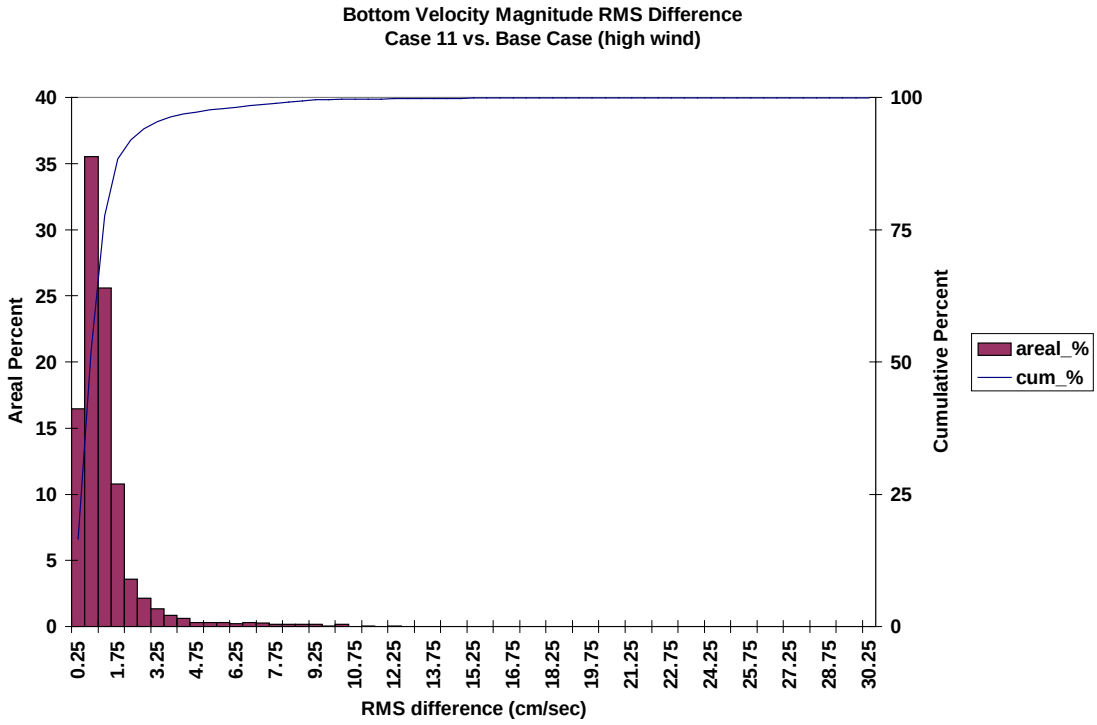

Figure 93. Frequency distribution of bottom velocity RMS difference for the Eastward and Westward Expansion (Option 7/5a, 55–foot channel) versus the Base Case during the high wind event of historical simulation.

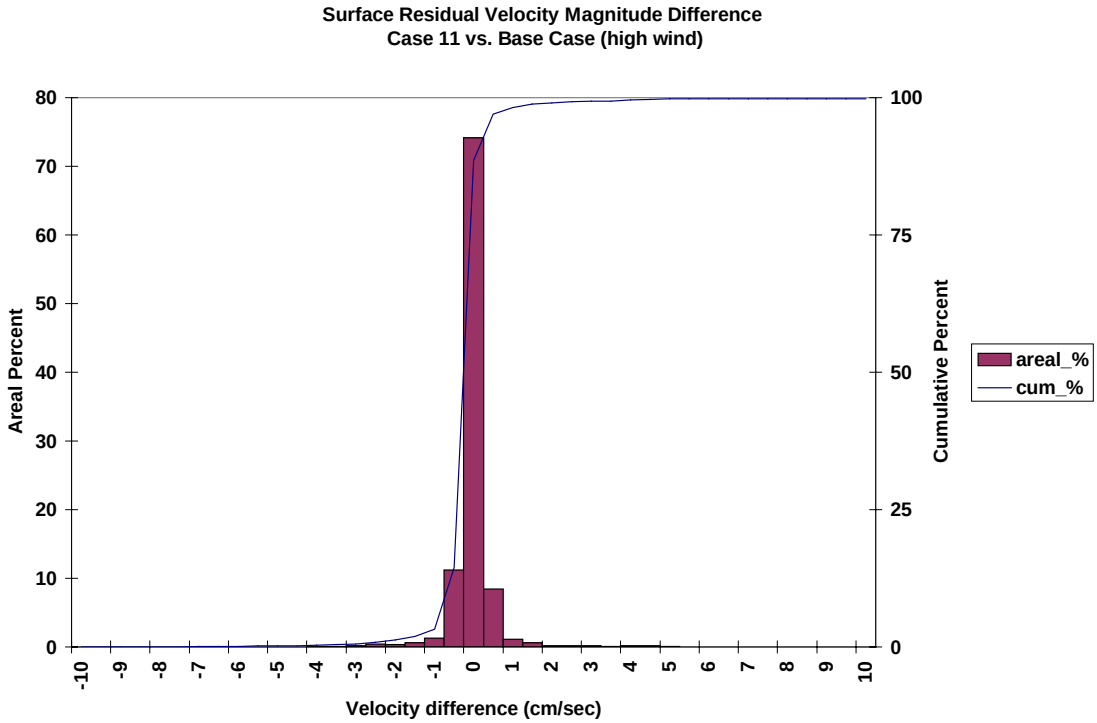

Figure 94. Frequency distribution of surface residual velocity magnitude difference for the Eastward and Westward Expansion (Option 7/5a, 55–foot channel) versus the Base Case during the high wind event of historical simulation.

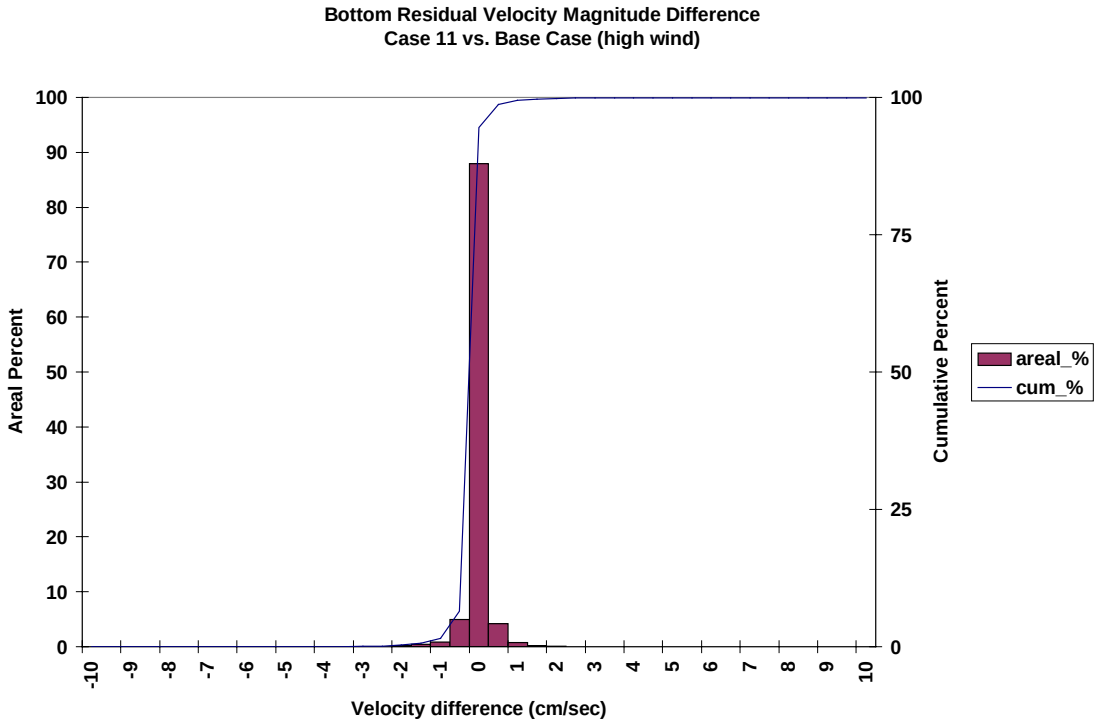

Figure 95. Frequency distribution of bottom residual velocity magnitude difference for the Eastward and Westward Expansion (Option 7/5a, 55–foot channel) versus the Base Case during the high wind event of historical simulation.

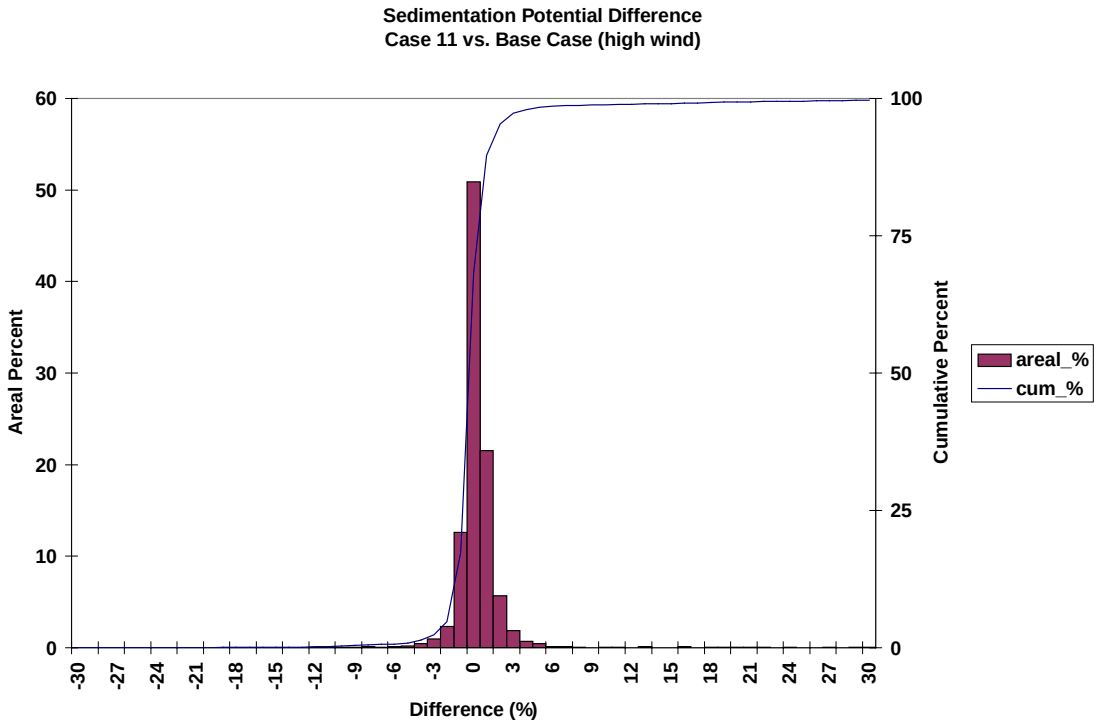

Figure 96. Frequency distribution of sedimentation potential difference for the Eastward and Westward Expansion (Option 7/5a, 55–foot channel) versus the Base Case during the high wind event of historical simulation.

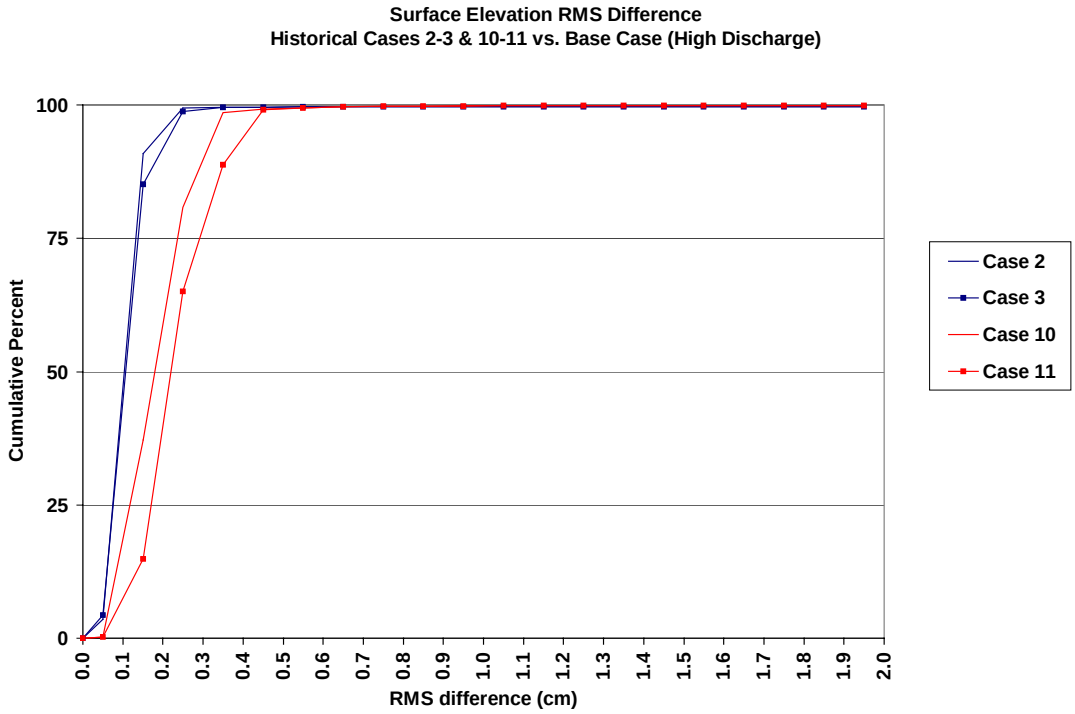

Figure 97. Cumulative percent curves of frequency distributions for surface elevation RMS differences for all Expansion Options versus the Base Case during the high discharge event of historical simulation.

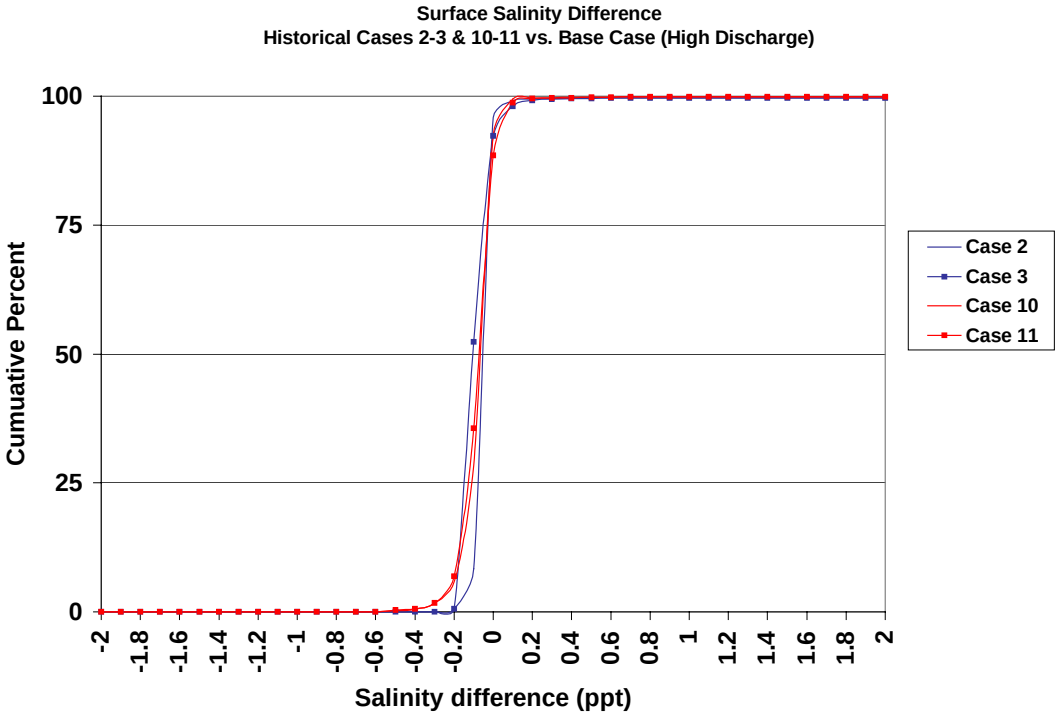

Figure 98. Cumulative percent curves of frequency distributions for surface salinity average differences for all Expansion Options versus the Base Case during the high discharge event of historical simulation.

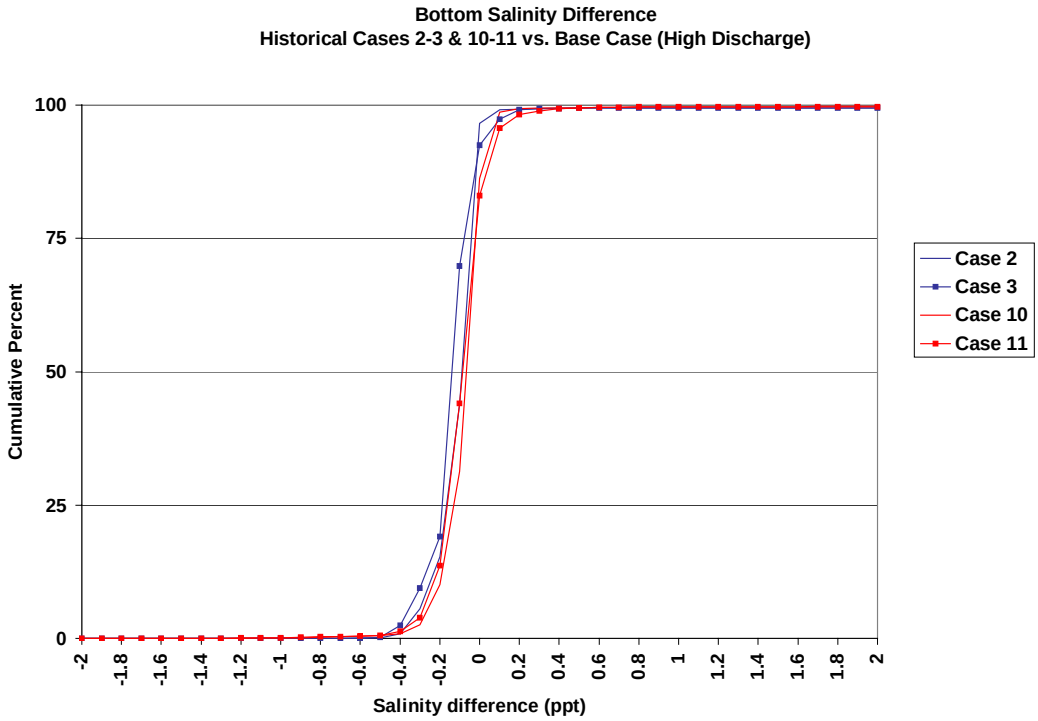

Figure 99. Cumulative percent curves of frequency distributions for bottom salinity average differences for all Expansion Options versus the Base Case during the high discharge event of historical simulation.

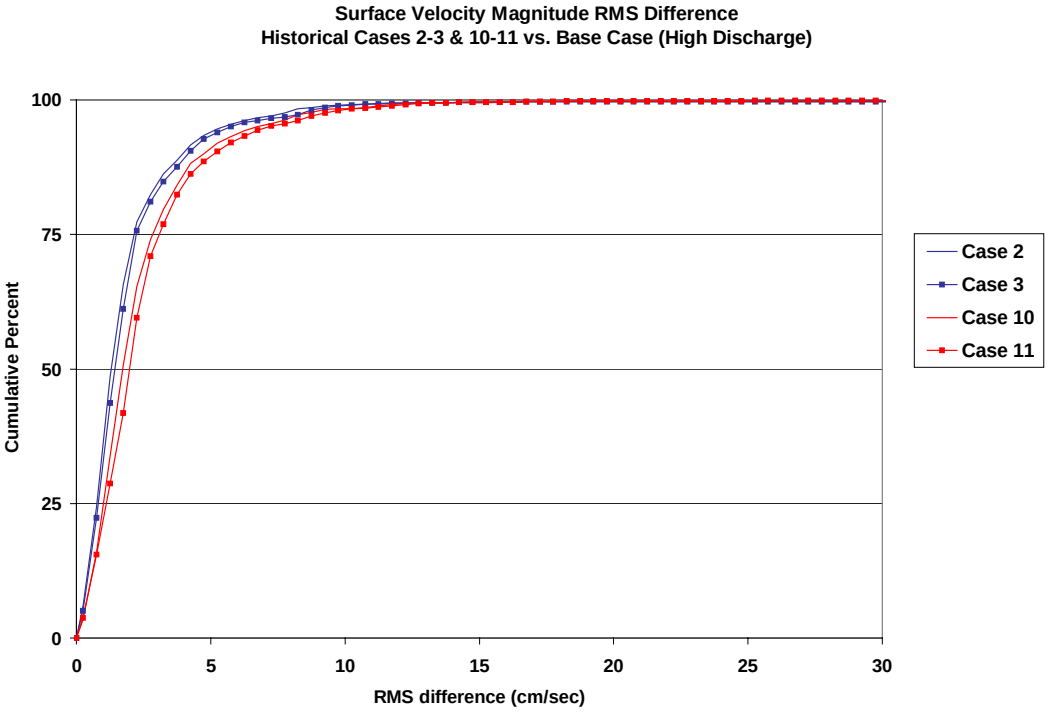

Figure 100. Cumulative percent curves of frequency distributions for surface velocity RMS differences for all Expansion Options versus the Base Case during the high discharge event of historical simulation.

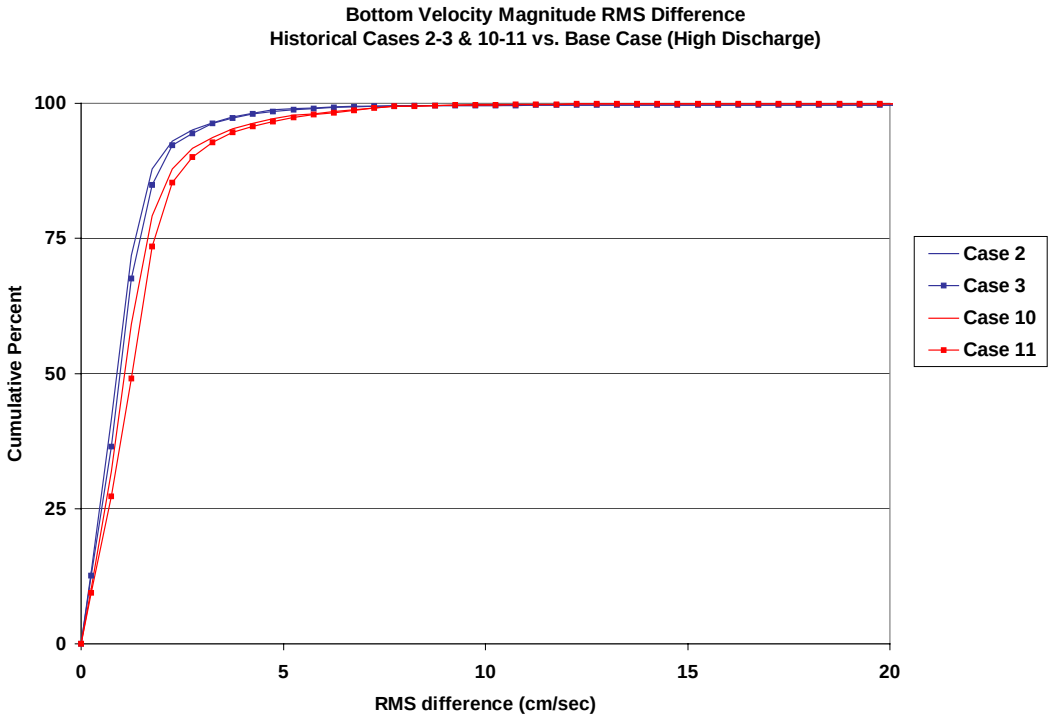

Figure 101. Cumulative percent curves of frequency distributions for bottom velocity RMS differences for all Expansion Options versus the Base Case during the high discharge event of historical simulation.

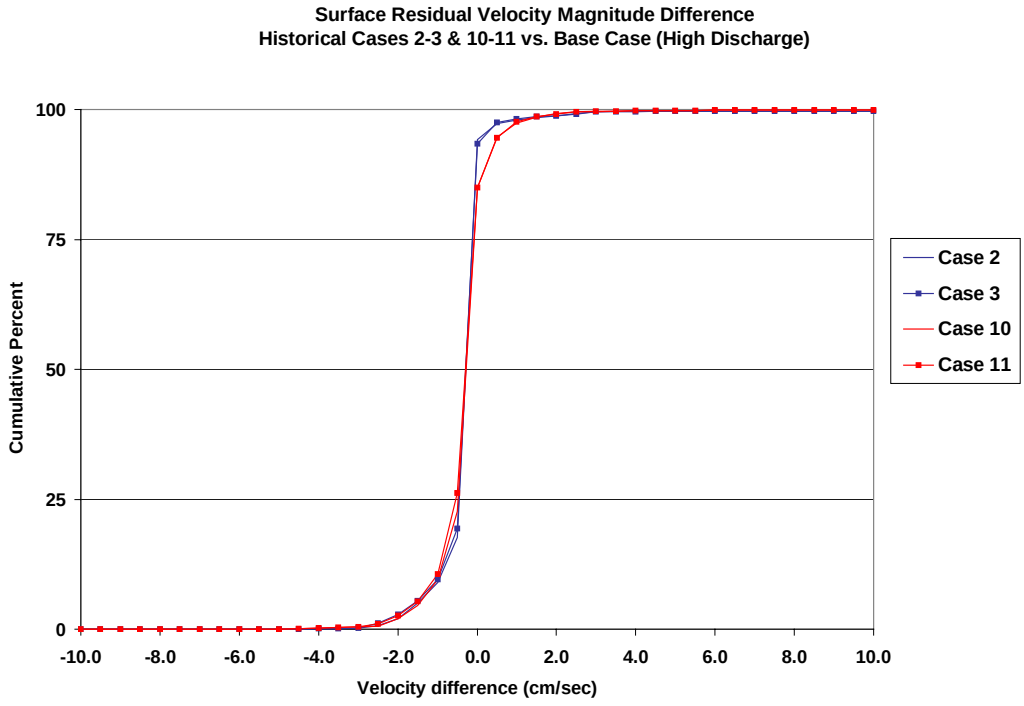

Figure 102. Cumulative percent curves of frequency distributions for surface residual velocity magnitude average differences for all Expansion Options versus the Base Case during the high discharge event of historical simulation.

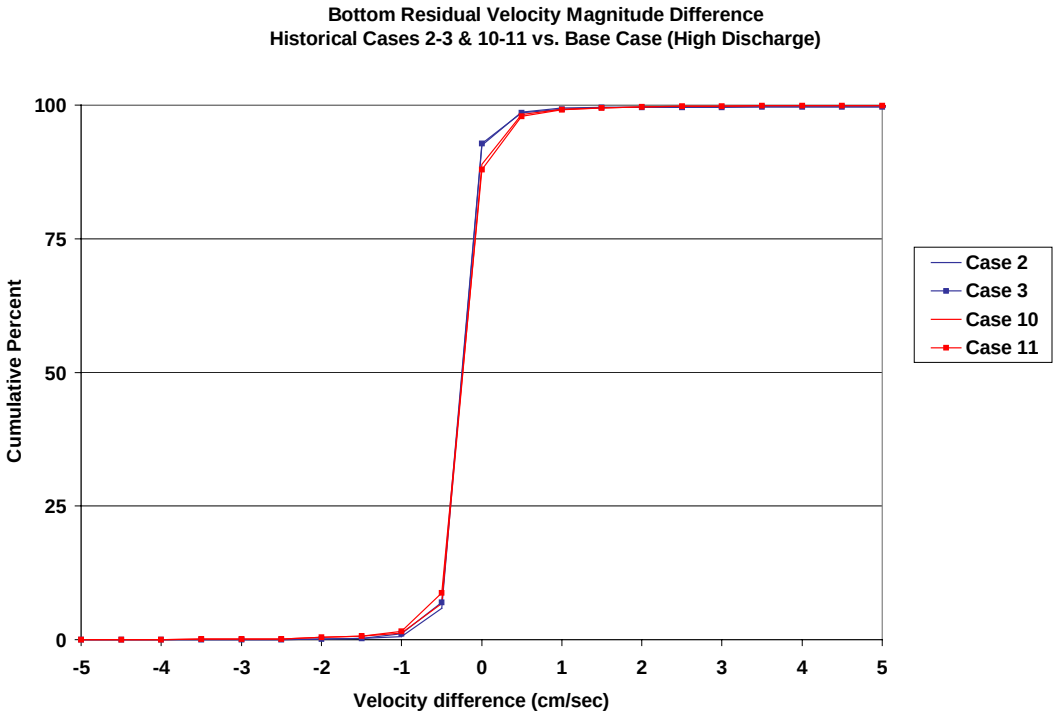

Figure 103. Cumulative percent curves of frequency distributions for bottom residual velocity magnitude average differences for all Expansion Options versus the Base Case during the high discharge event of historical simulation.

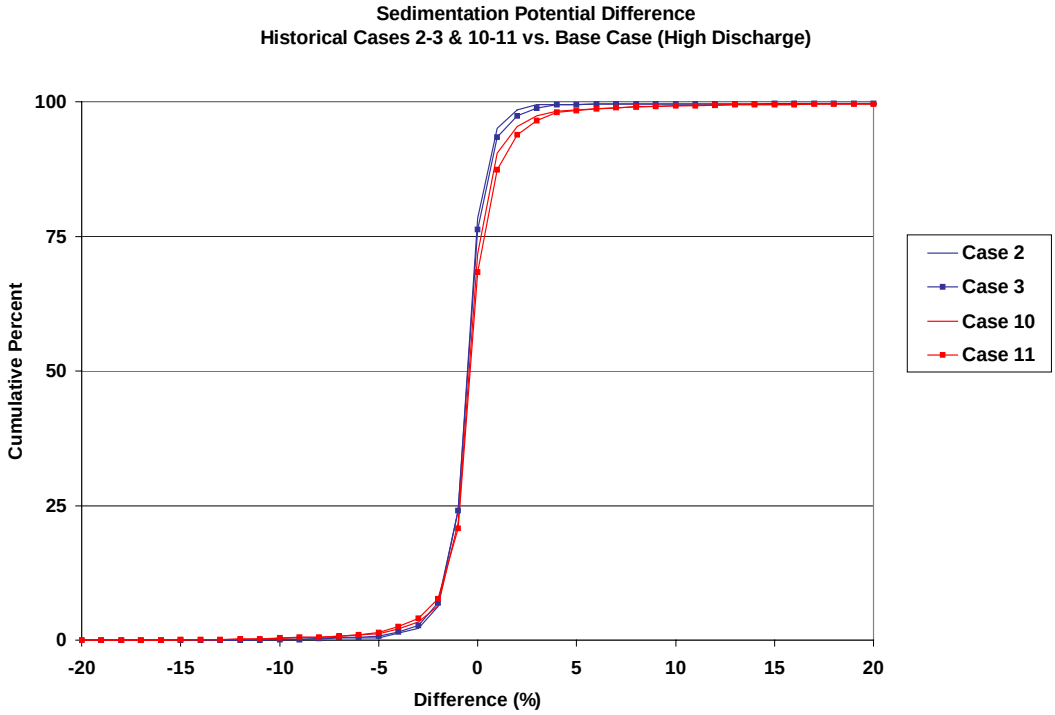

Figure 104. Cumulative percent curves of frequency distributions for sedimentation potential differences for all Expansion Options versus the Base Case during the high discharge event of historical simulation.

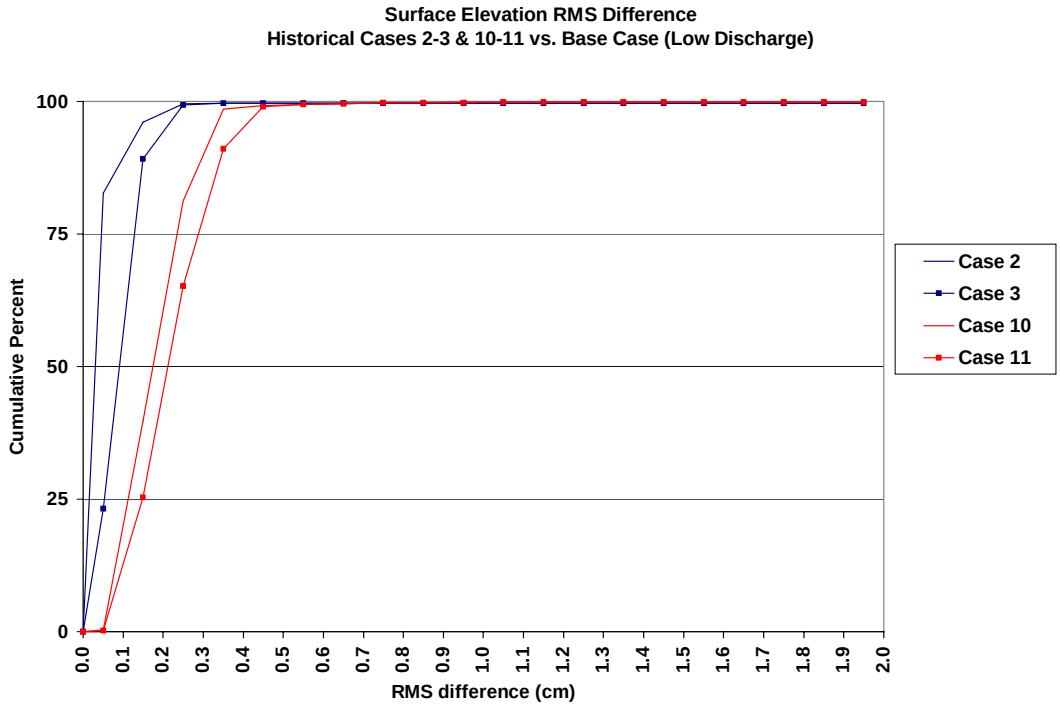

Figure 105. Cumulative percent curves of frequency distributions for surface elevation RMS differences for all Expansion Options versus the Base Case during the low discharge event of historical simulation.

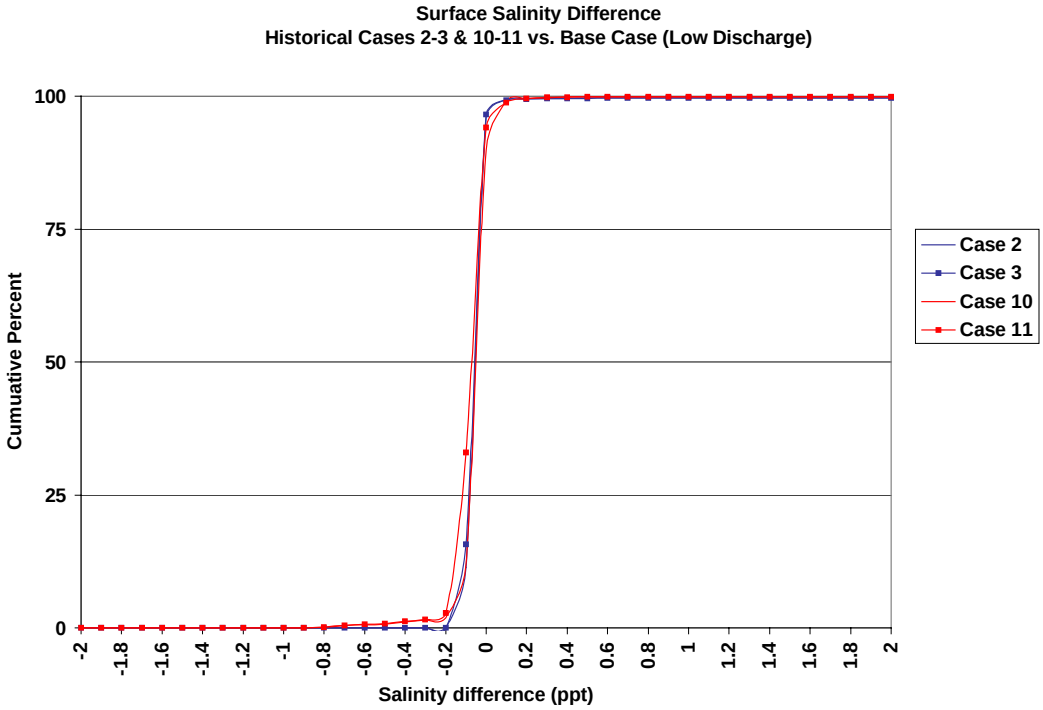

Figure 106. Cumulative percent curves of frequency distributions for surface salinity average differences for all Expansion Options versus the Base Case during the low discharge event of historical simulation.

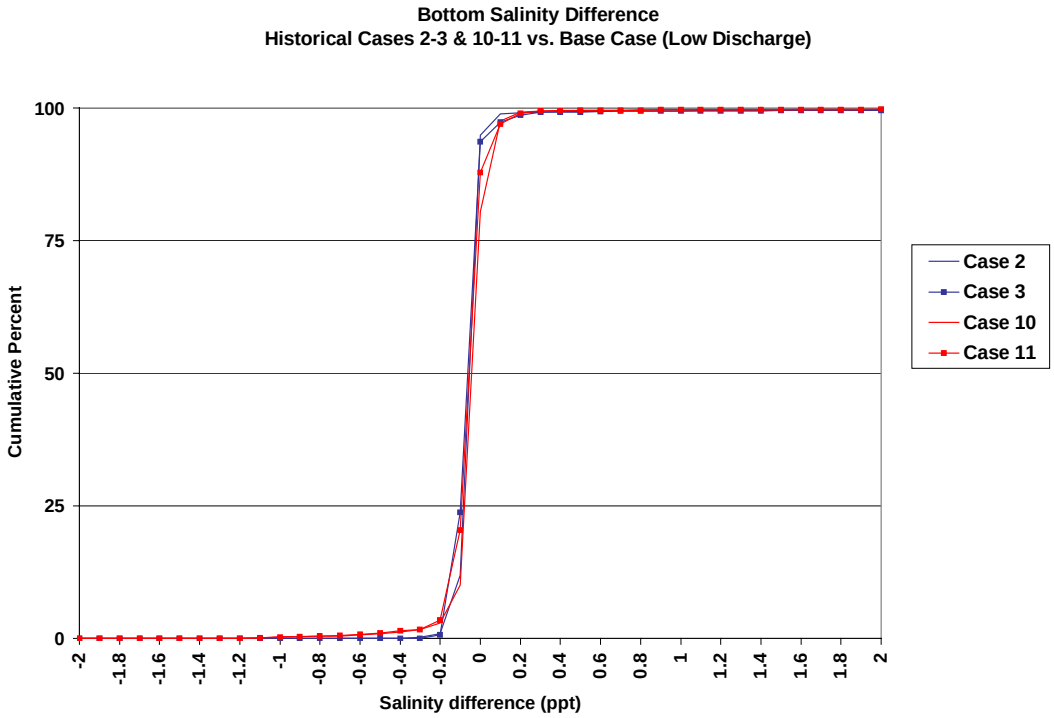

Figure 107. Cumulative percent curves of frequency distributions for bottom salinity average differences for all Expansion Options versus the Base Case during the low discharge event of historical simulation.

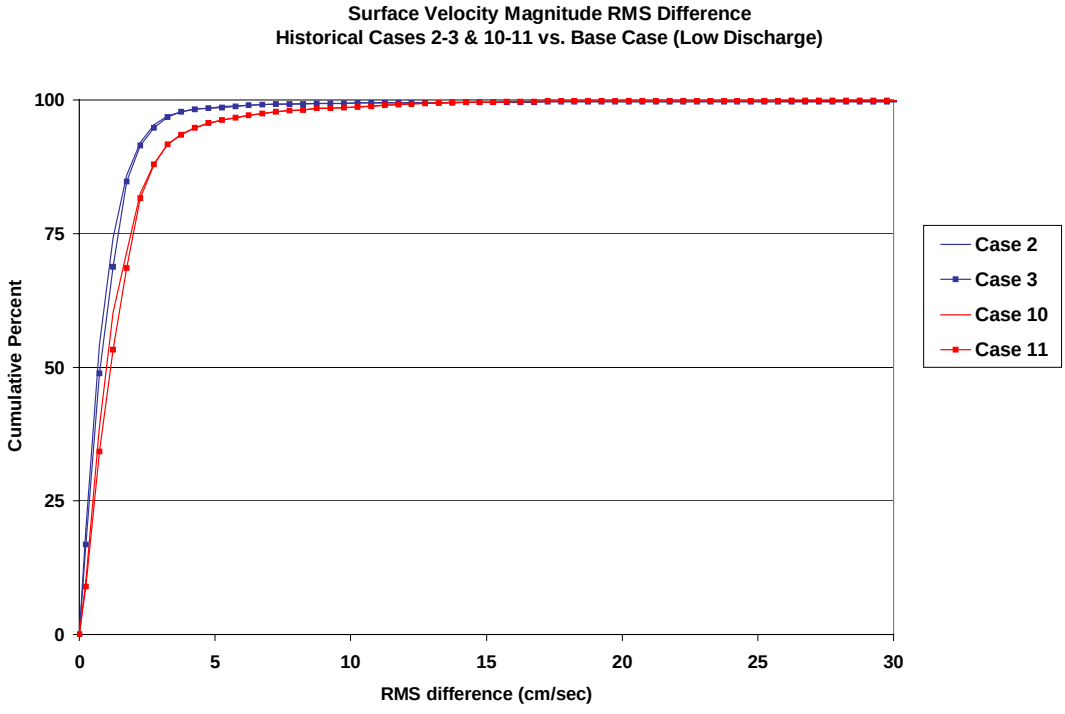

Figure 108. Cumulative percent curves of frequency distributions for surface velocity RMS differences for all Expansion Options versus the Base Case during the low discharge event of historical simulation.

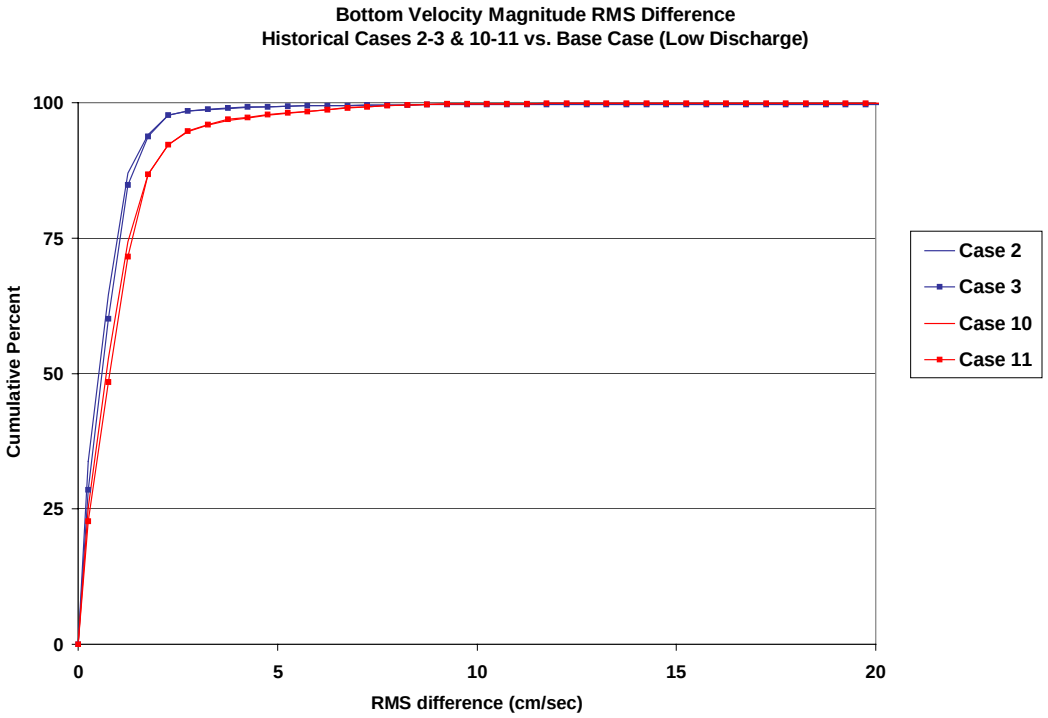

Figure 109. Cumulative percent curves of frequency distributions for bottom velocity RMS differences for all Expansion Options versus the Base Case during the low discharge event of historical simulation.

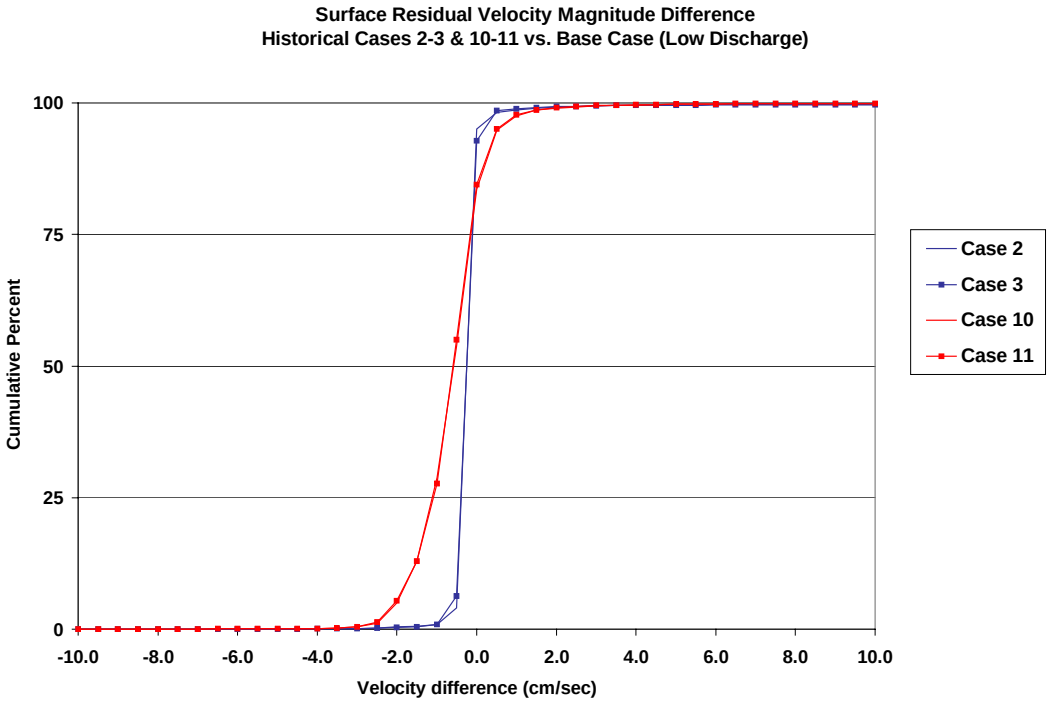

Figure 110. Cumulative percent curves of frequency distributions for surface residual velocity magnitude average differences for all Expansion Options versus the Base Case during the low discharge event of historical simulation.

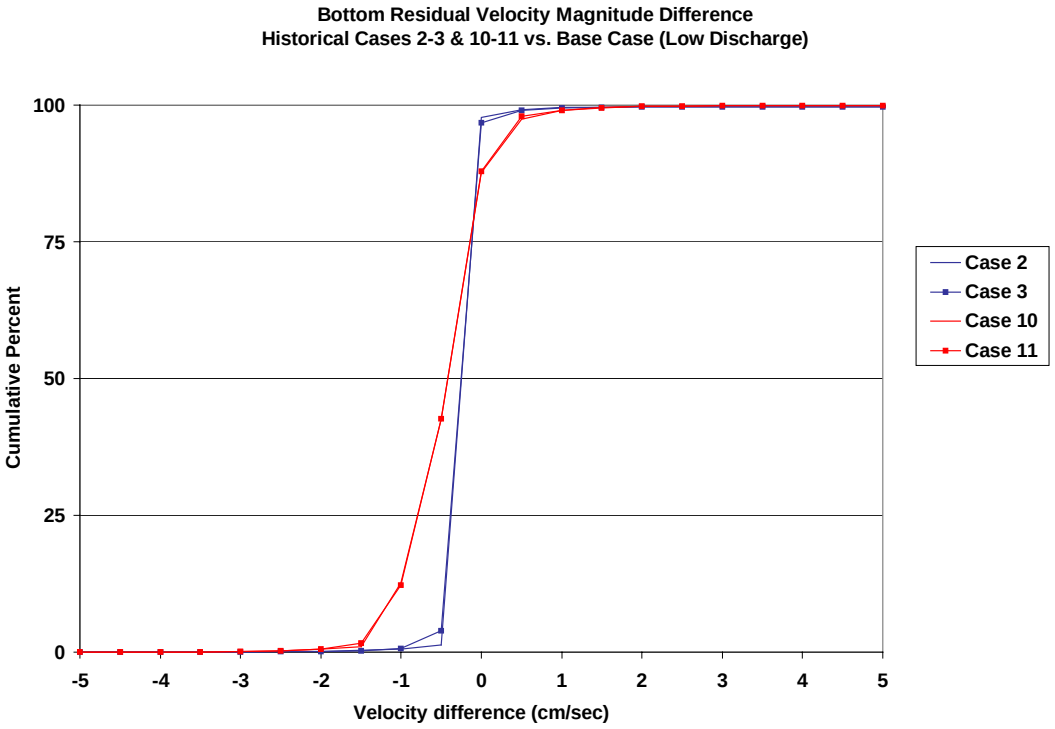

Figure 111. Cumulative percent curves of frequency distributions for bottom residual velocity magnitude average differences for all Expansion Options versus the Base Case during the low discharge event of historical simulation.

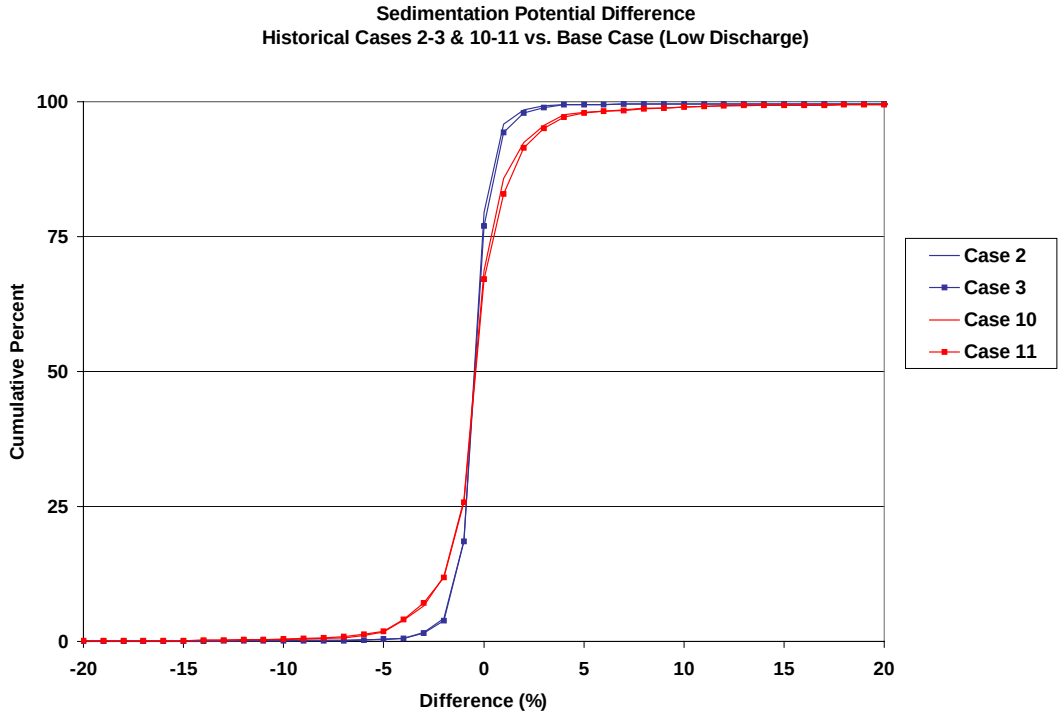

Figure 112. Cumulative percent curves of frequency distributions for sedimentation potential differences for all Expansion Options versus the Base Case during the low discharge event of historical simulation.

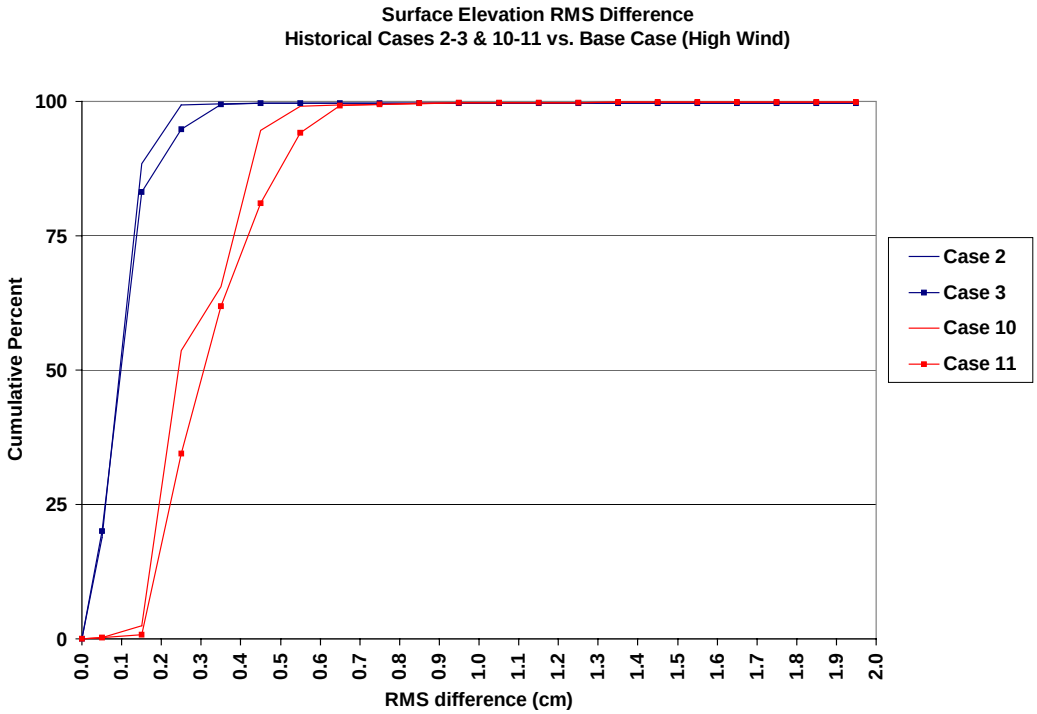

Figure 113. Cumulative percent curves of frequency distributions for surface elevation RMS differences for all Expansion Options versus the Base Case during the high wind event of historical simulation.

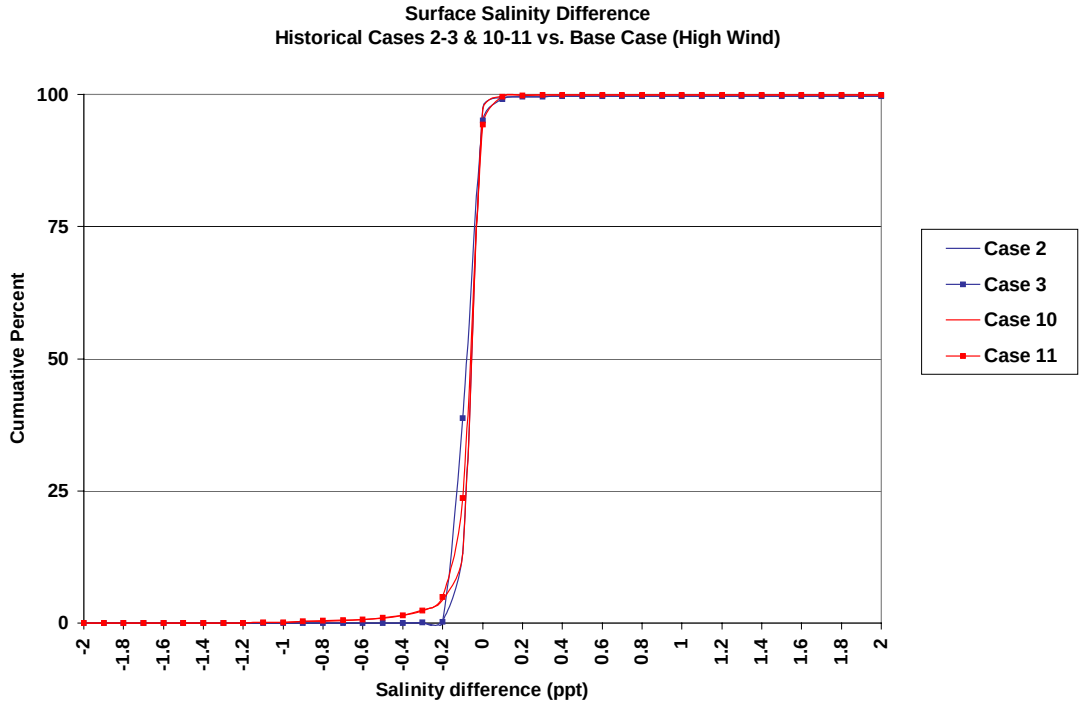

Figure 114. Cumulative percent curves of frequency distributions for surface salinity average differences for all Expansion Options versus the Base Case during the high wind event of historical simulation.

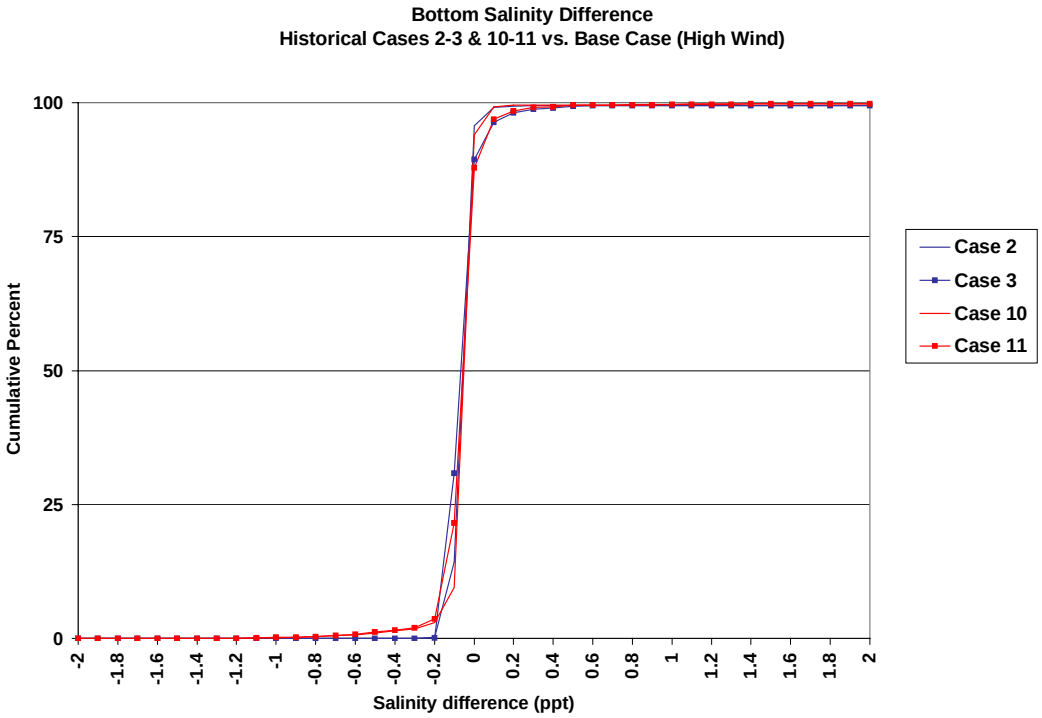

Figure 115. Cumulative percent curves of frequency distributions for bottom salinity average differences for all Expansion Options versus the Base Case during the high wind event of historical simulation.

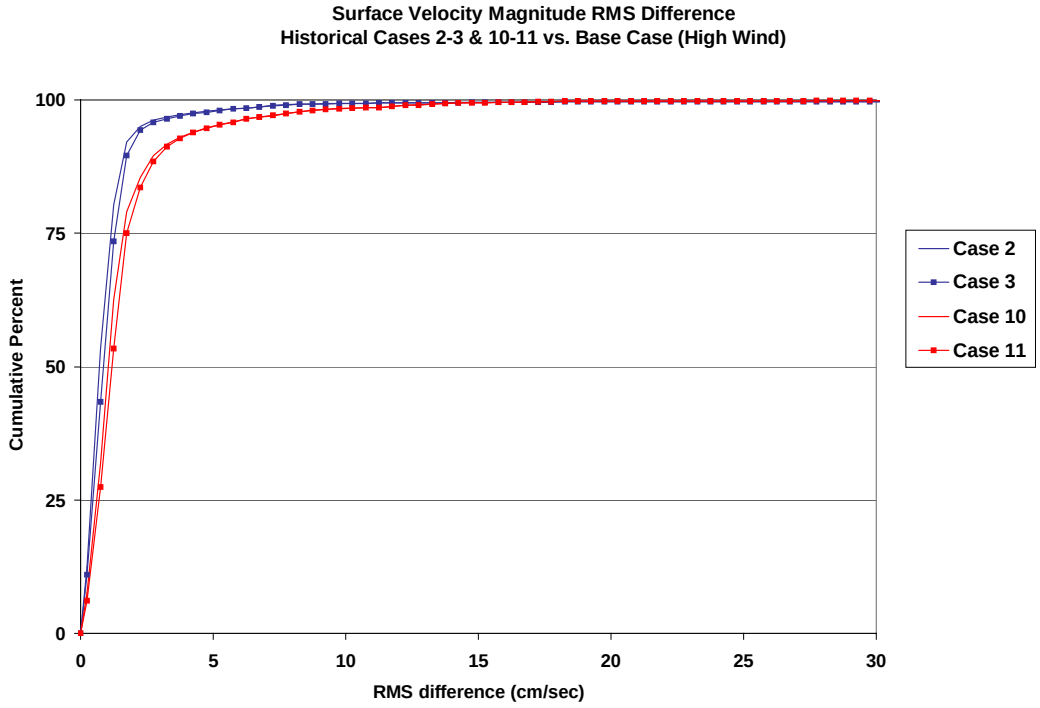

Figure 116. Cumulative percent curves of frequency distributions for surface velocity RMS differences for all Expansion Options versus the Base Case during the high wind event of historical simulation.

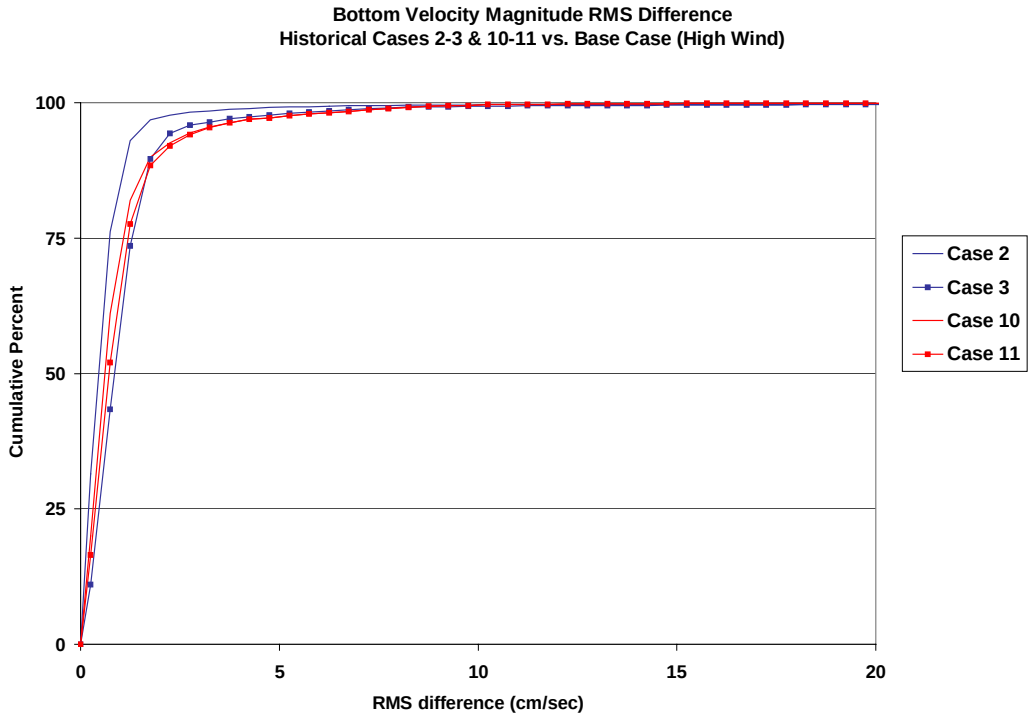

Figure 117. Cumulative percent curves of frequency distributions for bottom velocity RMS differences for all Expansion Options versus the Base Case during the high wind event of historical simulation.

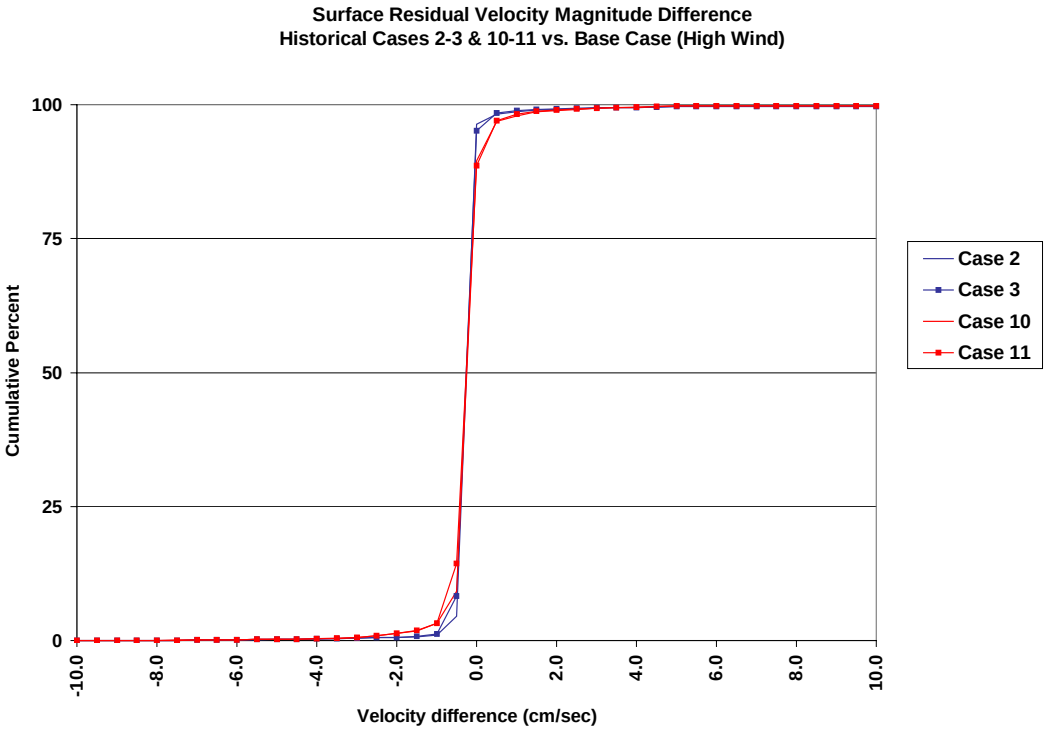

Figure 118. Cumulative percent curves of frequency distributions for surface residual velocity magnitude average differences for all Expansion Options versus the Base Case during the high wind event of historical simulation.

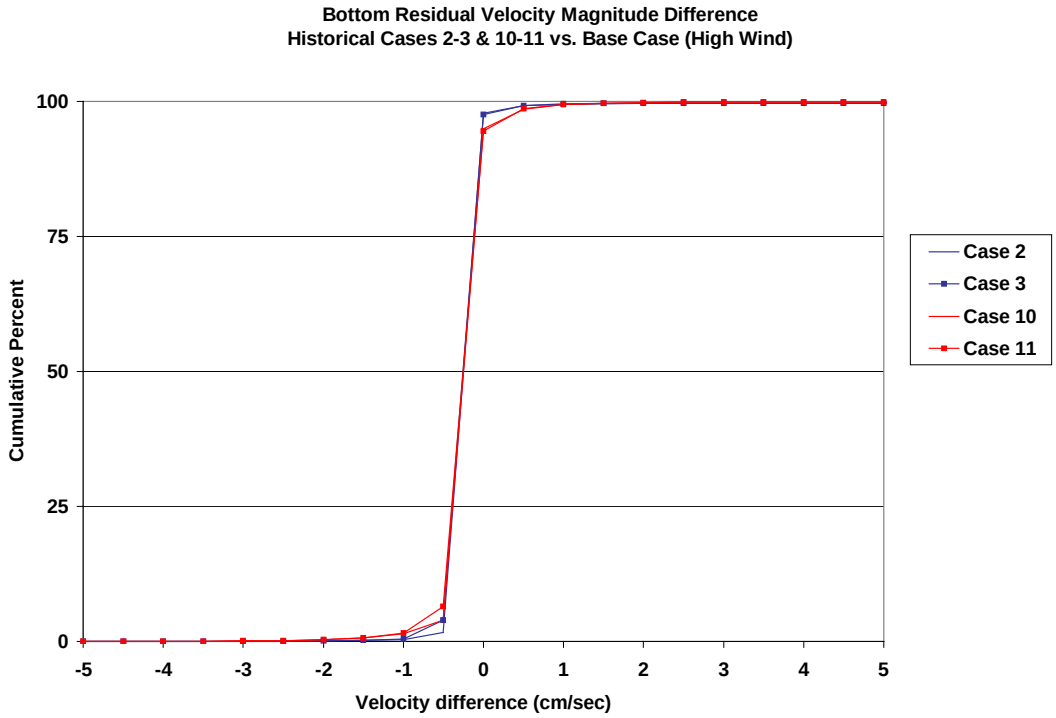

Figure 119. Cumulative percent curves of frequency distributions for bottom residual velocity magnitude average differences for all Expansion Options versus the Base Case during the high wind event of historical simulation.

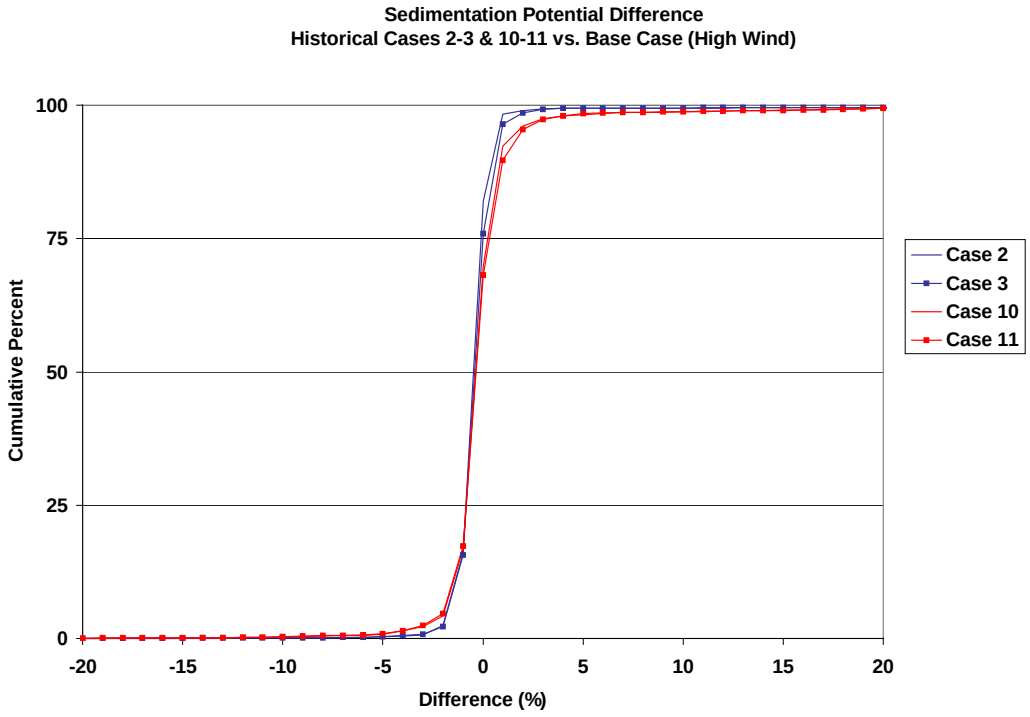

Figure 120. Cumulative percent curves of frequency distributions for sedimentation potential differences for all Expansion Options versus the Base Case during the high wind event of historical simulation.